2008 Beam Instrumentation Workshop

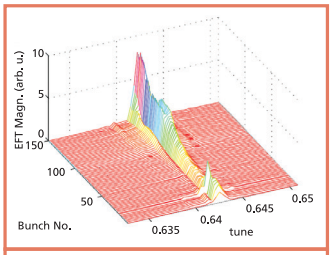

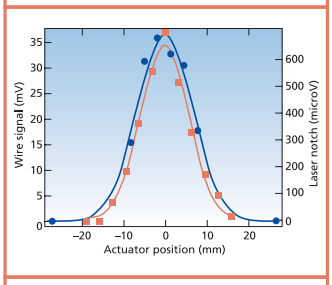

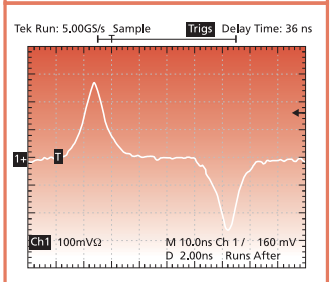

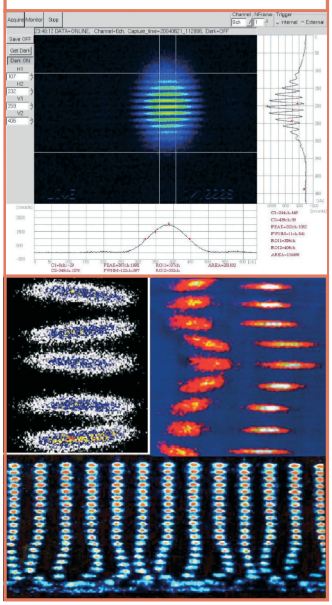

May 4–8, 2008
Granlibakken Conference Center and Lodge
Lake Tahoe, California, USA

www-als.lbl.gov/biw08

The 2008 Beam Instrumentation Workshop (BIW08) program committee is pleased to invite you to beautiful Lake Tahoe, California, for its 13th biannual meeting. Organized by the Lawrence Berkeley National Laboratory, the workshop will be dedicated to exploring the physics and engineering challenges of beam diagnostic and measurement techniques for charged-particle accelerators.

The meeting will feature

- Plenary and poster sessions
- Tutorials
- Vendor exhibits
- Multiple opportunities for informal discussions and collaborations
- Presentation of the 2008 Faraday Cup Award

Abstract submission deadline: February 29, 2008

Program Committee

Fernando Sannibale, Chair (LBNL)
Walter Barry, Co-chair (LBNL)
John D. Gilpatrick (LANL)
Robert Hettel (SLAC)
Ken Jacobs (SRC)
Kevin Jordan (JLAB)
Ralph Pasquinelli (FNAL)
Thomas Russo (BNL)
Hermann Schmickler (CERN)
Thomas Shea (ORNL)
Om Singh (BNL)
Steve Smith (SLAC)
Robert Webber (FNAL)
Jim Zagel (FNAL)

Local Organizing Committee

Joe Chew, Proceedings Editor
Martha Condon, Workshop Administrator
Grace Covarrubias, Workshop Secretary
Joy Kono, Administrative Coordinator
Elizabeth Moxon, Web/Communications
Fernando Sannibale, Chair
Tom Scarvie, Discussion Sessions & Banquet
Greg Vierra, Designer
Jonah Weber, Vendor Contact & Poster Session

Sponsors

Lawrence Berkeley National Laboratory

- Accelerator & Fusion Research Division
- Advanced Light Source Division
- Engineering Division

U.S. Department of Energy

- Office of High Energy Physics

For more information

Grace Covarrubias, Workshop Secretary
MS 80R0114, Berkeley Lab
One Cyclotron Road
Berkeley, CA 94720

Tel: +1 510·486·6466
Fax: +1 510·486·4960
Email: biw08@lbl.gov

BIW08 13th Beam Instrumentation Workshop May 4-8, 2008 BERKELEY LAB

FOREWORD

On behalf of the Beam Instrumentation Workshop Program Committee I want to thank you for your interest to the 13th meeting of the Beam Instrumentation Workshop (BIW08), which took place on the beautiful shores of Lake Tahoe, California. Sponsored by the Lawrence Berkeley National Laboratory, the workshop was dedicated to exploring the physics and engineering challenges of beam diagnostic and measurement techniques for charged-particle accelerators following the consolidated tradition of this series of workshops. The meeting featured plenary and poster sessions, tutorials, vendor exhibits, multiple opportunities for informal discussions and collaborations, and the presentation of the winner of the 2008 Faraday Cup Award.

Two new important events were added to this 2008 meeting:

- BIW08 offered partial financial support to help graduate and undergraduate students attend the workshop.
- The proceedings of BIW08 are being published in the Joint Accelerator Conferences Website (JACoW) database in addition to this book version.

With these new initiatives, the Program Committee hopes to boost interest in the field of beam diagnostics to the next generation of engineers and physicists, and, by publishing the proceedings online, facilitate a free and wider diffusion of the publications. This is of particular importance in this delicate period when, despite the richness of ideas and the possibilities for exciting scientific results, accelerator-based research is struggling to obtain sufficient funding for current and future projects—in the U.S. in particular, but also in other parts of the world.

The organization of BIW08 has been made possible thanks to the generous support of the Accelerator and Fusion Research (AFRD), the Advanced Light Source (ALS), and the Engineering Divisions of Lawrence Berkeley National Laboratory; the Office of High Energy Physics (HEP) of the U.S. Department of Energy; and last but not least, the participants and vendors attending BIW08.

Special thanks go to the members of the Local Organizing Committee whose enthusiastic and outstanding efforts made the workshop become a reality.

Fernando Sannibale, Chair, BIW08
August 2008

DEDICATION

R. Coles Sibley III
August 1957 – February 2007

This Workshop and Proceedings are dedicated to the memory of Coles Sibley, an active participant in the Beam Instrumentation Workshop series who died unexpectedly on 27 February 2007. Coles had also been a member of the BIW Program Committee for many years. He co-chaired both BIW 2000 at MIT-Bates (Cambridge, MA) and BIW 2004 at the Spallation Neutron Source (Knoxville, TN). At the time of his death Coles was working at Still River Systems in Massachusetts.

WORKSHOP SPONSORS

LAWRENCE BERKELEY NATIONAL LABORATORY DIVISIONS

DOE - OFFICE OF HIGH ENERGY PHYSICS

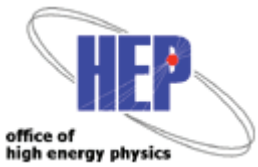

CORPORATE SPONSOR

GMW Associates

Contents

COMMITTEES

Program Committee

Fernando Sannibale, Chair (LBNL)
Walter Barry, Co-chair (LBNL)
John D. Gilpatrick (LANL)
Robert Hettel (SLAC)
Ken Jacobs (SRC)
Kevin Jordan (JLAB)
Ralph Pasquinelli (FNAL)
Thomas Russo (BNL)
Hermann Schmickler (CERN)
Thomas Shea (ORNL)
Om Singh (BNL)
Steve Smith (SLAC)
Robert Webber (FNAL)
Jim Zagel (FNAL)

Local Organizing Committee

Joe Chew, Proceedings Editor
Martha Condon, Conference Administrator
Grace Covarrubias, Conference Secretariat
Joy Kono, Administrative Coordinator
Elizabeth Moxon, Web/Communications
Fernando Sannibale, Chair
Tom Scarvie, Discussion Sessions and Banquet
Greg Vierra, Designer
Jonah Weber, Vendor Contact and Poster Section

FARADAY CUP AWARD

The Faraday Cup Award is intended to recognize and encourage innovative achievements in the field of particle accelerator beam instrumentation. It is donated by Bergoz Instrumentation, of Saint-Genis-Pouilly, France. The award consists of a certificate and $5000.00 (U.S.). These are presented every other year at the Beam Instrumentation Workshop (BIW), whose Program Committee is solely responsible for the selection of the recipient.

History

The Beam Instrumentation Workshop (BIW) was started to provide a forum for in-depth discussions of techniques for measuring charged-particle beams produced in high-energy accelerators. In the past, the large U.S. and European Particle Accelerator Conferences dedicated only a few sessions to instrumentation, thus making it difficult to have significant interaction among others in the field. It became apparent to Dick Witkover at Brookhaven National Laboratory (BNL) that a conference or workshop dedicated to instrumentation was needed.

After meetings with representatives from the other national labs across the U.S., the first Accelerator Instrumentation Workshop was held at BNL in 1989. During the last day roundtable discussion, the idea for the Faraday Cup Award was born as a means of encouraging young engineers and physicists to become more innovative. Discussions between Bergoz and the Organizing Committee continued through the next Beam Instrumentation Workshop (as it was now called) at Fermi National Accelerator Laboratory in 1990 with a final agreement on how to keep the Award fair and noncommercial reached in 1991. The procedures for selecting the winner were written primarily by Bob Shafer soon after, and they have remained virtually unchanged since then. The clever name of the Award, referring to both a trophy and a measurement device, is attributed to Bob Webber.

Selection Criteria

The Faraday Cup Award is presented to those who have made outstanding contributions to the development of innovative beam diagnostic instruments of proven workability. The prize is only awarded for demonstrated device performance and successful publication of the results.

At BIW08, the award (in its 10th edition) was assigned to Dr. **Suren Arutunian** of the Yerevan Physics Institute of Armenia for:

The invention, construction and successful test of the diagnostic system "A Vibrating Wire Scanner"

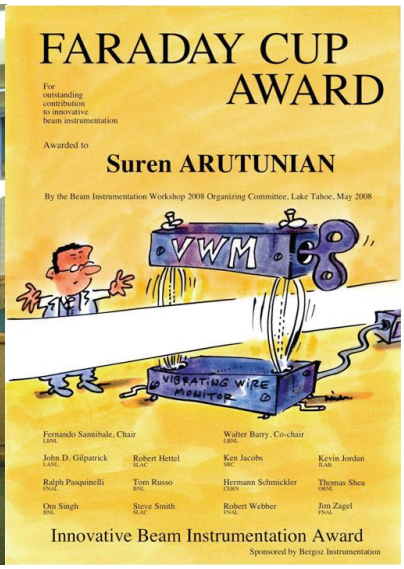

From left to right: Julien Bergoz (Faraday Cup Award sponsor), Suren Arutunian (2008 Faraday Cup Award Recipient), Fernando Sannibale (BIW08 Chair).

Past recipients of the Faraday Cup Award

2006 Haixin Huang, BNL, and Kazuyoshi Kurita, Rikkyo University
2004 Toshiyuki Mitsuhashi, KEK
2002 Andreas Jansson, CERN
2000 Kay Wittenburg, DESY
1998 Andreas Peters, GSI
1996 Walter Barry, LBNL and Hung-chi Lihn, SLAC
1994 Edward Rossa, CERN
1993 Donald W. Rule & Ralph B. Fiorito, NSWC
1992 Alexander V. Feschenko, INR

For more information: www.faraday-cup.com/

A WINNING TRADITION: THE FARADAY CUP AWARD

Michelle Wilinski,

Brookhaven National Laboratory, Upton, NY 11973, U.S.A.

The Faraday Cup Award is given for an outstanding contribution to the development of an innovative particle beam diagnostic instrument of proven workability. "Like a 'Nobel Prize' for the beam instrumentation community," is how the 2000 winner, Kay Wittenburg of DESY, describes the Faraday Cup Award. It is presented at the Beam Instrumentation Workshop (BIW), a biennial forum for in-depth discussions of techniques for measuring particle beams produced in accelerators. The Faraday Cup winner receives a US $5,000 cash prize, $1,000 for BIW travel expenses, and a certificate of award. An acceptance speech is given at the workshop by the Awardee in the form of a talk on the design and performance of the winning instrument.

Like many other awards, the Faraday Cup Award comes with a storied tradition. The first Beam Instrumentation Workshop was organized by Richard Witkover and held at Brookhaven National Laboratory in 1989 to stimulate interaction among those in the instrumentation field. The idea for an award was conceived during round-table discussions the last day of that meeting as a way to encourage innovation among young engineers and physicists. Agreement on policies for keeping the award fair and non-commercial was reached in 1991 based on nomination and selection procedures written primarily by Bob Shafer. Naming of the award is attributed to Bob Webber. Financial sponsorship of the Faraday Cup Award is donated by Bergoz Instrumentation.

The BIW Program Committee is solely responsible for selecting the Award recipient. The Committee accepts nominations for the award approximately 12 to 18 months in advance of each BIW. Self-nomination is permitted. The award is open to candidates of any nationality for work done at any geographical location. Instrument performance must be proven using a primary charged particle beam; mere concepts or "bench-top" demonstrations are not acceptable. A description of the device, its operation and performance must be published in a journal or conference proceedings that is in the public domain. In the event of deciding between works of similar quality, preference is given to candidates in the early stages of their beam instrumentation career. The award may be shared between persons contributing to the same accomplishment. Complete rules are available at *http://www.faraday-cup.com*.

Since the first Faraday Cup Award in 1992, thirteen people from laboratories around the world have received the Award (see Table 1) and have gone on to continued career success. Although each prize award is a one-time event, the rewards from the prize have continued for the winners.

Table 1: Faraday Cup Award Winners

Edition	Winner	Diagnostics
1992	Alexander V. Feschenko, INR	Longitudinal Bunch Shape Measurement using Wire Probe Secondary Emission
1993	Donald W. Rule & Ralph B. Fiorito, NSWC	Techniques for Measuring Bunch Shapes by OTR
1994	Edward Rossa, CERN	Technique for Measuring the 3-D Bunch Shapes
1996	Walter Barry, LBL and Hung-chi Lihn, SLAC	Sub-ps e^- Bunch Shape Measurement Techniques
1998	Andreas Peters, GSI	Cryogenic Current Comparator
2000	Kay Wittenburg, DESY	Beam Loss Monitor Using PIN Diodes
2002	Andreas Jansson, CERN	Quadrupole Beam Pickup
2004	Toshiyuki Mitsuhashi, KEK	Interferometric Profile Monitor Using Synchrotron Radiation
2006	Haixin Huang, BNL, and Kazuyoshi Kurita, Rikkyo Univ.	Innovative Proton Beam Polarization Monitoring System
2008	Suren Arutunian, YerPhI	Vibrating Wire Sensor for Beam Instrumentation

PhD students can have breakout results and winning instruments have emerged from their thesis work. In 1996, Walter Barry of Lawrence Berkeley National Laboratory and Hung-chi Lihn of the Stanford Linear Accelerator Center shared the Faraday Cup Award for development of techniques to measure the bunch shape of subpicosecond electron beams. Lihn, a PhD student at the time, sees the award as a great recognition, by experts in the field, of his

years of work and ideas. Now in industry, Lihn still calls upon the skills that he developed building his winning instrument. While he did not personally continue with further development of the device, Lihn's thesis and paper have been cited by a number of others and the ideas have been adopted in other labs.

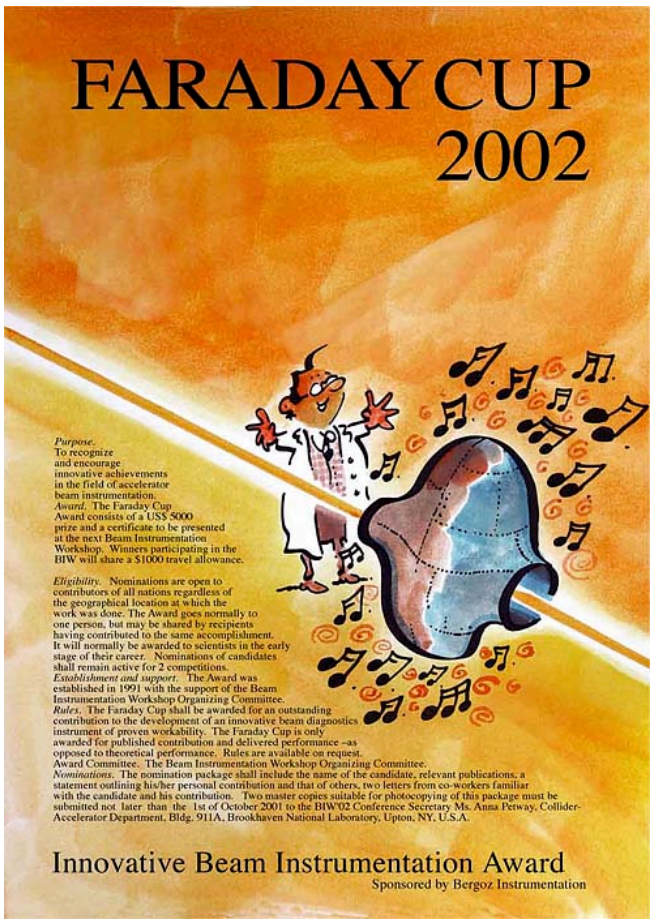

Figure 1. Example of Faraday Cup Award poster by the artist Pecub. More on the Faraday Cup Award web site (*http://www.faraday-cup.com*).

Development of a magnetic quadrupole pick-up began as a simple idea that eventually became a main theme of Andreas Jansson's PhD dissertation. Working many hours at CERN with a network analyzer by his side, Jansson won the 2002 award for his pick-up which measures the quadrupole moment, or ellipticity, of a particle beam. After BIW '02, nearing the end of a CERN postdoc position and looking to widen his horizons, he visited several US laboratories and then accepted a People's Fellowship at Fermi National Accelerator Laboratory, where he continues to work. Jansson credits some of his career success to his Faraday Cup Award win and the resulting visibility that came with it.

Like Lihn, who faced different challenges when moving to an industry position, Jansson had to call on his acquired skills in his new position at FNAL. The pick-up that he had developed for the CERN PS was not optimal for the Tevatron with its dual beams and helical orbits. He started work on other instruments such as Ionization Profile Monitors and Microwave Schottky Monitors. Jansson's fondness for his PhD work is evident as he tries to keep up with the development of various quadrupole detectors by others, including quadrupole mode cavities and electro-optical devices.

In its history, the Faraday Cup Award has recognized a wide range of innovations and advancements in beam diagnostics. The very first winner of the Award, Alexander V. Feschenko of the Institute for Nuclear Research in the Academy of Sciences of Russia, won for a technique to measure the longitudinal bunch shape of a charged hadron beam with picosecond resolution using secondary emission from a fine wire probe. Bunch shape information is used to study beam dynamics and to tune an accelerator.

A device to measure three-dimensional bunch shapes of picosecond e+/e- bunches in a single shot was the winning device for Edward Rossa in 1994. He developed this using a streak camera for the CERN Large Electron Positron collider. Synchrotron radiation emitted by particles creates images of the density distribution; Rossa's optical setup provides front, top, or side views.

Applications based on radiation emitted from charged beams have resulted in several prize-winning devices. In 1993, the first joint award of the Faraday Cup was given to Donald W. Rule and Ralph B. Fiorito for their work at the Naval Surface Warfare Center – White Oak using optical transition radiation (OTR). Together they developed several techniques to measure the divergence and emittance of charged particle beams utilizing OTR produced from thin intercepting foils.

In the years since the award, Rule pursued other fields of research, but has continued contributing to beam instrumentation development in small ways. He states that the recognition of receiving the award was an encouragement to remain actively connected to the beam instrumentation community and has offered great opportunities to meet and collaborate with many interesting and exciting colleagues. Fiorito echoes these statements, indicating that the national and international awareness provided by the award directly resulted in new professional opportunities which he believes would not have otherwise been possible.

Other benefits resulted from this award. At the time of their research, studies of beam physics had just recently been established at their laboratory. The Faraday Cup Award pointed out to the Navy, as well as to the accelerator community at large, that significant new ideas could be generated outside of a traditional accelerator laboratory setting. The award also stimulated a great deal of interest in transition radiation based techniques and gradually more scientists and engineers have implemented these and related techniques at facilities around the world.

The 2000 winner, Kay Wittenburg, triumphed for the design of a beam loss monitoring detector using PIN diodes in a coincidence configuration. His design discriminates between synchrotron radiation present in electron accelerators and radiation due to actual beam loss. The design eventually became commercialized and is now used in accelerators worldwide. DESY granted Bergoz Instrumentation a license to use the original concept of the PIN Photodiode Beam Loss Monitor, to further develop it, and to sell instruments based on this principle. Wittenburg, leader of DESY Machine Diagnostics and Instrumentation since early 2000, believes that the development of a new idea, the overall performance, and the reliable functioning of the system was greatly important to him.

Employing synchrotron radiation for a unique beam profile monitoring system won Toshiyuki Mitsuhashi of KEK (High Energy Accelerator Research Organization, Japan) the Faraday Cup Award in 2004. Mitsuhashi labored on the development of synchrotron radiation (SR) monitors for twelve years before receiving this award, with the development of the SR interferometer being the most significant topic. He conceived the idea in 1994 while investigating the coherence of SR and determined that he would be able to use the SR interferometer for measurement of beam profile and size.

The Faraday Cup has honored "bright" ideas based on synchrotron light, along with some "cool" ideas as well. Andreas Peters of GSI won the 1998 award for his work on the Cryogenic Current Comparator (CCC). This device measures nanoampere DC beam current by comparing it to a known current as both are passed through a cryogenic cylinder. Since Peters' development, several groups have worked on the CCC, especially in Japan where a CCC was built at TARN-II. CCC projects are now underway at DESY and again at GSI for the FAIR project. Peters declares that the "Faraday Cup Award was a great honor and a gratification for some years of hard, but exciting, work on the CCC project at GSI." He became the beam diagnostics group leader at GSI in 2000, and believes winning the award was the "kick" to this new position. At the end of 2006, Peters became head of the accelerator operations for the Heidelberg Ion Therapy project, a heavy ion cancer treatment facility of the Heidelberg University Clinics, and he still works on special beam diagnostics topics.

A joint award was given in 2006 to Haixin Huang of BNL and Kazuyoshi Kurita of Rikkyo University for an innovative proton beam polarization monitoring system. Their design uses ultra-thin carbon filaments and an array of silicon detectors to deduce the degree of polarization from proton-carbon elastic scattering. Huang calls the award a great milestone in his career and welcomes the recognition of his and Kurita's contribution to the device. In the two years since the award, the CNI polarimeters at BNL have been upgraded, most notably with a new target drive assembly for more precise target control. Kurita is now in charge of implementing the CNI polarimeter for polarized proton projects at the new 50 GeV J-PARC accelerator currently under construction in Japan.

Clearly, the Faraday Cup award has been a career highlight for past winners. They all overwhelmingly acknowledge and appreciate the recognition from experts in the field and from collaborators alike. Their stories prove that innovation can come from anywhere – a student or a professional, a government accelerator facility, university, or other lab, and any geographic location.

The BIW Program Committee is eager to receive nominations for devices that are pioneering and provide new insight into particle beam measurements. If you or a colleague has developed any instrument that meets the award criteria, please nominate it for the competition at the next Faraday Cup Award.

Author's Note: The author would like to thank Bob Webber and the BIW Program Committee for their support and ideas. Many thanks also go to the past recipients of the Faraday Cup Award for graciously sharing their insights. References for papers written about each of the winning devices can be found at www.faraday-cup.com.

VIBRATING WIRE SENSORS FOR BEAM INSTRUMENTATION

Arutunian, S.G.
Yerevan Physics Institute, Armenia

Abstract

Thermal sensors based on the vibrating wire principle are distinguished by high accuracy and stability. An important advantage of these sensors is that they produce a frequency signal that can be transferred large distances without disturbance. Original vibrating wire sensors and monitors for the measurement of beam transversal characteristics of charged-particle and photon beams are described. By means of these devices, measurements of an electron beam in the Yerevan synchrotron, a proton beam at PETRA (DESY), and a hard x-ray undulator beam at the APS (ANL) have been performed.

INTRODUCTION

The operating principle of Vibrating Wire Sensors (VWS) or Vibrating Wire Monitors (VWM) is based on the measurement of the change in the frequency of a vibrating wire, which is stretched on a support, depending on the physical parameters of the wire and environment in which oscillations take place. Today the area of application of this technique is expanding and the number of vibrating wire-based instruments has increased. Strain, displacement, piezometric level, pressure, angle and moment of rotation, viscosity of the media, and ultralow thermometry under 1 K are measured by VWS [1-7]. An interesting vibrating wire field-measuring technique has been developed for determination of magnetic center of units in accelerators (see, e.g., [8-10]).

The important advantages of properly constructed vibrating wire sensors are inherent long-term stability, high precision and resolution, good reproducibility and small hysteresis. The advantage of vibrating wire sensors is also that the frequency signal is imperturbable and can be transmitted over long cables with no loss or degradation of the signal. The reliability of the sensors becomes the overriding feature in the selection of a technology. It is also is important to ascertain a low drift and minimum change in sensitivity. An important parameter of vibrating wire-based sensors is their ability to operate in hard conditions (high operational power and temperature cycling, thermal shock, thermal storage, autoclaving, fluid immersion, mechanical shock, electromagnetic and electrostatic environments [11]).

We take an electromechanical resonator with a metallic vibrating wire excited by the interaction of a current with a permanent magnetic field as a basis for the VWS of electron and proton beams. In this paper we discuss an application of such resonators for precise profile measurement of particle and photon beams. The interaction of the beam with the wire mainly causes heating of the wire. Thus we expect that the frequency of natural oscillations of the wire will provide information about its temperature. The thermal method of measurement also allows registering neutron flux.

MAIN CHARACTERISTICS

The operating principle of vibrating wire sensors is measurement of the change in the frequency of a vibrating wire, which is stretched on a support, depending on the physical parameters of the wire and the environment in which oscillations take place. A detailed description of the vibrating wires sensors can be found in our publications (see [12] and cited references). Below we present a short description of the VWS and some aspects not discussed in previous publications.

Sensor main components

In Fig. 1 the sensor main components are presented. Wire (1) ends are pressed in the clips (2) and pass through the magnet field system (samarium-cobalt permanent magnets and magnet poles (3) and (4)). The magnet provides field strength on the order of 10 kG in the gap. Clips are fixed on the sensor support structure (5). Sensor is fastened on the scan feed arm by details (6) and (7).

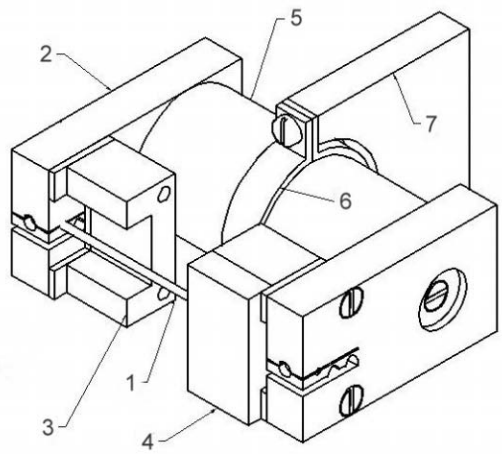

Fig. 1: Vibrating wire sensor main view.

By use of a simple positive feedback circuit, the magnetic system excites the second harmonic of the wire's natural oscillation frequency while keeping the middle of the wire exposed for detection of beam heating.

Wire oscillation excitation

Wire oscillations arise as a result of the interaction between the oscillating current through the wire and the applied magnetic field. When the oscillating current passes through the wire, the Lorentz force shifts the

wire in the transverse direction proportionally to the magnitude of the magnetic field and the peak current. The induced voltage is proportional to the time derivative of the current, which from the electrical viewpoint is equivalent to an inductance. The electrical equivalent of the wire can therefore be described as a series combination of a resistance and an inductance (see, e.g., [13]). Thus excitation of mechanical oscillations in the wire is possible because the wire acts like a tuned circuit when placed in an amplifier feedback arrangement. When the wire is connected to an amplifier circuit, a small amount of energy is fed back to the wire, which causes it to vibrate. This is similar to the excitation of electromechanical oscillations in quartz resonators (see, e.g., [14]). The frequency measurement is accomplished by counting the short impulses of the quartz generator inside a few periods of measured oscillations.

Wire under beam irradiation

The interaction of the beam with the wire mainly causes heating of the wire due to the energy loss of the particles in the wire. In case of permanent thermal flux falling on the wire, the equilibrium temperature profile along the wire is determined by the balance between the heat deposited on the wire and heat dissipation occurring in three ways: thermal conductivity along the wire, heat radiation and convective heatsink (in gas media) [15]. A change in wire mean temperature results in a change of wire strain, which is registered by measurement of the wire's natural oscillation frequency. The second harmonic frequency of natural oscillations (if wire elasticity is neglected) is written as

$$F = 1/l \bullet \sqrt{\sigma/\rho}\,, \qquad (1)$$

where ρ is the density of wire material, σ is the stress of the wire with ends pressed in clips on the distance l. Change of this value on Δl leads to a change in wire stress $\Delta\sigma = E\,\Delta l/l$ (E - modulus of wire elasticity). As a result, the relative change of frequency is

$$\Delta F / F = E/2\sigma \bullet \Delta l/l\,. \qquad (2)$$

The same effect arises if instead the wire is overheated by an amount ΔT. This can happen if a localized heat flux falls on the wire (e.g. a beam of the particles or photons). Then $\Delta l / l = -\alpha_S \Delta T$, where α_S is the coefficient of thermal expansion of the wire, and (2) is rewritten:

$$\Delta F / F = -E/2\sigma \bullet \alpha_S \Delta T \qquad (3)$$

This equation includes the large dimensionless factor $E/2\sigma$, which determines the high sensitivity of wire natural oscillation frequency to its heating. Thus for Stainless Steel E is of order 200 GPa, whereas σ is much less than tensile strength; of order of 500-800 MPa. If we measure the frequency with an accuracy of about 0.01 Hz, (this is the frequency measurement resolution at 1 s sampling) the corresponding temperature resolution is less than 0.001 K.

Frequencies resonant capture

So-called frequencies resonant capture [16] can be obtained in coupled mechanical oscillators with several wires. This phenomenon can happen for multiwire VWS if resonant frequencies are very close. This effect is stipulated by common clips and support that form a mechanical coupling between wires. Shown in Fig. 2 are data when resonant capture was aroused for two-wire VWS. Each frequency is measured by a separate electronic unit with a measurement gate of 30 s, which allows resolution down to 1 mHz. During the experiment the environmental temperature was also measured. Splitting of the frequencies occurred at 23:31 after which both frequencies moved to new values. This data allows for an estimation of the two measurement channel's accuracy by calculating the difference between the captured frequencies (see Fig. 3). One can see from the data that the frequency measurement channel accuracy is about 1 mHz.

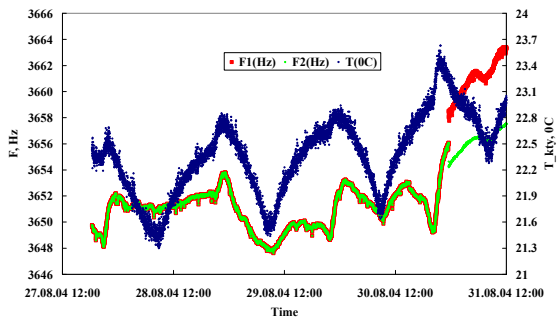

Fig. 2: Frequencies capture phenomenon for two wire resonator.

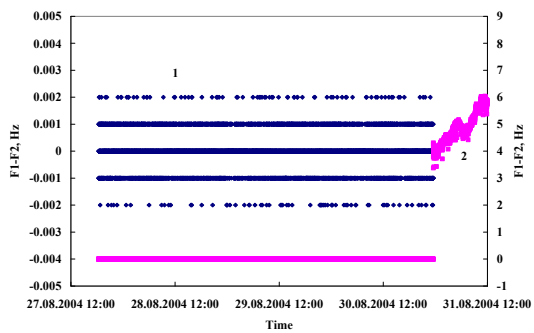

Fig. 3: Two oscillator frequencies difference at resonant capture. The same values are presented in two scales (1 – at left axis, 2 – at right).

Multiwire sensor wire thermal air coupling

If multiwire sensor is used in the air a thermal coupling between sensor wires occurs. In addition to the external heat source, (measured beam) the wire also reacts to temperature changes in neighboring wires. In this case, one must recover the necessary information

about contribution of external source from wire integral overheating. For effect estimation we performed an experiment with a five-wire sensor when the external source was modeled by DC current through the given wire. In Table 1 the wire overheatings are presented. Each row corresponds to a situation when current of about 10 mA passing through subsequent wire The offset between the wires was 0.5 mm (the second wire by technical reasons was omitted from measurements).

Table 1

wire 1	wire 2	wire 3	wire 4	wire 5
0.255	-	0.052	0.031	0.019
-	-	-	-	-
0.050	-	0.283	0.099	0.051
0.029	-	0.101	0.265	0.090
0.019	-	0.051	0.090	0.247

With good accuracy, (about 0.001 K) the values in the table are symmetric across the diagonal of the matrix. With respect to a linear heat transfer model, the heat coupling between the wires is determined by the following equations (Eq. 4):

$$Q_1=\alpha_{11}T_1+\alpha_{12}(T_1-T_2)+\alpha_{13}(T_1-T_3)+\alpha_{14}(T_1-T_4)+\alpha_{15}(T_1-T_5),$$
$$Q_2=\alpha_{12}(T_2-T_1)+\alpha_{22}T_2+\alpha_{23}(T_2-T_3)+\alpha_{24}(T_2-T_4)+\alpha_{25}(T_2-T_5),$$
$$Q_3=\alpha_{13}(T_3-T_1)+\alpha_{23}(T_3-T_2)+\alpha_{33}T_3+\alpha_{34}(T_3-T_4)+\alpha_{35}(T_3-T_5),$$
$$Q_4=\alpha_{14}(T_4-T_1)+\alpha_{24}(T_4-T_2)+\alpha_{34}(T_4-T_3)+\alpha_{44}T_4+\alpha_{45}(T_4-T_5),$$
$$Q_5=\alpha_{15}(T_5-T_1)+\alpha_{25}(T_5-T_2)+\alpha_{35}(T_5-T_3)+\alpha_{45}(T_5-T_4)+\alpha_{55}T_5.$$

Here T_i are the wire overheatings relative to the environmental temperature, Q_i is the power dissipated on the wire with index i. The right-hand sides of (4) define heat transfers with the environment (diagonal terms) and with the other wires. The coefficients α_{ij} can be obtained by special experiments, however it is possible to determine them by scan data processing using the statement that the unknown beam distribution is the same for all wires (see. below).

The problem also can be solved in a fashion similar to constant-temperature anemometery (see e.g. [17]). By use of additional DC currents, frequencies can be stabilized at some level and in case of wire overheating by another source can be held at the same value by a corresponding decrease in DC current. The value of decrease is characteristic of the unknown source.

Frequency dependence on environmental temperature

The wire oscillation frequency depends also on the environmental temperature. To minimize this dependence in our VWS, we used a compensation principle by choosing the coefficients of thermal expansion of the wire and support structure materials to be close to each other. For example, in the VWM005 the same grade of Stainless Steel was chosen both for the wires and the support. As a result, the dependence of frequencies upon environmental temperature variation decreases relative to characteristic value 40.2 Hz/K at frequency 4200 Hz for single wire (see Table 2). It is more convenient to compare the linear dependence of frequency squared on temperature (see. equation (1)). Multiple thermocycling of the five-wire sensor in the temperature range 300C – 700 C gives the values presented in Table 2. All values are much smaller than -3.38E+05 Hz^2/K for a single wire, but differ significantly from each other.

Table 2

	1	2	3	4	5
dF^2/dT, 1000* Hz^2/K	-5.5	-8.7	-7.4	-7.3	-8.3

Since all wires are made from the same coil of wire and are stretched on the same support, it follows that this difference is caused by the clips (plates of ceramics pressed by special elastic elements of sensor support). It seems that equal clamping of the wire ends will reduce the observed difference.

BEAM INSTRUMENTATION

The high sensitivity of the VWS to wire temperature variation makes it well-suited to a wide range of accelerator diagnostic applications. Vibrating wire sensors have been applied to measurements of electron, proton and ion beams. VWS can be used for photon beam monitoring with very wide spectral range from deep infrared to hundreds of keV. Weak laser beams were successfully measured with VWS. First experiments have been performed for monitoring hard x-ray beams, both in vacuum and in air.

Technical charachteristics

The main parameters of oscillators with wires from Stainless Steel and Tungsten are presented in Table 3.

Technical characteristics of 5-wire VWS in case of use in air are as follows: resolution of frequency measurement of each wire is 0.01 Hz, short time accuracy measurement (1 hour) is ± 0.01 Hz and accuracy in 24-hour interval is ± 0.04 Hz. response time is 0.26 s. These values correspond to wire mean temperature resolution of 0.00025 K and short- and long-time accuracy ± 0.00025 K and ± 0.001 K. By such device it is possible to measure deposited on the wire power as small as ± 1 μW in short-time mode and ± 4 μW in long-time mode. The nonlinearity of the pickup in its operational range 0-100 mW is 0.01 %.

Table 3

Material, conditions	A316 Vacuum	A316 Air	Tungsten Vacuum	Tungsten Air
$\Delta T_{mean}/\Delta Q$, K/mW	19.4	0.23	3.0	0.23
$\Delta F/\Delta T_{mean}$, Hz/K at 4200 Hz	-40.2	-40.2	-8.8	-8.8
$\Delta F/\Delta Q$, Hz/mW	-779.6	-9.3	-26.4	-2.0
response time, s	20.2	0.26	1.8	0.15

Electron beam

The first scanning experiments on a charged beam were done on an electron beam at the Injector of Yerevan Synchrotron with an average current of about 10 nA (after collimation) and an electron energy of 50 MeV [19].

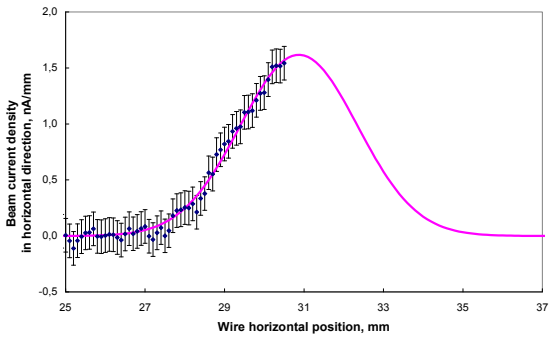

Fig. 4: Weak electron beam scan.

In Fig. 4 the result of the reconstruction of the beam profile for the first half-distance scan is shown. On the vertical axis the beam current density in the horizontal direction is presented. The solid line represents the profile of the beam approximated by the mean square method of a Gaussian function with a standard deviation of σ_x = 1.48 mm and a beam position at 30.87 mm.

Proton beam

A series of experiments with the VWS were done on a proton beam in the accelerator PETRA at DESY [12, 20-22]. The proton beam consisted of 10 bunches with an initial mean current of about 15 mA and an energy of 15 GeV. The transversal beam sizes were: $\sigma_x = 6$ mm, $\sigma_z = 5$ mm. A system of two scintillator-photomultiplier pickups were installed additionally to measure particles scattered on the wire. The park position of the wire was located at 40 mm ($6.7\,\sigma_x$) from the center of the vacuum chamber on the outside of the accelerator ring. The scanner was driven by a stepping motor toward the vacuum chamber center. A system of adjustable beam bumps allowed control the position of the beam inside the vacuum chamber at the scanner location.

An example of a beam scan is shown in Fig. 5. The signal from the VWS sensor changed from the beginning of the movement, while the signals from scintillators started to increase only at a distance of 13 mm from the VWS park position.

The whole scan range was 20 mm. During the experiment (20 min) the proton beam current decreased from 12 mA to 9.5 mA. Shown in Fig. 5 are data collected at a 1 Hz sample rate during a scan.

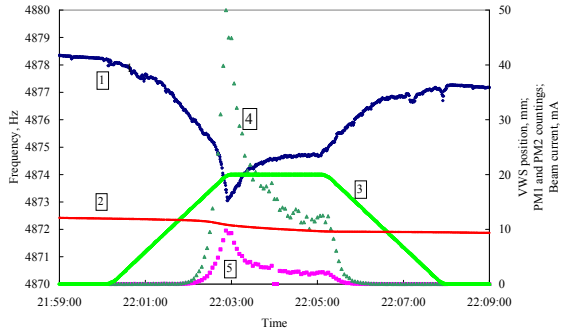

Fig. 5: Proton beam scan: 1 – frequency signal, 2 – proton beam current, 3 – scan depth, 5, 6 – photomultipliers response.

Ion beam

The vibrating wire scanner was also tested on an ion beam of the energo-mass-analyzer EMAL-2 [23, 24]. Approximately 16 pA of beam current interacted with the wire and a frequency decrement of about 0.15 Hz was measured. The interest to continue ion beam profiling by the VWS is stimulated by the fact that the vibrating wire scanning method is based on thermal action of the beam and accumulates effect from both charged and neutral particles. So by this method the effect of electrical neutralization of the ion beam by electron clouds can be overcome.

Laser beam

A laser beam was scanned in air by a vibrating wire sensor with two wires located at distance 1 mm from each other [25-27]. A semiconductor laser of about 1 mW power was used as a photon source. A typical scan is presented in Fig. 6. The laser beam was scanned at a speed of 66 μm/s forwards and backwards.

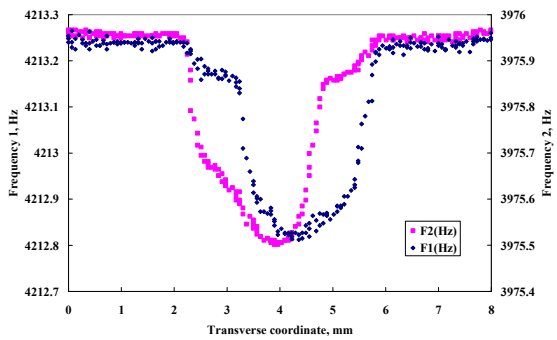

Fig. 6: Laser beam scan by two wire VWS.

Here we see the effect mentioned above of wire thermal coupling resulting in profile asymmetry.

Hard x-ray beam monitoring in vacuum

Hard x-ray flux measurements with a vibrating wire monitor with two wires were conducted at APS [28]. The insertion device was a standard APS undulator A.

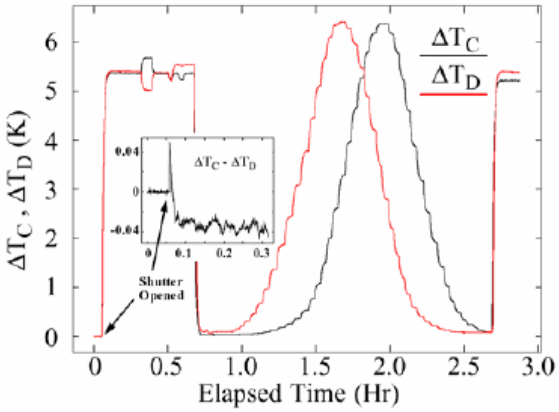

Fig. 7: Data collected during photon beam vertical angle scan.

A two-wire vibrating wire monitor was installed in a vacuum test chamber of beamline 19-ID. The initial frequencies were determined with the shutter closed at the start of the scan. Using these values, the temperature changes ΔTC and ΔTD were determined using equation (3), and these values are plotted in Fig. 7. The beam was steered downward by 100 microradians, and then steered in 5 microradian steps. A magnified view of the difference ΔTC - ΔTD is shown in the inset of Fig. 6. With the shutter closed, the fluctuations fall in the range ±0.001K, while after opening the shutter with the beam approximately centered, the fluctuations are significantly larger, most likely the result of real beam motion. At the detector location, this ±0.001K translates into a noise floor near 0.5 microns. Considering the 52 meter distance from the source, this translates into less than 10 nanoradians angular resolution, which is quite remarkable.

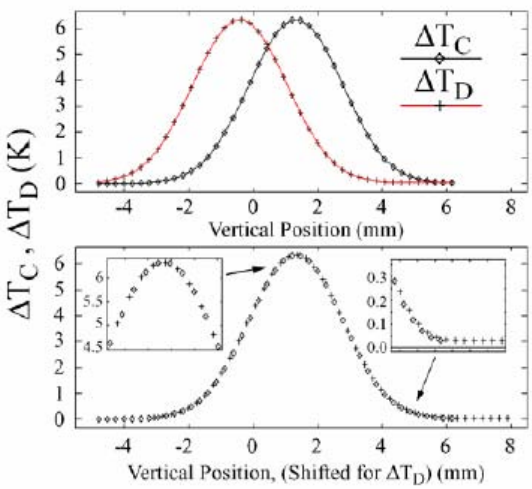

Fig. 8: VWM data corrected for thermal drift and beam current decay. The two data sets are offset in the lower panel for direct comparison.

Results of the scan after some data processing are shown in Fig. 8 (each of the 5-microradian step positions were fit to an exponential and thermal drift was subtracted). The plot of ΔTD was shifted by 1.730 mm in the lower plot, determined from the difference in centroid positions from the Gaussian fits. The wire separation measured later with a microscope was 1.717±.001 mm. Because it was placed in vacuum, the VWM time constant was about 31 s (compared with calculated response time of 20 s from Table 3).

Hard x-ray beam monitoring in air

Taking into account the extreme sensitivity of the vibrating wire sensors G. Decker suggested [28] placing the VWS outside of vacuum to detect only very hard x-rays that penetrate the vacuum chamber at selected locations (see also [29]). The addition of convective cooling reduces the response time substantially albeit with reduced sensitivity.

The VWM005 was mounted on the outboard side of a bending-magnet synchrotron radiation terminating flange in sector 37 at the APS storage ring, at a distance of about 7 m from radiation source. The synchrotron radiation power accepted in the horizontal angle corresponding to the VWM005 aperture (about 8 mm) is 99.1 W (at 100 mA beam current). Using spectral parameters for photon beam attenuation in Cu (material of flange) and Stainless Steel (material of wire), one can calculate the spectral distribution of synchrotron radiation transmitted through the flange and deposited into the wire (see Fig. 9). The synchrotron radiation power after attenuation by 6 mm copper is 420 mW, while power dissipated into the wire is 1.13 mW. One can see from the list of the VWM005 parameters that this value is sufficient for registration by this sensor.

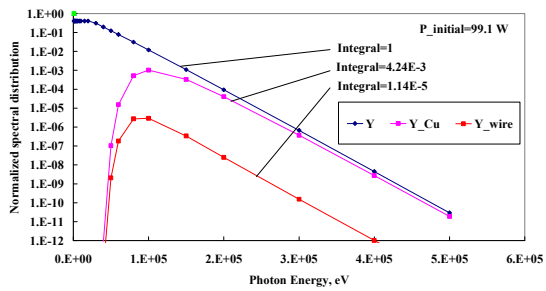

Fig. 9: Normalized spectral distribution of initial synchrotron radiation (Y), passed through the Cu flange (Y_Cu) and deposited into the wire (Y_wire).

In Fig. 10 we present the overheating data from the five-wire VWM when the electron beam angle was scanned vertically through a range of 300 microradians with 125 steps (for details see [30]). Profile asymmetries arise from the above-mentioned wire thermal coupling effect and some wire misalignment issues relative to the sensor housing.

Using a statistical data treatment, the heat coupling coefficients were found and accordingly (4) the profiles of the source were recovered (see Fig. 11).

In Fig, 12 we present the united profile from all wires. Profile widening, especially at the tails, takes place as a result of coefficient determination inaccuracy from equation (4).

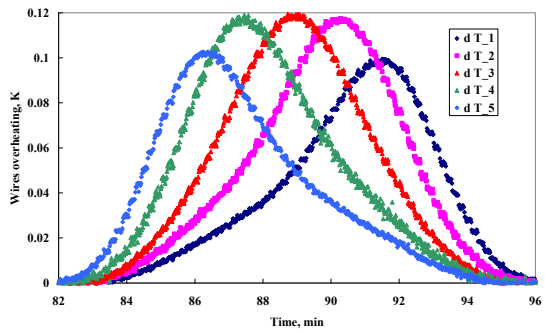

Fig. 10: APS vertical bending magnet angle scan results showing wire overheating temperatures.

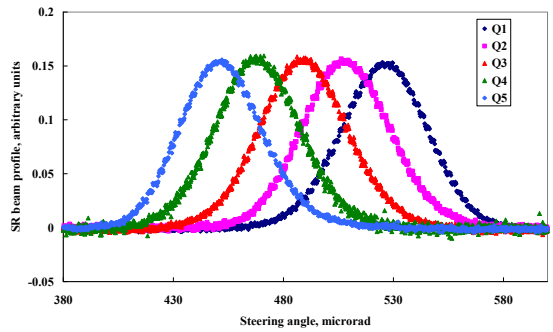

Fig. 11: Recovered profiles from separate wires.

.

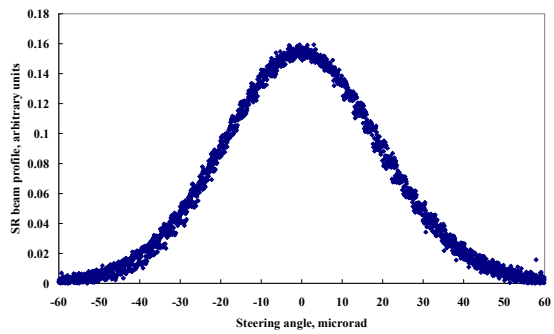

Fig. 12. Synchrotron radiation beam profile recovered from all wires.

DISCUSSION

As we mentioned above the vibrating wire sensors can be used for many types of beam diagnostics because only a small amount of heat transfer from the measured object to wire is needed. Therefore vibrating wire sensors can be successfully applied to electron, proton, ion and photon beam monitoring. It is very important that in each of mentioned areas, due to its extreme sensitivity, VWS can perform measurements that are impossible using any other existing technologies. For charged particle beam diagnostics, its can make weak beam measurements and provide beam halo and tails monitoring. For photon beams it is possibility to measure very hard spectral components. Because of this one can measure only necessary part of radiation from insertion devices and cut unwanted contributions from other accelerator sources. A possible area of VWS application is neutral beam diagnostics (neutrons, ion beams with uncompenstated positive and negative charged particles, plasma). Recent application of the VWS in air has allowed a dramatic reduction in response time, together with a reduction in system cost by a large factor. The VWS concept shows a lot of promise due to its very high sensitivity and overall simplicity in both the mechanical design and electronics.

ACKNOWLEDGMENTS

Author is grateful to all his co-authors with whom he worked many years. Many thanks to the YerPhI, PETRA and APS ANL stuff for their friendly help during the experiments. Special thanks to R.Reetz and J.Bergoz for permanent interest and essential support.

REFERENCES

1. McKenna G.T., “Grouted-in installation of piezometers in boreholes,” Geotechnical J. (1995), 32, pp. 355-363.
2. Agejkin D.I. et al., in Control and Regulation Pickups, Moscow, 1965.
3. Asch G., *Les capteures en instrumentation industrielle,* 1991.
4. T. Simmonds, “Vibrating wire tiltmeters and inclinometers, recent developments and experiences,” Monosys Guide in Monitoring (2000), Q-3, pp. 6-8.
5. Bourquin F., Joly M., “A magnet-based vibrating wire sensor: design and simulation,” Smart Mater. Struct. 14 (2005), 247-256.
6. Correia da Mata J.L.G., Fareleria J.M.N.A., Oliveria C.M.B.P., Wakeham W.A., “A new instrument to perform simultaneous measurements of density and viscosity of fluids using a dual vibrating-wire technique,”www.zae-bayern.de/ectp/abstracts/correia_da_mata1.html.
7. Krause A., Erbe A., Blick R.H., “Nanomechanical vibrating wire resonator for phone spectroscopy in liquid helium,” Nanotechnology 11 (2000), pp. 165-168.
8. Temnykh A., “The use of vibrating wire technique for precise positioning of CESR fase III super-conducting quadrupoles at room temperature,” Proc. of the 2001 Part. Accel. Conf. (Chicago, 2001), pp. 3469-3471.
9. Temnych A., “Vibrating wire field-measuring technique,” CORNELL CBN 96-7 (1996).
10. Temnych A., The magnetic center finding using vibrating wire technique. - CBN 99-22, 1999.
11. Ayazi F., Najafi K., “A HARPSS polysilicon vibrating ring gyroscope,” J. of Micromechanical Systems 10, 2 (2000), pp. 169-179.
12. Arutunian S.G., Mailian M.R., Wittenburg Kay, Nucl. Instrum. Methods A 572, 1022-1032 (2007).
13. Elcev Ju.F., Zakosarenko V.M., Tsebro V.I., “String magnetometer,” Transition processes in superconducting magnetic systems, Trudy FIAN, v. 150, Moscow, pp. 141-147.

14. “Fundamentals of Quartz Oscillators,” Application Note 200-2, Hewlett Packard, Electronic Counters Series.
15. Arutunian S.G., Dobrovolski N.M., Mailian M.R., Sinenko I.G., Vasiniuk I.E., “Vibrating wire for beam profile scanning,” Phys. Rev. Special Topics.- Accelerators and Beams, 1999, v. 2, 122801.
16. Abdelghani Zniber A., Dane Quinn D., “Resonance capture in a damped three-degree-of-freedom system: Experimental and analytical comparison,” Int. J. of Non-Linear Mechanics, 41, 10 (2006), pp. 1128-1142.
17. http://www.aoe.vt.edu/~simpson/aoe4154/hotwirelab.pdf
18. Cooper R et al. A program for neutron detector research and developmnet. – Oak Ridge National Laboratory, March 2003.
19. Arutunian S.G., Dobrovolski N.M., Mailian M.R., Vasiniuk I.E., “Vibrating wire scanner: first experimental results on the injector beam of Yerevan synchrotron,” Phys. Rev. Special Topics, Accelerators and Beams 6 (2003), 042801.
20. Arutunian S.G., Avetisyan A.E., Dobrovolski N.M., Mailian M.R., Vasiniuk I.E, Wittenburg K., Reetz R., “Problems of Installation of Vibrating Wire Scanners into Accelerator Vacuum Chamber,” Proc. 8th Europ. Part. Accel. Conf. (3-7 June 2002, Paris, France), pp. 1837-1839.
21. Arutunian S.G., Werner M., Wittenburg K., “Beam tail measurements by wire scanners at DESY,” ICFA Advanced Beam Dynamic Workshop: Beam HALO Dynamics, Diagnostics, and Collimation (HALO'03) (in conjunction with 3rd workshop on Beam-beam Interaction) (May 19-23, 2003 Gurney's Inn, Montauk, N.Y. USA).
22. Arutunian S.G., Bakshetyan K.G., Dobrovolski N.M., Mayilyan M.R., Oganessian V.A., Soghoyan A.E., Vasiniuk I.E., Wittenburg K., “Vibrating wire scanner parameters optimization.,” Proc. 9th Europ. Part. Accel. Conf. (5-9 July 2004, Lucerne, Switzerland), pp. 2457-2459.
23. Arutunian S.G., Bakshetyan K.G., DobrovolskiN.M., Mayilyan M.R., Oganessian V.A., Soghoyan A.E., Vasiniuk I.E., Wittenburg K., “Vibrating wire scanner parameters optimization,” Proc. 9th Europ. Part. Accel. Conf. (5-9 July 2004, Lucerne, Switzerland), pp. 2457-2459;
24. Aginian M.A., Arutunian S.G., Hovhannisyan V.A., Mailian M.R., Wittenburg K., “Vibrating wire scanner/monitor for photon beams with wide range of spectrum and intensity,” NATO Advanced Research Workshop on Advanced Photon Sources and Their Application (Nor Amberd, Armenia, August 29 - September 02, 2004)
25. Arutunian S.G., Dobrovolski N.M., Mailian M.R., Oganessian V.A., Vasiniuk I.E., “Nonselective receiver of laser radiation on the basis of vibrating wire,” Proc. Conference Laser 2000 (November 2000, Ashtarak, Armenia).
26. Aginian M.A., Arutunian S.G., Hovhannisyan V.A., Mailian M.R., Wittenburg K., “Vibrating wire scanner/monitor for photon beams with wide range of spectrum and intensity,” NATO Advanced Research Workshop on Advanced Photon Sources and Their Application" (Nor Amberd, Armenia, August 29 - September 02, 2004).
27. Aginian M.A., Arutunian S.G., Mailian M.R., “Vibration wire monitor for photon beams diagnostics: preliminary tests on laser beams,” NATO Advanced Research Workshop on Brilliant Light Facilities and Research in Life and Material Sciences, CANDLE (17-21 July, 2006 Yerevan, Armenia).
28. Decker G., Arutunian S., Mailian M., Rosenbaum G., “First vibrating wire monitor measurements of a hard x-ray undulator beam at the Advanced Photon Source,” DIPAC 2007.
29. B.K. Scheidt, DIPAC ’05, Lyon, France (2005).
30. Decker G., Arutunian S., Mailian M., Vasiniuk I., these proceeedings.

FUTURE ACCELERATOR CHALLENGES IN SUPPORT OF HIGH-ENERGY PHYSICS*

M. S. Zisman‡, LBNL, Berkeley, CA 94720 U.S.A.

Abstract

Historically, progress in high-energy physics has largely been determined by development of more capable particle accelerators. This trend continues today with the imminent commissioning of the Large Hadron Collider at CERN, and the worldwide development effort toward the International Linear Collider. Looking ahead, there are two scientific areas ripe for further exploration—the energy frontier and the precision frontier. To explore the energy frontier, two approaches toward multi-TeV beams are being studied, an electron-positron linear collider based on a novel two-beam powering system (CLIC), and a Muon Collider. Work on the precision frontier involves accelerators with very high intensity, including a Super-B Factory and a muon-based Neutrino Factory. Without question, one of the most promising approaches is the development of muon-beam accelerators. Such machines have very high scientific potential, and would substantially advance the state-of-the-art in accelerator design. The challenges of the new generation of accelerators, and how these can be accommodated in the accelerator design, are described. To reap their scientific benefits, all of these frontier accelerators will require sophisticated instrumentation to characterize the beam and control it with unprecedented precision.

INTRODUCTION

Scientific progress in high-energy physics has traditionally depended on advances in accelerator design. This trend has taken the community from the early electrostatic accelerators to cyclotrons, to synchro-cyclotrons, to synchrotrons, and finally to both circular and linear colliders. Achieving the full performance potential from each generation of accelerators requires corresponding advances in accelerator technology, including magnets, vacuum systems, RF systems, and instrumentation.

The critical scientific role played by accelerators is due to the fact that they permit the study of high-energy physics phenomena under (more or less) controlled conditions. However, the cost of today's proposed accelerator projects is high, and this has consequences for the community. Indeed, there is a danger at present of "pricing ourselves out of the market" if we are not conscious of costs in each aspect of the design. The practical way of mitigating project costs is to share the burden and, with this in mind, international cooperation and collaboration are key to our ability to successfully launch new projects.

*This work was supported by the Office of Science, U. S. Department of Energy, under Contract No. DE-AC02-05CH11231.

‡mszisman@lbl.gov

ACCELERATOR DELIVERABLES

Particle accelerators are designed to deliver two parameters to the HEP user—energy and luminosity. Of these, energy is by far the easier parameter to deliver, and the easier one to accommodate for the experimenters. Increased luminosity invariably presents a major challenge, not only to the accelerator builders but to the detector builders. Luminosity, L, is a measure of the collision rate per unit area and has dimensions of $\mathrm{cm}^{-2}\ \mathrm{s}^{-1}$. For a given event probability ("cross section"), σ, the event rate at a collider is given by $R = L\sigma$. For a collider having equal beam sizes at the collision point, luminosity is given by

$$L = \frac{N_1 N_2 f_c}{4\pi \sigma_x^* \sigma_y^*}, \qquad (1)$$

where N_1 and N_2 are the number of particles per bunch in beams 1 and 2, respectively, f_c is the collision frequency, and σ_x* and σ_y* are the horizontal and vertical rms beam sizes at the collision point, respectively. It is obvious from Eq. (1) that high luminosity demands intense beams and small beam sizes at the collision point.

PARTICLE PHYSICS QUESTIONS

In simple terms, there are two main thrusts of accelerator-based high-energy physics. The first of these, corresponding to experiments at the energy frontier, is to understand the origins of mass, that is, the mechanism that gives existing particles their widely different masses. Recent experiments [1] have shown the mass of the top quark to be comparable to that of a gold nucleus, whereas a neutrino mass (thought for a long time to be exactly zero) is likely to be only a fraction of an eV.

The second main thrust is understanding why we live in a matter-dominated universe. This is a quite fundamental question, as it basically addresses our very existence. It is believed that the Big Bang initially created equal amounts of matter and antimatter, yet these did not all annihilate. The survival of matter is related to differences in the reaction rates of particles and antiparticles, referred to as charge-conjugation–parity (CP) violation. CP violation has long been known in the quark sector [2], and two "B Factories" [3, 4] were built to study this phenomenon. Unfortunately, it turns out that CP violation in the quark sector is not enough to explain the observed baryon asymmetry in the universe. The prevalent view is that the additional CP violation needed occurs in the lepton sector. While this has never been observed, neutrinos are considered the hunting ground for finding it.

TODAY'S MACHINES

High-energy physics experiments typically make use of colliders, where counter-propagating beams collide at one or more interaction points ("IPs"). Until recently, colliders were single-ring devices that collided beams of particles and antiparticles, such as e^- and e^+. However, to get higher intensities and more bunches, modern colliders use two independent rings, and so no longer require the colliding beams to have equal momenta or opposite sign. Colliders are categorized based on the type of particles they utilize. Hadron colliders, exemplified by the Tevatron ($p - \bar{p}$), LHC (p –p), and RHIC (heavy ions, for nuclear physics), use protons or heavier ions. Lepton colliders, exemplified by CESR-c, PEP-II, and KEKB, all use electrons and positrons.

Hadron Collider Limitations

The main limitation associated with hadron colliders is that they are colliding composite particles. This means that only about 10% of the collision energy is actually available for the hard collisions that lead to new particles. To probe the 1 TeV mass scale, a hadron collider requires a collision energy of order 10 TeV. Such high beam energy has the disadvantage of requiring very strong magnets to store and focus the beams in a reasonable-sized ring. When using antiprotons, there is another disadvantage—these particles are difficult to produce, and it takes many hours to replace them if the beam is unexpectedly lost. The demand for high luminosity led to the LHC choosing a configuration with two separate rings, each containing many proton bunches, that are brought together at a few select locations. This configuration bypasses the antiproton production limitation, but not the other issues.

Lepton Collider Limitations

For these machines, synchrotron radiation emission is the biggest issue. In a circular machine, the emitted power is given by

$$P_{SR} = \frac{88.5\, E^4\, I}{\rho} \qquad (2)$$

where E is the beam energy in GeV, I is the beam current in A, and ρ is the bending radius in the ring dipoles, in m. An electron-positron collider in the LHC tunnel with 1 mA of circulating current would radiate roughly 2 GW of synchrotron radiation power into the vacuum chamber walls, and would require this amount of power to be restored by its RF system. This is a daunting requirement, to say the least.

For this reason, the high-energy e^-e^+ colliders on the drawing boards now (ILC [5] and CLIC [6]) are conceived as linear colliders. At a length of 31 km for ILC and 48 km for CLIC, these designs have the drawback of being too large to fit on any existing laboratory site. Furthermore, the single-pass acceleration scheme is relatively inefficient, because there is no reuse of expensive RF hardware. Despite such drawbacks, a linear collider is the only practical approach to an e^-e^+ collider in the TeV energy range.

Luminosity Performance

Electron-positron colliders have made great strides in delivering luminosity in recent years. In particular, as shown in Fig. 1, both KEKB and PEP-II quickly reached luminosities beyond 1×10^{34} cm^{-2} s^{-1}. It is likely that the performance of future machines will be judged according to this new standard.

FUTURE MACHINES

At present, there are several machines on the drawing board to address the high-priority questions of high-energy physics. For the precision frontier, there are three candidates: ILC, a muon-beam-based Neutrino Factory, and an e^-e^+ Super-B Factory. Candidate energy frontier machines include CLIC and a Muon Collider. Not all of the machines are at the same stage of development; ILC and CLIC are probably furthest along in terms of R&D progress.

In what follows, we will briefly discuss these machine designs and the R&D programs that support them. For reasons of personal taste and familiarity, the emphasis here will be on the muon-based accelerators. Although these are not the most advanced designs, they are undoubtedly the most novel.

Muon Accelerator Advantages

In contrast with other technologies, muon beam accelerators have the ability to address both of the physics questions discussed earlier.

For the neutrino experiments, the stored muon beam produces neutrinos as indicated in Eq. (3).

$$\mu^+ \rightarrow e^+ \nu_e \bar{\nu}_\mu \qquad (3a)$$

$$\mu^- \rightarrow e^- \bar{\nu}_e \nu_\mu \qquad (3b)$$

The decay kinematics is well understood, and there are minimal hadronic uncertainties in either the spectrum or the flux. Moreover, $\nu_e \rightarrow \nu_\mu$ oscillations result in "wrong sign" muons, which are easily observed in the detector.

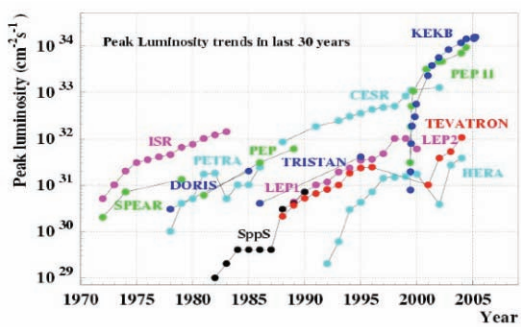

Figure 1: Peak luminosity trends. Both KEKB and PEP-II reached high luminosity much more quickly than any previous generation of collider.

For energy frontier experiments at a Muon Collider, the fact that muons are point particles makes the full center-of-mass energy available to produce new particles. Because the muon is much heavier than the electron, it produces negligible synchrotron radiation. Compared with an electron-positron collider, a Muon Collider has a reduced energy spread due to "beamstrahlung" and can be designed as a circular facility that fits on existing laboratory sites (see, e.g., Fig. 2).

Muon Beam Challenges

There are two major challenges associated with a muon beam accelerator. Firstly, muons are created as a tertiary beam, via the process p + target → π → μ. This process results in a relatively low production rate, so achieving the desired muon intensity requires a very intense proton beam, nominally 4 MW. Finding a target material that can tolerate such a beam intensity is not easy. Moreover, the decay process produces a muon beam with a very large transverse phase space and large energy spread. Handling this beam is difficult with standard quadrupole focusing devices, so strong, large-aperture solenoids are used to focus in both planes simultaneously. A rapid means to decrease the large transverse emittance is required and, even so, a large acceptance acceleration system and decay ring are needed.

Secondly, muons have a very short lifetime, only 2.2 μs at rest. Obviously, the short lifetime puts a high premium on rapid beam manipulations. Reducing the beam emittance requires the presently untested technique of "ionization cooling." This technique, described below, makes use of high-gradient RF cavities immersed in a strong solenoidal field—a configuration that has turned out to make it difficult to achieve high gradients.

Thirdly, the decay electrons produced give difficulties. In a Neutrino Factory, they create a substantial heat load in the midplane of the decay ring dipoles, and in a Muon Collider they give rise to substantial background in the detector.

For all these reasons, muon beams are difficult to produce and manipulate, and will make the accelerator designers work hard to obtain their obvious benefits.

Figure 2: Schematic layout of 1.5–4 TeV Muon Collider on the Fermilab site.

Ionization Cooling

Because ionization cooling plays a critical role in muon beam facilities, we describe the concept briefly here. Ionization cooling is analogous to the more familiar process of synchrotron radiation damping in an electron storage ring. In each case, there is an energy loss mechanism that reduces p_x, p_y, and p_z, along with an energy gain mechanism that restores only p_z. Repeated application of the process reduces p_x/p_z and p_y/p_z, and thus decreases the 4D emittance. In the electron case, the energy loss mechanism is synchrotron radiation emission, whereas for muons it is energy loss (dE/dx) in low-Z material. The energy gain mechanism, in both cases, is RF acceleration in the longitudinal (z) direction. Figure 3 illustrates schematically the ionization cooling concept.

For both electrons and muons, there is also a heating term. For electrons it is quantum excitation, whereas for muons it is multiple scattering in the absorber material. The balance between cooling and heating leads to an equilibrium emittance, given approximately by:

$$\varepsilon_{x,N,equil.} = \frac{\beta_\perp (0.014\,\mathrm{GeV})^2}{2\beta\, m_\mu X_0 \left|\frac{dE_\mu}{dx}\right|} \qquad (4)$$

where $\beta_\perp$ is the beta function at the absorber location, β is the relativistic velocity, m_μ is the muon mass, X_0 is the radiation length and dE_μ/dx the rate of muon ionization energy loss in the absorber material. Looking at Eq. (4), we see that a low equilibrium emittance results from a low $\beta_\perp$, large radiation length and large energy loss. This implies that hydrogen, though far from convenient, is the best absorber material.

ACCELERATOR DESCRIPTIONS

ILC

The ILC [5] is aimed at the 0.5–1 TeV energy range, with an initial energy of 0.5 TeV. As shown in Fig. 4, it comprises two superconducting main linacs, electron and positron sources, and a central complex with two damping rings. The damping rings must provide beams with a 2 pm-rad vertical emittance.

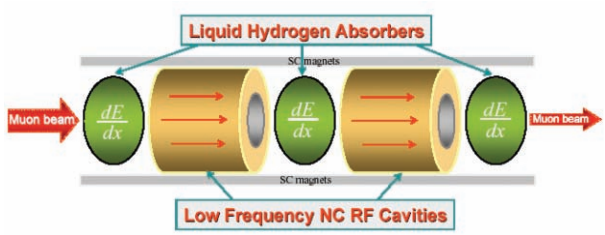

Figure 3: Schematic diagram of an ionization cooling channel. The best absorber material to use is liquid hydrogen. Its proximity to the RF cavities is an engineering challenge, as this represents a potential safety hazard if not implemented properly.

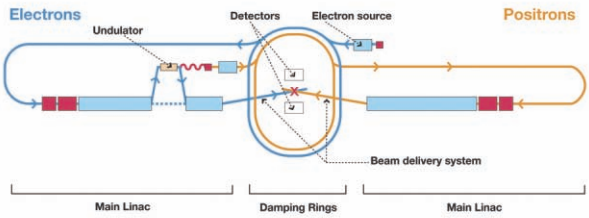

Figure 4: Layout of ILC facility. Its footprint is 31 km in length.

The design effort has been ongoing for a number of years, so the facility design is reasonably well defined. The main technical challenges for the design, which will be covered below, include reaching the specified gradient for the production cryomodules of 31.5 MV/m and obtaining the very low vertical emittance required by the linac.

Neutrino Factory

A schematic diagram of a Neutrino Factory [7, 8, 9] is shown in Fig. 5. It comprises many different systems. First, there is a proton driver capable of providing 4 MW of proton beam on a production target. The target—a free Hg jet immersed in a 20-T solenoid—is dispersed by the beam but "remade" by the time the next proton pulse arrives. A tapered solenoid channel captures the pions and the muons into which they decay.

The capture section is followed by a bunching and phase rotation section, where the muons are bunched into 201-MHz RF buckets and phase rotated in longitudinal phase space to transform the initial bunch having a small time duration and a large energy spread into a bunch train with a long time duration and smaller energy spread. The phase-rotated bunch train, with a mean momentum of about 200 MeV/c, is then cooled transversely in a cooling channel.

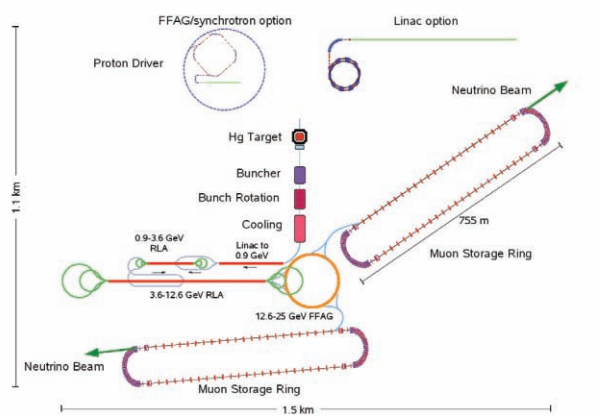

Figure 5: Schematic of a Neutrino Factory facility. Two separate decay rings are shown to permit simultaneous operation at detector baselines of 3000 km and 7500 km, respectively.

After cooling, the beam is accelerated to its working energy of a few tens of GeV using a linac, a pair of dog-bone recirculating linear accelerators (RLAs), and finally one or more fixed-field, alternating gradient (FFAG) accelerators. The last element is a decay ring with a long straight section aimed at a detector located 3000–7500 km from the ring.

Super-B Factory

The goal of this e^-e^+ collider facility is to greatly improve on the data sample at the Y(4S) resonance accumulated by the original B Factories [3, 4]. To do so, it aims at a peak luminosity of $\sim 1 \times 10^{36}$ cm^{-2} s^{-1}. The proposed design [10] involves two rings, with a single interaction region. The interaction region is designed to use a new approach, the "crab waist," to substantially reduce the effective beam size at the interaction point. The beams collide at a large crossing angle (see Fig. 6), but the overlap region is short in the *z* direction, permitting a low beta function without requiring a correspondingly short bunch length A pair of sextupoles in each ring is used to suppress synchro-betatron resonances. The likely site for the facility is Frascati, and their plan is to reuse most of the PEP-II components to reduce costs.

CLIC

CLIC [6] is an e^-e^+ linear collider designed to reach 3 TeV collision energy. It has a novel two-beam powering concept, as indicated in Fig. 7. A low-energy drive beam is created and then sent through passive structures that extract microwave energy at high frequency to power a second beam, with lower intensity but much higher energy. Using room-temperature accelerating structures for the main linac, the design goal is to operate at a gradient of 100 MV/m, some three times higher than that used in the ILC. The footprint of this machine, 48 km, is somewhat larger than that of ILC, but it is designed to operate at six times higher energy than ILC.

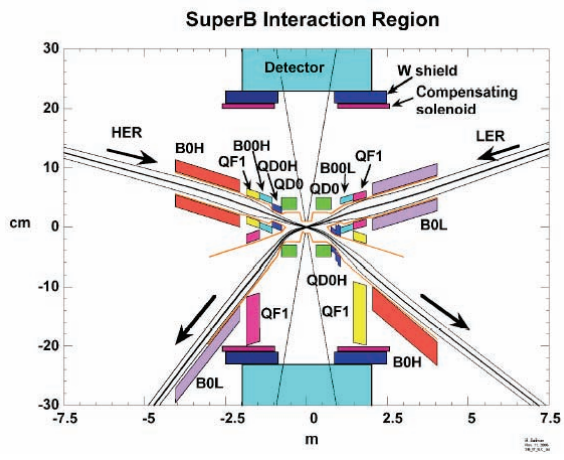

Figure 6: Anamorphic diagram of the Super-B Factory interaction region. The two beams cross at an angle of ±25 mrad. Note the substantial number of ring magnets that sit within the detector volume.

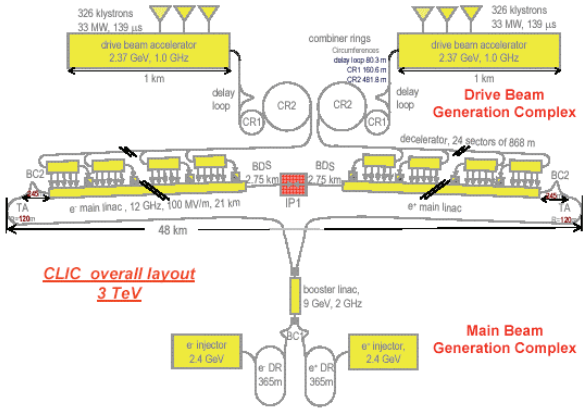

Figure 7: Schematic diagram of CLIC complex, showing drive beam generation system and main linacs.

Muon Collider

A scheme for a Muon Collider that would fit on the Fermilab site is shown in Fig. 8. The concept is based on using the existing Recycler and Main Ring at Fermilab, fed with protons from the Project X linac [11]. The early portion of the facility is essentially the same as that described above for a Neutrino Factory.

However, for a Muon Collider, the 4D cooling process described earlier is not sufficient to prepare the desired beam. The beam must be cooled in all six dimensions, that is, longitudinal as well as transverse. The concept of 6D cooling is shown in Fig. 9.

R&D ACTIVITIES

All of the potential projects described above have embarked on R&D activities to prove the physics concepts, validate technology choices, and develop realistic, defensible cost estimates. The choices for what must be studied can be complicated, as there are many "audiences" for the results and they do not all have the same concerns. These audiences include:

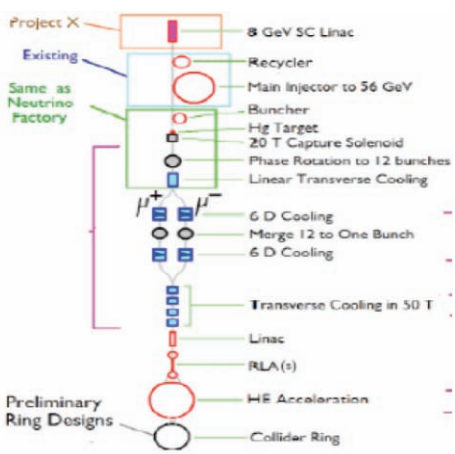

Figure 8: Muon Collider schematic. After the initial cooling section, the beam is split, cooled longitudinally, and then recombined for more transverse cooling. The final cooling stage makes use of extremely high field solenoids, up to 50 T.

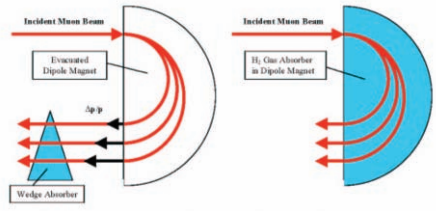

Figure 9: Schematic approaches to longitudinal cooling. On the left, a magnet creates dispersion so there is a correlation between horizontal position and momentum. The beam then passes through a wedge-shaped absorber such that low-energy particles have reduced energy loss compared with high-energy ones. On the right, the magnet is filled with a gaseous absorbing medium. Higher energy particles have a longer path length and hence experience more energy loss than do low-energy particles.

- project advocates
- the HEP community
- laboratory directors (at least one)
- funding agencies or governments (at least one)

Although it is not possible here to do justice to the large volume of R&D work in progress throughout the world, an attempt will be made in what follows to give a flavor of the R&D that is under way.

ILC

An noted earlier, a primary thrust of this program is to demonstrate that the cryomodule design gradient of 31.5 MV/m can be reached reliably in a production setting. Figure 10 shows results from a number of recent cryomodule tests. The trend is clearly headed in the right direction, but there remains work to be done. Because a large number of cryomodules must be built, the ability to demonstrate reproducibility is mandatory, and this requires a substantial, and thus expensive, production run.

Another technical concern for the ILC is the effects of the electron-cloud instability on the vertical beam emittance in the positron damping ring. Such concerns initially prompted a design with two positron damping rings (each with half the current). For cost reasons, this approach was eventually abandoned in favor of a single ring with appropriate mitigating features. Both clearing electrodes and "grooved" chambers (see Fig. 11) have been proposed and are being tested. Simulations indicate that solutions can be found, and plans for a detailed test program at Cornell (denoted "CESR-TA") are well along.

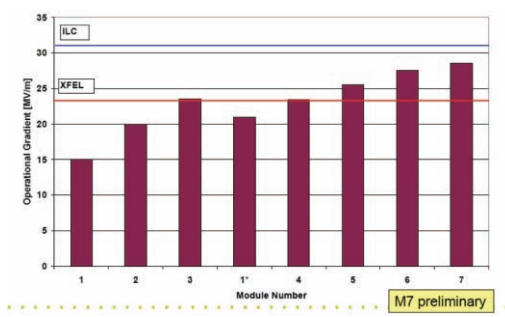

Figure 10: Recent results for ILC cryomodule gradients.

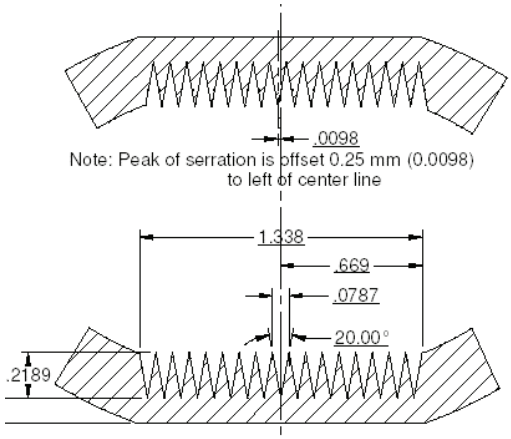

Figure 11: Grooved chamber approach to suppress e-cloud effects. Simulations indicate that the suppression is very effective if the sides of the grooves are steep. Unfortunately, this geometry is unattractive from an impedance perspective and trade-off studies must be made.

CLIC

The primary effort for CLIC is to demonstrate the feasibility of its two-beam technology and estimate its cost. The third generation of a CLIC test facility, CTF3, is now available at CERN, the injection portion of which is shown in Fig. 12. While centered at CERN, there are presently 19 countries represented in the CLIC R&D effort. There is technical coordination with the ILC program on areas of common interest, such as the damping ring instability referred to above.

Another key area of R&D is the study of high-gradient effects on the CLIC room-temperature RF structures. When using irises made from “hard” materials like Mo or W, gradients up to 190 MV/m have been reached. The limit, however, is the breakdown rate, which is specified to be below 10^{-6}. As shown in Fig. 13, to achieve acceptable breakdown rates, the gradient must be reduced substantially, which makes the distinction between harder materials and copper start to disappear. Moreover, the apparent gain in gradient performance at high frequencies also tends to disappear if one compares the performance at the same breakdown rate. This conclusion has led to the CLIC design frequency being reduced from 30 GHz to 12 GHz, which permits taking advantage of much of the work done at SLAC in support of the NLC design [12].

Super-B Factory

There are two primary questions to answer for this project:

- Does the crab waist scheme work as expected?
- Can the IP beta functions be made low enough to get a hundred-fold increase in luminosity with reasonable beam currents?

Tests of the crab waist scheme are getting under way now at DAΦNE to determine this. These tests have required significant modifications of the ring design, as shown in Fig. 14. Thus far, the results are encouraging. The beneficial effects of the crab waist sextupoles can clearly be seen in both reducing the beam size and increasing the luminosity.

Figure 12: Injection system for CTF3 facility at CERN.

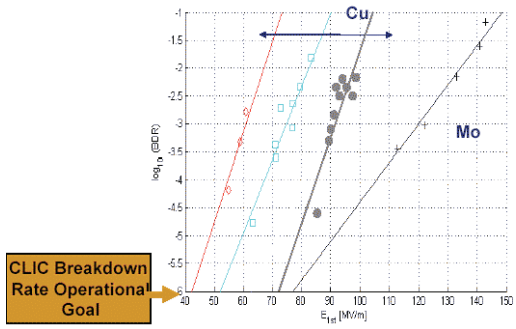

Figure 13: Breakdown rates (log scale) for several materials as a function of applied gradient. Although high gradients can be reached with a hard material like Mo, the breakdown rate is unacceptable for CLIC operation unless the gradient is substantially reduced, at which point Cu and Mo are no longer very different.

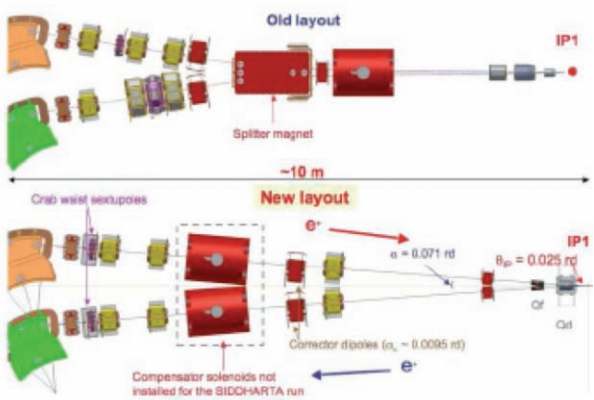

Figure 14: (top) Original layout of the DAΦNE ring, where the two beams collided head-on. (bottom) New layout for testing large crossing angle configuration, including crab waist sextupoles.

Muon Beam Program

There is a broad program under way worldwide to study the issues related to developing an intense muon beam facility. In large measure, the R&D program at this stage applies equally to a Neutrino Factory or a Muon Collider, so there is no need to make a distinction. In Europe, the work is supported by the BENE network and the UKNF program. In Japan, the NuFact-J group, supported by several universities and sometimes U.S.-Japan funds, has been active. In the U.S., the work is supported by the Neutrino Factory and Muon Collider Collaboration (NFMCC), augmented recently by effort from Fermilab's Muon Collider Task Force (MCTF).

Much of the work is being done by international collaborations involving participants from all these regions. These include:

- MERIT (beam test of a mercury-jet target in a 15 T solenoidal field at CERN) [13]
- MICE (muon ionization cooling demonstration at Rutherford Appleton Laboratory (RAL)) [14]
- EMMA (non-scaling FFAG demonstration at Daresbury Laboratory) [15]
- IDS-NF (international Neutrino Factory design study) [16]

In addition, there is component R&D under way aimed at development of suitable muon beam RF cavities and LH_2 absorbers.

The main component R&D at present involves the study of RF breakdown in a magnetic field. Interest in this is motivated by the NFMCC results for an 805-MHz test cavity, shown in Fig. 15. Although the cavity reached 40 MV/m in the absence of a magnetic field, the maximum gradient decreased markedly when an axial solenoidal field was applied. The effect is believed to be related to focusing the dark currents tightly enough to do damage to copper surfaces when the field is applied.

As the actual cooling channel design calls for 201-MHz cavities, a prototype has been built (see Fig. 16) at this frequency. The plan is to first test it in the fringe field of an existing solenoid at Fermilab, and then to test it with a more realistic field from a large diameter coupling coil identical to those to be used in MICE. In tests without magnetic field, the cavity easily reached 19 MV/m, limited only by the power of the RF amplifier tube.

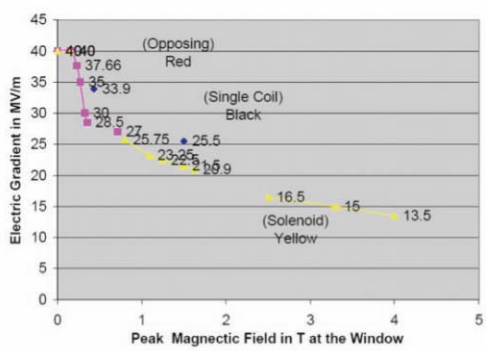

Figure 15: Degradation in achievable gradient *vs.* applied solenoidal field for an 805-MHz test cavity.

Figure 16: 201-MHz MICE prototype cavity installed in the MuCool Test Area at Fermilab.

The MERIT experiment [13] was designed to test the behavior of a mercury-jet target under realistic conditions. The experiment was carried out in October, 2007 using 24 and 14 GeV proton beams from the CERN PS. Figure 17 shows a diagram of the system and Fig. 18 shows the actual hardware being installed in the TT2A tunnel at CERN. Although the data are still being analyzed, preliminary indications are that the technology will work well at a beam power in excess of 4 MW and a proton beam repetition rate in excess of 50 Hz.

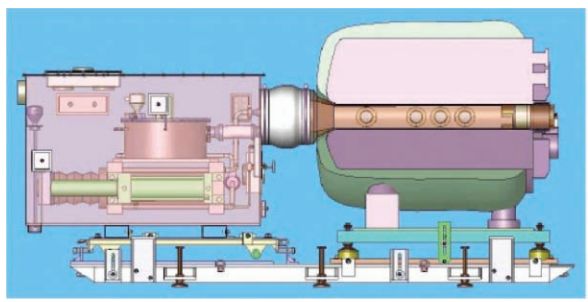

Figure 17: Drawing of the MERIT apparatus. The box on the left contains the Hg syringe pump, which creates a jet of Hg in the vessel within the solenoid on the right. Beam enters the apparatus from the right, so the jet pipe makes a 180° turn to aim along the beam direction. Optical diagnostics determine the effects of the beam on the jet.

Figure 18: MERIT apparatus being installed at CERN.

The international Muon Ionization Cooling Experiment (MICE) [14] is intended to demonstrate, for the first time, the process of ionization cooling of a muon beam. The layout of the experiment is shown in Fig. 19. The experiment uses the single-particle counting techniques of particle physics experiments to measure the incoming and outgoing emittance of each muon. Over the next several years, the experiment will test beams having a range of incoming emittance values and momenta. An important goal of this work is to validate the simulation tools used to estimate cooling channel performance. These tools will ultimately be used to design a facility and estimate its performance.

One of the challenges of MICE will be to operate liquid-hydrogen absorbers in close proximity to high-power RF cavities. With this in mind, safety has been a design criterion from the outset. There have already been two international reviews of the safety aspects of the experiment, and the RAL safety group has been kept in close contact with both the design and the R&D efforts.

There are some 140 scientists and engineers from Europe, Asia, and the U.S. collaborating on the experiment. Commissioning of the muon beam line, along with some of the upstream detectors, has recently gotten under way. The first pions were detected in the beam line in early April 2008. This beam was produced by operating a plunging Ti target in the halo of the ISIS synchrotron beam at a rate of roughly 1 Hz. Losses in ISIS must be kept to a minimum in order to keep radiation levels low enough for hands-on maintenance.

SUMMARY

In this paper, we have seen that HEP facilities now in the planning stage offer great potential to address the key outstanding questions in our field. There is little doubt that such new facilities will raise new questions as well. R&D toward the design of these new facilities is progressing on many fronts. While not all of these machines will be built, the work being done provides the HEP community and the funding agencies with the technical input needed to make good decisions about what should be done.

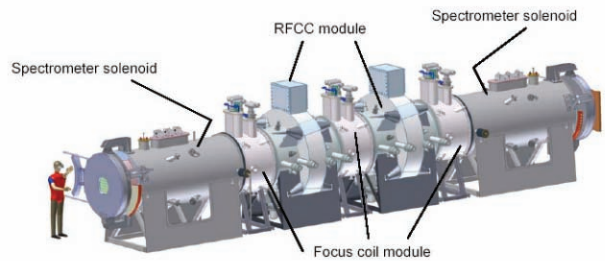

Figure 19: The MICE cooling channel. Spectrometer solenoids upstream and downstream house scintillating fiber tracker detectors to measure emittance before and after the cooling channel. Between the two spectrometers is one full cell of a cooling channel, comprising three focus coil modules housing liquid-hydrogen absorbers and two RF–coupling-coil (RFCC) modules.

As with all accelerator R&D, success will depend on a synergy between accelerator physics and accelerator technology. In particular, control of instabilities and emittance will require state-of-the-art instrumentation. The skills of the instrumentation designers and builders will undoubtedly be crucial to turning the accelerator physicists' dreams into the cutting edge scientific tools of the future.

From the U.S. perspective, going forward with Project X at Fermilab is a necessary step to provide for the long-term future. This accelerator provides scientific capability for carrying out improved neutrino experiments and paves the way for future muon-beam facilities. The technology being developed and used will also provide valuable technical information in support of ILC construction, should that be the eventual choice of the community.

REFERENCES

[1] Tevatron Electroweak Working Group, http://arxiv.org/abs/0803.1683.

[2] J. H. Christenson, J.W. Cronin, V. L. Fitch, and R. Turlay, "Evidence for the 2π decay of the K_2^0 meson," *Phys. Rev. Lett.*, vol 13, pp. 138–140, Jul. 1964.

[3] M. S. Zisman (ed.), "PEP-II, an Asymmetric B Factory, Conceptual Design Report," LBL-PUB-5379, SLAC-418, CALT-68-1869, UCRL-ID-114055, UC-IIRPA-93-01, June, 1993.

[4] S. Kurokawa and K. Oide (eds.), "KEKB B-Factory Design Report," KEK report 95-7, June 1995.

[5] N. Phinney, N. Toge, and N. Walker (eds.), "ILC Reference Design Report," see http://ilcdoc.linearcollider.org/getfile.py?docid=182&name=ILC_RDR_Volume_3-Accelerator&format=pdf.

[6] G. Guignard (ed.), "A 3 TeV e^+e^- Linear Collider Based on CLIC Technology," CERN 2000-008, see http://doc.cern.ch/yellowrep/2000/2000-008/p1.pdf.

[7] N. Holtkamp and D. Finley (eds.), "A Feasibility Study of a Neutrino Source Based on a Muon Storage Ring," Fermilab Pub-00/108E, see: http://www.fnal.gov/projects/muon_collider/nu-factory/ fermi_study_after_april1st/.
[8] S. Ozaki, R. Palmer, M. Zisman, and J. Gallardo (eds.), "Feasibility Study-II of a Muon-based Neutrino Source," BNL-52623, June, 2001, see http://www.cap.bnl.gov/mumu/studyii/final_ draft/The-Report.pdf.
[9] J. S. Berg *et al.*, "Cost-effective Design for a Neutrino Factory," Phys. Rev. Special Topics-AB, vol. 9, 011001 (2006).
[10] M. Bona *et al.*, http://arxiv.org/abs/0709.0451
[11] D. McGinnis (ed.), "Accelerator Issues of Project X," http://projectx.fnal.gov/AACReview/ProjectXAacReport.pdf.
[12] NLC Design Group, "Zeroth-Order Design Report for the Next Linear Collider," LBNL-5424, SLAC-474, UCRL-ID-124161, UC-414, see http://www.slac.stanford.edu/accel/nlc/zdr/
[13] H. G. Kirk *et al.*, "A High-Power Target Experiment at the CERN PS," in Proc. 2007 Particle Accelerator Conf., Albuquerque, June 25–29, 2007, pp. 646–648.
[14] P. Drumm (ed.), "MICE: an International Muon Ionization Cooling Experiment, Technical Design Report, see http://www.isis.rl.ac.uk/accelerator/MICE/TR/MICE_Tech_ref.html.
[15] R. Edgecock, "EMMA—the World's First Non-scaling FFAG," in Proc. 2007 Particle Accelerator Conf., Albuquerque, June 25–29, 2007, pp. 2624–2626.
[16] See https://www.ids-nf.org/wiki/FrontPage.

BEAM MEASUREMENTS AT LCLS*

J. Frisch, R. Akre, F.-J. Decker, Y. Ding, D. Dowell, P. Emma, S. Gilevich, G. Hays, Ph. Hering, Z. Huang, R. Iverson, R. Johnson, C. Limborg-Deprey, H. Loos, E. Medvedko, A. Miahnahri, H.-D. Nuhn, D. Ratner, S. Smith, J. Turner, J. Welch, W. White, J. Wu, Stanford Linear Accelerator Center, Menlo Park CA 94025, U.S.A

Abstract

The LCLS accelerator is presently in a commissioning phase[1] and produces a 14GeV beam with normalized emittances on the order of one mm-mr, and peak current exceeding 3000 Amps. The design of the beam measurement system relies heavily on optical transition radiation profile monitors, in conjunction with transverse RF cavities, and conventional energy spectrometers. It has been found that the high peak currents and small longitudinal phase space of the beam generate strong coherent optical emission that limits the quantitative use of OTR and other prompt optical diagnostics, requiring the use of wire scanners or fluorescent screen based measurements. We present the results of beam measurements, measurements of the coherent optical effects, and future plans for the diagnostics.

LCLS ACCELERATOR

The Linac Coherent Light Source is a SASE Free Electron Laser, designed to produce X-rays with wavelengths down to 1.5 Angstroms, using electron beam energies up to 13.6 GeV.

Table 1: Accelerator Design Specifications

Energy	4.3 to 13.6 GeV
Bunch Charge	200 pC to 1 nC
Design emittance	~ 1.2 mm-mr slice
Peak current	~ 3.4 KA.
Repetition rate	120Hz, single pulse

An accelerator layout with beam parameters is given in figure 1.

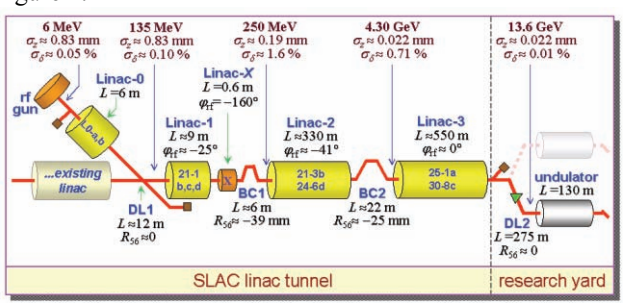

Figure 1: Accelerator layout.

Linac-2 and Linac-3 are only slightly modified from their configuration for the SLC [2]. The remainder of the machine is new, though it makes use of some old SLAC accelerator structures and magnets. As of April 2008, the beam is accelerated to the end of Linac-3 with nominal parameters, except that the repetition rate is presently limited to 30 Hz during commissioning.

BEAM DIAGNOSTICS AND MEASUREMENTS

The LCLS design relies heavily on beam-based control and feedback, necessitating the use of a variety of beam measurement devices:

- Position: Stripline BPMs
- Charge: BPMs, Toroids, Faraday Cups
- Beam Loss: Ion chambers and PMTs
- Profile: Wire Scanners, Optical Transition Radiation monitors, and fluorescent screens
- Emittance: Multiple profile monitors, or Quadrupole magnet gradient scans on a single profile monitor.
- Longitudinal Measurements: Spectrometers, Millimeter wave bunch length monitors, Transverse RF deflection cavities.

Beam Position Monitors

The LCLS injector, and a few locations along the Linac use self-calibrating strip-line BPMS based on digital down conversion: figure 2.

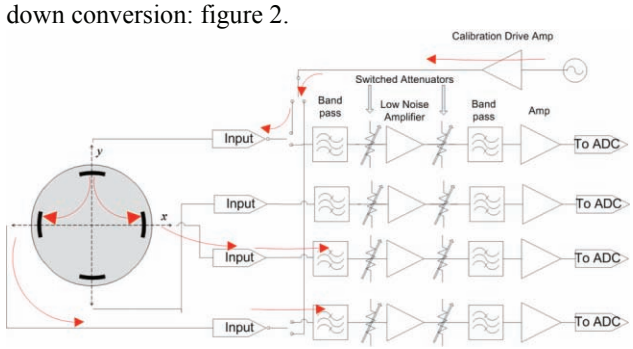

Figure 2: BPM Electronics

The BPMS operate at a center frequency of 140MHz, with a 7 MHz bandwidth. On every pulse, a tone burst is injected onto one strip, and the coupling to the perpendicular strips is measured. This corrects for gain changes in the readout channels and cables. [3]

The BPM noise is measured by performing a linear regression between the BPM under test, and the other BPMS in the accelerator, with the residual indicating the position noise, figure 3.

*Work supported by DOE Contract DE-AC02-76SF00515

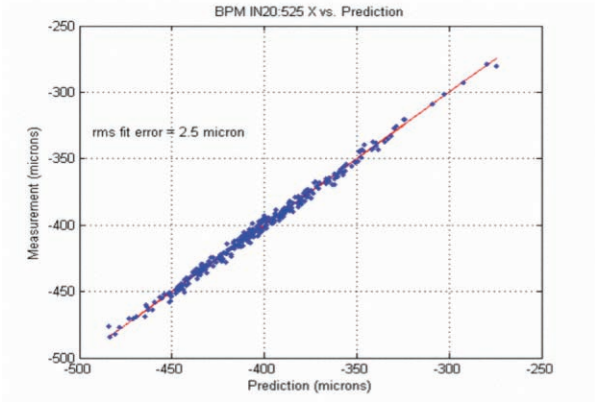

Figure 3, Example BPM noise measurement (at 350 pC) with 2.5 micron resolution demonstrated.

At 200pC, the BPMs meet the 5 micron RMS noise specification, with typical noise of 3 microns. Figure 4 shows the X and Y beam positions after BC1, measured over 24 hours. Note that the regular jumps are beam measurements. The beam motion is approximately 15 microns RMS at a location where the beam size is typically 50 microns RMS.

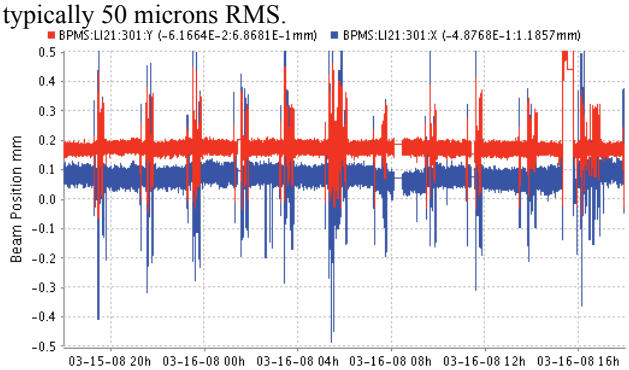

Figure 4, Beam position stability over 24 hours

Beam Charge Measurement

The LCLS BPMs provide a low noise ($7x10^{-4}$ RMS) relative beam charge measurement, but do not provide an absolute calibration. Absolute calibration is done using toroids in the LCLS injector, and existing (independently calibrated) toroids in the SLAC beam switchyard at 13.6 GeV. The two types of toroids agree within 5%.

The LCLS injector has 2 faraday cups at the 6MeV gun energy, with one in the straight-ahead line and one in the gun spectrometer. These faraday cups give a calibration that is 40% lower than observed with the toroids. These faraday "cups" are actually plates, and it is possible that a large amount of secondary electrons are lost, however the calibration error is not yet understood.

Beam Loss Measurement

The LCLS accelerator is designed to operate with minimal beam loss. The single pulse intensity is below the damage threshold for the accelerator; however average beam loss monitors are used to disable the beam to reduce the possibility of activation and electronics damage. Under normal conditions the beam loss is below the measurement limit of a few percent.

Beam Profile Measurement

The LCLS uses 3 different diagnostics for beam transverse profile measurement:

- Fluorescent Screens: These have good sensitivity, but saturate at high intensities (>~0.04pC/um^2) [4]. They are used in the LCLS injector at 135 MeV and lower energies.
- Wire Scanners: These have good resolution, and measurements are nearly non-invasive. However they only provide multi-pulse averaged, integrated profiles, and require long measurement times. Wire scanners are used in the LCLS energies of 135 MeV and above.
- Optical Transition Radiation Monitors: These have good resolution and linearity. OTR monitors are installed in the LCLS at 135MeV and higher energies, however, coherent optical effects prevent their quantitative use after the first bunch compressor.

Fluorescent Screens

The LCLS fluorescent screens use Ce:YAG crystals, 100 microns thick, oriented normal to the beam. 45 degree mirrors are located behind the crystals to reflect the light into cameras. This provides approximately 50 micron resolution.

The gun solenoid can be adjusted to image the cathode to the second YAG screen, located just before Linac-0. A mask placed at an image point in the drive laser beam, can produced a pattern on the cathode, and this will be imaged on the YAG screen. Figure 5 shows an electron beam image of a "LCLS" mask, at 6MeV. Imaging is performed at low currents ~30 pC.

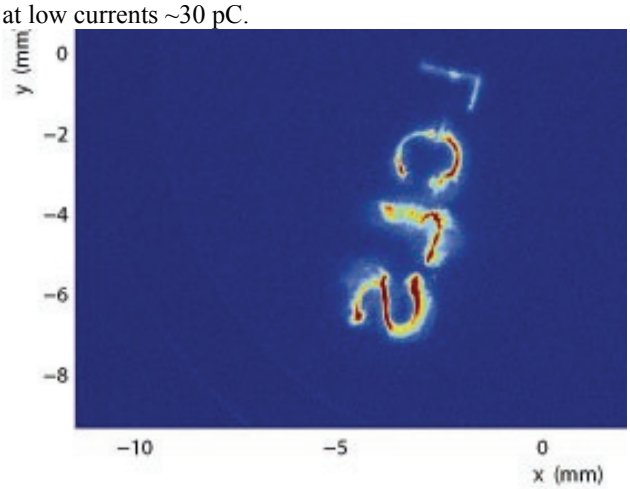

Figure 5, "LCLS" mask imaged onto YAG screen.

The imaging technique has proven useful for measuring the quantum efficiency of the cathode as a function of position. Typical quantum efficiencies are $5x10^{-5}$ at the nominal laser wavelength of 252nm. A cathode image is shown in figure 6 for 1.6mm diameter laser illumination.

Features in the emission pattern with a resolution of approximately 10 microns are observed.

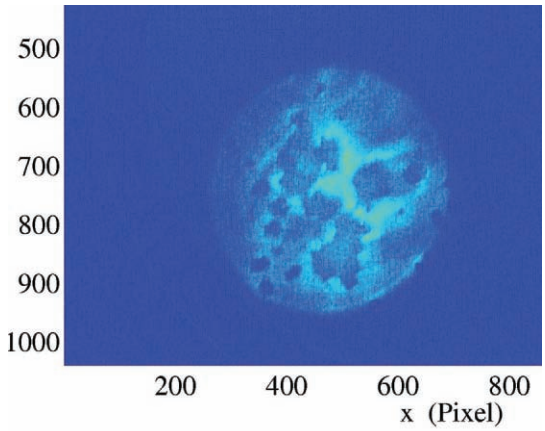

Figure 6. Electron beam cathode image with 1.6-mm spot diameter on the cathode

Wire Scanners

The LCLS wire scanners use 20-micron Tungsten wires driven by a stepper motor / leadscrew actuator. Scattered electrons are detected downstream by scintillators.

Initially the wire scanners used direct drive, with a step size of 5 microns. The wire vibration was found to be unacceptable and 10X gear reducers were added, reducing the vibration, but decreasing the maximum scan speed. With the reducers, the step size is now 0.5 microns. Figure 7,8 show a wire scan at 135MeV before and after the addition of the reduction gears.

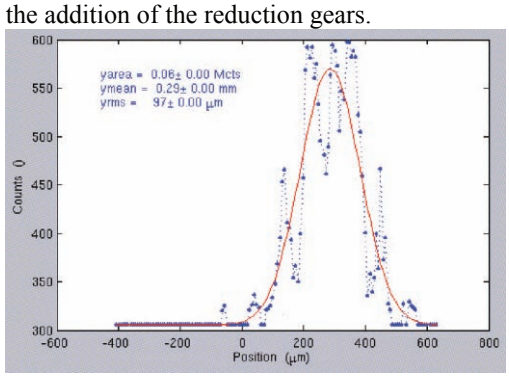

Figure 7. Wire scan at 135MeV

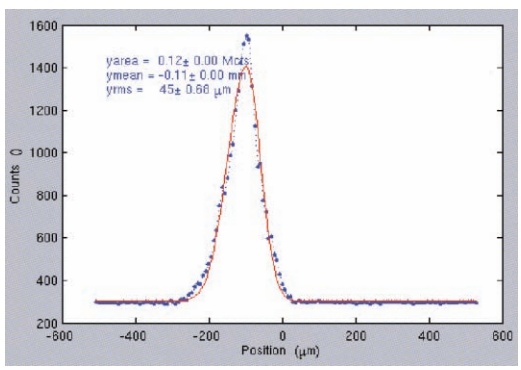

Figure 8. Wire scan at 135 MeV with 10X gear reducer added.

When wire scan or profile monitor data is used to provided a beam size, some fitting algorithm must be used to extract the RMS beam size. LCLS data analysis and emittance measurements use an asymmetric Gaussian fit, for the wire-scans, however results from other fit methods are recorded as well. Note that a choice of fit method can significantly change the measured beam size. Figure 9 shows an asymmetric Gaussian fitted to a beam with transverse tails (at 250 MeV, after the first bunch compressor).

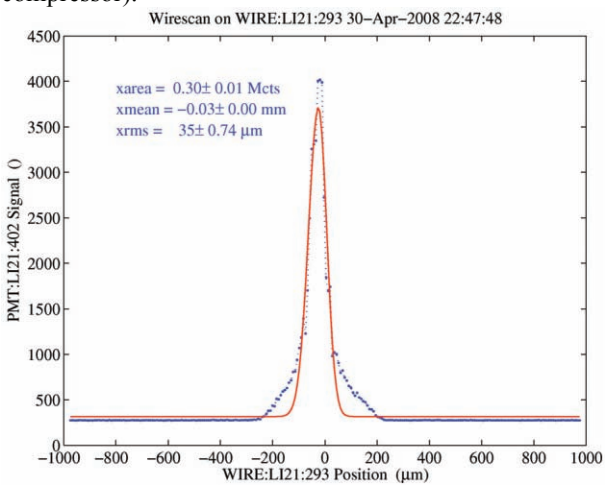

Figure 9. Wire-scan profile with fit (250MeV after BC1)

Optical Transition Radiation Monitors

At 135MeV and higher energies (after Linac-0), the beam size and charge in the LCLS are high enough to saturate fluorescent screens, and Optical Transition Radiation monitors with a 1-micron thick aluminum foil oriented at 45 degrees to the beam axis are used. The OTR camera is sensitive to wavelengths from 1 micron to 400 nanometers.

A beam image from an OTR at 135MeV is shown in figure 10. Note that the angle of the foil relative to the camera produces a position dependant focus, which limits the usable range to approximately +/-1 mm in the horizontal plane.

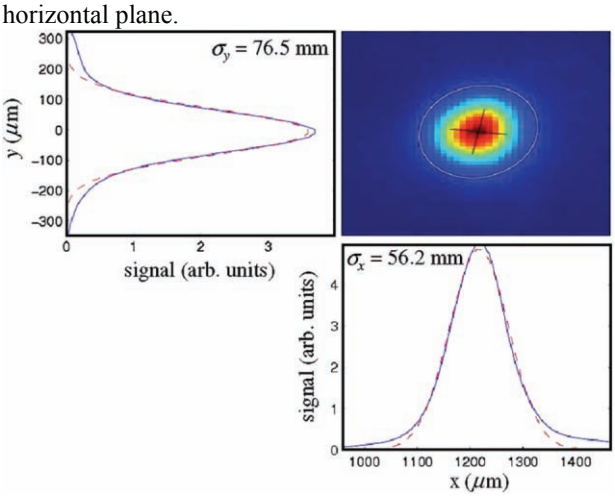

Figure 10. OTR Image at 135MeV

OTR profile monitors were intended as the primary transverse beam diagnostic in the LCLS. It has been discovered that the electron beam contains longitudinal structure at optical wavelengths, and that this distorts the OTR images.

Coherent Optical Transition Radiation

Optical transition radiation is emitted when an electron passes from vacuum into a conductor. For the extreme-relativistic beams used in accelerators, radiation is emitted broadband up to approximately the plasma frequency of the metal (~20eV). For details see [5]. In order for the radiated energy to be proportional to the electron charge, the emission from each electron in the beam must add incoherently.

If the beam has longitudinal structure on a scale comparable to the measurement wavelength, the beam can emit coherently, and the power will scale as the square of the charge. The LCLS beam contains on the order of 10^6 electrons in an optical wavelength, so even a density modulation of 10^{-3} will produce significant coherent emission.

Coherent OTR effects can be seen in the LCLS injector after DL1 (see Fig. 1), but before the beam is compressed. The field gradient of a dispersion correction quadrupole magnet in the DL1 bend is varied, and the image on an OTR screen at the end of L1 is recorded. For this experiment the RF in L2 is phased on the RF crest, and the bunch compressor BC1 is turned off (straight ahead beam, no dispersion). Figure 11 shows the integrated OTR intensity varying, and figure 12 shows the non-parabolic variation of measured Y beam size at the OTR. The measured beam size changes are not believed to represent actual changes in electron beam size, but rather changes in the distribution of the coherent optical signal. These changes (~25%) are large enough to invalidate emittance measurements. Note that the integrated optical signal is measured in uncalibrated "counts", the sum of the intensities of the pixels in the OTR image.

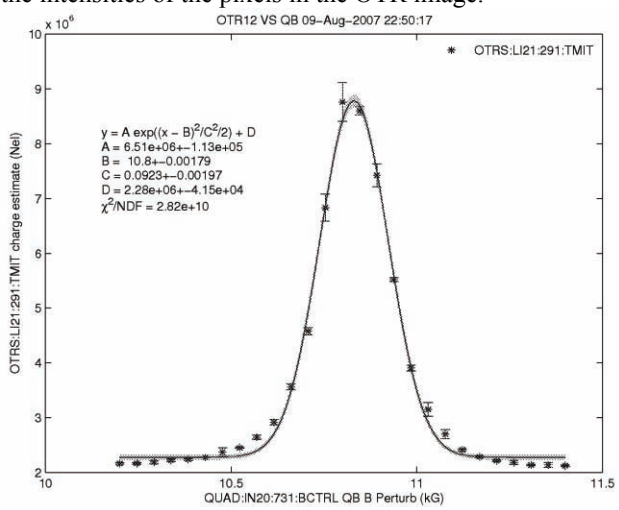

Figure 11. Integrated OTR intensity as the DL1 quadrupole magnetic field gradient is varied

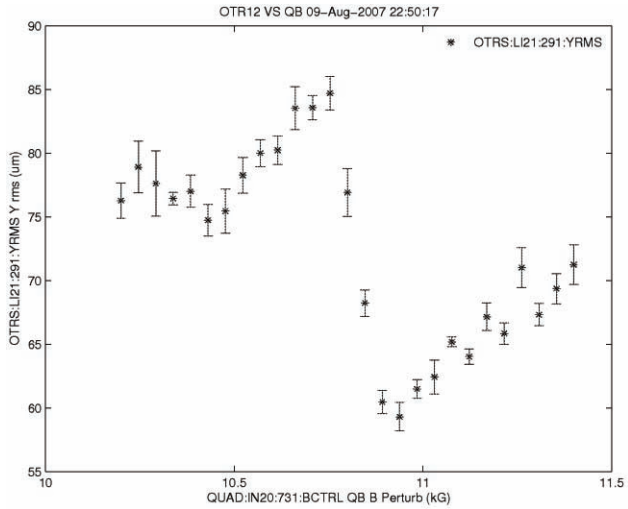

Figure 12. Measured Y beam size as the DL1 quadrupole magnetic field gradient is varied

The observed coherent OTR effects are larger after the first bunch compressor. This is presumably due to length compression of longitudinal structure on the beam, and longitudinal dispersion converting energy modulation into density modulation.

An OTR foil can be inserted in the first bunch compressor chicane. This has the effect of washing out any temporal structure on the beam, and also increasing the emittance at the end of the compressor. If we observe the OTR foil after the bunch compressor with the chicane foil inserted or removed, we see an approximate factor of 10 change in integrated optical signal level, Figures 13, 14.

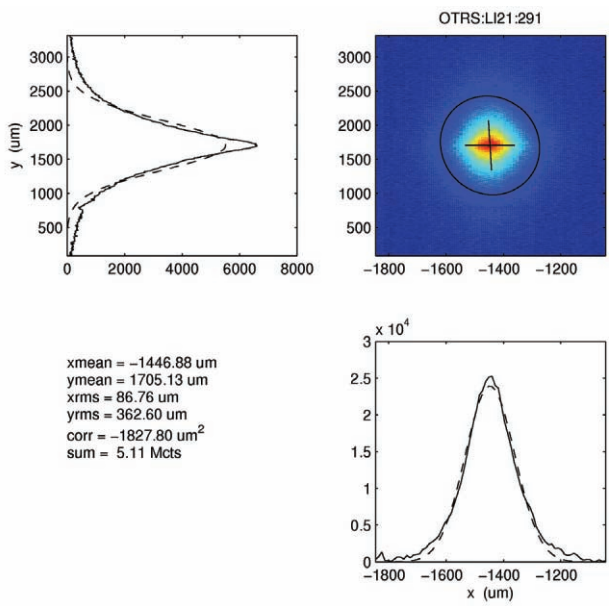

Figure 13, OTR with foil inserted in chicane. Integrated signal 5.11×10^6 counts.

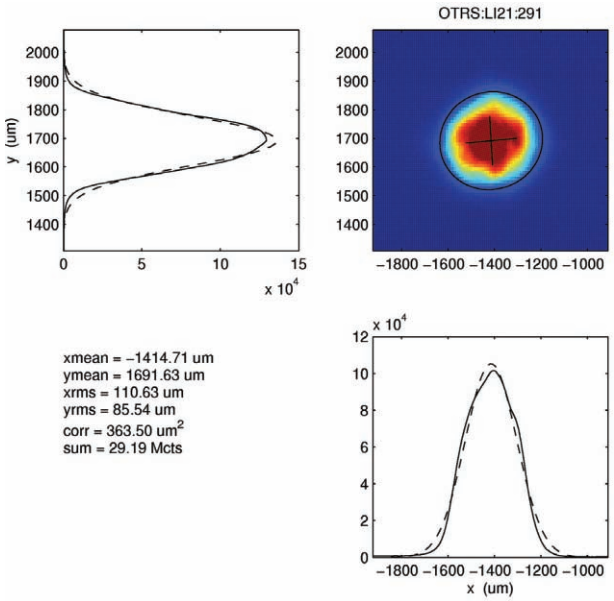

Figure 14, OTR with foil in chicane removed, integrated signal 2.9x107 counts . (6x107 counts without saturation)

If the phases of the structures in Linac-1 are adjusted to maximize compression in BC1, very dramatic COTR effects are observed. The toroidal shape is predicted from the circular polarization of the OTR emission. Interference produces an image that is proportional to spatial derivative of the original beam distribution [6]. Figure 15.

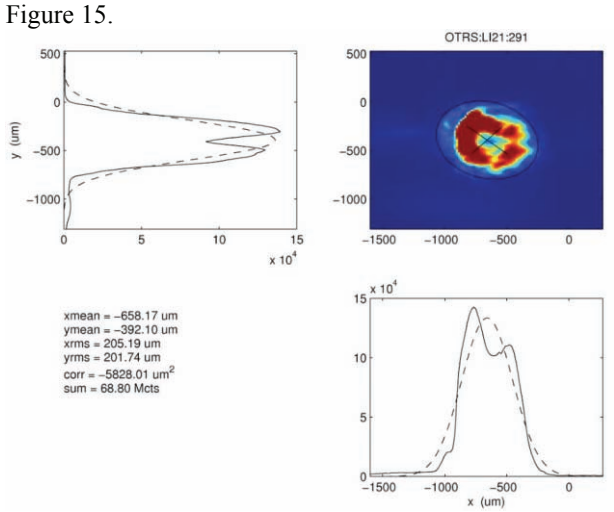

Figure 15. COTR with Linac-1 phases set for maximum compression in BC1. Integrated signal 100X incoherent.

In the second bunch compressor, the peak currents are higher, the coherent effects much stronger, producing distorted beam images, figure 16.

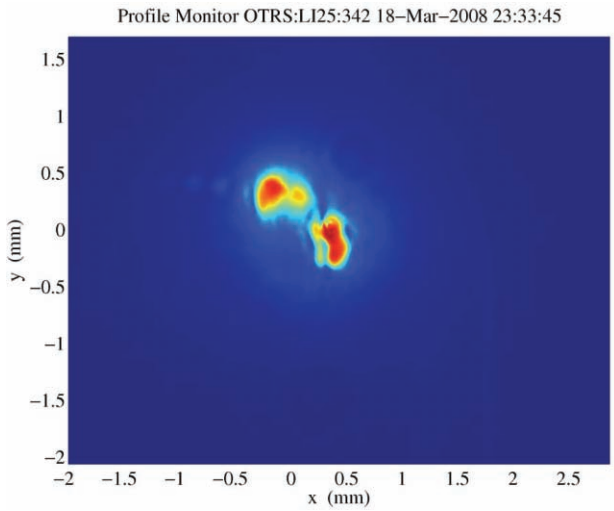

Figure 16. OTR image after second bunch compressor, normal compression, 1nC charge.

A diffraction grating was added to the OTR after the second bunch compressor to allow an approximate measurement of the spectrum of the coherent emission. The emission was found to be broadband over the camera's wavelength range of approximately 400nm to 1 micron (Figure17). This image is under normal compression conditions in BC1 and BC2. Note that the incoherent signal is too dim to observe in this image.

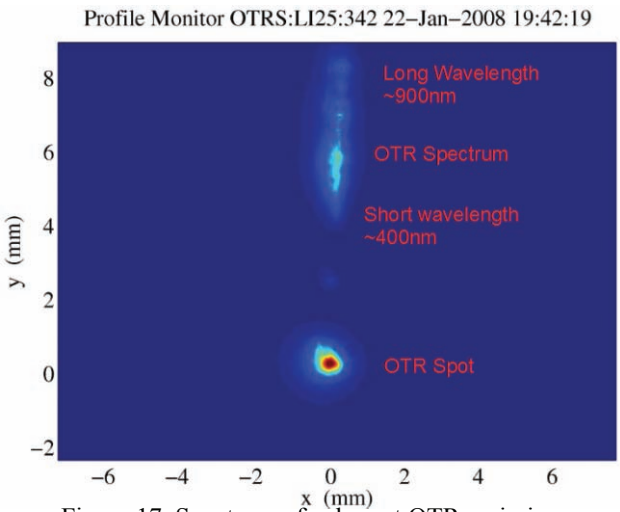

Figure 17. Spectrum of coherent OTR emission.

As expected, the strongest coherent OTR signal is seen when the bunch is maximally compressed in the second bunch compressor. The optical spectrum is seen to have spatial dependence, possibly due to a combination of coherent OTR effects and CSR beam breakup. Figure 18

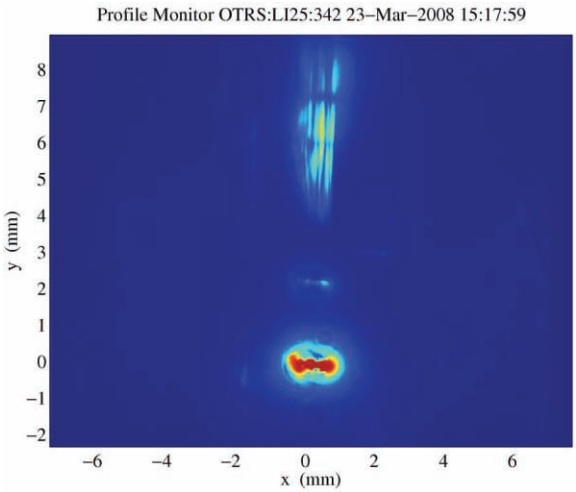

Figure 18. OTR image at maximum bunch compression in second bunch compressor.

Coherent Optical Transition Radiation Mitigation

The coherent optical effects make OTR profile monitors unusable for quantitative studies in the LCLS after DL1 (135MeV). The existing cameras are only sensitive to wavelengths longer than 400nm, and coherent effects are seen at this wavelength. We will investigate coherence at wavelengths as short as 200nm, roughly the limit of conventional optics, but the small longitudinal phase space of the beam may support modulations at even shorter wavelengths.

The LCLS plans to install a "laser heater" [7] before DL1 to increase the longitudinal phase space of the beam and reduce longitudinal space charge and CSR microbunching. This will likely also reduce or eliminate the coherent OTR effects. Until it is installed, however, the LCLS must rely on wire scanners for beam profile measurements.

The normal optics for the LCLS injector produces a ~50um beam waist after L0. Longitudinal space charge field at this waist may convert beam shot noise density fluctuation to energy modulation, at and near the optical wavelengths, which then produces amplified density modulation by DL1. Adjusting the optics to remove this waist may reduce the coherent OTR effects, but this has not yet been tested.

Emittance Measurements

The LCLS beam emittance is measured by one of two methods.

1. Scan a quadrupole magnet and measure the beam profile near the waist
2. Measure the beam profile at several locations with known phase advance.

Wire scanners are used for profile measurement throughout the machine, and an OTR screen can be used upstream of DL1 (at 135MeV).

The emittance measurement is completely automated by software that reads the machine model and drives wires scanners or OTR monitors for either quad-scan or multi-screen measurements. A quad-scan, wire scanner emittance measurement at 135 MeV, and 1nC is shown in figures 19 and 20.

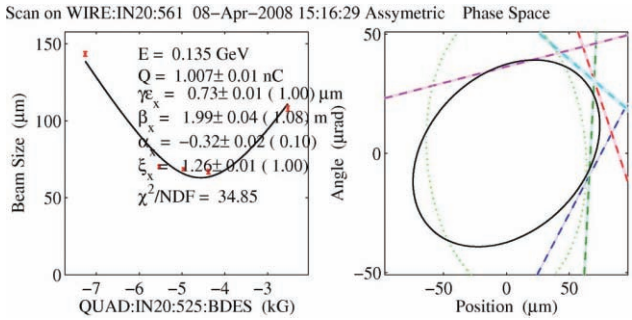

Figure 19, Horizontal emittance of 0.73um, at 1nC. And 135MeV, calculated using asymmetric Gaussian fits.

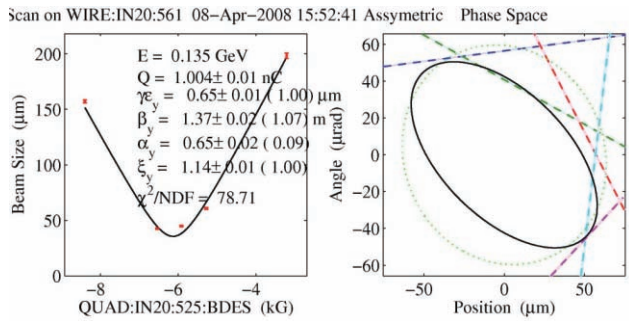

Figure 20, Vertical emittance of 0.65 um at 1nC and 135 MeV calculated using asymmetric Gaussian fits.

The measurements in figure 19 and 20 represent approximately the best measured emittance for the Gun / L0, at 1nC. More typical measurements are 0.8 to 1 micron. The emittance before the bunch compressor does not show a significant decrease at lower bunch charges, possibly due to the larger amount of time spent optimizing the system at 1nC.

The emittance is also measured after the first bunch compressor with a wire and quadrupole scan. Figures 21, 22 show an emittance x=1.15, y = 1.02 microns at 1nC. At 250pC, emittances of about 0.8 microns in both planes are commonly observed. Measurements were done at normal compression in BC1 (1 mm -> 200 microns). Horizontal emittances as 0.68 microns at 1nC have been measured. After BC1. The emittance measurements at the end of Linacx-3 show much more variable results ranging from 1 to 5 microns in both planes, with the best results observed with 250pC of bunch charge.

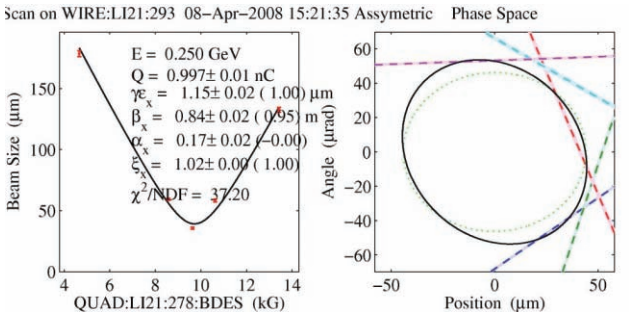

Figure 21. Horizontal emittance based on wire-scanner after first bunch compressor (1.15 microns)

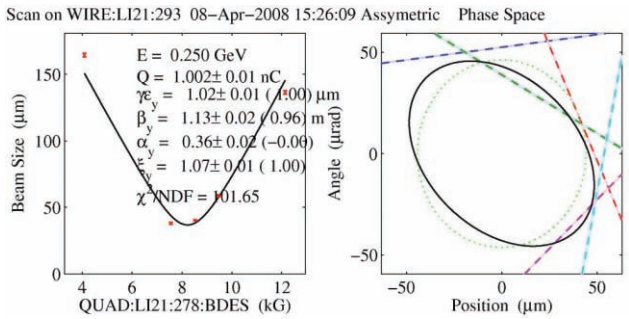

Figure 22.Vertical emittance based on wire scanner after first bunch compressor (1.02 microns).

Energy Spectrum Measurements

The beam energy spectrum can be measured at 5locations

- Gun spectrometer at 6 MeV, using a fluorescent screen.
- Injector Spectrometer, or DL1 bend at 135MeV (before compression), using an OTR screen.
- First bunch compressor at 250MeV, using an OTR screen.
- Second bunch compressor at 4.3 GeV using a OTR screen – however coherent effects make this a qualitative measurement only.
- Dump / spectrometer at the end of Linac-3 at 13.6 GeV, using a fluorescent screen.

The spectrometers are used to calibrate the energy gain of the gun and RF structures in the injector. They are frequently used with the transverse deflection cavities (next section) to provide energy vs. time measurements.

Bunch Temporal Measurements

An RF transverse deflection cavity, operating at a zero-crossing phase relative to the beam can be used to introduce a time-dependant transverse momentum. At a 90 degree betatron phase advance from the cavity, the temporal structure of the beam is transformed to transverse position. Transverse deflection cavities are located at 135MeV (before DL1 bend), and at 5 GeV (after the second bunch compressor) [8]. The transverse cavities deflect in the vertical direction to allow use in combination with the (horizontal) spectrometer magnets.

The coherent OTR effects prevent the use of the OTR screen originally intended for use with the transverse cavity after BC2 and instead a fluorescent screen at the end of L3 (13.6GeV) is used. Resolution, and the long fluorescence lifetime (~1 second) limit the accuracy of the measurement.

There is no transverse cavity directly after the first bunch compressor, however the second bunch compressor can be turned off, and L2 run at crest phase allowing the use of the transverse cavity located after BC2 to be used. Figure 23 shows the measured and *Elegant* simulated bunch length after the first bunch compressor (at 250 pC) as a function of the phase of the S-band system in Linac 1.

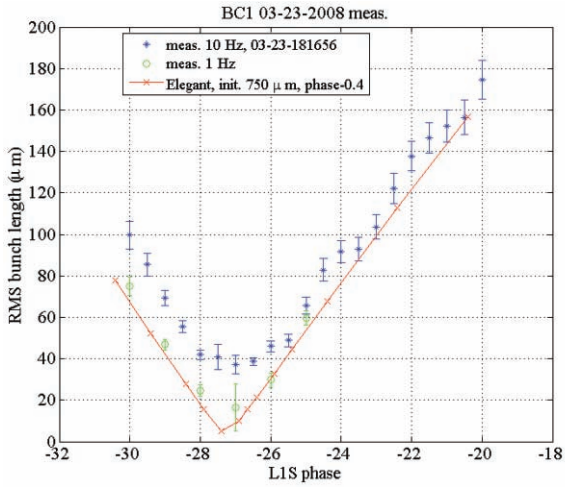

Figure 23. Bunch length after BC1 vs. pre-BC1 RF phase (see Fig 1) measured with BC2 off.

The perpendicular component of the RF phase in L2 can be adjusted to change the energy chirp and the compression in the second bunch compressor. Figure 24 shows the measured bunch length as the chirp is adjusted around the normal operating point, with a bunch charge of 250pC. A *Elegant* simulation, with an assumed input bunch length of 750 microns before BC1 is shown for comparison.

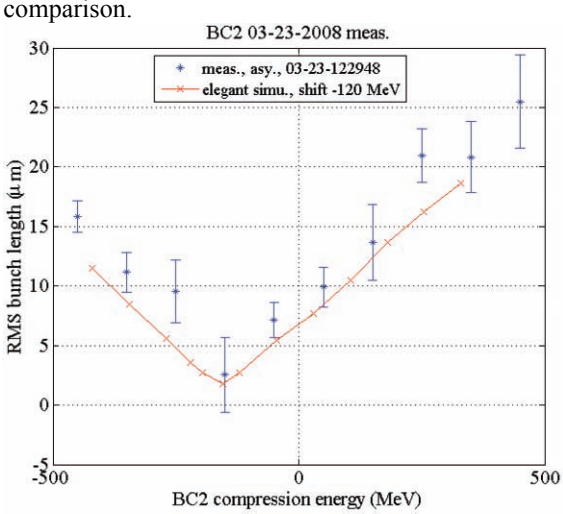

Figure 24. Bunch length after BC2 vs. RF chirp parameter. (250pC)

The minimum bunch length after BC2 is approximately 5 microns RMS. This represents the resolution of the transverse cavity system in conjunction with the fluorescent screen.

Energy vs. Time Measurements

The combination of transverse cavities and spectrometer magnets is a powerful tool for measuring the longitudinal beam phase space. Figure 25 shows the relative locations of the rf deflection cavity and the measurement locations.

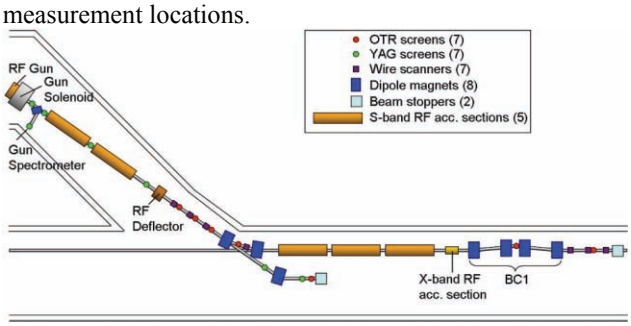

Figure 25. Transverse cavity location in injector

The injector RF deflector can be use in conjunction with either the injector spectrometer, or the DL1 bend to measure the longitudinal phase space of the beam after L0. (see figure 26).

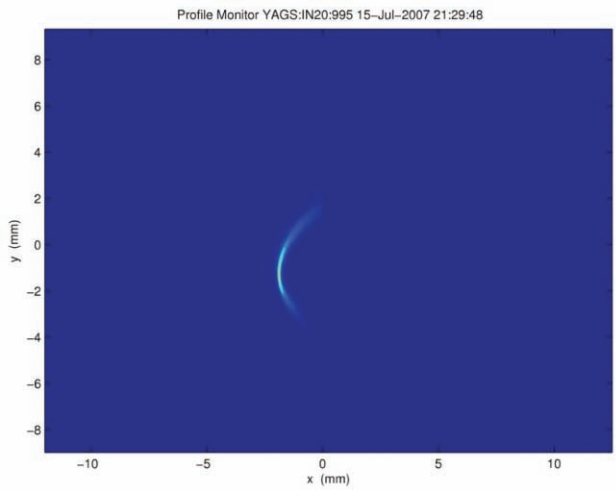

Figure 26. Energy vs. Time after L0 using the transverse RF deflector in the injector and spectrometer screen.

The first bunch compressor in the LCLS uses an 4th harmonic X-band RF (11.424 GHz) station to correct the phase space curvature (energy vs. time) which is introduced by the S-band RF structures. A plot of energy vs. time in the middle of BC1 allows adjustment of the X-band amplitude to linearize the energy chirp vs. time. Figure 27 shows energy vs. time in on the BC1 OTR screen without the X-band, figure 28 shows linear chirp with the X-band on. IN both cases the transverse RF deflector is switched on in order to provide a temporal measurement in the vertical direction.

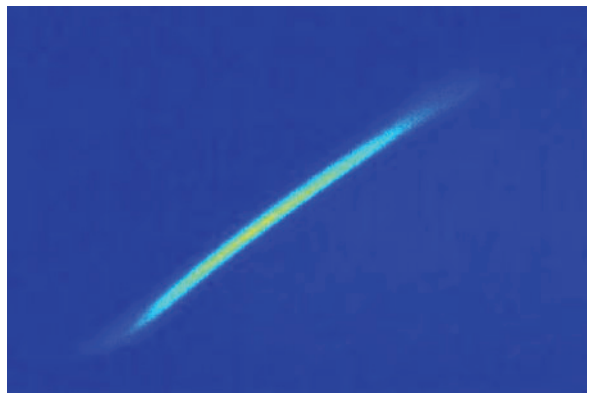

Figure 27. Energy vs. time in BC1, without X-band RF, (but with transverse RF deflector switched ON)

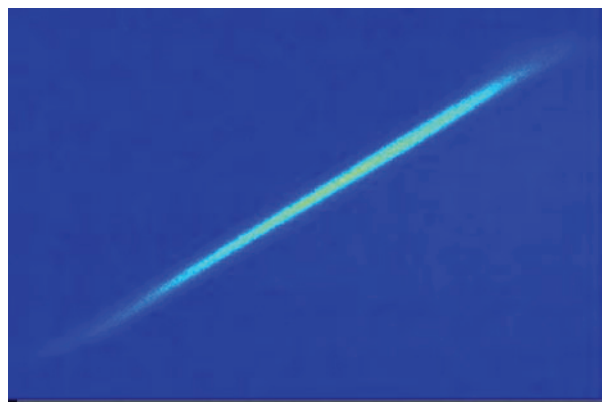

Figure 28. Energy vs. Time in BC1, with X-band RF (and with transverse RF deflector switched ON).

Relative Bunch Length Measurement

The transverse deflection cavities provide a high resolution and accurate bunch length measurement, but are invasive to beam operation. The RF phases in the LCLS drift over time and non-invasive bunch length monitors are required for feedback.

When an electron bunch passes through an impedance mismatch, it will emit electromagnetic radiation. For wavelengths long compared with the bunch length, the electrons in the bunch will radiate coherently. If we measure the radiated power at wavelengths comparable to the bunch length, the radiated power will vary with bunch length. This signal is not calibrated, but can be used to maintain a bunch length that has been set using the transverse cavities.

The bunch lengths after the first bunch compressor will produce radiation with wavelengths around 1 mm (300 GHz), while the beam after the second bunch compressor will be coherent at wavelengths below about 100 um, (3 THz).

Two relative bunch length monitors are installed after the first bunch compressor:

- Ceramic gap with waveguide coupled diodes at frequencies of 100 GHz and 300GHz.

- Diffraction / synchrotron / edge radiation monitor with an in-vacuum mirror and pyroelectric detectors.

The ceramic gap / RF diode monitor was simple to construct and provides a good bunch length signal (figure 29), however this technology does not work at the higher frequencies required for the second bunch compressor.

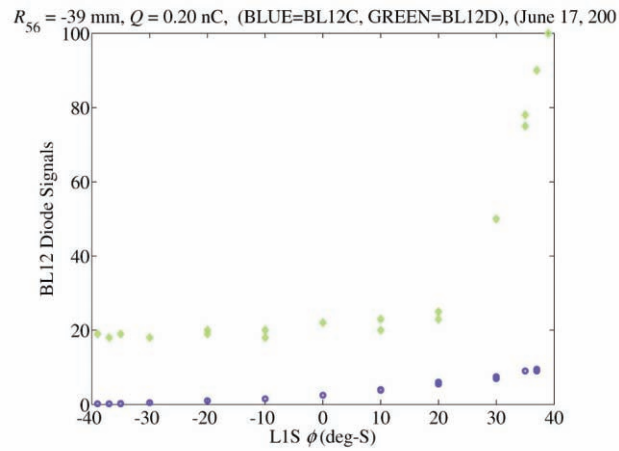

Figure 29. Ceramic gap / RF diode bunch length monitor, 100GHz and 300GHz diode signals as Linac 1 compression phase is varied.

The pyroelectric detector based bunch length monitor is located after the last bend magnet of the first bunch compressor. The signal is a combination of synchrotron radiation, end radiation, and diffraction radiation (figure 30). The bunch length monitor includes millimeter-wave filters to control the measurement frequency. For most operations however it was found that the unfiltered signal provided the lowest noise bunch length measurement. A scan of bunch length monitor signal vs. Linac 1 phase is shown in figure 31.

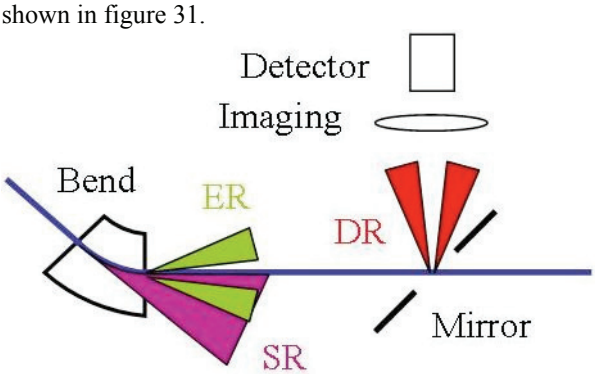

Figure 30. Pyroelectric bunch length monitor

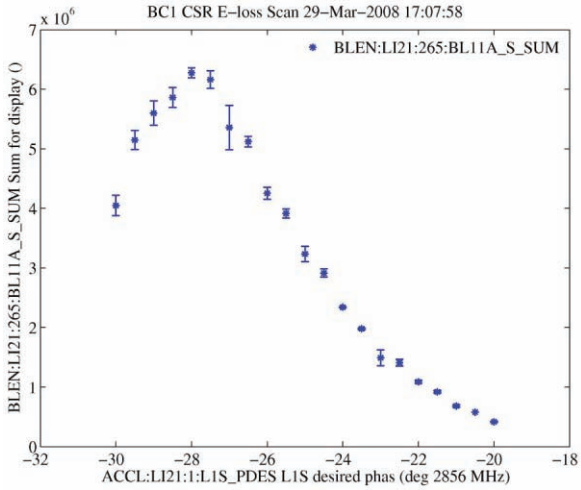

Figure 31. Signal from pyroelectric bunch length monitor as Linac 1 compression phase is varied.

The second bunch compressor uses a system very similar to the pyroelectric detector for BC1. A silicon vacuum window is used to provide transmission from 2 microns to millimeter wavelengths. Figure 32 shows the signal from this detector as the compression in BC2 is varied.

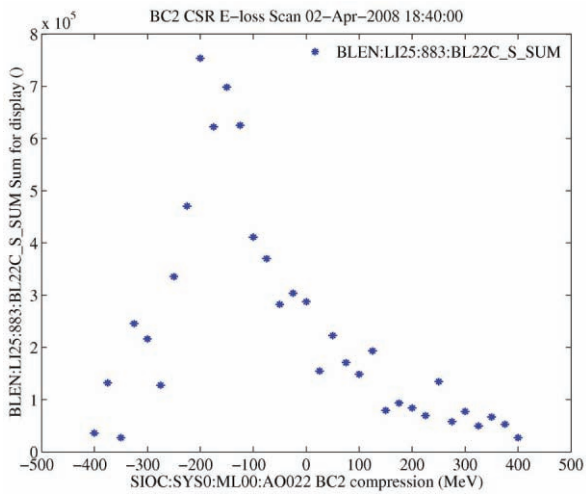

Figure 31. Signal from BC2 bunch length monitor as compression in L2 is varied.

Coherent Synchrotron Radiation

The coherent synchrotron radiation of a compressed bunch will produce increased energy spread, increased emittance and energy loss when the beam is close and over the full compression. The energy loss in the bunch compressor will result in the beam exiting the last compressor magnet with an x-angle. The X position (corresponding to energy loss) and emittance are shown and as the compression is change in BC1 are shown in figures 32 and 33.

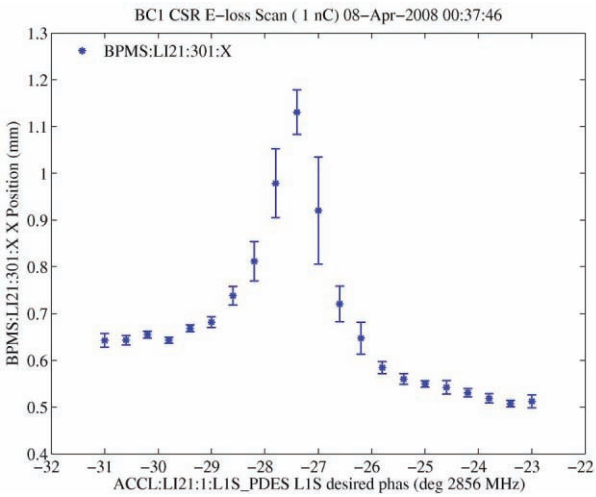

Figure 32. CSR energy loss in BC1 vs. RF phase

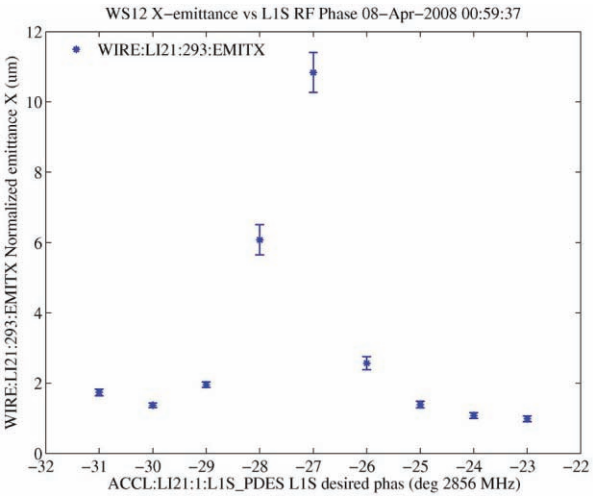

Figure 33. Horizontal emittance after BC1 due to CSR as compression (RF phase) is changed

A similar measurement of energy loss for the second bunch compressor is shown in figure 34.

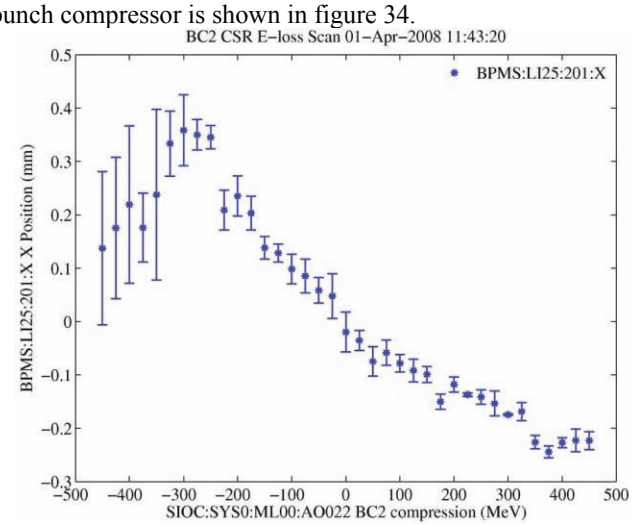

Figure34. Energy loss (as seen on BPM just downstream of BC1) due to CSR in second bunch compressor as compression is changed.

STATUS AND FUTURE WORK

The strong coherent optical transition radiation observed at LCLS has prevented the quantitative use of some diagnostics. In particular, there are no reliable beam profile measurements for the 900 meters of beamline between BC1 and the end of the L3 linac. A set of four wire-scanners were originally to be installed just upstream of BC2, but budget over-runs have forced a delay of these diagnostics. This lack of diagnostics has made beam tuning after the injector difficult.

There are several options to reduce the effects of COTR, including the addition of a “laser heater”, and optics changes in the injector, however the effectiveness of these is not yet known.

Despite the diagnostic limitations, the LCLS accelerator is operating at design charge, energy and bunch length. The emittance in the injector meets our requirements routinely, while the end of the linac is still quite variable. With additional tuning time, we expect to meet the emittance requirements at the end of the accelerator as well.

REFERENCES

[1] R. Akre et al, Phys. Rev. ST 11, 030703 (2008)
[2] R. Erickson, ed., “SLC Design Handbook”, Stanford (1984).
[3] E. Medvedko et al, “Stripline Beam Position Monitors for LCLS”, these proceedings.
[4] A. Murokh, “Limitations on Measuring a Transverse Profile of Ultra-Dense Electron Beams with Scintillator”, Proceedings 2001 Particle Accelerator Conference, Chicago.
[5] J. D. Jackson, “Classical Electrodynamics”, 1975, p685 .
[6] H. Loos, private communication
[7] Z. Huang et al. Phys Rev ST Accel Beams 8, 074401 (2004).
R. Carr, et.al. “Inverse Free Electron Laser Heater for the LCLS”, SLAC-PUB-11186, 2004.
[8] P. Emma et.al. “A Transverse RF Deflecting Structure for Bunch Length and Phase Space Diagnostics”, SLAC-PUB-8864, 2001

LHC MACHINE PROTECTION

B. Dehning, CERN, Geneva, Switzerland

Abstract

The LHC equipment is protected by passive and active components against beam-induced destruction. For the fast losses a passive system consisting of collimators, absorbers and masks is used. For the other losses an active system consists of beam loss monitors, a beam interlock system and the beam dump. The LHC protection requirements are different than those of other accelerators, mainly due to its energy, its stored beam intensity, and its dimension. At the LHC top energy the beam intensity is about 3 orders of magnitude above the destruction limit of the superconducting magnet coils and 11 orders above their fast loss quench limit. These extreme conditions require a very reliable damage protection and quench prevention with a high mean time between failures. The numerous amounts of loss locations require an appropriate amount of detectors. In such a fail safe system the false dump probability has to be kept low to keep a high operation efficiency. A balance was found between a reliable protection and operational efficiency. The main protection systems and beam instrumentation aspects of the measurement systems will be discussed.

DESTRUCTION POTENTIAL

The destruction potential of the LHC is illustrated by test measurements done in the SPS. The beam prepared for injection into the LHC has been directed onto a stack of copper and steel plates (Fig. 1). The beam, with a size

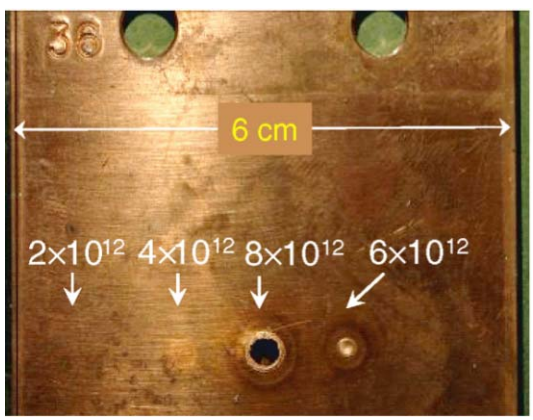

Figure 1: Destruction test of a Cu target in the SPS with an LHC beam.

of σ_x=1.1, σ_y=0.6 mm and intensities of several 10^{12} protons at 450 GeV, clearly damaged the copper plates at a penetration depth where the maximum energy is deposited. The steel plates were not damaged [1]. The safe intensity of 2 10^{12} represents only 0.6 % of the total intensity of 3 10^{14} at the LHC injection energy.

To illustrate the destruction potential of the LHC beam at top energy of 7 TeV, a simulation of the material phase transition in the longitudinal penetration channel is shown in Fig. 2.

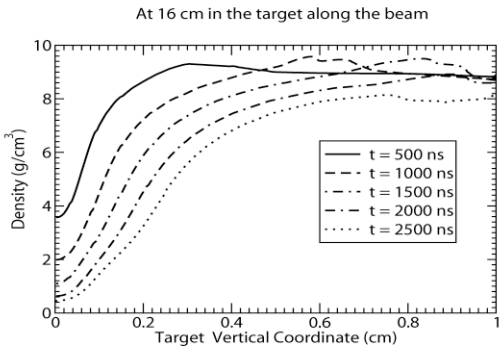

Figure 2: Density change of a Cu target material during the impact of 100 LHC bunches (bunch train duration 2500ns) with an intensity of 1.1 10^{11} proton per bunch at 7 TeV.

The energy deposition leads to a temperature increase, followed by a pressure increase, which causes a shockwave leading to a reduction of the density. The following bunches would interact with less material where the density is reduced and would penetrate even further. It is expected that the whole LHC beam would penetrate over 10 m through the material after impacting [2].

Beam induced destruction of equipment is one reason an accelerator might be rendered non-operational. Beam induced heating at the superconducting coils of the LHC magnets will cause a loss of their low resistance. In case of a failure, the tail of the beam will impact at the inner wall of the vacuum chamber and a secondary particle shower will deposit its energy in the vacuum chamber and in the surrounding coil (see Fig. 3). The lines of constant energy density show a decrease of the energy density in the radial direction. The largest temperature increase is not caused by energy deposition near the vacuum chamber, because a He cooling channel between the vacuum chamber and the coil transports heat to the heat bath region for steady state losses (> 1 s). Instead, the quench location is near the border between the inner and outer coils, where the heat flow is minimal (see Fig. 3, bottom) [3].

THE PROTECTION SYSTEM

Figure 4 shows a classification of the beam losses according to their duration. For the very fast losses (< 4 turns, 356 us) only passive components can protect the equipment. At LHC over 100 collimators and absorbers

are foreseen for installation. The BLM system is the main active system to prevent magnet damage from all possible multi-turn losses. It is the only system for short and intense particle losses, while at medium and longer loss durations it is assisted by the quench protection system and the cryogenic system. Quench prevention is ensured only by the BLM system.

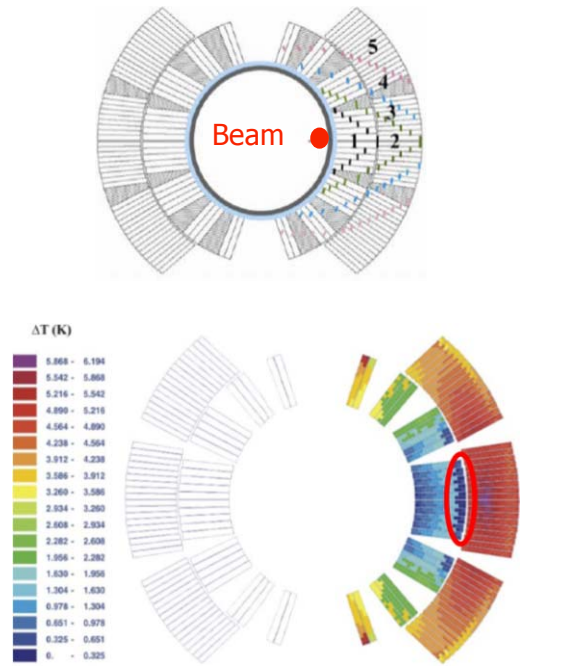

Figure 3: Top: Cross section of the superconducting coil of a LHC dipole magnet. The beam impact location and the lines of constant energy density are indicated. Bottom: Simulation of the temperature margin for the steady state (> 1 s) quench scenario. The quench location is in the midplane between the inner and outer coil (see ellipse).

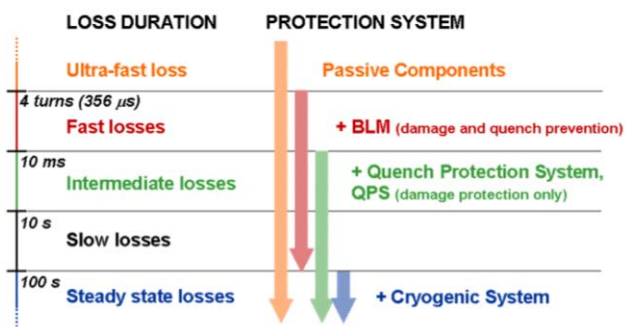

Figure 4: Classification of beam losses according to their duration and the applicable (passive, active) protection systems for the different loss classes.

Collimators and absorbers

The function of the collimators and absorbers is to protect of equipment against fast losses and to concentrate the steady state losses at locations where the secondary shower particles do not lead to quenches of superconducting coils. For the capture of the steady state losses the collimators and absorbers are installed at two locations, for betatron and momentum cleaning. The fast loss protection is also done by placing collimators near to the insertion magnets or near to magnets in the injection and dump region of the LHC.

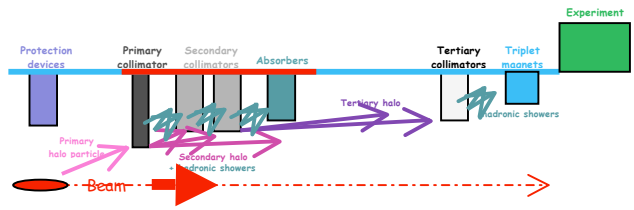

Figure 5: Sketch of the multi-turn LHC collimation system.

The setup for the multi-turn, 3-stage collimation system can be seen in Fig. 5. The beam halo is intercepted at the primary collimator (closest to the beam). In the primary collimator most of the protons undergo multiple Coulomb scattering and some of them will be caught by the secondary collimators, on average after some hundred turns. Most remaining protons will be caught by the tertiary collimator. The distribution of such losses along the circumference of the ring is shown in Fig. 6 [4].

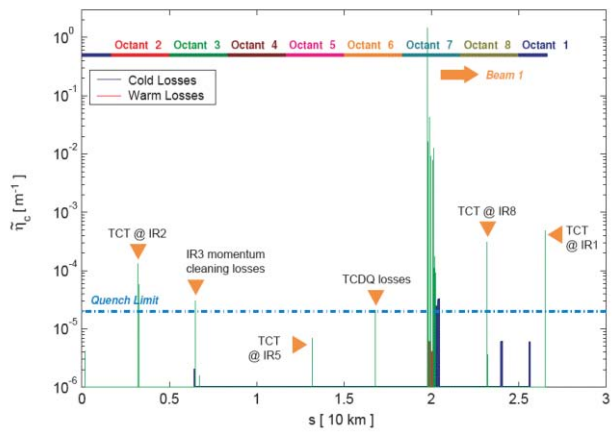

Figure 6: Distribution of the losses along the ring circumference.

The protons are mainly intercepted at the primary (TCP) und secondary (TCS) collimators at the collimation region in octant 7. Losses appear behind the collimator on the normal-conducting magnets (green) and further down stream on superconducting magnets (blue). Decreasing losses (beam direction left to right) can also been seen at the tertiary collimators (TCT) in octants 8, 1, 2 and 5.

DESIGN CONSIDERATIONS OF THE PROTECTION SYSTEM

For the design of a safety system, in addition to the standard specifications, like dynamic range, resolution and response time, a value for the "Mean Time Between Failures" (MTBF) is needed to quantify the level of the protection. The estimate of the MTBF value was based in the case of CERN's LHC on the SIL (Safety Integrity Level) approach [6]. Other approaches like "As Low As Reasonably Practicable" (ALARP) are also often used.

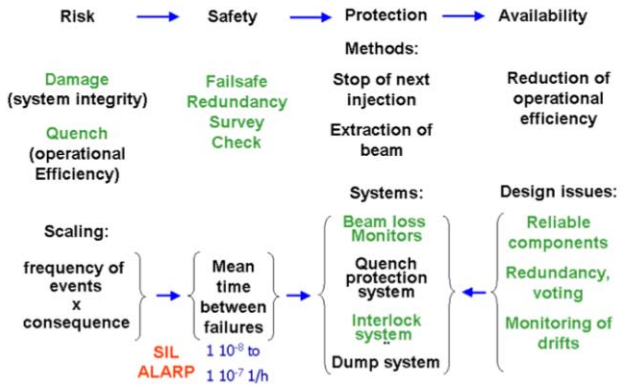

Figure 7: Schematic of the LHC protection system approach (items in green are discussed in this paper).

For both approaches the MTBF value is estimated by the calculation of the risk of damage and the resulting down time of the equipment [5]. In the case of a failure in the safety system itself, it will fall in a failsafe state with the consequence of making the protected system unavailable.

The design considerations of a beam loss monitor system and others for machine protection are schematically shown in Fig. 7. In the first row the key words discussed above are listed. A risk requires a safety system that provides protection, but the safety systen reduces the availability of the protected system. In the risk column the consequences (damage and quench) of a non-nominal operation (beam loss) are listed. A further consequence for both is the increase of the downtime of the accelerator. The risk scales with the consequences of the proton loss event and its frequency. From the risk the MTBF value is deduced. This main design criterion for the safety system is listed in the safety column as well as the means (failsafe, redundancy, survey, check) to reach the envisaged MTBF value. In the protection column the methods of protection are listed (stop of next injection and extraction of beam) for a one-path particle guiding system (linac, transfer line) and for a multi-path system (storage ring). The safety system consists of a beam loss measurement system, an interlock system and a beam dump system. If superconducting magnets are used, some protection could also be provided by the quench protection system. The availability column lists the means used in the design of the safety system to decrease the number of transitions of the system into the failsafe state. The effect of the components added to the system to increase the MTBF value results in a reduction of the availability of the system. This negative consequence of the safety increasing elements is partially compensated by the choice of reliable components, by redundancy voting, and the monitoring of drifts of the safety system parameters (see Fig. 7, fourth column). The key words listed in green will be discussed below.

Risk Examples: Stored Energy in the Beam

The damage potential at CERN's LHC is over two orders of magnitude higher than at all other existing accelerators (see Fig. 8), since the stored beam energy given by the product of the single particle energy and intensity is largest at LHC. The consequence of a dangerous proton loss event was "illustrated" by an accidental loss at Fermilab's Tevatron (200 times lower stored beam energy than at LHC) where the proton beam was lost within a few revolutions, melting some components. The loss was initiated by a moveable measurement instrument. The number of such moveable objects at LHC is also an order of magnitude higher than at Tevatron. This example may indicate the risk associated with the LHC-like beams, leading to downtimes of months or even years.

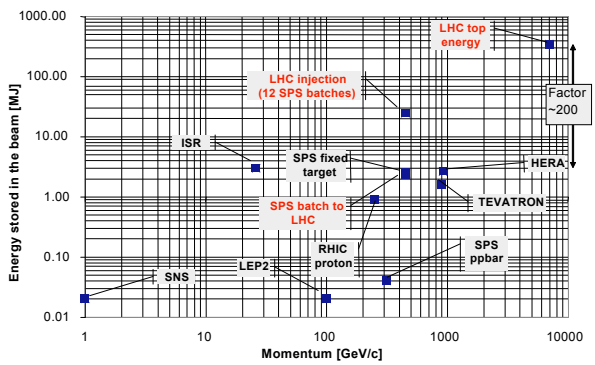

Figure 8: Comparison of the stored beam energy of different high energy physics accelerators as function of the beam momentum.

Risk Examples: Quench Levels and their Dependencies

The proton loss initiated quench of magnets depends on the loss duration and on the beam energy. A quench will create a downtime on the order of several hours in the case of LHC. To make the operation more efficient the beam could be dumped and a new store prepared. Figure 9 shows the expected loss dependence as function of the loss duration. The two curves indicate the levels for the injection and top energy of LHC. The two arrows indicate loss durations where the quench level of LHC is compared with levels at other storage rings (instant losses,

steady state,; see Table 1) [7][8]. It can be seen that the expected quench levels at LHC are lowest, resulting also in advanced requirements for the quench level detection.

The quench levels' dependence on energy is shown in Fig. 10. The quench levels decrease rapidly with the particle energy, leading to the requirement that the quench level thresholds need to be decreased during the energy ramp accordingly.

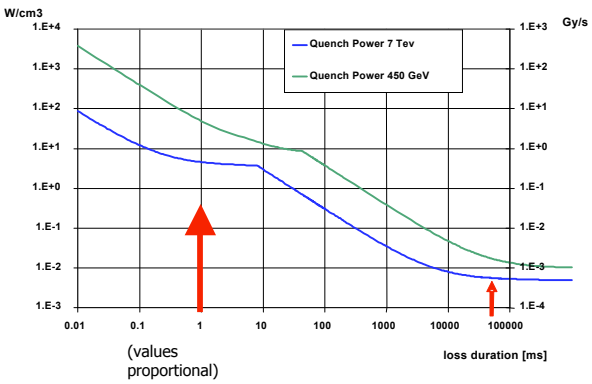

Figure 9: LHC bending magnet quench level curves as function of the loss duration.

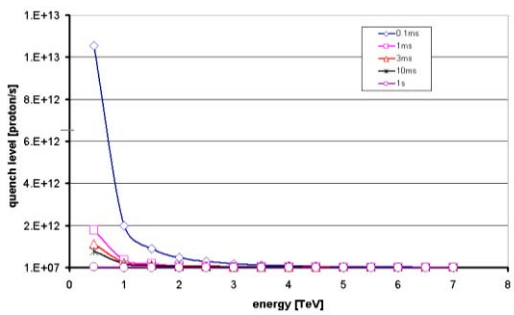

Figure 10: LHC bending magnet quench level curves as function of the beam energy. The parameterisation is for different loss durations.

Table 1: Instant and Steady State Loss Duration Quench Levels for Different Accelerators

	Instant (0.01-10 ms), J/cm^3	**Steady state, W/cm^3**
Tevatron	4.5×10^{-3}	7.5×10^{-2}
RHIC	1.8×10^{-2}	7.5×10^{-2}
LHC	8.7×10^{-4}	5.3×10^{-3}
HERA	$2.1\text{-}6.6 \times 10^{-3}$	

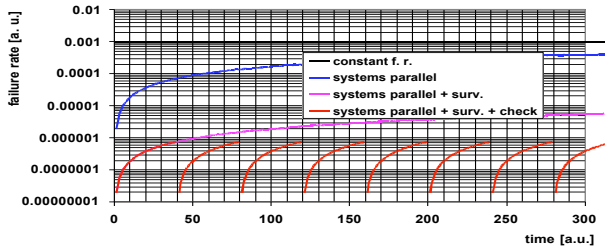

Figure 11: Calculation of the failure rates ranging from a simple system to redundant systems with surveillance and checks functionality.

Safety Means

The risk of damage could be reduced by safety means, which are incorporated in the safety system (see Fig. 7, second column). The most common safety feature of a system is the incorporation of the failsafe mechanism. In case of a failure of the safety system this system falls into a state where the protection is insured. If the system is doubled, redundancy is added, which will reduce the MTBF significantly for short time periods, but tends to reach the same value of the MTBF for long periods (see Fig. 11, failure rate = 1/MTBF) [10]. The use of a redundant and surveyed system will decrease the MTBF value for all durations compared to the simple redundant system. An even better result could be reached when a parallel system is not only surveyed but also its functionally is tested during the operation. This procedure will allow to assume that the status of the system after the test is identical to the status of the system as new. The frequency of the test will therefore determine the MTBF value.

Beam Dump Request Distribution

The beam loss measurement system is part of the equipment protection system. The protection as foreseen for LHC is schematically shown in Fig. 12 [10]. The number of beam dump request, which reaches the dump system over the machine interlock, is to 60 % operator initiated (inspired distribution by HERA [8]). The remaining dump requests are to 30 % caused by beam loss initiated dumps and to 10 % by various other reasons. The beam initiated requests are equally subdivided in losses with durations below 10 ms and above [7]. The short losses can only be detected by the beam loss system. The long losses can be detected in addition with the quench protection system (QPS, PIC). In this case two independent systems are available for the detection.

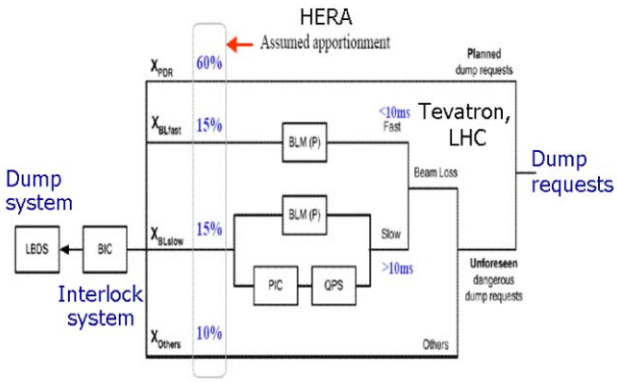

Figure 12: Dump request distribution and the employment of the beam loss system.

THE BEAM LOSS ACQUISITION SYSTEM

The electrical signals of the ionisation chamber and secondary emission detectors are digitized with a current to frequency converter and these pulses are counted over a period of 40 us (see Fig. 13). The counter value is transmitted every 40 us to the surface analysis electronics using a high speed optical link (with a cyclic redundancy check). The signal treatment and transmission chain is doubled after the current to frequency conversion to meet the required failure rate probability. The surface electronics calculates the integrated loss values and compares them to a table of loss duration and beam energy dependent threshold values.

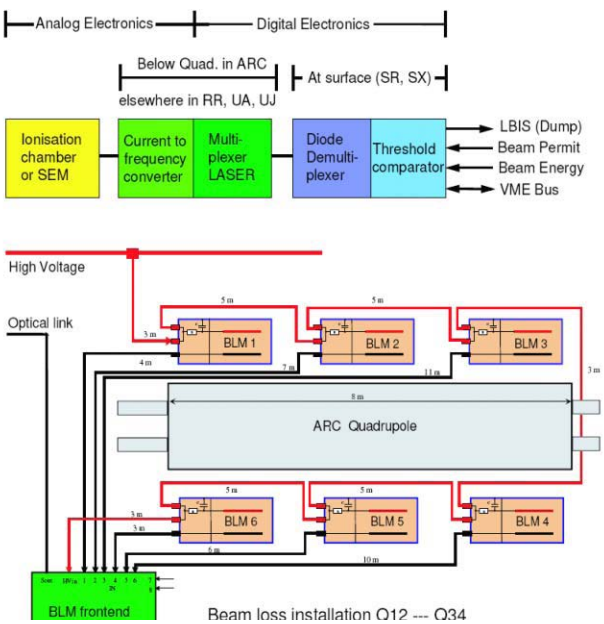

Figure 13: Schematic view of the signal transmission chain and the BLM installation at one arc quadrupole magnet. The beam permit and beam energy treatment is in this schematic simplified.

Warning information is transmitted by a software protocol. The beam abort signals are transmitted to the beam dump kicker magnets using the LHC beam interlock system (LBIS). The beam energy information is received over a dedicated link. Details of the readout system can be found in [11-16].

The analog electronics is located below the quadrupole magnets in the arc. For all detectors of the dispersion suppressor and the long straight sections the electronics is located in side tunnels to the LHC. All components of the tunnel electronics are radiation certified to 500 Gray. The dose expected at the electronics locations is about 20 Gray per year. No single event effect was observed during these tests. The temperature stability of the circuit was tested from 15 to 50 degrees Celsius. The analog signal transmission cables have a length of a few meters in the LHC arcs and up to 500 m in the long straight sections. This part of the transmission is subject to the injection of electromagnetic crosstalk and noise.

The BLM system will drive an online event display and write extensive online logging (at a rate of 1 Hz) and post-mortem data (up to 2000 turns plus averages of up to 10 minutes) to a database for offline analysis (see paragraph below).

System Tests

The testing procedures are described in [17]. They have been defined in order to achieve the required reliability and availability of the system. The functionality of all components will be tested before installation. Thereafter, there are three different inspection frequencies: tests after installation and during yearly maintenance, test before each fill and tests which take place with beam, in parallel to the data taking. Figure 14 lists the most important tests and their frequency.

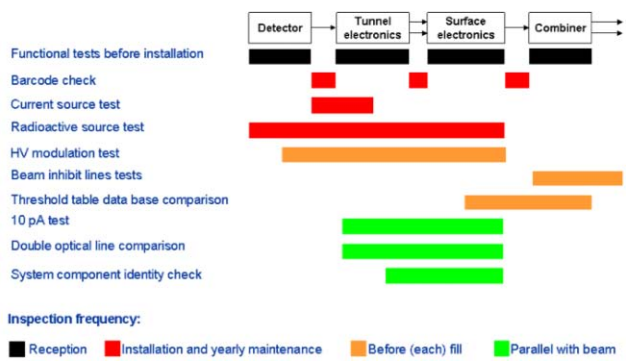

Figure 14: Schematic of test for the LHC beam loss system.

The availability of all electronics channels is constantly monitored and radiation dose induced drifts in the electronic channels are corrected (up to a maximum level, which corresponds to 10% of the lowest beam abort threshold value). The availability of all detectors, the

acquisitions chain and the generation and communication of the beam abort signal is verified for each channel before each injection into the LHC. The composition of the chamber gas is the only component in the BLM system that is not remotely monitored. The properties of the chamber gas are sufficiently close to the properties of air at ambient pressure (i.e., inside a detector that has developed a leak) so as not to compromise the precision of the BLM system, but sufficiently different to detect a leak during the scheduled annual test of all the chambers with a radioactive source. Environmental tests have taken place during the design of the tunnel electronics.

Redundancy voting

The redundancy voting procedure allows an increase in the availability of a system. An example is the cyclic redundancy check (CRC) comparison of a redundant transmitted signal (see Fig. 15). The CRC is calculated at the transmitter side and again at the receiver side for each link. For each link the CRCs are compared separately. In addition the CRC of both transmission links, which are calculated at the receiver side, are compared. In case that the comparison of the CRCs of one link is negative, the data of the other link are chosen independently of the result of the CRC comparisons of both links. The result of the comparison of both links allows identification of the location of the error in the data stream [15].

SOFTWARE AND DATABASE STRUCTURE

The LHC beam loss system consists of 4000 electronic channels. Each channel has threshold settings and can be connected to the interlock and dump system. The thresholds are stored in 2 dimensional tables. 12 values are needed for the integration intervals and another 32 values are needed to cover the beam energy variations. In total 384 values are needed per channel and for the whole system 1.5 10^6 values are used. The clients of the system request measurement data, which are integrated over different durations or/and triggered by different events. E. g. the collimation system will be supplied with measurements which are integrated over 2.5 ms lasting for 80 ms triggered by every movement of a collimator.

The overview of the software layout is shown in Fig. 16. The safety critical parts (red) are strictly separated from the parts that are not safety critical (green). The data streams are sent over the Ethernet to the different clients. The access to the single front-end VME crates by the clients is minimized by the usage of concentrators (e.g., display and logging concentrator, not all concentrators are shown).

The amount of threshold values and the request of having the threshold values frequently and safely changeable require well-defined setting management. The settings are stored in 3 databases: MTF, Layout and LSA (see left side of Fig. 16). The MTF DB holds all the hardware data and its history. The layout DB holds the connectivity and channel assignments. The settings needed for the operation of the system are propagated to the LSA DB, where also the threshold values are stored. In the LSA DB the reference settings are stored and the front-ends are loaded from this DB. The loading is done with a trim interface, which allows a secure transmission of the settings to the front-end. In the front-end itself the settings are stored in the thresholds comparators (VME card), in the FPGA memories (see right side of Fig. 16). The safety is given by the comparison procedure between LSA DB and FPGA memories (see lower part of Fig. 16). A process reads the LSA DB settings and the front-end memory values (FPGA memory) and writes back to the font-end the result of the comparison. If it is negative the combiner and survey module takes away the beam permit.

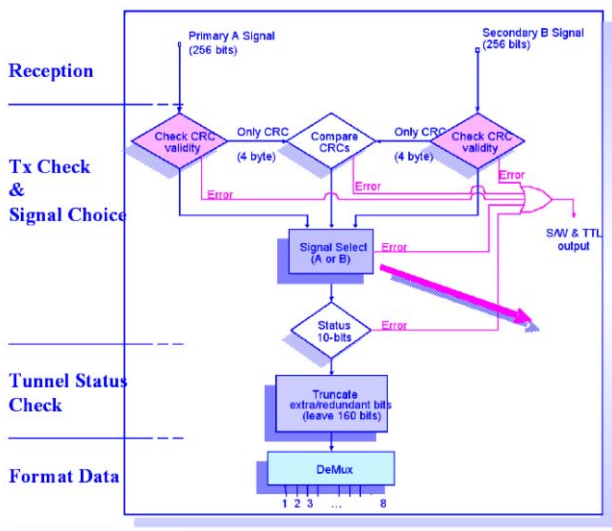

Figure 15: Schematic drawing of the redundant signal transmission comparison for the LHC design.

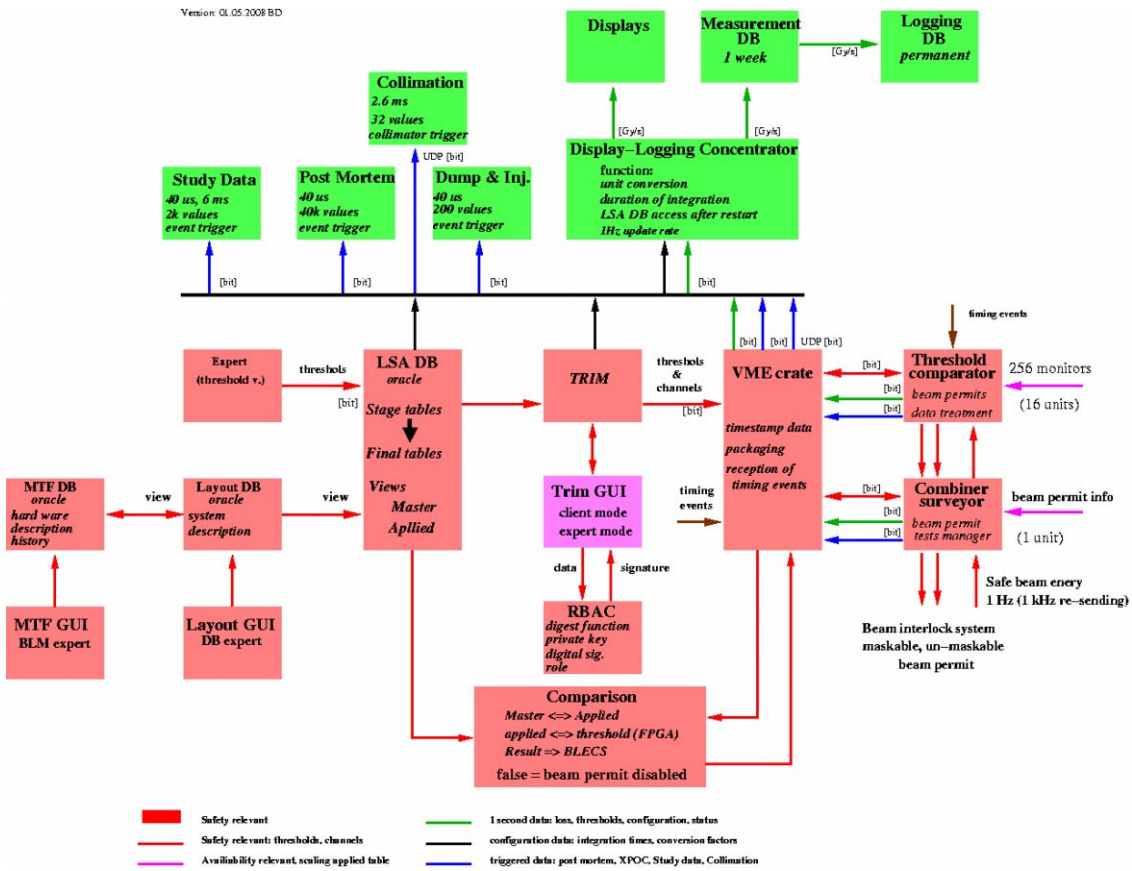

Figure 16: Schematic of the software structure for the LHC beam loss system. The green blocks are software entities that are not relevant for the safety of the system. The red blocks are safety critical.

The LSA data base layout is defined for safety reasons as shown in Fig. 16 and 17. The propagated layout DB settings are first stored in the stage tables as well as the threshold settings introduced by the expert GUI. After verification of the settings (history comparison) the settings are propagated to the final tables. In addition to this two level table system the information of the final tables is propagated to two views, the master table view and the applied table view.

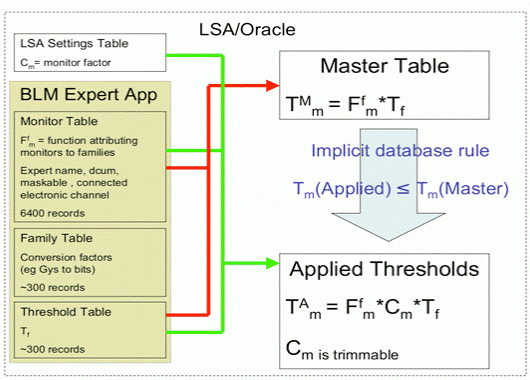

Figure 17: LSA database layout. Left side: the information of different tables are combined with views for the master table and the applied table.

The threshold values of the master table should be always higher as the values of the applied table. The access to the applied table is also possible with the trim GUI (see Fig. 16 and Fig 17, factor Cm) to allow the scaling of the threshold values. The safety of this procedure is again given by a DB internal comparison of master table and applied table.

UNSAFETY OF THE BEAM LOSS SYSTEM AND THE FOLLOWING INTERLOCK SYSTEM

The discussed aim of the beam loss measurement system is the protection of the accelerator equipment to allow an efficient operation. If the detectors are located at the likely loss locations (this aspect is not discussed in this paper), the MTBF value of the beam loss system will indicate the provided safety.

This value was calculated for the foreseen LHC beam loss system starting from the single component level and using tabulated or CERN measurements [5][17]. To identify the weakness of safety system components a relative comparison is shown in Figure 18. In the LHC design the ionisation chambers and their cabling contribute most to the unsafety of the

system. Even with no damage in 30 years of the ion chamber operation (SPS ionisation chamber experience), systems that are redundant and frequently checked contribute less to the unsafety. The availability of the system is decreased by false dumps. The components of the beam loss system which are most responsible for dumps are located in the very front end of the signal treatment chain, which are not redundant. For the LHC design it is a discharge switch of an analogue integrator.

The layout of the beam interlock system [19] is shown in Fig. 19. For each beam two rings are used to transmit the beam permit signal to the LHC dump at IR 6. A 10 MHz signal can be interrupted by clients (e.g., the beam loss system) at each location of the beam interlock controllers (BIC). If the beam permit signal is taken away the beam dump kicker magnets are triggered and after a maximum delay of one turn (waiting time for dump gap in bunch structure) the beam is directed into the dump channel.

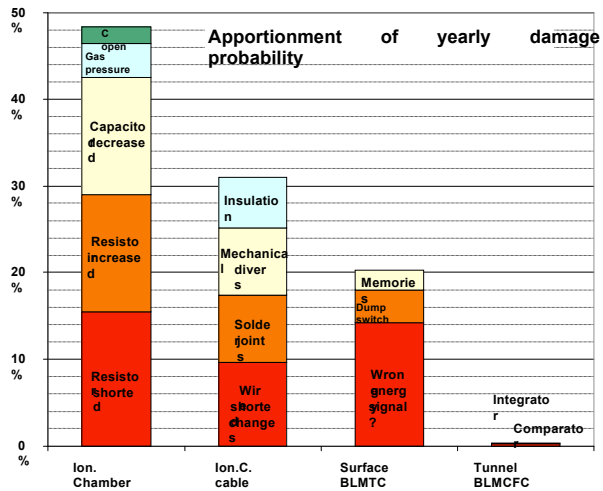

Figure 18. Relative probability of a system component being responsible for damage to a LHC magnet in the case of a loss.

The signal chain safety starting at the detectors of the beam loss system and including the interlock system has been addressed recently [18].

The components and the structure of the beam loss system and the beam interlock system have been modeled in a first step to estimate the damage risk and the false dump probability.

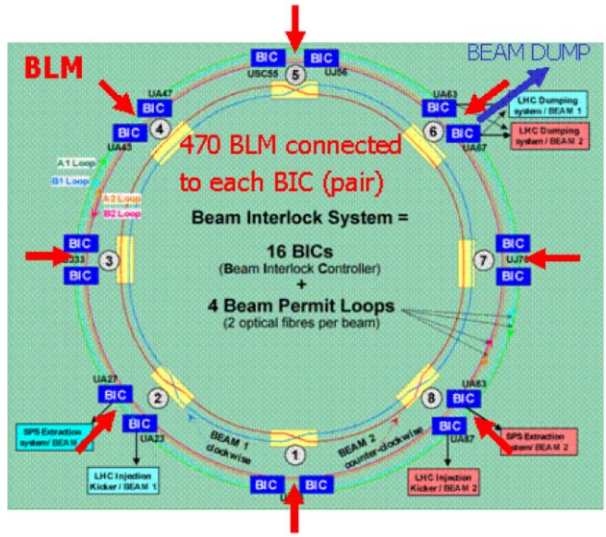

Figure 19: Schematic of the beam interlock system. Two redundant links for each beam link the client dump request to the beam dump system IR6.

Table 2: Listing of the Included Elements in the Safety Analysis

i	Component i	Number n_i
1	IC	3744
2	FEE	624
3	BEE	312
4	Combiner Card	24
5	VME crate	24
6	CIBU-S	8
7	BICbeam1	16
8	BICbeam2	16
	Total	4768

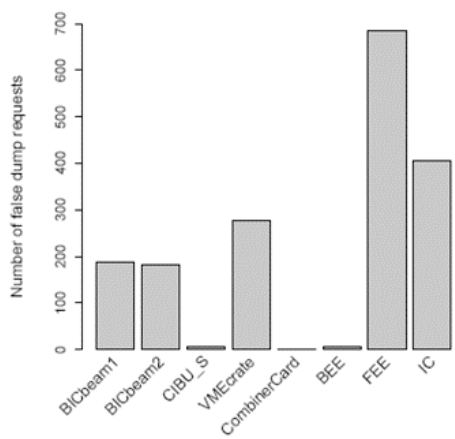

Figure 20: Distribution of contribution of the components to false dumps by triggering a false dump request.

The model predicts that the fraction of early ended missions triggered by beam loss event is 11.3%. The false dumps due to a false dump request contribute to the mission end by a component failure with 1.7%. The components which are most likely to create these false dump requests are components in the front-end electronics (FEE) and the ionisation chamber (IC) itself (see Fig. 20). The input data (failure rates of components) for this study are identical to the previous study. A new piece of information given by this study is the contribution of the beam interlock system components to the false dump requests.

REFERENCES

[1] V. Kain et al., "Material Damage Test with 450GeV LHC-type beam", 21st IEEE Particle Accelerator Conference, Knoxville, TN, USA, 16 - 20 May 2005, pp.1607.

[2] N. Tahir et al., "Impact of the 7 TeV/c Large Hadron Collider proton beam on a copper target", *J. Appl. Phys.* 97 , 8 (2005) 83532-1-8.

[3] D. Bocian et al., "Modelling of Quench Limit for Steady State Heat Deposits in LHC Magnets", MT 20 - 20th International Conference on Magnet Technology, Philadelphia, Pennsylvania USA, 2007, to published in IEEE Transactions on Applied Superconductivity.

[4] R. Démolaize, "Design and Performance Optimization of the LHC Collimation System, CERN THESIS-2006-069.

[5] G. Guaglio, "Reliability of Beam Loss Monitor Systems for the Large Hadron Collider", Proceeding of ICFA, AIP Conference Proceedings, 8 June 2005, Volume 773, Issue 1, pp. 191-196.

[6] "IEC 61508 International Standard", First edition, 1998-12.

[7] N. Mokhov, "Protecting Superconducting Magnets from Radiation at Hadron Colliders", Workshop, "Beam generated heat deposition and quench levels for LHC magnets", CERN, 3.-4. March 2005.

[8] K. Wittenburg, "Quench levels and transient beam losses at HERAp", Workshop, "Beam generated heat deposition and quench levels for LHC magnets", CERN, 3.-4. March 2005.

[9] E.B. Holzer, et al., "Design of the Beam Loss Monitoring System for the LHC Ring", 9th European Particle Accelerator Conference EPAC 2004 , Lucerne, Switzerland , 05 - 09 Jul 2004.

[10] R. Filippini et al., "Reliability Assessment of the LHC Machine Protection System", Particle Accelerator Conference PAC 2005, Knoxville, TN, USA, 16 - 20 May 2005.

[11] E. Effinger et al., "Single Gain Radiation Tolerant LHC Beam Loss Acquisition Card", 8th European Workshop on Beam Diagnostics and Instrumentation for Particle Accelerators, Venice, Italy, 20 - 23 May 2007.

[12] E. Effinger et al., "The LHC beam loss monitoring system's data acquisition card", 12th Workshop on Electronics For LHC and Future Experiments, Valencia, Spain, 25 - 29 Sep 2006, pp.108-112.

[13] C. Zamantzas et al., "An FPGA Based Implementation for Real-Time Processing of the LHC Beam Loss Monitoring System's Data", Nuclear Medical Imaging Conference, San Diego, CA, USA, 29 Oct - 4 Nov 2006, pp.1489 – 1492.

[14] C. Zamantzas, "The Real-Time Data Analysis and Decision System for Particle Flux Detection in the LHC Accelerator at CERN", Thesis, Brunel University : Brunel University, 2006. - 219 p.

[15] C. Zamantzas et al., "The LHC beam loss monitoring system's real-time data analysis card", 7th European Workshop on Beam Diagnostics and Instrumentation for Particle Accelerators, Lyons, France, 6 - 8 Jun 2005, pp.278; CERN-THESIS-2006-037.

[16] C. Zamantzas et al., "The LHC Beam Loss Monitoring System's Surface Building Installation",12th Workshop on Electronics For LHC and Future Experiments, Valencia, Spain, 25 - 29 Sep 2006, pp.552-556.

[17] G. Guaglio, "Reliability of the Beam Loss Monitors System for the Large Hadron Collider at CERN", thesis, Univ. Clermont-Ferrand 2 Blaise Pascal; Clermont-Ferrand 2, 2005. - 246 p.; CERN-THESIS-2006-012 ; PCCF-T-0509.

[18] S. Wagner et al., "Balancing Safety and Availability for an Electronic Protection System", paper accepted by ESREL 2008.

[19] R.Schmidt et al., "Protection of the CERN Large Hadron Collider", New Journal of Physics 8 (2006) pp 290.

HARD X-RAY SYNCHROTRON RADIATION MEASUREMENTS AT THE APS WITH VIBRATING WIRE MONITORS*

G. Decker[1], R. Dejus[1], S.G. Arutunian[2], M.R. Mailian[2], I.E. Vasiniuk[2]
[1] Argonne National Laboratory, Argonne, IL 60439
[2] Yerevan Physics Institute, Alikhanian Br. Str. 2, 375036, Armenia

Abstract

A 5-wire vibrating wire monitor (VWM005) was developed and tested at the Advanced Photon Source (APS). The sensor was mounted on the outboard side of a bending-magnet synchrotron radiation terminating flange in sector 37 of the APS storage ring. The parallel wires were separated vertically by 0.5 mm; however, due to the possibility of rotation about a horizontal axis, the effective distance between the wires was reduced by a significant factor. To increase the response speed, the sensor was installed in air, resulting in a step response time of less than one second. Due to the extreme sensitivity of the detector, the very hard x-ray component of synchrotron radiation was successfully measured after its passage through the terminating flange.

BACKGROUND

At the APS, insertion device photon beam position monitoring is integrated into DC orbit correction algorithms, providing submicroradian levels of pointing stability over periods greater than 24 hours. Existing photon beam position monitors (BPMs) make use of ultraviolet (UV) and soft x-ray photoemission from metallized diamond blades arranged in sets of four and positioned edge-on at the periphery of the photon beam. These monitors suffer from a number of insertion device gap-dependent systematic errors associated with unavoidable soft background radiation. This radiation is associated with strong steering correctors located immediately upstream and downstream from the undulator source; they are part of the so-called Decker distortion scheme for reducing stray radiation overall [1].

In an effort to further improve upon photon beam position monitoring, an effort was initiated in 2005 to develop a BPM that is completely insensitive to the UV and soft x-ray components of undulator beams. One active area of research is the development of PIN diodes arranged to sense copper x-ray fluorescence in the backward direction [2-4]. The present work is the culmination of a number of informal meetings that took place at DIPAC 2005, and is in fact a hybrid of Arutunian et al.'s vibrating wire monitor (VWM) concept [5] and Scheidt's work with very hard x-rays at ESRF [6].

First experiments with the VWM at the APS were conducted in vacuum with an undulator beam in early 2007 [7] using the same facility where the PIN diode measurements were made. The main conclusions from that work were that the VWM is sensitive to extremely low levels of x-ray flux, but the detector's time response is quite slow since the primary means of achieving thermal equilibrium in vacuum is through radiation. Nevertheless, the measurments and subsequent analysis have provided an interesting quantitative validation of the theory of undulator radiation. Shown in Fig. 1 are data collected for the two-wire detector installed in vacuum at APS beamline 19-ID during a vertical angle scan of the undulator source, which was a standard APS undulator A operating at a large gap of 60 mm. The principle for extracting temperature changes from individual wire acoustic resonance frequencies is described in reference [7] and in detail in reference [8], which also describes the operating principle of the device.

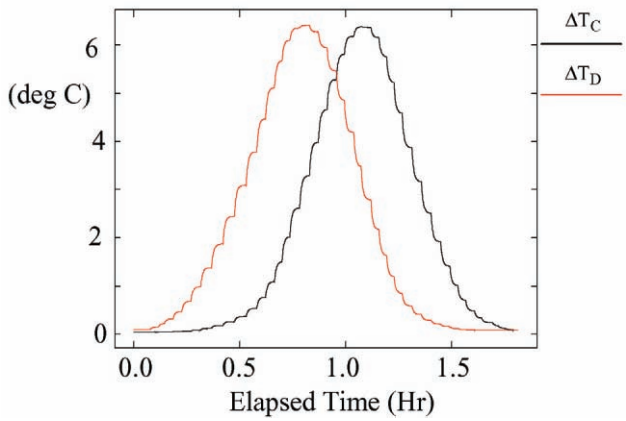

Figure 1: VWM data from undulator radiation during a vertical angle scan

The vertical angle was scanned in 5-microradian steps, pausing about three minutes after each change to reach equilibrium. As described in detail in reference [7], data analysis for this scan involved breaking the data set into 43 pieces, performing an exponential fit to each segment to extract an asymptotic temperature, executing an elaborate procedure to remove thermal drift with a linear drift model (0.01 degrees C / hour), and finally a performing normalization to stored beam current. The resulting profiles were seen to be very well approximated by Gaussians.

That the profile of an undulator beam should so closely match a Gaussian was somewhat surprising, given the known rather exotic profiles for individual undulator harmonics. To investigate this, the x-ray power density emitted from a standard APS undulator A with 60-mm gap (K = 0.023) was calculated after passing through 7 mm of beryllium [9]. This calculation included the particle beam dimensions, using a natural emittance of 2.5 nm-rad and 1% horizontal / vertical coupling. Shown

*Work supported by U.S. Department of Energy, Office of Science, Office of Basic Energy Sciences, under Contract No. DE-AC02-06CH11357.

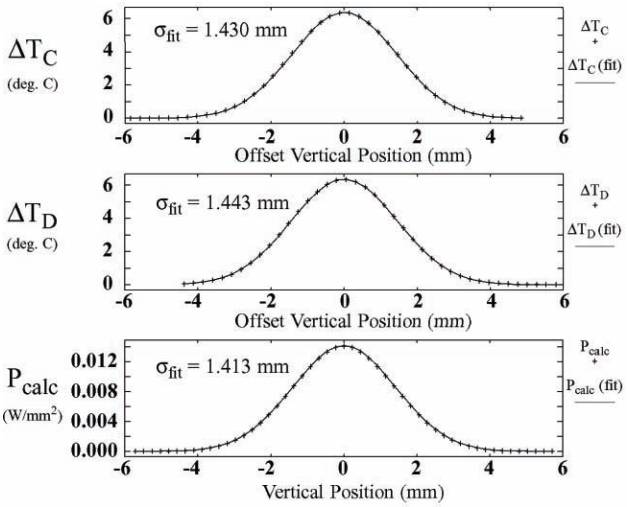

Figure 2: Comparison of experiment and theory: vertical profile of undulator radiation for APS undulator A, K = 0.023. Top and center: VWM data, shifted along the horizontal axis for the two wires C and D, with Gaussian fits. Bottom: calculated power density with Gaussian fit.

Fig. 2 is a comparison between the processed VMW profiles and the calculated power density.

As can be seen, the agreement is remarkable, to within about 2% in rms beam size. Nevertheless, the theoretical profile is non-Gaussian in detail. Shown in Fig. 3 are the residuals to the respective fits.

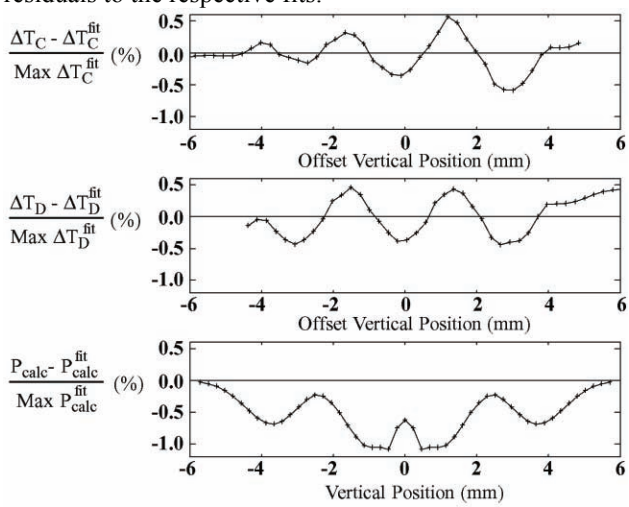

Figure 3: Undulator radiation Gaussian fit residuals.

The first thing to notice here is that the theoretical residual is unipolar. Since there is no ambiguity with regard to the zero-power baseline, the Gaussian fit was constrained to have zero baseline. This is clearly not the case for the experimental data, where unknown components of thermal drift introduce uncertainties as to the value of the baseline, which was used as a variable in the fit, along with centroid position and sigma. The scale of the residuals, and to some extent the shape, show good agreement. It is important to keep in mind that while the VWM provides a reliable measure of power deposited, in this case we are dealing with hard x-rays, and there clearly is a wavelength-dependent aspect to x-ray absorption in the wires. For the calculation, the total power density is computed, irrespective of material properties other than the 7-mm beryllium absorber placed in the path of the x-ray beam. An additional consideration, specifically with regard to the sigma values, is that the horizontal axis for the experimental data is wholly determined by the rf BPM calibrations, which are probably not accurate at the level of 2 to 3%.

IN-AIR DETECTOR

Inspired by efforts at ESRF to use unwanted very hard x-rays penetrating the accelerator vacuum chamber as a high-resolution beam size / position diagnostic, and considering also that an in-air vibrating wire monitor is expected to have a response time well below 1 second, a five-wire unit was designed and built at the Yerevan Physics Institute. This detector was designed to include five horizontally-mounted 100-micron-diameter steel wires with approximately 0.5-mm separation between them, to be mounted at an unused bending magnet radiation port in APS sector 37. Also included in the design was the ability to rotate the plane of the wires about a horizontal axis so as to reduce the effective vertical wire separation. The detector is shown in Figs. 4 and 5.

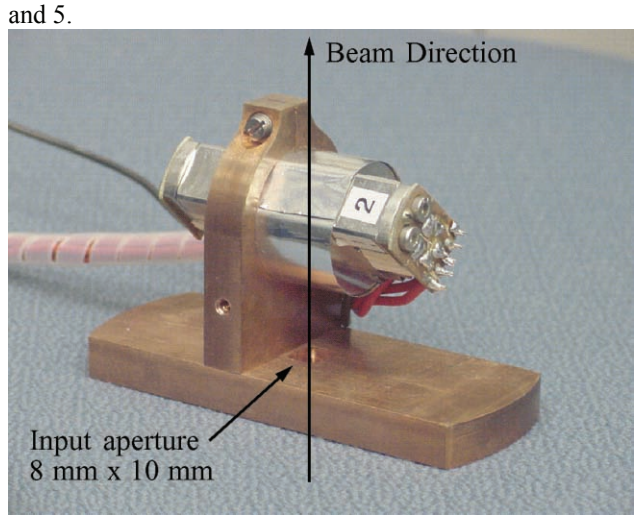

Figure 4: Five-wire in-air VWM unit showing rotational degree of freedom.

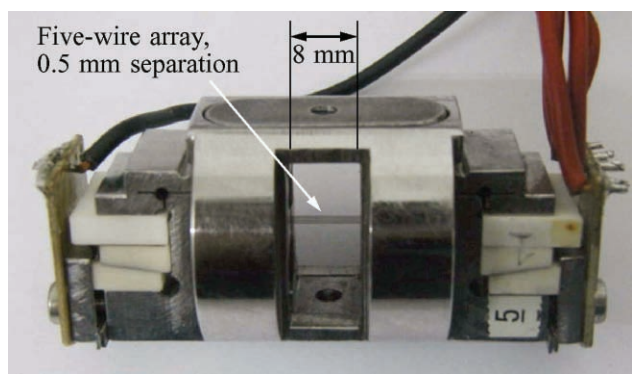

Figure 5: Five-wire VWM detector detail.

The wires themselves are 36 mm long and made of thermally-treated stainless steel [10]. The horizontal aperture of the detector is 8 mm, with a variable vertical aperture depending on the rotation angle. Acoustic resonance frequencies fall in the range from 4000 to 9000 Hz, with 0-1000 Hz variability from induced thermal heating allowed. The thermal calibration factor is nominally 40 Hz / K at 4200 Hz operating frequency. This results in a wire temperature range of 0 to 25 K, resolution of 0.00025 K, and long-term stability rated at +/- 0.00025 K and +/- 0.001 K over 1- and 24-hour periods, respectively.

The device shown in Fig. 4 (actually a second unit nearly identical to it) was installed at an unused bending magnet beamline exit port flange in sector 37. This sector is reserved for rf cavities, and as such no beamline will ever be constructed there. Shown in Figs. 6 and 7 are a photo of the photon beam dump absorber together with a line drawing, and a rendering of the installed detector.

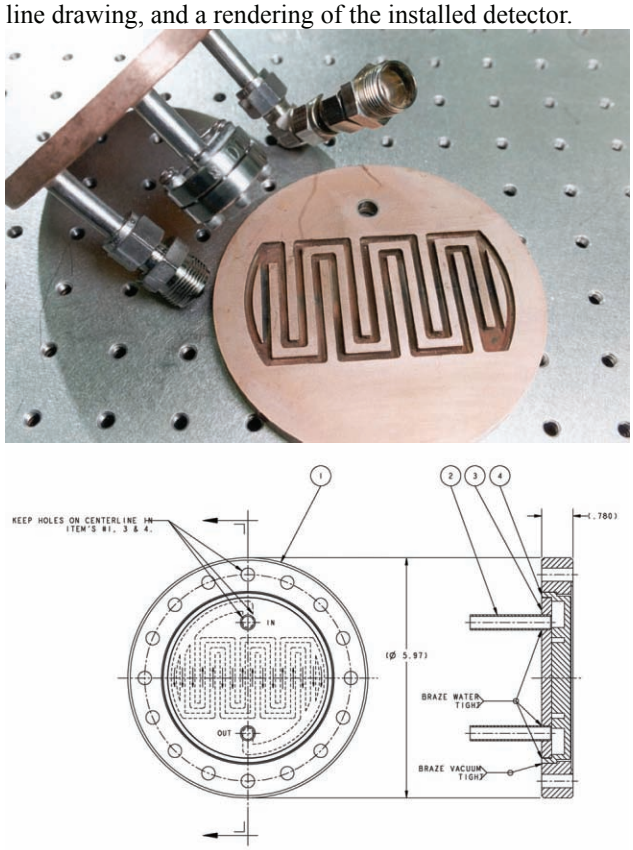

Figure 6: Bending magnet photon beam dump for unused exit port locations. Top: Disassembled unit showing internal cooling channels. Bottom: Assembly drawing.

The actual installation was significantly less tidy than shown in Fig. 7, but due to constraints of schedule pressure it was sufficient to produce acceptable results. The flange assembly is mounted 6.4 meters downstream of the bending magnet source point. At the APS, the source point is defined to be one-eighth of the way into the dipole magnet steel starting from the upstream end. A tangent line attached to the nominal curved particle beam trajectory at the one-eighth point in principle should strike the center of this flange. The flange thickness is 20 mm, which is the same as the copper thickness with the exception of the cooling channels. The flange diameter is 6 inches. A few variations of this design exist, as can be seen from the photo in Fig. 6 vs. the line drawing, which is what is actually installed in sector 37.

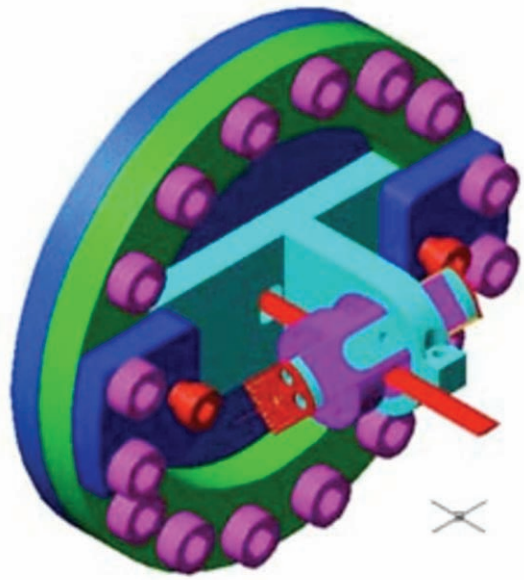

Figure 7: Conceptual rendering of the VWM installation.

DATA COLLECTION

After storing 102 mA in the APS storage ring, distributed among 324 individual bunches for long lifetime, a special vertical orbit bump was created to allow angle steering at the 37-BM bending magnet source point. An initial large-range scan had produced a measurable blip at an angle of -0.5 mrad relative to the nominal stored beam trajectory. This was due to a rather hasty installation effort that placed the detector's active area 3 mm below the machine midplane. After a second preliminary scan to define the optimal scan range, a series of scans over a 250 microradian range with 125 steps of 2 microradians each was collected. Typical results for one of these scans is shown in Fig. 8. While the orbit was scanned with 125 steps, VWM data was collected at a constant 1 Hz throughout.

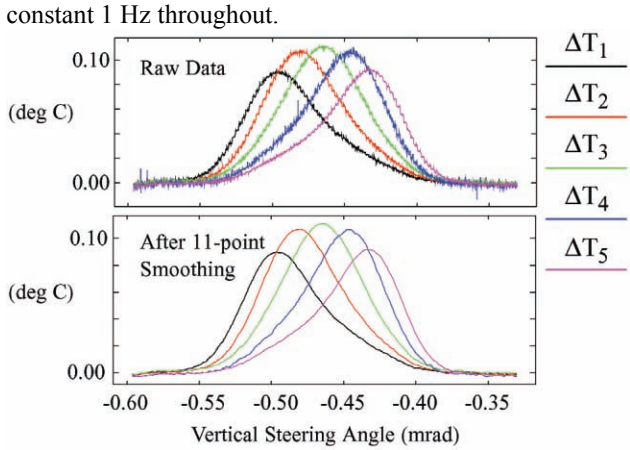

Figure 8: VWM-005 results from a vertical angle scan at source point 37-BM.

The horizontal axis is computed from rf BPMs straddling the source point, after correcting for a bunch-pattern-dependent change in gain. The dominant mode of operation at APS uses 24 bunches, but for 324-bunch operation, the rf BPM calibrations can change by 15% or more. Using 324 bunches has the side benefit of providing a longer beam lifetime. The lower panel of Fig. 8 shows the same data after running it through an 11-point smoothing filter with a despiking algorithm to eliminate outliers [11].

Immediately it is apparent that the in-air detector produces a different profile depending upon which wire is chosen. This is actually a cross-talk phenomenon where convective heat transfer is occurring between the wires, in spite of the fact that their temperatures differ by only small fractions of a degree. Using a linear heat-transfer model described in reference [8], the relative power striking each wire can be inferred from a matrix connecting the temperature differences between wires. This matrix is constructed semi-empirically, from the requirement that all wires produce the same power profile. The matrix used for the analysis presented here is contained in Table 1.

Table 1: Linear Heat Transfer Coupling Matrix

α_{ij}	ΔT_1	ΔT_2	ΔT_3	ΔT_4	ΔT_5
ΔT_1	2.50	0.633	0.353	0.319	0.170
ΔT_2	0.633	1.865	0.882	0.434	0.183
ΔT_3	0.353	0.882	1.692	0.932	0.424
ΔT_4	0.319	0.434	.932	1.820	0.489
ΔT_5	.170	.183	.424	.489	2.478

Starting from the smoothed data in Fig. 8, application of the heat transfer matrix results in the power profiles shown in Fig. 9, together with corresponding Gaussian fits. The data of Fig. 8 was first normalized to compensate for the slight decay in stored beam current over the course of the scan.

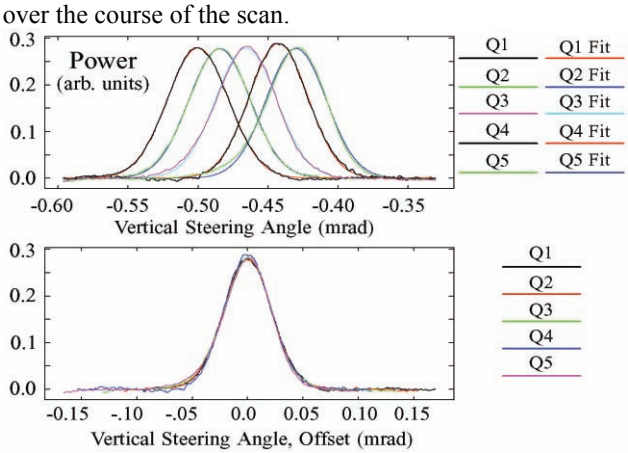

Figure 9: APS bending magnet power density profiles inferred from VWM data. Top: Measured profiles together with Gaussian fits. Bottom: The same measured data, shifted along the horizontal axis.

The upper panel in Fig. 9 shows the result of applying the coupling matrix to the smoothed data of Fig. 8, but with the additional step of subtracting a baseline power level for each curve, which is derived from the individual Gaussian fits. In the lower panel a similar offset has been introduced along the horizontal axis for direct comparison of the profiles from each wire. Only the data is shown in the lower panel, with no fit data displayed.

Shown in Table 2 are the Gaussian fit parameters for the curves of Fig. 9.

Table 2: Profile Fit Parameters

	gfit Centroid		gfit Sigma	
	mrad	mm	microrad	microns
ΔT_1	-0.5001	-3.201	21.96	140.5
ΔT_2	-0.4847	-3.102	21.95	140.5
ΔT_3	-0.4657	-2.981	21.87	140.0
ΔT_4	-0.4426	-2.833	21.01	134.5
ΔT_5	-0.4300	-2.752	21.51	137.7

The columns listed in mm / microns were derived from the angular data via multiplication by the 6.4-meter source-detector distance. Note that the sigma value for wire 4 deviates significantly from the values for the other wires. As can be seen from the original data, as well as in the lower panel of Fig. 9, this wire was producing data that was generally noisier than that of the other wires. A second observation is that difference between centroid values of wires 1 and 5 indicate an overall vertical extent of only 449 microns. Keeping in mind that the nominal separation between individual wires is 500 microns, this implies that the plane containing the wire is inclined at a shallow angle relative to the horizontal. Specifically, one expects an inclination angle of atan(0.449 / 2) = 12.65 degrees. This was cause for a bit of consternation since the spare unit had an angle nearer to 45 degrees. However, an inspection of the in-tunnel unit during a later maintenance period confirmed the shallow angle.

The values of rms beam size (gfit Sigma) in the table are certainly of the correct order of magnitude. An old calculation done by Ken Green many years ago showed that a Gausian fit to the power density for a bending magnet radiation source is fit quite well if one uses an rms angular size of 0.608 / γ, where γ is the relativistic factor, equal to 13700 for the 7-GeV APS [12]. This yields an rms size of 44 microradians. As shown in Fig. 10, however, the hard x-rays capable of penetrating 20 mm of copper have a considerably smaller profile than those at the critical energy. This is a plot of radiated power per unit solid angle for circular motion into revolution harmonic n as a function of vertical angle ψ. This is from a calculation done in 1945 by Schwinger [13,14]. In this case, the classical definition of the critical photon energy, which is 19.5 keV for APS bend magnets, corresponds to n = 3/2. The highest energy curve shown, curve J, corresponds to a photon energy of just under 100 keV. Unfortunately, in order to calculate the curves of Fig. 10, one is required to compute Bessel function of order n with arguments also of order n, where n is of order γ^3 = 3e12.

The data for Figs. 8 and 9 were collected with horizontal / vertical machine coupling set at 5.3%, corresponding to a vertical emittance of 0.15 nm-rad, a

vertical particle beam source size of 58 microns rms, and angular divergence of 3 microradians rms. This is quite a large amount of coupling, since the APS is normally run with 1% coupling, and was done intentionally using a skew quadrupole magnet to investigate whether the VWM could detect changes in vertical beam size. During an earlier scan, the coupling was set at an average 2.6% corresponding to a source size of 40 microns rms and angular divergence of 2 microradians rms. Because the initial steering angle was so large (-0.5 mrad), the coupling was influenced by forcing the trajectory to be so far off axis through a large number of sextupole magnets. This also caused the coupling to change significantly over the course of a single scan, from 3.6% at the extreme limit of the scan to 1.7% at the other end. Shown in Table 3 are the results of this earlier scan.

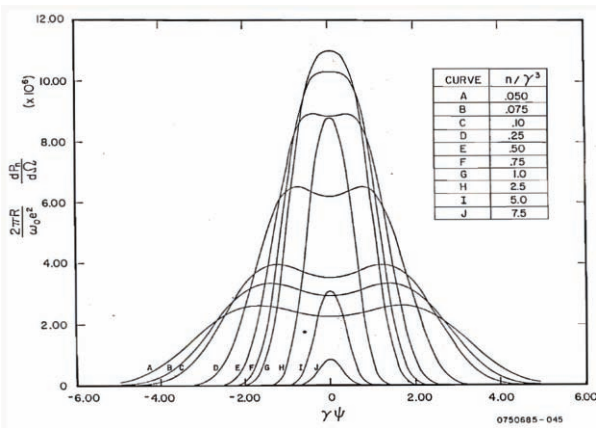

Figure 10: Synchrotron radiation power per unit solid angle into revolution harmonic n as a function of vertical angle ψ. The quantity γ is the relativistic factor.

Table 3: Fit Parameters for 2.6% Average Coupling

	gfit Centroid		gfit Sigma	
	mrad	mm	microrad	microns
ΔT_1	-0.4924	-3.151	19.88	127.2
ΔT_2	-0.4768	-3.052	19.96	127.7
ΔT_3	-0.4577	-2.930	20.00	128.0
ΔT_4	-0.4352	-2.785	19.29	123.4
ΔT_5	-0.4221	-2.701	19.43	124.3

From the table, it is clear that the effects of the coupling change are resolved by this detector. Due to the complex nature of off-axis trajectories through sextupoles it is difficult to make any quantitative statements; however, the observed resolution is very encouraging. Note that the measured distance between centroids for wires 1 and 5 is now 450 microns to be compared with 449 microns for Table 2.

CONCLUSIONS

Vibrating wire monitors have proven themselves as a reliable quantitative diagnostic of beam size and position for hard x-ray synchrotron radiation. For the five-wire design, using a shallow inclination angle allowed for an effective vertical wire separation distance of only 112 microns. Because of this, a five-sample beam profile monitoring vertical beam sizes with sigma values as small as 100 microns rms or lower can be provided in real time. As at ESRF, widespread use of monitors of this type could allow for local coupling correction around the ring. Further potential uses are envisioned, such as integrating an in-air monitor into an undulator photon mask assembly for clean hard x-ray position measurements.

REFERENCES

[1] G. Decker, O. Singh, Phys. Rev. ST Accel. Beams 2, 112801 (1999).
[2] R. Alkire, G. Rosenbaum, and G. Evans, J. Synchrotron Rad. 7, 61-68 (2000).
[3] G. Decker, G. Rosenbaum, and O. Singh, "Development of a Hard X-ray Beam Position Monitor for Insertion Device Beams at the APS," BIW '06, Batavia, IL, AIP Conf. Proc. 868, 202-207 (2006).
[4] G. Decker, P. Den Hartog, O. Singh, G. Rosenbaum, "Progress Toward a Hard X-ray Insertion Device Beam Position Monitor at the Advanced Photon Source," PAC '07, Albuquerque, May 2007, p. 4342.
[5] S.G. Arutunian et al., "PETRA Proton Beam Profiling by Vibrating Wire Scanner," DIPAC '05, Lyon, June 2005, p. 181.
[6] B.K. Scheidt, "Detection of Hard Xrays in Air for Precise Monitoring of Vertical Position and Emittance in the ESRF Dipoles," DIPAC '05, Lyon, June 2005, p. 238.
[7] G. Decker, S.G. Arutunian, M. Mailian, G. Rosenbaum, "First Vibrating Wire Monitor Measurements of a Hard X-ray Undulator Beam at the Advanced Photon Source," DIPAC '07, Venice Maestra, May 2007, to be published.
[8] S.G. Arutunian, "Vibrating Wire Sensors for Beam Instrumentation," these proceedings.
[9] R. Dejus, private communication, Argonne National Laboratory.
[10] Vibrating wire monitor VMW-005 users manual, HTM Reetz GmbH, Berlin, Germany, in cooperation with Yerevan Physics Institute.
[11] M. Borland, L. Emery, H. Shang, R. Soliday, "User's Guide for SDDS Toolkit Version 1.30," http://www.aps.anl.gov/Accelerator_Systems_Division/Operations_Analysis/manuals/SDDStoolkit/SDDStoolkit.html
[12] G.K. Green, "Spectra and Optics of Synchrotron Radiation," BNL report 50522.
[13] J. Schwinger, "On Radiation by Electrons in a Betatron," Office of Naval Research (1945), transcribed by M. Furman as Lawrence Berkeley National Lab note LBNL-39088 (1999).
[14] J. Schwinger, Phys. Rev. 70, 798 (1946).

THE PROGRESS OF BEPCII STORAGE RING DIAGNOSTICS SYSTEM

J.S. Cao#, L. Ma, H.Z. Ma, L. Wang, Q. Ye, J.H Yue, L. Zhang, X. Y. Zhao, Y. Zhao, Z. Zhao

Institute of High Energy Physics, Chinese Academy of Sciences, Beijing 100049, China

Abstract

In this paper, we will present the progress of BEPCII storage rings beam diagnostics system along with the BEPCII commissioning. Tools such as Libera BPM had been used for the BPR first turn measurement and the injection residual orbit research of BER. COD_BPM can satisfy the resolution requirement for the beam-beam scan in the interaction region, and for the COD measurement, BCM (bunch current monitor) can help us on the different injection pattern. The TFB system is important to suppress the strong multi-bunch instabilities during the higher beam current running. The tune meters, the beam-loss monitors, DCCT and SLM (synchrotron light monitor) are also described in this paper.

INTRODUCTION

As the upgrade project of Beijing Electron Positron Collider (BEPC), BEPCII is still serving the purposes of both high energy physics experiments and synchrotron radiation applications [1]. The BEPCII is a double ring electron-positron collider and a synchrotron radiation (SR) source with its outer ring, or SR ring. It can work on collision mode or dedicated synchrotron radiation mode. The design goals of the BEPCII are shown in Table 1.

Table 1: The design goals of the BEPCII

Beam energy	1-2.1 GeV
Optimum energy	1.89 GeV
Luminosity	1×10^{33} $cm^{-2}s^{-1}$ @1.89 GeV
Injector Linac	Full energy inj.: 1.55-1.89 GeV Positron inj. rate > 50 mA / min
Dedicated SR	250 mA @ 2.5 GeV

For the collision mode, the electron ring (BER) and positron ring (BPR) cross each other in the northern and southern interaction points (IP's) with a crossing angle. In the northern crossing region, a vertical orbit bump is used to separate the two beams, while the southern IP is used for BESIII detector. When BEPCII works in the dedicated synchrotron radiation mode (SR), the electron beam circulates in the two outer half rings. A bypass in the northern IP is designed to connect two outer half rings. In the southern crossing region, a special pair of superconducting magnet complexes, mainly including quadrupole magnets (SCQ) and bending magnets (SCB), are used for 1.5 cm β function in the y direction at the IP on colliding mode and to serve as the bridge connecting two outer half rings for SR operation, respectively. Because the construction schedule of the cryogenics system and superconducting magnets was little delayed compared to the other systems, it was decided to install conventional magnets in the interaction region (IR) as the backup scheme, so that we can provide beam to SR users as early as possible, and accumulate the beam commissioning experience on the colliding mode. The backup lattice is similar to that of the original design.

Two phases of commissioning of the BEPCII rings have been completed: collision mode commissioning, and providing beam to beamline users in the dedicated synchrotron radiation mode. Phase one commissioning started on Nov. 13, 2006 by using conventional magnets instead of SC magnets in the IR. Phase two commissioning started on Oct. 24, 2007 by using SC magnets (without the BESIII detector). In the two phases, the beam diagnostics system played important roles, such as using the Libera BPM for first-turn beam circulating and for injection residual orbit research on the BER, and transverse bunch-by-bunch feedback (TFB) system to suppress the strong multi-bunch instabilities in higher-beam-current running, and so on.

LIBERA BPM

In the storage rings of BEPCII, a total of 16 units of Libera BPM are used. Libera control platform is located in Central Control Room. We can implement the control of Libera and data acquisition through the local-area network. BEPCII event timing system provides the trigger signal through an event receiver (EVR) module. Then we use clock splitter to synchronize data acquisition in different Liberas.

The Libera BPM played an important role during the commissioning of the first-turn and first-several-turns beam-circulating in BER and BPR (Figure 1) We only took 3 hours and one day to realize the beam accumulation in BER and BPR, respectively.

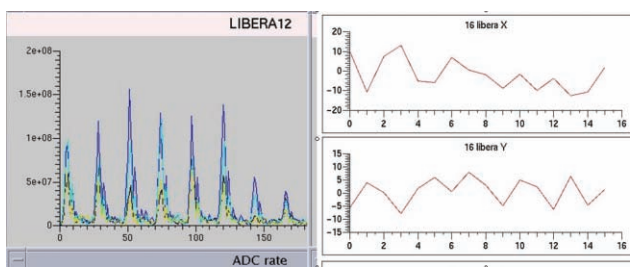

Figure 1: Libera BPM signal for first several turns of beam in the BER

Another important role Libera played is the optimization of timing delay of injection kickers and minimization of residual orbit oscillation in BER. The BEPCII includes two injection kickers and a Lambertson magnet for each

#caojs@ihep.ac.cn

ring. The injection layout of two rings is the same. Both kickers would kick the beam in the horizontal plane. The phase advance in the horizontal plane between two kickers is designed to be exactly 180° to decrease the disturbance to the circulating beams during the injection. During the beam injection in BER, we found the injection kickers frequently cause beam loss when the voltage intensities of two kickers are set almost the same. We use the Libera BPM to measure the turn-by-turn beam position data by changing the difference of two kicker intensities and try to analyze the residual orbit oscillation. When the difference of two kicker intensities becomes smaller, we observed that the amplitude of residual orbit oscillation becomes smaller in the X direction but bigger in the Y direction. We suspected a coupling between X and Y direction in the injection region. Later we finally found a short circuit in the R1OQ16 quadrupole magnet in the injection region. Before this problem was found and solved, we had to optimize the injection efficiency. We adjusted the voltage intensity and timing delay of two kickers to reduce the residual orbit oscillation, and the injection efficiency was improved. With a small residual orbit oscillation, we cold keep the two-beam colliding condition during injection [2]. Figure 2 gives the measurement results of residual orbit oscillation before and after optimizing the injection efficiency of BER.

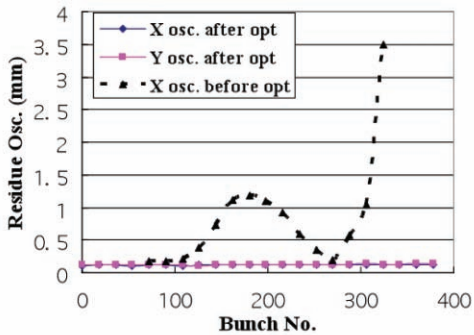

Figure 2: The measurement results of residual orbit oscillation in BER.

MX_BPM

In the BEPCII double rings with 240 m circumference, there are 67 BPMs in each ring (total 132 BPMs, two are for common) for the COD measurement and correction. A set of low loss coaxial cables brings up the pick-up signals of each detector to the local control room where the DAQ system is located. The lengths of cables vary from 60 to 90 meters depending on the locations of the detectors in the storage rings. Table 2 shows the main BPM and BEPCII parameters.

The COD BPM system consists of Bergoz MX_BPM, VME64x and ADC boards. Among various analog signals from a MX_BPM board, only the beam position (x and y), Σ and A, B, C, D (four buttons) signals are digitized for the regular operational database [3].

There are twenty 32-channel 60-kHz 16-bit ADC boards in each ring. The resolution of the position measurement is improved by averaging 30 raw BPM data in the microprocessor. It gives the 2 Hz data refreshing rate for double rings. Figure 3 shows the DAQ structure of the BPM system.

Table 2: Main parameters of BPM and BEPCII

Parameters	Unit	Value
BPM Accuracy	mm	0.1
BPM Resolution	mm	< 0.01
RF Frequency	Mhz	499.8
Harmonic Number	Colliding mode	396
Harmonic Number	SR mode	402
Bunch Current	mA	9.8
Total Beam Current	mA	910
Bunch Length	cm	~1.5
Crossing Angle	mrad	±11

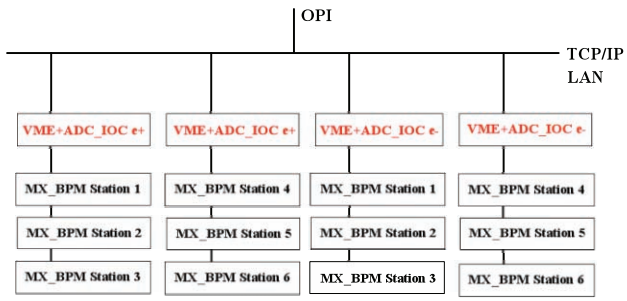

Figure 3: The DAQ structure of the COD BPM system.

Resolution

Normally, the main performance parameters of the BPM system are accuracy and resolution. The accuracy mainly depends on the alignment. This can be compensated by the BBA. By taking 16-bit ADC and averaging the raw BPM data, the system resolution is less than 2 μm in Y, within a measuring range of ±5 mm, and 4 μm in X within a measuring range of ±10mm. Figure 4 shows the BPM resolution during one standard shift (7 hours).

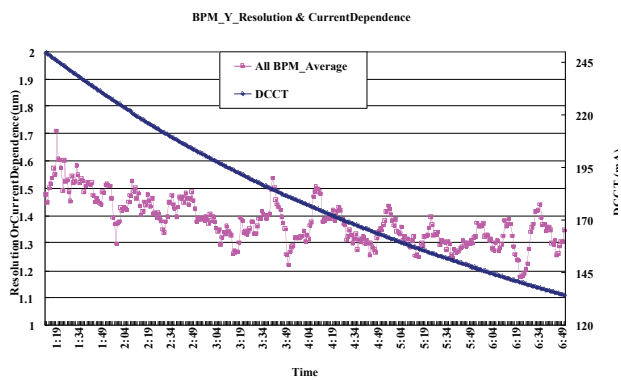

Figure 4: The BPM resolution in the Y direction over 7 hours.

For Beam-beam Scan

The vertical β function at the IP is one of the key parameters for luminosity. The small beam size means that the BPM system should have good resolution to satisfy the requirement for beam-beam scan (BBS) on collision

tuning. The first beam-beam scan with SCQ at IP was done by 2 μm steps on Nov. 18, 2007. For this purpose, an orbit bump around the IP in one ring is used to scan the beam position at the IP, while observing the beam orbit variation in the other ring due to the beam-beam deflection. Fig. 5 is a typical BBS result.

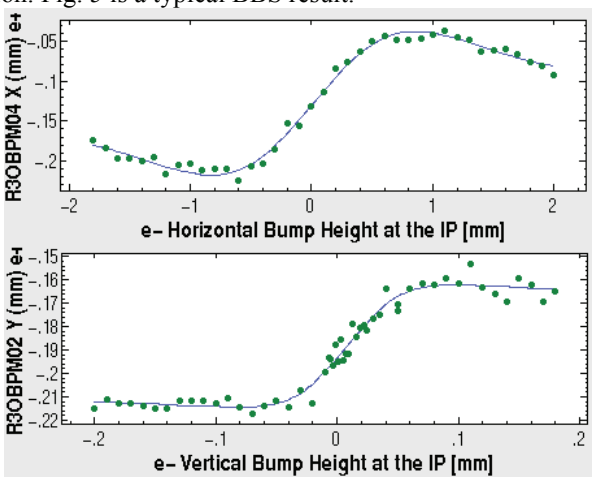

Figure 5: Positron beam orbit variation due to beam-beam deflection. The lines are the fitted curves for Gaussian bunches.

BUNCH CURRENT MONITOR

There are at least these two reasons for filling each ring with an equal charge in all bunches: to optimize the beam-beam tune shift and to control the stability of individual bunches.[4] The bunch current monitor (BCM) system consists of three parts in the hardware layer: the front-end circuit, the DAQ and the bucket selection system. The front-end circuit is located near the storage rings; the DAQ is in the local station of the beam instrument. The key component of DAQ is a FADC board with model of ECAD-1-081500-1 (1.5 GSPS, 8-bit VME board). Here the analog bunch current signal sent from the front-end circuits is processed by FPGAs and then the digital signal is sent to the shared memory board. The bucket selection system in the central control room reads the bunch current data from the shared memory board, then controls the beam pulse from the linac to be injected into the required bucket within 20 ms, which is the repetition period of the linac. Figure 6 shows the system structure with a dedicated optical communication system.

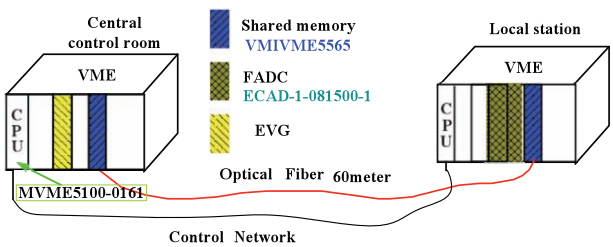

Figure 6: The BCM system structure.

In the software layer, the VME computer MVME5100-0163 in the local station of beam instrumentation runs real-time VxWorks program for the DAQ, while the same type VME computer in the central control room runs program based on standard EPICS I/O. For an 8-bit ADC with maximum input of 500 mV, the resolution of BCM system can reach 50 pC for an injection beam pulse. Figure 6 gives a measurement result from a 300 mA·300 mA multi-bunch collision.

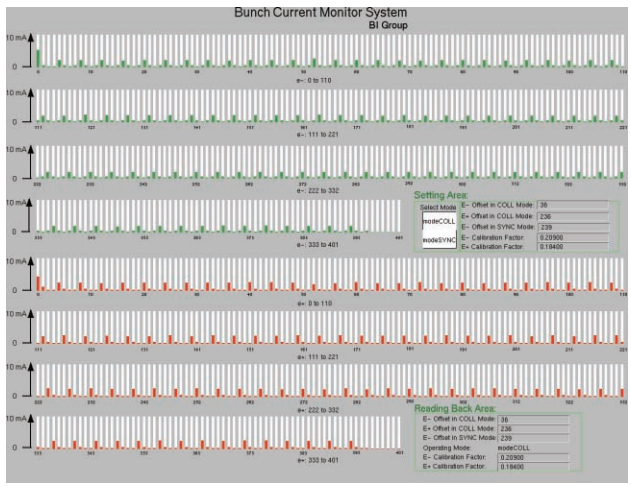

Figure 6: BCM measurement result on 300mA·300mA multi-bunch collision.

TRANSVERSE FEEDBACK SYSTEM

BEPCII is designed to operate with every other 4-bucket filled, with a bunch spacing of 8 ns (62.5-MHz bunch frequency) and high beam current (about 1 A) as shown in Table 2 in the colliding mode. Each ring has 93 and 99 bunches, with and without a small ion clearing gap, respectively. According to estimations of the growth time of most dangerous coupled bunch modes (4.3 ms for resistive wall and 0.5 ms for electron cloud) are shorter than the radiation damping time of 25 ms in the transverse direction. The design goal of the feedback damping time is set to 0.5 ms in the transverse direction.

Because the storage rings are small and the budget is limited, the transverse feedback system (TFB) is analog. To increase shunt impedance, the damping kicker length matches the 125-MHz bunch frequency. Two kickers were installed in the outer ring so the system can work in both colliding and SR modes. The front-end electronics, phase shifter, one-turn delay unit, notch filter and power amplifiers are shared by both modes.

The TFB system successfully operated in the phase two commissioning of BEPCII, including colliding mode and SR mode. Figure 7 gives the measurement results of synchrotron light monitor with the TFB system turning on and off during BEPCII operated in the SR mode.

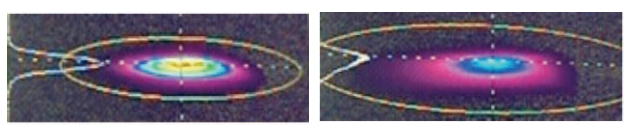

Figure 7: TFB turn on (left) and turn off (right)

In most cases of operation without TFB, a threshold of beam current often appeared when injecting beam into rings to over 200 mA. The capability of suppressing betatron sidebands can reach to 40 dB in both horizontal and vertical directions in the designed 125MHz system bandwidth. Figure 8 shows another beam spectrum measurement results in BPR when BEPCII operated in the colliding mode with 93 bunches and 243mA beam current.

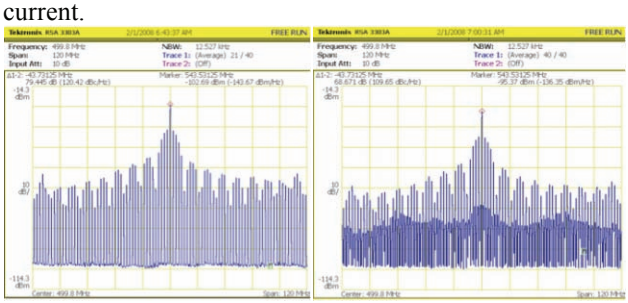

Figure 8: TFB turn on (left) and turn off (right)

BLM AND TUNE

The beam loss monitor (BLM) and tune measurement systems also played an important role for the first beam circulating in the outer ring for the dedicated SR mode (BSR) in phase one commissioning. They were also important for background study on BESIII (Figure 9 is an example of the beam loss measurement during the electron beam injection), tune-tune shift measurement for the luminosity estimation, and so on. By using the BLM and BPM, we found a wrong connection of a power supply to the R1OQ09 quadrupole magnet.

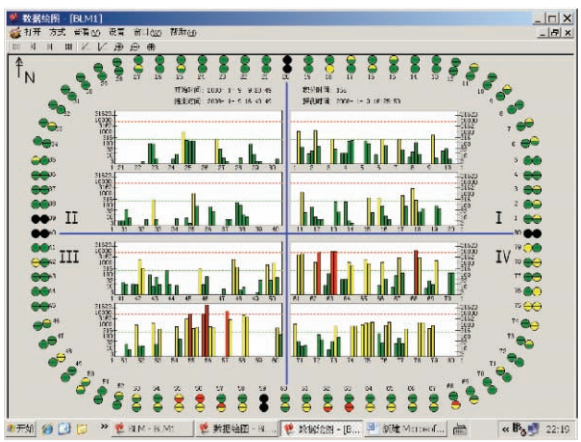

Figures 9: The beam loss measurement during electron beam injection.

Background study

The beam loss monitor (BLM) system usually is used for detecting or locating any possible excessive beam loss with the injection process, beam instabilities, bad vacuum, ion trapping, etc. This system is a useful supplement to the beam diagnostic system for the trouble-shooting. The detector is produced by Bergoz Company. It is the PIN diode type and not sensitive to photons. We try to use the BLM system for the BESIII detector background study. From the BLM measurement results, we found that:

- The electron beam injection brings more beam loss than positron beam injection.
- The collimators at present locations in the electron ring didn't show obvious effects to reduce the background, but the collimators at transport line show obvious effects to reduce the background during the electron beam injection.
- On the SR mode, the beam loss in IR is small.

Because BEPCII doesn't have a dedicated abort system for dumping the beam, so the beam abort became a problem. Similarly, according to the BLM measurement results, the new abort method was decided by using injection kickers and local orbit bump and it can obviously reduce the background in IR.

Tune-tune shift

The beam-beam tune shift can be used to evaluate the collision luminosity. Before the dedicated luminosity detector can offer the measured luminosity data for the accelerator commissioning, the sweep frequency method was used for the tune measurement while the transverse feedback kicker serving as the shaker to excite the beam oscillation. The perturbed tunes of each ring corresponding to the so called high tune (H) and low tune (L) modes have been observed with spectrum analyzer [1]. Figure 10 is a typical tune spectrum observed during two-single-bunches collision.

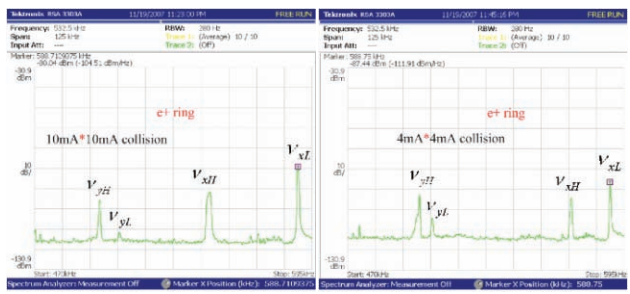

Figure 10: Measured tunes due to beam-beam effects.

SLM AND DCCT

Comparing with other diagnostics devices, like BCM, TFB, BLM and so on, synchrotron light monitors (SLM) just keep the same optics structure with BEPC used, only first mirror and its vacuum chamber were replaced by new one. It is used for the measurement of beam size, bunch length and to monitoring the beam instability. The calibration of the transverse magnification of the imaging optics had been done with beam by using the method of sliding the lens. The measurement error of beam size including chromatic error, depth of field error, diffraction error and curvature error are also analyzed.

The DCCT will be introduced in detail in the ref. [5]. Here only introduces the issues related to the high beam current. Along with beam intensity growth, particularly

when the beam current is higher than 500mA in colliding mode, the heating effect due to HOM appeared clearly in the DCCT. The temperature rise shows sensitivity to the bunch current. This problem had been considered in the shielding design, e.g., a copper layer to bridge the image current rerouting on the ceramic gap was adopted for RF shielding, but its capacity seems too small for some low frequency part of the image current. Therefore some capacitors will be connected during machine shutdown to improve the RF shielding.

SUMMARY

Two phases of BEPCII commissioning have been completed. Various beam instrumentation systems played important roles during each commissioning stage. However, there is still much work to do, such as eliminating the sporadic jitter in BCM, carefully tuning the phase to keep the TFB stable, solving the heating problem in DCCT, developing more functions for Libera in order to get more beam information, and so on.

ACKNOWLEDGEMENT

We appreciate many people from SLAC, LBNL and KEK for their continuous help. Dr. Alan S. Fisher from SLAC joined the first week of BSR commissioning, giving helpful advice. Dr. Tobiyama from KEK and Dr. John Byrd from LBNL give us help on the transverse feedback system commissioning. Dr. Michael Abbott from Diamond Light Source gives help on the code of Libera system. The companies of Bergoz and Instrumentation Technologies also give technical support on the application of their products. Thanks also go to R. Hettel, the BEPCII IMAC member.

REFERENCES

[1] J. Q. Wang, L. Ma and C. Zhang, The BEPCII: Status and early Commissioning, PAC'07, Albuquerque, June 2007.

[2] H. Z. Ma, J. S. Cao, et al, The Research of Residual Orbit Oscillation in BEPCII, Chinese Physics C, has been accepted.

[3] J. Y. Huang, S. J. Park, et al, Improved Closed Orbit Measurement System for PLS, PAC01, Chicago, June 2001.

[4] J. S. Cao, et al, The Design Report of Beam Instrumentation System for BEPCII, 2002.

[5] Y. Zhao, J. S. Cao, The BEPCII DCCT system, This proceedings.

MEASUREMENTS OF THE ELECTRON CLOUD DENSITY IN THE PEP-II LOW ENERGY RING*

J. Byrd, S. De Santis, K. Sonnad, LBNL, Berkeley, CA 94720, U.S.A.
F. Caspers, T. Kroyer, CERN, Geneva, Switzerland
A. Krasnykh, M. Pivi, SLAC, Menlo Park, California.

Abstract

Clouds of low energy electrons in the vacuum beam pipes of accelerators of positively charged particle beams present a serious limitation for operation of these machines at high currents. Because of the size of these accelerators, it is difficult to probe the low energy electron clouds over substantial lengths of the beam pipe. We have developed a novel technique to directly measure the electron cloud density via the phase shift induced in a TE wave that is independently excited and transmitted over a section of the accelerator. We infer the absolute phase shift with relatively high accuracy from the phase modulation of the transmission due to the modulation of the electron cloud density from a gap in the positively charged beam. We have used this technique for the first time to measure the average electron cloud density over a 50 m straight section in the positron ring of the PEP-II collider at the Stanford Linear Accelerator Center. We have also measured the variation of the density by using low field solenoid magnets to control the electrons.

INTRODUCTION

The accumulation of low-energy background electrons in regions of the beampipe of high-energy accelerators of positively charged beams presents one of the most serious challenges to increasing currents in these machines. Depending on bunch repetition rate, beam current and other machine conditions, electrons extracted from the beampipe walls, usually by synchrotron radiation, can be transversally accelerated by the circulating beam and extract even more electrons when they strike the beampipe again. This resonant mechanism leads to a buildup of these electrons, which can negatively affect the accelerator's operation in a variety of ways [1].

Because of its importance for a number of present and future high profile projects, such as the Large Hadron Collider and the International Linear Collider, the electron cloud dynamics, its effects on the beam and their cures have been the object of numerous studies in the past few years. From an experimental point of view, electron cloud effects have been observed in various high intensity synchrotrons and storage rings [2-4].

*Work supported by the U.S. Department of Energy under Contract Nos. DE-AC0-05CH11231 and DE-AC03-76SF00515

The methods used consist in the analysis of the beam's dynamic behaviour,, which can necessarily give only an averaged measurement of the electron cloud density (ECD) around the machine, and local detectors [5], which only measure the energy spectrum of electrons near the beampipe wall at a specific location.

In this paper we present a novel method featuring several positive characteristics, namely the possibility of being applied anywhere a pair of beam position monitors (BPM) are available, without the necessity of any dedicated hardware nor installation, and the ability of probing the electron cloud density directly along the beam path and not only in the vicinity of the beampipe walls.

The method consists in propagating an electromagnetic wave along the beampipe, between two sets of BPM's delimiting the region that one wants to measure.

The propagating wave does not interact with the ultrarelativistic beam, but is affected by the low-energy electron densities it encounters. This interaction essentially translates into a phase delay that can be theoretically evaluated, as shown in the next paragraph.

Besides this basic interaction mechanism it is also possible to obtain a resonant interaction in regions where a local magnetic field is of such strength as to define a cyclotron frequency equal to the frequency of the propagating wave. The theoretical treatment of this case is still object of work. We present nonetheless some preliminary results, with simulations and experimental measurements.

THEORETICAL EVALUATION OF THE ELECTRON CLOUD EFFECTS ON MICROWAVE PROPAGATION THROUGH THE BEAM PIPE

The derivation of the wave dispersion relationship for propagation of an electromagnetic wave through an electron plasma has been described in [6] and is limited to first order perturbations, so that the model does not anticipate any amplitude variation of the transmitted wave. The phase shift of a wave of angular frequency ω caused by a homogeneous density of cold electrons per unit propagation length is given by:

$$\Delta\varphi / L = \frac{\omega_p^2}{2c\sqrt{\omega^2 - \omega_c^2}} \qquad (1)$$

where ω_c is the beampipe cut-off frequency and ω_p is 2π times the plasma frequency f_p, which in turn is

approximately equal to 9 times the square root of the electron density per cubic meter n_e.

Figure 1 shows the theoretical phase shifts, based on Eq.(1) for a three different electron cloud densities in a beam pipe with a 2 GHz cut-off frequency. Numerical simulations using VORPAL agree very well with the above estimates [7].

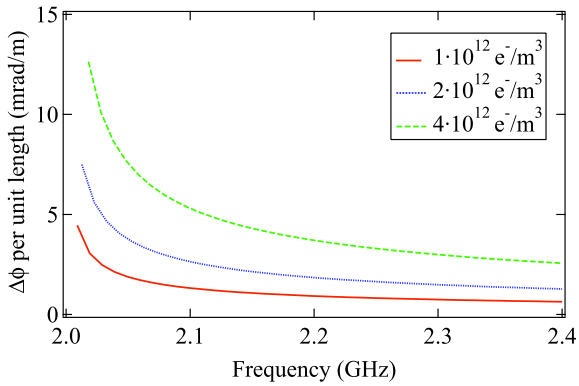

Figure 1: Phase shift per unit length for different electron densities. The cut-off frequency is 2 GHz.

It must be noted that as the propagating wave frequency increases the phase shift per unit length tends to zero, while it increases as the propagation frequency gets closer to the pipe cut-off the phase shift increases dramatically. However in the latter case the propagation attenuation increases as well, so that a compromise solution has to be found every time for the optimal frequency to be used in practice.

Based on Eq.(1), one can calculate the plasma frequency from the measured phase shift and obtain the average electron density in the beampipe length where the wave has propagated as:

$$\rho_e \approx \frac{f_p^2}{80} \ (e^- / m^3) \qquad (2)$$

The electron densities present in a vacuum chamber in most cases are below 10^{11} e^-/m^3 and that the maximum length of the beampipe region used for the measurement is limited by the presence of all those components (vacuum pumps, antechambered sections, ports, etc.) which greatly attenuate the wave propagation. As such, the total phase shift differences one tries to measure when using this method are of the order of a few milliradians. Trying to measure directly such a small difference and furthermore trying to do so in a noisy environment characterized by direct beam signals much stronger than the propagating wave, would be a desperate enterprise.

Our method instead takes advantage of the changes in the electron cloud densities introduced by the circulating beam itself: A gap in the fill pattern, if sufficiently long, can reduce the electron density and even eliminate them entirely. In general we can express the wave signal at the receiver in the form

$$s(t) = A\cos[\omega_{car}t + \Delta\varphi(t)] \qquad (3)$$

The modulating signal $\Delta\varphi(t)$ is directly related to the time evolution of the average ECD in the beampipe region between transmitter and receiver. In particular, it can be expressed as a Fourier series at frequencies multiples of the ring revolution frequency f_{rev} and, in the theoretical case of a simple sinusoidal variation of the ECD, the modulated spectrum would consist of just the carrier signal at f_{car}, with identical upper and lower sidebands at $f_{car} \pm f_{rev}$. The amplitude of these sidebands, relative to the carrier (one half of the modulation index β), is equal to one half of the maximum change in phase delay $\Delta\varphi$ and therefore of the ECD [8]. Although it would seem in principle that our method can only measure variations in the ECD and not its absolute value, is of course always possible to introduce a gap long enough to reduce the ECD to zero.

In more realistic cases, with the ECD time evolution encountered in practice, one observes a number of sidebands. Although phase modulation is not a linear process and a full demodulation of the received signal would be required to calculate $\Delta\varphi(t)$, the relative amplitude of the first sideband still gives a reasonably good estimate of the ECD in most cases and the number of observed sidebands (directly linked to the modulating signal bandwidth) offers a guideline on the clearing and build-up times of the ECD.

In the presence of a constant uniform magnetic field B, the above results are not valid anymore in the vicinity of the cyclotron frequency $f_{cycl} = eB / 2\pi m_e$. While a complete analytical treatment of the interaction between TE wave and electron in the vicinity of this frequency is currently object of study, simulations are available (Figure .2), which point out to a resonant behaviour, which we believe should result in a combination of amplitude and phase modulation, as the case seems to be also from preliminary experimental results.

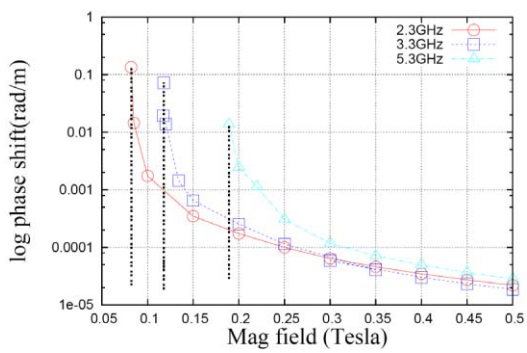

Figure 2: Calculated phase shift per unit length in a dipole region for a uniform cold electron plasma in a waveguide with 2 GHz cutoff frequency, the cloud density is assumed to be $1{\cdot}10^{12}$ e/m^{-3}. The vertical lines correspond to an electron gyration frequency equal to the wave frequency.

EXPERIMENTAL SETUP IN THE PEP-II LER

We ran experiments in two different regions of PEP-II: a 50 m field-free straight and a 5 m magnetic field section.

In the first region shown in Fig. 3, a couple of beam position monitor BPM buttons located in the long straight magnetic-free section of the LER Interaction Region 12 (IR12) was available for our measurement. These buttons are about 50 meters apart and long RF cables bring the signal in the experimental hall to our instrumentation. The beam pipe in the LER is surrounded by electrical cables generating a solenoid magnetic field. This field is used to confine the electrons near the beam pipe limiting their interaction with the positron beam and the emission of secondary electrons. In the region of interests, between our two BPM's there are two families of solenoids, each generating a magnetic field of about 20 gauss. During the two years of measurements, we didn't have a permanent setup. Our instrument suite always included an Agilent E4436B signal generator, capable of generating a CW signal at a fixed frequency up to 3 GHz. The emitted signal power can be selected up to around 15 dBm. We added a Comtech PST solid state 5W amplifier rated up to 2 GHz, but we verified it could still give +30dB amplification at 2.3 GHz.

On the receiver end we initially used an HP/Agilent E4408B and 8561EC spectrum analyzers; later on we also used a Rohde-Schwartz 42 GHz spectrum analyzer. In order to measure the power level at our output port we also used an HP 436A/8545A power meter. We performed measurements with a variety of beam currents, from no beam up to 2.5 A in about 1700 bunches. The PEP-II LER has a 476 MHz main RF frequency and the standard fill pattern is with every other RF bucket filled, except for a gap of 48 buckets (~100 ns long).

Figure 3: LER vacuum chamber in IR12 (upper beam pipe). The outer clearing solenoid can be seen.

In the second experimental region (Fig.4), we connected cables to a couple of BPMs located upstream and downstream of a new 4-dipole chicane recently installed to test the electron cloud effect in magnetic field regions of the future linear colliders. These buttons are about 5 meters apart and long RF cables bring the signal in the experimental hall to our instrumentation.

Two cables are used as transmitter and two cables as receivers. A Quadrature Hybrid 3 dB attenuator is connected in series in each receiver cable. The dipoles are 0.435 m long. The magnetic field of the chicane dipoles can be varied between 0 and 1.46 kG. The vacuum chambers at the chicane location are made in aluminum, partially coated with TiN. One magnet is located in the aluminum section and the other three magnets are located in the TiN section. The beam pipe is partially surrounded by electrical cables generating a solenoid magnetic field.

Figure 4: Chicane dipole magnets (right) installed in the LER (upper beam pipe) for electron cloud tests.

EXPERIMENTAL RESULTS

We detected electron cloud induced phase modulation in both the experimental setups described in the previous section. A more detailed analysis is reported also in [7].

Long straight

In order to measure a phase modulation in the 50 m-long straight section of the LER the clearing solenoids strength has to be reduced substantially.

Figure 5 shows the power spectrum of the received signal with the clearing solenoid set at the nominal 40 Gauss (black) and turned off (blue). The carrier signal is evident as well as two beam revolution harmonic signals with their small synchrotron sidebands. When the solenoid field is set to zero, the beam pipe fills with electrons, which are then periodically cleared by the 100 ns long gap in the fill pattern originating a phase modulation in the transmitted microwave.

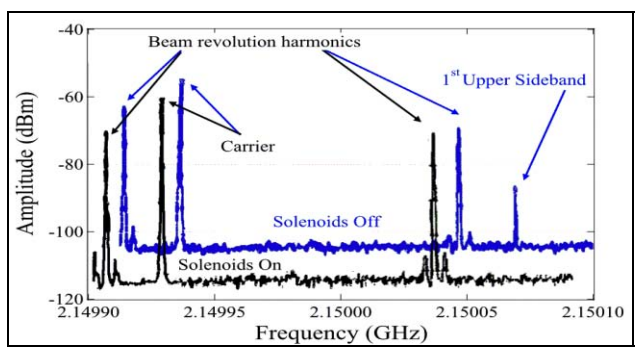

Figure 5: Spectrum analyzer traces showing microwave carrier and beam signals. A phase modulation sideband appears when the solenoid field is turned off (blue), allowing the electron plasma to fill the pipe.

If we assume for simplicity that this phase modulation is purely sinusoidal and that the ECD reaches zero during the gap, it indicates an average electron density of $6.6 \cdot 10^{11}$ e^-/m^3, according to Eqs. (1-2).

In practice, the presence of several other sidebands in the received signal points out to a more complex modulation than the simple sinusoidal one. From the analysis of the modulating signal bandwidth (i.e. the number of visible sidebands) it is already possible to estimate [9] growth and decay time of the electron cloud. We have also characterized the effectiveness of the solenoid field in controlling the ECD. Shown in Fig.6 is an estimate of the ECD derived from the first modulation sideband as a function of the solenoid strength. This measurement indicates that only small solenoid fields are required to confine the electron cloud near the beam pipe walls, thus limiting the ECD.

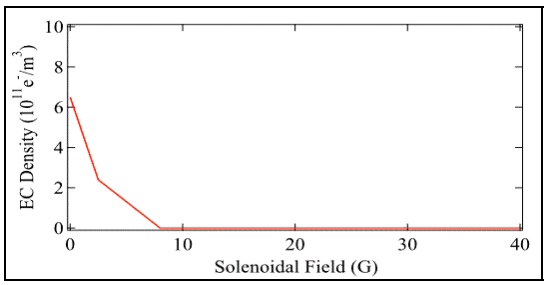

Figure 6: Average electron cloud density derived from the first modulation sideband as a function of the solenoid field strength.

Chicane

Figure 7 shows the phase delay of a TE wave propagating in the chicane at 2.015 GHz. When the dipole field is set so that its corresponding cyclotron frequency is equal to the microwave frequency, the total phase delay is greatly increased. The actual mechanism of this phenomenon is currently the object of investigation. The apparent difference between the propagation frequency of 2.015 GHz and the cyclotron frequency of the maximum phase shift in Fig.6 (~1.96 GHZ) is due to differences between the 700 G set point, the actual field in the four dipoles and its non-uniformity along the magnet length.

In this configuration, the phase shift reaches much higher values, so that it promises to yield a powerful tool for measuring even small electron densities.

CONCLUSIONS

We have shown the results of our TE wave transmission measurements on the PEP-II LER. We were able to detect modulation sidebands 136 kHz away from our transmitted signal at 2.295 GHz, which is consistent with a phase modulation induced by the presence of an electron cloud. Our results are in reasonably good agreement with theoretical estimates, which in turn have been checked with simulation codes.

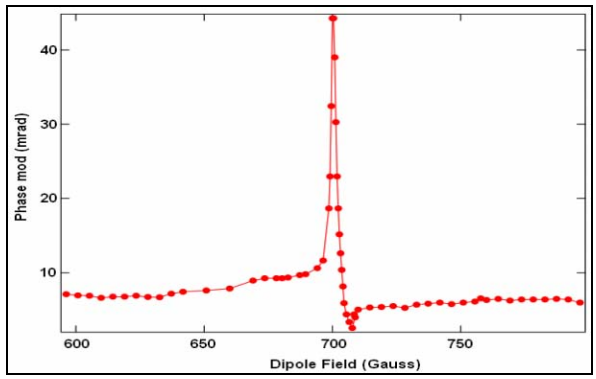

Figure 7: Phase delay as a function of the dipole field strength for a TE mode propagating in the chicane at 2.015 GHz.

We have shown how our method could be easily adapted to most machines as a tool for verifying experimentally the effectiveness of electron cloud clearing methods.

We have also successfully measured the signal in correspondence of a resonance with the electrons' cyclotron frequency in the presence of a fixed dipole field. The analytical study of this phenomenon is currently under investigation.

ACKNOWLEDGEMENTS

The authors wish to thank U. Wienand, M. Sullivan, F. Decker, F.-J. Decker, S. Hoobler, A. Krasnykh and A. Kulikov for their precious help in realizing the experiments.

REFERENCES

[1] K. Ohmi, Phys. Rev. Lett **75**, 1526 (1995).
[2] M. Izawa, Y. Sato, and T. Toyomasu, Phys. Rev. Lett. **74**, 5044 (1995).
[3] D. Neuffer, E. Colton, et al. Nucl. Instrum. Methods Phys. Res., Sect. **A 321**, 1 (1992).
[4] G. Arduini, K. Cornelis, et al. In Proc. PAC 2003, Portland, Oregon (2003)
[5] K. Harkay and R. Rosenberg, Phys. Rev. ST-AB **6**, 034402 (2003).
[6] H.S. Uhm, K. T. Nguyen, et al., Journal of Appl. Phys., 64(3), p. 1108-11115, 1988.
[7] K. Sonnad, M. Furman, et al. In Proc. PAC 2007, Albuquerque, New Mexico (2007).
[8] T. Koyer, F. Caspers, et al., in Proc. of the 31st ICFA Advanced Beam Dynamics Workshop, CERN-2005-001, (2005).
[9] J. Carson, Proc. IRE, **10**, 57 (1922).

THE BEAM DIAGNOSTIC INSTRUMENTATION OF PETRA III

K. Balewski, A. Brenger, H.-T. Duhme, V. Gharibyan, J. Klute, K. Knaack, I. Krouptchenkov, G. Kube, T. Lensch, D. Lipka, J. Liebing, Re. Neumann, Ru. Neumann, G. Priebe, F. Schmidt-Foehre, H.-Ch. Schroeder, R. Susen, S. Vilcins-Czvitkovits, M. Werner, Ch. Wiebers, K. Wittenburg
Deutsches Elektronen Synchrotron DESY, Hamburg, Germany.

Abstract

The former electron and proton preaccelerator PETRA at DESY is currently reconstructed and will be converted into a high brilliant storage-ring-based X-ray source called PETRA III [1]. Commissioning of the machine is scheduled for January 2009. PETRA III will operate at 6 GeV electrons or positrons with 100 mA stored current and a design emittance of 1 nm rad. Top-up operation is planned right from the beginning to reduce changes in heat-load and thermal drifts to a minimum,. Suitable beam diagnostic instrumentation and machine protection systems have to be established to guarantee the low emittance, sub-micron beam stability and save machine operation. To ensure a very high availability of the beam in top-up mode, injector and pre-accelerator diagnostic systems are refurbished as well. This paper presents a complete overview of the instrumentation and their latest developments to achieve these requirements.

INTRODUCTION

PETRA III will be a new high-brilliance synchrotron radiation source at DESY. The 6 GeV storage ring is on track to deliver the most brilliant storage-ring-based X-rays to users in 2009. The construction activities started in July 2007 when HERA went out of operation after 15 years of delivering high energy physics data. The 2.3 km long accelerator is completely redesigned, including the total rebuilding of one-eights of the storage ring where 14 undulators (incl. 5 canted) in 9 straight sections were installed. A new 300 m long experimental hall covering this octant with 14 independent beamlines (+ one diagnostic beam line) was recently build. In order to provide vibration-free conditions for the experiments the experimental hall rest on 99 piles of 1 m diameter that reach 20 m deep into the ground and a massive floor which consists of a 1 m thick monolithic slab of steel fiber enforced concrete. The remaining 7/8 of the storage ring are currently refurbished. Two damping wiggler sections were installed to achieve the designed low emittance of 1 nm rad. The vacuum system together with the beam position monitors (BPMs) was completely redesigned. PETRA III will run with a beam current of 100 mA (upgrade to 200 mA foreseen). Typically up to 100% of the ring circumference is filled with bunches of 8 ns distance (optional 2 ns) of nearly identical charge ($N = 5 \cdot 10^9$ $e^{+,-}$/bunch ± 10%) but other bunch patterns are possible. The bunch length will be 100 ps immediately after injection and 40 ps for stored beam.

In the following the beam diagnostic instrumentation of PETRA III will be described in detail.

BEAM POSITION MONITORS (BPMS)

PETRA III will be equipped seven different pickup types; their properties are summarized in Table 1. A total of 227 BPMs is foreseen, one BPM per standard FODO-cell and additional BPMs at the locations of insertion devices. The BPM-system has to serve for two major tasks resulting in different operational modes and requirements:

1) Machine commissioning and development: Single turn, single pass capability to acquire beam positions is required for:

-of the non-stored first turn and

-of each of consecutive turns

In these turn-by-turn operation modes the resolution requirement is relaxed (50...100 μm).

2) Orbit feedback and observation: In standard user operation the beam orbit of the stored beam has to be kept constant with respect to the reference (golden) orbit. All BPMs have to be squeezed to their maximum performance in terms of resolution (1/10 of the 1σ beam width) and reproducibility. To achieve this, the bandwidth of the BPM-readout can be reduced to 300 Hz and averaged position measurements of many turns will be acquired. In addition the BPM system has to provide position data with a frequency of about 130 kHz (turn by turn) to feed the fast orbit feedback system. Even at that bandwidth the resolution of a BPM must not exceed 50 μm.

All tasks are foreseen to be fulfilled with the LIBERA Brilliance BPM electronics from Instrumentation Technologies. A number of test measurements were performed in advance [2] to ensure, that the required specifications [3] will be covered by LIBERA. It was demonstrated that already the LIBERA Electron meets the required specifications and the new LIBERA Brilliance exceeds them. However, three parameters were discovered to be critical, namely 1) the temperature drift of LIBERA, 2) the bunch pattern dependence of the position readout and 3) the maximum input voltage of the channels:

1) A dependence on the bunch pattern was observed with LIBERA Electron, but LIBERA Brilliance should eliminate this behaviour. If there will be still a considerable dependency for extreme bunch patterns, it is planned to generate different “golden orbits” for certain fillings.

2) The temperature drift of 0.2 μm/°C allows operating LIBERA only in air-conditioned surroundings. Therefore all racks will be concentrated inside temperature

Location (number) -Chamber profile-	Chamber size [mm] (Button Ø [mm])	Required resolution σ (μm) vert.; hor.	Ultimate res. σ (μm) vert; hor.	current limits [mA]	Monitor const. k: vert.; hor.
Old octants (108) -elliptical-	80 x 40 (11)	10 ; 10	0.5 ; 0.5	8 – 100	16.9 ; 17.7
New octant (44) -octagon-	80 x 38 (11)	0.5 ; 2	0.5 ; 0.5	8 – 100	16.8 ; 17.5
Next to undulators (16) -elliptical-	66 x 11 (11)	0.3 ; 2	0.15 ; 0.15	4 – 100	5.26 ; 5.26
Canted undulator (5) -elliptical-	57 x 7 (4)	1 ; 1			2.34 ; 7.19
Straight sections (26) -round-	Ø 94 (15)	10 ; 10	1.0 ; 1.0	10 – 100	33.3 ; 33.3
Damping wiggler (26) -racetrack-	120 x 30 (11)	5; 5	0.5; 0.35	7 – 100	12.0 ; 16.4
Damping Wigglers (2) -octagon-	60 x 26 (11)	5; 5			10.24 ; 14.41

Table 1. Properties of the beam position pickups installed in PETRA-III and orbit resolution requirements at certain locations at a bandwidth of BW=300 Hz. The ultimate limits can be expected from the tightest requirement of a resolution of 0.5 μm for the new octant (taking into account the monitor constants). The lower beam current limit for which the ultimate resolution is valid is a result of the pick-up geometry, respectively the coupling to the beam. The Turn by Turn (TBT) position resolution is acquired by LIBERA Brilliance at a bandwidth of B = 0.3 ·130 kHz = 39 kHz. The accuracy requirements for the TBT measurement are relaxed from those in table 1. Since the resolution is proportional to 1/sqrt(B), the resolution requirements of 50μm (1 σ) are fulfilled.

stabilized cabins and in the new octant near the undulators (± 1 ^{o}C for both).

3) For the estimation of the signal levels at the LIBERA crossbar switch (limiting element), the transient signal at the input of the module was calculated for the various position monitors [4]. Beam offsets in the order of some mm (depending on the pickup type) resulted in amplitudes exceeding the allowed input amplitude of 80 V. Therefore additional 10 dB attenuators are foreseen. However, large beam excursions will still result in too high voltages and a nonlinear behaviour of the readout is expected. Such large beam offsets should be avoided when defining "golden orbits". To avoid measured orbit drifts due to different heating of the attenuators, they will be mounted thermally coupled on a solid metal board directly in front of the LIBERA input connectors. Calculations have shown that signals of reasonable small beam intensities are still in the useful range of the LIBERA electronics. More detailed specifications of the BPM readout system can be found in [3].

Movement detection

The position and movement of the pickups at critical locations will be measured with respect to the ground floor, respectively girder. All pickups in the new octant are attached to a "High Frequency Movement Monitor" (HF-MOMO) which determines pickup movements with a resolution of << 1 μm, based on the measurement of the distance between 4 terminated (50 Ω) striplines (two per plane) and a stiff solid wire of 2 mm diameter. The wire is mounted on a fork which is firmly connected to the ground or girder by a massive support. It is part of a matched 145 MHz λ/4-resonator and the striplines pickup this HF-signal. The 4 signals are processed like usual BPM signals to determine the position of the wire inside the pickup (monitor constant k = 3.0). The bandwidth of the system is about 1 Hz, sufficient to observe long term drifts. 4 ADCs (80 kHz, 16 bit) are attached to the 4 striplines, 16 monitors are multiplexed so that each monitor has a repetition rate of 16 s. The gap of the sensors limits the sensitive area to 8 x 8 mm^2, the linear response is in the range of ± 2mm in each plane. The readout electronics gives access to the ADC raw data to enable FFT analysis of measured frequencies.

The supports of the HF-MOMOs near the undulators are made from carbon fibers, designed for zero thermal expansion although the complete new octant (tunnel) will be temperature stabilized to 0.1 ^{0}C.

BEAM CURRENT MONITORS

Fast current transformer (FCT): A wide-band In-Flange FCTs with a bandwidth of 1.75 GHz (Bergoz) will measure the individual charge of each stored bunch. This measurement defines the required individual charge for the topping up injection. A resolution of < 1 μA/bunch with an analog bandwidth of 500 MHz (to meet the optional 2 ns bunch spacing) is intended. Its readout is performed by a scope type Wave-Runner 104Xi (LeCroy) with a sampling rate of 10 GS, a bandwidth of 1 GHz and 8 bit resolution. An average of about 50 turns of each bunch is displayed in the control room and sent via Ethernet connection to the control system. Two customized elliptical FCT (BW=800 MHz) are located in the injection area to determine the injection efficiency by comparing with the current in the pre-accelerators.

DC current transformers: The very high resolution measurement of the DC current will be performed by three parametric current transformers (PCT, Bergoz)

reused from PETRAII and HERAe and upgraded by the company. Experiences from HERA with this type of monitor showed a resolution of σ <<1 ‰ (absolute: 3 μA of 61.7 mA) [1] which is sufficient for the top-up operation of PETRA III. The readout is performed by a high precision DVM (Type HP 3458A with 16 - 24 bit resolution depending on sampling rate), connected to the Bergoz back-end electronics. The DVM averages over defined number of turns.

EMITTANCE

X-Ray Diagnostic Beamline

An x-ray diagnostics beamline will be located at the end of the new octant. Synchrotron radiation (SR) from a bending magnet with critical photon energy of 20.907 keV and a total emitted power of 6.96 kW is produced in the central field. The x-ray part of the emitted radiation will be used to image the beam spot onto a high resolution CCD camera system. Imaging will be performed with two interchangeable x-ray optics: A high resolution compound refractive lens (CRL) system (≈ 2 μm resolution) and a pinhole camera system for lower resolution standard operation (≈ 20 μm resolution). The CRL is made of 31 individual beryllium lenses, stacked behind each other in a very precise (1 μm) support fixed by a laminated spring. The pinhole consists of a 0.5 mm thick tungsten blade with a circular hole of 20 μm. In order to switch between they have to be moved ± 5mm in vertical direction by a stepper motor. Both optical systems are water-cooled, and two additional absorbers are installed in the photon path. The beamline has a vacuum system which is separated from the machine vacuum by a CVD window

For improvement of the spatial resolution a water cooled monochromator crystal (Si 311 in Laue geometry) will be used which is located 8.78 m behind the x-ray optics. At the nominal photon beam energy of $\hbar\omega$ = 20 keV the Bragg angle amounts 10.912^0.

The detector system (Hamamatsu AA50 beam monitor) will be installed about 68 cm away from the monochromator crystal outside of the vacuum system. It consists of a 10 μm thick LSO scintillator screen together with a microscope optics and a progressive scan interline chip CCD camera (Hamamatsu Orca C4742-80-12AG). The Peltier-cooled camera allows variable exposure times from 10 μsec up to 4200 sec. A remotely controlled filter wheel with molybdenum foils will be used together with different absorbers in order to adjust the incoming intensity and photon energy and to avoid saturation of the camera.

Optical Beam Line

For the main purpose of measuring the bunch lengths, an optical beam line is under construction. It uses the radiation from a standard dipole magnet. A mirror will extract the optical part of synchrotron radiation from the dipole and an optical relay system will guide the light to an experimental hut outside the tunnel. In the beginning it is foreseen to perform measurements of the bunch length with fast optical elements like streak camera or Avalanche Photo Diodes (APD). To be prepared for the measurement of the beam size in the optical regime as well, all optical elements are designed and proven to be as precise as possible (peak to valley wavefront aberration of $\lambda/20$ at λ=632 nm).

Laser wire scanner

A laser wire scanner is built to measure the beam emittance and its coupling. The laser itself is placed in a hut 6 m above the PETRA tunnel. A commercially available pulsed Nd:YAG laser capable of delivering 7.5 MW light pulses at 20 Hz is installed to produce high power light (532 nm). The laser system is injection seeded to eliminate mode-beating and to enable fast scans. The laser light will be transported from the laser hut to a vertical and horizontal optical table positioned around the cross chamber. Both tables are equipped with scanning, focusing and diagnostics optics.

A light polarization based, fast splitting technique will be applied. A Pockels cell at the laser hut allows pulse by pulse splitting of the laser beam to enable horizontal and vertical scans. Left/right helicity pulses made by the Pockels cell reach the tunnel and are converted into horizontal/vertical polarisations by a quarter wave plate followed by a Glan-laser prism-splitter. This prism guides laser pulses with vertical/horizontal polarization to different scanning arms (one for each plane). Each scanning arm will contain a bending transverse Pockels cell for scanning and a lens to focus the beam down to a laser spot size of about 5 μm.

A vacuum chamber with an outlet in the next dipole allows a safe transport of the scattered photons with few hundred MeV energies into the detector. The photon detector is a tungsten-scintillator sandwich with 2 segments to allow vertical position detection. The whole setup will allow a complete 2D transverse scan in about 30 s within a few percent accuracy [5].

MACHINE PROTECTION SYSTEM

PETRA III will be equipped with a ring-wide Machine Protection System (MPS) which will dump the beam in case of equipment failures, critical temperatures or too large beam offsets. One or more MPS crates are located in each of the 8 “old” PETRA halls. Each crate houses an interface to a field bus (SEDAC), a MPS-Controller (MPSC) and 1 to 10 Alarm-Input-Modules (MPSA). Each MPSA can sample up to 16 alarm inputs. Alarms might come from the BPMs (LIBERA interlock output), the temperature system (> 1500 PT100 sensors), from the vacuum pumps and valves, from the HF-system, from the power supplies, etc. The alarm-inputs can be enabled and disabled by software or automatically by predefined conditions. Certain conditions like low beam currents, large undulator gaps will disable individual inputs to allow machine studies without interference with the MPS.

Especially the beam current is directly connected to a special module to make the MPS independent from any network connection. The live-value of the current monitor (PCT) is always checked by test-pulses through a special test winding in the monitor. Various alarm conditions can be logically combined in one module

All crates are connected with an optical fibre dual loop (redundancy) via the MPSC. This loop synchronises all crates to the same beam turn. In case of an alarm the corresponding MPSC activates the dump and the post mortem trigger which is distributed to all other crates by the optical fibre loop. The dump trigger is connected to the RF-system which will stop to deliver power to the beam and the beam will be lost within ≈ 4 ms. The delay of the dump trigger with respect to the alarm does not exceed 100 μs. Two massive pieces of metal will also be driven into the beam pipe to ensure no survival of the beam (delay ≥ 100ms). A faster dump kicker (1 turn) triggered by the MPS is foreseen at a later stage. The MPS will keep the information of the channel which delivered the first alarm to simplify the search for responsible candidates. A post mortem trigger will be available at each crate to enable post mortem analysis of connected subsystems (e.g. BPM system, RF-system, etc).

ORBIT STABILIZATION, FEEDBACK AND TUNE

Orbit stabilization is the precondition for stable user conditions and it also prevents a blow up of the vertical emittance. The stabilization system has to suppress slow motions of the particle beam within time constants from several days to 300 Hz. The stability demand is about 10 % of the beam sizes, which is of the order of 4 μm for the horizontal and 0.5 μm for the vertical plane at the location of the undulators.

Slow orbit correction.

The slow orbit correction will be performed by the control system, based on the readout of the 220 BPMs. The LIBERA electronics are connected via Ethernet to the control system while its readout frequency is about 1 s for each. Singular Value Decomposition (SVD) is applied for simultaneous optimization of the closed orbit and the dispersion. Simulations have shown that the rms vertical dispersion can be kept below 5.0 mm in the whole ring. The maximum corrector strength needed is 0.5 mrad. The required resolution of the corrector power supplies has to be at least 16 bit. The slow orbit corrections will be performed with small horizontal and vertical magnets and backleg windings on selected magnets.

Fast Orbit Feedback System

The fast orbit feedback will reduce orbit distortion by about 20 dB at 50 Hz with a slope of -20 dB/decade. Its low frequency component does not overlap the high frequency range of the slow orbit feedback. Both systems will work independently. However it is foreseen to synchronize both systems at a later stage.

System setup: Each LIBERA brilliance box delivers 'raw' turn by turn position information to a signal combiner via their ultra fast rocket IO connector. 24 signal combiners are located near the BPM racks to which up to 15 LIBERA modules are connected. Each combiner generates a fast data stream into optical fibre lines (up to 200 MB/s synchronous data flow) which are connected in a star topology with a main processing unit. A second task of the signal combiner is the supply of timing signals e.g. machine clock and event triggers to the LIBERA front-ends. A main processing unit manages data collection, processing and distribution. The signal processing will be performed by using SVD and PID algorithms in FPGA technology. The output data stream is distributed (star topology) via fibre links to 82 digital power amplifiers (DPA) located in 12 racks. The DPAs have individual DSP based current controllers which are connected to 82 fast air coil correctors: 30 air coil magnets for each plane in the new octant and 11 for each plane in the seven old octants are designed. The DPA supplies have an average current of 10 A (max. 20 A). The frequency range spans DC to 1 kHz. The signal splitters, the main processing unit and all DPAs are accessible through standard USB interfaces by the orbit feedback server for control and maintenance. The whole setup is a complete end-to-end digital design with 16 bit resolution. A feed forward of mains frequency and its harmonics is also foreseen.

Multi Bunch Feedback Systems

The design current in PETRA III can only be achieved with the help of powerful bunch by bunch feedback systems. The required minimum bandwidth is 62.5 MHz (8 ns bunch distance).

Transverse feedback: The signals of two dedicated stripline beam position monitors are connected to an RF-front-end (in-house development) followed by a FPGA based signal processing board. It drives 4 feedback power amplifiers per plane (Bonn Elektronik, Type BSA 0125-250) with a frequency range of 9 kHz to 250 MHz and an output power of 250 W each. The amplifiers drive 4 stripline kickers (2 for each plane) which are designed and build in-house.

Longitudinal feedback: The signals of 4 buttons of a beam position monitor are combined to give an intensity signal which is insensitive to the transverse beam position. The longitudinal signal chain consists of an RF-front-end and a digital signal processing board as for the transverse system. The kicker devices consists of 8 cavities (modified DAFNE cavity [6]). These are well tuned and damped to get the required bandwidth of 62.5 MHz. The centre frequency is 1375 MHz and double sideband modulation will be used. A later modification for 250 MHz bandwidth is possible by changing the tuning and damping of the cavities and using single sideband modulation at the same centre frequency.

Tune

The tune measurement is part of the transverse multibunch feedback system. It contains a digital signal

generator to feed different kind of signals bunch-synchronized to the kickers. Single bunch as well as multibunch excitations can be performed. In the single bunch mode the number of bunches can be chosen while in multibunch mode the frequency of each mode can be adjusted. Different excitation schemes exist: 1) sinusoidal CW, 2) bursts with adjustable rate and length, and 3) bandwidth-limited "white" noise. Since the feedback systems will damp away any kind of excitation, the classical tune measurement can be performed only without feedback. However, a new idea of tune measurement with feedback will be tested at PETRA III: An adjustable broadband noise will be added to the RF front-end output (and therefore to the kickers). In the frequency response this will be seen as constant offset. At the tune resonance frequency a notch will appear due to the 180^0 phase shift of the feedback. These notches can be analyzed very precisely, even with running feedbacks and with a minimum of excitation. A detailed description of the system is in preparation [7].

X-RAY BEAM POSITION MONITORS

Blade-type x-ray BPMs obtain the information of the beam position from the halo of the undulator radiation. Their signals depend on the undulator gap and are strongly affected by stray radiation from bending and focusing magnets, making it not well feasible to use them in the photon beamlines for the experiments. To overcome these limitations an x-ray BPMs based on the ionization of residual gas was developed and tested. It uses the ions created by the x-ray beam in a small pressure bump of about 10^{-6} mbar. The ions are accelerated by a parallel electrical field towards a Micro Cannel Plate and an attached phosphor screen. This monitor type has the advantage of imaging the whole body of the beam so that the centre is well defined. Tests with a prototype at the ESRF showed a resolution of better than 5 μm. More details can be found in [8].

PREACCELERATORS

The PETRA III injector chain consists of the linear accelerator LINAC 2, the positron intensity accumulator PIA, the booster synchrotron DESY II and the interconnecting transfer lines. The whole chain is equipped with essential beam diagnostic instruments like BPMs, current monitors and screens:

LINAC2 is equipped with 5 BPMs, their readout electronics development started recently. The 3 GHz beam sub-structure needs a complete new type of readout electronics. The other pre-accelerators have a single bunch structure to provide filling and topping-up of PETRA III. The "Delay Multiplex Single Path Technique" is used to readout the beam position of the bunch. The technique was developed in 1978 for PETRA I by Ru. Neumann at DESY. An upgraded version will be used for the European XFEL [9].

All transfer lines, PIA and DESY II are equipped with in-house designed inductive current monitors (BW=150 MHz) to observe the bunch current behaviour in all stages of the filling of the PETRA III filling.

25 new designed phosphor screens (Ø 63.5 and 98 mm) are installed in the injector chain. They consist of a thin 8 μm Al screen covered with a thin layer of ZnS. The screens are viewed at 45^0 by commercial CCD cameras (radiation hard types in exposed areas) typically located about 800 mm below the beam inside a 50 mm thick lead shielding. The driving mechanism consists of a pressed-air cylinder to move the screen in and out, an electro-magnetic bar to allow the in-movement and a spring to ensure an automatic pullout of the screen in case of an air-pressure drop. Special screens are needed at the entrance and at the exit of the injection septum and one additional in PETRA III for observing the incoming beam. Their frameless screens consist of a 1 mm thick Al_2O_3 ceramic (66 x 38 mm) with a thin layer of ZnS. Special care is taken (by soft- and hardware) to avoid to move the PETRA-screen into a stored beam. The video signal treatment of the screens is described in detail in [10].

REFERENCES

[1] The Technical Design Report (TDR) "PETRA III: A low Emittance Synchrotron Radiation Source" Ed. K. Balewski et al., DESY 2004-035.

[2] K. Balewski, I. Krouptchenkov, K. Wittenburg, Examination of the Bunch Current and Bunch Pattern Dependence of the LIBERA BPM Electronic, Visit of ESRF". DESY-MDI internal Report Nr. 2006 – 1; September 2006

[3] K. Wittenburg et al., "PETRA III Beam Position Monitor Electronic: Requirements and technical Specifications; Tendering and Contract Management"; Version 1.92

[4] G. Kube, M. Werner, "Signal Level Calculation for the PETRA III Beam Position Monitor System" DIPAC 2007, Venice, Mestre, Italy and G. Kube, "Sensitivity Estimation for the PETRA-III Beam Position Monitors based on a Boundary Element Method", DESY technical note 2007-1

[5] A. Bosco et al., "A 2-Dimensional Laser-Wire Scanner for Electron Accelerators", Report accepted by Nuclear Inst. and Meth. in Physics Research, A.

[6] A. Gallo et al, "A Waveguide overloaded Cavity as Longitudinal Kicker for the DAΦNE Bunch-by-Bunch feedback System", International Workshop on Collective Effects and Impedance for B-Factories, Tsukuba, Japan, June 1995

[7] J. Klute, DESY, private communication

[8] P. Ilinski, et al., "Residual Gas X-ray Beam Position Monitor Development for PETRA III", (SRI, 9th), Daegu, Korea (2007), p. 782 – 785

[9] D. Noelle et al, "BPMs for the XFEL Cryo module", DIPAC 2007, Venice, Mestre, Italy

[10] I. Krouptchenkov, K. Wittenburg, "FPGA based Frame Grabber for Video Beam Diagnostics", DIPAC 2007, Venice, Mestre, Italy

LASER-BASED BEAM DIAGNOSTICS*

G. A. Blair, Royal Holloway Univ. of London, Egham, Surrey TW20 0EX,UK.

Abstract

Lasers are increasingly being employed in particle beam diagnostics. Laser-based techniques are attractive because they are essentially non-invasive to the beam under test and can not be destroyed by it. They also have the potential to be extremely fast. Uses include transverse beam profile measurement at electron machines using the Compton effect and at proton machines using laser-ionization of H- beams. An introduction is provided to Gaussian beam propagation and how this affects the laser properties and final focus optics needed for the various applications. Recent applications and results from ongoing research projects will be reviewed, with particular emphasis on the "laser-wire" systems recently employed at the PETRA and ATF machines. Future possibilities will be discussed, including higher order laser modes and interferometric techniques.

INTRODUCTION

Future electron machines will need accurate determination and monitoring of their transverse phase space in order to meet their challenging performance specifications. A detailed analysis of the issues and challenges involved in such measurements are presented in Ref. [1], with particular reference to the International Linear Collider (ILC) [2]; a brief summary of this work is presented below in order to motivate the challenges of the laser and optics prestented later.

The Laser-Wire (LW) is a key beam diagnostics, which is useful for beam profiles ranging from several tens of microns, down to the micron scale. Smaller beam profiles have been measured using laser interferometric techniques [3, 4] whereas traditional solid wires or screens can be used for larger profiles (although they are disruptive to the electron beams). Very challenging, low f-number, laser optics are necessary for the LW in order to achieve the required small laser spot-sizes and the subsequent performance is evaluated numerically and described in below. The laser systems necessary to power the LW are also very challenging and the necessary specifications are next derived and discussed.

TRANSVERSE EMITTANCE MEASUREMENT

The International Linear Collider (ILC) has demanding emittance goals that will need to be measured accurately in order to maximise the machine performance; the parameters of the ILC [2] are presented in Tab. 1, which provides the context for the requirements on measurement beam spot sizes and scanning speeds, discussed below.

Table 1: Nominal ILC Parameters

Beam energy	E	250(500) GeV
Norm. horiz. emittance	$\gamma\epsilon_x$	10^{-5}m rad
Norm. vert. emittance	$\gamma\epsilon_y$	$4 \cdot 10^{-8}$ m rad
Train repetition rate	f	5 Hz
Num. bunches per train	$N_{\rm train}$	2625
Inter-bunch spacing (ns)		369
Bunch length	L_b	300 μm
Num. electrons per bunch	N_e	2×10^{10}

Beam Phase Space

The phase-space of a general Gaussian particle beam can be described by four-dimensional (4d) matrix:

$$\sigma = \begin{bmatrix} \langle x^2 \rangle & \langle xx' \rangle & \langle xy \rangle & \langle xy' \rangle \\ \langle xx' \rangle & \langle x'^2 \rangle & \langle x'y \rangle & \langle x'y' \rangle \\ \langle xy \rangle & \langle x'y \rangle & \langle y^2 \rangle & \langle yy' \rangle \\ \langle xy' \rangle & \langle x'y' \rangle & \langle yy' \rangle & \langle y'^2 \rangle \end{bmatrix} \quad (1)$$

The standard approach to reconstructing the 4d coupled beam matrix with the least-squares fit method is presented in Ref [5]. At a scanner location in the beam-line it is possible to measure three values, $\langle x^2 \rangle$, $\langle y^2 \rangle$ and $\langle xy \rangle$, with the help of a horizontal (x), a vertical (y), and a tilted (u) wire scanner, as illustrated in Fig. 1, where the tilt-scanning angle, ϕ, is also defined.

The optimal value for ϕ is given by

$$\phi_0 = \tan^{-1}\left(\frac{\sigma_x}{\sigma_y}\right) . \quad (2)$$

and typical values of interest to the ILC beam delivery system (BDS) are presented in Tab. 2.

The ten independent entries of Eq. 1 can be obtained either by changing the optics in a controlled manner at the wire location [6, 5, 7] or by locating the wires at different positions in the beam-line. The latter technique will be relevant for routine fast-scanning operation at the ILC. Here it will be assumed that six laser-wire scanning stations are located at optimal locations in the BDS and that each laser-wire station measures x,y and u with the same relative measurement error. The emittance can then be inferred by inverting the relations between the transverse spot

* Work supported by the UK Science and Technology Facilities Council and by the Commission of European Communities under the 6th Framework Programme Structuring the European Research Area, contract number RIDS-01189.

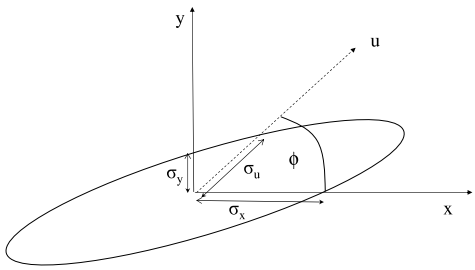

Figure 1: *Bunch with horizontal-vertical coupling, such that its major axis does not lie along the horizontal. In addition to vertical and horizontal scans, a scan of the u-axis is necessary, where u is at an angle ϕ to the vertical as shown.*

Table 2: *The relevant measurables for emittance measurement under the approximation $\langle xy \rangle \simeq 0$ for a set of electron beam sizes of interest at the ILC for the given beam energies E_b.*

E_b GeV	σ_x μm	σ_y μm	ϕ_0 deg	σ_u μm	σ_v μm
500	9	1.4	81.2	1.95	8.89
500	15	1.4	84.7	1.97	14.9
250	14	2	81.8	2.8	13.8
250	20	1.8	84.8	2.53	19.9

sizes as given by the R-matrices relating the beam twiss parameters at each location. This may lead to an unphysical result (a non-positive beam matrix) when the measurement is sufficiently noisy. A typical dependency of the fraction of non-positive matrices on the relative measurement error is shown in Fig. 2, where it can be seen that the relative error should be kept below about 10% if significant reconstruction inefficiency is to be avoided.

The quality of emittance reconstruction by performing this technique is shown in Fig 3, which motivates the need for LW systems that can measure beam spotsizes to a few percent (or better). Methods for achieving such accuracies will now be discussed.

GAUSSIAN BEAM OPTICS

Paraxial Approximation

Maxwell's equations in free space lead to electromagnetic field solutions of the form $E(x, y, z) \exp(ickt)$

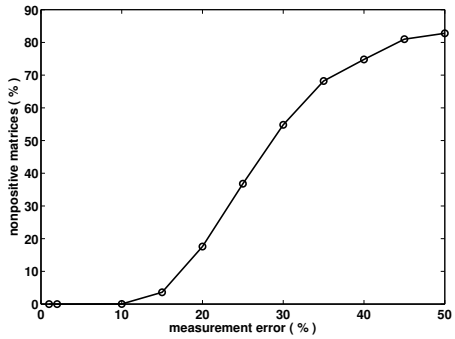

Figure 2: *Beam matrix rejection fraction vs. relative beam size measurement error level for the 4d ILC emittance measurement section with 6 scanners [1].*

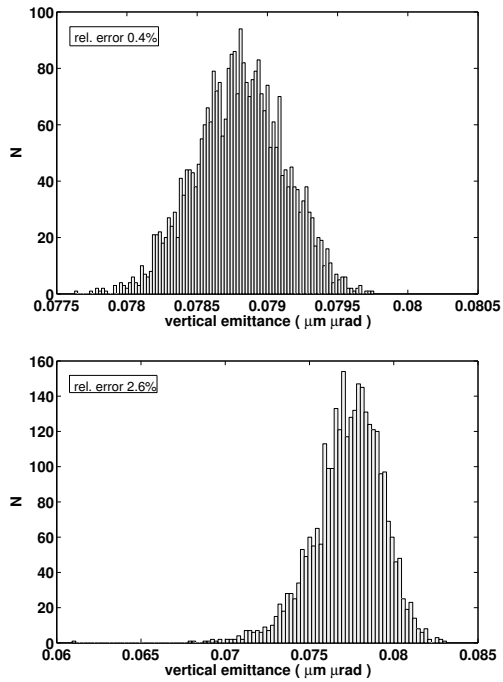

Figure 3: *Distribution of reconstructed vertical emittance with 1% (a) and 5% (b) random errors on the beam size measurement for a 4d diagnostics section (statistics corresponding to train length). Initial optical functions are perfectly matched. The true emittance is 0.079 $\mu m \cdot \mu rad$ [1].*

where:

$$\left(\frac{\partial^2}{\partial x^2}+\frac{\partial^2}{\partial y^2}+\frac{\partial^2}{\partial z^2}+k^2\right)E(x,y,z)=0 \qquad (3)$$

A pure plane wave travelling in the x-direction has the exact solution $E(x,y,z) = E_0\exp(ikx)$ but, due to diffraction effects, this is not in general sufficient to describe a laser beam of finite transverse size. Assuming a solution of the form $E(x,y,z) = u(x,y,z)\exp(-ikx)$ in Eq. 3 gives:

$$\left(\frac{\partial^2}{\partial z^2}+\frac{\partial^2}{\partial y^2}+\frac{\partial^2}{\partial x^2}-2ik\frac{\partial}{\partial x}\right)u(x,y,z)=0 \qquad (4)$$

In most practical situations, any variations along the beam (i.e. along x) will be gradual, which enables the $\partial^2 u/\partial x^2$ term to be ignored. As explained in Ref. [12], this so-called paraxial approximation is valid provided any rays within the beam are traveling at angles less than about 0.5 radians with respect to the optical axis, which is true for all the practical cases described later. The paraxial wave equation is then:

$$\frac{\partial u(x,y,z)}{\partial x}=-\frac{i}{2k}\left(\frac{\partial^2}{\partial z^2}+\frac{\partial^2}{\partial y^2}\right)u(x,y,z) \qquad (5)$$

The TM$_{00}$ Mode

Consider a Gaussian beam with an intensity (which is proportional to the square of the field strength) profile of the form:

$$I(x,y,z)=|u(x,y,z)|^2=\frac{I_0}{2\pi\sigma^2(x)}\exp\left(-\frac{y^2+z^2}{2\sigma^2(x)}\right) \qquad (6)$$

where I_0 is the (constant) total power of the beam and the first factor of $\sigma(x)^{-2}$ is the normalisation necessary to keep the total power constant as a function of x. For the simplest laser mode (TM$_{00}$) there is no azimuthal dependence and so the problem can be formulated using $r=\sqrt{y^2+z^2}$ and solving:

$$2ik\frac{\partial u}{\partial x}=\frac{\partial^2 u}{\partial r^2}+\frac{1}{r}\frac{\partial u}{\partial r} \qquad (7)$$

in the form

$$u(x,r)=\sqrt{\frac{I_0}{2\pi}}\frac{1}{\sigma(x)}\exp\left(-\frac{r^2}{4\sigma^2(x)}\right)e^{i\phi(x,r)} \qquad (8)$$

Substituting Eq. 8 into Eq. 7, and solving, yields:

$$\sigma(x)=\sigma_0\left[1+\left(\frac{x}{x_R}\right)^2\right]^{\frac{1}{2}} \qquad (9)$$

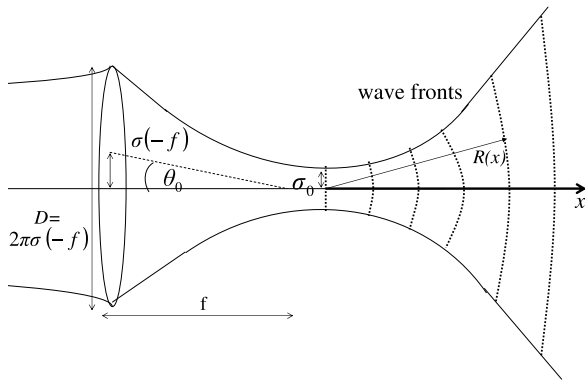

Figure 4: *The key features of the focussing of a Gaussian beam through a circular aperture of diameter D and focul length f. The beam has its waist at a distance $\simeq f$ from the lens, at which point its intensity distribution has Gaussian rms σ_0; this point also defines $x = 0$. The curvature of the wavefronts $R(x)$ varies as fuction of distance x from the waist, and is infinite at $x = 0$ and $x = \infty$. At large distances from its waist the beam diverges linearly with distance $\sigma = x\tan\theta_0$, where $\tan\theta_0 = \sigma(-f)/f$.*

where x_R, the so-called Rayleigh range, is given by

$$x_R=\frac{4\pi\sigma_0^2}{\lambda}, \qquad (10)$$

λ is the laser wavelength and

$$\phi(x,r)=\tan^{-1}\left(\frac{x}{x_R}\right)-\frac{2\pi}{\lambda}r^2\frac{\sigma'(x)}{\sigma(x)}. \qquad (11)$$

The first term of Eq. 11 shows that there is a phase shift of π (the Guoy phase shift) on passing through the focus, defined as where $\sigma(x)$ is a minimum; this point also defines $x = 0$. The second term of Eq. 11 is intepreted as due to the curvature of the wavefront, which can be written in terms of a radius of curvature $R(x)$ given by:

$$R(x)=x+\frac{x_R^2}{x}. \qquad (12)$$

This interpretation of the solution in terms of Gaussian-spherical waves is illustrated in Fig. 4; a more general treatment of this interpretation is given in Ref. [12].

When x is large compared to x_R, the beam diverges linearly:

$$\sigma(-f)\simeq\frac{\sigma_0}{x_R}f=\frac{\lambda f}{4\pi\sigma_0} \qquad (13)$$

and

$$\theta_0=\tan^{-1}\left(\frac{\sigma(-f)}{f}\right)\simeq\frac{\lambda}{4\pi\sigma_0} \qquad (14)$$

The usual practical convention [12] is to require 99% of energy in the Gaussian beam profile to be contained within

the lens aperture, here assumed to be circular with diameter D. For the TM_{00} mode this requirement means:

$$0.99 = \int_0^{D/2} \int_0^{2\pi} r dr d\phi \frac{1}{2\pi\sigma(-f)^2} \exp\left[-\frac{r^2}{2\sigma(-f)^2}\right] \quad (15)$$

so $D \simeq 2 \times \pi\sigma(-f)$ and by substituting this into Eq. 13

$$D \simeq 2\pi \frac{\lambda f}{4\pi\sigma_0} \quad (16)$$

$$\sigma_0 = 0.5\lambda f_{\#} \, . \quad (17)$$

where the f-number is defined by $f_{\#} = f/D$. In this case, the opening angle $\theta = 1/f_{\#}$ between the centre of the diverging Gaussian beam and its e^{-2} intensity cone is given by:

$$\theta = \frac{\lambda}{\pi\sigma} = \frac{1}{f_{\#}}$$

and so, for TM_{00} with f_1 optics, $\sigma_0 = \lambda/\pi$ and $\theta = 1$ rad, or $57°$. Thus, for $f_{\#} > 1$, the maximum angle of divergence of any ray in the beam is of order 0.5 rad, so the paraxial approximation is valid.

In practice, the laser beam must be transported over large distances involving many optical components and significant alignment challenges; so the practical final aperture D may be smaller than the nominal aperture of the final focus lens. For this reason it is safer to assume a more conservative final practical beam spot size $\sigma_\ell = k_p\sigma_0$ where k_p includes all the practical aspects of laser transport and alignment. In Ref. [1], and in the following analysis, $k_p \simeq 2$ is taken as a conservative estimate. So from now on the laser rms intensity at the waist, σ_ℓ, is given by the conservative estimate:

$$\sigma_\ell \simeq \lambda f_{\#} \quad (18)$$

The literature of laser optics contains several definitions of "laser spot size". It is common to find the beam size defined in terms of the diameter of the beam, where the radius of the beam is defined by the point $x = w$ at which the beam intensity is $1/e^2$ of its maximium value. In the above notation, this occurs at $x = 2\sigma$. To compare notation, $w = 2\sigma$ and the "laser spot size" is then $2w$, or 4σ. In the following, everything will be evaluated using σ but care is needed when comparing with formulae in other references.

Higher Order Laser Transverse Modes

In practice, the laser will not produce a pure TM_{00} mode but will also include higher order transverse modes. To illustrate the impact of such modes on the beam propagation issues, consider the TM_{01} mode where the condition that 99% of the light energy is contained within the lens aperture becomes:

$$0.99 = \int_0^{D_\ell/2} \int_0^{2\pi} r dr d\phi \frac{1}{2\pi\sigma_\ell^2} \left(\frac{r}{\sigma_\ell}\right)^2 \sin^2\phi \exp\left[-\frac{r^2}{2\sigma_\ell^2}\right] \quad (19)$$

which gives

$$0.01 = \left(1 + \frac{D_\ell^2}{8\sigma_\ell^2}\right) \exp\left[-\frac{D_\ell^2}{8\sigma_\ell^2}\right] \quad (20)$$

and hence $D_\ell \simeq 1.15 \times 2\pi\sigma_\ell$. So this means that the effective size of the beam is increased if TM_{01} modes are present. The same will be true for even higher order modes and their combined effect is included in a practical M^2 value for the laser, where $M^2 \geq 1$, with $M^2 = 1$ corresponding to a perfect laser.

The formulae outlined above for Gaussian laser optics are very similar to those used in accelerator physics, which describe a charged particle beam using a β-function and and emittance ϵ. The β-function is defined by the machine optical systems, such that the beam profile at any point is given by

$$\sigma_x = \sqrt{\epsilon\beta} \quad (21)$$

$$\sigma_{x'} = \sqrt{\epsilon/\beta} \quad (22)$$

$$\sigma_x\sigma_{x'} = \epsilon \quad (23)$$

where $\sigma_{x'}$ is the rms of the angular distribution. So, while the local profile of the beam depends on the β-function, the product $\sigma_x\sigma_{x'}$ at any location is invariant.

Comparing this with the formulae derived above for a perfect TM_{00} Gaussian laser beam; using Eq. 14 the corrsponding invariant is given by

$$\sigma_x\sigma_{x'} = \sigma_0\theta_0 = \frac{\lambda}{4\pi} \quad (24)$$

The effects of higher-order transverse modes are then taken into account by increasing the "emittance" of the laser beam to:

$$\sigma_x\sigma_{x'} = M^2\frac{\lambda}{4\pi} \quad (25)$$

If no re-tuning of the optical system is performed, then the effect of increasing M^2 is to increase both the local spot size and the angular divergence by a factor M, as shown in Fig. 5.

However, in practice, the laser spot size will be tuned to fill the aperture of the final focus lens. If the laser M^2 is then increased, the laser beam would clip the aperture and so the input beam will need to be re-tuned to reduce the size of the beam incicent on the lens by a factor M; this will consequently further increase by a factor M the spot size at the waist downstream of the lens. As a result the spot-size at the waist will have increased by a factor of M^2, as shown in Fig. 6.

In the following, the conventions used define y along vertical and x along the laser-beam direction. Including all the effects of M^2 and practicalities of light transport, the relevant formulae for Gaussian beam propogation are then modified as follows.

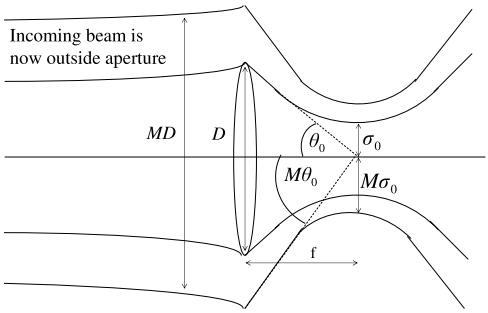

Figure 5: *Effect of $M^2 > 1$ on a LW final focus system initially set up to be optimised for $M^2 = 1$. In the unconstrained case, both the local angular divergence of the beam and its transverse spot dimension are increased by a factor of M.*

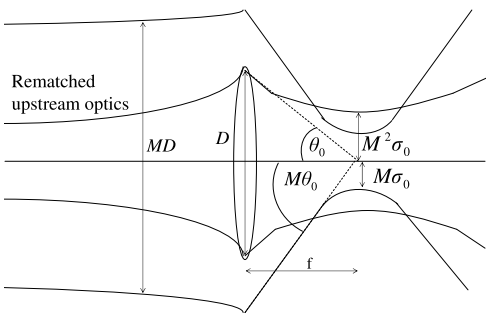

Figure 6: *Effect of rematching upstream optics for a beam with $M^2 > 1$ so as to maintain an optimised use of the final focus aperture. The final divergence of the lens must be reduced, by retuning the upstream laser optics, such that the beam is contained within the final focus aperture. This means that the transverse spot size at the waist must be further increased by a factor of M. Thus overal, the laser spot size at the waist is $M^2\sigma_0$.*

The light intensity of the laser has the form

$$I_\ell(x,y,z) = \frac{I_0}{2\pi\sigma_\ell^2}\frac{1}{f_R(x)}\exp\left[-\frac{y^2+z^2}{2\sigma_\ell^2 f_R(x)}\right] \quad (26)$$

$$f_R(x) = 1 + \left(\frac{x}{x_R}\right)^2 \quad (27)$$

$$\sigma_\ell = M^2 k_p \sigma_0 \quad (28)$$

where $\sigma_0 = 0.5\lambda f_\#$ and, conservatively, $k_p \simeq 2$.

$$x_R = M^2\frac{4\pi\sigma_0^2}{\lambda} \quad (29)$$

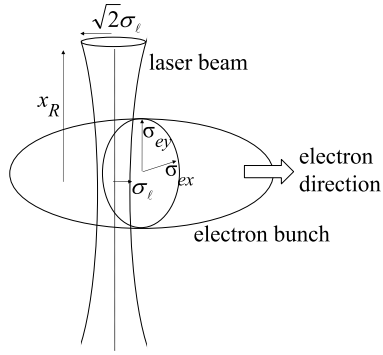

Figure 7: *Principle of operation of the laser-wire scanner with the key dimensions labeled. The figure shows the laser configured to scan the horizontal x-profile of the electron bunch σ_{ex}. x_R is the "Rayleigh range" of the laser beam as defined in Eq. 29; it gives the distance between the focus and the point where the laser spot-size has diverged to $\sqrt{2}$ of its minimum value.*

LASER-WIRE

Traditionally the transverse dimensions of an electron beam have been measured by scanning a tungsten or carbon wire across the beam and measuring the resulting backgrounds as a function of relative position of the wire. This method has the disadvantage of being highly disruptive to the electron beam and so it cannot be used during normal luminosity running. At the ILC, the electron beams in the BDS will have vertical transverse size of order 1-few μm; a normal wire scanner would not be able to measure beams of this size, nor would it be able to withstand the energy depositions from such high intensities. To solve these issues, the solid wire can be replaced by a finely-focused beam of laser light; such a system is called a laser-wire (LW).

Principle of Operation

The Compton collisions between laser photons and beam electrons are detected downstream and the Compton rate as a function of relative positions of electron and laser beams provides the measurement of the electron beam transverse profile. This principle is illustrated in Fig. 7, with a schematic experimental arrangement shown in Fig. 8. Two distinct methods have been employed to date. Operating the laser in continuous wave mode together with an optical cavity to enhance the power has been used [8] at the ATF at the KEK laboratory to measure the emittance of the damping ring; this technique would also be applicable to the ILC damping rings. In other parts of the machine, including the BDS, the beam is not circulating so a single-pass method based on high power pulsed lasers is required [9, 10, 11].

The Compton cross section decreases as the electron beam energy increases. For an electron beam energy E_b and laser photon energy $k = \frac{hc}{\lambda}$, the Compton cross sec-

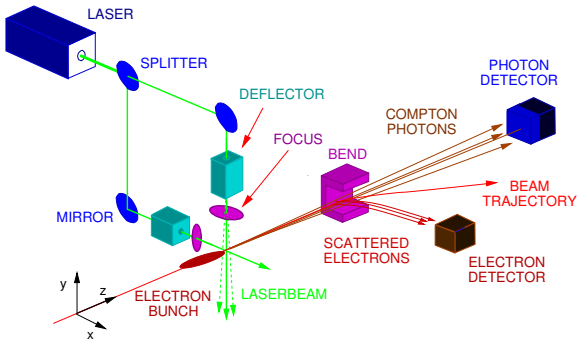

Figure 8: *Schematic of a practical LW system.*

Table 3: *Values of $f(\omega)$ for various laser wavelengths λ and ILC beam energies*

	λ(nm)			
E_b(GeV)	1064	532	355	266
5	0.96	0.92	0.89	0.86
50	0.72	0.59	0.51	0.45
150	0.51	0.38	0.31	0.27
250	0.41	0.30	0.24	0.20
500	0.30	0.20	0.16	0.13

tion is given by $\sigma_C(\omega) = \sigma_T f(\omega)$ where σ_T is the Thomson cross section = $0.665 \times 10^{-28}\mathrm{m}^2$, $\omega = \frac{kE_b}{m_e^2}$, and $f(\omega)$ gives the ratio of Compton to the Thomson cross section. Values of $f(\omega)$ for laser wavelengths and beam energies of typical interest at the ILC [1] are presented in Table 3.

In this section, the Compton rate for a set of laser-wire operating conditions is derived as a function of relative horizontal and vertical offsets, Δ_x and Δ_y respectively, between the centroids of the electron bunch and laser beam.

The number $N(\Delta_x, \Delta_y)$ of Compton photons produced will be proportional to the relevant overlap integral, $\epsilon(\Delta_x, \Delta_y)$. In Sec. , $\epsilon(\Delta_x, \Delta_y)$ will be evaluated in $\mu\mathrm{m}^{-1}$.

$$N(\Delta_x, \Delta_y) = N_0 \epsilon(\Delta_x, \Delta_y)$$

where

$$N_0 = \frac{P_\ell N_e \lambda f(\omega) \sigma_T}{hc^2} , \qquad (30)$$

P_ℓ is the instantaneous laser power at the laser-electron IP, and N_e is the number of electrons in the bunch. If η_{det} is the detector efficiency then, using realistic numerical values, the number of detected photons is $N_{\mathrm{det}}\epsilon(\Delta_x, \Delta_y)$, where

$$N_{\mathrm{det}} = 1212 \times \xi \qquad (31)$$

and

$$\xi = \frac{\eta_{\mathrm{det}}}{0.05} \frac{P_\ell}{10\ \mathrm{MW}} \frac{N_e}{2 \times 10^{10}} \frac{\lambda}{532\ \mathrm{nm}} \frac{f(\omega)}{0.2}\ \mu\mathrm{m} . \qquad (32)$$

Laser-Wire Overlap Integral

In the following, the electron beam is assumed to have a simple Gaussian charge profile, with σ_{ex} and σ_{ey} being the horizontal and vertical electron spot-sizes respectively. σ_z is assumed long compared to the laser spot-size, so the overlap integral in z integrates out trivially.

Scans Using the Laser TM_{00} Mode

The full overlap integral of a TM_{00} laser mode with a Gaussian electron bunch is now presented, including full effects of Rayleigh range. For the laser TM_{00} mode, performing the z- and y-integrals gives [1]

$$\frac{I_\ell I_e}{2\pi\sigma_{ex}} \int_{-\infty}^{\infty} \frac{dx}{\sigma_s(x,\Delta_x)} \exp\left[-\frac{x^2}{2\sigma_{ex}^2} - \frac{\Delta_y^2}{2\sigma_s(x,\Delta_x)^2}\right] \qquad (33)$$

where

$$\sigma_s(x,\Delta_x) = \sqrt{\sigma_{ey}^2 + \sigma_\ell^2 f_R(x-\Delta_x)}\ . \qquad (34)$$

In the approximation of an infinite Rayleigh range the equations reduce to the more familiar form with [4]

$$\sigma_m = \sqrt{\sigma_e^2 + \sigma_\ell^2} \qquad (35)$$

and

$$\epsilon(\Delta_y) = \frac{1}{\sqrt{2\pi}\sigma_m} \exp -\frac{(\Delta_y)^2}{2\sigma_m^2}\ . \qquad (36)$$

Similar additional formulae are provided in Ref [1] for laser-wire scans using the TM_{01} mode.

Results for the case of laser-M^2=1.3 and f_1 final focus optics are shown in Fig. 9 for an electron bunch transverse Gaussian profiles with (a) $\sigma_{ey} = 1\ \mu\mathrm{m}$, $\sigma_{\mathrm{ex}} = 10\ \mu\mathrm{m}$ and (b) $\sigma_{ey} = 1\ \mu\mathrm{m}$, $\sigma_{\mathrm{ex}} = 100\ \mu\mathrm{m}$; the effect of the Rayleigh-range is very apparent for the larger aspect-ratio.

Some recent experimental results obtained from the LW at the ATF extraction line are shown in Fig. 10, including a fit to function of the form of Eq 33. The detailed parameter extraction at the ATF is currently being analysed, however it is clear that the shape of the data is not pure Gaussian, and that the fit including Rayleigh range effects describes the data well.

Contributions to the Errors of a Laser-wire Measurement

A laser-wire scan will yield a measurement of the rate of Compton events as a function of position of the laser beam; this transverse scan size, σ_m, will be a convolution of machine related-effects and laser-related ones. The machine-related effects include bunch-to-bunch position jitter and residual dispersion at the laser-wire interaction point (IP) and are discussed in detail in Ref. [1]. The laser-related effects include laser pointing jitter, intensity (normalisation)

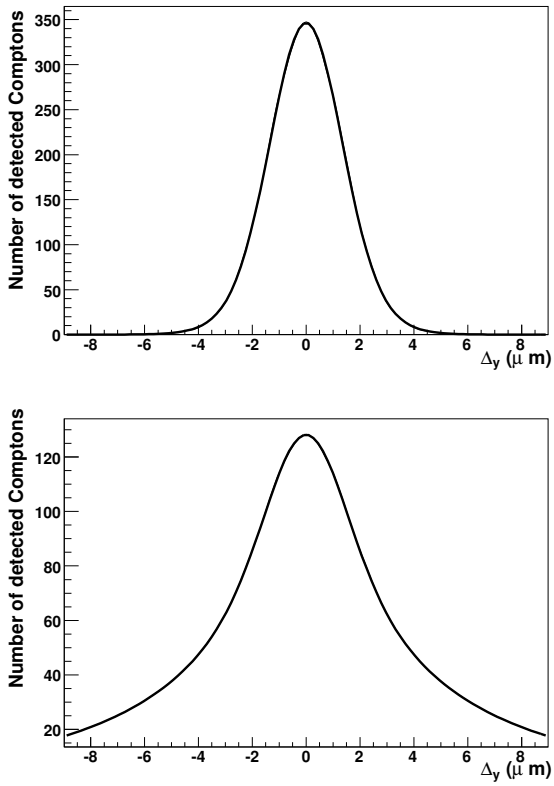

Figure 9: *Scan profile at the laser-wire IP for a laser with* M^2*=1.3 and wavelength 532* nm *operating in the* TM_{00} *mode and focused using* f_1 *optics. The electron bunch is assumed to have a Gaussian transverse profile. (a):* $\sigma_{ey} = 1\ \mu\text{m},\ \sigma_{\text{ex}} = 10\ \mu\text{m}$. *(b):* $\sigma_{ey} = 1\ \mu\text{m},\ \sigma_{\text{ex}} = 100\ \mu\text{m}$

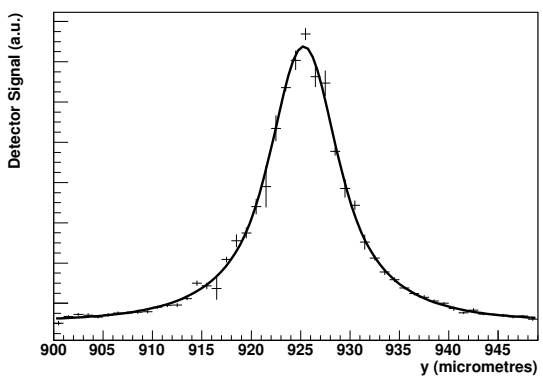

Figure 10: *Example scan from a laser-wire scan at the ATF extraction line. The non-Gaussian tails are clearly visible, which are well fit by including Rayleigh range effects, as given by Eq. 33*

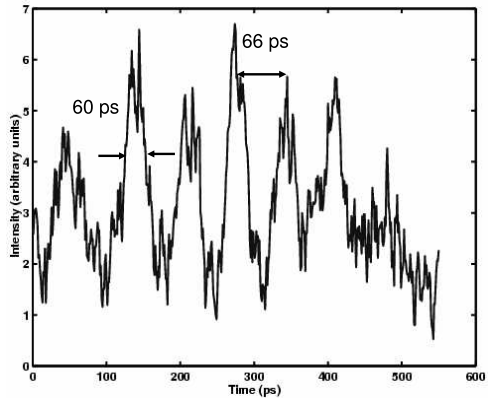

Figure 11: *Streak camera shot of a Q-switched laser. The temporal structure is due to longitudinal mode beating which, if the electron bunch lengths are less than or of order 50 ps, will have a serious impact on the effective rate at which a LW scan can be performed.*

fluctuations, and systematic errors associated with the uncertainty in the measurment of the light distribution at the IP, as discussed below.

Laser intensity fluctuations can be measured shot-by-shot using a fast photodiode; this works well for mode-locked systems, or for injection-seeded Q-switched ones. However, care must be taken with using unseeded Q-switched lasers because the presence of multiple longitudinal modes gives rise to a beating structure such as shown in Fig. 11, which is a streak-camera measurement of a Q-switched laser used in an early LW system at PETRAII. The PETRA bunch length is of order 50 ps, so shot by shot fluctuations of 100% are possible; this effect means that an average over several laser shots is required at each scan point. A later version of this system [10] used an injection seeded system, which enabled faster scan rates, as described below.

In the following a laser-wire scan is taken to consist of N_{scan} equally spaced values of y-displacements, Δ_y, of the laser with respect to the central value over a range $\pm 7\sigma_m$ (as defined in Eq. 35). The results presented here were obtained using $N_{\text{scan}} = 19$, however the statistical errors can be scaled in the usual way for other values. The contributions to the raw laser-wire scan can be broken down as follows:

$$\left(\frac{\delta\sigma_{\text{fit}}}{\sigma_{\text{fit}}}\right)^2 = \frac{19}{N_{\text{scan}}}\left(\frac{E_{\text{stat}}}{\sqrt{\xi}} + E_\xi\right)^2 + E_{M^2}^2 \qquad (37)$$

where E_{stat} is the relative statistical error of a 19-point fit to the raw scan curve, ξ is the event rate normalisation as defined in Eq.32, and E_ξ is the relative error arising from the shot-by-shot normalisation fluctuations.

E_{M^2} is the relative error on the extraction of σ_e introduced by any uncertainty in the laser light distribution at

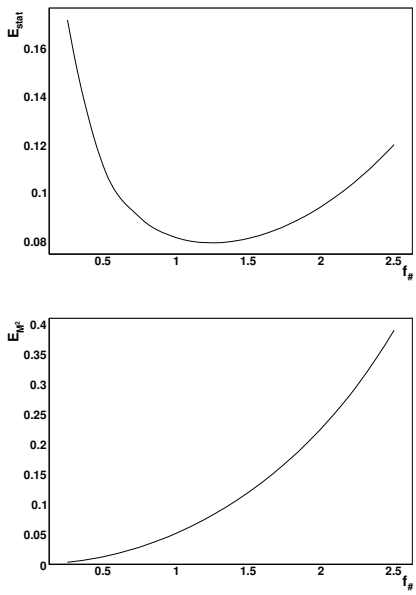

Figure 12: *(a): Statistical error $E_{\rm stat}$, (b): laser error E_{M^2} for $\xi = 1$ (Eq. 32) using $N_{\rm scan} = 19$ scan points versus the f-number of the final focus lens, using a laser with M^2=1.3 and operating in the TM$_{00}$ mode with $\lambda = 532\ nm$. The electron bunch is assumed to have a Gaussian transverse profile with $\sigma_{ey} = 1\ \mu$m and $\sigma_{ex} = 25\ \mu$m.*

the IP; this is characterized here by an error in the M^2 value of the laser and, for a real system, will need to be calculated including the effects of alignment errors etc. in the final-focus optics. Absolute M^2 measurements can be performed by slicing the laser-beam with a knife-edge at a set of longitudinal locations with respect to a laser-waist [17] and can be monitored relatively by capturing an image of the waist with a CCD camera.

E_{M^2} can be estimated by fitting the measured profile to σ_{ey} assuming a value of M^2 that is wrong by a factor $(1 + \delta_{M^2})$. In the following, the laser M^2 is thus assumed to be determined shot by shot to an accuracy of δ_{M^2}. Naively, without allowing for Rayleigh range effects, the error on the extracted value of σ_e from subtraction of the laser spot-size is

$$\frac{\delta\sigma_e}{\sigma_e} = \frac{\sigma_\ell}{\sigma_e^2}\delta\sigma_e \simeq \left(\frac{\lambda f_\#}{\sigma_e}\right)^2 M^2\delta_{M^2} \qquad (38)$$

Inserting representative values of $M^2 = 1.3$ and $\sigma_e = 1\ \mu$m gives:

$$\frac{\delta\sigma_e}{\sigma_e} = 1.08\left[\left(\frac{M^2}{1.3}\right)\left(\frac{1\ \mu\text{m}}{\sigma}\right)\left(\frac{\lambda}{532\ \text{nm}}\right)\left(\frac{f_\#}{1.5}\right)\right]^2\delta_{M^2}\,. \qquad (39)$$

A full numerical treatment [1] shows that this is a good approximation for small $\delta_{M^2} \simeq 1\%$ but is a slight underestimate for larger values.

The overlap integral Eq. 33 is now used to fit to a simulated laser-wire scan of interest to the ILC and thereby determine the laser-related errors on the extracted value of the electron vertical spot size σ_{ey}. Both $E_{\rm stat}$ and E_{M^2} will depend on the f-number of the laser optics employed. This dependence is illustrated in Fig. 12 for the case of $\sigma_{ey} = 1\ \mu$m and $\sigma_{ex} = 25\ \mu$m. For each set of σ_{ex}, σ_{ey}, there is an optimal f-number that gives the lowest statistical error for given values of ξ and $N_{\rm scan}$. However, as can be seen in Fig. 12, the minima are often fairly shallow, which must be contrasted with the difficulty of building low f-number optics. The difficulty is not just in building low f-number alone, but in producing a system that can maintain a small laser spot size approximately $\pm 10\ \sigma_\ell$ off axis, as needed during a scan. For these reasons, f-numbers of order 1.5 are likely to be optimal for ILC applications.

For larger spot-sizes and for the horizontal scans of the ILC electron bunch, the suitable f-number is determined primarily by the angular scan-range of the final focus lens plus scanning system. The laser optics for these dimensions will probably use diameter $D = 5$ cm optics (or similar). In this case, assuming again a scan range of $7\sigma_m$ the practical $f_\#$ is given by

$$f_\# = 1.4\left(\frac{\sigma_m}{10\ \mu\text{m}}\right)\left(\frac{5\ \text{cm}}{D}\right)\left(\frac{1\ \text{mrad}}{\theta_{\rm scan}^{\rm max}}\right)\,. \qquad (40)$$

In practice, for very large scan ranges, it may be preferable to use a stepping-motor system to move the final focus lens as opposed to scanning using optical ray deflection, which would enable smaller $f_\#$s to be employed. In that case, the scan would have to be very slow compared to the machine repetition rate. An additional consideration here is that the rate of Compton events is significantly lower for horizontal scans, due to the $1/\sigma_m$ factor in Eq. 36.

EXPERIMENTAL LW FACILITIES

Laser-wire at the PETRA Accelerator

A laser-wire system that can scan in both the horizontal and vertical directions was installed and operated [10] at the PETRAII accelerator. A schematic of this system is given in Fig. 13, which shows the stages used to find the beam and perform coarse scans using stepping motors. Faster, fine-grained, scanning was performed using mirrors attached to a piezo stack. Combined with the use of an inection-seeded Nd:YAG laser with wavelength λ=532 nm, high quality scans could be performed in about 50 s, this rate being limited by the repetition rate of the lase (20 Hz). Using both the horizontal and vertical scanning capability, the transverse beam profile was measured to be $46.5 \pm 0.6\ \mu$m in the vertical and $373 \pm 3\ \mu$m in the horizontal, where several single scans were used to obtain these measurements by fitting to the Rayleigh range formula of Eq. 29.

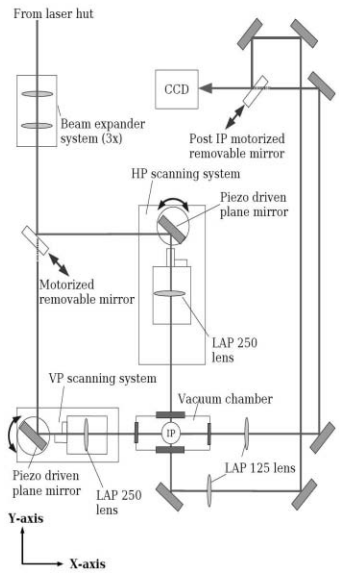

Figure 13: *Practical layout of a laser-wire system that can scan in both the horizontal and vertical dimensions. Such a system has operated at PETRAII [10]*

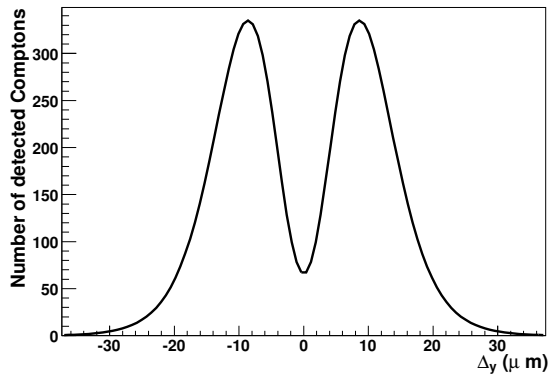

Figure 14: *Scan profile at the laser-wire IP for a laser with* M^2*=1.3 and wavelength 532* nm *operating in the* TM_{01} *mode and focused using* f_1 *optics. The electron bunch is assumed to have a Gaussian profile of* $\sigma_{ey} = 5\ \mu\mathrm{m},\ \sigma_{\mathrm{ex}} = 50\ \mu\mathrm{m}$

Laser-wire at H⁻ Accelerators

Laser-wires are also being used within H^- accelerators to measure the beam emittance [13]. They employ the photo dissociation technique, which is to ionize the H^- ions using lasers, which is possible because the threshold for this process is only about 0.75 eV and a Nd:YAG laser can thus be used as an effective light source. The laser light ionizes the H^- thus producing a free electron and a neutral H-atom. Both the electrons and the atoms can be used to determine detect the signal; the various components of the beam (H^0, H^- and e^-) are separated by a magnetic field and the electrons can then be detected in a Faraday cup to provide a fast signal that can also be used for a time-of-flight measurement in order to determine the longitudinal emittance of the electron bunch. The neutral atoms can be imaged by using a scintillation screen plus fast CCD camera [14]. The use of lasers in stripping the H^- ions to form an efficient source of protons is also being explored [15].

ALTERNATIVE MODES

Increased sensitivity to the electron spot-size can be obtained by using more sophisticated light distributions than the simple TM_{00} mode described above. Higher order laser-modes are one way to do this, another way is to create a laser interference pattern and scan the electron beam across the fringes; these methods are now discussed briefly.

TM_{01} laser mode

The case of operating the laser in TM_{01} mode with laser-M^2=1.3 and f_1 final focus optics are shown in Fig. 14 for an electron bunch transverse Gaussian profile with $\sigma_{ey} = 5\ \mu\mathrm{m},\ \sigma_{\mathrm{ex}} = 50\ \mu\mathrm{m}$; the benefit of the TM_{01} mode over similar scans using the TM_{00} mode (Fig. 9) is apparent due to the steeper variations of the signal as a function of Δ_y. The relative benefits of the TM_{00} and TM_{01} modes are discussed in Ref [1] , where it is shown that for $\sigma_{ey} > 1{-}2\ \mu$m there is a significant advantage for the statistical power by using the TM_{01} mode; this advantage has been demonstrated at the ATF [16]. However the sensitivity to the laser properties (as parameterized by a simple M^2 in these calculations) is greater for the TM_{01} mode and, for spot-sizes of order 1 μm, the relative statistical power of the TM_{01} to that of the TM_{00} mode decreases rapidly. The relative advantage of using higher order laser modes thus depends on where the system is located; laser-spot sizes of order 1 μm are of particular importance for the BDS LW system so the TM_{00} mode is more appropriate, whereas higher-order laser modes may be advantageous in other locations of the machine.

Interferometric Beam Size Monitor

The LW method of scanning across an electron bunch works well for electron bunch sizes greater than (or similar to) the wavelength of the light used (typically 0.5μm). For smaller electron bunches, an alternative technique has been demonstrated [4, 18], where a laser-beam is split into two and then the daughter beams superposed at a relative angle θ as shown in Fig 15. This sets up an interference pattern of the form [4]:

$$I(y) = I_0\left[1 + \cos\theta\cos\left(2k_y y\right)\right] \qquad (41)$$

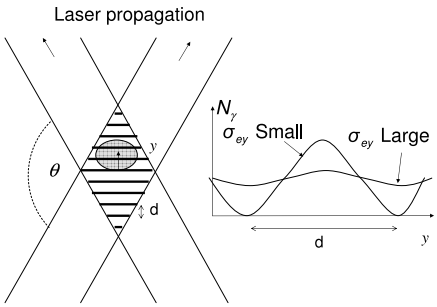

Figure 15: *Principle of an interferometric beam size monitor ("Shintake monitor"). The laser-beams are superposed at a relative total angle θ and the convolution of the resulting intensity fringes with a Gaussian electron bunch gives a number of Compton photons that varies as a function of relative position y between the fringes and the bunch. A measurement of the electron bunch size can be inferred from the magnitude of this signal variation, given by Eq. 42.*

where $k_y = 2\pi \sin(\theta/2)/\lambda$. This treatment applies only within that part of the region of overlap where a plane-wave approximation to Eq. 8 is valid (i.e. well within the Rayleigh range). If a Gaussian electron beam with rms size σ_{ey} is then incident on the region of overlap, the number of Compton photons N_γ is given by its convolution with Eq. 41:

$$N_\gamma = \frac{N_0}{2}\left(1 + \cos\left(2k_y y\right)\cos\theta \exp\left[-2(k_y\sigma_{ey})^2\right]\right) \tag{42}$$

This system, now frequently referred to as a "Shintake monitor", was employed [18] at the Final Focus Test Beam at SLAC, where the modulation of the Compton photon signal as a function of electron beam position determined the electron vertical spot size to be 73 nm. This system has since been transported to the ATF2 experiment [19] where it will be used to measure electron spot-sizes down to about 35 nm. In principle, through the use of shorter wavelength light, measurements of spot-sizes down to about 10 nm may eventually be possible using this technique, although this will require additional R&D both on the laser systems themselves and on the control of vibrations and jitter.

SUMMARY

Lasers are important elements of advanced beam diagnostics systems for transverse bunch profile measurements, with uses in both electron and proton machines. The main elements of such systems were described, including a derivation of the key formulae. A brief overview of exisiting laser-based systems was provided, with references to more detailed discussions in the literature.

REFERENCES

[1] I Agapov, G. A. Blair, M. Woodley. "Beam emittance measurement with laser wire scanners in the ILC beam delivery system". Phys. Rev. ST Accel. Beams **10**, 112801 (2007).

[2] Barish, B. and others. "ILC Reference Design Report" (2007). http://www.linearcollider.org/cms/

[3] Balakin, V. and others, "Focusing of submicron beams for TeV Scale e+ e- linear colliders". Phys. Rev. Lett. **74** 2479-2482 (1995).

[4] Tenenbaum, P. and Shintake, T., "Measurement of small electron-beam spots", Ann. Rev. Nucl. Part. Sci. **49** 125-162 (1999)

[5] Minty, M. and Zimmermann, F., "Measurement and Control of Charged Particle Beams" Springer (2003)

[6] Wiedemann, H., "Particle Accelerator Physics I",Springer (1999).

[7] Seeman, J., "Transverse and Longitudinal Emittance Measurements" in "Handbook of Accelerator Physics and Engineering", Ed. Chao, A. and Tigner, M., World Scientific, 559-562 (1999).

[8] Honda, Y. and others, "Upgraded laser wire beam profile monitor" Nucl. Instrum. Meth.,**A538** 100-115 (2005).

[9] Grishanov, B. I. and others, "ATF2 proposal. Vol. 2", physics/0606194 (2006)

[10] A. Bosco and others, "A Two Dimensional Laser-Wire Scanner for Electron Accelerators", to appear in NIM A (2008).

[11] Boogert, S. T. and others, "A laser-wire system at the ATF extraction line", Prepared for Particle Accelerator Conference (PAC07).

[12] Siegman, A. E.,"Lasers", University Science Books (1986).

[13] S. Assadi, "SNS Transverse and Longitudinal laser profile monitors desing, implementation and results", Proc. EPAC06 (2006).

[14] C. Gabor and others, "Laser-based Beam Diagnostic for the Front End Test Stand (FETS) at RAL", Proceedings of EPAC06 (2006).

[15] Danilov, V. and others, "Proof-of-principle demonstration of high efficiency laser-assisted H^- beam conversion to protons", Phys. Rev. ST Accel. Beams **10** 053501 (2007),

[16] Y. Honda, "Laser-wire at ATF Damping Ring", Proc. Laser-wire Mini Workshop, Oxford, (2006).

[17] T. F. Johnston, "Beam propagation (M^2) measurement made as easy as it gets: the four cuts method", Applied Optics **37**, 4840-4850 (1998).

[18] Balakin, V. and others, "Focusing of Submicron Beams for TeV-Scale e^+e^- Linear Colliders", Phys. Rev. Lett. **74** 2479-2482 (1995).

[19] Grishanov, B. I. and others, "ATF2 proposal. Vol. 2", physics/0606194 (2006).

Electro-optic techniques in electron beam diagnostics

J. van Tilborg*, Cs. Tóth, N. H. Matlis, G. R. Plateau, and W. P. Leemans
Lawrence Berkeley National Laboratory, Berkeley, California

Abstract

Electron accelerators such as laser wakefield accelerators, linear accelerators driving free electron lasers, or femto-sliced synchrotrons, are capable of producing femtosecond-long electron bunches. Single-shot characterization of the temporal charge profile is crucial for operation, optimization, and application of such accelerators. A variety of electro-optic sampling (EOS) techniques exists for the temporal analysis. In EOS, the field profile from the electron bunch (or the field profile from its coherent radiation) will be transferred onto a laser pulse co-propagating through an electro-optic crystal. This paper will address the most common EOS schemes and will list their advantages and limitations. Strong points that all techniques share are the ultra-short time resolution (tens of femtoseconds) and the single-shot capabilities. Besides introducing the theory behind EOS, data from various research groups is presented for each technique.

INTRODUCTION

Electron accelerators are playing a major role in today's scientific landscape. Compact relativistic electron bunches, containing $> 10^9$ electrons, with a transverse size of several microns and a temporal duration of 10's to 100's of femtoseconds, can be utilized for numerous applications. On one hand one can think of experiments where the electrons are utilized directly (for example: colliders, electron diffraction, and magnetic switching). On the other hand, these compact bunches can produce intense electromagnetic radiation such as X-rays, gamma rays, ultraviolet photons, and terahertz (THz) radiation, among others (think for example of synchrotron radiation or free electron lasers). For all these applications, the quality of the electron bunch is a critical parameter. One way to assign a parameter for bunch quality is through the introduction of a beam brightness, defined as

$$\text{Brightness} = \frac{\text{Charge} \cdot \text{E}_{\text{kin}}}{\text{Duration} \cdot (\Delta\text{E}_{\text{kin}}/\text{E}_{\text{kin}}) \cdot \text{Emittance}}, \quad (1)$$

where E_{kin} is the electron kinetic energy with spread $\Delta\text{E}_{\text{kin}}$, and where the emittance represents the transverse emittance.

Each of the parameters listed in Eq. (1) needs to be measured and controlled for optimized accelerator performance. The work presented in this paper will address characterization of the temporal bunch duration, with the emphasis on bunches of ultra-short (femtosecond) duration.

* JvanTilborg@lbl.gov

Coherent radiation from electron bunches

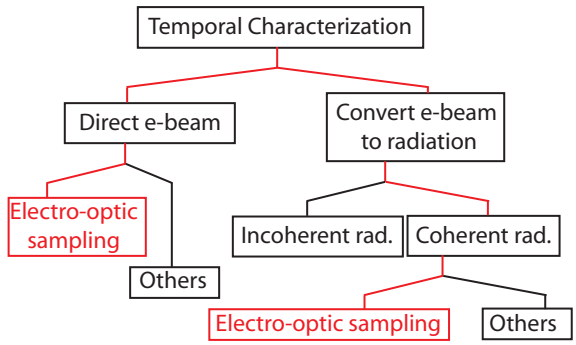

Figure 1: The technique of electro-optic sampling (EOS) can be applied to either the direct electron beam, or on the coherent radiation emission (typically at THz frequencies) that is produced by the electron bunch.

The temporal charge profile of an electron bunch can be labeled as $Q(t)$. The Fourier transformation of this profile is given by $Q(\omega) = \int dt Q(t) \exp(-\imath\omega t)$, where $\omega = 2\pi\nu$, with ν the frequency and ω the angular frequency. The spectral profile $Q(\omega)$ is complex (real and imaginary parts) and can be expressed as

$$Q(\omega) = |Q(\omega)|e^{\imath\phi(\omega)}, \quad (2)$$

where $|Q(\omega)|$ is the absolute spectrum and $\phi(\omega)$ the spectral phase. Note that only through measurement of both $|Q(\omega)|$ and $\phi(\omega)$ can the temporal profile $Q(t)$ be fully reconstructed.

As illustrated in Fig. 1, there are two paths to characterize the temporal duration of an electron bunch. The first path focuses on measurement of the field profile of the bunch itself (labeled as "Direct e-beam"), while the other path focuses on the emission of electro-magnetic radiation by the electron bunch. The mechanism for radiation emission can be transition radiation, diffraction radiation, Cherenkov radiation, Smith-Purcell radiation, or synchrotron radiation, among others. Since properties of the electron bunch duration are present in the emitted electromagnetic pulse, analysis of the radiation can lead to temporal bunch characterization.

The radiation can be categorized, see Fig. 1, as incoherent radiation (at wavelengths shorter than the bunch length) and coherent radiation (at wavelengths longer than the bunch length). It was demonstrated by Catravas *et al.* [1, 2] that through fluctuation interferometry of the incoherent radiation one can estimate the pulse duration. Also, a (sub)picosecond streak camera can be used to detect the pulse duration of the incoherent light [3]. Most

other radiation-based techniques focus on the coherent part of the spectrum, which is typically intense since it scales with the square of the number of electrons (while the incoherent part only scales linearly with the number of electrons). It has been shown that the field $E_{\rm coh}(\omega)$ of the coherent component of the spectrum can be described as

$$E_{\rm coh}(\omega) \propto Q(\omega)D(\omega), \qquad (3)$$

where $D(\omega)$ describes the effects of diffraction. The function $D(\omega)$ approaches $D = 0$ for long wavelengths and approaches $D = 1$ for short wavelengths. For example, for transition radiation, the function $D(\omega)$ was described by Schroeder *et al.* [4]. In Fig. 2 a coherent transition radiation pulse in the frequency domain (left) and in the time domain (right) is plotted for an electron bunch of duration τ_e =50 fs [root mean square (rms)], based on the definition $Q(t) = \exp\left[-t^2/(2\tau_e^2)\right]$. The diffraction [4] was based on a 500-μm transverse boundary size of the emission emitter. Note that the electric field profile of the coherent radiation pulse is almost identical to the field profile of the charge profile in both the time and frequency domain, except for the effects of diffraction. Diffraction will attenuate the spectrum at lower frequencies (see left plot in Fig. 2), while in the time domain a long negative field wing is introduced (see right plot). Through diffraction the condition $\int dt E_{\rm coh}(t) = 0$ is met, which is a condition required for any type of electro-magnetic radiation.

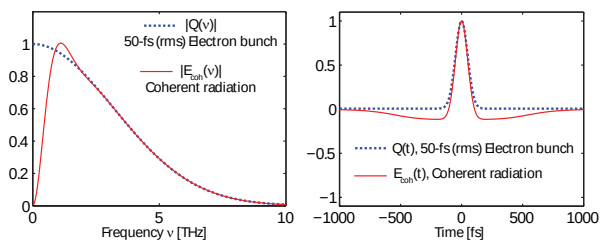

Figure 2: Example of a coherent radiation pulse (red solid curve) emitted from a 50-fs (rms) electron bunch. The left plot shows the similarity in the frequency domain (the difference is the attenuation due to diffraction at low frequencies), while the right plot shows the similarity in the time domain (the difference is the appearance of long-timescale negative field wings).

The spectrum on the left side of Fig. 2 also illustrates that both the charge profile and the coherent radiation pulse for a femtosecond electron bunch have spectral components in the terahertz (THz) regime. Therefore, both the electric field profile of the electron bunch and the coherent radiation pulse will share the same label "THz pulse" in the next sections of this paper, with field profile $E_{\rm THz}(t)$.

Several techniques exist for analyzing the absolute spectrum of the coherent radiation (and missing the spectral phase), such as spectral measurements with a far-infrared spectrometer (also referred to polychromator) [3, 5] or a Michelson or Martin-Puplett interferometer [3, 6, 7]. A more recently developed diagnostic technique is electro-optic sampling (EOS) [8, 9], which is a laser-based technique. This technique offers unique advantages, which include

- Temporal resolution on the order of 10's of femtoseconds
- Non-destructive to the electron beam
- Room-temperature operation (no bolometers)
- Single-shot capabilities
- Measures relative timing to other pump/probe beams
- Yields exact charge profile $Q(t)$, and not just $|Q(\omega)|$

As mentioned earlier, see Fig. 1, the temporal profile of an electron bunch can also be obtained through techniques measuring directly the field profile of the bunch. Examples are the radio frequency (RF) zero-phasing method [10, 11] (also referred to as the RF streak method), or laser-electron interaction experiments such as laser-induced electron deflection [12]. In addition to being applied to coherent radiation, EOS can also be applied directly to the electric field of the electron beam, as shown in the diagram in Fig. 1. Again, the same set of advantages for EOS as itemized earlier are valid. Note that EOS on the electron beam directly has to occur *in situ* (in the vacuum chamber), while coherent radiation could easily be transported out of the vacuum chamber to any location of choice, making it easier to access the EOS setup. Of course, by setting up a radiation beam path, issues such as clipping, aberrations, dispersion in transmissive optics, and spectral-dependent reflectivity have to be considered and could potentially effect the analysis [13].

BASICS OF ELECTRO-OPTIC SAMPLING

In electro-optic sampling [8, 9], the THz pulse (as mentioned before, this could refer to the electron bunch or the coherent radiation pulse since both have frequency components in the THz domain) induces a change in index of refraction in an electro-optic crystal. This change can be measured by a near-infrared (NIR) laser pulse $E_L(t)$. The electro-optic effect is a second-order nonlinear or $\chi^{(2)}$ effect. The EO crystal, having no or little birefringence in absence of THz fields, will become birefringent upon presence of a THz pulse. The birefringence can best be described by the index ellipsoid. This effect is sketched in Fig. 3. In this paper, the family of EO crystals of cut <110> is considered, for which the crystal axis (z' axis) lies in the plane of the cut. The relations between the crystal's z' axis, the THz field polarization vector, and the major and minor axes of the induced index ellipse are well described by Chen *et al.* [14].

Since the THz pulse field strength is time-dependent [$E_{\rm THz}(t)$], the change in index ellipse will also follow the THz pulse temporal profile. The change in index ellipsoid will leave an imprint on the accumulated phase of the laser pulse. The polarization of the laser pulse can be expressed in the coordinate system of the index

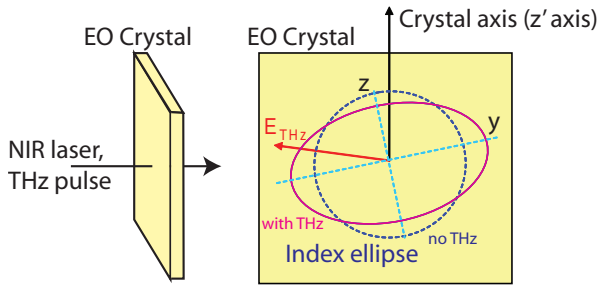

Figure 3: Overview of the field and crystal vectors involved in EOS. For <110> cut EO crystals, the crystal axis (or z' axis) lies in the crystal cut (crystal plane). Depending on the THz pulse field strength, the index ellipsoid for a NIR laser changes from circular (no birefringence) to elliptical, with major and minor axes z and y, respectively. The rotation orientation of the index ellipse is a function of the THz field vector with respect to the crystal z' axis.

ellipse y and z, see Fig. 3. We therefore can define $E_L(t) = E_{L,0}\exp(-\imath\omega_0 t)\exp[-t^2/(2\tau_L^2)]$, with τ_L the laser pulse duration (rms), and $E_{L,0} = E_y\exp(\imath\phi_{0,y})\ \vec{e_y} + E_z\exp(\imath\phi_{0,z})\ \vec{e_z}$. The polarization phase components $\phi_{0,y}$ and $\phi_{0,z}$ reflect the polarization state (linear, elliptical, or circular) and are constants determined by the optical elements in the laser's optical path such as quarter- and half-wave plates.

During propagation through the EO crystal, the change in index of refraction δn_z along the ellipsoid axes z, as well as δn_y along the ellipsoid axes y, is [14]

$$\begin{aligned}\delta n_z &= \frac{n_0^3 r_{41} E_{\mathrm{THz}}}{4}\left(cos\phi + \sqrt{1+3\sin^2\phi}\right)\\ \delta n_y &= \frac{n_0^3 r_{41} E_{\mathrm{THz}}}{4}\left(cos\phi - \sqrt{1+3\sin^2\phi}\right)\end{aligned} \quad (4)$$

with ϕ the angle between the crystal z' axis and the THz polarization. In this paper we will consider $\phi = \pi/2$, in which case the axes z and y are at 45 degrees with respect to the crystal z' axis [14]. Also, r_{41} is the electro-optic coefficient of the EO crystal and n_0 is the index of refraction at the central wavelength of the NIR pulse. The EO-induced phase shift for the laser's polarization component along axis j of the ellipse is given by $\delta\phi_j = \delta n_j L 2\pi/\lambda_0$, with $\lambda_0 = 800$ nm and L the EO crystal thickness.

Since E_{THz} in Eq. 4 has a temporal dependency one might at first sight expect the phase shift along the ellipse axis to be simply $\delta\phi_j(t) \propto E_{\mathrm{THz}}(t)$. However, several crystal effects can not be overlooked. Think of 1) absorption of some THz frequencies, 2) dispersion of the THz pulse, and 3) a velocity mismatch between the laser's group velocity and the individual THz phase velocities. These effects can best be described by a crystal transfer function $T_{\mathrm{crystal}}(\omega)$. The actual phase shift along axis j is defined as $\Gamma_j(t)$. In order to relate $\Gamma_j(t)$ to $E_{\mathrm{THz}}(t)$ and T_{crystal}, it is easiest to operate in the frequency domain, in which case [8, 15]

$$\Gamma_j(\omega) = \frac{2\pi}{\lambda_0} L\delta n_j(\omega) T_{\mathrm{crystal}}(\omega), \quad (5)$$

with δn_j defined by Eq. (4). It was shown [15] that $T_{\mathrm{crystal}}(\omega)$ is mainly dependent on the real and imaginary index of refraction of the EO crystal in the THz regime, and is given by

$$T_{\mathrm{crystal}}(\omega) = \frac{2}{1+n_{\mathrm{THz}}}\cdot\frac{\exp[\imath L(n_{\mathrm{gr}}-n_{\mathrm{THz}})\frac{\omega}{c}]-1}{\imath\frac{\omega}{c}(n_{\mathrm{gr}}-n_{\mathrm{THz}})}, \quad (6)$$

with n_{gr} the group velocity of the laser and $n_{\mathrm{THz}} = n_{\mathrm{THz}}(\omega)$ the complex index of refraction.

To summarize the previous discussion, let's label the modulated laser field as $E_M(t)$. The field projections of $E_M(t)$ along the y and z axis are $E_{M,y}(t)$ and $E_{M,y}(t)$. The field projection $E_{M,j}(t)$ is given by

$$E_{M,j}(t) = E_{L,j}(t)e^{\imath\Gamma_j(t)} \quad (7)$$

Note that a more detailed theoretical description has been written by Jamison *et al.* [9]. Here the modulated field profile was found to be $E_{M,j}(t) = E_{L,j}(t) + \frac{d}{dt}[E_{L,j}(t)\cdot\Gamma_j(t)]$. For THz frequencies much smaller than $\omega_0 = 2\pi c/\lambda_0$, and for THz-induced EO phase retardations less than 1 rad, this expression reduces to Eq. (7). It is therefore important to note that the expressions used in this paper are following those two assumptions.

There are a large variety of experimental configurations possible that detect the added phase term $\Gamma_j(t)$. The laser can have arbitrary polarization (linear, elliptical, or circular), its polarization vector can be at any arbitrary angle with respect to the index ellipse, and/or a polarizer can be added after the EO crystal. The next two sections will be devoted to various techniques that allow the user to measure $\Gamma_j(t)$, leading to $E_{\mathrm{THz}}(t)$ and $Q(t)$. In both sections, the phase dependent time $\Gamma_j(t)$ will be converted to an intensity modulation on the laser envelope. The first section will focus on techniques where the intensity-modulated laser beam is analyzed in the time domain, while the second section will focus on analyzing the modulated laser pulse in the frequency domain through measurement of the spectrum of the laser pulse.

ELECTRO-OPTIC SAMPLING IN THE TIME DOMAIN

The EOS schemes described in the remaining sections are based on the laser propagating through an EO crystal, oriented such that the major laser polarization axis, as indicated in Fig. 4, is at 45 degrees with respect to the ellipsoid axes. In Fig. 4 the laser polarization state is linear or elliptical, but with conservation of generality the case of circular polarization can be considered as well. The only difference between the various polarization states is the ratio of the field amplitudes E_y and E_z, as well as the difference in phase $|\phi_{0,y} - \phi_{0,z}|$. As indicated in Fig. 4 the polarizer, positioned after the EO crystal, is only transmitting the laser

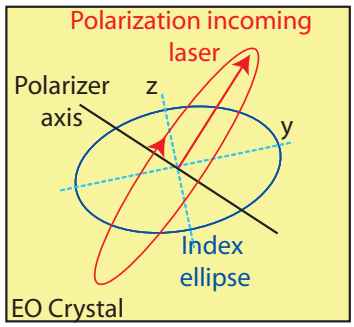

Figure 4: In most EOS schemes the THz-induced laser phase modulation is converted to a laser amplitude modulation. Typically, the laser's major polarization axis is at 45 degrees with respect to the index ellipsoid axes y and z. After propagation through the EO crystal, the laser beam passes through a polarizer (also referred to as analyzer), which only transmits the polarization component perpendicular to the incident laser's major polarization axis.

fields with a polarization component at 90 degrees with respect to the polarization vector of the laser. It was shown by Eq. (4), and using the geometry $\phi = \pi/2$, that the difference in index of refraction $\Delta n(t)$ is given by $\Delta n(t) = \delta n_z - \delta n_y = n_0^3 r_{41} E_{\mathrm{THz}}(t)$. This leads to a net phase shift following Eq. (5) of $\Gamma(\omega) = (2\pi/\lambda_0) L \Delta n(\omega) T_{\mathrm{crystal}}(\omega)$. A simple construction of Jones matrices [16] describes the evolution of the electric field vector (amplitude and phase) through any optical system, such as polarizers, wave plates, phase shifts induced in the EO crystal, etc. The Jones matrices allow for calculation of the electric field $E_M(t)$, and intensity $I_M(t) = |E_M(t)|^2$, of the laser passing through the polarizer. For example, for circular polarizer laser light, defined as $E_y = E_z$ and $|\phi_{0,y} - \phi_{0,z}| = \pi/2$, it can be shown that

$$I_M(t) = I_L(t) \cdot \frac{1}{2} \left[1 + \sin \Gamma(t)\right]. \tag{8}$$

For linear polarized light, for which $E_y = E_z$ and $\phi_{0,y} = \phi_{0,z}$, the transmitted laser intensity (or energy) is now

$$I_M(t) = I_L(t) \cdot \sin^2 \left[\Gamma(t)/2\right]. \tag{9}$$

Note that the sign information in this linear case is lost, although the sensitivity (change in transmitted intensity for a small THz field) has increased. In the next paragraphs, various experimental techniques to measure $I_M(t)$ [and therefore $\Gamma(t)$] will be considered. For simplicity we will assume a circular polarization state of the incoming laser pulse.

Scanning technique

In the first and simplest technique, the laser pulse length τ_L is short compared to the THz pulse length. Typically, laser pulse lengths of few tens of fs can easily be delivered to the EO crystal. A photo-diode can measure the time-integrated laser energy $I_{\mathrm{diode}} \propto \int dt I_M(t)$ that has passed through the polarizer. The diode signal (measuring energy I) versus time delay between laser and THz pulse, following Eq. (8), is then given by

$$\begin{aligned} I_{\mathrm{diode}}(\tau) &= \int dt I_L(t-\tau) \cdot \frac{1}{2} \left[1 + \sin \Gamma(t)\right] \\ &\simeq \frac{1}{2} \left[1 + \sin \Gamma(\tau)\right], \end{aligned} \tag{10}$$

where the second step is only valid for sufficiently short laser pulse lengths. In reality, the effect of the non-zero laser pulse length will come into play through the Fourier transformation of the envelope of the laser pulse intensity, or $I_{\mathrm{env}}(\omega) = \int dt \exp\left(-t^2/\tau_L^2\right) \exp\left(-\imath\omega t\right)$. In first approximation, the retrieved EO profile $\Gamma(\omega)$ is in fact $\Gamma(\omega) I_{\mathrm{env}}(\omega)$. The measurement of $\Gamma(\tau)$ needs therefore to be corrected for the laser pulse envelope. For example, a laser pulse with a rms (field) pulse duration of $\tau_L = 30$ fs, and thus an intensity full-width-at-half-max of $2\tau_L\sqrt{\ln 2} = 50$ fs, will result in a spectral cut-off [half-max of $I_{\mathrm{env}}(\nu)$] in the THz domain around $\nu = 9$ THz.

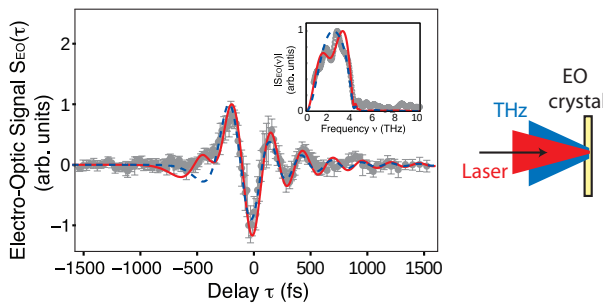

Figure 5: Example of a scanning EOS measurement of coherent radiation [$S_{\mathrm{EO}}(\tau) = I_{\mathrm{diode}}(\tau)$]. The radiation, together with the laser pulse, was focused on a ZnTe crystal. The data was published by van Tilborg *et al.* [17]. It was based on THz radiation from a laser wakefield accelerator. The inset shows the Fourier transformation of the data. The red curve is a fit based on a Gaussian electron bunch of length 50 fs (rms).

An example of a scanning measurement is presented in Fig. 5, published by van Tilborg *et al.* [17]. The data was taken on coherent transition radiation from a laser wakefield accelerator. The laser and THz beams were focused onto the EO crystal, such that the THz field strength was optimized and spatial overlap of the laser and THz profile was guaranteed. The Fourier transformation of the data is plotted in the inset. The data is also fitted with a modeled EO-modulated profile from a 50 fs (rms) electron bunch. Note that the sharp cutoff in the data at 4 THz is due to the crystal transfer function of 200-μm-thick ZnTe crystal. Note that the form factor $Q(\nu)$ a 50 fs (rms) electron bunch has a spectral half max at $\nu = 3.7$ THz, which falls just within the bandwidth of the ZnTe crystal. This limits the use of ZnTe crystal to bunches longer than ~50 fs (rms).

Because of the scanning nature of this technique, its success relies intrinsically on the stability of the electron accelerator and THz emission properties. Note that the use of elliptical or circular polarized laser light, see Eq. (8), yields sign-resolved THz field information. In the case of probing directly the fields of the electron bunch, this is not relevant and linear polarized laser pulses can be applied, which is more favorable since the polarizer throughput scales more dramatically with THz field strength in this configuration.

Since most accelerators do not possess excellent shot-to-shot reproducibility, either in the electron bunch properties or in the arrival time with respect to the laser, single-shot EOS techniques are strongly favorable. The next few section will introduce several single-shot detection schemes.

Spatio-temporal mixing or echelon-based technique

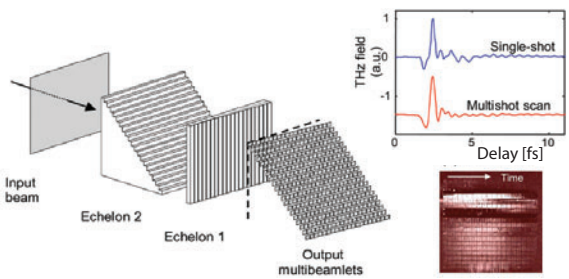

Figure 6: Overview of the experimental results from Kim *et al.* [18], in which two echelons (see left illustration) where used to create a series of beamlets out of the laser beam. Since each beamlet overlaps at the THz focus with a different time delay , the THz temporal profile (see figure top right) is imprinted in the spatial laser profile in the far field (see figure bottom right).

A simple extension of the previous technique is a technique demonstrated by Kim *et al.* [18]. Just as in the scanning geometry, a short laser pulse is used. However, through a combination of two echelons, see left part of Fig. 6, an array of beamlets is created out of the laser laser beam, each with a specific delay time. This is a direct consequence of the fact that each beamlet propagated through a different thickness of material in the echelons. Once this collection of beamlets is focused onto the EO crystal, each beamlet is overlapped with the THz pulse, but at a different relative temporal delay. In the far field, after propagating through a polarizer, the beamlets spread out again spatially and can be imaged by a camera, see the bottom right image in Fig. 6. By plotting the modulated measured energy of each beamlet a full THz profile can be reconstructed, see the top right part of Fig. 6. The retrieved waveform is compared to a waveform obtained with a standard scanning technique.

This technique is labeled as "spatio-temporal mixing technique" because the beamlets, which split up the larger laser beam into little spatial domains, represent different temporal delays at focus. The technique has not been applied yet to direct electron bunches or THz pulses produced by electron bunches, but was demonstrated [18] on a laser-based THz source. The same comments for the temporal resolution as for the scanning technique are valid, namely a resolution limited by the laser pulse length. Note that for ultra-short laser pulses (<30 fs), the beamlet-dependent dispersion through the echelons has to be accounted for and might limit its application.

Non-collinear cross-correlation between THz and laser pulses

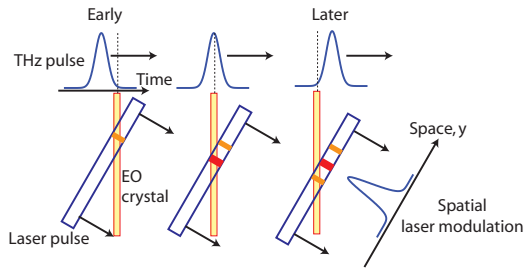

Figure 7: Illustration explaining the basic concept of non-collinear cross-correlation, in which the propagation vectors of the THz pulse and laser pulse are tilted with respect to one other. At early times (see left image), only a fraction of the transverse profile of the laser pulse is overlapped in the EO crystal with the front of the THz pulse. At later times (see right images), the overlap is occurring for a different spatial part of the laser beam, and the overlap also occurs at a different time slice of the THz pulse. Therefore, the temporal THz profile is imprinted on the spatial transverse intensity profile of the laser, which is an easy feature to measure with a camera.

Another single-shot technique that measures the THz modulation in the time domain is intrinsically based on non-collinear propagation of the THz pulse and the laser pulse onto the EO crystal, see Fig. 7. It is important that neither the laser beam nor the THz pulse are focused, but remain collimated. In fact, we have to assume that both beams have no spatial-dependent field features. At a specific moment in time, see for example the left plot in Fig. 7, the THz field in the EO crystal overlaps with only a spatial fraction of the laser pulse. There is direct correlation with the transverse spatial position within the laser beam and the relative time delay between both pulses. For example, subsequent plots in Fig. 7 show that different transverse spatial regions in the laser beam correspond to different relative delays. Therefore, by measuring (after propagating through a polarizer) the transverse energy distribution of the laser profile, a complete temporal THz profile can be reconstructed.

This technique was demonstrated on a laser-based THz source by Shan et al. [19], and demonstrated on the THz fields (direct electron beam) from an electron accelerator

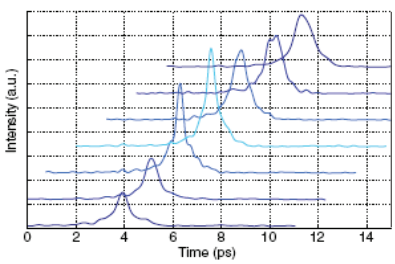

Figure 8: THz profiles obtained through the non-collinear cross-correlation technique, measured by Cavalieri *et al.* [20]. The electric fields of the electron bunch were measured directly by propagating the electron bunch close to the EO crystal. Each profile in the figure corresponds to a different accelerator tuning setting.

by Cavalieri et al. [20], as shown in Fig. 8. The electron bunches that they characterized were found to have a minimum pulse length of 270 fs. Another advantage of this technique is the relative large single-shot temporal window. For each shot, one not only gets the charge profile, but also the relative timing with respect to the laser pulse. Just as in the previous two subsections, time resolution is limited only by the laser pulse length. Disadvantages of this technique could be the reliance on a uniform transverse THz and laser profile. Also, the EO effect could be weak due to the lack of focusing. However, in case of measurement on the electron beam directly this last point is less critical since the electron bunch is typically dense with large transverse fields.

Non-collinear cross-correlation between laser and THz-modulated-laser pulses

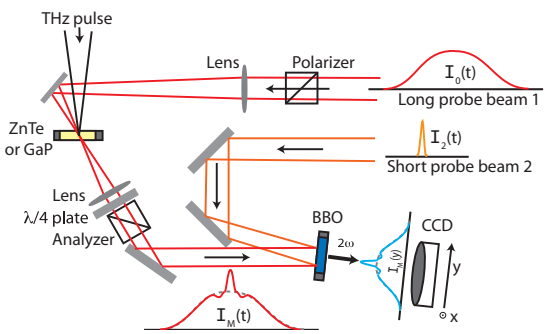

Figure 9: Overview of the setup for single-shot detection based on the non-collinear cross-correlation of a short laser beam (probe beam 2) and a long THz-modulated laser beam (probe beam 1). Through frequency doubling in the BBO crystal, the THz imprint on the envelope of probe beam 1 can be recorded by a camera in a single-shot.

Another non-collinear cross-correlation scheme was proposed by Jamison *at al.* [21] and demonstrated on electron accelerators by Berden *et al.* [11, 22] and van Tilborg *et al.* [13]. This technique is closely related to the previous cross-correlation technique, but there are a few critical differences. First of all, the laser beam incident on the EO crystal is now much longer than the THz pulse, see $I_0(t)$ in Fig. 9. This can be achieved by either suppressing the bandwidth of an ultra-short laser, or by chirping the laser. The laser and the THz radiation are both focused on the EO crystal for maximum EO effect. After propagating through the polarizer, see Fig. 9, the THz-modulated-laser beam has a time-dependent intensity modulation $I_M(t)$ as defined by Eq. (8). In second stage, the intensity-modulated long laser pulse can be measured in a single-shot with a second laser probe beam $I_2(t)$, which is now short (tens of femtoseconds), based on the same non-collinear cross-correlation geometry as discussed in the previous section. The second probe beam will define the temporal resolution of this technique. Through non-collinear frequency doubling in a BBO crystal, the spatial profile of the frequency-doubled beam $I_{2\omega}(y)$, as measured by a CCD camera, contains the THz imprint on probe beam I_0, or

$$\begin{aligned} I_{2\omega}(y) &\approx I_M(\tau) \\ &= \int dt I_2(t-\tau)\cdot I_0(t)\frac{1}{2}\left[1+\sin\Gamma(t)\right] \\ &\simeq I_0(\tau)\frac{1}{2}\left[1+\sin\Gamma(\tau)\right], \end{aligned} \tag{11}$$

By measuring the blue profile, and dividing it by a reference profile when no THz radiation was present, the THz profile $\Gamma(t)$ can be retrieved.

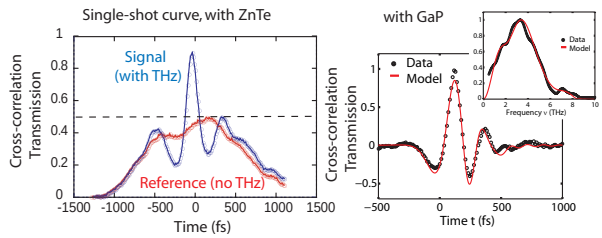

Figure 10: Data from van Tilborg *et al.* [13] using the non-collinear cross-correlation scheme between a short laser and a longer THz-modulated laser pulse. The left image shows a measurement on a ZnTe crystal, while the main figure on the right shows a GaP measurement. The Fourier transformation in the inset indicates the presence of THz radiation up to 7-8 THz. The red curve is a fit based on THz radiation from a 45 fs (rms) electron bunch.

Results from this technique, measured by van Tilborg *et al.* [13], are shown in Fig. 10. The data presented in Fig. 10 was obtained with the same accelerator of which scanning data was presented in Fig. 5. The left plot show a single-shot trace with a ZnTe crystal, while the right plots are based on EOS in a GaP crystal. The red curve for the right plots was based on modeled THz radiation from a 45 fs (rms) electron bunch. Note that the GaP crystal does not have a cut-off around $\nu = 4$ THz like ZnTe, but can resolve

the full THz spectrum up to $\nu = 8$ THz. The measured profile for $\Gamma(t)$ is in reality of convolution of the actual $\Gamma(t)$ with the laser pulse envelope of the second short laser probe $I_{\mathrm{env},2}$, and has to be taken into account. This technique seems to deliver all the necessary information in a single-shot. One can study shot-to-shot fluctuation in charge profile, or in timing jitter. Disadvantages of this technique are its complexity, resulting from a geometry based on 3 beams and 2 nonlinear crystals. Also, the power balance of the two laser beams is critical in order to obtain a clean frequency-doubled image but without damaging the EO crystal.

ELECTRO-OPTIC SAMPLING IN THE LASER'S FREQUENCY DOMAIN

Another set of techniques relies on measuring the spectrum of the THz-modulated chirped laser beam. Both the THz and laser beam are focused on the EO crystal. In these geometries an ultra-short laser is chirped to a pulse length much longer than the THz pulse. The expression for the electric field of the incident laser profile is given by

$$E_{L,j}(t) = \vec{e_j} \exp(\imath\phi_{0,j}) \exp\left[\frac{(1-\imath b/2)t^2}{2\tau_{\mathrm{FL}}^2(1+b^2/4)}\right] \exp[\imath\omega_0 t], \tag{12}$$

with b the chirp parameter and τ_{FL} the rms Fourier limited pulse duration. The actual rms pulse duration is $\tau_L = \tau_{\mathrm{FL}}\sqrt{(1+b^2/4)}$. Note that the instanteneous frequency $\omega_{\mathrm{inst}}(t)$ of the chirped laser pulse is given by

$$\omega_{\mathrm{inst}}(t) = \omega_0 + \frac{b}{2\tau_{\mathrm{FL}}^2(1+b^2/4)}t. \tag{13}$$

Just as mentioned earlier, after propagation through the EO crystal, an extra phase shift is introduced, leading to a modulated laser pulse $E_{M,j}(t) = E_{L,j}(t) \cdot \exp[\imath\Gamma_j(t)]$. Although the information on the THz profile could potentially be retrieved by measuring the power spectrum $|E_{M,j}(\lambda)|^2$ of the phase-modulated laser probe, the techniques described in this paper rely again on the conversion of the phase modulation to an amplitude modulation. Just as in last section, this can be done by using the polarization geometry of Fig. 4, and using a polarizer. This results in a time dependent intensity oscillation on the chirped laser pulse, as sketched on the right part of Fig. 11.

Spectral encoding for ps-type THz pulses

The simplest technique based on THz-pulse retrieval from the laser spectrum is only applicable for THz frequencies ν for which $\sqrt{\tau_{\mathrm{FL}}\tau_L} < 1/\nu$. For example, an electron bunch of length 400 fs (rms) contains THz frequencies up to 0.5 THz (spectral half-max at ν =0.46 THz). By using a laser pulse of τ_L =3.5 ps duration, from a Fourier limited pulse length of $\tau_{\mathrm{FL}} = 50$ fs, one can see that this requirement is met (indeed 418 fs $<$ 2 ps). This example is shown in Fig. 11. The THz pulse is plotted in the top left graph. The orange curve in the inset of the bottom left

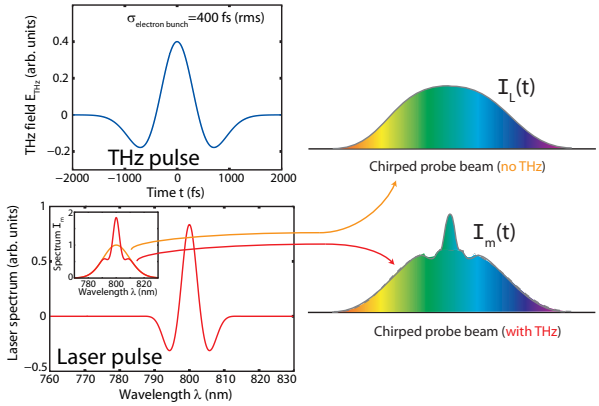

Figure 11: The right images show the intensity modulation of a THz pulse on the envelope of a chirped long laser pulse. The THz pulse itself is plotted on the top left plot, based on a electron bunch of 400 fs (rms) length. The spectrum of the modulated laser pulse $I_M(\lambda)$ is shown in the bottom left graph. Through a conversion of parameters $\lambda \rightarrow t^*$ (based on a linear chirp rate), it can be shown that the normalized spectral modulation is identical to the original THz pulse.

graph shows that laser spectrum without THz modulation, while the red curve is plotted with EO modulation considered. The normalized difference between both curves $[I_M(\lambda) - I_L(\lambda)]/I_L(\lambda)$ is also shown in the main figure on the bottom left.

It was shown by several groups [23, 24] that the modulated spectrum can be converted back to the time domain based on the conversion $\lambda \rightarrow t^*$, with $\lambda = 2\pi\omega_{\mathrm{inst}}/c$ based on Eq. (13). This conversion leads to the measurement of $I_M(\lambda) \rightarrow I_M(t^*)$. Since we know the relation of $I_M(t^*)$ to $\Gamma(t^*)$ through Eq. (8) we have reconstructed a complete sign-resolved THz profile. Indeed, the red curve in Fig. 11 is identical to the original THz profile after the conversion $\lambda \rightarrow t^*$ based on Eq. (13).

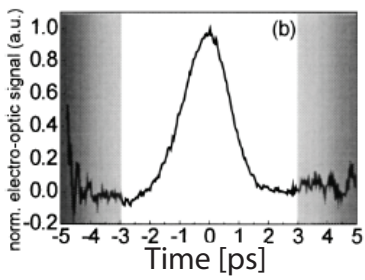

Figure 12: Data from Wilke *et al.* [25] based on the single-shot measurement of the spectrum of a THz-modulated laser pulse ($\tau_{\mathrm{FL}} = 30$ fs and $\tau_L = 4.5$ ps). The wavelength axis has been converted to a time axis based on Eq. (13). The electron bunch was found to have a length of 1.7 ps (FWHM).

An example of this technique is plotted in Fig. 12. The

data, published by Wilke *et al.* [25] was taken on the electric field of the electron bunch directly. The parameters for the laser were $\tau_{\rm FL} = 30$ fs, $\tau_L = 4.5$ ps, and the retrieved bunch length had a duration of 1.7 ps. The wavelength axis of the plot in Fig. 12 has already been converted to a time axis through the $\lambda \rightarrow t^*$ conversion based on Eq. (13).

Although the time resolution for the spectral encoding technique is limited to several hundreds of femtoseconds, this technique is otherwise quite advantageous. It relies on only one low-power laser pulse and only one nonlinear crystal (the EO crystal), and the alignment onto the spectrometer is fairly straightforward. The full THz field profile (amplitude and phase) is reconstructed in a single shot through a simple parameter conversion $\lambda \rightarrow t^*$. A calibration can be easily applied by adding a know temporal delay between the THz and laser pulse and observing the spectral shift.

Spectral encoding for fs-type THz pulses

Unfortunately, the previous analysis breaks down if THz frequencies are present in the THz pulse for which $\sqrt{\tau_{\rm FL}\tau_L} < 1/\nu$ is no longer valid. This is the case for electron bunches shorter than 500 fs. An example of the breakdown is shown in Fig. 13, where an electron bunch of 50 fs (rms) is plotted as the solid curve in the left plot. The top right image in the right plot again shows a sketch of the time-dependent intensity modulation, while the inset on the left of the same figure shows the modulated laser spectrum (red curve) versus the original laser spectrum (orange curve). The normalized difference between both curves $[I_M(\lambda) - I_L(\lambda)]/I_L(\lambda)$ is shown in the main plot of the right figure. As one can see, upon conversion of wavelength to time, the retrieved profile $I_M(t^*)$ does not resemble the original THz profile at all, mainly due to the presence of spectral oscillations.

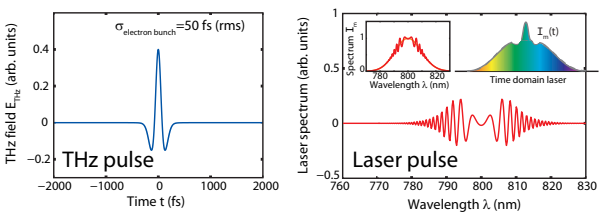

Figure 13: The left plots shows the THz profile of a 50 fs (rms) electron bunch. The spectrum $I_M(\lambda)$ of the THz-modulated laser pulse is plotted on the right. Due to the short bunch duration, the spectrum shows heavy modulation. Upon conversion of $\lambda \rightarrow t^*$, the retrieved profile $I_M(t)$ does not resemble the original THz profile.

It was shown theoretically by Yellampalle et al. [26], and demonstrated experimentally on laser-produced THz pulses by Kim et al. [27], that an algorithm can by applied on the heavy modulated spectral interferogram in order to retrieve the original THz pulse. The algorithm is based on detailed knowledge of the chirped laser beam (chirp parameter, Fourier-limited pulse length, and pulse shape). It has to be pointed out that the algorithm is ill-posed and highly susceptible to noise, as was stated by Kim et al. in a comment in a later paper [18].

Spectral encoding for fs-type THz pulses: spectral envelope information

An extension of the previously-mentioned spectral encoding technique into the high-temporal-resolution domain (no algorithms) does exist [28], and will be discussed now. Although the phase information of the THz pulse is lost, its spectral envelope is retrieved in a single shot with a spectral dynamic range only limited by the inverse Fourier-limited laser pulse length $1/\tau_{\rm FL}$. It is the spectral envelope that provides an indication of the bunch duration, therefore a useful and critical parameter to measure.

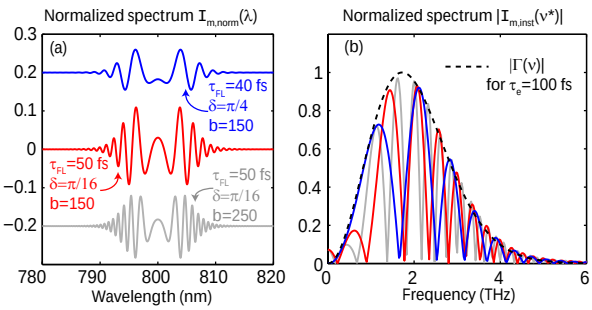

Figure 14: (a) Modeled spectral interferograms $I_{\rm m,norm}(\lambda)$ for various parameters for $\tau_{\rm FL}$, δ, and b. Through the wavelength-to-time parameter substitution $\lambda \rightarrow t^*$ in $I_{\rm m,norm}(\lambda)$ the function $I_{\rm m,inst}(t^*)$ is obtained, with its Fourier transformation $|I_{\rm m,inst}(\nu^*)|$ plotted in (b). The envelopes of the three solid curves in (b) match the original THz spectrum $|\Gamma(\nu)|$ (black dashed curve).

Modeled spectral interferograms are depicted in Fig. 14(a). For these curves the profile $\Gamma(t)$ was modeled based 100 fs (rms) Gaussian electron bunches [for simplification crystal effects are momentarily ignored ($T_{\rm crystal} = 1$)]. The amplitude of $\Gamma(t)$ was set at 0.1 rad. The blue curves in Fig. 14 correspond to various parameters for Fourier limited pulse duration, laser polarization, and the chirp parameter $(\tau_{\rm FL}, \delta, b) = (40\ {\rm fs}, \pi/4, 150)$, the red ones to $(50\ {\rm fs}, \pi/16, 150)$, and the gray ones to $(50\ {\rm fs}, \pi/16, 250)$.

Through Eq. (13) one can convert the wavelength parameter ($\lambda = 2\pi c/\omega_{\rm inst}$) to the time axis t^*. Doing so for $I_{\rm m,norm}(\lambda)$, defined as $[I_M(\lambda) - I_L(\lambda)]/I_L(\lambda)$, the new profile is labeled as $I_{\rm m,inst}(t^*)$. A Fourier transformation of $I_{\rm m,inst}(t^*)$ yields $|I_{\rm m,inst}(\nu^*)|$. The absolute spectra $|I_{\rm m,inst}(\nu^*)|$ for the three curves of Fig. 14(a) are plotted in Fig. 14(b). Also plotted in Fig. 14(b) as the black dashed curve is the THz spectrum $|\Gamma(\nu)|$. One can see that the envelopes of the oscillatory curves $|I_{\rm m,inst}(\nu^*)|$ match the THz spectrum $|\Gamma(\nu)|$. It is because of this matching that

analysis of the spectral interferogram results in single-shot information of the THz spectrum. This new result has been extensively studied and is found to be true for a wide parameter range for b, the amplitude of $\Gamma(t)$, τ_L, $\tau_{\rm FL}$, and τ_e, providing that $\tau_e > \tau_{\rm FL}$ and that $\Gamma(t)$ does not exceed $\simeq 0.3$ rad.

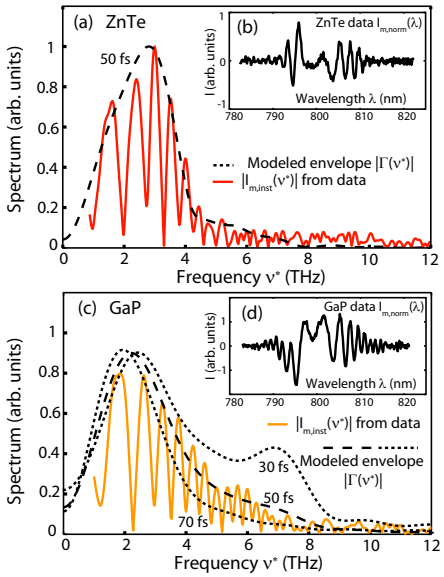

Figure 15: Data from van Tilborg *et al.* [28]. Experimentally obtained modulated laser spectra $I_M(\lambda)$, are normalized [yielding $I_{\rm m,norm}(\lambda)$] and plotted in (b) and (d). After the coordinate substitution $\lambda \rightarrow t^*$ [yielding $I_{\rm m,inst}(t^*)$], the Fourier-transformed curves $|I_{\rm m,inst}(\nu^*)|$ are plotted in (a) and (c). Also displayed in (a) and (c) as the black dashed curves are the THz spectra $|\Gamma(\nu)|$, based on coherent emission from a 50 fs (rms) electron bunch. Modeled curves for a 30 fs and a 70 fs bunch are also shown in (c) to highlight the optimum fit for a 50 fs bunch.

In order to experimentally verify the modeled predictions, we applied the setup to the THz pulses from the LWFA. Each modulated laser spectrum was recorded with a 512x512-pixel 16-bit camera with a resolution of 0.11 nm/pixel. Two typical measured normalized spectral interferograms $I_{\rm m,norm}(\lambda)$ are plotted in Figs. 15(b) and (d), based on a 200-μm-thick ZnTe and GaP EO crystal respectively. The parameters for the probe laser were independently measured with an autocorrelerator and FROG and were found to be $\tau_{\rm FL}$=40 fs (rms) and b=150. After the conversion $I_{\rm norm}(\lambda) \rightarrow I_{\rm inst}(t^*)$, the Fourier-transformed curves $|I_{\rm m,inst}(\nu^*)|$ are displayed in Figs. 15(a) and (c). Also depicted in Figs. 15(a) and (c) as black dashed curves is the spectrum of the THz pulse $|\Gamma(\nu)| = |E_{\rm THz}(\nu)T_{\rm crystal}(\nu)|$. Here the crystal effects [15] were not ignored. Note that the spectral cutoff [as can been seen in the data in Fig. 15(a)] for the ZnTe crystal is ν =4.1 THz. The function $T_{\rm crystal}(\nu)$ for GaP has a cutoff at a higher frequency (ν =8 THz). The black dashed curves in Figs. 15(a) and (c) for $|\Gamma(\nu)|$ are in good agreement with the data [the envelope of $|I_{\rm m,inst}(\nu^*)|$]. The fit was optimized by only varying τ_e to 50 fs (rms).

SUMMARY

In summary, several electro-optic techniques have been presented. In all techniques, the electric field profile of the electron bunch (or the field profile of its coherent emission) is imprinted onto a laser pulse after propagation through an electro-optic crystal. While a scanning technique is most sensitive to weaker THz fields, it intrinsically relies on shot-to-shot reproducibility. Techniques based on non-collinear cross-correlation do provide single-shot information, but the complexity of the systems increases. By analyzing the laser pulse in the frequency domain (through measurement of the laser spectrum) the complexity is reduced. However, the THz pulse information is not directly available, and post-processing of the data is required. Also, either the time resolution, or the phase information is compromised.

Application of EOS to a given accelerator depends on the specific goals and constraint available. Parameters such as the required time resolution, the available laser energy, the demands for online bunch length monitoring, among others, will determine which technique works best.

For now, EOS seems the ideal technique for characterization of sub-picoseconds bunches with single-shot capabilities. Several laboratories worldwide have implemented EOS on their accelerator, and this number will grow as the number of accelerators producing femtosecond bunches steadily increases. Eventually, even the time resolution of EOS (several tens of femtoseconds) will not be sufficient, and a new family of techniques will need to be developed.

This work was supported by the U.S. Department of Energy and the Defense Advanced Research Projects Agency (DARPA).

REFERENCES

[1] P. Catravas, W. P. Leemans, J. S. Wurtele, M. S. Zolotorev, M. Babzien, I. Ben-Zvi, Z. Segalov, X.-J. Wang, and V. Yakimenko, Phys. Rev. Lett. **82**, 5261 (1999).

[2] P. Catravas, E. Esarey, and W. P. Leemans, Phys. of Plasmas **9**, 2428 (2002).

[3] T. Watanabe, J. Sugahara, T. Yoshimatsu, S. Sasaki, Y. Sugiyama, K. Ishi, Y. Shibata, Y. Kondo, K. Yoshii, T. Ueda, and M. Uesaka, Nucl. Instrm. Methods Phys. Res. A **480**, 315 (2002).

[4] C. B. Schroeder, E. Esarey, J. van Tilborg, and W. P. Leemans, Phys. Rev. E **69**, 016501 (2004).

[5] Y. Shibata, T. Takahashi, T. Kanai, K. Ishi, M. Ikezawa, J. Ohkuma, S. Okuda, and T. Okada, Phys. Rev. E **50**, 1479 (1994).

[6] P. Kung, H. Lihn, H. Wiedemann, and D. Bocek, Phys. Rev. Lett. **73**, 967 (1994).

[7] B. Leissner, Ch. Berger, R. Siedling, M. Tonutti, M. Geitz, G. Schmidt, and P. Schmüser, Proceedings of the 1999 Particle Accelerator Conference, IEEE. Part vol. 3, 2172 (1999)

[8] G. Gallot and D. Grischkowsky, J. Opt. Soc. Am. B **16**, 1204 (1999).

[9] S. P. Jamison, A. M. MacLeod, G. Berden, D. A. Jaroszynski, and W. A. Gillespie, Opt. Lett. **31**, 1753 (2006).

[10] D. X. Wang, G. A. Krafft, and C. K. Sinclair, Phys. Rev. E **57**, 2283 (1998).

[11] G. Berden, W. A. Gillespie, S. P. Jamison, E.-A. Knabbe, A. M. MacLeod, A. F. G. van der Meer, P. J. Phillips, H. Schlarb, B. Schmidt, P. Schmüser, and B. Steffen, Phys. Rev. Lett. **99**, 164801 (2007).

[12] S. Banerjee, S. Sepke, R. Shah, A. Valenzuela, A. Maksimchuk, and D. Umstadter, Phys. Rev. Lett. **95**, 035004 (2005).

[13] J. van Tilborg, C. B. Schroeder, Cs. Tóth, C. G. R. Geddes, E. Esarey, and W. P. Leemans, Opt. Lett. **32**, 313 (2007).

[14] Q. Chen, M. Tani, Zhiping Jiang, and X.-C. Zhang, J. Opt. Soc. Am. B **18**, 823 (2001).

[15] J. van Tilborg, C. B. Schroeder, C. V. Filip, Cs. Tóth, C. G. R. Geddes, G. Fubiani, E. Esarey, and W. P. Leemans, Phys. Plasmas **13**, 056704 (2006).

[16] F. L. Pedrotti and L. S. Pedrotti, "Introduction to optics", Prentice Hall International Edition, 1993.

[17] J. van Tilborg, C. B. Schroeder, C. V. Filip, Cs. Tóth, C. G. R. Geddes, G. Fubiani, R. Huber, R. A. Kaindl, E. Esarey, and W. P. Leemans, Phys. Rev. Lett. **96**, 014801 (2006).

[18] K. Y. Kim, B. Yellampalle, A. J. Taylor, G. Rodriguez, and J. H. Glownia, Opt. Lett. **32**, 1968 (2007).

[19] J. Shan, A. S. Weling, E. Knoesel, L. Bartels, M. Bonn, A. Nahata, G. A. Reider, and T. F. Heinz, Opt. Lett. **25**, 426 (2000).

[20] A. L. Cavalieri, D. M. Fritz, S. H. Lee, P. J. Bucksbaum, D. A. Reis *et al.*, Phys. Rev. Lett. **94**, 114801 (2005).

[21] S. P. Jamison, J. Shen, A. M. MacLeod, W. A. Gillespie and D. A. Jaroszynski, Opt. Lett. **28**, 1710 (2003).

[22] G. Berden, S. P. Jamison, A. M. MacLeod, W. A. Gillespie, B. Redlich, and A. F. G. van der Meer, Phys. Rev. Lett. **93**, 114802 (2004).

[23] F. G. Sun, Zhiping Jiang, and X.-C. Zhang, Appl. Phys. Lett. **73**, 2233 (1998).

[24] Zhiping Jiang and X.-C. Zhang, Appl. Phys. Lett. **72**, 1945 (1998).

[25] I. Wilke, A. M. MacLeod, W. A. Gillespie, G. Berden, G. M. H. Knippels, and A. F. G. van der Meer, Phys. Rev. Lett. **88**, 124801 (2002).

[26] B. Yellampalle, K. Y. Kim, G. Rodriguez, J. H. Glownia, and A. J. Taylor, Appl. Phys. Lett. **87**, 211109 (2005).

[27] K. Y. Kim, B. Yellampalle, G. Rodriguez, R. D. Averitt, A. J. Taylor, and J. H. Glownia, Appl. Phys. Lett. **88**, 041123 (2006).

[28] J. van Tilborg, Cs. Tóth, N. H. Matlis, G. R. Plateau, and W. P. Leemans, Opt. Lett. **33**, in press (2008).

RADIATION DAMAGE IN DETECTORS AND ELECTRONICS

Ronald Lipton, Fermilab, Batavia, IL 60510, U.S.A.

Abstract

Coping with radiation-related effects is a constant challenge to the detectors and electronics deployed at high intensity and luminosity accelerators. Work associated with the LHC R&D collaborations has extended the range of understanding of these effects to unprecedented integrated dose levels. At the same time the availability of deep submicron technology and a variety of process variations available in IC production have redefined the tools available to build electronics to accommodate irradiation. This paper will briefly review our current understanding of the mechanisms of radiation damage and techniques to extend the lifetimes of detectors and electronics.

RADIATION EFFECTS IN SILICON AND SIO_2

I will concentrate here on the standard electronic materials – silicon and its oxide. We can divide the world of radiation damage into electromagnetic and bulk damage components. Ionizing radiation, such as x-rays, gammas, and electrons, create free charge in materials, which affects properties and performance. Hadrons (neutrons, pions, protons) can also produce "bulk" damage – damage to the silicon crystal lattice by displacing atoms from their usual sites. Electronics, because of the thin sensitive layer, tend to be most sensitive to ionization and the associated accumulation of charge in the material. Detectors are sensitive to both, with the most important damage often coming from bulk effects.

BULK DAMAGE – EFFECTS ON DETECTORS

Particle Physics detectors are unusual structures in the microelectronics world. They are fabricated with lightly doped, float zone, silicon, they use rather thick structures to collect a large signal, and they have a regular array of electrodes.

Displacement Damage in Silicon

Hadrons can interact and cause significant damage to the silicon crystal lattice. The amount and type of damage depends on the particle type and energy. The damage is usually quantified by the amount of Non-Ionizing Energy Loss (NIEL – KeV cm^2/g) or displacement damage (MeV-mb). For convenience damage is usually scaled to the NIEL of 1 MeV neutrons. However the pattern of energy loss depends on the type of particle and the pattern of damage clusters left by the particle.

Atoms scattered by inceident hadrons leave both vacated lattice sites (vacancies) and "free" atoms (interstitials) known as Frenkel pairs. The pattern of energy deposit is important – low energy transfers will leave sparse "point defects." Higher energy transfers can leave clusters of defects. Frenkel pairs in these clusters have a higher probability for recombination. The defects can have energies inside the bandgap, and act as additional donors or acceptors with energy levels different than the usual dopants. They can also act as generation centers for leakage currents. Other defects can act as traps for charge carriers and affect the charge collection efficiency of detectors. Vacancies and interstitials can also interact with the impurities in the silicon, and either be activated or passivated. Finally, they can recombine to anneal away some of the initial bulk damage.

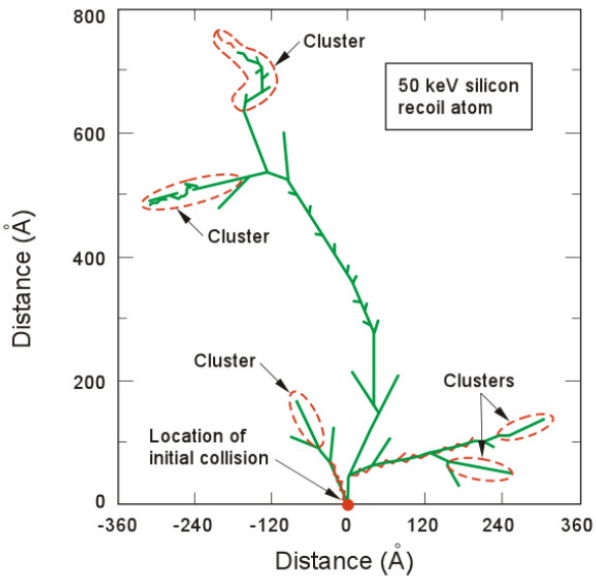

Figure 1. Simulation of damage caused by a 50 KeV silicon recoil nucleus [1].

The simplest effect, caused most efficiently by midgap states, is an increase in overall leakage current. This is a almost universal effect, and does not seem to depend on the details of doping, impurities, or processing. It is parameterized by:

$$I_{\det} = I_0 + \alpha \times flux \times Vol \qquad (1)$$
$$\alpha = 2 - 3 \times 10^{17} A/cm^2$$

There is a strong annealing effect in leakage current (Figure 2). The overall annealing time has several

components [3] but is independent of sensor doping or impurity concentration.

Charge traps are also generated by non-ionizing radiation. This effectively lowers the mean free path of the generated electrons and holes, resulting in a loss of signal charge as the integrated dose increases. A dose of 2.5×10^{14} cm^{-2} charged hadrons reduces the total charge collected by 20% in 280 micron-thick test diodes [2].

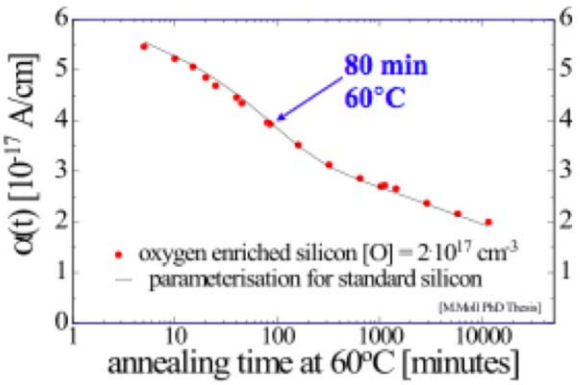

Figure 2. Damage constant as a function of annealing time at 60 deg C for standard (solid line) and oxygen enriched silicon [3].

The most significant effect for the lifetimes of LHC and Tevatron detectors is due to detector becoming more p-type as they are irradiated, due both to donor removal and acceptor creation. This is a complex process, which has been extensively studied by RD50. The most striking aspect is the "reverse annealing" that occurs when the detectors are exposed to temperatures above ~0 deg C. Defect complexes are generated by radiation which are not active at temperatures below ~-10. However, if the detectors are exposed to higher temperatures, these latent defect centers can be activated and contribute additional acceptors. The process has been characterized by [3]:

$$N_{eff}(\Phi) = N_{d0}e^{-c\Phi} + g_c\Phi + g_s\Phi e^{-t/\tau(t)} + N_Y(\Phi,t,T)$$

where the first term describes removal of donors, the second creation of acceptors, the third term describes "beneficial" annealing, and the fourth so-called "reverse" annealing. The reverse annealing term forces detectors exposed to high radiation doses to be kept cold to keep the effective p-type doping concentration low and maintain reasonable operating voltages. The parameterization is described in detail in reference [3]. Phi is the 1 MeV neutron equivalent flux. Silicon with a higher concentration of oxygen has been found to be less susceptible to reverse annealing for pion but not neutron exposure.

Detectors can be engineered to be more radiation hard by:

- Operating single-sided devices to eliminate capacitors, which need to stand off the bias potential, which increases as the devices become more p-type.
- Using oxygenated detectors.
- Design of implants and metallization to reduce internal fields and increase breakdown voltage.
- Utilizing thinned detectors, since depletion voltage is proportional to thickness squared. A subset of this technology comprises the "3D" sensors, which use deep holes etched into the silicon to reduce the effective distance between electrodes while keeping charge collection of a full thickness detector [4].

The most operating experience for heavily irradiated silicon detectors comes from the Tevatron, which has had large detector assemblies operating since 2002. Figure 3 shows the status of the operating voltage of the D0 silicon tracker as of May 2008.

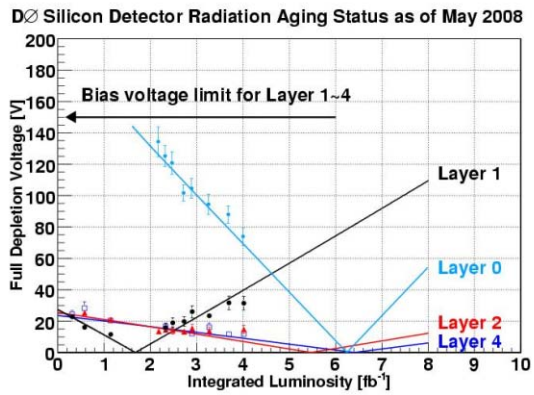

Figure 3. Depletion voltage as a function of integrated luminosity for several layers of the D0 silicon detector. Layer 0 is at ~1.6 cm, layer 1 at 2.5 cm and layer 4 at 9.6 cm. Points were measured during special runs where charge collection was measured as a function of bias voltage. Lines are fits to the model described in the text.

IONIZATION DAMAGE – EFFECTS ON ELECTRONICS

Although electronics are also affected by bulk damage to their crystal structure, modern electronics typically depend on highly doped structures near the surface of the silicon. This means that transistors, particularly CMOS, are sensitive to fields generated by charges induced in the silicon and SiO_2 structures by ionizing radiation.

Bipolar Transistors

Bipolar transistors depend on minority carrier diffusion from the emitter to the collector through a thin base. In this case the primary effect is bulk damage to the crystal structure. Traps are generated by displacement damage to the crystal structure. These can trap the charge diffusing from the emitter to the collector, effectively reducing the

transistor gain. The gain reduction depends on device geometry, type, switching frequency, temperature and current. For example, high currents through the base can saturate traps and increase the gain of irradiated bipolar transistors operating at high current [5].

CMOS

Modern high density electronics is based on the interaction of silicon and its oxide. The fact that precisely controlled thin SiO_2 insulating layers can be grown or deposited allows for fabrication of well-understood devices with extremely small feature size and excellent reliability. Radiation can affect the characteristics of the oxide, especially at the silicon-oxide interface, where there can be a high density of trapping states [6].

Figure 4 shows a typical MOS transistor with the current in an n or p channel controlled by a metal or polysilicon gate above a thin insulating silicon oxide layer. Ionizing radiation creates electron-hole pairs in the oxide. The electrons are relatively mobile and are collected by either the gate or channel fairly rapidly. Holes typically move more slowly, hopping from site to site until they reach the silicon-oxide interface. Here many of the holes are trapped by defects near the Si-SiO_2 interface. These trapped holes (Figure 5) generate a fixed positive charge, which can affect the characteristics of the transistor, generating shifts in the operating threshold of the device.

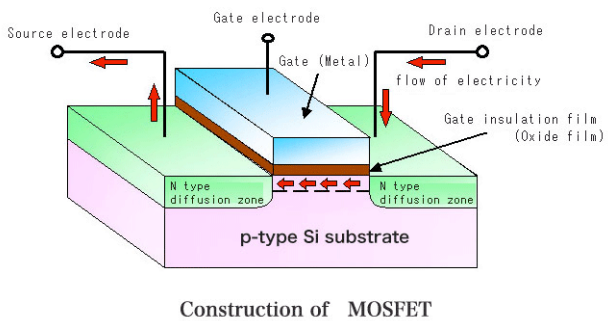

Figure 4. Schematic of a MOS transistor.

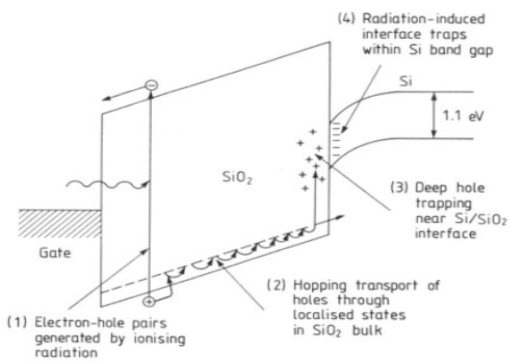

Figure 5. Energy band schematic of the motion of electrons and holes produced in a silicon gate oxide.

PMOS and NMOS have different damage characteristics, since holes in pmos are attracted to the gate rather than the channel. The art of radiation-hard design in the past primarily involved fabrication of high quality oxides, which low densities of interface states. Defects could also be passivated by additional dopants or treatment in a hydrogen-rich atmosphere [8].

Gate oxides used in modern deep submicron electronics are much thinner than the ~100 nm oxide layers used in the early 90's micron-scale feature size semiconductors. Typical oxides are now less than 10 nm thick. At that thickness electrons can tunnel through the potential barrier at the silicon-oxide interface and neutralize the trapped holes. These transistors are "naturally" radiation hard, because there is no longer a fixed gate oxide charge to generate transistor threshold shifts (Figure 6).

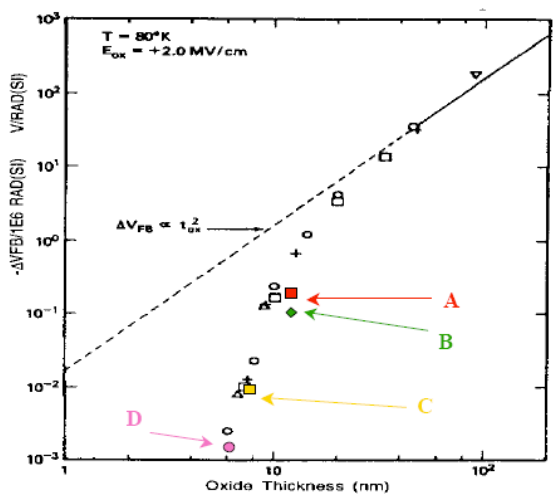

After N.S. Sacks, M.G. Ancona, and J.A. Modolo, IEEE Trans.Nucl.Sci., Vol.NS-31 (1984) 1249

Figure 6. Flatband voltage shift per megarad as a function of gate oxide thickness as predicted by Sacks et. al. [8].

However, the thin gate oxide is usually surrounded by a thicker field oxide. This field oxide will still trap charge and can provide a path for leakage current to flow from the source to the drain of the transistor. This effect can be avoided by altering the geometry of the transistor to a ringlike structure surrounded by a guard ring that does not provide a leakage path via the field oxide. This is usually called radiation hardness "by design" and is the basis for deep submicron electronics fabricated for readout of LHC detectors.

Single Event Effects

In addition to effects related to the total dose, local ionization caused by single particles can also affect electronics [9]. Charge deposition is usually characterized by the Linear Energy Transfer (LET), the energy loss per unit length of the ionizing radiation typically expressed in units of MeV·cm^2/mg of material.

Single event effects are characterized as:

- Single event upset (SEU). The change of state of a transistor due to radiation. This is usually reversible.
- Single event latchup (SEL). Latched change of state of a circuit due to radiation. May need to power cycle to reset.
- Single event burnout (SEB). Destruction of a circuit element due to radiation.

Modern three-dimensional device simulation programs allow designers to simulate the effects of ion impact on individual transistors (Figure 7).

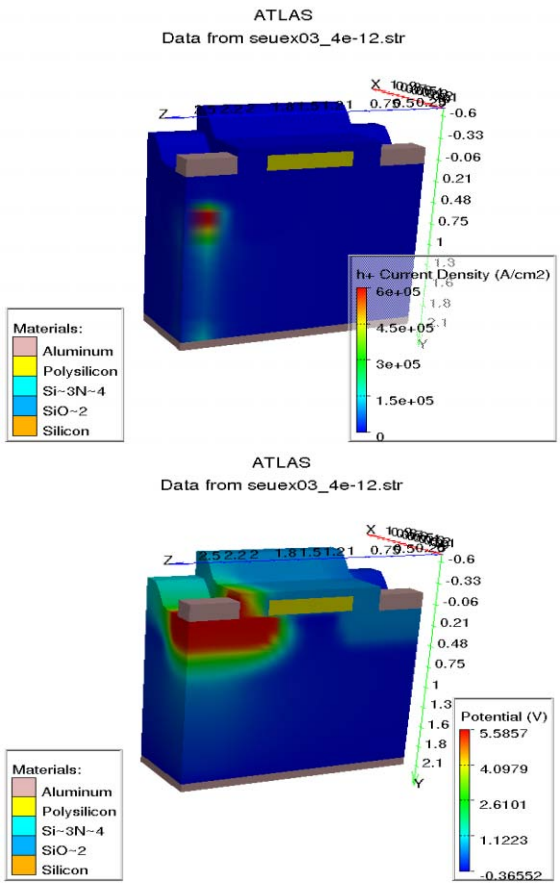

Figure 7. Simulation of the hole current density (top) and potential distribution (bottom) resulting from an ion impact on a typical MOS transistor structrure.

As transistor feature size goes down, less charge is needed to cause this state change, and single event effects become increasingly worrisome. Dynamic memory, which relies on the charge stored on a MOS capacitor is especially sensitive to SEU.

In CMOS, parasitic transistors can be formed in the implant/bulk/well regions. This can form a parasitic thyristor, which, if turned on by charge deposited in the bulk, can cause burnup if not current limited. The effects can by limited by:

- Use of thin, high resistivity epitaxial layers, which can limit parasitic currents.
- Trench isolation, which physically separates transistors.
- Silicon-on-Insulator (SOI) technology, which separates the device silicon from the bulk by a thin layer of oxide, reducing the area available for charge deposition.

Silicon-on-insulator is a particularly interesting technology [9]. SOI wafers are typically formed using a wafer bonding technology which can provide a structure with ~20nm thick device silicon on a 200-400 nm "buried" oxide bonded to a thick "handle" wafer. This structure isolates transistor from the bulk and lowers parasitic capacitance, allowing for faster response. However the buried oxide is still sensitive to trapped charge, which can act as a second gate, again affecting transistor characteristics [10, 11].

CONCLUSIONS

Increases in both understanding and technology have increased the range of total dose radiation hardness of silicon-based detectors and electronics by two orders of magnitude in the past two decades. Radiation damage Efforts by groups such as RD48 and RD50 [12-15] have revolutionized the understanding of bulk effects. Mitigation techniques based on detector design and high voltage operation allow for ~5-10 Mrad total dose exposures in the current generation of LHC detectors. New technologies, including thinned detectors, 3D electrodes, and devices with engineered defects promise further increase in the total dose tolerance. New parts must be carefully testing in a radiation environment that simulates the final environment [16].

Basic causes and effects in electronics have been carefully studied. However modern electronics constitute a moving target. The rapid advance of technology, with smaller feature sizes, thinner oxides, and innovative structures continue provide a new set of problems and opportunities.

REFERENCES

[1] A. Vasilescu and G. Lindstroem, Displacement damage in silicon, on-line compilation. http://sesam.desy.de/members/gunnar/Si-dfuncs.html
[2] G. Kramberger et. al, IEEE trans. nucl. sci., 2002, vol. 49(4), p. 1717.
[3] M. Moll, PhD Thesis, www.cern.ch/mmoll/thesis/.
[4] H. Gunther-Moser, Vertex 2007. Proceedings of Science: http://pos.sissa.it//archive/conferences/057/013/Vertex%202007_013.pdf
[5] H. Spieler, http://www-physics.lbl.gov/~spieler/
[6] Messenger, G.C. and Ash, M.S., The Effects of Radiation on Electronic Systems (van Nostrand Reinhold, New York, 1986).
[7] T. R. Oldham et. al., Semicond. Sci. Technol. 4 (1989) 986-999.
[8] N. Saks et al., IEEE Trans. on Nuc. Sci., vol. 33, no. 6, p.1185-90, Dec. 1986.
[9] J.R. Schwank et.al, IEEE Trans. on Nuc. Sci., Vol. 50, No. 3, June 2003P.
[10] Dodd, et. al, IEEE Trans. Nucl. Sci., vol. 51, p. 3278, Dec. 2004.

[10] P. Lestrat, C. Temer, F. Estreme, and L. H. Rosier, "SOI 68T020 heavy ions evaluation," IEEE Trans. Nucl. Sci., vol. 41, no. 6, p. 2240, 1994.
[12] http://rd49.web.cern.ch/RD49/MaterialRadCourse/RadCourseMaterial.htm
[13] lhc-electronics-workshop.web.cern.ch/LHC-electronics-workshop/2002/Links/A66.ppt
[14] R. Rausch, CERN SL 99-004 (CO)
[15] RD50/2004/002 CERN-LHCC-2003-058 and LHCC-RD-002
[16] http://radhome.gsfc.nasa.gov/radhome/papers/RHA98.pdf

.

PERFORMANCE OF FPGA-BASED DATA ACQUISITION FOR THE APS BROADBAND BEAM POSITION MONITOR SYSTEM*

H. Bui, G. Decker, R. Lill, A. Pietryla, W. E. Norum
Argonne National Laboratory, Argonne, IL 60439 USA

Abstract

The Advanced Photon Source (APS) monopulse beam position monitor (BPM) system, designed to measure single- and multi-turn beam positions, is one of three BPM systems currently in use to measure and control both AC and DC orbit motions. Recently, one sector of the monopulse BPM system was upgraded by replacing its 1992-era 12-bit signal conditioning and digitizing unit (SCDU) with a field-programmable gate array (FPGA)-based system for signal processing. The system consists of a repackaging of the broadband rf receiver modules together with a VME Extensions for Instrumentation (VXI) form factor housing eight 14-bit digitizers and one FGPA. The system will be described in detail, including an overview of its new functionality, and performance will be discussed. Of particular interest is the noise floor, which will be contrasted with the previous system and with other systems in use at the APS.

INTRODUCTION

The Advanced Photon Source broadband monopulse BPM system is designed to measure single- and multi-turn beam position used in a feedback system to control both AC and DC orbit motion. Presently, a VXI-based signal conditioning and digitizing unit (SCDU) is used for data acquisition. A monopulse rf receiver, located inside the SCDU, receives 10-MHz band-limited sum and difference signals from an in-tunnel filter-comparator and outputs beam intensity and normalized position [1]. Both signals are digitized via 12-bit analog-to-digital converters (ADCs), operating at the 271-kHz ring revolution frequency, and values are stored in registers. The Memory Scanner module, residing in the same VXI crate, reads the output registers and provides a programmable boxcar average. It also provides a high-speed fiber-optic port to stream data to the feedback system. The system has been in operation for more than ten years. Compared to today's technology, the SCDU is dated, and needs a technology upgrade. The planned upgrade was to remove the monopulse receiver from the SCDU for reuse, and replace the SCDU with an FPGA-based VXI data acquisition and processing module [2]. The new BPM Signal Processor (BSP100) contains eight ADCs, an embedded IOC, and a single Altera Stratix® II FPGA. It can acquire and process data for four monopulse receiver units. This paper describes the new system's functionalities and test results.

*Work supported by U.S. Department of Energy, Office of Science, Office of Basic Energy Sciences, under Contract No. DE-AC02-06CH11357.

SYSTEM OVERVIEW

The new monopulse BPM system (shown in Figure 1) consists of five subcomponents:

- In-tunnel hardware (capacitive button pickups, matching networks, filter comparator, Heliax® cables)
- Receiver chassis
- Power supply chassis
- Fan unit
- BPM signal processor (BSP100)

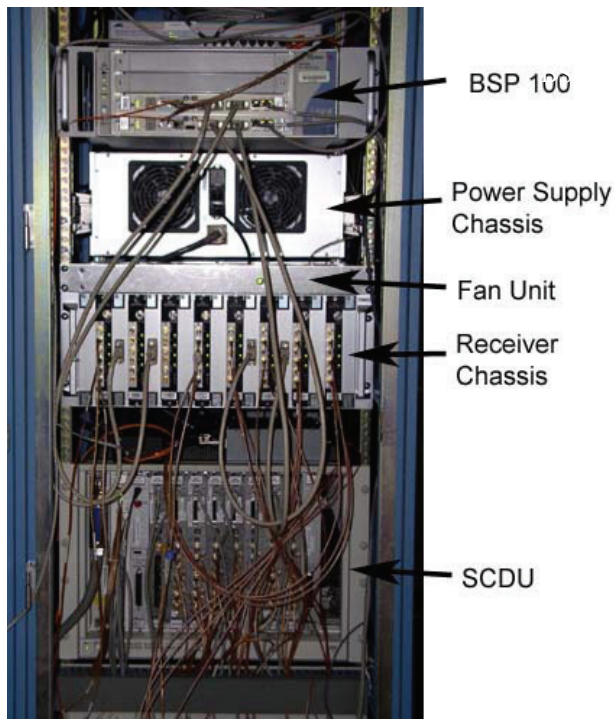

Figure 1: New monopulse BPM system installed at Sector 38.

The in-tunnel portion of the new monopulse BPM system, including capacitive button pickups, matching networks [3], filter comparator, and Heliax® cables, remains unchanged.

The monopulse receiver was removed from the SCDU and packaged together with an interface circuit board, mounted on a custom-designed heat-sink aluminum block, that can be plugged into a receiver chassis. The interface circuit board not only provides regulated power and filtering and I/O signal conditioning to the monopulse receiver, but also is capable of generating a 21-dBm,

351.94-MHz self-test rf signal that can be used to diagnose rf front end in-tunnel hardware.

The receiver and power supply chassis have a standard 4U height by 19" wide form factor and provide electromagnetic interference (EMI) shielding of 50 dBm at the fundamental frequency of 351.94 MHz. Mounted inside the receiver chassis is a custom-built backplane, which provides power and interconnections for up to eight receiver modules to interface with two BSP100 modules.

The power supply chassis consists of four linear power supplies providing all of the required voltages to the receiver chassis via a shielded multi-conductor cable. This chassis was designed such that it can be installed either in front or on the back of the cabinet. This allows the new system to be installed with a minimum amount of disturbance at the location where space might be tight due to other installed equipment.

A variable fan unit mounted above the receiver chassis provides cooling for the receiver modules. The fan speed is controlled by temperature sensors.

The BSP100 is the heart of the new monopulse BPM system. It is a stand alone Experimental Physics and Industrial Control System (EPICS) input/output controller (IOC); an FPGA-based, C-sized VXI form factor, consisting of eight high-speed 14-bit digitizers (Analog Device AD6645) running at 88 MSPS (one fourth of the APS rf frequency); an embedded IOC; and a Stratix® II FPGA. Although the BSP100 is a VXI form factor, the backplane connections are for power only.

The FPGA major functional blocks are:

- An APS timing system receiver
- An acquisition control block
- A preliminary processing block
- A continuous processing block
- A triggered processing block

APS Timing System Receiver Block

The APS timing system receiver block provides timing synchronization of the embedded IOC and generates triggered signals for single-turn acquisition, digital oscilloscope, turn history, and slow beam history used by the triggered-processing block.

Acquisition Control Block

The BPM data acquisition is controlled by setting the appropriate bit in the acquisition control RAM [4]. Configuration control bits are:

- Plane switch bit: selects the monopulse receiver X or Y channel.
- Commutation switch bit: commutates between 0 and 180 degrees on the sum channel for offset compensation.
- Use this sample bit: selects a sample for further processing.
- Save this sample bit: selects sample for use with the oscilloscope mode.
- Self-test gate: controls the monopulse receiver self-test oscillator.
- Wrap marker bit: marks the end of the acquisition RAM contents.
- Turn marker bit: indicates the beginning of a new turn.

The control RAM can be configured to provide sample-by-sample control for 324 samples per turn, for up to 12 storage ring turns. Acquired samples are forwarded to the appropriate blocks for processing.

Preliminary Processing Block

The preliminary processing block (shown in Figure 2) reads the ADC values in the horizontal (x) or vertical (y) planes specified in the control RAM, computes a turn-by-turn average, and sends it to several other blocks for processing. Setting the "Save this sample" bit in the acquisition control RAM allows oscilloscope acquisition of all ADC values for about 12.6 turns, a single sample per turn for 4096 turns, or any combination in between.

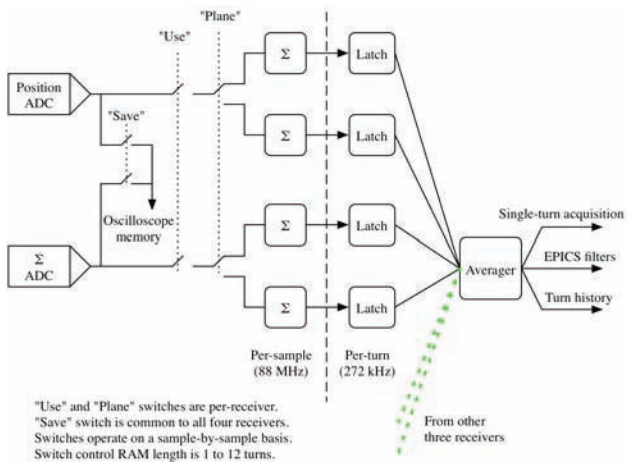

Figure 2: Preliminary Signal Processing.

Continuous Processing Block

The continuous processing block (shown in Figure 3) performs signal processing at a fixed rate. The sum and position signals for each plane are passed through a chain of low-pass decimating filters that result in three sets of process variables (PVs), labeled ms, msAve, and mswAve for historical reasons. The ms and msAve PVs have 10-Hz and 1-Hz signal bandwidth, respectively, and are updated at 10-Hz, whereas mswAve has additional averaging, with signal bandwidth, of 0.1 Hz, updated at 1 Hz. The noise power for sum and position signals for 1-Hz to 200-Hz and 1-Hz to 5-KHz bandwidths is also calculated in this block. Signal noise power is calculated by using the 'root-mean-square' (rms) technique. The averaged turn-by-turn values, from the preliminary processing block, are first bandpass filtered, squared, and then low-pass filtered to simulate the 'mean' operation. Finally the square-root is taken to obtain the rms values.

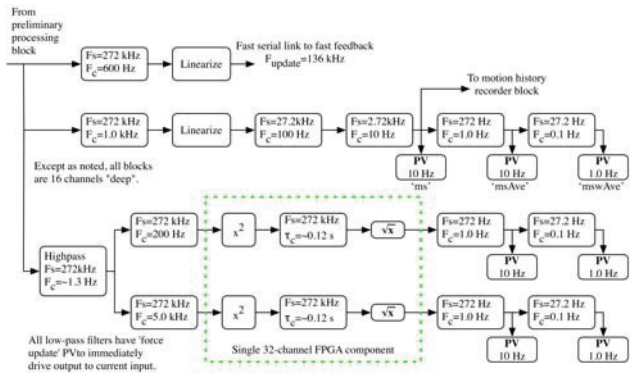

Figure 3: Continuous Signal Processing Block.

Triggered Processing Block

The triggered processing block provides data acquisition used for machine studies and postmortem analysis. Data is acquired and processed on an intermittent basis via a number of waveform recorders. Data acquisition is as follow:

1. An EPICS PV provides a signal to 'arm' the waveform recorder.
2. Upon being armed, it acquires data and stores it in a ring buffer.
3. After the specified number of pre-trigger samples have been acquired, it begins to look for a trigger condition.
4. When a trigger signal is detected, it continues acquiring and storing samples until the specified number of samples is reached, after which the recorder ceases acquisition and interrupts the EPICS IOC.
5. The EPICS generic transient recorder in the IOC reads the samples and makes them available as waveform records.

Oscilloscope Waveform Recorder

The oscilloscope waveform recorder records the raw signals from the ADC at the full sampling rate of 88 MHz. The buffers are 4096 samples deep with an equal number of pre- and post-trigger samples. The trigger signal is the logical OR of three sources; each can be individually inhibited. The sources are:

1. An EPICS PV aligned to the wrap condition from the acquisition control memory
2. An event programmed in the event receiver block
3. An external logic level

Turn-History Waveform Recorder

The turn-history waveform recorder records the turn-by-turn average sum and position values provided by the preliminary processing block at the turn rate of 272 kHz. The buffers are 262,144 samples deep. The trigger signal is the logical OR of four sources, each can be individually inhibited. The sources are:

1. An EPICS PV
2. An external logic
3. An event programmed in the event receiver block
4. A turn-average of a selected sum channel dropping below a specified threshold

The turn history tracks the average of predetermined 88-MHz samples collected during the preceding turn.

Slow Beam History Waveform Recorder

The slow beam history waveforms exist primarily for beam loss postmortem analysis The slow beam history waveforms are acquired and stored in the IOC generic transient recorder. Data samples are taken from the 2.72-kHz filter at a 100-Hz rate. The buffers are 2048 sample deep. The trigger signal is a logical OR of two sources, each of which can be individually inhibited. The sources are:

1. An EPICS PV
2. An event programmed in the event receiver block

Single-Turn Acquisition

The single-turn sum and position averaged values from the preliminary processing block are latched whenever a trigger signal is received. The trigger signal is normally derived from an injection trigger event. This allows information from the first through sixteenth turn to be acquired and will be used for injection optimization studies.

TEST RESULTS

Turn-History Waveform Recorder

Shown in Figures 4 and 5 are portions of the spectrum of horizontal beam motion during normal 24-bunch stored-beam operation. Here an EPICS soft trigger was used to trigger acquisition of a 262,144 (= 2^{18}) sample waveform. With each sample collected every 3.68 microseconds, the record length corresponds to 0.965 seconds. As a result, the FFT of the data has resolution down to 1.04 Hz and up to 135.8 kHz Nyquist, eliminating most aliasing problems.

Figure 4 shows the FFT spectral amplitude up to 5 kHz, while Fig. 5 shows the rms beam motion (square root of the integral of the power spectral density) in microns rms for the same data set.

These data were collected at a BPM location where the horizontal beta function is 3.8 meters. The largest contributions are from sources below 200 Hz, with prominent 60-, 120-, and 360-Hz components. Multiples of 360 Hz are also evident at 1440 and 1800 Hz. The 1.8-kHz line is amplified due to its proximity to the synchrotron tune, which is the broad peak extending from 1.8 to 2.1 kHz. It is likely that the 1.8 kHz is associated with the rf system high voltage power supplies, which induce small amounts of amplitude or phase modulation on the beam.

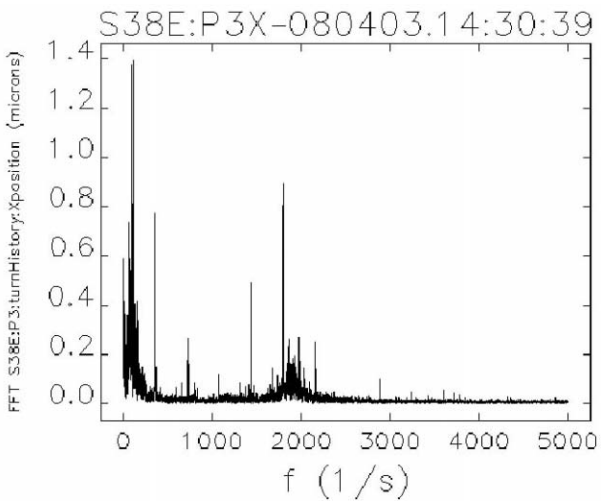

Figure 4: Frequency spectrum of horizontal beam motion during normal 24-bunch operation.

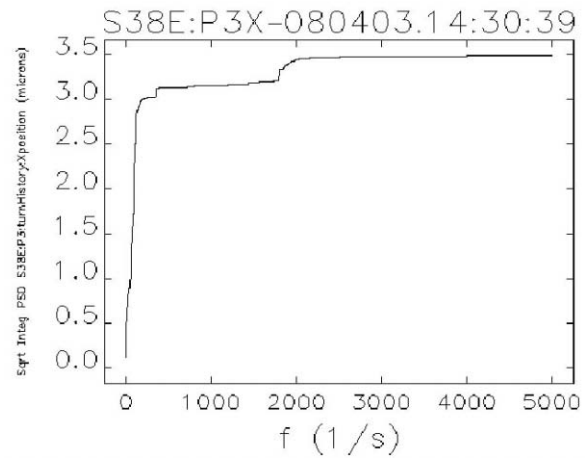

Figure 5: Integrated PSD of horizontal beam motion during normal 24-bunch operation.

An injection transient using the 2-Hz injection trigger derived from the EPICS event system was captured and is shown in Figures 6, 7, and 8 on vastly different time scales. In this case there were 24 bunches stored in the machine: however, the FPGA was configured to provide the average position of only the bunch being injected into. Six 88-MHz samples per turn for this bunch were averaged on a turn-by-turn basis vs. 6 * 24 = 144 samples per turn for Figures 4 and 5. In Fig. 6, data are shown for a full half second before and after the event.

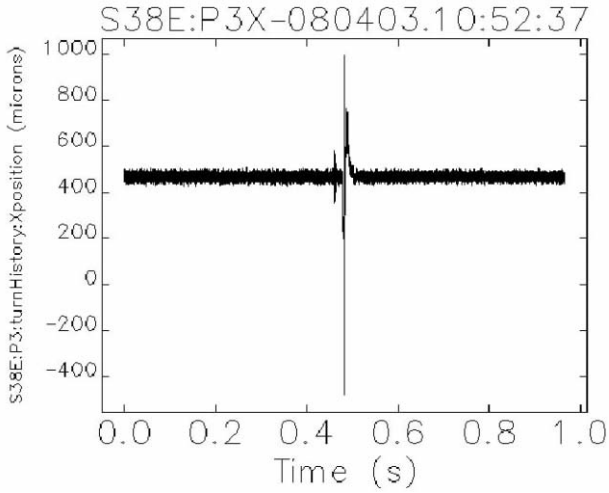

Figure 6: Beam motion during an injection transient captured with the turn history waveform recorder.

Figure 7 shows 80 milliseconds straddling the injection event. The slowest feature, resembling a sine wave starting just before 0.48 seconds, results from leakage fields from the injection thick septum magnet. The sharp spike occurring just after 0.48 seconds and shown in more detail in Fig. 8, is a residual 30-kHz betatron oscillation caused by the fast injection kickers. The small tone bursts near 0.46 seconds are of unknown origin, but also have a strong 30-kHz component and may be associated with the fast kicker power supplies.

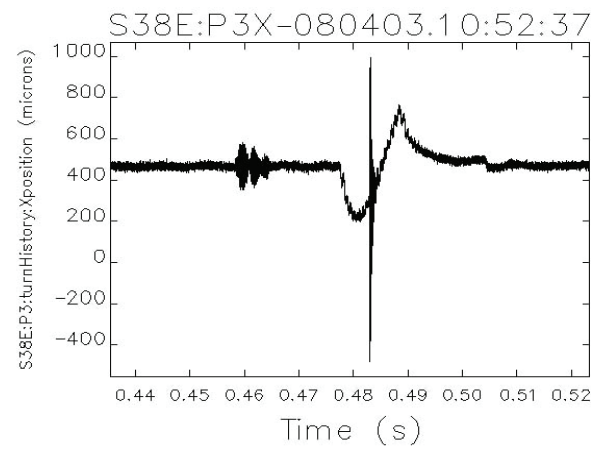

Figure 7: Beam motion during an injection transient (zoomed in).

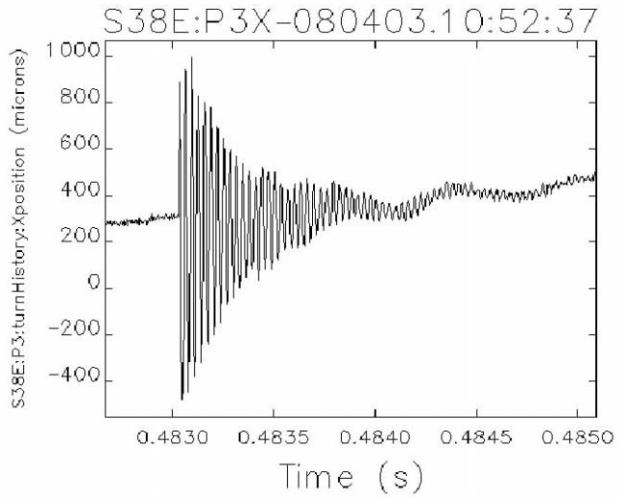

Figure 8: Residual 30k-Hz betatron oscillation.

Slow Beam History Waveform Recorder

Figure 9 shows the same injection transient event captured by using the slow beam history waveform recorder. As before, a 2-Hz injection signal was used to acquire 2048 samples at a 100-Hz sampling rate to obtain a waveform length of 20.48 seconds.

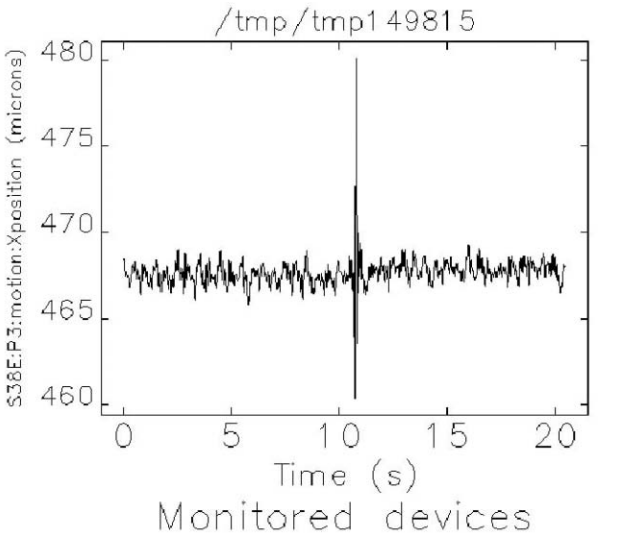

Figure 9: Beam motion during an injection transient captured with the slow beam history waveform recorder.

CONCLUSION

From the above results, one can clearly see the ability of the new monopulse BPM system to observe small beam motions over a large range of time scales. Coupled with the ability to trigger on injection, on beam dump, or on demand, it provides a set of very powerful diagnostics to support machine operation and accelerator physics.

REFERENCES

[1] E. Kahana, “Design of the Beam Position Monitor Electronics for the APS Storage Ring,” Proceedings of the 3rd Accelerator Beam Instrumentation Workshop, AIP Conference Proceedings 252, pp. 235-240 (1992).

[2] R. Lill, A. Pietryla, E. Norum, F. Lenkszus, “APS Storage Ring Monopulse RF BPM Upgrade,” 2004 Beam Instrumentation Workshop, AIP Conference Proceedings 732, pp. 358-265 (2004).

[3] Robert Lill and Glenn Decker, “Advanced Photon Source Monopulse RF Beam Position Monitor Front-End Upgrade,” 1998 Beam Instrumentation Workshop, AIP Conference Proceedings 451, pp. 318-324 (1998).

[4] Eric Norum, private communication.

NEW METHOD TO MONITOR THE TRANSVERSE DISTRIBUTION OF CURRENT IN PARTICLE BEAMS

M. J. Hagmann, NewPath Research L.L.C., P. O. Box 3863, Salt Lake City, UT 84110, U.S.A.

Abstract

A group of sinusoidally-wound coaxial toroidal coils can be used to determine the transverse distribution of a time-dependent current through their common aperture. The current is expressed in a basis of chapeau (pulse) functions over an array of pixels, and matrix methods are used to calculate the current in each pixel from the voltages induced on the coils. Optimum configurations of pixels are used, for which the condition number of the matrix is bounded by the number of pixels. For example, with 50 pixels the fractional errors in the currents are approximately 50 times the fractional errors in the measured voltages in addition to imperfections in the fabrication and placement of the coils. Numerical tests were made by specifying the currents, calculating the induced voltages, adding Gaussian noise to model measurement errors, and then using the algorithms to calculate the currents. These simulations confirm that the condition number is bounded by the number of pixels.

INTRODUCTION

Others have used a variety of different techniques to monitor the transverse distribution of the beam current in accelerators, including secondary emission monitors, wire scanners, multi-wire chambers, gas curtains or jets, residual gas monitors, scintillator screens, scrapers and measurement targets, synchrotron radiation, and Laser-Compton scattering [1], as well as optical transition radiation [2] and the deflection of a probe beam of electrons [3].

A Rogowski Coil is a non-ferrous current probe formed by bending a uniformly wound helical coil to follow a closed curve having arbitrary shape [4-6]. When a time-dependent current passes through the aperture that is enclosed by the bent helix a voltage is induced on the coil which is independent of the location of the current. However, currents that are located outside of the aperture do not induce a voltage on the coil. Deviations from a uniform winding are carefully avoided because they cause the induced voltage to depend on the location of the current within the aperture, but it will be shown that a group of coils having a specific type of nonuniformity may be used to accurately determine the transverse distribution of the current.

ANALYSIS

Figure 1 is a diagram used for deriving expressions for the open-circuit voltage induced on a non-ferrous toroidal coil that may have a nonuniform winding. The toroid has a mean radius R, and the cross-sectional area of the tube of the toroid is A. Consider the induction in an incremental winding of length Rdθ that is centered at (R,θ) or equivalently (X_1,Y_1), which is caused by a filament with current $I = I_{10}e^{j\omega t}$ that intersects the X,Y plane at point $P(X_2,Y_2)$. The dashed line L_1 is directed normal to the increment of winding. Dashed line L_2 is parallel to the magnetic field, and dashed line L_3 is parallel to the X-axis.

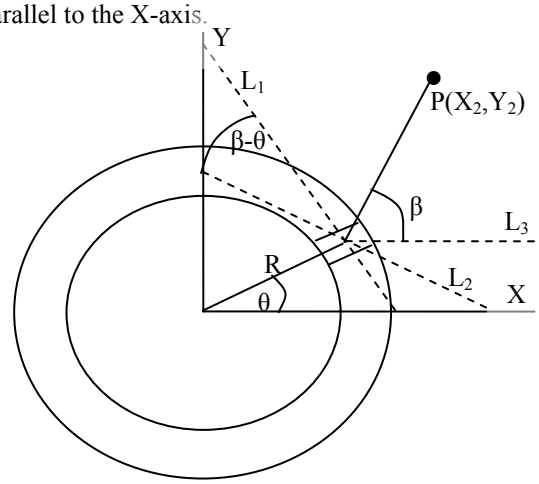

Figure 1: Diagram for analysis.

Let N'(θ) be the number of turns per unit length of the coil, as measured on a circle with radius R. For example, with a toroidal coil having a uniform winding, $N' = N_0' = N_T/2\pi R$, where N_T is the total number of turns. The number of turns in an increment of the winding is $dN = N'(\theta)\, R\, d\theta$. Thus, if the height and width of the tube are much less than R, the open-circuit voltage on the entire winding is given by

$$V_{OC} = -\int_0^{2\pi} \frac{j\omega\mu_0 N'(\theta) RAI \cos(\beta-\theta)\, d\theta}{2\pi\sqrt{(X_2-X_1)^2+(Y_2-Y_1)^2}} \quad (1)$$

Using trigonometry to obtain an expression for $\cos(\beta - \theta)$, Eq. (1) simplifies to give the following:

$$V_{OC} = \frac{j\omega\mu_0 AI}{2\pi}\int_0^{2\pi} \frac{N'(\theta)\left[1-\frac{X_2}{R}\cos\theta-\frac{Y_2}{R}\sin\theta\right]}{\left[\left(\frac{X_2}{R}-\cos\theta\right)^2+\left(\frac{Y_2}{R}-\sin\theta\right)^2\right]} d\theta \quad (2)$$

The expressions for N' are chosen from the following set, which constitutes the basis for a Fourier series:

$$N'(\theta) \in \left\langle N_0', \sum_{J=1}^{\infty} N_{JC}'\cos(J\theta), \sum_{J=1}^{\infty} N_{JS}'\sin(J\theta) \right\rangle \quad (3)$$

where the N_{JC}' and N_{JS}' are coefficients as is N_0'. By substituting the set in Eq. (3) into Eq. (2), and evaluating the integral, the open-circuit voltage that is induced on each coil is given by the corresponding term of the

following set:

$$V_{OC} \in j\omega\mu_0 AI_{10} \left\langle \begin{matrix} N_0', \sum_{J=1}^{\infty} \frac{N_{JC}'}{2}\left(\frac{R_2}{R}\right)^J \cos(J\theta_1), \\ \sum_{J=1}^{\infty} \frac{N_{JS}'}{2}\left(\frac{R_2}{R}\right)^J \sin(J\theta_1) \end{matrix} \right\rangle \quad (4)$$

where $R_2 < R$ so that the current must be located within the aperture.

Expressions for Currents with Known Locations

Consider the case where the locations of M filaments are defined and the currents in each of these filaments are to be determined, or equivalently, the cross-section of the aperture is divided into a group of M pixels which are small enough that the current in each one may be represented by a chapeau (pulse) function. Let the current and the coordinates of the Jth pixel be $I_J = I_{J0}e^{j\omega t}$ and (R_J, θ_J), respectively, for J = 1 to M.

It is convenient to require that M = 2K +1, an odd integer, and require coils with the number of turns per unit length being N_0', and both N_{IC}' and N_{IS}' (cosine and sine terms) having I = 1 to K. That is, there are a total of M coils. Furthermore, define the normalized radial coordinate $S_J = R_J/R$, and the impedances $Z_0 = \omega\mu_0 AN_0'$, $Z_{JC} = \omega\mu_0 AN_{JC}'/2$, and $Z_{JS} = \omega\mu_0 AN_{JS}'/2$, where the reactance of the self inductance of the N_0' winding is jZ_0. Thus, Eq. (4) may be generalized to give the following set of equations for the induced voltages:

$$V_{OC} = jZ_0 \sum_{J=1}^{M} I_{J0} \quad (5A)$$

$$V_{OCIC} = jZ_{IC} \sum_{J=1}^{M} S_J^I \cos(I\theta_J) I_{J0} \quad (5B)$$

$$V_{OCIS} = jZ_{IS} \sum_{J=1}^{M} S_J^I \sin(I\theta_J) I_{J0} \quad (5C)$$

where Eqs. (5B) and (5C) each hold for I = 1 to K. The 3 equations, (5A)-(5C) define a matrix which relates the M measured voltages to the M unknown currents.

Determination of the Ill-Conditioning

Consider the general matrix equation Ax = b, where A is a square matrix and x and b are column vectors. The "direct" problem is defined as solving for the column vector b when A and x are given, and the "inverse" problem is solving for the column vector x when A and b are given. For example, in the present work the direct problem would be calculating the open-circuit voltages when the currents are known and the inverse problem would be calculating the currents when the open-circuit voltages are known.

The errors in solving the inverse problem are frequently much greater than those in solving the forward problem because of what is called "ill-conditioning" of the matrix. It is possible to place an upper bound on the errors in solving the inverse problem as follows:

$$\frac{\|\Delta x\|}{\|x\|} \le \|A\|\|A^{-1}\| \frac{\|\Delta b\|}{\|b\|} \quad (6)$$

where $\|A\|\|A^{-1}\|$, which is the product of the norm of the matrix and the norm of the inverse of the matrix, is defined to be the condition number of matrix A. Several different norms have been used by others, but the Frobenius norm (or Hilbert-Schmidt norm) which is used here is defined as follows [7]:

$$\|A\| = \sqrt{\sum_{I}^{M}\sum_{J}^{M} a_{IJ}^2} \quad (7)$$

NUMERICAL TESTS OF ALGORITHMS

Reduction of Ill-Conditioning of the Matrices

Numerical tests were made to determine the condition number for the matrix that is defined by Eqs. (5A)-(5C), using the Frobenius norm with different values of θ_J, S_J, and the impedances.

In the first series of tests the current filaments were placed on a circle with a normalized radius $S_J = 0.5$, and the values of the θ_J were chosen to minimize the condition number, which requires that they are evenly spaced on the circle. Figure 2 shows an example for M = 3. It was determined that the condition number has a minimum value that is equal to M when $Z_{IC} = Z_{IS} = 1.5Z_0/S_J^I$ for all values of I so that all of the terms in the matrix have comparable magnitude. For example, with M = 7, the condition number has a value of 7.0 when $Z_{1C} = Z_{1S} = 3.0Z_0$, $Z_{2C} = Z_{2S} = 6.0Z_0$, and $Z_{3C} = Z_{3S} = 12.0Z_0$. For comparison, when $Z_{IC} = Z_{IS} = 0.5Z_0$ for all values of I, the condition number is equal to $2.403 \times 2^{(M+1)/2}$ which is much greater than M when M is large.

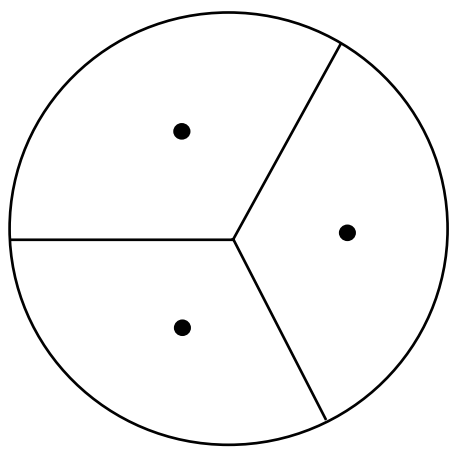

Figure 2: Partitioning of the aperture into 3 sectors.

Further numerical tests were made using pixels that are distributed over the full area of the aperture. Figure 3 shows an example with 9 current filaments that corresponds to the partitioning of a circular aperture into 9 pixels having equal area. In calculations for $Z_{1C} = Z_{1S} = Z_{2C} = Z_{2S} = Z_{3C} = Z_{3S} = Z_{4C} = Z_{4S} = 0.5Z_0$ the condition number equals 155. However, for $Z_{1C} = Z_{1S} = 2.0Z_0$, $Z_{2C} = Z_{2S} = 6.5Z_0$, $Z_{3C} = Z_{3S} = 11.0Z_0$, and $Z_{4C} = Z_{4S} = 23.0Z_0$, so that the matrix elements have comparable magnitude,

the condition number is reduced to a value of 46. The transverse distribution of current could be determined for this array of pixels by using the measurements made with 9 coils.

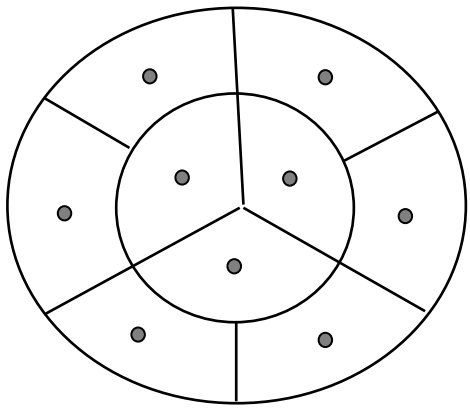

Figure 3: Partitioning of circular aperture into 9 segments.

Numerical Simulations

Numerical simulations were made by specifying the magnitudes, phases, and locations of the currents, calculating the induced voltages, adding Gaussian noise to model measurement errors, and then using the algorithms to calculate the currents and their locations. These results were compared with the input values to find the errors, so the degree of the numerical stability could be determined. Highlights of the results of these tests are as follows:

- For pixels that are evenly spaced on a single circle within the common aperture of a group of toroidal coils, the practical upper limit for the maximum number of pixels is set by the number of coils that can be used for the measurements and not by ill-conditioning of the matrix.

- The maximum number of pixels that may be used is significantly reduced when the pixels are distributed over an area within the aperture.

- It is not surprising that these results are consistent with the results of the numerical tests in which the condition number was determined for the matrices without specifying the magnitudes or phases of the currents.

CONSTRUCTION OF PROTOTYPES

It will be necessary to construct high-precision uniformly-wound and sinusoidally-wound toroidal coils having as many as 100 to 500 turns in order to be able to measure the transverse distribution of current.

Rapid Prototyping methods such as Stereolithography and 3D-Printing could be used to fabricate toroidal forms with grooves in which wires would be placed to form the coils. Typically models made using these techniques have a resolution of 10-100 μm. Prototype toroids having an outer diameter as large as 50 cm could be made with these methods, and one possible means for fabricating larger toroids would be to use Rapid Prototyping to prepare sections that would be connected together. Rapid Prototyping requires a data file with the (X,Y) coordinates for each Z value corresponding to the height of a given layer of the model.

Determining the Equation for the Coil

The (X,Y) coordinates for each Z value in the data file are determined from the coordinates on the surface of the toroid which are defined in Fig. 4, and the Cartesian coordinates may be determined from the coordinates on the toroid by Eqs. (8)-(10), where R is the mean radius of the toroid and r_0 is the radius of the tube of the toroid.

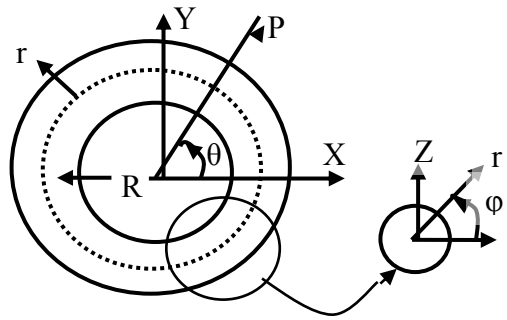

Figure 4: Definition of toroidal coordinates.

$$X = R\cos(\theta) + r_0\cos(\phi)\cos(\theta) \quad (8)$$

$$Y = R\sin(\theta) + r_0\cos(\phi)\sin(\theta) \quad (9)$$

$$Z = r_0\sin(\phi) \quad (10)$$

The equation for the path of the coil in a uniformly-wound coil on the surface of the toroid is given by

$$\phi = 2\pi RN_0'\theta \quad (11)$$

More generally, including non-uniform windings, the path of the coil is defined by

$$\frac{d\phi}{d\theta} = 2\pi RN'(\theta) \quad (12)$$

Thus, by integrating, the equation for the path of the winding for a general set of coils may be defined by extending Eq. (3) as follows:

$$\phi \in \left\langle \begin{array}{l} 2\pi RN_0'\theta, \quad \frac{2\pi RN_{JC}'}{J}\sin(J\theta), \\ -\frac{2\pi RN_{JS}'}{J}\cos(J\theta) \end{array} \right\rangle \quad (13)$$

Equation (13) may be inverted to derive the following expression which may be used to determine the series of values of θ at which the coil intersects each layer of the model:

$$\theta \in \left\langle \begin{array}{l} \frac{\phi}{2\pi RN_0'}, \quad \frac{1}{J}Sin^{-1}\left(\frac{J\phi}{2\pi RN_{JC}'}\right), \\ \frac{1}{J}Cos^{-1}\left(\frac{J\phi}{2\pi RN_{JS}'}\right) \end{array} \right\rangle \quad (14)$$

Generating the Data File for Rapid Prototyping

For each value of Z, corresponding to the height of a given layer of the model:

(1) Generate a file of (X,Y) coordinates on a grid with a resolution equal to the incremental step-size for the Rapid Prototyping instrument, such that these points approximate the two circles where the smooth surface of the toroid has the specified Z, requiring that these points have evenly-spaced values of θ.

(2) Define the inner circle, where $\pi/2 < \varphi < 3\pi/2$, and the outer circle, where $0 < \varphi < \pi/2$, or $3\pi/2 < \varphi < 2\pi$.

(3) Determine the first values for φ on each circle:
Inner circle: $\varphi = \pi - \mathrm{Sin}^{-1}(Z/r_0)$
Outer circle: $\varphi = \mathrm{Sin}^{-1}(Z/r_0)$ for $Z > 0$;
$\varphi = 2\pi + \mathrm{Sin}^{-1}(Z/r_0)$ for $Z < 0$.

(4) Use Eq. (14) to determine the corresponding values of θ where the coil crosses the inner and the outer circle.

(5) Add 2π to φ and use Eq. (14) to determine the second pair of θ where the coil crosses the inner and the outer circles.

(6) Continue step 5 to determine the subsequent values of θ until the argument of the inverse trigonometric function exceeds unity. Then use symmetry to determine the other values for θ on the rest of the way around the inner and the outer circles.

(7) Change the data file that was generated in step 1 to include grooves in this layer of the model at the values of θ where the coil crosses the layer.

SUMMARY AND CONCLUSIONS

- It is possible to determine the magnitude and phase of the currents in a number of wires having known locations by measuring the voltages that are induced on an equal number of coaxial toroidal coils that have these currents passing through their common aperture.

- This problem is equivalent to monitoring a continuous distribution of current that passes through a specified area which is divided into a number of pixels. These pixels must be small enough that the current is slowly varying within each of them. The well-known smoothing property of the integral operator makes a partial correction for the effects of the linear variation of the current within each pixel.

- It is convenient to use matrix methods to determine the magnitudes and phases of the currents when the number of wires is an odd integer M = 2K +1, and the coils have the number of turns per unit length constant, and proportional to the sin(θ), cos(θ), sin(2θ), cos(2θ), … , sin(Kθ), and cos(Kθ), respectively, where θ is the azimuthal coordinate.

- When the pixels are evenly spaced on a single circle within the common aperture of a group of toroidal coils, the practical upper limit for the maximum number of pixels is set by the number of coils that can be used for the measurements and not by ill-conditioning of the matrix. However, the maximum number of pixels that may be used is significantly reduced when the pixels are distributed over an area within the aperture. However, it is not necessary to have pixels in areas of the aperture where it is known that the current is negligible.

- Rapid Prototyping methods have adequate precision for fabricating the group of coils, and the equations that are needed to generate the data files which are required for Rapid Prototyping have already been derived.

REFERENCES

[1] H. Koziol, "Beam diagnostics for accelerators," Proceedings of the CERN Accelerator School, Fifth General Accelerator Physics Course, ed. S. Turner (1992).

[2] V. A. Verzilov, "Spatial resolution in optical transition radiation beam diagnostics," Phys. Rev. Special Topics –Accelerators and Beams 1 (1998) 062801.

[3] J. A. Pasour and M. T. Ngo, "Nonperturbing electron beam probe to diagnose charged-particle beams," Rev. Sci. Instrum. 63 (1992) 3027-3039.

[4] W. Rogowski and W. Steinhaus, "Die messung der magnetischen spannung," Arch. Electrotech. 1 (1912) 141-150.

[5] A. G. Klein, "Demonstration of Ampere's circuital law using a Rogowski coil," Am. J. Phys. 43 (1975) 368-370.

[6] M. J. Hagmann and T. M. Babij, "Non-invasive measurement of current in the human body for electromagnetic dosimetry," IEEE Trans. Biomed. Eng. 40 (1993) 418-423.

[7] G. Golub and C. F. Van Loan, Matrix Computations (Baltimore, Johns Hopkins University Press, 3rd ed., 1996).

NEW METHOD TO MONITOR THE CURRENT AND POSITION OF ONE OR TWO PARTICLE BEAMS

M. J. Hagmann, NewPath Research L.L.C., P. O. Box 3863, Salt Lake City, UT 84110, U.S.A.

Abstract

A group of sinusoidally-wound coaxial toroidal coils can be used to determine the magnitudes, phases, and locations of one or two time-dependent currents through their common aperture. A single current filament requires one uniformly-wound coil and two others having turn densities proportional to the sine and cosine of the azimuthal coordinate. Three simple algebraic equations give the magnitude, phase, and location of the current in terms of the voltages induced on the three coils, and there is no ill-conditioning. Two current filaments require two additional toroids with turn densities proportional to the sine and cosine of two times the azimuthal coordinate, and the solution is obtained using the method of steepest descent. Solutions for more than two currents become numerically unstable. Numerical tests were made by specifying the magnitudes, phases, and locations of the currents, calculating the induced voltages, adding Gaussian noise to model measurement errors, and then using the algorithms to calculate the currents and their locations. These simulations confirm that this method may be used with one or two currents

INTRODUCTION

Others have used a variety of different techniques to monitor the location of a single beam in an accelerator, including arrays of capacitive pickups, resistive wall gap monitors, electrostatic monitors, split-plate monitors, split-cylinder monitors, button monitors, longitudinal transmission lines, resonant cavities, and reentrant cavities [1]. Other techniques include secondary emission monitors, wire scanners, multi-wire chambers, gas curtains or jets, residual gas monitors, scintillator screens, scrapers and measurement targets, and synchrotron radiation [2], as well as the deflection of a probe beam of electrons [3]. Three groups have described work that is directly related to this paper. Two used four identical coils to determine the current and its location [4,5]. Murgatroyd and Woodland [6] made a short note that two coils with turn densities varying as sin(θ) and cos(θ) could measure the location of a single current, but they gave no analysis or experimental results and these authors could not be reached.

A Rogowski Coil is a non-ferrous current probe formed by bending a uniformly wound helical coil to follow a closed curve having arbitrary shape [7-9]. When a time-dependent current passes through the aperture that is enclosed by the bent helix a voltage is induced on the coil which is independent of the location of the current. However, currents that are located outside of the aperture do not induce a voltage on the coil. Deviations from a uniform winding are carefully avoided because they cause the induced voltage to depend on the location of the current within the aperture, but it will be shown that a group of coils having a specific type of nonuniformity may be used to accurately determine the current and its location.

ANALYSIS

Figure 1 is a diagram used for deriving expressions for the open-circuit voltage induced on a non-ferrous toroidal coil that may have a nonuniform winding. The toroid has a mean radius R, and the cross-sectional area of the tube of the toroid is A. Consider the induction in an incremental winding of length Rdθ that is centered at (R,θ) or equivalently (X_1,Y_1), which is caused by a filament with current $I = I_{10}e^{j\omega t}$ that intersects the X,Y plane at point $P(X_2,Y_2)$. The dashed line L_1 is directed normal to the increment of winding. Dashed line L_2 is parallel to the magnetic field, and dashed line L_3 is parallel to the X-axis.

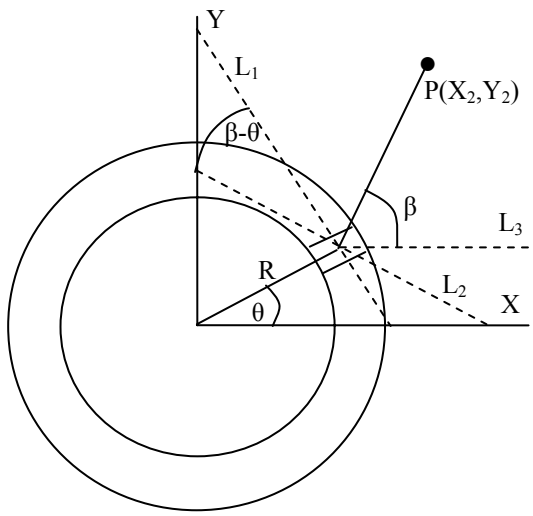

Figure 1: Diagram for analysis.

Let N'(θ) be the number of turns per unit length of the coil, as measured on a circle with radius R. For example, with a toroidal coil having a uniform winding, $N' = N_0' = N_T/2\pi R$, where N_T is the total number of turns. The number of turns in an increment of the winding is $dN = N'(\theta)\, R\, d\theta$. Thus, if the height and width of the tube are much less than R, the open-circuit voltage on the entire winding is given by

$$V_{OC} = -\int_0^{2\pi} \frac{j\omega\mu_0 N'(\theta) RAI \cos(\beta-\theta)\, d\theta}{2\pi\sqrt{(X_2-X_1)^2+(Y_2-Y_1)^2}} \quad (1)$$

Using trigonometry to obtain an expression for cos(β - θ), Eq. (1) simplifies to give the following:

$$V_{OC} = \frac{j\omega\mu_0 AI}{2\pi}\int_0^{2\pi} \frac{N'(\theta)\left[1 - \frac{X_2}{R}\cos\theta - \frac{Y_2}{R}\sin\theta\right]}{\left[\left(\frac{X_2}{R} - \cos\theta\right)^2 + \left(\frac{Y_2}{R} - \sin\theta\right)^2\right]} d\theta \quad (2)$$

The expressions for N' are chosen from the following set, which constitutes the basis for a Fourier series:

$$N'(\theta) \in \left\langle N_0', \sum_{J=1}^{\infty} N_{JC}'\cos(J\theta), \sum_{J=1}^{\infty} N_{JS}'\sin(J\theta) \right\rangle \quad (3)$$

where the N_{JC}' and N_{JS}' are coefficients as is N_0'. By substituting the set in Eq. (3) into Eq. (2), and evaluating the integral, the open-circuit voltage that is induced on each coil is given by the corresponding term of the following set:

$$V_{OC} \in j\omega\mu_0 AI_{10} \left\langle \begin{array}{c} N_0', \sum_{J=1}^{\infty} \frac{N_{JC}'}{2}\left(\frac{R_2}{R}\right)^J \cos(J\theta_1), \\ \sum_{J=1}^{\infty} \frac{N_{JS}'}{2}\left(\frac{R_2}{R}\right)^J \sin(J\theta_1) \end{array} \right\rangle \quad (4)$$

where $R_2 < R$ so that the current must be located within the aperture

Expressions for a Single Current Filament

If there is a single current filament, Eq. (4) may be used to show that the current and its coordinates may be uniquely determined from measurements that are made using three coils, by the following three equations:

$$I_{10} = \frac{-jV_{OC0}}{\omega\mu_0 AN_0'} \quad (5)$$

$$X_2 = R_2\cos(\theta_2) = \frac{2RN_0'V_{OC1C}}{N_{1C}'V_{OC0}} \quad (6)$$

$$Y_2 = R_2\sin(\theta_2) = \frac{2RN_0'V_{OC1S}}{N_{1S}'V_{OC0}} \quad (7)$$

Here V_{OC0}, V_{OC1C}, and V_{OC1S} are the open-circuit complex voltages induced on the three coils, for which the respective number of turns per unit length is N_0', N_{1C}'cos(θ), and N_{1S}'sin(θ). The derivation of Eqs. (5)-(7) implicitly assumes that $R << \lambda$, so these equations require that V_{OC1C}, and V_{OC1S} are in phase with each other and in phase quadrature with the current.

If the errors in the three measured voltages are small, but much greater than the effects of imperfections in the fabrication and placement of the coils, Eqs. (6) to (8) require that the fractional errors in the calculated current and its location are related to the fractional errors in the voltage measurements as follows:

$$\frac{\delta I_{10}}{I_{10}} = \frac{\delta V_{OC0}}{V_{OC0}} \quad (8)$$

$$\frac{\delta X_2}{X_2} = \frac{\delta V_{OC1C}}{V_{OC1C}} - \frac{\delta V_{OC0}}{V_{OC0}} \quad (9)$$

$$\frac{\delta Y_2}{Y_2} = \frac{\delta V_{OC1S}}{V_{OC1S}} - \frac{\delta V_{OC0}}{V_{OC0}} \quad (10)$$

Equations (6) to (8) show that the fractional error in the calculated current is equal to the fractional error in measurement with the uniformly wound coil. If the fractional errors in measuring the three voltages are comparable, then the fractional errors in the calculated coordinates have expectation values that equal the square-root of 2 times the fractional error in the calculated current. There is no ill-conditioning for the case of a single current filament.

Expressions for Two Current Filaments

If there are two current filaments, $I_1 = I_{10}e^{j\omega t}$ at (R_1, θ_1) and $I_2 = I_{20}e^{j\omega t}$ at (R_2, θ_2), Eq. (4) shows that the open circuit voltages on the first five coils from the set will be given by

$$V_{OC0} = j\omega\mu_0 AN_0'\left[I_{10} + I_{20}\right] \quad (11)$$

$$V_{OC1C} = j\omega\mu_0 A\frac{N_{1C}'}{2R}\left[I_{10}R_1\cos(\theta_1) + I_{20}R_2\cos(\theta_2)\right] \quad (12)$$

$$V_{OC1S} = j\omega\mu_0 A\frac{N_{1S}'}{2R}\left[I_{10}R_1\sin(\theta_1) + I_{20}R_2\sin(\theta_2)\right] \quad (13)$$

$$V_{OC2C} = j\omega\mu_0 A\frac{N_{2C}'}{2R^2}\left[I_{10}R_1^2\cos(2\theta_1) + I_{20}R_2^2\cos(2\theta_2)\right] \quad (14)$$

$$V_{OC2S} = j\omega\mu_0 A\frac{N_{2S}'}{2R^2}\left[I_{10}R_1^2\sin(2\theta_1) + I_{20}R_2^2\sin(2\theta_2)\right] \quad (15)$$

It may be seen that this set of 5 equations in 6 unknowns is a determined system by considering that the currents and voltages are complex variables requiring both phase and magnitude, but the phases of the measured voltages must have a common reference. It appears that Eqs. (11)-(15) cannot be solved directly. Thus, a cost function is defined as the sum of the squares of the residuals in these five equations, and the method of steepest descent is used to determine the values of I_{10}, R_1, θ_1, I_{20}, R_2, and θ_2 for which the cost function has a minimum.

Equations (11)-(15) were also used to derive two simultaneous equations having only the variables θ_1 and θ_2, so these two equations may be solved and then the other 4 unknowns may be determined. However, this procedure has been shown to have much lower numerical stability than in using the method of steepest descent as just described.

NUMERICAL TESTS OF ALGORITHMS

Numerical tests were made by specifying the magnitudes, phases, and locations of the currents, calculating the induced voltages, adding Gaussian noise to model measurement errors, and then using the algorithms to calculate the currents and their locations. These results were compared with the specified values to find the errors, so that the range of convergence and numerical stability could be determined. Highlights of the results of these tests are as follows:

- For one current filament, Eqs. (5)-(7) may be used for an explicit solution, or the method of steepest descent may be used to determine the solution by the minimization of residuals. Three coils are required, and

both procedures are highly accurate with errors that are consistent with Eqs. (8)-(10).

- For two current filaments, Eqs. (11)-(15) may be used with the method of steepest descent. Five coils are required, and the errors are consistent with the Gaussian noise that is introduced to model the measurement errors. An expression for the condition number of the matrix has not been determined, but the fractional errors are several times the fractional errors in the measurements.

- For two current filaments, two simultaneous equations in the variables θ_1 and θ_2 may be solved and then the other 4 unknowns may be determined from these two variables. However, this procedure has much lower numerical stability than the method of steepest descent as just described. Furthermore, there is a narrow range of convergence and the errors in determining the remaining 4 unknowns are much greater than the errors in θ_1 and θ_2.

- It would appear to be possible to use the method of steepest descent with the measurements from 2M +1 coils to determine the magnitudes, phases, and locations of M currents. However, the solutions are numerically unstable with more than 2 currents.

SUMMARY AND CONCLUSIONS

- Three coaxial toroidal coils may be used to determine the magnitude, phase, and location of one time-dependent current that passes through their common aperture. These three coils should have the number of turns per unit length constant, and proportional to the $\sin(\theta)$, and the $\cos(\theta)$, respectively, where θ is the azimuthal coordinate.

- Five coaxial toroidal coils may be used to determine the magnitudes, phases, and locations of two time-dependent currents that pass through their common aperture. These five coils should have the number of turns per unit length constant, and proportional to the $\sin(\theta)$, $\cos(\theta)$, $\sin(2\theta)$, and $\cos(2\theta)$, respectively.

- The magnitude, phase, and location of one current are determined from measurements of the magnitude and phase of the voltages that are induced on three coils, either by an explicit solution or by the method of steepest descent, with fractional errors that are approximately equal to the fractional errors in the measurements.

- The magnitudes, phases, and locations of two currents are determined from measurements of the magnitude and phase of the voltages that are induced on five coils by the method of steepest descent, with fractional errors that are several times the fractional errors in the measurements.

- It does not appear to be practical to use this method to determine the magnitudes, phases, and locations of more than two currents.

REFERENCES

[1] M. Minty, "Diagnostics," Deutsches Elektronen Synchrotron (DESY) Accelerator Division Internal Report (2004).

[2] H. Koziol, "Beam diagnostics for accelerators," Proceedings of the CERN Accelerator School, Fifth General Accelerator Physics Course, ed. S. Turner (1992).

[3] J. A. Pasour and M. T. Ngo, "Nonperturbing electron beam probe to diagnose charged-particle beams," Rev. Sci. Instrum. 63 (1992) 3027-3039.

[4] D. Berners and L. Reginato, "Beam position and total current monitor for heavy ion fusion beams," Accelerator Instrumentation Fourth Workshop, AIP Conference Proceedings No. 281 (1993) 168-174.

[5] P. Adderley, W. Barry, J. Heefner, P. Kloeppel, R. Rossmanith and M. Wise, "A beam position monitor for low current DC beams," Proceedings of the 1989 Particle Accelerator Conference (1989) 1602-1604.

[6] P. N. Murgatroyd and D. N. Woodland, "Geometrical properties of Rogowski sensors," IEE Colloquium on Low Frequency Power Measurement and Analysis 9 (1994) 1-10.

[7] W. Rogowski and W. Steinhaus, "Die messung der magnetischen spannung," Arch. Electrotech. 1 (1912) 141-150.

[8] A. G. Klein, "Demonstration of Ampere's circuital law using a Rogowski coil," Am. J. Phys. 43 (1975) 368-370.

[9] M. J. Hagmann and T. M. Babij, "Non-invasive measurement of current in the human body for electromagnetic dosimetry," IEEE Trans. Biomed. 40 (1993) 418-423.

INJECTION OF DIRECT-SEQUENCE SPREAD SPECTRUM PILOT TONES INTO BEAMLINE COMPONENTS AS A MEANS OF DOWNCONVERTER STABILIZATION AND REAL-TIME RECEIVER CALIBRATION*

J. Musson†, T. Allison, Thomas Jefferson National Accelerator Facility, Newport News, VA, 23606
Christopher Hewitt, Christopher Newport University, Newport News, VA, 23606

Abstract

Beamline components used for diagnostic elements often rely on thermal stabilization, continual physical maintenance (ie. tuning), and frequent beam-based calibrations to maintain specified performance. Direct-sequence spread spectrum (DSSS) pilot tones injected into a particular element and combined with the beam-derived signal can subsequently be separated and used to assess performance degradation. In addition, the DSSS tone can be used as a real-time calibration signal, without interference to the intended diagnostic signal. This paper demonstrates such a technique in the design of a Beam Current Monitor downconverter system, as an intended upgrade to the CEBAF Beam Loss Accounting system. A brief spread-spectrum primer is included, as well as a description of appropriate spreading codes and their generation.

INTRODUCTION

The Continuous Electron Beam Accelerator Facility (CEBAF) employs a system of passive 1497 MHz TM010 cavities as the basis for a beam current loss accounting system (BCM/BLA) for machine protection [1]. The 1497 MHz RF signal is downconverted, and routed to a VME-based IF receiver system capable of resolving hundreds of nanoamps of instantaneous beam loss [2,3]. In addition, a 1% absolute accuracy provides accelerator operators and experimenters with a convenient means of continuous, non-invasive beam current measurement. The present system has two limitations. Firstly, confidence tests of the cavity performance can only be preformed off-line, i.e. when the beam is not present. Secondly, the RF-to-IF downconverters, located in the beam enclosure, are no longer available and will require replacement for the 12 GeV CEBAF upgrade. A new system is desired, which is capable of continuous performance assessment, able to stay within calibration limits for long periods of time, and requires minimal operator or system expert intervention. The proposed design employs a CW pilot tone, orthogonal to the electron beam signal, as a means to evaluate proper performance in real time, as well as introduce a calibration reference for long-term stability.

DIRECT-SEQUENCE SPREAD SPECTRUM (DSSS)

The problem of intentional co-channel interference (ie. "jamming") has long been an issue with RADAR and tactical communications systems. An effective countermeasure involves spreading the carrier energy over an extreme bandwidth, often hiding beneath the thermal noise floor. If the mechanism with which the spreading is known, carrier reconstruction can be performed at the receiver using cross-correlation techniques [4].

The basis for DSSS involves multiplying the carrier with a pseudo-random bit sequence, which although looks like noise to other receiving stations, is actually a correlated, repeating sequence which has the effect of encrypting the carrier energy.

Spreading Codes

Mathematically, a spreading code serves to map the low-dimensional CW carrier tone to one having a high degree of dimensionality. Furthermore, each of the dimensions should consist of orthogonal signals, which form the new basis. Then, the D equiprobable and equienergy orthogonal signals within an n-dimensional space can be re-represented in the new signal space by considering an orthonormal basis, $\varphi_k(t)$, which is defined by [5]:

$$\phi_k(t);\ 1 \leqslant k \leqslant n$$

$$\int_0^T \phi_l(t)\phi_m(t)\,dt = \delta_{lm} = \begin{cases} 1 & l = m \\ 0 & l \neq m \end{cases} \quad .$$

Then, the new signal representation is:

$$S_i(t) = \sum_{k=1}^{n} S_{ik}\phi_k(t) \qquad 1 \leqslant i \leqslant D; \qquad 0 \leqslant t \leqslant T$$

where

$$S_{ik} = \int_0^T S_i(t)\phi_k(t)\,dt \quad .$$

The resulting average energy for each of the signals is represented by:

$$\int_0^T \overline{S_i^2(t)}\,dt = \sum_{k=1}^{n} \overline{S_i^2} = E_s; \qquad 1 \leqslant i \leqslant D$$

*Authored by Jefferson Science Associates, LLC under U.S. DOE Contract No. DE-AC05-06OR23177.
†musson@jlab.org

Since S_{ik} represents coefficients describing the space, they can be chosen, independently. The idea is to select them, such that their energies are uniformly distributed, have zero mean and correlation, and are only known by the intended receiver (hence unobservable by the primary BCM receiver). The energy occupied by each coordinate then becomes:

$$\overline{S_{ik} S_{il}} = \frac{E_s}{n} \delta_{kl} \qquad 1 \leqslant i \leqslant D$$

For the sake of illustration, the relatively narrowband beam signal can be represented by

$$J(t) = \sum_{k=1}^{n} J_k \phi_k(t); \qquad 0 \leqslant t \leqslant T$$

which results in a total energy

$$\int_0^T J^2(t)\, dt = \sum_{k=1}^{n} J_k^2 = E_J$$

and ultimately combines with the DSSS signal within the BCM cavity. Since each signal represents only a fraction of the other's energy, within the narrow bandwidth of the beam signal, an arbitrarily high SNR can be maintained, and is dependent on the dimensionality of the spreading code.

The resulting spectrum of a DSSS signal is shown in Figure 1. The envelope follows a $(\sin(x)/x)^2$ function, whereby the first nulls occur at +/- $1/f_c$, with f_c defined as the clock rate for the spreading code (known as the "chip" rate). Interestingly, the original carrier is further nulled by $1/n^2$, where n is the length of the sequence, resulting in a spectral notch [4].

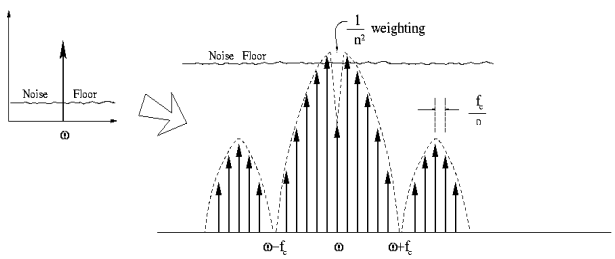

Figure 1. DSSS spectrum created from a CW carrier, showing $(\sin(x)/x)^2$ envelope, as well as $1/n^2$ notch.

A bench test was devised to examine the feasibility of generating necessary tones, and combining them within an actual BCM cavity, employing a pseudo-random (PRN) code generator, as shown in Figure 2.

A pair of 1496 MHz free-running oscillators were chosen for both the pilot tone and the beam signal, as a matter of convenience; the actual downconverter design will utilize 1497 MHz for both signals. Although the cavity resonance is centered at 1497 MHz, our test was contained within the 6dB passband, and therefore representative.

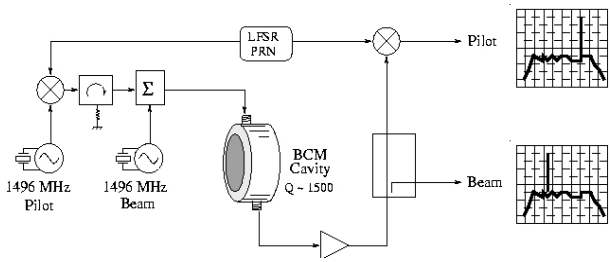

Figure 2. Bench test setup of DSSS system, utilizing near-frequency 1496 MHz oscillators to represent pilot tone and beam signals. PRN generates the sequence.

Figure 3 demonstrates the DSSS process for a single tone, with 2 spreading codes of n=15 and n=65535, respectively, after being passed through a 1497 MHz BCM cavity with 3dB bandwidth of ~ 1MHz. In each case (i.e. for any n), the envelope is the same, dictated solely by the 1 MHz chip rate. Within the envelope, the narrowband carrier (ie. pilot tone) is disassembled into n-dimensional components, which, although lacking in performance, is most easily seen in the n=15 case.

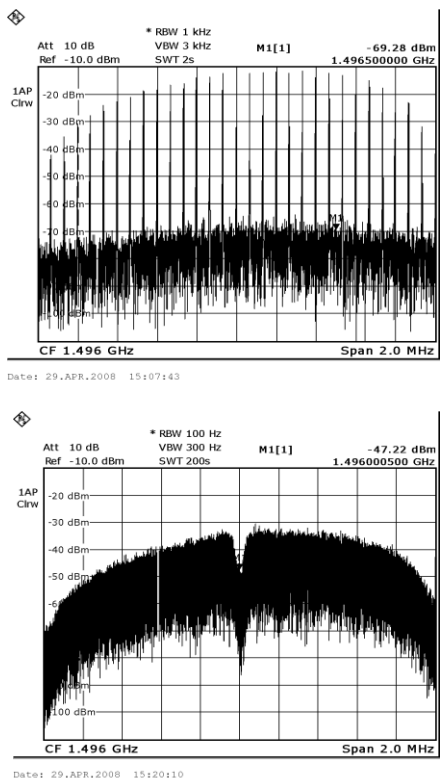

Figure 3. DSSS spectra of 1496 MHz tone for n=15 and n=65535. All cases were subsequently passed through a 1497 MHz cavity (Q ~ 1500), replicating in-situ conditions. The n=15 case clearly demonstrates the spreading process, whereby energy is "re-binned."

When this spectrum is subsequently cross-correlated with the original code, the carrier is re-assembled, but with some loss of accuracy as seen by degraded SNR for each of the three codes, given by Figure 4. The extent to which the SNR is retained is called "processing gain," simply stating that the carrier power is distributed evenly amongst n bins, and follows:

$$PG = 10 \cdot \log(n), \qquad n = sequence\ length$$

A designer can use this relation to determine the length of a PR code necessary to achieve a given SNR or carrier supression. The chip rate will then determine the first nulls in the actual spread spectrum.

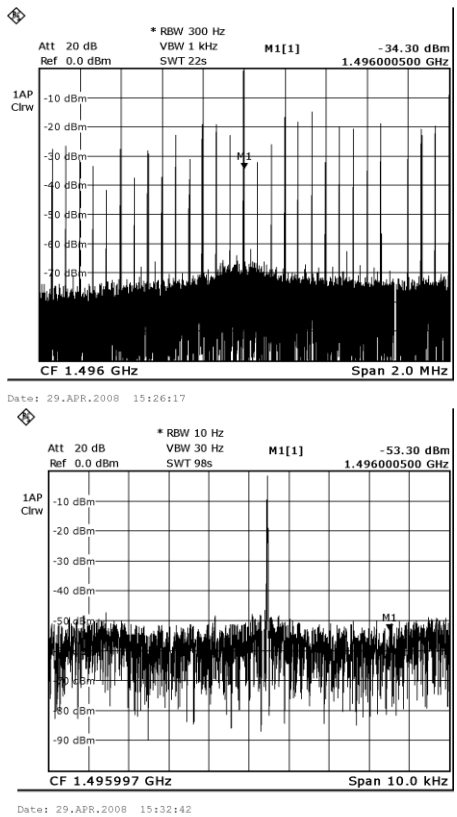

Figure 4. Reconstructed spectra for n=15 and n=65535. Processing gain (ie. SNR) follows the expected predictions of 12dB and 48dB, respectively, demonstrating the ability to spread and de-spread pilot tones to at-or-below the noise floor.

Linear Feedback Shift Register (LFSR)

Pseudorandom (PR) sequences are at the heart of cryptography and identity verification, which have each contributed countless methods for generating long PR codes. Although not completely random, in the strict sense, a good algorithm will produce a sequence (or set of sequences) which satisfy reasonable tests for randomness. These tests, or properties, include [5]:

Independence Property. Any preceding or subsequent sequence should not determine the present value.

Balance Property. There should exist an equal number of ones and zeros for the entire sequence.

Run Property. Continuous occurrences of all ones or all zeros should be minimized by $½^{(\text{number of consecutive occurrences})}$.

Correlation Property. Any bit-shifted version of a sequence should not cross-correlate with the original sequence.

For the application outlined in this paper, only loose adherence is required for the stated properties, allowing the use of a simple PR generation algorithm, known as a Linear-Feedback Shift Register (LFSR). A LFSR scheme uses a serial shift register of r bits, whose input is determined by exclusive-OR-ing (XOR) several of the output taps. Proper selection of feedback taps will result in a maximal-length sequence, which has a cycle length of 2^r-1, and inherently satisfies the PR properties [5,6]. A 16-bit (sequence length = 65535) LFSR algorithm was implemented on an Altera Cyclone II FPGA, with selectable sequence lengths, and clocked at 1 MHz [6].

DOWNCONVERTER

Replacement of the downconverter electronics will require that existing performance specifications are met. For this paper, the most relevant requirements are minimum and maximum beam loss values of 1 uA and 200 uA, respectively. Therefore, a minimum dynamic range of the system is 46 dB. As a proof-of-concept, we spread the pilot tone using a sequence of n=65535, thereby achieving at least 46 dB of processing gain. This resulted in the the supression of a 200 uA pilot tone to that of a representative BCM signal near 1 uA. The combined signals were then run through a de-spreader, reconstructing the pilot tone, but spreading the beam signal, as demonstrated in Figure 5.

It must be noted that mixer selection requires a very wideband (1 MHz – 1497 MHz) performance, particularly for the despreader. Several common units were tried, with varied output efficiencies. The output coupler provided a look at the simulated CW beam frequency with spread pilot tone, while the despreader output demonstrated the switch in spectra, maintaining 46 dB of SNR.

In practice, an additional 13 dB of margin is added so as to provide a S/N consistent with a false-alarm rate <=15min/yr (10^{-8}) [7]. A sequence of length n = 10^6 (20 bits) would then be required.

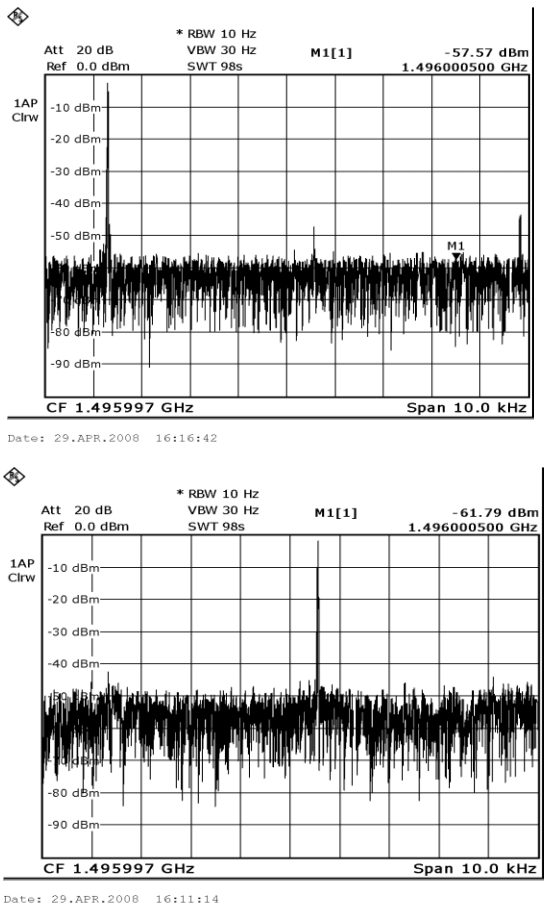

Figure 5. Signal representing beam is shown, with DSSS pilot tone, demonstrating 46 dB of supression (a). Upon reconstruction, the pilot tone re-emerges, while supressing the beam signal by the predicted 46 dB (b).

Figure 6 is the block diagram for the proposed 12 GeV downconverter, with pilot tone oscillator stabilization. Preliminary component analysis and SystemVue simulations are currently underway, and prototyping is expected for Summer, 2008.

IF RECEIVER IMPLEMENTATION

While the primary intent of the DSSS pilot tone was to provide downconverter gain stabilization and real-time performance information, it is not limited to synchronous demodulation. If the IF receiver is also capable of de-spreading the pilot tone, it can be used for comparative analysis with the demodulated beam cavity signal. Stabilization of the pilot tone oscillator to within the requirements of the BCM/BLA system (~0.25 dB) allows it to be used as an absolute reference, reducing the need for beam-based calibrations. The CEBAF BLA system uses a dual-channel, direct-digital downconverter receiver for IF signals. Currently, only one channel is used, with minimal processing. Since the DSSS pilot tone is present, along with the beam signal, it is possible to dedicate one receiver channel for de-spreading and detection of the DSSS tone. An approach commonly used for asynchronous despreading is known as a delay-locked loop [DLL], whereby a promptly arriving signal is compared with one which is ½-bit early and ½-bit late [5]. A triangular correlation function is produced by differencing the early and late signal amplitudes obtained by the correlator, which then adjusts the clock rate. The prompt signal emerges perfectly de-spread, since it is fed by the properly aligned sequence.

We would exploit the fact that only a few codes are used, and there is never more than a single DSSS signal present on any given BCM channel. Subsequently, all utilized codes (in the form of their LFSR implementations) reside in each IF receiver, and is tested by "sliding" against the incoming signal. If no match is found, the next LFSR code is tried, and so on. Each IF receiver is able to independently determine to which downconverter and cavity system it is connected, and applies the appropriate scaling constants, etc.

Oscillator stabilization could be accomplished through the use of a dual-channel, logarithmic comparator, used for cellular communication base stations. Although the ADL5519 is a wide-band part, narrowband stability over wide temperature ranges appears promising, with data sheets suggesting <0.25 dB stability, sufficient for use as an absolute reference to 1%. Frequency stabilization is not required; free-running oscillators for pilot tone and LO are acceptable, since no phase-sensitive measurements are performed. This removes any requirements for Master Oscillator signals.

CONCLUSIONS

DSSS provides a convenient method for creating orthogonal signals for pilot tone injection, as well as mulitplexing signals on a single channel. This work demonstrated the feasibility of simultaneously detecting beam and pilot tones, thus providing performance feedback for stabilization. In addition, real-time calibration and confidence testing can be run while beam is present in the accelerator. The choice of frequencies used in the demonstration were arbitrary, and are easily extended to many applications. The use of independent, free-running oscillators also demonstrated worst-case, asynchronous operation.

ACKNOWLEDGMENTS

The authors would like to thank Pavel Evtushenko for timely instrumentation assistance, as well as the JLAB I&C Group for supporting the development effort. Hari Areti's input and guidance were greatly appreciated.

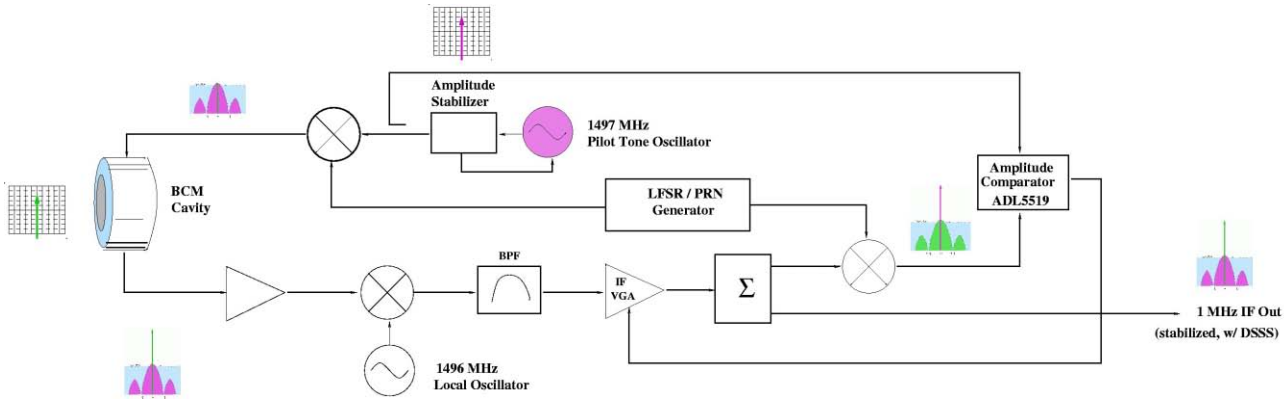

Figure 6. Block diagram for proposed downconverter. A 1497 MHz pilot tone is spread, and combined with the 1497 MHz beam signal, in the cavity. Despreading facilitates orthogonal detection of the 2 separate signals, for the purpose of gain stabilization.

REFERENCES

[1] R. Ursic, K. Mahoney, C. Hovater, A. Hutton and C. Sinclair, "CEBAF Beam Loss Accounting," Proceedings of the 1995 Particle Accelerator Conference, Dallas, TX, May 1-5, 1995. pp 2652-2654

[2] H. Dong, R. Flood, C. Hovater, J. Musson, "A Dual Digital Signal Processor VME Board for Instrumentation and Control Operations," ICALEPCS 2001, San Jose CA, November, 2001

[3] T. Powers et al., "Two Applications of Direct-Digital Downconverters for Beam Diagnostics," Proceedings of the 2000 Beam Instrumentation Workshop, Boston, MA, 2000

[4] L. Couch II, *Anal og and Digital Communications*, 3rd ed., Macmillan, NY, NY. 1990, ISBN 0-02-325391-6

[5] R.L. Pickholtz, D.L. Schilling, "Theory of Spread Spectrum Communications – A Tutorial, " IEEE Transactions on Communications, Vol. COM-30, No. 5, May, 1982

[6] "Linear Feedback Shift Register v3.0," Xilinx Technical Note DS257 (v1.0), Mar. 28, 2003

[7] M. Skolnik, Radar Systems, 2nd ed., McGraw-ill, NY, NY., 1980, ISBN 0-07-057909-1

THE BEPCII DCCT SYSTEM

Y. Zhao#, J.S. Cao

Institute of High Energy Physics, Chinese Academy of Sciences, Beijing 100049, China

Abstract

A DC Current Transformer (DCCT) as a standard diagnostic system for beam current plays an important role in BEPCII, the upgrade project of the Beijing Electron Positron Collider. Two DCCTs are operating now, separately in the electron and positron rings, to monitor the beam current, the beam injection rate, the beam loss rate and the beam lifetime. In this paper, the mechanical structure design, readout system and data processing are presented. The progress of DCCTs on each step of BEPCII commissioning, such as improving the beam lifetime and reducing the background noise, are also included.

INTRODUCTION

DCCT systems usually consist of three parts: sensor, electronics and the DAQ & control. The sensor is always affixed on the linear tube, for it is sensitive to the parasitic magnetic field caused by RF cavity, quadrupole magnet and the power cable, and must be far from those parts. Figure 1 shows the layout of the DCCT.

In BEPCII, two DCCT sensors are fixed in each outer ring, symmetrically around the south interaction points. The two sensors are individually used for the electron ring and positron ring when BEPCII operates in the collision mode. In dedicated synchrotron radiation mode, both of them are used for the electron ring. The sensor and electronics are made by the Bergoz Instrumentation Company. DCCT is an integrative system, so it works in single bunch or multiple bunch operation.

Tabel 1 gives the main technical parameters.

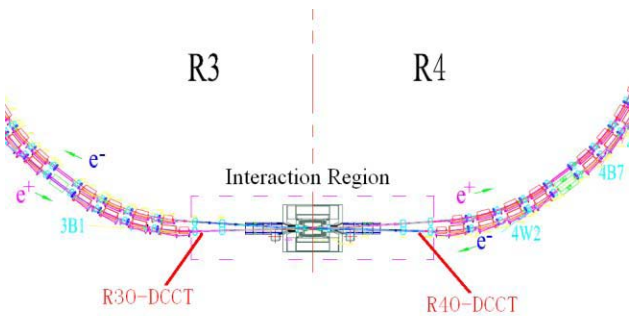

Figure 1: Layout of DCCT

Table 1: The main technical parameters of DCCT

Parameters	Value
Dynamic range	0.0~1.5A
Linearity	0.1 %
Zero drift	<0.05mA
Remarks	shielding needed
Detector size	350 mm with flange
Location	far from RF cavity

THE MECHANICS & INSTALLATION

A vacuum chamber with a ceramic gap has been used for avoiding the parasitic current caused by the chamber's electrical conductivity. Considering the 30 kHz bandwidth of the DCCT's signal, we decided to enhance the high frequency pass band to prevent the bunch frequency component from leaking from the gap when BEPCII operates in the single bunch mode. Thus the cut-off frequency could be lower than the bunch frequency but higher than the pass band of the DCCT. After calculation and simulation in the lab, the preparatory configuration of the system was confirmed. Figure 2 shows the structure and the parameters[3]. Copper foil and a layer of polyester film were used over the gap, to reduce the low-frequency signal leakage. Two magnetic shielding layers were adopted to protect the sensor from unorderly magnetic fields. The outer layer is electrostatic shielding against RF and for circulation of wall current.

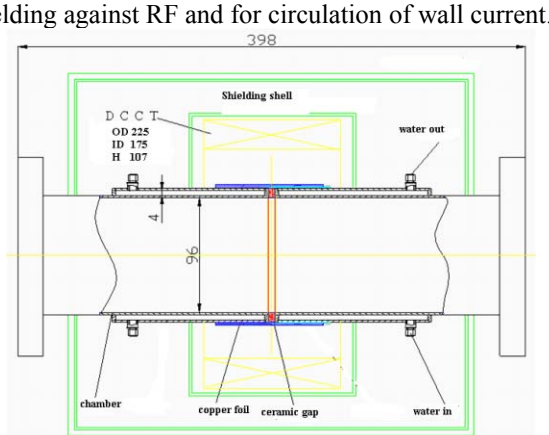

Figure 2: Structure of DCCT tube.

THE ELECTRONICS & DAQ

The electronics and the DAQ system of DCCT are in the local stations of beam instrumentation, and consist of 2 cassettes, 2 DVMs and an IPC. The sensors in the tunnel are connected to the electronics by 120 m of cable. Figure 1 shows the structure. In the earlier design, a low pass filter had been put between electronics and DVM to decrease 50 Hz interference; it has since been removed.

#zhaoying@ihep.ac.cn

The operating modes and ranges can be changed in the local station manually, according to the BEPCII working mode.

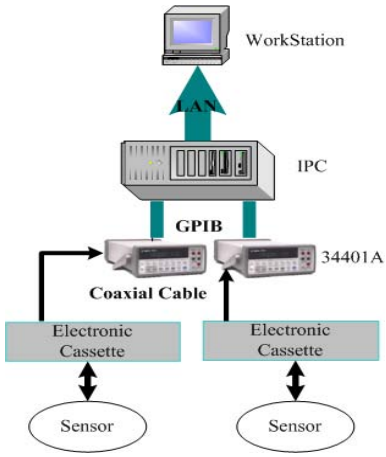

Figure 3: DCCT system structure

The DAQ system is based on DVM Agilent 34401A and GPIB. Programs running in the IPC complete data acquisition, processing and transmission. The program works as an EPICS soft IOC. Authorized users can access and acquire the data to calculate the beam injection rate and the beam loss rate. The historical data are not stored in the local IPC but can be checked in the Archive Database. Figure 4 shows the software structure and Fig. 5 shows the program interface.

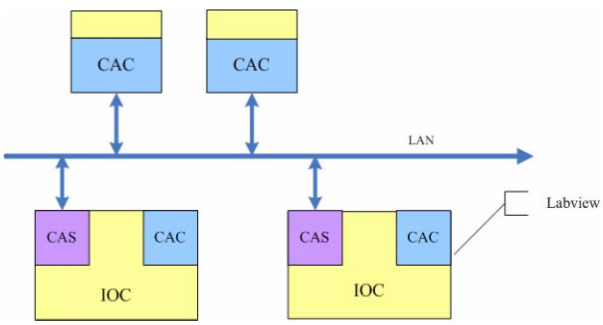

Figure 4: Software structure.

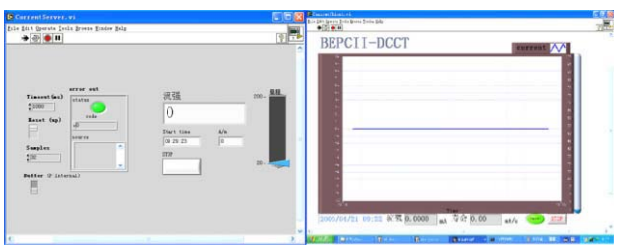

Figure 5: Program interface.

DATA ANALYSIS

The DCCT system in the electron ring played an important role since the first commissioning stage, running in dedicated synchrotron radiation mode.

The discrete lifetime solved

We found when the electron beam current was below 60 mA, the beam life time was somewhat "discreted." The beam lifetime often was related to the degree of vacuum, equipment state and closed orbit distortion, etc., and usually rises as current diminishes. Figure 6 shows the details of the waveform. [2]

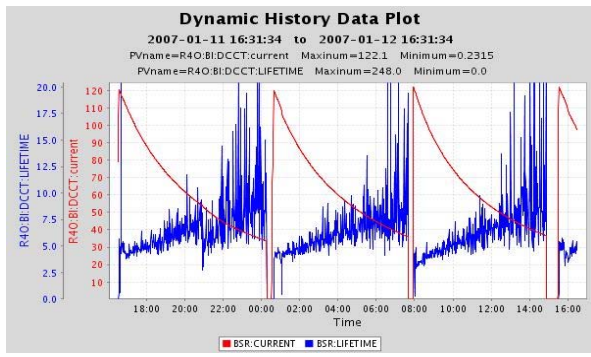

Figure 6: The details of the lifetime wave

The smooth red curve is what would be expected if all parameters of the storage ring were normal. The blue lifetime curve was abnormally shaped as current decreased. The lifetime discrete range was 7% when the current was 120 mA, 30% at the beginning. We thought the issue was noise dither and tried to solve it in the DAQ program. But the result was not satisfactory; even the readout rate was negative impacted.

We analysed the data again and tried to increase the sampling rate and improved the arithmetic for calculating lifetime. By changing the sampling rate of beam current from 5/s to 100/s, added the fitting spot and extended sampling range. The result was much better.

The magnetic field effect

We also found the sensors are sensitive to the magnetic field even with shielding. Figure 7 was the background data record from a machine study time. An obvious fall of current, about 0.3 mA, can be seen. The log showed that only the octupole magnet nearby was adjusted.

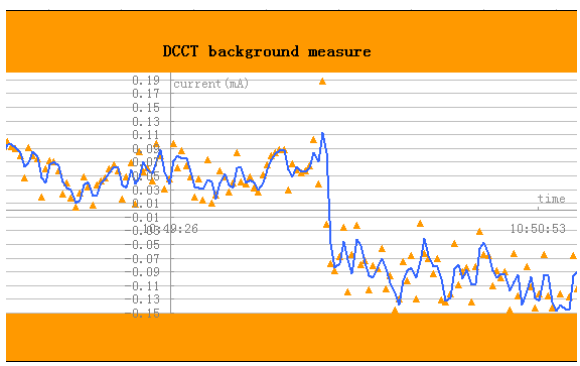

Figure 6: Intercepted from background data record.

So calibration was done periodically to insure the whole system's reliability. We used the standard current source (precision 0.01%) as the input signal entered the

electronics. The readout voltage signal was nearly linear with the current input.

Table 2 gives one of the calibration results. It shows the linearity of the beam current. When the current was 250 mA, the variance between experimental data and real current was about 0.15%. It completely met the demand.

Table 2: One of the demarcation results.

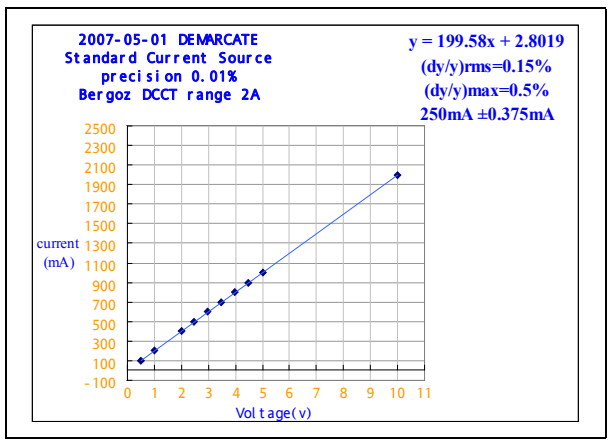

Troubleshooting

In the phase two commissioning, BEPCII was operating in collision mode. The DCCT system in the positron ring showed abnormal background drift from the beginning, comparing to the power of RF cavity; the read out data was incorrect. After calibration, we found that the linearity coefficient was changed 35%.

We did all-around examination and discovered that a signal wire's insulating layer in the cable head was torn and touched another pin, which affected the sensor's demagnetizer function. The tear may be due to careless installation. It was repaired and soon the whole system worked normally.

SUMMARY

BEPCII is undergoing maintenance and we are preparing for the next operation stage. Although the DCCT system is basically running well, there is still a lot to do and opportunity to make progress. As the heating problem of the DCCT sensor when beam current is higher than 500 mA, the automatic adjustment of the measurement range and the automatic adjustment of offset base on the BPM signal, and so on.

ACKNOWLEDGEMENT

I appreciate Dr Jianshe Cao, Dr Li Ma and Dr Chuang Zhang from IHEP for helping me a lot through the whole system. Special thanks to Dr Baogen Sun and Dr Ping Lu from NSRL for the support on the Epics. And The Bergoz Instrumentation Company give technical supports. Also thanks to all the group members from IHEP Acc-center for giving me a lot of useful advises.

REFERENCES

[1] Y. Zhao, J.S.Cao, The summarizing and analysis of the DCCT system, 2007.

[2] C. Zhang, The discussion of beam lifetime in BEPCII, 2007

[3] J.S. Cao, L. Wang, The report of the machine study of new and old DCCT, 2005

SCINTILLATION SCREEN INVESTIGATIONS FOR HIGH CURRENT ION BEAMS AT GSI LINAC

E. Gütlich, P. Forck, R. Haseitl, P. Kowina
Gesellschaft für Schwerionenforschung GSI, Darmstadt, Germany

Abstract

Scintillation screens are widely used for qualitative beam profile monitoring. However, precise measurements might yield ambivalent results, especially for high beam currents. We have investigated the optical properties of various scintillating materials with different beams in the energy range 5.5 to 11.4 MeV/u delivered by the heavy ion linac at GSI. Investigations were not only focused on well-known sensitive scinitillators but also on ceramic materials with lower light yield. Their properties (yield, beam width, higher statistical moments) were compared to different quartz glasses. The image of each macropulse was recorded by a digital CCD camera and individually evaluated. For some materials, a decrease of the light yield occurs. For a focused beam, the imaged width depends on the material. Moreover, the light yield and width depend significantly on the screen temperature, which is increased by beam impact.

DEMANDS AND SETUP

For decades, scintillation screens have been used for beam profile measurement in nearly all accelerator facilities. These screens are an essential part of a pepper-pot ermittance system used for the determination of the width of "beamlets" created by a plate with ≈100 small holes. The realization at GSI, as used for high current operation of UNILAC, is described in [1]. The angular distribution within the phase space is calculated from the intensity distribution of the beamlets. This requires an accurate measurement of the spot's light distribution. However, there had been doubts concerning the accuracy of the pepper-pot method [2], which might be related to possible image deformation by the scintillating screen.

We investigated the optical properties of 16 fluorescence materials with ∞5.5 and 11.4 MeV/u and different beam currents as delivered by UNILAC. Typical sizes for the focused beam were σ≈2mm. Sensitive scintillation screens, like YAG:Ce or ZnS:Ag were irradiated in addition with lower currents. Ceramic materials with less light yield, like BN, ZrO_2, ZrO_2 doped with Mg, pure Al_2O_3 and Al_2O_3 doped with Cr (Chromox) were investigated and compared to quartz-glass (Herasil 102) and quartz-glass doped with Ce (M382); see Table 1.

A movable target ladder, as shown in Fig.1, was equipped with 6 different screens of ∅30mm and installed in a vacuum chamber. The irradiations were performed with pressure of ≈$5x10^{-7}$ mbar. The target ladder allows beam observations without longer interruption, which ensures the same beam properties for all materials. The scintillation was observed by a digital CCD camera (AVT-Marlin) equipped with a monochrome chip of VGA resolution. A Pentax B2514ER lens system of 25 mm focal length equipped with a remote controlled iris was used for compensation of material dependent light yield. Moreover, the camera's inherent amplification was changed by the gain setting. The calculation of the light yield corrects both settings. The reproduction scale for the beam image was 10 pixel/mm. Data transmission was performed by the camera's Firewire interface to a high performance data acquisition system, [3] which enables the storage of an image from each macropulse for individual offline analysis.

Table 1: Compilation of investigated materials

Type	Material	Supplier
Crystal Scintillator	YAG:Ce, BGO, $CdWO_4$, CaF_2:Eu	Saint Gobain Crystals
Powder	ZnS:Ag	HLW
Ceramics	ZrO_2(Z700 20 A), ZrO_2:Mg (Z507), BN, Al_2O_3 and Al_2O_3:Cr (Chromox)	BCE Special Ceramics
Quartz-glass	Pure: Herasil 102, Ce doped: M382	Heraeus Quartz-glass

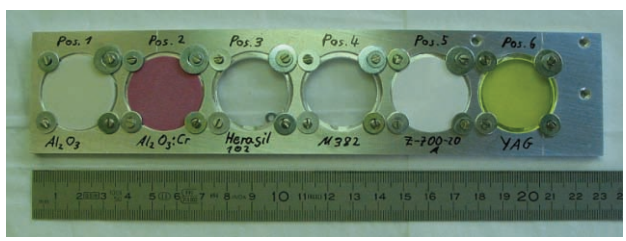

Figure 1: The target ladder equipped with ∅30mm screens is shown. The screen materials prior to irradiation are from left: pure Al_2O_3, Al_2O_3:Cr, Herasil, Quartz:Ce, ZrO_2 and YAG:Ce.

TYPICAL RESULTS AND ANALYSIS

The original beam image (an example is shown in Fig. 2 top) was projected to the beam's horizontal and vertical plane. A quantitative analysis was performed with the projection. In this work we show the horizontal projection but comparable results were obtained for the vertical direction. Two examples of such projections are shown in Fig. 2 bottom. For both displayed materials the total light yield decreases during irradiation. The shape of the peak is preserved for ZrO_2:Mg (shown left). For Al_2O_3 (shown right) the shape is modified mainly around the maximum;

this behavior is reflected by a broader width σ of about 11%. A typical increase of ≈10% corresponds to 0.2 mm, which is too small to be detected by a SEM-Grid, and is of minor importance in case of regular beam alignment. However, for the pepper-pot method it results in an over estimation of the emittance value. For the characterization of the distribution $p_i(x_i)$ not only the centre μ (1st moment) and standard deviation σ (2nd moment) were used, but also the skewness γ (3rd moment), describing the asymmetry and the kurtosis κ (4th moment), describing the peakedness of the distribution as given by:

Skewness: $$\gamma = \frac{1}{\sum p_i} \cdot \sum p_i \cdot \left(\frac{x_i - \mu}{\sigma} \right)^3$$

Kurtosis: $$\kappa = -3 + \frac{1}{\sum p_i} \cdot \sum p_i \cdot \left(\frac{x_i - \mu}{\sigma} \right)^4$$

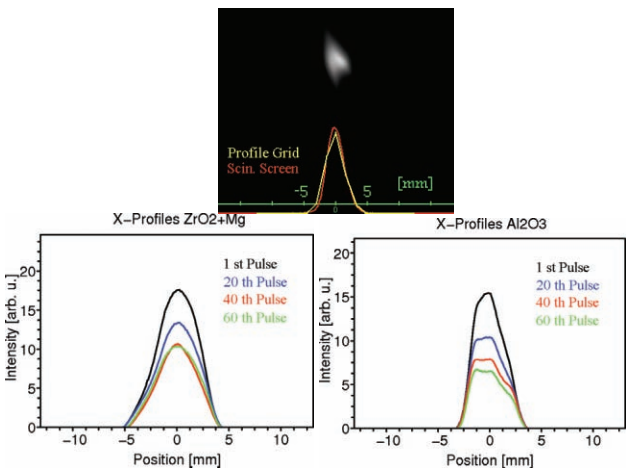

Figure 2: Examples of an original beam image (top) and the projection for ZrO_2:Mg (left) and Al_2O_3 (right) targets irradiated by 40 μA U^{28+} at 11.4 MeV/u. The variation from the 1st to 60th pulse for ZrO_2:Mg is width σ=1.78mm → 1.83mm, and kurtosis κ=-0.50 → -0.61. For Al_2O_3 the variation is significant: σ=1.30mm → 1.45mm and κ=-0.66 → -0.88.

SURFACE MODIFICATION

In Fig. 3 an example is shown for the irradiation with a high current 11.4 MeV/u Ar-beam of about $4x10^{10}$ particles per pulse (ppp), which corresponds to 0.7 mA and a 100 μs long pulse. The light yield of the BN screen decreased within the 1800 macro-pulses where as the beam width increased significantly caused by an irreversible damage of the screen. As expected from investigations of BN at CERN [4], the initially white surface became grey. Comparable surface modifications were observed for most ceramic materials with the least changes for ZrO_2:Mg. However, these modifications do not necessarily imply a lower light yield. In particular, ZrO_2 showed a very fast surface modification without significant decrease of the yield; this result confirms the finding in [4]. By baking ZrO_2 to 250^0C over 4 hours, this modification was reversible. The investigated quartz-glass Herasil showed no visible, permanent surface modification.

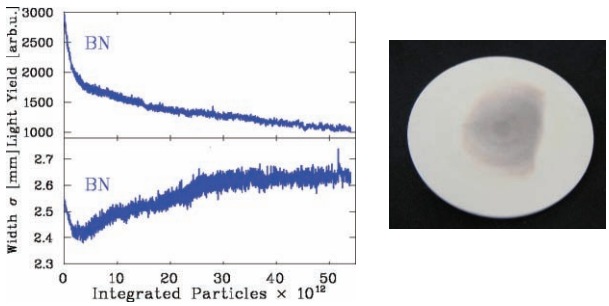

Figure 3: Left: Light yield and beam width σ for BN target irradiated by 1800 macropulses of ≈$4x10^{10}$ ppp Ar^{10+} at 11.4 MeV/u. Right: The ∅30mm BN screen after irradiation.

MEDIUM CURRENT INVESTIGATIONS

For a medium current of 30 μA and 100 μs delivery of Ar^{10+} beam at 11.4 MeV/u, the light yield and the beam width for different materials are compared in Fig. 4. As expected, the investigated materials have up to two orders of magnitude different light yield (integrated over 100 μs beam delivery) with Al_2O_3:Cr being the most and ZrO_2 the least sensitive material. This is consistent with a measurement reported by CERN [5]. The light yield was nearly constant during the irradiation for all materials. However, the determined beam width differed in a reproducible manner between the materials: For the given beam parameters, Herasil showed 22 % less width than ZrO_2:Mg. For three materials (BN, Al_2O_3:Cr and ZrO_2) the same width was recorded. As depicted in Fig. 5, the shape of the distribution differed for the materials, as rep resented by the relative peakedness. (The centre and the skewness were the same for all materials within the statistical fluctuations.) The described behaviour was reproduced with other ion beams of comparable parameters.

The average beam power for the parameters of Fig. 4 was 150 mW, resulting in an average temperature of 47^0 C on the backside of the ZrO_2:Mg screen as determined by aPT100 thermo-element. The peak power was 1.5 kW. Temperature effects will be discussed later on.

Presently, the reason for the different width reading is not well understood; it might be attributed to saturation effects or self-absorption. The different values of the kurtosis could help to clarify this topic. A more positive value is expected if absorption dominates, while a more negative value should occur for saturation. Moreover, a diffuse refraction at the surface and within the bulk material could contribute to a broadening. For ceramics it could be more pronounced due to the finite grain size. A laser-based method described in [5] let us estimate a spatial resolution for Al_2O_3:Cr ceramics to be ≈100 μm (compared to 50 μm for YAG:Ce and 35 μm for CsI, respectively). Since in all cases previously untreated materials were used, the broadening cannot be attributed to

any surface degradation caused by the beam, as discussed above for Fig. 3.

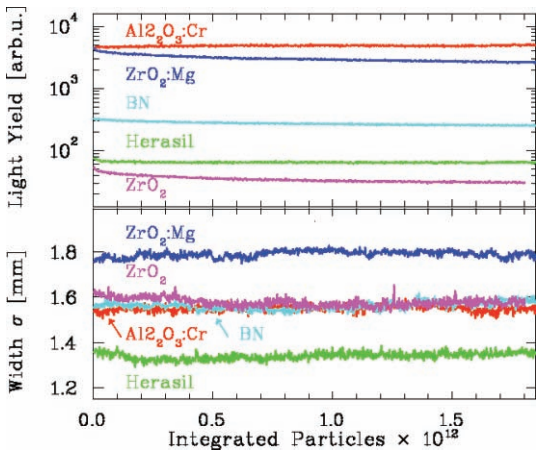

Figure 4: Light yield and beam width for different materials irradiated by 1000 macro-pulses of 1 Hz repetition rate with ≈2x10^9 ppp Ar^{10+} at 11.4 MeV/u.

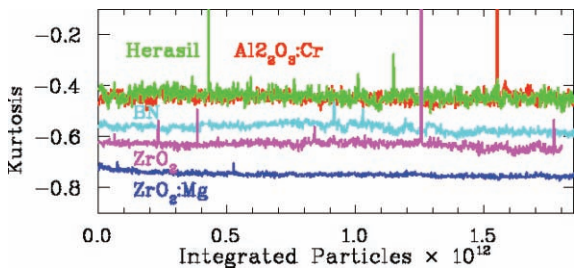

Figure 5: Kurtosis for the beam parameters of Fig. 4.

HIGH CURRENT INVESTIGATIONS

The interest of pepper-pot emittance measurements arises from the UNILAC high current operation with several mA. An example for high current measurement is shown in Fig. 6, where the screens were irradiated by Ar^{10+} with a current of 310 µA within 100 µs delivery time corresponding to 2x10^{10} ppp. The peak power was ≈14 kW while the average power was 3.8 W. As expected the light yield of the various materials differed of several orders of magnitude. In contrary to the medium current measurement of Fig. 4, the yield of ZrO_2:Mg relative to the other materials is lower.

For the four materials Quartz:Ce, ZrO_2:Mg, BN and Herasil the yields dropped significantly during the irradiation. The determined image widths vary within a factor of 2. The variation is larger as compared to the medium current measurement. A light yield decrease coincides with a smaller image width reading, but with a slightly different time constant. Since it was expected that the yield reduction is correlated with the screen temperature, a break in the beam delivery of 3 min was scheduled to let the screens relax to the original room temperature. For Herasil and ZrO_2:Mg the light yield and the beam width showed reproducible time behaviour and reached a constant value. BN suffered from permanent surface modification, as discussed for Fig. 3, while for Quartz:Ce the light yield is permanently reduced without visible surface modification. For Al_2O_3 the yield was constant whereas for Al_2O_3:Cr the yield even increased. In both cases, a broadening of the image width occurred in a reproducible manner.

For all materials, the reading of the beam centre and skewness was constant.

Using a PT100 thermo-element at the backside of ZrO_2:Mg screen the average temperature of 240^0 C was determined for comparable beam parameters with an average power of 2.3 W (compared to 3.8 W for the measurement of Fig. 6). However, the front-side temperature during 100 µs beam delivery was much higher due the ion range of about 20 to 170 µm (depending on the ion species and target density).

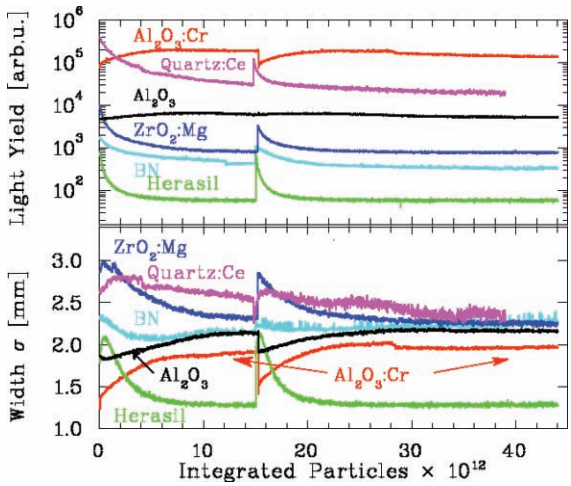

Figure 6: Light yield and beam width for different materials irradiated by 2200 macro-pulses of 2.6 Hz repetition rate with ≈2x10^{10} ppp Ar^{10+} at 11.4 MeV/u. After 5 min of irradiation, a 3 min break was introduced for relaxation to room temperature, followed by 10 min irradiation.

The interpretation of the temperature behaviour is difficult: As reviewed in [6,7] the light yield of scintillators depends significantly on temperature. For commonly used scintillators (like NaI:Tl, BGO, $CdWO_4$) the yield decreases as a function of temperature. It is related to a higher probability of non-radiative transitions from the upper scintillating levels competing with the fluorescence decay. Presently, we are lacking a detailed knowledge of these properties for the investigated materials. Moreover, the behaviour of the image width for Herasil and ZrO_2:Mg can be qualitatively described by the fact that the material is significantly stronger heated at the beam centre as compared to the beam edges. This results in a dominant decrease of the light yield at the peak area. After a certain (material dependent) irradiation time, a steady-state temperature distribution is reached, leading to a constant yield and width reading.

For Al_2O_3:Cr the yield increases with temperature. It might be related to an increased excitation probability from trapped states of the lattice (as it is the basis of thermo-luminescence). For BN and Quartz:Ce the discussed irreversible decrease of the light yield seems to dominate. Due to the different temperature dependent physical processes for the various materials, it does not astonish that the equilibrium width reading differs. For a quantitative interpretation, a detailed model is required, taking thermal diffusion, emissivity and temperature dependent light yield into account.

To investigate the temperature dependences, variable breaks between the irradiation were introduced to allow cooling to room temperature. As depicted in Fig. 7 for Herasil and ZrO_2:Mg, the length of the break did not influence the time constant for the yield reduction, equilibrium value, or width reading. It also proved the reproducibility for those materials.

LOW CURRENT INVESTIGATIONS

For comparison the properties of well known'scintillators under low current irradiation were investigated. In Fig. 8 the results are shown for the 17 nA C^{2+} beam of 100 µs length and 12.6 Hz repetition rate. The average power was 0.6 mW and the peak power 1.1 W. The yield of the materials differs by one order of magnitude, with YAG:Ce being a very efficient scintillator. However, even for these materials, quite different image widths were recorded. BGO showed the smallest value; YAG:Ce, $CdWO_4$ and CaF_2:Eu gave a ≈25% larger reading. This is remarkable, because YAG:Ce is frequently used for low current beam profile measurements. The powder ZnS:Ag shows a significant decrease of the yield and width reading even for this low current irradiation with light ions, i.e., low energy deposition.

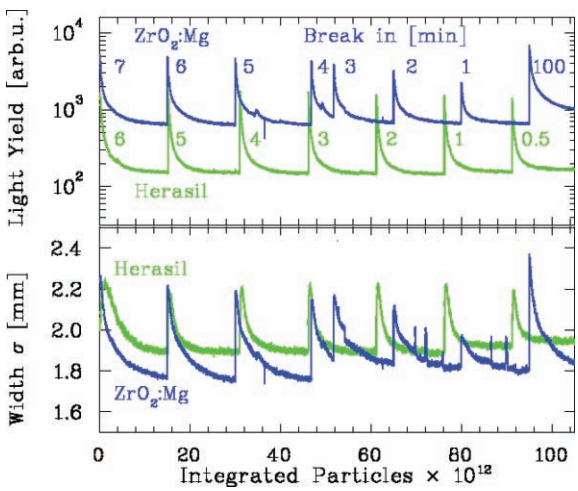

Figure 7: Light yield and beam width for ZrO_2:Mg and Herasil irradiated by 5500 macro-pulses of 2.4 Hz repetition rate with ≈$2.4x10^{10}$ ppp Ar^{10+} at 11.4 MeV/u; break durations are indicated. (The irradiation time varies.)

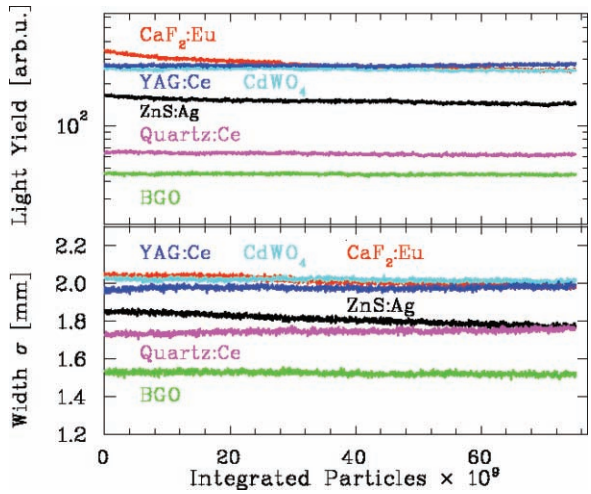

Figure 8: Light yield and beam width for different materials irradiated by 15000 macro-pulses of 12.6 Hz repetition rate with ≈$5x10^6$ ppp C^{2+} at 11.4 MeV/u. 10 macro-pulses are binned together.

CONCLUSION

Several scintillation materials were investigated under various beam conditions. Different readings of the image width for various materials were determined even for well known crystalline scintillators. The described behavior was reproducible under different beam conditions. Further data analysis is in progress to distinguish between saturation, diffuse refraction and self-absorbing of scintillation light. Statistical moments are considered for this purpose, but an interpretation might be difficult due to the presence of several effects. Additional beam-based tests are required to distinguish between these effects. For high current applications, the properties seem to be strongly dependent on the surface temperature, which is significantly increased during beam delivery. This knowledge is essential for choosing a well-suited material for the pepper-pot emittance device. Following the high current investigations at least BN and Quartz:Ce can't be used due to the permanent degradation. It seems that Herasil is a good candidate, because it shows a narrow image width and no significant surface modification even by high current irradiation. Being a transparent material, the diffuse reflections at the grain boundaries are avoided. However, its suitability has to be confirmed by ongoing beam-based investigations.

ACKNOWLEDGEMENT

We acknowledge the valuable discussion and practical support by T. Sieber and M. Frauenfeld from MPI-Kernphysik, Heidelberg. Moreover, we thank Z. Soares Macedo and G. C. Santana from University of Sergipe, Brazil for the supplier of several BGO ceramics [8].

REFERENCES

[1] T. Hoffmann et al., *Proc. Beam Instrum. Workshop Stanford*, p. 432 (2000).
[2] W. Barth, L. Groening, D. Liakin, *Proc. DIPAC03 Mainz,* p. 56 (2003).
[3] F. Becker et al., *GSI Scientific Report* 2007.
[4] C. Bal et al., *Proc. DIPAC05 Lyon*, p. 57 (2005).
[5] R. Jung, G. Ferioli., S. Hutchins, *Proc. DIPAC03 Mainz,* p. 10 (2003).
[6] G.F. Knoll, *Radiation Detection and Measurement*, John Wiley & Son, New York (1999).
[7] G. Blasse, B.C. Grabmaier, *Luminescence Materials,* Springer Verlag (1994).
[8] G. C. Santana, *J. Mater. Sci*. 42:2231 (2007).

COMMISSIONING OF ELECTRON BEAM DIAGNOSTICS FOR A SRF PHOTOELECTRON INJECTOR

T. Kamps*, D. Böhlick, M. Dirsat, D. Lipka, T. Quast, J. Rudolph, M. Schenk, BESSY, Berlin, Germany
A. Arnold, F. Staufenbiel, J. Teichert, Forschungszentrum Dresden, Dresden, Germany
G. Klemz, I. Will, Max Born Institut, Berlin, Germany

Abstract

A superconducting RF (SRF) photoelectron injector is currently under commissioning by a collaboration of BESSY, DESY, FZD and MBI. The project aims at the design and setup of a continuous-wave (CW) SRF electron injector including a diagnostics beamline for the ELBE FEL and to address R&D issues of high brightness CW injectors for future light sources such as the BESSY FEL. The layout and realization of the diagnostics beamline for the electron beam is presented including systems to monitor the momentum, charge, transverse emittance and bunchlength in various operation modes of the injector.

MOTIVATION

Future FEL light sources such as the proposed STARS FEL [1] and the ELBE facility [2] operate with superconducting RF (SRF) for electron acceleration to enable continuous wave (CW) operation generating flexible bunch patterns.

The SRF injector project combines the advantages of photo-assisted production of short electron pulses, high acceleration field at the cathode of an RF field and CW operation of a superconducting cavity. The main challenges are the design of the superconducting cavity with a suitable cathode insertion, the risk of contamination of the cavity with cathode material, and a method to control the transverse emittance of the electron beam. The SRF gun collaboration of BESSY, DESY, FZR and MBI sets out to tackle these issues. The target of the collaboration is to setup a SRF gun [3] together with a diagnostics beamline serving as a test facility for photoelectron injectors. The task of the diagnostics beamline is to ensure safe operation of the injector, check the theoretical model for the injector by measurements and to find an optimum working point for the setup of the injector parameters.

EXPERIMENTAL SETUP

The setup for the photoinjector consists of the SRF gun and the diagnostics beamline as depicted in Fig. 1. The electrons are generated by a pulsed laser beam impinging on the photocathode. The laser is designed to operate at 500 kHz repetition rate delivering pulses of 16 ps FWHM length with 1 μJ pulse energy at 263 nm wavelength [4]. The repetition rate of the laser can be reduced for alignment and beam diagnostics measurements. This laser serves two operation modes at high bunch charge. A second laser is under development for operation of the injector at higher repetition rate (13 MHz) with a reduced bunch charge of 77 pC. The three main operation modes of the injector are summarized in Tab.1. The photocathode is made of Cs_2Te

	ELBE	HC	FEL
RF frequency		1.3 GHz	
Beam energy		9.5 MeV	
Operation		CW	
Drive laser		263 nm	
Photocathode		Cs_2Te	
Pulse length FWHM	5 ps	16 ps	50 ps
Repetition rate	13 MHz	500 kHz	1 kHz
Bunch charge	77 pC	1 nC	2.5 nC
Trans. emittance	1.5 μm	2.5 μm	3 μm

Table 1: Design beam parameters of the three main operation modes: ELBE FEL, at high bunch charge (HC) and BESSY FEL (FEL).

with a quantum efficiency of better than 1 %. This cathode is placed at the entrance of a 3 1/2 cell cavity structure with a RF frequency of 1.3 GHz. The axis peak field of the accelerating mode is 50 MV/m (design value). The cavity structure is embedded in a liquid helium tank. At the exit of the SRF gun the electron beam is focused with a solenoid magnet. After that, the electrons pass the transfer section preparing the beam parameters for injection into the ELBE linac. Behind this section the diagnostics beamline is located, and the beam parameters will be measured.

BEAM CHARACTERIZATION

In order to characterize the performance of the photoinjector, the following beam parameters need to be considered:

- The energy distribution of the beam – the kinetic energy of the electrons and the energy spread. The beam momentum will vary between a few and 9.5 MeV. The minimum momentum spread as expected from simulations will be 36 keV for the low charge operation mode.
- The total beam intensity, together with the time structure. The bunch charge can vary between a few pC

* kamps@bessy.de

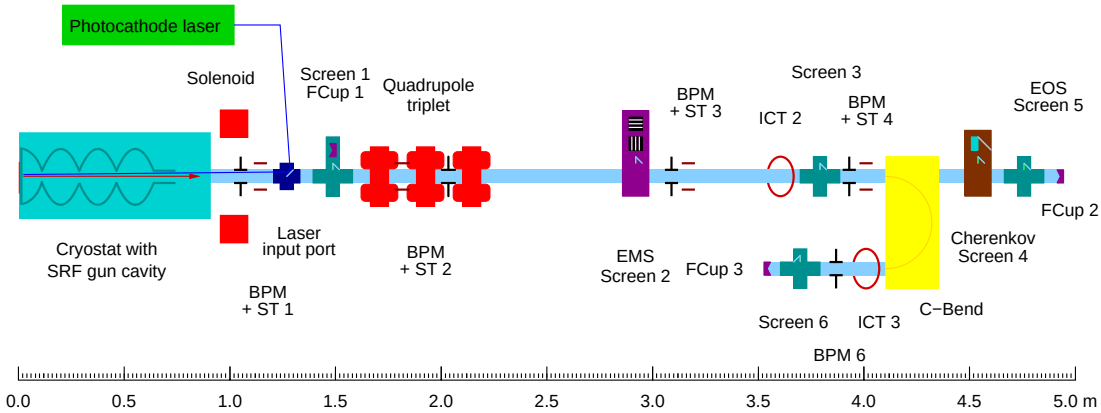

Figure 1: General setup of the SRF gun and diagnostics beamline.

during operation with a Copper cathode and 2.5 nC for nominal operation in the BESSY FEL mode.

- The optical properties, which can be described in terms of the transverse beam emittance. The normalized beam emittance is expected to vary between 1 and 10 mm mrad.

The optical properties are dependent on the intensity and energy distribution of the beam. Therefore all parameters need to be analyzed. In this paper the tools for the characterization of the electron beam are considered.

BEAMLINE OVERVIEW

A schematic overview of the diagnostics beamline and the SRF gun is given in Fig. 1. The diagnostics beamline consists of:

- Six viewscreens for transverse beam profile measurements, marked as Screens 1 to 6 in Fig. 1,
- Five beam position monitors (BPM N) and four steering coil pairs for orbit control (ST M),
- Two integrated current transformers (ICT 1 and 2) to control charge transmission through the beamline,
- One pair of slit masks to analyze the horizontal and vertical beam emittance (EMS),
- One 180 degree dipole spectrometer (C-bend) for momentum and momentum spread measurements,
- A Cherenkov monitor and electro-optical sampling system (EOS) to measure the time structure of the electron pulses, and
- Three Faraday cups, FCup 1 can be inserted at the beginning of the beamline and two (Fcup 2 and 3) are included into the beam dumps.

To keep the diagnostics beamline at low pressure (below 10^{-9} mbar), ion vacuum pumps and ion gauges are mounted below every viewscreen station. For the Cherenkov monitor a differential pumping scheme is applied. Valves are put along the beamline to divide the beamline into different vacuum sectors.

BEAM INTENSITY AND POSITION

Beam Intensity

Faraday cups and integrating current transformers (ICT) are used at several positions to measure the total beam intensity. The Faraday cup is insertable at the location of the first profile monitor port. Two additional Faraday beam dumps are implemented at the dispersive and straight end of the beamline. During commissioning of the beamline average beam currents as low as 50 nA (at 100 kHz repetition rate) have been measured with a sensitive Amperemeter directly connected to the first Faraday cup (FCup1).

Two integrating current transformers [5] are used to continuously monitor the bunch charge at two locations, before and in the dispersive arm of the spectrometer dipole. At low bunch charge and low repetition rate the signal from the ICTs will be amplified by 22 dB using low-noise amplifiers. Tests at the ELBE linear accelerator indicate that bunch charges as low as 10 pC can be resolved with 10% resolution.

Beam Position

The requirements for the beam position measurement are a resolution of better than 100 μm for single bunches for beam offsets as far as 5 mm. The readout electronics has to cope with all operation modes. We use stripline BPMs as implemented at the ELBE accelerator. The striplines have a length of 1/4 λ_{RF} and are mounted in a compact package. The readout electronics utilizes a logarithmic detector for direct RF to DC conversion and a logarithmic amplifier with a large linear dynamic range of 60 dB, the sensitivity of the BPM system is measured to be 0.8 dBm/mm [6].

BEAM PROFILE AND EMITTANCE

Beam Profile

The profile monitors are used to image the full beam at several locations along the beamline and to measure the size of the beamlets released by the emittance measurement slit mask. The relative resolution of the profile monitor has to be better than 10% for full and beamlet imaging. For this purpose thin Yttrium-Aluminum-Garnet (YAG) crystal sheets doped with the visible light scintillator Cerium are inserted into the beampath to produce an image of the transverse charge distribution. This beam image is detected by a CCD camera. The screen material has to be robust and UHV-compatible as the first screen is located in close proximity to the SRF cavity. To provide for the best image fidelity, the screens are mounted at normal incidence to the electron beam. An Aluminum mirror is placed downstream to deflect the fluorescent light out to the camera. Outside the vacuum beam pipe the light is deflected again by a mirror and then focused onto the sensitive area of a CCD camera. The optical focus and magnification can be calibrated by inserting a calibration target at the location of the screen. The minimum object size generated by the crystal screen is dominated by multiple scattering for beam energies below 10 MeV. At 2 to 3 MeV beam momentum the minimum resolution is around 40 μm and at 9.5 MeV the resolution is around 10 μm. During commissioning, the viewscreens were able to withstand operation conditions with several thousand nC per hour without any visible degradation of the beam image. In Fig. 2 the first beam images of the electron beam generated during commissioning are shown.

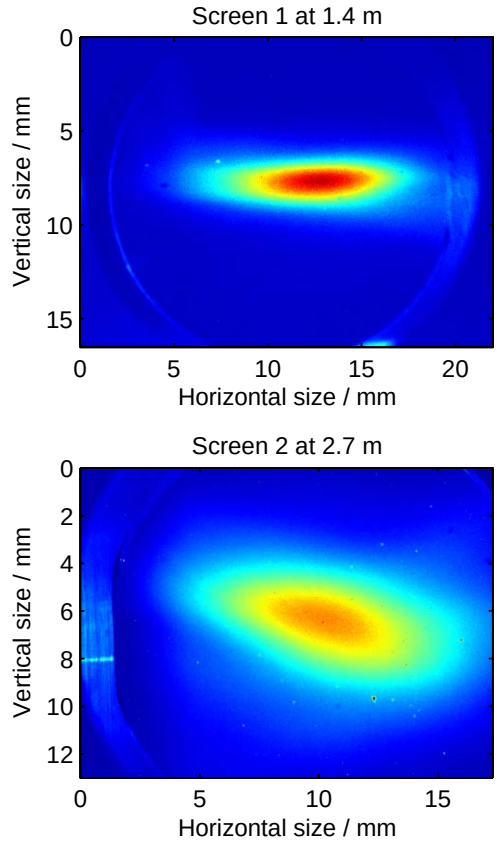

Figure 2: First beam images produced with the electron beam generated by the SRF injector.

Emittance Measurement Section

The electron beam generated in the injector is in all nominal operation modes space-charge dominated. For this reason a double slit-based phase space sampling method [7] is considered, where an actuator-mounted slit mask is moved perpendicular across the beam. The purpose of collimating the beam intensity with slits is two-fold. The first is to cut low current beam portions out of the high brightness beam. These small beamlets have the same divergence as the original beam with negligible effects due to space-charge. The second purpose is to separate the beam into many beamlets, whose intensity distribution at some downstream point can be measured to give the phase space distribution of the beam; the width of each beamlet gives a measure of the width of the transverse momentum distribution at each slit, and the centroid of the beamlets gives the correlated offset of the momentum distribution at each slit. The normalized beam emittance can then be calculated according to

$$\epsilon_n = \beta\gamma\sqrt{< x^2 >< x'^2 > - < xx' >^2}. \qquad (1)$$

Here $< x^2 >$ and $< x'^2 >$ are the RMS beam size and divergence of the beam, $< xx' >^2$ the correlation between size and divergence and $\beta\gamma$ the relativistic factors.

The contribution of the slit width towards the beamlet size should be small, but it must be large enough to supply the beamlets with sufficient charge. To meet the requirements of various operation modes, a slitmask with two pairs of slits with 100 μm and 50 μm width are constructed. For single-shot measurements of the beam emittance, an array with five 100 μm slits is also included in the slitmask. The size of the released beamlets will be measured with three viewscreen stations downstream in the diagnostics beamline. The stations are located 0.6 m, 1.6 m and 2.0 m after the slit mask. The beamlet sizes at these stations vary between 60 μm and 250 μm. The mask it-

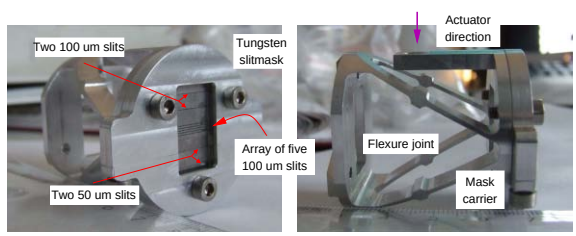

Figure 3: EMS slitmask inside the carrier, which can be tilted with respect to the beam by a flexure joint.

self is made of 1.4 mm thick Tungsten, being an optimum between acceptance and background due to Coulomb scattering. The slits were produced by electro-discharge machining the bulk material with a wire. The material is quite brittle and splinters were found in the slit opening. For this reason the 50 μm slits were produced by sandwiching two polished half-plates. The complete slitmask is placed inside a carrier (see Fig. 3), which can be moved by an actuator inside the beam path. The tilt of the slit mask can be changed by a movable flexure joint. This second actuator is mounted inside the large actuator moving the mask in and out. The size of the individual slits and the spacing of the multi-slit array have been measured by analyzing the Fraunhofer pattern of the slits illuminated by a monochromatic light source. The average slit width for the broad single slits is $d_{sgl} = 85 \pm 2$ μm and for the slit array $d_{arr} = 84 \pm 8$ μm. The spacing of the slit array is 499 ± 48 μm.

TEMPORAL PROFILE

To verify the shape and length of the temporal profile of the electron bunches, two techniques with ps time resolution will be used. Inside the Cherenkov monitor [8] the electron bunches pass a thin sheet of radiator. The radiator emits a Cherenkov radiation pulse with the same time structure as the electron bunch. A streak camera can be used to measure the shape and length of this radiation pulse with ps resolution. This technique is destructive to the electron bunches as the beam size increases during the passage through the radiator. The electro-optic sampling (EOS) diagnostic technique [9] inspects the electric field co-propagating with the electron bunch and enables non-destructive single-shot measurement with sub-ps resolution.

Cherenkov Monitor

The first temporal profile monitor is located after the spectrometer magnet in straight direction. The Cherenkov process is characterized by the Cherenkov-angle $\cos\theta_C = 1/(\beta n)$ (where β is the relativistic velocity factor of the electrons and n the refractive index of the radiator), under which a radiation cone is emitted. The number of emitted photons per pathlength in a bandwidth between wavelength λ_1 and λ_2 is

$$\frac{dN_\gamma}{dx} = 2\pi\alpha z^2 \cdot \sin^2\theta_C \cdot \frac{\lambda_2 - \lambda_1}{\lambda_1 \lambda_2} \qquad (2)$$

where z is the charge in elementary charge units and α the fine-structure constant [10]. Silica aerogel plates of small dimensions with refractive index of $n = 1.008$ and 1.028 are available [11] and considered as Cherenkov radiator. The threshold energy for $n = 1.008$ is 4.1 MeV, for $n = 1.028$ is 2.2 MeV. After emitting Cherenkov radiation, the electron bunch and the light pulse exit the Aerogel plate through a transparent quartz window. The light is then

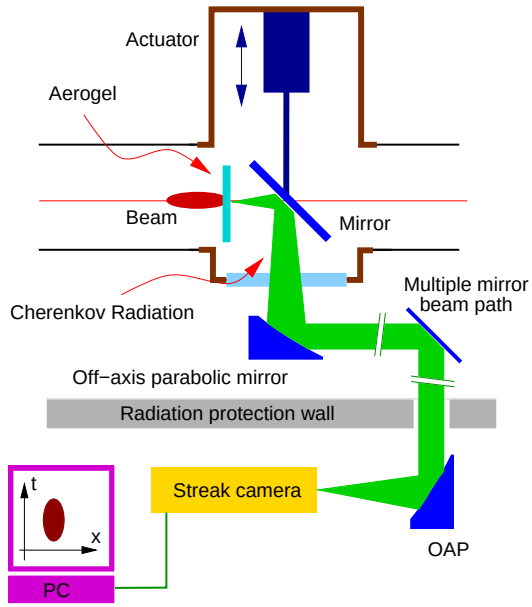

Figure 4: Schematic of the Cherenkov monitor.

reflected by a mirror and leaves the beam pipe through a viewport window (see Fig. 4). The Cherenkov light is then transported with mirrors to the streak camera [12] over a distance of roughly 20 m. The Cherenkov light exits the radiator with large divergence, therefore a relay imaging with focusing elements is necessary to achieve a high photon collection efficiency. Using lenses for this can cause dispersion of the short photon pulse up to several ten picoseconds. Therefore only reflective optical elements, plane and off-axis parabolic mirrors, were considered for the light transport. The setup was simulating with the ray-tracing code RAY [13]. The pulse broadening is dominated by the dispersion in the viewport window, which is $\Delta t = 1.4$ ps for the first viewport and $\Delta t = 3$ ps for the second. Both values are calculated assuming the collection of the wavelength region between 300 and 600 nm. The resolution can be enhance by limiting the wavelength band with bandpass filters.

Laser Pulse Measurements

First tests with the streak camera were perfomed to check the laser pulse length and the synchronisation of the streak camera to the master oscillator. The intensity of the laser pulses was attenuated by using several low reflectivity optical flats. Synchronization between laser and streak camera is achieved by a 250 MHz PLL synthesizer driven by a 13 MHz reference signal from the laser itself. The synchronization accuracy between laser and streak camera was measured to be better than 2 ps. In Fig. 5 the results for the pulse length measurement are shown. For each data point five streak images were taken. Each image was analyzed by applying a Gaussian fit to the time-projection axis data. The average RMS pulse length for the laser is $\sigma_{t,green} = 6.9 \pm 0.2$ ps and $\sigma_{t,UV} = 6.6 \pm 0.2$ ps. The laser

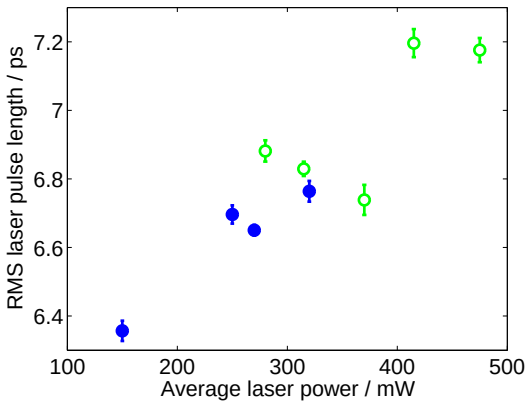

Figure 5: Results from laser pulse length measurements for the green (green and open points) and UV (blue and filled points) output of the laser for different average power levels.

pulse length does not depend on the average laser power. The RMS pulse length of the electron bunches after extraction out of the cathode as measured with a phase scan is $\sigma_e = 7.7 \pm 3.1$ ps.

MOMENTUM AND MOMENTUM SPREAD

The momentum distribution of the electron beam will be measured with a 180^o dipole magnet spectrometer. The spectrometer is a H-type dipole with a bending radius of $\rho = 200$ mm and a gap height of $g = 40$ mm. The field map of the magnet has been measured with a hall-probe on a movable stage. By moving the dipole and the hall-probe a two-dimensional map of the field distribution was measured. The relative homogeneity of the field between the pole shoes was measured to be $2.5 \cdot 10^{-4}$, which is below the value specified. A 180^o dipole magnet was chosen in order to unfold the contribution of the emittance and Twiss parameter to the beam size measured in the dispersive arm. The deconvolution can be done by putting a second screen in the non-bend plane in a location with the same $|R_{11}|$ and $|R_{12}|$ elements of the transfer matrix [14]as for the bend plane. Such a screen is placed at position of the Cherenkov monitor of the beamline (SC4 in Fig. 1). Simulating the setup with the particle tracking code ASTRA indicates that a momentum spread as low as $\Delta p = 6.3$ keV/c at 10 MeV beam energy and 1 nC bunch charge can be resolved using the setup and the deconvolution technique.

SUMMARY AND OUTLOOK

The diagnostics beamline currently under construction plays a vital role in the commissioning and successful running of the SRF injector. Results from first beam tests at low bunch charge indicate the efficiency of the individual devices.

ACKNOWLEDGMENTS

We want to thank the engineers and technicians from BESSY, FZD and the Max Born Institute who contributed to the SRF injector project. We are grateful bey the assistance received by DESY Hamburg and SLAC. We acknowledge the support by the German Federal Ministry of Education and Research Grant 05 ES4BR1/8.

REFERENCES

[1] M. Abo-Bakr *et al.*, "STARS: A two-stage high-gain harmonic generation FEL demonstrator," *Prepared for Particle Accelerator Conference (PAC 07), Albuquerque, New Mexico, 25-29 Jun 2007*

[2] P. Michel *et al.*, "The Rossendorf IR-FEL ELBE," *Prepared for 28th International Free Electron Laser Conference (FEL 2006), Berlin, Germany, 27 Aug - 1 Sep 2006*

[3] K. Möller *et al.*, "Development of a superconducting radio frequency photoelectron injector," Nucl. Instrum. Meth. A **577** (2007) 440-454.

[4] I. Will, G. Klemz, F. Staufenbiel and J. Teichert, "Photocathode laser for the superconducting photo injector at the Forschungszentrum Rossendorf," *Prepared for 28th International Free Electron Laser Conference (FEL 2006), Berlin, Germany, 27 Aug - 1 Sep 2006*

[5] Bergoz Instrumentation, "Integrating Current Transformer User's Manual Rev 3.0," 2006

[6] P. Evtushenko, "Electron Beam Diagnostic at the ELBE Free Electron Laser, " PhD thesis, presented at the Technical University Dresden, 2004

[7] J. Rosenzweig, G. Travish, "Design Considerations for the UCLA PBPL Slit-Based Phase Space Measurment System," UCLA PBPL Note 1994

[8] T. Watanabe *et al.*, "Overall comparison of subpicosecond electron beam diagnostics by the polychromator, the interferometer and the femtosecond streak camera," Nucl. Instrum. Meth. A **480** (2002) 315.

[9] I. Wilke, A. M. MacLeod, W. A. Gillespie, G. Berden, G. M. H. Knippels and A. F. G. van der Meer, "Single-shot electron-beam bunch length measurements," Phys. Rev. Lett. **88** (2002) 124801.

[10] C. Grupen, "Particle Detectors," Cambridge University Press (June 28, 1996).

[11] A. Y. Barnyakov *et al.*, "Development of aerogel Cherenkov detectors at Novosibirsk," Nucl. Instrum. Meth. A **553** (2005) 125.

[12] Hamamatsu Photonics, "Universal Streak Camera C5680 Series Manual," 2003

[13] F. Schäfers, "RAY, the BESSY raytrace program," BESSY Technical Report TB 202 (96).

[14] K. L. Brown, "A first and second order matrix theory for the design of beam transport systems and charged particle spectrometers," SLAC-R-075, Adv. Part. Phys. **1** (1968) 71.

STRIPLINE DEVICES FOR FLASH AND EUROPEAN XFEL

M. Dehler, G. Behrmann, Paul Scherrer Institut, Villigen PSI, Switzerland
S. Vilcins, M. Siemens, DESY, Hamburg, Germany

Abstract

A prototype fast intra-bunch train feedback system is currently under development which is to be tested at FLASH. For pickups as well as kickers, stripline devices have been developed. The new pickup is based on earlier designs used in the transfer lines of the Swiss Light Source as well as in the proton cyclotron PROSCAN at PSI; in particular, the stripline electrode output coupling is intentionally mismatched in order to increase the shunt impedance seen by the beam. Two versions have been designed for a center frequency of 1.65 GHz and a loaded Q of 35. Prototypes have been fabricated and built into FLASH. The stripline kicker consists of four main elements (all in-vacuum): two stripline electrodes fabricated from extruded aluminum and two metallic ground planes, held in place by ceramic spacers. The latter reduce the mutual inductance between the electrodes and optimize the RF match for asymmetries in the RF feed. Prototypes have been built, measured in the lab, and are now in the process of being installed into FLASH.

INTRODUCTION

As part of the Swiss contribution to the European XFEL project, the Paul Scherrer Institut is developing the prototype of an intra-bunch train. The feedback system has to correct for fast transverse orbit fluctuations within the bunch train, which are due to causes as beam loading and wake fields. Each plane, horizontal and vertical, has a dedicated system consisting of two upstream pickups for the measurement, two kickers for the correction of offsets, followed by a pair of downstream pickups used to calibrate the feedback gain. The electric signal chain consists of an analog RF front end, which down converts the pickup signals to base band, a fast, FPGA based, digital processing board with ADC and DAC mezzanines for the signal conversion, and high power broad band RF amplifiers feeding the kickers. For the European XFEL, two sets of systems are foreseen, one working after the injector region at 150 MeV and the other at the end of the main LINAC at 18 GeV (For more information on the general layout see [1]).

KICKER

The bunch distance within the bunch train is 200 ns; this time period should be matched by the total latency of the feedback system. Within the latency budget, a maximum fill time of 10 ns is foreseen for the kickers – a choice, which a priori excludes alternative options such as air coils. This requirement would lead to a maximum design length of 3 meters for a strip line kicker. For the prototype, we plan to replace existing stripline kickers at FLASH with the new designs, thus to be compatible an even shorter overall length of 1 meter was chosen.

Table 1: Kicker Specifications

Active length	1000 mm
Total length	1030 mm
Beam pipe diameter	34 mm
Bandwidth	50 MHz
Kick (P = 1W/port)	1 keV/c
Input impedance (differential mode)	50 Ω
Input impedance (common mode)	61 Ω

The required bandwidth, on the order of 2.5 MHz (coming from the 200 ns bunch spacing), is no problem given the fact that latency requirements lead to a far larger value. Table 1 gives an overview of the specifications.

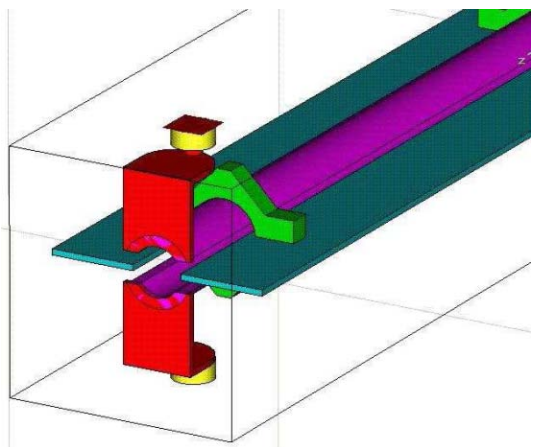

Figure 1: Front part of electrode assembly

The electrode assembly shown in figure 1 is a self supporting structure consisting of a pair of electrodes and two ground plates clamped together using ceramic spacers. The aluminum striplines are manufactured by extrusion in order to minimize twist and sag. Thus, an excellent stability and tolerance of the assembly is guaranteed.

The kicker is operated in differential mode with the electrodes at opposite polarity, the characteristic impedance seen by the amplifiers being 50 Ω. Phase and amplitude imbalances will show up as an additional common mode signal. This signal component itself is no problem for the beam itself, since it induces only a very minor longitudinal acceleration for the beam. The challenge lies in the mismatch at the input – for a standard electrode assembly without ground plates, the characteristic impedance is quite

a bit higher – which may cause problems for the amplifier electronics. This is the reason for the additional ground plate, which, while having no influence on the differential mode, lowers the characteristic impedance of the common mode to an acceptable 61 Ω.

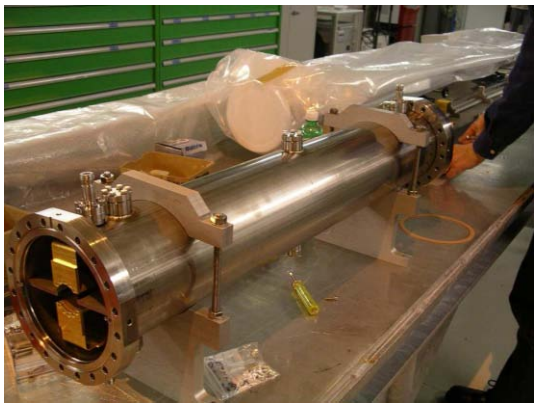

Figure 2: Photo of assembled kicker (Metallic front cap missing)

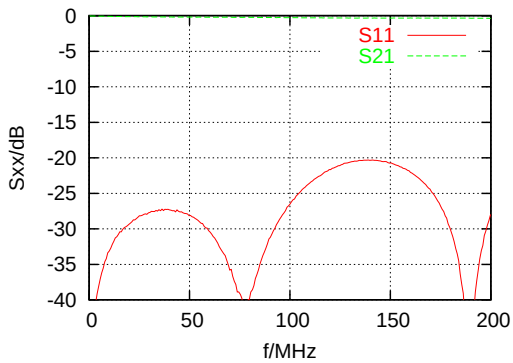

Figure 3: Measured scattering parameters

Three prototypes have been fabricated, two to be inserted into FLASH and one as a lab prototype for testing at PSI (Fig. 2). Figure 3 shows the measured reflection and transmission for the prototype. The maximum reflection within the bandwidth of interest of -27 dB is sufficient for our application. It is a little bit higher than the match of -32 dB predicted from numerical simulations using MAFIA [3], the difference probably comes from some last minute changes in the layout of the ceramics spacers.

The short range wakes and the longitudinal beam impedance were computed with CST Particle Studio [4], figures 4 and 5 show the results. The peak of the beam impedance is on the order of 700 Ω; with an average beam current of 5 mA during the EXFEL bunch train, this means a maximum wake of 3.5 kV, which is acceptable.

Currently, two prototypes of the kicker have been installed into FLASH to be tested with the beam.

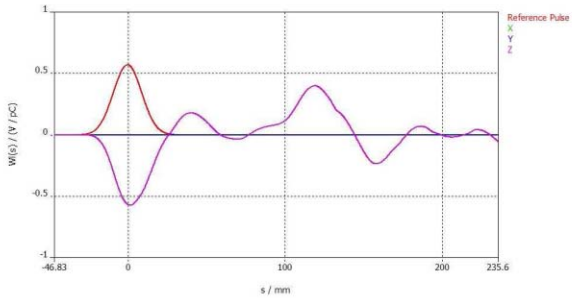

Figure 4: Short range wake field assuming a bunch charge of $Q = 1nC$ and an rms length of $\sigma = 9mm$.

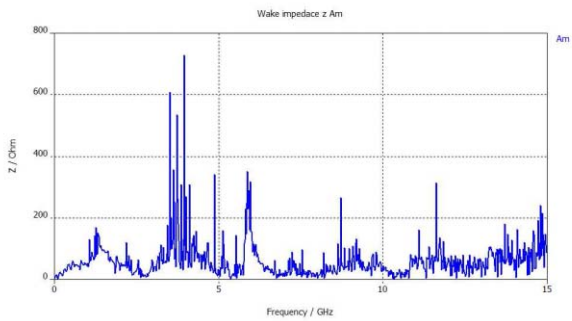

Figure 5: Computed longitudinal beam impedance

STRIPLINE PICKUPS

The conventional strip line design consists of strip line electrodes shorted on one side and perfectly matched to the output coupler. Its FIR pulse response consists of two peaks equivalent to a transfer impedance of

$$Z_T = \frac{U_{out}}{I_{beam}} = jZ_l e^{-j\omega\tau} \sin\omega\tau$$

where $\tau = l/c$ is the electrical strip line length and Z_l the characteristic impedance of the strip line and output coupler.

If the output coupler is shifted from the end of the stripline toward the grounded end of the electrode, the combined impedance of the short at the end plus the coupler is transformed to a narrow band peak with a corresponding increase of output power.

Given the coupling between the strip lines, there are three different resonant frequencies inside the structure, the the monopole/sum resonance, the difference/dipole resonances and a quadrupole resonance. The central frequency of the measurement should lie in between the monopole and the dipole resonances. The bandwidth/Q factor must be chosen suitably in order to give enough overlap for the measurement.

Since this approach was already used for the design of the stripline BPMs at the transfer lines of the Swiss Light Source as well as a prototype tested at the proton treatment

facility PROSCAN[2], it was decided to adapt it for the prototype of the intra-bunch train feedback system.

Current Design

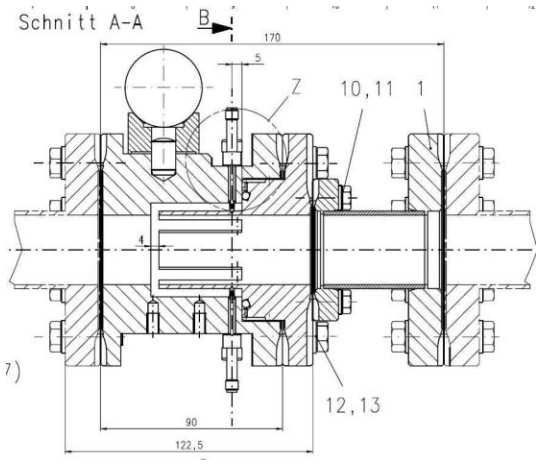

Figure 6: Cut view of stripline pickup

The center frequency was chosen as a multiple of the FLASH reference clock at 1.625 GHz. If we allow for a latency (corresponding to the roll off time of the pulse response) of 10 nsec, a quality factor of up to 50 is possible. In addition we have to keep in mind the required overlap between monopole/dipole resonances and the measurement frequency. With a difference between monopole and dipole of 35 MHz, this leads to a slightly lower limit of 45. For added security, the design goal was set to 35.

Figure 6 shows the cross section of the stripline and table 2 gives the respective specifications. The stripline is coupled out roughly 10 millimeters from the ground point, giving loaded Q factors of over 30 for the sum (monopole) and difference (dipole) modes. To avoid contact problems between the RF feedthroughs and electrodes as well at the contact surface of the vacuum tank, the inner part of the electrode assembly is gold plated.

Table 2: Specifications of Stripline BPM

Design frequency	1625 MHz
Sum resonance	1615 MHz
Shunt impedance sum mode	480 Ω
Loaded Q sum mode	32
Dipole resonance	1650 MHz
Loaded Q dipole mode	37
Sensitivity	10.1 mm

Figure 7 shows the reflection for monopole, dipole and quadrupole excitation. The minimum reflection of about 1.2 dB corresponds to an internal Q of 480. Power loss calculation using MAFIA would give Qs of 180 for a pure stainless steel device and 1200 for an ideal gold coating. Given that internal losses are relatively minor compared to the external ones, the actual value of the internal Q is anyway of negligible importance.

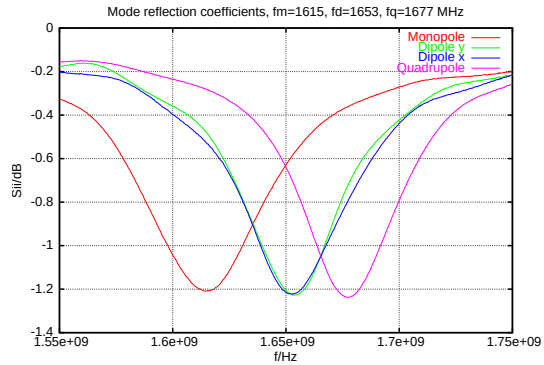

Figure 7: Measured reflection factors for monopole (all ports in phase), dipole (a pair of opposite ports in counter phase) and quadrupole excitation

Asymmetries in the structure were estimated by measuring the cross talk between the monopole and the dipole modes. As the sum (or intensity) signal also shows up as a dipole component, this corresponds to a shift of the electric center of the structure. For the devices measured, we obtained offsets up to 800 μm.

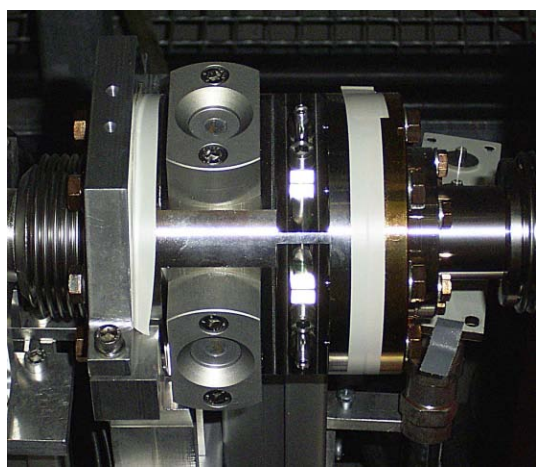

Figure 8: Stripline prototype inside FLASH

Further Developments

During the development of the stripline monitor as well as the RF front ends, the following critical aspects were observed. First, we are working at higher frequencies (compared to earlier versions), so that the quality of the contact between feedthrough and electrode can become a problem. Secondly, the difference in frequency between monopole and dipole mode creates a challenge for the development of fast latency RF front ends – phase rotations can create spurious signals in the down-converted output. A third minor, but visible effect is due to the quadrupole mode in the structure, which is responsible for quadratic nonlinearities in the measurement.

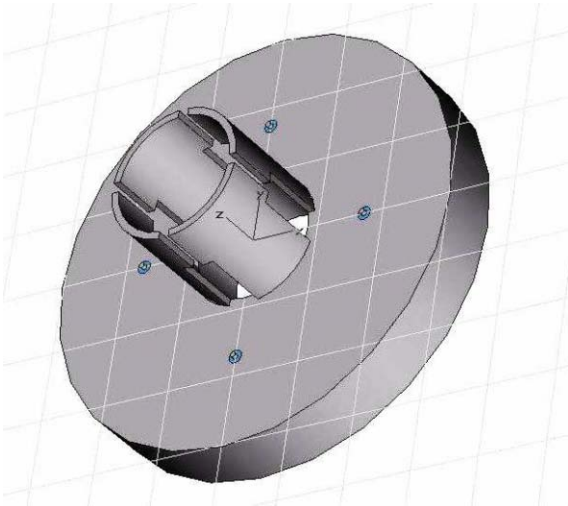

Figure 9: Electrode geometry giving equal resonance frequency for sum and difference mode.

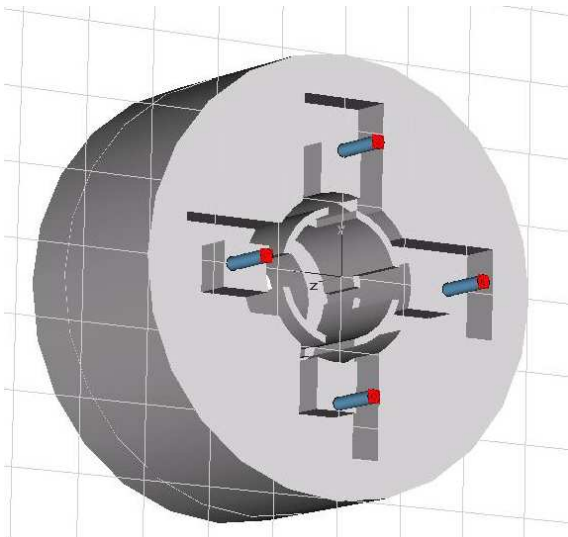

Figure 10: Coupling using a half-ridged waveguide to coaxial line transition

A new conceptual design addresses these points. The frequency difference between monopole and dipole depends on the mutual capacitive and inductive coupling between adjacent electrode, typically leading to a higher dipole frequency. If, as shown in figure 9, we add a capacitive load to the end of the striplines by widening them at their ends (which will only show an effect when the electrodes are at different potentials, as e.g. for the dipole mode), the dipole and quadrupole modes will move down in frequency toward the sum mode.

Contact problems at the electrode are eliminated completely by magnetic coupling using a half ridged wave guide, as shown in figure 10, which is followed by a transition to the coaxial feedthrough, which is easy to manufacture.

Nonlinearities stemming from the quadrupole mode are addressed as follows. The normal approach is to align the couplers with the electrodes, which leads to a homogeneous coupling to all modes. Now let us rotate the coupling slots by 45 degrees with respect to the stripline line. In this case, the coupler will see the average field (or voltage) of the two adjacent electrodes. The sum mode with equal voltage on all electrodes will couple the strongest, followed by the dipole mode. The quadrupole mode has alternating polarities on the electrodes, therefore the average is zero at the coupler and its nonlinear contribution is suppressed at the output. Damping of the quadrupole will be purely due to conductive losses inside the structure.

Table 3: Modal spectrum of improved design including internal losses (Material stainless steel)

Mode	frequency	Q factor
Monopole	1637 MHz	17
Dipole	1641 MHz	48
Quadrupole	1640 MHz	305

Table 3 lists the frequencies and Q factors for the modes. At first glance, the fact that sum and difference modes have different loaded Qs may look like a drawback. However, filtering the electrode signals down to the more restricted bandwidth of the difference signal will suppress part of the strongly dominating sum signal. The level of the difference signal will not be affected, the overall sensitivity of the system is effectively increased.

An alternative time domain technique would be to use a wide bandwidth front end to sample the signals, starting i.e. a few nanoseconds after the initial maximum, where the wide bandwidth sum signal has already decayed with respect to the difference signal. Figure 11 shows the respective signals.

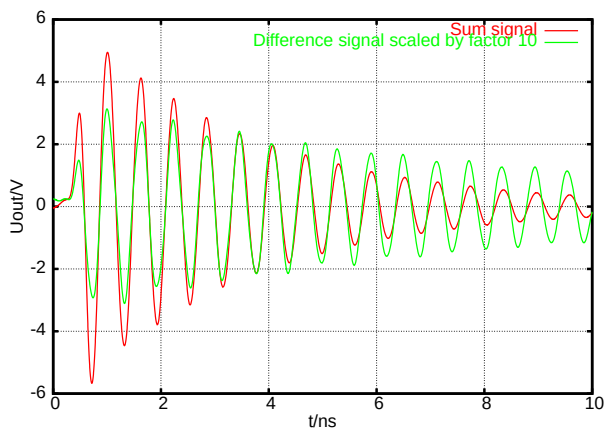

Figure 11: Sum and difference signals using signals from two opposite electrodes for a 1 nC bunch at 1 mm offset as computed with CST Particle Studio. Both signals were low pass filtered to eliminate signals from higher order resonances. To improve visibility, the difference signal was scaled up by a factor 10.

CONCLUSION AND OUTLOOK

As of the submission of the article, three prototypes of the stripline BPMs were built into FLASH and first tests with RF front end have been performed. In discussions between PSI and DESY, it has been decided, that cavity BPMs are going to used for the final system at the European XFEL, so further development of these devices (for this application) has been suspended for now.

Prototype stripline kickers are assembled and have been installed into FLASH. The final version will still need minor revisions to accommodate the differing size of the vacuum chamber and device length at the European XFEL.

REFERENCES

[1] B. Keil et al., "Design of an Intra-Bunch-Train Feedback System for the European X-Ray FEL", DIPAC07, May 20-23 2007, Venice, Italy, in press.

[2] M. Dehler, "Resonant strip line BPM for ultra low current measurements", DIPAC05, Jun. 6-8 2005, Lyon, France, pp. 284, http://www.JACoW.org.

[3] MAFIA rel. 4.0, http://www.cst.de

[4] Microwave Studio, http://www.cst.de

MEASUREMENTS AND ANALYSIS OF LONGITUDINAL HOM DRIVEN COUPLED BUNCH MODES IN PEP-II RINGS *

T. Mastorides†, C. Rivetta‡, J.D. Fox, D. Van Winkle
Stanford Linear Accelerator Center
Stanford, CA 94309, USA

Abstract

The growth rates of the longitudinal higher-order impedance-driven beam modes have greatly increased since the initial PEP-II design and commissioning. This increase is attributed to the addition of 6 1.2MW RF stations with 8 accelerating cavities in the HER and 2 1.2MW RF stations with 4 accelerating cavities in the LER, which allowed operations at twice the design current and almost four times the luminosity. As a result, the damping requirements for the longitudinal feedback have greatly increased since the design, and the feedback filters and control schemes have evolved during PEP-II operations.

In this paper, growth and damping rate data for the higher-order mode (HOM) driven coupled-bunch modes are presented from various PEP-II runs and are compared with historical estimates during commissioning. The effect of noise in the feedback processing channel is also studied. Both the stability and performance limits of the system are analyzed.

LONGITUDINAL INSTABILITIES

The PEP-II rings have exhibited coupled-bunch longitudinal instabilities since commissioning. The longitudinal instabilities in PEP-II are driven by two impedance sources: cavity fundamental and cavity HOM. The LLRF systems use direct and Comb loop feedback to reduce the effective impedance of the cavity fundamental. To further damp these instabilities two additional feedback systems are used: the Low Group Delay Woofer (LGDW) and the Longitudinal Feedback (LFB).

The band limited LGDW addresses the beam motion from in-cavity low-order modes via a signal from a beam pick-up and control paths through the RF stations [1], [2]. The cavity fundamental driven beam modes have been studied and predictions for higher currents, including studies of different configurations have been presented [3], [4].

The LFB is a wideband bunch by bunch channel that addresses all modes via a digital control filter and broadband longitudinal kickers. The LFB is needed to control instabilities from the cavity HOM impedance. It is a Digital Signal Processing (DSP) based flexible programmable system that can run FIR or IIR filters. A block diagram of the LFB system is shown in Figure 1.

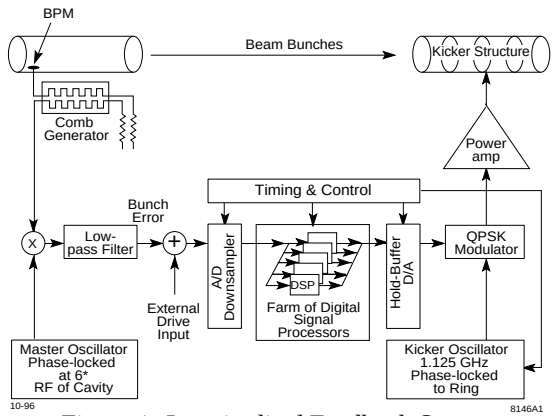

Figure 1: Longitudinal Feedback System.

This paper uses machine measurements in HER and LER to quantify the HOM driven growth rates, quantify the achieved performance of the broadband feedback, and highlight the performance limits in the systems as constructed [5].

HOM-DRIVEN MODES: GROWTH AND DAMPING RATES

During the PEP-II design and commissioning, the impedance driving beam instabilities was estimated from cavity measurements [6]. The impedance estimates allowed calculations of the expected growth rates for the HOM driven coupled-bunch modes, as shown in Figure 2 from [7]. The growth rates were calculated during commissioning for the design parameters of 1 A and 20 cavities for the HER and 2.25 A and 4 cavities for the LER. From this

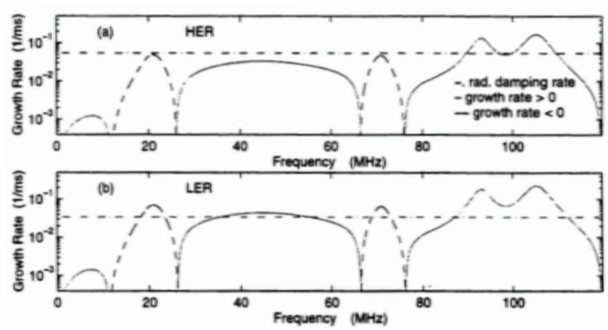

Figure 2: Growth Rate Estimates from Impedance Measurements for 1 A HER, 2.25 A LER.

figure one can see that there are two bands that excite instabilities. The strongest is a 9 MHz wide band that is aliased at around 105 MHz (mode 770) from the 238 MHz sampling and drives roughly 65 beam modes. The second band

* Work supported by the U.S. Department of Energy under contract # DE-AC02-76SF00515

† themis@slac.stanford.edu
‡ rivetta@slac.stanford.edu

is a 7 MHz wide band that aliases at around 93 MHz (mode 683). These wideband, instability driving impedances do not allow the use of narrowband feedback as employed for the cavity fundamental driven modes (LGDW). Furthermore, it is impossible to tune those impedances using adjustments in water temperature or cavity tuners. The dominant impedance driving these instabilities is the cavity HOM impedance, which is proportional to the number of cavities. The HOM driven coupled-bunch beam growth rates are proportional to the number of cavities and to the beam current.

At nominal current both rings exhibit coupled-bunch instabilities in the absence of the damping feedback systems. Therefore, to measure the beam growth rates, we open the LFB loop for a few milliseconds letting the unstable beam modes grow, and then turn it back on to recapture the beam [8], [9]. The time-domain data of the beam motion is transformed to a modal domain and fit versus time. The complex exponential fit provides an estimation of the modal growth rates and oscillation frequencies. This process allows the estimation of the fastest growing beam modes. Other techniques are possible to measure slower growing modes [10].

The highest HOM beam growth rates and the corresponding damping rates reported below are from a band between mode 790 and 810. This is very close to mode 770 that was estimated from the cavity data. The data reported are an average of the growth and damping rates over this mode range and multiple measurements.

HER For the HER, the HOM driven coupled-bunch modal growth rates are shown in Figure 3. Data points

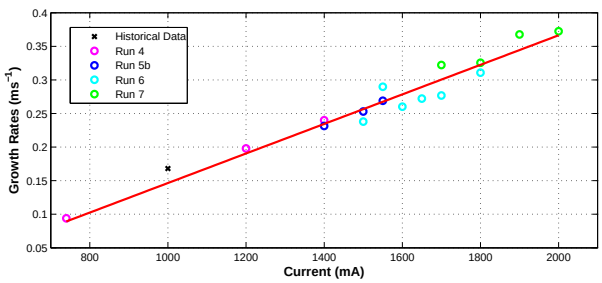

Figure 3: HER HOM driven coupled-bunch modal growth rates for modes 790-810.

over 4 years of PEP-II operations are collected. The data points show great linearity with current as expected. To correctly compare these data points, the data from run 4 have been multiplied by $14/13$ to account for the increase in the number of cavities from 26 to 28. The black point is a scaled version of the estimate based on the cavity data described above. The growth rate has been appropriately scaled by a factor of $28/20$ for the increase of the number of cavities from 20 to 28. Even though this point was estimated with limited resources more than ten years ago, it shows great agreement with our data.

The damping rates for the higher currents are shown in Figure 4. The LFB was configured with a 6 tap FIR filter centered around the 6 kHz synchrotron frequency. The kicker and digital processing gains are constant for all the

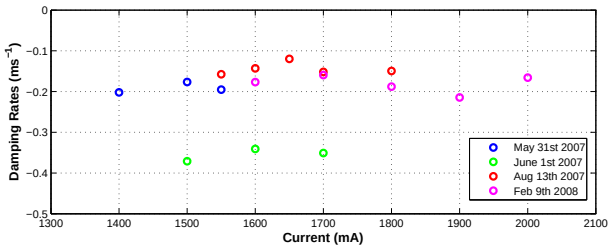

Figure 4: HER HOM driven coupled-bunch modal damping rates (growth plus feedback damping).

configurations shown. The filter gain is higher by a factor of 1.4 for the red and magenta data points. Even though the blue and green data points share the same configuration, they show a big difference in the modal damping rates. This difference is attributed to proper timing in the kicker. Changes in the order of tens of ps in the kicker timing exhibit huge improvement in the damping rates. Comparing the blue with the red and magenta data points, there is no improvement in the damping rate as expected with the higher filter gain due to the timing shifts. For the well-timed configurations, the damping margin was comparable to the measured growth rates, satisfying our margin criteria as defined in [4]. The lack of proportionality with current shows that the system is saturated. It should be noted though, that this saturation may be an artifact of the large longitudinal oscillations caused by the opening of the loop during our measurements. Even though we don't see this saturation during closed loop operation, it signifies that we are approaching limited headroom from saturation limits with this configuration.

LER For the LER, the HOM driven coupled-bunch modal growth rates are shown in Fig 5. The data is from

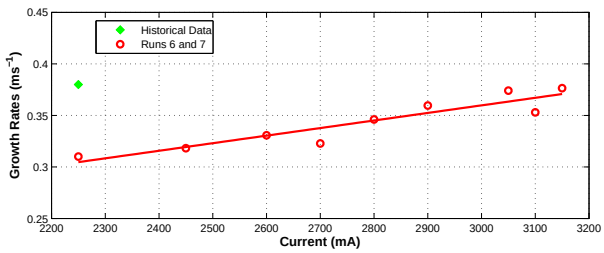

Figure 5: LER HOM driven coupled-bunch modal growth rates for modes 790-810.

runs 6 and 7 and shows great linearity with current as expected. Similarly to the HER, the green point is from the estimate based on the cavity data using the LER design parameters of 2 stations and 4 cavities. The growth rate has been appropriately scaled by a factor of 2 for the increase of the number of cavities from 4 to 8. Even though this point was estimated with limited resources more than ten years ago, it shows relative agreement with our data.

The corresponding modal damping rates are shown in Figure 6. The LFB was configured with a 10 tap FIR filter centered around the 4 kHz synchrotron frequency. The green and red data points share the same configuration. The filter gain of the blue data point is lower by a factor of 0.7,

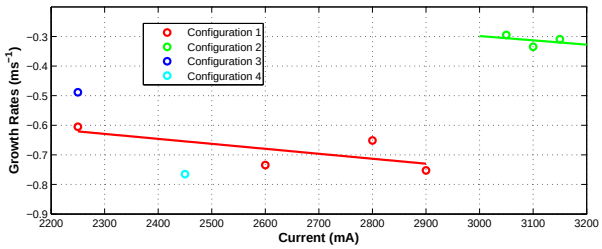

Figure 6: HER HOM driven coupled-bunch modal damping rates (growth plus feedback damping).

whereas the filter gain for the cyan data is higher by a factor of 1.4 from the green and red points. The red line is fitted to the red data points. As described in the HER case, the big difference between the red and green data points could be attributed to timing issues. Further analysis of our data will be conducted to determine whether there is a component of saturation reducing the performance at the higher currents. When the system is correctly timed, the damping margin was comparable to the measured growth rates, satisfying our margin criteria. The measurements agree with the expected behavior of increased damping rates with increasing gain and increasing current for the lower currents. The lack of direct proportionality though, signifies that we might be saturating our system.

Finally, Figure 7 shows the synchrotron frequencies for

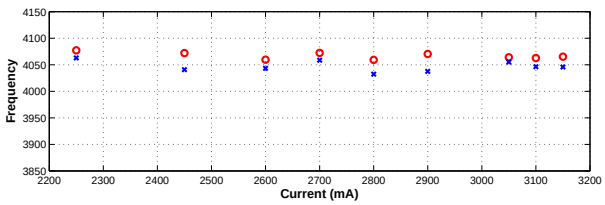

Figure 7: LER HOM driven coupled-bunch modal synchrotron frequencies.

the modal growth and damping rates with current. The two are in close agreement showing that the filter has been properly tuned for the system to introduce pure damping without affecting the modal oscillation frequency. The same check was performed in the HER with equally successful results.

FEEDBACK MODEL

To understand the effect of the system parameters in the LFB stability and performance, an analysis based on a dynamic model is presented. The model includes the dynamics of the multi-bunch beam, the loop filter, and the perturbing noise sources that degrade the performance and stability of the closed loop.

The multibunch system is a multiple-input, multiple-output (MIMO) system. It can be represented in a simplified version as depicted in Figure 8 [9], [11]. In absence of the LFB system damping the beam presents some unstable modes, defining an open loop unstable system. In addition, the system includes delays that in general limit the maximum open loop gain. The two main noise sources

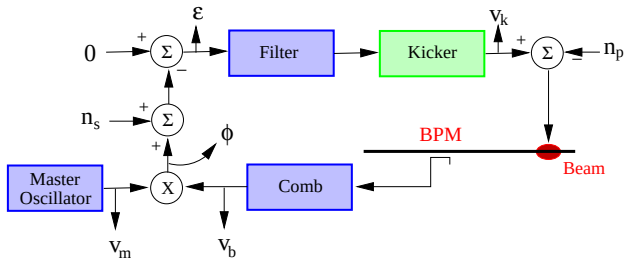

Figure 8: Simplified LFB Block Diagram.

in the system can be grouped in the process noise $n_p(t)$ and the sensor noise $n_s(t)$. The process noise collects mainly all the perturbations introduced by the RF stations, kicker timing, etc. The sensor noise describes mainly the collective effects of the noise in the receiver. This noise has sources in the Master Oscillator, kicker amplifiers, mixer, A/D sampler and cables connecting the BPM to the receiver. In a simple way, this noise can be analyzed assuming that the Master Oscillator produces a signal $v_m(t) = [V_m + n_m(t)]cos(\omega_0 t + \phi_m(t))$, where V_m is the amplitude of the sine wave, $\omega_0 = 6\,\omega_{RF}$, $n_m(t)$ and $\phi_m(t)$ are the amplitude and phase noise, respectively. The Comb filter responds to the beam impulses measured by the BPM with a finite duration signal $v_b(t, I_b) = [V_b(I_b) + n_b(t)]sin(\omega_0 t + \phi(t) + \phi_b(t))$, where $V_b(I_b)$ is the amplitude of the oscillation, proportional to the bunch intensity, $\phi(t)$ is the phase modulation in the beam produced by the noise $n_p(t)$ and the kicker signal, $n_b(t)$ and $\phi_b(t)$ are the amplitude and phase noise respectively, induced in the burst $v_b(t)$ by Johnson noise and pick-up.

The action of the mixer can be then simplified as $v_b(t, I_b)\, v_m(t) + n_x(t)$, where $n_x(t)$ is noise of the mixer at the output. Eliminating the upper sidebands at the mixer output by filtering, the detected signal is approximately $0.5\ [V_b(I_b)V_m sin(\phi)] + n_A sin(\phi) + n_\phi + n_x$, where $n_A = 0.5\ [V_m n_b + V_b(I_b)n_m]$ and $n_\phi = 0.5\ V_b(I_b)V_m cos(\phi)[\phi_b + \phi_m]$. To complete the model of the sensor noise $n_s(t)$, the ADC noise can be included giving $n_s(t) = n_A sin(\phi) + n_\phi + n_{ADC} + n_x$. It is important to notice that since the Comb generator output signal is proportional to the bunch intensity (beam current), the gain of the phase detector is proportional to the beam current and the noise of the receiver $n_s(t)$ increases also with the beam intensity.

The beam dynamics of each bunch are modeled as a discrete harmonic oscillator driven periodically ($6T_{rev} = 44.1\mu sec.$) by 6 equally spaced impulses with equal amplitude. This represents the effect of kicking individually each bunch at the revolution frequency by a system that has a downsampling factor of 6. Additionally, the destabilizing effect of the cavity HOM impedance is included in this model.

The set of transfer functions representing the ratio between the individual kicker signals $V_k(t)$ and the corresponding error signal $\epsilon(t)$ is defined mainly by the loop filter transfer function (FIR or IIR filters). This processing acts individually on the error signal generated by each

bunch and generates a control signal $V_k(t)$ that kicks the same bunch a few turns later.

Mathematically, the system depicted in Fig. 8 can be transformed into a modal domain using the transformation T, where the (m,l) element is defined by $T(m,l) = e^{-j2\pi\frac{ml}{N}}$. One advantage of the representation of the system in the modal frame is that the parameters defining the beam dynamic model for the unstable modes can be easily estimated form the growth rate measurements presented in the previous Section. Additionally, for the bank filter structure used in the LFB, where each filter processes the signal of an individual bunch, the transfer function of the filter is invariant with respect to the transformation.

The filter bank in the LFB is designed to stabilize the multibunch beam dynamics. There is a set of equal filters which stabilize the most unstable beam mode, and consequently all other beam modes. The design of the LER LFB loop filter follows. At $I_b = 2250mA$, from Figs. 5 and 7, the eigenvalues of the dominant unstable mode are $\Lambda = (+0.3 \pm j\ 2\pi\ 4.070)\ ms^{-1}$. The transfer function of the beam for that particular mode is shown in Fig. 9. For

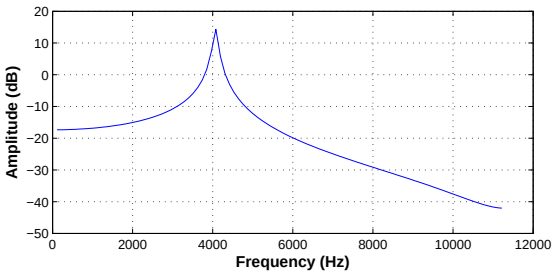

Figure 9: Beam Transfer Function - Most unstable mode.

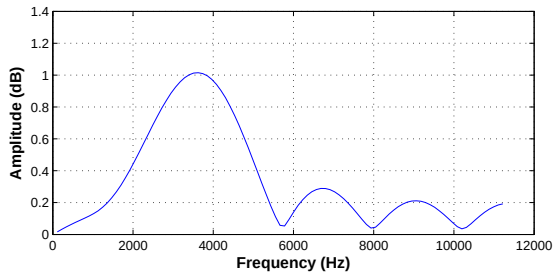

Figure 10: 10-Tap Loop Filter magnitude Transfer Function.

this system, a 10-tap FIR filter was designed. Its magnitude transfer function is depicted in Fig. 10.

When operating in closed loop, the eigenvalues of the composite system can be analyzed in the complex plane based on the Z-domain root locus analysis. Fig. 11 depicts the root locus for this particular system for open loop gains ranging from 0 to 3. Black squares show the location of the open loop eigenvalues of the composite system, as defined by the modal beam unstable eigenvalues and multiple eigenvalues defined by both the system and filter delays. The circles represent the zeros of the system defined mainly by the zeros of the filter. It is possible to evaluate the location of the closed loop eigenvalues for different gains for this particular beam mode. From the zoomed part in Figure 11 it is possible to observe that there is a min-

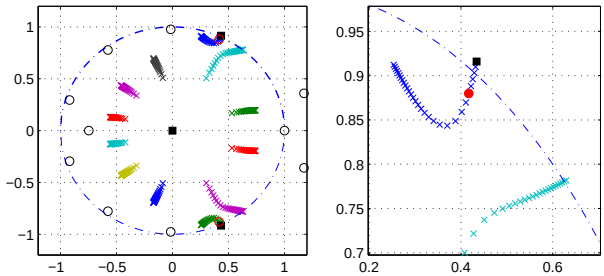

Figure 11: Root Locus.

imum gain to stabilize that particular beam mode, setting the closed-loop eigenvalues over the unity circle (open loop gain = 0.2). Additional gain is necessary to set the closed-loop eigenvalues to the red circle in the zoomed locus at $\Lambda = (-0.6 \pm j\ 2\pi\ 4.070)\ ms^{-1}$ (gain 0.5). This condition corresponds to Fig.8. For open loop gain greater than 3 one observes that the system is unstable.

NOISE FLOOR MEASUREMENTS

In order to quantify the effect of the noise sources in the LFB system in both PEP-II rings, several noise measurement were performed using the built-in data acquisition system of the LFB. The downsampled signal digitized at 238 Msamples/sec by the ADC is recorded for offline analysis. This corresponds to the error signal $\epsilon(t)$ depicted in Fig. 8. The acquired signal is post-processed to calculate the noise spectrum. We estimate the power spectrum bunch by bunch and a quadrature average provides the equivalent noise spectrum of mode 0 in the modal domain.

To analyze the impact of the different noise sources, measurements were conducted in several configurations. Terminating the ADC input with 50 Ohms provides a measure of $n_{ADC}(t)$ – the quantizing noise in the A/D and the noise in the internal sampler (as well as any systematic clock noise present in the processing). Turning off the gain in the Comb path at 3 GHz measures the noise contribution from the baseband channel plus the noise contribution through the mixer and Master Oscillator. Finally, measuring the system in the nominal channel configuration but in the absence of beam quantifies the sensor noise $n_s(t)$ – the noise contribution from the whole RF path and processing channel (including any coherent pickup in cables, BPM, etc). It is important to notice that the noise source $n_s(t)$ defined in our model includes noise terms that are amplified by the amplitude of the Comb generator signal $V_b(I_b)$. The other two measurement mentioned above cannot quantify completely these noise terms since $V_b(I_b) \simeq 0$ in these cases.

Measuring the noise of the system with beam quantifies the impact of both noise sources $n_s(t)$ and $n_p(t)$ in Figure 8. In closed loop the effect of these sources in the ADC is now affected by the transfer functions of the LFB system. These transfer functions will filter differently the perturbations due to the receiver noise $n_s(t)$ and the process noise $n_p(t)$.

LER noise measurements Figure 12 shows the noise levels for the four cases described above. Label 'A/D'

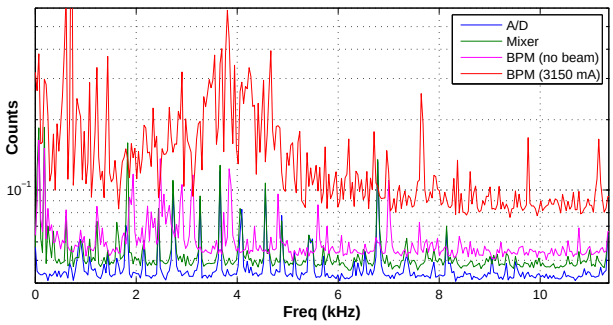

Figure 12: LER noise measurements.

identify the measurement of n_{ADC}, 'mixer' represents the case with the Comb gain turned off, 'BPM (no beam)' shows n_s, and 'BPM (3150 mA)' indicates the closed loop case with beam present. The measurements exhibit the expected order of noise power magnitude. For the LER, the noise in rms equivalent counts at the output of the ADC is approximately 0.66. To show the non-ideality and additional effects in the implemented A/D converter, a perfect quantizer, would have 0.32 rms counts of quantization noise. It is important to observe that the beam noise is dominant and much greater than the other measurements. Part of the noise is amplified by the system around the synchrotron frequency at 4.07 kHz. The noise spectrum with beam shows large noise interference at 720 Hz and 1440 Hz, which correspond to the RF klystron High Voltage power supply ripple. Again, since in the presence of beam we have almost 2 rms counts of noise, increasing the number of bits in the A/D would have no effect on the system noise. A 6 bit A/D would still have a noise level comparable to the beam noise. To improve the system closed loop rms noise floor we either have to improve our kicker amplifiers or to reduce the RF station noise (that drives the beam noise spectrum at low frequencies) through a narrower LFB filter or through other station improvements.

HER noise measurements Figure 13 shows measurements for the HER, exhibiting the same characteristics as the LER. We again see how the RF station noise amplified

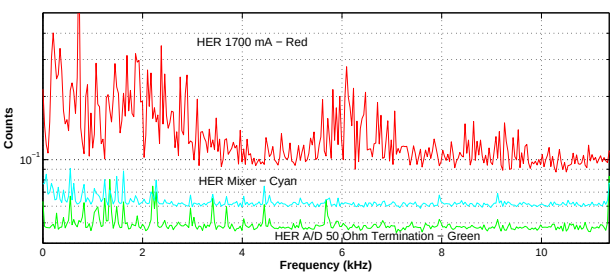

Figure 13: HER: Mixer, A/D downsampler and BPM at 1700mA.

through the beam dominates our system. In the HER case the synchrotron frequency is close to 6 kHz as can be inferred from the spectrum.

CONCLUSIONS

The LFB system was designed for much lower currents. Its programmable design allowed operations with much larger growth rates. Even though the system still had sufficient gain margin, the noise coupled to the beam from the RF station was very close to saturating the LFB at the highest beam currents. To operate at even higher currents, additional kicker power or improvements in the LLRF would have been necessary. Another important limitation was the kickers timing. We see that timing shifts in the ps level reduced the system gain – and thus the stability and margin – substantially.

ACKNOWLEDGEMENTS

The authors would like to thank D. Teytelman, S. Prabhakar, and H. Hindi for all their work, help and ideas that provided a substantial base to build on. We would also like to thank the PEP-II operations and accelerator groups for their consistent help with these measurements, the SLAC ART department and SSRL accelerator physics department for many helpful collegial discussions. We acknowledge our colleagues at LBL, LFN and KEK who have shared their ideas and interests on this subject.

REFERENCES

[1] D. Teytelman *et. al.*, "Operating Performance of the Low Group Delay Woofer Channel in PEP-II", PAC 2005.

[2] D. Teytelman *et. al.*, "Development and Testing of a Low Group-Delay Woofer Channel for PEP-II", EPAC 2004.

[3] T. Mastorides *et. al.*, "Analysis of Longitudinal Beam Dynamics Behavior and RF System Operative Limits at High Beam Currents in Storage Rings", submitted to Phys. Rev. ST-AB.

[4] C. Rivetta *et. al.*, "Modeling and Simulation of Longitudinal Dynamics for Low Energy Ring-High Energy Ring at the Positron-Electron Project", Phys. Rev. ST-AB, 10, 022801 (2007).

[5] D. Teytelman *et. al.*, "Control of Multibunch Longitudinal Instabilities and Beam Diagnostics Using a DSP-Based Feedback System", PAC 1997.

[6] R. Rimmer *et. al.*, "Updated Impedance Estimate of the PEP-II RF Cavity", EPAC 1996.

[7] S.Prabhakar, "New Diagnostics and Cures for Coupled Bunch Instabilities", Thesis, Stanford University Applied Physics Dpt., August 2001.

[8] S.Prabhakar *et. al.*, "Observation and Modal Analysis of Coupled-Bunch Longitudinal Instabilities via a Digital Feedback Control System", Part.Accel.57:175-187, 1997.

[9] D.Teytelman, "Architectures and Algorithms for Control and Diagnostics of Coupled-Bunch Instabilities in Circular Accelerators", Thesis, Stanford University EE Dpt., June 2003.

[10] J. Fox *et. al*, "Multi-bunch Instability Diagnostics via Digital Feedback Systems at PEP-II, DAΦNE, ALS and SPEAR", PAC 1999.

[11] H. Hindi *et. al.*, "Analysis of DSP-Based Longitudinal Feedback System: Trials at SPEAR and ALS", PAC 1993.

SUPPRESSION OF LONGITUDINAL COUPLED-BUNCH INSTABILITIES AT THE KEK-PF

T. Obina#, M. Tobiyama, T. Honda, M. Tadano, J. W. Flanagan, T. Mitsuhashi,
KEK, 1-1 Oho, Tsukuba, Ibaraki 305-0801, Japan
W. X. Cheng, J. D. Fox, SLAC, Menlo Park, CA, U.S.A
D. Teytelman, Dimtel Inc., San Jose, CA, U.S.A.

Abstract

A bunch-by-bunch feedback system has been developed to suppress longitudinal coupled-bunch instabilities at the KEK-PF. A longitudinal kicker based on a DAFNE-type overdamped cavity has been designed and installed in the ring, and a general purpose signal processor, called iGp, has been developed by the collaboration of the KEK, SLAC, and INFN-LNF. The entire feedback loop has been closed by the end of June 2007, and the feedback system has successfully suppressed the longitudinal dipole-mode instabilities up to 430 mA.

INTRODUCTION

The Photon Factory electron storage ring at the KEK is a dedicated synchrotron radiation (SR) source with an energy of 2.5 GeV. The ring is operated in both single- and multibunch modes. In both cases, longitudinal oscillations starting from very low currents are observed. In the single-bunch operation, the phase noise of a low-level RF circuit excites synchrotron oscillations of the bunch. In the multibunch operation, several coupled-bunch modes of instabilities are observed above 50 mA. Cavity-like structures in the storage ring are suspected to be the source of the instabilities, although the sources have not been determined thus far.

Phase modulation of the RF acceleration frequency at twice the synchrotron frequency ($2f_s$) can suppress the longitudinal instabilities considerably [1]. This easy and inexpensive technique has been utilized during SR user operation for years because this method is very effective not only in suppressing the instabilities, but also for increasing the beam lifetime, approximately by a factor of 1.5. The enhancement of the beam lifetime is desirable for many users. However, phase modulation increases the energy spread of the bunch. The effect is apparently observed in some insertion device beamlines at the dispersive section of the storage ring. In these beamlines, the intensity of the input SR fluctuates depending on the status of the RF phase modulation. In order to stabilize these fluctuations, a longitudinal feedback system has been developed and a feasibility study on top-up injection, which is indispensable for the compensation of a short beam lifetime, has been carried out.

The main parameters of the PF-Ring and the bunch-by-bunch feedback system are listed in Table 1.

Table 1: Main parameters of PF-Ring.

RF frequency [f_{RF}]	500.1	MHz
Harmonic number	312	
Revolution frequency [f_{rev}]	1.6029	MHz
Synchrotron tune [ν_s]	0.014	
Longitudinal damping rate	0.256	ms^{-1}
Beam current (single/ multi)	70 / 450	mA

FEEDBACK SYSTEM

The feedback system is composed of a front-end detection unit, a signal processing unit, and a corrector unit. The block diagram of the feedback system is shown in Fig. 1.

Front-end Detection Circuit

The output signals from two button-type pickup electrodes are summed by a hybrid (M/A-COM, model H-8) to cancel the transverse beam position dependence. A low-noise amplifier (LNA) is connected to a band-pass filter (BPF), which consists of three delay cables and a power combiner/splitter. The longitudinal position is detected with respect to the RF acceleration signal by synchronous detection at three times the RF frequency. The highest detection frequency is limited by the cutoff frequency of the vacuum chamber, approximately 1.8 GHz.

Though it is possible to change the RF detection phase (indicated as $\Delta\phi$ in the figure) along the bunch train, a constant phase is maintained (DC) because the difference in the synchronous phase between the head and the tail of the bunch train is not large even at 450 mA. A trombone delay adjusts the timing of the input signal and the clock of the ADC.

Digital Signal Processor

A general purpose signal processor, called the iGp, has been developed by a collaboration of the KEK, SLAC, and INFN-LNF [2,3]. iGp provides real-time baseband signal processing at an RF frequency of 500 MHz for 312 bunches at the PF. The longitudinal position of each bunch is digitized by an 8-bit ADC, processed by a 16-tap finite impulse response (FIR) filter, and transmitted to a DAC after an appropriate delay is introduced. The complete signal processing is sufficiently fast compared to the revolution time of the PF-Ring. A digital filter is implemented by using a field-programmable gate array (FPGA). The FPGA also provides a number of other

#takashi.obina@kek.jp

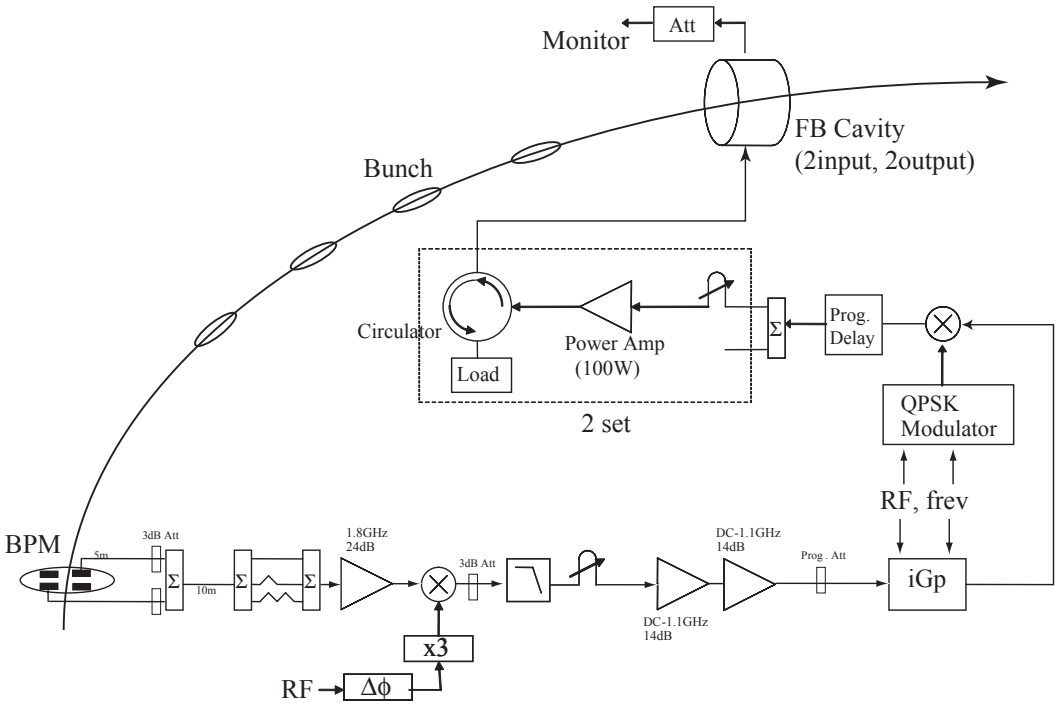

Figure 1: Block diagram of longitudinal feedback system. iGp is a fast real-time digital signal processor using FPGA. QPSK modulator has a carrier frequency that is 2.25 times the RF frequency.

interface features such as high-speed data acquisition memory (Static Random Access Memory, SRAM), slow analog and digital input/output, temperature monitoring, and power supply voltage monitoring. A USB interface in an embedded computer is used to program the FPGA. All the devices, including the signal processing unit, embedded computer, and power supply, are placed in a 19-in 2U-high chassis.

The embedded computer functions as an input/output controller (IOC) of the Experimental Physics and Industrial Control System (EPICS) [4], which is the standard control framework at the PF. The IOC runs on a customized Linux operating system and is connected to the control network. Many easy-to-use graphical user interface (GUI) panels are also provided for tuning and analysis. The FIR coefficients can be easily changed through the GUI.

High-power Component

The output of the iGp is a baseband signal. A QPSK modulator with a carrier frequency equal to the center frequency of the feedback cavity, converts the baseband signal to order to apply the energy kick to each bunch.

The feedback cavity has two input ports driven by a 100-W class-A amplifier (R&K, model A1012BW250). Two output ports are connected to a high-power attenuator (Bird, model 8327-300) to observe the beam-induced signal and output signal from the power amplifiers. In order to protect the amplifiers from the beam-induced signal from the cavity, two 10-kW wideband circulators (AFT Microwave) are installed.

Feedback Kicker Cavity

A longitudinal kicker based on the DAFNE-type overdamped cavity has been installed in the ring. Details of the cavity design and the calculated impedance are reported in ref. [5]. After mounting the cavity, the performance of the cavity is confirmed by using a mode-feedback system. Before the completion of high-speed signal processor, which can handle bunches with a 2-ns bunch spacing, an FPGA evaluation board was used to carry out 52-bunch feedback experiments. The details have already been reported in a previous paper [6]. In both the cases, the coupled-bunch instabilities up to 70 mA have been successfully suppressed.

Filter Design

A FIR filter for the feedback must have a 90° phase shift at a synchrotron frequency of 22 kHz. The impulse response of the FIR filter must be almost equal to the synchrotron period of 45 μs, which corresponds to 72 turns in the PF. Instead of using a 72-tap filter, the iGp has a 16-tap FIR filter and a downsampling feature. We selected different downsampling factors, *Nds*=4, 5 and 6; the total filter length is equivalent to 64, 80, and 96 turns, respectively. Figure 2 shows the two filter designs used in the experiment. The blue line labelled as “coef 1” is the original filter design. Since the quadrupole-mode oscillations of the beam become severe in a high beam current region, the filter with the design “coef 2” is designed to decrease the effects of the quadrupole-mode oscillations, which will be described in detail later.

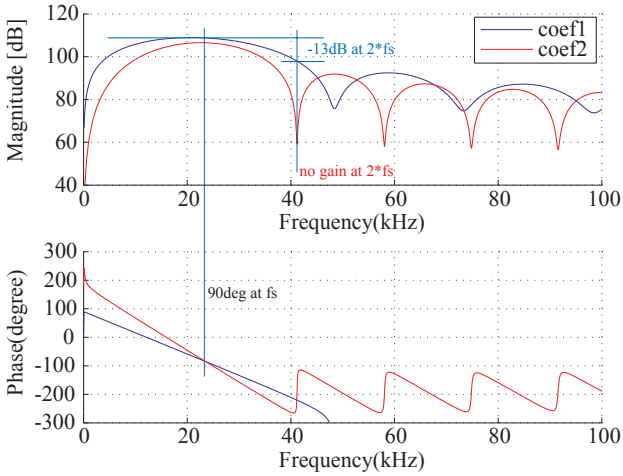

Figure 2: Gain and phase of two 16-tap FIR filter. Blue line (coef 1) corresponds to original filter design with *Nds* = 4. Red line (coef 2) corresponds to filter design with *Nds*=6; it shows almost no response to quadrupole-mode oscillations.

RESULTS

Timing Adjustment Using Single Bunch

The analog and digital delay time is adjusted precisely using a single bunch in the ring. As mentioned before, strong synchrotron oscillations caused by the main RF system are observed in the single-bunch operation. It is very difficult to completely suppress the single-bunch instabilities by using the bunch-by-bunch feedback system because the shunt impedance of the feedback cavity is considerably lower than that of the main RF system. However, it is possible to excite or suppress instabilities of approximately 3 dB in amplitude. This amplitude is sufficiently large for the timing adjustment of the feedback system. A wideband programmable delay unit (Colby Instruments, HPDL-100A-10.23NS) is introduced between the iGp and the power amplifiers to adjust precisely the timing for the kicker.

Feedback and Phase Modulation

Out of 312 buckets, 280 bunches are stored to prevent the onset of the transverse ion-trapping instabilities. The bunch spacing is 2 ns. In order to observe a difference from the present SR user's operation, we tested the four patterns of operation listed below. 'PM' indicates the RF phase modulation, and 'FB' indicates the bunch-by-bunch feedback system hereafter.

(A) FB OFF, PM ON : same as present user's operation
(B) FB ON, PM ON : both are turned ON
(C) FB ON, PM OFF: only feedback system; ideal case.
(D) FB OFF, PM OFF: no beam stabilization

The beam current is selected to be 430 mA. The beam spectra of the button type pickup electrode under the feedback conditions (A)–(D) are shown in Figs. 3 (A)–(D), respectively. The frequency range is from DC to 3 GHz. In Fig, 3(A), harmonics of the RF frequency is observed at 500 MHz, 1 GHz, 1.5 GHz, … Some spectral lines corresponding to the longitudinal coupled-bunch mode instabilities of mode number 276 (or mode –36) are also observed. In some cases, mode 276 disappears and another mode, mode 195 (–117), is observed (not shown in the figure).

When both PM and FB are turned ON, as shown in Fig. 3(B), all the instability lines disappeared and only the RF harmonics are observed. Beam stabilization appears to be successful, although the energy spread of the bunch is still large; hence this condition is not advantageous for SR experiments.

Without any stabilization, as shown in Fig. 3(D), several instability modes are observed. The strength of each mode is not constant and the peak height varies. The baseline of the spectra is raised because many modes exist within the resolution bandwidth (RBW) of the spectrum analyzer.

Figure 3(C) shows the beam spectrum without PM and with FB. This operation pattern is the ideal case for feedback system development. In the low-frequency region below 1 GHz, there is no peak due to the instabilities. On the other hand, a small peak corresponding to mode 276 exists in the high-frequency region above 2 GHz. Expanding the frequency range around the modes reveals that the peak is located at a distance of $2f_s$ away from the revolution harmonics, and there are no peaks around f_s. The dipole motion has been successfully suppressed by the feedback system and only the quadrupole-mode oscillations remain. A streak camera is used to directly observe the bunch shape as shown in Fig. 4. The top figure shows the longitudinal bunch shape without FB nor PM (case (D)), and the bottom figure shows case (C). It is apparent that the feedback system suppresses the dipole motion, and the bunch length varies along the bunch train. It should be noted that the adjacent bunches in the Fig.4 are actually 8 ns apart since the frequency of the fast-sweep signal of the streak camera is

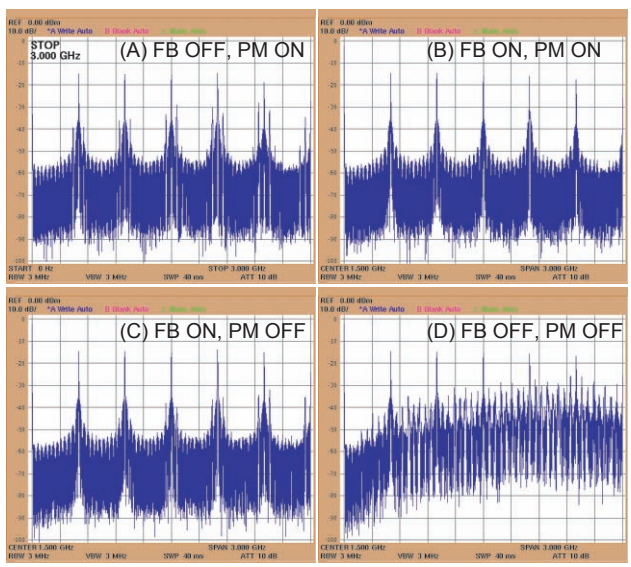

Figure 3: Beam spectra of button-type pickup electrode. FB indicates feedback, and PM indicates phase modulation of acceleration RF signal.

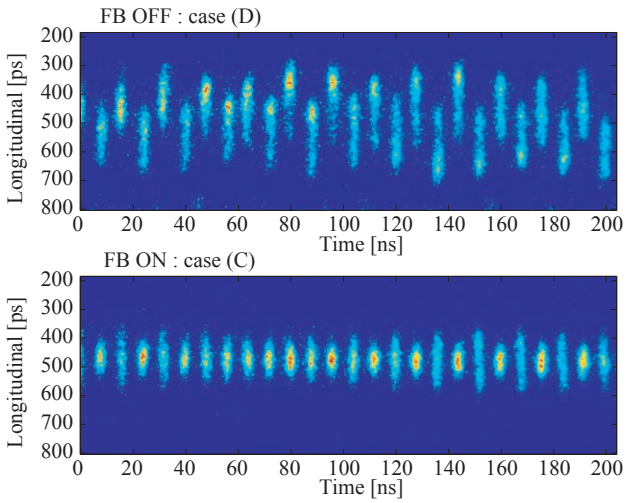

Figure 4: Longitudinal bunch shape measured by a streak camera. Top figure shows the profile without the feedback (case(D)), and bottom figure shows with the feedback (case (C)).

a quarter of the RF frequency. The bunch length is not constant. As time advances, the longer bunches become shorter, and vice versa. When a bunch arrives in the shortest time interval, the bunch length is shorter than the natural bunch length.

Figure 5 shows the transverse beam profile with and without FB (case (A) and (C)). Since the SR monitor is located in a non-zero dispersion region, the horizontal beam size includes the effects of energy spread of the bunches. By closing the feedback loop, the horizontal beam size decreases and the relative peak intensity increases by approximately 8%–9%.

It is possible to suppress the dipole motion of the beam above 430 mA, although the system sometimes goes out of the capture range of the feedback system, and the beam becomes unstable. In contrast to the transverse case, the longitudinal instabilities are difficult to be suppressed by just turning on the FB. In this case, to suppress the instabilities, the PM is turned on at first, then the FB is turned on, then finally the PM is turned off.

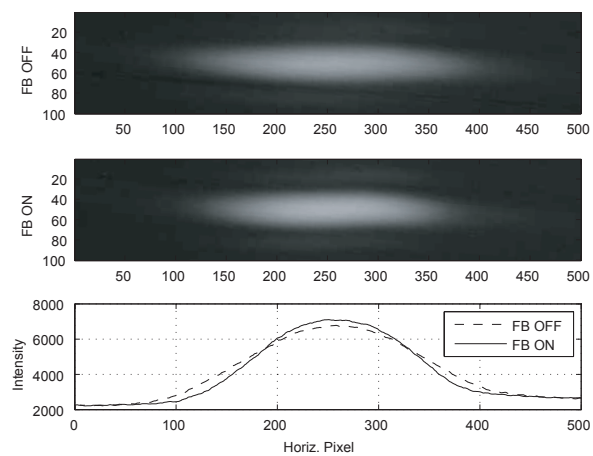

Figure 5: Transverse beam profile measured by a CCD camera in cases (A) and (C). The peak intensity increases with the feedback.

Mode Analysis of Instabilities

The iGp is equiped with two types data acquisition memories for beam diagnostics. One is the internal RAM of the FPGA, and the other is the external SRAM. They can store individual bunch positions up to 128 ksamples and 8 Msamples, respectively. The SRAM data for the mode analysis can be downloaded to the IOC through the USB, and transferred to other machines for analysis using high-level application tools such as MATLAB.

A grow/damp measurement at a beam current of 200 mA is shown in the left-hand-side figure of Fig. 6. There exist large zero-mode oscillations which are assumed to be driven by the main RF system. The growing and damping parts of mode 276 (–36) are fitted by exponential functions. The fitted growth and damping rates are obtained to be 1.1 and 0.8 ms^{-1}, respectively.

In the high beam current region, it is sometimes difficult to recapture the beam. The right-hand-side figure of Fig. 6 shows an example when the instabilities grow faster than the feedback damping time. Several modes are observed in the figure. The strongest mode has changed to mode 275 (–37) at 400 mA. Further investigations are required to identify the behavior of this variation, and the relationship between other parameters such as RF cavity temperature.

Effects of Longitudinal Feedback on SR Users

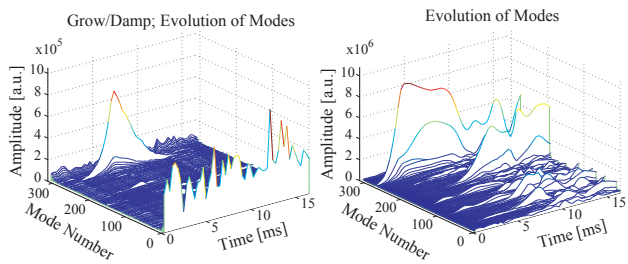

Figure 6: Evolution of modes during the grow/damp measurement. Left-hand-side figure shows the recaptured beam at a beam current of 200 mA, and right-hand-figure shows an example that the feedback cannot be recaptured at a beam current of 400 mA.

The effects of the longitudinal feedback on SR users were examined. The beamline users measured the intensity and stability of the SR while the machine was operated with pattern (A) through (D), approximately 2 h each. The initial beam current is selected to be 430 mA. The beam current and lifetime are plotted in Fig. 7. The difference in the lifetime between cases (C) and (D) indicates that the averaged bunch volume is increased by the quadrupole mode oscillation of the bunch. This is consistent with the beam spectrum or the streak camera measurement.

Figure 8 shows the intensity of the SR at beamline BL-17, which is a short-period small-gap undulator (SGU), in an in-vacuum configuration. Due to limitations of the lattice and available space, this undulator is installed at a non-zero dispersion region. In cases (A) and (B), the energy spread due to RF phase modulation causes

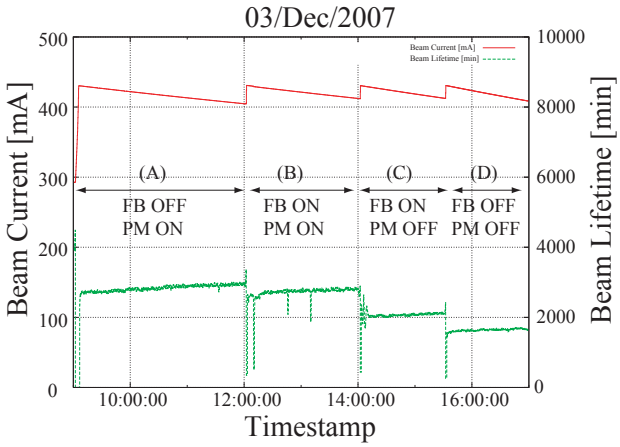

Figure 7: Beam current and the lifetime during the machine development period.

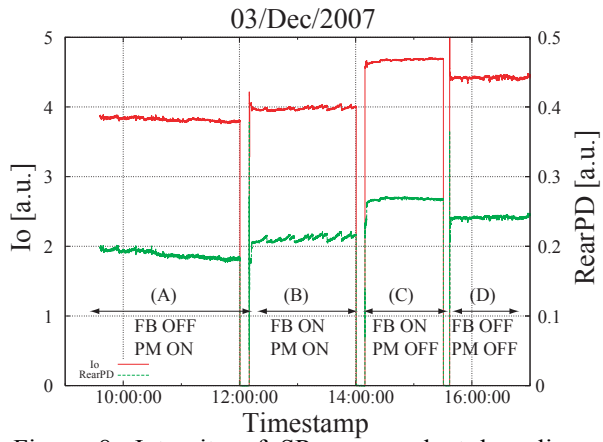

Figure 8: Intensity of SR measured at beamline BL17. Io indicates the intensity of the input light measured by an ion chamber, and RearPD indicates the output voltage of a photo detector placed after an X-ray diffractometer. Both scales are plotted in arbitrary units.

fluctuations and drifts in the intensity. On the other hand, when the feedback loop is closed, the intensity increases to approximately 30% in case (C). Further, the fluctuations and drifts are almost negligible in this case.

At beamline BL-5, an increase in the intensity of approximately 50%, and a decrease in the fluctuations from 5% to 3% with the feedback are observed. At other beamlines, the effects of longitudinal feedback are not significant, and the beam quality is not degraded by the feedback. The feedback system has been confirmed to be very effective.

Feedback Stability for Long-term Operation

The stability of the feedback system has been checked in operation for one week. Another purpose of this period was to check the effects of the short lifetime on SR users. The feedback system worked well during the week without any trouble.

When the beam current is lower than approximately 240 mA, the lifetime suddenly drops as shown in Fig. 9. There are no instability lines in the beam spectrum below this current. Further, in some beamlines, the SR intensity increases simultaneously with the drop in lifetime. There is a clear threshold and hysteresis phenomenon present in the quadrupole-mode instability. If the feedback loop is kept closed during the beam injection, the quadrupole-mode instability again appears above 300 mA. We continue to investigate the details of the hysteresis phenomenon along with the development of a quadrupole-mode suppression system.

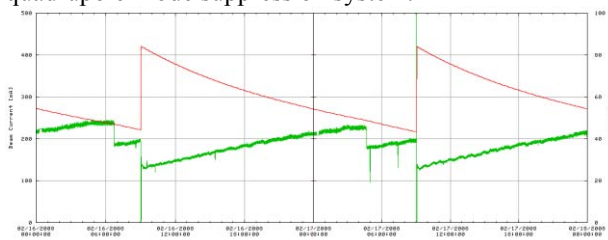

Figure 9: Beam current and lifetime for 2 days with the longitudinal feedback system in continuous operation.

SUMMARY AND FUTURE PLAN

A bunch-by-bunch feedback system has been developed to suppress the longitudinal coupled-bunch instabilities at the KEK-PF. The system can suppress the longitudinal dipole-mode instabilities up to 430 mA. The long-term stability of the system has been proven by operation of the feedback system for one week.

A regular SR operation starts at 450 mA in the multibunch mode. In order to improve the highest beam current for the dipole-mode suppression, two 500-W power amplifiers are ready to be installed in place of the present two 100-W amplifiers.

It is also important to suppress the quadrupole-mode instabilities to maximize the intensity of the insertion device beamlines with a non-zero dispersion. We are planning to develop another feedback system for the quadrupole-mode. One idea is to adjust the phase of the carrier signal to work on both the dipole and quadrupole components and design a new filter to suppress both of them [7]. The other idea is to develop another set of feedback processor and a cavity dedicated for the quadrupole mode. In both cases, it is not easy to develop a good detection circuit because button-type electrodes are less sensitive to the quadrupole motion. We continue to develop the feedback system along with the investigation on the sources of the dipole- and quadrupole-mode instabilities.

REFERENCES

[1] S.Sakanaka, *et al.*, Phys. Rev. ST Accel. Beams 3, 050701 (2000)
[2] D. Teytelman, *et al.*, Proc. EPAC06 (2006) 3030
[3] D. Teytelman, *et al.*, Proc. PAC07 (2007) 584
[4] EPICS homepage, http://www.aps.anl.gov/epics/
[5] W. X. Cheng, *et al.*, Proc. EPAC06 (2006) 3009
[6] T. Obina, *et al.*, Proc. PAC07 (2007) 233
[7] A. Drago, *et al.*, Phys. Rev. ST Accel. Beams 6, 052801 (2003)

LOCALIZATION OF NOISE SOURCES IN THE APS STORAGE RING USING THE REAL-TIME FEEDBACK SYSTEM *

Xiang Sun# and Glenn Decker, ANL, Argonne, IL 60439, U.S.A.

Abstract

There are two parallel feedback systems to correct the transverse orbit at the Advanced Photon Source (APS) storage ring: a real-time feedback (RTFB) system [1] that runs at 1.5 kHz using 38 fast correctors and up to 160 beam position monitors (BPMs), and a DC feedback system that runs at 10 Hz using up to 317 correctors and over 500 BPMs. An algorithm that uses the open-loop beam motion data to spatially locate strong noise sources in the storage ring is described. The orbit data are measured with 1.5-kHz data acquisition associated with the RTFB system. This system is limited to collecting 40 time-series waveforms synchronously. If synchronous data for the whole ring could be collected, source identification would be straightforward, because a sample-by-sample orbit could be reconstructed with the inverse response matrix. Since this is not the case, a synchronization procedure was developed allowing the splicing together of spatially overlapping double-sector single-frequency trajectories. This technique is applicable to narrow-band noise sources. By multiplying the truncated pseudo-inverse response matrix of the APS storage ring by the synchronous orbit data at a fixed frequency, noise sources at a fixed frequency can be located. The experiment and calculation results are presented.

INTRODUCTION

The real-time orbit feedback system is implemented digitally using digital signal processors (DSPs) [2,3] and consists of 21 VME crates – 1 master and 20 slaves. The 20 slave VME crates are distributed around the circumference of the 40-sector APS storage ring to manage interfaces to BPMs and correctors, and to compute orbit corrections. The master crate provides global controls to the other 20 slave crates and provides analysis tools such as "DSP scope," which works like a digital oscilloscope. The DSP scope can collect 40 channels synchronously, and each waveform has up to 4080 data points with 1.5 kHz sample rate.

While beam stability at the APS is quite good, there are a significant number of narrow-band spectral lines resulting in elevated levels of beam motion [4,5]. The problem comes from some potential spatially discrete, relatively strong sources of noise.

*Work supported by U.S. Department of Energy, Office of Science, Office of Basic Energy Sciences, under Contract No. DE-AC02-06CH11357

#xiang@aps.anl.gov

If one considers a full response matrix mapping all possible sources to all BPMs, a time series approximating each of these noise sources can be estimated by pseudo-inverting the full matrix and multiplying the orbit data that is collected synchronously.

The method for localizing narrow-band noise sources is described below. As a test case, a fast corrector in APS sector 10 was driven with a sine wave at 18.049 Hz. Because DSP scope collects only 40 waveforms at a time, it is not possible to collect data for the entire ring simultaneously. However, a synchronization procedure has been developed that results in a fixed-frequency orbit for the whole ring. After multiplying by the pseudo-inverse response matrix, the location of the known noise source can be reconstructed. This procedure was carried out driving both horizontally and vertically. Having validated the method, the same procedure was applied to a number of examples of unknown narrow-band noise sources.

EXPERIMENT AND CALCULATION TO LOCALIZE NOISE SOURCES

Measurement of the Orbit Changes

We measured the AC orbit by using as many BPMs as possible with the DSP scope tool's double-sector BPM acquisition function with the RTFB loop open. The double-sector BPM acquisition function synchronously collects 40 BPM waveforms at 1.5 kHz. This allows waveforms from ten BPMS per sector horizontally and vertically for two sectors to be acquired. Two such data sets with an overlapping sector can be synchronized with each other by making use of a common spectral line as a type of clock, provided that the spectral line is reasonably stable. By collecting 40 overlapping double-sector data sets in this fashion, one can reconstruct two complete orbits for the 40-sector ring.

We drove the fast correctors S10A:H3 and S10A:V3 separately with a sine wave at 18.049 Hz as a known strong source. The corresponding orbit changes were inferred from 1.5-kHz DSP scope data for 375 different BPMs. This test case was used to validate our method of narrow-band source localization. After stopping the 18.049-Hz excitation, we measured the ambient orbit motion with DSP scope at a 153-Hz sample rate to localize potential narrow-band noise sources in a lower frequency band. All of these measurements were conducted open loop: neither AC nor DC orbit correction systems were active.

The Overlapping Double-Sector AC Orbit Phase Correction Technique

For each of the 20 BPMs (ten per sector) in each data set (horizontal and vertical), the real and imaginary parts of the FFT at the single frequency of interest were extracted, producing a real and imaginary two-sector trajectory at that frequency. A phase rotation was then introduced in such a fashion as to maximize the rms real trajectory while at the same time minimizing the rms imaginary trajectory. If this same phase rotation technique is applied to two double-sector data sets, one finds that the real trajectory in the sector that overlaps is in agreement between the two data sets, outside of an overall sign. By bootstrapping from one double sector (say n and n+1) to the next (n+1 and n+2), while carefully keeping track of sign changes, it is possible to reconstruct a complete AC orbit at a single frequency.

Synchronization

After the orbit data were collected with DSP scope for the whole ring, a fixed-frequency AC orbit for a spectral line of interest was extracted using the technique just described.

Because there are 40 sets of double-sector BPM data for the whole ring, we can generate two independent orbits at a fixed frequency. A comparison between the resulting two orbits, labeled val1 and val2, along with their average, is shown in Figures 1 and 2 for the case of 2-Ampere peak 18.049-Hz oscillations being applied to correctors S10A:H3 and S10A:V3, respectively.

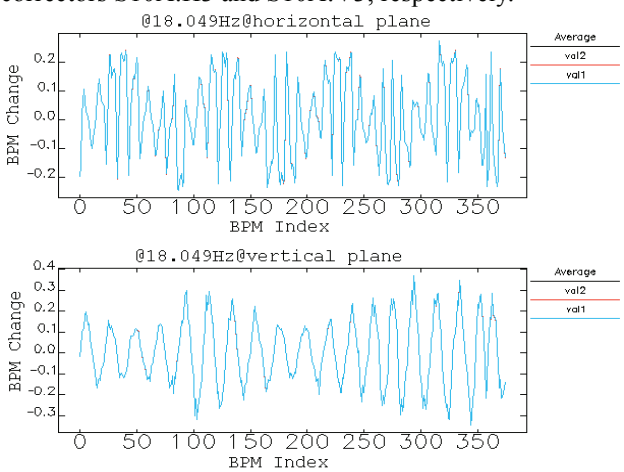

Figure 1: Two groups of synchronous orbit data and their average at 18.049 Hz for both horizontal (top) and vertical (bottom) planes, while driving the beam with a sinusoidal excitation in sector 10.

The two groups of synchronous orbit data (val1 and val2) in Figure 1 agree almost exactly. This indicates that the overlapping narrow-band double-sector phase correction technique is valid for sufficiently strong and stable narrow-band excitation. For the remainder of the analysis, the average of val1 and val2 is used as the best estimate for the AC orbit.

Shown in Figure 2 is a plot of a column of the response matrix for the corresponding steering corrector in sector 10 (labeled S10A:H3 or S109A:V3), together with the average AC orbit data from Fig. 1 (labeled CalAvg). The response matrix column represents the expected orbit using a corrected ring lattice model. Note that the beam position monitor calibrations are determined from the same algorithm used for the ring lattice corrections, and have been implemented in what follows. [6].

The agreement between measured and theoretical orbits in Fig. 2 is quite good, and in fact, the overlap algorithm used to produce Fig. 1 is a good way to very accurately determine the response matrix empirically.

Shown in Fig. 3 are narrow-band orbit data for two spectral lines observed without external excitation, at 2 Hz horizontally, and 59.98 Hz vertically. The two groups of data in Figure 3 agree well, but show noticeable differences between the two versions of the orbit (val1 vs. val2) in some sectors. This provides a measure of the stability of the measurements during the time required to collect data for the whole ring. Note that the size of these perturbations is two orders of magnitude lower than for the artificially driven results shown in Fig. 1.

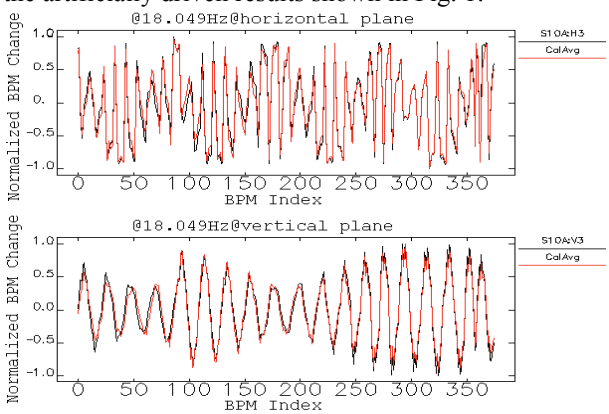

Figure 2: Expected orbit (a column of the response matrix) resulting from driving correctors S10A:H3 (top) and S10A:V3 (bottom). Data with legend CalAvg correspond to the measured average values from Fig. 1 after folding in small calibration corrections.

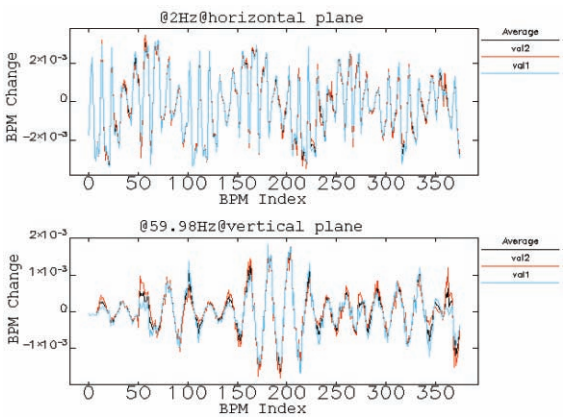

Figure 3: Two groups of synchronous orbit data and their average at 2 Hz in the horizontal plane (top) and at 59.98 Hz in the vertical plane (bottom) without artificial source.

Response Matrix

At APS, there are 375 rf BPMs out of a possible 403 available for monitoring by the real-time feedback system. While there are 317 steering correctors installed, only 38 of them have enough bandwidth for inclusion in the real-time feedback system. In the situation where a string of correctors are used with no BPMs between them, the full response matrix is singular, with infinite condition number. To address this problem, the matrix omitted correctors so that at least one BPM was located between any two successive correctors. After removing the affected correctors and a number of malfunctioning BPMs, the resulting response matrix used 375 rf BPMs and 307 correctors.

In each plane, the M x N response matrix maps N corrector changes to M BPM changes. When we measure M BPM waveforms simultaneously, we can get all N sources by multiplying the N x M pseudo-inverse matrix into the *M*-dimensional array of BPM data as shown in equation (1):

$$\Delta c = R^{+}_{pinv} \cdot \Delta b \,, \qquad (1)$$

where Δb is the array of synchronous BPM changes, Δc is the array of sources, and R^{+}_{pinv} is the truncated pseudo-inverse response matrix (see equation (3) below.)

SVD and Truncated Pseudo-invert Response Matrix

The response matrix of APS is analyzed by SVD [7] using equation (2)

$$R = U \cdot S \cdot V' \qquad (2)$$

where U and V are orthonormal matrices comprising the eigenvectors, and S is the diagonal matrix of singular values.

Very small singular values lead to large errors after multiplying the pseudo-inverse response matrix with the measured AC orbit, and consequently will result in an acceptable uncertainty for source localization. To deal with this, we zero very small singular values and truncate the pseudo-inverse response matrix as indicated in equation (3):

$$R^{+}_{pinv} = V \cdot S^{-1}_{truncated} \cdot U' , \qquad (3)$$

where U and V are the same matrices used in equation (2) and $S^{-1}_{truncated}$ is the inverse of the singular values matrix after the elimination of very small singular values.

If too many singular values are retained, unphysical effects such as noise-induced random step changes from one BPM to the next will result in very large corrector values. On the other hand, if too few singular values are retained, the corrector pattern will be spread over many sectors.

To demonstrate this, we vary the number of singular values for the AC orbit driven by a sine wave at 18.049 Hz on corrector S10A:V3 shown in the lower panel of Fig. 1. The localization results are shown in Figures 4 through 6, using 10, 80, and 150 singular values, respectively. It appears that retaining about 80 singular values is sufficient to localize the noise source for this test case.

Using the same procedure outlined above for the case of the driven 18.049-Hz horizontal orbit shown in the upper panel of Fig. 1, we get the predicted corrector strengths shown in Fig. 7. The peak value in this case corresponds to corrector S10A:H2, which is incorrect, but within one meter of the corrector that was actually causing the disturbance, S10A:H3.

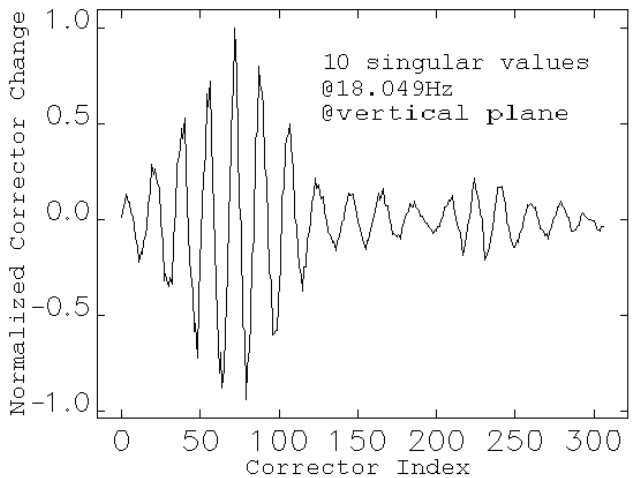

Figure 4: Predicted corrector values resulting from the multiplication of the pseudo-inverse matrix retaining only ten singular values [equation (3)] by the 18.049-Hz vertical orbit shown in the lower panel of Fig. 1.

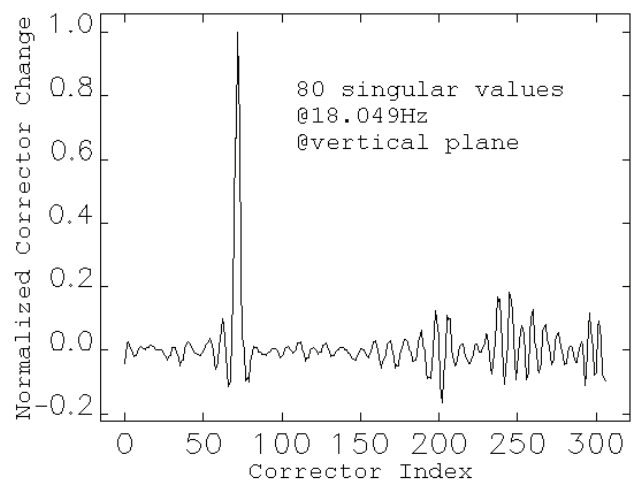

Figure 5: Predicted corrector values, generated in the same fashion as for Fig. 4, but retaining 80 singular values. The peak corresponds to corrector S10A:V3.

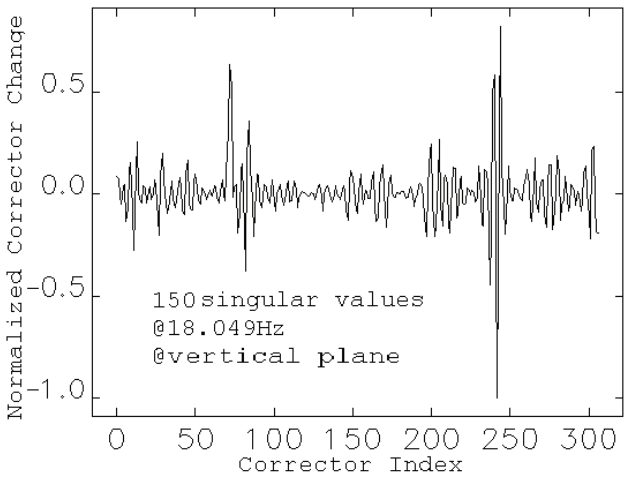

Figure 6: Predicted corrector values, generated in the same fashion as for Figs 4 and 5, but retaining 150 singular values.

.

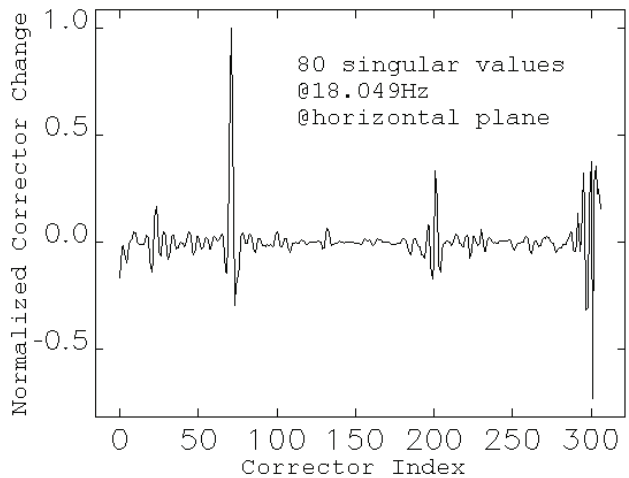

Figure 7: Predicted pattern of correctors derived from the 18.049-Hz horizontal orbit of Fig. 1, caused by deliberately driving corrector S10A:H3. A total of 80 singular values were retained.

Localization of the Unknown Noise Sources

The truncated pseudo-inverse response matrix using synchronous DSP scope BPM data can be used to localize artificial noise sources accurately. In this section we will apply the method to a couple of actual unknown narrow-band noise sources that caused the AC orbits shown in Fig. 3.

We measured the orbit by using the DSP scope tool's double-sector BPM acquisition function with a 154-Hz sample rate. By analyzing the spectra, we noticed spikes at 2-Hz in the horizontal plane and at 59.98-Hz vertically. By multiplying the horizontal truncated pseudo-inverse response matrix by the 2-Hz orbit, we localized the noise source to corrector S38B:H3, shown in Figure 8. With the same process, we localized the noise source at 59.98 Hz to the corrector S1A:V2 in the vertical plane, shown in Figure 9.

Note that for the 2-Hz horizontal case, a large number of singular values were retained in addition to the fact that there were repeatability problems in the derived AC orbit in this part of the ring. This is apparent by inspecting the upper panel of Fig. 3. These observations, coupled with the knowledge that only three out of a total of ten possible BPMs are available in sector 38, suggest that caution be applied before accepting the apparent noise source indicated by Fig. 8 as being genuine.

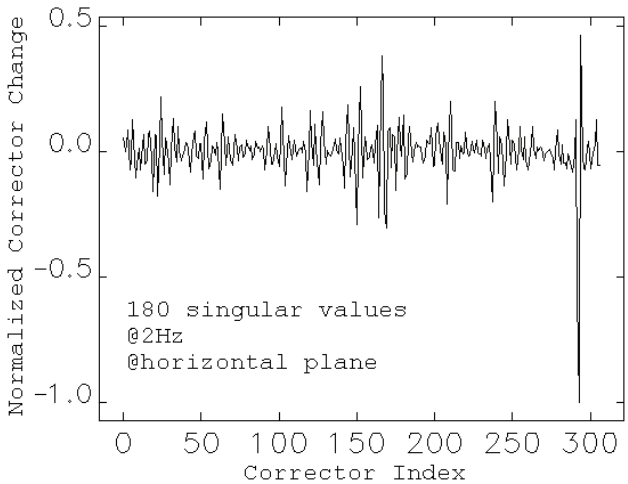

Figure 8: Predicted pattern of correctors corresponding to 2-Hz horizontal orbit of Fig. 3. The peak is located at corrector S38B:H3. Here, 180 singular values are retained.

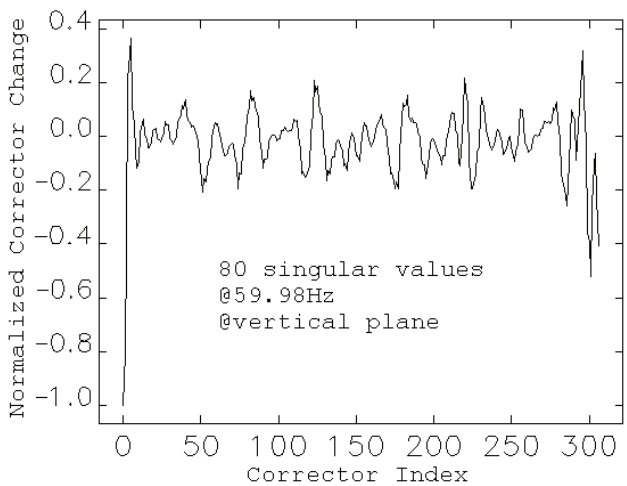

Figure 9: 59.98-Hz noise source in the vertical plane is most likely located at S1A:V2. The first 80 singular values in the ideal vertical response matrix are kept.

CONCLUSION

A technique for extracting AC orbits from 40 non-concurrent time-series data sets with each set comprising 40 waveforms has been developed for narrow-band noise sources. A judicious choice of correctors and singular values allows for the localization of these noise sources at the 1- to 2-meter level. The method has been applied successfully to externally driven AC sources at 18.049

Hz, and preliminary predictions for the locations of real-world ambient noise sources have been made. Further work remains to actually locate the components responsible for these narrow-band excitations and eliminate them.

ACKNOWLEDGEMENTS

The authors wish to acknowledge the contributions of V. Sajaev, H. Shang, L. Emery, and F. Lenkszus upon whose work much of the material presented is based.

REFERENCES

[1] J. Carwardine and F. Lenkszus, Real-Time Orbit Feedback at the APS, Proceedings of the 1998 Beam Instrumentation Workshop, Palo Alto, CA, AIP Conf Proc. 451, p. 125 (1998).

[2] J. Carwardine, G. Decker, K. Evans Jr., A. Hillman, F. Lenkszus, R. Merl and A. Pietryla, "Commissioning of the APS Real-time Orbit Feedback System," Proceedings of the 1997 Particle Accelerator Conference, Vancouver, B.C., Canada, http://www.JACoW.org, p. 2281 (1998)

[3] F. Lenkszus, "State-of-the-art Developments in Accelerator Controls at the APS," Proceedings of the 1999 Particle Accelerator Conference, New York, p.333 (1999); http://JACoW.org.

[4] G. Decker, J. Carwardine and O. Singh, "Fundamental Limits on Beam Stability at the Advanced Photon Source," Proceedings of the 1998 Beam Instrumentation Workshop, Palo Alto, CA, AIP Conf. Proc. 451, p. 237 (1998)

[5] Om Singh and Glenn Decker, "Beam Stability at the Advanced Photon Source," Proceedings of the 2005 Particle Accelerator Conference, Knoxville, Tennessee,, p. 3268 (2005) http://www.JACoW.org.

[6] V. Sajaev and L. Emery, "Determination and Correction of the Linear Lattice of the APS Storage Ring," Proc. of EPAC'02, Paris, p. 742 (2002); http://www.JACoW.org.

[7] W. Press, S. Teukolsky, W. Vetterling and B. Flannery, *Numerical Recipes in C 2nd ed*., Cambridge University Press, New York, 1992.

ALS FPGA-BASED TRANSVERSE FEEDBACK ELECTRONICS*

J. Weber, M. Chin, LBNL, Berkeley, CA, U.S.A.

Abstract

The Advanced Light Source Transverse Feedback System currently consists of a refrigerator sized analog delay line system. The new system is the 2nd generation Transverse Feedback System, derived from work done for PEP-II in 2004 [1]. It uses the latest generation Virtex-5 FPGA, and has 12-bit ADCs and DACs for bunch-bunch feedback at 500MHz. In addition, this system provides networked capability for setup and diagnostics.

INTRODUCTION

At the ALS, coupled bunch instabilities are driven by the RF cavity dipole higher order modes (HOMs) and the resistive wall impedance of the vacuum chamber [2]. The existing ALS Transverse Feedback (TFB) System adequately damps these beam oscillations, but does not provide any diagnostic information or remote control capability. Recent experiences using an ADC-FPGA-DAC architecture for bunch-by-bunch feedback systems have proven largely successful. These digital systems provide extensive diagnostic capability with deep memory capable of storing hundreds of turns of bunch data. Set points and diagnostic data can be transferred to and from the system via the control system network.

The existing TFB electronics consist of two microwave receivers for detecting horizontal and vertical moment, a system (shown as two variable attenuators) for mixing the signals from the two pickup stations, a delay, and a power amplifier for driving the kicker [2]. The electronics upgrade replaces the delay element (currently a long cable) with an FPGA-based digital system. Figure 1 shows the diagram of the upgraded electronics.

The new digital system will be based on the model of the PEP-II TFB upgrade [1]. Using the latest technology, the system is capable of feedback at the full ALS bunch rate of 500MHz. Data converters with 12-bit resolution clocked at 500MHz (effective) sample the pickups and drive the kicker outputs for bunch-by-bunch feedback. The Xilinx® Virtex™-5 LX50 FPGA provides filter, delay, data capture, and control system interface functions. This paper describes the design details of the new ALS TFB electronics.

HARDWARE

The new TFB system electronics consist of a two board set: a commercial FPGA evaluation board connected via a high-speed connector interface to a custom in-house designed board containing the high-speed analog interfaces. The block diagram for the TFB hardware is shown in Figure 2.

* This work was supported by the U.S. Department of Energy, under Contract No. DE-AC03-76SF00098

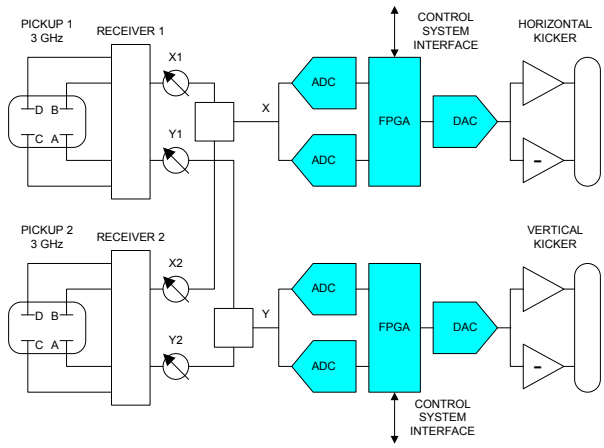

Figure 1: ALS Transverse Feedback Electronics.

The demo board chosen for this design is the Xilinx® Virtex™-5 LX Evaluation Kit from Avnet. This board contains many of the desired system components including a V5LX50 FPGA, EXP high-speed expansion connectors, 64MB DDR2 SDRAM, 16MB Flash Memory, and Ethernet PHY [3]. The FPGA contains sufficient programmable logic resources for the desired functionality and runs comfortably at the required clock speed of 250MHz. The EXP expansion connectors are controlled impedance Samtec QSE/QTE series connectors specified to run up to 750MHz for differential signals [4]. These connectors provide sufficient I/O to connect the FPGA to the high speed 12-bit data converters and other interfaces on the custom EXP daughter card. The SDRAM contains the software code to run the control system interface and the memory used for data capture diagnostics. The Flash Memory provides flexible boot options for the control system software. The Ethernet interface allows connectivity with the ALS Control System network.

The custom board is an EXP expansion daughter board that contains the high-speed data converters, clock distribution and programmable delay, and a moderate performance two-channel 16-bit DAC to set the kicker amplifier gains. Two 12-bit LTC2242-12 ADCs, sampling at $f_{RF}/2$ = 250Msps 180 degrees out of phase, sample the pickup signals on every bunch. The pickup data is transferred to the FPGA, clocked at 250MHz, which calculates the correction value to apply to the kickers on the two separate data paths. The correction data is fed through the FPGA DDR output buffers to the DAC at 500 MHz. The 12-bit MAX5886 DAC provides correction output to the kickers at 500Msps. This custom board receives the 500MHz bunch rate clock from the ALS timing system and divides and distributes it to the FPGA, DAC, and ADCs. Two MC100EP195 programmable clock delay chips can be used to fine tune the DAC and ADC clocks in 10ps increments over a 10ns range.

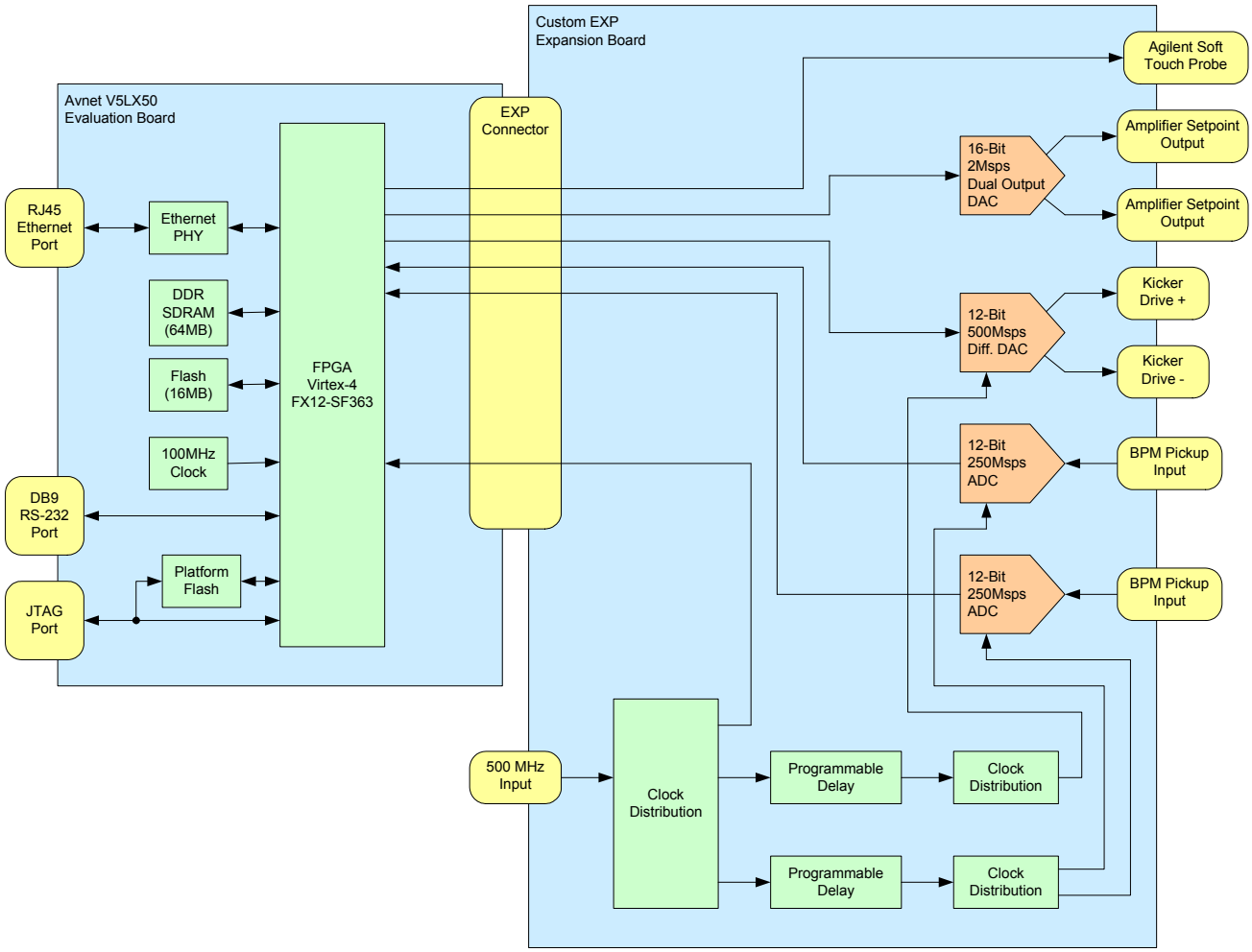

Figure 2: ALS Transverse Feedback Hardware Block Diagram.

FIRMWARE

The FPGA firmware consists of an embedded processor, standard peripheral interfaces, and custom cores for EXP board interfaces and feedback logic. A block diagram of the TFB firmware is shown in Figure 3. The PEP-II TFB design contained Virtex-2Pro series FPGAs with embedded PowerPC hard core processors running the control system interface software [2]. Since the Virtex-5 LX series FPGA on this board does not have an embedded PowerPC, the MicroBlaze soft core processor will be used. The processor runs the control system interface software, which initially will be a simple TCP interpreter based on an Avnet design example. Eventually, this interface could be replaced with an EPICS channel access server running on a version of the Linux operating system (OS). More details regarding the use of embedded processors in FPGA-based systems can be found elsewhere [5].

Several peripheral interface cores included in the development kit design templates are used in this design including an Ethernet controller (EMAC), Flash Memory controller, UART, Agilent Soft Touch Probe interface, Block RAM Controller, and SDRAM Mult-Port Memory Controller (MPMC2). These cores are developed by Xilinx and are pre-configured for the development kit hardware. The EMAC is used by the system software to communicate with the control system network. The Flash

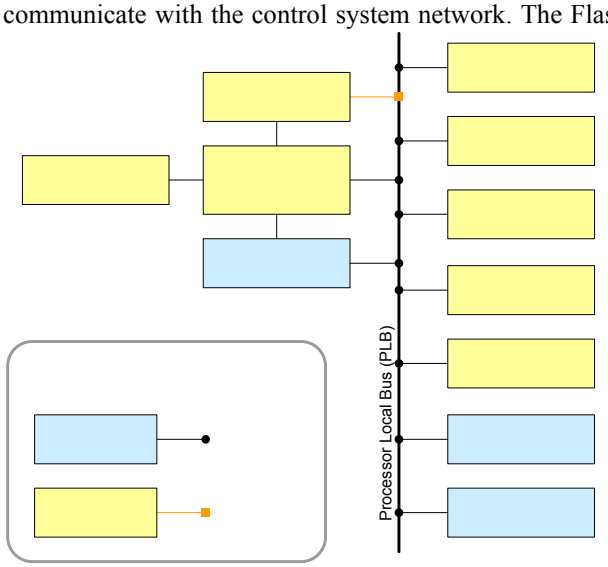

Figure 3: ALS Transverse Feedback Firmware Block Diagram.

can be used to store the OS or an OS bootloader application depending on the size. The UART and Soft Touch Probe can be used for status and debugging.

The Block RAM contains initial boot code for the processor. This code typically boots the OS or OS bootloader from the Flash. The MPMC2 allows simultaneous access to the SDRAM from multiple sources. The SDRAM stores all OS and program code that is accessed by the processor. It also stores bunch data written by the feedback core for diagnostic purposes.

The firmware also contains several custom cores. The feedback core provides access to the high-speed ADCs and DACs and implements the filter and delay logic for feedback. This core can write the ADC data to the SDRAM through a dedicated port in the MPMC2 core. Another core provides an interface to the lower performance DAC that controls the kicker amplifier gains. A third custom core controls the programmable delay chips to tune the ADC and DAC clock edges.

FUTURE CONSIDERATIONS

There are several aspects of bunch-by-bunch feedback systems that can be improved over the capabilities of the current generation of systems. One obvious limitation is the sampling speed of the ADCs. 12-bit 250Msps ADCs are near the edge of current performance limitations, but it is likely that there will be a 12-bit 500Msps part suitable for use in feedback systems in the next few years. While there is always a push for higher resolution parts, there is no proof of any performance advantage of 12-bit over 8-bit bunch-by-bunch feedback systems. We plan to run a side-by-side comparison of these systems to see if there is any performance advantage at the ALS.

Similarly, current FPGAs are incapable of single channel processing at 500MHz. The fastest FPGA speed grades boast routing designs running up to 550MHz, but with minimal design complexity the maximum routed performance decreases dramatically. With our new system using a Virtex-5 at the slowest speed grade, we are able to comfortably route complex designs at 250MHz. At the present rate of development, the performance of these devices will allow routing complex designs at 500MHz in the next few years as well.

With both ADCs and FPGAs running at 500MHz, systems will be capable of single channel feedback through the entire digital system. This is important because there are limitations to the current multi-channel sampling and processing designs. First, these designs cannot provide full resolution for particle accelerators with odd harmonic numbers due to errors in matching the multiple channels. With an odd harmonic number and a two channel sampling system like presented here, each bunch is sampled by the opposite ADC on each consecutive turn. Therefore gain and offset differences between the channels and clock jitter and mismatch can all affect the resolution of the sampled bunch data. This is not an issue for accelerators like the ALS with even harmonic numbers because each bunch is sampled by the same ADC on every turn (i.e. ADC0 samples even bunches and ADC1 samples odd bunches). However, for absolute bunch amplitude measurements, it is an issue for even harmonic number accelerators as well.

Improvements can also be made in the logic design of existing systems. One feature that we may add to the ALS system is the ability to provide a separate gain for each bunch. A table of gain values would be loaded into FPGA memory with a value for each bunch. This could be used for kick out or grow-damp studies of individual or arbitrary patterns of bunches.

An extension of this concept is to add bunch cleaning capability to the feedback system. The new ALS FPGA-based bunch cleaning hardware uses the same FPGA-DAC architecture as the ALS TFB system [6]. The bunch cleaning is currently connected to a spare set of kickers. Using the TFB electronics to run both the feedback and bunch cleaning algorithms by combining the logic into a single FPGA would require only a single electronic system and only one kicker.

CONCLUSION

Design of FPGA-based feedback electronics is not a new concept, but using only two 12-bit data converters to generate bunch-by-bunch feedback at 500MHz has not previously been achieved. This provides tremendous improvement over the existing analog system used at the ALS. Storage of bunch-by-bunch 12-bit data allows for advanced diagnostics and post-mortem analysis. The embedded Microblaze processor provides control system network accessibility to set points and diagnostic data. The electronics have been built and are being qualified with the plan to commission the system by the end of this calendar year.

REFERENCES

[1] J. Weber, et al, “PEP-II Transverse Feedback Electronics Upgrade”, PAC’05, Knoxville TN, May, 1995.

[2] W. Barry, et al, "Design of the ALS Transverse Coupled-Bunch Feedback System", PAC’93, Washington DC, May, 1993.

[3] Xilinx® Virtex™-5 LX Evaluation Kit User Guide, V1.0, November 11, 2006, http://www.files.em.avnet.com/files/177/xlx_v5_lx_dev-ug-rev1.3-123107.pdf.

[4] EXP Expansion Connector Specification, Revision 1.4, September 26, 2007, http://www.em.avnet.com/ctf_shared/evk/df2df2usa/exp_specification_v1_4.pdf

[5] J. Weber, M. Chin, “Using FPGAs with Embedded Processors for Complete Hardware and Software Systems”, BIW06, Batavia, NY, May 1-4, 2006.

[6] M. Chin, J. Weber, “ALS FPGA-Based Bunch Cleaning,” these proceedings.

STREAK-CAMERA MEASUREMENTS WITH HIGH CURRENTS IN PEP-II AND VARIABLE OPTICS IN SPEAR3*

Weixing Cheng,# Alan Fisher, and Jeff Corbett
Stanford Linear Accelerator Center, 2575 Sand Hill Road, Menlo Park, CA 94025

Abstract

A dual-axis, synchroscan streak camera was used to measure longitudinal bunch profiles in three storage rings at SLAC: the PEP-II low- and high-energy rings, and SPEAR3. At high currents, both PEP rings exhibit a transient synchronous-phase shift along the bunch train due to RF-cavity beam loading. Bunch length and profile asymmetry were measured along the train for a range of beam currents. To avoid the noise inherent in a dual-axis sweep, we accumulated single-axis synchroscan images while applying a 50-ns gate to the microchannel plate. To improve the extinction ratio, an upstream mirror pivoting at 1 kHz was synchronized with the 2kHz MCP gate to deflect light from other bunches off the photocathode. Bunch length was also measured on the HER as a function of beam energy. For SPEAR3 we measured bunch length as a function of single-bunch current for several lattices: achromatic, low-emittance and low momentum compaction. In the first two cases, resistive and reactive impedance components can be extracted from the longitudinal bunch profiles. In the low-alpha configurations, we observed natural bunch lengths approaching the camera resolution, requiring special care to remove instrumental effects, and saw evidence of periodic bursting.

INTRODUCTION

The Stanford Linear Accelerator Center (SLAC) has a long history of both high-energy physics (HEP) and synchrotron radiation (SR) research with storage rings. Recently, PEP-II and SPEAR3 (Table 1) together purchased a Hamamatsu C5680 streak camera with ~2-ps resolution, digital image capture, and dual-axis synchroscan sweeping to measure bunch length, characterize impedance, and observe beam instabilities.

PEP-II

The PEP-II *B* Factory completed its final run on April 7, 2008. Since the first beam in 1997, the PEP rings have run at a center-of-mass energy of 10.58 GeV, the Y(4S) resonance. Electrons at 8.97 GeV in the high-energy ring (HER) collide with 3.12-GeV positrons in the low-energy ring (LER) to produce $B\overline{B}$ pairs moving in the lab frame. For the final months of the 2008 run, the HER energy was shifted to collide at the 2S (10.02 GeV) and 3S (10.36), and then scanned up from just below the 4S to 11.2 GeV. This provided an opportunity to measure bunch length over a range of HER energies from 8.02 to 10.08 GeV.

Each PEP-II ring has a synchrotron-light monitor (SLM) observing visible dipole radiation [1]. The LER SLM collects positron emission from a dipole 30 m downstream of the interaction point (IP), while the HER SLM collects electron emission from an arc dipole. At each SLM, in-tunnel CCD cameras record beam images and interferometer fringes [2], and a visible-light transport line brings part of the beam to a focused image in an optics hutch outside the shielding wall for more sophisticated time-resolved cameras [3,4].

In the last year of PEP-II operations, the new streak camera was first installed in the LER hutch to resolve bunch-length discrepancies observed in 2004 when comparing a quick series of measurements with a borrowed streak camera to the high-frequency roll-off of the bunch spectrum [3]. The camera was then moved to the HER to track bunch length during the energy scan.

Since the beams collide at high current—typically 1.75 A in the HER and 2.6 A in the LER, for a peak luminosity of 1.0×10^{34} $cm^{-2}s^{-1}$—the gradual increase in beam loading following the 100-ns abort gap in the fill pattern causes a shift in synchronous phase, so that bunches further along the train arrive earlier in the RF period. At high-currents, the transient from first to last bunch is comparable to the natural rms bunch length (~40 ps in the LER). To measure bunch length without folding in the phase shift of the entire train required dual approaches to select a narrow interval: an electronic gate of the camera's microchannel plate (MCP), and an oscillating mirror that synchronously steers the light across the entrance optics.

SPEAR3

SPEAR3 is a 3-GeV storage-ring light source delivering UV to x-ray radiation into 13 beam lines (~30 branch lines) in a 500 mA, multi-bunch mode. The machine lattice was recently adjusted from achromatic (zero-dispersion) to finite-dispersion optics to reduce horizontal emittance, and tests have begun on low-momentum-compaction (low-α) lattices for dynamical pump-probe experiments. The SLM at SPEAR3 receives unfocused

Table 1: Key PEP-II and SPEAR3 parameters.

	PEP-II		SPEAR3
	HER	LER	
Energy (GeV)	9 (8–10)*	3.12	3
f_{RF} (MHz)	476	476	476.315
Harmonic No.	3492	3492	372
Bunches**	1722	1722	280
Spacing (ns)	4.2	4.2	2.1

* Energy varies during the CM-energy scan.

** Typical multi-bunch fill. PEP-II fills every 2nd bucket outside a 100-ns abort gap. SPEAR3 fills every bucket, with a single bunch in a 100-ns ion clearing gap.

* Work sponsored by U.S. Department of Energy Contract DE-AC03-76SF00515 and Office of Basic Energy Sciences, Division of Chemical Sciences.

chengwx@slac.stanford.edu

visible light through a 420-nm long-pass filter and a 6-in-diameter lens with a 2-m focal length. The light is relayed to several diagnostic instruments, including the streak camera [5,6]. The nominal bunch length is ~20 ps rms but can be as short as ~2 ps in the low-α mode, a value comparable to the C5680 streak-camera resolution.

STREAK-CAMERA OPERATION

Single- and Dual-Axis Synchroscan

The most basic operation of a streak camera uses a triggered sweep to measure the longitudinal intensity profile of a light pulse. Visible SR from the single passage of a bunch, however, is generally weak, producing an image dominated by shot noise that severely increases the χ^2 of a Gaussian fit. On the other hand, if more intensity is available, space charge at the photocathode can broaden the profile, again leading to erroneous results. Superposition of repeated low-light measurements is compromised by random trigger jitter. The dual-sweep mode (fast [ps] vertical, slow [100 ns to 100 ms] horizontal) is still subject to both shot noise and jitter in the fast-axis trigger.

An alternative is "synchroscan" mode, in which a large-amplitude sinusoid at a sub-harmonic of the storage ring's master oscillator drives the streak-camera sweep. Photoelectrons are dispersed across the MCP only during the linear part of the sine, near the zero crossings. Repeated low-light images are summed over a long exposure (typically 120 ms) on the camera's CCD to produce an image with little space-charge broadening, shot noise, or jitter.

At high currents in PEP-II, the slew in synchronous phase along the bunch pattern is comparable to the bunch length. Single-axis synchroscan overlaps bunches with centroids at different arrival times, broadening the measured length. In dual-axis synchroscan mode, the camera separates the image of each SR pulse in the bunch train, highlighting this slew. The instantaneous profile can be found by combining nearby bunches in software, but the Gaussian fits still suffer from noise. Instead, we combine single-sweep synchroscan with electronic and mechanical gating to repeatedly transmit light from only a few bunches along the train over a long exposure.

In SPEAR3, beam loading is not severe, but ~1-ps RF phase jitter eventually masks the true bunch-length measurements in the short-pulse mode as α is reduced. Attempts have been made to remove phase noise by fitting a series of pulse-by-pulse measurements in the dual-scan mode, but again shot-noise makes this method less satisfactory than synchroscan. Also, the low-α studies have seen a "bursting" phenomenon (discussed below), perhaps from a semi-periodic relaxation oscillation leading to emittance blow-up, which may be best explored using electronic/mechanical gating.

Electronic Gating

The PEP-II bunch length can be measured despite the synchronous-phase slew along the train by combining (single-axis) synchroscan with a narrow MCP gate locked to the ring clock, in order to superpose images from many turns, but from the same slice within the bunch train.

The MCP gate on the Hamamatsu C5680 has a minimum width τ_g = 50 ns and a maximum repetition rate f_g = 10 kHz. For accurate measurements, the MCP gate must provide sufficient extinction to block unwanted light from the remaining bunches. A 7.3-μs PEP-II turn contains 1722 bunches spaced by 4.2 ns ($2/f_{RF}$). Neglecting the 100-ns (1.4%) beam-abort gap, the necessary extinction ratio is $\tau_g f_g = 5\times10^{-4}$, easily within the factory specification of 10^{-6}. Since the PEP-II synchroscan drive is at $f_{RF}/4$ (119 MHz, half the bunch rate), a small phase shift from the zero crossing separates the even and odd bunches into two images located above and below the screen's center. Each spot combines bunches separated in time by 8.4 ns, putting 6 bunches in the 50-ns MCP gate.

Adding the MCP gate clearly reduces the image brightness. It drops further when the gate timing is centered on the abort gap, but does not completely darken. Instead the gap image shows a background spot slightly shifted from the bunch-train image and of comparable intensity (Fig. 1(a)). Further evidence of poor extinction is a variation seen in bunch length along the train, especially at the head where the synchronous phase changes most rapidly. While discussing this leakage with Hamamatsu, we pursued alternative ways to extract the true bunch length.

Scanning Mirror

In PEP-II, visible light is relayed to the streak camera through a 450-nm filter with a full width of 30 nm, and focused onto the entrance slit by a microscope objective. To improve the extinction ratio, we installed a scanning galvanometer (GSI Lumonics VM500S)—a small, flat mirror mounted on the shaft of a DC motor—upstream of the objective. Such devices are found in laser scanners for light shows, displays, and printers, and are often used in pairs for raster scans. Since they turn rapidly, one was used in a previous experiment that scanned light across the photocathode of a gated camera to observe the turn-to-turn evolution of transverse beam sizes in PEP-II during the onset of beam instability and during injection [4].

A driver board (also GSI Lumonics) pivots the mirror at an angle proportional to a control voltage. As a sinusoidal drive turns the mirror through ±2°, the incident SR light sweeps horizontally well beyond the acceptance of the objective, passing through it at each zero crossing of the angle. Sweeping the beam orthogonally to the (vertical) fast time axis avoids blurring the time resolution. Since mirror inertia limits the sinusoidal drive

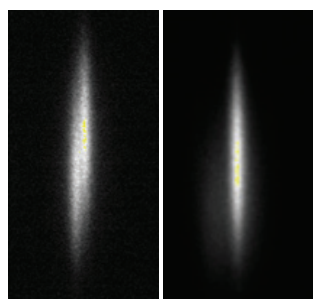

(a) (b)

Figure 1: (a) Streak image with synchroscan and 50-ns MCP gate. The image to the lower left is leakage through the gate. (b) Image with MCP gate plus rotating mirror, for minimal leakage.

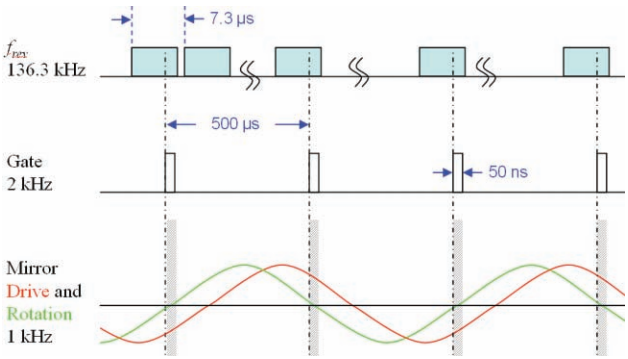

Figure 2: Timing of bunch pattern (top), streak-camera gate (middle) and rotating mirror (bottom).

to 1 kHz, we slow the MCP gate to 2 kHz (every zero crossing, Fig. 2).

To synchronize the MCP gate with the mirror's zero crossings, the 136-kHz ring-turn (f_{rev}) clock triggers a digital delay generator (SRS DG535) with four delays. One, set to 499 µs, slows the retrigger rate to ~2 kHz, locked to the next ring turn. Two delays start and stop the 50-ns MCP gate. The fourth triggers a function generator (SRS DS345) set to produce a single-period, 1-kHz sine wave, starting at −270° to provide a delay before its zero crossing. The DS345 waits for its 1-ms output to finish before retriggering. The result is a continuous 1-kHz sine wave rotating the mirror through ±2° at a phase locked to the ring-turn clock and to the MCP gate.

To align the mirror, we first set the drive amplitude to zero, using a DC offset from the DS345 to aim the light through the middle of the objective lens onto the center of the streak camera photocathode. Next the drive was slowly increased while an oscilloscope displayed both the drive and readback signals for the mirror angle. This allowed us to determine the maximum drive amplitude at 1 kHz (400 mV peak) and to measure the inertial lag of the mirror zero crossing (Fig. 2) relative to its trigger.

These settings were sufficient to see MCP-gated light on the streak camera at both of the mirror zero crossings. Small delays (tens of ns) of the gate then merged the two zero-crossing images. With this combined electronic and mechanical gating, the residual leakage in the abort gap was reduced to only a weak horizontal smear apertured on either side by the size of the objective lens. Most of this background was excluded from our analysis by software selecting a narrow region of interest for profiling; any remainder was measured and subtracted.

ANALYSIS OF BUNCH-PROFILE IMAGES

The impedance of a storage ring both stretches and skews the Gaussian form of the longitudinal bunch profile as the single-bunch current increases. Wakefields generated at the head of the bunch couple to the tail via resistive and reactive broadband impedance elements. The former elements steepen the head of the bunch compared to the tail, while the latter mainly increase bunch length (potential-well distortion) [7]. In general, the combination of wakefield impedance and energy spread distorts the longitudinal bunch distribution away from an ideal Gaussian as single-bunch current increases.

Consequently, we used an asymmetric Gaussian profile:

$$I(z) = I_0 + I_1 \exp\left\{-\frac{1}{2}\left(\frac{(z-z_0)}{[1+\mathrm{sgn}(z-z_0)A]\sigma}\right)^2\right\} \quad (1)$$

where A is a scalar asymmetry factor and z_0 locates the distribution offset, to fit projections of a user-specified region of interest in the synchroscan image. At low bunch currents, there is no asymmetry, and so we set A to 0 to reduce numerical noise.

Below the microwave threshold, we can fit the measured bunch lengthening versus bunch current I_b to Zotter's potential-well distortion formula [7]:

$$\left(\frac{\sigma_z}{\sigma_{z0}}\right)^3 - \frac{\sigma_z}{\sigma_{z0}} = \frac{1}{\sqrt{2\pi}}\frac{\alpha_c e I_b}{E_0 \nu_{s0}^2}\left(\frac{c}{\omega_{\mathrm{rev}}\sigma_{z0}}\right)^3 \mathrm{Im}\left[\left(\frac{Z}{n}\right)_{\mathrm{eff}}\right] \quad (2)$$

to find the reactive component of the effective impedance and so estimate the ring's broadband inductance L:

$$L\omega_{\mathrm{rev}} = \mathrm{Im}\left[(Z/n)_{\mathrm{eff}}\right] \quad (3)$$

Here E_0 is the beam energy and ν_{s0} is the low-current synchrotron tune.

Above the current threshold for the longitudinal microwave instability, energy spread further increases bunch length, according to Chao-Gareyte scaling [8]; then an asymmetric Gaussian provides an adequate but less accurate fit. This was a consideration only for SPEAR3 since PEP-II bunch currents are below this threshold.

MEASUREMENTS ON PEP-II

Data was taken under three conditions: in a full ring, during filling, and—for the LER—with a single test bunch filled in small increments. The first two cases involved parasitic measurements during routine collisions, and required both gates. The single-bunch data (which needed no gating) was obtained in a dedicated experiment in the final hours of the 2008 run.

PEP's bunch-current monitor (BCM) measures the charge in each ring's 3492 buckets at 1 Hz [1]. The bunch-injection controller (BIC) computer then arranges injection to fill each ring in a user-specified pattern (normally a uniform fill). After filling, the charge in each bunch is kept steady with small injections at a few Hz as needed ("trickle charge"). Thus streak-camera images taken with the ring current at its goal have a well-determined bunch charge within the MCP gate. During fills, the charge in the gate is less certain, as the linac timing shifts to fill different bunches, and histories of the BCM readings and filling sequence are not recorded.

Figure 3 shows measurements with 2150 mA in the LER, using a 50-ns MCP gate plus the rotating mirror, both delayed in 100-ns steps. Unlike measurements with only the MCP gate, here we see a constant the bunch length (36.9 ps) and Gaussian asymmetry factor (-0.06).

The synchronous phase clearly changes due to beam loading. Unfortunately, the RF phase at the LER optics hutch, at the end of the RF transport line, is poorly stabilized, drifting by 10 to 20 ps over hours and some-

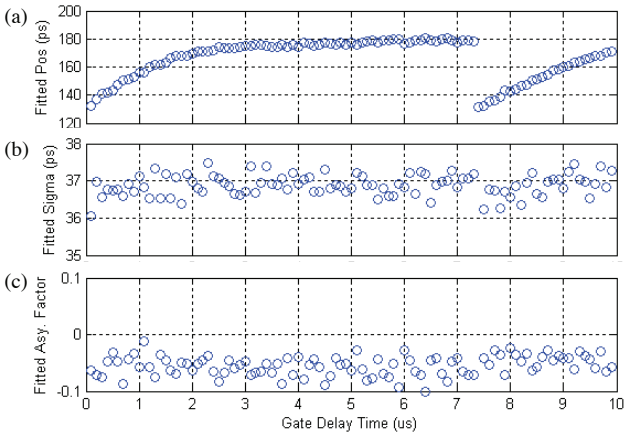

Figure 3: Measurements along a train of 1722 LER bunches, using a 50-ns gate delayed in 100-ns increments from the abort gap. (a) Location of fitted peak z_0, which slews by ~50 ps, corresponding to $\Delta\phi_s = 8.6°$ of RF. The gap returns after 1 turn, 7.3 μs. (b) Bunch length (rms) σ. (c) Asymmetry factor A.

times minutes. Consequently, the streak image moves on the screen, complicating relative phase measurements for scans in collision. However, the experiment varying the charge in a single test bunch from 0 to 3 mA (Fig. 4) included a comparable total charge in several low-charge reference bunches, placed 180° of the 119-MHz drive away from the test bunch. The images of the reference bunches then overlapped on the streak camera at a different location from the test-bunch image, allowing a measure of the phase slew independent of the RF drift.

In the HER, we measured the bunch length versus bunch current (Fig. 5) and energy (Fig. 6). The RF voltage was reduced from 16.5 to 14 MV for the low-energy point at the Y(2S) resonance. As with the LER, the phase transient along the bunch train due to beam loading required both the MCP gate and rotating mirror. The HER's bunch lengthening is smaller than the LER's due to a lower chamber impedance, and the asymmetry is negligible.

MEASUREMENTS ON SPEAR3

SPEAR3 recently retuned the original achromatic (AC) optics by adding finite dispersion in the ID straight sections. The corresponding change in lattice partition

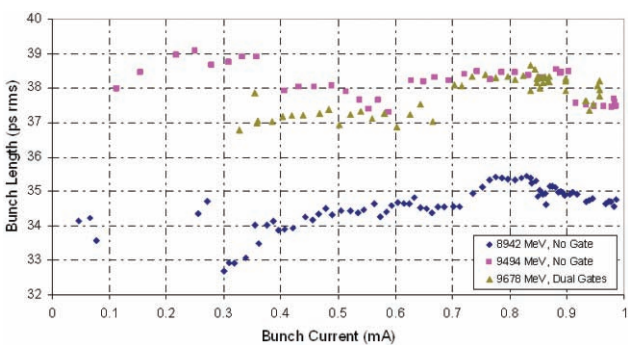

Figure 5: HER bunch length vs. bunch current at three energies. Using dual gates at 9.7 MeV reduced the measured length compared to 9.5 MeV without gating.

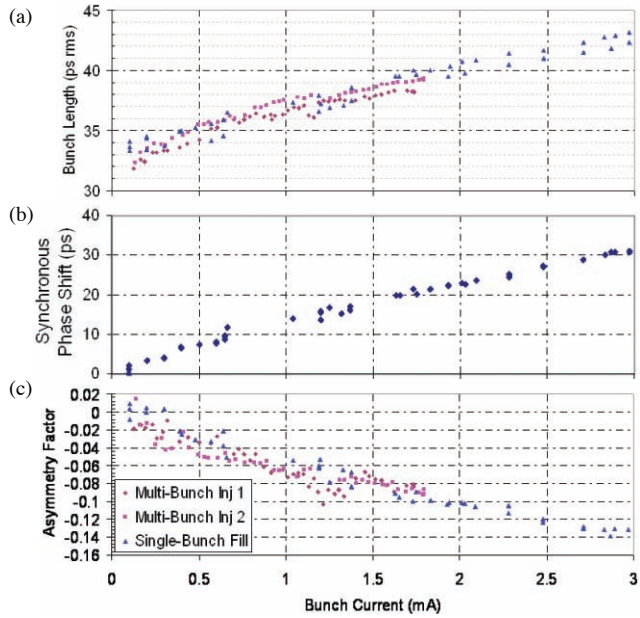

Figure 4: LER data vs. bunch current. (a) Bunch length σ. (b) Synchronous-phase shift $\Delta\phi_s$. (c) Asymmetry factor A.

numbers gives the new low-emittance (LE) optics an emittance just below 10 nm·rad, rather than 16, but increases the natural bunch length from 17 to 20.4 ps. As the ring moves toward top-off operation at 500 mA and adds more IDs, it is important to understand bunch lengthening, beam lifetime, and associated impedance effects with the LE optics. The low-α (LA) lattices are equally important, but in many ways more challenging [9], in part because the short bunches approach the resolution limit of the C5680 streak camera. Special care is therefore needed to verify the expected $\alpha^{1/2}$ scaling.

Bunch-length measurements were made for all three optical configurations as a function of single bunch current (Fig. 7) in single-axis synchroscan mode. For the AC and LE optics, the natural bunch length agrees with theory but can vary by 1 to 2 ps between measurements taken several weeks apart. Both lattices show a "knee" in the bunch-length curves near 7 mA, which may be the onset of the microwave instability; we are actively pursuing this effect. Fitting the low-current data to asymmetric Gaussian profiles and using Zotter's formula for potential-

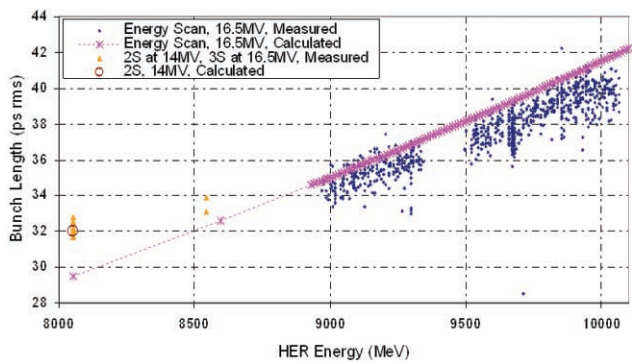

Figure 6: HER bunch length vs. energy for ring currents between 1500 and 1750 mA. V_{RF} = 14 MV for Y(2S) at 8 GeV, 16.5 MV for all others.

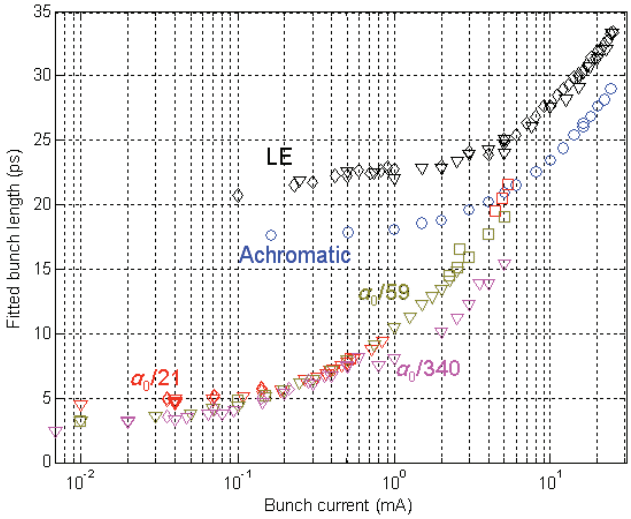

Figure 7: Bunch length (rms) versus single-bunch current in SPEAR3 for different lattices.

well distortion yields $|Z/n| \approx 0.28\ \Omega$ or L ≈35 nH.

The low-α case is more complicated because rapid bunch lengthening begins at very low current. Decreasing α by a factor of 60 lowers the natural bunch length below 2.5 ps rms, which is suitable for some short-pulse SR research, albeit at low single-bunch currents. The injected current must be kept below 10 μA to preserve the natural bunch length, yielding low light levels to experimentalists and on the photocathode.

Before correcting for streak-camera resolution, Fig. 7 shows low-current bunch lengths of 4.5, 3.2 and 2.5 ps rms for α_0/21, α_0/59 and α_0/340 respectively, whereas direct $\alpha^{½}$ scaling from the AC optics predicts lengths of 3.7, 2.2, and 0.9 ps rms. The common correction subtracts in quadrature the minimum spot size measured with the streak camera in "focus mode" (no streak deflection). We measured this value to be 5.0 pixels FWHM, which converts to 0.32 ps rms (0.75 ps FWHM) in the most sensitive range (R1), below the camera's specified resolution of 2 ps FWHM. However, other broadening effects apply, including dispersion of the photoelectrons emitted at the cathode and a lower space charge in focus mode. The 2-ps specification is also based on single-shot measurements with a short 800-nm laser pulse; dispersion is greater at our 550-nm wavelength. Synchroscan introduces additional broadening effects: jitter on the beam's RF (~1 ps rms) and the synchroscan drive, and dipole-mode synchrotron oscillations of the beam. As a result, an effective R1 resolution of ~2.4 ps rms (5.6 ps FWHM) is needed to make all three measurements consistent with predictions.

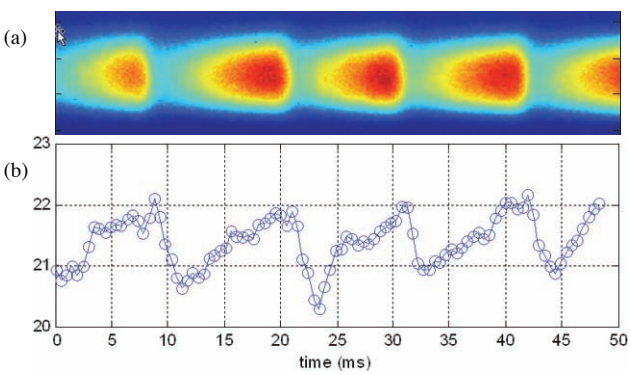

Figure 8: Dual-axis bursting in SPEAR3 at 5.3 mA with the α_0/21 lattice. (a) Dual-axis streak image. (b) Bunch length (ps rms) from this image.

Finally, with LA optics the total injected charge is limited to ~1 mA/bunch unless the RF voltage is reduced below 2 MV from 3.2 MV. Above ~3mA/bunch, the α_0/21 lattice exhibits quasi-periodic bursts in synchrotron-radiation intensity and increased bunch length (Fig. 8) [10].

SUMMARY

Streak-camera measurements of bunch length and profile asymmetry at high currents in the PEP-II rings require a novel electronic/mechanical gating configuration to remove the effect of slew in synchronous phase following the abort gap. Bunch-length measurements in SPEAR3 yield an inductive impedance of $|Z/n| \approx 0.28\ \Omega$ and with low-α lattices require careful evaluation of the camera's true resolution limit in synchroscan mode.

ACKNOWLEDGEMENTS

We gratefully acknowledge the advice and assistance of Alex Lumpkin, Walter Mok, Jim Sebek and Bill Cieslik.

REFERENCES

[1] A.S. Fisher, "Instrumentation and Diagnostics for PEP-II," BIW98, Stanford, CA, 4–7 May 1998, p. 95.
[2] A.S. Fisher, E.L. Bong, R.L. Holtzapple, and M. Petree, "Beam-Size Measurements on PEP-II Using Synchrotron-Light Interferometry," PAC01, Chicago, IL, 18–22 June 2001, p. 547.
[3] A.S. Fisher *et al.*, "Bunch-Length Measurements in PEP-II," PAC05, Knoxville, TN, 16–20 May 2005, p. 1934.
[4] A.S. Fisher *et al.*, "Turn-by-Turn Imaging of the Transverse Beam Profile in PEP-II," BIW06, Batavia, IL, 1–4 May 2006, p. 303.
[5] W.J. Corbett, C. Limborg-Deprey, A.Y. Mok and A. Ringwall, "The SPEAR3 Diagnostic Beam Line," PAC05, Knoxville, TN, 16–20 May 2005, p. 4057.
[6] W.J. Corbett *et al.*, "Bunch-Length Measurements in SPEAR3," PAC07, Albuquerque, NM, 25–29 June 2007, p. 4159.
[7] B. Zotter, "Potential-Well Bunch Lengthening," CERN SPS/81-14 (1981).
[8] A.W. Chao and J. Gareyte, "Scaling Law for Bunch Lengthening in SPEAR-II," Part. Accel. **25** (1990) 229.
[9] X. Huang *et al.*, "Low-Alpha Mode for SPEAR3," PAC 2007, Albuquerque, NM, 25–29 June07, p. 1308.
[10] W. Cheng *et al.*, "Bunch Length and Impedance Measurements at SPEAR3," EPAC08, Genoa, Italy, 23–27 June 2008.

DIFFRACTION EFFECTS IN COHERENT TRANSITION RADIATION DIAGNOSTICS FOR SUB-MM BUNCH LENGTH MEASUREMENT*

T. J. Maxwell, D. Mihalcea, Northern Illinois University, DeKalb, IL 60115, U.S.A.
P. Piot, Northern Illinois University, DeKalb, IL 60115, and Fermilab, Batavia, IL 60510, U.S.A.

Abstract

Electrons crossing the boundary between different media generate bursts of transition radiation. In the case of bunches of N electrons, the radiation is coherent and has an N-squared enhancement at wavelengths related to the longitudinal bunch distribution. This coherent transition radiation has therefore attracted attention as an interceptive charged particle beam diagnostic technique. Many analytical descriptions have been devised describing the spectral distribution generated by electron bunches colliding with thin metallic foils making different simplifying assumptions. For typical bunches having lengths in the sub-millimeter range, measurable spectra are generated up into the millimeter range. Analysis of this THz radiation is performed using optical equipment tens of millimeters in size. This gives rise to concern that optical diffraction effects may spread the wavefront of interest into regions larger than the optical elements and partially escape detection, generating a wavelength-dependent instrument response. In this paper we present a model implementing vector diffraction theory to analyze these effects in bunch length diagnostics based on coherent transition radiation.

INTRODUCTION

Relativistic electrons impinging on a metallic foil emit transition radiation (TR) as they move from one medium to the next. In the case where a bunch of electrons is incident on the foil, the slight time delay in the arrival of the charges at the foil introduces a phase delay between emission of this TR. Summing contributions to the emitted electromagnetic radiation of the individual charges over the length of the bunch, one finds for the emitted radiation spectrum

$$I(\omega) = N^2 I_e(\omega) f(\omega) \tag{1}$$

Here N is the number of charges in the bunch and $I_e(\omega)$ is the power spectrum for single electron TR. We assume N to be very large and leave in explicit dependence of the emitted TR spectrum on frequency. The last term $f(\omega)$ is referred to as the form factor of the bunch. For highly relativistic bunches under a one-dimensional line charge assumption, this is given roughly by

$$f(\omega) = \left| \int \rho_{long}(t) \exp(i\omega t) \right|^2 \tag{2}$$

In principle, this N-squared-enhanced coherent transition radiation (CTR) provides a signal strong enough to detect for sufficient bunch charge. However, analysis of the CTR spectrum emitted by beams with typical bunch lengths σ_z on the order of hundreds of micrometers, one must also consider the possibility of diffraction losses in any optical system used for spectral analysis due to the long coherence wavelengths. The goal of this research is to determine the response function $R(\omega)$ of such optical systems and the single-electron TR frequency dependency such that one can correct the modified equation

$$I_{Measured}(\omega) = N^2 I_e(\omega) f(\omega) R(\omega) \tag{3}$$

to recover the mod-squared Fourier transform of the longitudinal bunch distribution $f(\omega)$ from the measured signal.

SIMULATION

Extending previous work [1, 2] our approach is based on simulating ideal wavefront generation and propagation. Our model treats the radiation emitted at TR generation as the exact reflection of the relativistic electron's light-like electromagnetic field from the surface of the foil to generate $\vec{E}_e(\omega)$. At present the foil is treated as an ideal reflector, neglecting dielectric properties. Another approach to ensure proper treatment of the near-field electromagnetic radiation emission for low-energy electrons has been recently suggested in [3].

This source electromagnetic wave is then propagated through the optical system from one surface to the next using a fully three-dimensional vector diffraction integral as derived in [4]. While computationally expensive, this approach has demonstrated great accuracy over a wide variety of aperture size, diffraction distance, and wavelength ranges while preserving the detailed information necessary for reflections off of complex three-dimensional surfaces such as parabolic mirrors. Other methods have been suggested for accounting for these near-field phenomena via fast Fourier transform [5].

In taking this brute force approach to solving the diffraction problem, several enhancements have been added. The entire code is written in C++ and currently operates in a parallelized MPICH2 implementation. To work around the difficulty integrating over the electron's cusped source function in particular, the Cuba 1.4 [6] integration package has been added. Using Cuba's Cuhre adaptive cubature integrating routine, precision control over source integration to fix the overall energy scale of emitted TR wavefronts has been achieved and are in agreement with values predicted elsewhere [5].

Various benchmarks have been performed including comparison to other near-field ($D < \lambda \gamma^2$) TR predictions

*Work supported by US. Department of Energy, under Contract No. DE-FG02-06ER41435 with Northern Illinois University

and other basic diffraction patterns, some of which are outlined in [1]. Testing of repeated application of the diffraction integral as it is used in transporting the wavefront from one surface to the next has also been performed, tightly fixing constraints on the highest frequency that can be analyzed with reasonable accuracy.

SINGLE ELECTRON TRANSITION RADIATION

Further dissection the terms of Equation 3, we present simulated results of single-electron transition radiation as they pertain to the $I_e(\omega)$ term. TR simulations were done for radiation generated by γ = 50, 100, 500 and 2000 single electrons impinging at normal incidence with a 2" (50.8 mm) diameter foil. As shown in the literature, the emitted TR emanates in rings from the foil in the near field with the central ring having the greatest intensity. After reaching the TR formation length of $\lambda\gamma^2$, the radiation appears as a bright ring along a cone of opening angle $1/\gamma$.

The contour plot of Figure 1 (top) for γ = 100 shows the angular spectral fluence profiles with respect to frequency (horizontal axis) and the polar angle θ measured from the foil's normal (vertical axis). This was evaluated across a sphere of radius 50.8 mm. It has been previously noted [1] that the distribution takes a different form depending on the distance from the foil used to evaluate the TR wavefront. Changing the incident electron energy has shown only a change in the value of peak intensities with no change in the shape of the wavefronts. Integrating the resulting spectral fluence profiles for all the data over the entire half-sphere solid angle in the reflected back plane gives the resulting power spectra shown in Figure 1 (bottom).

The resulting power spectra given in Figure 1, bottom, demonstrate the diffraction limitations of the foil itself. All spectra plateau at $\nu = \gamma c / 3a$, where a is the radius of the foil, in agreement with [5]. For investigation of emitted CTR spectra at frequencies below this, the low-frequency TR suppression must be taken into account.

DIAGNOSTIC SYSTEM RESPONSE

The final component of Equation 3 to consider is any diffraction suppression due to partial acceptance of the diagnostic system's optics. As an example of such an effect, we consider again Figure 1, top. In practice the CTR foil is located inside the beam pipe with optics set up outside of the beam pipe to view and analyze the generated CTR. This is typically done through some viewing window situated on the side of the beam pipe to couple the radiation out of the vacuum.

However, if the radiated angular spectral fluence profiles is integrated out to some θ fixed by the maximum viewing angle through the window, a portion of the wavefront is suppressed. Integration over a partial solid angle yields a frequency-dependent signal suppression.

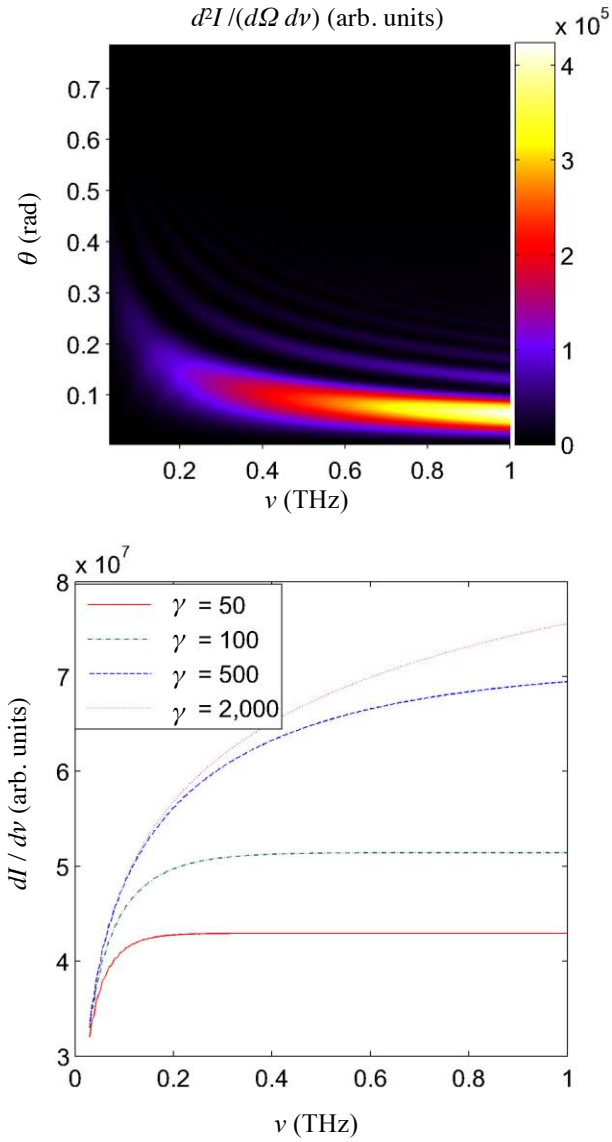

Figure 1: Angular spectral fluence profiles for TR of a γ = 100 electron at normal incidence with a 2" diameter foil at a distance of R = 2" from the center of the foil (top). Resulting emitted power spectra after integrating angular spectral fluence profiles over entire half-plane for several values of γ (bottom).

Work so far has suggested that this initial viewing window limitation as well as small final detector apertures are the typical sources for signal loss. All of these instrument-related effects are wrapped up in the response function for the system. In the computer model this is tabulated by propagating a TR wavefront through the entire instrument where it is integrated over the area of the final detecting surface. This final energy is then normalized by the total calculated input energy $I_e(\omega)$ to get a ratio of how much of the input signal survived.

The first system analyzed by the software was a Michelson interferometer. Details on its use to reconstruct the bunch form factor are presented in [7].

The resulting response curve for the device is shown in Figure 2. The flat high-frequency information still sees an overall suppression due to partial CTR wavefront acceptance at the 1" diameter quartz viewing window used to couple the CTR out of the vacuum.

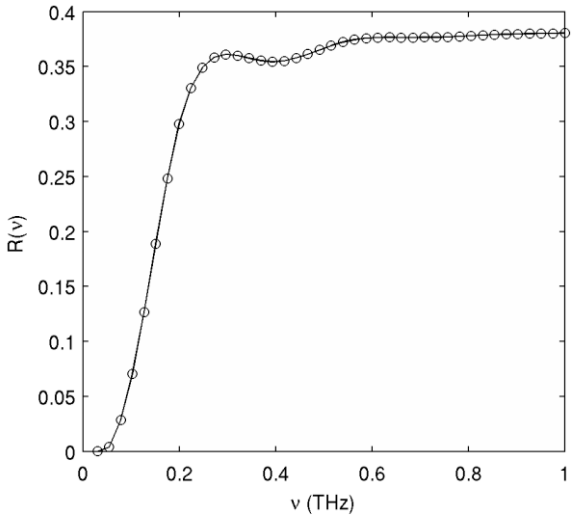

Figure 2: Response function $R(\omega)$ for the Michelson interferometer [7], including clipping at viewing window.

SIMULATED CTR-BASED BUNCH RECONSTRUCTION

Barring any dependence of the measured CTR signal on the TR strength Ie or a system response R as presented in Equation 3, one hopes to directly resolve the bunch form factor $f(\omega)$. To justify the frequency range of interest and how the results of the subsequent analyses pertain to an experimental electron beam, we have performed basic simulation of the ILC test accelerator (ILCTA) photo-injector currently under planning at Fermilab The photo-injector is composed of a radio-frequency gun followed by two TESLA-type superconducting cavities capable of accelerating the beam to approximately 50 MeV. The cavities, when ran off crest, can be used to chirp the electron bunch for longitudinal compression in a downstream magnetic chicane with momentum compaction factor R_{56} = -0.2 m. Though not comparable in energy, the typical root-mean-squared (RMS) bunch lengths under consideration also reflect projected International Linear Collider bunch lengths (σ_z = ~300μm after compression downstream of the damping rings at ~ 5 GeV).

The beam dynamics simulations of the production and low energy transport of the space-charge-dominated electron bunch was performed with ASTRA [8]. The resulting simulated 1.6 x 10^5 macroparticle bunch was used as an input in a one-dimensional, single particle longitudinal beam dynamics code. The off-crest phase of the cavity was adjusted to minimize the resulting bunch length to σ_z = 392μm (RMS).

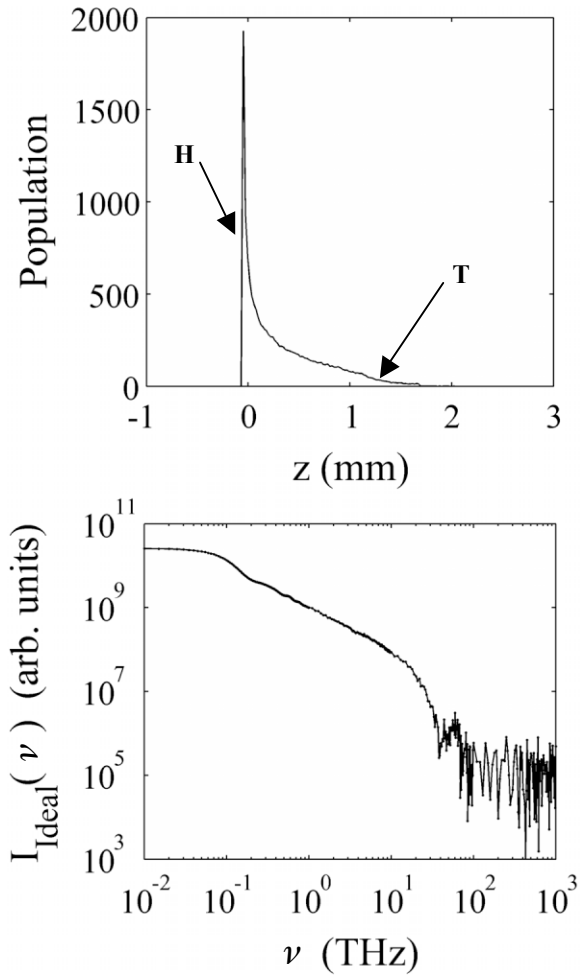

Figure 3: Simulated longitudinal bunch distribution with σ_z = 392μm (top). Corresponding ideal CTR power spectrum (bottom).

The resulting simulated longitudinal bunch distribution is shown in Figure 3 (top). Ideally, if the emitted single-electron TR and instrument had no frequency dependence, the emitted CTR power spectrum would be directly proportional to the form factor (Equation 2). This ideal power spectrum is shown on the log-log plot (Figure 3, bottom) for our modeled bunch in terms of frequency $\nu = \omega / 2\pi$. This theoretical power spectrum peaks at 2.53 x 10^{10}, just short of the expected N-squared value. The drop to incoherent noise sets in at $\nu \approx 10$ THz.

From Figure 3 we see that for a typical noisy beam, the detailed coherent spectral information on the bunch distribution lies at $\nu < 10$ THz corresponding to $\lambda > 30$μm. In principle, for a basic bunch length diagnosis, wavelengths on the order of σ_z are sufficient. For our subject bunch this corresponds to $\nu \approx 0.75$ THz.

Figure 4 shows the impact of the system response on a simulated measurement of the test bunch introduced in Figure 3. Trace A of Figure 4 is the mod-squared of the Fourier transform of the longitudinal bunch distribution, representing the ideal CTR signal [the bunch form factor $f(\omega)$]. Trace B is the corresponding spectrum that would

be measured by a detector at the end of the Michelson interferometer as calculated by Equation 3. For these calculations the detector is assumed the frequency response of the detector to be constant for all frequencies.

Figure 5 shows the equivalent bunch distributions. Shown for comparison are (A) the original bunch distribution as well as (B) the inverse discrete Fourier transform (IFDT) of $f(\omega)$. These show excellent agreement for the bunch shape for all $z > 0$, though the pathological drop of the simulated bunch is not recovered in the frequency analysis. Figure 5C shows the IFDT of the suppressed CTR signal shown in Figure 5B. This represents the bunch distribution from the suppressed signal as would be expected from experimental data.

Aside from the effective "DC offset" due to the severe zero-frequency suppression, the curve shown as Figure 5C shows little difference from the expected, noisy IFDT. While in an experiment this may be observed as a reduction in the observed tail, this can be avoided by careful analysis of the data.

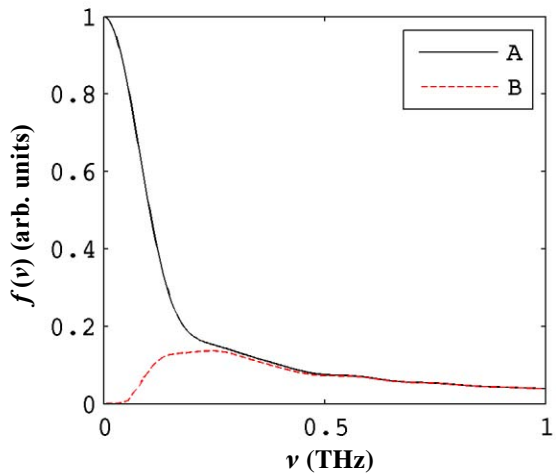

Figure 4: (A) Ideal power spectrum $f(\omega)$. (B) Simulated power spectrum $I_{measured}(\omega)$ as given by Equation 3.

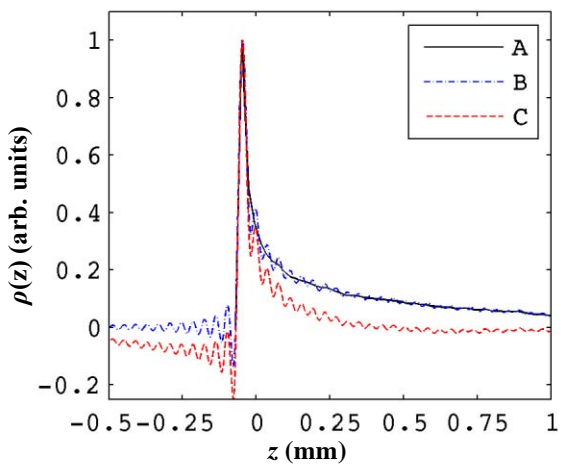

Figure 5: (A) Original bunch distribution $\rho(z)$. (B) Bunch distribution deduced by IDFT of $f(\omega)$ without phase information. (C) Bunch distribution deduced by IDFT of suppressed $f(\omega)$.

The overall qualitative agreement with the ideal signal stems from the peaked head of the bunch. The incoming longitudinal curvature results in a sharply peaked distribution with a full-width half-max (FWHM) on the order of tens of microns. Thus most of the frequency content is at frequencies higher than the characteristic frequency one would infer from the RMS value ($\omega \sim c/\sigma_z$). Comparing the FWHM values for the various bunches shows that the deduced suppressed longitudinal profile (Figure 5, trace C) is in agreement with the actual bunch profile (Figure 5, trace A) to within ~5%. This confirms that for the considered bunch distribution the critical frequencies needing to be analyzed lie in the 1 - 10 THz range where there is minimal diffraction reduction for the configuration analyzed here if the tail is of little concern.

REMARKS AND FUTURE PLANS

While this first case provided perhaps a very weak example of system response impact on longitudinal bunch diagnostics, further study is still warranted from what has been observed. Two factors minimized the expected effects including the sharply peaked longitudinal profile as well as the low beam energy. For bunches with broader bunch geometries, such as an ideal Gaussian distribution, the lower frequency information is expected to have a greater bearing on the final analysis. Furthermore, as seen in Figure 1 (bottom), higher energy bunches give $I_e(\omega)$ a frequency dependence penetrating higher into the spectrum. Early estimates show that going to 250 MeV beams roughly doubles the FWHM error of the bunch head to about 10%.

Bearing current ILC design considerations in mind, these higher energy (5 GeV downstream of the post damping ring bunch compressor) Gaussian bunch diagnostics by interferometry will be the first among upcoming analyses. Also to be studied are a very basic CTR-based phase scan device and multi-channel polychromator for single-shot bunch length estimation

REFERENCES

[1] T. Maxwell, *Diffraction Analysis of Coherent Transition Radiation Interferometry in Electron Linear Accelerators*, Master's Thesis, Northern Illinois University (2007).

[2] T.J. Maxwell, C.L. Bohn, D. Mihalcea, and P. Piot, Proceedings of 2007 IEEE Particle Accelerator Conference, 4015, Albuquerque, NM (2007).

[3] A. G. Shkvarunets and R. B. Fiorito, *Phys. Rev. Special Topics Acc. & Beams* **11**, 01281.

[4] A. S. Marathat and J. F. McCalmont, *J. Opt. Soc. Am. A.* **18**, 2585-2593 (2001).

[5] S. Casalbuoni, B. Schmidt and P. Schmüser, "Far-Infrared Transition and Diffraction Radiation", DESY Report TESLA 2005-15.

[6] T. Hahn, *Computer Science Communications* **168**, 78 (2005).

[7] D. Mihalcea, C.L. Bohn, U.Happek, and P. Piot, *Phys. Rev. Special Topics Acc. & Beams* **9**, 082801 (2006).
[8] K. Flottmann, *ASTRA: A Space Charge Tracking Algorithm,* available at http://www.desy.de/~mpyflo.

PROTOTYPE LASER EMITTANCE SCANNER FOR SPALLATION NEUTRON SOURCE (SNS) ACCELERATOR*

J. Pogge, Igor Nesterenko, Alexander Menshov, Dong-O Jeon, SNS Oak Ridge National Laboratory, Oak Ridge, Tennessee 37831, USA

ABSTRACT

Taking advantage of recent successes with the Laser Wire, a new prototype is being built to use the laser wire as both a profile monitor and a slit for an emittance measuring device. This improved system takes advantage of the steering dipole magnet prior to ring injection of SNS such that only the recently stripped H_0 protons continue forward to the emittance device. In this way we hope to make an emittance device that is both parasitic to neutron production and is capable of accurate measurements during full-power applications.

INTRODUCTION

As spallation neutron sources have demonstrated increasing power, it has become necessary to accurately measure the transverse phase-space distribution (emittance) of the H_0 beam prior to introduction into the storage ring. The high power of the proton beam and the necessity for non-destructive measurements make the use of a laser profile monitor as the emittance scanner slit especially attractive by replacing the more common and well known slit-grid (slit-harp) [1] mechanism used in lower power emittance measurements. The basic principal has been demonstrated in experiments with energies higher than 600 MeV [2,3,4]. This device will attempt to achieve results with a proton beam with energies as high as 1.4 GeV. The system is divided into two sections: the Laser Profile Monitor (LPM) and the Emittance Collection Device (ECD). The LPM is similar in capability to that of previous laser wire devices [5,6]. Specifications for this LPM are found in the following table.

Table 1. Laser Profile Monitor Specifications

X – Y Range	+/- 32 mm	100nm resolution
Laser /H- intersection	20 – 40 um	3% neutralization
Laser Energy	50 mJ	10 - 20 nS pulse
H- Beam	1.4 GeV	60 Hz

ENGINEERING CHALLENGES

The SNS Laser Emittance Scanner design takes advantage of the first dipole steering magnet in the ring injection section to separate the H^- representing 97% of the produced beam, from the recently generated H_0, 3% stripped by the LPM device. The primary LPM location also contains vacuum pumps, gate valves, and a key access point for moving equipment in and out of the tunnel in the HEBT section of the SNS accelerator. The design will be significantly more compact than its predecessor Laser Wire design used in 14 locations throughout the superconducting LINAC at SNS. This is primarily to allow for quick installation and removal of the LPM. The relatively low power of the separated H_0 allows the designers to evaluate either a scintillator camera device and a more traditional scanning harp assembly for the actual emittance collection system. This collection device will be located downstream in the LINAC dump area of the SNS accelerator approximately 11 meters from the LPM.

IMPROVED OPTICAL DESIGN

The prototype LPM under construction at SNS (Fig. 1) uses an improved optical system to increase repeatability and accuracy of the scanning optics with a decrease in overall size.

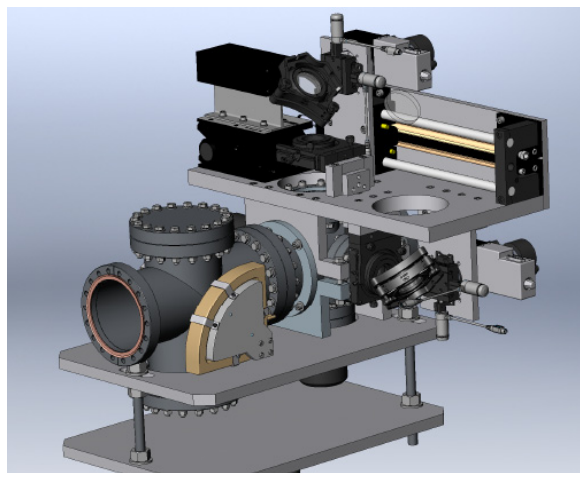

Figure 1: Improved LPM at SNS.

The new LPM also incorporates an embedded 50 mJ 1064 nm Nd:Yag pulsed laser, dramatically reducing the complexities of laser delivery to the optical scanning system. Stepper driven linear stages have been replaced with fixed angular scanning mirrors that have been precisely aligned and locked down prior to

installation. A focusing singlet is placed at a distance from the steering mirror equal to the lens focal point. The compact design (Figs. 1 and 2) allows the optical assembly to be easily removed and or replaced under repair conditions leaving the magnet and vacuum assemblies untouched. The optical scan mechanism's fast settling time and high repeatability, +/- .000025° with 80°/sec travel, allows the system to collect data at a maximum rate of 30Hz limited by the embedded laser pulse rate.

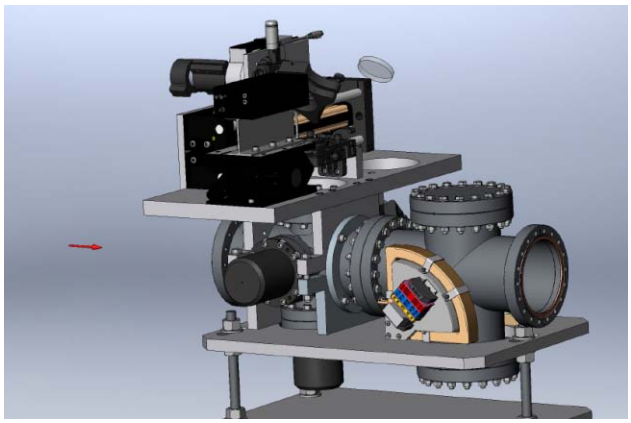

Fig. 2: Another look at the LPM at SNS.

Careful modeling of the optical system shows that the focal point of the laser beam, nominally 20–40 μm, stays well within desired size and intensity throughout the scanned region (Fig. 3) with only small distortion at the outside edges of the proposed +/- 35-mm scanning range.

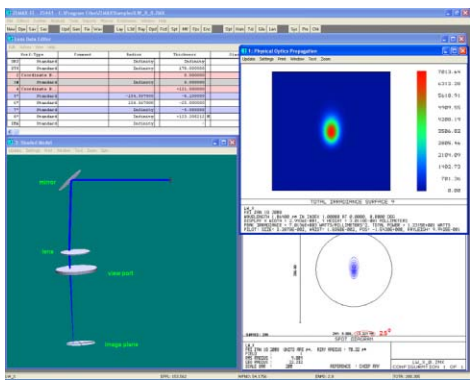

Fig. 3: Modeling of beam size and intensity.

The extreme edges of the scanning region modeled at 32mm from the center of the H_0 beam show a distortion due to the edge effects of the bi convex singlet. This distortion elongates the laser spot at the interaction point but maintains an acceptable spot size and intensity. Careful measurements will be made in this area to determine if any profile signal degradation occurs from this distortion. The modeled laser spot size appears in Fig.4.

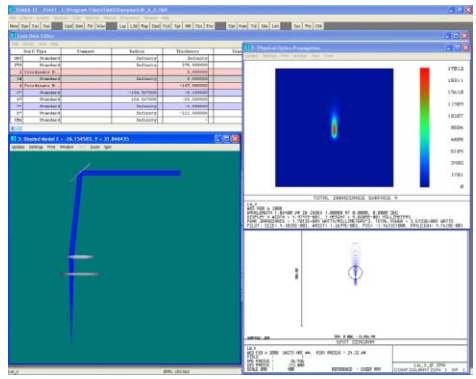

Fig. 4: Modeled laser spot size.

Several experiments have been added to the prototype assembly in order to facilitate additional information regarding the efficiency and operation of the LPM device. The high-frequency faraday cup is removed and a camera and scintillator are added temporarily allowing experimenters to capture and analyze the electron shower from the laser neutralization process. It is hoped such information may allow the designers to improve the faraday cup and magnet design.

EMITTANCE MEASUREMENT

Initially, a CsI Ti coated aluminum scintillator will be mounted in the collection vessel approximately 11 meters from the LPM. This vessel is placed in the LINAC dump line of the SNS accelerator taking advantage of the systems juxtaposition with the first ring injection dipole steering magnet. This magnet will act as the separator for laser-neutralized protons as the unaffected H-beam representing the majority of the SNS beam will continue on to the ring. Recently neutralized H_0 protons will strike the scintillator and the image will be collected using a 200-fps CMOS camera. Figure 5 shows a model of the H_0 beam intensity profile expected at the interface of the scintillator/harp collection point.

Prior to analysis of the efficiency of the laser slit, the scintillator and camera system will be used to determine if any stray H_0 beam is in the LINAC dump from alternative sources. If there is significant evidence of any residual H_0 present in the proton beam prior to neutralization. Any significant levels of non LPM generated H0 would make the use of a scintillator impractical. At this point the emittance collection device will switch to a more traditional electronically gated wire harp assembly. About 0.75 mrad resolution is needed,

for Harps with 0.75 mm inter-wire spacing, about 10 meter drift space is required. The harp assembly under construction is an array of 32 tungsten wires. A maximum 3% of proton beam is neutralized for a 0.02 mm-wide laser wire, indicating that 0.2~0.3% or less will be intercepted by a single harp wire. Given these system parameters, we modeled the expected SNS beam profile at the proposed collection site using ORBIT software as shown in Fig. 6. The estimated total emittance scanning range is +/- 2cm.

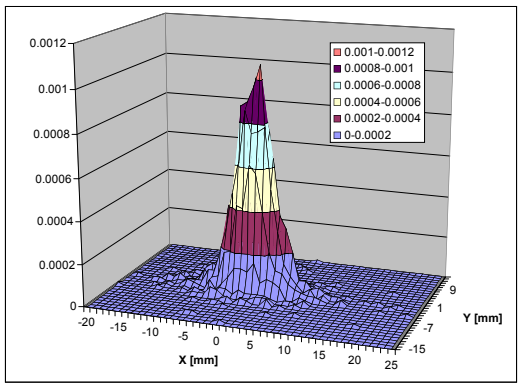

Fig. 5: Model of the H_0 beam intensity profile expected at the interface of the scintillator/harp collection point.

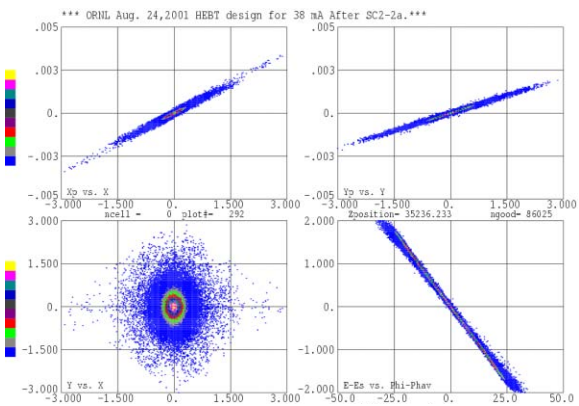

Fig. 6: ORBIT model of SNS beam profile at proposed collection site.

The region of interest is approximately 4 cm, with the majority ROI located within 3 cm. This model simulates the expected emittance when collected ten meters downstream from the LPM.

CONCLUSION

The design has passed all of the reviews to date and we have started assembling the LPM and ECD in the lab. The vacuum vessels will be installed this summer during a normal operations maintenance period, with initial experiments to measure the existence of stray H0 and collect information on the stripped electron spray pattern into the Faraday cup to start in early September. After reviewing the operation of the system we intend to collect parasitically the emittance of the SNS beam by January of 2009.

REFERENCES

[1] A.Ehrlich, J.Galtz, P.Strehl, GSI Gesellschaft für Schwerionenphysik, Darmstadt 1974, GSI-PB-3-74.

[2] V.W.Yuan *et al..,* "Measurement of longitudinal phase space in an accelerated H-beam", Nucl. Instr. Meth., A329, (1993).

[3] R.C.Conolly *et al.,* "A transverse phase-space measurement technique for high-brightness Hbeams", Nucl. Instr. Meth., A312, (1992).

[4] R. Connolly, P. Cameron, J. Cupolo, M. Grau, M. Kesselman, C-J. Liaw, R. Sikora, "JACoW, Laser profile measurements of an H- beam", DIPAC´01, Grenoble, May 2001, p.114, http://www.jacow.org.

[5] T. Tomisawa *et al.*, Proc. of DIPAC 2005, POW018.

[6] M. A. Plum *et al.*, Proc. of DIPAC 2003, IT08.

[7] C.Gabor et al. "Status Experimental Results of a non-destructive emittance measurement device for H- beams", Proceedings of 2005 Particle Accelerator Conference, Knoxville Tennessee.

LANSCE-R INVESTIGATION: IMPROVING THE WIRE SCANNER MOTION CONTROL*

J. Sedillo, J. D. Gilpatrick, F. Gonzales, J. Power, LANL, Los Alamos, NM 87545, U.S.A.

Abstract

The LANSCE accelerator facility utlizes 110 wire scanner devices to monitor the accelerator's charged particle beam. The LANSCE facility's existing wire scanner control systems have remained relatively unchanged since the LANSCE accelerator became operational in the 1970's. The evolution of motion control technologies now permits the development of a wire scanner motion control system that improves in areas of energy efficiency, precision, speed, resolution, robustness, upgradeability, maintainability, and overall cost. The purpose of this project is to research the capabilities of today's motion control products and analyze the performance of these products when applied to a wire scanner beam profile measurement. This experiment's test bed consists of a PC running LabVIEW, a National Instruments motion controller, and a LEDA (Low Energy Demonstration Accelerator) actuator. From this experiment, feedback sensor performance and overall motion performance (with an emphasis on obtaining maximum scan speed) has been evaluated.

INTRODUCTION

The Los Alamos Neutron Science Center (LANSCE) accelerator facility wire scanner system utilizes actuators and electronics that have existed since the accelerator's inception. The existing control system utilizes a motor drive that was developed and manufactured at LANSCE and is controlled directly by the LANSCE Operations Computers through LANSCE's Remote Instrumentation and Control Equipment (RICE) system. No feedback is employed for actuator positioning. Instead, wire scanner actuator position sensors are utilized to gauge the health of the actuator mechanics. The purpose of this study is to evaluate a previously utilized actuator, motor driver, and motion controller from the Low-Energy Demonstration Accelerator (LEDA) experiment to evaluate actuator movement performance and feedback sensor position accuracy. Furthermore, a resolver was also added so that its performance could be determined on this actuator.

SYSTEM DESCRIPTION

In order to evaluate sensor/actuator performance, we assembled a system utilizing a LEDA (Low Energy Demonstration Accelerator) wire scanner actuator powered by a Parker GT Stepper Drive. The motion was controlled by a PCI-7344 motion controller card within a Windows-based PC running LabVIEW. The

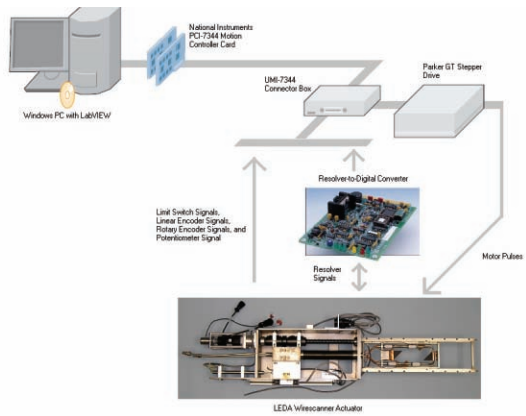

Figure 1: System Schematic

potentiometer and linear encoder maintained their original configuration of being coupled to the translational movement of the actuator. Furthermore, the rotary encoder maintained its original position as being coupled to the shaft of the stepper motor. A resolver was later added behind the rotary encoder and, like the rotary encoder, was directly coupled to the motor shaft. Details are shown in figure 2.

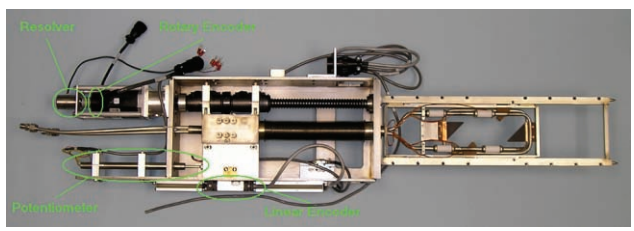

Figure 2: LEDA Wire Scanner Actuator with sensors highlighted

POSITION SENSOR TYPES UTILIZED

Linear Encoder

This sensor measures linear displacement through the use of a patterned film, two LED's, and two infrared photosensors. The pattern blocks the LED light in such a way that a quadrature signal is output from the sensor. This signal is used by the motion controller to detect sensor movement and direction. Although this sensor has a high degree of precision, the presence of semiconductor components in its manufacture increases its susceptibility to damage from ionizing radiation.

*Work supported by the United States Department of Energy.

Rotary Encoder

This sensor functions in a manner similar to the linear encoder above, but is designed to measure angular displacement. Like the linear encoder, this sensor is highly susceptible to damage from ionizing radiation.

Resolver

Resolvers are sensors that are similar in design to a typical electric motor. In order to be useful for angular position measurement, these sensors must be coupled with a Resolver-to-Digital (R/D) Converter. When connected to an R/D converter, a resolver-based system is capable of generating position signals similar to that of an encoder. Furthermore, a resolver's R/D converter may be placed over 150ft away from the resolver, thus allowing the R/D converter's semiconductor-based components to be placed in areas that are shielded from the damaging effects of ionizing radiation.

Potentiometer

This type of sensor is typical of what is used to measure the wire position of the wire scanner actuators at LANSCE. Variations of the shaft of this potentiometer result in a voltage variation that, once read through an analog-to-digital converter, may used to measure wire position. These sensors have proven to be very resistant to the effects of ionizing radiation.

FORWARD SCAN: SENSOR COMPARISSON

We first evaluated all four sensors together in order to determine their relative performance. The optimum result of this test would be a one-to-one relationship between the commanded position and the measured position. Throughout their 119-mm scan, all sensors appear to have made very linear measurements. Furthermore, all sensors values appear to be very close to the commanded position value. However, more details emerge when the error of these sensors is plotted as shown in figure 3. This figure depicts how each sensor has deviated from the commanded position. As is evident above, the linear encoder had the least deviation primarily because it was the sensor used for the actuator's feedback. Our reason for choosing this as the baseline feedback position sensor was because it was directly coupled to the motion of interest and had resolution exceeding that of the potentiometer-based feedback. The rotary encoder is the second best performer in this test with a maximum deviation of about 120 microns. In third place was the resolver, which followed the path of the encoder for most of the scan and then began to deviate by about 170 microns toward the end of the scan. The worst performer was the potentiometer, which had the most deviation.

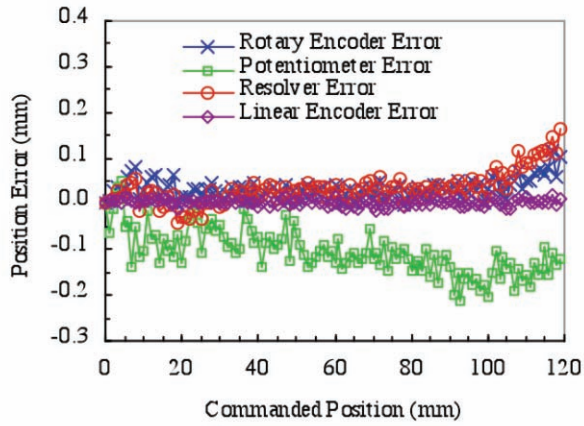

Figure 3. Deviation of each sensor from the commanded position

FASTEST 1-MILLIMETER MOVE

One of the primary objectives of this experiment was to determine how fast the actuator and its control system could perform a 1mm move (leading to a faster scan). Figure 4 shows that the fastest, most stable, 1mm move possible occurring within a timeframe of 50 ms. The criteria for this move involved a 60 mm/s peak velocity and a 3000mm/s^2 acceleration and deceleration. Increasing the acceleration and peak velocity beyond these values created an under damped response, resulting in a slower 1-mm move.

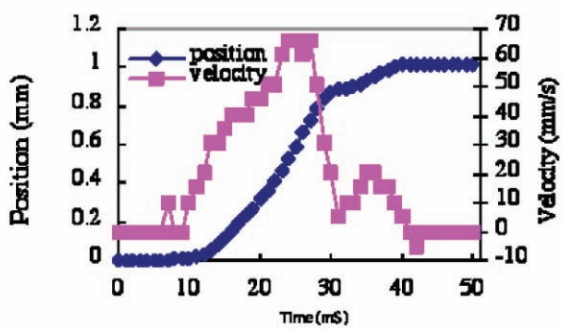

Figure 4: Velocity and linear displacement of fastest attainable move.

CLOSED-LOOP SENSOR ERROR

Table 1 presents the statistics of the error (arithmetic difference between commanded position and measured position) of each sensor when used as the feedback sensor. The data was collected by running ten, 119-mm scans at which a position sample was taken after every 1-mm moved. In total, the dataset for each test consists of 1200 data points. "Test 1" represents the statistical results of the scans set for a 25 mm/s peak velocity and 1000 mm/s^2 acceleration and deceleration. "Test 2" represents

the statistical results of the scans set for a 60 mm/s peak velocity and 3000 mm/s^2 acceleration and deceleration.

Sensor	Test	Average (mm)	Std. Dev. (mm)
Linear Encoder	1	0.0021	0.0067
	2	0.0092	0.0178
Rotary Encoder	1	-0.0004	0.0033
	2	-0.0002	0.0035
Resolver	1	0.0005	0.0108
	2	-0.0016	0.0178
Potentiometer	1	0.0007	0.0389
	2	0.0028	0.0469

Table 1: Statistical summary of the error of all sensors.

Linear Encoder

The results show that the linear encoder did not perform as well at a higher rate of speed and acceleration than it had at a lower speed and acceleration. This is evident by the increase in its standard deviation as well as the significant shift in its average value from 2.1 microns to 9.2 microns. A majority of the error associated with this sensor may be attributable to mechanical errors such as backlash, actuator fabrication errors, and perhaps, mechanical bending associated with quick movements.

Rotary Encoder

The rotary encoder appeared to perform nearly identically under both tests. A minor shift in the average error occurred, but the change was a minor 0.2 microns. This superb performance is mostly likely due to the motion controller's ability to act directly on the encoder due to its direct coupling to the motor shaft. In other words, the mechanical errors associated with (e.g. backlash) the actuator have no effect on the rotary encoder error.

Resolver

The resolver had a more significant shift in its average error than did the rotary encoder, but in general, the increased error is minor. Furthermore, the increased speed and velocity caused the standard deviation of the error to increase. This increase in error may have been caused by the frequency dependence of the resolver, from which, beyond certain accelerations, the resolver system experiences a reduction in its accuracy.

Potentiometer

The increased rate of movement caused a minor shift in average error and a minor increase in the error deviation. However, in general, the potentiometer's performance decrease is probably an insignificant one.

CONCLUSIONS

Many motion control technologies exist that have the potential to improve upon many aspects of LANSCE's wire scanner motion control system. In particular, motion feedback sensors such as optical encoders and resolvers may become welcome replacements for the potentiometer-based feedback sensor currently in use on every LANSCE wire scanner. However, since optical encoders are not highly radiation-resistant, resolvers may be employable in areas where radiation would otherwise damage a solid-state device. This study has compared the relative performance of each of these sensors and the results indicate that resolvers and optical encoders outperform potentiometers primarily in regard to positional accuracy. Deployment within LANSCE's accelerator will help gauge whether or not encoders and resolvers are capable of withstanding the effects of radiation to the extent of potentiometers.

REFERENCES

[1] "Things You Need to Know About Sizing and Applying Resolvers," Motion System Design, March 2001, p.61.

[2] "M50 - Synchro/Resolver User Manual," p. 25-30. September 8, 2003. www.men.de

[3] J. D. Gilpatrick, et. al., "Proposed Beam Diagnostics Instrumentation for the LANSCE Refurbishment Project," Albuquerque, June 2007, p 4099-4101.

[4] J. D. Gilpatrick, et. al., "Beam-Profile Instrumentation for a Beam-Halo Measurement: Overall Description, Operation, and Beam Data," Proceedings of the DIPAC2001–ESRF, Grenoble, May 2001, p. 76-78.

SPACE CHARGE WAVES AS A DIAGNOSTIC TO MEASURE TRANSVERSE BEAM SIZE OF SPACE CHARGE DOMINATED BEAMS

Jayakar C.T. Thangaraj* D.W. Feldman, R.A. Kishek, S. Bernal, M. Reiser, D. Stratakis,
R.Feldman, D. Sutter, B. Beaudoin, C.Papadopoulos, I. Haber, P.G. O'Shea
Institute For Research in Electronics and Applied Physics
University of Maryland, College Park, MD 20742

Abstract

Intense charged particle beams are of great interest to many wide areas of application ranging from high-energy physics, light sources and energy recovery linacs, to medical applications. The University of Maryland Electron Ring (UMER) is a scaled model to investigate the physics of such intense beams. It uses a 10 keV electron beam along with other scaled beam parameters that model the larger machines but at a lower cost. Multi turn operation of the ring (3.6 m diameter) has been achieved for highly space charge dominated beams. Such, multi-turn operation requires a non-intercepting diagnostic for measuring the transverse beam size. Localized density or velocity variations on a space-charge dominated beam travel as space charge waves along the beam. The speed at which the space charge waves separate from each other depends on the beam current, energy and g-factor. In this work, we propose a diagnostic using deliberately-induced space charge waves to measure the beam size with multi-turn operation. We present and compare experimental results with self-consistent simulation.

INTRODUCTION

Intense beams are of significant interest in next generation linear colliders, FELs and ERLs [1, 2, 3]. Beam quality is crucial in all these applications. For example, too high an energy spreaad can create havoc to the operation of XFEL [4] . Hence, the beam has to be well diagnosed for successful operation of the machine. Fluctuations in intense beams, either as density or energy, propagate as space charge waves [5, 6]. Such space charge waves convert the density modulations in laboratory beams to energy modulations [7]. Energy modulations present in the beam gets converted back to density modulations when the beam goes through a dispersive section of an accelerator e.g. bunch compressor in LCLS [2]. Such oscillations between the energy space and density space disrupts the beam quality and hence the operation of the machine. Whenever there is a localized density or energy perturbation in an intense beam, space charge waves are launched [8]. Space charge waves are created in pairs and are classified as fast wave, when the wave travels toward the head of the beam and slow wave, when the wave travels toward the tail of the beam.

* jtobin@umd.edu, Department of Electrical and Computer Engineering, University of Maryland, College Park, USA

Previous work on space charge waves concentrated on generating such waves using various methods [9, 10, 11]. The waves separate at a speed called as the sound speed, which was found to be proportional to the beam current, on which the waves were launched. Neumann [12]demonstrated that introducing perturbation on intense beams can be very good terahertz radiation sources. In this work, we propose and demonstrate using space charge waves as a diagnostic tool [13] to measure the beam size of an intense beam. using a laser or using a induction cell,the beam can be perturbed in density or in energy thereby launching space charge waves. Once the waves start propagating, by measuring the propagating speed and the main beam current, the beam size can be estimated.

The University of Maryland Electron Ring (UMER) [14] uses a 10 keV electron beam with scaled parameters which model other bigger machines at much lower cost. Recently, multiturn operation was achieved. A technique was needed to measure the beam size without intercepting the beam. Space charge waves are a suitable diagnostics for measuring beams of intense space charge. As the speed of propagation of waves is proportional to the intensity of the beam,the more intense the beam is, the faster the waves propagate and hence easier to resolve the waves and measure the speed. The work is presented as follows: In section I, the theory of space charge waves is discussed following which the experimental setup is discussed in section II. The actual experiment and results is discussed in section III, which is followed by conclusion.

THEORY: ONE DIMENSIONAL COLD FLUID THEORY

The linear theory of space charge waves is based on a cold-fluid model [8]. In this model, a small initial perturbation is assumed and then both momentum and continuity equations are solved. The solution shows that the perturbations propagate along the beam in the form of waves. One of them has a phase velocity greater than the beam velocity called as a fast space-charge wave, while the other one has a phase velocity smaller than the beam velocity and hence called a slow space-charge wave.

The linear continuity and momentum equations can be represented as:

$$\frac{\partial \Lambda_1}{\partial t} + v_0 \frac{\partial v_1}{\partial z} + \Lambda_0 \frac{\partial \Lambda_1}{\partial t} = 0, \qquad (1)$$

Table 1: List of symbols and parameters used in 1-D cold fluid theory

Quantity	Symbol [1]
Line Charge Density $[C/m]$	Λ
Beam Current$[A]$	I
Beam velocity $[m/s]$	v
Geometry factor	g
Strength of velocity perturbation	δ
Strength of current perturbation	η

$$\frac{\partial v_1}{\partial t} + v_0 \frac{\partial v_1}{\partial z} \approx \frac{eE_z}{m\gamma^3} = \frac{-eg}{4\pi\varepsilon_0 m\gamma^5} \frac{\partial \Lambda_1}{\partial z} \tag{2}$$

where

$$\begin{aligned} \Lambda(z) &= \Lambda_0(z,t) + \Lambda_1(z,t) \\ v(z) &= v_0(z,t) + v_1(z,t) \\ I(z) &= I_0(z,t) + I_1(z,t) \end{aligned} \tag{3}$$

Now we apply the initial and boundary conditions. (a) There are no perturbation along the z-axis when $t < 0$. (b) At $z = 0$, and $t > 0+$, the localized current and velocity perturbation can be represented in the form

$$\begin{aligned} v_1(0,t) &= \delta v_0 h(t) \\ I_1(0,t) &= \eta I_0 h(t) \end{aligned} \tag{4}$$

Where δ is a small quantity corresponding to the strength of the velocity perturbation, η is a quantity whose values depend on the strength of the initial current perturbation. η can be either negative or positive depending on the operating conditions of the gun. $h(t)$ is a smooth function representing the shape of the perturbation and its amplitude is unity. From the above equations and $I = \Lambda v$, after neglecting the second order terms, the line charge density perturbation becomes,

$$\Lambda_1(0,t) = (\eta - \delta)\Lambda_0 h(t) \tag{5}$$

Now, by applying double Laplace transform for both t and z, the equation is reduced to solving algebraic equation in v_1, Λ_1 and I_1 in the $k - s$ domain from $z - t$ domain. After solving for the unknowns, an inverse Laplace transform is done to obtain the perturbed beam velocity, density and current in the time-space domain:

$$\begin{aligned} \Lambda_1(z,t) = &-\frac{\Lambda_0}{2}\left[\delta\frac{v_0}{c_s} - (\eta - \delta)\right] h\left(t - \frac{z}{v_0 - c_s}\right) \\ &+\frac{\Lambda_0}{2}\left[\delta\frac{v_0}{c_s} + (\eta - \delta)\right] h\left(t - \frac{z}{v_0 + c_s}\right) \end{aligned} \tag{6}$$

$$\begin{aligned} v_1(z,t) = &\frac{v_0}{2}\left[\delta - (\eta - \delta)\frac{c_s}{v_0}\right] h\left(t - \frac{z}{v_0 - c_s}\right) \\ &+\frac{v_0}{2}\left[\delta + (\eta - \delta)\frac{c_s}{v_0}\right] h\left(t - \frac{z}{v_0 + c_s}\right) \end{aligned} \tag{7}$$

$$\begin{aligned} I_1(z,t) = &-\frac{I_0}{2}\left[\delta\frac{v_0}{c_s} - \eta + (\eta - \delta)\frac{c_s}{v_0}\right] h\left(t - \frac{z}{v_0 - c_s}\right) \\ &+\frac{I_0}{2}\left[\delta\frac{v_0}{c_s} + \eta + (\eta - \delta)\frac{c_s}{v_0}\right] h\left(t - \frac{z}{v_0 + c_s}\right) \end{aligned} \tag{8}$$

As it can be seen from the solutions, the beam current contains two terms one: the slow wave term $h\left(t - \frac{z}{v_0 - c_s}\right)$, which moves towards the beam tail with a velocity c_s; the fast wave term $h\left(t - \frac{z}{v_0 + c_s}\right)$, which moves towards the head of the beam with sound speed c_s.

The "sound speed" $C_s = \sqrt{\frac{qg\Lambda_0}{4\pi\varepsilon_0 m\gamma^5}}$ is the velocity of the space charge waves in the beam frame, in analogy to the propagation of sound in gas, where $g = 2\ln\frac{b}{a}$; b is the beam pipe radius and a transverse beam radius. It should be noted that the space charge waves have the same shape as that of the initial perturbation but their amplitude and polarity are dependent on the strength of the initial perturbation and initial conditions.The same conclusion can also be arrived by constructing the dispersion relation for the space charge waves [8, 7]. The group velocity is equal to the phase velocity of the waves and hence they are dispersion free. In other words, the perturbation travels unaffected.

EXPERIMENTAL SETUP

A Minilite II Q-switched Nd: YAG laser from Continuum forms the source of optical power. The full-width half-maximum of the laser (FWHM) is around 5 ns.The pulse repetition frequency is set at 15Hz. By using the proper nonlinear crystals, light at either 355nm or 266nm can be produced. In these experiments, the third harmonic at 355nm was used. After the UV light is reflected by suitable dielectric mirrors, the light passes through a quartz window and is reflected by another mirror installed inside the chamber (IC1) and hits the cathode [15, 10]

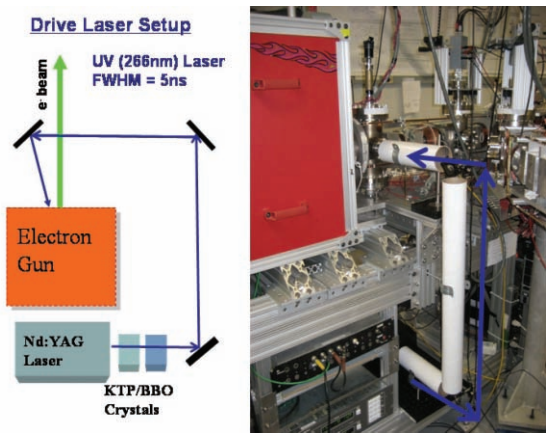

Figure 1: Schematic of the drive laser setup is shown on the left. The actual drive laser setup on UMER is shown on the right. The light path is shown with blue arrows.

DIAGNOSTICS

The induction cell [6] imposes an axial electric field in the beam direction by inducing a current through a parallel set of resistors straddling a glass section of the beam pipe. This glass section creates a discontinuity in the conduction path for the image current traveling along the beam pipe, such that the next path of least resistance is the housing that shields the termination end of the modulator. This path is essentially a short at low frequencies and yet contain an inductive component. So to increase the inductive term, as shown in the Figure,two high-frequency ferrite toroid are placed on either side of the glass gap region to choke off the high-voltage modulator and

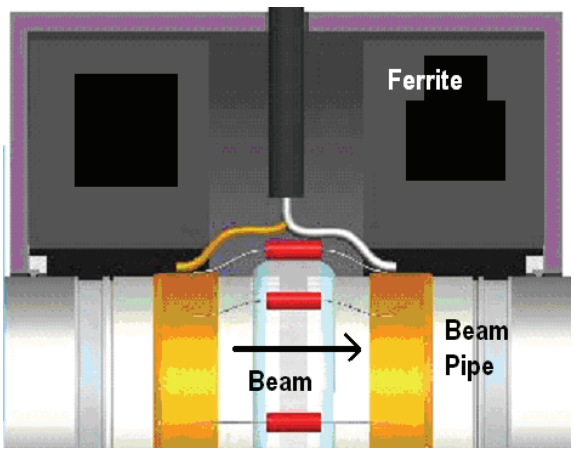

Figure 2: Induction Cell showing the ferrite toroid to choke the image current

allow an induced current to flow into the resistive path that straddles the glass gap region.

The modulator is composed of two BELKE high-voltage switches and circuitry to produce a positive and negative pulse with a full-width half-maximum (FWHM) of around 8nsec. The current modulator has a peak pulse voltage of 1kV with the capability of extending it too 3kV and a repetition rate that can be varied from 1Hz to 1MHz. As the beam propagates through the cell it can be pulsed at any point within the bunch, thus applying an axial electric field to accelerate and or decelerate any small segment of the bunch.

EXPERIMENT AND RESULTS

The beam is injected into the ring through injection optics and the beams goes around the ring for many turns. Every time it crosses the point of injection, a turn is counted. Beam loss has been observed for the first few turns. We believe it might be due to the injection optics. There are two current monitors to measure the total beam current. One is at z=3.83m (M1) and other one is at z=7.67m (M2) around the ring as shown in the Figure below. For the multi-turn beam, the signal from M1 and M2 is recorded in the scope without any density or energy modulation on the beam. Then a density modulation or energy modulation is introduced to the beam through the laser and the beam current signal from M1 and M2 is recorded with the perturbation. Care must be taken to ensure the perturbation is small compared to the main beam current. Typically values range from 5-10 percent of the main beam current. When the perturbation becomes too large, nonlinear effects starts to interfere with the measurment. In this experiment, we assume there is no loss in the beam current within a given turn. In other words, the beam current does not change between M1 and M2. This is a very good assumption confirmed by measurement of signals from M1 and M2. sound speed from experimental data, let us assume that the waves travel a distance of δz in a time δt in the beam frame. The waves will separate at twice the sound speed from each other. So,the sound speed C_s will be equal to half of $\frac{\delta t \cdot v}{\delta z / v}$. Once we get the value of the sound speed, we calculate the g-factor from the formula $C_s = \sqrt{\frac{qg\Lambda_0}{4\pi\varepsilon_0 m\gamma^5}}$, the g-factor is related to the beamsize as $g = 2\ln\frac{b}{a}$; b is the beam pipe radius and a transverse beam radius. . The measurement is repeated for various beam current and the value of the beamsize is recored for every turn.The variation of beam size for beam current with the turn number is shown in the graph below. Once the beam becomes emittance dominated, the waves move slowly and hence the beamsize cannot be calculated from the sound speed. A good guess, is the beam self-matches itself and hence the beam size remains constant thereafter.

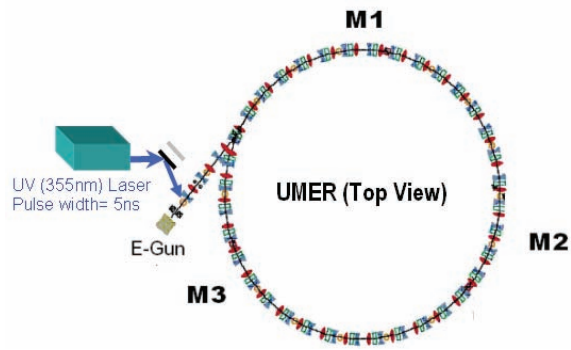

Figure 3: Top View of the University of Maryland Electron Ring (UMER)

CONCLUSION

An experimental technique to measure the transverse beam size of a space charge dominated beam is presented. Using a laser, space charge waves were launched on the beam and by measuring the speed at which the space charge waves separate the beam size was estimated over many turns. The experiment is conducted in UMER for various

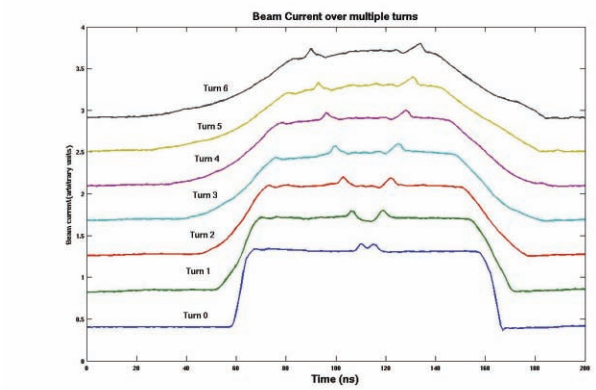

Figure 4: Space charge wave evolution over many turns. The spacecharge waves split into fast and slow waves

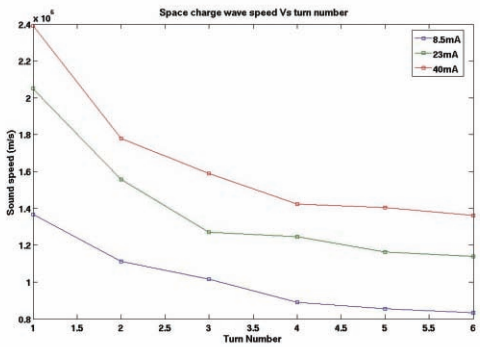

Figure 5: The speed of separation of the waves over multiple turns. As the beam current decreases, the speed of the waves decreases.

beam current and the shows good agreement with calculated values. By increasing the number of current monitors, the accuracy of this technique can be improved.The space charge waves technique can also be used to measure the g-factor in a FODO lattice for a long coasting beam.The space charge intensity [8] can be estimated using the space-charge wave technique after n turns. Estimating the emittance assuming a matched beam, we can calculate the space charge intensity at any turn.

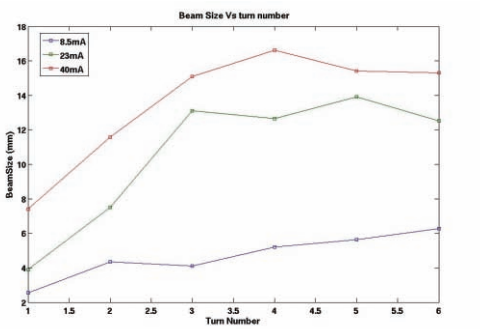

Figure 6: The transverse beam size Vs the number of turns. The beam seems to match itself to a specific value after few turns.

REFERENCES

[1] J. Brau et al., "International Linear Collider reference design report," ILC-REPORT-2007-001.

[2] J. Arthur et al., "Linac coherent light source (LCLS) conceptual design report," SLAC-R-593.

[3] M. Altarelli et al., "XFEL: The European X-Ray Free-Electron Laser. Technical design report," DESY-06-097.

[4] S. G. Biedron, Z. Huang, K.-J. Kim, S. V. Milton, G. Dattoli, A. Renieri, W. M. Fawley, H. P. Freund, H.-D. Nuhn, and P. L. Ottaviani, Phys. Rev. ST Accel. Beams **5**, 030701 (2002).

[5] J. Thangaraj et al., " Evolution of Laser Induced Perturbation and Experimental Observation of Space Charge Waves in the University of Maryland Electron Ring (UMER)," Proceeding of PAC,Albuquerque, NM, 2007.

[6] B. Beaudoin et al., "Application of induction module for energy perturbations in the University of Maryland Electron Ring," Proceeding of PAC,Albuquerque, NM, 2007.

[7] K. Tian et al., Phys. Rev. ST Accel. Beams **9**, 014201 (2006).

[8] M. Reiser, *Theory and design of charged particle beams* (WILEY-VCH Verlag GmBH & Co. KGaA,Weinheim, 2004).

[9] J. G. Wang, D. X. Wang, and M. Reiser, Phys. Rev. Lett. **71**, 1836 (1993).

[10] J. Harris, Ph.D. thesis, University of Maryland College Park (2005).

[11] H. Suk, J. Wang, and M. Reiser, Physics of Plasmas **3**, 669 (1996).

[12] J. Neumann et al., Nuclear Instruments and Methods in Physics Research A **507**, 498 (2003).

[13] J. G. Wang and M. Reiser, Review of Scientific Instruments **65**, 3444 (1994), `http://link.aip.org/link/?RSI/65/3444/1`.

[14] R. A. Kishek et al., "The University of Maryland Electron Ring (UMER) enters a new regime of high-tune-shift rings," Proceeding of 2007 PAC,Albuquerque, NM, 2007.

[15] Y. Huo, Master's thesis, University of Maryland College Park (2004).

BUNCH LENGTH MEASUREMENT AT THE FERMILAB A0 PHOTOINJECTOR USING A MARTIN-PUPLETT INTERFEROMETER*

Randy Thurman-Keup#, Raymond Patrick Fliller, Grigory Kazakevich (Fermilab, P.O. Box 500, Batavia, Illinois 60510)

Abstract

We present preliminary measurements of the electron bunch lengths at the Fermilab A0 Photoinjector using a Martin-Puplett interferometer on loan from DESY. The photoinjector provides a relatively wide range of bunch lengths through laser pulse width adjustment and compression of the beam using a magnetic chicane. We present comparisons of data with simulations that account for diffraction distortions in the signal and discuss future plans for improving the measurement.

INTRODUCTION

Application of Coherent Transition Radiation (CTR) diagnostics based on correlation techniques for bunch length measurements in the sub-millimeter range was proposed more than 10 years ago and numerous articles have been devoted to the problem, [1,2,3]. The diagnostic employs Transition Radiation (TR), [4], which is coherent at wavelengths approximately equal to or exceeding the bunch length. This technique suffers from a number of issues, some of which will be discussed in this paper.

The measurements in this paper were taken at the A0 photoinjector at Fermilab during 2007. Figure 1 is a schematic of the photoinjector as it existed at that time.

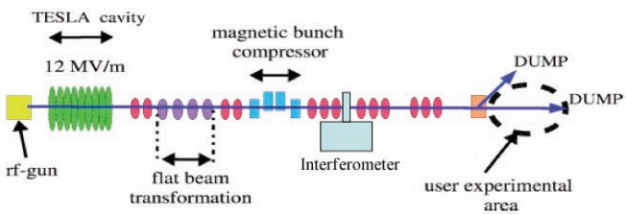

Figure 1: Schematic of the A0 photoinjector showing the main components. The interferometer is just downstream of the bunch compressor.

Beam is provided by a 1.3 GHz rf-gun with a CsTe photocathode. Typical charge is a few nC per micropulse. The micropulses are spaced by 1 μs and the overall rep rate is 1 Hz. The beam is accelerated via a TESLA 1.3 GHz SCRF cavity to energies around 16 MeV. A magnetic chicane does bunch compression of the beam just upstream of the interferometer with an expected compressed bunch length of 1-2 ps. The interferometer used for these measurements was obtained from DESY where it had also been used to make bunch length measurements. The thesis by Lars Frohlich [5] contains detailed descriptions of both the technique and the DESY measurements together with many references to previous work.

BUNCH LENGTH INTERFEROMETRY

Correlation between bunch length and spectrum

Interferometric bunch length measurements are possible because of the correlation between the bunch length and the spectral content of the CTR. This relationship is formally

$$I(\omega) = I_0(\omega) \cdot \left(N + N(N-1)\left|F(\omega)\right|^2 \right) \qquad (1)$$

where $I_0(\omega)$ is the single particle spectrum, and the complex form factor, $F(\omega)$, is the Fourier Transform of the longitudinal charge distribution

$$F(\omega) = \frac{1}{Q}\int dz\, \rho(z)\, e^{-i\omega z} \qquad (2)$$

where the transverse contributions are small, provided the observation point is close to the emission axis, and have been ignored.

Notice that the intensity is a function of only the magnitude of $F(\omega)$ and as such, in general, an exact determination of the longitudinal charge distribution cannot be obtained. However, for certain simple shapes, such as Gaussians, the approximations necessary to obtain the phase values do a fairly good job of preserving the main parameters of the bunch, such as width.

Reconstruction of the phase

Determination of the phase of the complex form factor involves writing the form factor as a product of a term without complex zeros and a term that contains just the zeros.

$$F(\omega) = e^{i\varphi(\omega)} = e^{i\eta(\omega)} e^{i\xi(\omega)}$$

$$\varphi(\omega) = \eta(\omega) + \xi(\omega)$$

The phase of the first term, $\eta(\omega)$, is termed the 'minimal phase' and in fact contains most of the information for a variety of simple shapes such as Gaussians. It also happens that the minimal phase can be obtained from a Kramers-Kronig equation. The phase of the second term, however, is not obtainable from just the magnitude of the form factor and hence ϕ must be approximated by just η.

The imaginary part of η, η_i, is just the logarithm of the magnitude of F. The real part of η, η_r, is related by the Kramers-Kronig relation to the imaginary part

* Fermilab is operated by Fermi Research Alliance, LLC under Contract No. DE-AC02-07CH11359 with the United States Department of Energy.

keup@fnal.gov

$$\eta_r(\omega) = \frac{2\omega}{\pi}\int_0^\infty d\omega' \frac{\eta_i(\omega) - \eta_i(\omega')}{\omega^2 - \omega'^2}$$
$$= \frac{2\omega}{\pi}\int_0^\infty d\omega' \frac{\ln\dfrac{|F(\omega)|}{|F(\omega')|}}{\omega^2 - \omega'^2}$$

This provides at least part of the missing phase information, which can be combined with the magnitude to complete the complex form factor

$$F(\omega) = |F(\omega)|e^{i\eta_r}$$
$$\propto \left|\sqrt{I(\omega)}\right| e^{i\frac{2\omega}{\pi}\int_0^\infty d\omega' \frac{\ln\frac{|\sqrt{I(\omega)}|}{|\sqrt{I(\omega')}|}}{\omega^2-\omega'^2}} \quad (3)$$

where, from Equation 1, $F(\omega) \propto \sqrt{I(\omega)}$ assuming the single particle spectrum is flat over the frequency range of interest (diffraction effects make this untrue as discussed in the next sections).

Diffraction effects in the CTR spectra

Diffraction effects have been discussed in a number of works [6,7,8]. In the last one, estimates were made of the systematic errors in determining the bunch length through the Fourier transform of the CTR spectra considering diffraction of the CTR due to the finite size of the TR screen. The diffraction distorts the TR angular distribution resulting in distortion of the CTR spectra. For CTR with wavelength, λ, the distortions become apparent at $\lambda\gamma > a$, $\lambda\gamma^2 > b$, where a is the TR screen radius, γ is the Lorentz factor, and b is the distance to the point of observation. Following [8] we consider the effect of the limited size of the OTR screen in the bunch length measurements at the A0 Photoinjector.

The angular distribution of the incoherent TR with frequency ω generated on the TR screen with radius a is expressed as, [8]:

$$\frac{d^2U}{d\omega d\Omega} = I(\omega,\theta) = 2\varepsilon_0 cR^2\left|\tilde{E}_x(\omega,\theta)\right|^2$$

where ε_0 is the permittivity of vacuum,

$$\tilde{E}_x(\omega,\theta) \approx \frac{e\omega^2}{(2\pi)^{3/2}\varepsilon_0\beta^2 c^3\gamma}\cdot\frac{e^{\frac{i\omega R}{c}}}{R}$$
$$\times\int_0^a J_1\left(\frac{\omega\rho\sin\theta}{c}\right)K_1\left(\frac{\omega\rho}{\beta c\gamma}\right)\cdot e^{\frac{i\omega\rho^2}{2cR}}\rho\, d\rho$$

where $J_1(u)$ and $K_1(p)$ are the Bessel function first and second kind, respectively, and $R = b/\cos\theta$ is distance between the OTR screen center (the origin) and the point of observation. Figure 2 shows the TR angular distributions for various wavelengths calculated for the single electron having an energy of 15 MeV with a TR screen size of a = 12.5 mm and a distance between the TR screen and the detector of 250 mm.

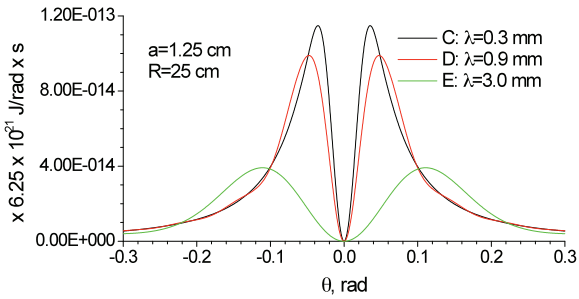

Figure 2: Angular distribution of the backward TR at 0.3 mm, 0.9 mm, and 3.0 mm wavelengths for 15 MeV electrons.

Figure 2 shows that the violation of the requirement $\lambda\gamma < a$ causes noticeable broadening of the angular distribution. For limited detector acceptance, this implies a distortion of the CTR spectra that depends on the bunch length.

Diffraction effects in the Bunch Length

CTR spectra were computed in assuming a Gaussian longitudinal distribution of the charge in a thread-like bunch. For small angles of observation the total CTR spectral power within the angle θ_0 is equal to, [6]:

$$I(\omega) = 2\pi N^2\int_0^{\theta_0} d\theta\left(e^{-\omega^2/2\sigma_\omega^2}\right)^2 I(\omega,\theta)\sin\theta\,.$$

Here N is the number of electrons in the bunch and σ_ω is σ of the bunch in the frequency domain. Calculated CTR spectra in 1 Hz bands with the current experimental acceptance limitations are shown in Figure 3 for several bunch lengths.

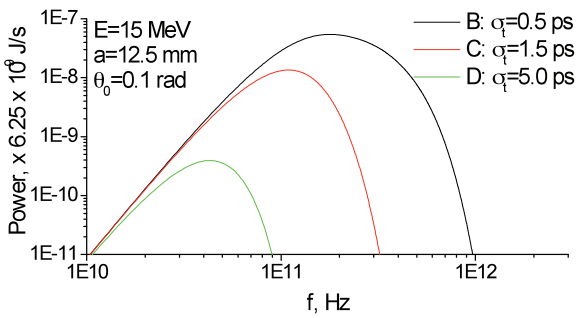

Figure 3: Calculated CTR spectra for 15 MeV, 1 nC bunch for different σ_t at a = 12.5 mm, θ_0 = 0.1 rad.

The calculations show that the diffraction effects noticeably shift the low frequency boundary of the CTR spectra to higher frequencies at limited size of the TR screen and limited detector acceptance. In fact these distortions of the CTR spectra lead to the "shortening" of the electron bunch length if it is computed using the inverse Fourier transform. Corresponding results are shown in Figure 4 for different σ_t values.

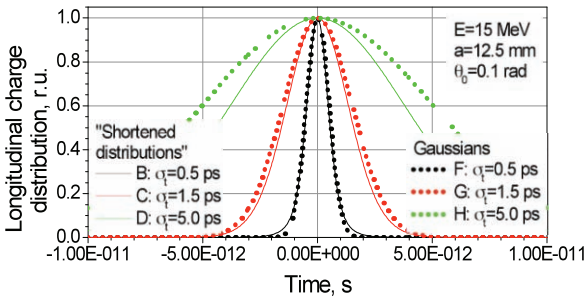

Figure 4: "Shortening" of the bunch length caused by diffraction. Curves *B, C, E* correspond to σ_t = 0.5, 1.5, 5 ps, corresponding to bunch lengths of approximately 0.3 mm, 0.9 mm and 3 mm, respectively.

Computed dependence of the "shortening" of the bunch length vs. the bunch σ_t is shown in Figure 5. The Systematic errors in determination of the bunch duration vs. the bunch σ_t are also plotted in this figure.

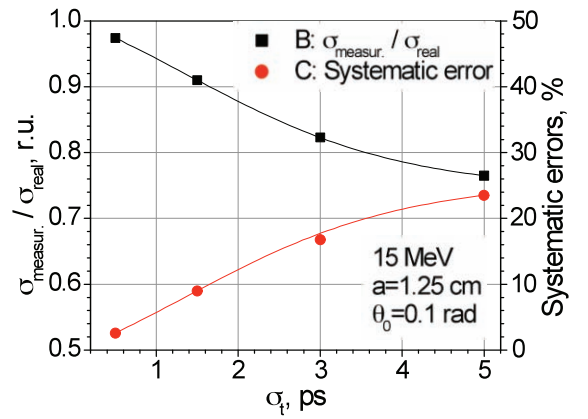

Figure 5: "Shortening" of the bunch length and the systematic errors caused by diffraction for correlation measurements using the A0 Photoinjector setup.

These plots show noticeable systematic errors in the bunch length caused by diffraction, if the distortion of CTR spectra is unaccounted for at longer bunch lengths. The effect is caused by a combination of the finite size of the TR screen (the Fraunhofer diffraction) and the finite acceptance of the detecting device (the Fresnel diffraction).

MARTIN-PUPLETT INTERFEROMETER

A Martin-Puplett interferometer is a polarizing type interferometer which in this case uses closely spaced wire grids for the polarizers and splitters (Fig. 6). The grids consist of 15 μm diameter gold-plated tungsten wires spced by 45 μm.

The CTR exits the beamline through a quartz window and is immediately collimated by a 200mm focal length off-axis parabolic mirror. Another flat mirror directs the light into the interferometer and through the horizontal input polarizer resulting in the following plane wave

$$\mathbf{E}(t) = E_0 \sin(\omega t)\mathbf{n}_h$$

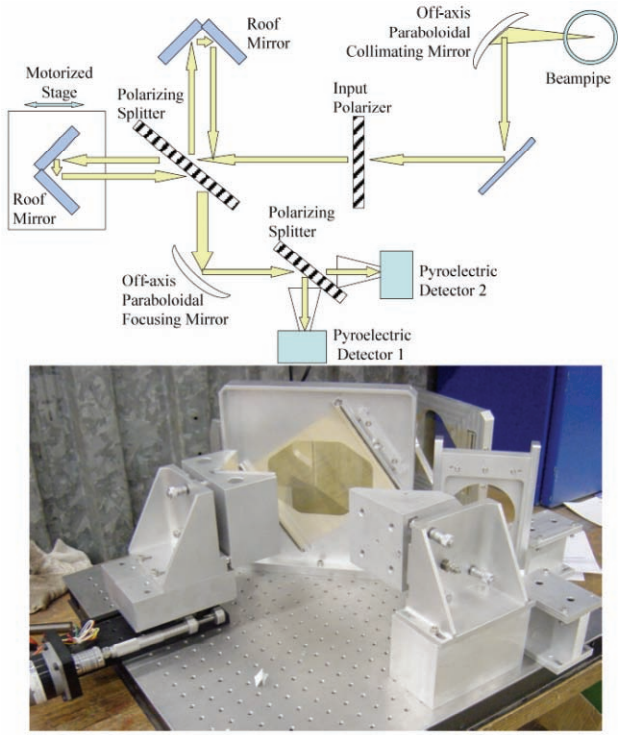

Figure 6: Schematic and photograph of interferometer. The large gold colored section in the photograph is the wire grid of the beam splitter for the two paths.

where $\mathbf{n}_h$ and $\mathbf{n}_v$ are horizontal and vertical unit vectors. This wave is split by the beam splitter, which is oriented diagonally, into the two polarizations

$$\mathbf{E}_1(t) = \frac{E_0}{2}\sin(\omega t)(\mathbf{n}_h + \mathbf{n}_v)$$

$$\mathbf{E}_2(t) = \frac{E_0}{2}\sin(\omega t)(\mathbf{n}_h - \mathbf{n}_v)$$

which then traverse their respective arms and arrive back at the beam splitter with a phase offset, ωτ, that depends on the path length difference

$$\mathbf{E}_1(t) = \frac{E_0}{2}\sin(\omega t - \omega\tau)(\mathbf{n}_h + \mathbf{n}_v)$$

$$\mathbf{E}_2(t) = \frac{E_0}{2}\sin(\omega t)(\mathbf{n}_h - \mathbf{n}_v)$$

The path length difference is controlled by a motorized stage on which is mounted one of the roof mirrors. The right angle roof mirrors adjust the polarization of the light such that what got transmitted(reflected) at the splitter now gets reflected(transmitted) so that it can be properly recombined into

$$\mathbf{E}(t,\tau) = \frac{E_0}{2}\Big[\big(\sin(\omega t - \omega\tau) + \sin(\omega\tau)\big)\mathbf{n}_h + \big(\sin(\omega t - \omega\tau) - \sin(\omega\tau)\big)\mathbf{n}_v\Big]$$

The recombined wave is then focused and split into horizontal and vertical polarizations, each of which are directed to a pyroelectric detector. The average intensity seen by each detector is

$$I_{h,v}(\omega,\tau) \propto \lim_{T\to\infty} \frac{1}{2T}\int_{-T}^{T} dt \left(\mathbf{E}(t,\tau)\cdot \mathbf{n}_{h,v}\right)^2$$

$$I_h(\omega,\tau) \propto \frac{E_0^2}{2}\cos^2\left(\frac{\omega\tau}{2}\right)$$

$$I_v(\omega,\tau) \propto \frac{E_0^2}{2}\sin^2\left(\frac{\omega\tau}{2}\right)$$

The sum of the intensities seen by the two detectors is proportional to the total intensity after the initial input polarizer. Defining the interferogram, $S(\tau)$, to be the intensity difference divided by the sum results in

$$S(\omega,\tau) = \cos(\omega\tau)$$

This result is for a single frequency, ω, but can be generalized to an arbitrary wave by Fourier composition. The intensities are then integrals over frequency space and the interferogram is

$$S(\tau) = \frac{\int d\omega\, I(\omega)\cos(\omega\tau)}{\int d\omega\, I(\omega)}$$

which is the real part of the Fourier Transform of $I(\omega)$. Inverting this gives

$$I(\omega) = \left|\Re\left[\mathbf{F}^{-1}\{S(\tau)\}\right]\right| \qquad (4)$$

where $\Re$ denotes the real part of a complex number, and $\mathbf{F}^{-1}\{\}$ indicates an inverse Fourier Transform.

The intensity outputs, $I_{h,v}$, of the pyroelectric detectors are attached to an oscilloscope from which the peak values from an average over 8 macropulses are obtained. The mirror position is set via a hand controller.

ANALYSIS

Several interferograms were taken over the course of 3 days. Figure 7 shows the interferogram and corresponding frequency spectrum from the 3rd day which used the widest path difference window. The interferometer is contained in an enclosure through which dry nitrogen can be flowed. For this particular sample, N_2 flowed for ~16 hours before taking data.

From Equation 2, $F(0) = 1$, and since the charge density is always positive, $F(0)$ is the upper bound on the magnitude of the spectrum. Because the detection system has a variety of low frequency cutoffs, the measured spectrum does not go to 1 at zero frequency. One way around this problem is to replace the low frequency region with a curve that goes smoothly to 1 at $\omega = 0$. The simplest curve to have this property is a parabola. Figure 8 shows both the raw and corrected spectra using a parabolic fit to

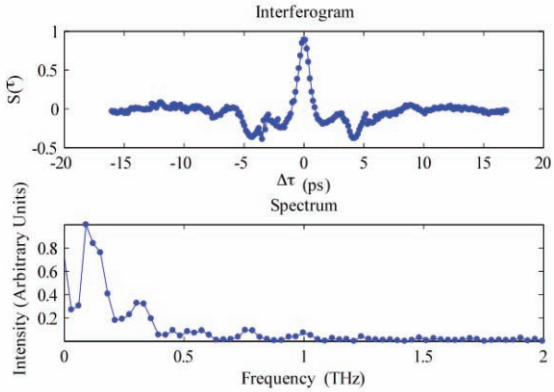

Figure 7: Interferogram (Top) and measured spectrum (Bottom) from compressed beam. One can see what appears to be interference fringes in the spectrum with a period of ~0.2 THz corresponding to 1.5 mm wavelength. This is comparable to what was measured by [9].

the 4th -8th points in the spectrum and replacing the first 3 points with the values of the parabola. To extract the bunch profile, Equations 2, 3, and 4 are combined to give

$$\rho(t) \propto \mathbf{F}^{-1}\left\{ \left|\sqrt{I(\omega)}\right| e^{i\frac{2\omega}{\pi}\int_0^\infty d\omega' \frac{\ln\left|\sqrt{I(\omega)}\right|}{\omega^2-\omega'^2}} \right\}$$

from which the bottom plot in Figure 8 is obtained.

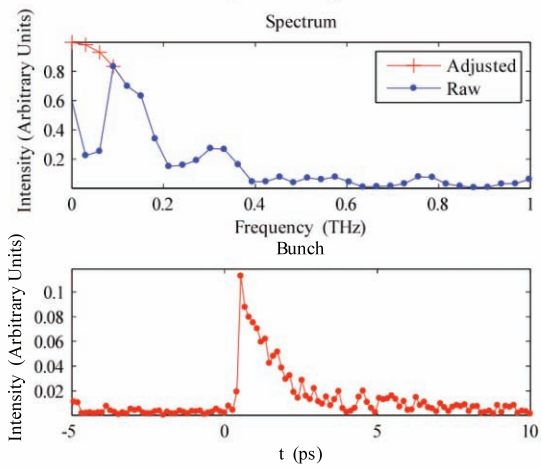

Figure 8: Top) Raw and adjusted spectra. The adjusted spectrum is the raw spectrum with the lowest 3 points replaced by the parabolic extrapolation values. Bottom) The bunch distribution in ps.

To obtain the bunch length, the width of the distribution in Figure 8 should be corrected for the diffraction effect. Since the width is under 1 ps, the diffraction correction from Figure 4 is fairly small (<5%).

To get a handle on systematic uncertainties, one can perform some conservative variations such as not adjusting the spectrum, or filling in the interference bumps in the spectrum (see Fig. 9). Table 1 lists these variations and the effect on the bunch length.

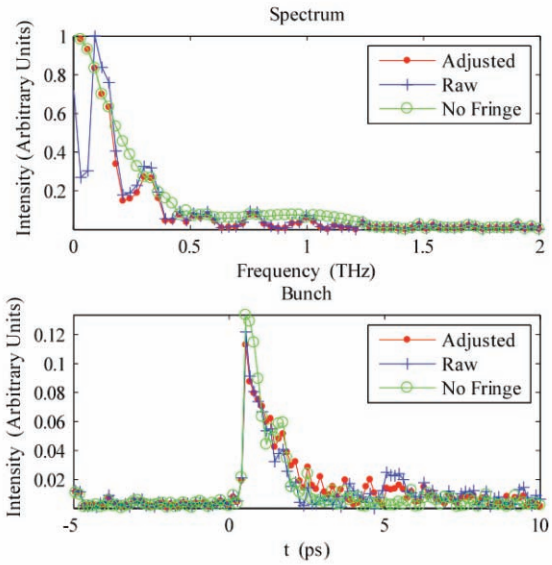

Figure 9: Impact on the bunch length of various corrections to the spectrum.

Table 1: Change in the bunch length with changes in the analysis techniques.

Technique	**Bunch Length (FWHM)**
Spectrum Adjusted	0.9 ± 0.1 ps
Raw Spectrum	0.8 ± 0.1 ps
Fringe Removal	0.7 ± 0.1 ps

A measurement without compression was also taken as shown in Figure 10. This measurement is difficult due to the fact that the spectrum is dominated by contributions in the poorly measured region below 200 GHz where the spectral response of the experimental setup is the main contributor to the shape. The measured width is ~3 ps. After correcting for diffraction, the FWHM bunch length is 3.3 ps.

Some items missing from the analysis are effects from diffraction of the optical elements, wakefields, water vapour, and interference in the pyroelectric detectors [9] and quartz window.

FUTURE

Currently, the interferometer is being reinstalled in a new beamline at the photoinjector. The chicane has been replaced with a double dogleg for an emittance exchange experiment. The interferometer will be after the second dogleg and shares a port with a streak camera which can be used for calibration purposes. The DAQ and mirror control is being automated which should allow for more regular measurements. New pyroelectric detectors with reduced interference have been obtained and there is the possibility of using broadband schottky diode antenna detectors in place of the pyroelectric detectors.

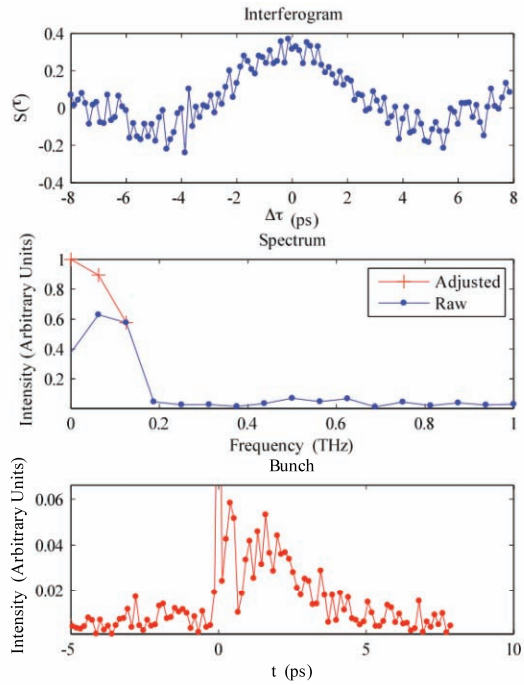

Figure 10: Top) Uncompressed beam interferogram. The window was probably not wide enough to obtain reliable results. Middle) Raw and adjusted spectra. Because beam is uncompressed, the spectrum is dominated by the poorly measured region. Bottom) Bunch distribution.

ACKNOWLEDGEMENTS

We would like to thank J. Santucci, C. Lundberg, and J. Ruan for their assistance in installing and aligning the interferometer. Also D. Milhalcea for discussions about bunch length interferometry.

REFERENCES

[1] S. Dobert *et al.*, Accelconf/e 96.
[2] P. Evtushenko *et al.*, THPPH064, Proceedings of FEL 2006.
[3] D. Mihalcea *et al.*, PRST-AB V **9**, 082801 (2006).
[4] V.L Ginzburg and I.M. Frank, J. Exp. and Theoret. Phys., Vol. 16, pp. 15-21, 1946.
[5] L. Frohlich, "Bunch length measurements using a Martin-Puplett interferometer at the VUV-FEL", DESY-THESIS-2005-011, DESY-TESLA-FEL-2005-02, Jun 2005. 60pp.
[6] M. Castellano and V.A. Verzilov, PRST-AB V **1**, 062801, (1998).
[7] R. A. Bosch, PRST-AB, V **5**, 020701 (2002).
[8] G. Kazakevich et al., TUPPH015, Proceedings of FEL 2007.
[9] C. Settakorn, H. Wiedemann, (APAC '01), Beijing, China, 17-21 Sep 2001. Published in 2nd Asian Particle Accelerator Conference 728.

THE ELECTRO-OPTIC SAMPLING STATIONS FOR FERMI@Elettra, A DESIGN STUDY

M. Veronese*, M. Danailov, M. Ferianis, Sincrotrone Trieste, Trieste, Italy

Abstract

FERMI@Elettra is a seeded FEL source, currently under construction at the Elettra Synchrotron Light Laboratory. On-line single shot and non destructive longitudinal bunch profile and bunch arrival time measurements are of great importance for this type of FEL source. These measurements will be performed by means of two Electro Optic Station (EOS) to be installed just upstream each of the two undulator chains. The paper describes the EOS stations design based on the spatial conversion scheme tested at SPPS and FLASH, and proposed for LCLS. The EOS will make use of two laser sources: a fiber laser at 780nm and the seed laser oscillator. A set of ZnTe and GaP crystal of different thicknesses will allow for flexibility in choosing high signal or high resolution configurations. The maximum resolution is expected to be of about100 fsec. The time profile mapped in a spatial laser profile will be acquired by a gated Intensified CCD.Calculations are presented for the expected EO signal and THz pulse broadening and distortion during propagation in the crystals.

MACHINE PARAMETERS

FERMI@Elettra is an single pass seeded FEL under construction at the Sincrotrone Trieste Laboratory, based on a normal conducting Linac (50Hz repetition rate), designed to laser in the range from 100nm to 10nm. A general description of the machine is presented in the FERMI Conceptual Design Report [1]. Two main operation configurations of the machine are foreseen: the *Medium Bunch* and the *Short Bunch*. The main machine parameters at EOS location are summarized in table 1. Two identical EOS stations are foreseen one per each of the two (FEL1 and FEL2) undulator chains. The aim is to provide a high resolution single shot non destructive longitudinal profile and bunch arrival time measurement with very low time jitter. The the SPPS-DESY spatial decoding scheme [2], [3] has beem adopted since it does not require an amplifier laser system and temporal resolution of about 150fsec has been demonstrated.

Table 1: FERMI@Elettra EOS main machine parameters.

Parameter	Medium Bunch	Short Bunch
Energy	1.2 GeV	1.2 GeV
Bunch Length FW	0.9 ps	0.17 ps
Charge	1 nC	0.5 nC
Beta (β_x, β_y)	(14m,7m)	(14m,7m)
Alpha (α_x, α_y)	(0.5,-0.5)	(0.5,-0.5)
Beam Size X (σ_x)	110 μm	110μm
Beam Size Y (σ_y)	77 μm	77 μm

LASER SOURCES

Femtosecond laser pulses from two different sources are foreseen for the spatial decoding scheme. The initial operation will be performed using a Menlosystems TC-780 fiber laser to be installed in the tunnel. The laser provides pulses at repetition rate of 78.895 MHz, with 120 fsec pulse width, and 0.8 nJ of energy per pulse. It offers noticeable performances in terms of temporal jitter with only 20fsec RMS (10Hz-1MHz) time jitter with respect to its electrical reference. This laser will allow operation from the very first days of the commissioning of FERMI in a very reliable way and is a *turn key* system.
When the ultrastable timing and synchronization distribution system will be installed we plan to use pulses from the fiber timing and synchronization distribution system (based on the MIT-DESY design). The pulses amplified by an EDFA amplifier and are used for second harmonic generation, bringing the wavelength down to 780nm. In this way we will intrinsically synchronized the ultra stable reference that will also be distributed to the users. The expected bunch arrival time jitter will then be only limited by the relative jitter between fiber links which we expect to be less than 10fsec RMS.

SETUP

The EOS stations will be located just upstream of the modulator, the first module of the FEL undulators chain. An optical table will support both fiber laser sources, all optical components and the vacuum chamber housing the EO crystals as well as the detector. For the whole length of the optical table the vacuum chamber will be supported on the table while at both ends bellows will isolate the EOS from the rest of the machine to guarantee maximum vibration isolation. A cavity BPM will be in the immediate vicinity and will allow for position measurements with micron accuracy. The whole setup including the vacuum chamber will be isolated from the rest of the tunnel by a light tight enclosure to prevent ambient light, air turbulence and for laser related safety issues too.
The EOS layout is sketched in figure 1. The laser source selection will be provided by a remotely movable mirror. A prism compressor is foreseen to reduce the temporal duration of the pulses to below 100 fsec. A remotely controlled

* marco.veronese@elettra.trieste.it

$\lambda/2$ and a polarizer will allow for adjustment of the laser power. A beam splitter will spill a small portion of the energy for laser diagnostics: on line measurements of power stability with a diode and pulse width measurements with a scanning autocorrelator. The main beam will be then directed to a motorized optical delay line to provide timing adjustment. A $\lambda/2$ wave plate will allow for polarization orientation control. Before entering the vacuum chamber the laser beam will pass trough a cylindrical lens to probe the electric field due to the e-beam only at specific distance avoiding averaging over distance. The laser beam will then be steered to the EO crystal with an angle of about 30 degrees with respect to the normal to the EO crystal (the normal is parallel to the electron beam direction). The angle is chosen to optimized for EO signal broadening effect due to group velocity mismatch between laser pulse and THz pulse propagation. Micrometric positioning in both transverse and vertical directions of the in vacuum crystal holder is needed. Multiple crystal (zinc-blende structure cut along (110) plane) are foreseen: 1mm thick ZnTe crystal will provide the highest EO signal and will be used for initial setup of the system, while maximum resolution will be achieved by a 60 μm thick GaP crystal, finally an 0.2mm thick ZnTe will be installed as a backup.

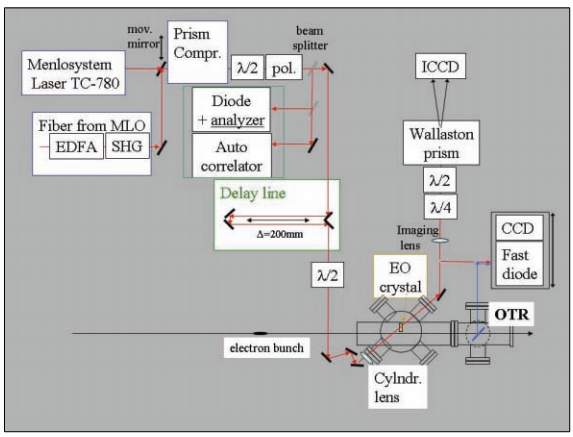

Figure 1: Electro Optical Sampling station layout.

After passing the EO crystal the laser pulse reaches the first lens which will image the EO surface on to the detector. Polarization analysis to extract the phase retardation information will be performed by a $\lambda/4$ zero order wave plate followed by a $\lambda/2$ zero order wave plate both mounted on motorized rotators that can be remotely controlled. Finally a polarizing cube or a Wollaston prism will be used to separate the two polarization components. The single shot image acquisition will be performed by a gated Intensified CCD. A gating time of 10nsec will be sufficient to extract the information from 78.895MHz fiber laser pulse train. Coarse timing alignment will be performed with a fast photodiode measuring at the same time the optical transition radiation from a metallic screen inserted on the electron beam path and the laser pulse.

EO CALCULATIONS

A numerical evaluation of the EO signal for the FERMI@Elettra case has been performed following [6]. Estimate the strength of the EO effect and the achievable resolution for our machine parameters are given.
For ultra-relativistic electrons the electric field has a large transverse component. For a single electron the electric field on axis at a distance b from the electron propagation direction is:

$$E_{y=b} = \frac{e}{4\pi\epsilon_0}\frac{\gamma b}{(b^2+\gamma^2 z^2)^{3/2}} \quad (1)$$

For an electron bunch with N_e electrons, the normalized longitudinal distribution $\rho(z)$ can be approximated for the FERMI case to a rectangular distribution that is conveniently modeled by the difference of two Heaviside functions: $\rho(z) = H(z + FW \cdot c/2) - H(z - FW \cdot c/2)$.
Then the total field along the axis is then:

$$E_{beam} = \int \rho(z - z')E_{0,b,z'}dz' \quad (2)$$

The seed laser travels collinear to the electron beam focusing from its entrance upstream the EOS to reach it minimum width at the center of the modulator. At the position of EOS the half width of the laser beam is expected to be 1.5mm posing a constraint to the minimum distance e-beam crystal. In practice we should consider for our purposes the minimum distance $b = 5$mm. Then for a rectangular distribution and the electron bunch parameters of table 1 we get: 13 MV/m for the $MediumBunch$ and 35MV/m for the $ShortBunch$.
To evaluate the amplitude of the EO effect we consider the case of a laser pulse probing a a crystal of zinc-blende crystal structure like ZnTe or GaP cut crystal along the normal to the (110) plane and a detection based on the $\lambda/4$ + Wollaston prism + balanced detector setup. Then the EOS signal is proportional to $\sin(\Gamma)$ where γ is the phase retardation induced by the electric field of the electron beam as from eq. 3.

$$\Gamma = \frac{\pi d}{\lambda_0} n_0^3 E_{beam} r_{41} \sqrt{1 + 3\cos^2(\alpha)} \quad (3)$$

Where d is the thickness of the crystal, λ_0 is the laser wavelength in vacuum, E_{beam} is the electric field due to the electron beam, r_{41} is the only independent element of electro-optic tensor for the chosen crystal structure, and finally α is the angle between the electric field of the electron bunch and the $[-1, 1, 0]$ direction. This translates for our laser and a crystal of 100μm thickness and $\alpha = 0$ to values for Γ of respectively: 0.3 and 0.8 for ZnTe and for GaP, large enough to allow for single shot EO measurement.
Temporal resolution is also of major importance, thus we have included in our study the frequency dependence and we have calculated the propagation and the distortion of the THz pulse associated to the transient electric field for

several thicknesses of both ZnTe and GaP. The approach we have applied to the analysis of the FERMI case, is the one described in [6]. The crystal parameters used in these calculations are described in table 2.

Table 2: Crystal parameters.

Parameter	ZnTe	GaP
C	-0.07	-0.53
ν_0	5.3 THz	10.98 THz
Γ_0	0.09THz	0.02THz
d_E	$4 \cdot 10^{-12} m/V$	$1 \cdot 10^{-12} m/V$
ϵ_{el}	7.4	8.7
S_0	2.7	1.8
L_{char}	$30 \mu m$	42 μm

The underling idea is to divide the crystal in smaller slices where for each slice the laser beam has an different pulse width to calculate the total phase retardation as the sum of the individual slice phase retardation $\Gamma(t) = \sum_j \Gamma_j(\tau)$. Equation 4 shows how the calculation is performed.

$$\Gamma(t) = \frac{2\pi n_0^3 d}{\lambda_0} \sum_j \left[\int E^j_{slice}(t_{j,ls}) \frac{\exp \frac{-(t-\tau)^2}{2\sigma_j^2}}{\sqrt{2\pi}\sigma_j} dt \right] \quad (4)$$

At each slice:

$$t_{j,ls} = d_j / v_{gr} + \tau \quad (5)$$

and the laser pulse of σ_0 initial sigma, undergoes a broadening passing through the crystal, described by:

$$\sigma_j = \sigma_0 \sqrt{1 + \left(\frac{d_j}{L_{char}} \right)^2} \quad (6)$$

At the $j-th$ slice the electric field is defined in terms of the field at the $j-1$ slice using the Fourier Transforms (FT) and anti-transforms (IFT):

$$E^j_{slice}(t) = IFT \left\{ FT(E^{j-1}_{slice}(t_{j,ls})) A_{tr}(\nu) B_{tr}(\nu) r_{41}(\nu) \right\} \quad (7)$$

where A_{tr}, the amplitude transmission coefficient is :

$$A_{tr}(\nu) = \frac{1}{1 + n(\nu) + ik(\nu)} \quad (8)$$

and B_{ph} accounts for the phase propagation,

$$B_{ph}(\nu) = exp \left(\frac{i2\pi d_j n(\nu)\nu}{c} - \frac{2\pi d_j \kappa(\nu)\nu}{c} \right) \quad (9)$$

Finally the complex dielectric function $\epsilon(\nu)$ and $r_{41(\nu)}$ electro optic coefficient are modeled as damped oscillators:

$$\epsilon(\nu) = \epsilon_{el} + \frac{S_0 \nu_0^2}{\nu_0^2 - \nu^2 - i\Gamma_0 \nu} \quad (10)$$

$$r_{41}(\nu) = d_E \left(1 + \frac{C\nu_0^2}{\nu_0^2 - \nu^2 - i\Gamma_0 \nu} \right) \quad (11)$$

$$(12)$$

Where ϵ_{el} is the frequency independent electron component while S_0,ν_0,Γ_0 are respectively the oscillator strength, the TO crystal resonance frequency and the oscillator damping constant (and similarly for $r_{41}(\nu)$). The results for the calculation for the THz propagation as a function of the thickness show clear EO signal broadening and shape distortion occurs as the thickness of the crystal is increased. The distortion effect gets more and more severe as the the electron bunch gets shorter. Calculation for THz propagation in ZnTe are shown for crystal thickness from $50\mu m$ to 1mm in figures 2 and 3 respectively for the *Medium* and *Short* bunch cases.

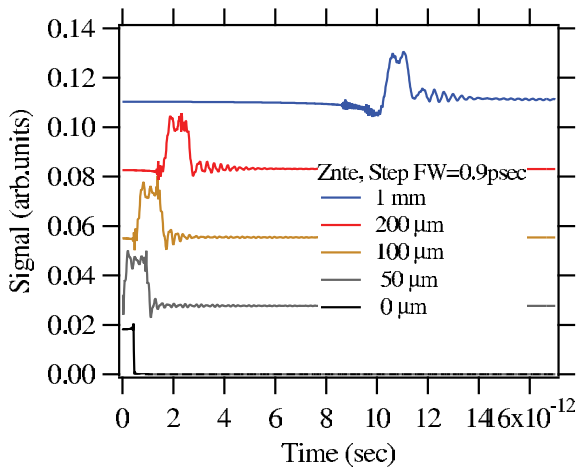

Figure 2: THz propagation through ZnTe crystal as a function of thickness for the *Medium Bunch*.

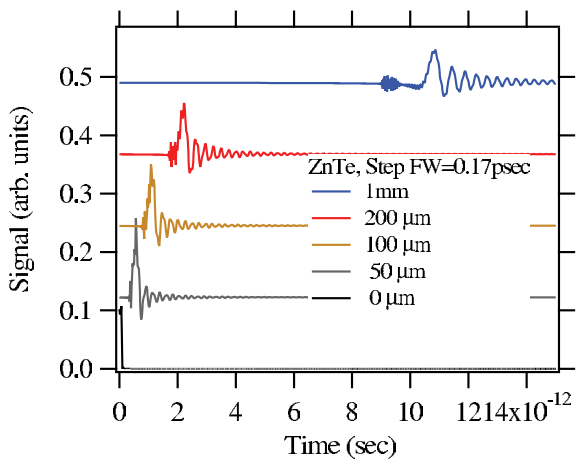

Figure 3: THz pulse propagation through ZnTe crystal as a function of thickness for the *Short Bunch*.

For the *Medium Bunch* negligible FWHM increase is found up to a Zn Te crystal thickness of 200 μm. Pulse shape distortion is present also for smaller thickness. For the *Short Bunch* the FWHM broadening is present even for $50\mu m$ and for 1mm thick ZnTe the width reaches 400fsec. Moreover strong pulse distortion is present for all thickness. Bet-

ter performances in terms of resolution and distortion are expected from GaP crystals due to its much higher crystal TO resonances which plays a crucial role in THz pulse propagation. We have performed for GaP the same kind of calculation done for ZnTe and the results are shown in figures 4 and 5 respectively for the *Medium* and *Short* bunch cases.

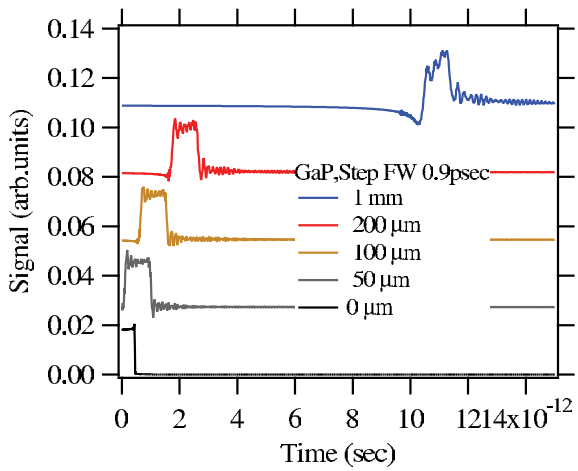

Figure 4: THz pulse propagation through GaP crystal as a function of thickness for the *Medium Bunch*.

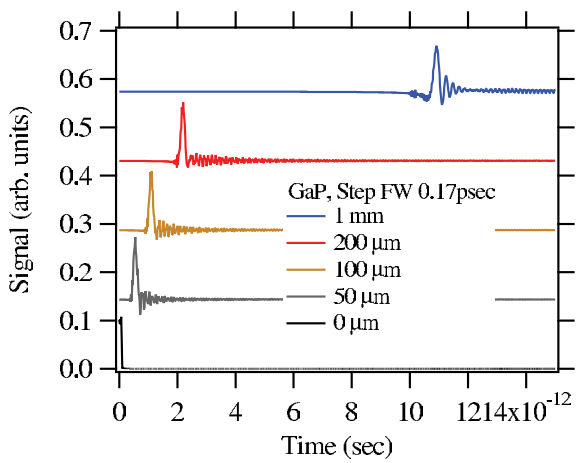

Figure 5: THz pulse propagation through GaP crystal as a function of thickness for the *Short Bunch*.

As expected GaP shows better performances in our case than ZnTe for both resolution and profile distortion in the both cases *Medium* and *Short bunch* but of course at the expense of a smaller electro optics coefficient. For the short bunch case FWHM is preserved within 10% for a GaP thinkness up to 200 μm but the THz profile is smoothed in the signal.

FEL ARRIVAL TIME

In a seeded FEL, the temporal jitter of FEL radiation depends not only on the arrival time of electron beam but and even more crucially from the temporal jitter of the seed laser. Timing of FEL radiation is of great interest for pump and probe experiments. Thee idea is to spill energy from the 800nm seed laser amplifier and use it for EOS measurements with the temporal decoding scheme. Temporal decoding has recently shown to be capable of 60 fsec resolution [4] better suited for the $ShortBunch$ mode of operation. For FERMI we could spill the radiation from the seed laser amplifier grating zero order beam and send it trough an evacuated transport line to the EOS. Considering the initial available energy and transport we estimate to have at the EOS station about 150μJ with a pulse length of 100fsec.

CONCLUSIONS

We have presented the design of the EOS stations for FERMI@Elettra. Major concepts and design choices have been introduced together with calculations of both expected EO signal strength and impact of THz e-beam electric field propagation in the EO crystals. Using the spatial decoding scheme coupled to a fiber laser source we aim at providing a robust and reliable system both to the machine operation and the user experiments. Benefits of expanding the EO stations to use the seed laser pulses for temporal decoding scheme are also discussed.

ACKNOWLEDGMENTS

The authors would like to thank P.Krejcik, D.Fritz for very useful discussion and suggestions on the spatial decoding scheme and S.P.Jamison for discussion and suggestions on the temporal decoding scheme.

REFERENCES

[1] FERMI CDR http://www.elettra.trieste.it/FERMI/

[2] A. Cavalieri et al. PRL 94 pg 114801 (2005)

[3] A. Azima et al. MOPCH011 Procs. EPAC 2006

[4] G. Berden et al. PRL 99, pg 164801 (2007)

[5] D.Fritz -LUSI team, private communication.

[6] S. Casalbuoni et al. TESLA Report 2005-01

STATUS OF THE CTF3 SYNCHROTRON LIGHT-MONITORING-SYSTEM

C.P. Welsch[1-4], E. Bravin[1], A. Dabrowski[1], T. Lefèvre[1]
[1]*CERN, Geneva, Switzerland*
[2]*University of Heidelberg,* [3]*GSI, Darmstadt, and* [4]*MPI-K, Heidelberg, Germany*

Abstract

Synchrotron radiation has proven to be a flexible and effective tool for measuring a wide range of beam parameters in storage rings, in particular information about the longitudinal beam profile.

It is today an established and widely used diagnostic method providing online measurements and thus allowing for continuous optimization of the machine performance. At the CLIC Test Facility (CTF3), synchrotron radiation is routinely used at a number of diagnostic stations, in particular in the Delay Loop and the Combiner Ring. Measurements with both standard CCDs and a streak camera showed the wide range of possible applications of this method, including determination of inter-bunch spacing, charge per pulse and monitoring of the manipulation of the effective path length by an undulator.

This contribution first addresses the critical points during the design phase of long optical lines with lengths of more than 30 meters as they had to be realized at CTF3. Second, a summary of the present installations is given and results from measurements are shown.

INTRODUCTION

CTF3 is being installed at CERN in the existing buildings of the LEP pre-injector accelerators LIL and EPA with the aim to demonstrate the technical feasibility of CLIC [1,2,3,4]. The complex starts with a 3 GHz linac that produces a pulsed electron beam with a present maximum energy of 150 MeV. The separation between individual bunches at the end of the linac is 20 cm - twice the linac RF wavelength. Moreover, the macro bunch is composed by alternated sequences 140 ns long of even and odd buckets, with the difference in phase between them being one RF wavelength.

The linac is connected by a transfer line to the Delay Loop [5] where a 1.5 GHz RF deflector deviates the odd bunch sequences to the left inside the DL and the even ones to the right, Figure 1. The DL length is 140 ns times the velocity of light c so that after this ring the odd sequence will be recombined with the incoming even sequence to fill the interleaved empty buckets. Precise adjustment of the longitudinal structure can be done with the integrated wiggler. The resulting macro bunch structure at the DL output presents 140 ns long trains of buckets separated now by 10 cm, followed by 140 ns long voids.

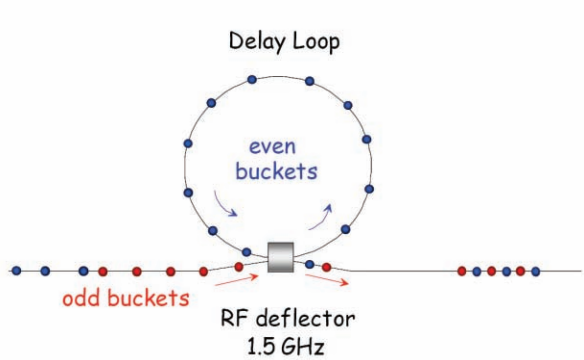

Figure 1: Schematic drawing of the injection scheme into the CTF3 Delay Loop [2].

The timing of the bunches of subsequent batches is adjusted such that they have a phase difference of 180 ° with respect to the 1.5 GHz RF of the deflector, Figure 2.

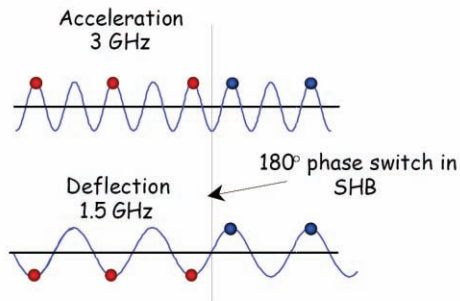

Figure 2: Illustration of required 180° phase switch between two batches of bunch trains [2].

An overview of the overall bunch combination process is shown in Figure 3. The necessary timing is controlled by the sub-harmonic bunchers working at 1.5 GHz in the injector region [6]. Every 140 ns the phase of the RF is changed by 180 degrees. This requires wide band sub-harmonic buncher structures as well as an RF power source capable of switching phase over a few bunches.

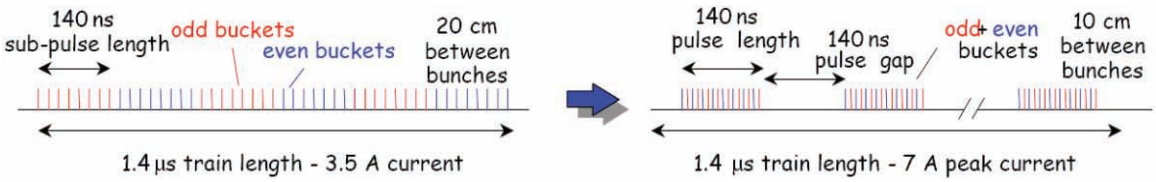

Figure 3: (x2) bunch frequency multiplication in the CTF3 Delay Loop [2].

High bandwidth travelling wave tubes (TWT) were chosen as an RF power source [7], which are pulsed giving the sub harmonic bunchers a 4 µs 40 kW RF pulse with a repetition rate of 5 Hz [8]. The voltage stability of the power supply is critical in order to achieve a phase variation on the output of the TWT that is less than 2° for a duration of 1.6 µs within the pulse. Since the beam loading is different in each of the three sub harmonic bunchers, the structures are individually detuned.

One possibility to analyze in detail the longitudinal behavior of the electron bunches in the DL as well as after the recombination process is to use a high speed streak camera with time resolutions down to a few picoseconds [9], Figure 4. In order to achieve a good time resolution, first the photons from the radiation to be analyzed are converted to electrons, which are then accelerated and deflected using a time-synchronized, ramped HV electric field. Thus the deflecting filed converts the time information into a spatial information much easier to analyze. The signal from the electrons is subsequently amplified with a micro channel plate (MCP), converted to photons via a phosphor screen and finally detected using an imager like a CCD array, which converts the light into a voltage signal.

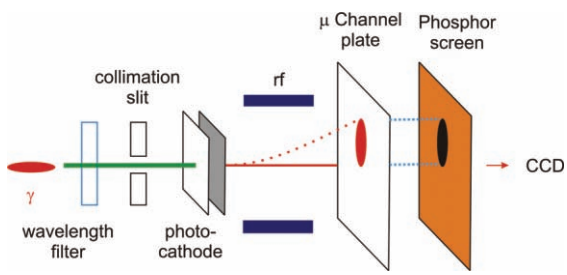

Figure 4: Principle of the streak camera.

PRESENT INSTALLATIONS

It is highly desirable to have the possibility to do time resolved measurements with a good time resolution with light originating from different places in the machine. Due to the high radiation level in CTF3 and the sensitivity of the streak camera, adequate measures have to be taken in order to protect the camera. A measurement close to the accelerator clearly is not feasible.

Thus optical lines had to be designed in order to guide the light to be observed to the streak camera. It needs to be ensured that a maximum of the created light is collected and projected onto the entrance slit of the streak camera. The distances that needed to be covered by these optical lines reached up to 40 meters and thus required a careful layout. The design steps can be summarized as follows:

- Transmission of light over large distances using telescopic arrangements, i.e. two identical lenses placed apart two times their focal length;
- Optimization of the overall system between collecting, transmitting and demagnifying optics;
- Minimization of the number of optical elements in order to maximize light transmission and reduce aberrations. Each lens will absorb about ~10% of the incident light.
- Optimization of the optical resolution. Even though (transverse) aberrations are not the most critical point in streak camera measurements, one would still like to have a final image where these are minimized.

In addition, constraints from the available space in the machine, type of lenses on hand and installations of other diagnostic equipment, using part of the optical lines in parallel, influenced the final layout of the optics to a high degree.

Further details on the design considerations, results from numerical simulations with the ZEMAX code [10], and on the optical elements used in the long optical lines can be found in [11,12].

As it is depicted in the following figure 5, synchrotron light is presently being extracted via three different viewports in the DL and via two viewports in the CR. While in the DL only one viewport is equipped with an optical line towards a streak camera laboratory (the other two being used for observation with a local CCD camera only), synchrotron light from both viewports in the CR is used for monitoring with a streak camera system and a CCD.

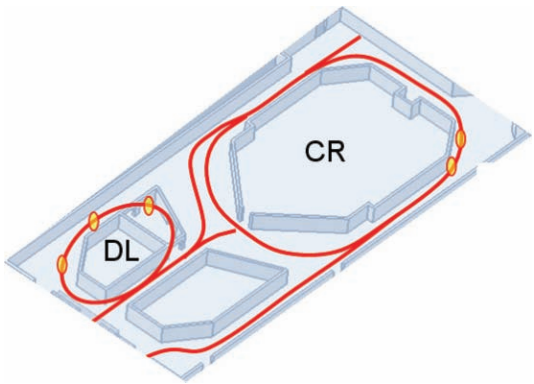

Figure 5: Synchrotron light viewports in the DL and CR.

Earlier measurements in the DL [10,11] clearly showed that the aberrations caused by the large distances between the light source and the point of observation reached a level where the quality of the measurements suffered. It was thus decided to build up a new dedicated laboratory for optical measurements in building 2012, adjacent to the CR.

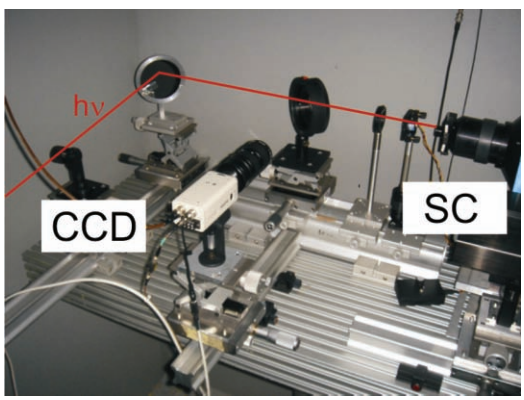

Figure 6: Setup for data acquisition in building 2012.

The two optical lines were aligned and tested early in 2008 with first results from measurements with both the Streak Camera and the CCDs being expected until end of May 2008.

MEASUREMENTS

The light from one of the synchrotron viewports in the DL as well as from an OTR screen in the transfer line between DL and CR were routinely used for beam observation in 2006 and 2007. Measurements with the streak camera allowed for determination of inter bunch separation, monitoring of the optimization of the DL track length with a wiggler, and for bunch length measurements. Some examples from measurements are shown in the following sections with more details being shown in [10].

Monitoring of RF Bunch Combination

As outlined in the beginning, the CTF3 DL is used for combining two 140 ns bunch trans with an inter bunch distance of 20 cm into a single 140 ns long bunch train where the individual bunches are 10 cm apart from each other. With one optical line monitoring the light from inside the DL and the other one from behind it, i.e. after bunch combination, the streak camera is the ideal tool for monitoring the longitudinal bunch profiles in both cases.

Measurements of bunch combination were done with a sweep speed of 250 ps/mm and an image of the measured bunch separation inside the DL is shown in the following Figure 12. The intrinsic resolution of the streak camera used for all the here-presented measurements is 0.25 ps.

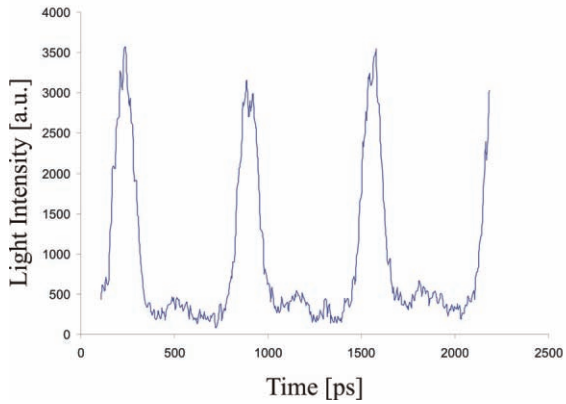

Figure 7: Measured bunch separation in the Delay Loop.

It can be seen that the train consists not only of the main bunches, but also of weaker satellite bunches of 8.5% of the main bunches' intensity. The spacing between individual bunches is 666 ps as can be extracted from the beam profile shown on the right of Figure 7.

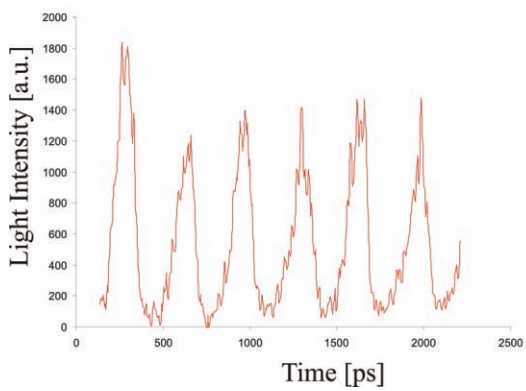

Figure 8: Measured bunch separation after RF recombination.

In a second step, the light emerging from the OTR screen at MTV0550 was used to monitor the combined bunch trains after RF deflection, Figure 8. Due to the lower transmission of the line the signal amplitude is not as high as in the previous case.

With the 1.5 GHz deflector the two bunch trains were successfully combined, resulting in a final bunch spacing of only 10 cm and double the current of the individual trains. In a future step, these trains will be further combined in the Combiner Ring [12,13] - another important step towards the demonstration of CLIC feasibility.

Track Length Modification

For the fine tuning of the machine, a compact wiggler magnet is integrated in the DL. It allows the modification of the ring circumference and thus the optimization of the timing between the two bunch trains to be combined.

In the following figure 9 the bunch from the DL is slightly off-centre the two bunches from the linac that are at a distance of 666 ps. This profile was measured with the wiggler off.

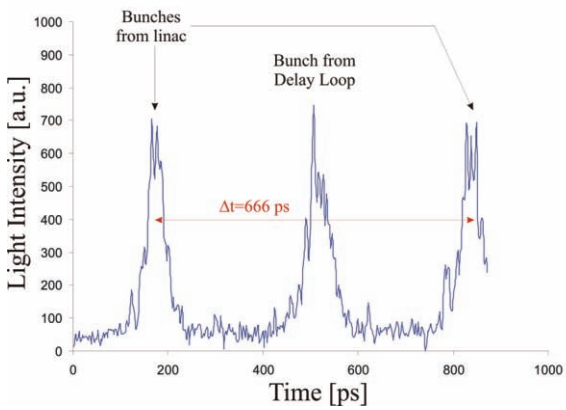

Figure 9: Measured longitudinal beam profile from MTV0550.

The wiggler was then used for optimization of the bunch spacing and an optimum value was found for a current of 62.5 A. Using the streak camera a change by 12 ps - or 3.6 mm - between the bunches was found, corresponding to about half of the total tuning range in the wiggler, Figure 10. Sweep speed in this measurement was 100 ps/mm.

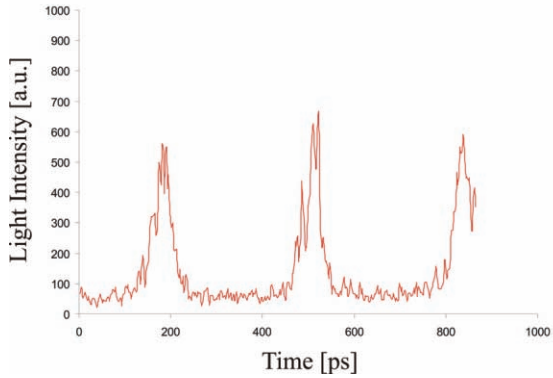

Figure 10: Measured longitudinal beam profile from MTV0550 with an initial offset time of 12 ps.

Bunch Length Measurements

When moving to the highest sweep speed of the streak camera of 10 ps/mm even bunch length measurements become feasible. Figure 11 shows measured profiles and corresponding τ-values for bunches in the DL and after the CTF3 linac for two different beam conditions.

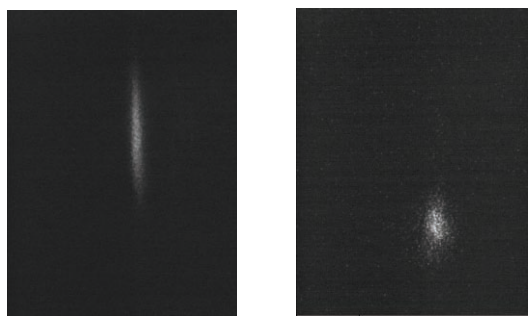

Figure 11: Measurement of single-bunch longitudinal beam profiles using the highest sweep speed (10 ps/mm) of the streak camera. Time is shown on the vertical axis. Left: Synchrotron radiation from MTV0361.

Measured σ = 8.9 ps. Right: Optical transition radiation from MTV0550. Measured σ = 4.5 ps.

This data was compared to calculations based on the optical functions of the machine and an assumed initial bunch distribution and good agreement with the measurements was found.

CONCLUSION AND OUTLOOK

The two streak camera lines installed in 2005/2006 allow in-detail monitoring of the longitudinal beam structure at CTF3. This gives access to e.g. bunch length monitoring, monitoring and optimization of the RF recombination as well as tuning of the machine with the integrated wiggler. The streak camera thus provides an ideal tool for measurements on shortest time scales.

With the new optical lines in the CR, detailed information about the longitudinal pulse structure in this ring will become available. These installations were just completed and first results from measurements are expected soon.

REFERENCES

[1] http://clic-study.web.cern.ch/CLIC-Study

[2] R.W.Assmann, et. al.,"A 3 TeV e^+e^- Linear Collider Based on CLIC Technology", CERN 2000–008

[3] G. Geschonke, A. Ghigo (ed.) et al.,"CTF3 Design Report", CERN/PS 2002-008 (RF)

[4] CLIC Study Team,"Proposal for Future CLIC Studies and a New CLIC Test Facility (CTF3)", CERN/PS 99-047 (LP) and CLIC Note 402 (1999).

[5] F. Sannibale,"Driving Beam Delay Loop Design for CTF3", CTF3 Note 023 (2001)

[6] P. Urschütz, H. H. Braun, G. Carron, R. Corsini, S. Döbert, T. Lefèvre, G. McMonagle, J. Mourier, J. Sladen, F. Tecker, L.Thorndahl, C. Welsch,"Beam Dynamics and First Operation of the Sub-harmonic Bunching System in the CTF3 Injector", Proc. Europ. Part. Acc. Conf., Edinburgh, Scotland (2006)

[7] G. McMonagle, "Operational Performance and Improvements to the RF power sources for the Compact Linear Collider Test Facility (CTF3) at CERN", CLIC note 663 and CERN-Open-2006-30

[8] G. McMonagle,"Technical specication for manufacture of three power supply systems to power TWT's in CTF", CERN Invitation to tender IT-3287-AB/CLIC

[9] http://www.zemax.com

[10] C.P. Welsch, H.H. Braun, E. Bravin, R. Corsini, S. Döbert, T. Lefèvre, F. Tecker, P. Urschütz, "Longitudinal Beam Profile Measurements at CTF3 using a Streak Camera", Journal of Instrumentation 1 P09002 (2006)

[11] C.P. Welsch, E. Bravin, T. Lefèvre,"Layout of the long optical lines in CTF3", CTF3 note 072, CERN, Geneva (2006)

[12] C. Biscari et al,"CTF3: Design of Driving Beam Combiner Ring", Proc. 7th European Part. Acc. Conf., Vienna, Austria (2000)

[13] https://edms.cern.ch/file/700154/3/CR_layout.ppt

MULTI-BUNCH BEAM SIGNAL GENERATOR FOR FEEDBACK RECEIVER DEVELOPMENT*

Jiajing Xu, John D. Fox, Daniel Van Winkle#,
Stanford Linear Accelerator Center, Menlo Park, CA 91, U.S.A.

Abstract

Bunched beam signals from button-style Beam-Position Monitor (BMP) electrodes can have spectral content up to 20-30 GHz and structure of narrow impulsive trains in time-domain. Multi-bunch feedback systems require receivers to process such beam signals and generate ΔX, ΔY, and ΔZ beam motion signals. To realistically test these receivers, we have developed a 4-bunch programmable impulse generator, which mimics the signals from a multi-bunch beam. Based on step-recovery diode techniques, this simulator produces modulated 100-ps impulse signals. The programmable nature of the system allows us to mimic Betatron and Synchrotron signals from 4 independent bunches with adjustable beam spacing from 1 to 8 ns. Moreover, we can observe nonlinear effects and study the noise floor and the resolution of the receiver. This paper presents the design of the system and shows typical achieved results.

INTRODUCTION

Beam Position Monitors to measure beam transverse coordinates and longitudinal coordinate are fundamental diagnostics. The BPM detects the centroid of the beam. The oscillatory component of the coordinate is useful for the feedback systems (the average position is useful for orbit measurements). For any of these purposes, the typical signals generated at button-type or stripline beam pick-ups are impulsive and have frequency components going out to high frequencies of order 1/(bunch length). The wideband signals with so many high frequency harmonics makes the design of the coordinate circuits interesting because non-linear effects may be present from the high frequency components. Filters can help remove harmonics out of the detection band but the feed-through and attenuation in these filters can effect the coordinate measurement.

One traditional way to lab test BPM and feedback systems is via narrowband sine waves. While convenient, this does not really explore the non-linear performance and system characteristics with signal that look very much like what we see from the real BPM. For this purpose, we investigated and put together a beam simulator that we can use to test various receivers.

METHODS

DIODE

The heart of our system is a step-recovery diode that makes impulsive signals at the RF driving frequency. Also called a snap diode, a p-n junction is doped to exploit the minority carrier storage inherent in the diodes. [2] It makes use of the abrupt transition from on to off that occurs once the stored charge has been removed and produces signals with extremely fast rise-time (~100 ps).

With a periodic input, the output spectrum consists of harmonics of the input fundamental. This way, a 100-MHz input signal can be used to generate gigahertz outputs. Step-recovery diodes are often used to make circuits such as frequency comb generators. The diode is typically used with a tuned bias circuit which has roughly 10% bandwidth, so that a given diode and tuned bias circuit is useful over a 10% operating fundamental bandwidth. Using the step-recovery diode, we are able to generate a train of narrow, high amplitude pulses, shown in Figure 1. We can clearly see this sharp 100-ps impulse generated by HP-33002 in Figure 1.

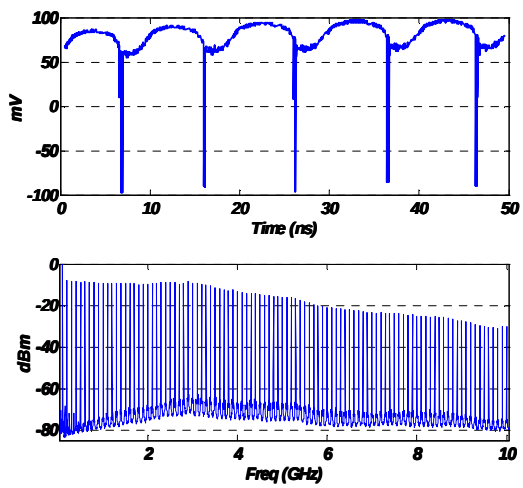

Figure 1: The impulse train generated using the 100 MHz HP-33002 snap diode in time domain (above, with 30 dB attenuation) and spectrum content (bottom, showing the 100 MHz comb)

The MODULATORS

We can modulate the impulsive output signal from the diode properly to mimic different beam oscillations, i.e. phase modulation for Synchrotron oscillation and amplitude modulation for Betatron oscillation. The next step is to make a good phase modulator and amplitude modulator.

Now we will look into making a good phase modulator to replicate Synchrotron oscillation. Phase modulation can be done by using a voltage controlled phase shifter.

* Work supported by U.S. Department of Energy under contract # DE-AC02-76SF00515
# {jiajing, jdfox, dandvan}@slac.stanford.edu

Applying a DC voltage plus 100 KHz small modulation applies phase modulation, as shown in the Figure 2.

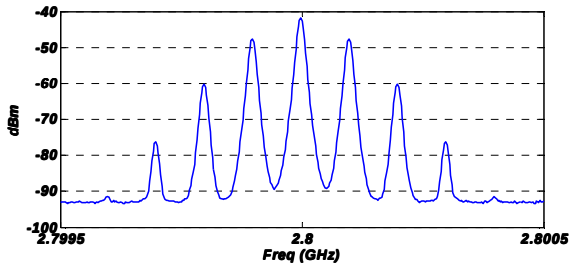

Figure 2: Simulated Synchrotron oscillation (DC voltage with 100 KHz modulation)

On the other hand, to simulate Betatron motion requires making a good amplitude modulator. If we want to look at signals with DC components and AC components, we have to think about the performance of the modulator in terms of small modulation with big DC offset. Let's look at some double-balanced mixers as modulators. We identify several mixers; each one is useful for a certain range of frequency, but none of them can be working in all bands. Figure 3 depicts how DC attenuation with a small amplitude modulation would affect the shape of the impulse.

In the lab, we tested three mixers: double balanced mixers M1G/M1J from M/A-COM and Marki M8 series mixer. We measure the frequency response of the mixers by passing a small modulation with DC value on both spectrum analyzer and network analyzer.

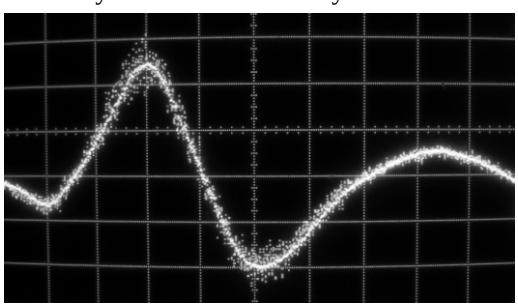

Figure 3: Close-up at the 100 KHz 20% amplitude-modulated impulse (notice the fuzzy samples around the tip of the impulse due to very small amplitude modulation, scale 10mV/div, time scale 100 ps/div)

Marki M8-0412 is specified from 4 GHz to 12 GHz. This is a high-level mixer (12 dBm drive level) and we were curious if it would behave differently than the standard 7 dBm level M1J and M1G. It has very flat response from 4 to 10 GHz, shown in Figure 4.

M1J Mixer from M/A-COM is specified in the frequency band ranging from 300 MHz to 2 GHz. It has relatively flat response in low frequency band and thus is useful for detection frequencies from 200 MHz up to 2 to 3 GHz.

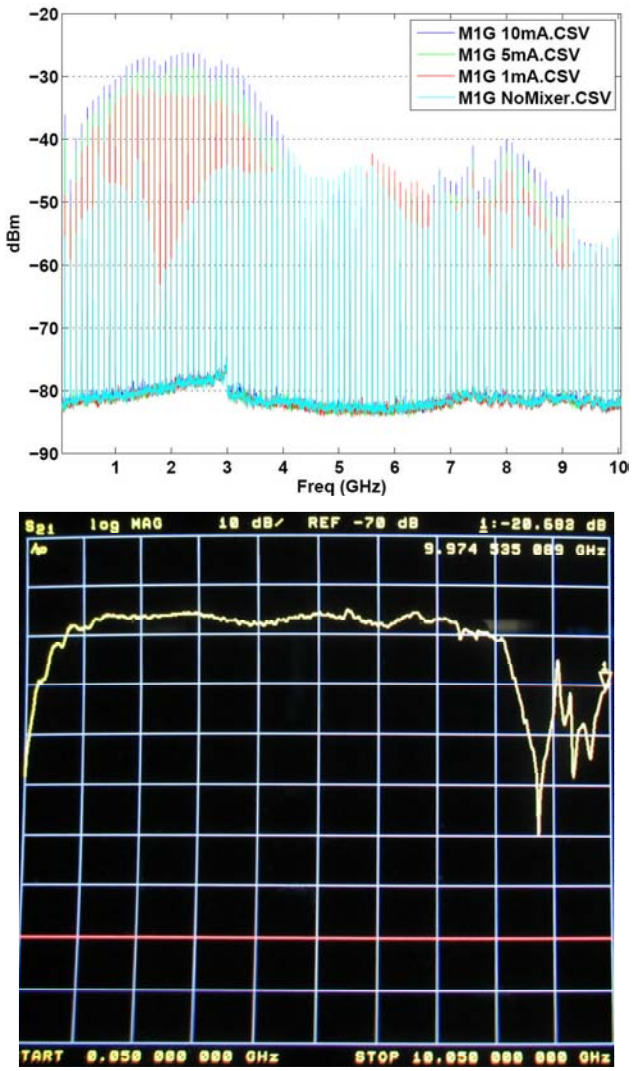

Figure 4: Lab measurement results of Marki M8-0412. The top figure is measured on the spectrum analyzer by driving M1J with a small modulation and a DC current of 1 mA (red), 5 mA (green), and 10 mA (blue). The bottom figure is from the network analyzer, frequency spanning from 50 MHz to 10.05 GHz, 10 dB/div.

M1G Mixer from M/A-COM is specified in the 1 GHz to 4.2 GHz frequency band. It has relatively flat response in wide frequency band and could be useful for detection frequencies of 1 to 4 GHz.

In summary, we identify several modulators; each one is useful for a certain range of frequency, but not for all. In low frequency band (200 MHz - 2 GHz), M1J is a good choice. M1G has better frequency performance in the 1 – 4 GHz band. On the other hand, Marki works well for higher frequency bands up to 10 GHz.

Selecting the Operation Point

We need to operate in the linear region of the mixer to represent Betatron motion. Thus we measured the DC attenuation characteristic of Marki M8-0412 at 2.865 GHz.

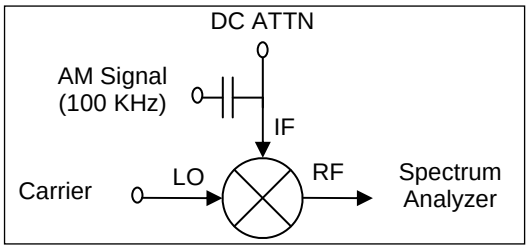

Figure 5: Lab setup to measure the DC attenuation characteristics

In the lab, the equipment is set up as Figure 5 describes. We put an amplitude-modulated signal (100 KHz) into the mixer and observe the carrier-to-sideband ratio on the spectrum analyzer. If the mixer is linear, we should expect the carrier-to-sideband ratio is going up because we have a fixed DC control current and increasing modulation depth. As we keep increasing the modulation depth, we gradually saturated the mixer and reach the limit of the carrier-to-sideband ratio. Figure 6 describes how the DC attenuation varies with different mixer drive level. If we put big DC control current (> 5 mA) into the mixer, we will saturate the mixer. We want good linearity and don't want to work in the saturation region. In Figure 7, we are operating in the linear region of the mixer.

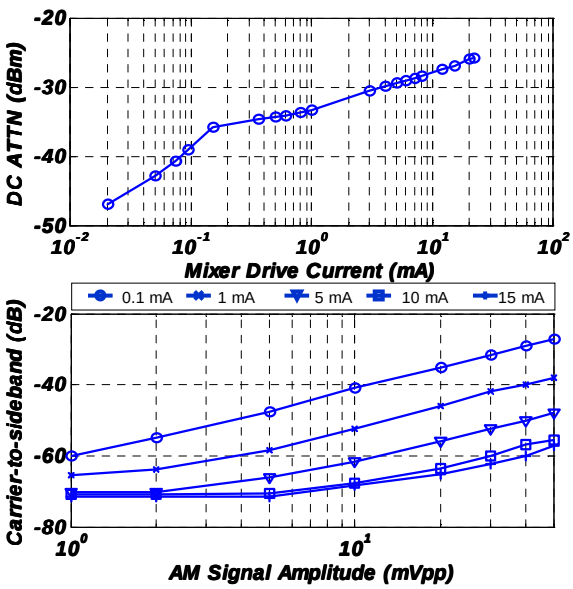

Figure 6: DC attenuation characteristic of Marki M8-0412 at 2.865 GHz

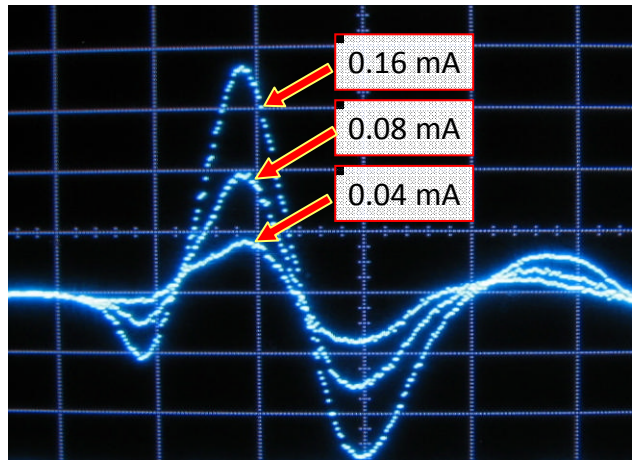

Figure 7: Linear Response of the Modulator. Snapshot of the impulse when the mixer is operating at DC control currents of 0.04 mA, 0.08 mA, and 0.16 mA. Time scale 10 mV/div, time scale 100 ps/div.

To test high resolution receiver, we want to generate beam signals that can be modulated with very small signal. For the chosen mixer, we have to carefully choose the operating point to achieve the high dynamic range. High dynamic range corresponds to high resolution, i.e. 60dB dynamic range will allow us to mimic <10 micron motion in 1 cm aperture. Figure 8 is typical result we achieved in the lab. The 60dB carrier-to-sideband ratio can be further improved by increasing the resolution of the spectrum analyzer and lowering the noise floor in the system.

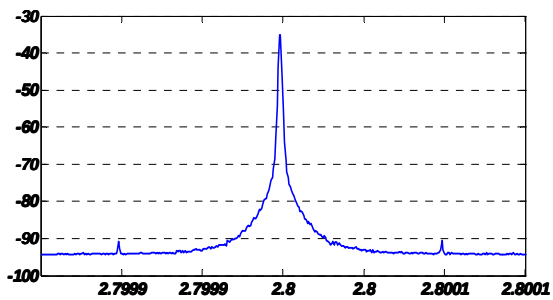

Figure 8: 60 dB carrier-to-sideband ratio, centered at 2.865 GHz, sidebands 100 KHz apart

One Bunch Block Diagram

Figure 9 shows the first bunch of our bunch signal simulator. A step-recovery diode driven at 100 – 125 MHz makes fast impulses; a phase modulator mimics Synchrotron oscillation. The 1-to-4 divider splits the signal into 4 button signals, each can be amplitude modulated by Betatron motion. This bunch signal repeats at the frequency the step-recovery diode is running at.

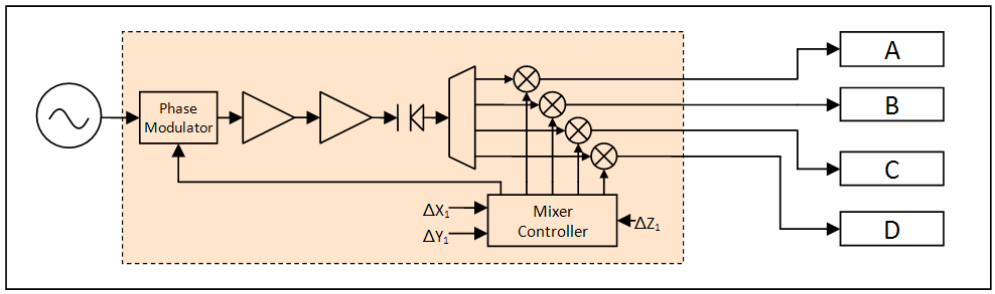

Figure 9: One Bunch system block diagram.

Four Button Signal Controller

We need an appropriate way to modulate the signals depending on the beam orientation at the pick-up. Thus we have built an analog baseband circuit to control the 4 modulators to generate desired voltage level on the four buttons. With this building block, we are able to simulate one bunch with Synchrotron oscillation and Betatron oscillation. It's going to be a bunch at the repetition rate of the step-recovery diode.

Figure 10 shows a typical button-style beam position monitor. For small displacements from the center of the beam duct, the beam position in terms of voltages on the four buttons is calculated by difference-over-sum algorithm [1]:

$$\Delta X = \frac{b}{2}\frac{(V_A + V_B) - (V_C + V_D)}{(V_A + V_B) + (V_C + V_D)}$$

$$\Delta Y = \frac{b}{2}\frac{(V_A + V_D) - (V_B + V_C)}{(V_A + V_D) + (V_B + V_C)}$$

With some math expression manipulation, we obtain the following equation for the voltage on the four buttons.

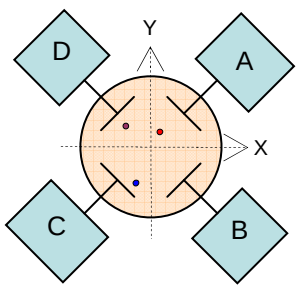

$$V_A = K_A - \frac{\Delta X - \Delta Y}{4}$$

$$V_B = K_B + \frac{\Delta X + \Delta Y}{4}$$

$$V_C = K_C + \frac{\Delta X - \Delta Y}{4}$$

$$V_D = K_D - \frac{\Delta X + \Delta Y}{4}$$

10: Button-style Beam-Position Monitor and the relationship between the Four-button voltages and the Beam Position

The analog baseband modulator is built with op-amps and has a bandwidth of 10 MHz, which is more than enough for the modulation we want to mimic. Potentiometers are used to adjust K_A, K_B, K_C, and K_D and signal Inputs represents ΔX and ΔY signals.

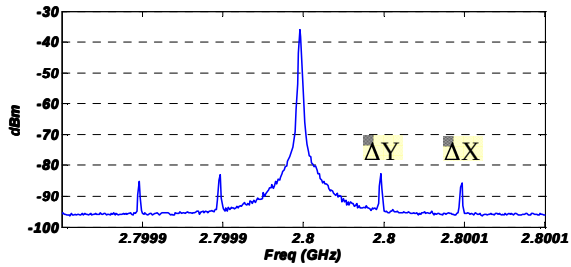

Figure 11: Spectral content of the one bunch signal with oscillations on ΔX and ΔY.

Combining Four Bunches

If we want to put more bunches and move them closer or a high frequency modulation pattern, what we do is to take four of these and combine them. Shown in the above diagram, for a 500 MHz system, we can operate each bunch at 125 MHz and superimpose the 4 signals. One advantage of doing this is the flexibility of choosing the bunch separation interval. Additionally this allows us to modulate each bunch's coordinates at relatively low baseband frequency (simulating coupled-bunch motion, and adjusting the phase between the 4 modulation oscillators to adjust high or low frequency coupled bunch mode). This is easier rather than modulating a single diode at 4 times the RF frequency over the full bandwidth of all coupled-bunch modes.

By selecting either 100, 119, 125, or 250 MHz as the base RF, we can simulate various machines with 100 to 525 MHz RF, and filling patterns up to every bucket. The system block diagram that combines four bunches is shown in Figure 12.

SUMMARY

In this paper, we present the design of a reprogrammable four-bunch beam signal generator system. Using step-recovery diode techniques, the simulator produces modulated 100-ps impulse signals that mimic realistic beam signals to test high-resolution BPM receivers. Our system generates a four-bunch beam impulse signal and the beam spacing can be individually re-configured for each bunch to adapt to different accelerators. The programmable nature of the system allows us to modulate the bunch signals in amplitude to simulate the transverse beam motion of low and high

frequency coupled-bunch modes and in phase for longitudinal beam motion. Since the system is working at RF/4 frequency, it increases the flexibility of the system and ease the modulation bandwidth requirement. It further allows testing and measurement of bunch-to-bunch coupling and isolation in multi-bunch feedback via use of 4 different modulation frequencies.

ACKNOWLEDGEMENTS

We thank the SLAC ARD department for support and Dr. Makoto Tobiyama from KEK for excellent discussions and tremendous help on these topics. We acknowledge the US-Japan Cooperative Program in High Energy Physics for providing important funding for this project.

REFERENCES

[1] S. R. Smith, “Beam Position Monitor Engineering”, Invited talk presented at the 7th Beam Instrumentation Workshop, Argonne National Laboratory, Argonne, Illinois (1996)

[2] T. H. Lee, “Planar Microwave Engineering: A Practical Guide to Theory, Measurements and Circuits”, Cambridge University Press (2004)

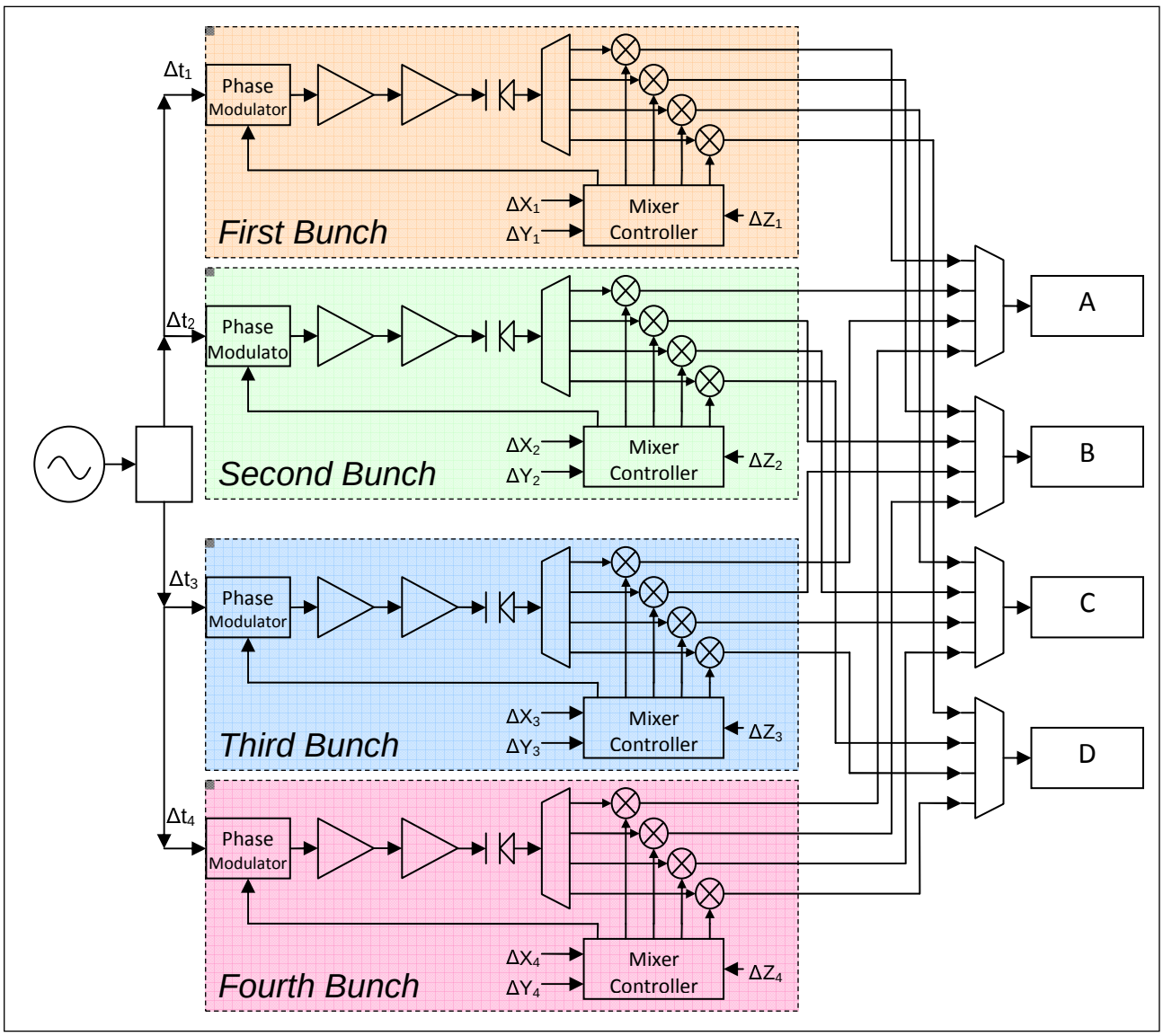

Figure 12: System (four-bunch) Block Diagram. Each dashed box is a separate bunch.

CRAB WAIST SCHEME LUMINOSITY AND BACKGROUND DIAGNOSTIC AT DAFNE

M. Boscolo, F. Bossi, B. Buonomo, G. Mazzitelli, F. Murtas, P. Raimondi, G. Sensolini
(INFN/LNF, Via E. Fermi 40 - 00044, Frascati, RM, Italy)
M. Schioppa
(Gruppo Collegato INFN, Via P. Bucci - 87036, Rende, CS, Italy)
F. Iacoangeli, P. Valente
(INFN-Roma, P.le Aldo Moro 5, Roma, Italy)
N. Arnaud, D. Breton, A. Stocchi, A. Variola, B. Viaud
(LAL, Univ Paris-Sud, CNRS/IN2P3, Orsay, France)
Paolo Branchini
(INFN Roma3, Via della Vasca Navale, 84 - 00146, Roma, Italy)

Abstract

Test of the crab waist scheme, undergoing at the Frascati DAFNE accelerator complex, needs a fast and accurate measurement of the luminosity, as well as a full characterization of the background conditions. Three different monitors, a Bhabha calorimeter, a Bhabha GEM tracker and a gamma bremsstrahlung proportional counter have been designed, tested and installed on the accelerator at the end of January 2008. Results from beam-test measurements, comparison with the Monte Carlo simulation and preliminary data collected during the SIDDHARTA run are presented.

INTRODUCTION

The promising idea to enhance the luminosity with the introduction of a large Piwinski angle and low vertical beta function compensated by crab waist [1], will be a crucial point in the design of future factory collider [2], where the luminosity is the fundamental parameter. The DAFNE accelerator, located in the National Laboratory of Frascati (INFN), optimized for the high production of Φ mesons (√s=1020 MeV), has been modified during last year to test the crab waist sextupoles compensation scheme. Since fall of 2007 the machine has restarted operations, and at the beginning of February various luminosity detectors have been put in operation in order to guarantee an accurate measurement of the luminosity and of backgrounds, as well as to provide powerful and fast diagnostics tools for the luminosity improvement.

Three different processes are used to measure the luminosity at DAFNE:

- The Bhabha elastic scattering $e^+ e^- \rightarrow e^+ e^-$; it has a very clean signature (two back-to-back tracks); the available angle is limited due to the presence of the low-β quadrupoles, however, in the actual polar angle range covered by our calorimeters, 18^0-27^0, the expected rate (~440 Hz at a luminosity of 10^{32} cm^{-2} s^{-1}) is high enough and the backgrounds low enough to allow an online clean measurement.
- The very high rate $e^+ e^- \rightarrow e^+ e^- \gamma$ (radiative Bhabha process); it has the advantage that 95% of the signal in contained in a cone of 1.7 mrad aperture, but it suffers heavily from beam losses due to: interactions with the residual gas in the beam-pipe, Touschek effect, and particles at low angles generated close to interaction region (IR).
- The resonant decay $e^+ e^- \rightarrow \Phi \rightarrow K^+ K^-$; a rate of about 25 Hz at 10^{32} is expected in the SIDDHARTA experiment monitor at ~90^o [3].

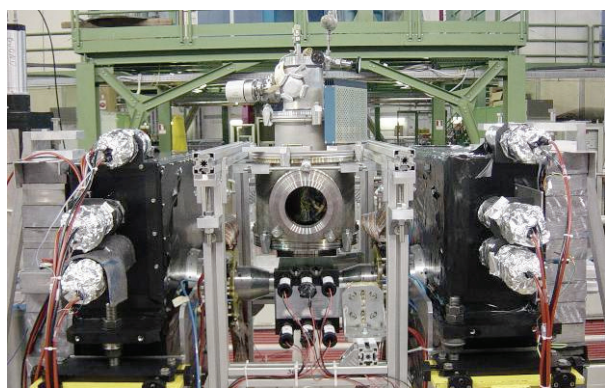

Figure 1: the SIDDHARTA preliminary setup installed at DAFNE. The Bhabhas calorimeters (black boxes) are visible on the left and right of the interaction region.

BHABHA MONITOR

The Bhabha monitors consist of two different detectors, a 4-module sandwich calorimeter, made of lead and scintillator, and two triple GEM annular trackers.

Calorimeters

Four modules of calorimeters surround the final permanent quadrupole magnets, located at a distance of 32.5 cm on both sides of the interaction region (IR), as shown in Fig. 1. They cover an acceptance of 18^o -27^o in polar angle, and are segmented in azimuthal angle in five sectors, 30^o wide. The choice of not instrumenting 1/6 of the acceptance, i.e. the ±15^o region, was dictated by the

consideration that most of the machine backgrounds are expected on the machine plane. Each sector is a sandwich of 12 trapezoidal tiles of 1cm thick scintillator, wrapped with Tyvek* paper, alternated with lead plates: eight 5 mm thick plates towards the interaction point and three 1cm thick plates in the back part, lead plates for a total thickness of 19 cm. This choice was driven by the compromise between the need of having a good longitudinal containment of 510 MeV electron showers (the total depth corresponds to about 12.5 X_0), and the necessity of having a detector not exceeding the permanent quadrupole length.

The 240 scintillator tiles have been produced with injection-molded technique in IHEP, Protvino. Each tile has three radial grooves on one face, 2 mm deep (one in the middle and two 1 cm from the edge of the tile) inside which wavelength shifting (WLS) fibers of 1 mm diameter are placed; the 36 WLS fibers (Fig. 2), are collected to an optical adapter to fit the photocathode of 20 Photonis-Philips XP 2262B photomultipliers, read by a prototype data acquisition system of the KLOE2 experiment: the analog signals are actively splitted to be digitized by a constant fraction discriminator for time measurement (using the KLOE TDC, 1.04 ns resolution), and for the pulse height measurement by the KLOE charge ADC, with a 0.25 pC resolution.

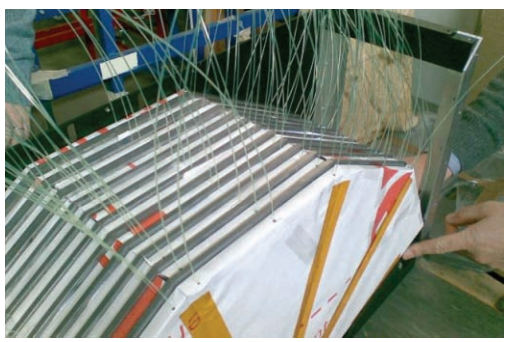

Figure 2: One of the four calorimeters modules during the assembly, wrapped tile, wavelength shifter, and lead plate are clearly visible.

The design energy resolution of 15% at 510 MeV is adequate to put a threshold for selecting Bhabha events.

The triple GEM tracker

In front of each calorimeter, at a distance of 18.5cm from the IR, a ring of triple-GEM detectors [4] is installed around the beam pipe. The two GEM trackers are divided in two units, with an half-moon shape; the top (bottom) half covers azimuthal angles between 14° and 166° (194° and 346°) respectively. Each of the four GEM units is segmented into 32 pads: eight cells in azimuth (covering 19° each) are arranged in four rings of equal radial extension. When a charged particle crosses the 3 mm drift gap, it generates electrons that will be multiplied by the three GEM foils separated by 2/1/2 mm. Each of the GEM planes is made of a thin (50μm) kapton foil sandwiched between two copper clads and perforated by a dense set of holes (70μm diameter, 140 μm pitch).

Figure 3: Gem ring (left, right) and SIDDHARTA scintillator K-Monitor (center) mounted on DAFNE IR.

As a high potential difference (about 400 kV) is applied between the copper sides, the holes act as multiplicating channels and the gain of each layer is about 20 (and hence roughly 8,000 in total).

The GEM trackers, as well as the gamma monitors, have been included into the main DAQ system.

GAMMA MONITOR

Two gamma monitor detectors are located 170 cm away from the IR, collecting the photons radiated by electron or positron beam.

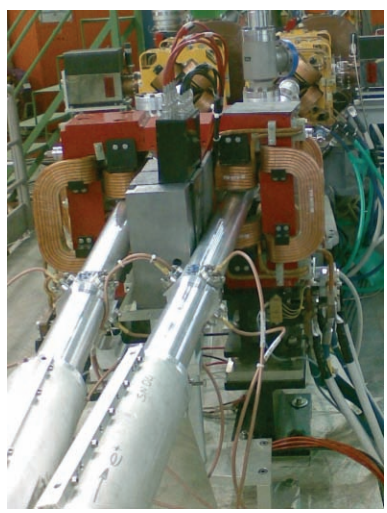

Figure 4: One of the gamma monitor installed between the two last correctors and the final permanent quadrupoles of DAFNE IR.

The detectors replace the gamma monitors previously installed in DAFNE [5] and are now made of four $PbW0_4$ crystals (squared section of $30\times30mm^2$ and 110mm high) assembled together along z, in order to have a 30 mm face towards the photon beam, and a total depth of 120 mm corresponding to about $13X_0$. Each crystal is readout by a Hamamatsu R7600 compact photomultiplier. Each of the crystal signals is splitted: one half is sent to the charge

* Tyvek™ is a trademark of DuPont company.

ADC of the KLOE2 data acquisition system, while the other is sent to an analog mixer. The analog sum of the four crystals is then discriminated and the counts are read by the DAFNE Control system, providing a prompt estimate of the luminosity for machine optimization.

Because of the boost introduced by the beam crossing angle, the trajectories of the photons are shifted towards the inner side (along x coordinate) of the machine; the gamma monitors and GEM trackers are then placed along the beam pipe at x=−5cm and rotated by 4° in the horizontal plane with respect to the beam axis.

Thanks to the high rate, those detectors are mainly used as a fast feedback for the optimization of machine luminosity versus background, more than providing a measurement of the luminosity, since the relative contribution of background is changing with the machine conditions. However, on the short time scale and as relative luminosity monitors, those counters have demonstrated to be extremely useful.

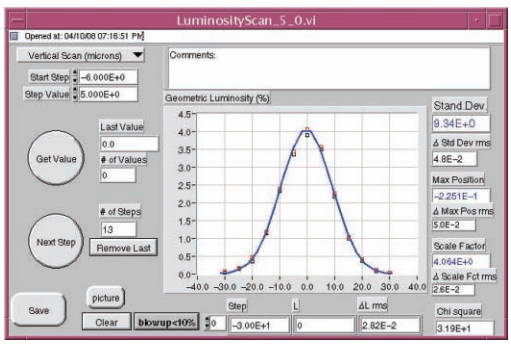

Figure 5: A vertical beam-beam scan performed by the crystal gamma monitor.

SIMULATION

In order to correct the Bhabha event rate measured using the calorimeters and the GEM trackers for the detectors' acceptance and selection efficiency, we developed a full simulation of the whole experimental set-up, based on the GEANT3 package. This includes all the materials and fields present in the interaction region as well as a simulation of the detectors response.

The BHWIDE package is used to generate Bhabha events with a full treatment of the radiation [6].

The contamination due to the Touschek background is investigated by interfacing an ad hoc generator [7] with the simulation.

Particular care was given to the implementation in the simulation of the materials and fields distribution all along the interaction region, since this impacts directly on the background level in the calorimeters as well as on the signal detection efficiency of the gamma monitors.

The simulation predicts a measured Bhabha event rate of ~440 Hz when the luminosity equals 10^{32} cm^{-2} s^{1}. The rate actually measured at the IP is compared with this number to derive the actual luminosity. The simulation is also used to evaluate the systematic uncertainties affecting this measurement. Tab. 1 lists the various contribution to this uncertainty. It's dominated by the alignment of the calorimeter and of the conical shielding in front of it ("Soyuz"), as well as by the definition of the energy threshold. Also the presence of the SIDDHARTA detector is taken into account. For a preliminary measurement involving only the calorimeters, an 11% uncertainty should be quoted. It drops to 7% when the GEMs are also in operation.

Table 1:Systematic errors according to the MC simulation

Sources	**No tracker σ_{syst}**	**GEM tracker σ_{syst}**
Calo alignment ± 2mm	4%	2%
Soyuz alignment ± 2mm	8%	6%
SIDDHARTA Exp.	2%	0%
Energy Th. ± 60MeV	5%	1%
BKG Accidentals	3%	0%
BKG γγ	0.1%	0%
Total (Σquad)	**11%**	**7%**

We also used the simulation to determine the optimal location for the GEMs. They're shifted in the horizontal plane by 5 mm in the direction of the boost to compensate for the loss of back-to-back-ness caused by this boost.

Finally, we based on the simulation to design the part of the beam-tests devoted to the measurement of the attenuation length of the scintillating tiles. This constant has to be precisely known for the simulation to describe accurately the energy reconstruction, thus the signal efficiency.

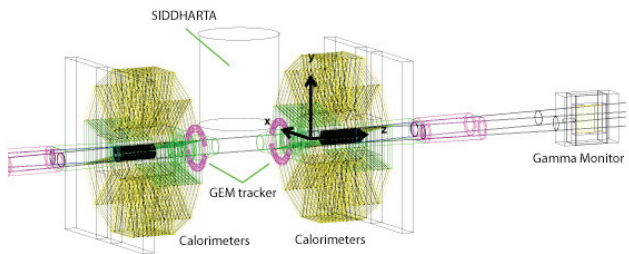

Figure 6: GEANT simulated setup

TEST BEAM

All the four modules have been tested and calibrated with 470 MeV electrons at the DAFNE Beam Test Facility [8], where linearity and energy resolution have also been measured.

Part of the test has been dedicated to comparison of data with Monte Carlo especially on edge effects, wave length fiber attenuation, dependence upon the position of the impact point on the tile due to attenuation of scintillation photons along their way to the fibers, etc.

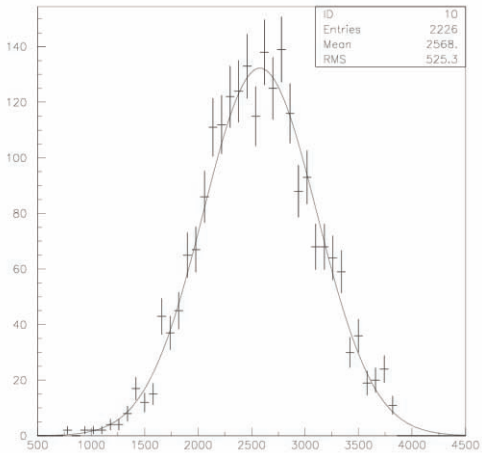

Figure 7: energy resolution of 14%√E(GeV) obtained at the test beam with 470 MeV electron impinging the center of one of the 20 sectors.

.

In the following figure Monte Carlo data are compared with test beam measured data: (read/bottom line)

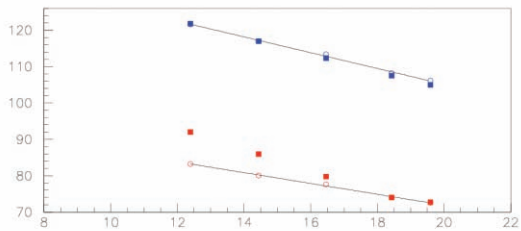

Figure 8: Photo-electron yield in data (open circles) and MC (plain squares) before the tile attenuation length was corrected in MC (red) and after this correction, based on test beam data (blue).

RESULTS

The four calorimeters, the GEM trackers and the crystal gamma detectors are acquired by KLOE2 farm data acquisition prototype. The trigger condition (T1FREE) consists of the coincidence of two opposite, upside down modules when the energy released in the modules is above 200MeV. Data can be acquired for offline analysis when particular studies have to been performed. All single and coincidence rate are acquired by the DAFNE control system, in order to provide a fast reading of luminosity and background condition very useful for machine parameters optimization.

Various analyses of trigger condition, luminosity and background have been performed in order to check the trigger efficiency and background contamination in the luminosity evaluation. For this reason an online filtering process has been implemented on the DAQ farm, providing an offline estimate of the rate (T2FARM), corrected by the percentage of background contamination in the coincidence. This correction is estimated analyzing blocks of 1000 events, and by looking at the time distribution of the time of the two triggering modules. The difference of the arrival time of a Bhabha candidate for the couple of triggering modules is shown in Fig. 9, as selected by the T1FREE hardware trigger. As expected, a Gaussian distribution peaked at $\Delta t=0$ is clearly visible. Superimposed on this narrow Gaussian ($\sigma\cong 2$ counts), a flat distribution due to background is also present. Indeed, the narrow peak completely disappears when the beams are longitudinally separated. The width of the background flat distribution is determined by the duration of the digital signals building the coincidence (≈25 ns).

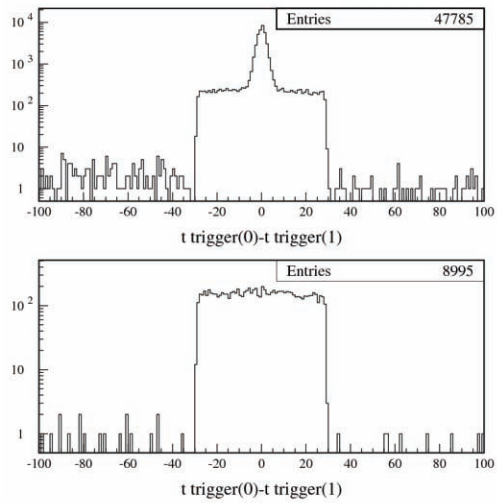

Figure 9: (top) Bhabha time of arrivals in the opposite modules as selected by the T1FREE hardware trigger. (bottom) background time of arrivals when the beams are not colliding (180 degree longitudinal separation)

In order to isolate genuine Bhabha's, the online filter selects events in a $\Delta t=\pm 3\ \sigma$ window (±6 counts). In order to estimate the amount of background beneath the peak, events in the sideband (12 counts wide) are counted and subtracted. In Figure 10 the energy distribution of events selected as good candidates are compared to the ones flagged as background.

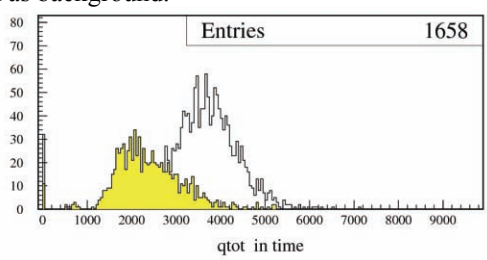

Figure 10: Bhabha total energy deposited: shaded histogram, out of time events, empty histogram, in time Bhabha candidates.

All online and filtered data are stored by DAFNE slow control system with a sampling time of 15 seconds and are available for offline analysis and on the word wide web for online performance presentation.

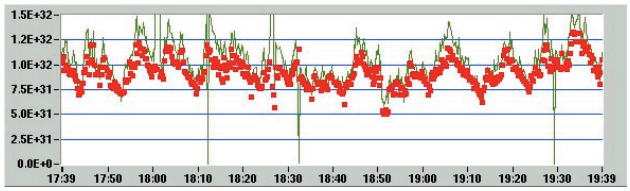

Figure 11: red dots T2FARM luminosity estimate; green line T1FREE uncorrected luminosity.

The GEM tracker is able to measure the Bhabha impact point with good precision and allows a better evaluation of the systematics on rate measurements. Fig. 12 shows the correlation between the impact point polar and azimuth angle of electron and positron tracks.

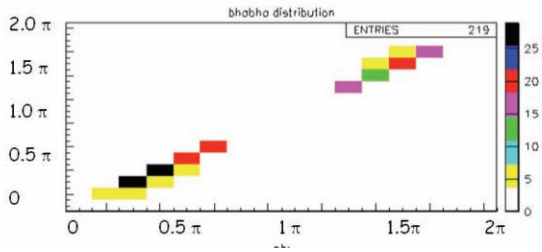

Figure 12: Azimuthally vs polar Bhabha angular correlation detected by GEM tracker.

CONCLUSIONS

The diagnostics installed on the new DAFNE IR in order to measure luminosity for the test of the new crab waist scheme, started to operate at the beginning of February 2008 and is collecting the first encouraging results from the machine (see Fig.13 and 14).

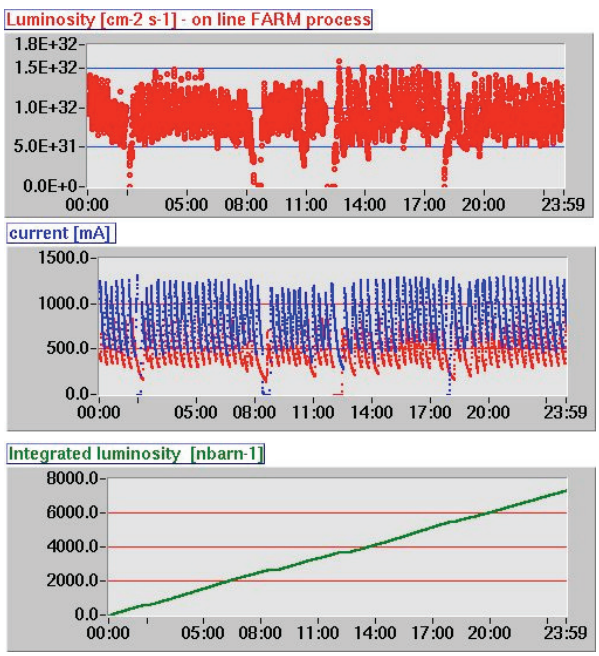

Figure 13: DAFNE WWW online data presentation.

All systems showed very good performance and fully achieved the design parameters. A total systematic uncertainty on the luminosity measurement of 11% can be estimated.

Detectors have been fully implemented in the machine controls, and data are available for the community on the world wide web DAFNE accelerator page.

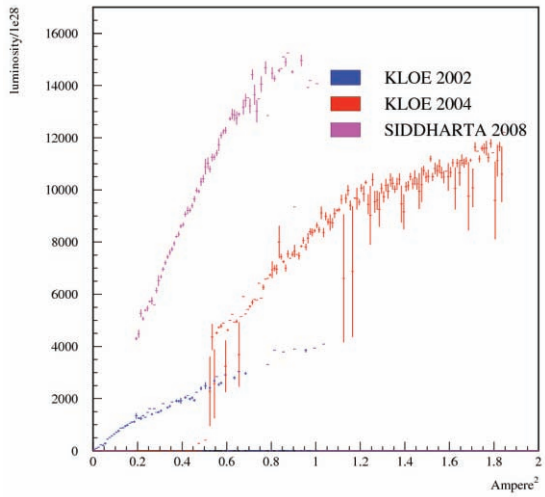

Figure 14: DAFNE performance (luminosity vs current product) during the tree major optics steps.

ACKNOWLEDGEMENTS

We would like to thank L. Iannotti, V. Romano and the LNF SSCR service for the mechanical works, and all the electronic staff of the Accelerator Division; G Corradi, M. Pistilli, D. Tagnani for the GEM electronics and detector construction. We also would like to thank W. Placzek for the support on BHWIDE code.

REFERENCES

[1] D. Alesini et al, LNF-06/033 (IR), 2006.
[2] M. Bona et al, INFN/AE-07-2, SLAC-R-856, LAL 07-15, 2007
[3] Marton et all, Proceedings to the XLV International Winter Meeting on Nuclear Physics, Bormio, Italy, 2007
[4] M.Alfonsi, et al. IEEE 53(1): 322-325 2006
[5] G. Mazzitelli et al, NIM.A486:568-589,2002.
[6] S. Jadach et al, Phys.Lett. B390 (1997) 298-308
[7] M. Boscolo et al, PAC2007, Albuquerque, New Mexico, USA, 2007.
[8] A. Ghigo, et al, NIM A 515 (2003) 524-542

BEAM DIAGNOSTIC FOR A WIDE RANGE BEAM TEST FACILITY

B. Buonomo, G. Mazzitelli, F. Murtas, L. Quintieri.
(INFN/LNF, Via E. Fermi 40, 00044, Frascati (Roma))
P. Valente
(INFN Roma, P.le Aldo Moro 5, Roma).

Abstract

The DAFNE Beam Test Facility (BTF), initially optimized to produce single electrons and positrons in the 25-750 MeV energy range, can now provide beam in a wider range of intensity up to 10^{10} electrons/pulse. The facility has been also equipped with a system for the production of tagged photons, and the possibility of photo-production of neutrons is under study. Different diagnostic tools have been developed and are available for high-energy physics and accelerator communities for testing beam monitor devices and for all studies of particles detectors performances. The facility diagnostic devices are here presented: the main characteristics and operation are described, as well as the performances and the experience of the experimental groups collected during these years.

INTRODUCTION

The Beam Test Facility (BTF) is part of the DAFNE collider, which includes a high current electron-positron LINAC and 510 MeV storage rings (Main Rings).

The e+/e- beam from the LINAC is stacked and damped in the accumulator ring for being subsequently extracted and injected into the Main Rings. When the injector is not delivering beam to the accumulator, the LINAC beam can be transported into the Beam Test area by a dedicated transfer line (BTF line). The main components of the line are described in the following[1].

The main parameters of the S-band LINAC (length 60 m) are listed in the table below:

Table 1. LINAC parameters

Particle	Electron	Positron
Energy	800 MeV	510 MeV
Max. Current	500 mA/pulse	100 mA /pulse
Transverse Emmittance	≤ 1 mm mrad at 510 MeV	≤ 10 mm mrad at 510 MeV
Energy spread	1% at 510 MeV	2.5 % at 510 MeV
Pulse duration	1 or 10 ns	
Repetition rate	1-50 Hz	

Electron (positron) beams in that energy range are suitable for many purposes: high energy detector calibration, low energy calorimetry, low energy electromagnetic interaction studies, detector efficiency and aging measurements, test of beam diagnostic devices etc. Since the end of 2005 a photon tagging system has been installed and started operation with the first users.

THE BTF TRANSFER LINE

The layout of the BTF transfer line is shown in Fig.1. The transfer line is about 21 m long, from the outlet of DHPTB101 (the pulsed dipole extracting the beam to the BTF line) to the bending magnet DHSTB002 in the BTF hall that is one of the two beam exits, and has an inner diameter of about 5 cm. All the line is kept under high vacuum (10^{-10} bar) with the exception of the final part (from the DHSTB002 inlet to the 2 beam exits in the experimental hall), that is working, at present time, at 10^{-4} bar. The part under high vacuum ends with a Be window of 0.5 mm thick. The 10 cm air gap between the Be window and the inlet of the DHSTB002 bending allows the insertion of the silicon micro-strip chambers needed for tagged photon production.

The injector system provides beam both to the DAFNE damping ring and to the test beam area. The DHPTB101 allows to drive each of 49 pulses per second either to accumulator or to the BTF line, thus allowing a quasi-continuous operation of the facility. Indeed, even when beams are injected into the DAFNE main rings, not all the bunches are used for machine filling, so that beam can still be delivered to the BTF, but with a lower repetition rate [2]. Obviously, in this operation scheme the pulse duration and the primary beam energy must be the same of DAFNE. This is not a strong limitation, since the facility is mainly operated in single particle mode (electrons/positrons), which is the ideal configuration for detectors calibration and testing. Once per second, one of the 50 LINAC pulses is bent by 6 degrees to the spectrometer line by another pulsed dipole magnet (DHSTP001), in order to measure the LINAC beam momentum with an accuracy of ≈ 0.1%.

The intensity and the spot of the beam inside the BTF line can be measured by a beam current monitor (BCM1 beam charge to charge output ratio 50:1) and a fluorescent screen of beryllium-oxide type (FLAG01).

The intensity of the beam can be tuned by means of a vertical collimator (SLTB01), located upstream respect to FLAG01 in the BTF transfer line. In the high multiplicity (10^{7} up to 10^{10} particles/bunches) range, the diagnostic elements of the line are completed by another beam charge monitor BCM2 (high sensivity, beam charge to output charge ratio 5:1) and two fluorescent screens FLAG02 (beryllium oxide), FLAG03(YAG:CE) mounted at the two exits of the line. In the following, the number of particles per bunch is also referred as “multiplicity of the beam”.

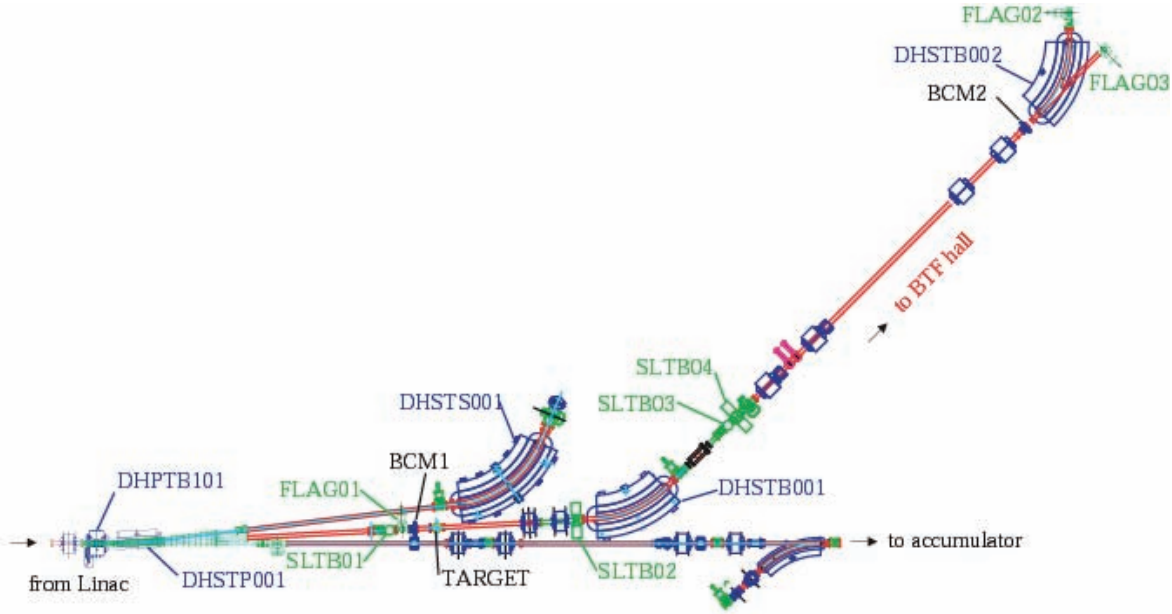

Figure 1. The BTF transfer line. In figure are shown the diagnostic elements mounting on the line, and the position of the target and the four collimator which is necessary to produce a beam with a variable number of particles

When the facility operates in low multiplicity range, it is necessary to strongly reduce the primary beam of the LINAC. The minimum beam current that can be detected by the BCM2 current monitors is $I \approx 1$ mA, and the corresponding number of electrons(positrons) is 10^7/pulse. It is thus necessary to strongly reduce the number of particles to reach the few particles range. The reduction of the particle multiplicity can be achieved with different methods; the one chosen for the BTF operation is the following: first the LINAC beam is intercepted by a variable thickness TARGET, in order to strongly increase the energy spread of the primary beam; then the out coming particles are energy selected by means of a bending magnet DHSTB001 and two horizontal collimators (SLTB02 and SLTB04).

This energy selector accepts a small fraction of the resulting energy distribution of particles, thus reducing the number of electron/positron by a large and tunable factor. The TARGET is shaped in such way that three different values of radiation length can be selected (1.7, 2.0, 2.3 X_0) by inserting it at different depths into the beam-pipe. The momentum of the selected particles has a resolution better than 1%.

After the energy selector, the beam is driven by a 12 m transfer line into the experimental hall by means of a focusing system of four quadrupoles. At the end of the BTF line a second bending magnet allows to use two separate beam-lines alternatively: a straight line is used when the magnet is off, while particles exit from a 45 degrees curved line when the magnetic field is properly set. In table 2 the beam parameters of the facility operated at different multiplicity are reported.

Table 2. BTF parameters for electron/positron beam; A) time-sharing with the DAFNE collider operation, B) continuous operation.

Operation mode	Time sharing	Dedicated
Energy range	25-500 MeV	25 – 750 MeV
Repetition rate	20-49 Hz	49 Hz
Pulse duration	10 ns	1 or 10 ns
Multiplicity	1 up to 10^5	1 up to 10^{10}
Duty cycle	80%	96 %
Spot size (σ_x*σ_y)	~ 2×2 mm (low multliplicity) ~ 10x10 mm (high multiplicity)	
Divergence	~2mrad- 10 mrad	
Energy resolution	< 1%	

BTF PHOTON TAGGED SOURCE.

During 2005, the tagged photon source has been designed, built and tested. The photons are produced by bremsstrahlung of electrons, on a pair of x-y silicon micro-strip chambers, placed at the inlet of the last

bending magnet DHSTB002. The photons are tagged in energy using the same bending dipole: the walls of the curved beam-pipe inside the magnet are covered by 10 modules of silicon micro-strip detectors (Fig 2.)

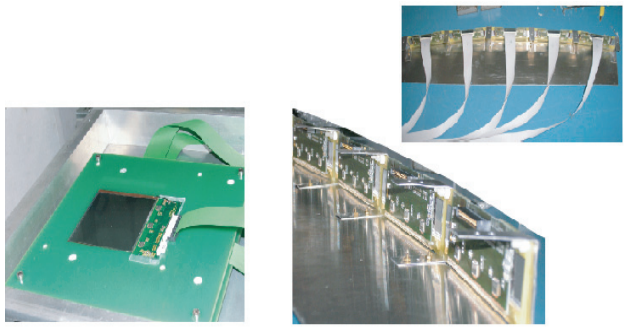

Figure 2. Hardware configuration of the photon tagging system. Left: the silicon microstrip chamber (active target). Right: one of the two supermodules of micro-strips (5x384) mounted on the internal wall of the DHSTB002.

Depending on the energy loss in the photon production, the electrons impinge on a different strip once the dipole current has been set to the nominal value. The correlation between the direction of the electron momentum measured by silicon chambers and the impinging position on the tagging module inside the magnet allows the tagging on the photons. Further details on this system can be found in Ref. [3].

BTF PERFORMANCE AND DIAGNOSTIC TOOLS.

Since November 2002, the facility has hosted many users that have worked in different conditions of beam parameters (wide range of energy and multiplicity). The following table shows the test beam allocated in the last 4 years.

Table 3. Test beam request in the last years.

Year	Days
2007	224
2006	244
2005	364
2004	282

The large range of operation of the facility requires the implementation of different diagnostic devices by mean of which it is possible to measure the beam characteristics (spot size, position, multiplicity). In the low multiplicity operation mode, the standard diagnostic beam devices do not reach the necessary sensivity for monitoring the beam. We have then employed a number of particle detectors (already existing or developed and built for this purpose) optimized for the measurement of the BTF beam. To define the multiplicity (1-100 particles/pulse) we have used different type of calorimeters: lead glass, PbWO4 crystal lead/scintillator fibers (KLOE type), NaI high resolution.

An example of calorimeter spectrum acquired with charge ADC is shown in Fig3. The individual peaks corresponding to the number of electrons can be easily identified. The total number of events in each peak should represent the probability of producing n particles: by fitting the distribution of the number of events in each peak with the Poisson function, the average number of particles can be determinated.

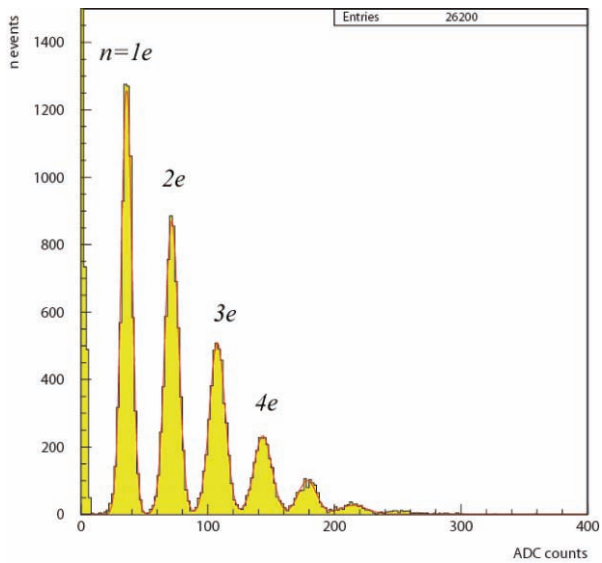

Figure 3. Calorimeter spectrum of BTF beam at low multiplicity

The beam spot profile and position are measured by a x-y scintillating fiber system with millimetric resolution and multi-anode PMT readout, in the range from single particle up to 10^3 particles/pulse[4].

In the low multiplicity range a silicon micro-strip chamber (the active target of the photon tagged source) can be used to measure the beam spot profile and position with ≈ 200 micron resolution (Fig 4).

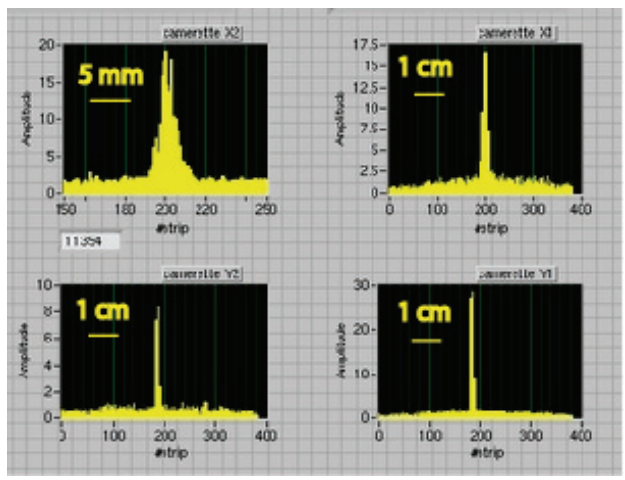

Figure 4. beam spot profile acquisited with a silicon microstrip chamber.

In the range of medium multiplicity (100-10^8 particles/pulse) we have used Cerenkov light emission counter to define the number of particles. This device has been cross-calibrated with the calorimeter at low multiplicity.

In order to have a high resolution beam position and size monitor in the intermediate multiplicity range another silicon microstrip detector, having a readout by front-end eletronics with tunable gain, has been developed and tested [5]. The dimension of this diagnostic device are 9.5x9.5cm^2, 400 μm thick silicon strip detector (HAMAMATSU Photonics). The 121μm pitch 768 DC-coupled strips are readout by 6x128 channels, charge integrating VA_SCM2 ASICs {IDEAS} characterized by 4 possible gains (corresponding to a charge range of 400-41000fC/channel) and a double sample & hold circuit enabling deadtime-less data acquisition. This detector can at the same time measure the beam profile and extract from the integral of the profile the beam multiplicity up to very high values (i.e.10^8 particles /pulse) (Fig5).

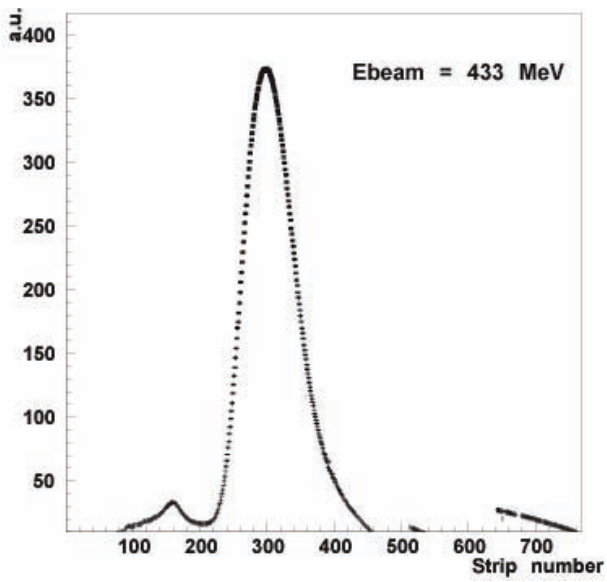

Figure 5. Beam profile with a 10^8 particles/pulse

CONCLUSIONS

The DAFNE Beam Test Facility showed very good performance, both from the point of view of operation reliability and the flexibility in order to cope with very different experimental needs. The diagnostic devices, data acquisition system and tools available for experiments are continuously improving.

In the last upgrade, the duty-factor of the facility has been greatly improved (up to 90%) thanks to the installation of a new dedicated pulsed dipole magnet (DHPTB101), capable of driving any of the 50 Linac pulses either to the accumulator ring or to the BTF transfer line.

First preliminary study has been done in order to develop a neutron source at the Beam Test Facility.

ACKNOWLEDGEMENTS

We deeply thank the DAFNE operators and the technical staff of the accelerator division for having continuously supported the upgrade of the Beam Test Facility . In particular, we thank M. Sperati for the mechanical support and O. Coiro, U. Frasacco, F. Galletti, E. Gaspari, C. Mencarelli, D. Pellegrino for their collaboration to improve the diagnostic devices.

REFERENCES

[1] G. Mazzitelli, A. Ghigo, F. Sannibale, P. Valente and G. Vignola, "Commissioning of the DAFNE beam test facility" Nucl Instr. Meth A 515 (2003) 516.

[2] B. Buonomo, G. Mazzitelli and P. Valente, "Performance and upgrade of the DAFNE Beam Test Facility", IEEE Nuclear Science symposium, Rome 2004.

[3] B. Buonomo et al, "A Tagged photon source at the Frascati Beam-Test Facility", DIPAC 2007, Venice, Italy, May 20-23, 2007.

[4] M. Anelli, B. Buonomo, G. Mazzitelli, and P.Valente, *A scintillating-fiber beam profile monitor for the* DAFNE BTF, LNF 04/24P (2004).

[5] B. Buonomo et al, "Profile Monitors for Wide Multiplicity Range Electron Beams", DIPAC 2005,Lyon, France, 6-8 June 2005.

A GATED BEAM-POSITION MONITOR AND ITS APPLICATION TO BEAM DYNAMICS MEASUREMENTS AT KEKB

T. Ieiri, H. Fukuma, Y. Funakoshi, K. Ohmi and M. Tobiyama, KEK, Ibaraki, Japan

Abstract

KEKB has transformed to an effective head-on collision by using of crab cavities from a crossing collision and gained a higher specific luminosity. A gated beam-position monitor, being capable of measuring the beam phase as well as the transverse position of a specific bunch in a bunch train, has been developed and is used to measure a beam-beam kick. The monitor estimated the effective horizontal beam size at the interaction point from a linear part of a beam-beam kick and demonstrated the effect of the crab cavities. The estimated horizontal beam size agreed with calculated size considering the dynamic beam-beam effect. Moreover, the monitor detected a displacement of the horizontal beam position along a bunch train under the crabbing collision.

INTRODUCTION

KEKB [1] is a multi-bunch, high-current, electron/positron collider for *B* meson physics. The collider consists of two storage rings: the Low Energy Ring (LER) for a 3.5-GeV positron beam and the High Energy Ring (HER) for 8-GeV electrons. Both rings store more than 1500 bunches, where the harmonic number is 5120 with an RF frequency of 509 MHz. Bunches are stored in two rings with a 3-bucket (6 ns) or 4-bucket (8 ns) spacing, forming a single bunch train followed by empty buckets that occupies about 5 percents of the circumference. Additional bunches, called pilot bunches, are placed just after the train, at different location in each ring so that they do not collide with each other.

The two beams collide at one interaction point (IP) with a horizontal crossing angle of 22 mrad. Crab cavities installed in 2007 can horizontally tilt a bunch without changing a central orbit using a dipole-mode kick operating at the RF frequency [2]. The crab cavities achieved an effective head-on collision at the IP. The crabbing collisions are successfully performed for the first time and increased a specific luminosity [3]. Since only one crab cavity per ring is installed, the effect of the crab kick could be observed in the whole ring.

The beam-beam effects are important issues from the viewpoint of beam dynamics, including the collision tunings to raise the luminosity. Since the beam-beam force depends on bunch-by-bunch parameters, a bunch-by-bunch measurement is required to study the beam-beam effect. Although a streak camera and an oscilloscope are useful tools to observe a bunch structure, it is not easy to handle them in the usual operations. Moreover, a direct measurement of the beams at the IP is difficult in the actual configurations. On the other hand, a gated beam-position monitor, being capable of measuring the beam phase as well as the transverse position of a specific bunch in a bunch train, is a simple tool to measure a beam-beam kick. The beam-beam kick can be measured by comparing a beam position between colliding and non-colliding bunches. Although a part of a gated beam-position monitor has already been reported [4], this note represents revised performances and new applications to beam dynamics measurements under the crabbing collision.

GATED BEAM-POSITION MONITOR

A gated beam-position monitor (GBPM), a fast switch selecting a specific bunch is attached with a turn-by-turn BPM, can measure the beam position of individual bunches. One application of a GBPM is to measure the beam-beam effect by comparing the beam parameters of a colliding bunch with those of the non-colliding pilot bunch. The signal processing is performed within a revolution period. This gated measurement has the following features:

- The position measurement is not affected by the global orbit correction.
- Imbalance in gains of the detector is cancelled out due to subtraction.
- However, the measurement is not simultaneous.
- An error would be enhanced, when the intensity between bunches to be measured is largely unbalanced.

Figure 1 shows the schematic diagram for a GBPM. Button type electrodes are mounted with a cylindrical vacuum pipe with a diameter of 64 mm to pick up a beam pulse. The optics parameters at the location of the pick-ups are listed in Table 1. The system can select an electron or a positron bunch and employs a common detector. A low-pass filter of a Bessel type with a cut-off frequency of 1.5 GHz is attached to a gate module so that high frequency components of a button signal would be eliminated. A gate selects a specific bunch in a bunch train with a pulse width of 8 ns, where a commercially available switch (Hittite-HMC234C8) is used. Owing to the IQ (In-phase and Quadrature phase) detection at the acceleration frequency of 509 MHz, the monitor can detect a longitudinal position or the beam phase of a bunch as well as the transverse beam positions [5]. Two orthogonal signals are put into 8-channel ADCs with a resolution of 12 bits. A peak of a detected pulse with 20 ns width is sampled in the ADCs at a rate of the revolution frequency of 100 kHz. The sampled data are stored turn by turn in a memory.

An on/off isolation of the gate module was tested in a bench. An isolation of more than 50 dB at 2 GHz is achieved, where two series of the switches are used to raise the isolation. The isolation of the system was also measured using real bunches placed with a spacing of 8

ns (4 buckets), while shifting the timing for the gate and for the clock of the ADCs in the unit of bucket. The isolation for the beam intensity was about 40 dB at a separation of 3 buckets as shown in Fig. 2. The degradation in the isolation would be due to a long tail of a button signal. Although the system can measure a beam position turn by turn, the beam position data are averaged over 2,000 turns for measuring a closed orbit. The standard deviation of the averaged position measurement was improved to 3 to 5 μm and the resolution of the phase is 0.10 degrees. The performances of the GBPM are summarized in Table 2.

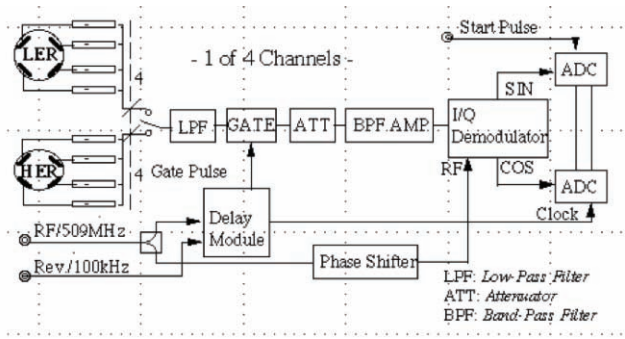

Figure 1: Schematic diagram of a gated beam-position monitor system.

Table 1: Optics parameters at GBPM

Ring	LER	HER
Location	QV1P.2	QX6E.2
Beta_x (m)	22.4	43.05
Betatron Phase Advance /2π from IP	22.68	23.31
Dispersion_x (m)	< 0.0001	0.001

Table 2: Specifications of GBPM

Pick-up Electrode	Button
Detector Bandwidth	509+/- 30 MHz
Resolution of Position	20 μm @ turn-by-turn
	3 to 5 μm @ average
Resolution of Phase	0.3 deg. @ turn-by-turn
	0.10 deg. @ average
Isolation of Gate	> 50 dB @ 2GHz
	40 dB @ 6 ns spacing

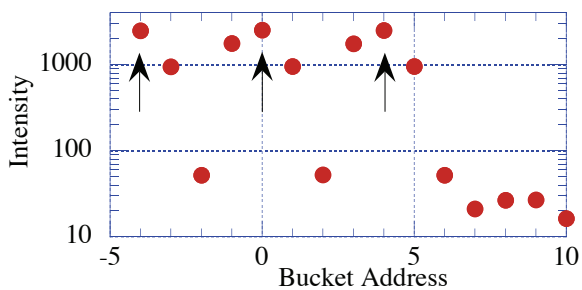

Figure 2: Measured intensity of positron bunches, while shifting timing for the gate and the sampling clock as a function of bucket address. Arrows indicate buckets with a bunch and the other buckets do not contain bunches.

BEAM-BEAM KICK

When two beams collide with an orbit offset, Δ^*_x at the IP, they are kicked by the electromagnetic force of the opposite beam and the orbits of both beams are distorted around the ring. A position monitor located at a phase advance of $\Delta\varphi_d$ from the IP detects a position shift due to the collision. A position shift at a detector is given by

$$\Delta X_{\mathrm{det.}} = \frac{\sqrt{\beta_{\mathrm{det.}}\beta^*}}{2\sin(\pi\nu)}\theta_{bb}\cos(\pi\nu - |\Delta\varphi_d|). \quad (1)$$

Here, $\beta_{\mathrm{det.}}$ and β^* are the beta functions at a detector and the IP, respectively and ν is the betatron tune and θ_{bb} is a beam-beam kick angle. Assuming that the vertical offset is zero, the horizontal beam-beam kick θ_{bb} is expressed using a rigid Gaussian model as

$$\theta_{bb} = \frac{-2r_eN_b}{\gamma}\Delta^*_x\int_0^\infty \frac{\exp(-\frac{\Delta^{*2}_x}{(t+2\Sigma_x^2)})}{(t+2\Sigma_x^2)^{3/2}(t+2\Sigma_y^2)^{1/2}}dt, \quad (2)$$

where, Σ_x and Σ_y are horizontal and vertical effective beam sizes, respectively, r_e is the classical electron radius, γ is the relativistic factor, N is the number of particles in a bunch. The effective beam size is defined by $\Sigma_{x/y} = \sqrt{(\sigma^+_{x/y})^2 + (\sigma^-_{x/y})^2}$. The superscript ± denotes positron or electron bunches. The beta function dynamically changes according to the beam-beam force, depending on the betatron tune. A calculation using the optics parameters shows that the product of the beta function is constant to be $\sqrt{\beta_{\mathrm{det}}\beta^*} \approx 4.0\,\mathrm{m}$. Thus, the position shift at the detector is proportional to the beam-beam kick. When the horizontal offset is smaller than the beam size, Eq. (2) is approximately given by

$$\theta^{\pm}_{bb} \approx \frac{-1.94r_eN^{\mp}}{\gamma^{\pm}}\frac{\Delta x^*}{\Sigma_x^2}. \quad (3)$$

We can estimate the effective horizontal beam size at the IP from the slope, $\theta^{\pm}_{bb}/\Delta x^*$ using Eq. (3).

Since the analytical formula in Eq. (2) is based on the head-on collision, a different configuration is required to calculate a beam-beam kick with a crossing angle. Figure 3 illustrates how to calculate the beam-beam kick under collision with a crossing angle of 22 mrad, assuming that a single particle collides with a Gaussian strong bunch. A particle is horizontally moved with a crossing angle. The each kick data are summed up, considering the longitudinal beam profile of the bunch. Figure 4 compares two beam-beam kicks of particles with and without the crossing angle under the same bunch intensity. Transforming the crossing scheme to the head-on collision from the crossing collision, the beam-beam kick is increased and the estimated effective beam size would decrease. Since the slope in a head-on collision around the linear part is roughly twice comparing with a crossing

collision, it is estimated that the relative beam size reduces by a factor of 1.4 due to the crabbing collision.

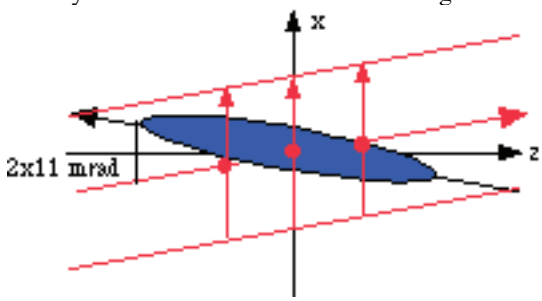

Figure 3: Schematics of calculating a beam-beam kick of a particle under a crossing angle of 22 mrad. The "x" and 'z" mean the horizontal and longitudinal directions, respectively. A particle moves in the horizontal direction with a slope of 22 mrad for a bunch.

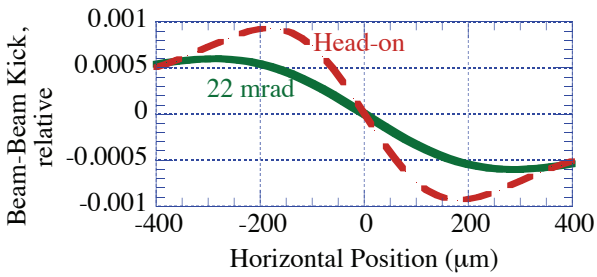

Figure 4: Relative beam-beam kick as a function of the horizontal position, dashed red is that with head-on collision and solid green line is that with a horizontal crossing angle of 22 mrad under the same beam conditions.

MEASUREMENTS

Beam-Beam Kick

Although a tilt of a bunch profile due to the crab cavities is directly observed by using a streak camera [6], its effect would be estimated from measuring a beam-beam kick at the IP, as estimated in the calculation. The GBPM compares a position between colliding and non-colliding bunches, while changing a relative orbit between the electron and the positron beams at the IP. After careful tuning of the crab voltage and the phase, the horizontal orbit scan was performed at the IP. Figure 5 shows the position shift with and without the crab cavity as a function of a setting value of the horizontal offset. It was confirmed that the horizontal offset agreed with the actual orbit displacement at IP within 10%. Both beam-beam kicks were taken under almost the same beam conditions except the crab voltage. There is a clear difference in the slope around the zero offset between two conditions. The estimated effective horizontal beam size using Eq. (3) is $\Sigma_x = 167 \pm 3\mu m$ with the crab voltage and $\Sigma_x = 230 \pm 3\mu m$ without the crab. The horizontal effective size at the IP reduced to 72 % by the crabbing collision. The measurement is consistent with the calculation. The reduction of the horizontal beam size could contribute an increase of the luminosity. Since the crab cavity is so effective, the operations are performed under the crabbing collision. The effective beam size was measured in the usual operations. The measured size was smaller than a calculated size without the beam-beam force as shown in Fig. 6. Since the horizontal betatron tune is close to a half-integer, the dynamic beam-beam effect greatly contributes to the beam size. Figure 6 shows that the dynamic effect with betatron tune of 0.51 or 0.54 can explain the measured beam size.

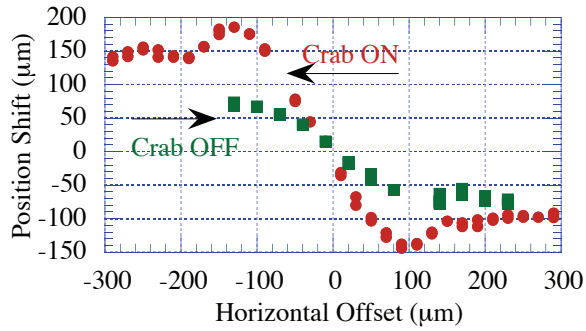

Figure 5: The position shift of a positron bunch detected at the monitor as a function of the horizontal orbit offset, red dots are measured under the crabbing collision and green squares are without the crab. The positron and electron bunch currents are 0.64 and 0.47 mA with the crab, 0.73 and 0.42 mA without the crab, respectively.

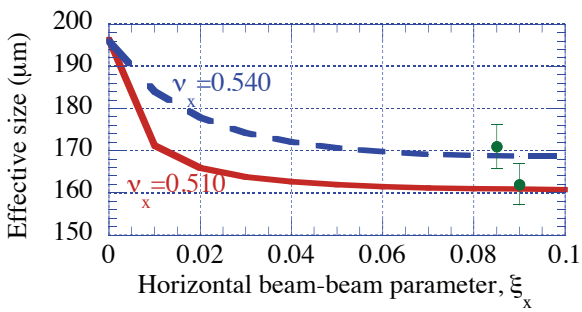

Figure 6: Measured effective horizontal beam size indicated with green dots as a function of the beam-beam parameter. The beam-beam parameter was estimated from a coherent beam-beam tune shift. Calculated sizes are shown in the case of two fractional tunes, 0.510 with a solid red line and 0.540 with a blue dashed line.

Beam Positions along a Bunch Train

The beam position and the beam phase along a bunch train were measured every 49 buckets using averaged data under the crabbing collision, where a bunch train contains 1584 bunches. Figure 7 shows the horizontal position, the vertical position and the beam phase as a function of the bucket number, measured in the LER. Similar measurements were performed in the HER as shown in Fig. 8. As shown in Fig. 7-(c) and Fig. 8-(c), the beam phase advances along a bunch train. The phase modulation is known as transient beam loading due to the gap after a train [7] and its maximum displacement is proportional to the beam current. Comparing Fig. 7-(c)

with Fig. 8-(c), there is a small difference in the phase advancing. The phase advance in the LER rapidly increases in the leading part and tends to saturate in the backward region. On the other hand, the phase in the HER almost linearly increases along a train. The difference would be due to the RF systems. KEKB employs two types of cavities, normal and super-conducting cavities. At the same time, we observed a peculiar phenomenon in the horizontal position, where the position drifts inside along a train in both rings. The horizontal orbit displacement between the head and the tail bunches is about 120 μm in the LER and about 280 μm in the HER. Note that the horizontal dispersion function at the location of the monitor is negligibly small in both rings. Since such a large horizontal displacement was not observed without the crab cavities, the horizontal displacement might be related to the crab kick. The vertical position did not show a peculiar displacement, except in the leading part in the LER.

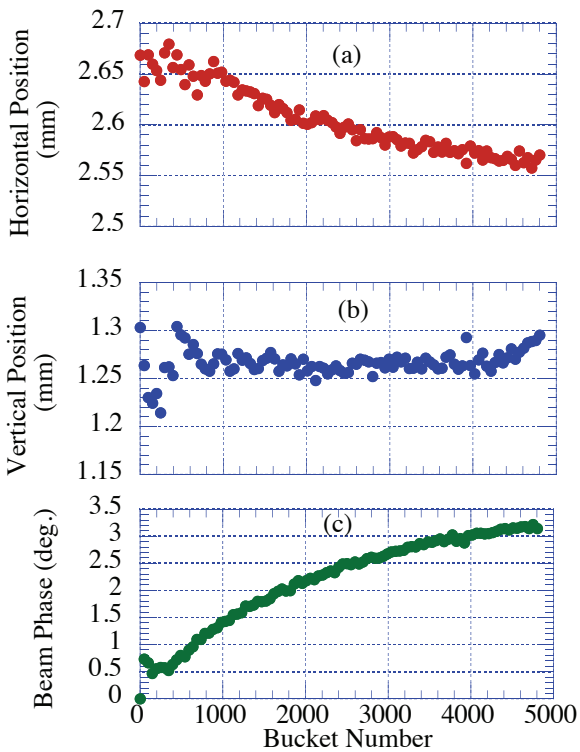

Figure 7: The horizontal beam position (a), the vertical position (b) and the beam phase (c) along a train in the LER measured at beam current of 1530 mA.

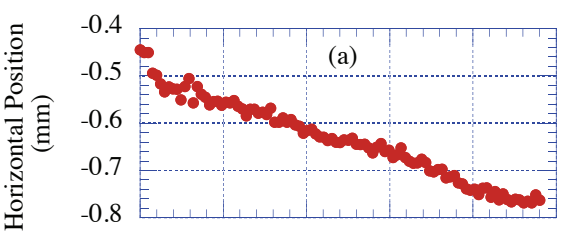

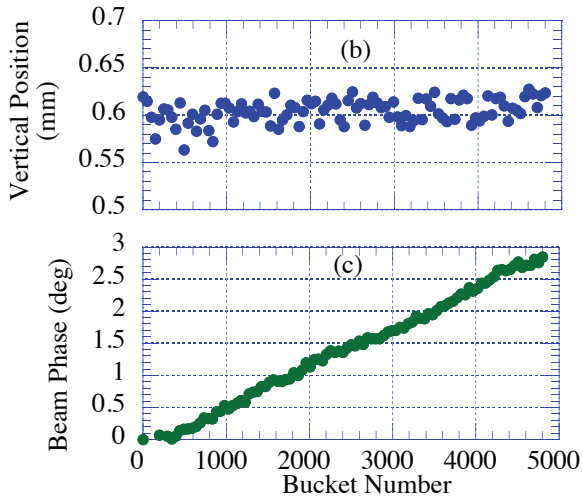

Figure 8: The horizontal beam position (a), the vertical position (b) and the beam phase (c) along a train in the HER measured at beam current of 800 mA.

Detail structure of the position along a train was measured. A bunch train has a periodic structure with a period of 49 buckets. Each period contains 16 bunches. In a period, only one bunch is placed with 4-bucket spacing and the others are placed with 3-bucket spacing. As shown in Fig. 9, we observed orbit displacements of about 60 μm in the horizontal and the vertical positions just before the 4-bucket spacing. The displacement in the vertical position reduced, when the beam current decreased.

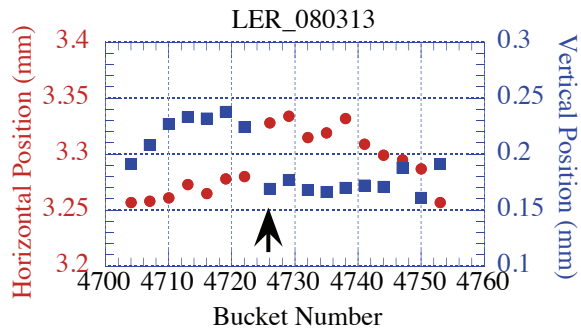

Figure 9: The horizontal (red dots) and the vertical positions (blue squares) as a function of bucket number, measured at total beam current of 1600 mA in the LER. Only one bunch indicating an arrow is placed with 4-bucket spacing. The others are placed with 3-bucket spacing.

DISCUSSION

The beam-beam kick angle can be obtained from the position shift data using the optics parameters. A measured beam-beam kick is represented together with calculated kicks as shown in Fig. 10. The measured kick agrees well with a calculated kick around the center, assuming a rigid Gaussian bunch with an effective size of 162 μm. However, the measured kick deviates from the calculated kick curve, when the horizontal offset is larger than about 100 μm. The measured kick is smaller than a

calculated one using a larger size of 196 μm there. The result suggests that a beam density at the peripheral region of a bunch profile reduces and somewhat expands, although the central part is shrunk by the dynamic beam-beam effect. The distorted horizontal profile might be related to a short lifetime observed at a high beam-beam parameter.

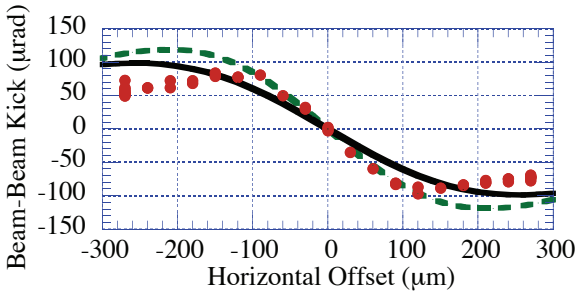

Figure 10: Measured (red dots) and calculated (dashed green and solid black) beam-beam kick as a function of the horizontal offset. The dashed green line indicates a kick with an effective size of 162 μm and the solid black with a size of 196 μm with a Gaussian profile.

As shown in Figs. 7 and 8, we observed the horizontal displacement as well as the beam-phase advance along a train in both beams. When a bunch shifting the synchronous phase passes through a crab cavity, the crab cavity kicks the bunch asymmetrically. As a result, a horizontal orbit displacement would be produced in the whole ring. The position-monitor detects the displacement as

$$\Delta X_{\mathrm{det.}} = \frac{\sqrt{\beta_{\mathrm{det.}}\beta_c}}{2sin(\pi\nu)}\Delta\phi_{crab}\cos(\pi\nu - |\Delta\varphi_d|), \qquad (4)$$

where β_c, $\Delta\phi_{crab}$, $\Delta\varphi_d$ are the beta function at the crab cavity, an asymmetric kick angle of the crab cavity and a betatron phase advance between the crab and the monitor, respectively. It is experimentally verified that a crab kick for a phase displacement of 4.8 μrad/deg is produced at crab voltage of 1 MV in the LER [8]. On the other hand, the phase amount in a train is measured to be about 3.2 degrees from Fig. 7-(a), which makes a position shift of 140 μm between the head and the tail bunches in a train. The estimated position shift agrees well with the measurement.

As shown in Fig. 9, position displacements were observed around changing the bunch spacing. In order to search the source, we tried to measure the beam position directly using an oscilloscope (Tektronix, DPO7254). Figure 11 shows a bunch signal picked up by a button electrode through a coaxial cable. A ringing is observed after a button signal with frequencies of 2 to 3 GHz. A large vertical position displacement was observed from a peak-to-peak measurement in the button signal, however, the displacement was reduced by using a low-pass filter with a cut-off frequency of 1.5 GHz. The ringing would be due to wake fields detected by button electrodes. It was confirmed that the low-pass filter attached to the gate module is effective to attenuate unnecessary high frequency components.

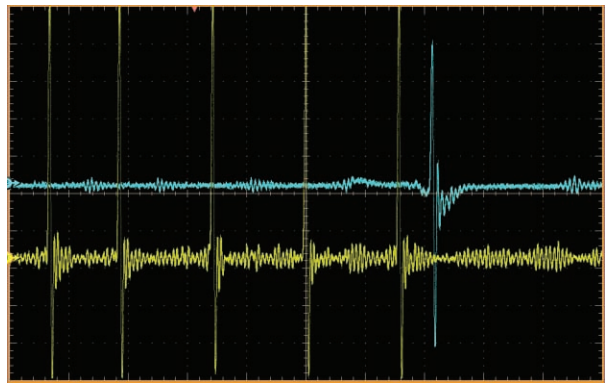

Figure 11: Button signals observed on an oscilloscope. Yellow trace is a bunch signal and upper blue one is a gated bunch signal. The horizontal scale is 5 ns /div.

SUMMARY

Under the crabbing collision, the beam-beam kick and the beam position along a bunch train were measured using a gated beam-position monitor at KEKB.

- The effect of the crab cavity was confirmed from measuring the effective horizontal beam size at the IP.
- The measured horizontal beam size at the IP is consistent with calculation with the dynamic beam-beam effect.
- However, the kick data suggest that a bunch profile deviates from a Gaussian in the peripheral region.
- Displacements of both the horizontal position and the beam phase were observed along a bunch train. The horizontal-position displacement is caused by an asymmetric kick of the crab cavity, which is based on the transient beam loading.
- Displacements in the horizontal and the vertical positions were observed around a change of bunch spacing. The source is still unclear and the displacements might not be real.

REFERENCES

[1] K. Akai et al., Nucl. Instrum. Methods Phys. Res., Sect. A 499, p.191 (2003).
[2] K. Hosoyama et al., to be presented in EPAC08, (2008).
[3] K. Oide et al., Proc. of PAC07, p.27 (2007).
[4] M. Arinaga et al., Nucl. Instrum. Methods Phys. Res., Sect. A 499, 100 (2003).
[5] T. Ieiri and T. Kawamoto, Nucl. Instrum. Methods Phys. Res., Sect. A 440, p.330 (2000).
[6] H. Ikeda et al., Proc. of PAC07, p.4018 (2007).
[7] K. Akai et al., Proc. of PAC01, p.2432 (2001).
[8] H. Koiso, Private communications.

MODIFIED DIGITAL FILTERING MAKES POSSIBLE "TRUE & PURE" TURN-BY-TURN MEASUREMENTS

A. Kosicek, V. Poucki, T. Karcnik, Instrumentation Technologies, Solkan, Slovenia
B. K. Scheidt, ESRF, Grenoble, France

Abstract

Libera, the beam position processor, features the so-called TbT (Turn-by-Turn) data output, the data rate being exactly the revolution frequency of the accelerator. This data is essential for commissioning of the accelerator as well as for various machine physics studies. However, due to the "natural" properties of correctly structured filters (respecting the Nyquist theorem), the smearing between adjacent TbT samples is not negligible. The purpose of the modified filters in DDC (Digital Down Converter) block is to efficiently reduce smearing between adjacent TbT samples, especially with partial fill patterns. The usage of Modified DDC filters provides excellent results for the studies based on TbT measurements, with the benefit of "true & pure" TbT results (no smearing). The method, its implementation and first results are discussed in this paper.

INTRODUCTION

The smearing of TbT beam position data can be problematic for the precise measurements of certain accelerator characteristics (i.e. lattice parameters, such as the local Beta-function values and phase-advance). The basic principle of such measurements is to first apply a single-turn, flat & uniform kick to the whole beam, and then to measure, with all the TbT BPMs in the accelerator ring, the resulting Betatron oscillations of the beam for a large number of turns after the kick. At the ESRF Storage Ring such measurements are done on a beam that fills 33 % of the Ring. The advantages of such fill pattern are:

a) The individual turns are clearly separated from each other, and

b) the application of pure single turn flat kick is practically possible.

With regards to these kicker specifications, for the ESRF it means a flat field of 1 μs and rise- and fall- times (to less then a few % of the flat field strength) of less than 0.9 μs [1]. To maintain these advantages it was important that the smearing, introduced by the standard, relatively narrow DDC filters inside the Libera BPMs, was addressed. The elaboration and implementation of adapted DDC filters was done at Instrumentation Technologies. Tests on real beam were subsequently carried out at the ESRF on 8 individual Libera BPMs in the Ring [2].

SIGNAL PROCESSING

The signal processing chain on Libera Brilliance is composed of analog signal processing, digitalization on fast ADCs (Analog to Digital Converters) and the digital signal processing, see Figure 1. Within the digital part, digital bandpass filtering is first applied, the signal afterwards being brought to DC by mixing. Then, the TbT data bandwidth is obtained by means of lowpass moving average filters. Finally, the TbT data rate is obtained with proper decimation.

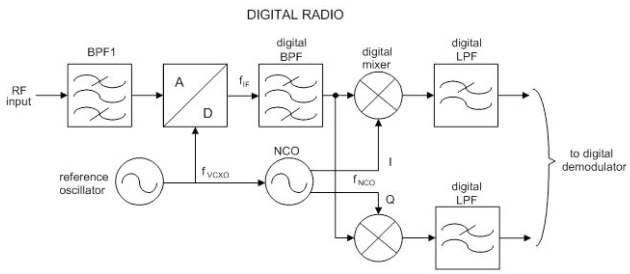

Figure 1: Signal Processing on Libera

Further signal processing to lower data rates for continuous data streams (serving fast feedback and monitoring) is not discussed in this article. Complete processing is implemented onboard a Virtex II Pro FPGA chip. Two main changes to the digital signal processing chain were introduced: wider bandpass digital filters and a narrower subsequent data acquisition window.

Digital Filters

The data coming into digital filtering has the bandwidth of approx 12 MHz, determined by bandpass SAW filters within the analog signal processing. The filters and procedures used for standard digital filtering are constructed by the book, as required by theory. To prevent unwanted aliasing, the 3dB bandwidth of the filters is always well below half of the output sampling rate. For the ESRF case, with TbT frequency of 355 kHz, the bandwidth of the TbT data reaches less than 150 kHz with standard filters. As it is known from the theory, the narrower the filters, the longer is the time response of the output data (i.e. 'ringing' of the filter response). It was therefore a logical choice to make the filters wider. The modified IIR bandpass filters (BPF1 on Figure 1) have been widened to approximately 3 times the TbT data rate.

Acquisition Window

The acquisition window of the standard moving average filters covers the whole TbT period, in the ESRF case this is 304 ADC samples or 2.81 μs. This is in principle correct since the useful signal is in principle distributed over the whole TbT period. But when the accelerator is filled with certain partial fills, the real signal will be distributed only on a certain sector of the TbT period, and the rest of the acquired data will consist mainly of noise. There is no sense to process the noise in

the average moving filters and it can be discarded. To discard the part of the signal without meaningful information, the adjustable acquisition window for these filters was introduced. The delay and the length of the acquisition window can be parametrically chosen, the resolution of both parameters being in ADC samples (~9 ns).

Combined Effect

The combination of these changes on filters and the acquisition window significantly reduces the amount of smearing. On one hand, wider filters reduce the tail of the single pulse signal, while on the other hand the gap between consecutive acquisition windows allows the tail to be flattened to an almost negligible amount: samples with low amplitudes are excluded from processing in moving average filters. Figures 2 and 3 show a schematic presentation of the amplitudes of consecutive TBT output samples. The beam is injected and damped after the first turn, after the standard (Fig. 2) and the modified (Fig. 3) digital processing. The resulting TbT samples are graphically presented as blue dots.

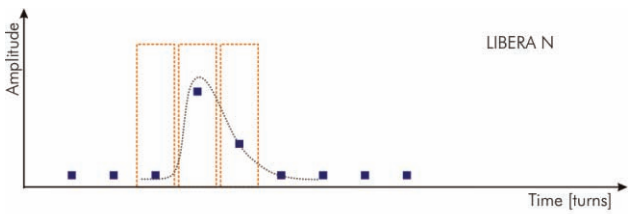

Figure 2: Standard filtering and acquisition window

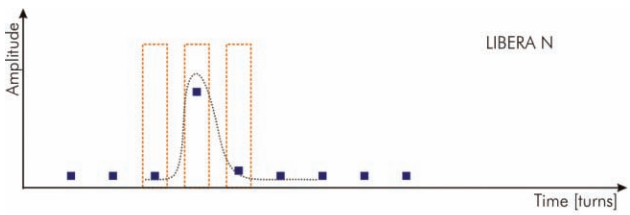

Figure 3: Wider filtering (reduced tail) and selectable acquisition window (in orange)

TESTS ON REAL BEAM

After initial laboratory tests of the modified signal processing, first beam tests were performed at the ESRF in Nov. 2007 on 8 independent Libera BPMs distributed around the Storage Ring. With the Ring in 33 % filling mode, the length of the acquisition window was set to a fixed value of 100 units (out of full width of 304 units per TBT period, i.e. corresponding to 33%). The correct delay (or phase) value for each BPM has been determined first, in order to precisely synchronize this window with the beam fill. This has been done by a simple routine that scans this window in the range of one TBT period and records the so-called Sum signals at each delay setting. The optimum delay value (at max Sum signal) was obtained and then programmed into each Libera. This optimum delay value needs to be determined only once after the installation of the Liberas and their cabling.

Pure Single Turn Measurement

The ideal way of checking whether each Libera unit around the Ring sees indeed only one single turn (i.e. no smearing) and also whether they all see that turn at the same turn-number, is to inject the 1us electron beam into the Ring and to totally suppress it after 1 single turn. This is easily obtained by setting a strong current in one of the last (vertical) orbit steerers before the injection zone: The beam makes 1 full turn and is then 100 % dumped in the vacuum chamber roof. Each Libera thus saw 1 μs of RF signal only. The injected current (at injector) was 2mA. This signal, as seen on Libera at ADC rate (107.9MHz), is plotted on Figure 4.

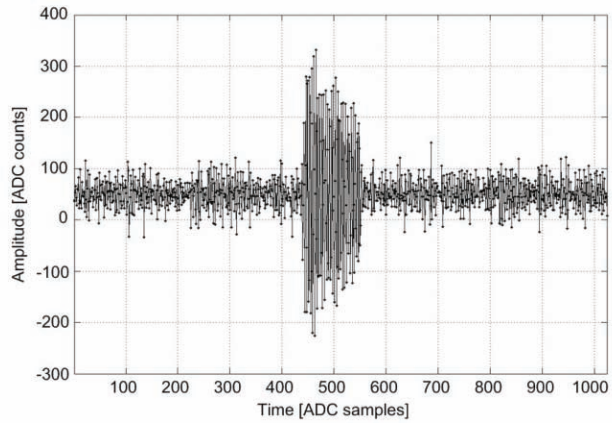

Figure 4: Single Turn, ~1μs long signal, in ADC samples on Libera

The effect of the modifications was expected to be seen on the TbT rate data (355 kSps): to remove smearing between adjacent TbT samples, especially with such, partial filling pattern. The Figure 5 shows exactly this in practice; the SUM output of the unit. Here the effect of the modified filters is evident: one single spike and no noticeable smearing. This result should be compared with the illustration on Figure 3.

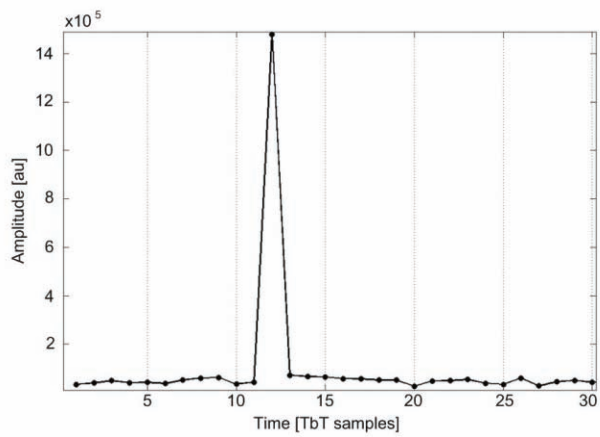

Figure 5: SUM signal at TBT data rate

Beam Arrival

The second experiment was performed by injecting the beam into the ring and allowing it to circulate (i.e., the beam was not dumped after the first turn). There was no RF power to the cavities and the beam survived for 60 to 70 turns. The arrival of the beam (similar current as for first measurement) on six Libera units around the ring is shown in Figures 6 (zoomed) and 7, the SUM signal being displayed. Again, one can observe independent measurement of each TbT sample.

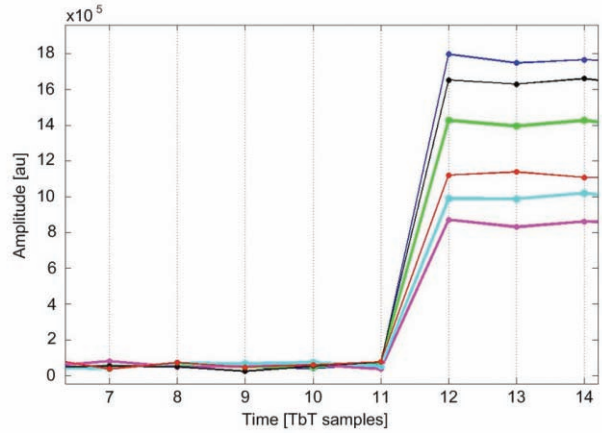

Figure 6: Arrival of the beam, sum signal

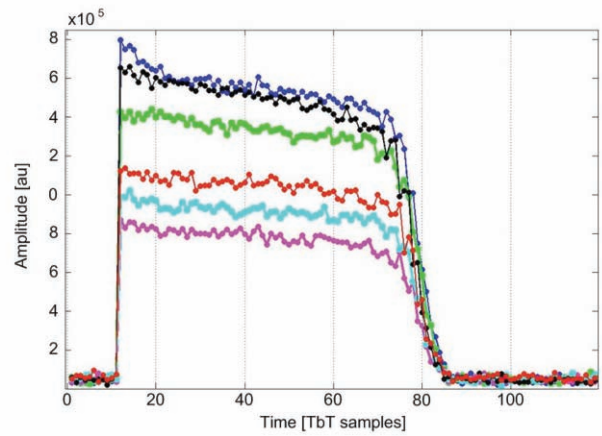

Figure 7: Arrival of the beam, surviving few cycles without RF power, sum signal displayed

Kicked Beam

Figures 8, 9 and 10 show the horizontal position after a kick with a 1μs flat kicker during a single passage of the beam (black line). In the ring, there was a current of approximately 38mA in 33% fill. For comparison, the position of the same beam without a kick was also measured (red).

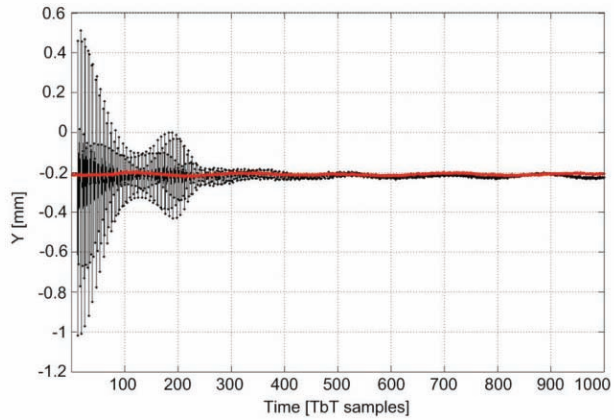

Figure 8: Kick of the flat 1us kicker to the beam, big picture

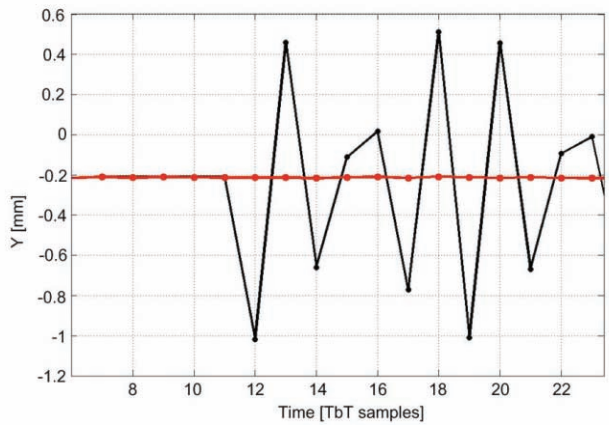

Figure 9: Kick of the flat 1us kicker, first samples

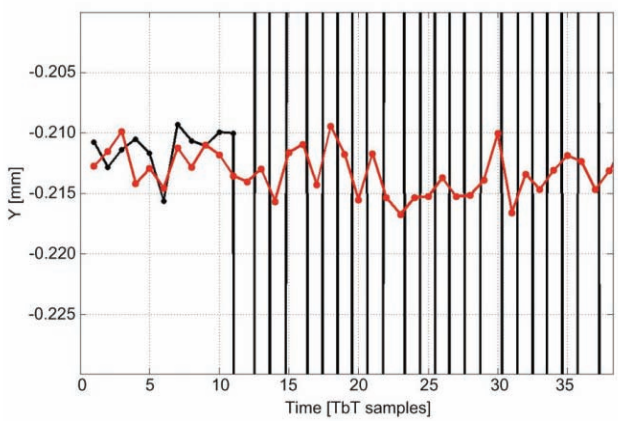

Figure 10: Kick of the flat 1us kicker, position zoom

From the Figures above it can be seen that the measured oscillation resulting from the kick was fast and flat. From the Figure 10 one can also estimate the RMS of the non-disturbed data (red), under such conditions (38 mA at 33 % fill), it is approximately 2um RMS.

SUMMARY AFTER THE MEASUREMENTS

The idea of using modified digital filtering has been confirmed in practice as a very efficient way to obtain true and pure TbT measurements without smearing of the adjacent TbT samples. This is an example of how the digital system can be successfully tailored to a special task just by a change in software. The test results gave very clean and expected results. The initial phase and synchronization adjustment of these filters with respect to the exact RF pulse arriving at each individual Libera BPMs from its BPM buttons is also very easy to perform thanks to programmable delays inside the Libera itself. We would like to emphasize successful collaboration between users (ESRF) and manufacturers of the instrument (Instrumentation Technologies).

Modified vs. Standard Filtering

The use of the modified filters is, as was expected, advantageous for a detailed study of machine parameters. For normal operation, the use of standard filters is still recommended, the main reasons being:

- Ease of use. The setting of delay and width parameters of the acquisition window is not straightforward and requires good understanding of synchronization issues.
- For the normal operation (beam monitoring, fast global orbit feedback …), the difference in performance seems to be negligible.
- The synchronization of the acquisition with the RF frequency must be perfect to keep the acquisition window synchronous with the signal. During normal operation, however, it is recommended to perform slightly asynchronous acquisition (controlled offset-tune) to enhance performance of Libera.

Possible Further Developments

To cover even more complex modes of operation, one improvement has been discussed already. Currently, the modified filters can deal with only one acquisition window within the TbT period. The use of a matrix structure may be considered to cover any possible combination. For example, the ESRF TbT period is composed of 304 ADC samples. There would be an option to choose which ADC samples are taken into consideration and which not. This would enable users to use modified filters, for example, in the four bunch mode, as is illustrated in Figure 11. All kinds of different hybrid modes could be covered. The benefit to users of such improvement is to be investigated.

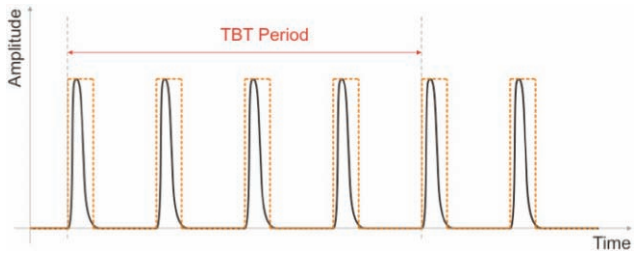

Figure 11: Modified filters and four bunch mode, acquisition windows in orange

REFERENCES

[1] B.K.Scheidt, “Breaking New Ground with High Resolution Turn-by-Turn BPMs at the ESRF”, DIPAC’01, Grenoble, 13-15 May 2001

[2] B.K. Scheidt, “ESRF-Liberas-Nov-2007-A.doc & ESRF-Liberas-Nov-2007-A.ppt”, test report

STRIPLINE BEAM POSITION MONITORS FOR LCLS*

E. Medvedko, R. Johnson, S. Smith, R. Akre, D. Anderson, J. Olsen, T. Straumann, A .Young
Stanford Linear Accelerator Center, Menlo Park, CA, 94025

Abstract

The Linac Coherent Light Source (LCLS) must deliver a high quality electron beam to an undulator for production of coherent X-ray radiation. High resolution beam position monitoring is required to accomplish this task. Critical specifications are a dynamic range of 0.08-8.0 nC with 5 micron resolution at 200 pC in a stripline pickup of 1 inch diameter. Processor electronics were designed, based on band-pass filtering the signals followed by direct digitization of the resulting pulse train. The processor consists of Analog Front-End (AFE) and Analog-to-Digital Converter (ADC) boards, packed into 19-in rack mount chassis, 1U high. The AFE board has a very low input noise, approximately 3 micro V rms in a 7 MHz bandwidth centered at either of two frequencies, 140 or 200 MHz, depending on the length of the stripline BPM used. The maximum gain is 34 dB with programmable attenuation of up to 46 dB in 1 dB steps. An on-board pulser sends a short calibration tone burst to the striplines to perform calibration between beam pulses. The ADC board has four 16-bit digitizers with a sampling frequency of 120 MHz. For the LCLS injector 22 prototypes of the processors were built and installed in 2007. Measured resolution at 200 pC is typically 3-5 microns. A production run of 53 improved processors are currently being installed and commissioned.

OVERVIEW

A beam position monitor consists of four stripline electrodes connected with low loss cables to a BPM Processor (Fig. 1). The BPM processor chassis consists of the Analog Front-End, ADC, and clock boards in a 19" rack-mounted chassis. A processor on the ADC board talks with the VME IOC (Input-Output Controller). The digitizer and the data acquisition system are described in references [1] and [2].

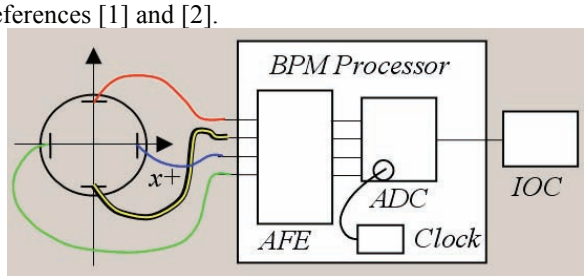

Figure 1: BPM system block diagram.

Twenty-two prototypes and 16 new production chassis are distributed along the Linac injector. Forty-three new BPM Processor chassis will be installed on LCLS this summer.

*Work supported by U.S. Department of Energy contract DE-AC02-76SF00515

Requirements

There are two critical requirements – dynamic range and resolution at 200 pC beam charge.

Table 1: Requirements for the LCLS BPM system

Parameter	Value	Comments
Dynamic Range	0.08 – 8 nC	40 dB
Resolution @ 0.2 nC	5 μm	
Stability	5 μm per hour	

ANALOG FRONTEND

Modern technology provides a variety of high dynamic-range, low noise RF amplifiers and low insertion loss filters applicable for the precision analog front-end design. Three RF amplifiers and three band-pass filters provide low noise amplification with gain programmable by two digital attenuators per channel, providing a total dynamic range control of 46 dB (Fig. 2).

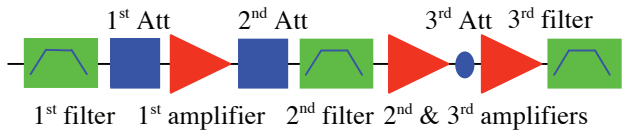

Figure 2: One channel of the Analog Front-End

Two rather different lengths of stripline pickups are used in LCLS: the typical linac BPM strips are 10 cm long, while the striplines intended to provide higher resolution for the linac-to-undulator section have 50 cm long striplines. Due to the difference in frequency response of the two type of striplines we construct BPM processors at two different frequencies, 140 MHz and 200 MHz. Bandpass filters define a bandwidth of 7 MHz at the operating frequency, either 140 MHz or 200 MHz.

Taking the component parameters from Table 2 we calculate an input-referred noise of 3 microvolts rms.

Table 2: Insertion loss (IL), Noise Figure (NF), Gain, IP3.

	IL, dB	NF, dB	Gain, dB	IP3, dBm
1st filter	2.5			
1st att	0.5			
1st amplifier		2.8	20.4	39
2nd att	0.5			
2nd filter	5			
2nd amplifier		3.3	14.9	40
3rd att	6			
3rd amplifier		3.3	14.9	40
other	1.4			

The output noise power density is measured at -134.5 dBm/Hz or 42 nV/√Hz or 110 μV rms in a 7 MHz bandwidth (see Fig. 3). The channel gain is 34 dB so the input noise is about 2.2 μV rms, close to the calculated 3 μV rms.

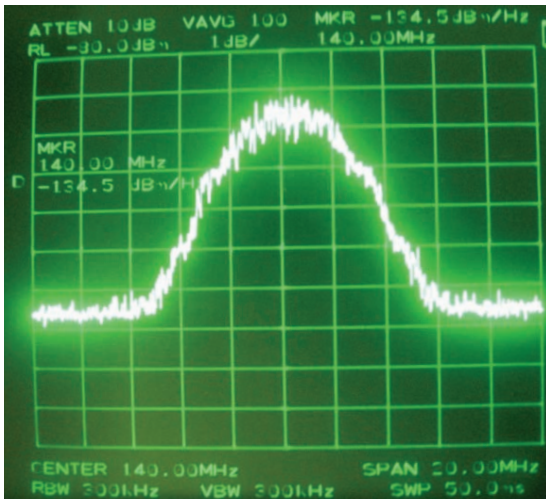

Figure 3: Analog Front-End noise spectrum. Vertical and horizontal scales are 1 dB/div and 2 MHz/div respectively.

Online Calibration

The BPM processor continuously self-calibrates between beam pulses. The AFE transmits short (~260 ns) tone-bursts at the processor frequency alternately on one of the striplines on each of the BPM axes (typically the Y^+ and the X^- striplines). The ratio of amplitudes of the signals detected on the two adjacent striplines calibrates the gain ratio of these processor channels and their associated cables. The calibration tone drive amplifier can put out as much as 2 Watts, adjustable via programmable attenuator down to 2 mW.

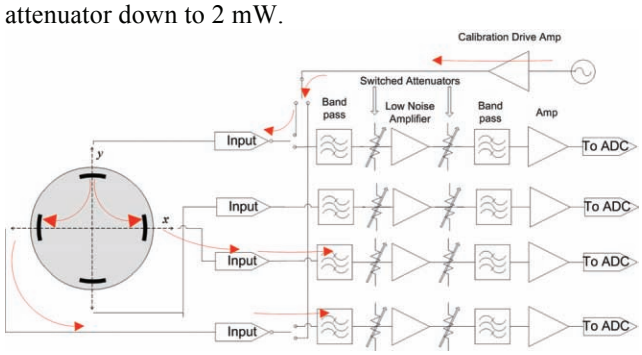

Figure 4: Calibration scheme block diagram.

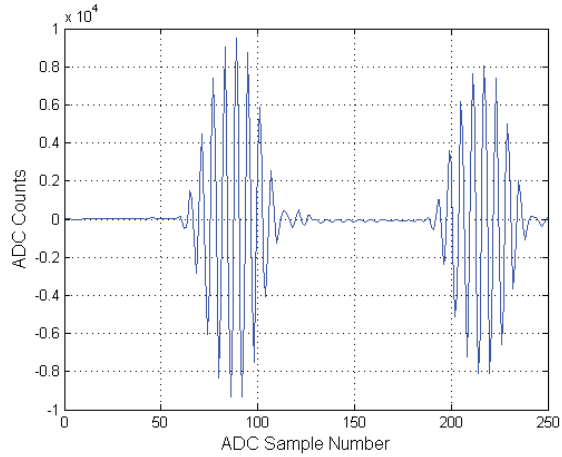

Figure 5: Calibrator tone burst detected by left and right striplines.

Output Limiter

An unwelcome feature that comes with high dynamic range amplifiers, used in the signal channels to achieve high linearity, is that the potential output power levels can overdrive the ADC inputs to damage. The AFE board therefore contains fast comparators at its channel outputs that shut down the outputs as an overvoltage is approached. The limited bandwidth of the signal channel allows a reasonably fast comparator to prevent transient overvoltages.

Control

A Xilinx FPGA controls programmable attenuators, generates the timing sequences for the calibrator and limiter, and communicates with the processor on the ADC board via a QSPI (queued serial peripheral interface) link.

ADC BOARD

The digitizer board is the Phase and Amplitude Detector[1] (PAD) board developed for LCLS low-level RF control carrying four Linear Technology Corp. LTC2208 16-bit ADCs capable of sampling at 130 MHz. We expect close to 12.4 effective bits on a 140 MHz signal according to specifications. The ADCs are clocked at 120 MHz. Since the input signal frequency is higher than the sampling frequency, the ADC under-samples the data, aliasing the 140 MHz signal to 20 MHz, while the 200 MHz signal are aliased to 40 MHz.

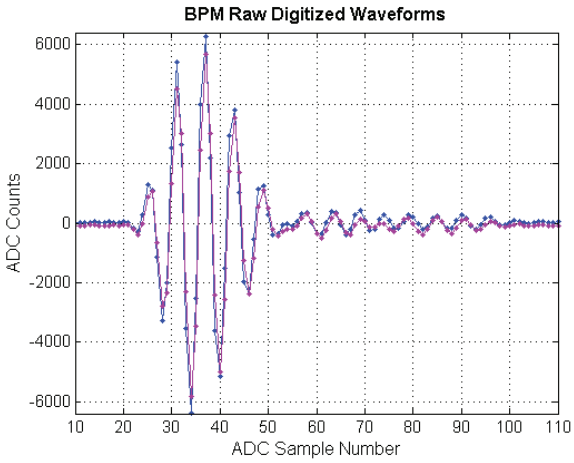

Figure 6: Beam signal digitized at 120 MHz.

A processor on the PAD board acquires BPM waveform data from the ADCs and transmits it over a dedicated network link to a local BPM IOC. A separate network links the PAD processor to the accelerator network for configuration and control.[2]

RESOLUTION

We evaluate BPM resolution in the presence of beam jitter which is much larger than the resolution by acquiring position synchronously over a large number of beam pulses from many BPMs. Then we use a least-squares linear fit to the shot-by-shot beam position in each BPM as a linear function of the positions measured in all the others. Using 17 of the LCLS stripline BPMs in the linac over 120 consecutive beam pulses we find an average position resolution of 4.8 microns rms at a bunch charge of 220 pC. Figure 7 shows pulse-by-pulse measurement of beam position at one particular BPM, the X and Y positions measured there versus that predicted by the best-fit linear combination of 16 other BPMs, and the X and Y positions with the beam jitter predicted by the other BPMs subtracted. The scatter of the measured position after beam jitter subtraction is taken as an estimate of BPM resolution.

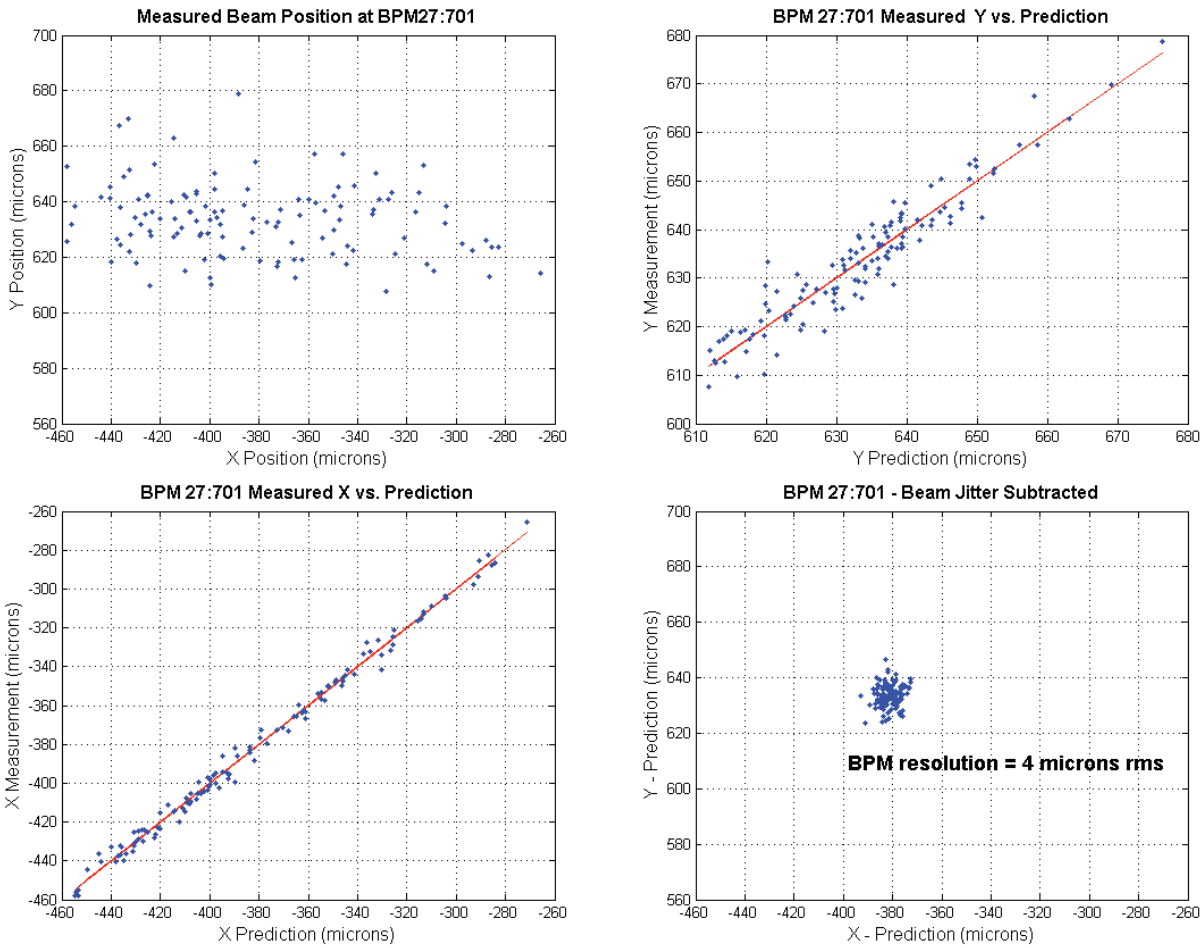

Figure 7: (a) X,Y position measured at BPM 27:701, (b) Measured Y versus Y predicted here from the other 16 BPMs, (c) Measured X versus X predicted here from the other BPMs, and (d) X ,Y with the beam jitter removed.

SUMMARY

Twenty-two prototype BPM processors were installed in the linac and commissioned in 2007. The prototypes design was revised, improved, and 53 production modules assembled and tested in February through April of 2008. The first 14 of these have been installed and commissioned with beam, demonstrating 5 micron rms resolution at 200 pC as required. The remaining BPMs will be installed this summer.

REFERENCES

[1] D. Kotturi, R. Akre, T. Straumann, "130-MHz, 16-Bit Four-Channel Digitizer", ICALEPCS'07, Knoxville, October 2007.

[2] T. Straumann, et al, "LCLS Beam-Position Monitor Data Acquisition System", ICALEPCS'07, Knoxville, October 2007.

MEASUREMENTS ON LIBERA ELECTRON AND LIBERA BRILLIANCE BPM ELECTRONICS

A. Olmos, F. Pérez, ALBA-CELLS, Bellaterra, Barcelona, Spain

Abstract

ALBA synchrotron light source is a 3rd generation machine being constructed by the CELLS consortium near Barcelona, Spain. Orbit correction system will be based on the Libera Brilliance electronics and its goal will be the stabilization of the beam at the submicron level. Important parameters to reach such corrections have been measured and are reported in this document, like electronics resolution, beam current dependence, latency (among others). Comparison of the two different Libera products offered by the company (Libera Electron and Libera Brilliance) is also reported in order to analyze the benefits of choosing Libera Brilliance.

INTRODUCTION

Synchrotron machines constructed nowadays require beam position stability in the order of hundreds of nanometres. Such stabilities can only be accomplished with a dedicated system, usually known as Fast Orbit Feedback System (FOFB). The FOFB system is in charge of the following:

- Measurement the beam position drifts around the machine.
- Transmission of all the position measurements to the computational unit/s.
- Calculation of the correction values and actuation on the beam through corrector magnets.

ALBA will use the Libera Brilliance electronics, developed by Instrumentation Technologies company, to perform the measurements and the transmission of the beam position [1]. Brilliance are an upgraded version of the already existing Libera Electron units. A vast laboratory test has been done on each of the units in order to check their specs and prove the Brilliance improvements vs. the Electron.

LABORATORY MEASUREMENTS

Here are reported some of the results obtained during the Site Acceptance Test [2] (SAT) of the electronics. Until now, a total of 31 Electron units and 66 Brilliance ones have been tested.

Laboratory Setup

Units were tested one by one using the test setup showed in Figure 1. A remote industrial PC sets the Libera parameters and retrieves the data through a Matlab based GUI [3] (both slow rate and fast rate data). An RF generator simulates the electron beam, while two function generators are used to generate the needed clock signals and events. A small modification of that setup allows us to perform latency measurements using the Libera interlock output.

We report here the measurements done on the Brilliance units. Electron units results are showed on the comparison chapter.

Electronics Resolution

Vertical RMS resolution of 8 Libera units is showed on Figure 2. As seen, the needed sub-micron resolution is achieved on the electronics down to ~5.5mA beam current (-45dBm Libera input), on a 10kHz measurement rate.

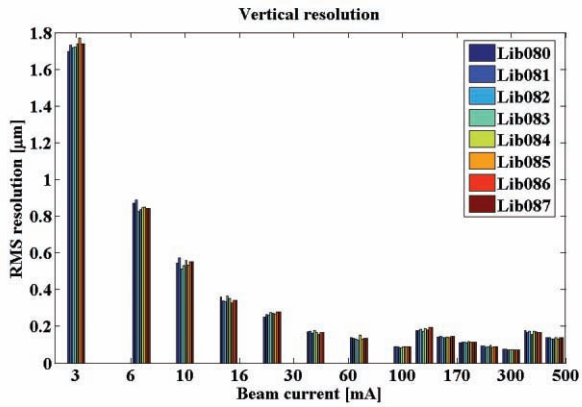

Figure 2: Vertical resolution of 8 Liberas @ 10kHz rate

Resolution is improved a factor 10 for slower rates, i.e. at 10Hz rate for control systems acquisitions.

Beam Current Dependence

Beam Current Dependence (BCD) of the position readings on the stored beam has been improved on the Libera Brilliance electronics (Figure 3).

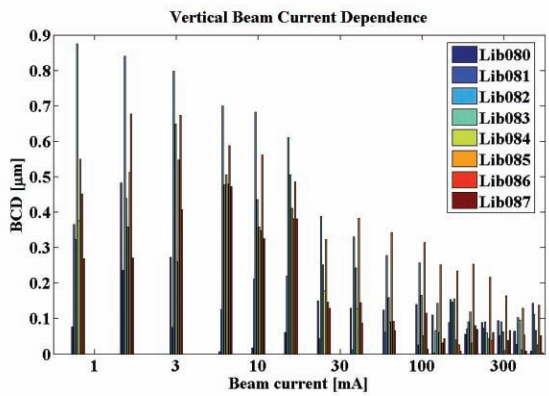

Figure 3: Vertical BCD of 8 Liberas @ 10kHz rate

Position measurement dependence, or independence, remains below 1µm even at very low beam currents. Once ALBA will be running on Top-Up mode, the BPM

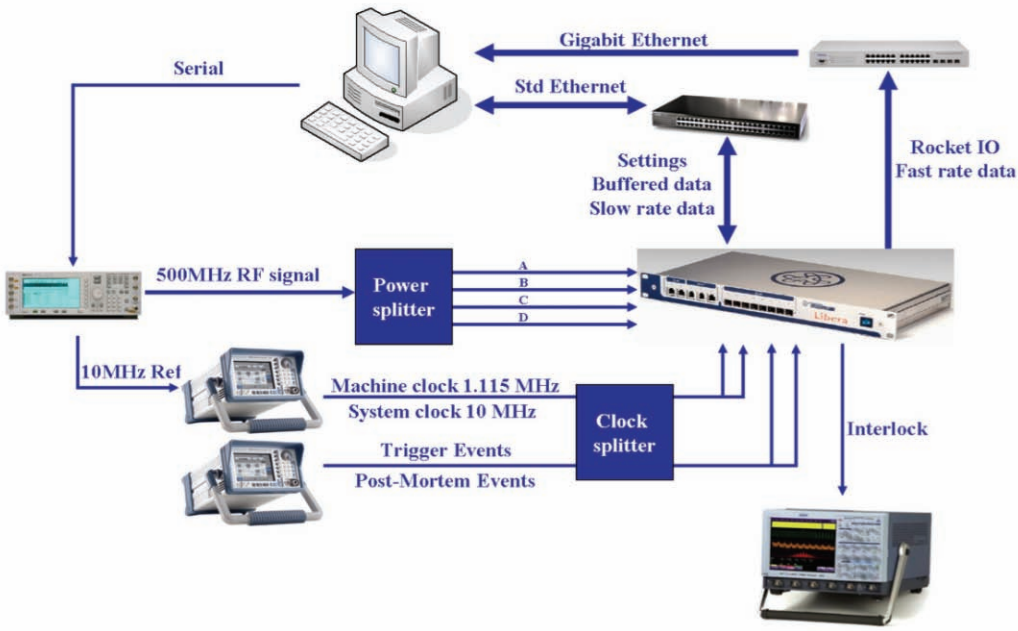

Figure 1: Laboratory test setup for Liberas measurements

readout electronics contribution to the BCD will be negligible. After testing all the 161 Libera units that ALBA has purchased, a sorting of best quality Liberas will be done for those machine places where a better BCD and/or resolution are needed.

Synchronization Stability

Global acquisitions of position reading around the ring are synchronized over the revolution clock (1.1153MHz for ALBA storage ring). Each Libera accomplishes the synchronization using an internal phase locked loop (PLL) locked to the revolution clock. Figure 4 shows its stability during 24 hours.

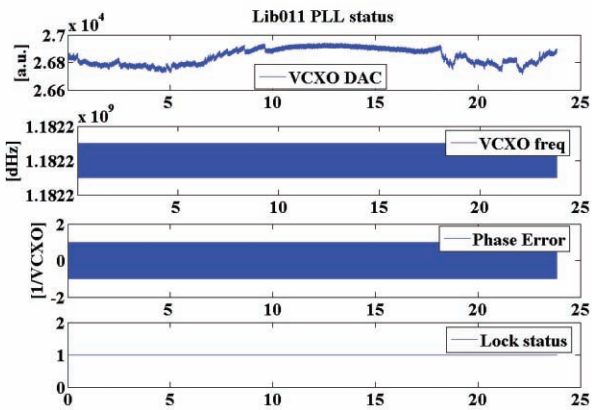

Figure 4: PLL stability during 24 hours.

The PLL remains "locked" during the whole time, as well as the phase error never gets out of the +1/-1 stable region. It can be recognized the night period when the temperature in the lab was more stable and therefore the DAC voltage driving the oscillator didn't change much.

Latency Measurements

Latency is a key parameter when implementing global beam correction systems, as it determines how fast we can run the FOFB system. The BPM electronics turned out to be one of the main contributors to the overall latency on the FOFB.

Interlock output of the Libera was used to measure the latency. Figure 5 illustrates the test setup.

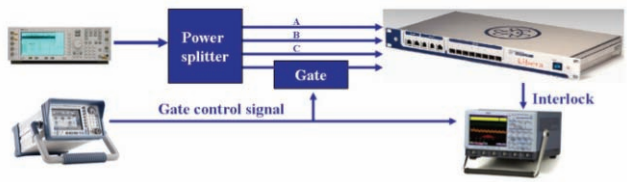

Figure 5: Test setup for latency measurements

A steep change on the Libera inputs moves the position readings out of thresholds, triggering the interlock output. Time difference between input change and interlock trigger determines the latency value.

Table 1: Latency for different interlock thresholds on an offset corrected beam

Threshold [mm]	Min Latency [µs]	Max Latency [µs]	Δ [µs]
700	132	255	123
800	153	260	107
1000	173	268	95
1200	181	297	116
1500	205	308	103

Difference around 100µs between min and max latency results are inherent to the interlock source. Interlock signal is triggered based on 10kHz fast data positions.

ELECTRON VS. BRILLIANCE

One objective of the reported study is the analysis of Libera Brilliance benefits versus Libera Electron. The hardware difference between them is mainly on the analog board, which has improved its Analog to Digital Converters (ADC) from 12 to 16 bits. There's in principle no software difference, which make both units compatible from the controls point of view.

Electronics Resolution

Figure 6 shows a comparison of the vertical resolution between the units (very similar results are obtained for the horizontal).

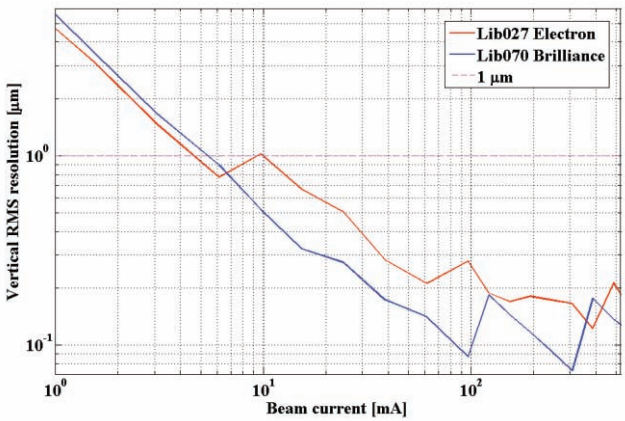

Figure 6: Comparison of the vertical RMS resolution

A non substantial resolution improvement from the Electron has been achieved on Brilliance; nevertheless both units have excellent results.

Beam Current Dependence

Highest improvement on Brilliance is on the BCD (Figure 7). The higher dynamic range of the ADCs allows them to stay working in a more linear area, reducing the position dependence function on the electronics input signal level.

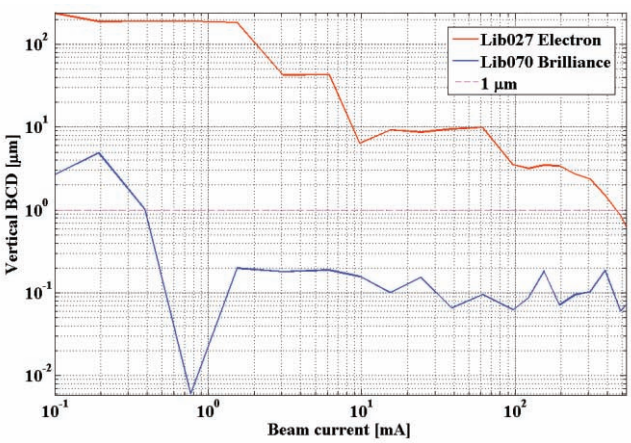

Figure 7: Comparison of the vertical BCD

Note that with Electron the BCD is always above the micrometer level (for ALBA, the maximum current is 400mA) while the Brilliance unit is almost independent of the beam current (based on a simulation of 100% filling).

Filling Pattern Dependence

Since we have introduced the filling pattern issue, Figure 8 shows the comparison between the two units function of different patterns.

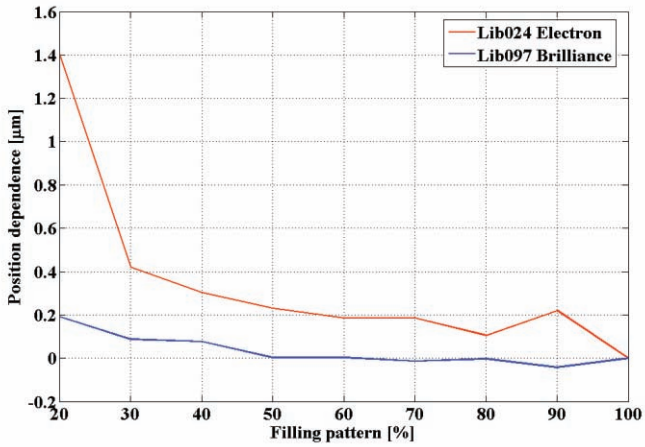

Figure 8: Comparison of filling pattern dependence

Electron results were already quite good and they have been improved a bit on the Brilliance units.

CONCLUSIONS

Laboratory characterization of all the BPM electronics showed that the Brilliance units should fulfill the requirement of a 3rd generation light source in terms of resolution, stability and beam dependence.

Changes on the analog board of the Libera Electron to make it Brilliance improve the long term parameters, easing the electronics calibration when changing the current or the filling patterns of the machine.

REFERENCES

[1] A. Olmos, "ALBA Fast orbit feedback topology", CELLS internal document AAD-SRDIFOFB-A-0001, February 2008

[2] A. Olmos, "Liberas 2nd batch SAT", CELLS internal document AAD-SRDILIBERA-A-0002, March 2008

[3] www.cells.es/Divisions/Accelerators/RF_Diagnostics/Diagnostics/OrbitPosition/eBPM_Readouts/MatlabLiberasGUI/

COMPARISONS OF SELECTED COTS AND CUSTOM HARDWARE FOR BEAM POSITION AND PHASE MEASUREMENTS FOR LANSCE*

J. F. Power, J.D. Gilpatrick and D. Martinez, LANL, Los Alamos, NM 87545, U.S.A.

Abstract

Beam Position and Phase Monitors (BPPMs) planned for the LANSCE diagnostics refurbishment will be required to measure beam position and phase of the 201.25-MHz bunched beam in the proton linac. One method to do this is direct down conversion to in-phase and quadrature-phase data of the BPPM signals using either commercial digitizers or custom designed hardware. We are evaluating selected hardware for systems with emphasis on commercial-off-the-shelf COTS hardware to the extent practical. Approximate system requirements include a beam current range of 27 db, position resolution of 0.25% of beam aperture and relative phase measurement with 0.25 degree resolution at 201.25 MHz [1]. We present our results to date on two approaches, ZTEC Instruments ZT-410 digitizers, and a custom four-channel ADC analog front end board combined with National Instruments, Inc. digital I/O board. These two systems use PCI cards in a standard PC running Windows® XP. Our primary points of comparison include measured position resolution, phase resolution, phase linearity, minimum cycle rate and approximate cost for these portions of a BPPM system.

INTRODUCTION

As in our previous designs, such as those for the Spallation Neutron Source, we are planning to add phase measuring BPPMs to the LANSCE linac [2-4]. Rather than analog downconversion, we plan to use direct down conversion, and we want to use COTS hardware where practical.

In this paper we compare the performance of a pair of ZTEC Instruments ZT-410 oscilloscope cards (two channel, 250 MHz BW, 14-bit, 500 MSPS PCI) with a custom designed (four-channel 700 MHz, 16-bit, 130 MSPS) analog front end (AFE) mated to a pair of National Instruments NI PCI-6542 digital I/O cards. Each of these solutions represents $11k-$12k in hardware costs.

Both systems were evaluated using the same PC running Windows XP and a BPPM application written in LabVIEW®. The BPPM application contains all of the functionality needed for correctly calibrating, calculating and displaying the beam position and phase. Additional gain and analog calibration circuits will be required on the real system and these will be a custom design.

TEST CONFIGURATIONS

The computer PCI cards and their interfaces are shown in Figure 1. The ZTEC cards have BNC inputs that we use for top, bottom, right and left signals. The clock and trigger signals are routed in parallel to each card in both the ZTEC and the NI system

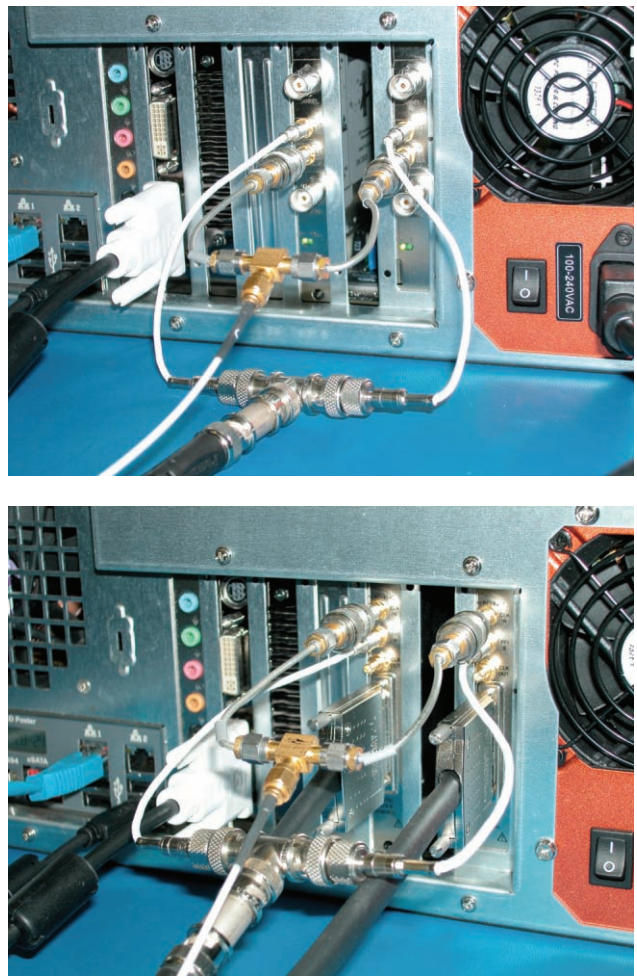

Figure 1: BPPM computer interfaces showing the ZTEC cards (top) and the NI/custom AFE (bottom).

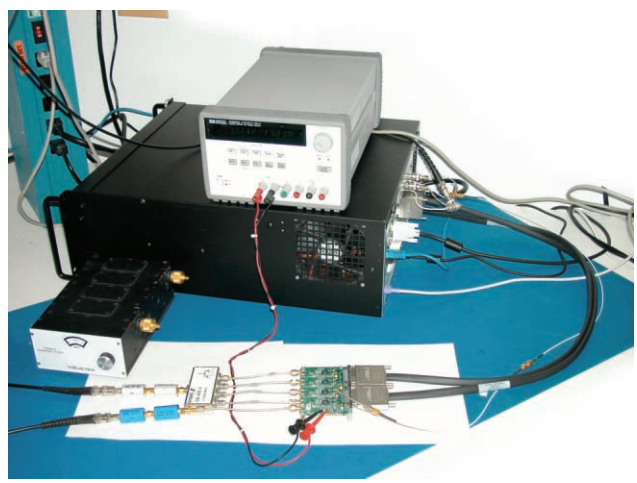

Figure 2: The custom AFE connected to the NI digital I/O cards. The filters and splitter are used to test both systems.

*Work supported by the U.S. Dept. of Energy

The custom AFE and RF cables can be seen in Figures 2 and 3. Both systems are driven from a three-channel IFR 2026 RF generator which provides coherent sampling clocks and RF drive to the 4-way splitter with relatively low phase noise.

The ZTEC cards are clocked at 230 MHz, which is internally divided by each card to 115 MHz. The custom AFE is clocked at 35 MHz. These frequencies are correct for I/Q sampling of 201.25 MHz. Unfortunately the ZTEC cards cannot run as low as 35 MHz (after division) and the NI cards cannot be clocked higher than 100 MHz, therefore the systems must be compared as we would probably use them and not under exactly the same clocking rate. The NI cards could be clocked at other frequencies higher than 35 MHz and less than 100 MHz, but we would have had to build a custom synthesizer to generate the clock.

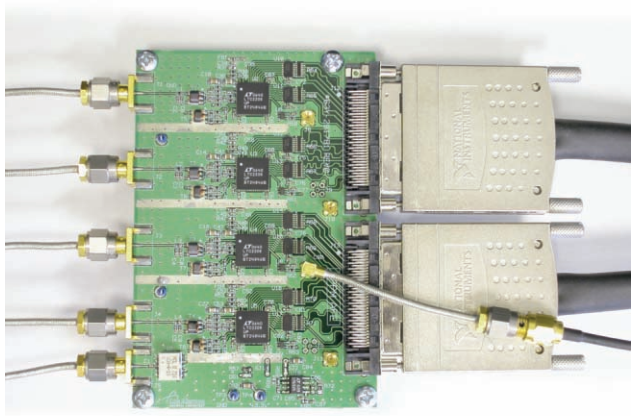

Figure 3: The custom four-channel AFE using Linear Technology LTC2208 ADCs. RF inputs are on the left and connections to the PCI cards are on the right.

DATA TAKING AND ANALYSIS

The metrics we use for comparison are system update rate, position resolution (relative to a 44.5-mm aperture LANSCE BPM), phase resolution and phase accuracy.

A typical screen shot of one tab of the BPPM test application is shown in figure 4. Here we see the raw magnitude and phase data for the four channels, after I/Q processing, but before gain and phase normalization on the NI/custom system.

Maximum Update Rate

While we don't need the BPPM measurements to update at the maximum 120 Hz machine rate, we want the rate to be as high as practical for human machine tuning procedures. For LANSCE operation we need to take beam data for up to1 ms.

The maximum cycle rate for the ZTEC system was about 1.3 Hz with a 1-µs averaging window and 1.39 Hz with 5-µs or longer averaging windows. The NI/custom AFE system ran at 12.8 Hz and 25.4 Hz respectively. The averaging reduces the number of final position and phase calculations performed by up to a factor of 1/t, where t is the averaging time, so the rates increase for lower measurement bandwidths.

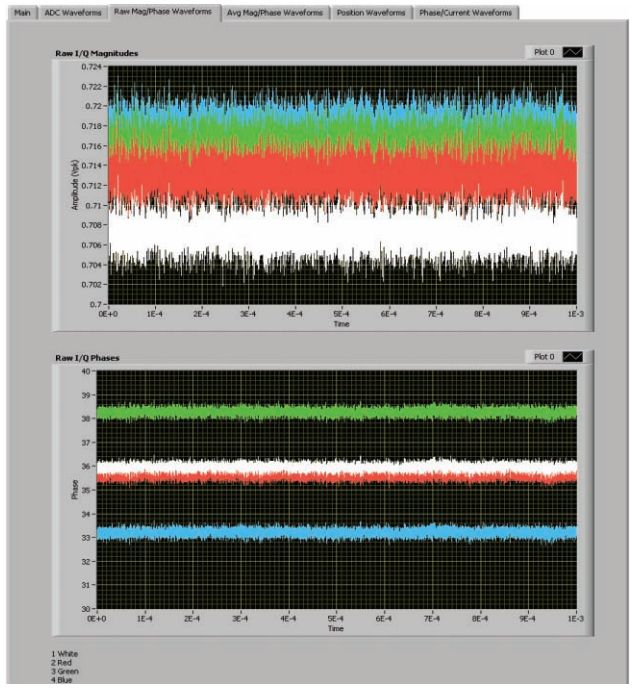

Figure 4: An example LabVIEW application screen showing the four channels of data before gain and phase normalization for the NI/custom AFE system.

Position and Phase Resolution

The LANSCE machine primarily operates at about 1 mA of peak beam current and can run with up to near 20 mA in some cases. Lower peak currents are not required, so the beam current range of interest about 26 dB.

We have selected a 6-dB headroom before ADC overflow, and we assume the centered-beam-amplitude to be 15 dB below that, or -21 dBFS for the ADCs. For these tests we define -21 dBFS as 20 mA, and -41 dBFS as 1 mA of centered beam respectively. We measured the position and phase resolution for each system at these two levels and for various averaging times of from 1 to 100 µs. The resulting data is presented in Figure. 5.

The NI/custom AFE system has no gain adjustment, so there were no changes made to the setup between the 1 and 20 mA beam cases. The ADC is set to 1.5 Vpk-pk as full scale, or 7.5 dBm for a 50-ohm differential input impedance. The ZTEC oscilloscope has multiple gain ranges of from 0.1 to 10 Vpk-pk, so we used the 2 Vpk-pk setting for the 20 mA beam case and the 0.1 Vpk-pk case for the 1 mA beam case.

The results of the resolution measurements show that either system can meet our requirements which are 22 µm-rms position resolution for the 44.5 mm pickups and 0.25 degrees-rms of phase resolution. Note that either system requires at least 10 µs of averaging to meet the position resolution specification, which is acceptable for our requirements.

Phase Linearity

The phase linearity of the two systems was measured under the larger beam current condition, as harmonic distortion is largest in this case. The linearity data is shown in the upper graph in Figure 5, where the ZTEC data is in blue. Both systems show excellent linearity; much better than ±0.5 degrees. Not surprisingly, the NI/custom AFE shows less distortion as there are no amplifiers on the front end of the ADCs. In reality, gain will be necessary for this system, so careful selection of amplifier harmonic distortion will be required.

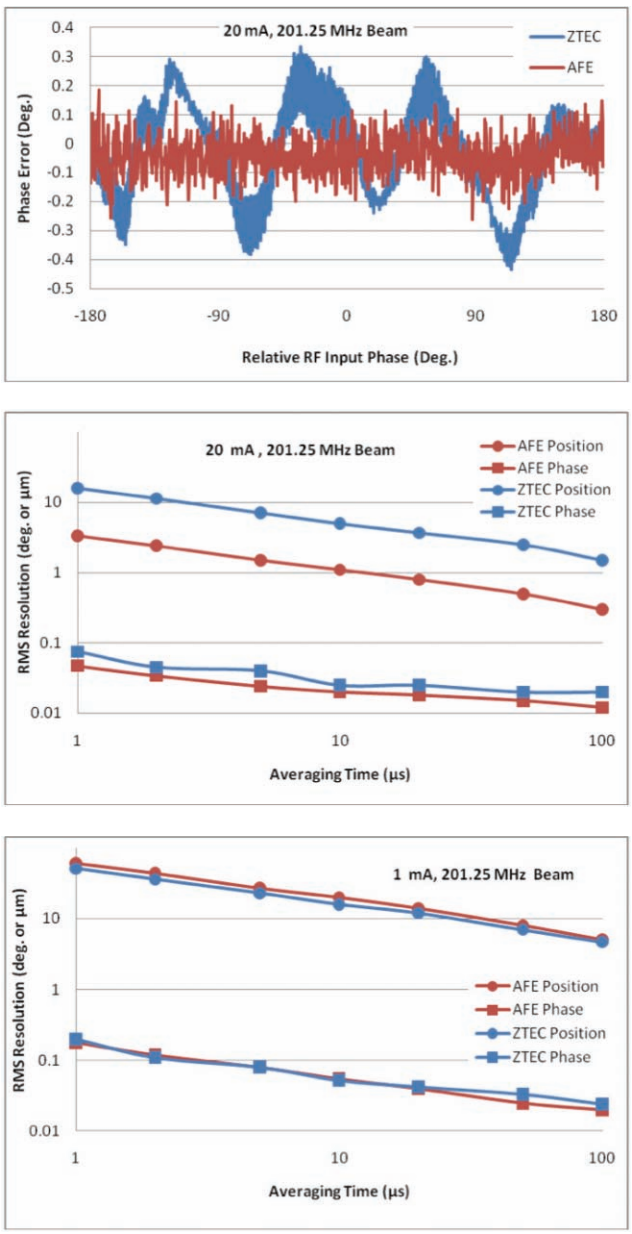

Figure 5: Comparison of phase linearity for 20 mA beam (top), RMS position and phase resolution for 20 mA beam (middle) and RMS position and phase resolution for 1 mA beam (lower) for the ZTEC and custom AFE systems.

Other Observations

There are differences between the two systems that don't directly relate to our requirements that were observed and worth mentioning.

The ZTEC sampling clock is internally divide by two, which requires more care in keeping the two independent digitizer cards synchronized at a known phase. Choices of sampling frequencies are also limited to those above 40 MHz, requiring more data to be transferred over the PCI bus, which may not be done as a DMA transfer. The NI PCI-6542 does not seem to work at sample rates much below 20 MHz in addition to being limited to 100 MHz.

Programmable gain of the ZTEC card is nice, and in fact is required to be used to meet the resolution requirements. Leaving the cards at the same gain settings for both current ranges leads to poor resolution performance at the lower current condition.

The ZTEC cards have an analog bandwidth of 250 MHz while the custom AFE has an analog bandwidth beyond 700 MHz. It is in fact very usable at 201.25, 402.5 and 805 MHz, all of the cavity frequencies used at LANSCE. Even at 805 MHz, this system would meet all of our requirements at averaging times of 20 µs or greater.

The worst case channel-to-channel isolation of the ZTEC cards is about 41 dB at 201.25 MHz. The custom AFE has over 80 dB of isolation at 805 MHz and below.

CONCLUSION

Both of these two prototype systems meet most our basic requirements for beam position and phase measurement. They are of similar cost and performance. Based on the superior performance of the custom AFE and its faster cycle cycling rate, it is our preferred choice between these two. We hope to evaluate additional systems before a final selection is made.

REFERENCES

[1] J. Douglas Gilpatrick, "Proposed Beam Position and Phase Measurements for the LANSCE Linac," DIPAC '07, Venice, May 2007, pending publication, http://www.jacow.org.

[2] J. Power, J. O'Hara, S. Kurennoy, M. Plum, M. Stettler, "Beam Position Monitor for the SNS Linac," PAC'01, Chicago, June 2001, p. 1375, http://www.jacow.org.

[3] J. Power, L. Day, M. Plum, M. Stettler, "Beam Position Monitor Systems for the SNS Linac," PAC'03, Portland, May 2003, p. 2429, http://www.jacow.org.

[4] John F. Power, Mathew W. Stettler, LANL, Alexander V. Aleksandrov, Saeed Assadi, Willem Blockland, Paul Chu, Craig Deibele, John Galambos, Cary D. Long, James Pogge, Anthony Webster, ORNL, Linac '06, Oak Ridge, August 2006, p. 249, http://www.jacow.org.

HIGH RESOLUTION UPGRADE OF THE ATF DAMPING RING BPM SYSTEM*

N. Terunuma, J. Urakawa, KEK, Tsukuba, Japan
J. Frisch, J. May, D. McCormick, J. Nelson, A. Seryi,
T. Smith, M. Woodley, SLAC, Menlo Park, CA 94025, U.S.A.
C. Briegel, R. Dysert, N. Eddy, B. Fellenz, E. Gianfelice, W. Haynes, D. Nicklaus
P. Prieto#, R. Rechenmacher, D. Slimmer, D. Voy, M. Wendt, Fermilab, Batavia, IL 60510, U.S.A.

Abstract

A *beam position monitor* (BPM) upgrade at the KEK *Accelerator Test Facility* (ATF) damping ring has been accomplished in its first stage, carried out by a KEK/FNAL/SLAC collaboration under the umbrella of the global ILC R&D effort. The upgrade consists of a high resolution, high reproducibility read-out system, based on analog and digital donwconversion techniques, digital signal processing, and also tests a new automatic gain error correction schema. The technical concept and realization, as well as preliminary results of beam studies are presented.

MOTIVATION

To achieve a high luminosity in the next generation, linear acceleration-based e^+/e^- *high energy physics* (HEP) collider, low-emittance beam generation and preservation are mandatory. In frame of the *International Linear Collider* (ILC) R&D program, the goal of the beam studies at the KEK ATF damping ring[1] is to generate and extract a beam with an ultra-low vertical emittance < 2 pm [2]. This requires various optimization methods to steer the beam along an optimum ("golden") orbit with minimum disturbance of non-linear field effects. A high resolution BPM system is one of the important tools to achieve this goal, which requires a resolution in the 100 nm range in a "narrowband" mode.

The "ATF DR BPM Upgrade Project" is a KEK/SLAC/Fermilab collaboration that addresses the problem by installing and commissioning of new hard-, firm- and software for the signal processing to read-out the button type BPM pickups in the ATF damping ring:

- 714MHz-to-15MHz downmix and calibration module (located in the ATF tunnel).
- VME-based digital signal processing and timing electronics, based on the commercial *Echotek* digital receiver.
- Various FPGA-firmware, control and diagnostics drivers and software (C++, LabVIEW, VxWorks, Linux) and an EPICS interface to the ATF control system.

As proof of principle, 20 (out of 96) installed button BPMs are currently equipped with the new read-out system. To minimize the expenses, the experiment is based on available spare units, rather than implementing the latest generation of digital signal processing technology.

*This work supported by a high energy physics research program of Japan-USA cooperation, and by the Fermi National Accelerator laboratory, operated by Fermi Research Alliance LLC, under contract No. DE-AC02-07CH11359 with the US Department of Energy.
#prieto@fnal.gov

THE ATF DAMPING RING

Figure 1 shows the KEK Accelerator Test Facility with S-Band linac, damping ring and extraction line, as of year 2008. Indicated is the staged upgrade process of BPM stations.

Table 1: ATD DR machine and beam parameters

beam energy E	=	1.28 GeV
beam intensity, single bunch	≈	~1.6 nC ≡ 10^{10} e^- (≡ I_{bunch} ≈ 3.46 mA)
beam intensity, multibunch (20)	≈	~22.4 nC ≡ 20 x 0.7 10^{10} e^- (≡ I_{beam} ≈ 48.5 mA)
f_{RF}	=	714 MHz (≡ t_{RF} ≈ 1.4 ns)
f_{rev}	=	f_{RF}/330 ≈ 2.16 MHz (≡ t_{rev} ≈ 462 ns)
bunch spacing t_{bunch}	=	2/ f_{RF} ≈ 2.8 ns
batch spacing	=	t_{rev}/3 = 154 ns
repetition freq. f_{rep}	=	1.56 Hz (≡ t_{rep} = 640 ms)
beam time t_{beam}	=	460.41 ms (≡ 996170 turns)
vert. damping time τ	≈	30 ms
hor. betaron tune (typ.)	≈	15.204 (≡ f_h ≈ 441 kHz)
vert. betaron tune (typ.)	≈	8.462 (≡ f_v ≈ 1 MHz)
synchrotron tune	≈	0.0045 (≡ f_s = 9.7 kHz)

Table 1 lists some relevant machine and beam parameters of the ATF damping ring. In standard operation a single bunch in injected on axes from the S-Band linac. After ~200 ms all injection oscillations are fully damped, and the beam stays for another 400 ms in the ring, before being extracted. Optional multi-batch/multi-bunch operation can be set up on a cycle-by-cycle basis (no extraction), with up to three equally spaced batches, each containing 1…20 bunches, spaced by 2.8 ns.

THE ATF DR BPM UPGRADE

A 10-20 μm RMS resolution, measured on the currently installed BPM read-out system, does not meet the

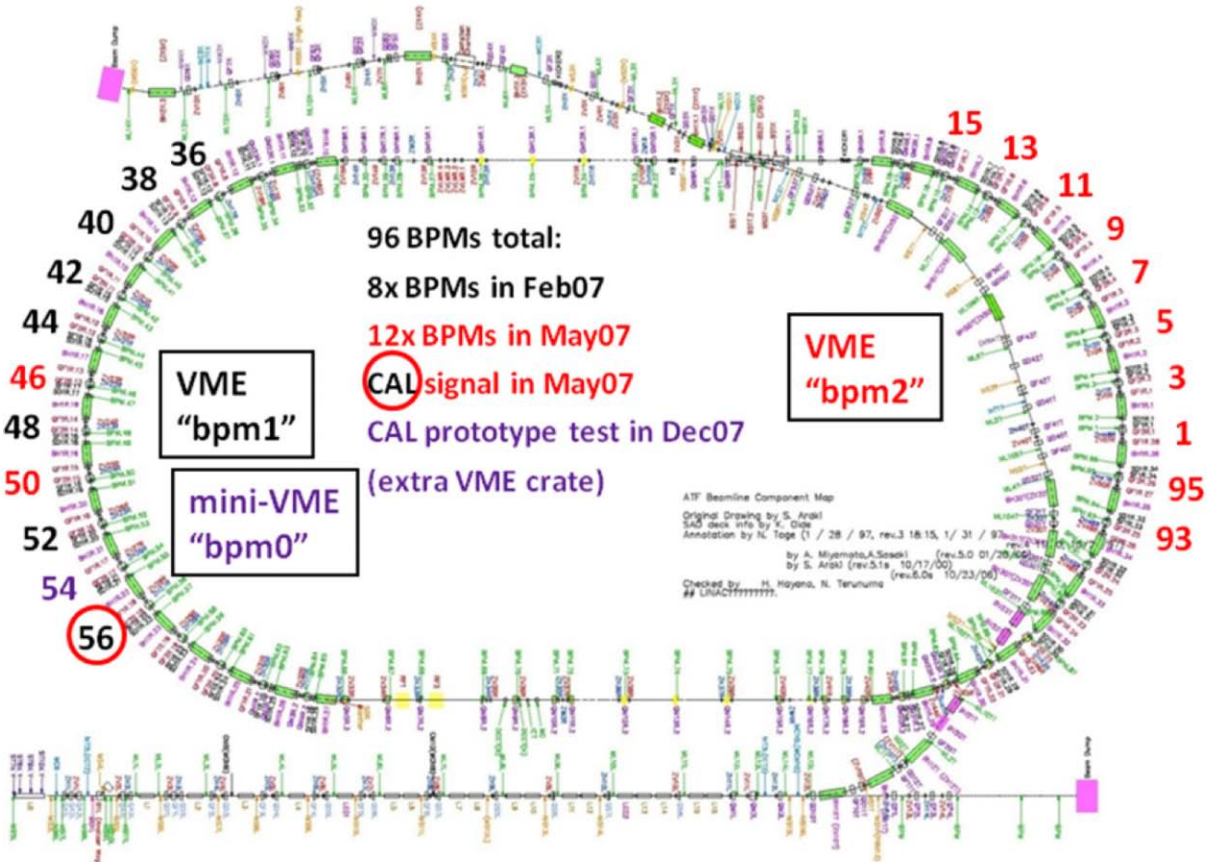

Figure 1: Layout of the ATF damping ring, indicating 20 upgraded BPM stations in the arcs.

requirements for the corrections of non-linear effects in the ATF damping ring, required to achieve the ultimate low vertical beam emittance. A first initiative to upgrade the BPM read-out system was started already in 2006, based on analog downmix modules and commercial *Echotek* digital receivers, achieving 1-2 µm RMS resolution, followed by the 2007/2008 collaboration to the current upgrade status of 20 BPMs:

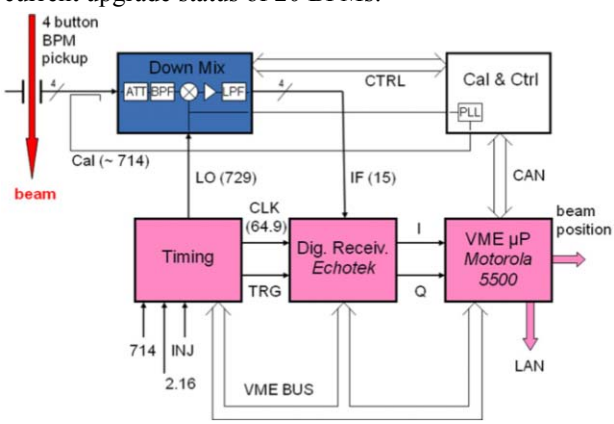

Figure 2: Upgraded BPM hardware.

Figure 2 gives an overview of the new BPM read-out hardware, shown for a single button-style pickup. Each of the four button-style BPM electrode signals are processed separately up to the VME CPU, where the actual position normalization and calibration takes place. All analog hardware, i.e. downmix modules and calibration signal generation (under development), is located in the tunnel:

- The **downmix module** receives the four signals from the button-style pickup, filters the 714 MHz frequency content (BW ≈ 10 MHz), and down-converts this signal to a 15.1 MHz output signal. The analog signal processing includes low-noise amplifiers in RF and IF sections with switchable gain. A 729 MHz local oscillator signal (LO) generated in the VME timing module is distributed in the tunnel to every donwmix modules.
- A **calibration/test signal** is currently in an early development stage. The LO signal is split off and used to locally generate a phase locked test signal of ~714 MHz, to be used to observe the long term stability of each analog channel. The signal is close, but not at the 714 MHz readout frequency, but still in the passband of the system. It is injected through a 10 dB directional coupler and couples through the pickup electrodes.

All digital hardware is located in two VME crates in the corresponding west and east arc huts, each holds:

- A set of 5 ***Echotek* digital receiver** modules, each has 8 channels to read-out two BPMs. The Echotek digitizes the 15.1 MHz analog signal at a rate of 69.236 MS/s and downconverts them to baseband. Data filtering and decimation is processed depending on the requested operation mode, e.g. wideband turn-

by-turn mode, narrowband mode. The in-phase and quadrature BPM data is stored into the FIFO memory and DMA transferred to the VME CPU controller board.

- A **timing module** generates all required trigger, clock and RF signals, with input signals f_{RF} = 714 MHz, f_{rev} = 2.1636 MHz and the 640 ms injection trigger. Output signals are f_{LO} = 729.15 MHz, f_{CKL} = 69.236 MHz (both phase-locked to f_{RF}), and an injection trigger delay able in steps of 2.8 ns.
- A ***Motorola* 5500 CPU controller** board for data collection and post-processing.

Button-style BPM Pickup

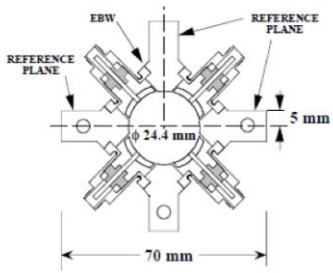

Figure 3: ATF damping ring button BPM.

The ATF damping ring is equipped with a total of 96 button-style BPM pickup stations. The button electrodes are mounted under 45^0 rotations into the beam pipe of circular cross-section (24.4 mm diameter), to avoid the direct synchrotron light (see Figure 3). The 12 mm diameter button electrodes span ~15.7 % (equiv. 56.4^0), which results in an electrical beam-to-electrode coupling of ~15.9 % for a centered beam.

The highpass-like transfer impedance of the button electrode can be approximated:

$$|Z_b(f)| = \phi R_0 \left(\frac{\omega_1}{\omega_2}\right) \frac{2\pi f/\omega_1}{\sqrt{1+(2\pi f/\omega_1)^2}} \qquad (1)$$

with: $\omega_1 = \frac{1}{R_0 C_b}$, $\omega_2 = \frac{c_0}{2r}$, $\phi = \frac{r}{4b}$

$C_b \approx 5$ pF (button capacitance),

$R_0 = 50\ \Omega$ (load impedance),

$b = 12.2$ mm (beam pipe radius),

$r = 6$ mm (button radius),

$c_0 = 2.998\times10^8$ m/s (speed of light).

which results in $Z_b \approx 0.735\ \Omega$ at the operating frequency f_{in}=714 MHz.

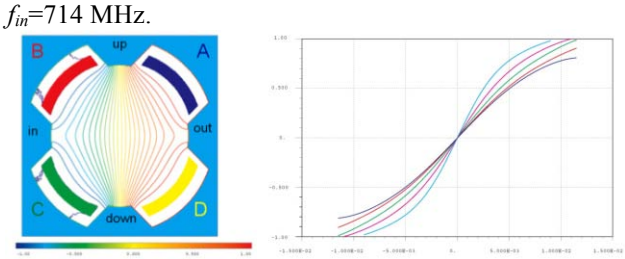

Figure 4: Button BPM characteristics (horizontal).

The position characteristic of the ATF DR button BPM pickup was analyzed numerically by solving the Laplace equation of the pickup cross-section (two-dimensional). Figure 4 (left) shows a corresponding plot of equipotential lines in the form

$$\phi_{hor} = \frac{(\phi_A + \phi_D) - (\phi_B + \phi_C)}{\sum \phi} \qquad (2)$$

Figure 4 (right) shows a parametric plot of the horizontal position characteristic for different vertical displacements of the beam. A 5th order 1D polynomial fit of this numerical result $\mathit{Ø}_{hor}(y=0)$, resp. $\mathit{Ø}_{vert}(x=0)$ is implemented in the read-out software for calibration of the BPM pickup signals:

$$Pos[mm] = 9.35\phi + 1.00\phi^3 + 7.79\phi^5 \qquad (3)$$

Analog Signal Processing

The analog bandwidth and sampling rate of the analog-to-digital converter (ADC), as well as other hardware specifications, limit the uses of the digital signal processing in the *Echotek* digital receiver to signal frequencies ~40 MHz. The transfer impedance of the button electrodes is poor at frequencies < 100 MHz, thus a higher signal frequency has to be used to ensure a good S/N-ratio. For this reason an analog downconverter, including filters and gain-stages, is inserted in front of the Echotek digital receiver for signal conditioning. Figure 5 shows a simplified block diagram of one (of four) downmix channel. The unit is located in the tunnel close to each BPM pickup station to minimize cable insertion losses. An improved downmix prototype offers a remote controlled step-attenuator between input BPF and LNA, as well as other remote functionality.

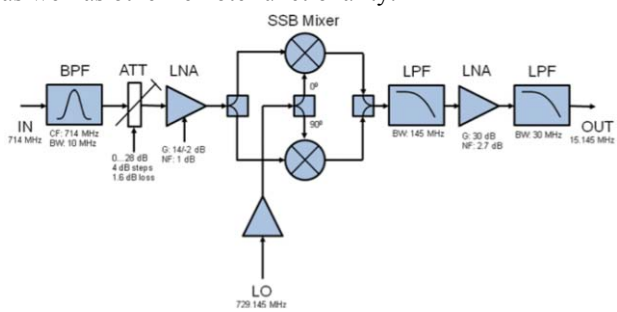

Figure 5: BPM downmix module.

Calibration and Remote Control System

High reproducibility, as well as high resolution is important for the measurements of beam orbits. Uncontrolled drifts in gain stages and RF-switches, filter components, etc. due to temperature variations or aging effects cause unwanted drifting of the *BPM offset* (according to Eq. (2) and (3) a 0.1 dB gain error results in a 27 µm offset error). A prototype calibration system was tested separately on BPM #54 with a mini-VME crate, using two (programmable) CW signals 400 kHz off the 714 MHz operating frequency. The signals are generated with a PLL locked to the 729 MHz LO and fed into the

system using a 10 DB directional coupler (see Figure 6). The CAL signal transmitted through the BPM pickup, and the reflected CAL signal are detected simultaneously with the beam signal, and processed in parallel in the *Graychip* DDC. The calibration unit also incorporates a CAN-bus based remote control and read-back of various function of the downmix module, e.g. input attenuator, LO-signal level, supply voltages and currents, temperature, etc.

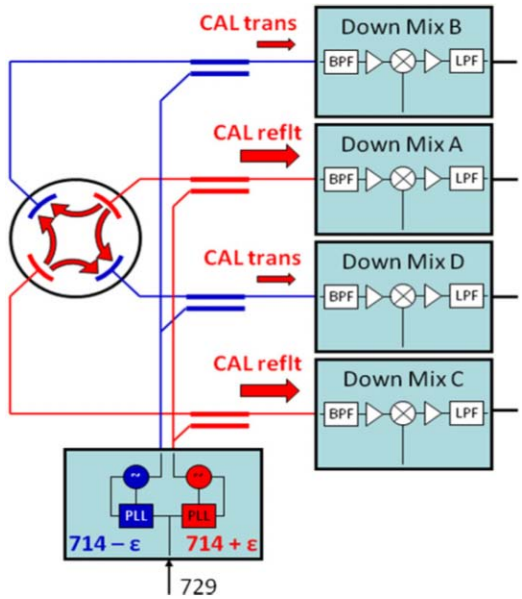

Figure 6: BPM calibration system.

Digital Signal Processing

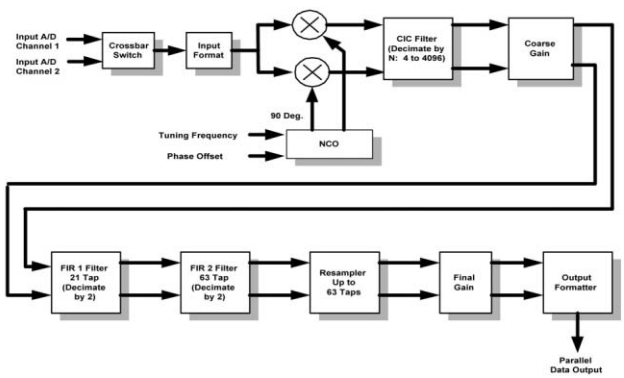

Figure 7: Digital signal processing in the *Graychip* DDC.

Key to the digital signal processing is the 4 channel GC-4016 ASIC (*Graychip,* see Figure 7), which is part of the 8-channel *Echotek* digital receiver VME board. Each signal is digitized at 69.24 MS/s, generating 32 samples / turn. This DDC input data is I-Q demodulated (NCO), low-pass filtered, and decimated using CIC and FIR filters (see Fig. 7). Further data processing takes place in the front-end hard- and software to produce a final button value computed by taking the square root of the sum of the squares of the I-Q data. This result is used to compute a beam position in combination with three other BPM channels, according to Eq. (2) and (3).

All DDC NCO's are programmed to 15.14545 MHz, shifting the IF frequency to baseband. The CIC and FIR filter coefficients and decimation settings used in:

- **Wideband (turn-by-turn, TBT) mode** (see Fig. 8)
  5-stage CIC: decimate by 4
  CFIR: 7-tap boxcar, decimate by 2
  PFIR: 1-tap, no decimation
- **Narrowband mode** (see Fig. 9)
  5-stage CIC: decimate by 2746
  CFIR: 21-tap raised cosine, decimate by 2
  PFIR: 64-tap raised cosine, decimate by 2

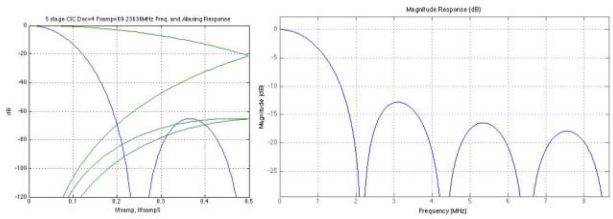

Figure 8: CIC and CFIR filter responses in wideband (TBT) mode, bandwidth ≈ 1 MHz.

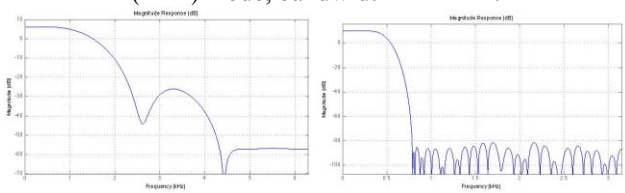

Figure 9: CFIR and PFIR filter responses in narrowband mode, bandwidth ≈ 500 Hz.

Auxiliary Hardware

Besides the core components, the BPM upgrade includes power supplies, VME controller (*Motorola* 5500), VME-64 crates, RF-amplifiers, and an in-house developed FPGA-based VME time generator (TGF). The TGF generates all required clock, trigger, and the LO-signal, and also provides programmable delays in steps of 2.8 ns (see Fig. 2).

Software

The layered software isolates components and enables configuration of the system. The software is primarily written in C++. The interface to the digitizer is through a VxWorks driver and functions to optimally control the operation of the board. The ADC class provides a transparent path to the hardware for making measurements. This class is instantiated and invoked by the BPM class. The measurement is controlled with several memory-resident filter specifications and the type of measurement (either diagnostic or a single flash spanning a number of turns.) Timing specifications are set in conjunction with a coordinated trigger for all ATF BPM's. This suite of software provides measurements to a supported LabVIEW client for diagnostics. Turn-by-turn or closed orbit data is provided to EPICS clients, serving data to the ATF control system.

PRELIMINARY RESULTS

Automatic Calibration System

At BPM #54 an error correction term:

$$X_{corr} = \frac{A_{CAL} + B_{CAL} + C_{CAL} + D_{CAL}}{4\, X_{CAL}} \qquad (4)$$

is generated from the (transmitted and reflected) CAL tone signal for each channel X $\{A, B, C, D\}$. The correction (4) is added to the measured values Φ_X in (2).

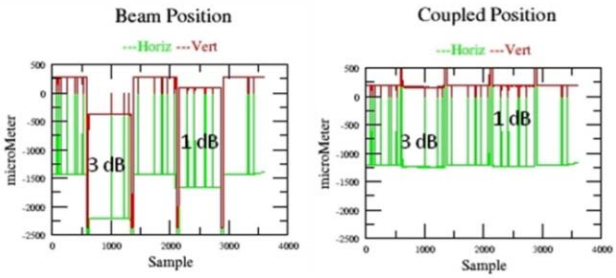

Figure 12: Uncorrected (left) and corrected (right) beam position measurements using the CAL system.

Fig. 11 shows the proof of principle using the automatic calibration correction when introducing a 1 or 3 dB artificial gain error (attenuator pad) in one of the BPM channels.

Narrowband Mode

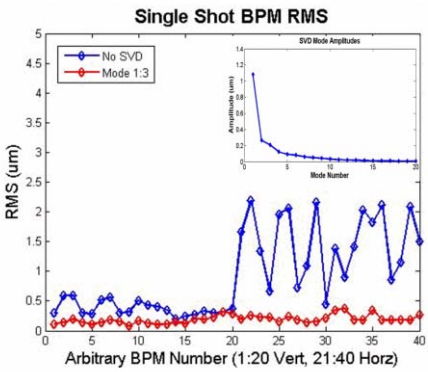

Figure 10: Calculated RMS resolution for the filtered position data, with(out) removing SVD modes.

The obtained narrowband mode resolution was derived using Singular Value Decomposition (SVD) analysis techniques applied to the beam data [3]. For a single injection, the BPM's are triggered at the 500,000th turn and data is collected out of the filter for about 200 ms resulting in 1280 position measurements per BPM at 6.3 kHz. The data is further averaged by a 126 tap box filter specifically chosen to remove 50 Hz harmonics, interfered by the main bus supplies. The resolution is calculated as RMS value on the position data for each BPM, this yields an average BPM resolution of 800 nm. As shown in Fig. 10, the resolutions are much larger for horizontal BPMs. The SVD technique is applied to the data to remove correlated motion from the BPM data. Just removing modes with strong horizontal correlations yields an average BPM RMS of 200 nm. Other modes show strong correlations in both horizontal and vertical data, but because the SVD modes can mix physical modes, it is difficult to separate beam motion from correlated BPM noise. This analysis requires a good understanding of the machine performance and is still under study. With the machine power supplies off, a signal generator was used in the tunnel to provide a simulated beam signal to the system. A BPM resolution of 30 nm was obtained using the signal generator, giving a lower limit of the achievable narrowband resolution.

Wideband Turn-by-Turn (TBT) Mode

The TBT mode was tested by Fourier analyzing the BPM response to coherent beam oscillations [4], excited by a kicker (pinger) in the horizontal plane, and by miss-steering the injection in the vertical one. The data quality in the last case is rather poor, since the oscillations lasted only a few hundred turns. The spectral analysis shows betatron and synchrotron tunes, but also unwanted harmonics at lower frequencies, probably due to EMI of the main power bus to the BPM downmix electronics in the tunnel.

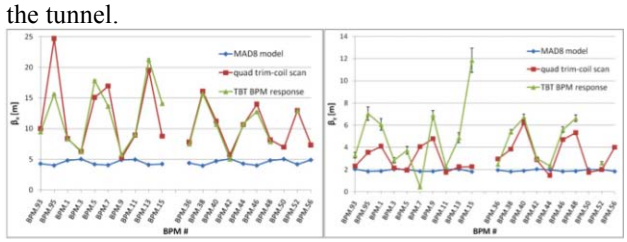

Figure 11: Comparison of measured and theoretical β-functions.

We computed the twiss function values at the BPM locations from the Fourier transform of the TBT oscillations. While the comparison to the model is poor, the results are in good agreement with the betatron amplitudes measured by a scan of the quadrupole trim coils (Fig. 11). The betatron amplitudes computed through the TBT Fourier analysis is determined a constant factor apart, the oscillation amplitude. In Fig. 11 such scale factor was computed by fitting to the data measured by the quad trim-coil scan. TBT response data points are missing at BPM #50 and #56 due to defect electronics channels.

REFERENCES

[1] J. Urakawa, PAC'97, Vancouver, B.C., Canada, May 1997, pp. 444-448.
[2] Y. Honda, et.al., Phys. Rev. Lett. 92, 054802 (2004)
[3] C. Wang, et.al., PAC'01, Chicago, IL, U.S.A., June 2001, pp. 1354-1356.
[4] J. Borer, C. Bovet, A. Burns and G. Morpurgo, EPAC'92, Berlin, Germany, March 1992, pp.1082-1084.

DEVELOPMENT OF BUTTON ELECTRODE WITH IMPROVED TIME RESPONSE

M. Tobiyama*, J. W. Flanagan, KEK Accelerator Laboratory, 1-1 Oho, Tsukuba 305-0801, Japan
T. Obina, M. Tadano, KEK-PF, 1-1 Oho, Tsukuba 305-0801, Japan

Abstract

Good time response in a button electrode is essential to realize the bunch-by-bunch feedback / diagnostic systems for future short-bunch spacing accelerators such as an energy recovery linac (ERL) or super B-factory. The impedance matching and the time-domain response of the electrodes especially around the vacuum seal have been studied using 3-D electromagnetic codes (HFSS, MAFIA and GdfidL). Several candidates have been fabricated to examine the tolerances of mechanical pressures and heat stress due to the welding process. The real beam response from a short linac bunch has also been studied using a test beam line at the KEK-PF beam transport section.

INTRODUCTION

The requirements on the bunch-by-bunch beam position diagnostics systems for future short-bunch spacing accelerators, such as energy recovery linac (ERL) or super particle factories such as SuperKEKB, are much harder than those of present accelerators because the systems play a major role in operating the accelerators or to realize the fairly difficult specifications. Since the signal inputs of the system which couples to the beam (head) limit the absolute performance of the system, it is necessary to design good electrodes such as button-type electrodes or stripline electrodes including feedthrough which fulfill the requirements.

The requirements on the front-end parts of bunch-by-bunch diagnostic systems might be summarized as follows:

- Good impulse response without long trailing signals, such as ringing from the bunch signal. It is also necessary to be free from trapped modes which not only make the response worse but easily damage vacuum sealing in high beam current conditions.
- High enough output voltage to keep good signal to noise ratio on succeeding detection circuits.
- Mechanically tough structure with respect to both signal induced heating and possible impacts such as mechanical pressure coming from fastening and unfastening the RF connectors or cable stress. Note it is also necessary to be strong enough in the construction process such as welding them to vacuum chamber.

For the KEKB bunch-by-bunch feedback systems, we designed and fabricated modified-SMA type button electrodes about 10 years ago[1]. We have done 3-D EM simulations such as MAFIA310 or HP-HFSS ver.3 using fairly poor computing power compared those available to now. The installed BPMs have been working excellently under tough conditions, with a maximum beam current of 2A, minimum bunch spacing of around 4ns (about 15nC / bunch), and a bunch length of about 7mm in standard deviation, without any troubles. Good frequency response of the electrodes also helps to investigate beam characteristics such as beam-beam effects or unknown beam instabilities. For an accelerator with a much shorter bunch length, say about 3mm, or with much shorter bunch spacing, however, the electrode might not be suitable.

Since the large permittivity of alumina-ceramics (e_r~9.7) used to seal vacuum makes impedance matching difficult, we have employed a glass of low permittivity (ε_r~4) as vacuum seal of the feedthrough and examined the frequency and time response using current 3D-electromagnetic field simulation codes (GdfidL, HFSS) [2, 3]. Several candidates have been fabricated to examine the frequency response, and tolerance to mechanical and heat pressures. The time response of the electrodes has been studied using the very short linac bunch using the test-beam line at KEK-PF beam transport section. The target specification of the electrodes for SuperKEKB and the ERL test facility proposed in KEK are shown in Table.1.

Specification		**unit**	
Bunch length	3 <0.9	mm mm	SuperKEKB ERL
Bunch charge	20 7.7	nC pC	SuperKEKB ERL
Time response	<0.5 <0.3	ns ns	SuperKEKB ERL

Table 1 Design target of new button electrodes.

BUTTON ELECTRODE FOR KEKB FEEDBACK SYSTEMS

The structure of the present button electrode used in the KEKB feedback systems is shown in Fig. 1.For support

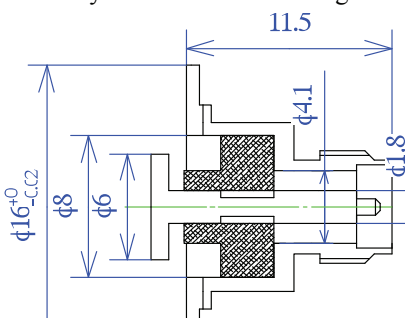

Fig.1 Button electrode for KEKB feedback systems.

*mailto:makoto.tobiyama@kek.jp

and vacuum sealing, aluminum-ceramic of ε_r=9.7 (Kyocera A473) is used. The outer metal is Kovar (Fe-Co-Ni). The beam response from the KEKB-LER (positron ring) 1st bunch, of bunch charge of about 9 nC, is shown in Fig. 2, with a 43dB attenuator and about 5dB and 15 dB cable loss at 2GHz and 10GHz, respectively. The analogue band-width of the HP54121 oscilloscope was 20 GHz.)

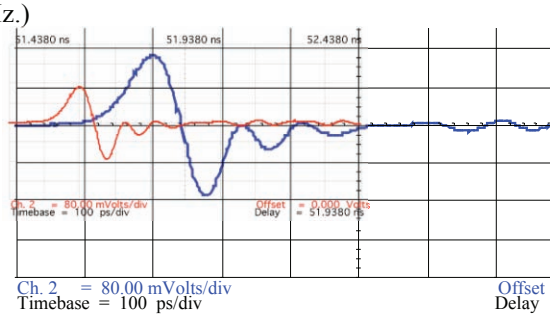

Fig.2 BPM signal from 1st bunch of KEKB-LER at bunch charge of 9nC. The BPM is mounted on a circular vacuum chamber of diameter of 64 mm.

The results of the time domain simulation using GdfidL for a bunch of σ_z=7mm, I_b=1nC are shown in Fig.3 and Fig.4, with time-domain response and the power spectrum, respectively. Taking into account the frequency dependence of the cable loss, the numerical simulation shows good agreement with the real signal.

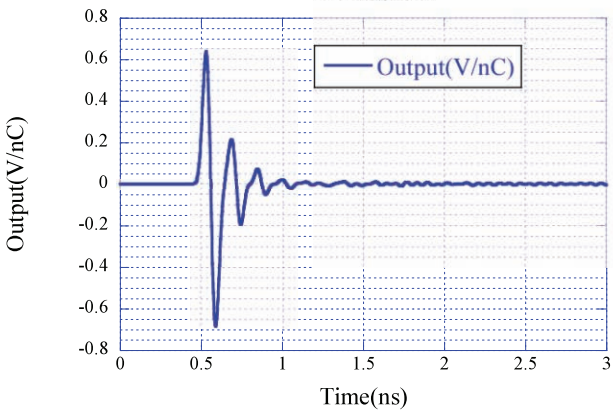

Fig. 3 Simulated time response of KEKB-FB BPM.

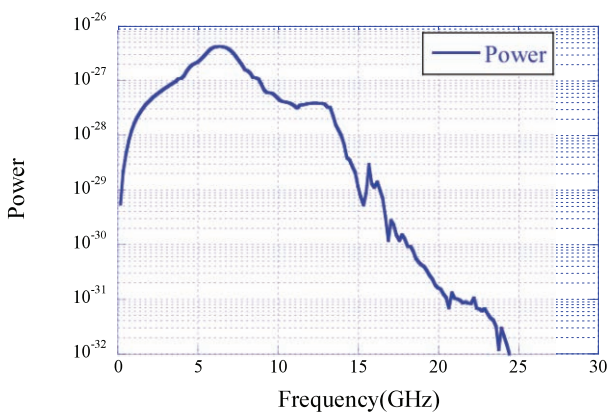

Fig. 4 Power spectrum of KEKB-FB BPM output.

The S-parameter of the electrode is also calculated with Ansoft HFSS (ver.11) under the condition of both button and SMA terminal being completely matched ports as shown in Fig. 5.

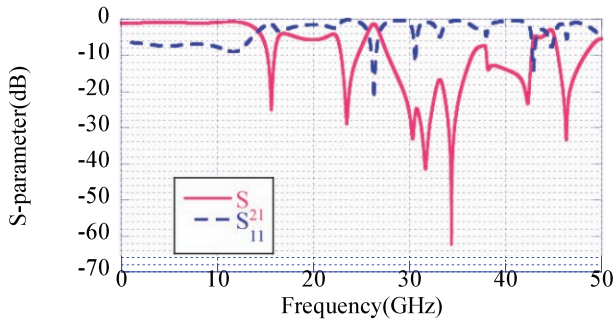

Fig. 5 Simulated S-parameter of KEKB-FB button electrode.

As is clearly shown, the lowest trapped mode of the electrode sits as around 16GHz. At KEKB, this resonance can be ignored because of the longer bunch length. However in future accelerator with much shorter bunch lengths, this characteristic makes the situation fairly difficult. Figure 6 and 7 show the simulated response in the case of σ_z=3mm.

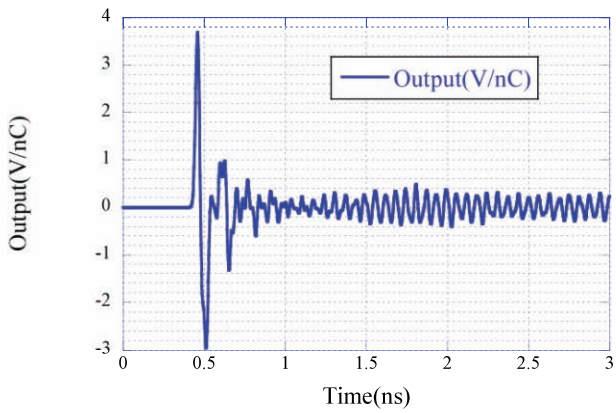

Fig. 6 Simulated time response of KEKB-FB BPM with bunch length of 3 mm. Note that we have used the narrower pipe (24 mm in diameter) for the simulation.

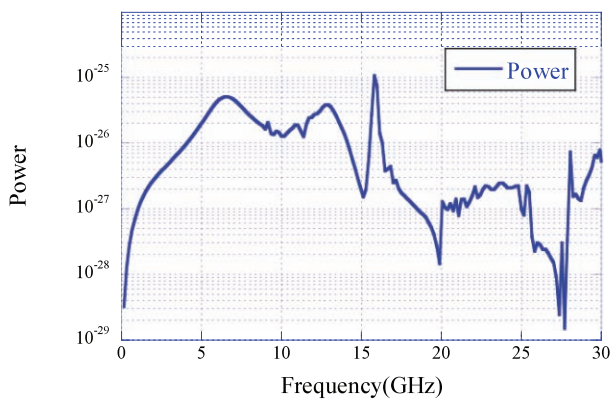

Fig. 7 Power spectrum in the case of bunch length of 3 mm.

The high-Q resonance around 16 GHz which is estimated to be coming from the ceramic part makes a long ringing tail. For a high beam current machine, this may heat up the ceramic which will cause fatal breaking of the vacuum seal.

BUTTON ELECTRODE WITH GLASS SEALING

To make impedance matching easier and to shift the possible trapped modes to higher frequencies, employing a low permittivity material as vacuum seal is always promising. We have designed the electrode using glass-type sealing with ε_r~4 (Kyocera KC-1), as shown in Fig. 8 (D01-type). The simulated S-parameter is shown in Fig. 9. Clearly it shows no suspicious structure up to 50 GHz. MAFIA 2D (e420) calculations also showed no trapped modes inside the glass seal under 50 GHz.

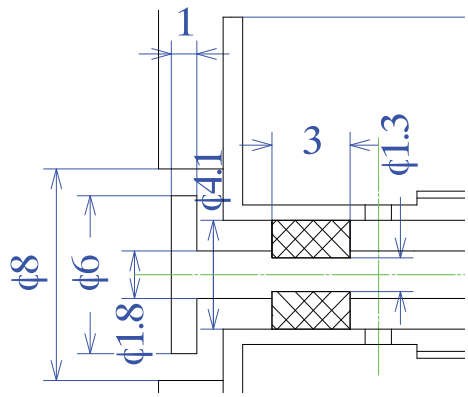

Fig. 8 Button electrode with glass sealing (D01-type).

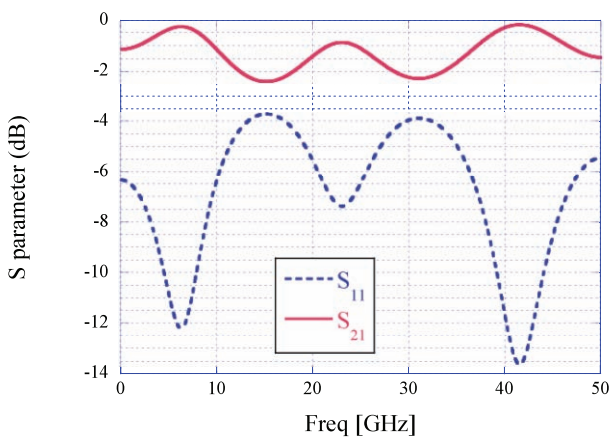

Fig.9 Simulated S-parameter of the D01-type BPM.

The feedthroughs must sustain various mechanical impacts such as fixing and releasing of the RF connectors. We have fabricated several test pieces that fit a pulling test machine with the same vacuum sealing structure, and have measured the breaking points. Figure 10 shows the results of D01-type feedthroughs and other simple feedthroughs with various diameters of inner conductors using KC-1 glass. Also the results of the KEKB-FB type feedthrough are plotted. In general, the mechanical strength of the feedthrough will be proportional to the area of bonding if the materials on both sides of the bonds

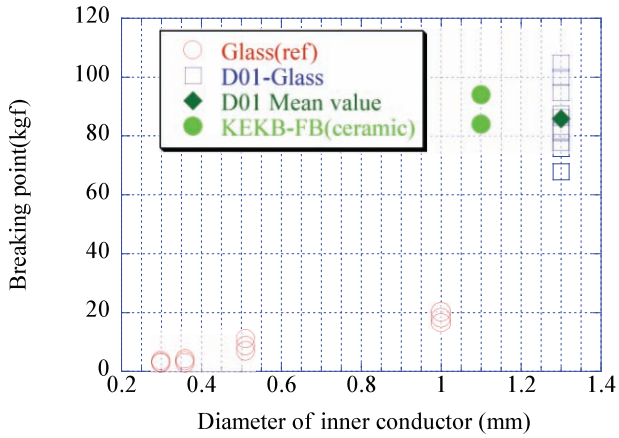

Fig. 10. Breaking points versus diameter of inner conductor.

are the same, as shown by the reference glass seal data. The D01-type feedthroughs show much higher tolerances. Note all the breaking of D01-type occurred in the inner conductors, not in the glass seal. The mean value of about 80 kgf is comparable to that of the KEKB-FB type.

The time response of the electrode is also calculated by GdfidL with the condition of 3mm bunch length and 1nC charge. Figures 12 and 13 show the time response and the

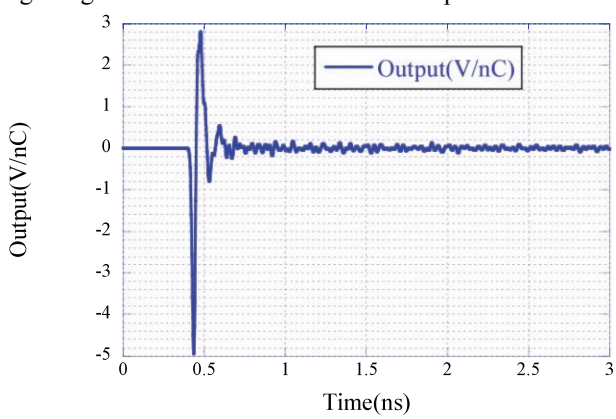

Fig. 12. Time response of D01 type electrode.

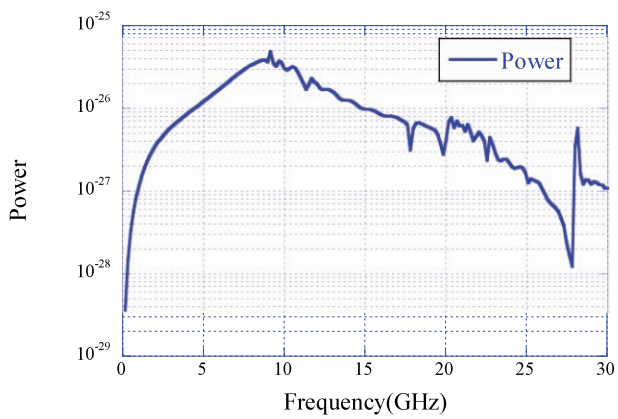

Fig. 13. Power spectrum of D01 type electrode.

power spectrum, respectively.

Next, we started to construct the bunch-by-bunch feedback monitor chamber of inner diameter of 64 mm made of stainless steel (SUS 304) on which we welded 16 D01-type electrodes and 4 KEKB-FB electrodes as reference. Very unexpectedly, during the welding process of the electrodes, we found 4 out of 16 D01-type feedthroughs had become damaged to show slow a vacuum leak, around the order of 1×10^{-10} Pa m^3/s. Though the monitor chamber itself was finally completed without a leak, we were afraid the leak would return again during beam operation. Since manufacture failed to find the cause of the leak, we have tried to examine the welding process by welding the feed-through on simple ICF070 flanges under completely controlled conditions.

The rate of the leaking feedthrough still exceeded 20%. Therefore, we decided to halt the installation of the chamber in the ring and to develop a much stronger feedthrough than the D01-type.

MODIFIED GLASS-SEALING TYPE ELECTRODE

The diameter of the inner conductor at the glass seal of the D01-type feedthrough is reduced from 1.8mm to 1.3mm. Due to this narrow cross section, it is needed to make the glass part in two halves and melt them together in the assembly process. Though this narrow part contributes to good impedance matching, we have decided to omit this part as shown in Fig. 15 (D02 and D03 type). Also we have added a small circular dip near the welding edge and made the thickness around the glass thicker than in the D01-type. For the glass-seal, two different materials have been selected. The first one is the same as the D01-type (ε_r=4, Kyocera KC-1):D02-type, and the other has larger ε_r =5 (Kyocera BH) but has better affinity to Kovar (D03-type). The S_{21} simulated by HFSS is shown in Fig. 16.

Though there still seem no obvious resonance structure up to 50GHz in all cases, both the D02 and D03 types have worse frequency response even with lower frequencies (around 10GHz) showing the impedance matching has been deteriorated by the modification to some degree.

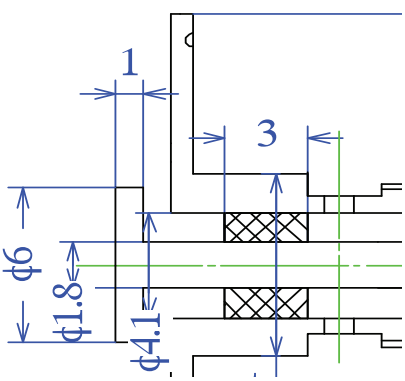

Fig. 15. Modified glass-type sealed electrode (D02 and D03 type).

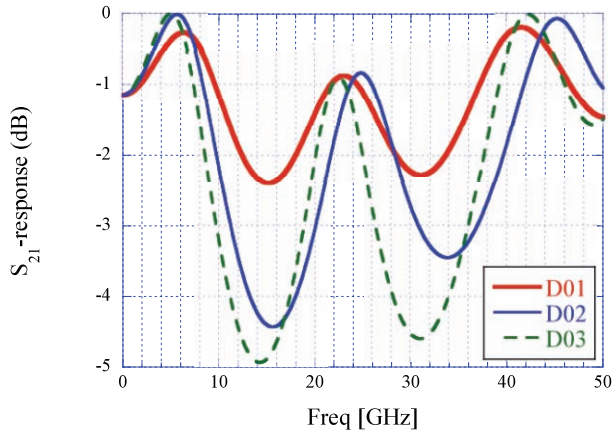

Fig. 16. Simulated S_{21} for three types of the electrodes.

Comparison of the results of time-domain simulation and power spectra by GdfidL for the three types are shown in Fig. 17 and 18, respectively

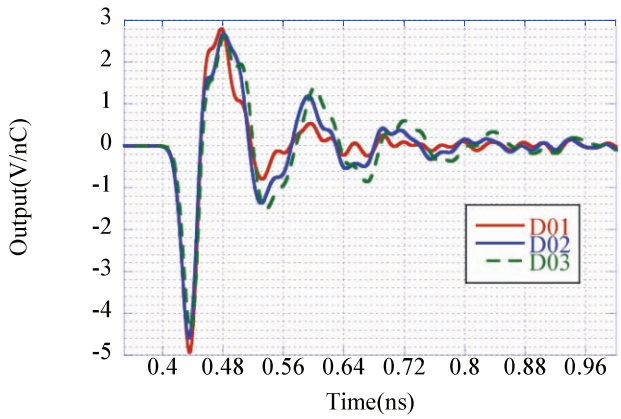

Fig. 17. Comparison of the time-domain simulation for three types of feedthrough.

The differences among the three cases are not so large, though the D01 type still shows the smallest ringing response among the three.

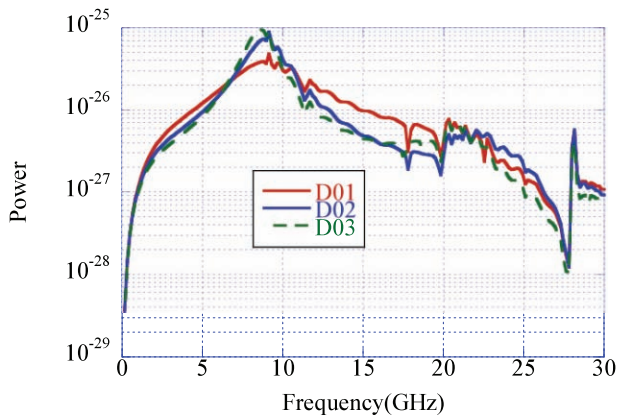

Fig. 18. Comparison of power spectra of three types of electrodes.

To obtain the real beam response of those electrodes, we made a test monitor chamber with KEKB-FB, D01,

D02 and D03 type electrodes mounted and installed in the beam test line recently constructed near KEK-PF beam transport line from the 2.5GeV linac [4]. The bunch length is about 8 ps in FWHM. Note by tuning the R56 and T566 parameters, we can compress the bunch length down to 0.5 ps. Since we do not have a good timing line between the linac gun and the test line, we have used an ultra-wideband real time oscilloscope, the Tektronix DPO71604 (BW=16GHz, 50GSPS). Figure 19 shows the measured beam response for (A: KEKB-FB, B: D01, C: D02, D: D03).

Obviously the response of the D01 type electrode is the best of the four. Also, the KEKB-FB type electrode shows a long ringing tail similar to the simulation (the frequency of larger than 10 GHz) and it seems it is radiating the ringing components into the vacuum chamber and is detected with the other electrodes afterwards. The difference between D02 and D03 is not so clear.

DISCUSSION

We have fitted the first part of the response (starting near the falling edge to about 250 ps) by the derivative of a gaussian distribution. Since the sampling frequency was 50 GHz, it has about 14 points for the fit. Though all the fitted widths are within fitting error, the χ^2 parameter showed the relation, D01 << D02 < D03 ~ KEKB-FB. The deviation comes not only in the tail part but also near the falling edge, especially in the D02 and D03 types.

The differences between the D01, D02 and D03 types are not large, and all of them might be acceptable for bunch-by-bunch diagnostic systems in storage rings, such as SuperKEKB. For applications at much shorter bunch lengths, the response of the D01-type will not be sufficient. Since the mechanical tolerance around the inner conductor might be regarded as large enough, we can try to reduce the diameter for better impedance matching. To improve the heat tolerance in the welding process, further study and investigation will be needed.

SUMMARY

We have designed and tested button-type electrodes with improved time response. The mechanical tolerance of the feedthroughs including the shocks due to construction of the monitor such as the welding process have also been examined. The real beam response of the electrodes has been tested using a test beam line with very short bunches from a linac. Further development for better time response with enough strong mechanical structure is underway.

The authors wish to thank Prof. T. Mitsuhashi for the preparation and help of the test beam line experiment at the KEK-PF. The discussions with the KEKB beam instrumentation group have been very fruitful.

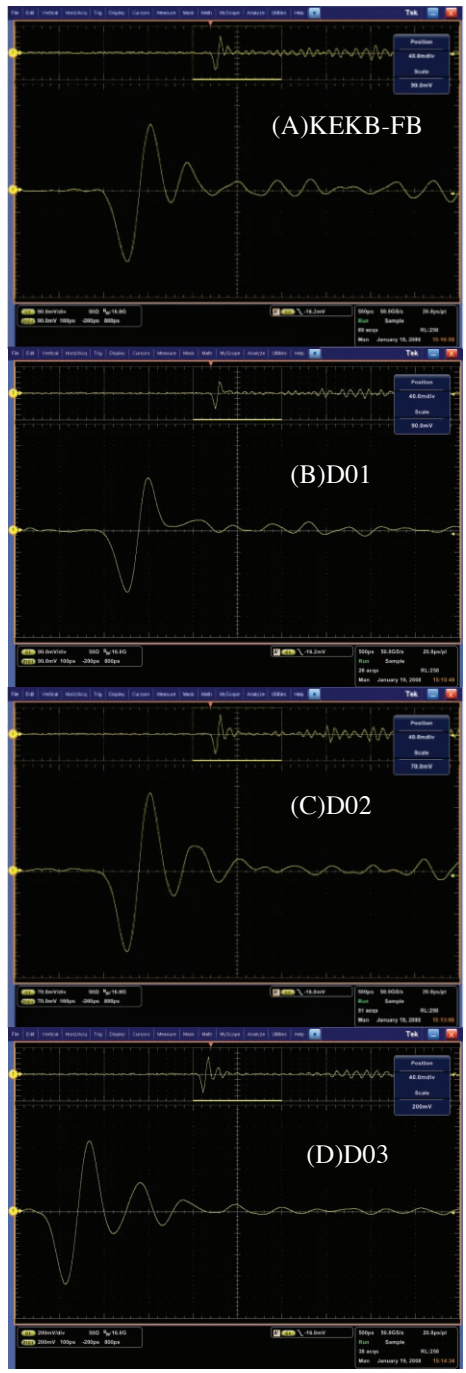

Fig. 19. Beam response of BPMs from linac beam.

REFERENCES

[1] M.Tobiyama and E.Kikutani, “Bunch-by-bunch feedback systems for KEKB rings”, in proceedings of 1st APAC (APAC98), Tsukuba, Japan, 1998.
[2] W. Bruns, GdfidL (http://www.gdfidl.de/)
[3] Ansoft HFSS Ver.11.0 (http://www.ansoft.com/hfss)
[4] K. Furukawa, et, al, “Beam instrumentation for KEK ERL test facility”, in proceedings of ERL07, Daresbury, UK, 2007.

BEAM QUALITY MEASUREMENTS AT THE SYNCHROTRON AND HEBT OF THE HEIDELBERG ION THERAPY CENTER

T. Hoffmann[1], D. Ondreka[1], A. Peters[2], A. Reiter[1], M. Schwickert[1]

[1]Gesellschaft für Schwerionenforschung (GSI), Darmstadt, Germany
[2]Heidelberg Ion Therapy Center (HIT), Heidelberg, Germany

Abstract

The Heidelberg Ion Therapy Center (HIT) for tumor treatment is presently being commissioned using the beam diagnostic devices designed and produced by the GSI beam diagnostic department. To fulfil the requirements for hadron therapy a high-resolution analysis of the particle distribution within the slowly extracted beam is necessary. We present spill-structure measurements for carbon ion beams at energies from 88 MeV up to 430 MeV, also with respect to the spill-pause and abort functionality of the rf-knock-out extraction method. The spill-structure, as measured by internal intercepting ionization chambers (IC) is compared to data recorded with external beam loss monitors (BLM). The high-resolution data acquisition system with sampling rates up to 10 kSa/s and the connected detectors are described and the achievements during the commissioning phase are discussed.

INTRODUCTION

The Heidelberg Ion Therapy center (HIT) is a new dedicated hadron accelerator facility for medical treatment of tumor patients. The advantage of using hadrons in cancer therapy is their characteristic energy loss profile in irradiated materials. When applied to tumor tissue this leads to a DNA destructive maximum at the Bragg peak immediately before the particles come to rest. To reach penetration depths of 20-300 mm in water, which is almost comparable with human tissue, ion energies of 50-430 MeV for carbon ions are required. The tumor is irradiated in sliced fractions (iso-energy-layers) by means of cycle-to-cycle energy variation. Within such a layer the intensity controlled raster-scan method applies a pencil beam which is moved from voxel to voxel (3D-pixel) by two fast scanner-magnets. Due to this technique some accelerator characteristics have to be taken into account to assure the fulfilment of the manifold requirements of medical radiotherapy.

In this contribution the spill-pause and abort functionality are analyzed. During raster-scan operation within a synchrotron cycle the spill-pause functionality spares healthy tissue in cases where irradiation areas are spatially separated. Secondly the spill-pause is an important tool to optimize treatment planning, and machine efficiency. The qualities of the rising and falling edges and the intensity of the residual particles within the pause, and after the spill-abort have to be investigated. To gain a homogeneous irradiation per fraction the spill-structure has to be optimized as spike effects and small interrupts increase the failure rate. The spill-structure is influenced by many factors such as the rf-knock-out extraction (KO) method, the power supplies, and the beam bunching parameters.

HIT ACCELERATOR COMPLEX

Presently HIT is in the final phase of its commissioning. All treatment areas can be served with carbon ion beam in the designed energies range from 88 MeV up to 440 MeV. As shown in Fig.1, the complex consists of two ECR ion sources, a 7 MeV RFQ/IH Linac (A), a Synchrotron (B) with magnetic rigidity of Bρ=0.38-6.5 Tm, two horizontal

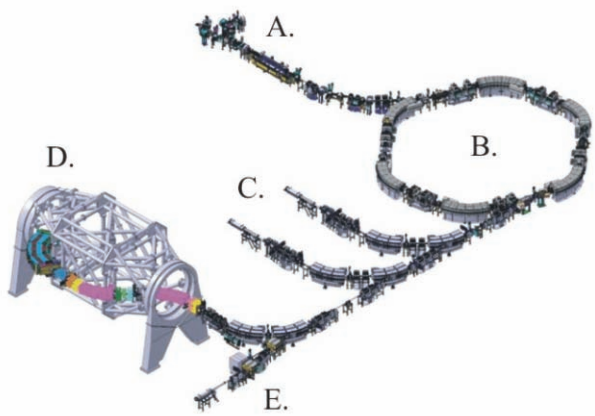

Figure 1: Isometric drawing of the HIT accelerator complex.

treatment places (C), a 360º patient irradiation gantry (D), and a quality assurance section (E). A more detailed description of the facility and its diagnostics is given in [1] and [2].

BEAM DIAGNOSTICS AND DATA ACQUISITION

The complete beam instrumentation, from layout and production to the final installation including the final proof of operability with beam, was managed by the GSI beam diagnostics group. All beam diagnostic devices were categorized into separate device classes on the base of the detected beam parameter such as current, energy, beam profile, position, phase and others. One of these device classes is the “event counting” class, which is from its functional point of view a down-sized reproduction of the GSI ABLASS system [3]. It combines all particle

counting devices such as plastic scintillators, ionization chambers with I/f converters [4], and beam loss monitors (BC400 plastic scintillator, 20x20x75 mm^3), which all can be used to investigate the spill-structure beneath the standard usage for intensity, transmission and beam loss measurements. The analogue signals of the scintillators are shaped and digitized by standard NIM modules (Fan In/Out, Discriminator, Level adaptor). All signals are finally fed into the data acquisition system (DAQ).

The general concept of the LabViewRT based DAQ at HIT is to use "commercial off the shelf" products (COTS) as the facility is operated by a university hospital and therefore needs the most practicable standard for operation and maintenance. In addition, standardized DAQ modules reduce the spares inventory and improve the facility-wide exchangeability of components. The DAQ consists of PXI front-end systems using many types of PXI modules. Four eight-channel PXI-6602 Scalers from National Instruments were installed for the "event counting" class. In default mode the scalers sample and deliver data of all 32 channels with 1 kSa/s. In addition, data of three selected channels may be acquired with a sample rate of 10 kSa/s using the DMA mode. The spill-structure measurements presented in this paper were observed by using this fast mode.

SPILL-STRUCTURE

The detectors and the DAQ system of the "event counting" device class allow a detailed analysis of the synchrotron spill-structure that fulfills the demands of the ongoing commissioning as well as the requirements of

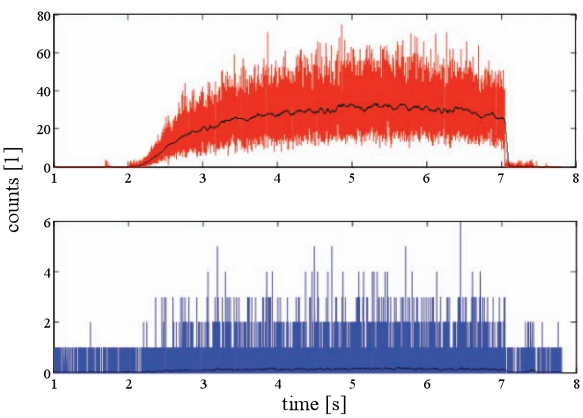

Figure 2: Spill-structure measurements with $^{12}C^{6+}$ at 430.10 MeV and $8 \cdot 10^7$ p/spill. Top: IC. Bottom: BLM.

routine operation. The spill shape is usually observed by ionization chambers (Fig. 2, top), here in front of the first treatment area in the high energy transfer line (HEBT). In addition, one of the movable non-intercepting BLMs (Fig. 2, bottom) placed at the electrostatic septum of the synchrotron is used to examine the spill. The count-rate of the BLM in this measurement is low as the machine is well tuned and only negligible beam loss is created at the extraction section of the synchrotron.

The spill data measured with the IC can be used for spill-structure optimization purposes by calculating the count-rate ratios of minimum to average and maximum to average values [5]. The interspace between the two

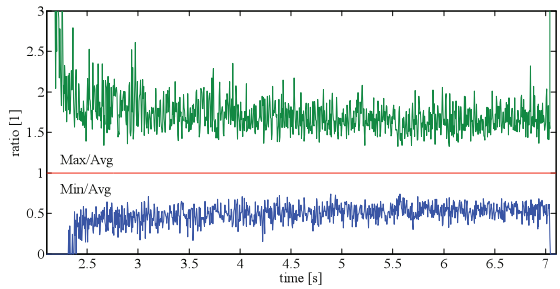

Figure 3: Ratios of Min and Max values divided by the average (5 ms integration window). Minimization of the interspace of both functions smoothes the spill-structure.

graphs shown in Fig. 3 has to be minimized for best results. The shown value below 2 for the Max/Avg ratio is already satisfactory. The influences of machine settings such as the KO-extraction parameters, which are significantly affecting the spill-structure, are currently studied as part of the machine commissioning.

SPILL PAUSE AND SPILL ABORT

At present the implementation of the spill-pause and spill-abort functionality is still in progress. The pause is

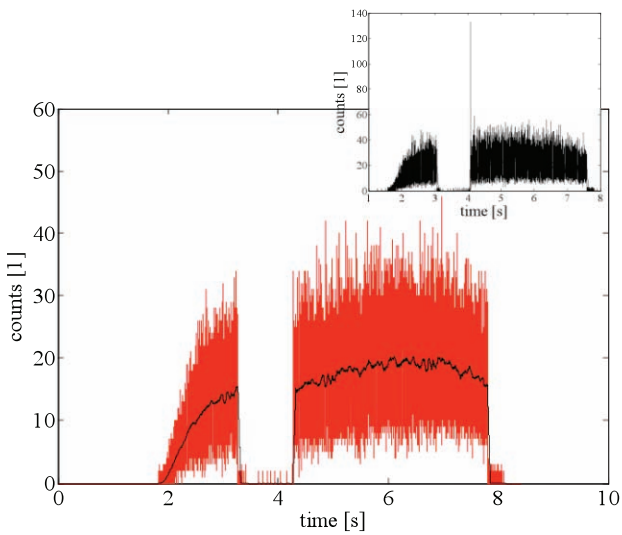

Figure 4: Slowly extracted $^{12}C^{6+}$ beam at 270 MeV with 1s spill-pause, 10 kSa/s. The black line is the result of a rolling average filter of 500 points window-size. Top right: spill with re-entry spike.

created by shifting the synchrotron rf out of the KO-extraction noise band. In order to completely dump accidentally extracted particles within a spill-pause, a spill abort magnet (SPAM) is installed in the 1st section of the HEBT behind the extraction septum as a second safety arrangement. These mechanisms together ultimately

prevent unwanted beam transport, e.g. inside a spill-pause to the treatment places. Fig. 4 shows a spill with 1s pause and the final beam abort.

Examinations of these pauses are essential since unwanted spikes at the pause edges may occur as shown in the top right corner of Fig. 4. The rise- and fall-times of the pause should be constant for all possible energies. Otherwise, energy-dependent corrections have to be

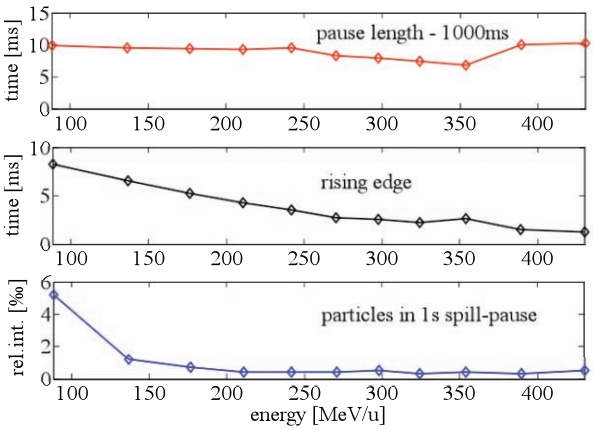

Figure 5: Energy-dependent effects: Top: variation in time of the real spill-pause minus 1s (pause set-value). Middle: rise time at the pause end. Bottom: intensity of residual particles in spill-pause.

added to the extraction parameters.

With measurements from 88.83 up to 430.10 MeV the time behavior of the edges as a function of energy were analyzed. In the top graph of Fig. 5 almost no influence on the pause length can be seen. The length was calculated by linear regression on both edges, and subtracted by the set pause length of 1 s. The middle graph represents the pause-end flank, which shows a significant decrease of the rise-time with increasing energies. The residual particle amount within a spill-pause of 1s is estimated by finding the minimum of a 1s-integration window shifted across the recorded spill data. The results are shown in the bottom graph of Fig. 5. Only at lower energies (88-130 MeV) max. 0.52% of the average spill intensity is leaking through the spill pause mechanism. This preliminary measurement indicates very good particle suppression. Even without using the spill abort magnet for spill pauses, the intensity is already very low. The final value of accepted residual particles in the pause is yet to be defined in the ongoing risk assessment.

FFT ANALYSIS

The spill-structure data is passed to a Fast Fourier Transformation (FFT) algorithm to discover objectionable ripples of machine parts such as the mains, power supplies or vacuum pumps. Fig. 6 shows 10 averaged FFTs for synchrotron cycles at 88.83 MeV (top) and 430.10 MeV (bottom). At both energies the harmonics of the 50 Hz mains are visible, but, for unknown reasons, only at the lower energy the 50 Hz itself is present. The

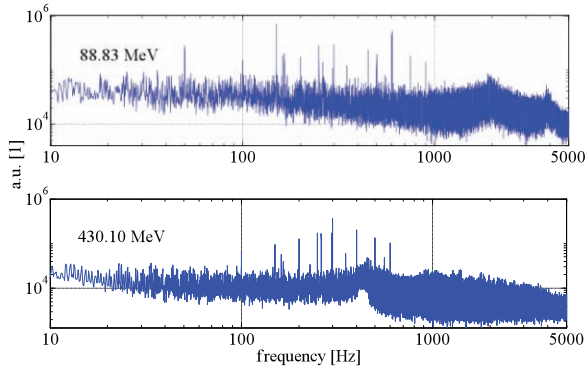

Figure 6: Averaged FFTs at 88.83 MeV (top) and 430.10 MeV (bottom) are showing significant ripples of the mains (50Hz, Germany) and of unknown sources.

influence of the synchrotron frequency of 2 kHz at 88.83 MeV and of 456 Hz at 430.10 MeV is clearly visible. The noticeable peaks at 165 and 262 Hz give a hint to minor ripple influence of the synchrotron equipment and are subject of further investigations.

CONCLUSION

By means presented here the spill-structure, spill-pause, and spill-abort functions are studied in the course of HIT commissioning. The applied FFT routines give good information about unspecific machine effects, which yield to separate investigations. The usage of a non-intercepting BLM for online spill-structure measurements is possible, but at the relatively low beam intensities at HIT scintillators with a greater active volume are required to achieve useful count rates in DMA mode.

With a view to the requirements of a hospital based accelerator facility the described beam diagnostic devices and DAQ are meeting all demands for commissioning, maintenance and daily operation. The authors would like to thank Dmitry Liakin for helping on the data evaluation and many fruitful discussions.

REFERENCES

[1] H. Eickhoff, Th. Haberer, B. Schlitt, U. Weinrich, “HICAT- The German hospital-based light ion cancer therapy project”, EPAC’04, Lucerne (CH), p. 290-294.

[2] A. Peters, T. Hoffmann, M. Schwickert, “Beam diagnostic devices and data acquisition for the HICAT facility”, DIPAC’05, Lyon (F), p. 143-145.

[3] T. Hoffmann, P. Forck, D. A. Liakin, “New spill structure analysis tools for the VME based data acquisition system ABLASS at GSI”, BIW’06, Batavia (USA), p. 343-350.

[4] H. Reeg, “A current digitizer for ionization chambers /SEMs with high resolution and fast response”, DIPAC’99, Chester (UK), p. 147-149.

[5] P. Forck, H. Eickhoff, A. Peters, A. Dolinskii, “Measurements and improvements of the time structure of a slowly extracted beam from a synchrotron”, EPAC’00, Vienna (A), p. 2237-2239.

CREATING A PSEUDO SINGLE BUNCH AT THE ALS — FIRST RESULTS*

G. Portmann, S. Kwiatkowski, J. Julian, M. Hertlein, D. Plate, R. Low, K. Baptiste, W. Barry, D. Robin, Lawrence Berkeley National Laboratory (LBNL), Berkeley, CA 94720 U.S.A.

Abstract

Typically storage ring light sources operate with the maximum number of bunches as possible with a gap for ion clearing. The Advanced Light Source (ALS) has 2 nanoseconds between bunches and typically operates with 276 bunches out of a possible 328. For experimenters doing timing experiment this bunch separation is too small and would prefer to see only one or two bunches in the ring. In order to provide more flexible operations and substantially increase the amount of operating time for time-of-flight experimenters, it is being proposed to kick one bunch on a different vertical closed orbit. By spatially separating the light from this bunch from the main bunch train in the beamline, one could potentially have single bunch operation all year round. By putting this bunch in the middle of the ion clearing gap the required bandwidth of the kicker magnets is reduced. To test this new method of operation on the beamlines one kicker magnet running at the ring repetition rate (1.52 MHz) has been installed at the ALS. This paper will show some first results running the kicker at 1.52 and 1.52/5 MHz.

INTRODUCTION

The concept of using a camshaft bunch started many years ago and originated out of the needs of time-of-flight experimenters. Some time ago, NSLS at Brookhaven experimented kicking one bunch in the train at low repetition rates, [1]. This will introduce relatively long transient oscillations until the synchrotron radiation damps the bunch back to the closed orbit. To our knowledge no accelerator in the world has taken the next step to kick the camshaft bunch on a different closed-orbit to create a pseudo single bunch mode. Accelerators like the APS and ESRF can achieve similar functionality by installing choppers in the beamlines. However, even with state-of-the-art choppers this solution requires relatively large gaps in the bunch train, so it's presently only feasible on large accelerators. It also requires each beamline to purchase a relatively expensive and often difficult to use and maintain chopper. At the ALS the largest gap in the bunch train is presently 104 nanoseconds, which is out of reach for x-ray choppers.

There are a number of beamlines at the ALS interested in exploring a pseudo single bunch operational mode. A major reason is so that experiments using the camshaft bunch will not have to use gated detectors. The ability to use integrating detectors increases the variety and quality of the experiments that can be done. For instance, the combination of the pseudo single bunch mode and a chopper with an open time of just more than one turn allows for an effective single bunch operation at 1-10 kHz.

A POSSIBLE NEW OPERATIONAL MODE

By kicking the camshaft bunch on a different closed-orbit, it may be possible to create a pseudo single bunch operation during a multi-bunch user run. There are a number of different ways the orbit of the camshaft bunch can be shaped depending on the number and location of the fast kicker magnets. The easiest thing to do is install one kicker magnet and place the camshaft bunch on a different global closed-orbit. This may not be optimal for all single bunch or multi-bunch users, but it would be a relatively easy thing to do to experiment with the method. Another obvious thing to do is locally bump the camshaft bunch in one part of the ring. This would isolate the disturbance to a relatively small section of the ring. A third option is to install kicker magnets all around the ring and profile the orbit much like global orbit correction. This paper will show results for the one kicker scenario. A more detailed explanation of the entire system can be found in [2][3]. Details of the kicker magnet and pulser design can be found in [4].

GLOBAL ORBIT DISTORTIONS

The ALS is a 12 sector, triple bend achromat with 4.5 meter straight sections for insertion devices. A convenient location to install an experimental kicker happens to be in the straight section 2.

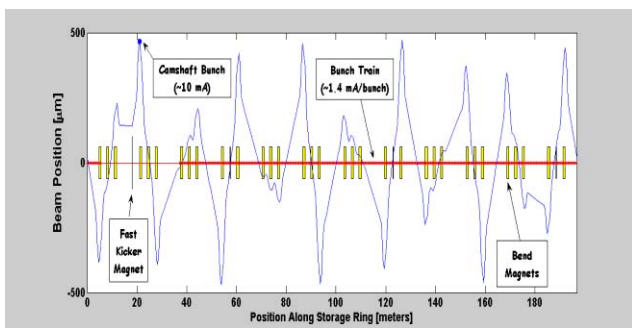

Fig. 1: Orbit Change for a One Kicker Magnet.

Using one fast kicker magnet running at the revolution rate (1.52 MHz) the camshaft bunch can be permanently put on a different closed orbit. Fig. 1 shows the change in

* This work was supported U.S. Department of Energy under Contract No. DE-AC03-76SF00098 and DE-AC03-76SF00515.

the closed orbit for the camshaft bunch for a 60 μradian kick (the design goal). As shown in the figure, this configuration would be suitable for a number of beamlines. Many of the outer bend beamlines and some of the insertion device and center bends beamlines would see a sizeable separation. Fig. 2 is the same data with the beam sizes included.

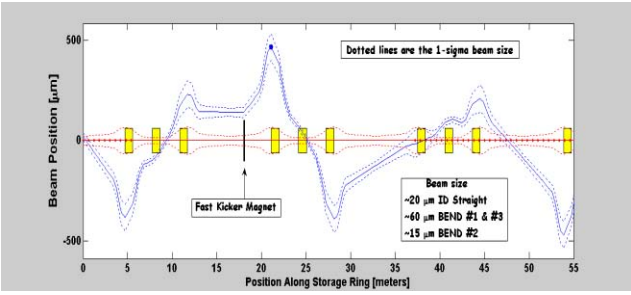

Fig. 2: 1- Kicker Magnet – First 3 Sectors.

BEAMLINE USER INPUT

A workshop was held to determine the user requirements for a pseudo-single bunch operation. The three basic issues are kick size (displacement), repetition rate, and contamination. There are also potential negative effects on storage ring operations.

Kick Size (displacement and/or angle)

The kick size is the required displacement or angle separation of the kicked bunch from the main bunch train. The present design calls for a 5-10 beam sigma displacement. This requirement could possibly be verified by scanning a closed-orbit bump in normal multi-bunch mode.

One of the challenges here is every beamline is different and the quality of the optics plays a big role in determining the required separation. Experimental data from BL 5.3.1 is shown in Fig. 3 for a beam sigma of .1 mm. Due to imperfect optics the beam profile distribution is only Gaussian to about 3.5 sigma. So there is only nominal improvement in bunch purity by kicking the beam past about 8 sigma. This beamline is roughly looking for a 10^{-3} reduction of the signal from the main bunch train.

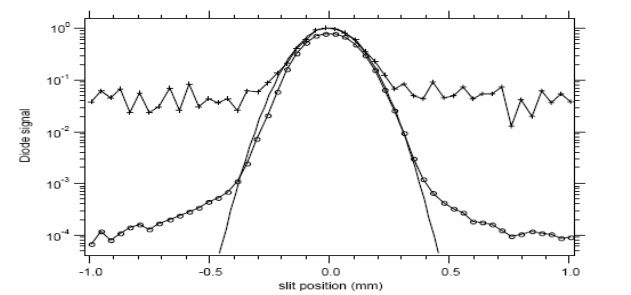

Fig. 3: Measured horizontal profile at BL 5.3.1 at 5 keV. The crosses and circles represent two amplifier gains and the line without symbols shows a Gaussian fit (Data provided by Robert Schoenlein).

Repetition Rate

The upper bound on the repetition rate is revolution frequency of the electrons – 1.5 MHz. Certain user experiments may require slower rates. For instance, experiments using lasers tend to be in the 1-10 kHz range. When using local bumps it is possible to run at any fraction of the revolution rate.

Contamination

There is a serious question about whether or not the multi-bunch users can handle this new beam profile.

- Contamination effects due to changes in the background radiation (not a Gaussian beam profile anymore).
- Effects of small periodic changes to the beam current in the main bunch train in the local bump case with frequencies less than 1.5 MHz.

Considerable attention will be given to understanding the contamination issues for each beamline.

Potential storage ring operational problems also need to be studied. For instance, the average orbit as reported by the beam position monitors (BPM) will change with the kick size and current of the camshaft bunch (which has a shorter lifetime). Non-repeatability of the kicker magnet would add noise to the bunch train and possibly a beam size increase due to diffusion. And if kicking at 1.5/n MHz, the transverse bunch-by-bunch feedback system would need to be modified.

FIRST RESULTS

A kicker magnet was installed in January 2008. Fig. 4 shows the difference orbit with and without the kicker on. A calibrated model was used to determine the 73 μradian maximum kick strength.

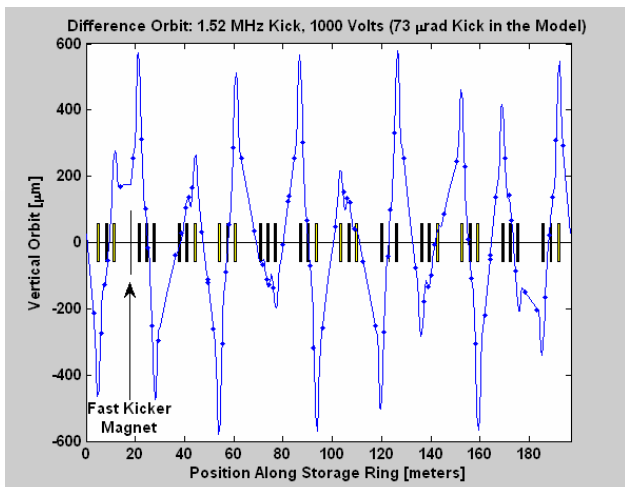

Fig. 4: Model (solid line) and measured (dots) difference orbit with the kicker at 1 kV.

When triggering the kicker every other turn, the effect at the synchrotron light monitor is quite obvious (Fig. 5). Fig. 6 shows the model orbits at the location of the light monitor for this case.

Fig. 5: Synchrotron light image when kicking every other turn.

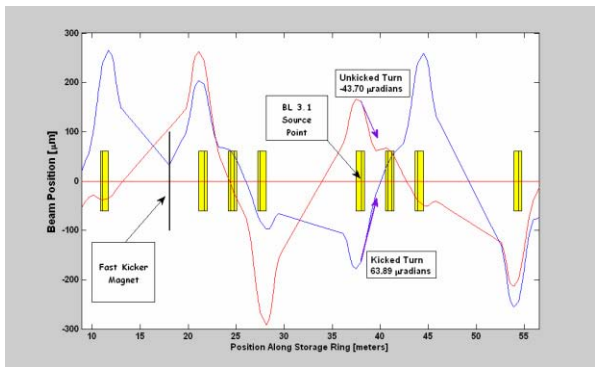

Fig. 6: Model orbits for each turn (1.5/2 MHz).

Reduce the Repetition Rate by 1.5/n MHz

If a beamline is not at favorable location with respect to a single kicker magnet in Sector 2 (Fig. 1), it may not be the end of the story. Being able to test this method on many different beamlines is extremely important. Instead of adding more kicker magnets, one can get interesting orbits by kicking at less than the revolution rate – 1.5/2, 1.5/3, 1.5/4, etc. When kicking at 1.5/n MHz it takes n turns for the orbit to close. Fig. 7 shows the closed orbits when kicking at 187.5 kHz (n=5). Since the electron BPMs measure the center of charge, the bottom plot in the figure compares the average of the 5 orbits in the model to the actual BPM measurement.

The picture gets quite confusing if one skips too many turns before kicking, however, this method can extend the reach of a single kicker magnet. For instance, a user in straight section six sees mostly an angle change in Fig. 1 but will see reasonable positional changes if kicking every fifth turn, Fig. 7.

Since the vertical fractional tune in the ALS is .2, kicking the bunch every fifth rotation will be in resonance with the beam. Basically, the $1/\sin(\pi\nu)$ term for a closed orbit change due to corrector blows up. If the tune was exactly .2, the bunch would be kicked out of the accelerator. However, if the tune is changed a small amount off .2, the kick will be just off resonance and a potential large amplification of the bump can be achieved. Fig. 7 shows the result for a vertical tune of 9.188. This factor of 3 amplification comes from $1/\sin(9.2\pi)$= -1.7 and $1/\sin(5*9.188\pi)$=-5.33 or 3.14 times the kick for free. There are two problems with using this method. First, all the different orbits in Fig. 7 may be a bit difficult to work with. That said, many of the beamlines would see one track which shows a large positional separation from all the other tracks. Second, the size of the orbit kick is directly dependent on the tune and the more amplification one tries to achieve the more sensitive it becomes to tune variation. For test purposes, one could also move the vertical tune to be on near resonance when kicking every 4th turn.

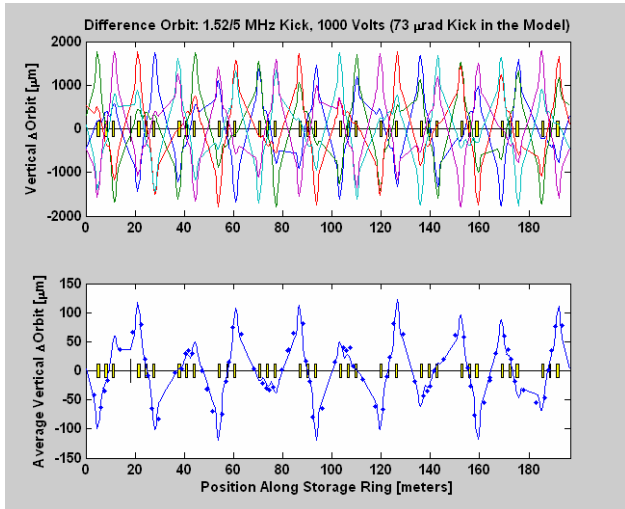

Fig. 7: Kicking Every Fifth Turn. Top plot shows the 5 model orbits. Bottom plot shows the average of the 5 model orbit as well as the actual difference orbits (dots).

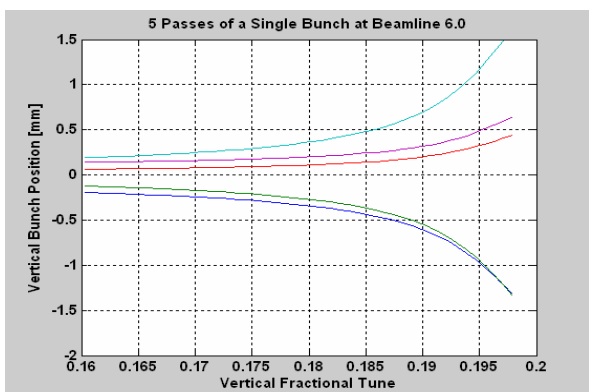

Fig. 8L Separation of the five passes vs. tune.

The first user experiment was done on beamline 6.0 (an insertion device BL located in the upstream end of sector 6 straight section). Fig. 8 shows the separation of the five separate passes of the singe bunch as a function of the tune. Fig. 9 shows the 1024 turns measured at a BPM just upstream of the beamline for various storage ring tunes. The turn-by-turn data is quite noisy however the separation of the different passes is quite apparent.

The profile of each of the five passes can be measured in the beamline using an avalanche photon diode, Fig. 10. The beamline data, the electron BPM data, and the model all agree reasonably well. However, Fig. 11 shows a limitation of this method. When the beam profile is measured at BL 6.0 for different tunes (this data was for pass #5), a large change in orbit is observed but the beam size also appears to change when approaching the resonant condition (.2 fractional tune). The cause of this increase is presently under investigation. A likely scenario is that the tune jitter translating to orbit jitter when sufficiently close to the resonances is too large. In the beamline orbit jitter looks like beam size blowup when integrating many turns with the APD. One particular power supply is responsible for most of the tune jitter in the ALS. It may be possible to improve the stability of this supply (or buy a new one).

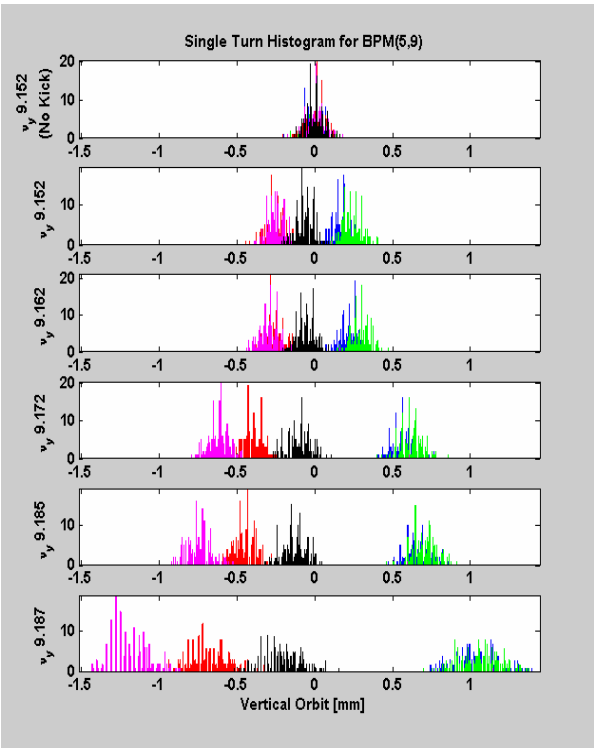

Fig. 9: Turn-by-turn BPM data for the 187.5 kHz (n=5) case. The vertical tunes are only approximate numbers.

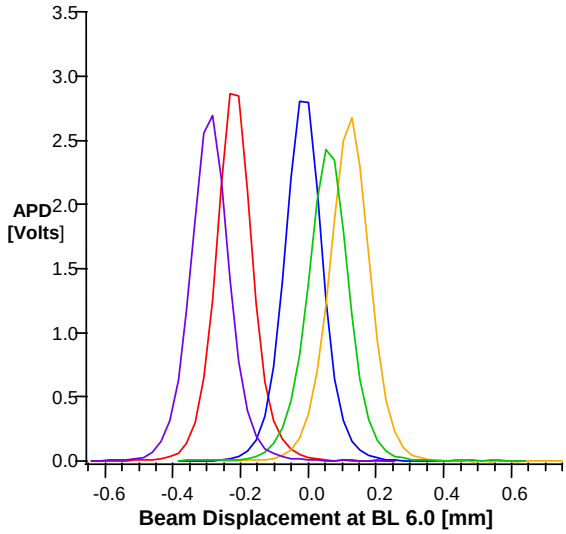

Fig. 10: Beam profile in BL 6.0 (tune ~9.162).

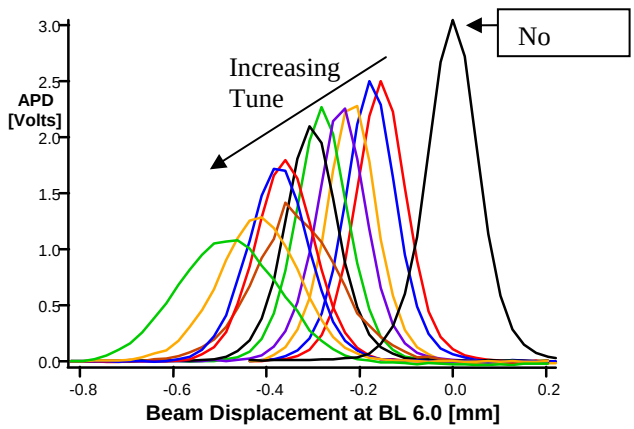

Fig. 11: Beam profile at different tunes for pass #5.

Repartition Rate Tradeoff

Unfortunately kicking at too low a frequency will produce some interesting but probably not useful beam characteristics. When kicking relatively slowly, a transient will be introduced which defuses in phase space (beam blowup) then finally damps back to the closed-orbit of the main bunch train.

The advantages of using a single magnet system is it takes up less than .5 m in the storage ring, it reaches a large number of users per kicker magnet, and it's relatively simple to operate. The disadvantage is it's a fixed frequency (1.5 MHz or a close fraction there of) and the fixed beam path may not be optimal for all users (or non-users). And the separation of the camshaft bunch from the main bunch train will vary depending on the beamline location.

FAST KICKER MAGNET DESIGN

The main parts of the fast kicker are the pulser and the magnet. The magnet is a stripline kicker similar to the fast feedback kickers which were designed at the ALS, Fig. 12.

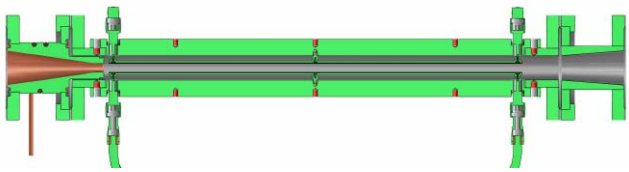

Fig. 12: Stripline Kicker

The pulser circuit provides the voltage to the kicker. The goal of the pulser is to supply high voltage when the camshaft bunch is present and zero volts the rest of the time. There was some hope of purchasing the pulser from industry but the 1.52 MHz requirement puts too big a heat load on all commercial units that were considered. For beamline requiring only 10 KHz or less repartition rate, there may be an off-the-shelf commercial unit with fast enough rise/fall time to meet the specification. However, running much less then 1.52 MHz can only be done using local bumps.

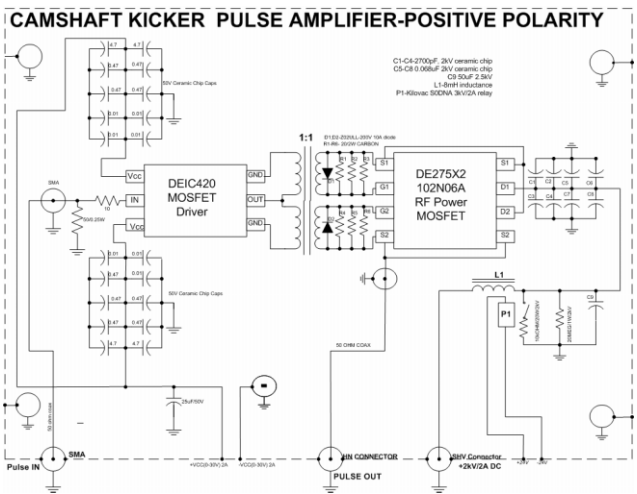

Fig. 13. Pulser Circuit (S. Kwiatkowski)

The circuit design for the pulser is shown in Fig. 13. It has a push-pull MOSFET pair that can run at 1.52 MHz (or less) and providing 1 kV between the electrodes (1 kW average power, 10 kW peak power). Fig. 14 shows the pulse shape. At 45 nanoseconds there is potentially some room to reduce the gap in the bunch train if that is desired in the future.

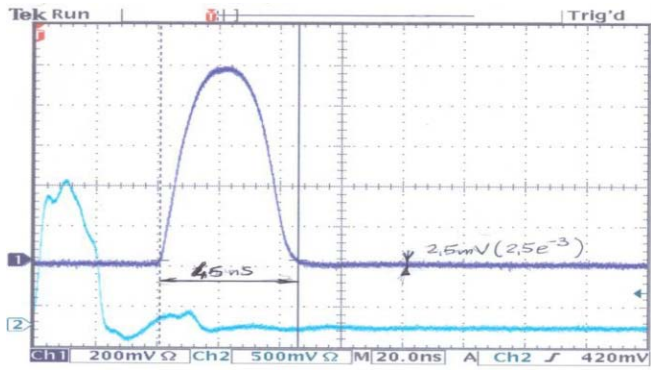

Fig. 14: Fast Kicker Pulse.

MORE TESTING

Depending on the operational mode and the location of the beamline with respect to the kick, there can be negative effects on beamlines using the multi-bunch beam. Since there are many beamlines with unique optics, it's difficult to predict the impact on every beamline. The next set of experiments with users at the ALS will be to study the benefits and contamination issues of this method.

ACKNOWLEDGEMENTS

We would like to acknowledge Brian Kincaid who suggested this approach many years ago and Janos Kirz for providing the support and encouragement to pursue it.

REFERENCES

[1] L. Blumberg, "VUV Wobbler," BNL Memorandum, May 29, 1980.
[2] G. Portmann, S. Kwiatkowski, D. Plate, J. Julian, R. Low, K. Baptiste, W. Barry, D. Robin, "Creating a Pseudo Single Bunch at the ALS," PAC, June 2007.
[3] G. Portmann, J. Kirz, S. Kwiatkowski, D. Plate, D. Robin, W. Barry, "A New Operational Mode at the ALS: Pseudo Single Bunch," 37th ICFA Advanced Beam Dynamics Workshop on Future Light Sources, Hamburg, Germany, May 2006.
[4] S. Kwiatkowski, W. Barry, J. Julian, R. Low, D. Plate, G. Portmann, D. Robin , "Camshaft Bunch Kicker Design for the ALS Storage Ring," EPAC'06.

ELECTRON BEAM DIVERGENCE MEASUREMENTS AT LOW ENERGIES USING A NOVEL OPTICAL DIFFRACTION RADIATION TRANSMISSION INTERFEROMETER

A.G. Shkvarunets, R.B. Fiorito, P. G. O'Shea, IREAP, University of Maryland, College Park, MD 20742, USA
J.G. Power, M.E. Conde and Wei Gai, ANL, Argonne, IL 60439, USA

Abstract

We have used an optical diffraction-transition radiation interferometer (ODTRI) in a transmission mode to measure the divergence of the low energy 8 MeV ANL-AWA electron beam. The interferometer employs a metallic micromesh first foil, which is used to overcome the inherent limitation due to scattering in the solid first foil of a conventional OTR interferometer, and an optically transparent dielectric foil. The interferences of forward directed ODR from the mesh and radiation from the dielectric foil is observed in transmission. This geometry allows a small gap between the foils (0.9 mm), which is required to observe fringes from two foils at low beam energies. The measured beam divergence is in a good agreement with that obtained using simulation code calculations. ODTRI measurements indicate that a single Gaussian distribution is insufficient to describe the angular distribution of the measured beam and that a second Gaussian beam faction or halo beam component is required to fit the data.

INTRODUCTION

Conventional OTRI cannot be used for low emittance beams because scattering in the first foil of the OTR interferometer dominates and obscures the beam divergence (1μm of Aluminium scatters 8 MeV electrons by RMS θ ~ 5mrad). To overcome this problem we have devised a perforated foil (mesh) – solid mirror foil reflection interferometer [1, 2] which is useful at moderate beam energies (E > 50 MeV).

For low energy beams the inter foil spacing ($L \sim \gamma^2\lambda$) is too small to observe the interferences of forward ODR from the mesh and backward OTR from the mirror in a standard reflection geometry. For example, at beam energy E = 8 MeV and λ = 632nm, L < 1 mm. To overcome this problem, we have developed a transmission interferometer [3, 4]. This interferometer uses a transparent dielectric foil as a second foil. The forward ODR produced by the mesh passes through the dielectric foil and interferes with forward radiation produced by the dielectric itself. A transport mirror is used to redirect the interfering radiations into the optical measurement system.

The radiation from the mesh is produced by two beam fractions: 1) unscattered electrons passing through the holes and 2) electrons heavily scattered in the mesh wires. Each component produces diffraction radiation ODR. Since no analytic theory for diffraction radiation from a matrix of holes in a metallic foil exists, we devised a simulation code (BEAMDR) to calculate the ODR from the two beam fractions.

A second code (CONVD) is then used to convolve the interferences of the ODR and OTR from the dielectric foil DOR with a given distribution of particle trajectory angles (typically a Gaussian distribution) and optical filter function. The latter is needed to produce distinct visible fringes for a given range of divergence. The essential part of code CONVD is the fitting procedure which varies the beam and interferometer parameters, and calculates the RMS deviation between the calculated and measured intensity distributions within some angular interval. The goal is to find a set of parameters which produces the minimum deviation. Beam divergence is one of the fitted parameters. A complete description of these codes is given in [2].

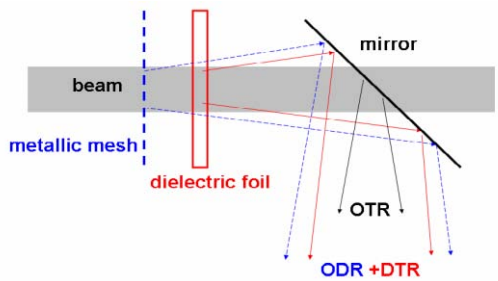

Figure 1: Mesh-dielectric foil interferometer.

There is a challenge in using dielectric foil in the interferometer, namely is to correctly prescribe the properties of optical dielectric optical radiation (DOR). In this work we use an additional measurement of OTR from metallic foil in order to "calibrate", the DOR from the kapton foil used in our interferometer and thus determine the parameters of the kapton foil.

EXPERIMENTAL SETUP

An ODR-DOR interferometer was designed and used to measure the electron beam divergence of the Argonne National Lab's Advanced Wakefield Accelerator

operating at 8 MeV. The average current of this machine is about 0.1 μA, and the repetition rate is 5 Hz.

A 5 μm thick, rectangular aperture nickel micromesh (2000 lines per inch, 12.7 micron period, 36% transparency) is the first foil and a ~ 9 μm thick Kapton foil with refraction index n ~ 1.8, the second foil. The transparency of the Kapton foil is ~ 95% at λ = 632nm. The inter foil spacing L ~ 0.9 mm. The wires of the mesh scatter electrons producing a calculated rms scattering angle of about 30 mrad which is much larger than the expected rms beam divergence, θ_{rms} ~2-4 mrad. The dielectric foil also produces a large amount of scattering (~ 10 mrad), but this does not affect the performance of the interferometer, since the phase and hence the interferences are primarily determined by the interfoil distance; see [3] for details.

The optical system is shown in Fig. 2. It consists of an aluminized silicon mirror mounted at 45 degrees w.r.t. the beam direction mounted in a vacuum chamber, a primary lens (diameter 76mm, focal length f_1 = 320mm), a second camera lens (f_2 = 105mm) and an interchangeable bandpass filter and a CCD camera. The second lens refocuses the image of the AD formed at the focal plane of the first lens onto the CCD. The distance between the interferometer and transport mirror is 220 mm, between the mirror and main lens is 150 mm, and between main lens and camera lens is 1880 mm.

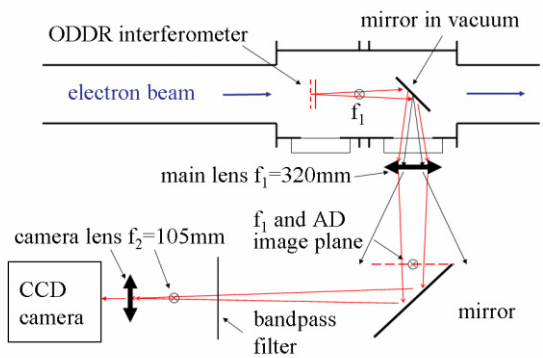

Figure 2: Experimental setup.

The light from interferometer is transported by the optics to the CCD camera lens, but the OTR from the transport mirror is heavily defocused by the main lens (distance mirror-lens = 150mm < f_1 = 320mm) and hence only a negligible fraction of the OTR produced by the mirror is accepted by the aperture of second lens.

An Apogee Instruments Inc., 16 bit, Peltier cooled, high QE CCD camera (model Alta E47) is used to acquire the interference patterns. The camera is equipped with an electronically controlled shutter which allows us to integrate the light produced from multiple electron beam pulses. An optical band pass (632 x/ 10 nm) filter is used to observe the interferences.

DATA FITTING CODES AND CALIBRATION OF FOIL RADIATION

In order to calculate the interference pattern produced by the ODR from the mesh and the dielectric foil radiation, we use code BEAMDR which is described in [1] and code CONVD, which is the modification of our original code CONV [1] to properly include the radiation from the dielectric foil.

The radiation from the dielectric layer is described by Pafomov's formula [5]. Alternatively, as a means of simplifying the calculations and the fitting procedure, we have previously shown [3] that dielectric foil radiation can be modelled as the interference of radiations from front and back interfaces of the layer assuming that each interface radiates as a perfect conductor. In contrast to OTR from a single interface, the amplitude of the thin dielectric foil radiation is proportional to $2-2\cos\left[2\pi n\beta d/\lambda(n-\beta)\right]$, where n is the refractive index and d is a thickness of the foil. Roughly speaking then, the thin dielectric foil can be considered to equivalently radiate OTR with an intensity amplitude factor which can vary between 0 and 4. As a result, a small uncertainty in the foil thickness leads to a great uncertainty in the intensity of the radiation.

Code CONVD includes the full radiation properties of the dielectric and also takes into account the refraction, reflection, attenuation and phase shift of radiation from the mesh within the dielectric foil. However, he exact values of thickness and refractive index of the dielectric foil are needed for CONVD. In order to find them we measured the OTR produced by the focused and accordingly heavily diverged 8MeV beam passing through a single metallic foil. Also we measured the radiation from interferometer produced by the same beam. Figure 3 shows the angular distributions of OTR and radiation from interferometer - red curves as well as the best fit distribution calculated by CONVD. The best fit of OTR takes place for an RMS angular divergence θx = θy = 21mrad. The best fit parameters of interferometer are: foil spacing d = 0.89mm, beam energy E = 8 MeV, scattered beam θx= θy = 24 mrad, unscattered beam θx= θy = 7 mrad, λ = 632nm, n = 1.8, d = 9.27μm. Note that the radiation from kapton is about 2.7 times larger than the OTR from a metal.

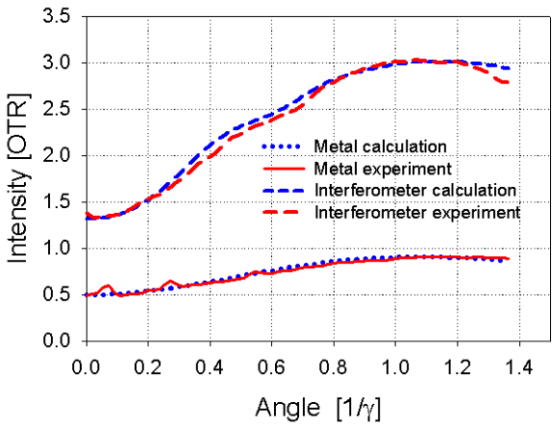

Figure 3: Measured and calculated radiation from metallic foil and interferometer produced by the strongly diverged beam.

EXPERIMENTAL RESULTS

The primary goal of this experiment was to demonstrate the capability of method to measure angular divergence of a low energy (8 MeV) electron beam. Doing the experiment we were primarily interested to see how the beam tuning affects the fringe visibility and accordingly, the angular divergence of the beam. The first tune was a beam sharply focussed in both X and Y . Accordingly beam had large angular divergence $\theta x = \theta y =$ 7 mrad and exhibited very small fringe visibility (Fig. 3). Then the beam was largely un-focused allowing the smallest angular divergence (Fig.4) and thus showed the maximum fringe visibility.

The last two tunes produced a horizontal or (X waist (Fig. 5) and a vertical or Y-waist (Fig.6) condition.

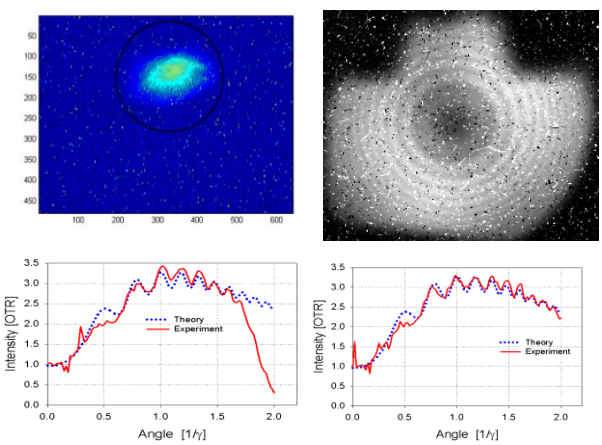

Figure 4: Unfocused beam (no-waist, solenoid only). Top – beam spot distribution (black circle is an interferometer aperture with diameter 15mm); top right – image of the angular distribution of intensity; bottom left and right are the horizontal-x and vertical-y scans of angular distribution

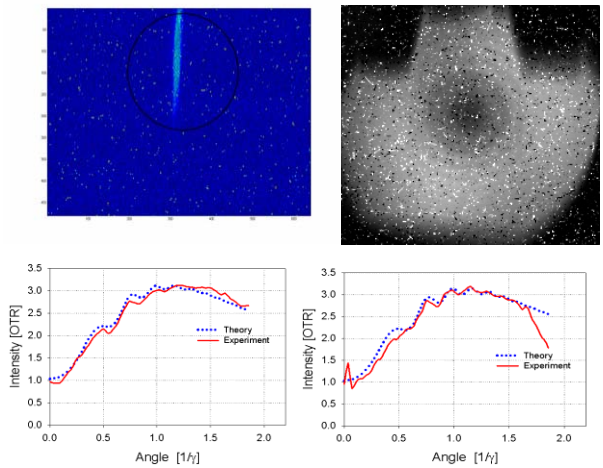

Figure 5: Same as Fig.4 for horizontally focused beam (x-waist)

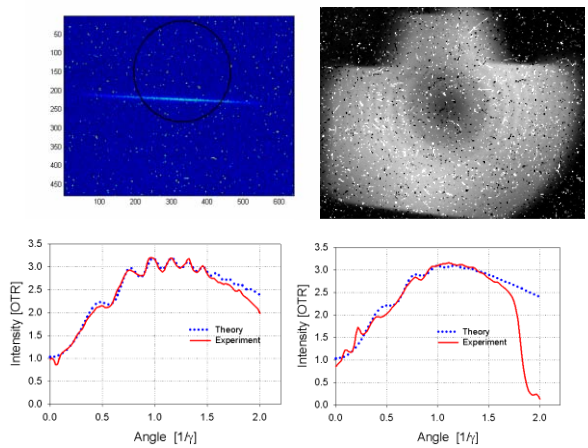

Figure 6: Same as Fig.4 for vertically focused beam (y-waist)

Horizontal and vertical line scans of the interference patterns were taken by averaging over the arcs to smooth the noise [2]. The sector averaged data scans are shown in Fig. 3, 4, 5 and 6 as red lines. The calculated distributions are also plotted in these figures as blue dotted lines for the set of parameters which gives the best fit for each scan.

The best fit parameters for the unfocused beam (Fig.4) are: interferometer foil spacing d = 0.89mm, beam energy E = 8 MeV, RMS angular divergence of the scattered fraction of the beam θs = 18mrad. The unscatterd beam is split to two Gaussian fractions: 1) a narrow angle component and 2) a wide angle (halo) component. The best fit parameters are: first beam fraction(62%), $\theta x = \theta y$=1.15 mrad; second beam fraction (38%) , $\theta x = \theta y$=6 mrad.

From Fig.5 and 6 it is seen that waist tuning of the beam increases the angular divergence and washes out the fringes. In two last cases the best fit requires the splitting the beam into two approximately equal fractions each with a different angular distributions. Best fit parameters for all cases are presented in Table 1.

Table 1. The measured best fit parameters of the beam.

RMS, mm, mrad	no-waist	x-waist	y-waist	double waist
X spot size	2.7	<0.2		<1
X divergence	1.15/6	3.3/6	1.75/8.4	7
Y spot size	2.1		<0.2	<1
Y divergence	1.15/6	3/6	4.6/8.4	7

Table 2. Simulated parameters for pulse duration 2.5 ps.

RMS, mm, mrad	no-waist	x-waist	y-waist
X spot size	2.7	0.068	
X divergence	1	7.5	
Y spot size	2.7		0.068
Y divergence	1		7.5

Table 2 shows the results of Parmela code simulation for the beam parameters. In the comparison of the observed and simulated beam note that the resolution of the imaging system used to measure the beam spot size was approximately 0.2mm. This means that we were not able to measure the spot size predicted by simulation with any accuracy.

Another restriction is that the simulated beam assumes a single component beam whereas the our fits to the angular data shows two component. Roughly speaking we cannot distinguish between these two components, i.e "core" and "halo". For instance, in the case of no-waste condition tune, the simulation result matches the small divergence component of the beam. In the cases of the x and y-waists, the simulations fit the large divergence component. In the case of double waist, it is likely that the simulation fits the observed beam if we assume that the double waist focusing is a linear combination of the x and y waist focusing.

CONCLUSIONS

We have successfully applied an ODR-dielectric foil transmission interferometer to measure the unperturbed angular divergence of a 8 Mev ANL-AWA electron beam. Simulation and fitting codes allowed us to fit the measured distributions and determine the RMS divergences of the beam. Also we have developed procedure which allows to measure required parameters of the dielectric foil.

REFERENCES

[1] A.G. Shkvarunets, R.B. Fiorito, P.G. O'Shea, , Nuc. Instrum. and Methods B 201, (2003), p.153-160.
[2] R.B. Fiorito, A.G. Shkvarunets, T. Watanabe, V. Yakimenko, D. Snyder, , Phys. Rev. ST Accelerators and Beams, **9**, (2006) 052802.
[3] R.B. Fiorito, A.G. Shkvarunets, and P .G. O'Shea, paper WPPG056, PAC 2003, Portland, OR, May 14, 2003.
[4] A.G. Shkvarunets, R.B. Fiorito, P. G. O'Shea, J.G. Power, M.E. Conde and Wei Gai, paper FRMPS034, PAC 2007, Albuquerque, USA, June 25 – 29, 2007.
[5] V.E. Pafomov, Proc. of the P. N. Lebedev Physics Institute, Consultants Bureau, New York, NY, V.44, (1971) pp.25-157.

OVERVIEW OF BEAM INSTRUMENTATION AND DIAGNOSTICS FOR THE NSLS-II PROJECT*

Om Singh#` and Igor Pinayev, NSLS-II Project, BNL, Upton, NY 11973, U.S.A.

Abstract

A new, ultra-bright 3rd generation light source, the NSLS-II Project, is planned to be built at Brookhaven National Laboratory. The light source being developed will have unprecedently small beam horizontal emittance and will provide the radiation sources with a brightness of 3×10^{21} photons/sec/0.1%BW/mm^2/mrad^2. In this paper we present the detailed specifications and a comprehensive description of the planned beam instrumentation system and the first results of the ongoing instrumentation R&D activities on beyond state-of-the-art subsystems.

INTRODUCTION

The NSLS-II project will be a state-of-the-art synchrotron radiation facility [1,2] featuring ultra-high photon brightness with extremely low emittance. It consists of a 170–270 MeV S-band linac, 0.2–3 GeV ramping booster, transport lines and 3 GeV storage ring [3,4,5] with the latest available beam instrumentation and diagnostics systems. The storage ring consists of 15 identical superperiods, each consisting of two mirror symmetric DBA cells. There are alternating ID straights of 8.6-m long with high horizontal β for injection, RF, damping wigglers (DW), and high flux user ID's; and 6.6-m long with low β for narrow gap ID's for high brightness X-ray beams. Top-off injection once per minute will be necessary to maintain the stored beam current at 500 ± 5 mA. The main beam diagnostics related parameters for the storage ring are shown below in Table 1.

Table 1: NSLS-II Storage Ring Parameters

Parameter	Nominal Value
Energy	3.0 GeV
Circumference	792 m
RF frequency	499.68 MHz
Harmonic number	1320
Revolution period, T_0	2.642 μs
Number of bunches filled	1056 (~80%)
Tunes - Q_x, Q_y	32.42, 15.15
Emittance Bare Lattice ε_0 (H/V)	2.05/0.01 nm-rad
Emittance with 8-DWs ε (H/V)	0.51/0.008 nm-rad
Bunch length, rms natural	2.9 mm; 10 ps
β-function at 8.6m ID (β_x, β_y)	20/3.0 m
β-function at 6.6m ID (β_x, β_y)	2.0/1.3 m
X,Y,E Damping times at 3 GeV	5.4/5.1/2.5 ms
Synchrotron frequency, f_s	3.0-3.6 kHz

*Work supported by the U.S. DOE under contract No DE-AC02-98CH10886
#singh@bnl.gov

To realize the benefits of the high brightness and small sizes of NSLS-II sources, photon beams must be exceedingly stable both in position and angle to the level of better than 10% of beam sizes and divergence. Table 2 provides the electron beam sizes and angular divergences for selected NSLS-II sources.

Table 2: The Electron Beam Sizes and Divergence

Types of source	8.6m ID	6.6m ID	Bend magnet	1-T 3-Pole wiggler
σ_x (μm)	108	29.6	44.2	175
$\sigma_{x'}$ (μrad)	4.6	16.9	63.1	14
σ_y (μm)	4.8	3.1	15.7	12.4
$\sigma_{y'}$ (μrad)	1.7	2.6	0.63	0.62

The most stringent beam measurement and stability requirement will be for the vertical position at the short ID source (σ_y=3.1 μm); this will require special consideration for measuring both electron and photon beams. Instrumentation requirements for measurements are further discussed in the storage ring section.

INJECTION DIAGNOSTICS

The diagnostics for the injection system will be procured with the subsystems with exception of beam transfer lines. The specifications for the required instrumentation will be provided for vendors by NSLS-II project team.

Linac

The linac beam instrumentation comprises two integrating current transformers for monitoring total bunch train charge and one fast current transformer (FCT) to monitor the distribution of charge. In routine operations, the beam trajectory will be monitored with three monopulse beam position monitors. Fluorescent screens will complement beam position monitoring during studies periods and for measuring beam emittance and energy spread at the linac exit. Wall current monitors formed by equally spaced broadband ceramic resistors mounted on a flexible circuit board, wrapped around a short ceramic break, will also give information on beam charge as well as longitudinal profiles of electron bunches. Linac diagnostics are summarized in Table 3.

Booster

The following booster beam parameters will be monitored:

- orbit,
- working point (tunes),
- circulating current and filling pattern,
- emittances for both planes,
- bunch length.

Table 3: Linac Diagnostics

System	Quantity	Monitor type	Beam parameter
Electron source	3	Wall current monitor	intensity, longitudinal beam characteristics
Linac	3	Fluorescent screen	position, profile
	2	Current transformer	intensity

Booster instrumentation is summarized in Table 4.

Six fluorescent screens will be installed to facilitate booster commissioning and troubleshooting. The screen material will be YAG:Ce, which has excellent resolution of the beam image and exhibits high sensitivity and high radiation hardness. Booster orbit will be monitored with 20 BPMs with turn-by-turn capability. The BPM receivers will be the same as in the storage ring, to simplify maintenance. The sum signal from the receivers can be used to monitor fast history of the beam current.

Table 4: Beam Instrumentation for the Booster Ring

Monitor	Quantity	Beam parameter
DC current transformer	1	Beam current
4-button pick-ups	20	Beam position, beam current
Fluorescent screens	6	Injection position, beam profile
Set of striplines and amplifier	2	Betatron tunes, bunch cleaning system
Fast current transformer	1	Filling pattern
Optical beamline with streak-camera	1	Bunch length
Firewire camera	1	Beam position, profile (emittances)

Circulating current will be measured with DCCT installed over ceramic break in the vacuum chamber, while bunch pattern will be monitored with a fast current transformer. For tune measurement, the electron beam will be excited with white noise using striplines. The beam response will be observed with a real-time spectrum analyzer connected to the dedicated BPM buttons with the front end. There will be an extra set of striplines for a bunch cleaning system, for users who need a specific fill pattern in the storage ring.

Synchrotron radiation from a dipole will be used to observe the beam during ramp and emittance measurements. The capability to monitor bunch length with a streak-camera will be also provided.

Transfer lines

Transfer line diagnostics will consist of monopulse BPMs for measuring beam position in the top-up mode, and fluorescent screens, which will provide information on beam position and size. After the septum in the storage ring injection straight there will be a screen with two active positions. At the first position the beam will be intercepted immediately after the septum. In the second position beam will be observed after the first turn. During regular operation this screen will be fully retracted. Integrating current transformers will provide information on beam charge at different locations and hence on the beam losses during the injection cycle.

STORAGE RING DIAGNOSTICS

RF Diagnostics

The beam diagnostics system is designed to provide a complete characterization of the beam and the accelerator system, including beam closed orbit, size, tune, circulating current, fill pattern, lifetime, chromaticity, beam loss pattern, beam density distribution, emittance, and bunch length. A large number of beam monitors/ drivers and beam loss monitors will be installed on the storage ring. The types and quantities of these devices are given in Table 5.

Table 5: NSLS-II SR Particle Beam Monitors (total number of cells = 30)

#	Beam Monitors/ Drivers	Quantity
1	DC Current Transformer	1
2	Fast Current Transformer	1
3	4-button pick ups	6 to 9 per cell
4	Stripline Monitors	2 sets 1 set = 4 electrodes
5	Stripline Drivers	2 sets – 1 set = 4 electrodes
6	PIN Diode Type Loss Monitors	2 per cell
7	Scintillation Loss Monitors	10
8	Scrapers	2 sets per plane 1 set = 2 blades

Circulating current DC measurement – A high-precision DC current measurement will be provided by using a commercially available radiation-hardened new parametric current transformer (NPCT). The NPCT device provides a resolution of better than 1μA/√Hz and has large dynamic range/ bandwidth, making it a versatile device for measuring lifetime and injection efficiency. Such a small noise will allow measurement of the expected 60 hours lifetime for 25 mA circulating in 1 minute with 2% accuracy (assuming a 1 Hz update rate).

Filling pattern measurement – A high-speed current transformer (FCT) will provide electrical signal proportional to the charge of individual bunches (bandwidth >1.75 GHz and rise time <200 ps). A fast ADC digitizer, sampling at RF or a multiple of RF frequency, will enable measurement of the fill charge distribution of each bunch. This information is critical for top-up operation to smooth out the fill pattern as much as possible.

Beam position monitors – Fig. 1 provides a layout of one cell, showing RF and X-ray beam position monitors and magnets. Each cell will have six standard RF BPMs mounted on elliptical chambers, up to three user RF BPMs located in the ID straight section; and up to two X-ray photon BPMs per beamline. The number of user RF and X-ray BPMs will be determined by the type of beamline. For example, a canted beamline will require three user RF BPMs.

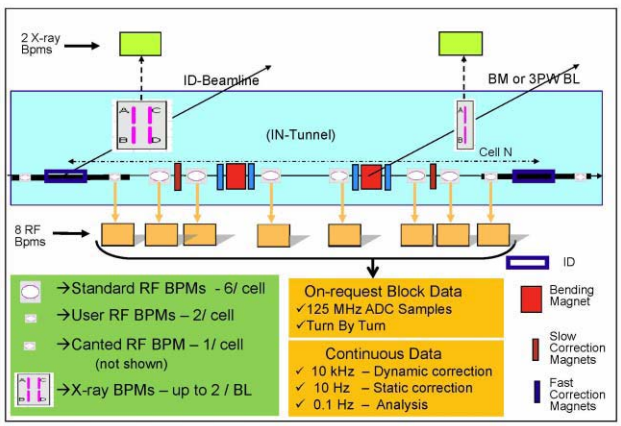

Fig 1: Layout of RF and X-ray BPMs and magnets in a storage ring cell

To achieve the highest level of orbit measurement resolution, the optimization of the button geometry for both standard and user BPMs is in progress [6]. The four high-precision pick-up electrodes will be mounted on elliptical or small-gap chambers with optimized button diameter size and geometry locations. Although, the vertical separation of buttons is pretty much defined by chamber vertical apertures, the horizontal separation of buttons will be optimized to obtain a high level of BPM resolution. The Table 6 provides sensitivities results with three cases of buttons' horizontal separation for elliptical chamber. Case 1, with 32 mm horizontal separation, can be achieved by using a commercially available 34-mm flange, but this results in the worst vertical sensitivity (0.04 mm^{-1}). As horizontal separation is reduced to 10 mm (case 3), vertical sensitivity improves three fold; however to achieve this separation, either BPM buttons mounted on 34 mm flanges have to be mounted longitudinally or custom flange, housing two buttons, needs to be developed. Other effects such as linearity and operational range will be further explored. Case 2, 18 mm of horizontal separation, may be an acceptable solution with two-fold improvement in vertical sensitivity. Although horizontal sensitivity reduces as horizontal separation reduces, the resolution requirement is less stringent in this plane.

Table 6: Sensitivities (Δ/Σ) vs. Horizontal Separation (Button Diameter=10mm; Vertical Separation = 25mm)

#	Buttons Horizontal Separation	Vertical Δ/Σ, mm^{-1}	Horizontal Δ/Σ, mm^{-1}
1	32 mm	0.04	0.12
2	18 mm	0.08	0.10
3	10 mm	0.12	0.06

The user BPMs will be located in the ID straight section and will require high mechanical and thermal stability. This is discussed further in the R&D section.

Commercially available, fast digital design based BPM electronics are being considered to meet various requirements and provides outputs such as 1) 125 MHz block and turn-by-turn block data for fast diagnostics, 2) 10 kHz data for fast orbit feedback, 3) 10 Hz data for slow orbit correction and 4) 0.1 Hz data for analysis and logging (shown in Fig 1). Table 7 gives a comprehensive position measurement resolution requirement within several time scales and intensity levels for standard BPM. The requirements for 100 mA to 500 mA are further subdivided, based on electronics and mechanical effects, so that there is a budget for each kind of effect. The

Table 7: Position Measurement Resolution Requirements

Parameters/Subsystems				Conditions	Standard BPM System Requirements	
					Vertical	Horizontal
Single bunch, single turn resolution (@378 kHz)				0.05 nC charge	500 μm rms	500 μm rms
				5.0 nC charge	20 μm rms	20 μm rms
Single bunch, stored beam resolution (0.017-200 Hz BW)				0.02 mA	10 μm rms	10 μm rms
				2.0 mA	1 μm rms	1 μm rms
100-500 mA stored beam resolution, 20-100% duty cycle	BPM receiver electronics	Assuming no contribution from bunch charge/fill pattern		0.017-200 Hz	0.2 μm rms	0.3 μm rms
				200-2000 Hz	0.4 μm rms	0.6 μm rms
				1 min to 8 hr	0.2 μm pk-pk	0.5 μm pk-pk
		Bunch charge/fill pattern effects only		DC-2000 Hz	0.2 μm rms	0.3 μm rms
	Mechanical motion limit at pick-up electrodes assembly (ground and support combined)		Vibrations	50-2000 Hz	10 nm rms	10 nm rms
				4-50 Hz	25 nm rms	25 nm rms
				0.5-4 Hz	200 nm rms	200 nm rms
			Thermal	1 min to 8 hr	200 nm rms	500 nm rms

resolution requirements for user BPMs are expected to be better by a factor of 2.

Tune measurement – The vertical and horizontal betatron tunes will be monitored using a network analyzer. The signal from the receiver pick-up electrodes will be combined with hybrids to produce vertical or horizontal signals, which will be down-converted below the revolution frequency and fed to the input of the network analyzer.

Transverse feedback – A broadband signal, measuring the position of the individual bunches, will be provided by the stripline monitors. It will be sampled at 500 MHz fast ADC, and a digital filter will calculate the correction. The correction kicks, using a DAC, will be fed through a broadband amplifier and drive the electron beam using the second set of striplines. The detailed design of the striplines and a feedback system is in progress.

Loss monitors – NSLS-II will utilize a distributed beam loss monitoring system based on p-i-n diodes, which are commercially available. Two beam loss monitors per cell will be used for monitoring the special distribution of beam losses. For the temporal distribution of the last particles (on the scale of one turn) scintillation detectors (10) will be used. These can also be used for monitoring the losses of injected electrons near the injection and RF straights.

Scrapers – Two pairs of two-plane adjustable-position scrapers will be installed on the ring to be used both as protective devices as well as diagnostics instruments for accelerator studies. One set of scrapers (H/V) will be installed in the dispersive section to measure the energy distribution of the electron beam. Another set will be installed in a straight section with zero dispersion in order to have information on the transverse size of the electron beam, and to eliminate possible beam halos capable of affecting the insertion devices.

Photon diagnostics

The photon diagnostics for the NSLS-II storage ring will utilize visible and X-ray synchrotron radiation generated in a bending magnet and insertion devices. Table 8 shows the types and quantity of optical diagnostics for the NSLS-II storage ring.

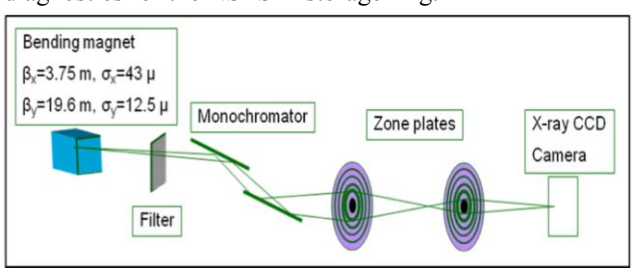

Fig 2: Emittance monitor layout with two zone plates

For measuring the ultra low vertical emittance of the storage ring, we included in the baseline design the direct imaging of the electron beam with two zone plates. This method was developed at KEK [7] for measuring ultra small beam sizes. A double crystal monochromator selects the observation wavelength. The first zone plate focuses the monochromatic beam to small spot, while the second zone plate magnifies the image, making it suitable to observe by X-ray CCD camera. The optical setup is shown in Fig. 2.

The pinhole camera will utilize synchrotron radiation from a three-pole wiggler [8]. Its main function will be measurement of the electron beam energy spread and monitoring vertical beam size. Presently, we are optimizing the design of the pinhole camera beamline (see Research and Development section). If the obtained resolution will be sufficient, we will be able to measure vertical emittance with it.

Table 8: Complement of the optical diagnostics for the NSLS-II storage ring.

Monitor	Quantity	Function
Emittance monitor	1	Emittances in the both planes
Streak-camera	1	Bunch length
Pinhole camera	1	Beam size, energy spread
Photon BPMs	Up to 2 per BL	Position (angle) of ID radiation
Diagnostics undulator with pinhole camera	1	Horizontal emittance, energy spread, momentum compaction factor
Firewire camera	1	Beam profile

A double-sweep streak-camera will be used to measure the longitudinal beam dynamics. Its versatility and high sensitivity make it an excellent choice for monitoring the bunch length with high resolution and studying beam instabilities. The synchroscan feature provides low-phase jitter for synchronous summing of signals and tracking phase dynamics. The dual sweep is also available. We are considering to utilize either Optronis model SC-10 or Hamamatsu C5860 streak-camera.

Photon beam position monitors (PhBPMs) made by FMB-Berlin (shown in Fig. 3) are being considered for monitoring radiation from the insertion devices. The blades, of course, will be designed and optimized to suit the requirements of NSLS-II.

Fig. 3: Photon beam position monitor.

The PhBPMs are based on a development by Dr. Karsten Holldack at BESSY. The information obtained on the position of the photon beam will be incorporated into the orbit feedback system to provide the beam stability

required for user applications. In the baseline design we have one PhBPM per beamline. The PhBPM assembly will be mounted on a stable post and its location (elevation and transverse position) will be adjusted with 2D translation stages. Similar devices at APS enable pointing stability of the photon beam with peak-to-peak drift of less than 2 μrad over six days [9].

An IEEE1394 (Firewire) camera will be used to observe the visible radiation from the electron beam. Such an approach eliminates the need for a frame-grabber and makes display of the beam on the control computer straightforward. The camera has an external trigger capability and exposure control from 10 μsec to 5 sec.

The diagnostics undulator will allow independent measurement of the energy spread and horizontal emittance. The momentum compaction factor can be also measured. We plan to utilize one of the user beamline undulators in a 5 m straight; therefore, this tool is not included in the baseline design. This beamline will be equipped with an additional high-resolution fluorescent screen and a retractable pinhole. Use of the radiation from the undulator for diagnostic purposes will be restricted to periods when it is not needed by the users.

RESEARCH AND DEVELOPMENT

The beam diagnostics research and development program is aimed at the most critical items for the NSLS-II project: beam stability and low emittance. Research on beam stability includes the evaluation of BPM receivers and the development of ultra-stable support for "user" BPMs surrounding insertion devices.

The user BPM consists of a special BPM block with BPM buttons, cooling fins and end flanges (Fig. 4). This assembly is mounted via four invar rods to the BPM support stand, made from carbon fiber composite. A carbon fiber composite can have thermal coefficient as low as 0.2 μm/m/^{o}C. With tunnel temperature controlled to 0.1^{o}C, one meter BPM stand will have a thermal expansion of no more than ±20 nm.

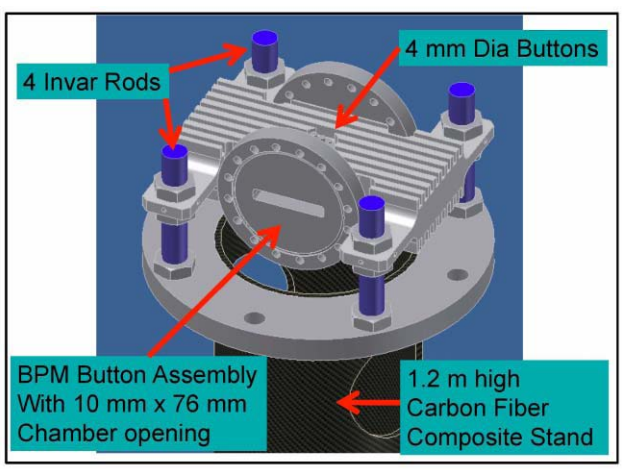

Fig. 4: User BPM support stand with a BPM block mounted at its mid-plane

The second focus of diagnostics R&D concerns an evaluation of ability for robust measurement of beam parameters. The vertical beam emittance of the electron beam will be extremely small to provide synchrotron radiation sources with diffraction limited size. The pinhole camera using a three-pole wiggler as a light source will provide measurement of energy spread and possibly also has sufficient resolution for measurement of vertical emittance [8]. The original plan was for emittances to be measured with a zone plates imaging system utilizing synchrotron radiation from a bending magnet. During R&D we will evaluate the replacement of this system with a less expensive and more robust pinhole camera as well, providing it has sufficient resolution with feasible design.

SUMMARY

We have presented an overview of beam instrumentation and diagnostics for the NSLS-II project. The critical diagnostic systems, addressing beam stability and low emittance monitoring, are being investigated in the FY08 R&D program. Preliminary simulations optimizing the RF BPM buttons have been completed, providing insight into the selection of RF button geometry for prototype assembly. Preliminary design on various diagnostics systems has begun.

REFERENCES

[1] S. Ozaki, et al, "Philosophy for NSLS-II design with sub-nanometer horizontal emittance", Proc. of PAC07, Albuquerque, New Mexico, USA.
[2] http://www.bnl.gov/nsls2/project/CDR/
[3] J. Rose, et al., "Design consideration of the NSLS-II Injection Linac," Proc. of PAC07, Albuquerque, New Mexico, USA.
[4] T. Shaftan, et al., "Conceptual design of the NSLS-II Injection," Proc. of PAC07, Albuquerque, New Mexico, USA.
[5] N. Tsoupas, et al, "Design of beam transfer lines for NSLS-II; Proc. of PAC07, Albuquerque, New Mexico, USA.
[6] I. Pinayev and O. Singh, "Evaluation of BPM button geometry for NSLS-II project," NSLS-II Technical Note.
[7] K. Iida, et al., "Measurement of an electron-beam size with a beam profile monitor using Fresnel zone plates," Nucl. Instr. and Meth. A506 (2003), pp. 41-49.
[8] I. Pinayev, "Evaluation of pinhole camera resolution for NSLS-II project," these proceedings.
[9] G. Decker and O. Singh, "Beam Stability at the Advanced Photon Source," Proc. of PAC 2005, pp. 3268–3270

LOW ENERGY BEAM DIAGNOSTICS AT THE VENUS ECR ION SOURCE*

D.S. Todd#, D. Leitner, and M. Strohmeier, LBNL, Berkeley, CA 94720, U.S.A.

Abstract

A dedicated effort to accurately simulate beam extraction and transport from the superconducting electron cyclotron resonance (ECR) ion source VENUS (Versatile ECR for NUclear Science) using particle-in-cell methods has been underway at Lawrence Berkeley National Laboratory (LBNL). The wide range of beam diagnostics used along the VENUS transport system has been essential in benchmarking simulation against experiment. Measurements with some of these devices are presented and are compared with simulation.

INTRODUCTION

The fully-superconducting electron cyclotron resonance (ECR) ion source VENUS at LBNL serves as the prototype injector for the future radioactive ion beam accelerator in the United States [1]. Additionally, a dedicated effort at LBNL has been underway to develop a highly-adaptable, particle-in-cell simulation code to serve as a design tool for future sources and accelerators [2]. Benchmarking simulations against experiment plays a crucial role in model development, and for this reason the transport system for the VENUS ion source has been outfitted with a wide range of diagnostic devices.

Plasma confinement in an ECR ion source is provided through the superposition of solenoidal and sextupolar magnetic fields. Solenoids at each end of the source and a surrounding sextupole produce a confining magnetic field whose magnitude increases in all directions from the source center. This source-centered minimum is surrounded by a series of closed surfaces of constant magnetic field magnitude, and by supplying microwave heating at a frequency matching the electron cyclotron frequency on one or more of these surfaces electrons can be resonantly heated to produce and maintain a plasma through step-wise ionization.

Though the field geometry in ECR ion sources has proven very effective for producing high-current, multiple-charged ion beams, there are inherent characteristics of these sources which make difficult both analysis and simulation of extracted beams including:

- Superposed magnetic field confinement produces asymmetric plasma distributions at extraction
- Plasma is maintained through step-wise ionization, therefore extracted heavy ion beams are typically composed of thirty or more ion species
- Positional distribution of different ion species at the plasma extracting face is unknown
- Beams are extracted at a peak solenoidal magnetic field of up to 3 tesla which falls to zero over the first half-meter of travel giving each extracted ion species a different dynamical behavior
- Beam space charge self fields must be taken into account

From the outset, beam diagnostics have played an important role in the improvement of VENUS ion beam models. As an example, initial simulations of ion distributions at the plasma aperture indicated that while the plasma distribution had a triangular cross section, as expected, this distribution was much larger than the 8-mm diameter beam extraction aperture, was homogenously filled, and should have resulted in an axially-symmetric extracted beam. However, as can be seen in figure 1, imaging of a single species ion beam (He^+) on a 0.25-mm thick tantalum sheet just after extraction shows a triangular cross-section, making it clear that the initial conditions used for the simulation were invalid. As the initial ion beam distribution at the source extraction aperture is unknown and cannot be directly measured or computed, we are using various ion beam diagnostics to refine our simulation model as described in the following sections.

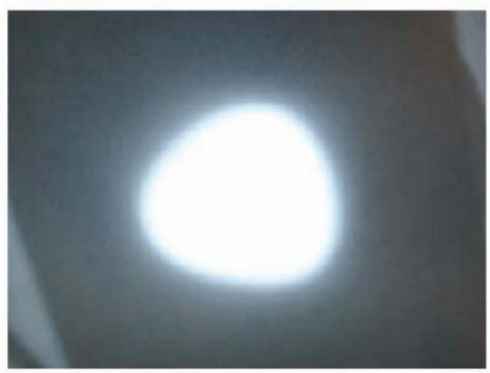

Figure 1: Beam imaging of a He^+ beam with the tantalum sheet, left, shows triangular beam structure 80 cm after extraction.

PARTICLE-IN-CELL SIMULATION OF VENUS EXTRACTION AND TRANSPORT

The layout of VENUS and its accompanying beam transport system are shown in figure 2. Beams are extracted across potentials of up to 30 kV, and the shape of the extracting surface of the plasma can be optimized by a movable accel-decel extraction system. A solenoid lens and a mass analyzing dipole magnet serve as the only two optical elements after the source when used for ion

* Work supported by the Director, Office of Energy Research, Office of High Energy & Nuclear Physics, Nuclear Physics Division of the U.S. Department of Energy under Contract DE AC03-76SF00098
#dstodd@lbl.gov

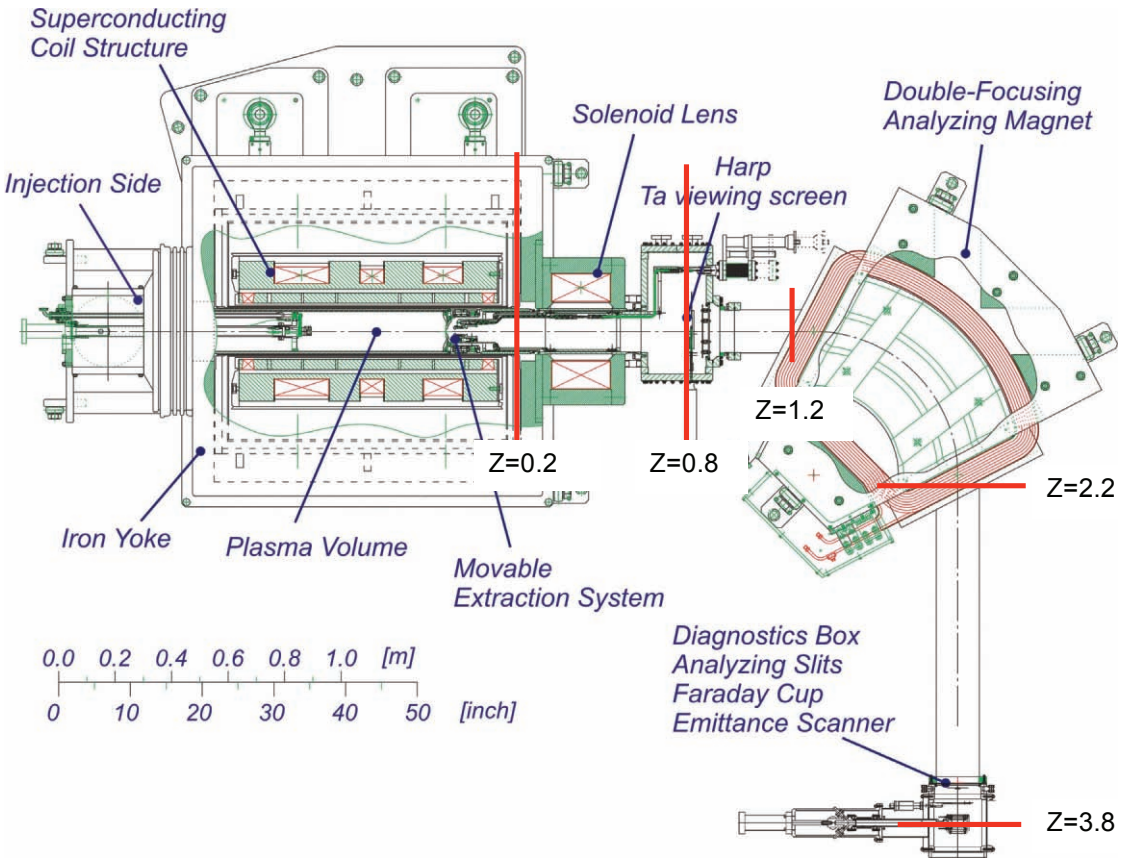

Figure 2: VENUS ion source and transport system layout viewed from above. The indicated lines indicate points at which beam profile measurements will be compared with simulation in the following sections.

beam analysis. The result of this layout is that there are two primary diagnostic regions for the VENUS system: the first is located between the solenoid lens and the analyzing dipole, and the second is located after the analyzing dipole. As the first region is located before the dipole, all ion species are present in the beam complicating analysis greatly. After the dipole magnet analysis is simplified by the presence of only one ion species, but the strong beam asymmetries introduced to this ion species by those charge states over- or under-bent in passing through the dipole complicate the post-dipole beam as well.

Particle-in-cell (PIC) modeling was chosen as the method of simulation for the VENUS system as PIC codes are capable of accurately simulating systems made up of multiple types of interacting particles [3]. The three-dimensional PIC code WARP is well-tested in beam transport modeling and capable of simulating beam transport including both external and self electromagnetic fields [4]. We have enhanced this code by adding a three-dimensional plasma extraction model to allow for the simulation of multiple-species ion beams from asymmetric plasma sheaths. With the addition of this extraction model it is now possible to use WARP to simulate the entire transport system including the plasma extraction in one self-contained code.

For simulations of the VENUS transport system the cross section of the plasma at extraction has been set using field line tracing from experimentally-measured, highly-localized plasma ion sputter marks on the source chamber surface [2]. This method assumes that the ions sputtering the chamber are representative of the ion distribution throughout the source along field lines. In other words, scattering between the plasma and chamber walls doesn't largely affect the measured distribution and it can be as an indicator of the distribution within the plasma. This method of tracking field lines from sputter marks has the distinct advantage that it leads to a triangular ion distribution at the extraction plane that is smaller than the aperture based on measurable properties. The simulations shown in figure 3 are cross sections at the four locations along the transport system indicated in figure 1 for a multi-species and multiple charge state oxygen beam (primarily oxygen with hydrogen and carbon impurities) where a constant triangular distribution based on the plasma sputter marks has been assumed for all ion species.

BEAM DIAGNOSTICS

Viewing screens before dipole

The tantalum viewing screen discussed in the introduction is very useful for imaging single species ion beams of sufficient current to heat the tantalum to glowing. However, for multi-species beams the rotation of the various ion species upon extraction blurs out the

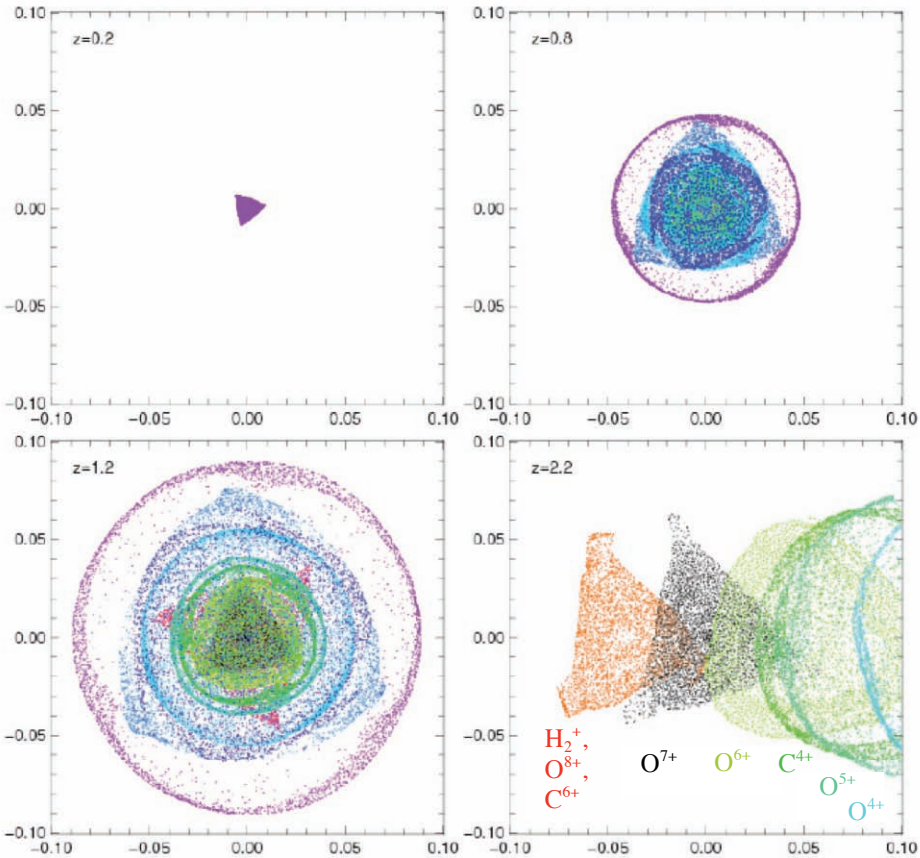

Figure 3: Simulated beam cross sections are plotted for a multi-charge state oxygen beam at four locations along the VENUS transport system: 0.2, 0.8, 1.2, and 2.2 m after the extraction aperture from left to right, top to bottom, respectively). Different colors represent different oxygen charge states and the axes are of meter scale. The development of hollow beams for some species can be seen beginning at 0.8 m, and beam separation immediately after the magnet is clear at 2.2 m.

triangular structure using this method. Therefore, in addition to the tantalum we have used quartz viewing screens that can be inserted into the beam line both before and after the analyzing dipole. As can be seen in figure 4 where the quartz was inserted at 0.8 m after extraction, the triangular structure for multiple ion species is visible for the imaged oxygen beam. In particular, figure 4 should be compared to the simulation shown in figure 3 at 0.8 m.

Beam profile measurement (harp)

Quantitative current density distribution measurements before the analyzing dipole are performed with a harp scanner composed of 62, 0.1-mm diameter wires contained in a 5.0 cm square window, with half of the wires running in parallel to the vertical and half parallel to the horizontal directions.

To investigate beam asymmetry from the VENUS source we extracted single component, He^+ beams in two modes: normal operation and an operational mode with the confining sextupole magnets turned off. In turning off the sextupole the resulting plasma is axially symmetric (axial mirror field only), however this mode is not used for typical operation as the plasma confinement, and hence performance, is greatly reduced.

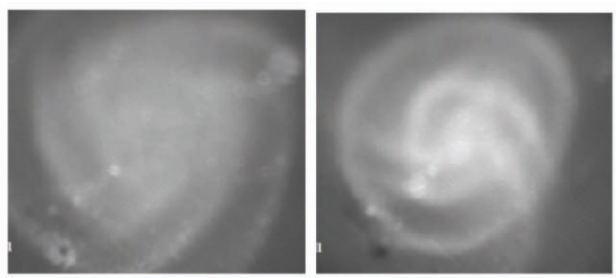

Figure 4: Beam imaging of an oxygen beam using the quartz viewing screen 80 cm after extraction for two solenoid lens current settings: 400 A, left and 500 A, right. Multiple ion species are visible as rings and triangular structure which rotate and focus with increased lens current.

Figure 5 shows measurements with the harp of the beam cross section in the vertical and horizontal

directions when producing a He^+ beam with the sextupoles off for two settings of the solenoid lens. As can be seen in this figure, the measured beam is symmetric and decreases in width as the solenoid lens current is increased (beam is focused).

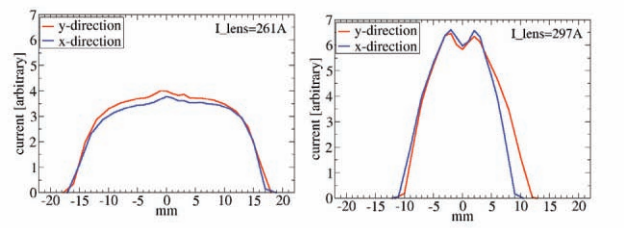

Figure 5: He^+ current density profile measurements in the horizontal and vertical directions using the harp for two solenoid lens currents when the source is operated without the sexutpole resulting in an axially symmetric beam. The small tip in the middle of the profile is believed to be the overfocused, low-current He^{2+} component of the beam.

Energizing the source sextupole produces the measurable beam asymmetry of a triangular beam which rotates and shrinks with increasing focusing strengths of the solenoid lens. Figure 6 shows the measured horizontal profile with the sextupoles on for two solenoid settings along with simulation of the same beam. Reasonable agreement between experiment and simulation were achieved at this location.

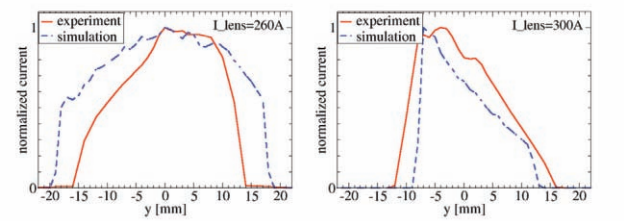

Figure 6: Simulated He^+ current density profiles, dashed, compared with experimental measurement at the harp, solid, for two solenoid lens current settings

Degree of neutralization

Ionization of background gas by the passing beam produces both low energy electrons and ions inside of the beam envelope. These new electrons can be confined by, and effectively reduce, the beam's positive potential, while the newly created ions are ejected from the beam because of the beam potential. We have designed and constructed two retarding potential analyzers, shown in figure 7, to measure the kinetic energy of the ejected ions by measuring the stopping potential distribution for these ions. The devices have three meshes and an electrically isolated plate which is used to measure the ion current. The mesh nearest the beam is at the beam line potential (ground), the voltage of the second is varied to measure the stopping potential of the ions, and the third and closest to the measuring plate is biased negatively to prevent secondary electrons created by ion impact from leaving the measuring plate.

Using an early prototype version of this device at normal operating pressures (~10^{-8} torr) preliminary data showed that stopping potentials were near those one would expect for a beam with no electrons screening the beam space charge, and that the stopping potential decreases significantly as the pressure is raised, as can be seen in the curves plotted in figure 7. This result indicates that although the beam is operated for up to weeks at a time in CW mode (allowing for electron buildup in the beam), the loss rate of confined electrons must exceed the rate of their trapping. However, these surprising results need to be confirmed with the higher resolution energy analyzers.

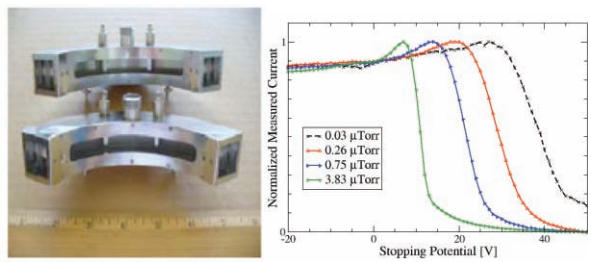

Figure 7: Retarding potential analyzers, left. Measurements of the measured ion current as a function of stopping potential are plotted at right.

Imaging of mass analyzed beams

After the dipole only one species is present, therefore beam analysis is made much simpler. Using a quartz viewing screen mounted at the end of the transport system individual ion species from multiple species beams are imaged. Figure 8 shows an O^{7+} beam imaged on the quartz viewing screen located at z=3.8 m along with the same beam from simulation.

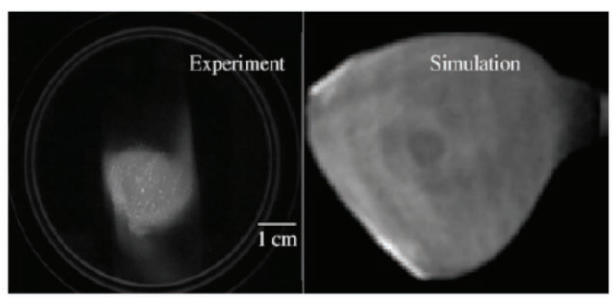

Figure 8: Experimentally imaged O^{7+} beam, left, and the simulated current density plot, right, on the same scale.

As can be seen in figure 8, the general shape of the O^{7+} is reproduced in simulation after passing through the analyzing magnet, but the beam sizes are not in agreement. Imaging and simulation of a C^{4+} from the same extracted beam are shown in figure 9, and once again there is a mismatch in size although the hollowing feature present in the experimental beam is also seen in simulation. Further investigations are needed to determine the source of this discrepancy.

Emittance measurement of mass analyzed beams

In this location quantitative phase space measurements are taken using a pair of Allison-type emittance scanners [5], one aligned horizontally and one vertically to measure x-x' and y-y' distributions. With these devices it has been found that the measured emittance decreases with charge state, whereas analysis of expected emittance growth due to beam extraction in a magnetic field would increase with charge state [1]. This reduced emittance with charge state could be due to smaller initial distributions for highly charged ions at extraction. Alternatively, the hollowing that has been found to occur for low charge state beams [2,6] would decrease emittance with charge state. This hollowing effect can be seen in the simulations in figure 2 at z=2.2 m, where the lower charge state beams, moving right, have hollow distributions while the higher charge state beams, moving left, are closer to constant density.

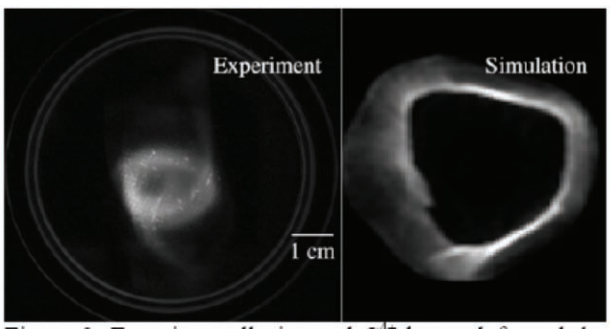

Figure 9: Experimentally imaged C^{4+} beam, left, and the simulated current density plot, right, on the same scale.

Pepper pot---under development

Pepper pot emittance measurement systems have long been in use allowing for the simultaneous measurement of both x' and y' distributions for each hole of the utilized mask [7]. By measuring these distributions over a number of different holes it is possible to obtain a full four-dimensional phase space current density distribution of an ion beam, $f(x_i,y_j,x',y')$, whereas our slit scanners cannot measure transverse correlations. Having this capability is especially important for ECR sources for phase space measurement of measured hollow beam structure, as this hollow structure is much more difficult to extract without cross-correlated phase space information (x-y, x-y', or y-x').

To add this diagnostic capability, a pepper pot system for the VENUS beam line composed of a hole mask, fluorescing material, and CCD camera is under development. We are currently testing hole mask sizes and shapes as well as necessary distances between the mask and the fluorescing material. We have tested three fluorescing materials (quartz plates, Ba_2F, and KBr crystals) and have found the KBr crystals to have the best light response. A measured O^{4+} beam incident on a KBr crytal with a test hole mask is shown in figure 10 along with an analyzed spot showing measured spot structure.

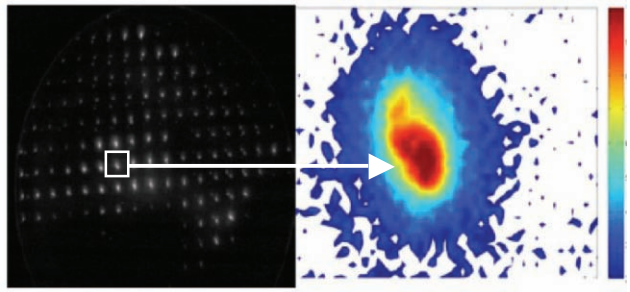

Figure 10: Pepper pot test image of O^{4+} beam, left, with a beam spot's analyzed brightness distribution, right.

FUTURE MEASUREMENT AND SIMULATION

Using the diagnostics we have at present we have found qualitative agreement between experiment and simulation for beam analysis both before and after the dipole with overall shapes and features found experimentally appearing in simulation. However, there are clearly disagreements with regards to properties such as beam size. One free parameter in simulation that needs to be investigated is the level of beam potential screening along the beam line. In simulations to date we have assumed zero beam neutralization as measurements with the retarding potential analyzer have indicated stopping similar to those expected analytically for a nonneutralized beam. However, this analytical check has been done using the approximation of a round beam with a total effective current related to the total extracted current. With the three dimensional extraction simulations it is possible to get a better approximation for the potential at the beam center (and hence necessary stopping potential) for a nonneutralized beam and adjust the level of neutralization accordingly.

Additional simulation improvement will come with the installation of the finalized pepper pot design. Use of this device before the dipole with a simple beam such as He^+ will allow a better understanding of initial conditions while after the dipole it will yield more complete distribution information to investigate beam hollowing.

REFERENCES

[1] D. Leitner, C.M. Lyneis, S.R. Abbott, Nucl. Inst. Meth. B **235**, (2005) 486.
[2] D.S. Todd, D. Leitner, C.M. Lyneis, and D.P Grote, Rev. Sci. Instrum. **79**, 02A316 (2008).
[3] C.K. Birdsall, IEEE Trans. Plas. Sci. **19**, 65 (1991).
[4] Alex Friedman, David P. Grote, and Irving Haber, Phys. Fluids B **4**, 2203 (1992).
[5] D. Wutte, M.A. Leitner, C.M. Lyneis, Physica Scripta **T92**, (2001) 247.
[6] G. Machicoane, et. al., Rev. Sci. Instrum. **79**, 02B714 (2008).
[7] L.E. Collins and P.T. Stroud, Nucl. Instrum. Meth. **26**, (1964) 157.

PHASE MEASUREMENTS FOR GANIL AND LANL

B. Baricevic, T. Karcnik, Instrumentation Technologies, Solkan, Slovenia

Abstract

Libera Brilliance has proved successful in the field of beam diagnostics. High performance, system reliability and its high level of integration into accelerator control systems makes Libera a very accurate, robust and powerful measuring system. Although Libera Brilliance has been developed mainly for applications involving frequency domain processing, the flexibility makes it a good time domain measuring system for single pass applications. Moreover, there are other applications dealing with pulses, where a modified version of Libera Brilliance can be used. This is the case of beam phase and position measurements in accelerators, like Spiral2 (Ganil) and LANSCE (Los Alamos), dealing with heavy particles (protons, deuterons and heavy ions). The phase information extracted by the measurement in such systems is used to control the acceleration process of such heavy particles. This paper shows the approach adopted in processing the signals produced by such bunch trains. A modified Libera Brilliance unit, configured for the LANSCE bunch trains, has been tested by means of extensive laboratory measurements. Performance has been evaluated by applying different digital signal processing.

INTRODUCTION

Libera Brilliance is a very accurate beam position measuring system. Although its performance was improved for applications in circular electron machines, the Libera Brilliance processing structure is flexible enough to fulfil the requirements of applications requiring an accurate signal measurement in time domain too.

The scope of the phase measurement is to control the acceleration processes of heavy particles. Two applications with similar requirements for the beam position and phase measuring system were taken as reference.

The first application is the LANSCE linac, where bunches of H^+ and H^- are accelerated. The bunches in the fundamental scheme have a repetition frequency of 201.25 MHz and are grouped in 0.625 ms long "macropulses" at the repetition rate of 30 Hz that results in a duty factor of 1.875%.

The second application is the Spiral2 linac (Ganil), where the deuteron or ion bunches are accelerated with bunching frequency of 88.0505 MHz, and are organized in "macropulses" with minimum duration of 100 us and repetition rate between 1 and 10 Hz. The minimum duty factor is in this case 0.01 %.

Table 1 compares the mentioned parameters for the two applications. The very low duty factors indicate that the signals produced by such beam signals need a time domain processing scheme, since the power is spread between the "macropulse" repetition rate harmonics.

Table 1: Macroplulse structure comparison

	LANSCE linac	**Spiral 2 linac**
Bunch rep. rate	201.25 MHz	88.0505 MHz
Macropulse length	0.625 ms	>0.1 ms
Macropulse rep. rate	30 Hz	1÷10 Hz
Duty factor	1.875 %	>0.01 %

The particles with the specified time structures cross stripline BPM pickups and excite bipolar pulses on four coaxial lines. The bunch repetition rate defines the main frequency component. Since the BPM pickup is time-invariant, the beam longitudinal shifts with respect to the RF reference are linearly transformed into a phase deviation of the main frequency component from the RF reference and therefore a phase measurement of the fundamental frequency can be used to adjust the set points of the LLRF system that controls the acceleration process.

MEASURING SYSTEM REQUIREMENTS

An amplitude and phase measurement is performed on the main bunch frequency component, at the bunch repetition rate. The phase is measured with respect to an RF reference signal, provided by the accelerator timing system, at the same frequency of the bunch repetition rate. Table 2 shows the main requirements relevant to the measurement.

Table 2: Measurement requirements and additional parameters

Parameter	**LANSCE linac**	**Spiral 2 linac**
Bunch rep. rate	201.25 MHz	88.0505 MHz
Input power range	50 dB	40 dB
Position repeatability	100 um	±10/±100 um
Phase repeatability	0.25 deg	±0.5 deg
Pickup position sensitivity	1.26 dB/mm	2.5 dB/mm

The signal level varies inside the specified input range depending on the particles' charge. The pickup position sensitivity is a geometrical parameter defined by the pickup dimensions. The phase repeatability is expressed

in degrees at the bunch repetition rate. In both the cases the signal levels are inside the range from -60 dBm to -10 dBm.

DEVELOPED MEASURING SYSTEM

Brief description of Libera Brilliance processing structures

Libera Brilliance unit is composed of an analog and a digital processing system. The analog part processes the RF signals produced by the BPM pickups. The gain of each RF chain is adjusted by means of an active AGC system, while the signal bandwidth is limited by means of band pass filters removing the unwanted frequency components. Furthermore the analog crossbar switch, at the beginning of each RF chain, gently exchanges the paths of the four input signals through the RF board resulting in a very precise calibration system that preserves short term performance and guarantees submicron long term stability. The signals are then sampled by means of four 16 bit ADCs. The sampling clock is generated by a VCXO locked to the external reference by means of a software PLL loop. The external reference is provided by the accelerator timing system at the revolution frequency. The PLL can be programmed in order to have an offset tune respect the provided reference.

The digital processing is implemented inside an FPGA and includes the digital signal conditioning, the filtering, the digital down conversion, several decimation stages and subsystems for full integration of the data streams into the accelerator feedback and control systems.

Adopted measuring technique with modified Libera Brilliance system

The phase and amplitude measurement is based on the quadrature sampling technique. Table 3 shows some choices for the sampling clock for the LANSCE linac and Spiral2 linac cases.

The quadrature sampling technique, also known as IQ sampling, has the property that it implicitly extracts from the samples of a sine signal the in-phase and in-quadrature components like an IQ demodulation process does. Depending on the choices of the phase step and the time axis origin, the ADCs are streaming out a sequence of input signals expressed with I and Q components. (E.g. in the case of a phase step of 630 deg. the ADC will produce the sequence I, –Q, –I, Q, I, -Q, –I, Q …etc…). Figure 1 shows the block diagram of the analog processing chains.

Table 3: Sampling clock frequency choices for quadrature sampling in the case of LANSCE linac and Spiral2 linac

Phase step	**Sampling frequency (LANSCE f_{rf}=201.25 MHz)**	**Sampling frequency (Spiral2 f_{rf}=88.0505 MHz)**
90 deg	805 MHz	352.202 MHz
270 deg	268.3 MHz	117.40 MHz
450 deg	161 MHz	70.44 MHz
630 deg	115 MHz	50.31 MHz
810 deg	89.4 MHz	39.13 MHz

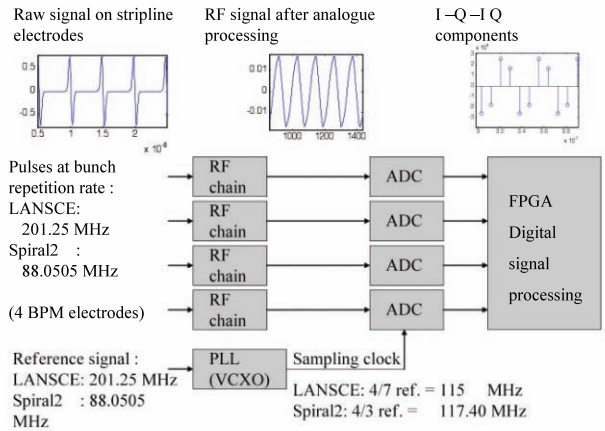

Figure 1: Block diagram of analogue signal processing and quadrature sampling scheme.

In order to measure the mentioned signals in the specified signal ranges (see table 1) the Libera Brilliance RF chain gain and bandwidth have been adapted. Moreover the VCXO used to generate the sampling clock has been closed in a much tighter PLL loop implemented inside a low jitter clock distribution circuit. The scope of the PLL circuit is the generation of the sampling clock from the reference frequency. In the case of the LANSCE linac a 630 deg phase step was chosen, since this maximizes the amount of information taken by the ADC. In this case the 115 MHz sampling clock is produced by multiplying the RF reference signal at 201.25 MHz by 4/7. This frequency multiplication is accomplished by the PLL circuit. The signal produced by the PLL at 115 MHz is phase locked to the reference signal; therefore the BPM signal is sampled in quadrature.

In the case of Spiral2, where the bunches have a repetition rate of 88.0505 MHz, the phase step of 270 degrees has been chosen and therefore the PLL is locked with a ratio of 4/3 resulting in a sampling clock of 117.40 MHz.

Adopted digital signal processing

The digital signals produced by the ADCs are processed in the FPGA by means of digital signal processing. The quadrature sampling scheme converts the frequency component at the bunch repetition rate to $f_s/4$, where f_s is the chosen sampling clock frequency (see table 3). Figure 2 shows the processing blocks. The signals are first processed by three stages of programmable second order IIR bandpass filters tuned at exactly $f_s/4$. The transfer function of each IIR section is

$$F(z) = \frac{z}{z^2 - k} \tag{1}$$

where k is a real parameter that can be used to adjust the filter bandwidth and has to be -1<k<0 for stability reasons.

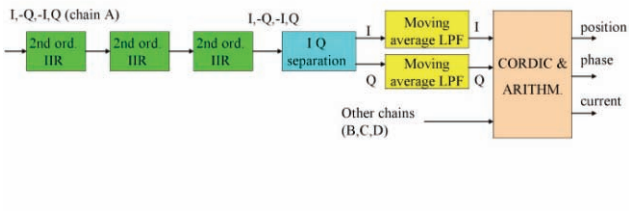

Figure 2: Block diagram of digital signal processing

Once the signals are filtered the separation of I and Q components is performed and there after the I and Q components are filtered by means of configurable moving average low pass filters. Afterwards amplitudes and phase are computed from the stream of filtered I and Q components by means of a cordic algorithm. The phase computation is based on the vector sum of signals on different electrodes, therefore I and Q signals are summed on the four channels. The position is computed with the standard delta over sum equation involving two electrodes with sensitivity coefficient specified in table 2.

MEASUREMENTS

One modified Libera Brilliance unit has been tested by means of extensive laboratory measurements. The PLL circuit has been programmed for the LANSCE linac 630 deg phase step (see table 3). The board was equipped with a VCXO with a center frequency of 115.404 MHz and a tuning range of ±90 ppm. The measurements were performed with a slight detune with respect to the designed 115 MHz sampling clock for the LANSCE linac. The reference signal for the PLL was therefore detuned by the same amount to preserve the PLL ratio 4/7. Consequently the bunch repetition frequency of the laboratory setup was fixed to 201.957 MHz. The adopted testing setup is depicted in figure 3.

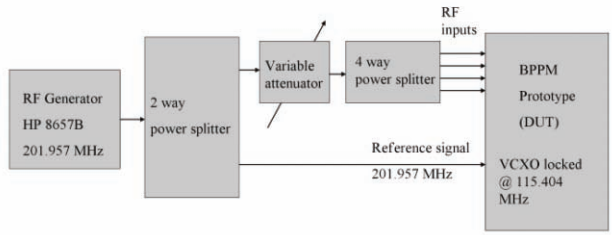

Figure 3: Block diagram of the measurement setup

An RF signal generator at 201.957 MHz is used to simulate the beam signal. This RF signal is passively split by means of a 2 way splitter. One branch of the split signal is attenuated by means of a variable attenuator and therefore equally distributed to the four RF inputs of the measuring system by means of a 4 way splitter that simulates a centred beam. The variable attenuator is used to simulate the charge excursion in the 50 dB dynamic range. The remaining branch from the 2 way splitter is used as the reference signal for the phase measurement.

Figures 4 and 5 show diagrams of the acquired samples and the relative phase measurement.

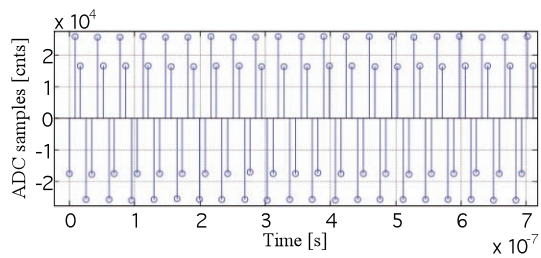

Figure 4: Acquired ADC samples

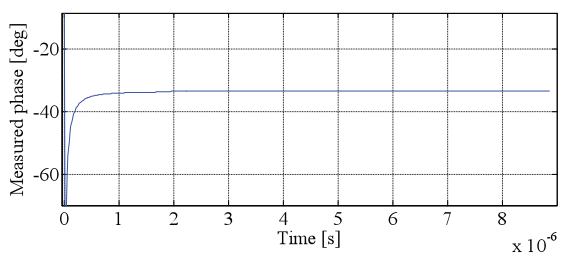

Figure 5: Typical phase measurement

Figure 4 shows the periodic pattern of I and Q components resulting from the quadrature sampling. Figure 5 shows the phase stream after the processing. After a short transient, introduced by the processing, the phase reaches a stable value.

Two different sets of filtering coefficients were adopted during the measurements:

- Filtering 1: 1 stage of IIR with coefficient k=-0.8 and moving average of 100 samples.
- Filtering 2: 3 stages of IIR with coefficient k=-0.9 and moving average over 500 samples.

The position and phase repeatability has been measured by means of the standard deviation computation on consecutive position and phase samples. The plots of the position and phase repeatability as function of the input power are shown in figure 6 and figure 7.

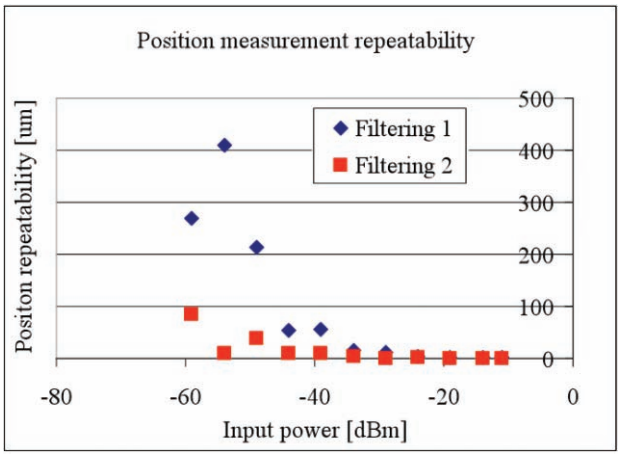

Figure 6: Position repeatability measurement vs. input power for two different settings of filtering coefficients.

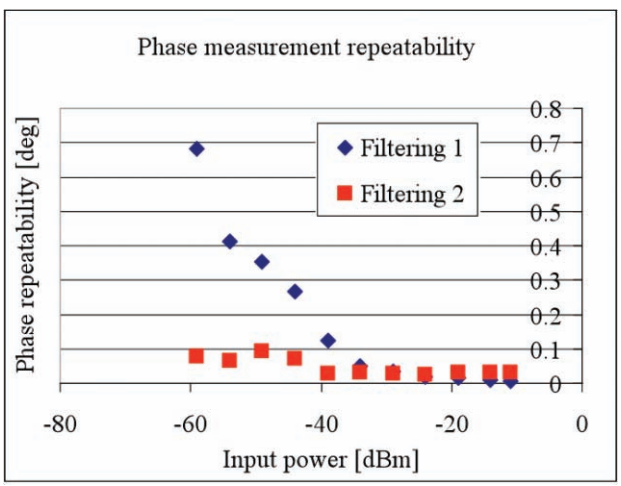

Figure 7: Phase repeatability measurement vs. input power for different sets of filtering coefficients.

At higher input levels, down to -40 dBm, the two different setting of the processing schemes give similar results in terms of repeatability. At lower input power levels, the signal is progressively deteriorated by noise and therefore the repeatability is affected. The second filtering scheme is more effective in terms of repeatability, since it is filtering out more noise. When the second filtering scheme is used, both position and phase repeatability are inside the LANSCE requirements (see table 2).

CONCLUSIONS

A modified version of Libera Brilliance has been successfully tested for time domain phase measurements inside an input power range of 50 dB. The quadrature sampling scheme has been successfully implemented inside Libera Brilliance by means of a hardware PLL. Digital signal processing has been applied to the quadrature sampled signal. Two different filtering schemes were evaluated for the data processing. The schemes give very similar results at higher input level. The second scheme is more effective in the lower input power range. It was shown how the flexibility of the processing schemes allows the user to configure the digital algorithms and therefore improve measuring performance.

REFERENCES

[1] J. D. Gilpatrick, B. Blind, S. Kurennoy, R. McCrady, J. O'Hara, C. Pillai, J. Power, L. Rybarcyk, "Proposed beam position and phase measurements for the LANSCE linac", DIPAC'07, Venice, May 2007.

[2] P. Ausset et al., Ganil, Orsay, France, private communication.

Beam Induced Fluorescence (BIF) Monitor for Intense Heavy Ion Beams *

F. Becker[1†], C. Andre[1], F. M. Bieniosek[3], P. Forck[1], P. A. Ni[3], D.H.H. Hoffmann[2]
[1]GSI, Darmstadt, Germany; [2]TUD, Darmstadt, Germany; [3]LBNL, Berkeley, USA

Abstract

Non-intercepting **B**eam **I**nduced **F**luorescence (**BIF**) monitors measure transversal beam profiles by observation of fluorescence light originating from excited residual gas molecules. Thus they are an alternative to conventional intercepting devices. Single photon counting is performed using an image intensified digital CCD camera. We investigated the BIF process in the energy range of 7.7 keV/u to 750 MeV/u in residual nitrogen. Experiments at low beam energies were performed at a Marx-accelerator (NDCX) at Berkeley Lab [1] whereas mid and high energy experiments were carried out at GSI accelerators [2, 3]. Especially in the vicinity of targets the neutron-generated radiation level limits the monitor's signal to background ratio. Therefore the radiation background was investigated for different ion species and particle energies. Background simulations using a Monte Carlo transport code are compared to experimental data taken with scintillators, thermo luminescence detectors and the BIF monitor. Alternative image intensifier techniques are presented as well as shielding concepts. Furthermore the dynamics of ionized nitrogen molecules in the electric field of intense ion beams is discussed.

THE BIF METHOD AND APPLICATION

When beam ions collide with residual gas molecules, some molecules are ionized remaining in an excited state with a certain probability. In a N_2-dominated residual gas composition, a strong fluorescence at 390 nm $< \lambda <$ 470 nm (blue), of about 60 ns lifetime, is generated by a transition band to the N_2^+ electronic ground state ($B^2\Sigma_u^+(v') \rightarrow X^2\Sigma_g^+(v'')+\gamma$, for vibrational levels v) [4]. 'Single-photon counting' was performed with a commercial image intensifier [5], equipped with a double Micro-Channel Plate (MCP) for up to 10^6-fold photo-electron amplification. Green light from a P46 phosphor screen of 300 ns decay time is taper-coupled to a digital CCD camera with a IEEE-1394a interface [6]. The device is mounted on a fused silica viewport at a distance of 20 cm from the beam axis. Remote controlled CCTV lenses with focal distances of 8 to 25 mm, lead to typical resolutions of 100-500 μm/pixel. Beam profiles were recorded on a single shot basis. To select specific transitions, 10 nm narrow band interference filters were installed in the optical path. A more detailed description of the experimental setup can be found in [7, 8, 9, 11].

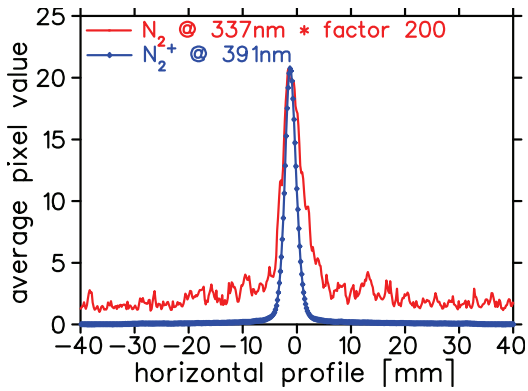

Figure 1: Beam profiles of a 10μA 5.4 MeV/u Ni^{6+} beam in 10^{-3}mbar nitrogen, recorded with spectral filters [9]. The N_2^+ profile @ 391nm shows a σ of 1.1mm whereas N_2 profile @ 337nm has a σ of 2mm.

This paper will focus on issues related to the challenging beam parameters of the FAIR-facility [3] like energies well above 100 MeV/u in considerable loss induced radiation environments and E-field induced profile falsifications for intense and strongly focused beams. During the last years the BIF method was applied successfully at the GSI heavy ion LINAC for various ion species and energies between 5 and 11.4 MeV/u [7, 8, 9]. An additional setup was installed behind the heavy ion synchrotron SIS-18 in a high energy beam transfer line (HEBT) close to a dump. Due to the beam energy between 60 and 750 MeV/u this location allowed to determine the radiation impact on the detector performance. In addition this part of the beam pipe was separated by vacuum windows so that residual gas densities from base-pressure 10^{-8} mbar up to atmospheric pressure could be applied. Systematic investigation of profile falsifications have shown that beam profile width remains constant up to nitrogen pressures of about 1 mbar and also, that N_2 transitions lead to increased profile width $\geq$40% compared to ionic N_2^+ transitions [9], see Fig.1. Cross sections for heavy ion induced transitions in N_2^+ are predominant compared to electron induced transitions. Unlike transitions in neutral working gases (N_2) which show enlarged beam profiles due to the secondary electron halo [10]. Although the contribution of N_2 transitions is $\leq$ 20% and in the near UV, it should be suppressed by optical filters and discriminated against the desirable N_2^+ transitions at (391, 428, 470nm) [9]. For typical beam parameters at GSI LINAC and high energy beam transfer lines, profiles recorded with the BIF-monitor complied with SEM-grid (Secondary Electron Monitor) measurements within 10% [11], see Fig.2.

* Work supported by EU, project FP6-CARE-HIPPI
† Frank.Becker@gsi.de

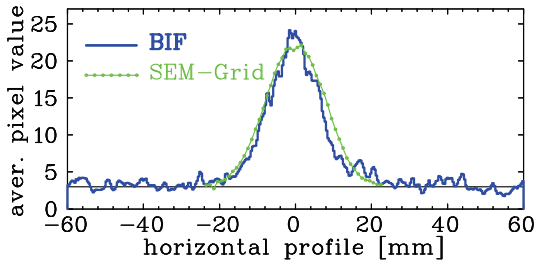

Figure 2: Beam profiles recorded with the BIF-Monitor and a SEM-Grid agree within 10%. 1.5 μs pulse of $2{\cdot}10^9$ Xe^{48+} at 200 MeV/u in HEBT line [11].

RADIATION IMPACT ON THE MONITOR

In the vicinity of production targets like the $\bar{p}$-target, the Super Fragment Separator-target (SFRS), or solid targets for plasmaphysics, a considerable amount of beam ions generates radiation which cannot be avoided. Our experimental area in a SIS-18 HEBT line is located just 2.1 m from the beam dump (Fe). Since all beam particles are stopped in the dump, the generated dose is comparable to fixed target experiments [12, 13]. Therefore radiation impact on the BIF-monitor was investigated in a realistic environment. During the first campaign a specific scaling of signal amplitude and background level with the beam energy was recognized [11]. Recent measurements for slowly extracted uranium ions of complementary energies are in good agreement with the 2005 data, although an Intensified CCD-camera (ICCD) with a different response characteristic and reproduction scale had to be used, see Fig.3. However, the signal amplitude scales with the Bethe Bloch law, whereas the background level scales with $\propto E^2$. With Li^6 Li^7 thermoluminescence dosimeters $\geq$83% of the total dose was determined as neutrons [14]. A semi-empirical neutron production yield for heavy ion projectiles $\geq$5 MeV/u in thick heavy metal targets estimates neutrons per incident projectile, where N_T is the neutron number of the target and E_P is the incident projectile energy in MeV/u, see Eq.1 [13].

$$Y = \frac{1.5 \cdot 10^{-6}}{N_T^{1/3}} E_P^2 (A_P^{1/3} + A_T^{1/3})^2 N_P \frac{A_P}{Z_P^2} \qquad (1)$$

This neutron yield scales with E^2, like the background level recorded with the BIF-monitor. Therefore the neutron flux in our experimental cave as well as the neutron energy- and TOF spectra were simulated with the Monte Carlo transport code PHITS for a 200 MeV/u Xe^{48+} beam [12]. With fast plastic-scintillator-based, neutron sensitve detectors we recorded decaying background levels which complied with the simulated TOF-spectra [11]. The total simulated neutron flux per incident projectile and area integrated over all neutron energies is equally distributed and amounts between 10^{-3} and 10^{-6}, which is more than 1000 neutrons on the $5cm^2$ photo cathode for 10^9, 200 MeV Xe-ions per pulse. The simulated neutron energy spectrum (see Fig.4) predicts energies $E_n \geq$1 MeV for $\leq$20% of the

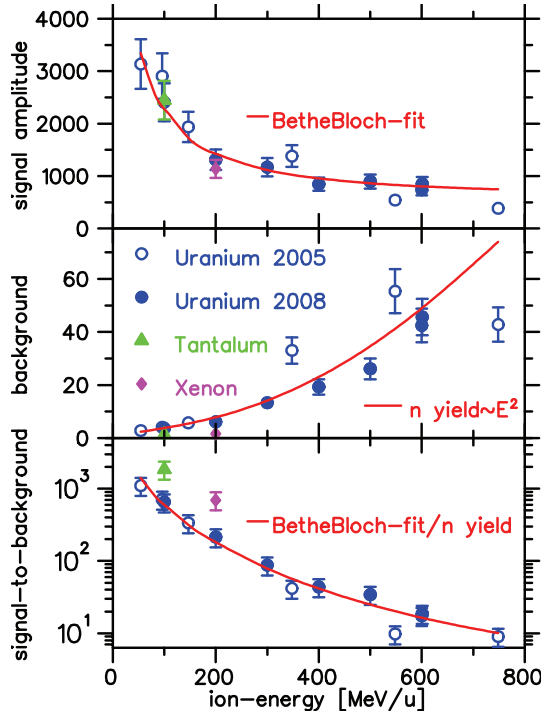

Figure 3: The total signal amplitude (top), background level (middle) and signal-to-background ratio (bottom) as a function of energy for the investigated ions. The signal amplitudes for Xe and Ta were normalized by their charge and mass with respect to U. The background was normalized with respect to the mass only.

generated neutrons. Since the thermal neutron peak at $\sim 4{\cdot}10^{-8}$MeV [15] was cut off in that simulation, the low-energy part of the spectrum is even more predominant. As charged particles have even shorter ranges in matter (dump, beam-pipe, camera housing), shorter lifetimes $\leq$ms , or both - the essential contribution to the total radiation dose at the detector is neutrons and neutron-induced gammas. The signal to background ratio decreases by two orders of magnitude for E_P from 60 to 600 MeV/u. One order is due to increasing background level in this energy range. Thus the radiation impact on the intensified camera system has to be reduced.

ICCD VS. EMCCD CAMERA

One way to reduce the background contribution concerns the camera sensor and the radiation total cross section for alternative sensor materials. Our ICCD camera is equipped with a S-20 multi-alkali (Na_2KSb)Cs photocathode which was identified to cause the background signal [11]. Another competing technique is the silicon- based Electron Multiplying EM-CCD camera which has an additional gain register, based on avalanche diodes between the shift register and output amplifier, for single-photon detection applications [16]. The specific EMCCD sensor [17] we used was thinned to 15 μm, back illuminated and Peltier-cooled down to -80°C. Neutron and photon total cross sections

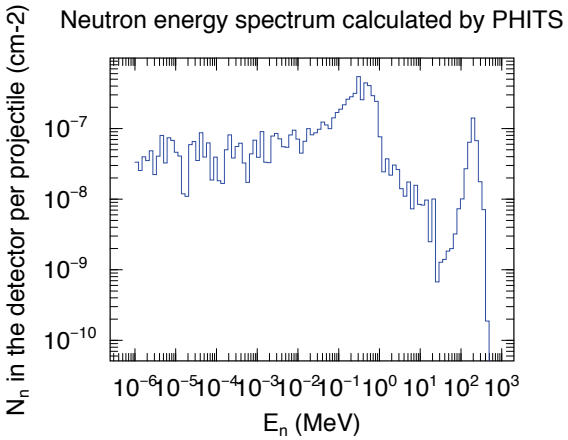

Figure 4: Energy spectrum as counting rate per incident projectile in log energy bins, at the BIF-monitor position, 2,1m from the dump - for a 200 MeV/u Xe beam [12].

from accessible databases [18] have been weighted stoichiometricaly for S-20 and silicon, see Fig.5. S-20 shows a $\sim$1 order of magnitude higher radiation total cross section for neutrons and gammas over the whole energy range, except for energies with nuclear resonances from 10^{-1} to 10 MeV. If the cross section is normalized to the detector surface and mass densities following Eq.2 (EMCCD/ICCD), the silicon data (blue) has to be multiplied by a factor of 2.37 to obtain the relative camera sensitivity. Nevertheless this estimation still predicts a lower radiation sensitivity for the EMCCD camera.

$$\frac{A_{em} \cdot d_{em} \cdot m_{A,em}}{A_{iccd} \cdot d_{iccd} \cdot \bar{m}_{A,iccd}} = \frac{0.66cm^2 \cdot 15\mu m \cdot 28}{4.91cm^2 \cdot 0.5\mu m \cdot 46} = 2.37 \quad (2)$$

In order to check this prediction, we set up an experiment to compare both camera systems [5, 19] with identical source to sensor distances (c-mount $\widehat{=}$ 17,52 mm + 4 mm for Pb-shielding), see Fig.6. As radiation sources, we used ^{60}Co (76 MBq) and ^{241}Am (3.52 MBq) as γ-emitters and a ^{241}Am-Be hybrid source as neutron emitter ($2.1 \cdot 10^4$n/(s 4π)). All γ energies are listed in [18] and neutron energy spectra have been measured with a TOF-energy spectrometer as E_n between 1 and 10 MeV with peaks at 3 and 5 MeV [20]. For the Am-Be source we had to discriminate the neutron radiation against the ^{241}Am γ radiation with a 4 mm Pb shielding between source and camera system. This way there was just $\sim$1 primary γ left per 100 neutrons at the detector surface. In this experiment we averaged over 100 images of 1 s integration time. Radiation background levels are listed in Tab.1. The EMCCD camera showed a 12-times higher dark noise level but in the radiation tests, the ICCD camera was between 2.0 and 3.4-times more sensitive for γ radiation and still 1.5-times more for neutrons and neutron induced γ radiation, which a priori cannot be distinguished from each other.

Second part of this comparison was the camera performance working as a BIF-monitor in single photon detection mode. For that purpose we installed both systems one after another at the GSI LINAC beamline with reproducible beam parameters (1.2 ms, 60 μA, Ni^{13+}), N_2 pressures and the same lens (f=16 mm, f/1.4). Exemplary for five different pressures, relative signal amplitudes are shown in Tab.2. For pressures $\geq 5 \cdot 10^{-6}$ mbar the ICCD camera showed a 30-times higher signal amplitude, for pressures below it was even better, due to its negligible dark noise level Tab.1. This aspect can be understood with respect to Fig.7 and Fig.8, where BIF images and corresponding projections are plotted. However, the EMCCD camera had a 5-times higher resolution, because of constantly small single photon spots, even at highest gain levels compared to the ICCD which showed increasing spots sizes for increasing gain levels.

Table 1: Relative radiation background levels normalized to the 8 and 16-bit dynamics, dark noise subtracted.

Source	E[keV]	ICCD	EM	I/EM
darknoise	-	$9.4E^{-5}$	$1.1E^{-3}$	$8.5E^{-2}$
^{241}Am/γ	13.9;59.5	$8.8E^{-2}$	$2.6E^{-2}$	3.4
^{60}Co/γ/Pb	1173;1332	$4.3E^{-1}$	$2.1E^{-1}$	2.0
Am-Be/n	10^3-10^4	$1.9E^{-3}$	$1.3E^{-3}$	1.5

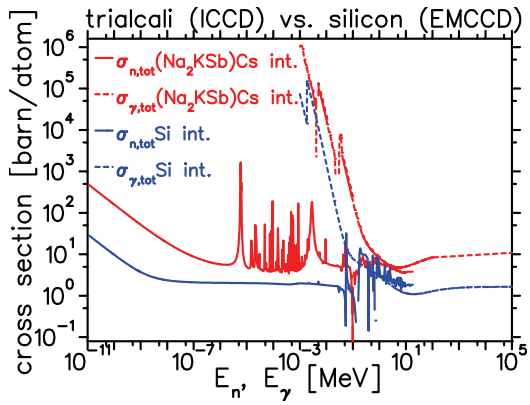

Figure 5: Total neutron and gamma cross sections for S-20 (weighted, red) and silicon (blue) from databases [18].

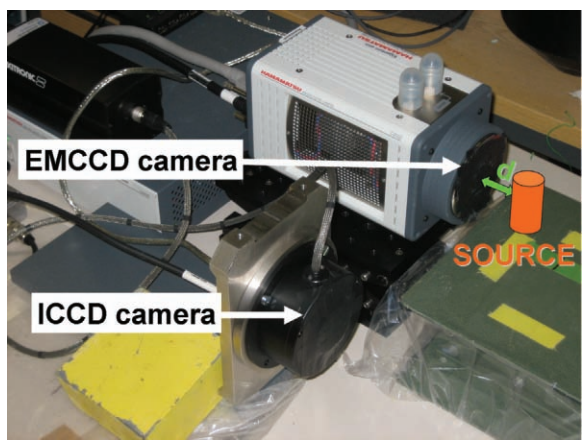

Figure 6: Photograph of the experimental setup. Radiation tests with Am, Co γ sources and a Am-Be neutron source in front of EMCCD and ICCD camera.

Table 2: Relative signal amplitude normalized to the 8 and 16-bit dynamics, dark noise subtracted.

p_{N_2} [mbar]	ICCD	+FB	EM	I/EM
$1{\cdot}10^{-6}$	$5.5E^{-3}$	-	$7.6E^{-5}$	72
$5{\cdot}10^{-6}$	$3.2E^{-2}$	-	$1.1E^{-3}$	29
$1{\cdot}10^{-5}$	$6.8E^{-2}$	-	$2.6E^{-3}$	26
$5{\cdot}10^{-5}$	$2.9E^{-1}$	$7.1E^{-3}$	$9.7E^{-3}$	30
$1{\cdot}10^{-3}$	-	$1.8E^{-1}$	$2.3E^{-1}$	-

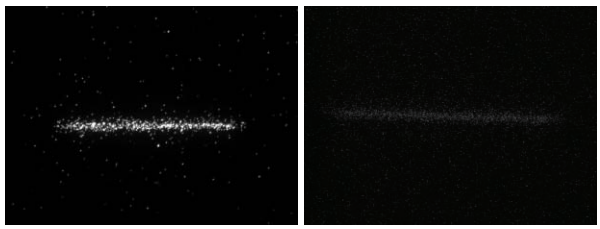

Figure 7: BIF-images of an 1.2 ms, 60 μA, Ni^{13+} beam in $10{-}4$ mbar N_2, recorded with a ICCD (left) and a cooled EMCCD (right) [19].

FIBEROPTIC IMAGE BUNDLE

Another way to approach the radiation issue is to enclose the detector system in an appropriate shielding. A multi-shell concept for moderation and capture of MeV neutrons and absorption of neutron induced γ radiation requires a shielding thickness of $\sim$1 m [21]. Since the imaging is sensitive to the solid angle Ω by $1/r^2$, it has to be conserved. This can be realized by a telescope setup or a fiberoptic image bundle, which maintains mechanical flexibility, see Fig.9. In order to preserve the optical resolution of the whole imaging system, the fiber size, packing density and active surface were adapted to parameters of the MCP (10 μm, 60 lp/mm, 12x12mm). Only for practical reasons the fiber bundle was coupled to the ICCD with a 1:1 relay optics. The actual losses in the relay optics, compared to direct coupling will be measured shortly, but a conservative estimate for the acceptance is NA$\sim$ $[n \cdot sin(arctan(1/(2\kappa)))]^2 = 3.1\%$ with $f = 2.8$. The 1.2m image bundle is specified to have a spectral tranmission of 35% at 400 nm. We measured the total performance of the ICCD coupled to an image bundle at BIF-setup at GSI UNILAC. As shown in Tab.2 (third column), relative signal amplitude decreases by a factor of 40 ($5{\cdot}10^{-5}$ mbar), compared to the ICCD without the image bundle. Whereas signal quality is maintained in this setup, see Fig.10 and in particular, see Fig.11.

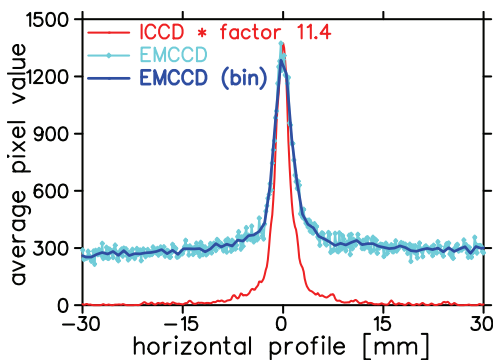

Figure 8: Projected beam profiles of a 60 μA, Ni^{13+} beam in 10^{-4} mbar N_2, recorded with ICCD (8-bit) and EMCCD (16-bit) camera. To compensate the 5-times higher resolution of the EMCCD, profile was binned by a factor 5.

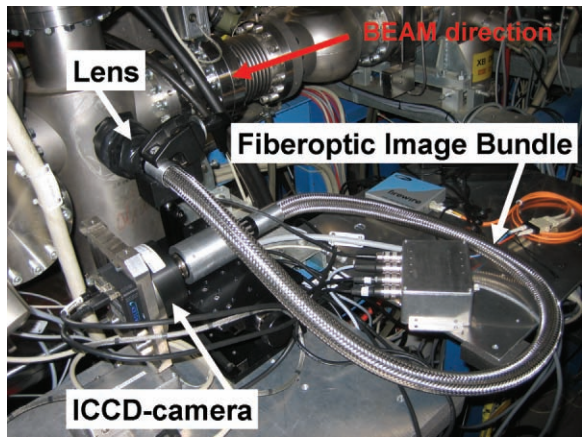

Figure 9: The 1.2 m fiberoptic image bundle mounted at the UNILAC test setup. In a later shielding assembly, the fiber bundle will not be furled.

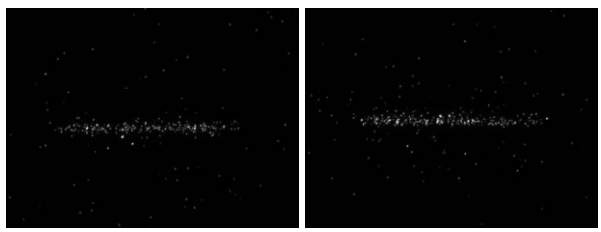

Figure 10: BIF-images of an 1.2 ms, 60 μA, Ni^{13+} beam, recorded with a ICCD in $2.5{\cdot}10^{-5}$ mbar N_2 (left) and with the ICCD mounted on the 1.2 m fiberoptic image bundle in 10^{-3} mbar N_2 (right), see Figure 9.

HOW THE E-FIELD AFFECTS PROFILES

Singly charged N_2^+ ions are accelerated in the E-field of an ion bunch. Their trajectories from the position of ex-

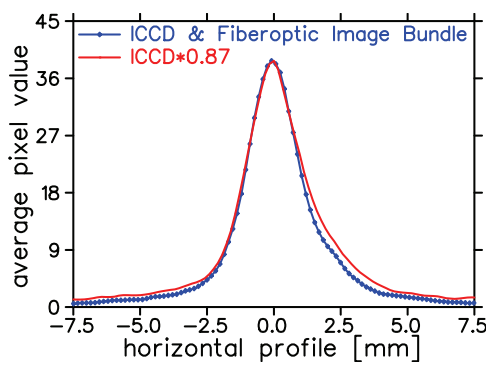

Figure 11: Experimental conditions of Fig.10. Comparison of profiles with the fiber bundle (blue) and without (red). Averaged over 100 images to improve statistics.

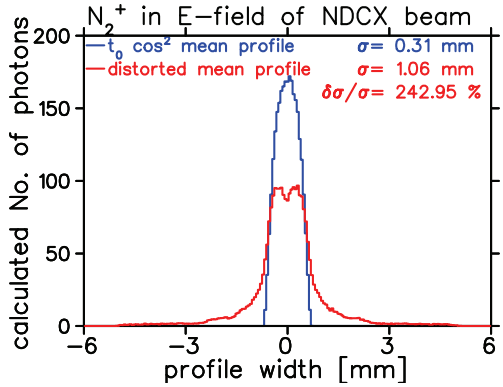

Figure 12: Monte Carlo simulation of projected N_2^+ trajectories in the electric field of $5{\cdot}10^{11}$ K^+ @ 7,69 keV/u in 3 μs, focused down to 0.3 mm as in the NDCX target chamber [1].

citation to the crucial position of spontaneous decay and photo-emission after a specific lifetime can be calculated. Precise E-field modeling is the basis for a Monte Carlo simulation code [22]. As for $\cos^2$ charge distributions, Maxwell's equations can be solved analytically, this distribution was chosen to approximate the Gaussian charge distribution in ion bunches. Trajectories had to be weighted incrementally in time with the decay-frequency of excited states (τ=60ns). Finally all simulated trajectories ($\sim$25000 points per data-set) are projected and plotted as counting rate, representing a beam profile. A $5{\cdot}10^{11}$ K^+ beam @ 7,69 keV/u of 3μs bunch length was simulated as the blue $\cos^2$ distribution, see Fig.12. For $E_{r,max}$=65 kV/m and $\tau_{N_2^+}$ a hollow shaped distribution (red) was obtained. GSI beam parameters are currently not as critical as those, but we are considering different working gases with shorter life times.

CONCLUSION

The comparison between ICCD and EMCCD cameras as BIF-monitors showed an intrinsically lower radiation sensitivity for the EMCCD camera, namely a factor of 1.5 to 3.4, see Tab.1. Although the EMCCD's relative signal performance is a factor of 30 lower, it resolves beam profiles comparable to the ICCD-type, see Tab.2. This was achieved due to its higher resolution (factor 5) with applied binning and due to its higher dynamic range (16-bit for that specific model). For lowest light-intensity applications with few photons, another point for the EMCCD is the 4-times higher quantum efficiency (for thinned, back-illuminated sensors) leading to less shot noise and better statistics [17]. Since former experiments with a front-illuminated EMCCD, cooled to -12°C showed a significantly higher noise level ($\sim$2.5 orders of magnitude), it seems to be important that CCD and avalanche diodes are cooled further down, even for short integration times (1μs). Especially in areas with critical radiation levels, EMCCD cameras should be considered as serious alternative to the established MCP based ICCD systems. Second part of this investigation proofed the principle of a fiberoptic image bundle as an mechanically flexible alternative to telescope optics. Even though its signal performance was a factor of 40 lower than for the ICCD camera without the bundle, see Tab.2, we expect avoid most of the losses by direct coupling to the sensor. In this case the performance of the bundle should be limited just by its spectral transmission, which is still 35% for the relevant wavelength. With the BIF monitor embedded in an effective shielding, the image bundle opens up the field of application to radiative environments. We will set up a shielded BIF-monitor in a HEBT-line during the next beam time shortly. Dynamics of working gas ions have been simulated and identified as a considerable source of error for high intense or strongly focused ions beams, see Fig.12. To overcome this issue we currently are testing alternative working gases with shorter lifetimes.

ACKNOWLEDGEMENTS

We gratefully acknowledge T. Lehmann from the radiation and safety group for the discussion and his support with radioactive sources, H. Iwase and D. Schardt for their work and advice concerning numerical PHITS simulations. We wish to thank B. Lohmueller from Hamamatsu who provided the EMCCD camera for this measurements. This work was supported by the EU, project FP6-CARE-HIPPI.

REFERENCES

[1] P. K. Roy et al., *Nuclear Instruments and Methods in Physics Research*, **A577**, p. 223 (2007)
[2] GSI accelerators, further information on: www.gsi.de
[3] FAIR Baseline Technical Report, Darmstadt, p. 1-38 (2006) www.gsi.de/fair/reports
[4] R.H. Hughes et al., *Phys. Rev.* **123**, 2084 (1961), L.W. Dotchin et al., *J. Chem. Phys.* **59**, 3960 (1973)
[5] Company Proxitronic, www.proxitronic.de
[6] Company Basler, www.baslerweb.com
[7] P. Forck, A. Bank, *Proc. EPAC 02*, Paris, p. 1885 (2002) and A. Bank, P. Forck, *Proc. DIPAC 03*, Mainz, p. 137 (2003)
[8] see e.g. P. Forck et al., *Proc. DIPAC05*, p. 223, Lyon (2005)
[9] F. Becker, C.Andre, P.Forck, *Proc. DIPAC07*, Venice (2007)
[10] A. Ulrich et al., priv. communications, TU Munich (2008)
[11] F. Becker, P.Forck, *Proc. EPAC06*, p. 1013, Edinburgh (2006) and F. Becker, A. Hug, P. Forck, P. Ni, D. Varentsov, *Las. and Part. Beams*, **24**, p. 541-551, Cambridge (2006)
[12] H. Iwase et al., priv. communications, GSI, Darmstadt (2006) and H. Iwase et. al., *JNST* **39 11**, 1142 (2002)
[13] T. Kurosawa et al., *Phys. Rev.* **C 62**, 044615 (2000)
[14] F. Becker - *diploma thesis*, p. 34, Darmstadt (2006)
[15] D. Schardt et al., priv. communications, Darmstadt (2008)
[16] EMCCD detectors, general information, www.emccd.com
[17] Comp. e2v, CCD097, back illuminated, www.e2v.com
[18] free data basis: www.nndc.bnl.gov, www.nist.gov
[19] Comp. Hamamatsu, (C-910013), www.hamamatsu.com
[20] S. T. Park et al., *J. of Rad. and Nuc. Chem.*, Vol. **256**, No. **1**, p. 163-166, (2003)
[21] N. Pyka, private communications, GSI, Darmstadt (2008)
[22] P. Strehl, textbook: *Beam Instrumentation and Diagnostics*, Darmstadt, Germany Springer-Verlag, (2006)

A SOFTWARE UPGRADE FOR THE SNS WIRE-SCANNER*

W. Blokland, C. Long, ORNL, Oak Ridge, TN 37831, U.S.A.

Abstract

The SNS Beam Instrumentation Group has designed new software for all wire scanners at SNS. The original wire-scanner software was written by one of the Spallation Neutron Source (SNS) partners, Los Alamos National Laboratory. This software was designed for the types of wire-scanners initially planned and their usage at that time. New variations in the wire-scanner hardware added gearing, different position read-back methods, and a timing card. The new software handles these hardware variations in a flexible manner through configuration control files. The software upgrade allows the user to synchronize the stepping of the fork with external applications, such as with loss monitors to calibrate energy dependence of the beam losses caused by the wire. Another new functionality allows physicists to select what part of the beam pulse is used to determine the transverse profile after the data has been taken. This avoids time-consuming rescans in case the timing was not initially correct. The new software, also a LabVIEW program, is structured around a state-machine with sequence capabilities to manage the complexities of stepping through a scan and interacting with the user. This paper discusses the new software features, the implementation, and the obtained results of field tests.

INTRODUCTION

Wire-scanners are used in the warm linac and the transfer lines to determine the transverse profiles of the accelerated particle beam. During a scan a fork holding three wires, one horizontal, one vertical, and one diagonal wire is stepped through the beam. As the beam hits each wire, it deposits on or strips charge from the wire. The resulting signal is low-pass filtered (30kHz) to reduce noise and sampled by a digitizer (up to 1Mhz). The sum of the trace at each step is plotted versus the wire position to create the transverse profiles.

The SNS accelerator was built in phases with different labs designing and supplying the wire-scanner hardware.

The software for these scanners was implemented by LANL and tested with the first wire-scanners at Berkeley, [1]. This software has now been successfully used for over 5 years. However, due to several factors it was decided that the software needed to be upgraded.

One factor was that new wire-scanner actuators, see Figure 1, has been developed that uses different motors, gearing, and position read-back methods. The old software has trouble handing these new variations leading to incomplete scans. Its code would have to be modified for each new style resulting in different versions, or a significant rewrite of the old code would have to be done.

Another factor is that the old software uses the ActiveX interface to Channel Access. This was the only available LabVIEW to Channel Access interface available to us at the time. Now most SNS diagnostic instruments use the Shared Memory IOC, which has faster processing and has a quicker response than the ActiveX interface.

Another motivation is the need for additional features. One important feature is the synchronization of the scan, the stepping through the beam, with an external application such as the Loss Monitor. By giving the loss monitor program control over the stepping of the wire-scanner, we can determine the energy dependency of the loss monitors.

Taking a scan from single wire-scanner can take several minutes. Often a scan has to be redone because the timing was not quite right. During studies the beam parameters are often adjusted, for example from a chopped beam to an unchopped beam. This change in the beam also requires a change in the setup parameters of the wire scan. To get these scan parameters just right can take several scans. At several minutes per scan this can become quite time-consuming.

All these factors combined lead us to the decision to rewrite the program.

Figure 1. Photo of a new CCL wire-scanner actuator.

* ORNL/SNS is managed by UT-Battelle, LLC, for the U.S. Department of Energy under contract DE-AC05-00OR22725

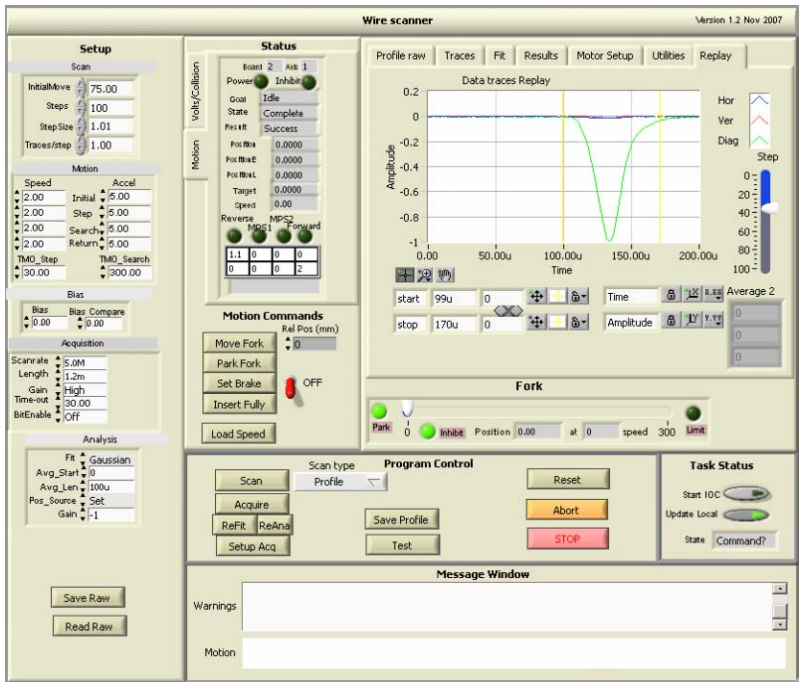

Figure 2. The front panel of the LabVIEW-based wire-scanner application.

IMPLEMENTATION

One of the standard SNS templates for LabVIEW-based instruments is the state machine. The template includes support for the Shared Memory IOC and configuration files that are stored in the Oracle database, [2].

The application's front-panel, see Figure 2, shows the setup for the scan, motion, digitizer, and analysis on the left. The middle of the figure shows the status of the motion and motion commands. The program maintains continuous information about the motion to verify that the fork is not stuck. The top right of the figure shows the results of the scan including the Gaussian fit to estimate the width of the beam.

Program Structure

For this particular application where the application must control a series of steps and acquisitions, we chose to use the state-machine with sequencer. The sequencer allows the programmer to define a scan as a sequence of simple actions, such as move fork 1 mm, acquire trace, and analyze trace that are each mapped into a state of the state machine. Parameters can be passed to each state to describe items such as the length of the move of the fork or what type of analysis must be done. The sequence can be as complex as needed and generated from a routine using specific parameters or read in from a file. During the execution of the sequence, after exiting a state, the state-machine returns to the "Command?" state where it checks if there was user input, e.g to stop the sequence, before continuing to the next step. This allows the program to be responsive during the execution of a sequence using the same state that is called when the program is idle. This does require that each state is executed relatively quickly and can't linger around waiting for a condition, such as the completion of a move, to become true. The sequence can call the Wait state to check for this condition and the sequence is not allowed to progress unless the condition has been met. The state machine structure is shown in Figure 3.

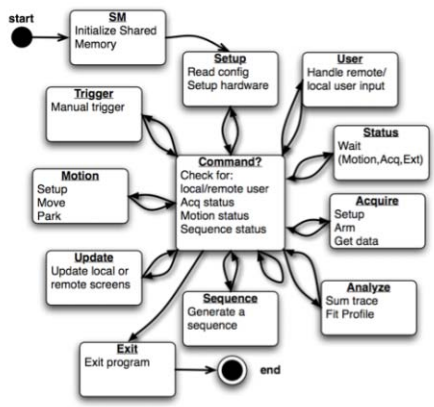

Figure 3. The State-machine structure.

Hardware variation

The new program handles the variation of the hardware from the ground up. From the main program, a technician can start a program to input the specifications of the individual parts such a gear, motor, and position readout device, to create the entries for the configuration file. An additional tool tests the motion of the fork independent of the main program.

Timing Adjustment

To support changing the timing after the data has been taken, more data is stored in memory than is actually used for a single profile. The old program only takes the data it uses for the profile as defined. The new program takes data before and after the data required for the currently defined profile. During a wire scan the SNS beam is limited to at most 100 usecs. The chopped or unchopped beam, will not be further away than 200 usec either direction so that a trace of only about 500 usec will capture the beam under almost any circumstances. Even with oversampling at 1 Mhz this requires only 500 samples per trace. With about 120 steps and perhaps two to four multiple traces per position to do averaging, the program has to store less than 1 million data points. This is not a problem with PCs having now 512 Mbytes to 1Gbytes of RAM. After the scan the user can modify the start and stop locations for the integration and immediately see the effect. This feature also allows us to instantaneously see to some degree (the signal is lowpass filtered) the difference in profiles between the head and the tail of the beam.

Synchronization

Synchronization with other applications is easily implemented with the state-machine. It already has a "Status" state to see if the motion or acquisition has completed. The "Status" state can now also be asked to wait on a change to a Channel Access Process Variable (PV). The loss monitor program can use this PV to halt the stepping until it is done with its loss measurements.

RESULTS

First the program was tested without any motion or digitizer hardware. Data was simulated to test the logic of the program and the analysis routines. The next step tested the program in the lab with an actuator but with no signal to the digitizers. Next, the program was been tested in the HEBT section of the SNS accelerator. Figure 4 shows the beam pulse for which the transverse profile was being measured.

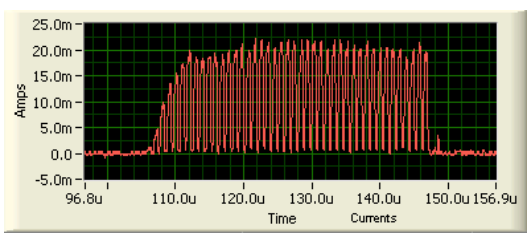

Figure 4. Plot of the beam being measured.

Figure 5 shows the data traces as the beam hits the vertical wire. Figure 6 shows the profiles for all the wires from a different scan. Obtaining these results mean that the program was able to complete a full scan and analyze the data. The interface to the control system has not been finalized.

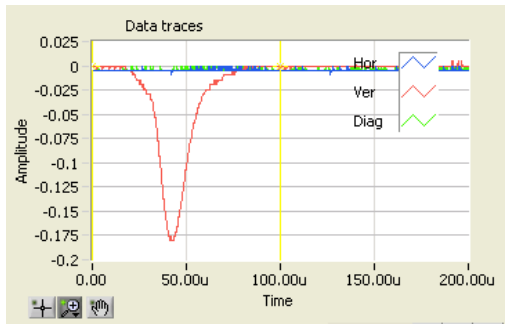

Figure 5. One data trace for the diagonal wire

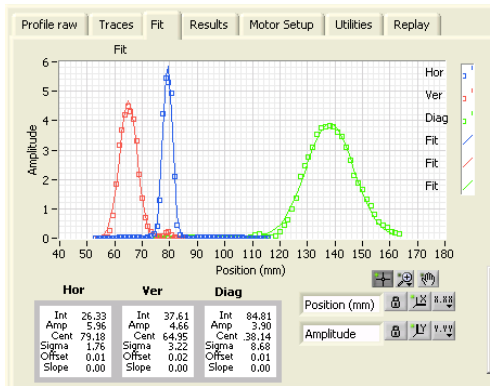

Figure 6. The profiles.

FUTURE

While the program has been tested with two types of wire-scanners, we will have to test it with the other types as well before starting to update all the wire scanners. As many wire-scanner use PCs that are around 5 years old, we will also replace the older PCs at the time of the software upgrade.

Besides being operator controlled through standard EDM screens, the wire-scanners are also accessible through applications of the physics groups using the XAL Java-based framework, [4]. Therefore the switch over has to be carefully coordinated to make sure that all wire-scanner whether running the old software or the new software are accessible.

REFERENCES

[1] M. Plum et al. "The SNS Linac Wire Scanner System, PAC'03, Portland, May 12-16, p2485-7.

[2] W. Blokland et al, "Network Attached Devices at SNS", DIPAC'03, Mainz, Germany May-5-7, 2003, pp 146-8.

[3] W. Blokland and C. Long, "An In-Line Emittance Scanner Based On A LabVIEW Style State Machine With Sequencer", ICALEPCS'05. Geneva, 10 - 14 Oct 2005, PO1.057-6.

[4 J. Galambos et al., "XAL Application Programming Structure," http://accelconf.web.cern.ch/ AccelConf/p05/PAPERS/ROPA001.PDF, PAC'05, Knoxville, TN

CLOSED LOOP WIRE SCANNER ACTUATOR CONTROL FOR LANSCE ACCELERATOR BEAM PROFILE MEASUREMENTS*

Stanley Cohen, Sandeep Babel (BiRa, Albuquerque, New Mexico),

J. Douglas Gilpatrick, James D. Sedillo (LANL, Los Alamos, New Mexico),

David A. Bonal, Murali M. Ravindran (National Instruments, Austin)

Abstract

The design and test of a new beam-profile wire-scanner actuator for the LANSCE (Los Alamos Neutron Science Center) 800-MeV proton linear accelerator is described. Previous actuator implementations use open-loop stepper-motor control for position indexing. A fixed-frequency, fixed-duration pulse train is sent to the stepper motor driving the linear actuator. This has lead to either uncertainties in position due to mechanical resonances and electrical noise or slowing down actuator operation..

A real-time, closed loop control system is being developed and tested for more repeatable and accurate positioning of beam sense wires. The use of real-time controller allows one to generate a velocity profile for precise, resonance-free wire position indexing. High radiation levels in the beam tunnel, dictate the use of an electro-magnetic resolver, typically, used in servo applications, as the position feedback element. Since the resolver is an inherently analog device, sophisticated digital signal processing is required to generate and interpret the waveforms that the feedback mechanism needs for positioning. All of the electronic and computational duties are handled in one the National Instruments compact RIO real-time chassis with a Field-Programmable Gate Array (FPGA)

DESIGN CONTRAINTS

Timing and Physical Environment

Beam-profile wire scanners present a number of electrical and mechanical challenges for designers.. Achieving accurate, repeatable and rapid wire positioning is a key function that must be addressed to obtain reliable beam-intensity data in a timely manner. The high beam intensity, itself, limits the parameter space of what kinds of electronics and materials can be used in the wire-scanner design.

This report is focused on controlling wire-scanner position using the National Instruments cRIO system and getting the actuator movement in the FPGA of cRIO under close-loop conditions., For this first set of tests we are using a wire scanner assembly from the decommissioned LEDA project[1,2]. Operating the wire scanner with closed-loop control is one of the essential requirements for the beam diagnostics refurbishment of the 30-year-old LANSCE proton linear accelerator at Los Alamos [3, 4].

* Supported by LANL Contract SBA 030608

Incorporating closed-loop motion control for the positioning the wire will provide a more accurate picture of the proton beam profile than practice of using open-loop stepper-motor positioning.

Motion control in this design demands that the position for each intensity measurement be achieved during the 8ms between beam macropulses. That is the mechanism must move and settle, between beam pulses, before there is request to measure the beam intensity at that location.

ACHIEVING CLOSED-LOOP MOTION WITH A STEPPER MOTOR

Mechanically Quantized Motion

Using a stepper motor within a closed-loop motion control context introduces quantized motion into the system. The rotational motion of the motor cannot be moved to an arbitrary rotational angle. This can be mitigated somewhat, by microstepping the motor, but this slows down its rotational speed, hence the maximum linear velocity of the wire housing. Motion is, ultimatedly controlled by a computer. This has implications for the motor-control algorithm, since all I/O must be digitized. The wire cannot be positioned with arbitrary accuracy, using an analog to digital converter, (ADC) in conjunction with a linear encoder, may further limit the position accuracy. This limitation and the former quantization effects means that the wire can be positioned to the commanded position within, ±ε, a small error. This will determine the convergence criterion for reaching a position setpont.

Wire Scanner Physical Environment and Constraints

Why use a stepper motor, at all, since servo motors are available? A stepper has the advantage of having detent torque or “holding torque”, when it’s stopped. This keeps the wire stationary without an explicit program for the stopped motion. It is assumed that the detent torque is great enough to overcome competing mechanical forces on the wire assembly. The stepper motor comes to a complete stop, when command signals are inhibited. This is advantageous for keeping the beam-sense wire steady for sensing the particle beam charge.

Linear Position Feedback Elements

The choice of feedback elements for the LANSCE-accelerator is limited, since radiation levels are high

enough to destroy some internal elements for an optical encoder. We want to close the feedback-control loop with a sensor that samples the linear motion of the wire carrier directly. We are limiting our choices to a resolver [5], linear variable differential transformer (LVDT) [6] or magnetostrictive linear displacement device (MLDT) [7]. We've chosen to postpone the decision on which transducer to use and focus on developing closed loop motion control software. For this proof-of-principle project, a linear potentiometer was chosen to close the feedback loop. We are developing all of the programming using relatively low-level modules available in Labview. National Instruments propriety "SoftMotion" package does not have the bandwidth required for the fast positioning performance we are demanding.

Compact RIO and FPGA loop control

The heart of the motion control system we are developing runs on a National Instruments(NI) hardware chassis (See Figure 1) based upon NI's Compact RIO (reconfigurable I/O) architecture. The system consists of five major parts. See Figure 2.

1. Real-time controller
2. Chassis-mounted signal conditioning modules
3. A Virtex II FPGA (field programmable gate array) that is the intermediate processor between the RT and the I/O modules.
4. Ethernet interface to the rest of the world.
5. Shared variable engine

The power of this configuration is contained in the FPGA which can run multiple, simultaneous processes. This is a true parallel process environment at a minimum of 40 MHz

The beauty of this arrangement is that the FPGA is programmed in Labview, not VHDL. Three pieces of software must be written, but the all use the common graphical programming paradigm of Labview, the virtual instrument (VI).

The FPGA allowed us to create our own stepper-motor-pulse train generator, signal conditioners, and digital I/O that are running as independent processes on the FPGA.

Figure 1 Compact RIO Hardware

The first control algorithm for our LEDA test bed consists of an FPGA module with stepper-motor speed and direction pulse control analog input from the linear-encoder potentiometer and a number of digital inputs whose state can be passed to the real-time controller.

The control loop is closed in the real time controller a simple PD algorithm is used which has been tweaked to compensate for the quantized motion and position data. See details below.

A shared-variable engine passes start stop and set point information to a VI running on a Windows XP, personal computer on a TCP/IP network. This mimics the topology of the future implementation of the system. Our goal is to pass the exact process variables used by the EPICS control-system drivers. See Figure 3.

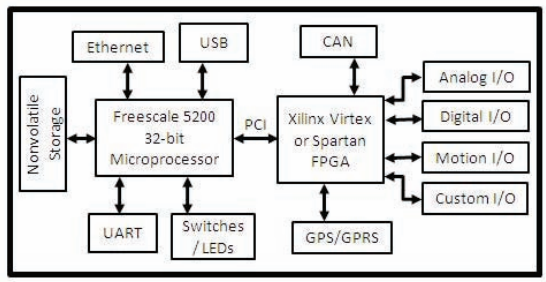

Figure 2. National Instruments cRIO architecture

Control Algorithm

The requirement that the wire assembly moves every 8 ms during operation implies that the response to a step input overrides long-term stability of the control loop. A successful control scheme is one that will move quickly and accurately to the commanded setpoint (linear position).

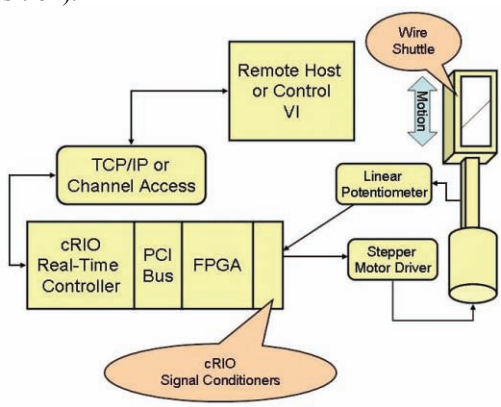

Figure 3. Wire Scanner Control Architecture

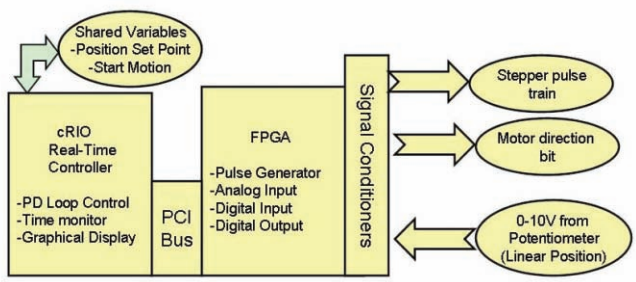

Figure 4. Distribution of processing tasks

Using the conventional model of proportional, integral, differential (PID) control, the integral part becomes irrelevant, compared to the mechanical time constants of the wire positioning system. The loop bandwidth dictates

a fast feedback loop. Preferably, "closing the loop" in the FPGA. That is, placing the entire closed-loop control algorithm in hardware. No data required for loop convergence will need to be passed to the PCI bus to the real-time portion of cRIO during the 8 ms of wire motion.

These first tests, whose results are described here, sacrificed speed for understanding the system behavior. Therefore, loop convergence calculations were done in the real-time portion of the cRIO system. See Figures 4 and Figure 5.

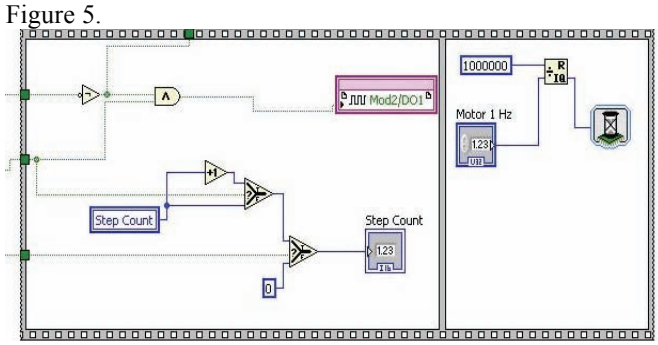

Figure 5. FPGA programming is done with Labview.

PRELIMINARY TESTS AND RESULTS

Loop Parameters and Stepper Motor Control

A minimum number of channels were used with the cRIO hardware for this series of tests. An NI 9215 cRIO analog input module read the linear potentiometer. A single 16 bit channel was set up to read at 50 µs intervals. Pulses and direction digital an NI 9474 handled information, 1 MHz digital output module.

The inclusion of the FPGA in the cRIO system allowed us to create and modify stepper-motor control signals at that were, essentially hardware. For these tests, we used an IMS MForce motion controller [8] that takes a square wave pulse train to control the motor's rotational speed and a single bit to specify direction of rotation. The motor will move one step (a specific rotational angle) with each transition of the pulse train. MForce is a micro stepping controller that allows one to change the number of steps per one complete rotation of the motors shaft. This can be adjusted "on the fly" via an Serial Peripheral Interface (SPI) [9].. For these tests the motor rotates 0.45 degrees for each pulse. If required, one could step this up to 1.8 degrees to facilitate a rapid retraction of the wire shuttle.

The linear potentiometer supplied absolute position as feedback which made loop calculations very straightforward. Input parameters for control consisted solely of specifying a target position (setpoint) and a start command. The motor moves toward the new position and stops its position is within ε of the target. Optimization of the motion was achieved by varying sample time, maximum motor speed (which is analogous to proportional gain), and differential gain. A further enhancement is a threshold parameter that reduces the proportional gain linearly as the position error approaches the target value.

By changing the parameters one can get the loop to exhibit ringing and milder overshoot, as well as critically-damped behavior. See Figure 5

Preliminary results achieved performance of 87 ms to move 1 mm with an accuracy of 0.1 mm. We estimate that, at least, 50 ms of that time is communication overhead from the real-time processor and the host monitor computer.

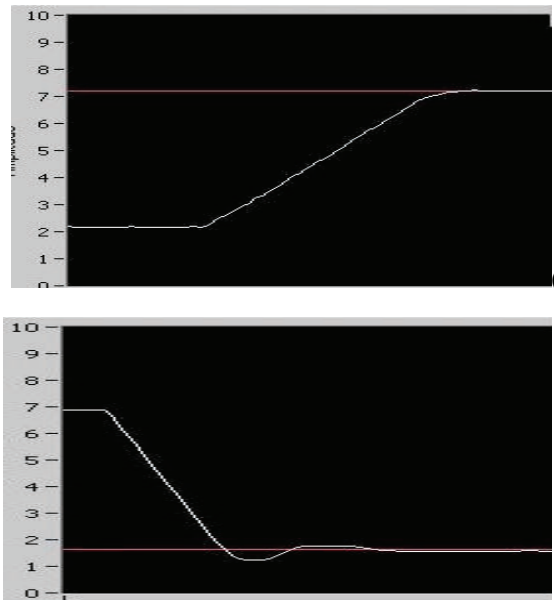

Figure 6. Actual recorded motion of wire shuttle (a)Critically and (b)Under-damped motion.-- Red - Set point White - Shuttle Motion

REFERENCES

[1] R. Valdiviez, , et. al.,The Final Mechanical Design, Fabrication, and Commissioning of a Wire Scanner and Scraper Assembly for Halo-Formation Measurements in a Proton Beam. PAC2001, Chicago, IL

[2]. D. Barr, et.al.," Design and Experience with the WS/HS Assembly Movement Using LabVIEW VIs, National Instrument Motion Controllers, and Compumotor Electronic Drive Units and Motors., PAC2001 Chicago, IL

[3] K. W. Jones, et. al., The LANSCE Refurbishment (LANSCE-R) Project, PAC07, Albuquerque, NM

[4] J. D. Gilpatrick, et.al., Proposed Beam Diagnostics Instrumentation for the LANSCE Refurbishment Project, PAC07, Albuquerque, NM

[5] http://www.inductosyn.com/linear_transducers.htm

[6] http://www-ssrl.slac.stanford.edu/ble/lvdt.htm

[7]._http://www.directindustry.com/prod/novotechnik/absolute-magnetostrictive-linear-position-sensor-13745-210991.html

[8]_http://www.imshome.com/Product%20Datasheets/MFM_Micro.pdf

[9]http://www.embedded.com/story/OEG20020124S0116

ELECTRON BEAM TIMING JITTER AND ENERGY MODULATION MEASUREMENTS AT THE JLAB ERL*

P. Evtushenko#, D. Sexton, Jefferson Lab, Newport News, VA USA

Abstract

When operating JLab high current ERL a strong reduction of the FEL efficiency was observed with the increase of the average current of the electron beam. Investigating the FEL efficiency drop-off with the electron beam average current we have measured the electron beam phase noise and the fast energy modulations. The phase noise is a variation of the time arrival of the electron bunches to the wiggler. It could be a very effective way of reducing the FEL efficiency especially when the driver accelerator for the FEL is operated with the RMS bunch length of about 150 fs. Under a fast energy modulation we denote a modulation which can not be followed by the FEL due to its time constant, defined by the net FEL gain. Such a modulation also could be a possible cause of the efficiency drop-off. Making the measurements we could rule out the FEL efficiency drop-off due either the fast energy modulation or the phase modulation. We also have learned a lot about instrumentation and techniques necessary for this kind of beam study.

ELECTRON BEAM PHASE NOISE MEASUREMENTS

Investigating the FEL efficiency drop-off with the electron beam average current we have measured the electron beam phase noise and the fast energy modulations. The so-called phase noise is essentially a variation of the time arrival of the electron bunches to the wiggler. That could be a very effective way of reducing the FEL efficiency if one takes in to account that the accelerator is routinely operated with the RMS bunch length of about 150 fs [1]. Under a fast energy modulation we denote a modulation which can not be followed by the FEL due to its time constant, defined by the net FEL gain. Such a modulation also could be a possible cause of the efficiency drop-off. The two effects are strongly connected in the FEL driver accelerator due to the longitudinal phase space transformation, i.e., longitudinal bunch compression. The simplified view of the longitudinal phase space transformation is a rotation of a long and low energy spread beam at the injector by ~90 degrees in the longitudinal phase space so that the bunch length minimum is located in the wiggler [2]. Under such a transformation an energy modulation in the injector would get transferred in to a phase modulation at the wiggler and a phase modulation in the injector would gets transferred in to an energy modulation at the wiggler.

The technique we use for the phase noise characterization of the electron beam was originally

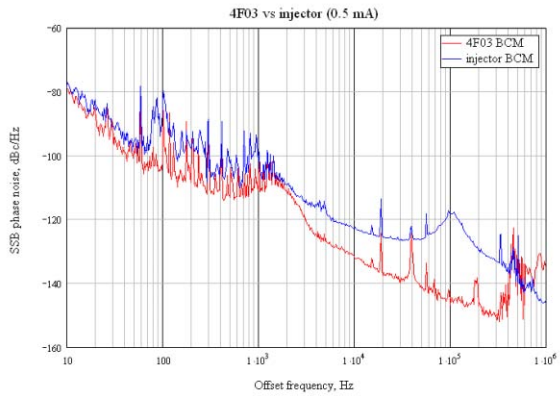

Figure 1 a: Single sideband spectrum measured at 0.5 mA

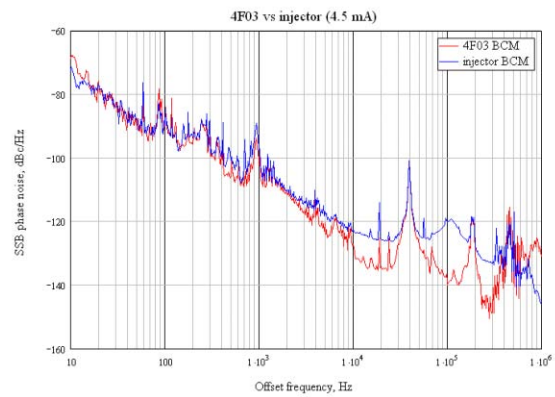

Figure 1 b: Single sideband spectrum measured at 4.5 mA

developed for noise characterization of ultra fast lasers [3]. It was shown that both phase noise and amplitude noise information can be extracted from the power spectrum measurements of the electron beam intensity. The power spectrum of the electron beam is a comb with spectral lines separated by the frequency of the bunch repetition rate. The envelope of the spectrum is determined by the longitudinal profile of a single bunch. Both the amplitude AM and phase modulation PM (or noise) of the beam intensity manifest themselves in the power spectrum as the sideband modulations of the spectral lines of the comb spectrum. It was shown in [3] that amplitude of the sideband modulations seen relative to the carrier amplitude changes differently with the harmonic number for AM and PM. The relative amplitude of the sidebands due to the amplitude noise does not change with the harmonic number, whereas the relative amplitude of the phase noise increase as μ^2, where μ is the harmonic number. Thus measurements of sideband

* Work supported by the U.S. DOE contract # DE-AC05-06OR23177
# Pavel.Evtushenko@jlab.org

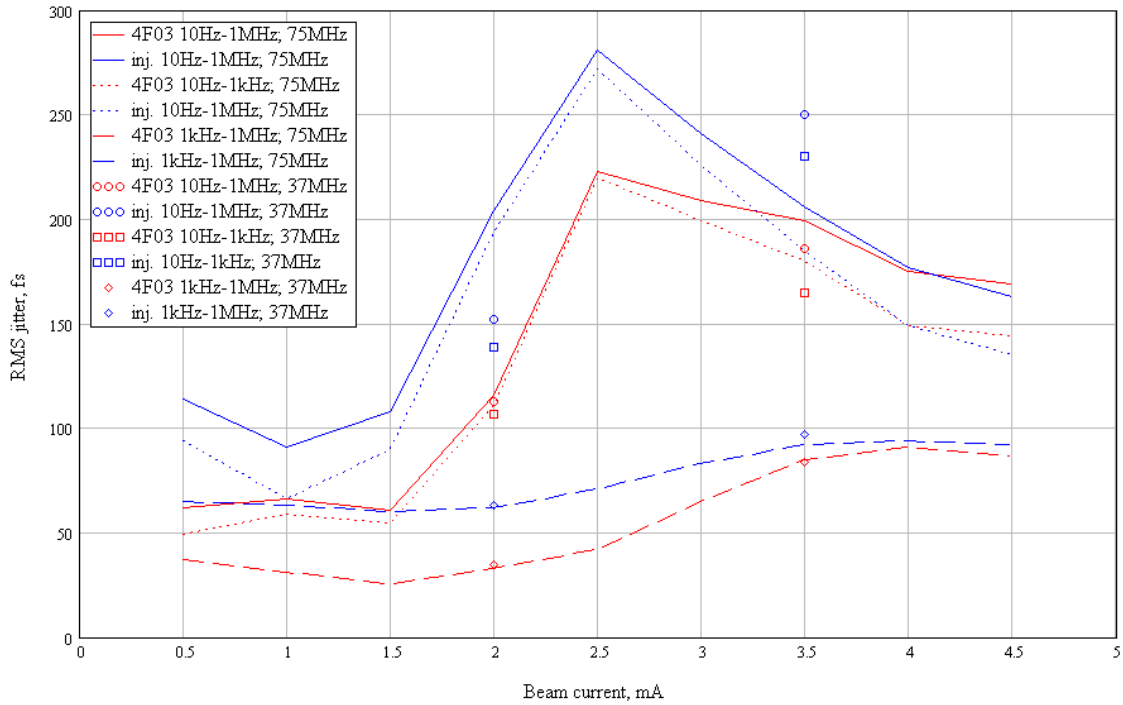

Figure 2: RMS phase noise as a function of the average beam current

spectrum at the DC contain only the amplitude noise (modulations) and measurements made at very high harmonic number will be dominated by the phase noise (modulations).

Beam current monitor (BCM) cavities and Agilent E5052A Signal Source Analyzer were used for the electron beam phase noise measurements. The BCM is a pill box cavity with the fundamental mode tuned to 1497 MHz. Since the maximum repetition rate of the electron beam is 74.85 MHz the cavity is measuring at least 20th harmonic of the beam. Hence it is reasonable to assume that the sideband spectrum will be dominated by the phase noise. Two cavities used for the measurements are installed at the injector and upstream the wiggler. Signal of such a cavity is strong enough to be used for the phase noise measurements without additional amplification. The E5052A Signal Source Analyzer is a commercially available state of the art device designed for the phase noise measurements of RF sources.

In one set of the measurements the electron beam phase noise was measured as a function of average beam current in the range from 0.5 mA through 4.5 mA. As an example, Fig. 1 shows the phase noise spectra measured at the injector and in the vicinity of the wiggler side by side. Figure 1.a shows the spectra measured with 0.5 mA beam current and Fig. 1.b shows the spectra measured at 4.5 mA.

Figure 2 shows summary of the measurements made with the BCMs. Most critical question in the data interpretation is the question of the data “pollution” by the amplitude modulation AM. The signal source analyzer from its operational principal would not distinguish between phase and amplitude modulation. Even when we do the measurements at the relatively high harmonic number due to a very low phase modulation residual amplitude modulation could be present in the signal. We are convinced that there is AM present in the phase noise spectrum we measure and one should keep that in mind when evaluating the measurements results.

As one sees on the Fig. 2 we did measurements in three different ranges of the offset frequency, namely: 10 Hz ÷1 MHz, 10 Hz ÷1 kHz, 1 kHz ÷1 MHz. There are two reasons for doing the measurement this way. First of all in the preliminary measurements we saw a strong drop of the phase noise at 4.5 mA. On the spectrum one sees that the drop is due to the less noise at low frequency, i.e., below 1 kHz. But the higher frequency components did not went down, and if they reduce the FEL efficiency it could explain why the efficiency did not go up as the RMS jitter went down at the 4.5 mA. That was one reason to separate the range of the phase noise measurements in to two and also make the measurements in the whole range. The other reason is, when looking at the FEL noise data one sees that there are a lot of noise below ~1 kHz and much less above that. This is why we decided to separate the "low" and "higher" frequencies at 1 kHz.

Certainly it is important to compare the measured phase noise (modulation) with the specification. The spec derived from the requirement that the FEL intensity would be reduced not more than by 10 % due to the variation in the electron bunch time arrival can be summarized as following; the RMS jitter at frequency f_m has to be less

than $6 \cdot 10^{-9} / f_m$ [4]. Figure 3 shows the comparison of the spec and the measured phase spectra at 0.5 mA and 5 mA. The measured spectra are shown as the yellow curve; the spec is shown as the red line.

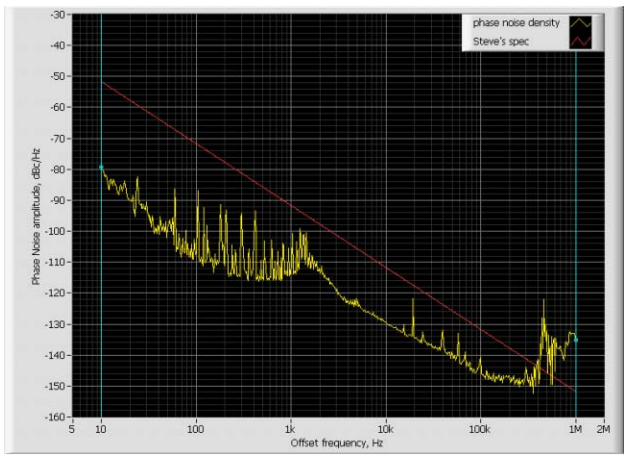

(a) measurements at the average current of 0.5 mA

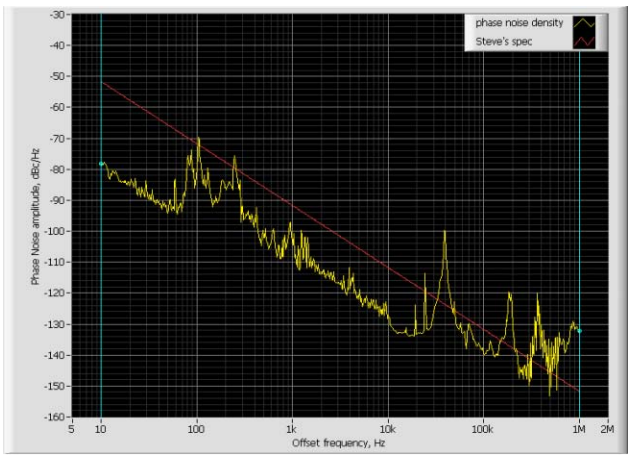

(b) measurements at the average current of 4.5 mA

Figure 3: Comparison of the measured phase noise spectrum with the requirements imposed by the FEL stability

Comparison of the spec and the phase noise spectrum measured at 5 mA average beam current from the first sight tells that the measured phase noise exceeds the one allowed by the spec. However it was established that the peaks at ~100 Hz, ~250 Hz and ~ 40 kHz are due to amplitude modulation of the electron beam caused of by the amplitude modulation of the drive laser. The peaks do not represent the phase modulation of the electron beam and therefore our conclusion was that the measured phase noise does not exceed the required one.

ENERGY MODULATION MEASUREMENTS

As was explained above the phase and energy modulation are strongly connected in the FEL driver due to the beam dynamics. Energy modulation can also originate from the LINAC, for instance due to misbehaving RF system. For this reasons we also did measurements of the "fast" up to 1 MHz electron beam energy modulation. The measurements were done at the injector and at the section with dispersion right upstream of the wiggler. Beam position monitors (BPM) were used for the measurements in a combination with the special set of the BPM electronics. The BPM electronics used for the measurements is essentially the analog part of the log-amp based BPM electronics [5], which we have been developing to upgrade our BPM system. The analog part of the electronics was used in a combination with high speed 4 channel simultaneously sampling ADC card. Essential part of the measurements was proper calibration of the electronics and making sure that the electronics will detect the beam position modulation properly. Such tests made in a lab have shown that this type of the BPM electronics would detect the modulation properly, thus our calculation and measurements in the lab were agree on the 2 % level. The measurements in the lab also have shown that the system noise floor is at the level of 0.5 microns, which we consider to be quite remarkable. Figure 4 shows the lab noise floor measurements of the BPM electronics with the fast ADC. The peak in the X spectrum at the 20 kHz is our artificially introduced test modulation.

Our estimates are that the level of the energy modulation in the injector, which would lead to the phase modulation at the wiggler of a concern level, also would show up as a ~100 μm beam position jitter at the dispersion section in the injector. Thus we would be able to detect such a motion very easily. The first result of the measurements was that there is no significant change in the energy jitter in the injector when the average beam current is increased form 0.5 mA up to 5 mA, so that there is no correlation between the FEL efficiency drop-off and the injector energy modulation. The second result was that beam motion we are measuring in the injector dispersion section is on the level of ~ 1 micron, i.e., much less that the level of concern. The same system was used to measure the fast energy modulations in the dispersion section right upstream of the wiggler. Here again we could not see any dramatic change in the energy modulation with the average beam current. Also the beam energy modulation which we have measured was extremely low and several times smaller that the intrinsic beam energy spread.

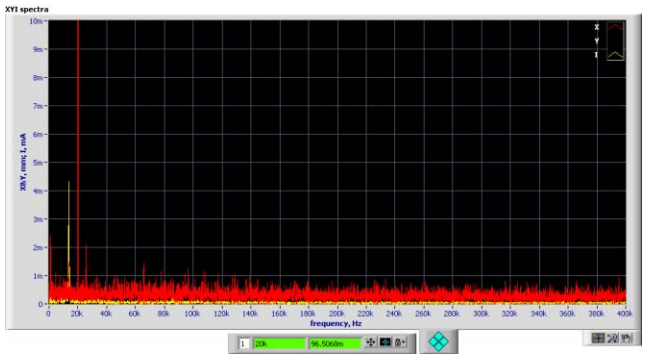

Figure 4: Noise floor in the fast beam position measurements and injected calibration signal

Making the above described measurements we could rule out the FEL efficiency drop-off due either the fast energy modulation or the phase modulation. We also have learned a lot about instrumentation and techniques necessary for this kind of beam study. We think that it will have an impact not only on our future electron beam diagnostics and instrumentation but also on the instrumentation for other ERL accelerators.

REFERENCES

[1] P. Evtushenko et al., Proceedings of 12th Beam Instrumentation Workshop, 2006, Fermilab, Batavia, IL, USA
[2] D. Douglas, Proceedings of PAC07, Albuquerque, New Mexico, USA
[3] D. von der Linde, Appl. Phys. B 39, 1986, p. 201
[4] Steve Benson, private communication
[5] D. Sexton et al., Proceedings of 12th Beam Instrumentation Workshop, Fermilab, Batavia, IL, USA

COUPLING CORRECTION IN NSLS X-RAY RING

M. Fedurin#, I. Pinayev, BNL, Upton, NY, 11973, U.S.A.

Abstract

In this paper we present an algorithm for coupling correction in storage ring based on monitoring the vertical size of a stored beam, while varying skew quadrupoles. The details of the algorithm are realized as a Matlab script and experimental results of its application are presented.

CORRECTION METHOD

There are 17 skew quadrupoles (Table 1) distributed around the X-ray ring, as well as beam profile, could be measured on pin-hole camera monitor (Fig.1). All this is enough to try to find the optimal skew quad configuration to minimize vertical beam size.

Varying one skew quad setting in defined range will affect the beam size change. So, one iteration cycle has this sequence: 1) find optimal quadrupole setting for minimal vertical beam size; 2) set it up and then turn to vary next quads; 3) make one pass for all quadrupoles; and 4) correct beam displacement after each pass or keep beam position feedback on all the time.

Optimal skew quadrupole setting

The quadrupole variation range was made small, to avoid disturbing beam position too much or reaching the trim-current saturation limit if orbit feedback is running all the time. The skew quadrupole current was varied in 5 equal steps and beam size was measured by pin-hole camera beam profile monitors at every step. Then a polynomial curve fit on measured data was used to find the local extremum. Three possible types of extrema could be found in that way (Fig. 2): 1) extremum located on one of the edges of the range; 2) inside range; and 3) value corresponding to maximim, not minimum, beam size—in this case, sign check of second derivative always followed finding the value .

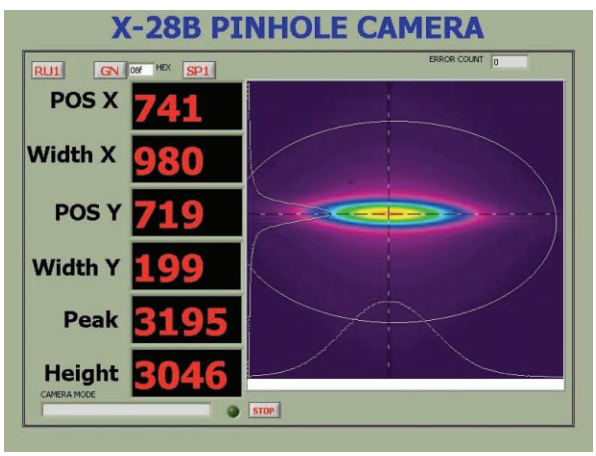

Figure 1: Pin-hole camera monitor located at X28 beamline used for beam profile measurements.

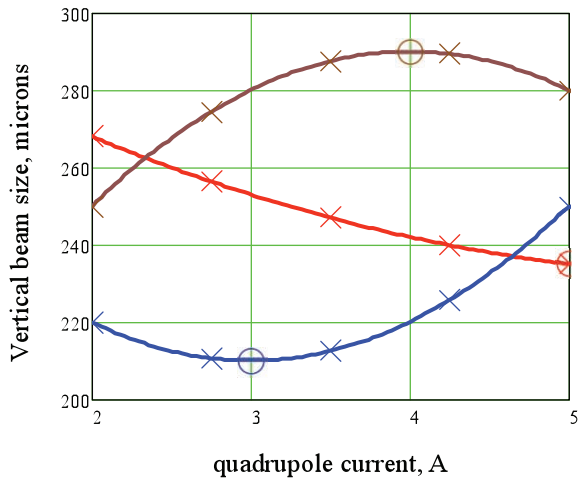

Figure 2: Three different types of local extremum: extremum located on one of the edges of the range (red curve), inside range (blue curve), and extremum value correspond maximum beam size (brown curve)

CORRECTION SCANS

Before starting the correction process, all skew quadrupoles are set to zero. After the first pass, skew quadrupole settings bring vertical beam size down from 570 μm to 425 μm. Each other iteration step changes size value down, and after 9 passes goes below 300 μm. Every beam profile measurement is averaged over 10 seconds, so each quadrupole scan takes about 1 minute, and a whole pass about 20 minutes.

Skew quadrupole scan history is presented in Fig. 3 and vertical beam size changes in Fig. 4. It is noticeable that some quadrupoles reach saturation when making big steps in iterations. During the scan all three types of local extrema were observed but logic in the script code makes it choose the correct value.

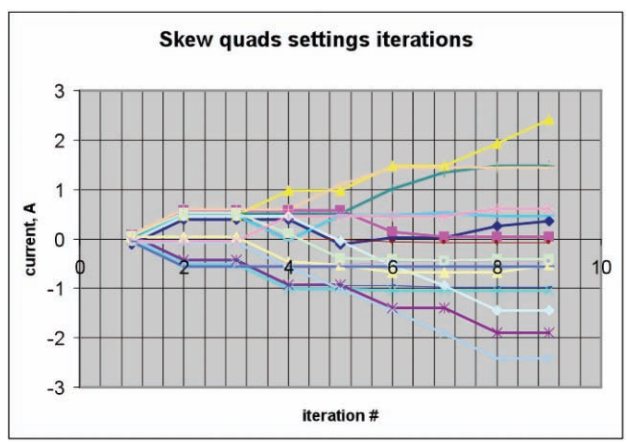

Figure 3: History of skew quadrupole current settings.

SUMMARY

The skew quad iteration method was verified on NSLS X-ray storage ring. After 9 passes coupling was significantly reduced but still exceeds current operational value. Present iteration method needs improvement to speed up convergence of iteration passes—for example, increasing the variation range or finding the optimal skew quad sequence.

ACKNOWLEDGEMENTS

We wish to thank Jack Tallent, Susila Ramamoorthy, and other people from Operations Group for technical support.

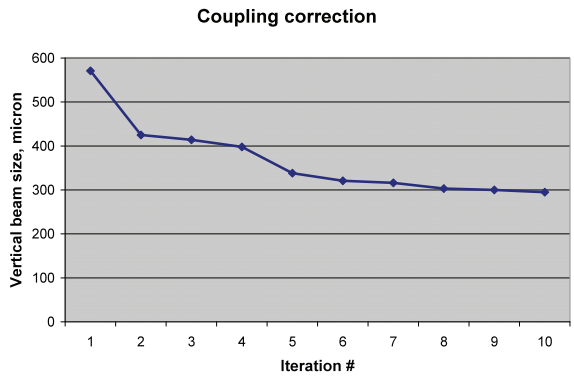

Figure 4: Changes of the vertical beam size after every iteration pass.

CONSIDERATIONS ON ODR BEAM-SIZE MONITORING FOR GAMMA = 1000 BEAMS*

A.H. Lumpkin, Fermilab, Batavia, IL, U.S.A. 60510
C.-Y. Yao, Argonne National Laboratory, Argonne, IL U.S.A. 60439
E.Chiadroni, M. Castellano, LNF-INFN, Frascati, Italy, A. Cianchi, Univ. of Rome Tor Vergata

Abstract

We discuss the feasibility of monitoring the beam size of γ=1000 beams with 3000 times more charge in a video frame time and with a more sensitive 12- to 16-bit camera than were used in the previous electron beam studies at 7 GeV at the Advanced Photon Source. Such a beam would be generated at Fermilab in a new facility in the coming years. Numerical integrations of our base model show beam size sensitivity for ± 20% level changes at 200- and 400-μm base beam sizes. We also evaluated impact parameters of 5 σ_y and 12 σ_y for both 800-nm and 10-μm observation wavelengths. The latter examples are related to a proposal to apply the technique to an ~ 0.98 TeV proton beam, and this study shows there are trades on photon intensity and beam size sensitivity to be considered at such gammas. In addition, we report on first results at γ=1800 on a superconducting rf linac.

INTRODUCTION

Characterization of the high-power electron beams of the superconducting rf (SCRF) accelerator to be installed in the New Muon Laboratory (NML) building at Fermilab will be an important aspect of the project [1]. Beam size, position, divergence, emittance, and bunch length measurements are all of interest. Due to the projected high beam power with 3000 micropulses of up to 3 nC each in a macropulse at 5 Hz at eventually up to 1800 MeV, the need for nonintercepting (NI) diagnostics is obvious. Although position is readily addressed with standard rf beam position monitors (BPMs), the transverse size, and hence emittance, are less easily monitored noninterceptively in a linear transport system. Besides an expensive laser-wire system, one of the few viable solutions appears to be the use of optical diffraction radiation (ODR) [2-8] which is emitted when a charged-particle beam passes near a metal-vacuum interface. Appreciable radiation is emitted when the distance of the beam to the screen edge (impact parameter) $b \sim \gamma\lambda/2\pi$, where γ is the Lorentz factor and λ is the observation wavelength. Previous near-field imaging experiments at the Advanced Photon Source (APS) with 7-GeV beams used an impact parameter of 1.25 mm from a single edge of a plane as compared to the scaling factor of ~1.4 mm (with an assumed operating wavelength of 0.628 μm) [7]. The near-field images were obtained with a single, 3-nC micropulse using a standard CCD camera. Since for the NML case, with its much lower gamma, the fields are reduced exponentially as $e^{-2\pi b/\gamma\lambda}$. We either have to use the longer wavelengths in the NIR or FIR or have more charge integrated in the image and a more sensitive camera. The NML design-goal beam intensity gives a factor of 3000, and the intensified or low-noise camera should give another factor of 1000. These two factors combined should allow visible to IR near-field imaging of a beam that is up to 10 to15 times lower in gamma than the APS case, if similar impact parameters can be used.

We considered focus-at-the-object or near-field imaging optics and established that the perpendicular polarization component of ODR has the beam-size sensitivity that would be needed for a transport line with 400- to 1000-μm rms sizes in the x-plane. These parameters are compatible with the proposed test-area location in the lattice after the SCRF linac [1] as shown in Fig. 1. In addition, we evaluated the possible extension of the technique to a very high intensity hadron beam with γ~1000 as would be found in the Fermilab Tevatron [2,10]. In the latter application, we also consider a larger impact parameter constraint and the possible compensation of the consequently reduced signal by going to much longer wavelengths. We show there are trades to be considered in this paradigm.

ANALYTICAL BACKGROUND

The basic strategy is to convert the particle–beam information into optical radiation and to take advantage of the power of imaging technology to provide two-dimensional displays of intensity information. These images can be processed for beam size information. Possible radiation sources are optical transition radiation (OTR), ODR, and optical synchrotron radiation (OSR). For completeness, the near-field ODR model as described in Ref. 6 is provided here.

As stated before, ODR is produced when an electron beam passes near a region where different dielectric materials are present. This is generally a vacuum-to-metal interface, and the theory [3-6] is usually for the *far-field* diffraction pattern produced by a beam passing through apertures or slits in conducting planes. In the present case, we effectively integrate over angle and frequency since our optical system is focused on the ODR source itself, i.e. the *near-field* image on the screen. Therefore we proposed a simplified model of the

*Work supported by U.S. Department of Energy, Office of Science, Office of High Energy Physics, under Contract No. DE-AC02-06CH11357.

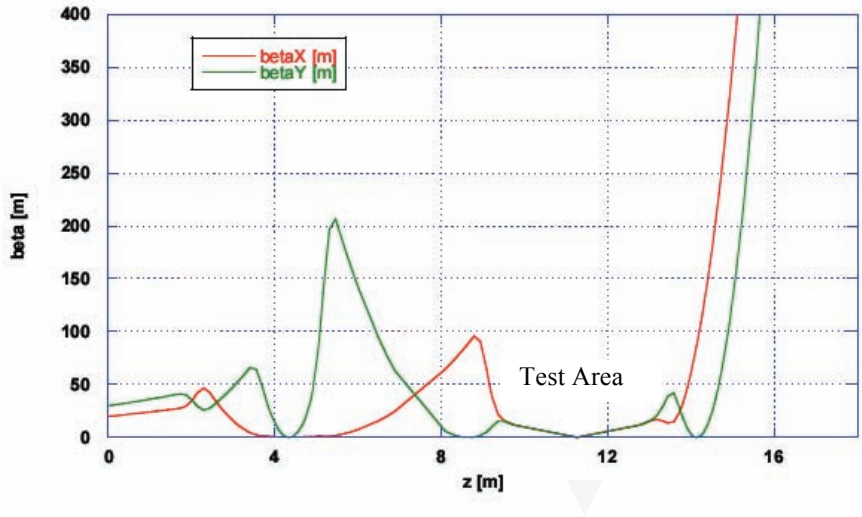

Figure 1: Lattice functions (case 2 waist at z~11 m) for the NML Downstream beamline with the proposed three-station configuration indicated by the arrows (lattice plot courtesy of Mike Church, Fermilab).

near field based on the method of virtual quanta described by Jackson [9] in dealing with the photon-like fields of relativistic beams. One convolves the electron beam's Gaussian distribution of sizes σ_x and σ_y with the field expected from a single electron at point *P* in the metal plane. One wishes to calculate the incoherent sum of radiation from all beam particles in a pulse emitted from a given point on the ODR radiator, i.e. at $\boldsymbol{u} = \boldsymbol{P} - \boldsymbol{r}_o$, where $\boldsymbol{P}$ is the field point with respect to the origin and $\boldsymbol{r}_o$ is the position of the beam centroid with respect to the origin. The impact parameter is $\boldsymbol{b} = \boldsymbol{u} - \boldsymbol{r}$, where $\boldsymbol{r} = \boldsymbol{r}(x,y)$ denotes a position in the beam measured from the beam centroid. One then can write the differential spectral intensity as:

$$\frac{dI}{d\omega}(\mathbf{u},\omega) = \frac{1}{\pi^2}\frac{q^2}{c}\left(\frac{c}{\mathrm{v}}\right)^2 \alpha^2 N \frac{1}{\sqrt{2\pi\sigma_x^{\,2}}}\frac{1}{\sqrt{2\pi\sigma_y^{\,2}}} \times \int\int dx dy K_1^2(\alpha b) e^{-\frac{x^2}{2\sigma_x^{\,2}}} e^{-\frac{y^2}{2\sigma_y^{\,2}}} \quad (1)$$

where ω = radiation frequency, v = particle velocity ≈ *c* = speed of light, *q* = electron charge, *N* is the particle number, $\alpha = 1/\gamma\lambda$, and $K_1(\alpha b) = K_1\left(\alpha\sqrt{(u_x - x)^2 + (u_y - y)^2}\right)$ is a modified Bessel function. Since one measures light intensity *I*, this should be proportional to $|E_x|^2 + |E_y|^2$, resulting in the K_1^2 dependence. The incoherent photon intensity is proportional to *N*, the number of electrons, in contrast to the case of coherent diffraction radiation in the far infrared (FIR), which is enhanced by N^2.

The APS experiments actually started with a single plane which was inserted vertically. We evaluated the beam size parallel to the single edge. In Fig. 2 we show a calculation of the signal distribution in the optical near field based on this new model for a 7-GeV beam at an impact parameter of 1250 μm. The beam size was 1375 μm by 200 μm [7].

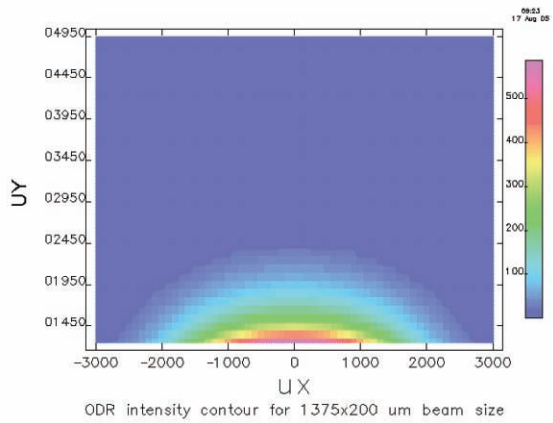

Figure 2: Calculated ODR image for a beam size of 1375 μm by 200 μm and an impact parameter starting at 1250 μm.

NUMERICAL RESULTS

The numerical integrations were done as described previously at PAC07 [11]. In this case the parameters were adjusted to assess the γ=1000 regime, initially for approximately 500-MeV electrons that are anticipated in the NML at Fermilab. In this case a superconducting linac would be combined with a high-average-current photo injector. Under the scenario of a single semi-infinite metal plane inserted from above the beam axis, we assessed the ODR monitor beam-size sensitivity at a value centered at 200 μm. In Fig. 3 we show both the parallel (px) and perpendicular (py) components of the ODR profiles for a series of impact parameters. For this beam size near 200 μm and impact parameters, the near-field ODR parallel

component is a two-lobed structure, while the perpendicular component is a single lobe and more directly tracks the beam size. The profile intensities are normalized to one, and it is noted that the vertical profile falls off almost exponentially with impact parameter. The perpendicular polarization component is also 3-4 times more intense than the parallel one.

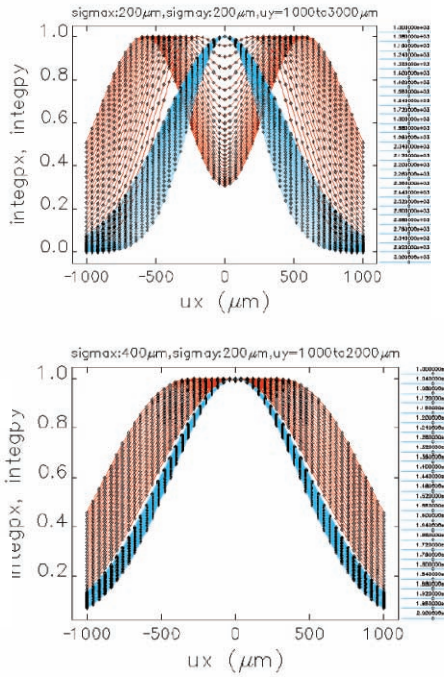

Figure 3: Calculated parallel (red) and perpendicular polarized (blue) ODR profiles for 200 μm (upper) and 400 μm (lower) for impact parameters starting at 1000 μm.

In Fig. 4 we show the ODR perpendicular polarization component for a beam size at 200 μm (upper) and around 400 μm (lower). The observed ODR profile is of course larger than the actual beam size, but the profiles do detectably change in size with the beam size change. A 20% change in beam size from 200 μm, gives ~ 12% change in ODR profile size. We note the calculated ODR profile size is 257 μm for the reference size. We stepped the beam sizes while using fixed input parameters for wavelength of 800 nm and an impact parameter of $5\sigma_y$ = 1000 μm.

As an additional issue we addressed the beam size sensitivity for a 400-μm beam size, but with an impact parameter of 12 σ_y = 5000 μm in Fig. 5. Using an 800-nm wavelength, we still calculate some sensitivity to beam size changes of 12 % in the upper plot, but the 10-μm wavelength case shows very little sensitivity in its much larger horizontal profile in the lower plot. A previous proposal [10] had suggested a 14-μm wavelength could be used to increase the photon emission number in an application for protons in the Tevatron using a far-field imaging technique, but the trade is not at all favorable in our near-field technique. So it appears that signal-level permitting, the 800-nm regime would be the better choice as has been used in far-field experiments at 680 MeV by the Frascati team using a 16-bit CCD camera[12].

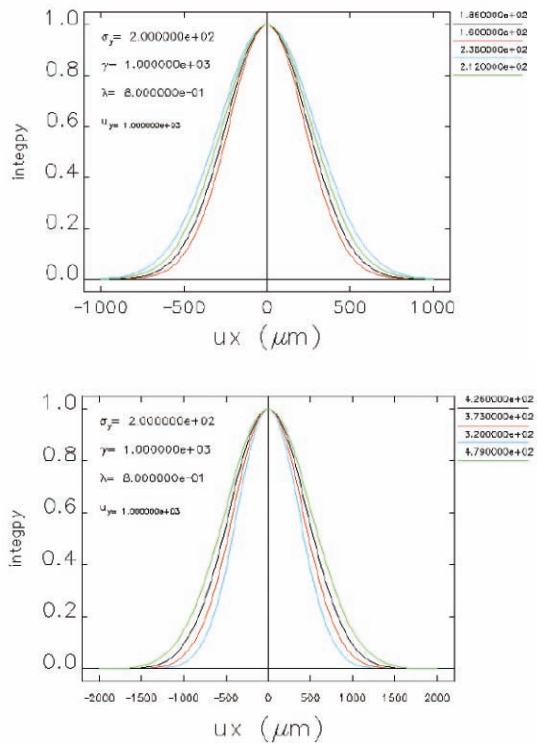

Figure 4: Calculated perpendicular component of horizontal ODR near-field profiles for the variation around 200 μm (upper) and 400 μm (lower).

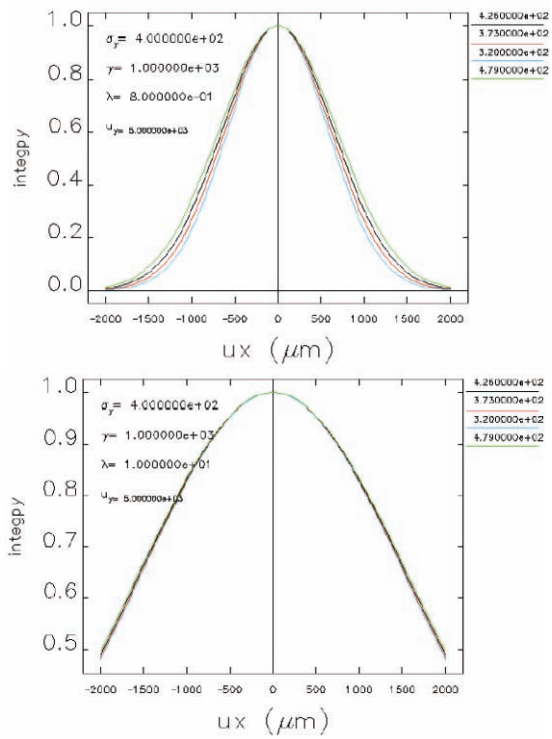

Figure 5: Numerical calculation of the near-field ODR perpendicular component for stepped beam sizes near 400 μm with b= 5000 μm, γ=1000, and λ= 800 nm (upper) and λ=10 μm (lower). The beam-size sensitivity is basically washed out using 10-μm ODR and with this impact parameter of ~12 σ_y.

ODR EXPERIMENTAL RESULTS

An opportunity to test the feasibility of the near-field monitor at 900 MeV was identified in discussions with staff at FLASH in Germany and Frascati in Italy. In this case a complementary test was proposed to the ongoing far-field ODR experiments of the Frascati team [12]. The converter consisted of an aluminized Si nitride wafer with a slit chemically etched of 1–mm height. A test beam with 6 bunches and 1 nC per bunch operating at 5 Hz was generated in the FLASH facility and transported to the test station. Ultimately 10 images were summed to improve statistics for the ODR signal obtained using an 800 x 80 nm band pass filter. The beam was positioned on the top edge of the slit, and then the actuator was stepped in 100-μm steps. An example of the image obtained with a 400-μm beam offset from the top edge is shown in Fig. 6. The dark current from the photoinjector has been subtracted from the total beam intensity. The dim ODR image is seen near both top and bottom edges. The ROI sampled only the top image and gave an ODR profile width of about σ_x=360 μm as shown in Fig. 7, as compared to the original OTR-measured beam size of 205 μm.

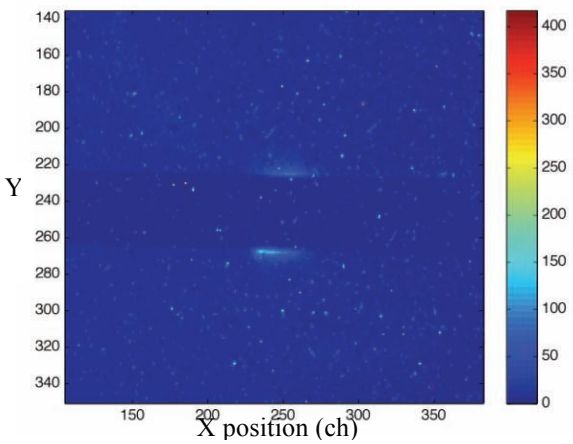

Figure 6: Initial near-field ODR image of the 900-MeV electron beam at FLASH passing through 1–mm tall slit at a location 400 μm below the top edge. This is a 10-image sum with the dark current subtracted from the 16-bit digitized CCD camera data.

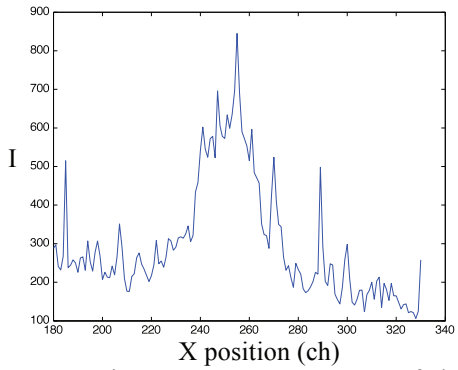

Figure 7: Horizontal profile projection of the ODR top image from Fig. 6. The observed rms width is about 360 μm compared to the OTR image's profile size of 205 μm. The calibration factor is 36.4 μm per channel (ch).

With the first experimental results in the near-field at γ=1800, we performed post-experiment modeling for these specific parameters. The results of the numerical evaluations are shown in Fig. 8. The top plot shows the total intensity profile for different impact parameters starting at 500 μm. The ODR x profile was calculated to range from 286 μm to 400 μm for impact parameters from 500 to 1200 μm for total intensity, in reasonable agreement with the experiment. The lower plot shows the calculated beam-size sensitivity for the 200 μm ± 20% horizontal size. The ODR x-profile clearly tracks the changes with its roughly 30-μm change in sigma per step or 10-12% relative changes. In these cases, the dots on the curves are the ODR results and the solid lines are the Gaussian fits to those points. It is clear the Gaussian assumption is appropriate.

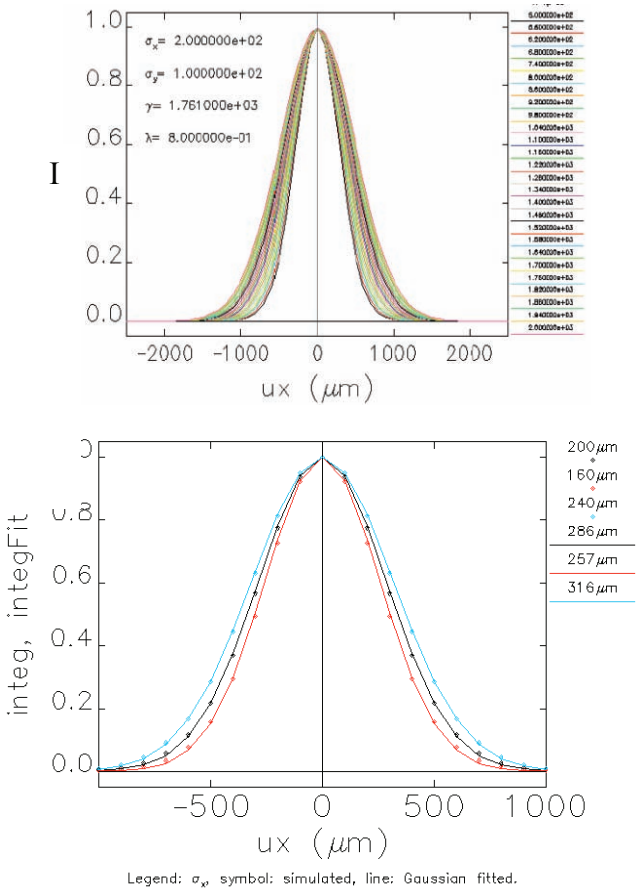

Figure 8: Calculated near-field ODR horizontal profiles for the FLASH case with the variation of impact parameter (top) and the 20% variation of initial beam size around 200 μm (lower).

SUMMARY

In summary, we have extended our investigations on the feasibility of near-field ODR monitoring of particle beams as a noninterceptive method. Our modeling was extended to the challenging γ=1000 regime to address the potential applications at Fermilab for electrons and possibly protons. With the recent successful proof–of–principle near-field experiment at FLASH at γ~1800, the scaling to these high-charge, lower gamma beams in the linac now seems more realistic with 800-nm to 1600-nm ODR and an ultra-sensitive CCD camera. The Tevatron proton case is much more difficult due to constraints on the minimum impact parameter allowed and other considerations [13].

ACKNOWLEDGEMENTS

The authors acknowledge support from M. Wendt and S. Nagaitsev of Fermilab and K.-J. Kim of the Argonne Accelerator Institute. We also thank M. Church of Fermilab for the NML lattice calculations and T. Sen for hadron discussions.

REFERENCES

[1] S. Nagaitsev, ILC-TA Workshop, November 2006, Fermilab.

[2] Alex H. Lumpkin, "Possible ODR Imaging Diagnostics for ILCTA", presented at ILC-TA Workshop, Fermilab, November 28, 2006.

[3] M. Castellano, Nucl. Instrum. Methods Phys. Res., A **394**, 275 (1997).

[4] R. B. Fiorito and D. W. Rule, Nucl. Instrum. Methods Phys. Res. B **173**, 67 (2001).

[5] T. Muto et al., Phys. Rev. Lett. **90**(10), 104801 (2003).

[6] P. Karataev et al., Phys. Rev. Lett. **93**, 244802 (2004).

[7] A.H. Lumpkin, W.J. Berg, N.S. Sereno, D.W. Rule, and C.Y. Yao, Phys. Rev. ST-AB, 10,022802 (2007).

[8] A.H. Lumpkin et al., "Far-Field OTR and ODR Images Produced by 7-GeV Electron Beams at APS", Proceedings of PAC07, Albuquerque, June 25-29, 2007.

[9] J.D. Jackson, *Classical Electrodynamics*, (John Wiley and Sons, New York, 1975) Sec. 15.4.

[10] T. Sen, V. Scarpine, R.Thurman-Keup "Prospects of Diagnostics with ODR in Hadron Colliders", Proc. of PAC07.

[11] C.-Y. Yao, A.H. Lumpkin, D.W. Rule,"Numerical Simulation of ODR from a 7-GeV Beam", Proc. of PAC07, FRPMS001, Albuquerque, NM.

[12] E. Chiadroni et al., "Non-Intercepting Electron Beam Transverse Diagnostics with ODR at the DESY FLASH Facility",Proc. of PAC07, Albuquerque, NM.

[13] Alex H. Lumpkin, "ODR Imaging of Charged Particles: Recent Experiments", presented at the LARP CM10 Meeting, Port Jefferson, NY April 23, 2008.

INITIAL SYNCHROSCAN STREAK CAMERA IMAGING AT THE A0 PHOTOINJECTOR*

A.H. Lumpkin and J. Ruan, Fermilab, Batavia, IL U.S.A. 60510

Abstract

At the Fermilab A0 photoinjector facility, bunch-length measurements of the laser micropulse and the e-beam micropulse have been done in the past with a single-sweep module of the Hamamatsu C5680 streak camera with an intrinsic shot-to-shot trigger jitter of 10 to 20 ps. We have upgraded the camera system with the synchroscan module tuned to 81.25 MHz to provide synchronous summing capability with less than 1.5-ps FWHM trigger jitter and a phase-locked delay box to provide phase stability of ~1 ps over 10s of minutes. This allowed us to measure both the UV laser pulse train at 244 nm and the e-beam via optical transition radiation (OTR). Due to the low electron beam energies and OTR signals, we typically summed over 50 micropulses with 1 nC per micropulse. We also did electron beam bunch length vs. micropulse charge measurements to identify a significant e-beam micropulse elongation from 10 to 30 ps (FWHM) for charges from 1 to 4.6 nC. This effect is attributed to space-charge effects in the PC gun as reproduced by ASTRA calculations. Chromatic temporal dispersion effects in the optics were also characterized and will be reported.

INTRODUCTION

The opportunity for a new series of streak camera experiments at the Fermilab A0 photoinjector was recognized in the last year. The enabling upgrade was adding the synchroscan option to the existing C5680 Hamamatsu streak camera mainframe. By locking this module to the 81.25 MHz subharmonic of the rf system, the synchronous summing of micropulses could be done with trigger jitter of <1.5 ps (FWHM) for both the UV drive laser component at 244 nm and the e-beam via optical transition radiation (OTR) measurements [1,2]. The synchronous summing of the low OTR signal from the 15-MeV electron beam micropulses allowed the needed bandpass filters to be utilized to reduce the chromatic temporal dispersion effects inherent to the broadband OTR source and the transmissive optics components. In addition, the C6768 delay module with phase feedback was also acquired, and this stabilized the streak camera sweep relative to the master oscillator so that camera phase drift was much reduced to the ps level over 10s of minutes. This latter feature allowed a series of experiments to be done on the bandwidth effects and transit time effects in the respective transport lines. After characterizing the UV laser bunch length, a series of e-beam experiments on the A0 beamlines was performed. We have measured a significant bunch-length elongation versus micropulse charge for the present conditions and show that this is consistent with ASTRA calculations. We also observed a micropulse slice emittance effect for charges of 4 nC per micropulse. In the course of our experiments, we have done a series of tests on the chromatic temporal dispersion effects for this particular input optics barrel with UV transmitting optics and our optical transport lines. We show our effects our less than that reported at SSRL at PAC07 with optical synchrotron radiation (OSR) [3], but ours still have to be characterized carefully to allow accurate bunch-length measurements using the OTR in our case. Finally, we report measurements of the bunch compression in a double-dogleg transport line as a function of the upstream 9-cell accelerator rf phase.

*Work supported by U.S. Department of Energy, Office of Science, Office of High Energy Physics, under Contract No. DE-AC02-07CH1135.

EXPERIMENTAL BACKGROUND

The tests were performed at the Fermilab A0 photoinjector facility which includes an L-band photocathode (PC) rf gun and a 9-cell SC rf accelerating structure which combine to generate up to 16-MeV electron beams [4]. The drive laser operates at 81.25 MHz although the micropulse structure is usually counted down to 9 MHz. Previous bunch length measurements of the drive laser and e-beam [2] were done with the fast single-sweep module of the Hamamatsu C5680 streak camera with an inherent shot-to-shot trigger jitter of 10 to 20 ps. Such jitter precluded synchronous summing of the short pulses. We have upgraded the camera by acquiring the M5676 synchroscan module tuned to 81.25 MHz with a trigger jitter of less than 1.5 ps (FWHM) and the C6878 phase-locked delay unit which stabilizes the camera phase over 10s of minutes. Due to the low, electron-beam energies and OTR signals, we typically synchronously summed over 50 micropulses with 1 nC per micropulse. The tests were performed in the straight-ahead line where energizing a dipole sends the beam into a final beam dump. The setup includes the upstream corrector magnets, quadrupoles, rf BPM, the YAG:Ce/OTR imaging stations, and the beam dump as schematically shown in Fig. 1. The initial sampling station was chosen at Cross #9, and an optical transport system using flat mirrors and a parabolic mirror brought the light to the streak camera. A short focal length quartz lens was used to focus the beam image more tightly onto the streak camera entrance slit. The quartz-based UV-Vis input optics barrel transferred the slit image to the Hamamatsu C5680 streak camera's photocathode.

Alternatively, the 4-dipoles of the emittance exchange line could be powered and experiments done at an OTR station, Cross #24, after the fourth dipole.

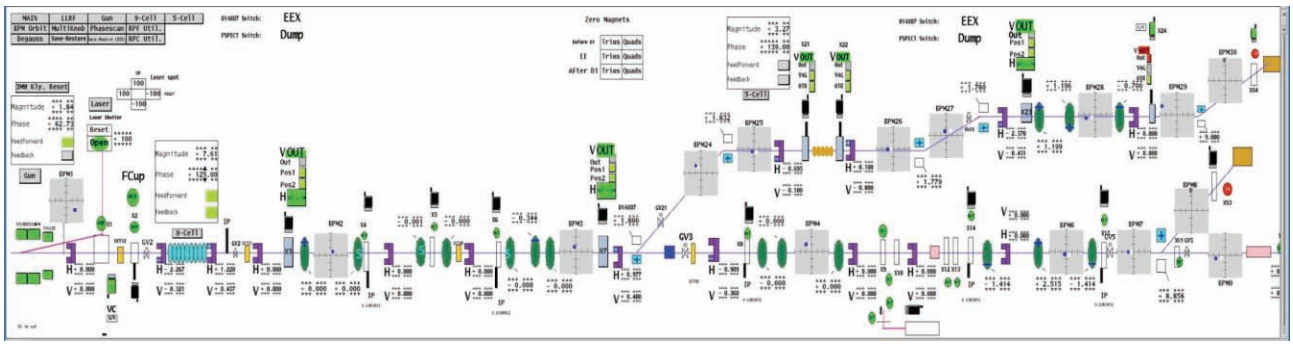

Figure 1: A schematic of the A0 photoinjector test area showing the PC gun, 9-cell cavity, the rf BPMs, the OTR/ODR station, the optics with camera, and the second beamline when the two dogleg dipoles are powered.

A second optical transport line brings the OTR to the streak camera. In the EEX line the bunch compression effects were observed, and the shorter bunches were used to help delineate the chromatic temporal dispersion effects for various band pass, long pass, and short pass filters The OTR converter is an Al-coated optics mirror that is 1.5 mm thick with a zerodur substrate, and is mounted with its surface normal at 45 degrees to the beam direction on a stepper assembly. The assembly provides vertical positioning with an option for a YAG:Ce scintillator crystal position. We still suspect the larger beam sizes may have resulted in incomplete signal collection over angle space. A two-position actuator and a 4-position translation stage were used in the optical path in front of the camera to select band pass filters. The OTR streak readout camera images were recorded with a PCI-compatible video digitizer for both online and offline image analyses. The charge was monitored by an upstream current monitor.

RESOLUTION AND BANDWIDTH EFFECTS

The first step in verifying streak camera operations is to determine the static spread function contribution to temporal resolution. This is the vertical beam spot size of the entrance slit mapped through the imaging system when in camera "focus" mode. The major contribution is the slit height itself for values larger than 30 µm or so. In our early experiments with 10-50 nC of charge integrated in the micropulse sum, we used a slit height of 80 µm, which resulted in a limiting vertical spot size of 9 pixels. The limiting resolution is then found by multiplying this by the sweep-speed calibration factor. We did a careful determination of the two fastest ranges, range 2 and range 1 by using a laser pulse-stacker configuration. By splitting the laser beam energy, we could separately delay one pulse relative to the other by a set of movable mirrors. We then tracked the observed pulse separations in the streak camera images. A plot of the observed time separations is shown in Fig. 2 for range 2 and Fig. 3 for range 1. The reciprocals of the fitted slopes gave us 1.55 ps/pixel and 0.32 ps/pixel, respectively. This means our initial resolution terms were 14.0 ps and 2.9 ps (FWHM), respectively. In the second series of experiments we reduced the slit height to 40 µm with a corresponding vertical spot size of 4.7 pixels (FWHM). This then gives us resolution terms of 7.3 ps and 1.50 ps (FWHM), respectively, for range 2 and range 1. This was needed for the bunch compression tests particularly.

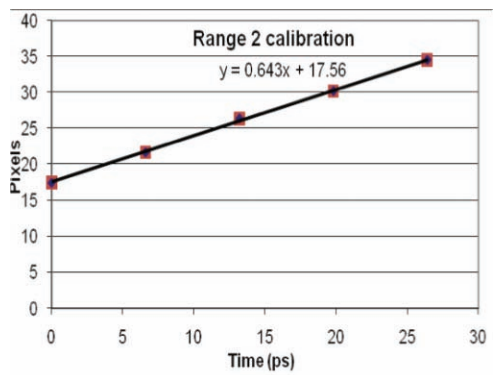

Figure 2: Calibration of the streak camera Range 2 using the laser pulse stacker. The separation of the split laser beam pulses was adjusted with the mirror spacing.

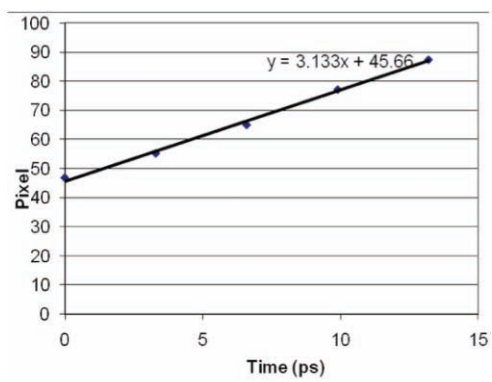

Figure 3: Calibration of the streak camera Range 1 using the laser pulse stacker. The separation of the split laser beam pulses was adjusted with the mirror spacing.

One of the practical issues we addressed was the chromatic temporal dispersion that occurred for the broadband OTR light as it was transported through the

transmissive components of the optical transport line. Since the input optics barrel of the streak camera was actually UV transmitting, it consisted of quartz optical components. This material has less variation of index of refraction with wavelength than flint glass or other materials used in the other standard Hamamatsu input optics, but still results in a measurable effect that limits effective temporal resolution with broadband light. Our effect was shown to be smaller than the SSRL setup of 0.2 ps/nm reported at PAC07 [3]. The basic concept is expressed by the simple relationship for the transit-time change, $\Delta t = L\,(v_{g2}-v_{g1})/(v_{g1} \times v_{g2})$, due to the difference in group velocities v_{g1} and v_{g2} for two wavelengths through a characteristic material thickness, L [5].

This effect is represented in Fig. 4 where a 3-ps FWHM actual pulse is shown as arriving at different times for different wavelengths with a 4-ps shift across the bandwidth of the measurement. The resulting superposition of these Gaussian profiles can be fit to a single Gaussian of 4.21 ps (FWHM). In the actual MATLAB model, a series of over 1000 Gaussians was used. In our case the temporal shift was 8 to 9 ps within the 550-nm shortpass filter bandwidth and caused an effective limiting resolution term of about 4.4 pixels (FWHM) for range 2 in quadrature with the static spread function of 4.7 pixels.

We then can calculate the actual pulse length by subtracting from the total observed pulse width in pixels the contributing terms of static spread function, bandwidth, and trigger jitter. Since the jitter term appears to be small compared to our bunch lengths, we have absorbed it into the actual bunch length term for the time being. Then for range 2 and range 1 we would have respectively:

$$\delta t(FWHM) = \sqrt{Pixel^2 - 4.7^2 - 4.4^2} \times 1.55 ps/pixel$$

$$\delta t(FWHM) = \sqrt{Pixel^2 - 4.7^2 - 22^2} \times 0.32 ps/pixel$$

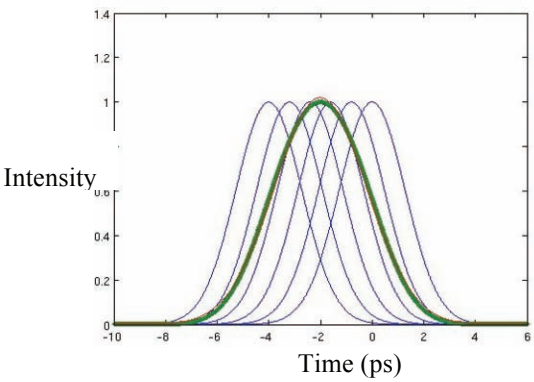

Figure 4: A simple representation of the group velocity dispersion effect on the streak image for a 3-ps FWHM initial pulse and a 4-ps temporal shift in the bandwidth used. The blue curves represent the series of Gaussians time shifted with wavelength. The resultant streak image profile has a 4.21 ps (FWHM) size (green curve).

STREAK CAMERA OTR RESULTS

The experiments were usually initiated by verifying the OTR-deduced spot sizes and centering of the beam on the screen centerline and the downstream rf BPM coordinates. We would optimize the signal transported through the entrance slit of the streak camera while in Focus mode. We then switched to either range 2 or range 1, set the delay for viewing the streak images, and phase locked the delay box.

In the case of the straight-ahead line, we first tried to use larger charges in the micropulse and integrated over 10 pulses. Figure 5 shows the results for both range 2 and range 1 with 5.3 nC per micropulse and 10 micropulses synchronously summed in the image. For these data we actually used a 550 x 40 nm bandpass filter so the bandwidth effects are negligible. After subtracting a larger limiting resolution of 9 ch (FWHM) from each image for this setup, the bunch length was determined as 31± 2ps in range 2 and 32 ± 2 ps in range 1. This was a somewhat larger value than expected so we next did a series of bunch length measurements in which we varied the micropulse charge only. The drive laser bunch length was maintained at about 7.9 ps (FWHM), as verified by a separate streak camera measurement. The results are shown in Fig. 6 where a significant elongation of the e-beam micropulse from 10 to 30 ps occured as we varied the charge/micropulse from 1 nC to 5 nC. For comparison we also show a previous measurement reported in Rodion's dissertation on this photoinjector which has a decidedly different slope [2]. We attribute this difference to the laser spot size being previously reported as 1.77 mm rms compared to the present measured value of 1.15 mm rms. Since the bunch lengths were within 10 % in each case, the space charge effects should be stronger in our data. This is consistent with the ASTRA results (black curve) that simulate our present situation and shown in Fig. 6 as well. The previous ASTRA simulation curve falls very close to the reported experimental data [2].

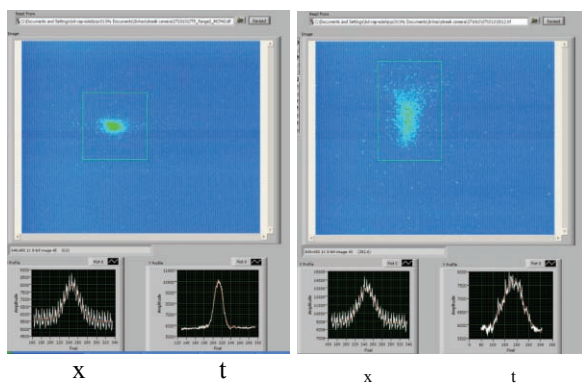

Figure 5: Streak camera image using range 2 (left) and range 1 (right). In the images the vertical axis is the time axis, and the horizontal display axis is the x spatial axis. The bunch length profile is at the lower right of the image and has a width of 32±2 ps (FWHM).

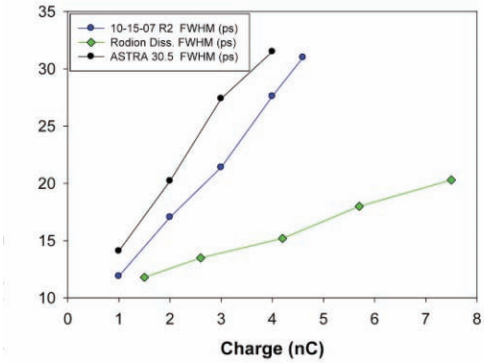

Figure 6: Comparison of the variation of bunch length FWHM with micropulse charge as measured [in Oct. 2007] (blue curve) and as simulated by ASTRA (black curve) and a previous measurement by Rodion (green curve).

As part of these studies we also noted an apparent beam size variation *within* the micropulse time scale as shown in Fig. 7 for a micropulse charge of 4 nC. The observed synchronous sum beam size in the center (green) region of interest (ROI) is about 34.5 ch (FWHM), while it is 50.4 ch at the upper end (red ROI). A beam-size ratio of 1.46 for that portion in the end ROI over the middle ROI was found. The bunch length is about 28 ps (FWHM).

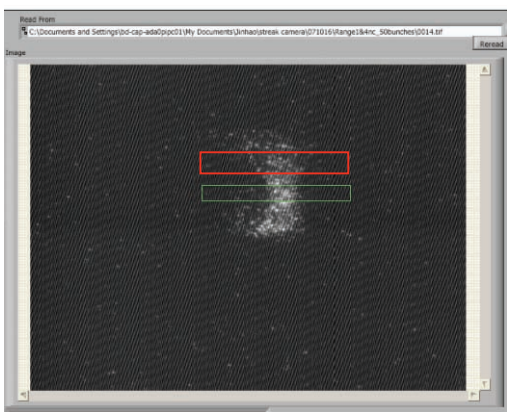

Figure 7: Evidence for slice beam-size effects on the micropulse time scale for a 4-nC micropulse charge. The x beam size sampled at each end of the time profile is about 50% larger than that sampled in the middle (green ROI) of the pulse.

The next series of investigations was done in the other beam line that is setup for emittance exchange experiments [6]. A 5-cell TM_{110} rf superconducting deflector cavity is positioned between two transport doglegs. Compression of the e-beam can be done by proper phasing of the upstream 9-cell cavity. In Fig. 8 we show the results of our initial experiments. The 9-cell rf accelerator phase is varied from 5 degrees off crest to about 25 degrees off crest [7]. The reference phase is 148 degrees in this case. The minimum bunch length is expected at about 21 degrees off crest based on simulations. Due to lower OTR signal transport, we used 100 micropulses of 1 nC per micropulse summed in the images. The bunch length is seen to vary from 22 ps down to 3.8 ps (FWHM) for these conditions. We used both R2 and R1 with the 550 nm short pass filter, and then one additional scan another day was done with the 550 nm LP filter in place with R1. The data were matched in phase at the local minimum. The overlap of points for the different ranges and filters are all in good agreement. This supports the validity of our analysis of the various contributions to resolution.

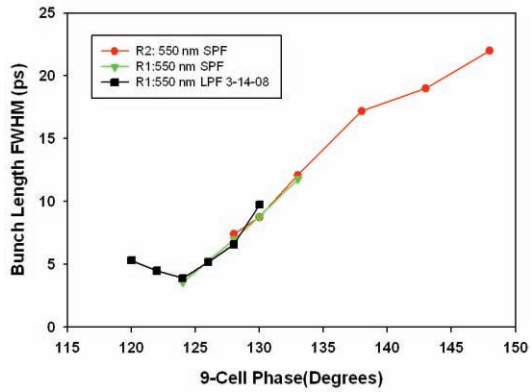

Figure 8: The variation of bunch length with 9-cell phase as measured by the streak camera after the two transport doglegs.

Also the trajectory change with beam energy can be studied via the transit time changes through the doglegs as shown in Fig. 9. The phase-locked streak images allow the change in image time position to be used to track the arrival time change. One can see that a ±1% change in momentum causes an about ±6 ps change, respectively, in transit time through the bends. These data were used to evaluate one of the transport matrix elements of the emittance exchange line.

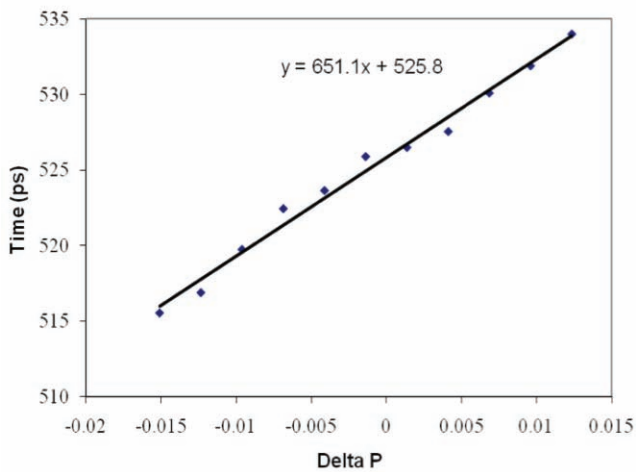

Figure 9: A plot of the change in transit time through the doglegs for different 9-cell rf amplitudes, and hence momentum changes, Delta P.

SUMMARY

In summary, we have extended the investigations on streak camera imaging of the 15-MeV electron beam in the transport lines of the A0 photoinjector using OTR as the conversion mechanism. The enabling technology for these measurements was the synchroscan module installed in the streak camera mainframe combined with the new phaselocked delay box. These allowed synchronous summing of micropulses with much lower jitter than the single sweep unit and with the phase stability locked over 10s of minutes. We were able to measure space-charge effects in the gun, bunch compression effects, transit time effects, and chromatic temporal dispersion effects in our optics. Further investigations are planned on these effects, and a dual sweep unit for the streak camera will be added to the options to explore macropulse time-scale effects.

ACKNOWLEDGEMENTS

The authors acknowledge support from M. Wendt and H. Edwards of Fermilab and A0 technical assistance from J. Santucci, R. Fliller, T. Koeth, and M. Davidsaver.

REFERENCES

[1] Alex H. Lumpkin, "The Next Generation of RF FEL (Free Electron Laser) Diagnostics: Synchroscan and Dual-Sweep Streak Camera Techniques," Nucl. Inst. and Meth. in Phys. Res., A304, 31 (1991).

[2] Tikohoplav Rodion, PhD thesis, "Low Emittance Electron Beam Studies", FERMILAB-THESIS-2006-04.

[3] J.Corbett et al., "Bunch Length Measurements in SPEAR3", Proc. of PAC07, FRPMS065.

[4] R. P. Fliller, H. Edwards, W. Hartung, "Time dependent quantum efficiency and dark current measurements in an RF Photocathode injector with a high quantum efficiency cathode", proc. of PAC05, Knoxville, USA.

[5] H.Staerk, J. Ihlemann, A. Helmbold, "Group Velocity Dispersion: Its Consideration in Picosecond Spectroscopy with Streak Cameras", Laser und Optoelektronik, **28**, 6 (1988) in english.

[6] T. Koeth, L. Bellantoni, D. Edwards, H. Edwards, R. P. Fliller III, " A TM110 Cavity for Longitudinal to Transverse Emittance Exchange", PAC 07, THPAS079, Albuquerque , NM , USA

[7] Ray Fliller (Fermilab, Private communication, Jan. 2008.)

OBSERVATIONS OF ENHANCED OTR SIGNALS FROM A COMPRESSED ELECTRON BEAM*

A.H. Lumpkin, Fermilab, Batavia, IL U.S.A. 60510
N.S. Sereno, M. Borland, Y. Li, K. Nemeth, and S. Pasky,
Argonne National Laboratory, Argonne, IL U.S.A. 60439

Abstract

The Advanced Photon Source (APS) injector complex includes an option for photocathode (PC) gun beam injection into the 450-MeV S-band linac. At the 150-MeV point, a 4-dipole chicane was used to compress the micropulse bunch length from a few ps to sub 0.5 ps (FWHM). Noticeable enhancements of the optical transition radiation (OTR) signal sampled after the APS chicane were then observed as has been reported in LCLS injector commissioning. A FIR CTR detector and interferometer were used to monitor the bunch compression process and correlate the appearance of localized spikes of OTR signal (5 to 10 times brighter than adjacent areas) within the beam image footprint. We have done spectral dependency measurements at 375 MeV with a series of band pass filters centered in 50-nm increments from 400 to 700 nm and observed a broadband enhancement in these spikes. Discussions of the possible mechanisms will be presented.

INTRODUCTION

During the commissioning of the LCLS injector in 2007, unexpected enhancements of the signals in the visible light optical transition radiation (OTR) monitors occurred after compression in a chicane bunch compressor [1]. These signals were attributed to a microbunching effect of some kind and the generation of coherent OTR (COTR). Since the Advanced Photon Source (APS) injector complex includes a flexible chicane bunch compressor that is similar to that at LCLS, we have an option to use an rf photocathode (PC) gun, and we had experience with SASE-induced microbunching [2], a series of experiments was performed to explore the phenomena. We initially performed studies on OTR measured at three screens located after the bunch compressor. We used focus-at-the-object or near-field imaging optics and established that there were clear enhancements of the OTR signals at maximum bunch compression. The compression was also monitored with a FIR CTR monitor and interferometer. The shortest bunches generally generate the strongest FIR signals, and the appearance of the enhanced OTR was strongly correlated with the maximum FIR signal, although there appeared to be a slight phase shift between the two maxima. We also accelerated the compressed beam to the end of the linac and evaluated the enhancements at 375 MeV. The localized spikes in the beam distribution were still visible at this energy. At this latter station we have the light transported outside of the tunnel to a small optics lab that allowed us to perform additional spectral dependency measurements. Moreover, the use of a thermionic cathode gun pulse train with only 40 pC per micropulse did not show the OTR enhancements when the bunch length was compressed comparably to that of the PC gun beam. Discussions of the possible mechanisms will be presented for the APS case which is similar, but not identical to that of LCLS.

*Work supported by U.S. Department of Energy, Office of Science, Office of High Energy Physics, under Contract No. DE-AC02-06CH11357.

EXPERIMENTAL BACKGROUND

The tests were performed at the APS facility which includes an injector complex with two rf thermionic cathode (TC) guns for injecting an S-band linac that typically accelerates the beam to 325 MeV, the particle accumulator ring (PAR), the booster synchrotron that ramps the energy from 0.325 to 7 GeV in 220 ms, a booster-to-storage-ring transport line (BTS), and the 7-GeV storage ring (SR). In addition, there is an rf photocathode (PC) gun that can also be used to inject into the linac as shown schematically in Fig. 1. An extensive diagnostics suite is available in the chicane and after the chicane area as also shown in Fig. 1. The tests were performed in the linac at the three imaging stations (indicated by a flag symbol) after the chicane bunch compressor and at the end of the linac where another beam imaging station is located. A FIR coherent transition radiation (CTR) detector (Golay cell) and Michelson interferometer [3] are located between the three-screen emittance stations. A vertical bend dipole and diagnostics screens in this short beamline allow the monitoring of tranverse x-beam size and energy following compression.

The CTR converter is an Al-coated mirror with an 18 mm diameter clear aperture on a zerodur substrate, and it is mounted with its surface normal at 45 degrees to the beam direction on a pneumatic actuator assembly. A synthetic quartz lens at the port of the cross collimates the beam into the interferometer box. A remotely controlled translation stage steps the position of one arm of the interferometer for the autocorrelation tests. An EPICS interface allows the acquisition of the autocorrelation data. The YAG:Ce and OTR were directed by turning mirrors and relay optics to a Pulnix CCD camera located 0.5 m from the source. These Chicane stations also have options for low- and high-resolution imaging of the beam spot by selecting one of two lens configurations [4].

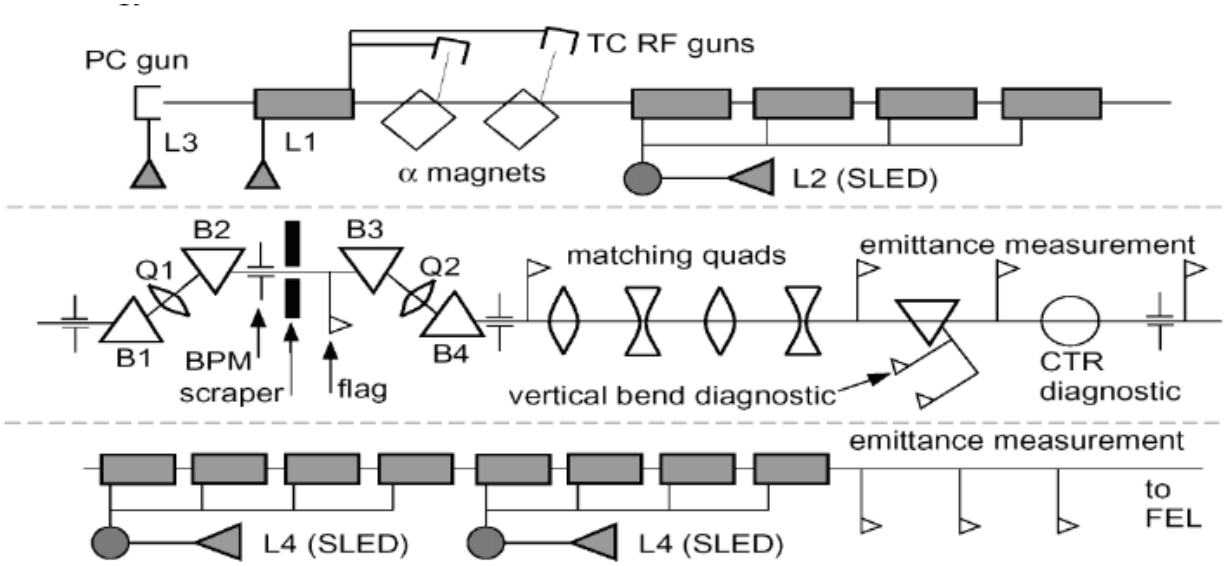

Figure 1: A schematic of the APS linac test area showing the PC gun, the two TC rf guns, the accelerator structures, the chicane, and the diagnostics suite. This includes rf BPMs, beam profile screens (flags), FIR CTR diagnostic, and the vertical bend diagnostic line.

The near-field, low-resolution magnification resulted in calibration factors of 48.8 μm per pixel in x and 38.9 μm per pixel in y. The OTR signal strength with a 400 pC micropulse was too low to use the high-resolution mode. The signal intensity was adjusted with a remotely-controlled iris (with no absolute position readback) in the path to the camera. The OTR and YAG:Ce images were recorded with a Datacube MV200 video digitizer for both online and offline image analyses, and a video switcher was use to select the camera signal for digitizing.

At the end of the linac, the imaging station included the optical transport of the visible light out of the tunnel to a small, accessible optics lab where the CCD camera was located. This allowed the access for exploring the spectral dependency of the enhanced OTR. A set of bandpass filters with center wavelengths in 50-nm increments from 400 to 700 nm and 40-nm band width as well as a 500-nm shortpass filter and 500-nm long pass filter were used in the tests. The beam energy was 375 MeV at this station.

Data were also recorded from the electron spectrometer at the end of the linac, but this focal plane converter screen was made of Chromox.

INITIAL CTR AND OTR RESULTS

The experiments were initiated by transporting the PC gun beam accelerated to 150 MeV to the chicane area. The rf phase of the L2 accelerator structure located before the chicane was used to establish the appropriate conditions for compression in the chicane. The degree of compression was tracked with the Golay cell signals as shown in Fig. 2. A very strong variation of the FIR signal with L2 phase is observed. There is almost no signal seen when uncompressed and 300 units seen at the peak compression. The autocorrelation scan was then done and showed a profile width of ~65 um (FWHM) as seen in Fig. 3. Two separate scans are displayed in the plot. This would mean a roundtrip time of 130 μm, or about 430 fs (FWHM). The initial PC gun bunch length was 3 to 4 ps (FWHM) as determined by the drive laser pulse.

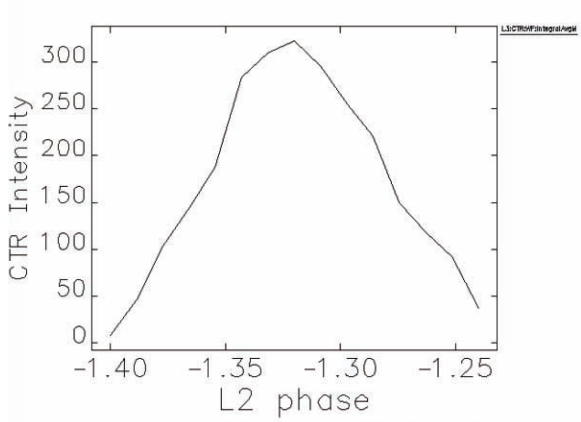

Figure 2: FIR CTR signal from the Golay cell variation with the upstream L2 phase setting (reading in V).

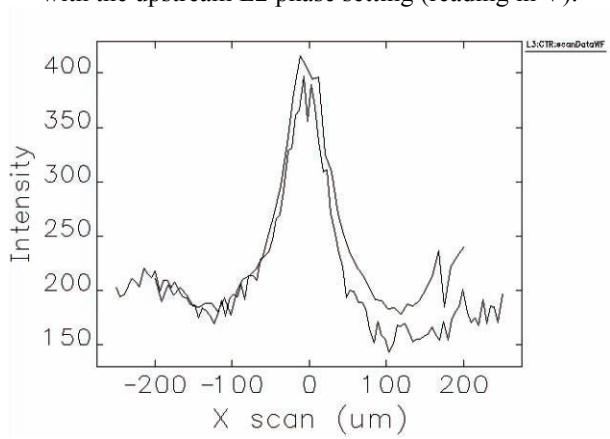

Figure 3: FIR CTR autocorrelation performed after the chicane near maximum compression setup for the PC gun. The two scan profile widths are about 65 μm (FWHM).

Having determined we had good compression from the Golay-cell data, we then sampled the beam images at the three screens after the chicane in the emittance measurement area. The samples shown are from FS5, the third screen of the set. At the point of minimum compression the OTR image is weak, but visibly tilted in x-y space. No sharp features are seen as shown in Fig. 4. The profile is sampled a little off center of this image, but it is representative of its flatness and low intensity of 15-25 counts. In contrast, the image taken near full compression as indicated by the FIR CTR signal has significantly enhanced localized spikes of about 250 μm extent as shown in Fig. 5. The pseudo-color intensity scale at the right of the image shows that the red areas are high intensity. The profile at the right shows the peak intensity of 180 counts, almost 10 times the adjacent intensities in the beam-image footprint. We do not see the ring-like structure in the enhancement reported at LCLS, but we also don't have a harmonic cavity for linearizing longitudinal phase space before the chicane as LCLS has. On this particular run, we noted that there seemed to be a preferred location in the beam image to be enhanced. The enhanced vertical band in Fig. 5 is the same area that shows less enhancement with less compression.

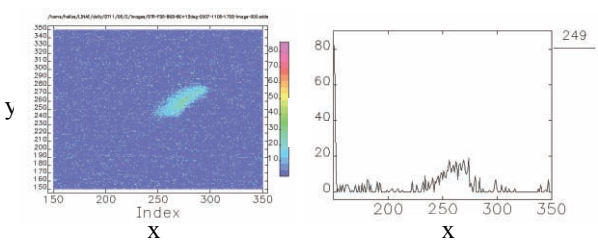

Figure 4: OTR beam image (left) and horizontal profile (right) sampled through distribution after BC with L2 phase = 12 degrees, close to minimum compression.

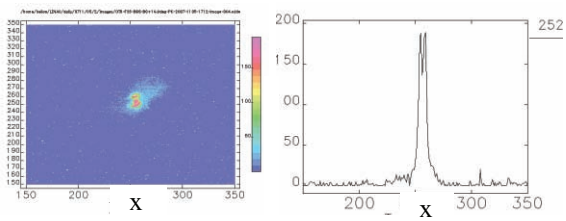

Figure 5: OTR beam image (left) and horizontal profile (right) through spike in distribution after BC with L2 phase = 14.9 degrees, close to maximum compression.

An additional indication of the effect is shown in Fig. 6, where the peak intensities from the vertical profiles taken though the images at each phase setting show the rapid increase in the enhanced OTR signal in just a few degrees of L2 phase change. The order of magnitude enhancement is clearly seen in this plot. A similar plot for horizontal profiles was done, and this showed a slight shift of the intensity peak compared to the CTR data by 0.4 degrees in L2 phase. Integrated areas of the ten images at each phase setting do not show this degree of enhancement, but

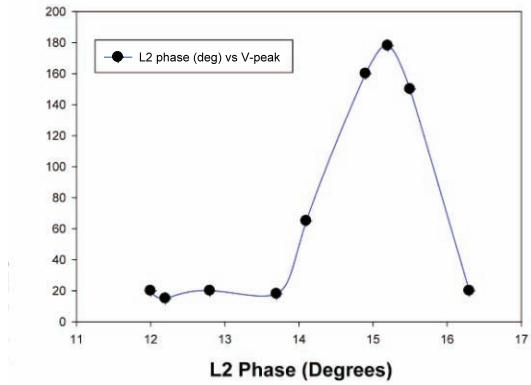

Figure 6: Plot of the peak intensities from the OTR image vertical profiles taken near the enhanced regime coordinates as a function of L2 phase in degrees.

about a 1.6-2 times larger counts integral at peak compression was seen with larger fluctuations in the compressed conditions as shown in Fig. 7 (top). The peak intensities on average increase by 3-4 as shown in the lower plot of Fig. 7. This fact is consistent with the premise that the charge transport intensity is not the cause of the effect nor CSR- induced clumping of electrons, but rather a coherent enhancement of some kind is involved.

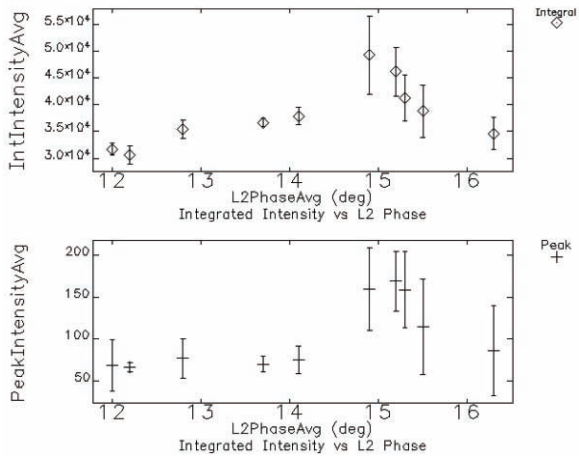

Figure 7: Plot of the OTR image integrals (top) and OTR peak intensities (bottom) using automated post processing versus L2 phase (degrees). The enhancements occur near the FIR CTR signal maximum.

In order to assess the spectral dependency of the OTR enhancements, we accelerated the beam to 375 MeV and again imaged the beam spot with OTR at a downstream station. As described previously, this station included transport of the signal outside of the tunnel to a small optics lab. First, we still see enhanced localized spikes when we have compressed the beam as shown in Fig. 8. We also confirmed that these spikes were present at even a compression level of ½ the CTR signal, although their intensity varied more from shot to shot. In Fig. 9 we show the post-processed image intensity integrals (top) and the peak intensities (bottom) versus the L2 phase set point at this location. In this case enhancements of the OTR signals when at maximum compression are about 3-6

times the normal intensity. The strong fluctuations of these enhanced areas are again suggestive of a coherent process, perhaps seeded by noise. (We also recall that previously our self-amplified spontaneous emission (SASE) free-electron laser (FEL) experiments indicated preferred hot spots in the spatial distribution of the compressed beam.)

At full compression we checked the spectral dependency of the enhancements by inserting the bandpass filters in front of the CCD camera. Our preliminary results are that the enhancements were seen at all central wavelengths from 400 to 700 nm (in steps of 50 nm), although relatively weaker in the 400 to 500-nm regime than at 550 nm. We subsequently checked the spectral dependence of incoherent OTR from the TC gun beam and saw a similar intensity rolloff in this short wavelength interval which we attribute to the CCD camera response to these different wavelengths. We also saw more enhancement of intensity in the 500-nm longpass filter than in the 550-nm shortpass filter.

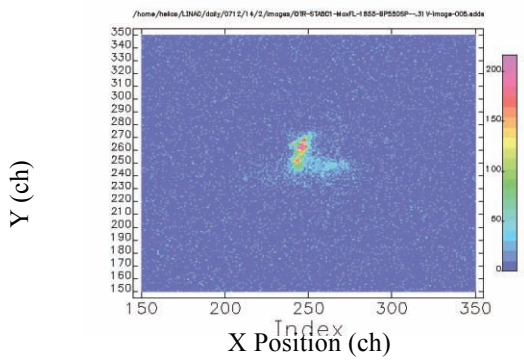

Figure 8: OTR image at 375 MeV showing the enhancements are still present after acceleration beyond the bunch compressor.

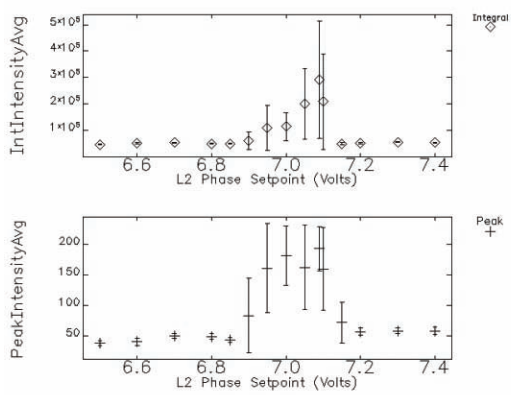

Figure 9: Plot of the OTR image integrals (top) and OTR peak intensities (bottom) at 375 MeV using automated post processing versus L2 phase setpoint (volts). The enhancements occur near the FIR CTR signal maximum.

CTR AND OTR RESULTS WITH TC RF GUN BEAM

In the course of our studies, we decided to test the effect with the TC rf gun beam. In this case we could generate about 40 pC per micropulse in a macropulse of 25 micropulses that contained about 1 nC total. So the integrated OTR signal should be similar to that of the PC gun beam. We also have no drive laser involved. With the combination of compression in the alpha magnet of the TC gun system and the chicane, we were able to generate an autocorrelation profile width of ~62 μm (FWHM) as shown in Fig. 10. This result is very similar to the PC gun result in Fig. 3, so we have again about a sub-0.5 ps FWHM micropulse at a beam energy now of 150 MeV. The main difference at the chicane is there is now 10 times less charge in the micropulse compared to the PC gun beam, and 10 times lower peak current. One would expect a significant reduction in any coherent mechanisms. We observed no localized OTR enhancements at the screen after the chicane, nor at the downstream location at the end of the linac. The integrated intensities were the same to about 10% throughout the L2 phase scan. An image from the latter screen under full compression conditions is shown in Fig. 11. The beam size is larger than that of the PC gun beam due to the larger emittance from the source. We repeated the spectral intensity measurements with the filters and determined the nominal overall response of the system to the OTR spectrum and the CCD sensitivity factors. The intensity vs. wavelength curve is very similar to that of the PC gun beam images with enhancements. Therefore, we have no evidence yet of a specific wavelength enhancement in the visible light regime, such as might be due to longitudinal microbunching. We are planning tests with a UV-IR spectrometer in the near future.

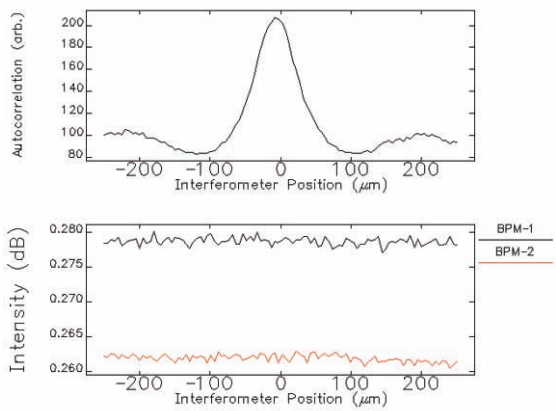

Figure 10: FIR CTR autocorrelation performed after the chicane near maximum compression setup for the TC gun. The scan profile width (top) is about 62 μm (FWHM). The BPM sum signals (bottom) from positions after the chicane were also tracked and show little change during the scan.

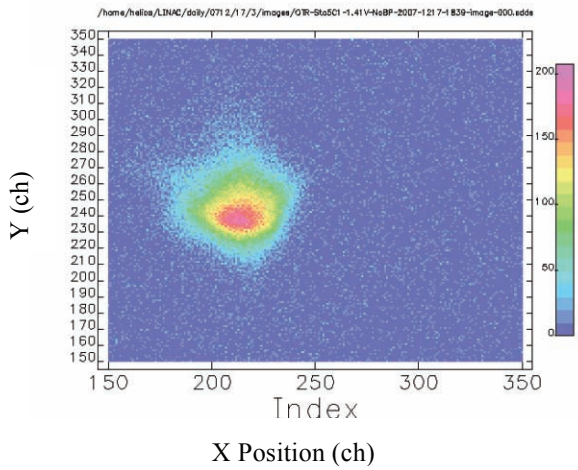

Figure 11: An example OTR image of the TC rf gun beam at the 375-MeV station with maximum compression in the chicane. No localized spatial spikes are evident.

DISCUSSION

We have identified several characteristics of the enhanced OTR signals that may be used to evaluate which mechanism is involved. If we consider electron number constancy, photon number enhancements, and spectral structure observed, we may be able to discriminate among microbunching, a longitudinal spike, and CSR-induced clumping. We initially wondered whether there were microbunching from the drive laser interaction with the low-energy photoelectrons such as found under high laser power conditions [5], but a simple calculation of the laser field strengths showed this effect would not be measurable. Since we accept the transported charge through the chicane is basically constant to 10 % during the phase scan, we cannot explain the large photon number enhancements as only due to CSR-induced clumping of the charge distribution. Finally, our preliminary spectral sampling across the visible light region with 40-nm band widths showed a broadband character like that of incoherent OTR. Our data seem more consistent with coherent enhancements due to longitudinal structure such as a leading-edge spike.

SUMMARY

In summary, we have initiated investigations on enhancement of OTR signals in the visible light regime following bunch compression of our PC rf gun beam at APS. Although the enhancements are not as high as that reported at LCLS, we do see order of magnitude signal increases in localized spatial spikes. At this time the coherent enhancement appears consistent with a fine spike in the longitudinal distribution that develops after bunch compression. The practical effect is that we cannot simply evaluate emittance of the beam for different compressions using the OTR screen images, but we normally use the Yag:Ce screens. We did not see the effects in the TC gun beam when compressed similarly, but this involved only 40 pC per micropulse and a macropulse charge of ~1 nC. The growing interest in these COTR effects is indicated by the time allowed for discussion in the planned high brightness beams workshop at Zeuthen in May 2008 [6].

ACKNOWLEDGEMENTS

The authors acknowledge support from R. Gerig and K.-J. Kim of the Argonne Accelerator Institute and M. Wendt of Fermilab.

REFERENCES

[1] D.H. Dowell et al., “LCLS Injector Commissioning Results”, submitted to Proc. of FEL07, Aug. 26-30, 2007, Novosibirsk.

[2] A.H. Lumpkin et al., “First Observation of z-dependent Microbunching using Coherent Transition Radiation,” Phys. Rev. Lett., Vol. 86(1), 79, January 1, 2001.

[3] A.H. Lumpkin et al., “Initial measurements of CSR from a Bunch-Compressed Beam at APS.” Proc. of FEL05, JACoW/eConf C0508213, 608 (2005).

[4] B.Yang et al., “Design and Upgrade of a Compact Imaging System for the APS Linac Bunch Compressor”, BIW2002, AIP Conf. Proc. 648, 393 (2002).

[5] Karoly Nemeth et al., PRL 100, 095002 (2008).

[6] Agenda for Mini Workshop on “Characterization of High Brightness Beams,” Zeuthen, May 26-30, 2008.

BEAM TRANSVERSE PROFILE MONITOR FOR IFMIF-EVEDA ACCELERATOR

P. Abbon, É. Delagnes, F. Jeanneau, J. Marroncle, J.-P. Mols, J. Pancin,

CEA Saclay, DSM/IRFU, France

Abstract

In the framework of the IFMIF-EVEDA project, a high deuteron beam intensity (125 mA - 9 MeV) prototype accelerator will be built and tested at Rokkasho (Japan). CEA-Saclay group and Ciemat-Madrid (Spain) are responsible of the beam instrumentation from the ion source to the beam dump. One of the most challenging diagnostic is the Beam Transverse Profile Monitor (BTPM). CEA-Saclay group investigates such a monitor based on residual gas ionization. This monitor uses a high electric field to drive the products (electrons and ions) of ionization to micro-strips. A priori, no primary amplification is required due to the high beam intensity. Nevertheless, in order to study the feasibility, a prototype will be tested in a proton beam.

INTRODUCTION

This paper is devoted to the description of a non-destructive profiler prototype for the IFMIF-EVEDA project. In a first part, the context of this project will be briefly given. The second part will present the prototype, its principle, the expected counting rates, the design and some issues addressed to a future preliminary test.

CONTEXT

The International Fusion Materials Irradiation facility (IFMIF) aims at producing an intense flux of 14 MeV neutrons, in order to characterize materials envisaged for future fusion reactors. The primary mission of IFMIF is to provide a materials irradiation database for the design, construction, licensing and safe operation of the Fusion Demonstration Reactor (DEMO) [1]. In such a reactor, high neutron fluxes may generate up to 30 dpa/fpy (displacements per atom / full power year). IFMIF facility is based on two high power cw drivers (175 MHz) delivering 125 mA deuteron beams at 40 MeV each, colliding a liquid lithium target.

In the framework of the "Broader Approach", the IFMIF-EVEDA (Engineering Validation and Engineering Design Activities) project includes the construction of an accelerator prototype with the same characteristics as IFMIF, except 9 MeV instead of 40 MeV for the incident deuteron energy. Most of the components of the accelerator are developed by France, Italy and Spain. Commissioning of this accelerator at Rokkasho is foreseen for 2013.

France (CEA-Saclay) and Spain (Ciemat-Madrid) are responsible of the beam instrumentation from the RFQ to the beam dump.

One of the relevant IFMIF issues is to avoid lithium boiling at beam-target crossing (5×20 cm^2), thus placing stringent conditions on the beam spot. In particular, beam intensity fluctuations must be kept below ±5 %. Consequently, non-destructive beam profile monitors have to be designed to drive safely the beam in a very hard radiation background of neutrons and γ, and to precisely monitor the transverse beam profile and intensity fluctuations, especially just upstream the target. CEA-Saclay has decided to investigate such a monitor based on residual gas ionization.

BEAM TRANSVERSE PROFILE MONITOR (BTPM) PROTOTYPE

The BTPM prototype is based on the ionizations, induced by the beam particles, of the residual gas contains in the beam pipe of the accelerator. It will be first tested with a proton beam.

Accelerator parameters

Below are listed the parameters of the IFMIF accelerator:

- Deuteron cw linear beam (175 MHz ≡ 5.7 ns).
- Energy range: 5 to 9 MeV (40 MeV for IFMIF).
- Beam intensity: 125 mA which represents 4.5 10^9 deuterons/burst (250 mA close to IFMIF target).
- Vacuum pipe: 10^{-5} mb (target region) and 10^{-7} elsewhere.

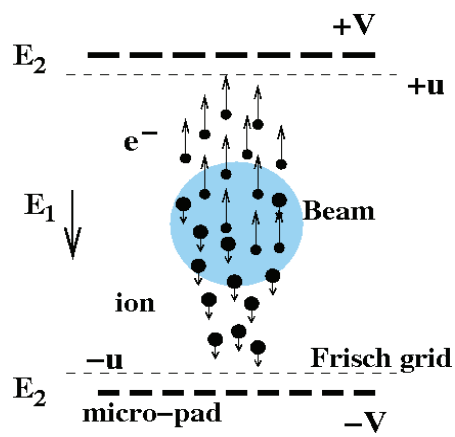

Figure 1: Transverse cross-section of a BTPM. Ionized pairs are sketched in the electric field.

Principle

Along the passage of the charged beam particles, some molecules of the residual gas are ionized, leading to the creation of electron/ion pairs, as sketched in Figure 1.

If a transverse electric field is applied, the produced particles, electrons and ions, drift along the field lines toward the anode and the cathode respectively. The motion of these particles induces currents, which can be detected on micro-pad. The Frisch grid, transparent to particles provided a good field ratio E1/E2, allows shielding against the beam electromagnetic field and restricts the active volume in which the current is read by the micro-pad.

Feasibility

Counting rate has been estimated to determine if amplification is required or not. Unfortunately, ionization data for deuteron are sparse. Thus, proton data have been used and extrapolated to 40 MeV [2]. The dominant residual gas is H_2 [3], so calculations were done using the $H^+ + H_2 \rightarrow H^+ + H_2^+ + e^-$ cross-section reactions. Taking into account the conditions defined above, the number of electron/ion pairs is around 3500 per burst, for a 1 cm detector thickness. The induced currents due to ionized particles are 100 nA for the electrons and 25 nA for the H_2^+ ions. With such currents, no amplification should be required. Usually, Multi Channel Plates (MCP) are used as amplifiers when primary currents are too weak. However, MCPs are very radiation sensitive and would not cope with the hard IFMIF radiation environment.

The time taken by electrons and ions are 5 ns and 280 ns respectively, for a 20 cm drift distance. Since position resolutions are better with ions than electrons [3][4], the profiles will be extracted from ion signals. Nevertheless, electron signals are big and fast, and could be exploited to give some rough information with wider strips…

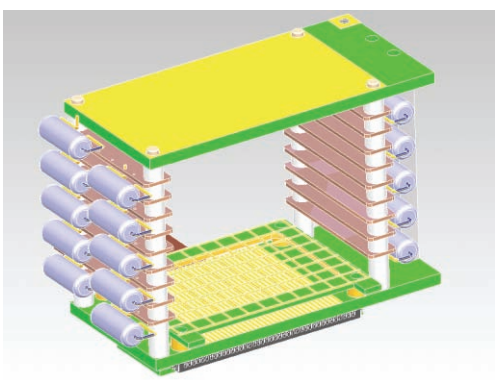

Figure 2: BTPM prototype.

The BTPM prototype design

In order to check the response of our BTPM, we have designed a first version of prototype, which will be tested at Saclay proton beam. Figure 2 shows the drawing of this prototype. This prototype is 5x5x4 cm^3 (4 cm in beam direction) with a 4x3 cm^2 micro-pad area made of 32 strips. The electric potential is applied to the upper plate while micro-pad is grounded via electronics. The electric field uniformity is insured by 9 rod pairs (left and right sides) degrading regularly the field by means of resistors.

Preliminary test

A first test is foreseen in July 2008 at Saclay, with the SILHI source [5], which delivers a proton beam of 95 keV up to 100 mA. In order to measure ion and electron signals, we will change the polarity of the voltage. Rotating the monitor by 90° will give access to vertical or horizontal axis. Below are listed the various topics we want to check or investigate:

- Principle of the detector.
- Optimization of voltage versus beam intensity and energy.
- Noise, background shielding.
- Counting rates: at 95 keV, ionization cross-sections are ~ 300 times greater than for 40 MeV.
- Position resolution measurement.
- Data acquisition.

This test will permit improvements to adapt a new detector to our requirements (simultaneous electrons/ions detection, new electronics, mechanical shape…). This one will be tested on the Saclay IPHI proton beam [6] of 3 MeV up to 100 mA, in fall 2009.

If this prototype is validated, a final design will be launched, leading to the delivery at the end of 2012 at Rokkasho.

Conclusion

We have presented a prototype of a non-destructive Beam Transverse Profile Monitor for IFMIF-EVEDA project. Such a BTPM has to deal with huge flux of neutrons and γ. A preliminary test is foreseen in June 2008 to answer various issues like the possibility to work without charge amplifier.

REFERENCES

[1] IFMIF Comprehensive Design Report, January 2004.
[2] E. Surrey at al., Report for TASK EVEDA technology programme, 2007.
[3] R. Anne et al., NIM A329 (1993) 21-28.
[4] K. Wittenburg, "Experience with the residual gas ionization beam profile monitors at the DESY proton accelerators", EPAC'92, Berlin, March 1992, p.1133.
[5] R. Hollinger et al., "High current proton beam investigations at the SILHI-LEBT at CEA/Saclay", Linac 2006, Knoxville, August 2006, p. 232.
[6] P.-Y. Beauvais et al., "Installation of the French high-intensity proton injector at Saclay", Linac 2006, Knoxville, August 2006, p. 153.

EVALUATION OF PINHOLE CAMERA RESOLUTION FOR NSLS-II STORAGE RING *

I. Pinayev #, NSLS-II Project, BNL, Upton, NY 11973, U.S.A.

Abstract

The NSLS-II Storage Ring will provide ultrabright radiation sources with extra-small sizes of the circulating electron beam. The beam dimensions will be monitored with a pinhole camera. In this paper we discuss the possible design and ultimate achievable resolution of the system. Modeling is based on the SRW code as well as numerical calculations using MATLAB.

INTRODUCTION

The pinhole camera has been a workhorse for measuring electron beam size on the storage ring-based light sources since it was first utilized at ESRF [1]. The NSLS-II storage ring will utilize an electron beam with diffraction limited source size in the vertical plane [2] in order to achieve unprecedented brightness. The goal of the study described in this paper is to define parameters that most affect resolution of the imaging system and optimize beamline design.

BEAMLINE LAYOUT

The expected layout of the pinhole camera beamline is shown in Fig. 1. The bending dipoles of the storage ring have low magnetic field of 0.4 T in order to reach small horizontal emittance [2]. Therefore the expected critical energy of the dipole synchrotron radiation is rather low, namely 2.4 keV. To improve resolution by utilizing a shorter wavelength we will employ a three-pole wiggler as a source. The field of the central pole is 1.14 T, the critical photon energy is 6 keV, and the useful synchrotron radiation spectrum extends to 50 keV. The electron beam parameters at the location of the three-pole wiggler are η_x=0.17 m, β_x=4.1 m, and β_y=19.3 m. Taking emittances ε_x=1 nm and ε_y=8 pm and relative energy spread σ_E/E=0.1% one can easily find the transverse dimensions of the source: σ_x=180 microns (defined mostly by energy spread) and σ_y=12.4 microns.

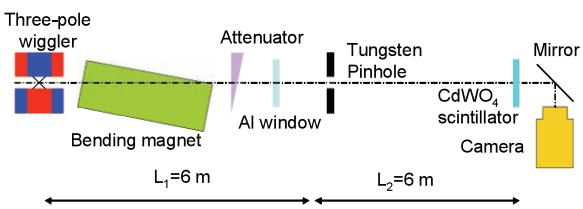

Fig.1 Layout of the pinhole camera beamline.

The first element of the pinhole camera beamline is a variable filter/attenuator. It constitutes a wedge, mounted on a linear actuator to set desirable transmission level. The filter serves two functions: the first is to bring intensity down to an acceptable level. The second function is to suppress long-wavelength radiation, in order to improve resolution. The filter is followed by an aluminum window so synchrotron radiation can exit to the atmosphere. Usually the material of the wedge is copper but we found it unsuitable due to substantial transmission of low-energy photons (Fig. 2).

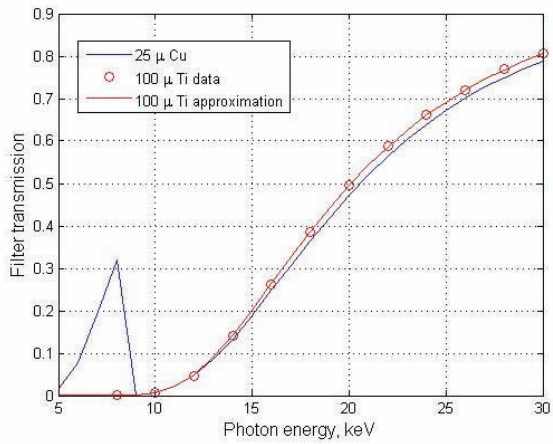

Fig. 2. Transmission curves for 25 microns of copper and 100 microns of titanium. Data from [4].

For our design we plan to use titanium, which does not have absorption lines in the spectral range of interest and has excellent vacuum compatibility. The Ti filter transmission curve also is shown in Fig. 2. Fig. 3 shows on-axis brightness of a three-pole wiggler source after being filtered by 50 microns of titanium.

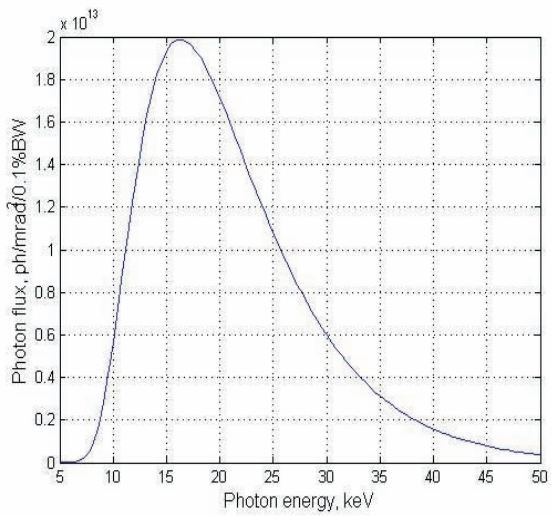

Fig. 3. Spectral brightness of the three-pole wiggler source after a 50 micron Ti filter.

*Work supported by the U.S. Department of Energy with Contract No. DE-AC02-98CH10886

#pinayev@bnl.gov

The 100 micron aluminum window provides sufficient mechanical strength and has substantial transmission above 10 keV (Fig. 4). Because all low-energy photons are absorbed by the filter, the thermal load on the window is about 0.3 W/mm^2.

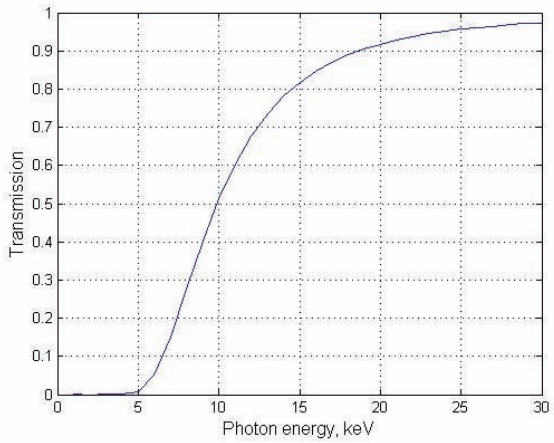

Fig. 4 Transmission of aluminum window 100 microns thick.

The pinhole installed after the aluminum window will be made of tungsten and will have fixed size (we will consider usage of variable pinhole, as well). Putting the pinhole assembly outside the vacuum chamber simplifies the design and service of the beamline. The distance from the pinhole to the source is defined by available physical space and is expected to be approximately 6 meters. The image of the electron beam will be observed with $CdWO_4$ phosphor and a camera equipped with a zoom lens.

SIMULATIONS

In our simulations we assumed a 6 meter distance from the source to the pinhole, and the same distance from the pinhole to the phosphor screen. We disregarded the loss of resolution in the phosphor screen and optical imaging system, thus concentrating on the fundamental factors affecting resolution.

For specified photon energy one can easily find the resolution of a pinhole camera using SRW code [5]. However, in our case the source has a continuous (and quite wide) spectral range. To handle such a situation it is possible to find profiles of photon flux for multiple wavelengths and then perform summing, but this is quite labor extensive. We chose a different approach. The effective resolution of the system at particular wavelengths was estimated using natural units $u = \sqrt{\lambda L_1 L_2/(L_1+L_2)}$ and $v = \sqrt{\lambda(L_1+L_2)L_2/L_1}$ introduced in [6]. Well-known analytical solutions exist for small apertures (Fraunhofer diffraction) as well as for large ones (geometric shadow). The curve (E) for monochromatic Fresnel diffraction shown in Fig. 13 in [6] was approximated using the formula below:

$$\sigma = v\sqrt{u^2/8 + 0.13/u^2}\cdot\left[1 - \frac{0.476}{1+\left((\ln u - 0.385)/0.341\right)^2}\right]$$

The first term is a quadrature sum of the width of resolutions due to geometric shadow and Fraunhofer diffraction. The term in square brackets is a correction multiplier accounting for Fresnel diffraction. Such fit provides good agreement with SRW calculations as well. The fit curve is shown in Fig. 5.

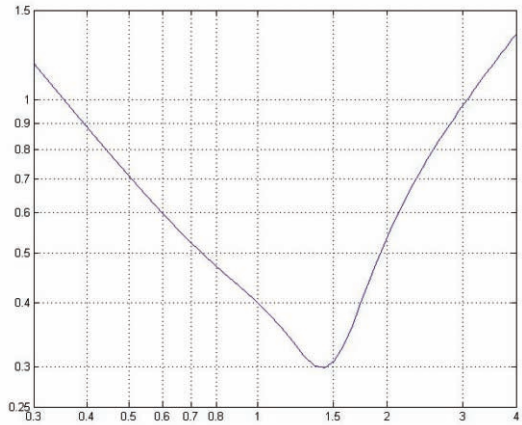

Fig. 5. Effective resolution of pinhole camera in natural units.

To estimate photon flux on the phosphor we needed also to calculate the spectral density of synchrotron radiation from the three-pole wiggler. For this we used a well-known formula for synchrotron radiation from a bending magnet:

$$\frac{dN}{d\Omega}[photons/sec/mrad^2] = 1.325\times10^{16}\frac{\Delta\omega}{\omega}E^2[GeV]\cdot I[A]\left(\frac{\lambda}{\lambda_c}\right)^2 K^2_{2/3}\left(\frac{\lambda}{2\lambda_c}\right)$$

The spectrum was multiplied by the transmission coefficients of the filter and aluminum window. In order to evaluate the attenuation of the titanium filter, the penetration depth of X rays was approximated with the following formula:

$$\lambda[\mu m] = 0.0157E_{h\nu}^3 + 0.04221E_{h\nu}^2,$$

and for aluminum

$$\lambda_{Al}[\mu m] = 0.0740E_{h\nu}^3 + 0.0944E_{h\nu}^2.$$

where $E_{h\nu}$ is photon energy in keV.

In the dedicated MATLAB® script, numerical integration over the spectral range from 6 to 50 keV was performed in order to estimate photon density on the phosphor screen. For each particular wavelength, the number of photons that passed through the pinhole was found, and photon density in the image plane was calculated using a Gaussian curve which width corresponds to resolution. The point spread function was found by summing over all wavelengths (such as shown in Fig. 6) and was fitted with a Gaussian curve. The

resulting effective width was used as the resolution of the system.

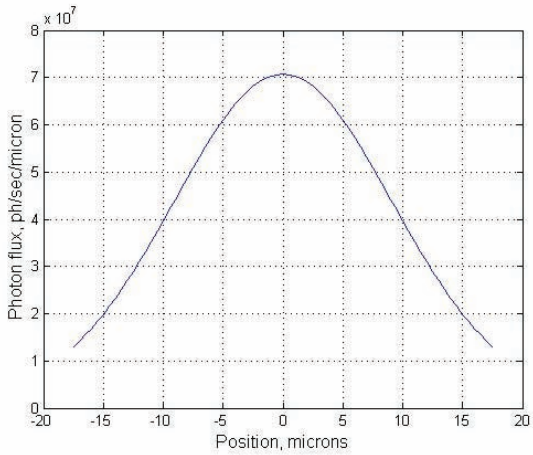

Fig. 6. Point spread function in phosphor plane for 20 microns pinhole and 120 micron Ti filter.

To optimize the design the described procedure was applied to the set of pinhole sizes and filter thicknesses. The 3D curve for calculated resolution dependence on filter thickness and pinhole size is shown in Fig. 7.

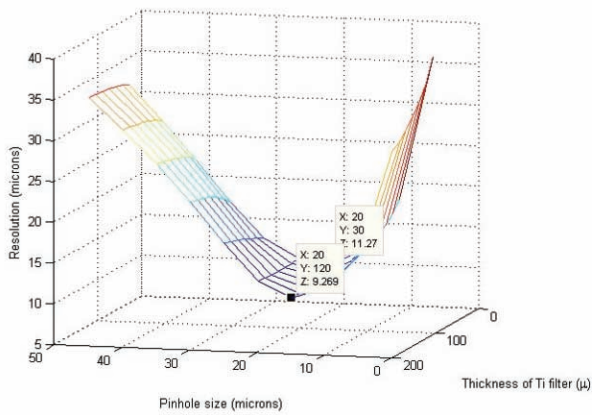

Fig. 7. Dependence of pinhole camera resolution on aperture size and thickness of Ti filter.

The best resolution is achieved with a pinhole of about 20 microns and has weak dependence on the thickness of the filter. The resolution of the system is slightly below r.m.s. vertical beam size but is certainly suitable for measuring the horizontal beam size.

To verify calculations we used SRW to generate 2D profiles of photon flux at the image plane with 20 micron pinhole and 50 micron filter at different wavelengths. Summing the intensities gave us total photon flux density and therefore the profile of the image of a realistic electron beam. The resulting image is shown in Fig. 8. There is excellent agreement between the SRW simulation and the approximations used in this paper.

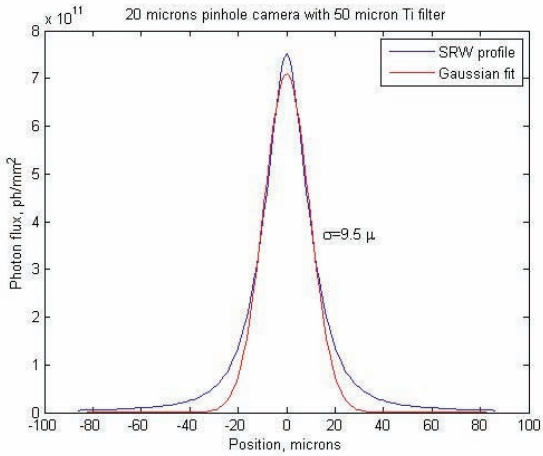

Fig. 8. Point spread function of pinhole camera obtained by summing of photon beam profiles generated by SRW.

To improve resolution we estimated a solution where a pinhole will be placed in the vacuum chamber in place of a crotch absorber. In such a situation distance from the pinhole to the source is 3 meters and it is easy to obtain 5-fold magnification by placing a fluorescent screen 15 meters from the pinhole. The results of the simulations are shown in Fig. 9.

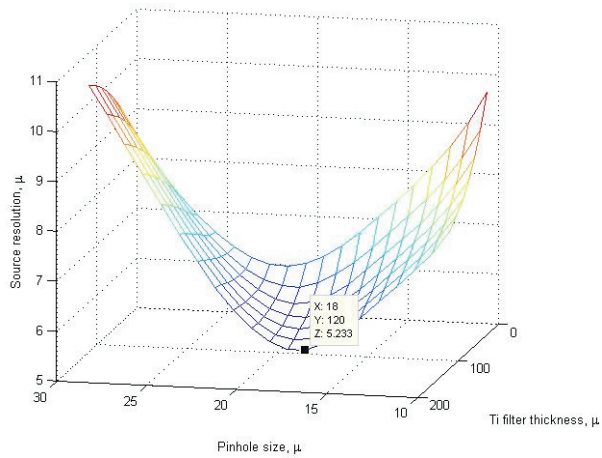

Fig. 9. Resolution of pinhole camera with 5-fold magnification.

The proposed design improves resolution by a factor of 2 and makes the pinhole camera suitable for measuring vertical beam size. Also, due to the magnification, the resolution of the imaging system is of less concern. However, there are certain technical difficulties, such as provisions for adjusting the pinhole, which need to be overcome.

CONCLUSIONS

The pinhole camera planned for installation on the NSLS-II storage ring will not have sufficient resolution for robust measurement of vertical beam size if it is positioned outside the vacuum chamber, but the camera can be a useful tool for monitoring fluctuations of beam

emittance during regular operations. If the pinhole will replace a crotch absorber inside dipole vacuum chamber then the required resolution can be achieved.

The resolution in the horizontal plane is quite adequate in both cases and the camera can be very useful for monitoring beam energy spread, which defines the beam size at location of the three-pole wiggler.

NOTICE

REFERENCES

[1] P. Elleaume et al., J. Synchrotron Rad. (1995). 2, 209-214.

[2] S. Ozaki et al., "Philosophy for NSLS-II design with sub-nanometer horizontal emittance," PAC'07, pp. 77-79 (2007).

[3] NSLS-II Preliminary Design Report, available at http://www.bnl.gov/nsls2/project/PDR

[4] "X-ray Filter Transmission" available at http://henke.lbl.gov/optical_constants/filter2.html.

[5] O. Chubar and P. Elleaume, "Accurate and Efficient Computation of Synchrotron Radiation in the Near Field Region" EPAC98, THP01G, pp.1177-1179.

[6] B. Yang, "Optical System Design for High-Energy Particle Beam Diagnostics," BIW'02, AIP Proc. 648, 2002, pp.59-78

OPERATIONAL LIMITS OF WIRE SCANNER ON LHC BEAM

M. Sapinski*, Tom Kroyer, CERN, Geneva, Switzerland

Abstract

A heat flow equation with beam-induced heating and various cooling processes for a carbon wire passing through a particle beam is solved. Due to the equation nonlinearity a numerical approach based on discretization of the wire movement is used. An estimation of the wire sublimation rate is made. Heating of the wire due to the beam-induced electromagnetic field is taken into account. The model is tested on SPS data. Results are discussed and conclusions about limits of Wire Scanner operation on LHC beams are drawn.

INTRODUCTION

Wire Scanners [1] are devices widely used in accelerators to measure the beam profile. They provide direct and accurate measurement with resolution down to $1\ \mu\mathrm{m}$ and they are considered as a reference for calibration of other instruments.

During the scan, the wire is moved through the beam. It is heated by the RF-coupling to the beam. When it enters into the beam it is irradiated, heated up and cooled down by heat transport along the wire, by thermal radiation and by thermionic emission. In high temperatures it sublimates and it might melt if the pression due to thermal stress is high.

The wire breakage has been observed many times with different beams. The cross-section of the broken wire has been photographed and analysed [2, 3]. These photographs indicate different breakage mechanism depending on beam conditions.

The mechanisms leading to the wire damage during the scan can be: brittle failure, plastic failure, sublimation, melting and thermal fatigue. In case of normal operation, when the wire breaks after thousands of scans, a combination of the above factors is relevant. For instance, as seen in some photographs in [2], the wire has significantly sublimated before breaking. The sublimation removes the external part of the wire which contributes the most to its total strength, as it contains crystals which are more oriented then the ones in the core [5]. In case of LHC beams the heating is slower than the sound speed therefore the thermal shock does not develop.

The LHC beam poses very demanding conditions for the wire. If scanning of the full beam would be possible the total energy deposited by the direct beam interaction during a scan would be about 0.1 J in a time of $900\ \mu\mathrm{s}$, in $1\mu\mathrm{g}$ of fiber. No material can withstand such conditions.

* mariusz.sapinski@cern.ch

In this paper the modeling of the wire temperature during the scan is presented. Separate models describe RF-heating and beam heating as they apply to different length scales along the wire. Conclusions about operational limits of Wire Scanners on LHC beams are drawn.

INDUCTIVE HEATING FROM BEAM

The wire heating due to RF-coupling to the beam field has been observed even when the scanner was in the parking position [6], with the wire hidden in a cavity. After this experience RF-absorbing ferrites have been fixed in the parking cavity what cured the wire breaking problem. In this paper the wire heating during the scan is calculated.

Ansoft HFSS was used for the simulation of the beam power loss on the wire [4]. The model parameters are summarized in the Table 1.

Table 1: Parameters used in the simulation.

parameter	unit	value
beam pipe side length	mm	60
structure length	mm	40
RMS beam size	mm	1
wire radius	μm	15
wire conductivity	S/m	$4 \cdot 10^4$
relative permittivity		1

The losses on the wire scale with the square of the beam current density. They increase with the distance from the beam pipe center and with frequency as shown in Figure 1. Due to symmetry no current is generated in the wire center therefore there are no losses in the place which later is heated by direct interaction with the beam.

For a given beam the power deposited in the wire can be calculated by weighting the relative losses from Figure 1 with the beam spectrum. The field power in the 40 MHz harmonics of the nominal LHC beam at top energy is depicted in Figure 2.

The power deposition has been used in the wire model which contains thermal conductivity. Other cooling processes are not adequate for the temperatures reached by the wire. The thermal conductivity gives relatively small effect due to weak thermal conductivity of the wire. In Figure 3 the temperature evolution along the wire during the scan is presented. The characteristic pattern with large losses on the sides of the wire and almost no heating in the wire center, observed in LEP wire scanners [7], is confirmed.

The temperature of the wire center, in case of scan of 25% of LHC injection beam, increases only by a few de-

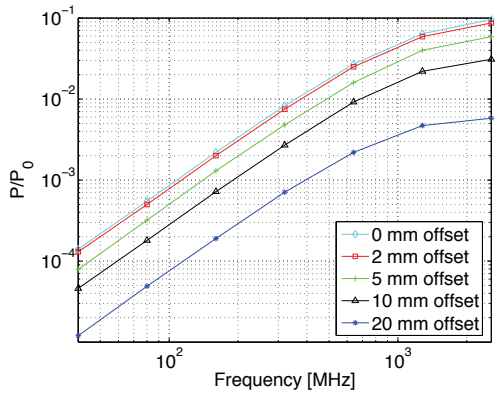

Figure 1: Total relative loss on the carbon wire as a function of frequency. Different curves are for different distances of the wire from the beam.

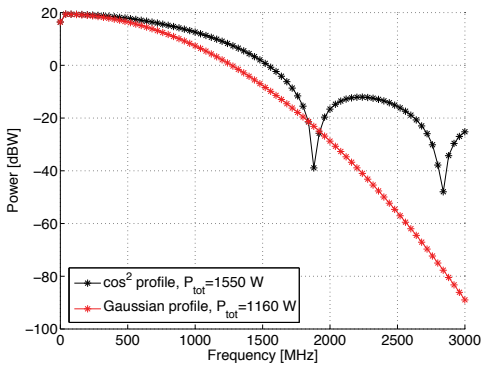

Figure 2: The power in the harmonics of nominal LHC beam at top energy, 4σ bunch length 1.06 ns. From experience with the SPS a Gaussian profile is believed to be more realistic.

grees. It can be concluded that in case of LHC wire scanners the RF-heating during the scan is small.

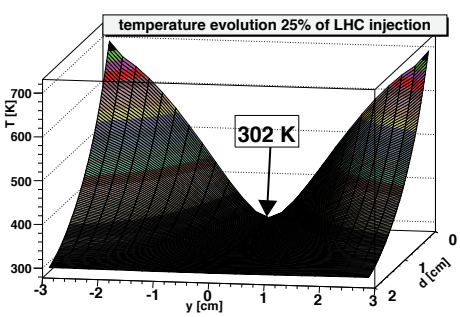

Figure 3: The wire temperature evolution due to RF-heating. A 25% of LHC injection beam is assumed.

WIRE HEATING MODEL

The temperature evolution of a wire placed in a particle beam is described by Equation 1. The left side of the Equation represents heating of the wire by the beam and the right side represents the wire heat capacity and four cooling processes: radiation, heat transport along the wire, thermionic emission. and sublimation. The description of variables used in the Equation 1 is presented in Table 2.

$$\begin{aligned} E_{dep}\frac{dN_{hits}}{dt} &= \rho_C V c_p(T)\frac{dT}{dt} \\ &- A_{rad}\epsilon\sigma(T^4 - T_{amb}^4) - \lambda(T)A_d\frac{dT}{dy} \\ &- A_{rad}(\phi + \frac{2k_B T}{q_e})J_{th} + C(y)J_{th} \\ &- \Delta H_{sub}\frac{dn}{dt} \end{aligned} \quad (1)$$

Table 2: Variables of the wire model.

variable	description
E_{dep}	energy deposited by a proton
ρ_C	graphite density
$c_p(T)$	graphite specific heat
A_{rad}	the surface of the wire which radiates heat
ϵ	the emissivity
σ	Stefan-Boltzmann constant
T_{amb}	temperature of environment
$\lambda(T)$	is the graphite thermal conductivity
A_d	wire cross-section $\pi d^2/4$
k_B	Boltzmann constant
ϕ	carbon work function
J_{th}	thermionic current
q_e	elementary charge
$C(y)$	current compensating the thermionic current
ΔH_{sub}	is the entalphy of sublimation
dn	amount of material sublimated

The wire is divided into bins with volume V, along the wire length (y-axis), in which the temperature is uniform. The bin size, Δy, is chosen as a fraction of the beam width σ_y. The total wire length considered in the calculation is $6\sigma_y$. The scanning process is divided into steps where, during the time Δt the wire moves by distance Δx. For every step a contribution from all processes is calculated. The initial temperature is set according to results of the RF-heating model.

BEAM ENERGY DEPOSITION

A Geant4 (in version 4.9.0.p01) simulation has been carried out in order to estimate the beam energy deposition in a thin target, where the Bethe-Bloch approach does not

apply directly due to significant energy removal by escaping electrons. The distribution of energy deposited in the wire is presented in Figure 4. The low energy part of the distribution has been fitted with a Landau curve which is a good approximation for thin targets [8]. The discrepancy between the fit and the simulation for energies above 70 keV is interpreted as an effect of energy transfer to electrons which are knocked-off from the material [9]. The spectrum of particles emited from the wire is dominated by those electrons.

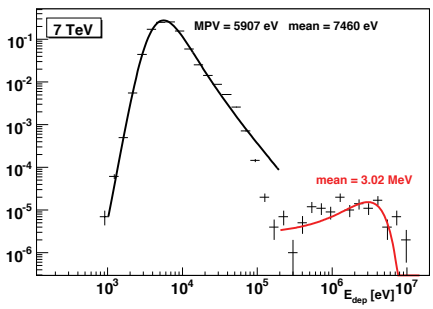

Figure 4: The energy depositions in the wire by a 7 TeV proton beam (Geant4 simulation).

The nuclear interactions with the wire material give tail of high energy depositions (red curve) but the contribution to the total deposited energy is below 1%.

In the following calculations the value of energy deposited per proton has been taken as the mean value of the distribution in Figure 4. To correct for the cylindrical shape of the wire, the total energy deposited is multiplied by a factor $\pi/4$. The error in the estimation of the mean value of energy deposition in Geant4 simulation is below 10%.

COOLING PROCESSES

Because of a very small cross section of the wire the heat transfer plays negligible role in heat distribution during the scan. Nevertheless its relative contribution is important for temperatures below 1300 K.

In the temperature range between 1300 K and 3200 K the main cooling process is the radiative cooling. It is proportional to the wire surface, fourth power of the wire temperature and to emissivity which quantifies deviation from ideal black-body radiation. The last parameter is poorly known and can have values between 0.4 and 0.8.

The thermionic emission is a dominant cooling process for temperatures above 3200 K. It determines the wire temperature for scans of the high intensity beams like the LHC or SPS ones. The electric current emited by the hot body is described by Richardson-Dushman Equation:

$$\mathrm{J_{th}} = \mathrm{A_R} \cdot \mathrm{T}^2 \cdot \exp(-\frac{\phi}{\mathrm{k_B T}}) \qquad (2)$$

where $\mathrm{A_R}$ is Richardson constant. The power dissipated by the thermionic current is proportional to the surface of the wire and depends exponentially on the temperature.

The thermionic emission removes electrons which are replaced by a current flowing from the fork supporting the wire. This current, described in Equation 1 as $\mathrm{C(y)J_{th}}$, is taken into account as an additional source of heating, but it has a negligible contribution.

The thermionic emission may lead to a phenomena observed in Figure 7, where the temperature is stabilized at about 3600 K due to equilibrium between beam heating and thermionic cooling. For very narrow LHC beams this equilibrium is not observed because the heating is faster than characteristic time of cooling processes. In this case the maximum temperature is determined mainly by the heat capacity of the wire.

The relative contribution of different cooling processes is illustrated in Figure 5.

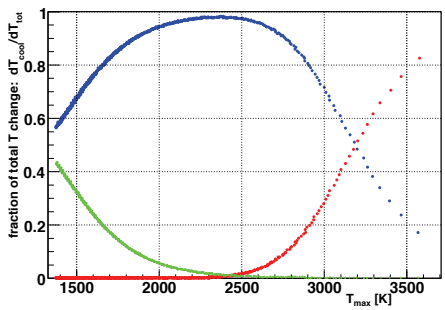

Figure 5: Relative contribution of cooling processes to the total temperature change as a function of temperature. Blue points are for radiative cooling, red for thermionic emission and green are for the heat transfer.

ESTIMATION OF WIRE SUBLIMATION RATE

The wire sublimation rate has been estimated from a simple model [10] which assumes that in a thin layer around the wire the carbon vapour pressure is in equilibrium with the wire material. The second assumption is that the carbon vapour is an ideal gas, therefore it does not have internal degrees of freedom. Both assumptions are conservative therefore the amount of sublimated material is overestimated.

The vapour pressure data have been obtained from [11]. The error on this data is significant and it is the main source of uncertainty of the model.

The depth of the layer sublimated in the time $\Delta\mathrm{t}$ can be expressed by:

$$\mathrm{d_{sub}} = \frac{1}{2}\mathrm{v_{vap}}\rho_{\mathrm{vap}}\Delta\mathrm{t}/\rho_{\mathrm{C}} \qquad (3)$$

where:

$$\rho_{\mathrm{vap}} = \frac{m_{mol}}{V_{mol}}\frac{T_{std}}{p_{atm}}\frac{p_{vap}(T_{vap})}{T_{vap}},$$

$$v_{vap} = \frac{1}{2}\sqrt{\frac{8kT_{vap}}{m\pi}}$$

The total amount of sublimated material depends on the maximum temperature reached during the scan and the time the temperature remains high. The removal of the material from the wire leads to decrease of the wire heat capacity and cools down the wire because of sublimation entalphy. The contribution of this cooling to the total cooling at high temperatures is only about 1.5%.

In Figure 6 the maximum temperature of the wire during the scan is confronted to the decrease of wire radius. The sublimation process starts sharply at temperature of about 3300 K for vapour pressure of a few Pa.

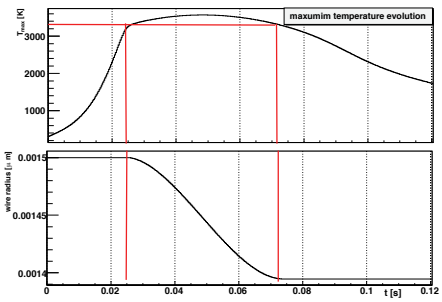

Figure 6: Illustration of the temperature evolution and corresponding decrease of the wire diameter in the sublimation model. The scan conditions correspond to SPS experiment with wire velocity of 10 cm/s.

RESULTS

The different sets of beam parameters, presented in Table 3, have been used to test the calculation against the known experimental results and to predict the wire scanner operational limits for LHC.

Table 3: Values used in the calculations for different beams.

parameter	unit	SPS	LHC	
			inject.	coll.
beam σ_x	cm	0.163	0.053	0.016
beam σ_y	cm	0.065	0.080	0.023
No of protons in beam $(\cdot 10^{13})$		2	32	32
protons energy	TeV	0.45	0.45	7
wire velocity	cm/s	10	100	100

SPS experiment

The model has been tested on the results of an experiment made in 1988 on SPS beam. During this experiment the consecutive scans were performed with decreasing wire velocity. The wire has been broken at velocity of 10 cm/s [12] in beam conditions described in Table 3. At velocity of 20 cm/s the wire was still not broken, although probably it was significantly weakened. At 1 m/s the scans of this beam were safe for the wire.

The evolution of the maximal temperature during the scans with different velocities is visualized in Figure 7. The arrows show the moment when the wire passes the beam center.

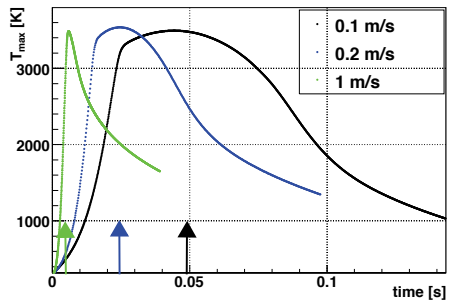

Figure 7: temperature of the central bin of the wire for 3 scan velocities: 10 cm/s (black curve), 20 cm/s (blue curve) and 100 cm/s (green curve).

For all velocities the maximum temperature is about 3550 K. The fastest scan passes the center of the beam 4.9 ms after the beginning of the scan and the wire continues to absorb beam energy without a visible influence from cooling processes until it reaches the maximal temperature at 6.2 ms. The period of high temperature lasts relatively short leading to sublimation of a 0.3% of the wire material in the central bin.

For the scan with 10 cm/s, after 30 ms from the beginning, when the temperature of the wire reaches about 3300 K, the thermionic cooling slows down the wire heating substantially. The maximum temperature is reached when the wire crosses the beam center at 49 ms from the beginning of the scan, but temperature increase between 30 ms and 49 ms is small. The total material sublimated is about 7% of the wire diameter.

The thermionic cooling is the main cooling mechanism therefore the poor knowledge of the carbon work function is an important source of uncertainty. The work function variation by 20% results in the maximal temperature change between 3100 K and 3800 K.

LHC injection beam

The LHC beam is much more dense than the SPS one. It contains 16 times more protons and the beam dimensions are smaller. From the other hand the revolution time is almost 4 times longer.

At 1 m/s wire speed the heating from the beam would destroy the wire. A fraction of the nominal beam intensity which reproduces the safe scans on SPS is found to be between 22% and 25%. The maximum temperature is about 3600 K for 22% and 3700 K for 25% of nominal intensity.

The total material sublimated is between 0.02% and 0.5% of the wire diameter. In Figure 8 the evolution of the beam temperature along the wire is presented for scan of 25% of the nominal beam intensity.

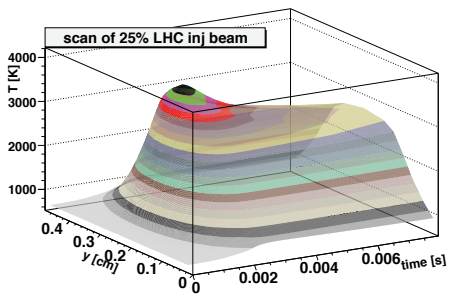

Figure 8: Distribution of wire temperature during a scan of LHC injection beam with 25% of the nominal intensity.

LHC colliding beam

During the acceleration the LHC beam not only gains energy but also is squeezed by a factor of almost 4.

Using the same criteria for safe operation as for injection it is found that between 6% and 7% of the nominal beam intensity can be safely scanned. In Figure 9 the temperature evolution during the scan of 6.5% of the LHC beam is presented. The beam center is reached after 0.48 ms and the maximum temperature of about 3670 K is reached 0.67 ms after the beginning of the scan. The total material sublimated according to calibrated model is about 0.16% of the wire diameter. The comparison of the temperature evolution of different-diameter wires is also shown.

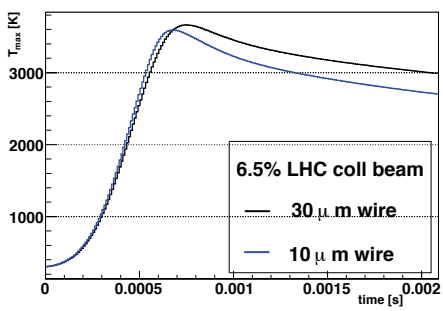

Figure 9: Distribution of wire temperature during a scan of LHC collision beam with 6.5% of the nominal intensity.

CONCLUSIONS

A model of the heating and cooling of the carbon wire has been obtained, tested on SPS data and solved for LHC beams. The main conclusion is that the maximum intensity which can be safely scanned is between 22% and 25% for injection beam and between 6% and 7% for collision beam.

The other outcomes of this research are the following:

- thermionic current plays crucial role as a cooling process in temperatures above 3200 K,
- the main factor affecting the maximum temperature is the wire heat capacity,
- RF-heating does not affect significantly the maximum wire temperature in case of LHC beam,
- sublimation rate becomes significant above 3300 K, but for fast scans of narrow beams the total amount of material sublimated is small,
- the model critical parameters: the carbon work function and vapour pressure are poorly known.

The LHC wire scanners work in critical conditions. The most valuable development would be to assure fast and automatic exchange of the broken wire, operate at higher speeds and use a thin carbon fiber with optimized mechanical properties.

ACKNOWLEDGMENTS

Authors would like to thank Jan Koopman, Bern Dehning, Fritz Caspers, Barbara Holzer and Delio Ramos for inspiration, ideas and numerous discussions.

REFERENCES

[1] K. Wittenburg, *Prepared for 39th ICFA Advanced Beam Dynamics Workshop on High Intensity High Bightness Hadron Beams 2006 (HB2006), Tsukuba, Japan, 29 May - 2 Jun 2006*

[2] "Examen par MEB de cause de cassure de 2 fils torsads en carbone et de 3 fils neufs pour dtecteur de profils PS/Booster", CERN TS/MME-MM investigation report

[3] C.Field, D.McCormick, P.Raimondi, M.Ross, "Wire breakage in SLC wire profile monitors", SLAC-PUB-7832, May 1998

[4] T.Kroyer, CERN-AB-Note-2008-018

[5] J-B.Donnet, R.C.Bansal, "Carbon fibers", Marcel Dekker, New York (1990)

[6] F. Caspers, B. Dehring, E. Jensen, J. Koopman, J. F. Malo, F. Roncaloro, "Cavity Mode Related Wire Breaking of the SPS Wire Scanner and Loss Measurement of Wire Materials", CERN-AB-2003-067-BDI

[7] C. Fisher, R. Jung, J. Koopman, "Quartz wires versus Carbon fibres for improved beam handling capacity of the LEP Wire Scanners", CERN-SL-96-009-BI

[8] B. Rossi, "High Energy Particles", Prentice-Hall, Inc., Englwood Cliffs, NJ, 1952.

[9] J. Bosser et al., "The micron Wire Scanner at the SPS", CERN SPS/86-26

[10] P. Thieberger, "Upper Limits for Sublimation Losses from Hot Carbon Targets in Vacuum and in Gasses", MUC-0186, Brookhaven National Labolatory

[11] S. Grigoriev, E.Z. Meilikhov, "Handbook of Physical Quantities", CRC Press 1997, 324-337

[12] Gianfranco Ferioli, private communication

FAST PINHOLE CAMERA FOR OPTIMISATION OF TOP UP INJECTION

C.A. Thomas, G. Rehm, Diamond Light Source, Oxfordshire, U.K.

Abstract

Top up is increasingly becoming a standard mode of operation for synchrotron light sources. Although it brings a very stable source in terms of intensity and position, the regular injections potentially perturb the beam. In order to investigate the perturbation of the beam from imperfections of the injection kickers (i.e. non-closure of the bump), we use an X-ray pinhole camera equipped with a fast CMOS-sensor giving a rate of up to 3200 frames per second to monitor the image of the beam. The analysis of the observed beam size as well as position allows quantifying the perturbation from the kickers that can be seen on beamlines. In addition we compare the observed motion to bunch-by-bunch position data recorded in both vertical and horizontal planes, which reveals to be very complementary.

INTRODUCTION

In almost all third generation synchrotron light source like Diamond there are plans to operate the machine in top up mode [1, 2, 3, 4, 5, 6, 7]. This operational mode presents many advantages for the machine and for the users. However, it implies injecting a small amount of charge regularly to compensate for the losses. By doing that, there is a necessity to take into account the perturbation of the stored beam by the injection kickers and their consequences on beamlines activities. In this paper we present a method to measure the perturbation of the stored beam by the kickers from the view point of a beamline. This method consists of using a fast camera, operating from 200 to 3200 frame per second (FPS), in a X-ray pinhole camera setup. We firstly present the system and its performance. Then we show some results obtained at Diamond to finally discuss the potential use of such a system and give some concluding remarks.

INSTRUMENTATION AND PERFORMANCE

The system we use is the X-ray pinhole camera setup that is currently used to measure the beam size, and thus calculate the emittance, the relative energy spread and the coupling emittance of the electron beam [8]. But instead of using our standard CCD camera, we use the Pulnix TM-6740GE from JAI[1]. This camera achieves 200 FPS with full frames of the 640 by 480 CMOS sensor and transmits the image data through Gbit Ethernet. The pinhole has a 25×25 μm^2 aperture, and the system pinhole + screen + camera provides a good resolution for the measurement we intend to do, i.e. measuring the centroid and the beam size vs. time. The resolution has been evaluated to $\Delta \approx 16\mu$m when using a 0.5 mm thick $CdWO_4$ screen [9]. The other important parameter of the measurement is the flux reaching the camera in order to have a low noise floor on the images. To this end we used the flux from a stored beam with our nominal two third fill at 125 mA. In this case, the average number of photons on the scintillator screen is of the order of 10^{11} s^{-1} [8].

The camera software provided by JAI is extremely basic but sufficient to allow us to acquire all the frames desired. We setup the camera to 1200 FPS by selecting a small region of interest, 224 by 160 pixels. Higher rates can be obtained by bining the pixels up to 4x4, which provides rates up to 3200 FPS on the whole sensor size but with 4 times less resolution.

MEASUREMENT OF THE KICKED BEAM

Top up mode requires regular injections of a small amount of charge, either after a fixed period of when the stored current drops below a certain threshold. During injections, the stored beam is kicked through a theoretically closed bumped. In practice, a residual angular kick resulting from the four kicks not adding up to precisely zero, or from leakage field from the septum, will perturb the beam. As the residual kick typically originates from a mismatch in the shapes of the kicker pulses, it shows fast changes within the duration of the pulse. This leads to different kicks seen by individual bunches along the bunch train and causes a damped oscillating motion of varying amplitude along the bunch train. As a result of this, using a beam position monitor with turn by turn acquisition (which averages the position of the beam over one turn) to judge when the bunch motion is minimised is fundamentally flawed, as opposite motion of the head and tail can cancel out.

Recording the position bunch by bunch (see figure 1) will reveal the full extent of the residual kick on the first turns after the injection, but it cannot correctly record the full temporal evolution of the damped oscillation. Decoherence of the electrons inside each bunch leads to the oscillation appearing to damp faster as a beam position monitor is only able to record the centre of mass motion.

The disturbance of the stored beam can best be investigated with our fast pinhole camera setup as it records the beam as seen from a beamline and the perturbation can be quantified. We have been acquiring images at 1200 FPS while kicking the electron beam and followed this with an image by image analysis of the horizontal and vertical centroid, the image beam size and the intensity across a given aperture. The beam size is measured by fitting each image

[1] www.JAI.com

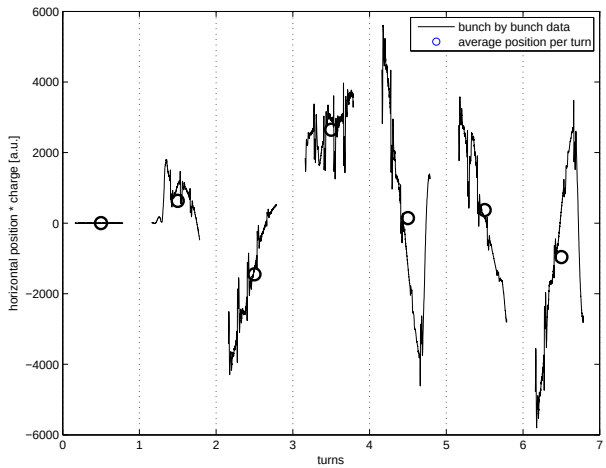

Figure 1: Bunch by bunch data recorded every turn from the injection kick.

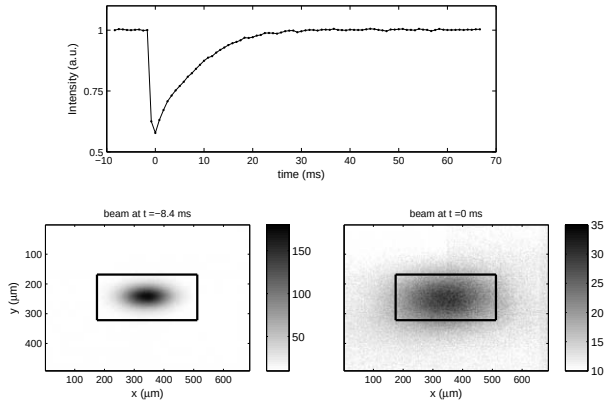

Figure 2: Image of the beam before and at the kick. The square represents an aperture 6 times the r.m.s beam size in both planes. The top graph shows the intensity integrated across the aperture.

with a 2-dimensional Gaussian. When the electron beam has been kicked, it is oscillating in both dimensions, at least due to the coupling between the two planes when the injection kick is only horizontal. The image seen by the camera is the integration of this motion over 800 μs. Therefore, the distribution seen by the camera is not always Gaussian during the kick. After the kick the centroid of the beam undergoes a parametric curve described as a Lissajous curve. As a consequence, the image at the kick shows a more rectangular beam, shown in the figure 2.

In order to simulate the impact of this temporary beam blow-up for a beamline, we integrate the intensity over a 'virtual aperture' of $\pm 3\sigma$, i.e. 110×50 pixels at the center of the camera. The effect of the kick is then seen as a temporary drop in intensity (see figure 2). Finally, figure 3 shows the temporal evolution of the transverse beam dimensions as well as the contours of the line 50% intensity from the maximum at different times before and after the kick. The beam size seen by the camera grows to more than 2.5 times the unperturbed beam size. The analysis of the decay is fitted well with a single exponential decay of $\tau \approx 9$ ms in the vertical plane. In the horizontal plane, the data cannot be fitted well with a single decay, there appear to be a faster decay mechanism with $\tau_1 \approx 1$ ms and a slower with $\tau_2 \approx 9$ ms. In both planes, it takes about 35 ms for the beam to recover its natural size.

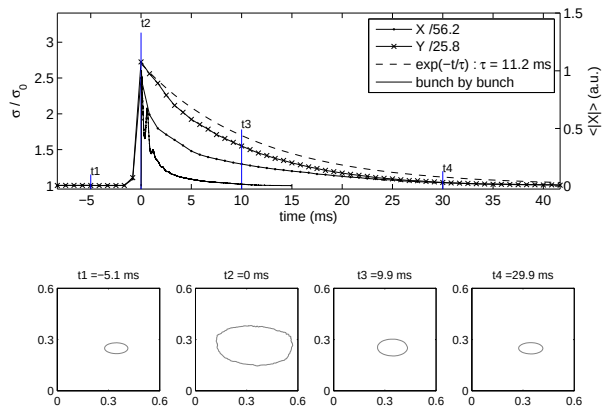

Figure 3: Contour plot showing the FWHM of the beam at several time after a kick. The upper figure shows the beam size, horizontal and vertical (X,Y) after the same kick and the times selected for the contour plots. The theoretical transverse decay is also shown in dash line on the graph. On the right side axis is the decay observed by the bunch by bunch system.

DISCUSSION AND CONCLUDING REMARKS

A X-ray pinhole setup equipped with a fast camera can be used for investigation and optimisation of the injection bump. The pinhole camera system provides sufficient accuracy for the beam size and centroid measurement at the ms scale. However, faster camera would imply either a larger flux or a more sensitive camera. Analysis of images permit to quantify the perturbation of stored beam and to assess the perturbation that should be observed on beamlines. We have chosen the normalise the measurement to the beam size as this is generally a stability and quality criteria for beamlines. Most beam beamlines, however, will not have fast enough detectors to observe the transient change of the beam shape, so they will mainly see a brief drop in intensity for typically about 3 transverse damping times. A fast camera with 1200 FPS is well adapted to the measurement as it is fast enough to accurately record the damping of the beam after it has been kicked. The camera sees an integrated motion, which can be a limiting factor for the measurement, but at the same time this is a good diagnostic for investigating the effect to a beamline. Complementary measurement

can be done using a bunch by bunch measurement system. Such a system is faster than the camera, and most of the movement can be rebuild with the bunch by bunch data, but at the same time it cannot show the correct decays as the signal is attenuated by decoherence of the beam.

REFERENCES

[1] F. Iazzourene, S. Bassanese, A. Carniel, K. Casarin, R. De Monte, M. Ferianis, F. Giacuzzo, M. Lonza, G. Tromba, and A. Vascotto. Elettra top up requirements and design status. Proceedings of EPAC 2006, pages 3350–3352, Edinburgh, 2006.

[2] L. Emery and M. Borland. Top-up operation experience at the advanced photon source. Proceedings of PAC 1999, pages 200–202, New York, 1999.

[3] A. Ludeke. Operation of the swiss light source: Top-up for highest performance. Proceedings of EPAC 2004, pages 2281–2283, Lucerne, 2004.

[4] H. Tanaka, T. Aoki, T. Asaka, S. Dat, K. Fukami, Y. Furukawa, H. Hanaki, N. Hosoda, T. Kobayashi, N. Kumagai, M. Masaki, T. Masuda, S. Matsui, A. Mizuno, T. Nakamura, T. Nakatani, T. Noda, T. Ohata, H. Ohkuma, T. Ohshima, M. Oishi, S. Sasaki, J. Schimizu, M. Shoji, K. Soutome, M. Suzuki, S. Suzuki, S. Takano, M. Takao, T. Takashima, H. Takebe, K. Tamura, R. Tanaka, T. Taniuchi, Y. Taniuchi, K. Tsumaki, A. Yamashita, K. Yanagida, H. Yonehara, T. Yorita, M. Adachi, K. Kobayashi, and M. Yoshioka. Top-up operation at spring-8 - towards maximizing the potential of a 3rd generation light source. Proceedings of EPAC 2004, pages 222–225, Lucerne, 2004.

[5] M.J. Boland, G.S. LeBlanc, D.J. Peake, and R.P Rassool. Preliminary studies for top-up operations at the australian synchrotron. Proceedings of PAC 2007, pages 3856–3858, Albuquerque, 2007.

[6] G.H. Luo, H.P. Chang, J Chen, C.C. Kuo, H.J. Tsai, T.Z. Ueng, D.J. Wang, and M.H. Wang. The status of top-up injection at NSRRC. Proceedings of APAC 2004, pages 224–226, Gyeongju, Korea, 2004.

[7] G. H. Luo, H. P. Chang, J. C. Chang, C. T. Chen, J. Chen, J. R. Chen, C. S. Fann, K. T. Hsu, C. S. Hwang, C. C. Kuo, K. B. Liu, Y. C. Liu, R. J. Sheu, T. S. Ueng, D. J. Wang, and M. H. Wang. Overview of Top-up Injection at Taiwan Light Source. In *Synchrotron Radiation Instrumentation*, volume 879 of *American Institute of Physics Conference Series*, pages 13–16, January 2007.

[8] Thomas, C. A. and Rehm, G. DIAMOND Storage Ring Optical and X-ray Diagnostics. Proceedings of BIW 2004, Knoxville, Tennessee, 2004.

[9] Thomas, C. A. and Rehm, G. Pinhole Camera Resolution and Emittance Measurement. Proceedings of EPAC 2008, Genoa, 2008.

COMPLEMENTARY METHODS OF TRANSVERSE EMITTANCE MEASUREMENT*

James Zagel, Martin Hu, Andreas Jansson, Randy Thurman-Keup, Ming-Jen Yang (Fermilab, Batavia, Illinois, USA 60510)

Abstract

Several complementary transverse emittance monitors have been developed and used at the Fermilab accelerator complex. These include Ionization Profile Monitors (IPM), Flying Wires, Schottky detectors and a Synchrotron Light Monitor (Synchlite). Mechanical scrapers have also been used for calibration purposes. This paper describes the various measurement devices by examining their basic features, calibration requirements, systematic uncertainties, and applications to collider operation. A comparison of results from different kinds of measurements is also presented.

SYSTEMS IN USE

Several emittance measuring systems exist across the Fermilab accelerator complex. Booster has both IPM's and Crawling Wires. Main Injector has IPM's, Flying Wires, and Multiwires. Recycler has Flying Wires and Schottky detectors. Tevatron has IPM's, Flying Wires, Schottky detectors, Synchrotron Light Monitors, and Optical Transition Radiation (OTR) [1] instruments. We will discuss the comparative measurements from only those instruments used in the normal course of stacking and storing, protons and antiprotons (pbars). Crawling Wires, Multiwires (secondary emission monitors,) and OTR are used for studies of injection and tolerate only a few turns of beam.

MAIN INJECTOR

Three types of instrumentation devices are installed in the MI10 straight section of Main Injector Ring for transverse emittance measurements; a horizontal and vertical Flying Wire, horizontal and vertical IPM[2], and one magnetic electron IPM[3]. The straight section, being of zero dispersion function by design, ensures that measurements are free from effects of longitudinal beam motion.

For collider operation, beam emittances of both horizontal and vertical plane are measured using the Flying Wire system and logged for every pbar transfer from Accumulator to Recycler Ring, Recycler Ring to Tevatron, and each proton transfer from Booster to Tevatron. In Main Injector, these measurements are taken at 8 GeV/C injection and at 150 GeV/C flat-top, before transfering beam to Tevatron.

The Flying Wire system measures beam loss profiles as a 33um carbon filament flies through the beam. Flying at 6 meters/second the wire takes about 5 milliseconds, or 450 revolutions, to traverse the entire width of beam. Quasi-stationary beam is a necessary condition for measurement to make any sense. . Unlike the flying wire system, the ion profile monitor records a complete profile from each successive turn of beam

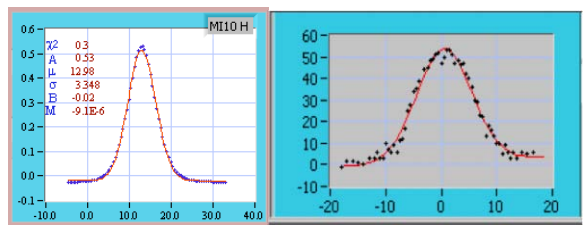

Figure 1. Main Injector Flying Wire And IPM Profile.

The IPM's are placed directly next to the flying wire system, of corresponding plane, to make comparisons more straight forward. Only one magnetic electron IPM for the horizontal plane is installed. A second unit is anticipated for the vertical plane in the near future. This is expected to be an improvement over the ion IPM for measurements at or above 120 GeV.

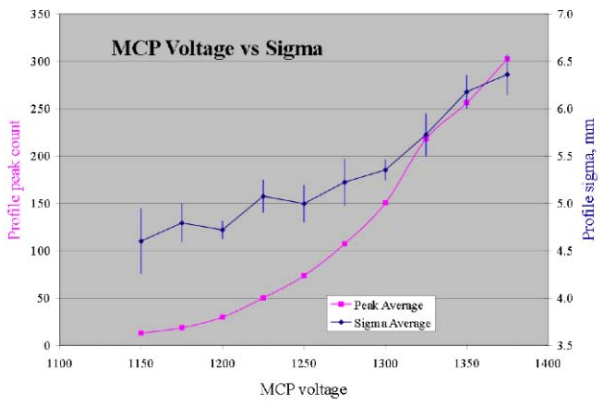

Figure 2. Sigma and peak count vs MCP Voltage

The full characterization of IPM response has so far not been completed. Figure 2 shows a measurement of beam profile sigma with varying high voltage to the Micro Channel Plate. While the increase in peak count is expected the dependency of sigma on high voltage is of concern. The best setting allows for good signal to noise measurement without saturation, or sag, at the peak of the profile. Two straight forward comparisons have been made. A simultaneous measurement of sigmas on both systems with increasing intensity and, in a separate measurement, a position bump was implemented through

*Operated by Fermi Research Alliance, LLC under Contract No. DE-AC02-07CH11359 with the United States Department of Energy

the Q102 straight section to compare the positions measured. Figure 3 shows a comparison of profile sigma from both flying wire and IPM's with varying number of Booster turns at injection for different beam intensity, and inherently varying beam width. The IPM single turn profiles show a consistently smaller sigma than the 100 turn average or the flying wire due to dilution by position oscillations.

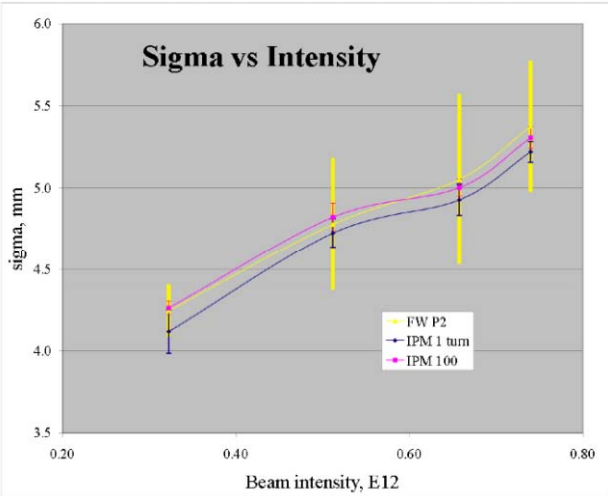

Figure 3. Sigma vs beam intensity for Flying Wire and IPM.

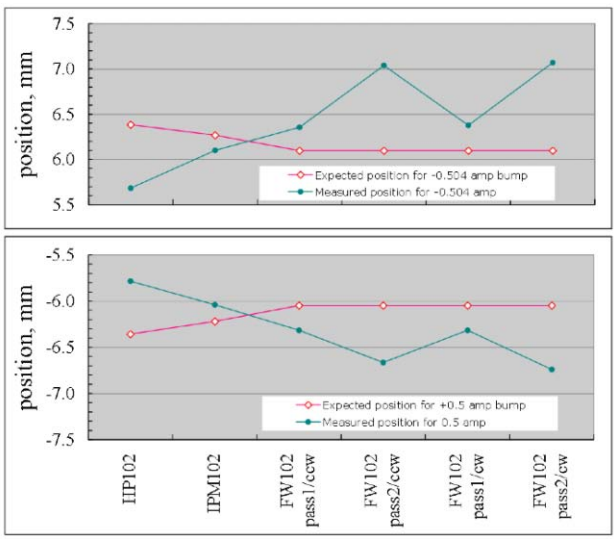

Figure 4. Position reading with known orbit bumps to verify position calibration.

RECYCLER

The Fermilab Recycler is a 3.3-km 8.9-GeV/c fixed momentum storage ring located in the Fermilab Main Injector tunnel. The Recycler has been an essential and integral part of the substantial Run II luminosity improvements since 2005. For beam stability and efficiency in generating a bright pbar beam, it is critical to have precise knowledge of the transverse emittances and beam profile. For transverse emittance monitoring, two complimentary systems are used: the flying wires, and the 1.75 GHz Schottky detectors.

Flying Wires

The Recycler Flying Wire System[4] consists of two cans (for horizontal and vertical measurements) installed at low dispersion locations. Each can is equipped with an ion pump and a TSP for vacuum maintenance. Wires were initially 33 micron monofilament carbon fiber, but the transverse emittance growth due to the wire-beam interaction is proportional to the wire diameter squared.

$$\frac{1}{\pi}\Delta\epsilon_N = 3\gamma\beta\left(\frac{fd}{v_{tr}}\right)\left(\frac{\pi d}{4}\right)\left(\frac{1}{L_{rad}}\right)\left(\frac{13.6\,MeV}{Pv}\right)^2$$

Where d is the diameter of the fiber, vtr is the transverse speed of the fiber, and Lrad is the radiation length of the fiber. The normalized emittance growth is proportional to the wire diameter squared. Emittance growths on the order of 0.5 π-mm-mr per measurement, (4 wire-beam crossings) were observed with the 33 μm wires. A system upgrade was performed in the 2006 shutdown, in which high tensile strength 5 μm Toray T1000G carbon fiber replaced the 33 μm fiber. Since the impact on emittances due to wire-beam interaction has been thus minimized, the flying wires have been employed in routine emittance monitoring of all modes (stored beam, newly injected beam and beam to be extracted).

Schottky detectors

In addition to the flying wires, a Schottky detector system is used to monitor the betatron band power, and therefore the transverse emittance, of the beam. Details about the Recycler 1.75 GHz Schottky detectors can be found in [5]. The narrow band, high impedance waveguide pickups measure sum and difference components of the beam signal. The difference components, mixed down to 2~5 MHz, are processed on a VSA (Vector Signal Analyzer) for background subtraction and band power calculation. The computed betatron power is then scaled to reflect the transverse emittance of the beam based on the constants obtained from calibration with the mechanical scrapers [6].

Comparison of the two detector systems

Flying wires measurements were compared to the measurements from the 1.75 GHz Schottky detector system. The tradition at Fermilab is to report the 95% normalized emittances. The Schottky detector measures the rms size of the beam, and converts it to the 95%

normalized emittance based on the assumption that the beam distribution is Gaussian. The Flying wires measure the time-averaged projection of the beam profile and obtain the σ from a Gaussian fit. It was verified that the two detectors agreed to within 10% when measuring a cooled pbar beam, which has a known Gaussian profile. Furthermore, it was demonstrated that the two detectors diverge when the transverse profile was known to be non-Gaussian, as when strong electron cooling is employed. The Schottky detector reports larger emittances when the distribution had a tail bias (large rms), and the Flying wires reports larger emittances when the tails of the distribution were truncated (small rms).

One of the key utilizations for the Flying wires in daily operation is the measurement of the transverse emittances when the rms momentum spread of the beam is more than 4 MeV/c, at which point the betatron and momentum bands (at h ~ 20,000) overlap and it becomes impossible to measure the betatron band power accurately due to the loss of baseline information.

Emittance measurements in a Tevatron shot

The following is an example, taken on the 19th of April, this year, of a sequence of emittance measurements for a typical set of antiproton transfers from the Recycler to the Tevatron. All emittances are 95%, normalized. Initially, recycler Schottky measurements reported 2.3 and 2.7 π-mm-mr shortly before the RF manipulation for extraction. The Recycler flying wires reported 2 π-mm-mr for the first partition of beam measured shortly before its extraction. The discrepancy has been understood to be due to a non-Gaussian distribution of the transverse beam profile of a stochastically and electronically cooled antiproton beam. The emittance measured on the horizontal Main Injector flying wire was 2 π-mm-mr at injection, before acceleration from 8 to 150 GeV, as the injection position errors are typically minimal. The horizontal Main Injector flying wire measurement made slightly later at 150 GeV showed a 25% increase in the normalized emittance. The increase can be attributed to the change in the momentum spread due to the coalescing of the bunches and the small but non-zero dispersion at the horizontal flying wire. In the Tevatron, the horizontal flying wire measurement after the first injection was 3.5 π-mm-mr, partially as a result of intended position errors made at injection on the order of 1mm to lessen beam-beam effects due to the brightness of the antiproton bunches.

In addition to distribution-dependent uncertainties, the uncertainties in the Recycler and Main Injector emittance measurements are dominated by the 15% or so uncertainty in the lattice functions used in the computation of the emittances. In the Tevatron, the field non-linearity and the orbit changes contributed to about 20% of the uncertainty in the lattice function; additionally, the uncertainty in the dispersion function at the wires was about 10%.

TEVATRON

The Fermilab Tevatron has several systems capable of measuring transverse emittance. The primary instruments used in operation are the Flying Wires, but there is also a Synchrotron Light Monitor, Ionization Profile Monitors and Microwave Schottky detectors.

Flying Wires

The Tevatron flying wire system[7] is similar in design to the other flying wires in Tevatron machines, and consists of three cans. One horizontal and one vertical system is installed at low dispersion locations, and an additional horizontal system is installed in a high dispersion location.. The idea of the high dispersion system was to independently measure the momentum spread from dispersive size of the beam but this was found to be unreliable and hence the high-dispersion system is rarely used.

Since the original 33um carbon fibers were changed to 5um, for the same reason as in the Recycler, the wires are used routinely in every stage of operation. Wires are flown following most proton injections, after each pbar injection, several times during ramp, squeeze and halo removal (scraping), and every hour during HEP stores.

Synclite

When a charged particle passes through a magnet, it undergoes acceleration perpendicular to its direction of motion and emits electromagnetic radiation. For certain energies and magnetic fields, part of this light is in the visible spectrum and can be detected with generic optical devices. Since each particle in the beam emits this light, one can point a telescope at it and produce a transverse image of the beam. The Synclite system[8] does this and thus offers a non-destructive method for measuring the transverse emittances of the Tevatron beam.

For the Tevatron, synchrotron radiation is non-negligible only when the beam energy gets above 600-700 GeV. The peak emission wavelengths are related to both the beam energy and the magnetic field ($\propto E^3 \cdot B$) and the intensity drops dramatically at shorter wavelengths. It was pointed out by [9] that there should be an enhancement of the emissions on the short wavelength side resulting from transitions into or out of magnetic fields. The Tevatron dipoles have peak wavelengths in the micron range, and as such observation would be difficult due to the lack of near infrared devices and the inherent diffraction caused by the longer wavelengths. Fortunately, the light emitted from the edge of the dipoles is enhanced in the blue optical region which helps with both of the aforementioned shortcomings.

The physical layout of the Synclite system is shown in Figure 5 and comprises a vacuum insertion mechanism to which is attached a pickoff mirror, and a light tight box containing the necessary optics for forming an image. The optical path contains a single lens for focusing, motorized mirrors for positioning the image, a 440/10 nm band pass filter (400/40 nm for pbars), and a gated, Image Intensified CID (Charge Injection Device) camera for obtaining the image. The image is retrieved from a frame grabber in a PC running Windows XP and LabVIEW.

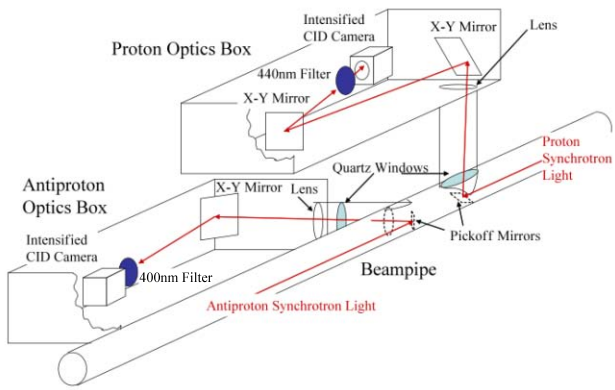

Figure 5. Synchrotron Light Monitor.

The image has its background subtracted before the beam sizes are extracted from fits to the horizontal and vertical profiles in a window around the peak. The fits are simple Gaussians with linear baselines. The values of the fits are then corrected for non-linearities in the intensified camera response and for theoretical distortions in the image. The theoretical distortions are determined via a numerical calculation [10] and contain most notably the broadening of the peak due to diffraction and the impact from the longitudinal extension of the source.

The light emitted from the accelerated particles is emitted in a cone with a half-width of roughly $1/\gamma$, which at 980 GeV is $\sim 10^{-3}$ radians. This narrow cone is the optical equivalent of a circular aperture which results in a diffractive broadening of the image after propagating it through the lens. At 10^{-3} radians, the impact is 100 μm on a beam size which for pbars is in the range of 200-400 μm.

The second main effect is from the longitudinal extent of the emission source. Light is emitted along the entire body of the magnet. At the wavelengths used in Synclite, the dominant emission source is the edge of the dipole, but there is still a significant distortion from the light emitted from the body of the magnet which is neither in focus nor at the same transverse position due to the constant bending through the magnet. This effect on the image must be accounted for in determining the beam size.

Comparisons can be made with other profile measurements such as the flying wires.

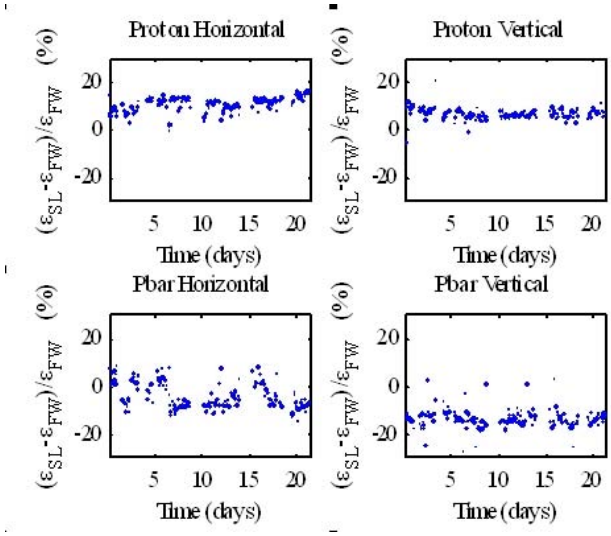

Figure 6 shows the percentage differences between the Synclite and Flying Wire emittances for a handful of beam stores.

Schottky detectors

The Tevatron has microware Schottky detectors that are identical to the ones installed in the Recycler. The acquisition electronics, software and data analysis is different, however. The Tevatron microwave Schottky is mainly used to measure tunes during stores, but the total power in the Schottky band is also reported. In the case of true incoherent Schottky signals, this signal is proportional to emittance. It has been observed, however, that during ramp and squeeze, early in stores, and sometimes for brief periods during stores, that there is significant coherent power in the Schottky spectrum. For most of the store however, this signal scales reasonably well with the Flying Wire emittance.

IPM

The Tevatron IPM's were designed to be single turn, single bunch devices, in order to resolve any turn-by-turn beam size oscillation caused by injection mismatch, and were not optimized for average emittance measurement.. However, data from multiple turns can be combined in software to create an average beam profile from which the emittance can be calculated.

The IPM measures ionization electrons collected using a parallel electric and magnetic field. A localized pressure bump obtained by controlled injection of pure N2 is required to obtain single turn sensitivity. The magnets and gas injection is left on continuously, while the high voltage sweep field is pulsed only for acquisitions. The detector granularity is 1/4 mm, and the readout uses electronics borrowed from HEP experiments, enabling close to single electron sensitivity.

Comparison of the detector systems

Both proton and pbar emittances change significantly during the course of a normal HEP store and this can be used to compare the various emittance readings. In general, the different measurements scale well within a store, but the absolute values can be off up to 10-20% In addition, the ratio between different instrument readings sometimes change up to 10% from store to store. This is the case for all the different measurement methods and is generally attributed to variations in the beta functions.

CONCLUSION

It is clear that there is more work to do and we will continue to identify and execute more complete studies. Ultimately these devices measure beam size and not emittance directly. We depend on a good knowledge of the Beta functions to convert these measurements to emittance. Additional work is on going to understand and reduce the systematic errors in the measurements of the beam size.

REFERENCES

[1] V. E. Scarpine, A.H. Lumpkin, and G. R. Tassotto, "Initial OTR Measurements of 150 GeV Protons in the Tevatron at FNAL", proc of AIP Conf 868, (BIW08), Bataiva, IL, 1-4 May 2006, pp 473-480

[2] J. Zagel, J. Crisp, A. Hahn, P. Hurh, "Fermilab Main Ring Ion Profile Monitor System", proc of IEEE Particle Accelerator Conference (PAC 1997), Vancouver, B.C. Canada, 12-16 May 1997, pp2166-2168

[3] J. Zagel, B. Brown, H. Glass, D. Harding, L. Kozien, S. Pruss, J. Volk, "Permanent Magnet Ion Profile Monitor at the Fermilab Main Injector." ,proc of IEEE Particle Accelerator Conference (PAC 2001), Chicago, Illinois, 18-22 Jun 2001, pp 1303-1305.

[4] M. Hu, R. Carcagno, Yu. Pishchalnikov, J. Krider, E. Lorman, A. Marchionni, S. Pordes, P. Wilson, J. Zagel (Fermilab) . "Beam profile measurement with flying wires at the Fermilab Recycler Ring." Proc of Particle Accelerator Conference (PAC 05), Knoxville, Tennessee, 16-20 May 2005, pp 2182-2184.

[5] Cullerton, E. and Pasquinelli, R., "A 1.75 GHz Schottky Detector for the Recycler," Fermilab RF Department technical note, Dec. 2003.

[6] Hu, M.,"Calibration of the Recycler Transverse Schottky Detectors," Fermilab Beams-doc-372.

[7] W. Blokland, J. Dey, G. Vogel, "A New Flying Wire System for the Tevatron" proc of IEEE Particle Accelerator Conference (PAC 1997) , Vancouver, B.C. Canada, 12-16 May 1997, pp2032-2034

[8] A.A. Hahn, P. Hurh "Results from an imaging beam monitor in the Tevatron using synchrotron light" In *Hamburg 1992, Proceedings, High energy accelerators, vol. 1* 248-250. (Int. J. Mod. Phys. A, Proc. Suppl. 2A (1993) 248-250).

[9] R. Coisson, "Angular-spectral distribution and polarization of synchrotron radiation from a 'short' magnet", Phys. Rev. A 20 (1979) 524.

[10] O. Chubar, P. Elleaume, "Accurate And Efficient Computation Of Synchrotron Radiation In The Near Field Region", proc. of the EPAC98 Conference, 22-26 June 1998, p.1177-1179.Synchrotron Radiation Workshop (SRW) http://www.esrf.fr/Accelerators/Groups/InsertionDevices/Radiations/Software/SRW

ADVANCED LIGHT SOURCE FGPA-BASED BUNCH CLEANING*

M. J. Chin, J. M.Weber, F. Sannibale, W. M. Barry, LBNL, Berkeley, CA 94720, U.S.A.

Abstract

At the Advanced Light Source (ALS), imperfections in the injection system plus electron diffusion result in storage ring RF bucket contamination. A Virtex-4 FPGA is used to generate a Direct-Digital Synthesized (DDS) sinewave waveform at the vertical betatron tune frequency, which is synchronously gated on or off at the 1.6MHz ring orbit frequency. Any pattern on/off/invert in 328 buckets by 2ns at the ring orbit frequency can be set. An embedded Power-PC core in the FPGA provides TCP access for control and monitoring via a remote PC running LabVIEW.

INTRODUCTION

The ALS has several fill patterns (camshaft, 2-bunch) that require a filled bucket be surrounded by empty buckets. This requires actively "cleaning" by selectively exciting the empty buckets at the vertical tune [1]. The major components of such a system include transverse kickers, kicker amplifiers and a signal source.

The ALS signal source uses a Xilinx FPGA demo board, the ML403 [2] together with a custom add-on board that has a 12-bit 500MHz DAC. By clocking the FPGA and DAC at the 500MHz master oscillator rate f_{RF}, any of the 328 bunches can be set to an independent value. Bunches to be cleaned are then selectively kicked at the tune frequency, while the isolated filled bunch is left un-stimulated. Additionally, due to tune shift, the kick frequency is swept in a few KHz bandwidth.

BUNCHCLEANER HARDWARE

The BunchCleaner board in Figure 1 was designed to investigate the LTC 2242-12 ADC (12-bits, 250MHz clock speed, 1.2GHz bandwidth) and the MAX5886 DAC (12-bits, 500MHz clock speed, 450Mhz bandwidth, 375ps rise/fall times) using the ML403 for FPGA interfacing and system design. Both ADC and DACs use LVDS digital I/Os. The DAC takes advantage of the double-data rate I/Os of the Virtex-4 to allow full speed updates at 500MHz while allowing the gate array internal clock to run at 250MHz.

For BunchCleaning, only the DAC is used, but the ADC was also successfully tested for transverse feedback.

ML403 Interfacing

There are two DIN-style connectors intended for user expansion that connect to FPGA pins and provide power. These connectors are not impedance controlled, and not specified for any maximum speed. Nevertheless, there are nearly 1 ground pin per 2 signal pins, and acceptable signal distortion was measured when used in 100ohm LVDS (the lower trace of Figure 2).

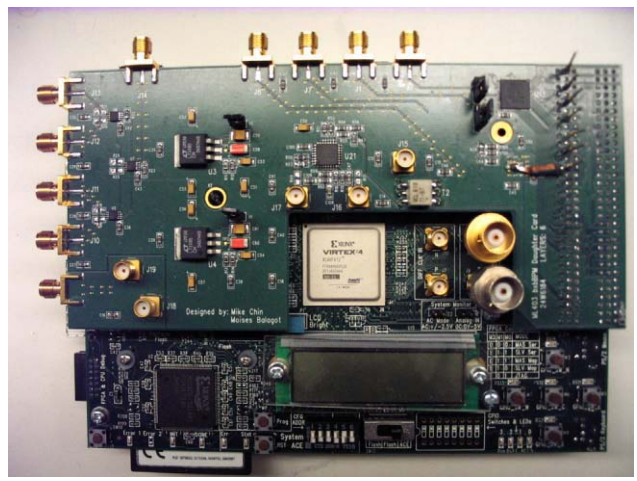

Figure 1: BunchCleaner mounted to ML403

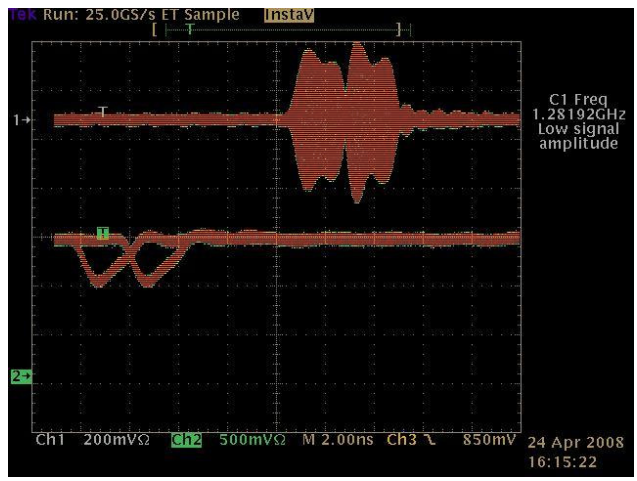

Figure 2: Top trace is DAC Output, lower trace is LVDS to DAC. Pattern is 1,-1 (rest are 0's)

500MHz is brought into the ML403 on two of its onboard SMAs, which are hooked up to an LVDS clock input of the FPGA. An RF transformer is used for a single-ended to differntial converison

FPGA DESIGN – BUNCHCLEANER

The main goal of the bunch cleaning is to generate a gated-sinewave where the stimulus is only on for bunches to be kicked out. Due to the 250MHz bandwidth of the Amplifier Research kicker amplifiers, a simple on-off approach does not work, because they cannot turn fully on

*This work was supported by the Director, Office of Science, Office of Basic Energy Sciences, of the U.S. Department of Energy under Contract No. DE-AC02-05CH11231

or off fast enough to change between adjacent 2ns bunches. Instead, the sine-wave is polarity inverted, to allow a zero crossing to coincide with the bunch to be kept.

The main parts of the bunch cleaning are the direct-digital synthesis, a pattern-generator, a multiplier, and a multiplexer-to-DDR output converter (mux-ddr). All of these blocks are clocked at $f_{RF}/2$ = 250MHz. They are either self-contained VHDL cores, or netlists provided by Xilinx design tools.

DDS Core

The Xilinx utilty program CoreGen was used to generate a direct-digital synthesis (DDS) core, with a 27-bit phase accumulator and 12-bit output. It is nominally set for an output of approximately 1.4MHz.

Pattern Generator Core

The pattern-generator is basically a 1K by 4 bits dual port memory. One side is written under software control, and is essentially write-only. The 4 bit value represents 2 bunch position controls, with "00" meaning zero output, "01" meaning normal output, and "10" meaning inverted output. This means only 328/2 address locations are actually used.

The other side of the memory is read out under hardware control, with an 8-bit counter generating sequential address 0 to 163 at 250MHz.

Multiplier Core

The multiplier is also generated from Coregen, parameterized as a 12-bit inputs with a 12-output. It serves as a software-settable gain control of the stimulus to the kicker amplifier. One input is fed by the output of the DDS core, the other by a parallel I/O port.

Mux-DDR Core

The output of the multiplier goes to one input of the mux-ddr. The other input port of the mux-ddr comes from the pattern generator. The two output ports D1 and D2 of the mux-ddr feed a 12-bit DDR output port on the FPGA, according to Figure 3.

Pattern	D1	D2
0000	Zero DAC code	Zero DAC code
0110	Multiplier +	Multiplier -
0101	Multiplier +	Multiplier +
1010	Multiplier -	Multiplier -

Figure 3: mux-ddr output D1 and D2.

Thus a pattern of "0110" would result in D1 being Multiplier+ and D2 being Multiplier-. With the DAC updating at f_{RF} =500MHz, this allows a sign inversion of the DDS stimulus in a single 2ns period. The upper trace in Figure 2 shows the DAC output for this pattern.

The custom core connection is shown in Figure 4. All cores except for the GPIO run at 250MHz.

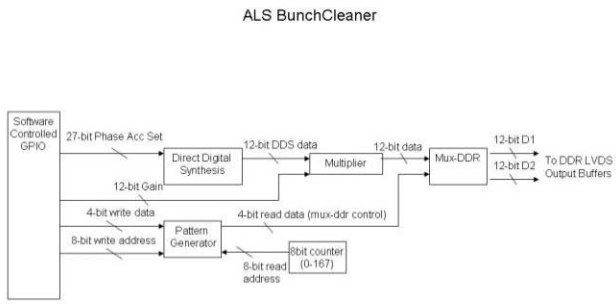

Figure 4: BunchCleaner.

FPGA DESIGN – EMBEDDED SYSTEM

The system design for the ML403 takes advantage of Xilinx-supplied cores designed for embedded processor systems; these include the Power-PC 405 hardcore, the UART, DDR SDRAM, System-ACE, and 100-baseT Ethernet. These cores are supported for the ML403 in an "push-button" template design provided in the Xilinx Embedded Device Kit. Similar FPGA embedded processor systems have been developed for the ALS Mini-IOC[3].

Although there are many lines of Verilog or VHDL describing each of these cores, most of the complexity is hidden through the use of parameterized description files. The entire BunchCleaner design is described in a 500 line text file (MHS file). Figure 5 is the sub-section of the MHS used to describe the FPGA's UART.

```
BEGIN opb_uartlite
 PARAMETER INSTANCE = RS232_Uart
 PARAMETER HW_VER = 1.00.b
 PARAMETER C_BAUDRATE = 9600
 PARAMETER C_DATA_BITS = 8
 PARAMETER C_ODD_PARITY = 0
 PARAMETER C_USE_PARITY = 0
 PARAMETER C_CLK_FREQ = 100000000
 PARAMETER C_BASEADDR = 0x40600000
 PARAMETER C_HIGHADDR = 0x4060ffff
 BUS_INTERFACE SOPB = opb
 PORT OPB_Clk = sys_clk_s
 PORT Interrupt = RS232_Uart_Interrupt
 PORT RX = fpga_0_RS232_Uart_RX
 PORT TX = fpga_0_RS232_Uart_TX
END
```

Figure 5 – UART description in MHS file

BunchCleaner Custom Core Interfacing

Since software setup of the BunchCleaner custom cores is very low performance, they do not require mapping into the high-performance bus structure connecting the Xilinx cores; it was sufficient to use dedicated internal ports from Xilinx parallel I/O cores to control the user-settings. This allows software bit-twiddling to control DDS frequency, pattern loading or multiplier gain.

System Software

The system software is written in C for a Xilinx-supplied RTOS called xilkernel. It provides multi-threading, timer interrupt, task prioritization, and an LightWeight IP implementation. A modification of the Xilinx-supplied web server demonstration program is used to implement a command interpreter using a simple read/write TCP buffer. The software takes about 500Kbytes. Both FPGA firmware and software are stored in a single System-ACE file on the Flash Memory Card, allowing power-up initialization.

The software in the FPGA sets the patterns, DDS frequency and amplitude. Since the excitation tune is variable over a few kilo-hertz range, an upper and lower stimulus frequency range is varied at a user-specified rate under software control. Although random frequency settings were tried, empirically we find that simply ramping the rate up and down works best.

Control Room Software

A PC running a LabVIEW Virtual Instrument (VI) is used to send the parameters to the FPGA software. Buffers up to 2048 bytes are transferred using TCP-Write and TCP-Read VI functions. Initial setups are done with a laptop at the transverse kicker racks. During user operations the same VI is used in the control room PC's to turn the stimulus on/off and to adjust the stimulus frequency range as required.

CONCLUSION

The ALS BunchCleaner project shows that the Xilinx Virtex-4 FPGA can be used for a versatile gated signal generator. It combines the functionality of an arbitrary waveform generator with capabilities normally associated with accelerator timing systems. Using the ML403 demonstration board greatly speeds up the proto-typing process, and enhances the implementation of an embedded processor system to support networked user control of the BunchCleaning .

REFERENCES

[1] F. Sannibale, et al, "Tests of a New Bunch Cleaning Technique for the Advanced Light Source," EPAC-06 Edinburgh, Scotland, 2006

[2] Xilinx® ML403 Virtex-4 FX Evaluation Platform Product Brief, 2005, http://www.xilinx.com/.

[3] J. Weber, M. Chin, "Using FPGAs with Embedded Processors for Complete Hardware and Software Systems", Beam Instrumentation Workshop, Batavia, NY, May 1-4, 2006..

A SOLID-STATE PINGER TUNE MEASUREMENT SYSTEM FOR THE INTENSE PULSED NEUTRON SOURCE (IPNS) RAPID CYCLING SYNCHROTRON (RCS)*

J. C. Dooling†, L. Donley, M. K. Lien, and C. Y. Yao
Argonne National Laboratory, Argonne, IL 60439, U.S.A.

Abstract

A cw tune measurement system for the IPNS RCS is described. The pinger magnets are energized by a solid-state, transformer-coupled power supply operating at 30 Hz. In its present configuration, the power supply provides a 160-A pulse to a pair of series-connected, single-turn ferrite magnets. The magnet pair separately drive x- and y-plane orbit bumps in the h=1 beam. The dipole oscillations generated in the beam are sensed with pairs of split-can, pie electrodes. Raw signals from the H and V electrodes are carried on matched coax cables to 0/180-degree combiners. The output difference signals are recorded with gated spectrum analyzers. Bunch circulation frequency varies from 2.21 MHz at injection to 5.14 MHz at extraction. With a fixed frequency span of 24 MHz, between four and ten bunch harmonics and sidebands (SBs) are present in the difference spectra. Software has been developed to use the multi-harmonic SBs present over the span to improve the accuracy of the tune measurements. The software first identifies and then fits the multiple SBs to determine the tune. Sweeping the beam across the momentum aperture provides a method for measuring the chromaticity.

RCS PINGER DIAGNOSTIC

The IPNS RCS operated for almost 25 years without a dedicated tune diagnostic system [1]. Finally in February 2006, a ferrite pinger magnet set was added [2]. The horizontal and vertical magnets were initially driven by a thyratron-switched transmission line, essentially using 1/4 of the extraction kicker system. Assisted by an AC septum and a combined-function, horizontally defocusing singlet, the kicker provides 24 mrad of deflection, sufficient to extract the 450-MeV proton beam in a single turn. By contrast, the pinger supply need only provide a beam deflection on the order of 0.1-0.5 mrad. Therefore one of the goals of this work is to build a lower power, lower maintenance supply relative to the thyratron-based system. Another goal is to develop a diagnostic that can determine tune and chromaticity values more quickly than the single-shot measurements previously described [2]. In that case, pie-electrode data are recorded on a fast, deep memory oscilloscope. An optimized spectrum is then generated off-line; this process tends to be CPU intensive. In the present study, spectral data are recorded directly using two Agilent E4402B spectrum analyzers (SAs). Signals are first collected in each plane from a pair of split-can pie electrodes [3]. Each signal pair is fed on matched transmission lines to 0/180-degree combiners producing an A-B output. The x- and y-difference signals are recorded on the gated SAs.

*Work supported by U.S. DOE, Office of Science, Office of Basic Energy Sciences, under contract number DE-AC02-06CH11357.
†jcdooling@anl.gov

Pinger Power Supply

The power supply combines the properties of SCR-Marx and transformer step-up circuits. The amp-turns of four Marx circuit outputs are summed through a transformer to provide the final output to the pinger magnet load as shown in Figure 1. In addition to the series-connected horizontal and vertical magnet pair, the pinger load includes a 6.2-Ω resistor in parallel with 0.040-μF of ceramic disk capacitance. The terminating load is shown in Figure 2 prior to installation. To roughly match the terminating load impedance, eight 50-Ω, RG-217 coaxial cables are run in parallel from the pinger supply to the terminating load. Each cable is 7.6-m (25-ft) in length. To provide current protection for the 2N6405 SCRs, a 1.4-Ω series resistor is placed between each Marx stage. Initial testing of the pinger was conducted with two turns on each primary side winding and four turns on the secondary output side. The terminating impedance was connected in series to a single horizontal test magnet.

Several different values of capacitance in parallel with load resistance were tried to see if rise time could be reduced. In Figure 3, pinger output current waveforms are presented for terminating capacitances of 5 and 40 nF. The risetime is seen to improve from 186 to 174 ns as capacitance is raised between these two capacitance values; however, greater oscillations in output voltage and current also occur as the load impedance drops below a matched condition. To reduce hysteresis in the output transformer ferrite, each core is gapped to 0.38 mm (15 mils), lowering the energy per cycle lost in the NiZn core

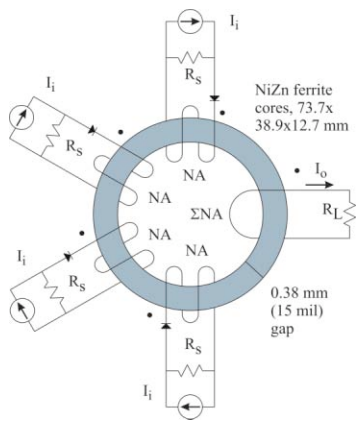

Figure 1: Output transformer schematic.

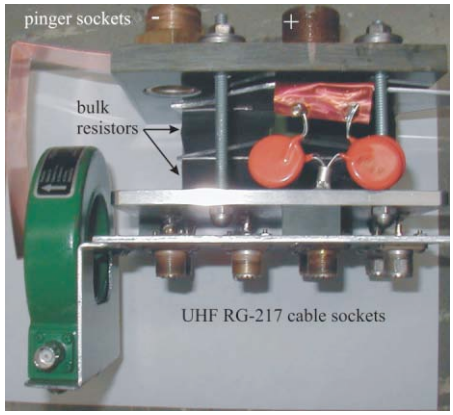

Figure 2: Pinger teminating load.

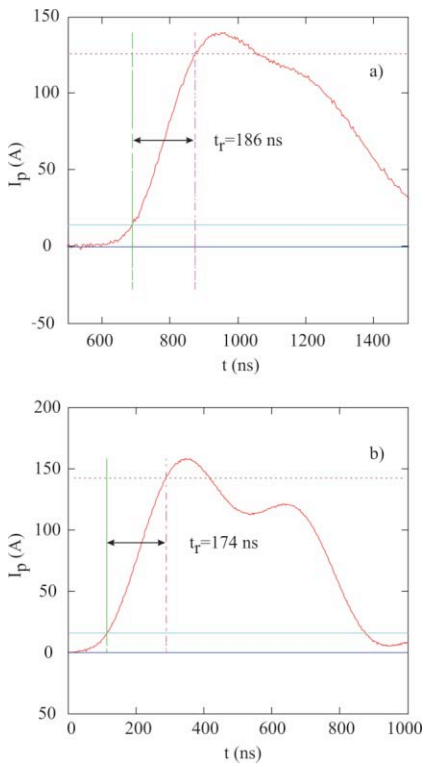

Figure 3: Comparison of 4-turn pinger output current waveforms and risetimes for a) 5 nF and b) 40 nF bypass capacitance.

material. However, this also lowers the inductance of the transformer, which must remain much higher than either the source or load impedances for efficient transformer response. Just prior to installation, the number of toroidal cores in the transformer was increased from five to seven. At the same time, the number of turns on the primary side was reduced from two to one; and the secondary winding was lowered from four to two turns. The pinger was placed into service in this configuration; see Figure 4. Its output was tested into the single test magnet without the terminating load since the load had already been installed in the RCS tunnel. Figure 5 presents the output voltage and current waveforms, the charge voltage on a single Marx capacitor, and the trigger signal at maximum output.

Once the pinger supply was installed, its output current into the actual dual-pinger magnet set and terminating load was monitored with a Pearson Model 6600 current toroid (0.05 V/A, 50 Ω) mounted to the terminating load, as shown in Figure 2. The current waveform into the magnets at the terminating load is presented in Figure 6 for a nominal voltage of 40 percent maximum output. A clear reduction is seen in the FWHM output pulsewidth relative to that shown in Figure 5. Examples of x- and y-difference spectra recorded at 40 percent of maximum output voltage, 10 ms after injection are given in Figure 7.

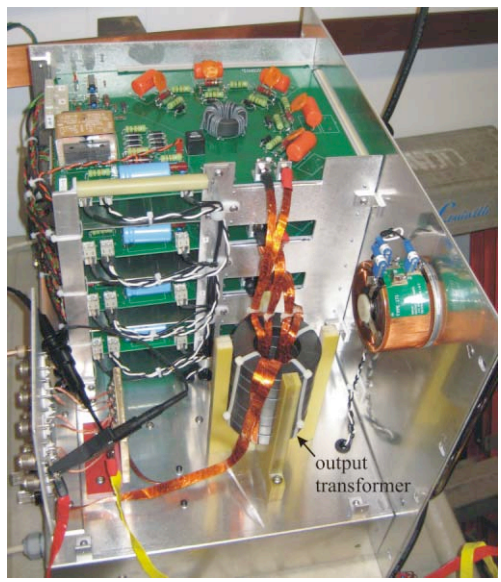

Figure 4: Final pinger configuration (two turn output).

Tune Algorithm

The algorithm for finding the tune from a recorded spectrum is as follows: For a given time in the acceleration cycle, the fundamental frequency is estimated using a fourth-order polynomial. The algorithm refines this estimate by locating all of the harmonic peaks within a fixed frequency range of 0-24 MHz. The 24-MHz span is represented by 801 points, making the bin width 30 kHz. Video and Resolution Bandwidths (VBW and RBW) are both set to 30 kHz on each SA. The number of harmonics participating in the analysis varies from ten

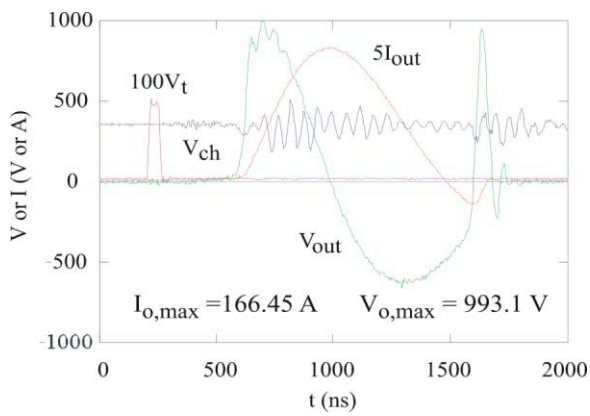

Figure 5: Two-turn output into unterminated magnet load.

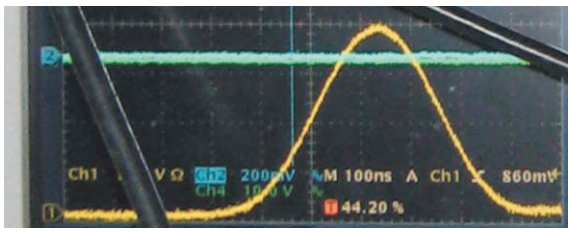

Figure 6: Pinger current waveform (partially obscured), two-turn output, into the terminated load; horiz. scale: 100 ns/div; vert. scale: 1 V/div (50 Ω, term.) = 20 A/div. Output voltage set to 40 percent.

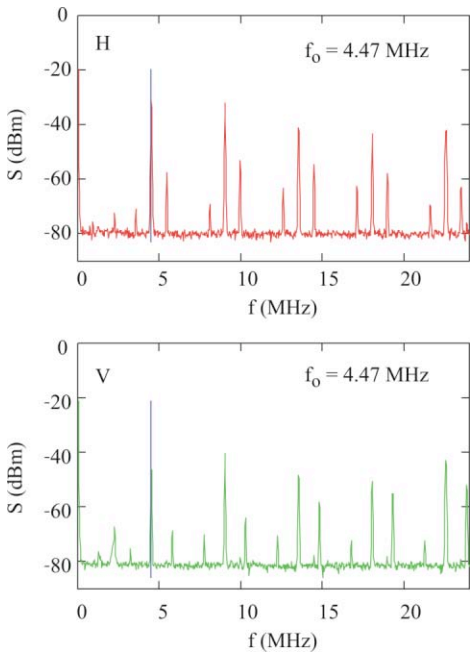

Figure 7: Difference spectra, 10 ms, nominal radial position (central orbit).

near injection (f_0=2.21 MHz) to four prior to extraction (f_0=5.14 MHz). It is required that all component sidebands of a principal harmonic must be present in the 0-24 MHz span to be included in the tune calculation. The exact location of each peak is determined by calculating the parabola described by the three measured spectral intensities, S_1, S_2, and S_3, about the local maximum. Within the 2Δf range (60 kHz) including the peak, the spectral amplitude is expressed as,

$$S(f) = a_0 + a_1 f + a_2 f^2, \quad (1)$$

where the coefficients a_0, a_1, and a_2 are given as,

$$a_0 = \Delta^{-1}\left[S_1\left(f_2 f_3^2 - f_3 f_2^2\right) + S_2\left(f_3 f_1^2 - f_1 f_3^2\right) + S_3\left(f_1 f_2^2 - f_2 f_1^2\right)\right],$$
$$a_1 = \Delta^{-1}\left[S_1\left(f_2^2 - f_3^2\right) + S_2\left(f_3^2 - f_1^2\right) + S_3\left(f_1^2 - f_2^2\right)\right],$$
$$a_2 = \Delta^{-1}\left[S_1\left(f_3 - f_2\right) + S_2\left(f_1 - f_3\right) + S_3\left(f_2 - f_1\right)\right], \quad (2)$$

and Δ is the determinant The peak intensity occurs when dS/df=0 or f_p=-a_1/2a_2. The value of the bunch frequency is expressed as the weighted average of all the visible principal harmonics. The locations of the x- and y-sidebands are measured in a fashion similar to the principal harmonics. The tunes are then determined from the total separation of the upper and lower sidebands relative to the bunch frequency. The horizontal fractional bare tune is near 0.18; therefore, the search is made in a range from 0.14-0.22. Fast and slow waves are both present, so the search extends below as well as above the harmonic frequencies. The vertical fractional bare tune is 0.32, and the search in the vertical plane covers a fractional tune range from 0.24-0.33. Space-charge usually lowers the vertical tune. The RCS Tune software display, presented in Figure 8, shows first an acquired vertical spectrum followed by the peak search results.

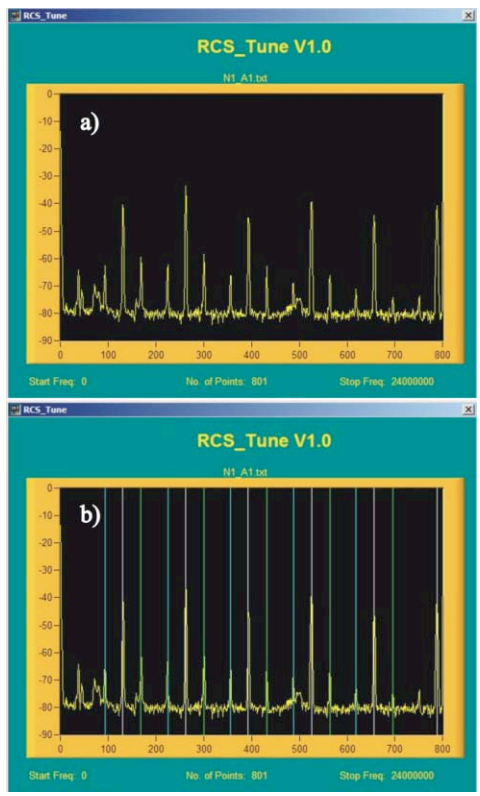

Figure 8: An early version of the RCS Tune software screen a) after reading a difference spectrum and b) after the first localization of peaks. The vertical spectrum is acquired 8 ms after injection.

RESULTS

Tune measurements are made at 1-ms increments during the 14.2-ms acceleration cycle, beginning 1 ms after injection. The period immediately after injection is avoided due to an early, vertical microwave instability. Measurements are made at reduced intensity to minimize the effect of space-charge-dependent tune-shift. Whereas typical injection involves 3.6x10^{12} protons (580 nC), for

tune measurements, approximately 0.5×10^{12} protons are injected (80 nC). At a given time in the cycle, chromaticity is evaluated by stepping the beam across the horizontal aperture using a local change in the frequency.

Examples of tune measurements made with the SS pinger are presented in Figures 9-12; these data were collected 11 and 12 ms after injection. SS Pinger data, obtained in November 2007 are compared with earlier data collected using the thyratron-based diagnostic in May 2007. Central orbit tune and chromaticity data are compared for these two periods in Figures 13 and 14. In general, small variations exist in the central horizontal and vertical tunes. The most significant shift is in the vertical plane where the November data are higher throughout the cycle. Regarding chromaticity, the horizontal data late in the cycle show the November results approaching positive values; in the past, positive x-chromaticity was cited as a reason for a head-tail instability that limited the current in the RCS; see the next section for further discussion.

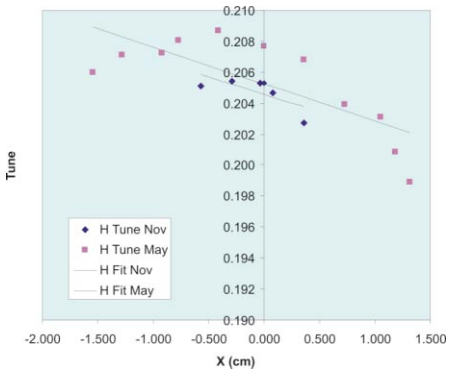

Figure 9: x-tune vs. x-position at 11 ms.

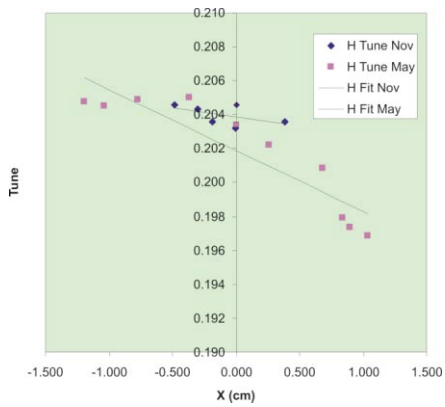

Figure 10: x-tune vs. x-position at 12 ms.

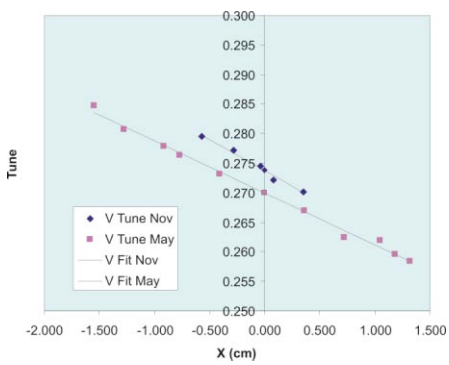

Figure 11: y-tune vs. x-position at 11 ms.

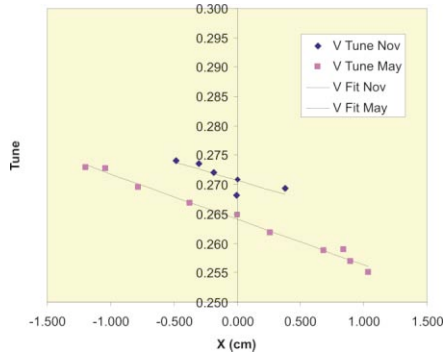

Figure 12: y-tune vs. x-position at 12 ms.

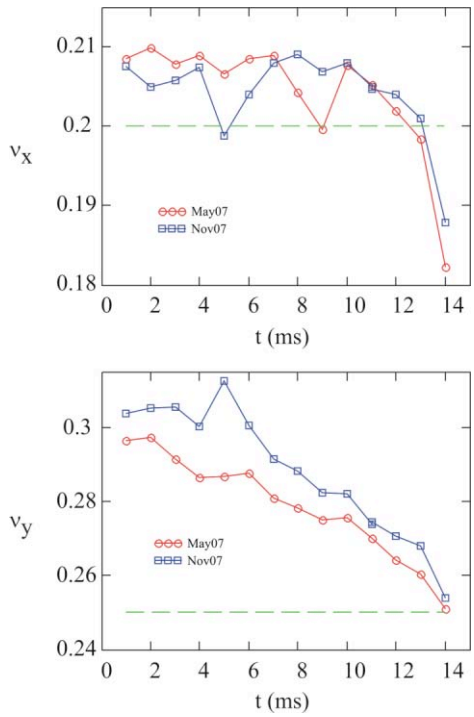

Figure 13: x- and y-tunes throughout the RCS cycle recorded in May and November, 2007.

DISCUSSION AND CONCLUSIONS

Chromaticity, the change in focusing relative to a change in momentum or energy, is expressed as

$$\xi(x,s) = \frac{d\nu}{\left(\frac{dp}{p}\right)} = \frac{\nu'(x)dx}{\left(\frac{\Delta x}{D(s)}\right)} \approx \nu'(x)D(s), \quad (3)$$

where D(s) is the local value of dispersion at the pie electrode. When normalized by the tune, chromaticity takes on a value close to -1 for a FODO lattice ring below transition [4]. Pulsed sextupoles are used to control both

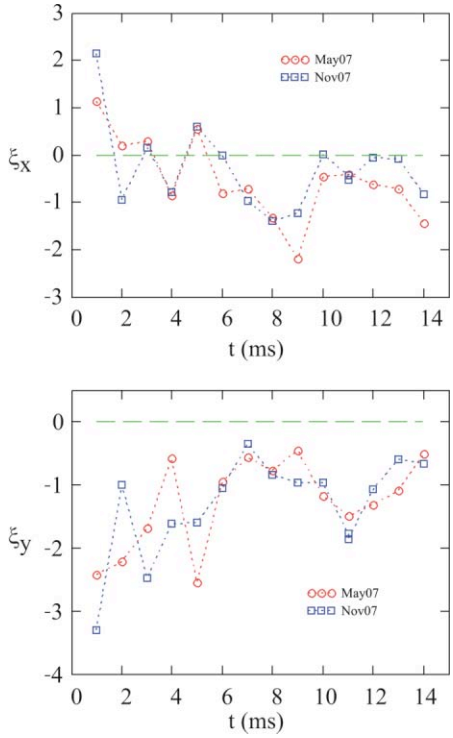

Figure 14: x- and y-chromaticities throughout the RCS cycle recorded in May and November, 2007.

x- and y-chromaticities during acceleration. These magnets were found to be important for stabilizing a horizontal head-tail instability early in the history of the RCS [5,6]. Stabilizing the head-tail allowed the current in the machine to be more than doubled from 4-5 μA to 10-11 μA. At the higher current level a new, vertical instability appeared later in the cycle (>10 ms). The vertical instability is not curable with sextupoles; instead, phase modulation (PM) at twice the synchrotron frequency that leads to quadrupole oscillations and a subsequent high-frequency microwave effect appears to add enough Landau damping to allow operation up to 16 μA. The form of the tune across the horizontal aperture can be represented with a polynomial. The horizontal data shown in Figures 9 and 10 suggest the order of the polynomial should be 2 or higher, indicating the presence of at least octupole terms in the focusing; however, sextupoles can only affect the linear term.

One of the main motivations for the pinger was to try to understand the nature of the instabilities in the RCS that limit its current. It was mentioned that the pulsed sextupole magnets play an important role in stabilizing the beam from destructive head-tail (HT) instabilities. During 2007, the HT reappeared. An example of the change that took place in the horizontal spectrum between 2006 and 2007 is shown in Figure 15. In the former case, at 11 ms in the cycle, only principal beam harmonics were observed; however, in 2007, horizontal sidebands appeared. Average beam current in most cases during this latter period was limited to under 15 μA. Several

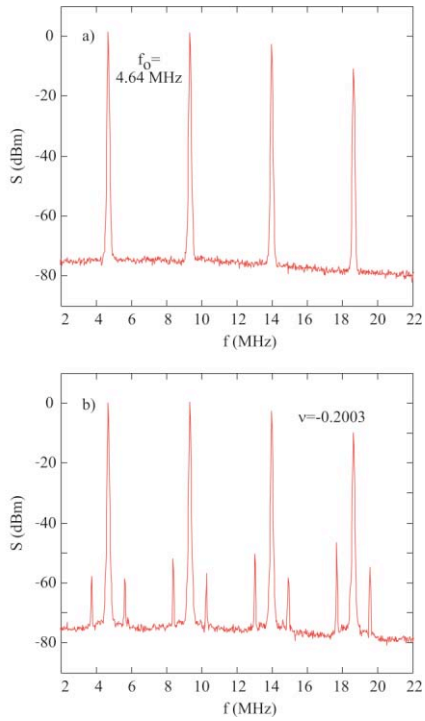

Figure 15: RCS full intensity beam spectra from a single-ended horizontal pie electrode 11 ms after injection a) December 2006 and b) December 2007. The oscillations indicated by the sidebands in b) are self-excited.

attempts were made to adjust sextupoles during 2007, but they proved to be unsuccessful. Having faster tune and chromaticity measurements, as the SS pinger diagnostic was beginning to provide, might have allowed a more coherent effort to mitigate the instability.

In conclusion, the SS pinger system did allow tune and chromaticity results to be obtained more quickly and with comparable accuracy relative to the single-pulse diagnostic.

ACKNOWLEGEMENTS

On January 1, 2008 the IPNS program was terminated. IPNS set the reliability standard for accelerator-based neutron user facility operations. It was a pleasure to work with the dedicated people that made the IPNS function so smoothly.

REFERENCES

[1] A. V. Rauchas et al., IEEE Trans. Nuc. Sci. **28**(3), 2331 (1981).
[2] J. C. Dooling et al., BIW06, AIP-868, 2006, p. 281.
[3] A. V. Rauchas et al., IEEE Trans. Nuc. Sci. **28**(3), 2338 (1981).
[4] S. Y. Lee, *Accelerator Physics*, World Scientific, Singapore, 1999, p. 121.
[5] Y. Cho, A. V. Rauchas, IEEE Trans. Nuc. Sci. **28**(3), 2585 (1981).
[6] C. Potts et al., IEEE Trans. Nuc. Sci. **28**(3), 3020 (1981).

AN OVERVIEW OF THE LHC TRANSVERSE DIAGNOSTICS SYSTEMS

M. Gasior, A. Boccardi, R. Jones, R.J. Steinhagen, CERN, Geneva, Switzerland

Abstract

The unprecedented intensity and energy of the LHC proton beams will require an excellent control of the transverse beam dynamics in order to limit particle loss in the superconducting systems. Due to restricted tolerances of the machine protection system and a tight beam emittance blow-up budget only small beam excitation is allowed, making precise measurements of the transverse beam parameters very challenging. This overview outlines the systems measuring the tune, chromaticity and betatron coupling of the LHC beams, referred to in the paper as the transverse diagnostic systems. As manual correction of the parameters may reach its limit with respect to required precision and expected time scales, the LHC is the first proton collider that can be safely and reliably operated only with automatic feedback systems for controlling transverse beam dynamics. An outline of these feedback systems is also presented.

INTRODUCTION

During nominal operation the LHC has a stored beam energy of about 350 MJ per beam circulating inside a cryogenic environment, which tolerates energy depositions in the order of only a few mJ/cm³. This requires an excellent control of particle loss, which for the LHC is provided by its Machine Protection and Beam Cleaning System [1-3]. The function of these systems depends critically on the stability of orbit, energy, tune (Q), chromaticity (Q') and betatron coupling (C^-), and imposes significant constraints on the maximum allowed beam excursions, traditionally required to measure Q and Q'. The transverse oscillation 'budget', which at nominal is below a few tens of μm, must be shared between several accelerator systems, such as the orbit and energy feedback, the Q phase-locked loop (PLL) and the bunch-by-bunch transverse damper feedback. As a result, the amplitudes of the explicit beam oscillations used by the transverse diagnostic systems for nominal beam operation are limited to a few μm. The non-zero dispersion at the collimator locations and available RF power relates this to an effective limit in the order of 10^{-5} on the maximum allowed momentum modulation Δp/p, with a maximum modulation frequency of about 5 Hz.

Due to persistent currents, the related decay and snap-back phenomena (inherent to superconducting magnets) and other perturbation sources, the induced changes in Q, Q' and C^- will exceed LHC beam stability requirements by orders of magnitude, as summarized in Table 1. Assuming that a large part of these perturbations are reproducible from fill-to-fill, these effects may be partially compensated by feed-forward systems. However, due to the intrinsic uncertainties related to the mentioned processes and the tight tolerances requested on Q, Q' and C^-, beam-based measurements and their exploitation in automated feedback systems will be mandatory for a safe and reliable LHC operation.

The nominal requirements of the LHC transverse diagnostic systems can be summarized as follows:

- sensitivity, allowing operation with excitation amplitudes in the 1 μm range for the rms beam sizes about 0.2-1 mm;
- resolution and measurement speed;
- robustness, required to reliably operate automatic feedback systems under varying beam conditions.

This overview focuses on the measurement and control of Q, as both Q' and C^- are usually derived from it. While C^- can be calculated using cross-amplitude terms of the tune eigenmode oscillations [4, 5], the base-line LHC Q' measurement employs the classic method, based on tracking the Q' dependent tune changes ΔQ as a function of momentum modulation Δp/p. The underlying relation, also defining the unit of Q', is given by

$$\Delta Q = Q' \frac{\Delta p}{p}$$

Table 1. Parameters and requirements of the LHC transverse diagnostic systems [6].

Parameter	Tune [f_{rev}]	Chromaticity [Q']	Coupling [C^-]
Nominal value	0.31, 0.32	2	< 0.001
Nominal stability	< 0.001	±1	< 0.001
Perturbations	0.14	70	0.01
Worst-case perturb.	0.18	300	0.1
Max drift per sec.	< 0.001	1.3	–

TUNE MEASUREMENT

The biggest challenge in measuring tunes of high intensity beams is the dynamic range of the processed signals, as the small signal related to transverse beam oscillations is carried by large, short pulses. For example, the nominal 1 ns long LHC bunches induce some 50 V on the 40 cm electrodes of the Q measurement stripline pick-ups. For the 80 mm pick-up diameter and 1 μm beam oscillation amplitudes the modulation of the pick-up output pulses is in the order of 10^{-5}, i.e. a few mV. An efficient way to filter out the betatron modulation signal from its inconvenient carrier is to use the Direct Diode Detection (3D) [7, 8]. The principle of this technique is shown in Fig. 1, with the simplified signal waveforms sketched above the corresponding circuit paths.

The pick-up electrode signals are processed by diode peak detectors, which can be considered as fast sample-and-hold circuits, with the sampling self-triggered at the bunch maxima and 'held' by the parallel capacitors. The purpose of the parallel resistors is to slightly discharge the capacitors so that the next bunch with a potentially smaller amplitude also contributes to the detector output signal.

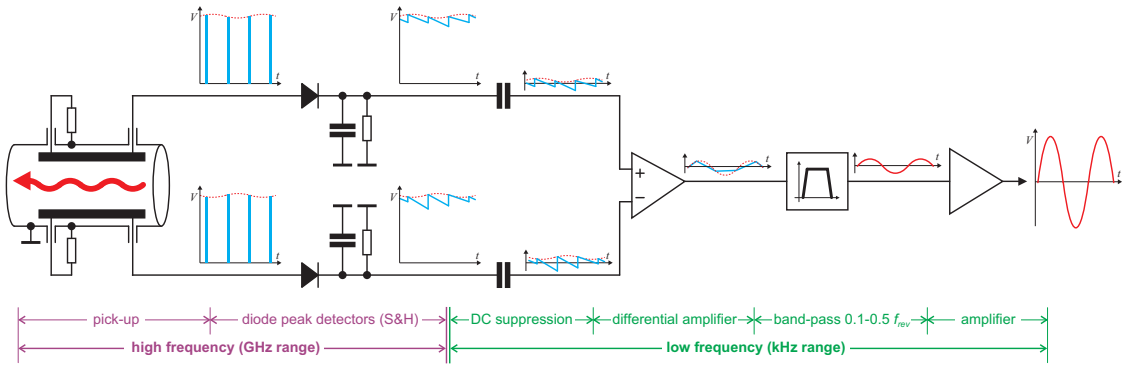

Figure 1: Direct diode detection principle with simplified signal shapes in the key nodes of the circuit.

Bunch sampling by the peak detectors at the bunch repetition rate down-converts the beam energy from a few GHz frequency range to the baseband. In the baseband in the kHz range the signals can be efficiently and cost-effectively processed by powerful audio-frequency components.

The 3D technique requires simple, low frequency and thus inexpensive electronics, and gives very high sensitivity for large beam signals, which could otherwise not be processed without prior attenuation or filtering. It does not require beam synchronous timing due to the intrinsic down-sampling property and can work with any position pick-up.

The 3D technique as described above yields an 'averaged' tune for all bunches, with those of dominating amplitudes contributing more than smaller ones. This can be improved with a preceding fast, large signal gate, selecting only bunches of interest, however, at the cost of potentially reduced sensitivity and increased system complexity. Such a solution is currently being studied.

The block diagram of the LHC tune and coupling measurement system, based on the 3D technique, is shown in Fig. 2. The 3D analogue front-end (AFE) signals are digitised at the revolution frequency rate of 11.2 kHz by 24-bit audio ADCs. Samples are subsequently send through an LVDS link to an LHC standard VME data acquisition card, which is also used for other LHC instrumentation systems. The acquisition card houses a large FPGA and memory, allowing an efficient, fast, real-time, turn-by-turn processing of the digital samples.

The tune measurement system can operate either using spectral analysis (FFT) or as a PLL system resonantly locked on the tune eigenmodes.

In the 'FFT' mode the FPGA calculates the fast Fourier transform of the ADC samples arranged in frames of length from 256 to 256K, prior to the application of one of the commonly used windowing functions. The FFT acquisition frames can be triggered to start at specified time intervals, at the end of the previous frame ('back-to-back' mode) or to overlap with adjacent frames by up to 50%, as all samples are double buffered. The internal FPGA processing is done with 32-bit precision, resulting in a 180 dB dynamic range of the calculated spectra [9].

The acquisition card is connected to a VME front-end computer, through which the user can continuously retrieve the real and imaginary parts of the FFT spectra, the power spectra and the original raw signal samples via a fast Ethernet link, using the CERN common middle ware communication protocols.

The FFT mode offers several types of measurement options. The system can operate with no explicit excitation relying on the residual beam oscillations ('passive' operation), with dedicated tune kickers or with fast frequency sweeps ('chirp' signals). The chirp signals are generated digitally inside the FPGA and converted into analogue signals by 24-bit DACs. To get sufficient resolution the trigonometric functions required for the windowing and chirp signal generation are calculated 'on-the-fly' in the FPGA. The DAC chirp signals are sent to the LHC transverse damper system which amplifies the signal and excites the beam through pairs of electrostatic deflection plates.

A typical FFT measurement example is shown in Fig. 3. The measurement has been done with the LHC prototype system installed in the CERN SPS using a chirp excitation in the vertical plane. For the 2007 start-up the prototype was adapted for regular SPS operation and has since been working as the primary SPS tune meter.

In the PLL mode the beam is sinusoidally excited at a small amplitude (typically less than a μm) through either the transverse damper or through a dedicated 1 m stripline kicker, which will be driven with a current of a few A. For the baseband excitation frequencies (around 3.5 kHz) the stripline electrodes will be short-circuited at one end to allow operation with low voltages (a few V), limiting power dissipation in the driving amplifier to some 20 W. The stripline will be RF terminated only for beam pulses at higher frequencies.

The PLL scheme is based on mixing the beam signals from the AFE with the sine and cosine components of the excitation signal. Then IIR low-pass filters are used to remove higher order mixing products. The remaining signals are treated by a rectangular-to-polar converter that separates the signal phase and amplitude, which can further be treated by two independent controllers. In comparison to classic phase detectors based on mixers, this scheme provides a twice the dynamic range for the

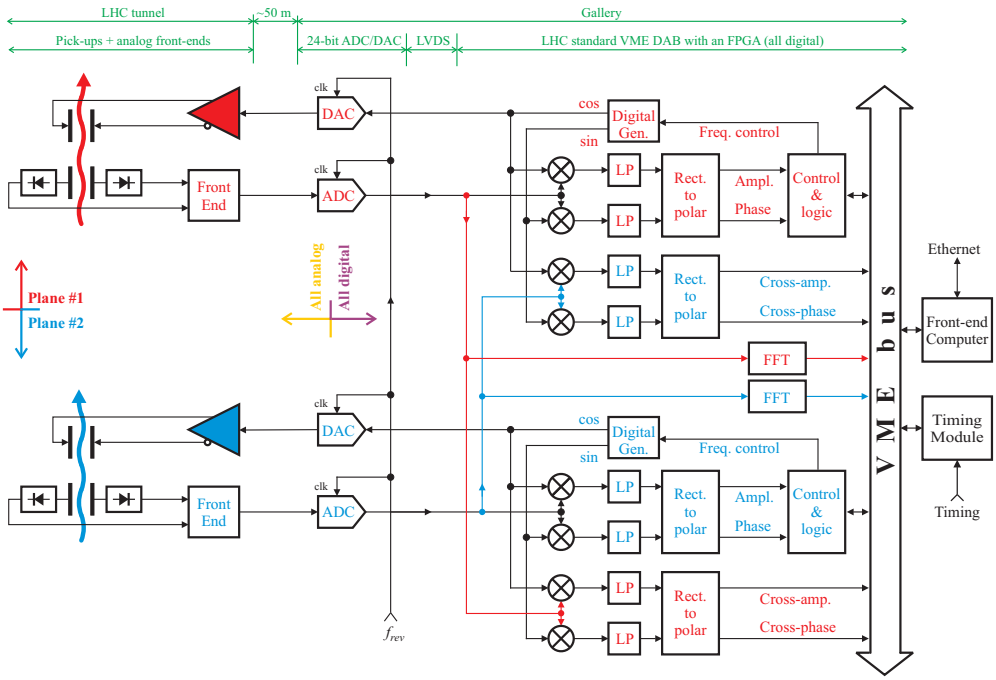

Figure 2: Block diagram of the LHC tune and coupling measurement system (two planes of one beam).

phase and a true decoupling from the amplitude, which proves to be advantageous in situations when the phase and amplitude change at the same time. The FPGA further compensates for other non-beam related contributions to the measured phase shift, such as constant lag due to data processing, cable transmission delays, filters in the AFE and the response of the beam exciter itself. Most of the controller parameters can be updated during operation for the optimum trade off between the required measurement resolution and tracking speed, depending on beam conditions.

The prototype LHC PLL system has been successfully tested at the SPS. Complementary studies have also been carried out at BNL RHIC in the framework of US-LARP activities [4, 10-14]. The RHIC PLL tune measurement system is based on the same 3D technique, with however different architecture.

The system in the PLL mode measures C^- by correlating the tune eigenmode signal in the excited plane with that of the response in the unexcited plane, i.e. horizontal tune in vertical plane and vice versa [5]. While the base-line for coupling measurement is the PLL, it has also been shown that the same C^- estimate can be equally derived using the chirp excitation, as shown in Fig. 3.

The LHC tunes will be measured by three independent operational systems per beam. While requiring only one system per beam, it is believed that this redundancy will provide an increased flexibility and thus reliability for LHC operation.

Of the three systems per beam, one is dedicated for passive beam spectra observation, ensuring a continuous data logging for post-mortem analysis, passive beam quality monitoring and fixed displays in the control room. While not being directly connected to a dedicated exciter, this passive system nevertheless observes any beam excitation introduced by the other systems connected to one of the excitation sources.

The second system is dedicated to tune PLL operation, with the excitation signals routed to either the dedicated stripline kickers or the transverse damper. The third system, connected to either the stripline kicker or damper, is intended for 'on-demand' tune measurement which may require frequent acquisition parameter configuration changes, temporary pausing or synchronization of the acquisition to other machine timing driven events (e.g. operation of the tune kickers).

An additional fourth system, dedicated for beam instrumentation and diagnostic development purposes, can replace any of the operational systems in case of hardware problems.

CHROMATICITY MESUREMENT

The base-line LHC chromaticity measurement is based on the classical momentum modulation method. Similarly to the tune tracking itself, the main Q' measurement constraints derive from the tight limits on the transverse beam position by the collimation and RF acceleration system, which reduces the usable momentum modulation to a few 10^{-5} with modulation frequencies of less than about 5 Hz. This puts very challenging demands on the resolution of the Q measurement, which must therefore also be of the same order. The feasibility of the Q' measurement with this unprecedented small momentum modulation has been demonstrated at the SPS in 2007. One such a measurement is shown in Fig. 4. The tune variations due to a peak momentum modulation of 1.8×10^{-5} and the reconstructed chromaticity are shown.

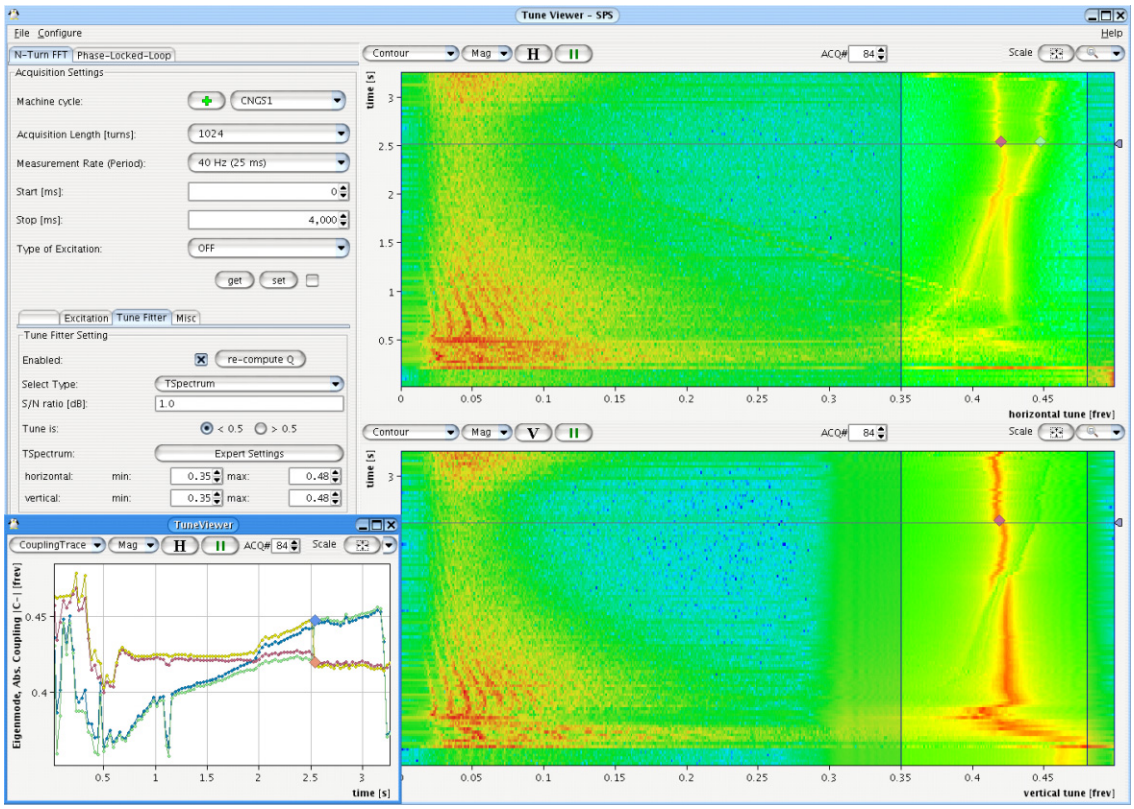

Figure 3: A typical SPS FFT measurement with vertical chirp excitation in presence of coupling. Measured and reconstructed unperturbed crossing tunes are shown on the plot in the left bottom corner. Synchrotron sidebands of the revolution frequency (down-converted to DC) can be seen at lower frequencies. The synchrotron frequency becomes small at the transition (around 0.5 s).

The achieved Q resolution was in the order of 10^{-6}, resulting in a chromaticity resolution of better than 1 unit. It was shown that the Q' tracking loop was able to operate up to chromaticity values of at least 36 units, which provides some margin for operation in a regime where a classic Q kicker based measurement using BPMs would fail due to very fast de-coherence times [15].

Attempts have been made to assess the information on chromaticity without an explicit momentum modulation, based on collective effects such as the head-tail phase shift [16, 17], decoherence time and related tune width, which can be exploited through additional side-exciters placed around the primary tune PLL exciting frequency [18]. All these methods have in common that they are also dependent on other effects, such as impedance, non-Q' related detuning with amplitude and other higher order effects that may drive non-linear particle motion. Nevertheless, provided that the relevant non-Q' beam parameters are small, these techniques could ultimately allow a direct measurement of Q' using the PLL system without the need for momentum modulation. This will, however, require further evaluation with LHC beams for acceptance in terms of robustness and reliability. Thus the base-line Q' measurement method is and will be based on the more established classic momentum modulation technique.

FEEDBACKS

Due to the tight beam parameter requirements and expected large perturbation sources, the LHC will be the first accelerator that requires continuous beam-based feedbacks for safe and reliable machine operation during nearly all operational phases. It is thus foreseen to deploy fully automated feedbacks on orbit, tune, chromaticity, coupling and beam energy. This paper concentrates on tune, chromaticity and coupling feedbacks, with the control of orbit and energy described in detail in [19].

The operation of multiple feedback loops acting on the same beam requires a proper addressing of cross-constraints, cross-talk and possible coupling between the loops already at the design stage. In the LHC two basic decoupling strategies are deployed:

- decoupling of beam parameters, e.g. orbit and energy (dispersion orbit), or tune and betatron coupling;
- separation of feedback bandwidths.

The foreseen nested LHC feedback control scheme is shown in Figure 5. The orbit and energy feedback are the inner-most loops surrounded by the tune PLL measuring and correcting the global tune and coupling parameters.

In order to minimize the cross-talk introduced between the chromaticity and orbit/energy feedback via the

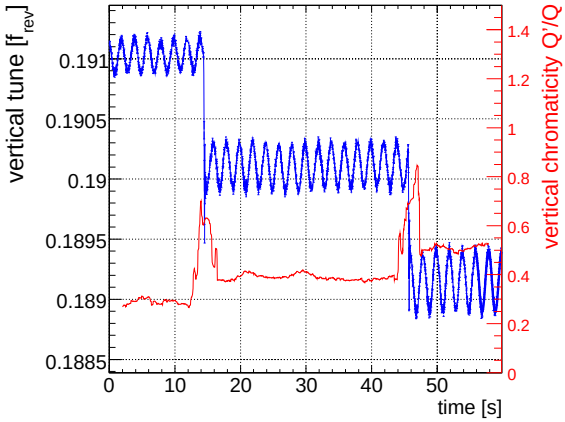

Figure 4: Q' measurement by momentum modulation.

dispersion orbit, the foreseen orbit/energy feedback filters and separates the dispersion orbit from the measured closed orbit prior to performing any orbit or energy correction (radial steering).

The Q tracking PLL is first nested within the tracking loop that measures and controls the chromaticity and is then surrounded by the actual Q feedback loop controlling the global tunes and coupling. The decoupling is obtained by choosing gradually reduced bandwidths for the Q tracking PLL ($f_c \approx 8$ Hz), chromaticity ($f_c \approx 1$ Hz) and tune feedback ($f_c < 1$ Hz). This nesting hierarchy is required in particular to eliminate the cross-talk between the Q and Q' feedback, as the tune feedback would otherwise minimize the momentum-driven modulation and thus compromise the chromaticity measurement.

An alternative scheme, to correct for the momentum-driven tune perturbations by the quadrupole and to derive the chromaticity through the quadrupole current modulations, has been tested at RHIC [13]. However, at the LHC these modulations would be too small and the knowledge on the quadrupole transfer function not sufficient in the targeted tune modulation regime to exploit this scheme.

CONCLUSIONS

The LHC will require a continuous, automatic control of orbit, tune, chromaticity, betatron coupling and energy for safe and reliable machine operation. The collimation and machine protection systems impose tight constraints on the allowed transverse beam oscillations, traditionally required to measure Q and Q'. These constraints have led to the development of the high sensitivity direct diode detection technique. Combining this detection technique with a tracking PLL and small momentum modulation has allowed all transverse beam parameters to be measured with unprecedented accuracy using minimal excitation. The performance of such systems has been shown to be compatible with nominal LHC requirements during regular operation and tests both at the CERN SPS and BNL RHIC. The LHC will therefore start-up with a comprehensive suite of instruments for the measurement and correction of the transverse beam parameters.

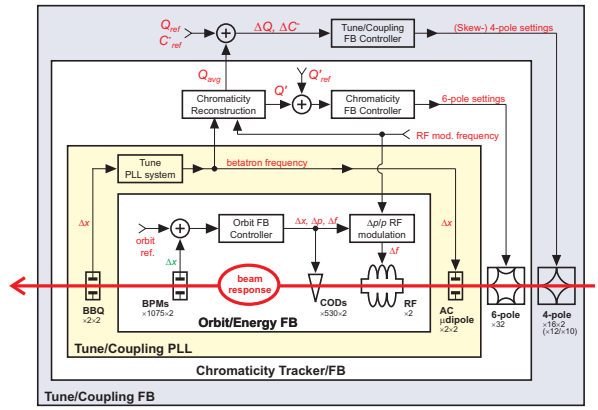

Figure 5: Block diagram of the LHC feedback systems.

REFERENCES

[1] R. Assmann, "Collimation and Cleaning: Could this limit the LHC performance?", Proceedings of Chamonix XII, 2003.
[2] S. Redaelli, "LHC Aperture and Commissioning of the Collimation System", Proceedings of Chamonix XIV, 2005.
[3] V. Kain et al., "The Expected Performance of the LHC Injection Protection System", CERN LHC Project Report 746, 2004.
[4] P. Cameron et al., "Advances Towards the Measurement and Control of LHC Tune and Chromaticity", DIPAC'05.
[5] R. Jones et al., "Towards a Robust Phase Locked Loop Tune Feedback System", DIPAC'05.
[6] R. J. Steinhagen, "Real-time Feed-Forward/Feedback Required", Proceedings of Chamonix, 2006.
[7] M. Gasior, R. Jones, "The Principle and First Results of Betatron Tune Measurement by Direct Diode Detection", CERN LHC Project Report 853, 2005.
[8] M. Gasior, R. Jones, "High Sensitivity Tune Measurement by Direct Diode Detection", DIPAC'05.
[9] A. Boccardi et al., "The FPGA-based Continuous FFT Tune Measurement System for the LHC (…)", PAC'07.
[10] P. Cameron et al., "The Effects and Possible Origins of Mains Ripple in the Vicinity of the Betatron Spectrum", DIPAC'05.
[11] P. Cameron et al., "Summary of Coupling and Tune Feedback Results during RHIC Run 6, and Possible Implications for LHC Commissioning", EPAC 2006.
[12] P. Cameron et al., "Simultaneous tune and coupling feedback (…)", PRST 122801 (2006).
[13] P. Cameron et al., "Tune, Coupling, and Chromaticity Measurement and Feedback During RHIC Run 7", DIPAC'07.
[14] P. Cameron et al., "Progress in Tune, Coupling, and Chromaticity Measurement and Feedback during RHIC Run 7", PAC'07.
[15] R. J. Steinhagen et al., "Results of Continuous Chromaticity Measurements in the CERN-SPS (…)", EPAC'08, tbp.
[16] M. Sands, "The Head-Tail Effect: An Instability Mechanism in Storage Rings", SLAC-TN-69-008, 1969.
[17] R. Jones et al., "The Measurement of Chromaticity via Head-Tail Phase Shift", BIW'98.
[18] R. J. Steinhagen et al., "Influence of Varying Tune Width on the Robustness of the LHC Tune PLL (…)", PAC'07.
[19] R. J. Steinhagen, "LHC Beam Stability and Feedback Control – Orbit and Energy", CERN-AB-2007-049.

PROGRESS WITH THE DIGITAL TUNE MONITOR AT THE TEVATRON*

V. Kamerdzhiev#, V. Lebedev, A. Semenov, FNAL, Batavia, IL 60510, USA

Abstract

Monitoring the betatron tunes of individual proton and antiproton bunches is crucial to understanding and mitigating the beam-beam effects in the Tevatron collider. To obtain a snapshot of the evolving bunch-by-bunch tune distribution a simultaneous treatment of all the bunches is needed. The digital tune monitor (DTM) was designed to fulfill these requirements. It uses the standard BPM plates as a pickup. The vertical proton monitor is installed and allows us to gain valuable operational experience. A major upgrade is underway to implement an automatic bunch-by-bunch gain and offset adjustment to maintain the highest possible sensitivity under real operational conditions. We present the concept of the DTM along with its technical realization as well as the latest experimental results. Major challenges from the design and operation point of view are discussed.

INTRODUCTION

In the TEVATRON 36 proton bunches collide with 36 anti-proton bunches at the center of mass energy of 1.96 TeV. The bunches of each species are arranged in 3 trains of 12 bunches circulating around the ring with the revolution frequency f_{rev} = 47.7 kHz. The bunch spacing within a train is 396 ns corresponding to 21 RF buckets (53.1 MHz). The bunch trains are separated by 2.6 μs abort gaps corresponding to 139 RF buckets. The betatron tunes of individual bunches are affected, among other phenomena, by the head on and long range beam-beam interaction [1]. These mechanisms limit the performance of modern colliders. In order to be able to mitigate the beam-beam effects, the knowledge of the bunch-by-bunch tune distribution is crucial. Three transverse tune monitors are presently available at the Tevatron: the 21.4 MHz Schottky, the 1.7 GHz Schottky and the Direct Diode Detection Base Band Tune (3D-BBQ) detector [2]. The 21.4 MHz Schottky is used to measure the horizontal and vertical tunes of the 36 proton bunches without the possibility of gating on individual bunches. The 1.7 GHz Schottky is capable of measuring the horizontal and vertical tunes of a single proton and anti-proton bunch but needs a few minutes of averaging time to get the precision of 10^{-4}. Furthermore, the significant width of the betatron sidebands at high frequency and the presence of transverse coupling in the machine result in additional uncertainty of the reported tune values. The 3D-BBQ detector is under development and allows to gate on proton and anti-proton bunches. This monitor showed promising results (individual proton and anti-proton tunes have been observed without additional beam excitation) and is presently used to cross-check the tunes measured by the two other monitors. The Digital Tune Monitor (DTM) [3], the subject of this paper, has the potential to report the horizontal and vertical tunes of each proton and anti-proton bunch, at a repetition rate of 1 Hz.

EXPERIENCE WITH THE DTM

The DTM was successfully used to acquire proton vertical spectra in numerous HEP stores [4]. The theoretical estimates show that detecting the betatron oscillation of individual bunches without additional beam excitation might be possible. However, under real operating conditions the ultimate achievable sensitivity and the dynamic range are limited by the orbit drifts (Fig.1), low frequency beam motion (Fig.2) and the bunch to bunch intensity and position variation.

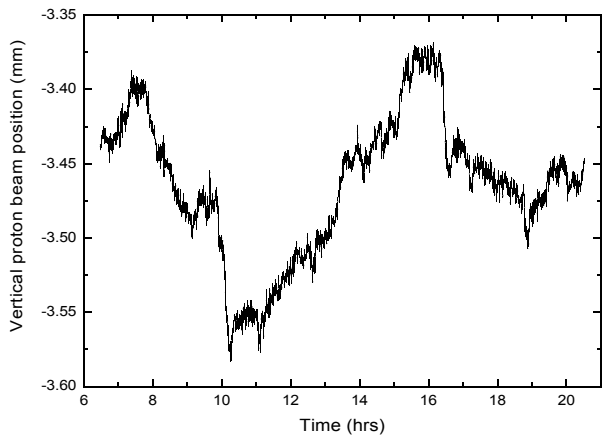

Figure 1. Vertical proton beam position reported by the Tevatron BPM over the course of a store.

The present DTM design makes use of a linear discriminator in a feedback loop in the difference channel. This technique allows for compensation of the slow beam motion (based on the average position measured over several turns).

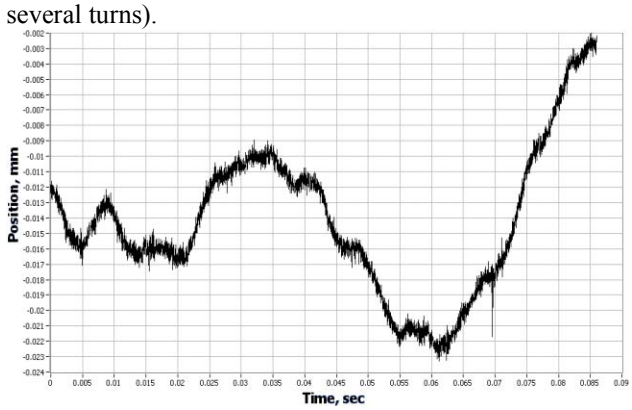

Figure 2. An example of the vertical proton beam position as seen by the DTM. Full scale is 22 μm, ~4000 turns.

*Work supported by the U.S. Department of Energy under contract No. DE-AC02-07CH11359

#vsevolod@fnal.gov

The application of this method led to reproducible results but additional beam excitation is still necessary. The position resolution of the DTM in the FFT averaging mode was estimated to be of the order of 100 nm. The frequency resolution is better than 12 Hz.

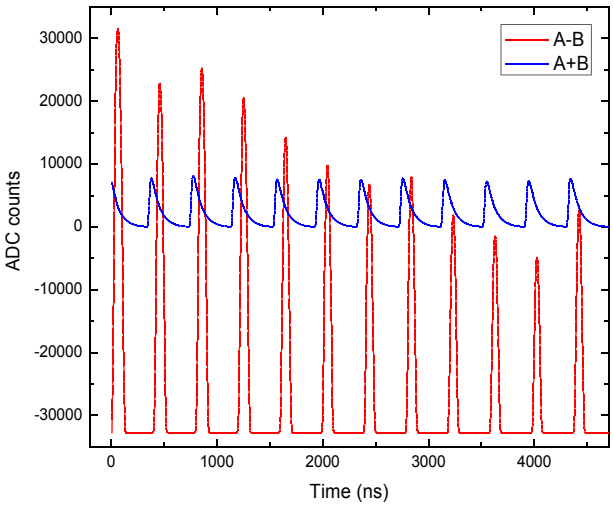

Figure 3. The integrated sum and difference signals in time domain (ADC FIFO) measured 3.5 hrs into store # 6051. Proton bunches 1-12 are shown.

As mentioned above the bunch to bunch variation in intensity and position significantly limits the dynamic range and the achievable sensitivity. Fig.3 shows a snapshot (content of the ADC FIFO) of the A-B and A+B signals. The data represents a single passage of the beam by the pickup. The vertical scale corresponds to the full ADC range. The gain in the A+B channel is much lower than in the A-B channel. One can see that in this particular case the bunch to bunch amplitude variation, caused by the long range beam-beam effects and the different bunch intensities, consumes more than half of the available ADC range in the A-B channel. In extreme cases it can be the full range. Furthermore, beam motion can cause temporary saturation for some bunches leading to elevated noise floor in the spectra or even to data loss.

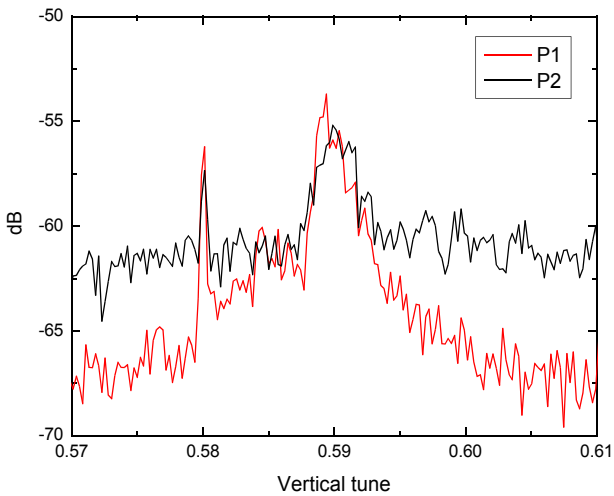

Figure 4. The vertical DTM spectra for proton bunches 1 and 2 measured 3.5 hrs into store # 6051.

An example of the vertical proton spectra acquired with the DTM is shown in Fig.4. The noise floor in the P2 spectrum is about 5 dB higher than in P1 spectrum – a sign of possible dynamic range problems. The data was taken during a HEP store using additional beam excitation (band limited noise). Since the excitation power is very low and is needed for less than 2 s the DTM does not affect the Tevatron operation in any way.

In order to provide adequate beam excitation the DTM now includes a subsystem consisting of a two channel digital signal generator and two power amplifiers (PA). Since the betatron sideband of interest corresponds to 19.6 kHz, inexpensive commercially available audio PAs are used. Fig.5 shows how the kicker and pickup are shared with other Tevatron systems.

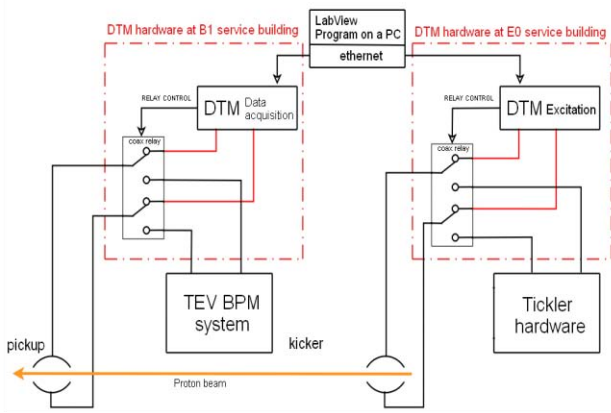

Figure 5. A block diagram illustrating the pickup and kicker sharing.

THE NEW DEVELOPMENT

In order to cope with the issues described in the previous section the DTM is undergoing a major upgrade. Based on the operational experience we acquired, several additional techniques are being currently implemented. Fig.6 shows the block diagram of the latest design. In order to be able to effectively suppress the beam position offset at the pickup location the signals from individual plates are now integrated, amplified and digitized separately. In addition, a fast linear discriminator (LD) and a variable gain amplifier (VGA), both controlled by the FPGA by means of two fast DACs are used for compensating the bunch to bunch amplitude variation. All the signal processing, including four parallel FFT engines and a DSP is realized in the large CYCLONE III FPGA. The DSP takes care of the data formatting and communication via 100/1000Mbit Ethernet link. The LD threshold is calculated using the orbit data (all bunches over several revolution periods) and the data describing the properties of each individual bunch. Before each tune measurement, the DTM goes through a “learning period” (several turns) when the data tables describing the individual bunches are derived. During the actual data taking these tables are used to adjust the LD and the VGA for predictable bunch parameters. Additional adjustment can be made on the turn-by-turn basis.

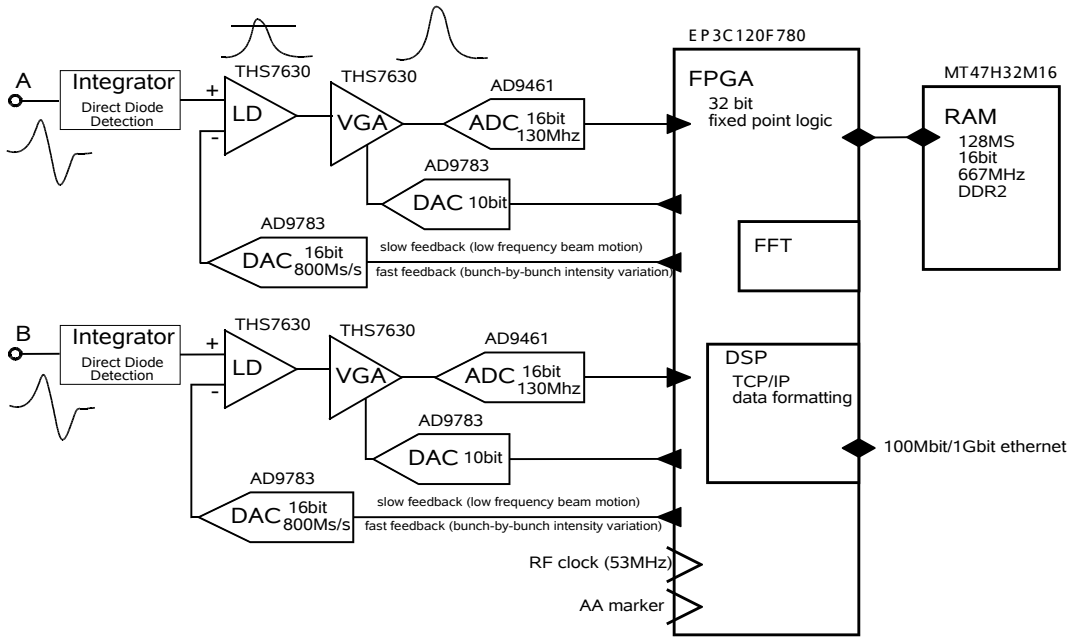

Figure 6. The block diagram of the new DTM design.

SUMMARY

Based on the experience gained while operating the Digital Tune Monitor in numerous HEP stores, several additional features are now being added to the DTM design. The new hardware has been assembled; the FPGA code development is underway. The new design will allow compensating for the detrimental affects of the orbit changes and bunch to bunch intensity and position variation. These measures are expected to result in significant improvement of sensitivity and reliability of the DTM.

ACKNOWLEDGEMENT

We would like to thank J.-P. Carneiro, B. Fellenz, V. Scarpine, J. Simmons, V. Shiltsev, and R. Webber for their contributions to the project.

REFERENCES

[1] V. Shiltsev *et al.*, "Beam-beam effects in the Tevatron", Phys. Rev. ST Accel. Beams 8, 101001 (2005).

[2] M. Gasior and R. Jones, "The Principle and First Results of Betatron Tune Measurement by Direct Diode Detection", LHC Project Report 853, August 2005. See also "High Sensitivity Tune Measurement by Direct Diode Detection", Proceedings of DIPAC 2005, same authors.

[3] J.-P. Carneiro *et al.* "A possible new method to measure the betatron tunes at the TEVATRON ", FNAL Beam-doc-1911, August 2005.

[4] A. Semenov *et al.* "Status of the FNAL Digital Tune Monitor", Proceedings of PAC 2007.

AN FPGA-BASED TUNE MEASUREMENT SYSTEM FOR THE APS BOOSTER SYNCHROTRON*

C.-Y. Yao#, W. E. Norum, Ju Wang
Advanced Photon Source, ANL, Argonne, IL 60439, U.S.A.

Abstract

The Advanced Photon Source (APS) injection booster is a 7-GeV electron synchrotron with a ramping time of 226 ms and a repetition rate of 2 Hz. A real-time tune measurement system is needed in order to monitor and correct tune drift during the 226-ms energy ramp. Such a drift occurs during user beam operations, especially during continuous top-up operations, and results in shot-to-shot efficiency fluctuations. We designed and developed an FPGA-based system that pings the beam at variable intervals and measures tunes. An operational system has been built and commissioned. It has achieved a time resolution of better than 2 ms and a tune resolution of better than 0.001. This report describes the system design and main parameters, and results from our preliminary commissioning. We also briefly discuss the application of such a system in ramping correction and ring diagnostics.

INTRODUCTION

A real-time tune measurement system is needed for the APS booster synchrotron in order to monitor the tune drift during the 226-ms energy ramp. Such drift may occur during user beam operations and results in inconsistent performance of the booster synchrotron. We designed and developed an FPGA-based tune measurement system that can measure booster tune using a pulsed pinger and an FPGA processor. The system is operational, and its performance is better than the VSA-based configuration we used previously in terms of speed, cost, and the ability to continuously monitor tunes.

PEAK DETECTION MECHANISM

The Numerical Analysis of Fundamental Frequency (NAFF) method [1,2] has been widely used to analyze frequency components of various objects. Transverse betatron oscillations of a bunch can be observed by kicking or chirping the bunch in the plane of observation. A turn-by-turn position signal is acquired from a beam position monitor (BPM). The instantaneous tune is obtained by maximizing the absolute value of the correlation term

$$I(\nu_m)=\sum_{n=1}^{N} x_n[\cos(2n\nu_m)+j\sin(2n\nu_m)]w(n),$$

where N is total number of turns from which the tune is measured and W(n) is a window function. Typically several iterations are necessary to reach the desired accuracy.

*Work supported by U.S. Department of Energty, Offices of Science, Office of Basic Energy Sciences, under contract No. DE-AC02-06CH11357.
#cyao@aps.anl.gov

Another frequency analysis method was reported by Gasior et al. [3] This method first performs fast Fourier transform (FFT) with N data points, and then interpolates the result with a parabolic or Gaussian function. The frequency peaks are then derived from the fitted curve. This method improves the FFT resolution and not only produces the peak frequency but also generates a full spectrum, which is useful for diagnostics purposes. It is easier to implement, very efficient, and more appropriate for our application. We adopted the latter method in the current version of the FPGA firmware.

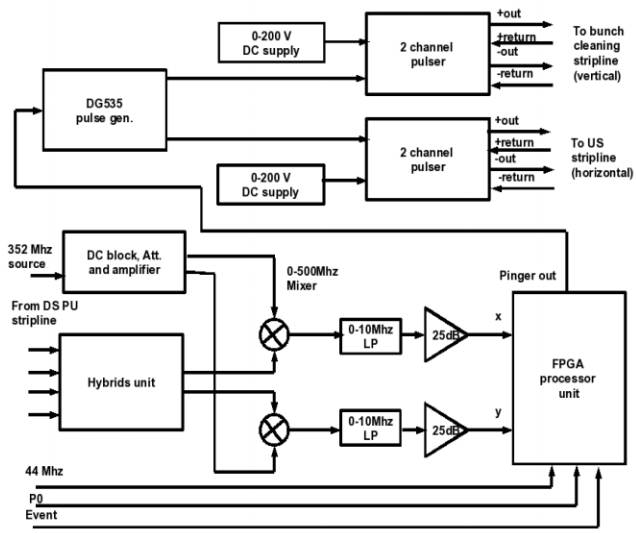

Figure 1: Block diagram of booster tune measurement system.

SYSTEM DESCRIPTION

Figure 1 shows a diagram of the booster tune measurement system. The booster is a ramped accelerator in which beam energy ramps from 325 MeV to 7 GeV in 226 ms. We use two bipolar pulsed supplies to drive two sets of striplines, one in the vertical plane and another in the horizontal plane. The output pulses are half sinusoid with a width of around 600 ns, half of the booster revolution period, and a repetition period of 1.5 ms to 10 ms. The time intervals between the pings can be programmed by writing an array to the FPGA.

The front-end electronics consists of a hybrids converter box that converts signals from four diagonal blades into x, y, and sum signals, a mixer that down-shifts the stripline signal into base-band; and a low-pass filter with a bandwidth of 23 MHz.

Signal acquisition and processing is performed by a Stratix II FPGA processor [4]. There are two separate channels, one each for the x and y planes. Figure 2 shows the block diagram of the FPGA processor firmware. FFT is performed after each pinging and the tune traces are

made available as EPICS waveform records. Turn histories and ADC waveform records are also available for troubleshooting and off-line processing. Tune peak detection is performed by a peak detect block of the FPGA and the tune data are currently available as waveform records. A serial digital data stream will be added for real-time tune corrections. Pinger strength change is realized through the adjustment of the pinging signal timing relative to beam arrival time at the pinger. A COLDFIRE board in the FPGA processor unit provides EPICS support. All the waveform records are available as waveform PVs.

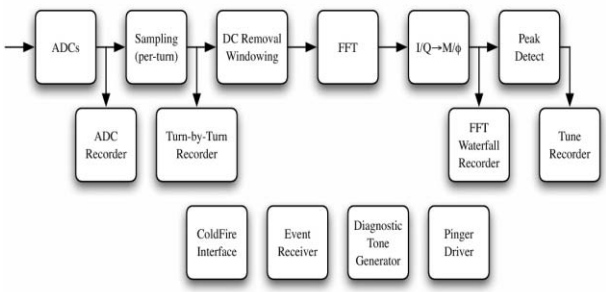

Figure 2: Block diagram of the FPGA firmware.

PULSER FOR THE PINGER

For transverse pinging applications a stripline is similar to a kicker magnet. When properly terminated, both the magnetic field and the electrical field contribute to the total kick. During the booster ramping cycle, kick amplitude is adjusted according to beam energy. This is achieved by shifting the timing of the pulse waveform relative to the bunch. Overall waveform amplitude can be changed by adjusting the output voltage of the DC supply for the pulser. The specifications for the pulsed supply are listed in Table 1. Figure 3 show the main circuits of the pulser.

Table 1: Parameters of the pinger source

Maximum voltage	2.5 kV
Load impedance	50 Ω
Pulse width	500 to 800 ns
Pulse interval	1.5 ms to 20 ms
Waveform	Half sine with adjustable amplitude
Flat top time	> 50 ns

SYSTEM OPERATIONS

The system is designed to continuously monitor the booster tune during normal beam operation. A workstation-based GUI interface was developed to save, archive, and display the tune spectra. Figure 4 shows the main control screen. The entries on this screen set the delay of ADC samples relative to the revolution clock of the accelerator, additional samples per turn for average, and the delay of FFT records after the pinger pulse. The two tune peak detection channels (A' and B') can be switched to either one of the ADC channels though the graphic crosspoint switch. Each channel is provided with a start and end input to narrow down the detection range.

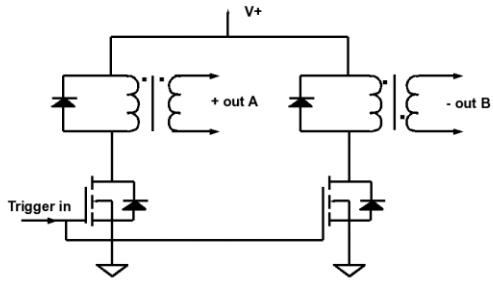

Figure 3: Main circuits of the pulser.

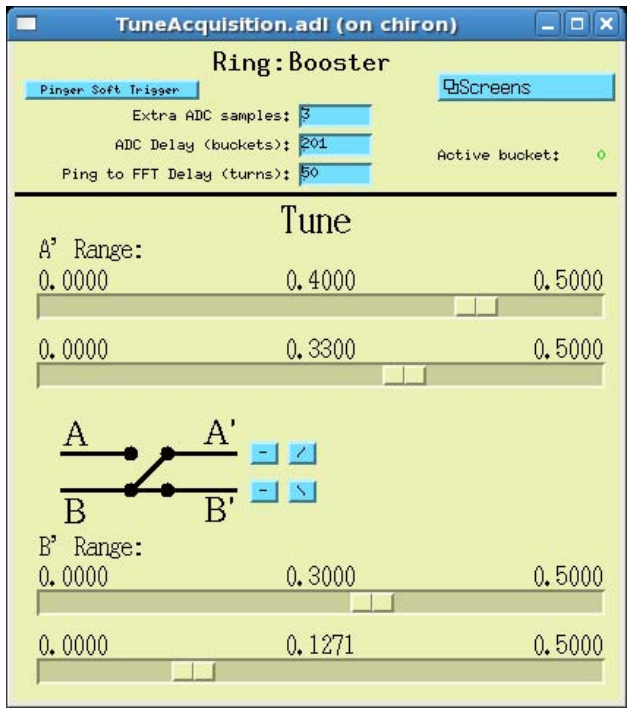

Figure 4: Tune measurement main screen.

Figure 5 shows the ADC raw waveform screen, which is used mainly to align the ADC sample timing with the beam signal. The two top traces are raw waveform from the two ADC channels. The bottom trace shows the location of the first sample clock for each turn.

Figure 6 is the MEDM screen for events and trigger control. APS distributes all injection and storage ring events through a coded event system. The FPGA is designed to work with any one of the storage ring, booster, and particle accumulator ring (PAR) machines. This control screen selects an appropriate event for triggering. Typically the linac trigger is for a PAR application, booster inject is for the booster application, and storage ring inject for a storage ring application.

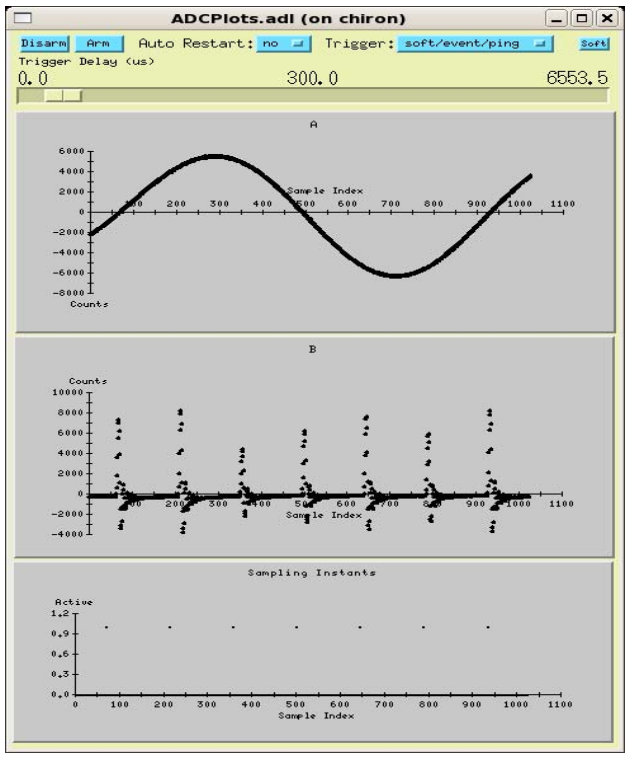

Figure 5: ADC waveform and sample points display. Top two traces are raw waveforms. The bottom trace is the sample point indication.

Figures 7 and 8 show plots of horizontal and vertical APS booster tunes, respectively, for the 132 nm lattice. One can also see the synchrotron sidebands at the beginning of ramping. The straight lines on the spectrum are believed to be some unknown artifacts or noises.

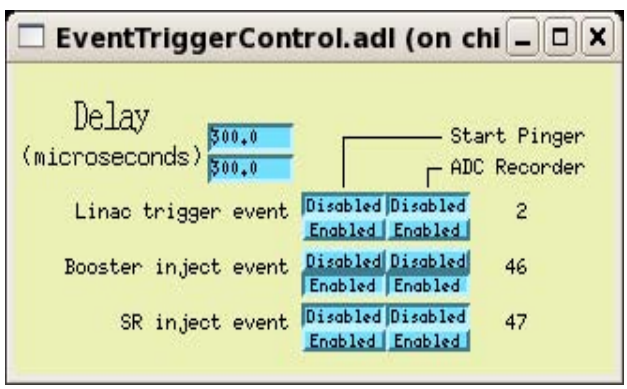

Figure 6: Events and Trigger Control screen.

Figure 9 shows the detected tune peak waveform of both x and y planes. These tune waveforms will be made into digital streams for fast tune corrections.

Figure 10 shows the GUI for the main application. The basic functions provided are: acquire and view only tune waveform, review plots, archive tune data, and review archive spectra. Other functions are: turn on/off the pinger pulse; set pinger timing; scan ADC acquisition time delay; and switch between x, y, and sum signals. The sum signal is used for synchrotron tune detection and works very well. Other functions will be added as the need arises.

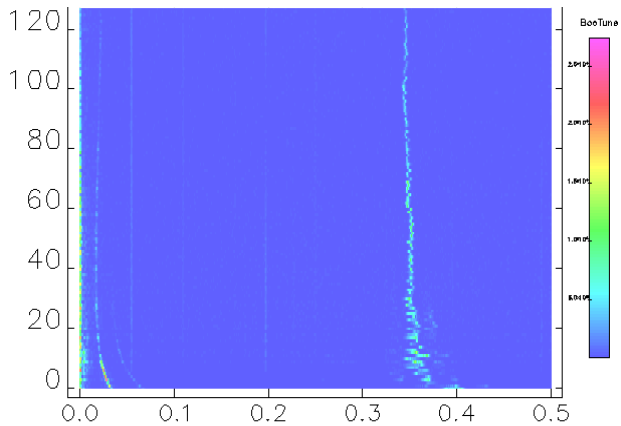

Figure 7: Horizontal tune spectrum.

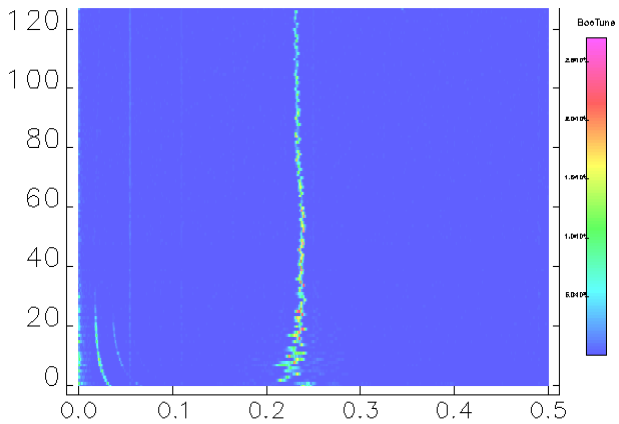

Figure 8: Vertical beam spectrum.

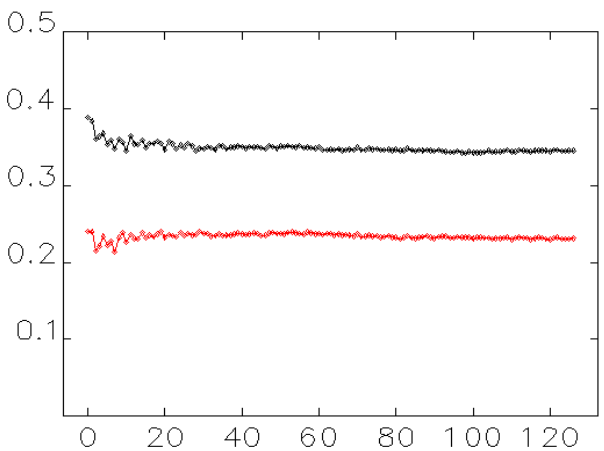

Figure 9: Detected tune waveform for both planes; black: x tune; red: y tune.

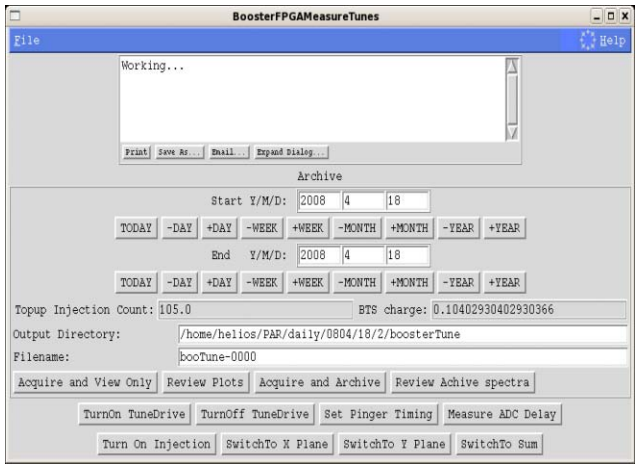

Figure 10: Graphic interface of booster tune measurement application.

POTENTIAL APPLICATIONS

We plan to implement a similar design to the PAR and storage ring in which we will add a fast digital tune waveform output channel so that the information is available for real-time applications, such as feedback with quadrupole magnet currents for tune corrections.

ACKNOWLEDGMENTS

The authors would like to thank Nick Sereno, Michael Borland, Glenn Decker, Frank Lenkszus, and Bob Lill for their interest in and discussion of this subject. We also would like to thank Hahn Bui, Hairong Shang, Chuck Gold, Bob Laird, Pat Dombrowsky, Adam Brill, Randall Zabel, and Gary Sprau for their help in assembling all the hardware and software.

REFERENCES

[1] A. Terebilo *et al.*, "Measurement of the variation of machine parameters and the effect of the power supplies ripple on the instantaneous tunes at SPEAR," Proc. PAC 97, pp. 1490-1492; http://ww.jacow.org.

[2] H. Dumas, J. Laskar, "Global dynamics and long-time stability in Hamiltonian systems via numerical frequency analysis," Phys. Rev. Lett. 70, 2975 (1993).

[3] M. Gasior and J.L. Gonzalez, "Improving FFT Frequency Measurement Resolution by Parabolic and Gaussian Spectrum Interpolation," 2004 Beam Instrumentation Workshop, AIP Conf. Proc. 732, pp. 276-285 (2004).

[4] "Stratix II EP2S60 DSP Development Board Data Sheet," http://www.altera.com/literature/ds/ds_stratixII_dsp_dev_board.pdf

ACCELERATOR VACUUM 101, MADE EASY???*

T. Anderson, FNAL, Batavia, IL 60510, U.S.A.

Abstract

This paper, FERMILAB-CONF-06-568-AD and MSDN – ME – 000069, has been formatted for presentation as background material for the BIW08 tutorial on vacuum issues. The original paper is used as a vacuum primer for engineers and technicians at Fermilab's Accelerator Division, Mechanical Support Department. This version is without the appendix, which has specific examples to illustrate how this material is used. The full document can be obtained from the Fermilab, AD/MS Department.

INTRODUCTION

This paper presents a condensed, simplified, and practical discussion of the principles, procedures, and operating parameters of particle accelerator vacuum systems as practiced at Fermilab. It is intended to provide a basis for designers, builders, and operators of accelerator systems to communicate with each other about the needs and impact of the vacuum system. Rigorous analytical development of the equations and concepts are not given. It is assumed that the reader has some limited understanding of the subject. Practical examples of real world experiences are used to illustrate the concepts outlined. Examples of how to use this material is given in appendix 1 and references for further study are given in appendix 2. The following advice is given for people who design, build, or operate accelerator vacuum systems:

A) Keep it simple.
B) Keep it clean.
C) Establish guidelines and standard practices; then follow them.
D) Always stop and think about what the outcome will be before you do something to the system.
E) Test and certify everything you can before it goes in the system.
F) Despite the abundance of "hot air" around physics laboratories, air is not the only gas we need to think about.
G) There is no vacuum gauge on this planet that, in and of itself, gives you the real picture.

Vacuum can be a complicated subject, but on a base level it does not need to be. Some may view this discussion as over simplified, but they should realize others don't have their level of understanding. Others may find it complicated and they should realize that they need to have a base understanding in order to meet operational goals.

* Work supported by Fermi Research Alliance, LLC under Contract No. DE- AC02-07CH11359 with the U.S. Department of Energy.

All need to realize that they need to communicate with each other on some base level. Most of the problems that arise in vacuum practice are a result of a lack of knowledge or communication. Complicated technical issues can be addressed by physicists and experts. Practical issues are usually addressed by engineers and technicians. Having a base understanding by all involved is essential to ensure a successful outcome for the projects they work on.

WHY VACUUM?

Most all vacuum texts start out with a discussion on the ideal gas law (PV = nRT). For this discussion it would be nice to avoid this, but it is simply too fundamental to ignore. In particle accelerators the purpose of the vacuum system is to remove gas molecules from the path of the beam. So, for accelerators it is more appropriate to think of the ideal gas law in terms of the number of moles in a volume. Pressure is nothing more than a measure of the number of molecules that can interfere or interact with the beam.

$$n = P\,V / R\,T \qquad (1)$$

Where: n = Number of Moles
P = Pressure (Torr)
V = Volume (L)
R = Universal Gas Constant (62.3632 Torr-L/K-mol))
T = Temperature (K)

THE VACUUM WORLD ACCELERATORS LIVE IN

Figure 1, below, is a graphic representation of the vacuum bounds associated with accelerator vacuum systems. The information depicted is intended to be a guide or a starting point when thinking about accelerator vacuum systems. Given a pressure range that a system needs to operate in, the chart gives a reasonable estimate of the out-gassing rate needed, the time scale that will be needed to achieve a given pressure, and the likely pump types that will be needed.

The chart shows $1(10)^{-3}$ Torr as the transition point between the viscous and molecular flow regimes. This is not strictly the case, though. Molecular flow can exist above $1(10)^{-3}$ Torr and there is the transition flow regime between viscous and molecular. For all practical purpose in accelerator vacuum systems $1(10)^{-3}$ Torr is a good place to start thinking about molecular flow.

For the systems encountered in accelerators the range between atmosphere and $1(10)^{-3}$ Torr is not of a lot of concern. The roughing pumps and turbo molecular

pumps (turbo) used usually pump the system down to $1(10)^{-3}$ Torr within hours if not minutes. The main exception to this is insulating vacuum on cryogenic systems. These systems can take many hours to days to reach $1(10)^{-3}$ Torr.

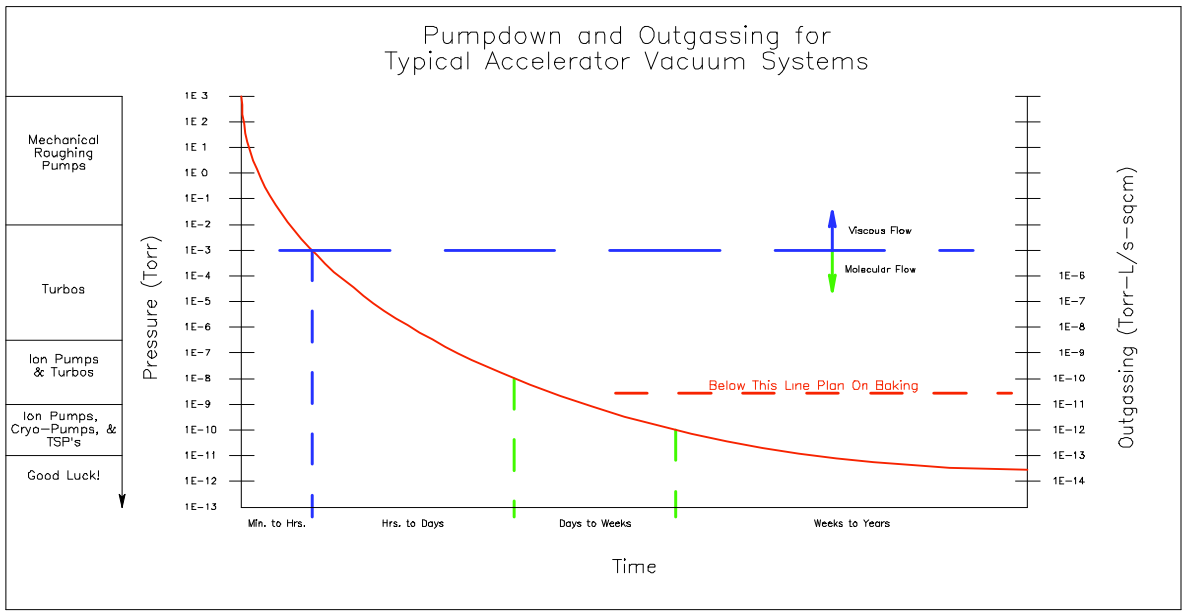

Figure 1. The vacuum world accelerators live in. Note: Information depicted is intended for general reference and may or may not be representative of any real system.

The range between $1(10)^{-3}$ and $1(10)^{-6}$ Torr is usually achieved using turbos and can take hours or days depending on the system cleanliness and the amount of water vapor attached to the system walls. If the system "hangs-up" in this range it is often necessary to bake the system to release the water vapor. Ion pumps can operate at pressures above $1(10)^{-6}$ Torr, but it is usually not advisable. The usable life-time of ion pumps operating above $1(10)^{-6}$ Torr is reduced significantly, which, may cause operational problems. At Fermilab, the ion pump power supplies are generally set to trip off at $2(10)^{-6}$ Torr or lower and are often interlocked to vacuum sector valves. If the ion pump trips, the valves close and interrupt the particle beam.

In ranges below $1(10)^{-7}$ Torr system pumps are almost exclusively capture pumps (ion pumps (IP), titanium sublimation pumps (TSP), cryogenic pumps (cryo-pump), or non-evaporable getter pumps (NEG)). These pumps capture the pumped gasses permanently or temporarily and the system is a closed system. When TSP's, cryo-pumps, or NEG's are used some number of IP's are also used to pump the gasses not pumped by the TSP's, cryo-pumps, or NEG's. In general TSP's and NEG's don't pump noble gasses, methane, or ethane. Cryo-pumps will pump all gasses at some level depending on the temperature of the cryogenic surface.

At pressures below $5(10)^{-9}$ Torr it is almost always necessary to do an in-situ low temperature bake to remove water vapor from the system. A useful low temperature water bake is time and temperature dependent. The temperatures need to be at least 100° C, and are often as high as 300° C. Bake durations run from 24 hours to a couple of weeks. If the system is unusually water loaded, an in-situ low temperature bake may also be necessary to achieve pressures higher than $5(10)^{-9}$ Torr.

There are two topics that are not explicitly shown on the chart, but that should be covered in this discussion. They are connections and materials. The materials used for vacuum systems are generally ceramics or metals, specifically stainless steel, aluminum, and copper. There are synthetic materials that can be used, but most should be avoided at pressures below $1(10)^{-7}$ Torr. At pressures lower than $5(10)^{-9}$ Torr it is usually necessary to degas metals to remove the trapped H_2 in them. This is another time/temperature dependent process and is done under vacuum. For stainless steel this can be partially accomplished by baking at 500° C for 24 hours or more. The standard practice is to bake at 950° C for 2 hours. Care must be taken when heating and cooling between 600° and 850° C. In general, the heating and cooling in this range needs to be as fast as possible to prevent carbide precipitation to the grain boundary.

It is almost always best to use welded or brazed connections in vacuum systems operating below $1(10)^{-8}$ Torr. The exception is on components and devices that need to be removed periodically for maintenance or repair, in that case flanges should be used. The seals used for the flanges should be metal (copper or aluminum). Elastomer seals can be used at pressures above $5(10)^{-9}$ Torr, but they should be used sparingly.

Elastomers will permeate water and helium and have a significant out-gassing rate. Helium permeation will interfere with leak checking by lowering the sensitivity and slowing clean-up time.

BASIC EQUATIONS FOR VACUUM

Equations 2 through 5 constitute the basic equations for most all vacuum work. Knowing these relationships and how to apply them is essential for understanding what is happening with regard to any vacuum systems. In most cases accelerator vacuum work can be simplified to this level. References [1] & [2] in appendix 2 are excellent sources for learning how to apply and understand these relationships. In these sources, additional formulas for calculating the conductance based on an assortment of geometries and gasses are presented. Figure 2 illustrates the effect of geometry on the conductance for round tube.

For molecular flow the following apply:

$Q = S\,P$ (Eq. 2) (Relationship between Flow, Pump Speed, & Pressure at the Pump)

$Q = C\,\Delta P$ (Eq. 3) (Relationship between Flow, Conductance, & Pressure Drop)

$C = k\,A\,\alpha$ (Eq. 4) (Relationship between Conductance, Gas Species, & Geometry)

$1/S_{eff} = 1/S + 1/C$ (Eq. 5) (Relationship between Effective Pump Speed, Rated Pump Speed, & Conductance)

where: Q = Gas Flow (Torr-L/s)
S = Pump Speed (L/s)
P = Pressure (Torr)
C = Conductance (L/s)
k = Flow Constant for Specific Gas (L/s-cm^2)
A = Cross-Sectional Aperture Area (cm^2)
α = Transmission Probability
S_{eff} = Effective Pumping Speed (L/s)

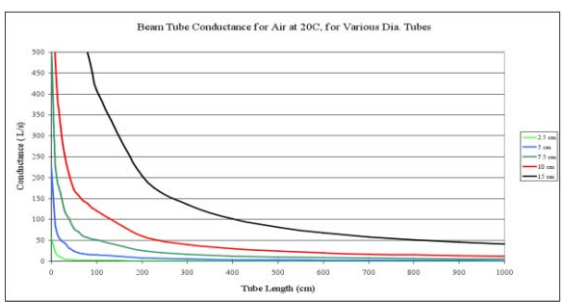

Figure 2. Conductance for round tube. Multiply by $(29/M_m)^{0.5}$ to adjust for other gases, where M_m = molar mass (g/mol) of gas.

SYSTEM DESIGN

At this point in the discussion it is useful to outline the basic design parameters used in designing accelerator vacuum systems. Figure 3 shows the basic layout for most accelerators. In general there is some vacuum space (generally a stainless steel tube) with pumps connected to it at some defined spacing (L_p). The spacing is often dictated by the length of the magnets used for steering the beam. The aperture of the tube can be round, elliptical, or rectangular and is mostly dictated by the beam size and the magnet pole tip spacing. The vacuum levels required are dictated by the beam and operational reliability. Equations 6 through 8 [1] are the governing relationships for the system design.

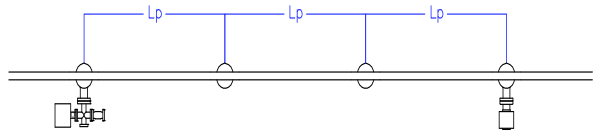

Figure 3. Basic accelerator vacuum system layout.

$P_m = P_p + \Delta P$ (Eq. 6) (Pressure between pumps)

$P_p = q_D\,B\,L_p / S$ (Eq. 7) (Pressure at the pump)

$\Delta P = q_D\,B\,L_p / (4C)$ (Eq. 8) (Pressure drop in a beam tube from midpoint to pump)

Where: P_m = Midpoint Pressure (Torr)
P_p = Pump Pressure (Torr)
q_D = Specific Outgassing Rate (Torr-L/s-cm^2)
B = Inside Tube Perimeter (cm)
L_p = Pump Spacing (cm)
C = Conductance Over Length $L_p/2$ (L/s)

Although the beam size and magnet geometry dominate the geometry for the vacuum system, vacuum considerations must be taken into account early in the magnet and tube size selection. This is necessary to make sure the vacuum system will perform as needed. To illustrate this, example 1 is given in appendix 1.

COMPONENT AND DEVICE DESIGN

This brings us to the point in the discussion where we need to address components and devices that get placed where magnets aren't. For the purpose of this discussion, components are any part of the vacuum system that is not the beam tube. Components would include bellows, fittings, flanges, valves, and any other parts whose primary function is as part of the vacuum system. Devices are components whose primary function is beam related. Examples would be RF cavities, separators, collimators, Lambertsons, and instruments such as BPM's, IPM's, flying wires, etc.

Given that there is a basic system design, a system will have some gas load per unit length. If Q = S P, then S P / L_p equals the gas load/cm for the system. Any component or device to be installed has to have a gas load, per unit length, equal to or less than the above load. If the gas load is larger, additional pumping must be supplied. In general the pressure at any additional device or component has to have a pressure equal to or less than the average in the system. Devices and components installed in accelerators tend to have very large internal surface areas relative to their length. In addition, the materials used are not always the best choice for use in vacuum systems. Therefore, very high gas loads can be expected. Examples 2 and 3 are given in appendix 1 to illustrate these basic concepts.

Someone knowledgeable in vacuum practice should always be involved in the design, manufacture, and assembly phases of these components and devices. The best way to assure that these are built so that they will do no harm to the vacuum system that they will reside in is to test the components before they go into the assembly and certify the assemblies before they go in the system. If components and devices are installed without certification there is a very real risk that the entire system can become contaminated.

Figure 4 is a sketch of a test chamber for testing parts that will be used in devices. The set-up would be the same for certifying an assembly, with the assembly replacing the chamber. With a set-up like this, one can test for out-gassing rates, total gas load from a part, identify contaminants, and determine the gas composition in the assemblies. Tables 1 & 2 are examples of the results obtained from tests done with this set-up.

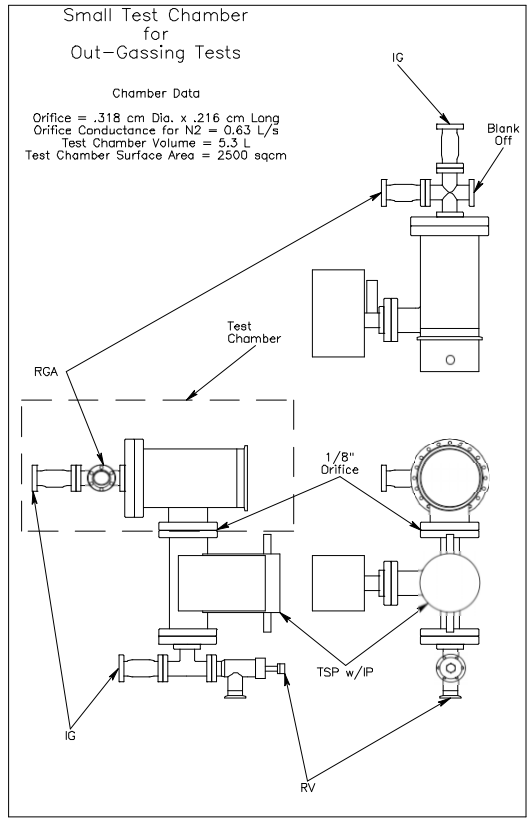

Figure 4. Vacuum test chamber set-up.

Table 1: Out-gassing Rates (Torr-L/s-cm^2) of Various Materials

Material	Totals	H_2	CH_4 Methane	H_2O	CO / N_2	C_2H_6 Ethane	Ethyl Alcohol	O_2	Ar	C_3H_6 Cyclo - propane	CO_2
Stainless Steel (unbaked)	1.0E-10	5.0E-11	2.0E-13	5.0E-11	1.0E-12	5.1E-14		3.0E-16		1.0E-14	1.0E-13
Stainless Steel (baked, no degas)	5.1E-11	5.0E-11	2.0E-13	8.0E-14	2.0E-13	5.1E-14		3.0E-16		1.0E-14	8.0E-14
Stainless Steel (baked & degassed)	6.7E-13	6.2E-13	1.0E-14	1.3E-14	1.3E-14	5.4E-15		1.7E-16	4.8E-16		5.7E-15
Torlon (baked)	3.1E-08	4.2E-09	6.2E-11	2.5E-08	6.7E-10	9.6E-11		8.2E-11	2.6E-12	7.5E-12	9.1E-10
Armalon (baked) (Glass filled Teflon)	3.1E-10	3.0E-10	2.0E-12	6.0E-12	4.0E-12	3.0E-13	3.0E-14	2.0E-15	1.0E-14	4.0E-13	2.0E-12
Rulon (baked)	6.7E-11	6.1E-11	1.7E-13	4.2E-12	1.4E-12			1.4E-15			1.3E-13
MF190 (baked)	6.5E-11	4.0E-11	2.5E-13	1.1E-11	6.0E-12	1.1E-12		3.8E-14	3.3E-15	5.7E-14	6.2E-12

Table 2: Out-gassing Rates (Torr-L/s) of Various TeV IPM Flex Circuit Components

Sample Material	Total	H_2	CH_4 Methane	H_2O	CO / N_2	C_2H_6 Ethane	Ethyl Alcohol	O_2	Ar	C_3H_6 Cyclo - propane	CO_2
Test Chamber Baseline	2.3E-08	2.2E-08	1.2E-10	2.2E-11	6.8E-10	1.2E-11			5.3E-13	3.7E-13	3.6E-11
Flex Circuit Sample 1	1.0E-07	8.7E-08	6.9E-11	1.9E-09	1.3E-08	5.0E-10	1.2E-10	4.9E-12	3.1E-11	1.3E-10	6.2E-10
Flex Wires	2.3E-08	2.2E-08	1.7E-10	1.5E-11	9.9E-10	2.5E-12					3.9E-11
Flex Circuit Sample 2	1.7E-08	1.6E-08	7.1E-11	4.0E-11	9.7E-10	2.1E-12	1.2E-11				3.4E-11
Flex Circuit Sample 3	3.9E-08	3.1E-08	4.6E-10	7.0E-10	5.6E-09	5.4E-11		3.9E-11			5.6E-10
Peek Connector, before bake	1.3E-04	3.6E-05	1.1E-07	8.5E-05	2.0E-06	2.2E-07		6.4E-06	6.4E-08	1.1E-09	3.3E-06
Peek Connector, after bake	7.2E-07	4.0E-07	1.4E-09	2.7E-07	2.4E-08			8.1E-09			1.7E-08

A CAUTIONARY TALE

Earlier the potential for contamination was mentioned, Figure 5 is a residual gas analyzer (RGA) scan of a device (Flying Wire) that was installed in Fermilab's Recycler. The black peaks are from a scan taken before installation. This device was not properly certified prior to installation. There was no low temperature bake done to get an accurate picture of the assembly and the RGA was only on for a couple of hours. RGA's need to be on for many hours to days before reasonable scans can be taken. The scan seen here (black peaks) is typical of an RGA being on for only a few hours. The clusters of peaks that repeat about every 12 to 14 mass units are hydrocarbons.

If there is no contamination they are the result of the RGA filament heating up and degassing. On a clean system, with a clean RGA, this can be seen to clean up over several hours. On this particular device these clusters were observed to be decreasing over a period of a couple hours.

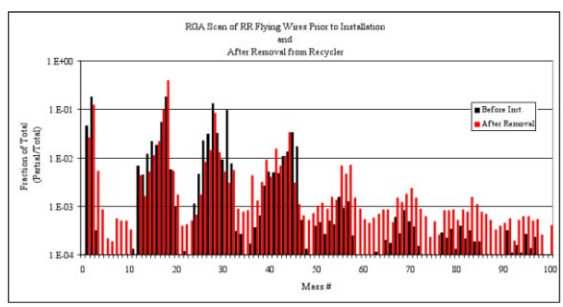

Figure 5. RGA scan of recycler flying wire.

There was a push to install this device during a shutdown and the decision was made to go ahead with the installation without a proper certification. The

device was subsequently installed and baked in-situ at 150º C. The bake appeared to go well and the system came down to $1(10)^{-9}$ Torr after the bake. After the shutdown was over and the machines started running it was noticed that the vacuum was degrading in this sector. Over the course of a week the pressure degraded to $1(10)^{-8}$ Torr and stabilized. Another access was made and the TSP's were reactivated and the pressure again was $1(10)^{-9}$ Torr. Within a week the pressure was again $1(10)^{-8}$ Torr and stabilized. This went on for several months with periodic accesses to leak check and other attempts to find the problem. Eventually an RGA was installed on the system and the scan showed something very similar to the red peaks in Figure 5.

It turned out that a bearing in the rotary feedthrough on the device had a grease lubricant with a high vapor pressure. The original bearings specified for the feedthrough were dry, but the supplier had sent some that had grease. To make matters worse, the initial 150º C bake had spread the contamination through the entire sector and the change in tunnel temperature while running (about 15º C) would accelerate the out-gassing by an order of magnitude. The TSP's would spoil in about a week. Figure 6 shows the effect of the small temperature rise. Ultimately the entire sector had to be replaced.

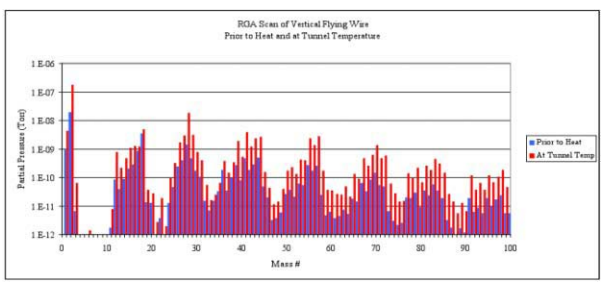

Figure 6. Change in out-gassing due to small temperature rise.

This tale is told to illustrate several points that have been made in this discussion:

1) Establish guidelines and standard practices, then follow them.
2) Always stop and think about what the outcome will be before you do something to the system.
3) Don't guess – test and certify everything you can before it goes in the system.
4) Someone knowledgeable in vacuum practice should always be involved in the design, manufacture, and assembly phases of components and devices that will reside in the vacuum system.

KEEP IT CLEAN

If I have learned anything in my 18 years at Fermilab, it is that everything that goes in the vacuum system needs to be clean. In my opinion, this is the single most important factor affecting the quality of a vacuum system. The equipment will run better, last longer, and be more reliable if the system is clean. The gas composition will be more acceptable to the beam and the desired pressure levels will be achievable. I have this sign on my office wall (Figure 7) and it is the single most important guiding principle when I look at vacuum systems.

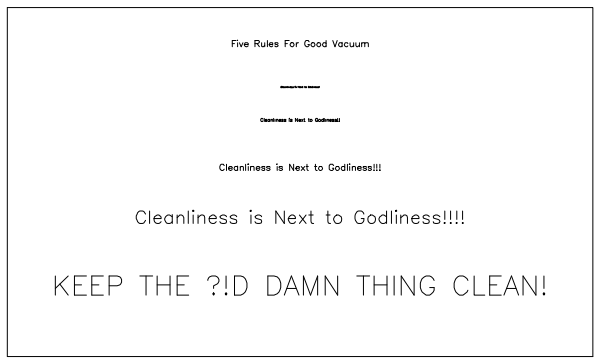

Figure 7. Terry's five rules for good vacuum.

The obvious next question is; what constitutes a clean vacuum system? And, the answer is; that depends. The better question is; what is a contaminant? And, that answer is easy. Any gas in the system that does not need to be there, that interferes with the beam, or prevents the system from reaching the required ultimate pressure is a contaminant. Figure 8 is an RGA scan of a very clean system. H_2 is over 95% of the gas composition with the next highest component being CO at about 1%. N_2 is slightly less that than CO and CH_4, H_2O, C_2H_6, and CO_2 are all some fraction of 1%. These are all contaminants, but it may not be possible to do any better. If the pumping is sufficient the system should be able to reach a desired ultimate pressure and at that pressure the beam/gas interaction should be acceptable.

Figure 9 is an RGA scan of a dirty system, and is the one discussed earlier with the grease in the bearing. The hydrocarbons in that system did not need to be there, they interfered with the beam (caused large losses and short life times), and they prevented the system from reaching the required ultimate pressure.

It is always asked what the best cleaning procedure is? The best cleaning procedure is the one that works best for a given application. There are any number of procedures that work, so be flexible when specifying cleaning procedures. An understanding of the processing that a part has been through is a prerequisite for determining the proper cleaning procedure. Specify the vacuum performance you want, and then choose the cleaning procedure that works. Once a part or device is clean, great care should be taken to keep it clean. Clean assemblies should always be vented with dry N_2 and clean parts should always be stored under vacuum or in hermetically sealed UHV grade containers, back-filled with dry N_2. Clean parts should always be

handled with clean latex (or equivalent) gloves. Transfer of solvents, grease, and dirt by handling is the number one way a system is contaminated.

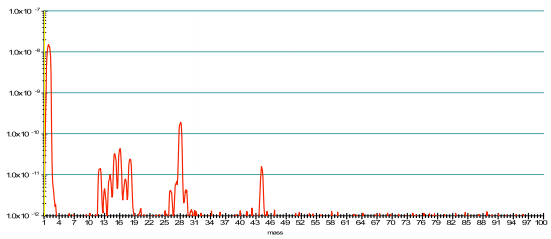

Figure 8. What a very clean system looks like.

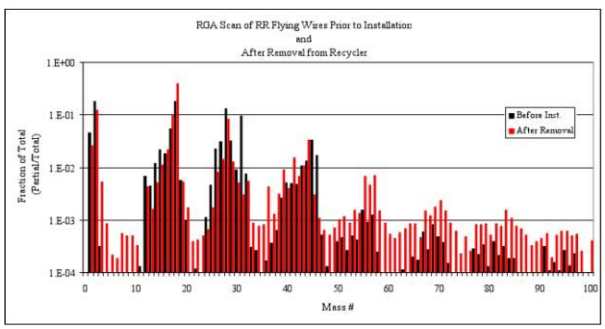

Figure 9. What a dirty system looks like.

The most common procedure used is ultrasonic cleaning with an acid or alkaline based detergent. This is followed by several thorough clean water rinses (usually distilled or de-ionized water). If it is a metal part and needs to be cleaner than the above procedure can achieve, follow it with a vacuum bake at 400 to 500° C, and that will be about as good as it gets.

VACUUM QUALITY AND OPERATION

To this point the discussion has centered on how a system is designed and a little bit about how that design is achieved. But ultimately, what really matters is how the system performs and how easy it is to maintain and operate. The only performance that really matters is the interaction (or lack of) with beam. This goes back to how much gas and of what species is in the vacuum space. Two different gasses (say H_2 and H_2O) at the same pressure can have dramatically different effects on the beam. It basically comes down to the size of the molecules; larger molecules present a bigger target for the beam to hit. Physicists use a number, Z_{eff} (Eq. 9), as a measure of the molecular size of the gas mixture that the beam encounters. This is really nothing more than the effective atomic number of the gas mixture. Higher values for Z_{eff} present a greater potential for beam/gas interactions than smaller values, thereby increasing losses and decreasing beam lifetimes.

$$Z_{eff} = \Sigma(x_n n_i Z_i / n_n) \qquad \text{(Eq. 9)}$$

where n_i = The number of atoms of the i^{th} species in the molecule.
Z_i = The atomic number of the i^{th} atom in the molecule.
x_n = The fractional concentration of the n^{th} gas.
n_n = The number of atoms of the n^{th} molecule.

So, when one talks about accelerator vacuum quality, it is really the combination of the system pressure (a measure of the number of molecules in the space) and the species of the gasses remaining in the system.

Operationally this means that there is some standard (quantitative and qualitative) that has to be maintained for any given system. Most of this is addressed in the design and building phase of a system through proper selection of materials, processing methods, and careful construction. But, at some point the system has to operate and invariably will need modifications. Additions and modifications to a system must follow the same rules that were used to design and build it.

Maintaining the system operationally requires an understanding of what was done before and what will happen in the future if something is done now. More precisely this means that the people responsible for maintaining the system need to know what the system design parameters are, what the vacuum quality (both quantitative and qualitative) needs to be, and what has been done over the course of time that could have changed the vacuum quality. At a basic level this means good record keeping.

They also need to know what the effect will be if something is done that changes the system's equilibrium temporarily or permanently. An example of this is the simple act of letting-up a system to atmospheric pressures. Figure 10 is a plot of a system that was first baked at 200° C, and then vented by two different methods. The first method was venting with clean dry N_2 and then pumping back down without a bake. The second method was to vent to outside air and remain exposed for two hours, then pumping back down without a bake.

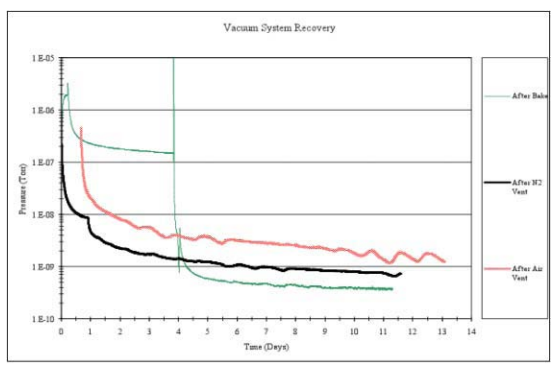

Figure 10. What happens when a system is vented?

It can be seen that there is a difference in both total pressure and the time taken to reach any given pressure. Zero time in all cases is the start of initial pump down. The bake was approximately 4 days, but could have been as short as two days with about the same results. As far as total pressure goes, there is about a factor of two between the subsequent processes. From a strictly pressure point of view this is not very significant. But, if the gas mixture composition is looked at (Figure 11) the difference is significant.

There is a significant increase in the carbon containing molecules (CH_4, CO, C_2H_6, and CO_2), H_2O, and N_2. The increase in the carbon compounds is probably driven by the hot filaments on the ion gauge and RGA. This will probably clean up in time and has a large affect because the vessel is small relative to the number of filaments. What is significant though, is the increase in H_2O and N_2. For the system vented with air there is an increase in the level of H_2O of almost two orders of magnitude. This is due to mono-layers of H_2O accumulating on the surfaces from the moisture in the air. Without a bake this will take a very long time (months to years) to pump away. There is also an increase in the H_2O level as a result of venting with clean dry N_2. This is because the vent line and exterior of the system valve had all been exposed to air for a very long time. Additionally, there is always a slug of air in the vent line; unless it is permanently connected to the system, purged of air, and baked to remove the H_2O. The N_2 level has increased in both cases and will continue to remain high for some time, but will eventually pump away. Below the chart are values for Z_{eff} in the three cases.

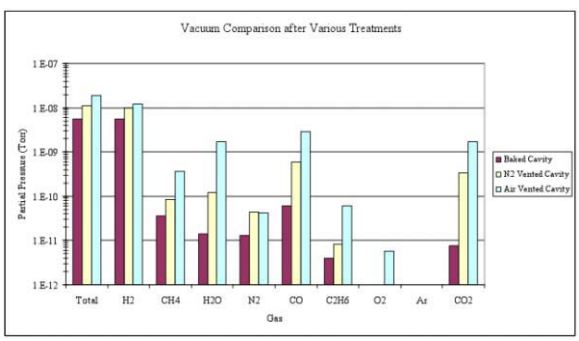

Figure 11. Vacuum quality after venting, Z_{eff} for baked system = 1.1, Z_{eff} for N_2 Vented System = 1.57, Z_{eff} for Air Vented System = 2.75

GAUGES

To this point, the discussion has really said nothing about gauges except a statement in the introduction that; there is no vacuum gauge on this planet that, in and of itself, gives you the real picture. We could probably leave it at that and go on with life in blissful ignorance. But, if you really want to understand what a vacuum system is doing an understanding of this is required. In practice, gauges are the only indicator of a system's health. And, that is all they are; indicators. Almost all gauges used in the vacuum regimes that are of interest to accelerators are calibrated for N_2 as the only gas in the system. As was shown earlier this is almost never the case. In addition, most of the gauges used (primarily ion gauge and cold cathode) are total pressure gauges. So they treat all the gas species as one gas. The relationship between the gauge pressure and actual pressure for a specific gas for a Bayard-Alpert type ion gauge is given in equation 10.

$$P_{gasX} = (P_{ind} / r_{gasX})(K_{N2,\,cont} / K_{N2,\,gauge}) \qquad (10)$$

Where P_{gasX} = The pressure of gas X.
P_{ind} = The N_2 equivalent pressure indicated by the gauge.
r_{gasX} = Gas sensitivity for gas X.
$K_{N2,\,cont}$ = Controller sensitivity for N_2.
$K_{N2,\,gauge}$ = Gauge sensitivity for N_2.

Values for $K_{N2,\,gauge}$, $K_{N2,\,cont}$, and r_{gasX} can be found in the literature and manufacturers' catalogs. $K_{N2,\,gauge}$ is typically between 10 and 25 /Torr. If the controller and gauge are calibrated the same the K terms drop out. Typical sensitivity values for some gasses are listed in Table 3.

Table 3: Gas Sensitivity Table

Gas	H_2	CH_4	H_2O	CO	N_2	C_2H_6	O_2	Ar	C_3H_6	CO_2
Sens., r	0.46	1.4	1.12	1.05	1.0	2.6	1.01	1.29	3.6	1.4

To get a better picture, a gauge that differentiates between the various gasses is needed. At first glance an RGA would seem to do this, but there are also calibration issues there. An RGA differentiates between the masses of the various gasses, but thinks everything is still N_2 when it comes to the magnitude of the pressure. In addition, there is always a question of how well any gauge (ion gauge, cold cathode, or RGA) is calibrated for N_2. As a general rule, I treat all high or ultra-high vacuum gauges as only being accurate to with in a factor of two. Most RGA's are moved from system to system as needed. This is mostly because they cost so much. Even when they are permanently installed on a device or system, it is usually only the analyzer that is installed and the head and electronics are moved from analyzer to analyzer. In this case calibration becomes a real slippery slope, and can be off by orders of magnitude.

To combat all these inaccuracies and uncertainties I try to only use an RGA in conjunction with an ion gauge. The RGA is used only to get a qualitative measure of the gasses in the system and a sense of the relative concentrations of the gasses. An ion gauge is then used as the total pressure measurement and the RGA data is normalized to that. As an example

assume that the RGA scan in Figure 8 indicates the relative partial pressures of the gasses as shown in Table 4. The ion gauge on the system near the RGA shows a total pressure of $2.7(10)^{-9}$ Torr. The fractional contribution of each gas to the total is also shown in the table. Setting both K's in Equation 9 equal to 1 and making use of the fact that the sum of the partial pressures is equal to the total pressure an equation can be written to correct for the gauge calibration.

$$P_{Tact} = P_{TIG} / \Sigma((P_i / P_{TRGA})\, r_i) \qquad (11)$$

where P_{Tact} = Actual total pressure (Torr).
P_{TIG} = Indicated ion gauge pressure (Torr).
P_{TRGA} = Total indicated RGA pressure (Torr).
P_i = Partial pressure of the i^{th} gas (Torr).
r_i = Gas specific sensitivity for the i^{th} gas.

It can be seen that the actual total pressure is 5.6×10^{-9} Torr, which is about two times the indicated 2.7×10^{-9} Torr. The individual partial pressures are then the fractional contributions of each gas times P_{Tact}.

Table 4: RGA Analysis Normalized to an Ion Gauge

	Totals	H_2	CH_4	H_2O	N_2	CO	C_2H_6	CO_2
RGA Partial Pressure (Torr)	1.54E-08	1.50E-08	1.00E-10	3.90E-11	3.50E-11	1.70E-10	1.10E-11	2.10E-11
Fractional Contribution to Total	1.00	0.976	0.007	0.003	0.002	0.011	0.001	0.001
Gas Specific Sensitivity (r)		0.46	1.40	1.10	1.05	1.05	2.60	1.40
Adjusted Partial Pressure (Torr)	5.64E-09	5.51E-09	3.67E-11	1.43E-11	1.28E-11	6.24E-11	4.04E-12	7.71E-12

CONCLUSION

The topics discussed here are by no means complete. Anyone needing an in-depth knowledge of the subject is encouraged to pursue further study with the references suggested. This discussion does, however, provide a core of knowledge for those working with accelerator vacuum systems. The intention was to condense and simplify the basic concepts, design, and operating parameters that are encountered in most accelerator vacuum systems. This discussion should be of particular use to those that design and build components and devices that reside in the vacuum system, but who typically have no involvement in the design, building, or operation of the vacuum system itself. For those that are actively involved in the design, building, and operation of a vacuum system, this discussion provides a base point to build on. The primary purpose of this discussion is to give all those that are in some way contributors to the vacuum system, whether directly or ancillary, a common means to communicate with each other.

REFERENCES

[1] Roth, A., Vacuum Technology, 3rd ed, 1990 (Elsevier Science B.V.)

[2] Lafferty, J.M., Foundations of Vacuum Science and Technology, 1998 (John Wiley & Sons, Inc.)

[3] Turner, S., et al., CERN Accelerator School Vacuum Technology, 1999 (CERN)

[4] Chao, A.W. & Tigner, M., Handbook of Accelerator Physics and Engineering, 1999 (World Scientific Publishing Co.)

[5] Drinkwine, M.J. & Lichtman, D., Partial Pressure Analyzers and Analysis (AVS)

[6] Manufacturer's Catalogs (Varian, Leybold, Alcatel, SAES, Granville Philips, and others)

TRANSITION, DIFFRACTION AND SMITH-PURCELL DIAGNOSTICS FOR CHARGED PARTICLE BEAMS*

R. B. Fiorito†, Institute for Research in Electronics and Applied Physics, University of Maryland, College Park, MD 20742, U.S.A.

Abstract

I review the state of the art of diagnostics based on transition, diffraction and Smith Purcell radiation in the optical to millimeter wave band, which are currently being used to measure the transverse and longitudinal parameters of charged particle beams. The properties and diagnostic capabilities of the incoherent and coherent forms of these radiations are described. Examples of TR, DR and SPR diagnostics for electron and proton beams are presented.

INTRODUCTION

The spatial, angular and spectral distributions of radiation produced from a charged particle beam interacting with a material object or field, e.g. magnetic field, carries information about the beam properties. In this paper we review the state of the art in the diagnostic application of three important beam based radiations: transition, diffraction and spatially coherent diffraction from a grating, i.e. Smith Purcell radiation. These radiations, and indeed all radiation from charged particles, can be analysed using some fundamental concepts: 1) the radiation impact parameter; 2) the coherence length of radiation from a moving charge; 3) the resonance radiation condition for spatially coherent radiation from N_r radiators; and 4) the bunch coherence of radiation from N charges.

The radiation impact parameter $\alpha = \gamma\lambda/2\pi$ is the distance where the radial field of the charge is significant and therefore provides a convenient scale length for significant interaction of the charged particle's field with a medium. This property is analogous to the usually defined impact parameter which is the distance where a moving charged particle interacts with another charge.

For relativistic particles, the parameter α is also the effective source size of a virtual photon of wavelength λ, which is associated with the field of the moving charge. If the size of the radiator $r >> \alpha$, the radiator can be considered to be infinite and the radiation is transition radiation whose spectral angular density is frequency independent. If, however, $\alpha >\sim r$, or if the radiator is an aperture whose size $r <\sim \alpha$, the radiation produced is diffraction radiation (DR) and the spectral angular density is dependent on frequency and on the ratio r/α.

The radiation field of DR from a hole in an infinite radiator, TR from a complementary finite size solid radiator and TR from an infinite radiator are related by Babinet's principle[1] ,

$$E^{TR}_{\infty Screen} = E^{DR}_{Hole} + E^{TR}_{FiniteScreen}. \quad (1)$$

In this sense, TR from a finite screen can be considered to be a form of DR as Figure 1 suggests.

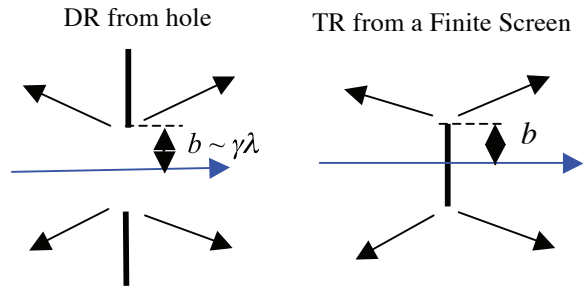

Figure 1. Diffraction and transition radiation from two complementary screens.

The coherence or "formation" length, as it is sometimes referred to in the literature, is the distance where the fields of the charge and the photon generated in the interaction defer in phase by π radians [2]. There are two types of coherence lengths, i.e. the vacuum coherence length, $L_v = (\lambda/\pi)(\gamma^{-2} + \theta^2)^{-1}$, which applies to the radiation produced when a charge moves from a medium into vacuum or vice versa; and the material coherence length, L_d which applies to a charge moving within a material with dielectric constant ε. Note that L_v is a function of the Lorentz factor γ for a relativistic charge while L_d is independent of γ. The definition of L_v indicates that for high energies and observation angle $\theta \sim 1/\gamma$, the coherence of TR or DR fields and the field a co-moving charge is maintained over distances in proportion to the square of the Lorentz factor. The phenomenon of interference of TR/DR from two foils or apertures in the path of a relativistic particle is an example where the vacuum coherence length plays a major role.

When the charge interacts with a series of radiators spaced periodically, e.g. a stack of foils or the periods of a grating, the radiation can be resonant, i.e. in phase, for a particular observation angle or wavelength [3]. Examples of resonance radiation are TR from a stack of foils and Smith Purcell radiation.

The last concept of interest to us is the coherence of charges in a bunch radiating in or out or phase. The general expression for the spectral angular density of any type of beam base radiation can be written in the form:

* Work supported by ONR and the DOD Joint Technology Office
† rfiorito@umd.edu

$$\frac{d^2 I_N}{d\omega d\Omega} = \frac{d^2 I_e}{d\omega d\Omega}\{N + N(N-1)S_\perp(k_\perp,\sigma_T)S_z(\sigma_z,k_z)\}, \quad (2)$$

where $S_{\perp,z} = \left|F(\rho_{\perp,z})\right|^2$ are, respectively, the transverse and longitudinal form factors, i.e. the squared moduli of the Fourier transforms of the corresponding charge densities and the first term on the RHS of Eq. (2) is the spectral-angular density of radiation produced by a single charge. When both of the form factors are of order unity, the radiation intensity is proportional to N^2 where N is the number of particles. This occurs at wavelengths close to or larger than the bunch length and the radiation is said to be fully *coherent*. At wavelengths much less than the bunch length the radiation is proportional only to N and the radiation is said to be *incoherent*. Both types of radiation serve useful purposes for charged particle beam diagnostics.

APPLICATIONS OF INCOHERENT RADIATION

Near Field Imaging using OTR and ODR

For most applications in rf accelerators the bunch micro pulse duration is of the order of 1 ps corresponding to a bunch length of about 300 microns. Hence the longitudinal form factor is small for observations of TR, DR and SPR at optical wavelengths and the radiation in this band is incoherent.

By far the most common use of incoherent OTR is beam imaging. For this purpose simply focusing a camera on the generating foil produces a linear, high resolution image of the beam. This application is commonly referred to as 'near field' imaging though the use of this term is not strictly accurate. For most situations OTR is the preferred beam imaging technique for monitoring the beam spatial profile. Figure 2 shows a comparison of OTR with other types of imaging screens,

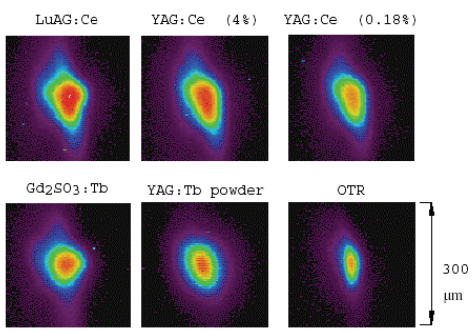

Figure 2: Comparison of e beam images using various screens at the 50 MeV BNL/ATF; from ref. [4]

i.e. phosphors and YAG crystals, which, although they produce a higher yield of photons, do not have the spatial and temporal resolution offered by OTR. OTR has been successfully used to image beams with micron spatial resolution (usually limited only by diffraction in the optics) and sub ps temporal resolution.

A number of theoretical studies [5-8] as well as experimental data have confirmed that the spatial resolution of OTR is primarily independent of energy and not related to the effective virtual photon source size $\gamma\lambda$ as some authors had previously claimed. An especially strong experimental confirmation of this fact is the successful OTR imaging of 100 micron size beams (confirmed by wire scanners) at a beam energy of 30 GeV, where $\gamma\lambda$ at optical wavelength is tens of millimeters [9].

OTR has been successfully used to image both relativistic electron and proton beams, e.g. the 120 MeV proton beam at FNAL [10], as well as non relativistic beams, e.g. the CLIC facility's 80 keV gun [11] and the University of Maryland's 10 keV electron beam ring (UMER)[12]. For the UMER source, OTR images have been taken in 10ns gates within a 100ns pulse showing the evolution of the beam profile[13].

Recently ODR near field imaging been demonstrated and used to determine horizontal beam position with respect to an edge radiator with an accuracy of 40 microns [14]. Experiment data comparing beam sizes using OTR as a baseline and ODR also indicated that ODR can provide relative beam sizes if the beam is Gaussian in x and y.

Figure 3. shows a comparison of an OTR image of a 7 GeV electron beam compared to the ODR image induced by the beam on a polished edge radiator that is 1.25mm away from the beam centroid as indicated by the dotted line. For 7 GeV the radiator impact parameter is about 1 mm at a wavelength of 500nm so that ODR is expected to be observed and the picture confirms this.

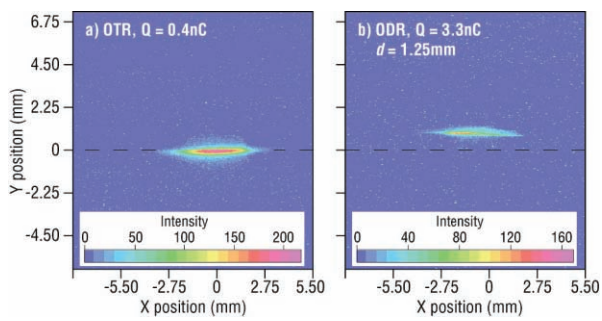

Figure 3: Near field mages of OTR (left) and ODR (right) from a 7 GeV beam passing through and near a polished metal edge, from ref. [14].

If the beam is moved in the horizontal direction, the centroid of ODR image tracks the motion as observed by beam position monitors in the walls of the accelerator tube. The results shown in Figure 4 indicated that the ODR centroid measurement linearly tracks the BPM signal to within 40 microns. The ultimate accuracy of this

ODR beam position monitor is expected to be 10 microns or less.

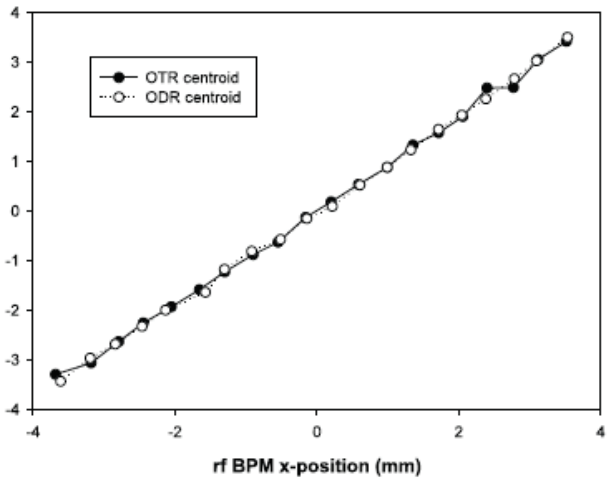

Figure 4: Centroid of ODR and OTR images vs. horizontal BMP signals illustrating the tracking of ODR with horizontal beam position; from ref. [14]

Far Field Imaging of OTR and ODR

The far field images of OTR from a single foil, and interference of OTR two foils and ODR-OTR produced when the first foil is a metal micromesh, have all been demonstrated to be useful as beam divergence and energy diagnostics for relativistic electron beams.

In order to use such far field images to measure divergence, a model for the distribution of trajectory angles is assumed, e.g. a single Gaussian distribution function, f(x',y'). This expression is then convolved with the angular distribution for a single electron. Horizontal (x') or vertical (y') line scans of the resulting angular distribution are then fit to the experimental data to provide the divergences.

Figure 5 shows *single foil* OTR angular distributions for three different beam conditions at the 48 MeV CLIC test facility, along with corresponding intensity line scans. Fits of these scans produce divergences show on the line scan graph. Using the angular distribution of OTR from a single foil, divergences as low as 0.1/γ can be measured.

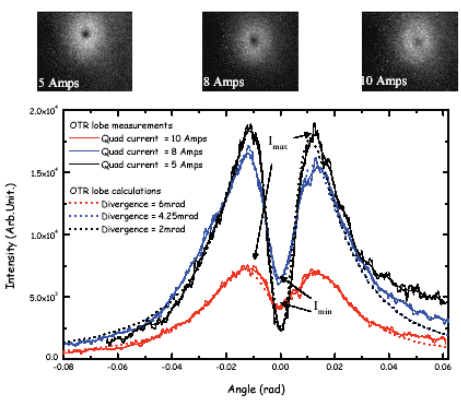

Figure 5: Far field single foil OTR patterns for three different divergences (top); line scans (bottom); from [15]

Figure 6 shows an two foil OTR interferogram which was taken to measure the divergence of the NPS 100 MeV linac, which has an average current of about 0.1 μA. The picture was taken with a high quantum efficiency cooled CCD camera and an optical interference filter with sufficiently narrow band pass to insure that the visibility of the fringes is dominated by beam divergence.

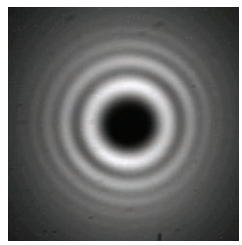

Figure 6: OTRI from a 100 MeV electron beam.

Divergences as low as 0.01/γ have been measured with two foil OTRI and ODTRI [16]. Simultaneously, the energy of the beam can be determined from the interference peaks with accuracy of about 1% and under the right conditions, energy spread can also be determined [17].

If the beam is magnetically focused to an x or y waist condition at the second foil of the interferometer, and simultaneous imaging of the spatial and angular distributions is performed, a corresponding x or y *rms* emittance measurement can be made [18]. This can be accomplished with a variable focus lens, or two cameras one focused on the foil, the other to infinity.

An extension of this technique called optical phase space mapping can also be done with the help of a movable optical mask. In this method the beam is first imaged onto a pinhole mask. The far field AD pattern emerging from the pinhole is then analysed with the same technique described above to provide a localized (i.e. within the beam distribution) measurement of the divergence and ensemble trajectory angle. By scanning the pinhole over the beam image, which is monitored by another camera focused on the back of the mask, a map of the (x,x') or (y,y') trace space of the beam can be constructed [19].

The angular distribution of ODR from a single edge, slit or any type of symmetric aperture can also be used as a diagnostic. However, unlike OTR, the AD of ODR depends not only on the divergence but the beam size and offset from the center of the aperture used to create the radiation. Hence the analysis of the AD of ODR a diagnostic for a particular parameter is more complex than OTR. Nevertheless, a number of methods employing the near field and far field distributions of ODR have been suggested [20,21].

For beams with very low divergence, the AD of ODR is mainly dependent on the beam size or position within the aperture [21]. For an aperture with vertical or horizontal symmetry e.g. a slit, the position effect can be neutralized by positioning the beam in the center of the aperture. In

cases where the effect of divergence cannot be neglected two orthogonal slits can be used to separately measure the (x,y) sizes and the (x',y') divergences [22]. Efforts to provide beam size diagnostics using the far field ODR AD are underway by a number of groups [23,24].

Measured and fitted scans of a far field ODR angular distribution pattern from a 700 MeV passing through the center of a 0.5 mm slit is shown in Figure 7 which is taken from [24]. The beam size and divergence from

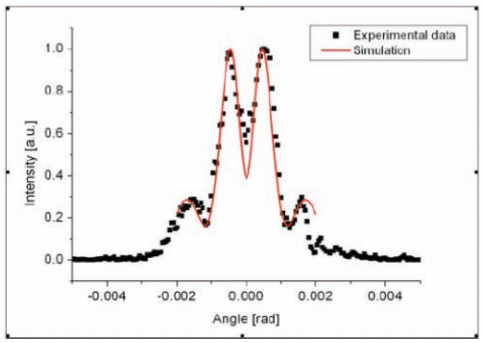

Figure 7. Measured and fitted vertical scans of AD image of ODR with a 800nm band pass filter

the fit are: 70μ and 30μrad respectively. A significant problem in obtaining useful far field ODR data is the interference of optical synchrotron radiation produced by from upstream magnets with ODR from the slit.

Far field ODR can also be used in conjunction with OTR as in an ODR-OTR interferometer to measure divergence [16]. In this configuration a micromesh foil with hole dimensions d ≤10μ << R, the beam size. The ODR is produced both from the wires and holes of the mesh interfere with OTR from a mirror and create interferences. The wire thickness and density is chosen so that the fringes created by ODR and OTR from electrons intersecting the wires are heavily scattered so that their visibility is zero. The ODR-OTR fringes from the unscattered particles passing through the mesh holes then seen above a smooth background; the visibility of these fringes provides a divergence diagnostic. Note that the divergences measured with this technique is not limited to beam divergences which exceed the mean scattering angle in the first foil, as is the case with a conventional OTR interferometer.

Figure 8 shows scans from an ODTR and an OTR interferograms for the same beam conditions and the

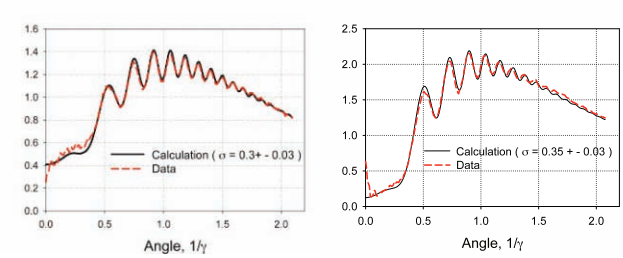

Figure 8: Comparison of divergence measurements with an ODTR (left) and OTR (right) interferometers [16].

same measured divergence. The foil thickness and material of the first foil of the OTR interferometer was chosen to introduce negligible scattering to validate the ODTRI divergence measurements.

COHERENT RADIATION BUNCH LENGTH DIAGNOSTICS

The use of fully coherent radiation such as transition, diffraction and Smith Purcell radiation have been used to diagnose transverse as well as longitudinal properties of beams. We will confine our discussion to longitudinal beam diagnostics making use of the dependence of the coherent radiation on the longitudinal form factor of the beam, cf. Eq. (2). The chief advantages of frequency based diagnostics are their bandwidth which easily exceeds the equivalent temporal limit imposed by conventional streak cameras (currently about 0.3 ps) and lower cost.

The most common types of spectral measurements are: 1) direct spectroscopy, which employ dispersive gratings and/or multiple detectors; 2) autocorrelation techniques which use scanning or single shot interferometers; and 3) electro-optic sampling techniques. Items 1) and 2) have been well described in the literature and item 3) is reviewed in the invited talk by van Tilborg presented in these Proceedings [25].

We will therefore discuss only two recently developed techniques which both employ the frequency dependence of the *angular distributions* of coherent TR, DR and Smith Purcell radiation (SPR) to measure bunch length.

CDR and CTR Angular Distribution Method

We have noted above that the angular distributions of TR from a finite sized foil and DR from an aperture are both forms of diffraction radiation and hence the single electron spectral angular densities of both radiations are frequency dependent, i.e. the first term on the RHS of Eq. (2). This frequency dependence adds an additional complication to the analysis of the spectrum of coherent radiation, since it is the goal of spectral analysis to measure the form factors in order to determine the bunch size.

It is possible to use and optimize the sensitivity of the AD of CTR and CDR for a given bunch length and beam energy to frequency in the band required to adequately sample the form factor. To do this we control the size of the radiator r, so that the radiation impact parameter $\alpha \sim \gamma c \Delta t_b / 2\pi \sim r$ where Δt_b is the expected bunch length and $1/\Delta t_b$ is the frequency band of interest. For a 10 MeV and a 1 ps bunch width, e.g. the optimum radiator size is about 8mm.

The broad band AD is calculable from theory by taking the radiated power of CTR or CDR for a given radiator and geometry per electron from theory, assuming a model for the bunch distribution, e.g a Gaussian, calculating the resultant form factors, multiplying by the form factor for a particular bunch length and integrating over the

appropriate frequency range. The mathematical details are presented in [26,27], so we will only present results for the example mentioned above.

The frequency band necessary for the calculations is determined by both the high frequency role off of the bunch form factor and the low frequency role off due to the finite size of the radiator. These are illustrated in Figure 8 for three Gaussian longitudinal distributions.

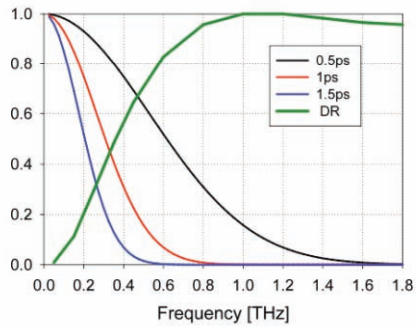

Figure 9: Gaussian bunch form factors in black, red and blue for bunch lengths 0.5, 1.0 and 1.5ps respectively; green: DR spectrum for an 8mm diameter disk.

To illustrate the effect of bunch length on the AD of DR from a finite radiator, we calculate line scans of the projected AD on a plane 300mm away from the source. Sample frequency dependent scans within this range of frequencies are shown in Figure 10, and total (frequency integrated) angular distributions scans for three different bunch lengths are presented in Figure 11.

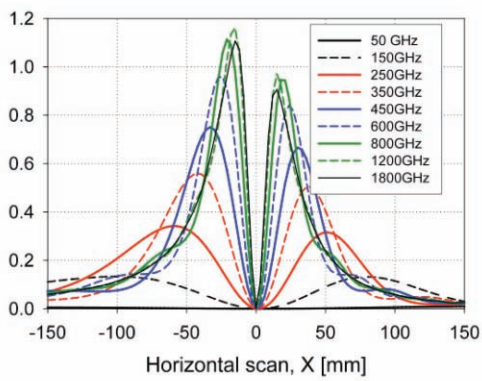

Figure 10: Horizontal line scans of the angular distribution of CDR from an 8mm disk projected onto a plane at 300mm from the source for various frequencies in the band 50-1800 GHz.

A proof of principle experiment using the AD of CTR from a finite rectangular plate and CDR from a slit has recently been performed at the Paul Scherrer Institut's SLS 100 MeV linac [26]. Two different bunch compressor settings produced bunch lengths: 0.7 and 1.0 ps, which have been previously measured at PSI using an electro-optic sampling method. Simple vertical and horizontal line scans through the AD's of the CTR and

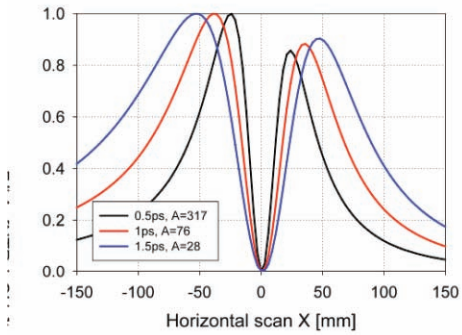

Figure 11: Broad band (frequency integrated) scans of the projected AD's of CDR at 300mm from the source; A is the amplitude scale factor for each curve.

CDR were measured by a Golay cell placed on an x, y translation stage. The frequency response of the cell is nearly flat over the frequency range 50-2000 GHz.

Figure 12 shows the results of fitting the AD of DR from a 10 mm slit in a 40x40mm plate produced using the procedure mentioned above assuming a Gaussian beam pulse with a 0.78 ps full width at half maximum with data obtained by vertical line scan of the measured AD. Data from a solid 40x40mm rectangular plate, used to generate CTR, was also fit with the same bunch width used for the fit of the slit CDR scan data shown in Figure 12. The Figure shows the overall *rms* deviation of the fit. PBU0 identifies the bunch compressor setting used to produce a sub ps bunch. The bunch lengths measured with the slit

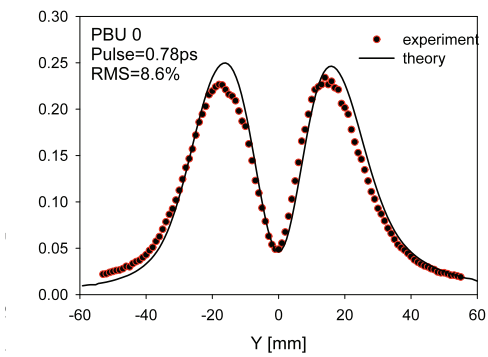

Figure 12: Vertical line scan of AD of CDR from a slit at 300mm from the source; from [26].

and the solid rectangular targets agree with each other, within experimental uncertainty, as well as with previous EO measurements, indicating the consistency and validity of the method.

Coherent Smith Purcell Bunch Length Monitor

The final diagnostic method to be reviewed in this paper is the coherent Smith Purcell effect. The SP effect is observed when an electron beam passes over a grating [28]. A spectrum of light is observed emanating from the grating as shown in Figure 13. The condition for generation of SP radiation follows the relation:

$$\lambda = \frac{l}{n}(\beta - \cos\theta) \qquad (3)$$

where λ is the observed wavelength, l is the number of grating periods, n is the order of the radiation, and θ is the angle of observation. One can conclude from our earlier discussion of DR and the condition for resonance radiation that the SP effect is actually resonant DR from a series of edges and it has been analyzed as such [29].

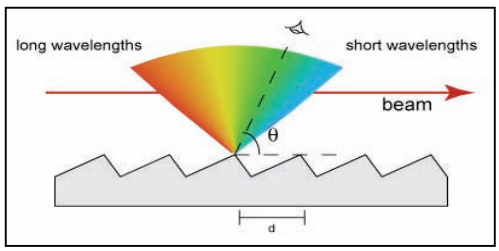

Figure 13: Illustration of the Smith Purcell effect.

Thus it is clear that 1) substantial generation of incoherent SP radiation will occur when the distance between the beam and the grating is close to the radiation impact parameter α; 2) a fully coherent form of the radiation (CSPR) is possible when the emitted wavelengths are comparable to or longer than the bunch size; 3) like DR from any radiator, the wavelength and bandwidth of CSPR depends on the properties of the radiator itself, in this case the grating period and the geometry of one period of the grating; and 4) that the band width can be optimized for a given beam energy to measure the bunch form factor for the expected bunch size.

Several international efforts are presently studying CSPR as a bunch length diagnostic. These cover a range of electron beam energies from 6 MeV to 30 GeV [29-33]. However, I will confine my discussion to what in my assessment is the most developed of these, i.e. the work by the MIT-Bates group [32,33].

The intensity of SPR for a single electron has been derived [34]. If this relation is put into Eq. (2) and integrated over the transverse form factor of the bunch one obtains an expression for the frequency dependent spectral density of the radiation [32]. The resonance condition given by Eq. (3) links the wavelength or frequency of SPR with the angle of observation. Thus a scan of the angular distribution of CSPR is linked to the spectral distribution.

If one models the longitudinal distribution, e.g. by a single Gaussian, multiplies the spectral density of the SPR by the corresponding form factor (also a Gaussian) and fits this to measured angular-spectral distribution, one can measure the bunch length in a manner similar to what is described above. Unlike in the case of normal DR from a single aperture or medium, it is not necessary to integrate the SPR over the bandwidth since the angle and frequency are correlated via Eq. (3).

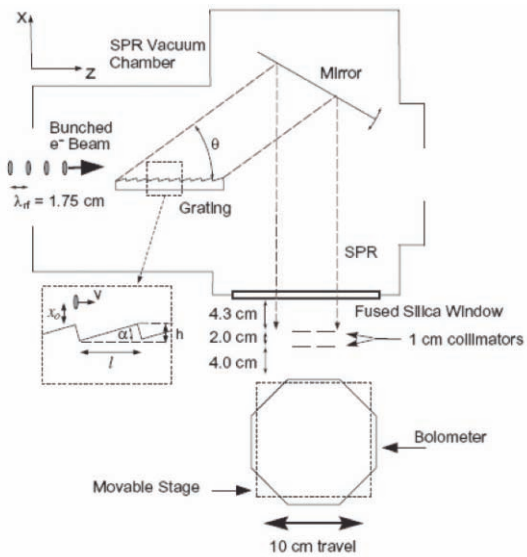

Figure 14: Schematic of the MIT experimental setup to measure the angular/spectral distribution of CSPR.

Experiments at 15 MeV for various bunch lengths in the range of 0.5 to 1ps have been performed at the MIT Bates accelerator laboratory where mm wavelength CSPR has been observed. The experimental setup is shown in Figure 14 which is taken from ref. [32]. A scanning bolometer is used to observe the angular distribution of the radiation in a manner similar to the CDR experiments described above.

Figure 15 also from [32] shows the measured and fitted angular distribution of CSPR assuming a single Gaussian bunch shape with a bunch length of 0.6±0.2 ps. This value has been confirmed by independent measurements.

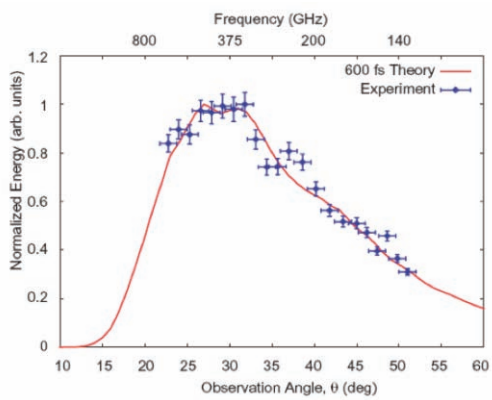

Figure 15: Data and fit of the angular distribution of CSPR for a Gaussian longitudinal distribution with a FWHM of 600 fs.

CONCLUSIONS

We have briefly reviewed the state of the art in TR, DR and SPR diagnostics for charged particle beams. Diagnostic applications of these beam based radiations continue to advance and become more refined. DR and SPR diagnostics hold particular interest since they are non -interceptive in nature and therefore are potentially applicable to diagnose very high current density beams. ODR diagnostics in particular have the potential to measure multiple beam parameters by observation of the near and far field distributions of the radiation.

Both the incoherent and coherent forms of these radiations can be utilized to measure the transverse and longitudinal properties of the beam. Examples of several diagnostic applications of the spatial and angular distribution of incoherent OTR and ODR for imaging the beam and measuring its divergence and energy have been presented. Additionally two methods employing the angular distributions of CDR and CSPR to measure bunch length in the FIR-mm band have been reviewed here. The observation of coherent transition radiation at shorter wavelengths, i.e. in the optical band, have been reported in the literature and in one case the effect of the *transverse* form factor on the far field angular distribution of COTR interferences has produced a novel beam size diagnostic [35]. Coherent optical TR, DR and SPR also have the potential to serve as diagnostics for micro bunching at optical wavelengths, which has recently been observed e.g. at LCLS [36].

REFERENCES

[1] A. G. Shkvarunets, R.B. Fiorito and P.G. O'Shea, Nuc. Instrum. and Methods B., 201 (1), pp. 153-160 (2003).

[2] L. Wartski, et. al., J. Appld. Phys., 46, 3644 (1975).

[3] M. Ter-Mikaelian, High Energy Electromagnetic Processes in Condensed Media, Wiley-Interscience, (1972).

[4] A. Murokh, et. al., Proceedings of 2001 Particle Accelerator Conference, IEEE, pp. 1333-35, (2001).

[5] D.W. Rule and R.B. Fiorito, AIP Conf. Proc. No. 229, p. 315,(1991).

[6] X. Artru, et. al. Laboratoire de l'Accelerateur Lineaire Report No. 97-30, (1997).

[7] M. Castellano and V. Verzilov, Phys. Rev. ST Accel. Beams 1, 062801 (1998).

[8] V. A. Lebedev, Nucl. Instrum. Methods Phys. Res., Sect. A, 372, p. 344 (1996).

[9] P. Catravas, et. al., IEEE, Proc. of PAC99, vol. 3, p. 2111-2113 (1999).

[10] V. Scarpine, et. al. , Proc. of PAC07, p. 2639, (2007).

[11] C. Bal, et. al., Proc. of DIPAC03, p. 95, (2003).

[12] R. Fiorito, et.al., Proc. of PAC07, p. 4006, (2007).

[13] K. Tian, et. al., Phys. of Plasmas, 15, 056707 (2008).

[14] A. Lumpkin, et. al., Phys. Rev. ST Accel. Beams 10, 022802 (2007).

[15] E. Bravin and T. Lefevre, Proc. of DIPAC03, p. 92, (2003).

[16] R. Fiorito, A. Shkvarunets, T. Watanabe, V.Yakimenko and D. Snyder, Phys. Rev. ST Accel. and Beams, 9, 052802 (2006).

[17] R. B. Fiorito and A.G. Shkvarunets, Proc. of DIPAC03, Mainz, DE, p.89 (2003).

[18] R.B. Fiorito and D.W. Rule, AIP Conf. Proc. 319, p.21-37, ed. R. Shafer (1994).

[19] R. Fiorito, A. Shkvarunets and P. O'Shea, AIP Conf. Proc. 648, p. 187-194, ed. G.A. Smith and T. Russo, AIP (2002).

[20] M. Castellano, Nucl. Instrum. Methods Phys. Res., Sect. A , 394, 275 (1997).

[21] R.B. Fiorito, D.W. Rule and W. Kimura, AIP Conf. Proc. 390, ed. A. Lumpkin, pp. 510-517, (l997).

[22] R.B. Fiorito and D.W. Rule, Nuc. Instrum. and Methods B, 173, 67-82 (2001).

[23] P. Karataev, et. al,, Phys. Rev. Lett. 93, 244802 (2004).

[24] E. Chiadrioni, et. al., paper FRPMN027. Proc. of PAC07, Albuquerque, New Mexico, USA (2007)

[25] J. van Tilborg, "Electroptic Techniques in Beam Diagnostics,",Paper TUIOTIO01, Proc. of BIW08.

[26] A.G. Shkvarunets, R.B. Fiorito, V. Schlott and F. Mueller, Paper WEPC21, Proc. of DIPAC 07

[27] A.G. Shkvarunets and R.B.Fiorito, Phys. Rev ST Accel. and Beams, 11, 012801 (2008).

[28] S. Smith and E. Purcell, Phys. Rev. 92, 1069 (1953).

[29] A. Potylitsin, Nuc. Instrum. and Methods B, 145, Number 1, 2, pp. 60-66(7) (1998).

[30] G. Doucas, et. Al. Phys. Rev. ST Accel. Beams 5, 072802 (2002).

[31] G. Kube,et al., Phys. Rev. E 65, 056501 (2002)

[32 S. Korbly, et. al. Phys. Rev. ST Accel. Beams 9, 022802 (2006).

[33] S. Korbly, et. al. Phys. Rev. Lett. 94, 054803 (2005).

[34] P.M. van den Berg, J. Opt. Soc. Am. 63, 1588 (1973).

[35] A. Lumpkin, et. al., Proceedings of the 2004 FEL Conference, p. 519-522, Trieste, Italy (2004).

[36] D. Dowell, et. al.,Proc. of the 2007 FEL Conference, p. 276, Novosibirsk, Russia (2007).

THE CLIC TEST FACILITY 3 INSTRUMENTATION

T. Lefèvre, CERN, Geneva, Switzerland

Abstract

Built at CERN by an international collaboration, the CLIC Test Facility 3 (CTF3) aims at demonstrating the feasibility of a high luminosity 3TeV e^+-e^- collider by the year 2010. The CLIC project is based on the so called 'two-beam acceleration scheme' where the RF accelerating power is provided by a high current high frequency electron beam. The required performances put high demands on the diagnostic equipment and innovative monitors have been developed during the past years. This paper gives an overview of the instrumentation developed at CTF3 with a special emphasis on short bunch length measurements, nanometer beam position monitors, femtosecond synchronization technique and high dynamic range beam imaging system.

INTRODUCTION

In the framework of the Compact Linear Collider (CLIC) project [1], a test facility named CTF3 [2] is constructed at CERN by an international collaboration. It shall demonstrate by 2010 the key technological challenges for the construction of a high luminosity 3TeV e^+-e^- collider. The two main issues to be addressed on CTF3 are the development of 100MV/m 12GHz accelerating structures and the generation of the CLIC RF power source which is based on the production of a high frequency high current electron beam, called Drive Beam. The layout of the CTF3 machine is depicted in Figure 1.

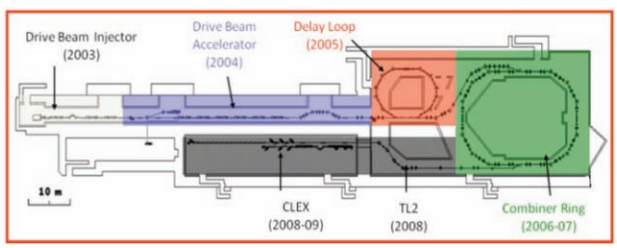

Figure 1: Overview of the CTF3 complex

In the present scheme, a long train of bunches with a bunch spacing of 20cm is converted into an eight times shorter train with a 2.5cm bunch spacing. The complex starts with a 3GHz linac (twice the bunch frequency) that produces a pulsed electron beam with a present maximum energy of 150MeV. By means of RF manipulation in the Delay Loop (DL), the beam is converted of four consecutive bunch trains, each of them having 7.5A average current and 10cm bunch spacing. The electrons are then injected into the Combiner Ring (CR) using a 3GHz RF deflector [3]. After the 4th turn, the bunch trains are combined into a single one with a current of 30A and a 2.5cm distance between bunches.

The beam is finally extracted and sent to the CLIC experimental area (CLEX) where several beam lines are under construction at the moment. A 'Test Beam Line' [4] will study the reliability and the stability of the Drive Beam decelerator which must operate with a low level of beam losses. A 'Two-Beam Test Stand' is devoted to the test of a relevant CLIC module [5] with Power Extraction and Transfer Structures (PETS) on the Drive Beam side and 12GHz accelerating structures on the Probe Beam side [6].

This paper presents an overview of the CLIC Test Facility 3 instrumentation. The first paragraph is dedicated to essential beam diagnostic to measure position, intensity and size. The second paragraph presents the beam diagnostics specifically developed for the need of CTF3. The third and final paragraph discusses some CLIC specific instruments which are currently tested on CTF3.

ESSENTIAL INSTRUMENTS

Beam Position and Intensity Monitors

Beam position and intensity monitors are the first instruments used when the accelerator is turned on. An overview of the different types of pick-up developed for CTF3 is shown in Figure 2.

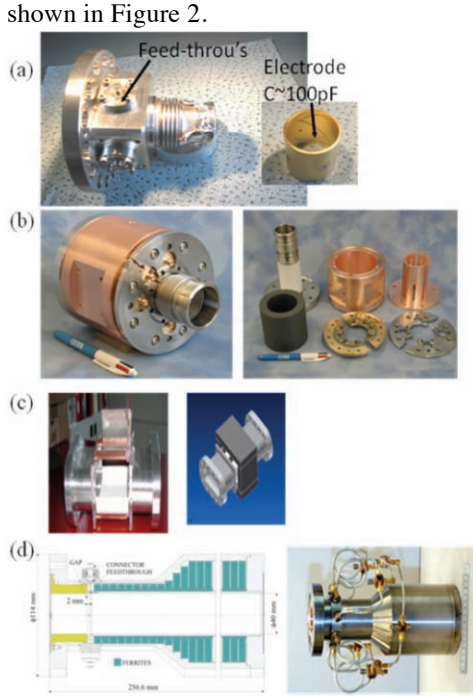

Figure 2: CTF3 Beam position and intensity monitors (a) BPE, (b) BPM, (c) BPI, (d) WCM

In the first part of the accelerator, electrostatic beam position and intensity monitors (BPE) have been installed. They present the advantage of functioning inside the

magnetic of the solenoids. Along the linac, inductive pick-ups (BPM) [7] have been developed. They detect the beam image current circulating on the vacuum chamber using eight electrodes. Similarly, inductive pick-ups (BPI) are used in the rings. Their design is slightly modified compared to the BPM, with a racetrack vacuum chamber and a reduced number of electrodes (4). The spatial resolution of the position measurements is better than 100μm, and with a frequency bandwidth ranging from 1kHz up to 200MHz they are sensitive to fast signal fluctuations and can observe the 1.2μs long pulse without any signal droop.

In addition to these pick-ups, Wall Current Monitors (WCM) [8] have been installed all along the machine in order to provide intensity measurements with an absolute precision better than 1%. Their high frequency bandwidth of 7GHz allows them to measure bunch to bunch intensity variations. A preliminary design of the CTF3 machine protection system was based on the measurement and the comparison of consecutives WCM signals [9].

Several acquisition systems have been developed and tested during the last few years. In the linac and in the combiner ring, a front-end electronic system is installed close to the monitors. It combines the signals from the BPM electrodes to generate the intensity and position signals, which are then amplified and sent via long cables onto 100MS/s digitizers located in a nearby technical gallery. In the Delay Loop, the four signals from the BPI's electrodes are directly sent to the digitizers via long cables. The beam position and intensity are computed numerically afterwards. In CLEX, a third choice has been made. The front-end electronic is kept in order to increase the signal to noise ratio but the signals are digitalized in the tunnel using a radiation compatible electronic system developed by LAPP [10]. It has the advantage to reduce by a large amount the cable cost but cannot be used without a control and software interface.

With a total of 104 devices installed in 2008, CTF3 is becoming one of the largest test facility ever built.

Beam Size for Emittance and Energy Measurements

In the list of essential beam diagnostics, the beam profile monitors would come in second. In a linac they are classically used to check the beam optics and measure the beam emittance. Beam profile monitors are also used in spectrometer lines to measure the beam energy and its energy spread.

In CTF3 ten TV stations have been distributed all along the machine for emittance measurements [11] and seven additional units are installed in spectrometer lines. All of them are based on the observation of Optical Transition Radiation. The most recent designs of CTF3 TV stations are presented in Figure 3.

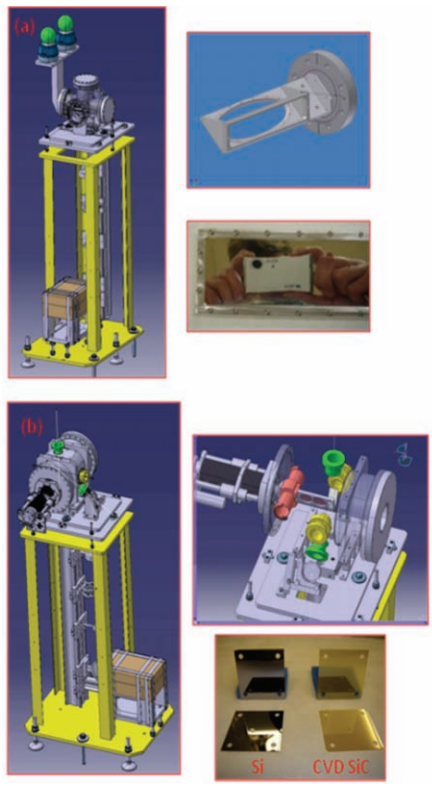

Figure 3: Beam profile monitors based on OTR screens. (a) Designed for energy measurement, (b) Designed for emittance measurement

In the case of emittance measurement, OTR screens are mounted on a 4 positions remotely controlled moving support. The system is designed to provide a spatial resolution that can be adjustable between 20 to 100μm. The 15° tilt angle between the OTR screen and the beam trajectory has been chosen to minimize field depth errors. A high reflectivity silicon screen coated with a thin aluminium layer is used to observe the lowest beam intensity. Higher beam charges are imaged using a CVD Silicon Carbide screen. When the screens are not used, a replacement chamber is put in place to ensure the continuity of the beam line. It suppresses wakefield effects that would become problematic, specially at the exit of the combiner ring, where the beam current increases up to 30A. A calibration plate can be inserted as well to quantify the resolution of the optical system.

In our spectrometer line, a bending magnet kicks the beam horizontally onto an OTR screen where the beam position and its transverse width are monitored. Because the electrons are dumped just after the TV station, the system has been simplified compared to the OTR system developed for emittance measurement. A 45° tilt angle OTR screen is mounted on a fixed support. The dimension of the screen, 100x50mm, fits the large horizontal beam size induced by dispersion. The spatial resolution of the system is typically 250μm. For electron energies higher than 100MeV, the intensity of the synchrotron radiation emitted in the dipole magnet

becomes comparable to the OTR light level and perturbs the measurement. Therefore, in order to suppress this effect, a carbon foil has been implemented just in front of the screen and acts as a SR shielding. Moreover, the OTR screen surface is parabolic along the x axis [12,13]. It refocuses the OTR photons onto our camera and improves the linearity of the measurement with respect to the beam position.

In addition to OTR-based monitors, seven TV stations are installed in the machine observing the synchrotron radiation emitted from dipole magnets in the magnetic chicane, the delay loop and the combiner ring.

For all systems, the light is sent onto a CCD Camera via a 1.5m long optical line. Optical density filters mounted on a remotely controlled wheel adjusts the light intensity if necessary. The camera itself is surrounded by a lead shielding but nevertheless due to the high radiation level generated in the machine, cameras must be replaced in average every two years.

These 24 TV stations are controlled by CERN made VME cards [14] which can switch on and off the camera, move the screens in and out of the beam tube, turn on and off a lamp and digitize the image.

CTF3 SPECIFIC INSTRUMENTS

Time resolved spectrometry

In order to optimize the overall efficiency of the Drive Beam generation, the accelerating structures [15] are operated in fully beam-loaded condition, meaning that all the RF power, except for ohmic losses, is transferred into beam energy. In this mode of operation, the RF-to-beam transfer efficiency has been measured at 96 % [16]. The resulting energy spectrum shows a strong time dependency with higher energies in the first 10-50 nanoseconds of the pulse. Time-resolved spectrometry is therefore an essential beam diagnostic to correctly tune the phase of the accelerating structures.

Time resolved beam diagnostics have been developed with the aim of measuring beam energy spread with 50MHz bandwidth. Three spectrometer beam lines are now routinely used along the linac as shown in Figure 4. For low and intermediate beam energies as they are in the first two spectrometer lines, segmented beam dumps are used as detector [17]. They consist of 32 parallel metallic plates designed to stop the incident particles. By measuring the deposited charge in each segment, the horizontal beam profile can be reconstructed. The material and the dimension of the segments must be chosen correctly to provide the required spatial resolution. With our beam parameters, 2mm thick 40mm long tungsten plates have been chosen. Because of the high power carried by the beam, thermal changes represent a crucial issue and radiation effects influence the long term behavior the detector. Therefore, a multi-slit collimator has been installed just upstream of the segmented dump. Its role is to capture as much beam power as necessary to ensure a good signal to noise ratio, but to keep the deposited power in the plates low enough so that they do not need water cooling. Radiation hard ceramics have been chosen as insulating material in between each segment.

For electron energies higher than 100MeV, the input collimator does not work as efficiently and multiple scattering inside the segments degrades the resolution of the monitor [17]. At the end of the linac, an alternative solution has been proposed and uses a 32 channels linear multi-anode photomultiplier (MAPMT) [18]. The latter is installed on the OTR screen of the spectrometer line, where an optical beam splitter has been added and divides the OTR light intensity in two parts, guiding 70% of the photons onto the MAPMT and the remaining 30% onto the camera.

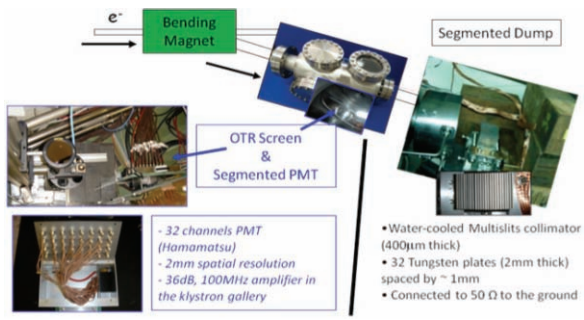

Figure 4 : Spectrometer line equipped with time resolved monitors

An example of the beam spectrum measured on the first spectrometer is shown in Figure 5. The time resolution is better than 10ns, limited in the present set-up by the bandwidth of the digitizers (100MS/s).

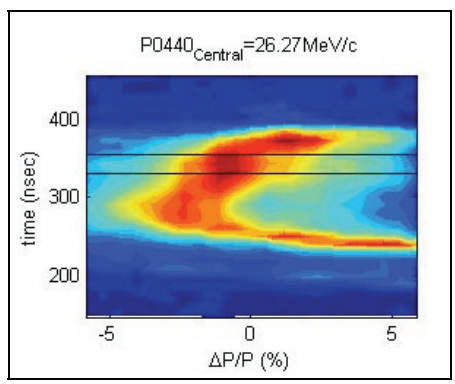

Figure 5: Time resolved energy profile measured at the exit of the CTF3 injector.

Bunch frequency multiplication

The Drive Beam generation relies on the production of high current high frequency electron beam based on a flexible bunch multiplication frequency technique. This is currently performed by means of RF manipulation and RF injection in a delay loop and a combiner ring.

The role of the delay loop is to rearrange the 1.2μs beam-pulse from the drive-beam linac into four 140ns long pulses, separated by 140ns gaps, increasing at the same time by a factor 2 both the current and the bunch repetition frequency. The procedure is schematized in Figure 6.

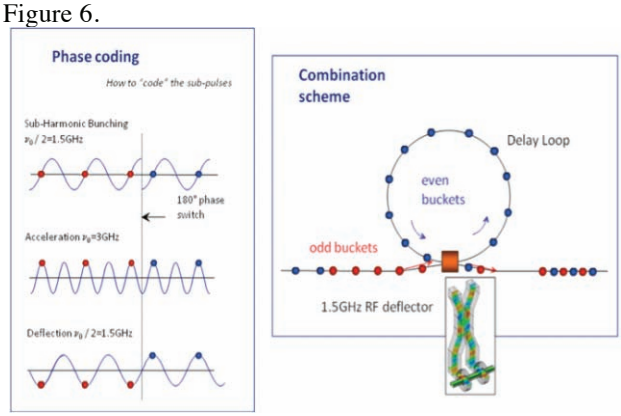

Figure 6 : Operation of the Delay Loop

A transverse RF deflector working at 1.5 GHz sends the first phase-coded sub-pulse (labeled as "even buckets" in the figure) into the delay loop. The loop length of 42 m corresponds to the sub-pulse length of 140ns, thus the "even" bunches are coming back at the deflector at the same time as the "odd" bunches of the next sub-pulse from the linac. The delay loop length can be precisely tuned to be an integer number of the RF wavelength, thus odd and even bunches arrive with opposite phases and receive opposite kicks. However their incoming angles are also opposite, so they are interleaved and combined into the same orbit. The bunch spacing is halved to 10cm and the beam current is doubled. The process also naturally produces a gap of 140ns, essential in the next stage for clean injection in the combiner ring.

The four 140ns pulses are then combined in the ring using a similar principle as depicted in Figure 7. The combiner ring length is equal to the distance between pulses (280ns) and for a four-fold bunch interleaving it is precisely tuned to $(n + ¼)\ \lambda$, where n is a (large) integer.

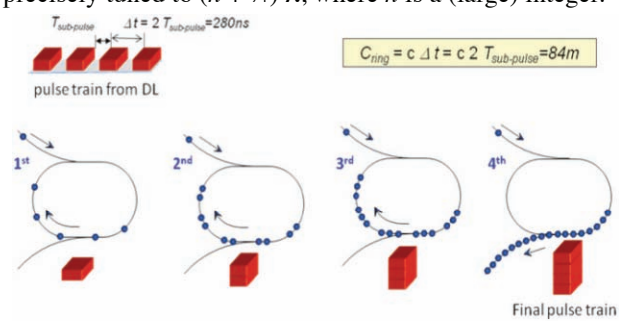

Figure 7 : Schematic operation of the Combiner Ring

A 3GHz RF deflector located after the injection septa kicks each incoming pulse into the closed orbit. Another deflector before the septa is synchronized with the first one to generate a closed bump, such that whenever the injected pulses come round they are kept on the closed orbit. After four turns, the first injected pulse would experience the maximum kick and hit the septum from the inside. Before this happens, the four pulses combined into one are extracted by the kicker on the other side of the ring to be sent to the CLEX area. The beam current is now eight times the initial one and the bunch distance is 2.5 cm, i.e., 12 GHz.

Streak cameras combined with OTR or synchrotron radiation have been used for decades for longitudinal profile measurements. In CTF3 long optical lines have been implemented to connect the OTR screen in the linac and the synchrotron radiation emitted in the rings to the streak camera laboratories [19].

The sub-harmonic bunching (SHB) system is responsible for the phase coding of 'even' and 'odd' RF bucket introducing a 180° phase switch every 140ns. Successfully operated since 2006, the results on the SHB performances can be found in [20]. Streak cameras images have been acquired in order to study the phase coding as presented in Figure 8. The phase switch is performed in 6ns and the presence of 8% satellite bunches at 3GHz that will be lost in the combiner ring gives an indication of the 1.5GHz SHB system efficiency.

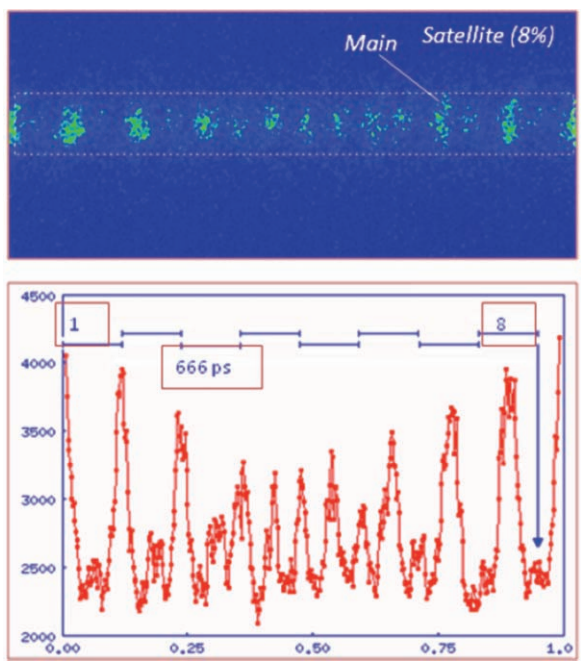

Figure 8 : Observation of the SHB 180° phase switch with a streak camera

The first commissioning of the delay loop was done in 2006 [21] and a bunch multiplication frequency by a factor of two was measured as presented in Figure 9.

In order to control the bunch interleaving, the beam time-of-flight in the ring must be precisely equal to an integer number of RF deflector periods. This is adjusted

using an undulator installed in the delay loop, which tunes the path length of the electrons accordingly as shown in Figure 10.

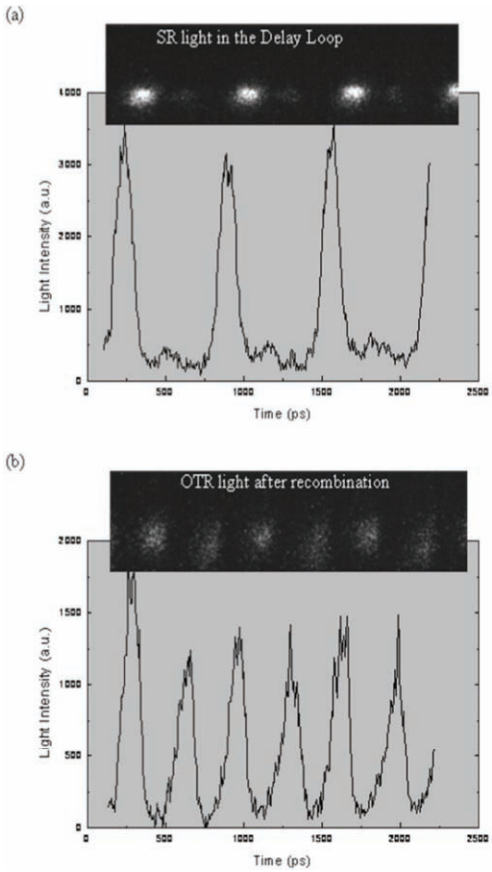

Figure 9 : Streak camera image taken with a sweep speed of 250ps/mm. (a) Bunch spacing of 20cm measured using SR in the delay loop (b) Bunch spacing of 10cm measured after recombination using OTR light.

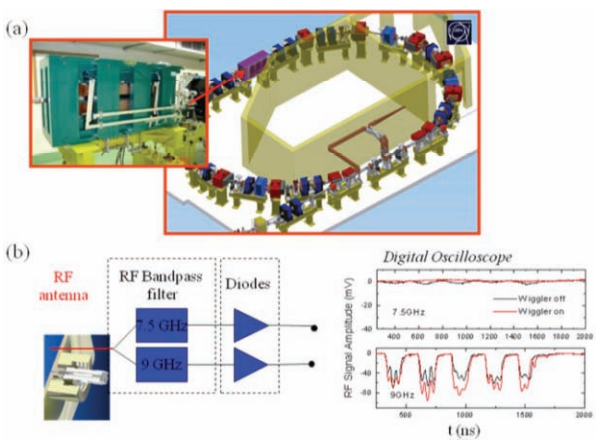

Figure 10 : (a) Picture of the delay loop undulator (b) Principle of the phase monitor with some measured signals taken during the optimization of the bunch train combination in the delay loop.

For the same purpose, a non-intercepting monitor, called 'Phase monitor' [22], was installed at the exit of the delay loop. The detector is an RF antenna as shown in Figure 10, which was already tested several years ago at a previous test facility [23]. It measures the amplitude of the electromagnetic field emitted by the particles at harmonic frequencies of 1.5 and 3GHz. In the case of a perfect frequency multiplication from 1.5 to 3GHz, the signal at 7.5GHz would completely disappear whereas the signal at 9GHz would increase accordingly. A typical measurement is presented in Figure 10, where the signal at 7.5GHz is strongly reduced for an optimized tuning of the delay loop length.

Bunch Length Monitors

The bunch length needs to be controlled precisely in the CTF3 complex [24]. In the linac the bunches must remain short to keep the energy spread as low as possible, but need to be stretched before the rings to minimize emittance dilution due to coherent synchrotron radiation. Two magnetic chicanes have been implemented in the machine. The first one, located after the injector, is used to adjust the bunch length before the beam enters in the linac. A second magnetic chicane, installed at the end of the linac, is currently used as a stretcher before the electrons enter in the rings. Typical streak camera measurements are presented in Figure 11.

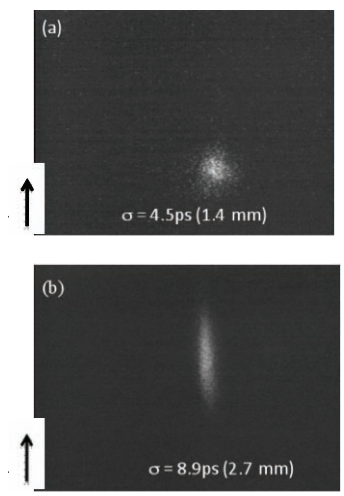

Figure 11 : Streak cameras images taken with a sweep speed of 10ps/mm: (a) Short bunch length from the linac. (b) Stretched bunches at the entrance of the Delay Loop.

In addition to the streak camera, other techniques to measure short bunch lengths have been studied. One of the most promising alternative techniques is based on the use of RF deflecting cavities. As the bunch is passing through the cavity, it experiences a time dependent deflection which converts time into spatial information. By measuring the beam size at a downstream location, the longitudinal profile can be extracted. The time resolution depends on the deflecting power, the beam optics at the location of both the deflector and the beam profile

monitor, and finally on the spatial resolution of this monitor. With this method time resolutions of 10fs have already been obtained [25]. In CTF3 RF deflectors are already used for injection in the rings and bunch length measurements can be performed using the same hardware; see Figure 12.

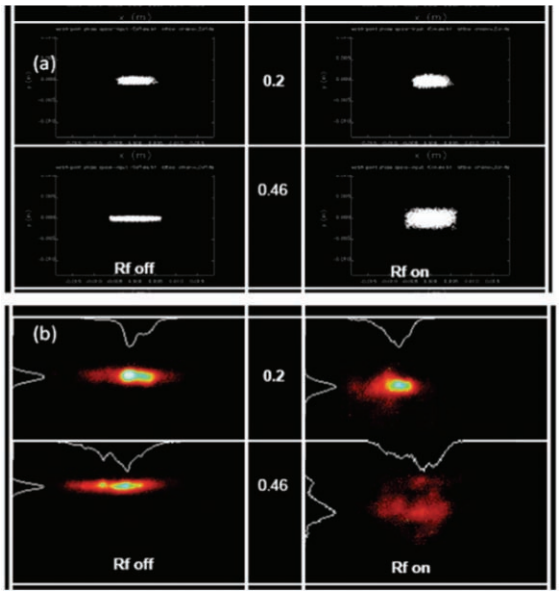

Figure 12 : RF deflector measurements at CTF3 performed for two different bunch compression factors in the magnetic chicane: (a) Estimated beam sizes from simulations (b) Corresponding measured beam sizes.

The deflection is done using the 3 GHz cavity installed just after the 'stretching' magnetic chicane and the beam size is then monitored by an OTR screen. The bunch length is obtained by comparing the measured beam sizes with and without RF power in the deflector. Bunch lengths of 1.2 and 6ps were measured in these cases.

At the same time, non-intercepting bunch length monitors have been developed, in particular through the use of an RF pick-up. The device picks-up and analyzes the power spectrum of the electromagnetic field emitted by the electrons. A simple version, called BPR, has been implemented in the machine since 2003 in order to tune the bunch compression in the first magnetic chicane. Pictures of the BPR components are depicted in Figure 13. The monitor relies on the detection of beam emitted power at 30GHz. The signal from the WR28 waveguide is strongly attenuated using two horns deliberately off centered the one with respect to the other. The RF signal is then bandpass filtered at 30GHz and measured using a schottky diode. The signal is finally digitalized using 100MS/s ADC's.

Three additional BPR's have been installed after the stretcher chicane and in the rings. Reliable and robust, this device gives a signal proportional to the bunch length but cannot provide any absolute measurement.

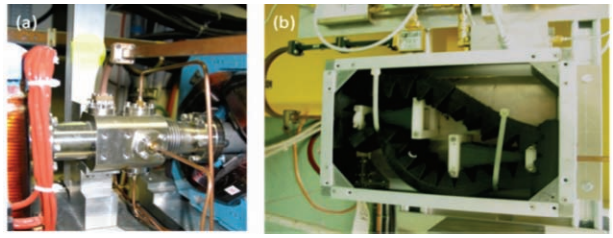

Figure 13: BPR monitor (a) Vacuum assembly installed on the beam line (b) WR28 waveguide components used for the measurement.

A more sophisticated detection system has been developed recently in order to get single shot non intercepting sub-picosecond bunch length measurements [26]. The vacuum assembly of the BPR remains the same but the RF window in alumina is replaced by a thin diamond window, which improves the transmission for high frequencies. Using a series of down-converting mixing stages and filters (see Figure 14), the signal amplitude and phase are measured simultaneously in four different frequency bands: 30-39GHz, 45-69GHz, 78-90GHz and 157-171GHz. Each signal is then digitized using ADCs with a bandwidth of 2 GHz. The system is capable of performing single shot bunch length measurements with a 300fs time resolution.

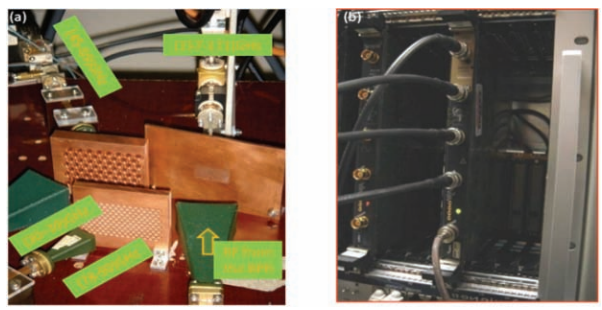

Figure 14 : Bunch length measurement with an RF Pick-up: (a) Waveguide assembly using reflecting brass filters and two consecutives down mixing stages in four different frequency bands (b) 4 channels, 2GHz, 8GS/s digitizer.

The pick-up is installed close to the 1.5GHz RF deflector such that cross-calibrations can be obtained easily. Detailed results of the recent commissioning of the detector are presented in [26].

CLIC-RELATED DEVELOPMENTS

High Precision Beam Position Monitor

In CLIC, the beam position has to be controlled very precisely to minimize emittance growth along the main linac. Beam dynamic simulations have shown that to guarantee the performance of the collider, beam position measurements must be performed with an absolute precision of 10μm and a resolution of 100nm. One approach, which has already demonstrated good

performance [27,28], is to develop cavity BPM's. Another alternative pursued at CERN is to scale down the inductive pick-up already developed for the CTF3 linac [7]. The beam tube diameter is reduced by a factor 10 compared to the initial design down to 4mm and the number of electrodes is reduced from 8 to 4 as shown in Figure 15.

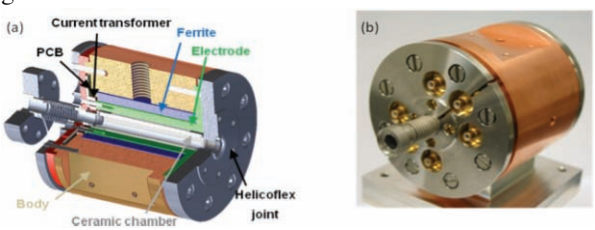

Figure 15 : Nanometer BPM: (a) 3D drawing (b) Pictures of the final assembly.

Three nanometer BPM's have already been build and tested on a vibration free stabilized bench. Calibration results are illustrated in Figure 16. Scaled to the CLIC beam parameter the achieved resolution corresponds to 200nm.

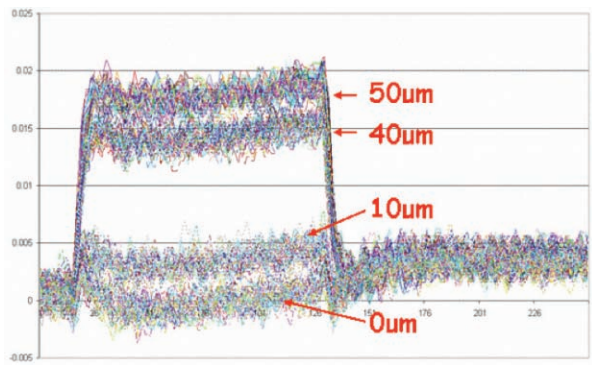

Figure 16: Calibration of the BPM using a stretched wire traversed by a 100mA pulsed current. Each curve represents a different transverse position of the wire.

The three BPM's have been installed at the end of the CTF3 linac (see Figure 17) and a beam test is planned sometime this year.

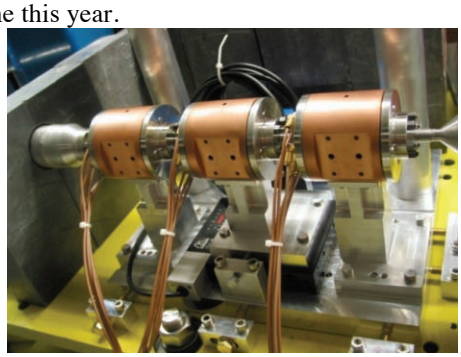

Figure 17: Picture of the nanometer-BPM test in CTF3.

Beam Halo Monitors

For future linear colliders, it must be ensured that particle losses are minimized, as activation of the vacuum chambers or other components makes maintenance and upgrade work time consuming and costly. It is imperative to have a clear understanding of the mechanisms that can lead to halo formation and to have the possibility to test available theoretical models with an adequate experimental set-up. Measurements based on optical transition radiation are a well-established technique for measurements of the transverse beam profile. However, in order to be suitable for halo measurements as well, the dynamic range of the final image acquisition system needs to be high, being able to cover at least five orders of magnitude in intensity changes. In CTF3, high dynamic imaging system has been investigated since 2004. Beam core suppression techniques were tested on CTF3 using a coronagraph [29]. The central part of the beam is masked so that the beam halo can be observed without saturating the camera. The performances at that time were limited to 10^4 dynamic range measurements because the mask had a fixed size which was not adaptable to the real beam size.

Innovative camera based on charge injection device (CID) technology [30], which potentially can reach dynamic ranges up to 10^6, as well as improved beam core suppression technique using adaptive optics [31] have been investigated since then. The latter is based on digital light processing technology using micro mirror arrays as depicted in Figure 18. Composed of individually controllable mirrors, they have the possibility to produce a mask of any geometrical form which can fit perfectly to the beam dimension.

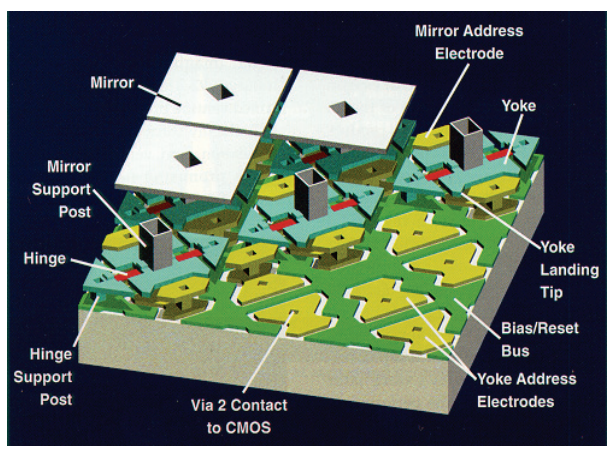

Figure 18: Schematic of a Micro Mirror Array.

In Figure 19, the performance of a standard acquisition system as it is used in the CLIC test facility (CTF3) is compared with CID camera system and measurements performed with a micro mirror array. Adaptive optics and CID technology allow reaching dynamic range higher than 10^5 to be compared with the 10^3 dynamic range of classical CCD cameras.

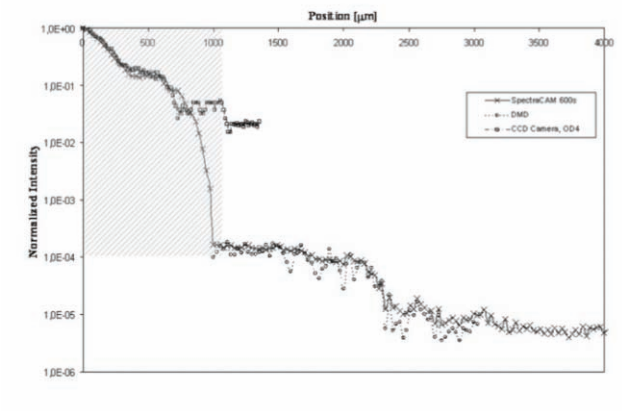

Figure 19: Laser beam profile measured with a CCD camera, a CID camera and a micro mirror array (DMD).

Femtosecond Phase Monitor and Feedback

One important aspect of the two beam acceleration scheme is to synchronize precisely the Main Beam with respect to the RF power produced by the Drive Beam. Timing errors lead to energy variations in the main linac and would have an impact on the collider performance. A jitter of 15fs would give a luminosity reduction of around 2% [32]. It is extremely doubtful that this required tolerance could be met without feedback, feedforward or both types of beam-based correction.

As shown in Figure 20, a possible scheme [33] for CLIC is to measure the arrival time of the Drive and the Main beam in the transfer line between the injector complex and the main linac.

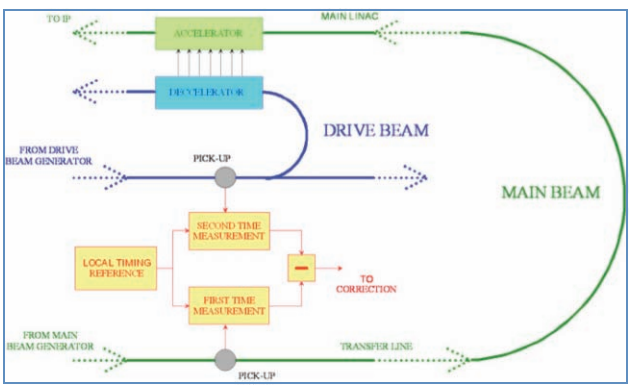

Figure 20: Phase measurement in CLIC.

A precision local clock would be required to keep time from the arrival of the reference until the end of the drive beam train, 92µs later. Precise time measurements of both beams are performed and compared, and depending on the observed difference, a correction on the drive beam would be applied. Corrections could be done using RF structures, either with deflecting cavities or by varying the energy before the final drive beam bunch compressor. The system relies on a precise timing measurement with a resolution better than 20fs.

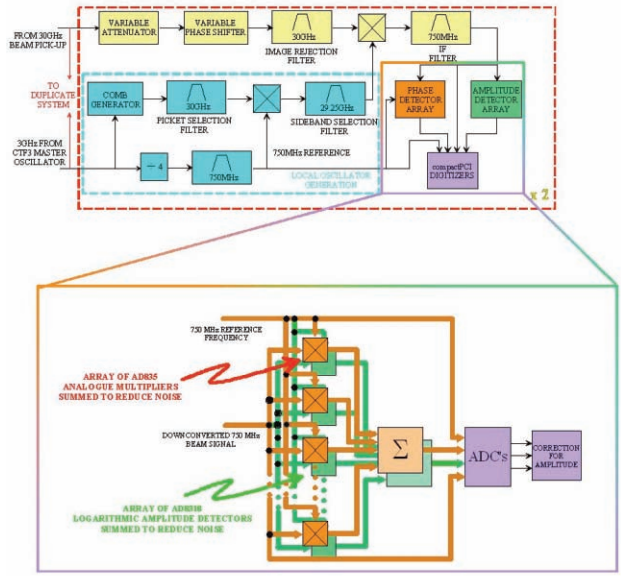

Figure 21: Layout of the femtosecond timing measurement in CTF3.

On CTF3, a heterodyne approach has been taken, measuring the phase of the 10th harmonic of the 3GHz bunch frequency as depicted in Figure 21. The 30GHz component of the beam was sampled in a pick-up and then mixed down to an IF of 750MHz. The phase and the amplitude of this signal are then measured with respectively an array of 8 analogue multipliers and 8 logarithmic amplitude detectors, with their outputs summed and averaged. The phase difference of two independent phase monitors is then computed so that the noise level of the measurement can be estimated. A resolution better than 10fs for a beam timing measurement over 9dB amplitude has been already demonstrated [34].

CONCLUSIONS AND PERSPECTIVES

Since 2003, a large number of beam diagnostics have been developed in the framework of the CLIC test facility 3. New challenges in terms of beam instrumentation development would have to be faced with the construction of the Test beam line [4] and the Two-beam test stand [5] in the CLEX area.

A major step for the CLIC study will be to provide a conceptual design report by 2010. In this context an exhaustive review of beam instrumentation has been initiated. It will critically review all the technical solutions envisaged so far. This work will be based on the expertise gained on CTF3 and also based on the numerous developments performed in the framework of the International Linear Collider project and of the 3rd or 4th generation light sources.

REFERENCES

[1] H.H. Braun *et al*, "Updated CLIC parameters 2005", CLIC note 627, (2005)

[2] G. Geschonke, "Status of the CLIC Test Facility 3 (CTF3)", Proceeding of LINAC 2006, Knoxville, Tennessee, USA, pp.11

[3] C. Biscari *et al*, "CTF3: Design of Driving Beam Combiner Ring", Proceeding of EPAC 2000, Vienna, Austria, pp.450

[4] S. Döbert, "Progress on the CTF3 Test Beam Line", Proceeding of EPAC 2006, Edinburgh, UK, pp.783

[5] V. Ziemann *et al*, "The Two-Beam Test-Stand in CTF3", Proceeding of EPAC 2006, Edinburgh, UK, pp.2445

[6] A. Mosnier *et al*, "The Probe Beam Linac in CTF3", Proceedings of EPAC 2006, Edinburgh, UK, pp.679

[7] M. Gasior, "A Current Mode Inductive Pick-Up for Beam Position and Current Measurement", Proceeding of DIPAC 2005, Lyon, France, pp.175

[8] P. Odier, "A New Wide Band Wall Current Monitor", Proceeding of DIPAC 2003, Mainz, Germany, pp.216

[9] D. Belohrad, "First Tests of the Machine Protection System for CTF3", Proceeding of DIPAC 2005, Lyon, France, pp.255

[10] L. Bellier et al, "CTF3 BPM Acquisition System", Proceeding of ICALEPCS 2007, Knoxville, Tennessee, USA, pp.395.

[11] P. Urschütz *et al*, "Beam Dynamics Studies and Emittance Optimization in the CTF3 Linac at CERN", Proceeding of EPAC 2006, Edinburgh, UK, pp. 798

[12] C.P. Welsch, E. Bravin and T. Lefevre, "Optimization of OTR Screen Surface Materials and OTR Screen Geometry at CTF3", Review of Advanced Material Science 16 (2007) 73-79.

[13] C. Welsch, E. Bravin and T. Lefevre, "Investigations of OTR Screen Surfaces and Shapes", Proceeding of EPAC 2006, Edinburgh, UK, pp.1220

[14] S. Burger *et al*, "A New TV Beam Observation System for CERN", Proceedings of DIPAC 2005, Lyon, France, pp.214

[15] E. Jensen, "CTF3 Drive Beam Accelerating Structures", Proceeding of LINAC 2002, Gyeongju, Korea, pp. 34. CERN-PS-2002-068

[16] P. Urschütz *et al*, "Efficient Long-pulse Fully Loaded CTF3 Linac Operation", Proceeding of LINAC 2006, Knoxville, Tennessee, USA, pp.31; CLIC note 697

[17] T. Lefèvre *et al*, "Segmented Beam Dump for Time Resolved Spectrometry on a High Current Electron Beam", Proceeding of DIPAC 2007, Venice, Italy, pp. ; CERN-AB-2007-030-BI

[18] T. Lefèvre *et al*, "Time Resolved Spectrometry on the CLIC Test Facility 3", Proceeding of EPAC 2006, Edinburgh, UK, pp. 795; CERN-AB-2006-079

[19] C. Welsch *et al*, "Longitudinal Beam Profile Measurements at CTF3 Using a Streak Camera", Journal of Instrumentation, 1, (2006), P09002

[20] P. Urschütz *et al*, "Beam Dynamics and First Operation of the Sub-Harmonic Bunching System in the CTF3 Injector", Proceeding of EPAC 2006, Edinburgh, UK, pp. 795

[21] R. Corsini *et al*, "Commissioning Status of the CTF3 Delay Loop", Proceeding of EPAC 2006, Edinburgh, UK, pp.771

[22] A. Ferrari *et al*, "Development of a Bunch Frequency Monitor for the Preliminary Phase of the CTF3", Proceeding of DIPAC 2003, Mainz, Germany, pp.211

[23] R. Corsini *et al*, "Experimental Results on Electron Beam Combination and Bunch Frequency Multiplication", Phys. Rev. STAB 7, 04101, (2004)

[24] A. Ghigo *et al*, "Commissioning and First Measurements on the CTF3 Chicane", Proceeding of PAC 2005, Knoxville, Tennessee, USA, pp.785

[25] P. Emma *et al*, "A Transverse RF Deflecting Structure for Bunch Length and Phase Space Diagnostics", LCLS-TN-00-12, (2000)

[26] A. Dabrowski *et al*, "Non Destructive Single Shot Bunch Length Measurements at CTF3", Proceeding of the PAC 2007, Albuquerque, New Mexico, USA, pp.4069

[27] M. Slater *et al*, "Cavity BPM System Tests for the ILC Energy Spectrometer", Slac-Pub-13031, EuroTeV-2007-059

[28] S. Walston *et al*, "Performance of a High Resolution Cavity Beam Position Monitor System", Nuclear Instruments and Methods A578 (2007) p.1–22

[29] T. Lefèvre *et al*, "Beam Halo Monitoring at CTF3", Proceeding of EPAC 2004, Lucerne, Switzerland; CLIC note 610

[30] C.P. Welsch *et al*, "High dynamic range beam profile measurements", CERN-AB-2006-068; CLIC-Note-686; CTF3-Note-081 ; C.P. Welsch *et al,* "Alternative Techniques for Beam Halo Measurements", Measurement Science and Technology 17 (2006) 2035–2040

[31] C.P. Welsch, E. Bravin and T. Lefèvre, "A Beam Halo Monitor Based on Adaptive Optics", Proceeding SPIE Europe Optical Metrology (2007), Munich, Germany

[32] D. Schulte, E. J. N. Wilson and F. Zimmermann, "The Impact of Longitudinal Drive Beam Jitter on the CLIC Luminosity", CLIC Note 598

[33] A. Andersson and J.P.H. Sladen, "Precise Beam Timing Measurement System for CLIC Synchronization", Proceeding of EPAC 2006, Edinburgh, UK, pp. 1211

[34] A. Andersson and J.P.H. Sladen, "RF-based Electron Beam Timing Measurement with sub-10fs Resolution", CERN-AB-2008-003-RF, CLIC note 734

NEAR-FIELD OPTICAL DIFFRACTION RADIATION MEASUREMENTS AT CEBAF*

P. Evtushenko#, A. P. Freyberger, C. Y. Liu, Jefferson Lab, Newport News, VA USA
A. Lumpkin, Fermilab, Batavia, IL USA

Abstract

An optical diffraction radiation (ODR) diagnostic station was recently designed and installed on a CEBAF transfer beam line. The purpose of the setup is to evaluate experimentally the applicability range for an ODR based non-intercepting beam size monitor as well as to collect data to benchmark numerical modeling of the ODR. An extensive set of measurements was made at an electron beam energy of 4.5 GeV. The ODR measurements were made for both pulsed and CW electron beam of up to 82 μA. The wavelength dependence and polarization components of the ODR were studied using a set of insertable bandpass filters (500 nm short and 500 nm long pass filter) and polarizers (horizontal and vertical). The typical transverse beam size during the measurements was ~150 microns. Complete ODR data, wavelength and polarization, were recorded for different beam sizes and intensities. The beam size was also measured with optical transition radiation (OTR) (using the surface of the ODR converter) as well as a wire scanner located next to the ODR station. In this contribution we describe the experimental setup and present the results of the measurements with the comparison to the numerical simulations.

INTRODUCTION

Optical diffraction radiation is generated when a charged particle passes near a conductor at a distance comparable or smaller than $\gamma \cdot \lambda/2\pi$, where γ is the relativistic Lorenz factor and λ is the wavelength of the radiation. The theory of the diffraction radiation is well developed [1]. In the case of a highly relativistic particle beam with large γ, a conductor located at a distance bigger than the transverse beam size will generate a significant amount of diffraction radiation in the optical wavelength range. Several ODR based schemes were suggested for non-intercepting beam size measurements [2-6]. Some of them utilize the angular distribution of the ODR whereas others make use of imaging of the radiator surface, i.e., near-field measurements. The near-field ODR was observed experimentally previously [7, 8]. A common condition in such measurements was that the integrated charge used to generate the ODR was several nC.

The Continuous Electron Beam Accelerator Facility (CEBAF) is a multipass superconducting LINAC delivering CW electron beam with an energy up to 6 GeV and average current up to 100 μA for nuclear physics experiments on fixed targets [9]. A typical beam size in CEBAF at high energy is 100 μm. The total charge delivered by CEBAF within the time a standard video camera uses to integrate one field of a video signal (16.6 ms) and when running 100 μA beam is 1.66 μC. The combination of the these parameters, GeV range energy, 100 μm beam size and μC charge integrated within 16.6 ms, makes CEBAF an ideal facility to study develop and implement an ODR based non-intercepting beam size diagnostic, as was pointed out previously [10]. At the same time, from an operational point of view it is very desirable to have such a non-intercepting beam size monitor. It can be used to detect drifts leading to a change in the betatron match early and therefore can improve beam availability for the nuclear physics experiments. A set of such beam size monitors positioned properly along a transport beam line could also provide online emittance monitoring as well as emittance measurements virtually at any bunch charge when running CW beam. With such motivation in mind we have designed built and installed an ODR diagnostic station which would serve in a first place as an evaluation setup for the ODR, but also would be a prototype of such a diagnostic setup for CEBAF.

EXPERIMENTAL SETUP

The most important part of the ODR diagnostic station is the ODR radiator. The optical transition radiation (OTR) was used for reference beam size measurements. Thus we have designed and built a radiator which could be used for both OTR and ODR measurements. The radiator is shown in Fig. 1. The ODR part of the radiator is a 300 μm thin silicon wafer optically polished and aluminized on one side. The thickness of the aluminum layer is about 600 nm. The wafer is mounted on an

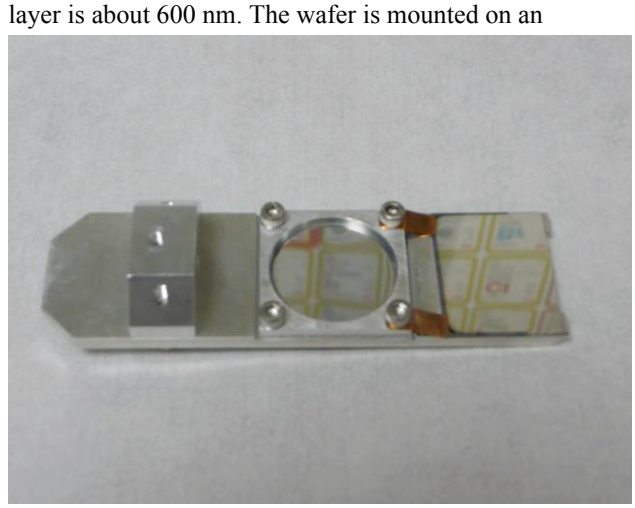

Figure 1: ODR-OTR radiator

* Work supported by the U.S. DOE contract # DE-AC05-06OR23177
# Pavel.Evtushenko@jlab.org

aluminum holder in such way that its edge does not have any frame underneath. This edge of the wafer was put close to the beam to generate the ODR. Since we wanted to be very careful with the ODR radiator and did not have experimental results which would indicate how much current can be sent through the wafer without destroying it, it was not our favorite option to use the ODR radiator to generate the OTR. Also, minimizing the beam scattering in the OTR screen and reducing the beam losses downstream of the radiator is always desirable. Therefore next to the ODR radiator we have put a separate OTR radiator. The radiator is a 6 μm thin Kapton foil aluminized on one side and stretched on a frame so that it is flat. Surfaces of both radiators look as an optical mirror. The aluminization of both radiators is done to increase radiation yield, since for both OTR and ODR it is proportional to the reflectivity of the surface.

The radiator is mounted on a stepper motor actuator with a lead screw. The actuator can position the radiator with accuracy better than 10 μm. The radiator is mounted on the actuator at an angle of 45 degrees relative to the direction of the beam propagation. Fig. 2 shows schematically the ODR diagnostic station. The setup was installed on an existing very stable girder in the beginning of the Hall-A beam line. The radiator is installed on the downstream side of the girder. Another very important part of the experimental setup is an alignment laser, which was installed on the upstream side of the girder. The laser beam is coupled in to the beam line with the help of an insertable mirror. To set up and align the optical system, first the alignment laser was set to be at the same position and angle at the ODR radiator as the electron beam. To do that the laser is equipped with ×10 beam expander. The laser spot position would be measured on the ODR radiator itself and on a beam viewer located approximately 30 m downstream of the ODR station. Thus we could setup the angle of the alignment laser with accuracy 100 μrad relative to the beam trajectory. All optical components are mounted on two optical rails as can be seen in the Fig. 2. There are two 2″ mirrors on the vertical rail to redirect the OTR and ODR light to the horizontal rail. Two 2″ diameter achromatic lenses are used to image the surface of either radiator on a CCD camera. For the measurements we used a JAI-A50 CCD camera. The camera is neither cooled nor intensified. The most important feature of the camera is the signal to noise ratio (SNR) of 60 dB. There are two insertable polarizers, vertical and horizontal, installed in the optical system to study effects of polarization on the ODR measurements. There are also three motorized and remotely controlled filter wheels where band-pass and neutral density filters are installed. The video signal of the CCD camera was digitized with 10-bit frame grabber. Due to the SNR of the camera and the resolution of the frame grabber the dynamic range of our measurements was about 10^3. There are two wire scanners installed on the same girder where the ODR diagnostic station was installed. This gave us the capability to cross check the ODR as well as OTR measurements with the wire scanners measurements.

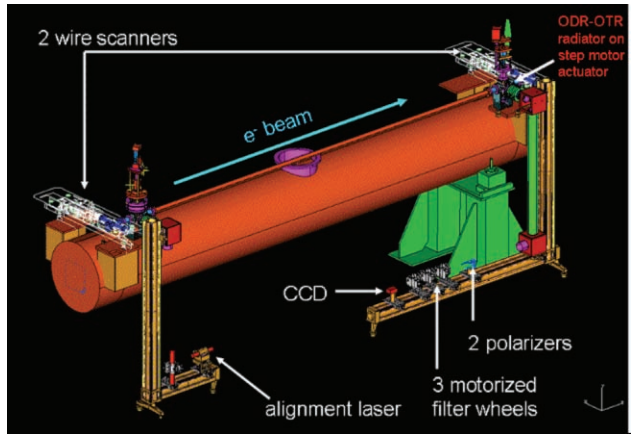

Figure 2: Schematic of ODR station

EXPERIMENTAL RESULTS

We started our measurements by determining the beam size with the help of the OTR and the wire scanners. Unfortunately the thin Kapton OTR radiator surface happened to be somewhat misaligned with the surface of the ODR radiator. The optical system was aligned reflecting the alignment laser from the surface of the ODR radiator. As a result the OTR image from the Kapton radiator was considerably dimmer and appeared somewhat shifted. For that reason we had to use the surface of the ODR radiator for the OTR measurements.

Since our goal is to develop a non-intercepting beam size measurements technique, one of the measurements we did was to change the beam size using upstream quadrupoles and measure the changes in the ODR pattern. As mentioned above the OTR and wire scanners were used to determine the beam size. We have observed that using polarizers made a difference for the measured beam size. For instance, if without polarizer we would measure the vertical and horizontal beam sizes of σ_x=149 μm and σ_y=157 μm, then when the horizontal polarizer was inserted we have measured σ_x=150 μm and σ_y=130 μm

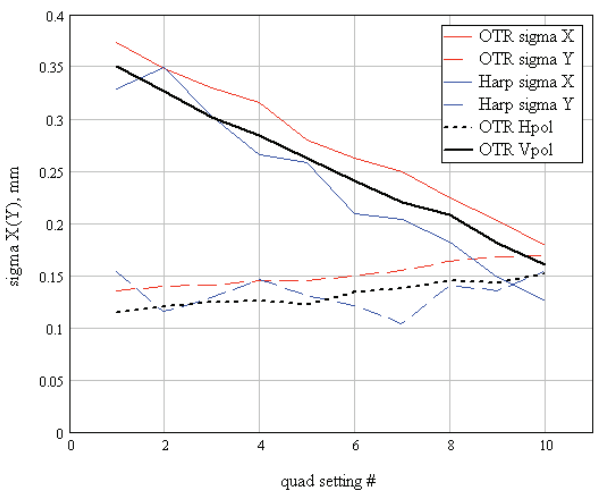

Figure 3: Layout of papers.

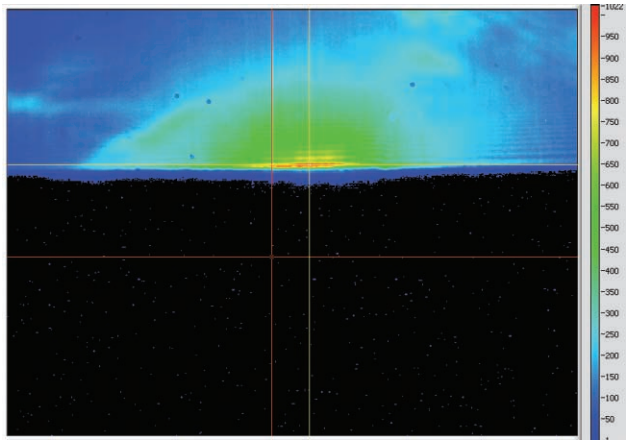

Figure 4 a: Unpolarized ODR pattern

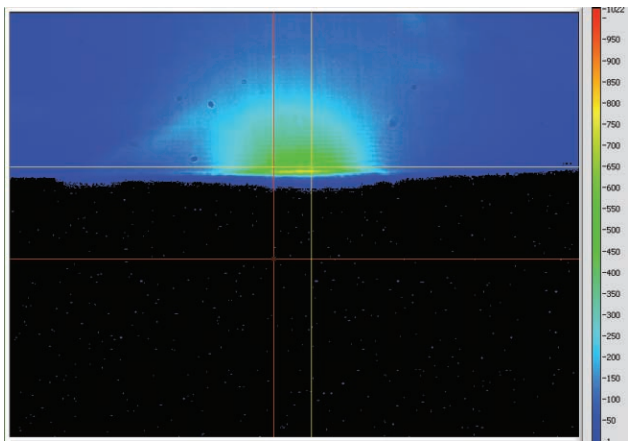

Figure 4 a: Vertically polarized ODR pattern

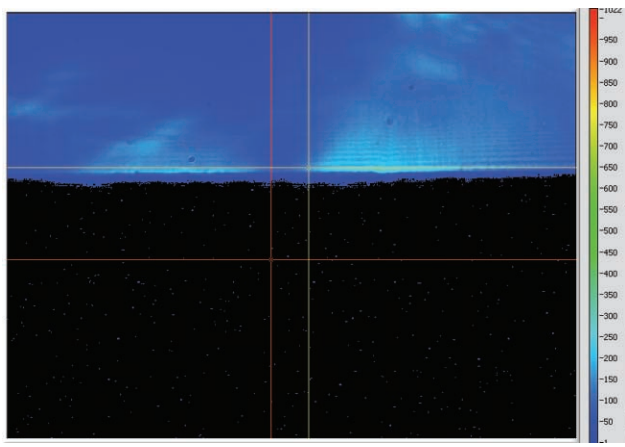

Figure 4 a: Horizontally polarized ODR pattern

and when the vertical polarizer was inserted the measurements were σ_x=124 μm and σ_y=160 μm. That is for either polarization the beam size measured in perpendicular direction would appear to be smaller by about 20 % and the beam size measured in the direction of polarization essentially would not change. Figure 3 shows a comparison of the beam size measurements with the wire scanner, unpolarized OTR and polarized OTR for ten different quadrupole settings. The polarized OTR data are systematically much closer to the wire scanner data than the unpolarized data. At this time the polarized OTR data have much smaller statistical spread which manifests in much smoother data curves.

For the ODR measurements it is be desirable to position the edge of the ODR radiator as close as possible to the beam without generating beam losses. Before inserting the ODR radiator close to the beam and running higher current beam the vertical beam size was reduced to 110 μm. The edge of the ODR radiator was positioned above the beam at 1.1 mm from the beam centroid, which is $10\times\sigma_y$. Gradually increasing the average beam current of CW beam we would record the image shown in Fig. 4 a. The image is recorded at an average current of 10 μA. No beam loss was detected with the ODR radiator inserted. The field of view of the image is 6.9 mm by 5.2 mm. Note that at this beam intensity we started to saturate the CCD camera at the maximum of the intensity of the ODR pattern. The measurements are made with the beam energy of 4.5 GeV. With the vertical polarizer inserted the ODR pattern appeared to be considerably narrower (Fig. 4 b) and with the horizontal polarizer inserted we could clearly observe the double lobe pattern (Fig. 4 c). Both these observations are in agreement with the model prediction [7].

We use the following quantity as a measure of the ODR pattern's width. In the ODR image a small, approximately 100 μm wide, region of interest (ROI) close to the edge of the radiator was selected. The intensity of all lines in the ROI was added and normalized to the number of lines. Using a nonlinear least square fit, a best approximation of the normalized intensity profile in the ROI by a Gaussian function was found. The sigma of the Gaussian distribution found by the fit was taken as a measure of the ODR pattern. For the previously determined ten settings of the upstream quadrupole we have measured the width of the ODR patterns without any polarizers and with vertical polarizer inserted. Results of the measurements are shown in Fig. 5 where the horizontal axis is the beam size measured via vertically polarized OTR. For both unpolarized and vertically polarized ODR data a systematic increase of the ODR pattern width is measured when the horizontal beam size was increased. The same experimental observation was made previously in [7]. Based on the result of these measurements one can conclude that the near-field ODR can be used at least as a beam size monitor, but would need a prior calibration. However, ultimately we would like to be able to use ODR for beam size measurements without such a cross-calibration, i.e., based only on the ODR data. As a first step towards such measurements we would like to see a good agreement between the measured data and the prediction of the model. Since we had the beam size measured with the OTR and we know the distance from the beam centroid to the edge of the ODR radiator, we can calculate the expected ODR pattern distributions for these conditions. We can apply then the same procedure to the model data as we did with the experimental data. The results of this would be the expected sigma of the best

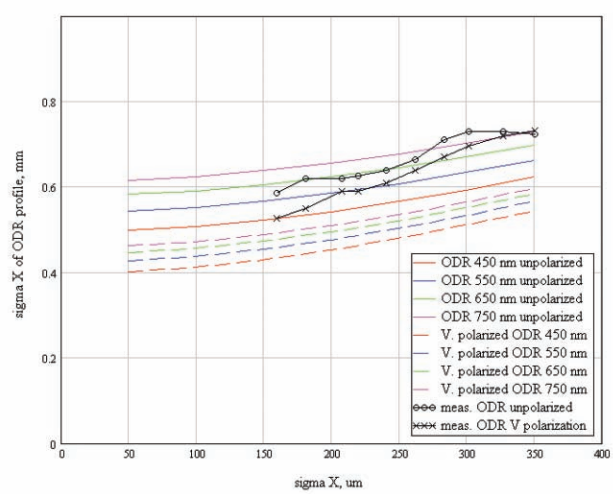

Figure 5: Layout of papers.

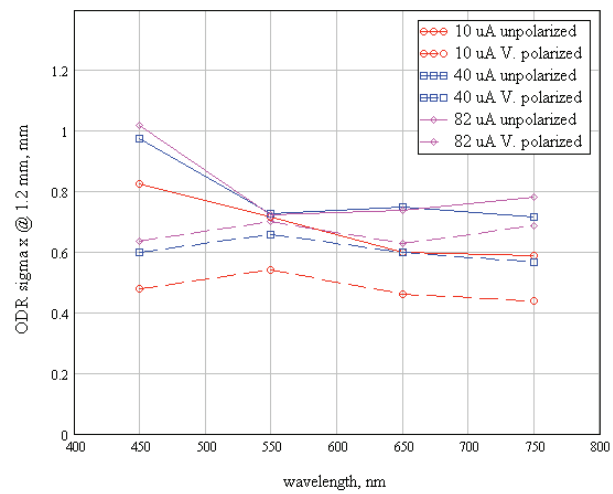

Figure 6: Layout of papers.

Gaussian fit. We did such calculations for a horizontal beam size in the range 50 μm through 350 μm; the vertical beam size in the calculations was kept constant and equal to 150 μm. The calculations were made for four different wavelength 450 nm, 550 nm, 650 nm and 750 nm, for unpolarized and vertically polarized ODR distributions. The results of the calculations are shown in Fig. 5 with the results of the measurements. Note that the measurements are broad band, and the calculations are narrow band. It is reasonable to assume that when the quantum efficiency of the CCD camera is taken in to account the broad band data or calculations will be somewhere in the range between 450 nm and 750 nm. Comparing the calculation and the measurements in the Fig. 5 we can conclude that the unpolarized data are in reasonable agreement with the model predictions whereas the vertically polarized data agree less with the model. However, the disagreement between the vertically polarized ODR data and the model is only about 20 %. It is also easy to notice that the trends in the experimental data are somewhat different from the model. As can be seen in Fig. 4 there is a background present in the raw ODR data. Possible sources of the background are visible synchrotron radiation and visible edge radiation from the upstream dipole, which is located only 8 m upstream of the ODR radiator. The presence of the background in the data certainly affects the results of the Gaussian fits. We consider the background to be the main reason for the discrepancy between the model prediction and the experimental results.

Another set of the data was taken to study experimentally dependence of the ODR distribution on the wavelength of the radiation. Thus using CW electron beam with three different values of the average current, namely 10 μA, 40 μA and 82 μA, we have measured the width of the ODR distributions at four wavelengths 450 nm, 550 nm, 650 nm and 750 nm using insertable bandpass filters with a bandwidth of 10 nm for 450 nm, 550 nm, 650 nm filters and 40 nm for the 750 nm filter. Results of the measurements are shown in Fig. 6. The first observation is that whereas the model predicts broader distributions for longer wavelengths at any distance from the beam centroid and for any beam size, as can be seen in Fig. 5, this trend does not show up in the experimental data. Here we do not provide an explanation of this observation. We are planning to examine achromaticity of the imaging optics and magnitudes of the aberrations introduced by different bandpass filters as well as make more measurements to understand the experimentally observed wavelength dependence. One more observation is that the ODR data at any wavelength, both unpolarized and vertically polarized, suggest that when the beam current was changed from 10 μA to 40 μA the beam size has changed while when the beam current was changed from 40 μA to 82 μA the beam size has not changed. Note that at the maximum CW beam average current of 82 μA (the limitation factor was the quantum efficiency of the photocathode) no measurable beam loss was observed. One can consider the fact that we could run a CW electron beam with an average current of 82 μA, have the ODR radiator 1 mm away from the beam, and not see detectable beam loss as a milestone for the ODR based diagnostics development.

We would like to discuss two more observations we made during the ODR measurements. When measuring the ODR patterns with the horizontal polarizer inserted we were clearly observing the double lobe distributions. However the distributions we have observed were not symmetrical as the model predicts. One possible explanation for that can be a slightly misaligned polarizer. Maximum asymmetry seen in the data was 60 %. To cause such asymmetry in the measurements the horizontal polarizer would have to be misaligned by approximately 4.5 degrees. Another cause for the asymmetry can be a background intensity distribution which is not symmetric relative to the beam position at the ODR radiator. We are planning to install one single polarizer on an insertable rotation stage and make more measurements to clarify this observation.

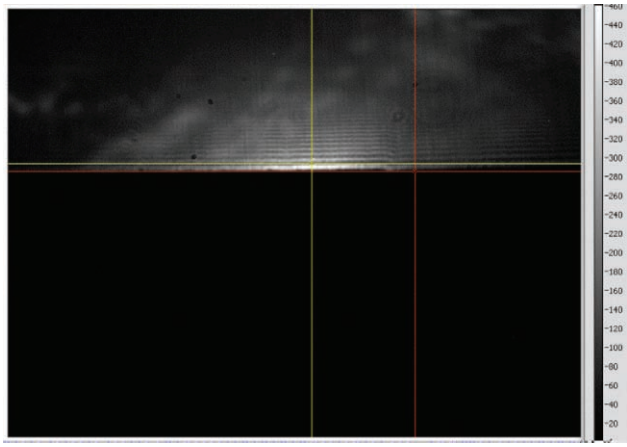

Figure 7: Layout of papers.

Another interesting effect we have seen during the measurements is demonstrated in Fig. 7. Most of the ODR patterns we have measured are modulated by diffraction fringes. The diffraction fringes are parallel to the edge of the radiator and look very similar to the classical diffraction pattern from a straight edge observed in the far-field. The fringes are most visible at 550 nm and 650 nm and considerably less visible at 450 nm and 650 nm. The data evaluation aimed at understanding this phenomena is in progress and in this paper we do not present its complete explanation. We would like to point out, however, than a coherent wavefront is required to generate the diffraction on the edge. We suggest that due to the fact the transverse field size is $\sim \gamma \cdot \lambda\!\!\!^{-}$ and is much bigger

in our measurements than the transverse beam size, the phase difference between the fields of different electrons across the beam is very small which result in transverse coherence of the virtual photons originated from the electron beam. Another aspect which needs to be mentioned here is the fact that the formation length $\sim \lambda \cdot \gamma^2$ for the optical radiation in our experiments spans from 32.4 m at 400 nm through 60.8 m at 750 nm. The formation length is considerably smaller than the distance between the ODR radiator and the upstream dipole which is 8 m. That makes the synchrotron and edge radiation from the dipole somewhat coherent with the ODR since the electron brings the phase information with it from the dipole to the ODR radiator. To our knowledge this effect has not been predicted by models and has not been observed in experiments before. The effect influences the data analysis making it less accurate and needs to be understood to make the data analysis and the beam size reconstruction from the ODR patterns more accurate and reliable.

CONCLUSION

We have made measurements of the ODR patterns distribution using CEBAF CW electron beam at the beam energy of 4.5 GeV. The distributions were measured as a function of the beam size, wave length of the radiation and polarization of the radiation. We were able to run CW beam with an average current up to 82 μA with the ODR radiator edge placed 1.1 mm from the beam centroid, which was about ten times the vertical beam size. No measurable beam loss was detected at these conditions. That gives us the reason to think that the ODR based non-intercepting beam size diagnostics will be applicable to the CEBAF beam. It was demonstrated that at the above mentioned beam parameters the ODR can be used for non-intercepting beam size monitoring when the beam size varies in the range from 150 μm through 350 μm. We also observe significant background in the ODR data that affects the data analysis and is considered to be the main reason for the ~ 20 % discrepancy between the model and the experiment. As a next step we are planning to improve the experimental setup mainly to mitigate or completely eliminate the background in the ODR data. With the improved setup we are planning to investigate in more detail the applicability range of the ODR based beam size measurements and use the ODR station in the CEBAF Hall-A beam line for non-intercepting beam size measurements.

ACKNOWLEDGMENTS

Authors would like to thank their colleague Lia Merminga, George Neil, Gwyn Williams and Steve Benson for stimulating and useful discussions. This work is supported by the U.S. Department of Energy under contract number DE-AC05-06OR23177.

REFERENCES

[1] M. L. Ter-Mikaelian, High Energy Electromagnetic Processes in Condensed Media (Wiley/Interscience, New York, 1972)

[2] D.W. Rule and R. B. Fiorito, "The Use of Transition Radiation as a Diagnostic for Intense Beams", NSWC Tech. Report 84-134, July 1984

[3] D.W. Rule , R. B. Fiorito and W.D. Kimura, Proc. of BIW , 7th Workshop, AIP Conf. Proc 390 pp. 51-517 (1997)

[4] M. Castellano, Nucl. Instrum. Methods Phys. Res., Sect. A394, 275 (1997).

[5] A. P. Potylitsyn, Nucl. Instrum. Methods Phys. Res., Sect. B 145, 169 (1998).

[6] P. Karataev et al., Phys. Rev. Lett. 93, 244802 (2004)

[7] A. H. Lumpkin, W. J. Berg, N. S. Sereno, D. W. Rule, and C.-Y. Yao, Phys. Rev. ST Accel. Beams 10, 022802 (2007)

[8] E. Chiadroni, et al., Proceedings of PAC07, Albuquerque, New Mexico, USA, p. 3982

[9] C.R. Leeman, D.R. Douglas, and G.A. Kraft, Annu. Rev. Nucl. Part. Sci. 51, 413-50 (2001).

[10] A. H. Lumpkin et al., Proceedings of PAC07, Albuquerque, New Mexico, USA, p. 4381

COMMISSIONING OF SOLEIL FAST ORBIT FEEDBACK SYSTEM

N. Hubert, L. Cassinari, J-C. Denard, J-M. Filhol, N. Leclercq, A. Nadji, L. Nadolski, D. Pédeau;
Synchrotron SOLEIL, Gif-sur-Yvette, FRANCE

Abstract

The SOLEIL Fast Orbit Feedback system has been integrated in the BPM electronics, using the FPGA resources of the LIBERA modules. On top of their position measurement, the FPGAs compute the orbit correction and drive the power-supplies of the 48 dedicated air coil correctors. Position data are distributed all over the ring by a dedicated network connecting the 120 BPMs modules together. The correction rate is 10 kHz and is applied with low latency. Even if at almost all the source points, the high frequency stability specifications have already been achieved thanks to great care in the design of the machine, remaining vibrations are still observed in the 46-54 Hz band and during the changes in gap and phase of some insertion devices. Those perturbations can be efficiently damped by the Fast Orbit Feedback system. While the BPM system has been operational for some time, the Fast Orbit Feedback system is presently in its commissioning phase. The design and first results of the latter are reported.

INTRODUCTION

The SOLEIL BPM system has been in operation from the start of the Storage Ring commissioning in May 2006 [1, 2]. There are 120 BPMs, 72 are located in the arcs and there is one at each end of the 24 straight sections. The electronic processing has been defined and designed by SOLEIL and Instrumentation Technologies, a company in Slovenia [3]. The BPM electronics consists of one crate per BPM called "LIBERA". It is plugged into the 50 Hz mains and the Ethernet control network. It has been designed from the start for supporting a Fast Orbit Feedback embedded into the BPM processing FPGA. The BPM digital electronics has subsequently equipped most of the new storage rings around the world.

The stability of the beamline at the source points are required to be better than $1/10^{th}$ the rms size and angular divergence of the photon beam.

Photon Source	$\sigma_x/10$ µm	$\sigma'_x/10$ µrad	$\sigma_z/10$ µm	$\sigma'_z/10$ µrad
Bending magnets (≤ 35 keV)	N/A	N/A	1.5	5.3
Hard X-ray IDs (≤ 18 keV)	39	1.5	0.55	0.51
Soft X-ray IDs (≤ 1.6 keV)	18.3	3.4	0.65	1.6
UV IDs (≤ 0.04 keV)	32	4.6	6	4.2

Table 1: Beam stability requirements at source points with ε_H = 3.75 nm.rad and K = 0.4%

These parameters for the main beamline types depend on their location on the machine and on their maximum photon energy. They are shown in table 1.

SLOW AND FAST ORBIT FEEDBACK

A Slow Orbit Feedback (SOFB) based on an SVD algorithm with the 120 BPMs and 56 correctors in each plane is operational since May 2007 [2].

Initially, the FOFB was mainly meant to suppress the residual vibrations at frequencies higher than 1 Hz; the slow drifts, below 0.01 Hz being corrected by the SOFB. The SOFB acts on 56 correctors built in the sextupoles. One of the technological innovations at SOLEIL is the extensive use of NEG coated aluminium vacuum chambers in the arcs and straight sections. It improves the vacuum pressure and beam lifetime without increasing the broadband wall impedance. However, the eddy currents in aluminium suppress the magnetic field over few Hz in the vacuum chamber.

In each plane the FOFB acts on 48 fast air correctors that are installed around stainless steel BPM bellows, at the ends of the 24 straight sections. The correctors can yield orbit kicks in the ±20 µrad range, which is much less than that of the slow correctors (±0.8 mrad in H and ±0.6 mrad in V, values necessary for the closed orbit distortion), but its cut-off frequency due to eddy currents is ≥ 2.5 kHz. The power-supplies can provide currents in the ±10A range within ±24V voltage limits.

The Slow and the Fast Orbit Feedback systems do not use the same set of correctors, which is not a problem if the two systems are kept well separated by functioning in different frequency ranges. Actually, we found that the FOFB is very efficient at suppressing two unexpected sources of orbit perturbation: i) use of the overhead cranes in the experimental hall during photon beam delivery ii) imperfections of the feedforward correction process during undulator gap changes. At the moment, the feedforward steerers correct the orbit very well before and after gap changes, but not well enough during the transitions. The cause of the problem is currently being addressed (better synchronization between the four feedforward correctors and smooth interpolation between consecutive points of the correction tables). It should be corrected by the end of the year, but in the mean time, the FOFB would greatly help.

The tests conducted so far were aimed at demonstrating that the FOFB can stabilize the beam position alone (without SOFB) for about 8 hours without saturating the air correctors.

BEAM NOISE SPECTRUM

We identify three different ranges in the beam spectrum: i) the "high frequency" noise from 1 to 150 Hz, ii) the beam movements due to crane operation and

undulator gap changes in the 0.01 to 1 Hz bandwidth, and iii) the slow drifts, mainly from thermal effects, from DC to 0.01 Hz.

The high frequency noise without orbit feedback is shown in figure 1. The integrated noise amounts to 3 µm in horizontal and 1 µm in vertical. The natural beam stability is within specifications (see table 1) in horizontal but needs to be improved by a factor of two in vertical. The main contribution to the vertical beam noise is at 50 Hz, the frequency of the mains. The lines at 46 Hz and 54 Hz correspond to the first eigen modes of the girders.

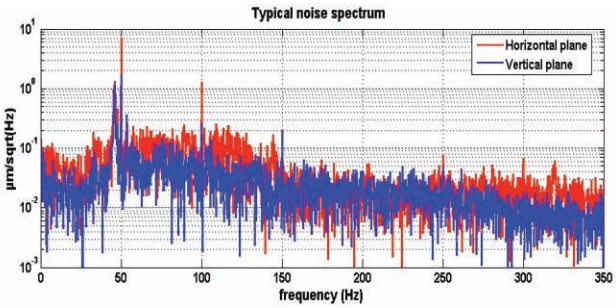

Figure 1: Natural beam spectrum without feedback. Most of the beam noise is below 150 Hz.

The beam movements during crane operation or gap changes can reach up to 10 μm in vertical and need to be damped in both H and V planes. The slow drifts, after machine warm-up, are in the 20 μm range over an 8 hour shift.

DATA DISTRIBUTION

In order to have a global system, the position data from each BPM module has to be distributed to all the points where the processing is done. As the processing is distributed in the BPM FPGAs, we have implemented a communication system between them. This is done with a dedicated network, linking all BPM modules together. Two different kinds of link are used:

- Copper cables links are used for the small length connections inside each cell, (Fig. 2).
- Multimode optics fiber links are used for 30 meter connections between cells, (Fig 2 and 3).

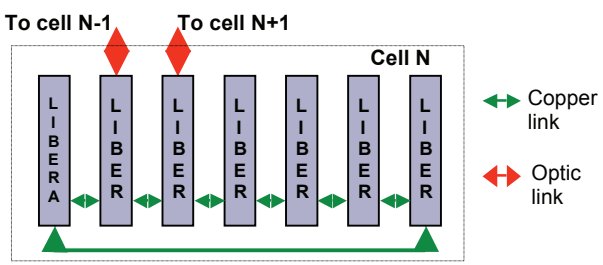

Figure 2: Topology of the dedicated network. In one cell, LIBERA modules are connected with a 'ring' topology with copper links. Two modules per cell are connected to neighbour cells with optic fibers.

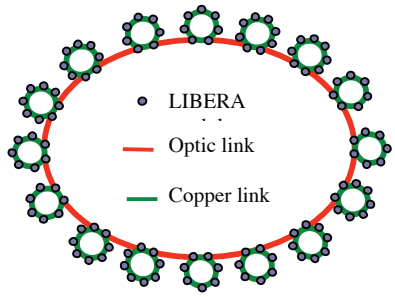

Figure 3: Topology of the dedicated network.

Data distribution all over the ring is controlled by a Communication Controller (CC) implemented in the FPGA of every BPM module. This CC has been designed by Diamond Light Source [4]. At the beginning of each time frame, the CC reads the data provided by its own BPM, and sends it over the network to its neighbours. Then, new incoming data from other BPMs are stored and forwarded to all the neighbours. In order to avoid network overflow, incoming data that is received for a second time is simply discarded. The main advantage of this protocol is that it fits any kind of topology for the dedicated network. The topology needs to be optimised for minimizing the number of BPMs a frame has to go through. With the present SOLEIL topology the data distribution process takes about 25 µs. The time-out for data distribution is configured to 60 µs in order to keep some margin in case of link failures.

DATA PROCESSING

FPGA Implementation

The FOFB algorithm has been fully integrated in the BPM modules FPGAs. On top of the processing for position measurement (provided by Instrumentation Technologies), we added our own Fast Feedback application. The coding has been done in VHDL (*Very high speed integrated circuit Hardware Description Language*) and simulated, before its integration into the FPGA. The application can be split into 5 main blocks (Fig. 4):

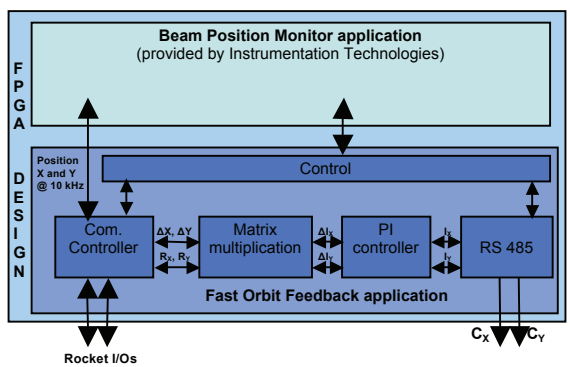

Figure 4: FPGA implementation.

• Communication Controller: This block allows the data distribution between BPM modules (see previous paragraph).

• Matrix Multiplication: To compute the correction this block has to perform 120 multiplications and additions for each plane. In order to save FPGA resources, multiplications are done serially, and one plane is computed after the other.
• PI Controller: In order to adjust the gain and the uncorrected error of the loop, we need a controller. The proportional part is applied offline when configuring the system, by multiplying the inversed response matrix by the appropriate coefficient. The integrative part is implemented in the FPGA as a simple integrator with an adjustable coefficient (Eq. 1).

$$I_N = \Delta I_N + coeff * I_{N-1} \quad (1)$$

With:
I_N : The next corrector setting
ΔI_N: The matrix multiplication result
coeff: The integrative coefficient
I_{N-1}: The previous corrector setting
• RS 485: This block shapes and serializes the correction set-points before sending them to the power-supplies on a RS 485 link. The communication over this link is only one way, from BPM module to power-supply. Each frame is 22 bits long: 16 bits for data, 2 for parity and 4 for synchronization (Fig. 5). The transmission rate is 1.25 Mbits/s and the transmission delay is around 20 µs.

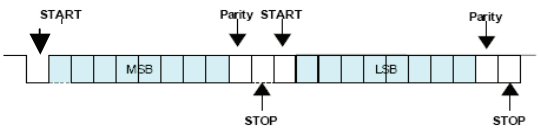

Figure 5: Communication protocol over the RS 485 link.

• Control: This block allows the control and the monitoring of the Fast Feedback Application. Each BPM module sends to the control system some statistics on the computed correction values for both planes (average, minimum, maximum). Those data are refreshed at 10 Hz.

Latency

The main part of the system latency is caused by the processing of the position data (BPM functionality). Time allowed for data distribution could be reduced by increasing the redundancy in the dedicated network (Table 2).

Position processing	190 µs
Data Distribution	60 µs
Matrix Multiplication	5 µs
PI Controller	1 µs
Serialization and transmission to Power Supply	20 µs
Total of FPGA delays	**~280 µs**
Power supply latency	20 µs
Eddy current in vacuum chamber	~60 µs
Total of delays	**~360 µs**

Table 2: Decomposition of the system latency

OPEN LOOP MEASURMENTS

Two series of open loop measurements have been performed.

Before implementing the algorithm, the whole electronics response was measured, from the power supply to the LIBERA outputs, thus including corrector, vacuum chamber transmission and beam response. This was done by applying a sweeping frequency signal on the power supply input and recording the resulting motion measured on the LIBERA output. The measured 3dB bandwidth is higher than 2 kHz in both planes (Fig. 6).

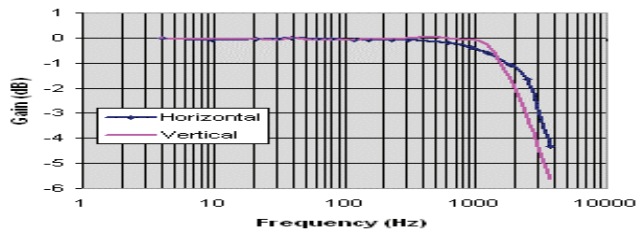

Figure 6: Bandwidth of the power supply + corrector + vacuum chamber + beam, measured on a BPM.

A second series of open loop measurements was performed during the commissioning with the whole open loop, including the computing delays in the FPGA. This was done by using an Agilent 35670A signal analyser equipped with two PR30A current probes, allowing to get amplitude as well as phase response. The 35670A source sweeping frequency signal was connected to the input of a voltage driven power supply;and the power supply output to the air-corrector. The corrector current was measured with a PR30A probe connected to the 35670A first input; meanwhile, the matrix output measured by the second probe was connected to the second input.

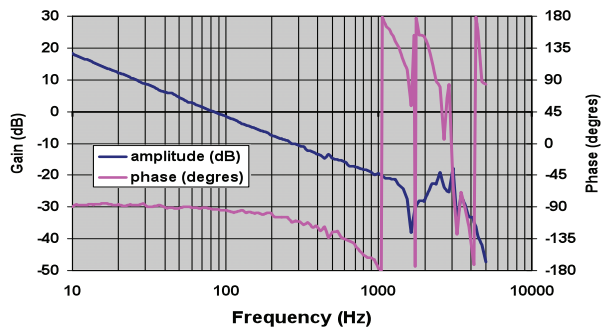

Figure 7: Open Loop Frequency Response (Horizontal plane with accumulator; 48x48 matrix 48 eigen values; gain=25).

The loop stability and the expected closed loop performance were deduced from these measurements and could be compared with the experimental behaviour of the feedback, and were found to be in good agreement (Fig. 7,8).

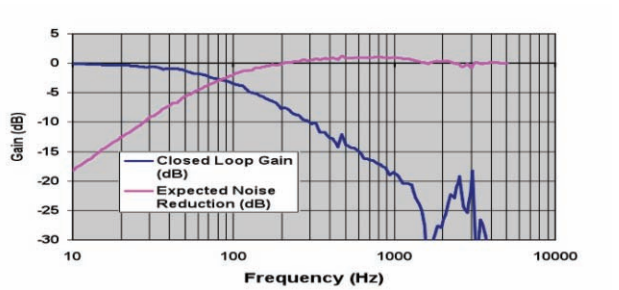

Figure 8: Expected Closed Loop Frequency Response (Horizontal plane with accumulator; 48x48 matrix 48 eigen values; gain=25).

COMMISSIONING

First tests of the SOLEIL Fast Orbit Feedback were started in December 2007 and are still currently in progress. The modularity of the system makes quite easy any change in configuration, allowing quick changes in gain, PI Controller coefficients, as well as the numbers of correctors, BPMs and matrix eigen values involved in the feedback loop. Up to now, ten 8-hour Machine shifts have been dedicated to these tests, allowing to solve a few bugs and to address several issues.

Bugs and issues

Among the bugs, a very simple (once solved), but quite disconcerting one was due to division of signed numbers. Because of encoding, the rounding of the division was to the lower nearest integer for positive numbers but also for negative ones (instead of higher nearest integer in this case). This lead to a non-zero mean value noise, which gave rise to diverging values when using accumulator for integration.

The other main issue during these first tests was communication reliability of the network. In a previous version of the network, all the LIBERAs were ordered in a serial (single ring) network, resulting in poor redundancy and long communication delays in case of link failures. This lead to large spikes (several hundreds of µm) on the orbit any time a communication problem was occurring (up to every few minutes in the worst cases). The new network scheme now implemented reduced the whole communication delay by a factor 2 when no communication hitch occurs (from 50 to 25µs), and allows to work even with a permanent open link.

Test set-up

During these test shifts, only 2 configurations were tested: 48 and 120 BPMs, both using 48 correctors.

The loop gain was optimized experimentally, and the experimental behaviour was compared with the expected performance deduced from the open loop measurements.

Up to now, tests were performed without the SOFB running, assuming that the Fast Orbit Feedback should be able to correct even DC components (drifts or crane displacement or slow moving insertion gap induced beam movements). In order to measure these effects, several tests were performed: i) comparing long time (several hours) orbit records with and without feedback, while changing insertion gaps and moving the cranes ii) frequency spectrum analysis on BPMs, and on the few X-BPMs currently available on the dipole beamlines.

EXPERIMENTAL RESULTS

The FOFB reduces the high frequency noise (1 to 100 Hz) within the σ/10 goal for all source points, especially in the case of the hard X-ray beamlines in the vertical plane (fig. 10). There is a strong positive effect up to 50 Hz, but with some noise addition above 100 Hz. Integrated noise is suppress by nearly a factor of two in the band 1-350 Hz.

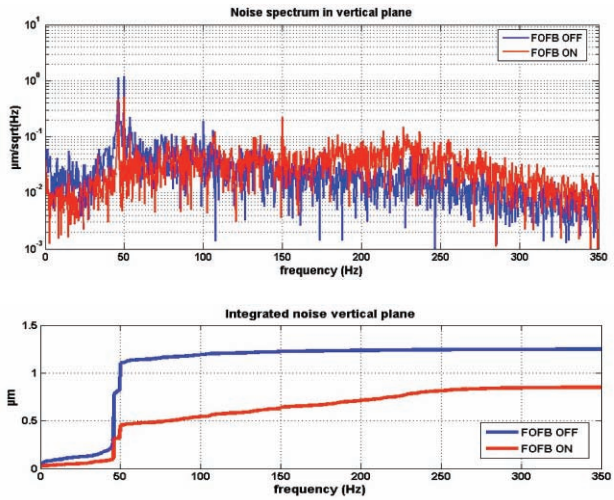

Figure 9: Vertical beam noise with and without feedback (external sensor).

In order to measure the effects in the 0.01-1Hz BW we have repeated 4 times the same transitions in gap and phase of some insertion devices with 4 configurations: no Orbit Feedback, SOFB ON, FOFB ON with 48 BPMs and FOFB ON with 120 BPMs.

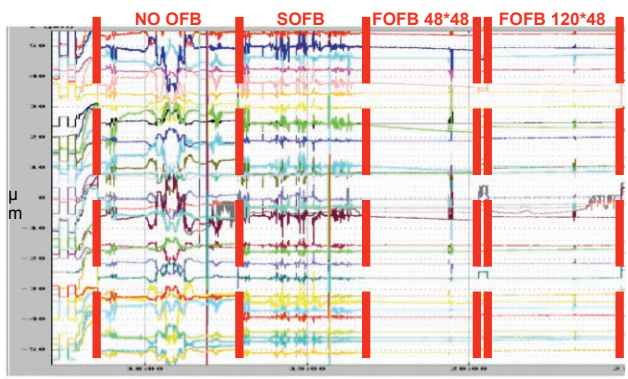

Figure 10: Good suppression of beam position perturbations during gap changes(0.01 Hz-1 Hz BW).

From table 3, the optimum configuration is 120 BPM x 48 correctors in the vertical plane in order to have an action on the bending magnet source points, but this is not an issue in the horizontal plane, and the 48 BPM x 48

corrector is better. The air-corrector strength after a few hours of operation remains relatively small which gives confidence for operation up to an 8-hour shift, between two injections.

Photon Source		ΔX µm	ΔX angle µrad	ΔZ µm	ΔZ angle µrad
Bending Magnet ≤ 35 keV	σ/10	N/A	N/A	1.5	5.3
	no FOFB 3.5h	4.5	11	17	1.6
	48x48 for 2h	1.5	0.9	4.1	0.6
	120x48for3h	0.2	0	0.3	0.1
Hard X-ray IDs	σ/10	39	1.5	0.55	0.52
	no FOFB 3.5h	15	1.5	3.2	1.6
	48x48 for 2h	0	0	0	0
	120x48for3h	0.3	0	0.3	0.1
Soft X-ray IDs	σ/10	18	3.4	0.65	1.6
	no FOFB 3.5h	10	2.5	5.8	1.6
	48x48 for 2h	0	0	0	0
	120x48for3h	0.5	0.1	0.5	0.1
UV ID	σ/10	32	4.6	6	4.2
	no FOFB 3.5h	12	0.5	4	0.3
	48x48 for 2h	0	0	0	0
	120x48for3h	0	0.1	0.6	0

Table 3: few-hour stability with FOFB, from DC to 0.01 Hz (slow drifts).

Some optimization is currently under progress on the number of eigen values selected for the SVD inversion. This leads to even more promising results (suppression by a factor of 3 of the integrated vertical noise in the 1-350 BW)

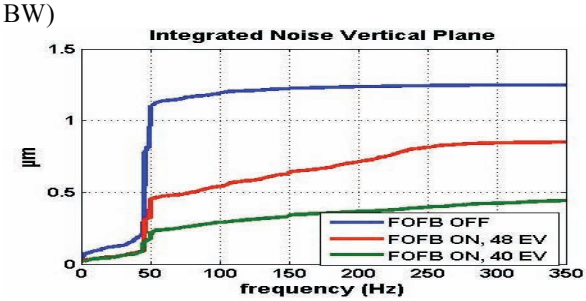

Figure 11: Optimization on the number of eigen values.

COMPATIBILITY WITH SOFB

As said previously, we have a different set of correctors for the Slow and the Fast Orbit Feedback systems. The Slow Orbit Feedback operates from DC to 0.05 Hz (limited by the latency of its power-supplies). At the moment, the Fast one is operating from DC to 100 Hz. With different correctors and a common operating frequency band, the 2 system will not be compatible.
Two options are still considered:

- The first option is to separate the operating frequency bands of each system. In this case, the FOFB 'area' will have to start at 0.1 Hz instead of DC. It has the main advantage to keep the two systems completely independent. But it will also create a frequency dead-band (from 0.05 Hz to 0.1 Hz) where beam movement will not be corrected at all (Fig. 11 a).
- The second option is to keep the Fast Orbit Feedback system working from DC. In this case, the Slow Feedback system will have to read the DC part of the current in the fast corrector and integrate it before applying its correction. The Slow System correction rate could be decrease as its main role would be mainly to relieve the fast power-supplies and correct the RF frequency. The two systems are no more independent and a reliable communication has to be implemented between them. The main advantage of this solution is to have a continuous frequency band where the beam movement can be suppressed (Fig. 11 b).

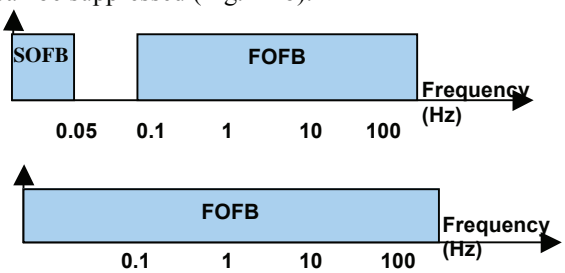

Figure 12: Two options: a) 2 independent systems with a dead-band, b) FOFB correcting from DC.

CONCLUSION

The Slow Orbit Feedback suppresses efficiently the slow drifts due to thermal effects, but has no significant effect on beam movements and vibrations faster than 0.05 Hz. The Fast Orbit Feedback corrects efficiently the latter and seems able to correct well enough the slow drifts. The initial idea of having the two feedback systems working simultaneously but separated in the frequency domain by a dead band may not work properly for suppressing the perturbations caused by the cranes and by the undulator gap changes. The perturbation spectrum is likely to cover the dead band and would not be suppressed. We are investigating the possibility of using the FOFB with an occasional relief of its DC correction by the Slow System.

The Fast Orbit Feedback system gives very promising results and is expected to be available for user operation in the coming months.

ACKNOWLEDGEMENTS

We thank I. Uzun and G. Rehm from Diamond Light Source and E. Plouviez from ESRF for their collaboration. We are also grateful to the Instrumentation Technology staff involved in the LIBERA project.

REFERENCES

[1] J-C. Denard, "Behavior of the BPM system during the first weeks of SOLEIL commissioning", EPAC'06.

[2] N. Hubert, "The SOLEIL BPM and Orbit Feedback Systems", DIPAC'07.

[3] A. Kosicek, "Libera Electron Beam Position Processor", PAC'05.

[4] I. S. Uzun, "Initial Design of the Fast Orbit Feedback System for Diamond Light Source", ICALEPS'05.

BEAM DIAGNOSTICS AT DAΦNE WITH FAST UNCOOLED IR DETECTORS

A. Bocci, A. Clozza, A. Drago, A. Grilli, A. Marcelli, M. Piccinini, A. Raco, R. Sorchetti,
INFN/LNF, Frascati, Italy
Lisa Gambicorti, INOA, Firenze, Italy
A. De Sio, E. Pace, Università degli Studi di Firenze, Firenze, Italy
J. Piotrowski, Vigo System Sa, Warsaw, Poland

Abstract

Bunch-by-bunch longitudinal diagnostics is a key issue of modern accelerators. To face up this challenging demand, tests of mid-IR compact uncooled photo-conductive HgCdTe detectors have been recently performed at DAΦNE. Different devices were used to monitor the emission of e^- bunches. The first experiments allowed recording of 2.7 ns long e^- bunches with a FWHM of a single pulse of about 600 ps. These results address the possibility to improve diagnostics at DAΦNE and to this purpose an exit port on a bending magnet of the positron ring has been set-up. An HV chamber, hosting a gold-coated plane mirror that collects and deflects the radiation through a ZnSe window, is the front-end of this port. After the window, a simple optical layout in air allows focusing IR radiation on different detectors. The instrumentation will allow comparison in the sub-ns time domain between the two rings and to identify and characterize bunch instabilities. Moreover, to improve performances tests of new photovoltaic detectors with sub-ns response times are in progress. We will briefly summarize the actual status of the 3+L experiment and will discuss future applications of fast IR photovoltaic detectors and the development of fast IR array detectors.

INTRODUCTION

Beam diagnostics is an essential component of a particle accelerator. All storage rings emit synchrotron light and different radiation energies can be used for beam diagnostics. Indeed, the synchrotron radiation emission covers a wide energy range from IR to X-ray energies with a pulsed structure that depends by the temporal characteristic of the stored beam. The radiation can be used to monitor the beam stability and to measure the longitudinal profiles of the accumulated particles. However, due to the time structure of the synchrotron radiation, to perform beam diagnostics fast detectors are required. At third generation synchrotron radiation sources useful devices for the diagnostics of accelerated particles need response times from the ns to the ps range while the future FEL sources need response time in the fs domain.

The main advantage of photon diagnostic is that it is a direct and non-destructive probe. Diagnostic based on synchrotron light is typically used for imaging and allows the measure of the beam cross section as well as the longitudinal structure such as the bunch length of stored particles. The determination of the bunch length is an important operational parameter of storage rings that allow monitoring the beam dynamics.

The main requirements of a beam diagnostic system could be: fast, at least in the sub-ns regime to guarantee the installation in all accelerators, compact and robust. However, it could be also easy to manage, possibly vacuum compatible and at low cost.

Standard beam diagnostic methods use a streak camera, an extremely fast photon detectors that takes an instantaneous image of the particles running along the orbit. Images of the temporal structure of a beam have resolution time of ~1 ps or below [1]. Streak cameras are powerful detectors whose principal drawback is the cost. Moreover, streak cameras are complex and fragile devices and usually are not used for permanent full-time beam diagnostics. As a consequence fast, cheaper and compact photon detectors may represent an important alternative for photon beam diagnostics. Photon devices are also easier to manage with respect to a streak camera. The availability of uncooled infrared devices optimized for the mid-IR range, based on HgCdTe alloy semiconductors, already now allow obtaining sub-ns response times [2]. These detectors can be used for fast detection of the intense synchrotron radiation IR sources and then for beam diagnostics. Preliminary measurements of the pulsed synchrotron light emission have been performed with uncooled IR photo-conductive detectors at DAΦNE, the e^+-e^- collider of the LNF laboratory of the Istituto Nazionale di Fisica Nucleare (INFN), achieving a resolution time of about few hundred of picoseconds [3,4]. In this contribution we will present and discuss preliminary results obtained with such photo-conductive detector.

Experiments have been performed at SINBAD (Synchrotron Infrared Beamline At DAΦNE), the IR beamline operational at Frascati since 2001. Moreover, to improve the DA_NE diagnostics a new experiment, 3+L (*Time Resolved Positron Light Emission*), funded by INFN, started the installation at the exit of one of the bending magnet of the DAΦNE positron ring. The installation, when completed, will allow monitoring the positron bunch lengths at DAΦNE with the main aim to study and characterize the instabilities of the positron beam and in order to possibly increase the positron current and the collider luminosity.

A short description of the 3+L experiment, the optical simulations and the actual status of the experiment will be

presented. Finally we will discuss how to improve the time resolution using faster IR photovoltaic detectors and how to perform transverse diagnostics with new IR array detectors working at room temperature.

MEASUREMENTS OF THE ELECTRON BEAM ON THE SINBAD BEAMLINE

Preliminary measurements of the pulsed signal of the electron beam have been carried out at DAΦNE with uncooled IR detectors. Experiments have been performed using the IR emission collected at the end of the optical system of SINBAD [5]. As showed in Fig. 1 the IR beam is extracted from a bending magnet located in the external arc section of the electron ring. DAΦNE is the Frascati e^+/e^- collider, with a center of mass energy of 1.02 GeV, designed to operate at high current (>2 A) and up to 120 bunches [6]. Different bunch patterns can be stored at DAΦNE but the minimum bunch distance is 2.7 ns with a maximum achieved single-bunch current of ~20 mA. Bunches have a quasi-Gaussian shape with a length in the range of 100 - 300 ps FWHM. For the first experiments we used a single-element uncooled photo-detector trying to resolve the time structure of the IR light emission. The detector has been placed at the focus of the last optical mirror just at the entrance slit of the interferometer.
The emission of 105 bunches and the gap between the last and the first bunch was measured with an average current of ~3 mA per bunch. The photo-conductive detector was biased through a bias tee with a current of about 20 mA. The output signal was amplified by a voltage amplifier with a bandwidth of 2.5 GHz and a gain of ~40 dB. Acquisitions have been performed with a scope (model Tektronix TDS 820) with a bandwidth of 6 GHz. The average response time of the detector was of ~600 ps and the rise time of the signal emitted by a single-electron bunch was ~400 ps. The amplified signal of the IR detector has been used also to perfom measurements of the longitudinal feedback of the electron ring using a spectrum analyzer. In the multibunch mode, the electron synchrotron frequency has been measured as well as the correct longitudinal feedback behaviour [4].

POSITRON BEAM DIAGNOSTICS: THE 3+L EXPERIMENT

To test and characterize a simple set up based on such uncooled IR detectors and with the objective to perform bunch by bunch beam diagnostics on the positron ring, a compact experimental installation was set up inside the DAΦNE hall in the framework of the 3+L experiment. In Fig. 1 is showed the layout of the DAΦNE complex and the location of the 3+L exit port. The experimental system is placed after the IP2 interaction region collecting the light from a bending magnet having a critical energy of 273 eV, on the only available exit port of the positron ring.

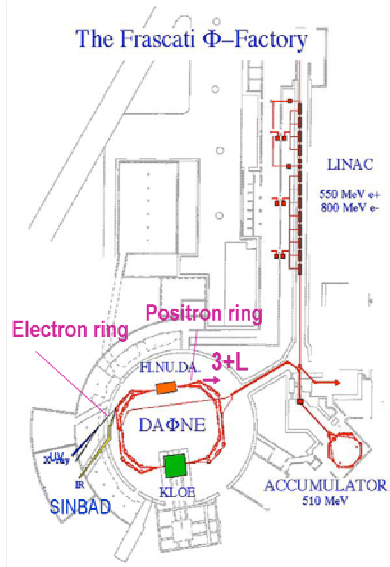

Figure 1 : Layout of the DAΦNE collider. The 3+L exit port inside the hall and of the SINBAD beamline are also showed.

The experiment under installation on this exit port is outlined in Fig. 2. It consists in a simple front-end where a HV chamber hosts a gold-coated plane mirror that collects and deflects the IR radiation through a ZnSe window. This latter window allows transmission of IR radiation between 0.6 to 12 μm. After the window, a simple optical layout composed by 5 mirrors in air will focus the radiation on IR detectors as illustrated in Fig. 2.

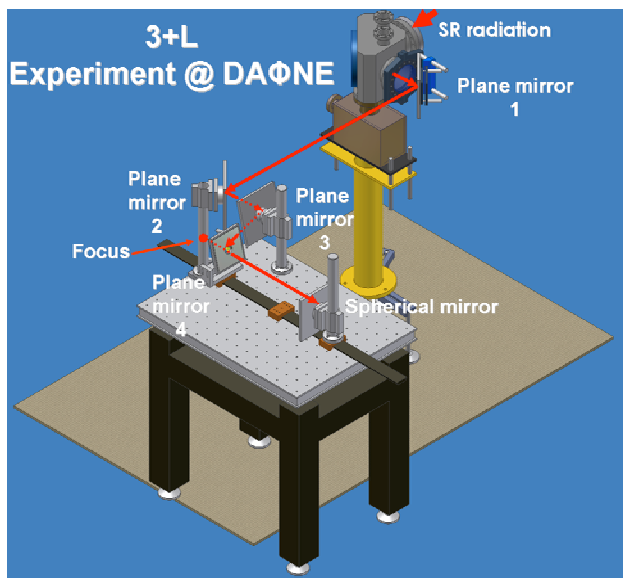

Figure 2 : CAD drawing of the optical system of the 3+L experiment. The IR beam path is outlined by red lines showing the last mirror with the central hole.

Ray tracing simulations have been performed to design and optimize the optical system. The optical layout is based on four plane mirrors that transport 60 x 20 mrad^2 of the emitted radiation to the optical table where a spherical mirror will focus the radiation on the IR detector.

Different detectors could be aligned and tested thanks to a motorized and remotely controlled xyz stages. The remotely controlled scope connected to a PC by a GPIB I/O controller will be used to collect data. A dedicated software package for acquisition has been developed under the Labview platform.

To optimize the optical system and to compare the measured intensity of the IR source we performed simulations at the wavelength of 10 μm with the SRW software package [7]. In particular, we calculated the intensity and the distribution of the vertical and horizontal intensity of the IR synchrotron radiation source at the exit port before the first gold coated mirror installed inside the HV chamber.

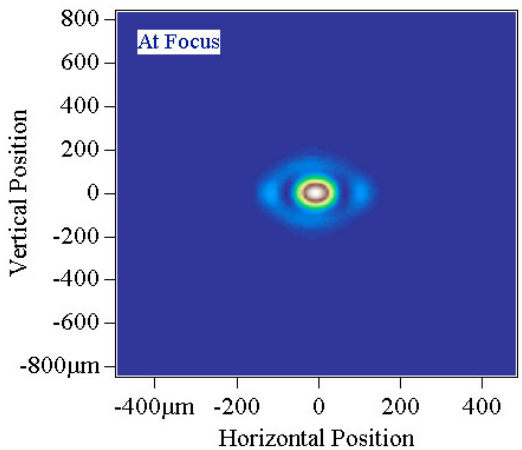

Figure 3 : The spot size at 10 μm simulated at the focus of the optical system outlined in Fig. 2.

To calculate the flux of the source at the focus of the optical system we performed different simulations. To characterize the power of the source at the exit of the window with a calibrated NIST power meter we have also performed preliminary measurements. Data have been collected with the power-meter model Melles Griot 13 PEM 001/J with different IR filters in the range 5-20 μm. The power of the source measured after the first reflection on the first mirror of the optical system is ~0.08 mW. A comparison between the measurements, the simulations and the calculated data is now in progress.
From simulations we obtain that more than 50 % of the energy of the source at the exit port, in the range 0.6-10 μm is contained inside a 400 x 400 micron^2 spot at the focus of the optical system. The simulated spot size at 10 μm is showed in Fig. 3.

When the optical system will be installed and aligned a measurement of the power available at the focus of the beam will allow a reliable evaluation of the beam loss of the mirror layout.

When completed, the main goal of the 3+L experimental apparatus will be the systematic acquisition of the positron bunch profiles in order to identify with a real-time method beam instabilities and to improve the existing DAΦNE diagnostics on the positron ring. Positron bunch instabilities have been observed at DAΦNE and actually limit the maximum available current to ~1.3 A. These instabilities have been associated to the occurrence of e^- cloud effect inside the pipe [8,9]. Detailed and simultaneous measurements and comparison of bunch lengths in both electron and positron rings by fast photon detectors could be very helpful to characterize these phenomena, not only to improve the DAΦNE performances but also to shed light on the origin of the instabilities. We will try also to understand the possible role of e^- cloud effects and how it may affect the maximum current in the DAΦNE positron ring. In conclusion, this optical diagnostics approach could be important to increase the accumulated current in the DAΦNE e^+ ring and consequently the collider luminosity.

FUTURE APPLICATIONS

New photo-voltaic IR detectors operating at near room temperature (from 300 K to 205 K temperature) with faster response time will be also test to further improve longitudinal beam diagnostics. The response time of such devices is of the order of 100 ps or lower. Also these devices are based on HgCdTe multilayer heterostructures grown by MOCVD on (211) and (111) GaAs substrates [10,11]. Preliminary characterization of these photo-voltaic devices has been performed at SINBAD with success but recently additional tests were performed and analysis is in progress.

Finally a fast IR array detector has been developed in collaboration with the VIGO SA [3]. The array showed in Fig. 4 is a customized uncooled IR photoconductive matrix constituted by 32x2 pixels. The size of each single pixel is about 50x50 _m and their response time is about 500 ps. A first experimental characterization of the array is planned on the SINBAD beamline after the completion of the electronics that is foreseen before summer.

With such device a bunch by bunch imaging of the IR source and investigations of the transverse bunch instabilities will be also possible.

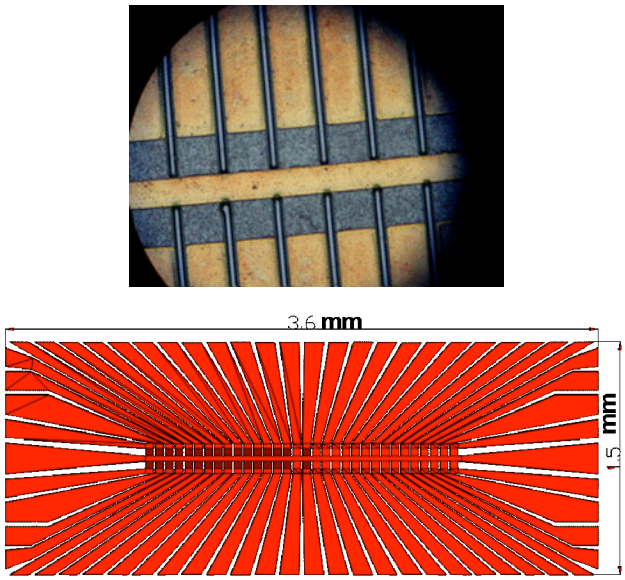

Figure 4 : Top: a small detail of the IR photoconductive array detector. Bottom: layout of the array showing its real dimension.

CONCLUSIONS

A new method to perform bunch-by-bunch longitudinal and transverse measurements is under test at the DA_NE collider. To monitor the bunch profile on both rings of this low energy and high current collider this optical method employs fast IR devices. The IR photo-conductive or photo-voltaic devices we use are made by MCT semiconductors and work at near room temperature. They are fast, robust, vacuum compatible, easy to manage and in particular are available at much lower cost if compared with fast alternative devices such as streak-cameras.

Measurements performed at DAΦNE at SINBAD beamline with uncooled photo-conductive detectors looking at the time structure of the electron bunches showed a sub-ns response time. To improve beam diagnostics on the positron ring a novel experiment is under installation at the exit port of one of the bending magnet of the positron ring. The instrumentation will be used to monitor the bunch profiles of the stored positrons, i.e., measurements of bunch-by-bunch lengths and to identify and characterize positron beam instabilities. Data could be useful to increase the current on the e^+ ring and the collider luminosity. Future foreseen applications of the technology are based on faster photo-voltaic devices with <100 ps response time and IR uncooled array detectors to achieve bunch by bunch imaging of the source and to investigate simultaneously transverse bunches instabilities on the DAΦNE rings. A first prototype made by 32x2 pixels each 50x50 μm^2 will be soon characterized on the SINBAD beamline.

ACKNOWLEDGMENTS

Special thanks are due to the DAΦNE accelerator group for running dedicated beamtime at the 3+L experiment, to M. Pietropaoli and G. Viviani for the technical assistance in the DAFNE-Light laboratory, to M.A. Frani for the support on the software development, to G. Cinque for fruitful discussions and support with the SRW SW package.

REFERENCES

[1] B.K.Scheidt,"Review of Streak Cameras for Accelerators: Features, Applications and Results", EPAC2000, Vienna, 2000 http://accelconf.web.cern.ch/AccelConf/e00/PAPERS/WEYF202.pdf

[2] J. Piotrowski, A. Rogalski, Infrared Physics & Technology 46 (2004) 115–131.

[3] A. Bocci et al., Nucl. Instr. Meth. Phys. Res. A., 580, 1 (2007), 190-193.

[4] A. Bocci et al., "Bunch-by-bunch longitudinal diagnostics at DAΦNE by IR light", DIPAC'07, Venice, May 2007, WEPB29, http://felino.elettra.trieste.it/papers/WEPB29.pdf.

[5] M. Cestelli Guidi et al., Jour. Opt. Soc. Amer. A22, (2005), 2810.

[6] A. Drago et al., Proc. PAC2003, Portland, Oregon, (2003).

[7] O. Chubar and P. Elleaume, Proceedings EPAC98 1998, 1177-1179.

[8] A. Drago and M. Zobov, Particle Accelerator Conference (PAC2005), Knoxville, Tennessee, USA - May 16-20, 2005.

[9] A. Drago, C. Vaccarezza, M. Zobov: "Analysis of Mechanisms Driving the Horizontal Instability in the DAFNE Positron Ring", G-67, 25/5/2006.

[10] J. Piotrowski and A. Piotrowski, Proc. SPIE 5957 (2005) 117.

[11] A. Piotrowski et al., Proceedings of the SPIE, Volume 6542, (2007) 65421B.

DIGITAL SIGNAL PROCESSING USING FIELD PROGRAMMABLE GATE ARRAYS

J. Serrano, CERN, Geneva, Switzerland

Abstract

This paper presents an introduction to digital hardware design using Field Programmable Gate Arrays (FPGAs). After a historical introduction and a quick overview of digital design, the internal structure of a generic FPGA is discussed. Then we describe the design flow, i.e. the steps needed to go from design idea to actual working hardware. Digital signal processing is an important area where FPGAs have found many applications in recent years. Therefore a complete chapter is devoted to this subject. The paper finishes with a discussion of important peripheral concepts which are essential for success in any project involving FPGAs.

HISTORICAL INTRODUCTION

Digital electronics is concerned with circuits which represent information using a finite set of output states [1]. Most of the applications use in fact just two states, which are often labeled '0' and '1'. Behind this choice is the fact that the whole Boolean formalism becomes then available for the solution of logic problems, and also that arithmetic using binary representations of numbers is a very mature field.

Different mappings between the two states and the corresponding output voltages or currents define different logic families. For example, the Transistor-Transistor Logic (TTL) family defines an output as logic '1' if its voltage is above a certain threshold (typically 2.4 V). For the same family, if we set the input threshold for logic '1' as 2 V, we will have a margin of 0.4 V which will allow us to interconnect TTL chips inside a design without the risk of misinterpretation of logic states. This complete preservation of information even in the presence of moderate amounts of noise is what has driven a steady shift of paradigm from analogue to digital in many applications. Here we see as well another reason for the choice of binary logic: from a purely electrical point of view, having only two different values for the voltages or currents used to represent states is the safest choice in terms of design margins.

Historically, TTL chips from the 74 series fuelled an initial wave of digital system designs in the 1970s. From this seed, we will focus on the separate branches that evolved to satisfy the demand for programmability of different logic functions. By programmability, we mean the ability of a designer to affect the logic behavior of a chip after it has been produced in the factory.

A first improvement in the direction of programmability came with the introduction of Gate Arrays, which were nothing else than a chip filled with NAND gates that the designer could interconnect as needed to generate any logic function he desired. This interconnection had to happen at the chip design stage, i.e. before production, but it was already a convenient improvement over designing everything from scratch. We have to wait until the introduction of Programmable Logic Arrays (PLAs) in the 1980s to have a really programmable solution. These were two-level AND-OR structures with user-programmable connections. Programmable Array Logic (PAL) devices were an improvement in performance and cost over the PLA structure. Today, these devices are collectively called Programmable Logic Devices (PLDs).

The next stage in sophistication resulted in Complex PLDs (CPLDs), which were nothing else than a collection of multiple PLDs with programmable interconnections. FPGAs, in turn, contain a much larger number of simpler blocks with the attendant increase in interconnect logic, which in fact dominates the entire chip.

BASICS OF DIGITAL DESIGN

A typical logic design inside an FPGA is made of combinatorial logic blocks sandwiched in between arrays of flip-flops, as depicted in Fig. 1. A combinatorial block is any digital sub-circuit in which the current state of the outputs only depends, within the electrical propagation time, on the current state of the inputs. To this group belong all the well known basic logic functions such as the two-input AND, OR and any combination of them. It should be noted, that logic functions of arbitrary complexity can be derived from these basic blocks. Multiplexers, encoders and decoders are all examples of combinatorial blocks. The input in Fig. 1 might be made of many bits. The circuit is also supplied with a clock, which is a simple square wave oscillating at a certain fixed frequency. The two flip-flops in the circuit, which might be flip-flop blocks in the case of a multi-bit input, are fed with the same clock and propagate the signals from their D inputs to their Q outputs every time there is a rising edge in the clock signal. Apart from that very specific instant in time, D is disconnected from Q.

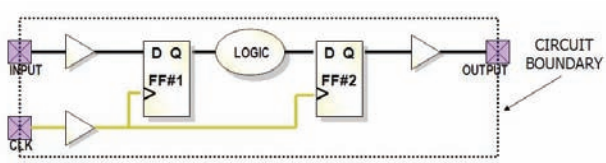

Fig. 1: A typical digital design

The structure of the circuit is thus very simple, and its application as a template covers the vast majority of digital design requirements in standard applications, such

as the control of particle accelerators. The designer only needs to ensure that the worst-case propagation delay between any of the inputs to the combinatorial logic block and any of its outputs is less than one clock period. If that condition is satisfied, the inputs to the second stage of flip-flops will be stable by the time the next clock edge reaches them. As we shall see later, the process of ensuring this timing closure is nowadays automated, so the designer need only be concerned with the specification of the logic behavior of the circuit.

The main merit of this design strategy, called synchronous design, is that the analysis of the possible timing failures and race conditions is greatly simplified. One might design otherwise, feeding for example the clock input of a flip-flop from the output of a combinatorial clock, in what is called a 'gated clock' circuit, and that design might give good results during simulation. But then, slight changes in the different delays of the signals might result in circuit malfunction. Slight changes of delays in the synchronous design paradigm can be easily accommodated by taking some safety margin in the maximum allowed time for any combinatorial signal path. This simple recipe contrasts with the 'many-body problem' of examining effects of delay changes in asynchronous designs.

FPGA STRUCTURE

A typical modern FPGA (see Fig. 2) provides the designer with programmable logic blocks that contain the pool of combinatorial blocks and flip-flops to be used in the design.

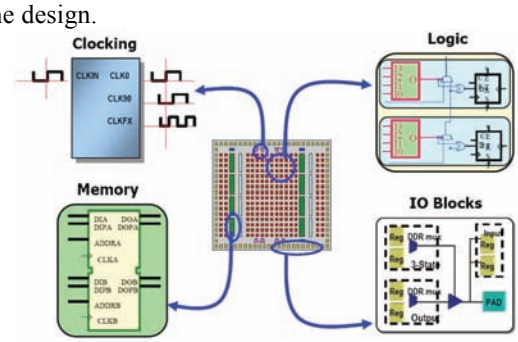

Fig. 2: Internal structure of a generic FPGA (courtesy Xilinx, Inc.)

In addition, vendors acknowledge the fact that logic is often used in conjunction with memory, and typically include variable amounts of static Random Access Memory (RAM) inside their chips. Clock conditioning has also become commonplace, and support in the form of Delay Locked Loops (DLLs) and Phase Locked Loops (PLLs) is also provided inside the same silicon chip. Finally, an FPGA chip does not lead a solitary life isolated from the rest of the world. It needs to be easily interfaced to other chips or external signals. In order to make this interfacing easier, FPGA vendors have invested a great deal of effort in enhancing the flexibility of the input/output blocks behind the chip pads. Each pad can serve as an input, an output, or both. The list of electrical standards supported is extensive, and novel techniques for maximizing bandwidth, such as clocking data in using both edges of the clock, are widely supported.

All the components shown in Fig. 2, however, typically account for less than 20% of the silicon inside an FPGA chip. What is not shown is the large amounts of programmable interconnect and the auxiliary circuits which 'program' the generic blocks to become a well-defined piece of logic. This silicon inefficiency is the price to pay for programmability, and is also the reason why FPGAs have traditionally been more successful in high-end, low-volume applications in the past, with Application Specific Integrated Circuits (ASICs) taking a leading role for high-volume applications. With Moore's law, however, the line between high-end and low-end applications is continuously shifting, and FPGAs are more and more used in domains which used to be dominated by ASICs and Digital Signal Processors (DSPs).

To overcome the silicon inefficiency problem, FPGA vendors often include hardwired Intellectual Property (IP) cores inside the chips for functions identified as recurrent in many designs. These non-programmable blocks include general purpose processors, high speed serial interfaces, arithmetic blocks and Ethernet Medium Access Control (MAC) units.

DESIGN FLOWS

The designer facing a design problem must go through a series of steps between initial ideas and final hardware. This series of steps is commonly referred to as the 'design flow'. First, after all the requirements have been spelled out, a proper digital design phase must be carried out. It should be stressed that the tools supplied by the different FPGA vendors to target their chips do not help the designer in this phase. They only enter the scene once the designer is ready to translate a given design into working hardware.

The most common flow nowadays used in the design of FPGAs involves the following subsequent phases:

- Design entry. This step consists in transforming the design ideas into some form of computerized representation. This is most commonly accomplished using Hardware Description Languages (HDLs). The two most popular HDLs are Verilog and the Very High Speed Integrated Circuit HDL (VHDL) [2]. It should be noted that an HDL, as its name implies, is only a tool to describe a design that pre-existed in the mind, notes and sketches of a designer. It is not a tool to design electronic circuits. Another point to note is that HDLs differ from conventional software programming languages in the sense that they don't support the concept of sequential execution of statements in the code. This is easy to understand if one considers the alternative schematic representation of an HDL file: what one sees in the upper

part of the schematic cannot be said to happen before or after what one sees in the lower part.

- Synthesis. The synthesis tool receives HDL and a choice of FPGA vendor and model. From these two pieces of information, it generates a netlist which uses the primitives proposed by the vendor in order to satisfy the logic behavior specified in the HDL files. Most synthesis tools go through additional steps such as logic optimization, register load balancing and other techniques to enhance timing performance, so the resulting netlist can be regarded as a very efficient implementation of the HDL design.
- Place & route. The placer takes the synthesized netlist and chooses a place for each of the primitives inside the chip. The router's task is then to interconnect all these primitives together satisfying the timing constraints. The most obvious constraint for a design is the frequency of the system clock, but there are more involved constraints one can impose on a design using the software packages supported by the vendors.
- Bit stream generation. FPGAs are typically configured at power-up time from some sort of external permanent storage device, typically a Flash memory. Once the place and route process is finished, the resulting choices for the configuration of each programmable element in the FPGA chip, be it logic or interconnect, must be stored in a file to program the Flash.

Of these four phases, only the first one is human labor intensive. Somebody has to type in the HDL code, which can be tedious and error-prone for complicated designs involving, for example, lots of digital signal processing. This is the reason for the appearance, in recent years, of alternative flows which include a preliminary phase in which the user can draw blocks at a higher level of abstraction and rely on the software tool for the generation of the HDL. Some of these tools also include the capability of simulating blocks which will become HDL with other blocks which provide stimuli and processing to make the simulation output easier to interpret. The concept of hardware co-simulation is also becoming widely used. In co-simulation, stimuli are sent to a running FPGA hosting the design to be tested and the outputs of the design are sent back to a computer for display (typically through a Joint Test Action Group (JTAG), or Ethernet connection). The advantage of co-simulation is that one is testing the real system, therefore suppressing all possible misinterpretations present in a pure simulator. In other cases, co-simulation may be the only way to simulate a complex design in a reasonable amount of time.

DIGITAL SIGNAL PROCESSING USING FPGAS

Clearly the main advantage of FPGAs over conventional DSPs to perform digital signal processing is their capability to exploit parallelism, i.e. replication of hardware functions that operate concurrently in different parts of the chip. Figure 3 shows how a Finite Impulse Response (FIR) filter could be implemented in both platforms. While the DSP needs 256 clock ticks to calculate an output sample, the FPGA generates a new sample for every clock cycle. Even if DSP chips can be clocked faster than FPGAs, the difference is in no case larger than a factor of 10. If one adds that many such filters can exist concurrently and interact inside the same FPGA, it is easy to see that DSPs are no match for FPGAs in high performance signal processing applications [3].

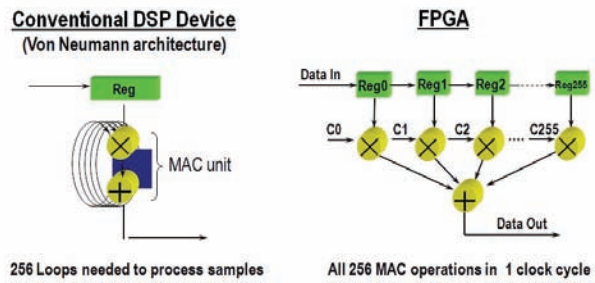

Fig. 3: FIR filter comparison between DSP and FPGA

Another advantage of FPGAs is the flexibility for trading off between area and speed until very late in the design cycle. Figure 4 shows three different implementations of a sum of products, from a full expansion using more silicon to a minimalist implementation which takes more clock cycles to generate a result.

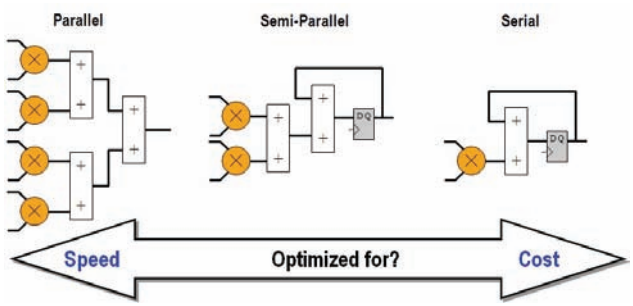

Fig. 4: Illustrating the speed/area trade-off in FPGAs

In this section, we give a basic introduction to fixed-point arithmetic and then touch briefly upon two interesting techniques for processing fixed-point signals: distributed arithmetic and the COordinate Rotation DIgital Computer (CORDIC) algorithm. The interested reader will find more details in the references at the end of this document.

Fixed point arithmetic

In FPGA design, one typically uses a two's complement fixed-point representation of numbers. Floating point design is perfectly feasible, but the high-performance applications typically targeted by FPGAs can very often be served adequately by using enough bits in a fixed-point representation. This is another advantage of FPGAs: the possibility to tailor the bus widths in different parts of the design to satisfy the final precision requirements. Figure 5 shows an example of fixed-point

two's complement representation, where we have taken 3 of the bits for the integer part and 5 for the fractional part. In reality, as we shall see, an adder or any other arithmetic circuit does not know about our decision on how many bits to interpret as fractional. This is purely an interpretational issue, so for all practical purposes, one can think of fixed-point arithmetic as integer arithmetic.

digit worth								decimal value
$-(2^2)$	2^1	2^0	2^{-1}	2^{-2}	2^{-3}	2^{-4}	2^{-5}	
-4	2	1	0.5	0.25	0.125	0.0625	0.03125	
0	0	0	0	0	0	0	1	0.03125
0	0	0	0	0	0	1	0	0.0625
1	0	1	0	0	0	0	0	-3.0
1	1	0	0	0	1	1	1	-1.78125
1	1	1	1	1	1	1	1	-0.03125

Fig. 5: fixed-point two's complement representation of signed numbers using 3 integer bits and 5 fractional bits

As an introductory example, let's see how one can make a circuit that performs simple addition or subtraction of 4-bit numbers using logic gates. This will be a combinatorial circuit with 9 inputs (4 per input and 1 for controlling if we add or subtract) and 5 outputs (the final result). Notice that we need to have one extra bit in the output because the addition/subtraction of two 4-bit numbers can result in a 5-bit number.

We start with the full adder circuit of Fig. 6. It is easy to see that this circuit made of AND, OR and XOR gates takes two bits and a carry (maybe from a preceding stage) and generates a proper sum and carry out.

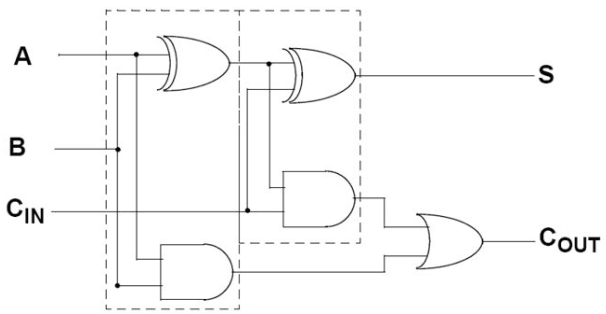

Fig. 6: a full adder circuit

Out of many of these Full Adder (FA) cells, one can build the circuit of Fig. 7, which takes two 4-bit signed numbers and adds them together if the Control signal is '0'.

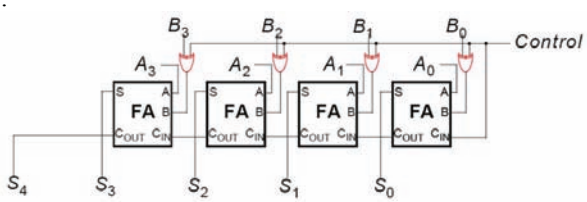

Fig. 7: 4-bit full add/subtract

Otherwise, a subtraction is performed. Although these days one would generate this circuit with a simple HDL statement, it is enlightening to understand what the underlying hardware looks like. More complicated blocks to multiply, divide, take a square root, etc can be synthesized using these basic blocks and the reader is referred to the specialized literature for details [3].

One question that arises immediately is what to do with this arithmetic bus that gets wider and wider as we cascade more and more operations one after the other. At some point, the bus width will become inconveniently large. We will be wasting bits with unnecessary information, and our timing constraints could be compromised as the combinatorial paths traverse more layers of logic before hitting the next flip-flop. One example could be a feedback system that generates an analog signal towards a Radio Frequency (RF) cavity using a 16-bit Digital to Analog Converter (DAC) fed by an FPGA. There would be no point in keeping an internal representation of say 50 bits and then collapse it all at the very end to feed the DAC with only 16 bits. The solution to this problem is to control the width after each operation by judiciously choosing a suitable number of bits to represent the intermediate results. Figure 8 shows two ways of doing this: truncation and rounding. In truncation, some of the fractional bits are taken out before feeding the result to the next stage. In rounding, a '1' is added to the most significant bit (of the ones to be taken out) before truncation.

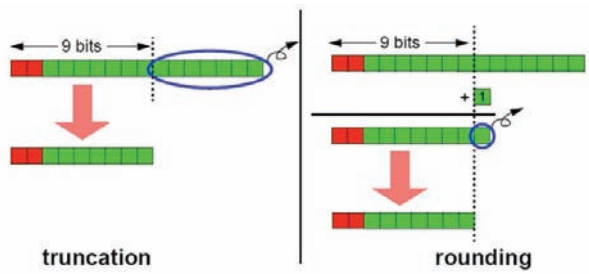

Fig. 8: truncation vs. rounding in fixed-point representation

Notice that in two's complement, truncation is a biased operation. The output of truncation will always be a smaller number than the input. If an unbiased scheme is needed, then rounding should be used at the expense of the extra addition involved. The loss in precision incurred by taking some of the bits out can be studied statistically by modeling rounding or truncation as a source of white noise with an amplitude dependent on the number of bits eliminated [4].

Distributed Arithmetic

Digital signal processing is all about sums of products. For example, if a generic filter is fed with an input sequence x[n], we can write its output as

$$y = \sum_{n=0}^{N-1} c[n] \cdot x[n] \qquad (1)$$

where c[n] are the filter coefficients. If these coefficients are constant, and assuming the input signal to be B bits wide, we can rearrange the terms in a sequence

that will end up suggesting an alternative hardware implementation. We begin by re-writing (1) as

$$y = \sum_{n=0}^{N-1}\left(c[n] \cdot \sum_{b=0}^{B-1} x_b[n] \cdot 2^b \right) \quad (2)$$

where $x_b[n]$ is bit number b of x[n], i.e. either '0' or '1'. After rearranging:

$$y = \sum_{b=0}^{B-1} 2^b \cdot \left(\sum_{n=0}^{N-1} c[n] \cdot x_b[n] \right) \quad (3)$$

and the term in parentheses can be implemented as a Look Up Table (LUT) with N inputs, as suggested in Fig. 9.

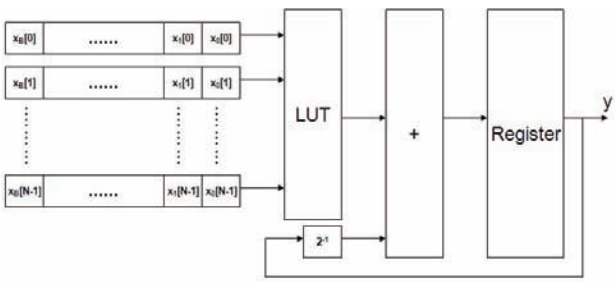

Fig. 9: Distributed Arithmetic implementation of a filter

The filter implemented in this way has no need of hardware multipliers, and generates a result every B ticks, independent of the filter length N. By increasing the number of LUTs and replicating hardware, one can trade-off latency versus area. The extreme case would be full parallelization: replicating B times to get one output sample per clock tick.

The CORDIC algorithm

The CORDIC is a circuit that iteratively rotates an input vector (x(1), y(1)) and generates an output vector (x(2), y(2)), where x and y are the Cartesian coordinates of the vectors. There are two modes of operation. In rotation mode, an angle accumulator is set to the desired rotation angle, and the CORDIC approximates that angle by performing elementary rotations of decreasing angles. The output is the input vector rotated by the specified angle. In vectoring mode, the CORDIC block rotates the input vector using the same table of decreasing angles until the resulting vector is aligned with the horizontal axis. In this mode, the result is the angle accumulated throughout the whole rotation process. The trick in the CORDIC algorithm is to constrain the set of angles to those whose tangent can be expressed as 2^{-i}, i being the iteration index. Then the rotation operations for these angles do not need any specific multipliers, since a multiplication by 2^{-i} is just a right-shift by i places. This produces a very efficient hardware implementation in terms of area and speed. Each iteration generates roughly an extra bit of precision in the result. Among the several things one can calculate with a CORDIC, we can highlight the following:

- Magnitude of a vector: it is found on the x of the output vector after operating the CORDIC in vectoring mode.
- Sine and cosine of an angle: found by feeding an input vector with x=1, y=0 and setting the CORDIC to work in rotation mode with the specified angle.

More uses of the CORDIC as well as a detailed description on its internal features and ways to accelerate it can be found in the references [5].

FPGAS IN REAL WORLD DESIGNS

This section is devoted to design aspects which are encountered in real projects. The FPGA designer will find none of these problems while simulating behavioral HDL in a computer, but they are paramount for the success of any FPGA project.

Performance boosting techniques

We already discussed the benefits of synchronous design. The place & route tool will analyze the timing constraints and optimize the placement and routing in such a way as to meet these constraints. But what if it can't? If the delays due to propagation through individual gates are already higher than the specified clock period, there is nothing the tool can do to meet the specification. Remember the tool's degrees of freedom are just related to where to place blocks and how to interconnect them. The interconnect delay will never be less than 0, and it has to be added to gate propagation delays which are fully determined by the synthesized netlist. So if the gate propagation delays already exceed the specified clock period, it's mission impossible for the place & route tool.

Delays in modern designs can be as much as 90% due to routing and 10% due to logic. The routing bit is due to long routes and capacitive loading on the nets. Many synthesis tools automatically insert buffers in some nets to provide more current to drive the capacitive loads, therefore decreasing routing delay, as depicted in Fig. 10.

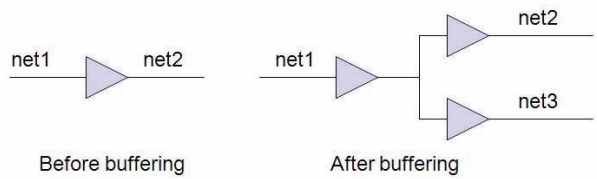

Fig. 10: Automatic buffer insertion example

The automatic replication of registers is another useful technique. This can be set as an option for those synthesis tools that support it, or it can be done by hand at the HDL level. Figure 11 illustrates the principle. The nets coming out of the flip-flop after the producer are going to four different destinations, potentially covering great lengths inside the chip. After the flip-flop is duplicated, each of the outputs only has to serve two destinations, so the timing constraints become easier. If there were combinatorial logic after the first flip-flop, it would also be replicated. The HDL specification is therefore fully

respected.

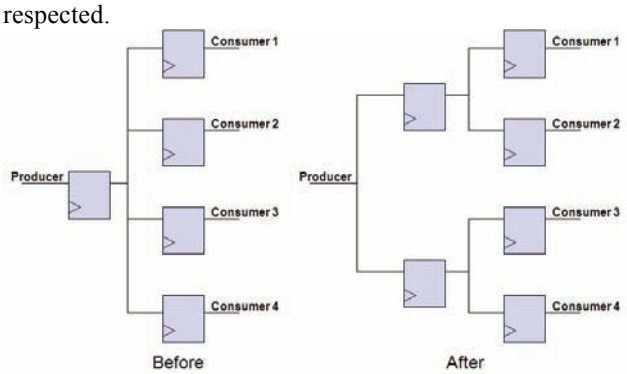

Fig. 11: Automatic replication of registers

Another problem case concerns long combinatorial delays between flip-flop stages. As we said earlier, there is nothing that the place and route tool can do in this case. The solution must come from the synthesis tool or the designer. Retiming – also known as register balancing – is a technique that can be used in these cases. Figure 12 shows how it works. Some of the combinatorial logic is passed to the next stage in the pipeline so that the maximum delay in each stage remains within the specifications.

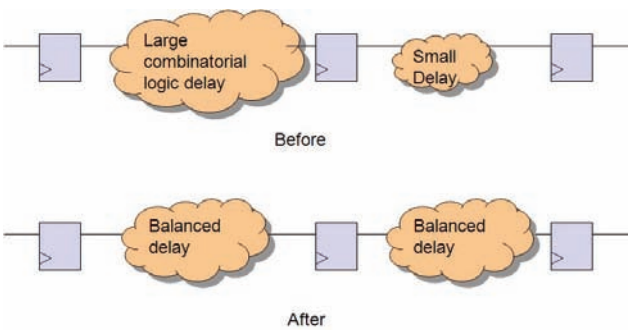

Fig. 12: Retiming

If retiming is not possible, one can always try pipelining, provided the circuit is not sensitive to the latency in the extra number of clock cycles. The principle is explained in Fig. 13. It consists in breaking up the large combinatorial delay by inserting flip-flop stages after intermediate results. In this case, it is better to modify the original design rather than using the synthesis tool, since this could lead to an incoherency between HDL sources and final hardware.

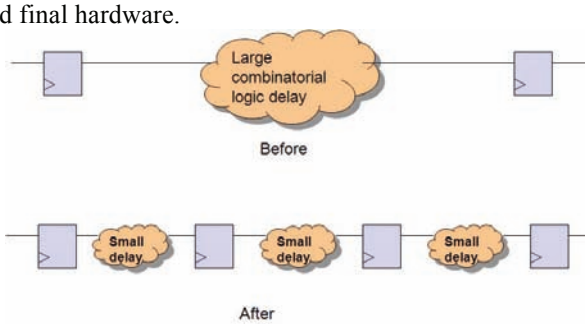

Fig. 13: Pipelining

Finally, time-multiplexing in conjunction with hardware replication can also be a powerful tool to prevent timing pathologies. The principle, depicted in Fig. 14, consists in splitting a data path in two, making each branch work at half the speed, and recombining the results at the end to regenerate a data flow at the design clock frequency.

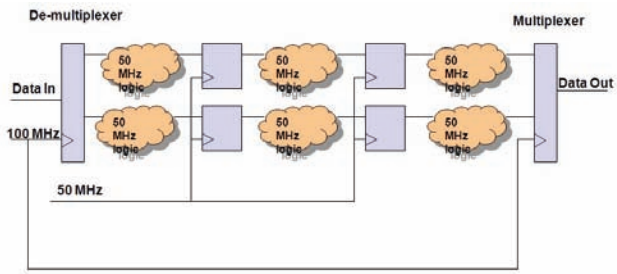

Fig. 14: Time multiplexing.

As an example of how these tools can be used in practical cases, let's examine a performance problem that arouse in the phase filter of a PLL used to track bunch frequency in CERN's PS. Figure 15 shows the original filter design, a first order Infinite Impulse Response (IIR) filter implementing the transfer function y[n+1] = a y[n] + b x[n]. Signal y goes back to the output flip-flop through a multiplier and an adder, and these combinatorial delays are not compatible with the clock frequency. What can we do?

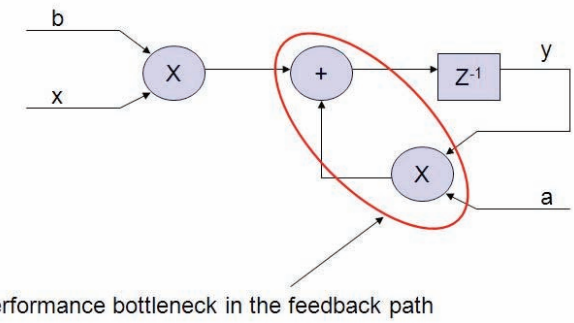

Fig. 15: A simple IIR filter with a performance problem

We can calculate y[n+2] = ay[n+1] + bx[n+1] = a2y[n] + abx[n] + bx[n+1], and see what the resulting direct implementation would look like in Fig. 16.

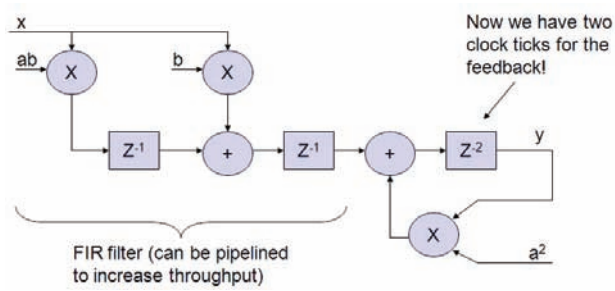

Fig. 16: Look-ahead scheme for IIR

The circuit looks now much more favorable for timing improvements. The leftmost part looks like an FIR and can be pipelined as much as necessary. The second part now contains two flip-flops in series in the feedback path, which can be used for retiming. The technique we used is called 'look-ahead' and is very common for boosting the speed of digital circuits.

Powering FPGAs

FPGAs are typically powered from various supply rails. They need different voltages for the internal logic, the Input/Output (I/O) circuitry and some analog blocks like PLLs. Typical specifications include a +/-5% tolerance on the actual value of the voltage and monotonic ramping of the supplies during power-up. While it is not proven that ramping in a non-monotonic way would not work, FPGAs are not tested that way after manufacturing, so it is better to guarantee a monotonic ramp in order to avoid surprises. Devices also specify a minimum and a maximum ramping time for the voltage rails. Again, this is just how they are tested after production, and it is very wise to follow these guidelines.

An important aspect to bear in mind concerns in-rush current at power-up due to the decoupling capacitors on the power supply rails. If C is the total capacitance, $Ic=C*\Delta V/\Delta T$, so one might want to slow the ramping process down using a soft-start circuit in order to avoid the kick-in of protection mechanisms in regulators, which could in turn compromise monotonicity.

Sequencing of supply voltages, i.e. making one available, then another one and so on, was a required practice in old technologies, and nowadays it is only recommended. It seems sensible that the I/O stages get power only after the internal logic is properly configured. A Supply Voltage Supervisor (SVS) chip can be used to control the process. Sequencing is also good to make sure that the main (typically 5V) rail feeding the regulators is well established (i.e. all capacitors charged) before they begin requesting current from it. Otherwise the 5V protection could trip and spikes could appear in the output of the regulators.

The design of a proper bypassing network using capacitors is also a critical issue. A decoupling network should look like a short to ground for all the frequencies of power supply noise we want to reject. At high frequencies, like the ones of interest for this discussion, a capacitor chip can be modeled as an equivalent RLC circuit to take into account the various imperfections in its design. The parasitic inductance dominates at high frequencies, and is (almost) exclusively determined by the package type of the capacitor. The global frequency response presents a downward slope at low frequencies whose value depends on the capacitance, and an upward slope at high frequencies whose value depends on the parasitic inductance. The minimum of the curve thus depends on the capacitance value, and can be made arbitrarily wide by selecting a suitable set of capacitor values and placing them in parallel. High-value capacitors take care of low-frequency perturbations and can be placed relatively far away from the chip, while low values of capacitance (typically 10 nF), can be placed close to the chip – ideally below it – to take care of the fast perturbations. Reference [6] can be consulted for further details.

Interfacing to the outside world

Modern FPGAs have very versatile I/O blocks which make them easy to interface to other chips. In this section, we look in particular at issues which could appear when interfacing to Analog to Digital Converters (ADCs) or DACs.

Whenever a design deals with high speed, high pin count parallel busses, as is often the case when interfacing FPGAs and ADCs/DACs, there is potential for noise problems. This is because the I/O drivers in the FPGA commute state all at the same time, creating large current surges in the Power Distribution System (PDS). The PDS should be well decoupled using the appropriate mix of capacitors as discussed above, but it cannot filter all the noise at all frequencies. In addition, sampling many bits at a high frequency can pose synchronization problems. If the clock edge is very close to the transition of any of the data bits, a problem known as metastability – to be explained later – can arise. It is therefore desirable to avoid simultaneous fast-switching of large busses if possible. One example where this is possible is in the sampling of high frequency, low bandwidth analog signals. According to sampling theory, there is no need to sample them in their main Nyquist zone, i.e. with at least twice their frequency. It is sufficient to sample them at least faster than twice their bandwidth – which can be significantly slower. This can be a solution for systems where latency is more or less a secondary concern, but it might not be possible for feedback systems. Another possibility for mitigating noise problems is to choose ADC and DAC chips which use differential signaling for the data bits and the clock. Currents in differential signals go in through one line and out of the other, without any net demand on the PDS. The use of differential signaling also creates negligible ground bounce. Ground bounce is caused by the fact that the impedance between the ground pins and the ground plane is not exactly zero. This can cause a perceived change in ground level, as seen by the digital chip, when it consumes significant current. This impedance has a resistive component but also a very important inductive component which will create voltage jumps as a function of dI/dt. Therefore, another way to improve the noise problem is to feed the digital outputs of the ADC with the lowest realistic supply voltage. Current generation ADCs can accept digital supplies in the range 2.0-2.5V. In addition, current can be reduced by placing resistors in series with the ADC outputs.

Another aspect to bear in mind when designing FPGA systems is the state of I/O drivers during power-up. Most FPGA chips provide a possibility, through external jumpers, of selecting whether the I/Os will be pulled-up or tri-stated during the power-up process. The tri-state option lets the designer control the power-up state of each

pin through external pull-up or pull-down resistors. This is important if glitch-free operation is requested during startup.

Clock domains and metastability

Oftentimes a designer is faced with an input signal that is not synchronized with the system clock, i.e. its rising and falling edges do not maintain a constant delay with respect to the rising edge of the clock signal. Let's imagine for example that we have a card where an FPGA is clocked by an on-board 100 MHz oscillator, and the card is fed with an external input representing the revolution frequency of a synchrotron. Let's also assume that the revolution tick has to be fed to two different state machines inside the FPGA, and that the correct functioning of this design relies on both state machines detecting the revolution tick during the exact same period of the system clock, which is used as the clock for the state machines.

A naïve design might split the revolution tick signal in two before feeding it to the state machines. The problem with this solution is that the revolution tick might eventually, after going through several layers of combinatorial logic, find itself at the D inputs of two different flip-flops inside the FPGA. But because the propagation delays of the revolution signal going through the two paths are different, one flip-flop might already clock it in as '1' while the other still sees a '0'.

A less naïve designer would then propose to feed the revolution tick to the D input of a flip-flop to begin with, and only then split in two. Indeed, the rate of failures would go down, but every now and then we would still see an incoherency between the two state machines. The culprit is an effect known as 'metastability' which afflicts flip-flops when a transition at their D input occurs too close in time to the rising edge in the clock input. In that case, their Q output hesitates until it finally settles to one of the two possible output values. The resolution time can be arbitrarily long as we push the two edges closer and closer in time. In our second design, from time to time the Q output of the synchronizing flip-flop will go metastable, with a resolution time such that – on the next system clock tick – one of the two subsequent flip-flops will already see a '1' when the other one still sees a '0'.

While it seems that this could become a never ending story, in fact, for all practical purposes, the circuit in Fig. 17 will fix the problem.

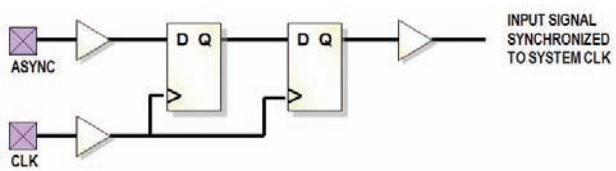

Fig. 17: Two flip-flop synchronizer

Now, for typical system clock and asynchronous input frequencies, the chances that the second flip-flop goes metastable after the first one did on the previous cycle of the system clock are vanishingly small. One can easily design a circuit that will fail on average once every million years.

The discussion above applies equally well to any design with more than one clock domain where data must be transferred from one domain to the other. By clock domain, we mean a part of the design which is clocked by a single common clock. Let's imagine a designer needs to transfer a 16-bit number from one domain to another. Inserting a synchronizer for each bit would not help, since different flip-flops will see different set-up times of the data with respect to their clock. Indeed, these set-up times vary with time in a random way! The solution is to design the emitter block so that it asserts a data strobe when the data are ready, and holds the data stable for a suitable amount of time. The receiver circuit can then sample the strobe with a two flip-flop synchronizer and clock the data in once it senses a '1' on the strobe line. A variation on this circuit includes a handshake whereby the receiver sends back an acknowledge line to the emitter, which in turn synchronizes it into its clock domain. Once the emitter senses a '1' on the acknowledge line, it knows it can change the state of the data lines to prepare the next transfer.

Sometimes the above scheme will not work because data comes in bursts at a speed which makes it impossible to perform the full handshake. In those cases, a First-In-First-Out (FIFO) block is needed with each of its sides clocked by a different clock.

Safe design

There is at least one asynchronous signal in almost all designs: the external reset. In many cases, it is very important to handle this signal properly in order to guarantee coherency of different parts of a design. If we return to the example of the two different state machines within an FPGA, both running off the same system clock, and we require that they both 'wake up' during the same clock tick after the de-assertion of the reset signal, we find ourselves with a need to treat the reset signal as we treated the revolution tick above, i.e. we need to feed it to a synchronizer before using it in the design.

The best reset strategy, not always possible, is to synchronize the reset to the system clock and then use it as a synchronous reset. This means that the reset line is treated as any other synchronous signal. It will enter some combinatorial block and affect its output, which will then be feed to the D input of a flip-flop. Chances are that the output of that combinatorial logic block will go to a predefined 'reset' state irrespective of other inputs if the reset line is active, but there is really nothing special about the reset line in this case from a topological point of view.

Things change if, for some reason like saving resources, the designer wants to use the asynchronous reset input present in all flip-flops. There is still a certain guarantee of coherency if the reset fed to these inputs has been properly synchronized in advance, but this will greatly depend on the clock period and the delay to reach

each asynchronous reset input. Typical place & route tools will not include these paths in their timing analysis because they don't go from Q outputs to D inputs. It is really best if the asynchronous reset can be avoided altogether.

Another important topic in safe design is that of complete state coverage in state machines. If a state machine has 5 different states, it will need at least 3 signal lines to represent its current state. But with 3 lines one can have 8 different states, 3 of which will be illegal. It is the designer's responsibility to detect these states and take the state machine to a safe state if it goes to one of them. Now, how can a state machine go to an illegal state if no combination of inputs and states are supposed to take it there? The state vector is made of three lines, and each of these lines is – we can assume this without loss of generality – fed from the Q output of a flip-flop. High energy particles crossing the FPGA can induce what is called a Single Event Upset (SEU), flipping the state of one of the flip-flops to a new one, which might make the new three-bit combination illegal. With process geometries shrinking, one no longer needs a high energy accelerator to produce SEUs. Atmospheric particles will produce them at a rate high enough to make it a major concern for safety critical systems.

Sometimes in high energy accelerator applications, an FPGA must live in a highly radioactive environment. This is a completely different game. Here are three techniques designers use frequently to make their designs more robust under such adverse conditions:

- Antifuse technology. An antifuse is an element that creates a short circuit when overheated, i.e. exactly the opposite of what a fuse does. FPGAs based on antifuse technology are inalterable at least as far as the configuration memory is concerned. But we know that, among the RAM bits of a typical FPGA, the vast majority of them are configuration bits, so antifuse technology is a major improvement in terms of resistance to radiation. The negative side is the price of antifuse chips and also their lower densities. These devices are roughly one generation behind in terms of silicon processes.
- Scrubbing. This is a protection scheme for the configuration memory of SRAM-based devices. As we said, most of the FPGA RAM bits that are susceptible of being affected by a SEU are in fact configuration bits. One can read the configuration stream back repeatedly to check if there has been any corruption, and then take corrective action if needed. The device that scans the configuration bits must itself be more robust than the FPGA being checked. It is typically antifuse-based.
- Triple Mode Redundancy (TMR). This technique consists in replicating the same piece of logic three times and adding a set of voters to detect whether there was a SEU in one of the blocks. It is complementary to scrubbing because it takes care of design bits instead of configuration bits. Figure 18 shows the principle for the simple example of a counter. If a mismatch is found, the losing counter will be informed and correct its value accordingly.

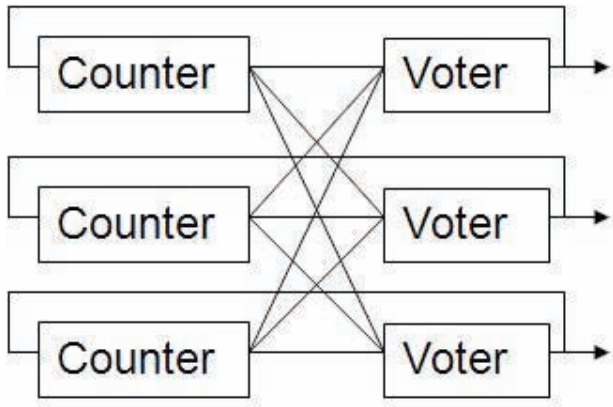

Fig. 18: TMR with state feedback

It is assumed that the probabilities to have a double upset that will affect two counters at the same time are negligible, but this may not be a very realistic assumption with the ever-diminishing process geometries. A single high-energy particle can indeed affect more than one transistor around the impact area. This is why some vendors are developing software that automatically generates TMR logic and places the different parts of the ensemble in different, geographically distant, areas of the chip. Notice also that our FPGA contains now three counter outputs instead of one. With only one output, a SEU in one of the output transistors could defeat the whole TMR scheme. If the counter value is to be used outside the FPGA, decision logic must be implemented outside using a radiation-hard scheme in order to figure out the current value of the counter.

For unmatched reliability, radiation-hard antifuse products are available. Every flip-flop in these devices is TMRed in silicon, with feedback TMR built in. Needless to say, these devices are extremely expensive and reserved for the most demanding applications in terms of radiation hardness. The extra logic needed for the TMR scheme and the state feedback are also a problem if excellent timing performance is required.

ACKNOWLEDGEMENTS

I would like to acknowledge many fruitful and interesting discussions on this topic with several colleagues. Special mention goes to Tony Rohlev (Elettra), Andrea Boccardi, Christos Zamantzas, Greg Kasprowicz, Uli Raich (CERN), Matt Stettler (LANL) and Larry Doolittle (LBL).

For presentation material, I would like to thank specially Jeff Weintraub (Xilinx University program) and Prof. Stewart (University of Strathclyde).

REFERENCES

[1] John F. Wakerly, Digital Design: Principles and Practices, 4th ed. (Prentice Hall, 2006).
[2] Andrew Rushton, VHDL for Logic Synthesis, 2nd ed. (John Wiley & Sons, 1998).

[3] Uwe Meyer-Baese, Digital Signal Processing with Field Programmable Gate Arrays, 3rd ed. (Springer, 2007).
[4] John G. Proakis, Dimitris K. Manolakis, Digital Signal Processing, 4th ed. (Prentice Hall, 2006).
[5] Ray Andraka, A survey of CORDIC algorithms for FPGAs, Proc. 1998 ACM/SIGDA 6th International Symposium on Field Programmable Gate Arrays, Feb. 22-24, Monterrey, CA, USA, pp. 191-200. URL: http://www.andraka.com/files/crdcsrvy.pdf.
[6] Mark Alexander, Power Supply Distribution (PDS) Design: Using bypass/decoupling capacitors, Xilinx application note 623. URL: http://www.xilinx.com/support/documentation/application_notes/xapp623.pdf.

RECENT BEAM MEASUREMENTS AND NEW INSTRUMENTATION AT THE ADVANCED LIGHT SOURCE*

F. Sannibale[#1], K. Baptiste[1], W. Barry[1], M. Chin[1], D. Filippetto[2], L. Jaegerhofer[4], J. Julian[1], S. Kwiatkowski[1], R. Low[1], D. Plate[1], G. Portmann[1], D. Robin[1], T. Scarvie[1], G. Stupakov[3], J. Weber[1], M. Zolotorev[1],

[1]Lawrence Berkeley National Laboratory, Berkeley, CA 94720, U.S.A.
[2]Istituto Nazionale di Fisica Nucleare, Laboratori Nazionali di Frascati, 00044 Frascati, Italy
[3]Stanford Linear Accelerator Center, Stanford, CA 94309 U.S.A.
[4]Vienna University of Technology, 1040 Vienna, Austria

Abstract

The Advanced Light Source (ALS) in Berkeley was the first of the soft x-ray third generation light source ever built, and since 1993 has been in continuous and successful operation serving a large community of users in the VUV and soft x-ray community. During these years the storage ring underwent through several important upgrades that allowed maintaining the performance of this veteran facility at the forefront. The ALS beam diagnostics and instrumentation have followed a similar path of innovation and upgrade and nowadays include most of the modern and last generation devices and technologies that are commercially available and used in the recently constructed third generation light sources. In this paper we will not focus on such already widely known systems, but we will concentrate our effort in the description of some measurements techniques, instrumentation and diagnostic systems specifically developed at the ALS and used during the last few years.

INTRODUCTION

The Advanced Light Source (ALS) at the Lawrence Berkeley National Laboratory (LBNL) was the first soft x-ray source built among the so-called third generation synchrotron light sources [1]. In this kind of storage rings, fully dedicated to and optimized for the production of synchrotron radiation, insertion devices in the straight sections allow for many order of magnitude increased brigthness respect to those of the previous generation light sources. After the ALS many other 3rd generation sources have been and are still being built around the world under the always increasing requests from users. Despite its age, the ALS performance as a storage ring as well as a light source compare well with those of the younger machines in the category. This is due to the fact that during these years the machine underwent to a number of upgrades of the lattice, of the ring and beamline components, and of the instrumentation and beam diagnostics systems.

In this paper, after a brief introduction of the ALS and its instrumentation, we focus on the description of three new systems developed at the ALS that improve the beam measurements capabilities and potentially allow for the operation of the ring in a new mode of operation.

* Work supported by the Director, Office of Science, of the U.S. Department of Energy under Contract DE-AC02-05CH11231.
# FSannibale@lbl.gov

THE ADVANCED LIGHT SOURCE

Figure 1 shows the "clock diagram" of the ALS with its collection of beamlines. More than 40 beamlines with source points inside dipoles or insertion devices allow for more than 2000 users per year, using photons from the far-infrared to the hard x-rays. Figure 1 also shows the injector system composed by a 50 MeV linac and by a booster ring that ramps the beam energy up to 1.9 GeV before the injection into the storage ring.

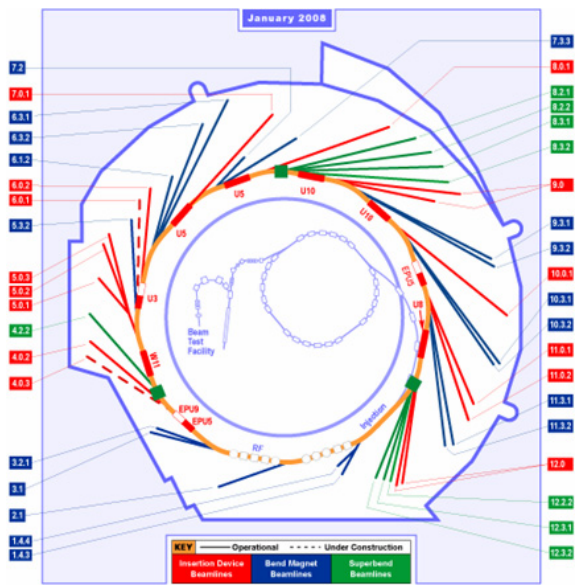

Figure 1: Clock diagram of the ALS showing the different beamlines now in operation.

Table 1 contains the main parameters of the storage ring. During standard user operation, 400 mA of electrons are stored in about 280 of the 328 available buckets. The 12 triple bend achromat cells distributed over a circumference of ~ 197 m allow for the small emittance value of 6.3 nm. A cost effective upgrade of the ALS is being proposed that will reduce the emittance by about a factor 3 by replacing four corrector magnets in each sector

of the ring with the same number of hybrid elements with both dipolar and sextupolar field components [2].

Table 1: ALS ring parameters

Parameter	Value
Circumference	196.8 m
Particle Species	electrons
Beam Energy	1.9 GeV
Beam Current	400 mA
Emittance	6.3 nm
Energy Spread	0.1% rms
Radio Frequency	499.642 MHz
Harmonic Number	328
Bucket Spacing	2 ns
Lattice Cell Type	Triple bend achromat
Number of Cells	12

A CONTINUOUS EVOLUTION

Table 2 enumerates most of the beam diagnostic systems and instrumentation presently in operation at the ALS and at its injector.

Such a set is pretty complete and allows for the measurement of all the electron and photon beam relevant physical quantities and for the full control of the stability of the beam at the required level.

The majority of these individual systems have been added and/or upgraded during the years by using the latest available commercial technologies or by in house developments.

NEW INSTRUMENTATION AND BEAM DIAGNOSTICS SYSTEMS AT THE ALS

In this section we describe three in–house-developed systems that have been installed in the ALS in the last few years. A novel type of absolute bunch length monitor, the instrumentation that should allow running the ALS in a new operation mode defined as "pseudo-single bunch", and finally a FPGA based system that allow for the removal of undesired electrons from nominally empty buckets ("bunch cleaning").

Absolute bunch length from incoherent radiation fluctuation analysis

Charged particles can radiate in many ways, by synchrotron radiation, Cerenkov radiation, transition radiation, etc. In all radiating processes the presence of incoherent radiation is due to the fact that the particles are randomly distributed along the beam.

For example, in the case of an ideal coasting beam composed of a large number of particles equally separated by a longitudinal distance d and moving along a circular trajectory, there is no synchrotron radiation emission apart at those wavelengths where $\lambda = nd$, with n being an integer. Additionally, for those wavelengths the radiation from different particles is in phase and the emission is fully coherent. For all other wavelenghts, the interference between the radiation emitted by the evenly distributed electrons will produce a vanishing net radiation field.

Table 2: ALS instrumentation and diagnostic systems

Monitor	Quantity
Synchrotron Light Monitors	2
Beam Position Monitors (electromagnetic, photon)	~140
DCCT's	2
Beam Loss Monitors	~24
Streak Cameras	1
Fluorescent Screens	12
Integrated Current Monitors	4
Fast Current Transformers	1
Pinger Systems	1
Slow and Fast Orbit Feedbacks	2
Bunch by Bunch Longitudinal Feedbacks	1
Bunch by Bunch Transverse Feedbacks	2
Network Analyzers	1
Real Time Spectrum Analyzers	1

In a more realistic coasting beam, the same particles are now randomly distributed along the orbit causing a small modulation of the beam distribution. The effect of such a random modulation is that the interference is not fully destructive anymore and a net nonzero radiation field shows up. If the turn by turn position of the particles along the beam changes (due for instance, to longitudinal dispersion or to path length dependence on transverse position), then the modulation changes and the energy radiated in a single pass fluctuates turn by turn. By measuring the radiation intensity over multiple passages, we would observe that for a sufficiently large number of samples, the measured average spectrum converges to the characteristic incoherent spectrum of the radiation process under observation (synchrotron radiation in our example).

The passage from the coasting to the bunched beam case introduces a strong coherent emission at those wavelengths comparable or longer than the bunch length, but does not modify the short wavelength part of the spectrum.

It has been shown [3] for the case of a bunched beam, that by measuring the pulse to pulse intensity fluctuation

of the radiation within a bandwidth $\Delta\omega$ in a region of the spectrum where no coherent emission is present, it is possible to perform absolute measurements of the bunch length. Experimental schemes exploiting such a technique and using a high resolution spectrometer have been already proved experimentally [4-6].

At the ALS, we developed a remarkably simpler version that does not require complex and expensive intrumentation and that allows for accurate absolute measurements of the rms bunch length. The scheme is non-destructive and can be applied in both circular and linear accelerators including cases where the very short length of the bunches makes difficult the use of other techniques.

The energy radiated by the bunch in a single pass is measured. The photons are collected within a narrow bandwidth in a wavelength region where no coherent emisssion is present. The values of radiated energy per passage W are measured and recorded for many passages of the beam. The method is quite general and can be applied to arbitrary bunch and bandwidth shapes. Nevertheless, in the simple but important case where both the bunch and the bandwidth shapes are Gaussian, the system equations can be integrated and an analytical solution can be derived. This case is quite realistic because commercial narrowband interferometric filters have usually a Gaussian shape and electron bunches in storage rings are usually Gaussian as well. If we use one of such filters with rms bandwidth σ_ω to measure a Gaussian beam with rms length σ_τ (measured in time units), W fluctuates passage to passage with a relative rms variation δ given by [3, 4]:

$$\delta^2 = \frac{\sigma_W^2}{\langle W \rangle^2} = 1\Big/\sqrt{1+4\sigma_\tau^2\sigma_\omega^2} \qquad (1)$$

This last expression shows that if σ_ω is known, then by measuring δ one can derive the absolute value of the rms bunch length. For nongaussian distributions the system equations need to be integrated numerically, but it can be shown that equation (1) can be still used with a few percent accuracy for most of the distributions, as long as they are represented by their rms length and do not include microstructures with characterisitc length much smaller than the bunch length.

For $\sigma_\tau >> 1/(2\sigma_\omega)$, we have that Eqn. (1) becomes $\delta^2 \sim 1/(2\sigma_\tau\,\sigma_\omega)$, and using the fact that the longitudinal coherence length for an electromagnetic mode with frequency content σ_ω is $\sigma_{tc} = 1/(2\sigma_\omega)$** we can write:

$$\delta^2 = \sigma_{tc}/\sigma_\tau = 1/M \qquad (2)$$

where M is the number of modes contained in the bunch. Equation (2) leads to the nice physical interpretation that the intensity fluctuation is due to M independent modes radiating randomly within the bunch. In fact, the radiation from a single mode is a stochastic Poisson process whose intensity shows 100% fluctuation. When M of such modes radiate in a combined but independent way the resulting fluctuation scales as described by Eq. (2).

The results presented so far assumed a bunch with no transverse size. By including the effect of the finite transverse size for the example case of Gaussian transverse distributions one obtains:

$$\delta^2 = \left(1+\sigma_\tau^2/\sigma_{tc}^2\right)^{-\frac{1}{2}}\left(1+\sigma_x^2/\sigma_{xc}^2\right)^{-\frac{1}{2}}\left(1+\sigma_y^2/\sigma_{yc}^2\right)^{-\frac{1}{2}} \qquad (3)$$

with σ_x and σ_y the rms horizontal and vertical beam sizes respectively and σ_{xc} and σ_{yc} the coherence sizes of the related transverse electromagnetic modes at the wavelength of operation. Such quantities are defined by the properties of the radiation process and include diffraction effects due to limiting apertures. For simple cases analytical expressions for σ_{xc} and σ_{yc} can be derived and for more complex cases codes as SRW [7] can to be used.

It can be shown that the statistical error on δ^2 when N_s samples are collected is given by:

$$\sigma_{\delta^2}/\delta^2 = \sqrt{2/N_s} \qquad (4)$$

We tested the described theory with the ALS beam and the results were compared with the ones from streak camera measurements. Figure 2, shows the layout of the experimental setup used for the measurements performed at the beamline BL7.2. Such a beamline collects the synchrotron radiation from a dipole magnet and has a total angular acceptance of 5.5 mrad and 2.8 mrad for the horizontal and vertical plane respectively (represented by the limiting aperture in Fig. 2). BL7.2 spectrum ranges from the far-infrared up to the top part of the visible portion.

In our application we used visible light, which is in the incoherent part of the spectrum and allows using the large variety and relatively inexpensive optical components and detectors readily available for such a frequency range. A 1 m focal length lens was used to focus through a flat mirror the beam on the photocathode plane of a streak camera (Hamamatsu C5680). The mirror could be retracted in order to allow for the light to go into another branch for the fluctuation measurement. An interferometric filter (Melles Griot), with gaussian transmission curve centered at 632.8 nm and with peak transmission of 55%, selected the photons within a bandwidth of 1 nm FWHM. The first lens focal length was chosen for keeping the angle between the incoming photon trajectories and the normal to the filter plane small enough to avoid broadening of the filter bandwidth. Downstream of the filter the transmitted photons were finally focused by a microscope objective (Edmund DIN 10, F 0.25) on the 0.2 mm^2 sensitive area of an avalanche

** For a Gaussian pulse the uncertainty principle requires $\sigma_\tau\,\sigma_\omega = 1/2$.

photodiode (Perkin Elmer C30902S, gain 250, ~600 MHz bandwidth, ~ 60% quantum efficiency at 632.8 nm). The signal from the photodiode was amplified (Hamamatsu C5594, 50k-1.5G Hz bandwidth, 36 dB gain) and sent to a digital oscilloscope (LeCroy Wavepro 7300 A, 3 GHz bandwidth and 20 Gsamples/sec) for data recording and analysis. The oscilloscope was triggered with the ~ 1.5 MHz revolution clock of the ALS.

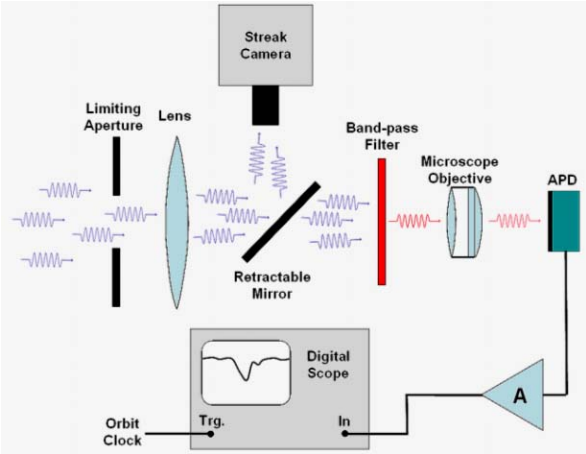

Figure 2: Schematic diagram of the experimental set-up used for the measurement at BL 7.2.

Figure 3 shows the typical signal visible at the scope when measuring the light from a single passage of a single ALS bunch. The typical rms length of the electron beam is ~ 25 ps so that the shape of the pulse in Fig. 3 was totally defined by the response of the measurement system. The oscilloscope was set in order to measure the areas S_{AB} of the signal between points A and B, and S_{CD} between points C and D in Fig. 4. S_{AB} is proportional to the number of photons impinging on the detector plus the contribution due to the noise in the signal, while S_{CD} is a measure of this noise contribution. The "lengths" of the segments AB and CD were set to be the same.

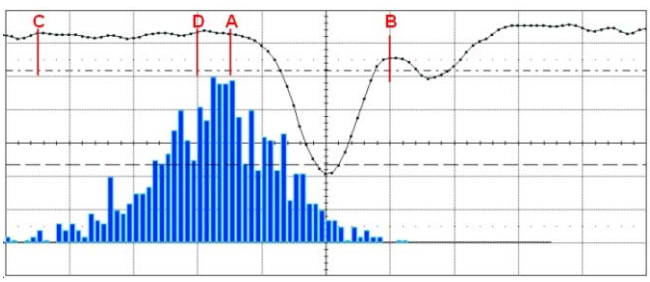

Figure 3: Oscilloscope window showing the track of a typical signal from the photodetector and the histogram of the measured values of the signal area between points A and B. The horizontal scale is 500 ps/div while the vertical is 50 mV/div.

The scope was also set to calculate the average values for such areas and their standard deviations over 5000 samples per each bunch length measurement (~ 1 min per measurement) in order to keep according to (4), the statistical error at ~ 2%. In this configuration, $\langle W \rangle$ the average energy radiated per passage by the electron beam is proportional to $\langle S_{AB} \rangle - \langle S_{CD} \rangle$, while its variance σ_W^2 is proportional to $\sigma_{SAB}^2 - \sigma_{SCD}^2$. By comparing different amplitude signals, we also verified that the shape of the signal itself did not depend on the amplitude.

Simulations and analytical calculations showed that in our configuration, the diffraction due to the finite beamline acceptance fully defines the shape for both the transverse modes, which can be well described by the $[\sin(\xi)/\xi]^2$ function typical of a plane wave diffracting through a finite aperture. Nevertheless, calculations also showed that it is still possible to use the Gaussian formula (3) if one fits the central peak of the $[\sin(\xi)/\xi]^2$ function with a gaussian, and uses for the coherence length the rms width of the fit divided by the $\sqrt{2}$ factor. For $\lambda = 632.8$ nm and for the acceptances of BL7.2 we obtained $\sigma_{xc} = 29.8$ μm and $\sigma_{yc} = 59.5$ μm. The ALS measurements were performed at the two beam energies of 1.2 and 1.9 GeV. The rms beam sizes at BL7.2 source point are $\sigma_x = 64.8$ μm and $\sigma_y = 6.3$ μm at 1.2 GeV and $\sigma_x = 103.0$ μm and $\sigma_y = 10.0$ μm at 1.9 GeV.

Equation (3) was derived in the framework of classical field theory, the proper quantum treatment requires the addition of the shot noise term $1/\langle N \rangle$, with $\langle N \rangle$ the average number of photons impinging on the detector. Additionally, photodiodes, avalanche photodiodes and photomultipliers all exploit stochastic phenomena for the photon-electron conversion and amplification. This must be accounted by using a modified shot noise term $\kappa^2/\langle N \rangle = \zeta/(\eta \langle N \rangle)$, where ζ is the excess noise factor, a constant ≥ 1 related to the avalanche process and η is the detector quantum efficiency. Putting all the contributions together and indicating with δ_M^2 the measured fluctuation variance one finally obtains for the rms length of the bunch:

$$\sigma_\tau^2 = \frac{1}{4\sigma_\omega^2}\left[\left(\delta_M^2 - \frac{\kappa^2}{\langle N \rangle}\right)^{-2}\left(1+\frac{\sigma_x^2}{\sigma_{xc}^2}\right)^{-1}\left(1+\frac{\sigma_y^2}{\sigma_{yc}^2}\right)^{-1} - 1\right] \quad (5)$$

The κ^2 term can be measured by performing 2 or more measurements of δ_M^2 for the same bunch length for different number of photons impinging on the detector (using neutral density filters for instance). All the terms on both sides of (5) remain the same with the exception of the shot noise one. From that, and considering that $\langle N \rangle \propto (\langle S_{AB} \rangle - \langle S_{CD} \rangle)$, κ^2 can be evaluated.

Figure 4 shows two examples of measurements performed for different beam conditions. The agreement with streak-camera data acquired right after each fluctuation measurement is remarkably good especially considering that no parameter has been adjusted to match the data.

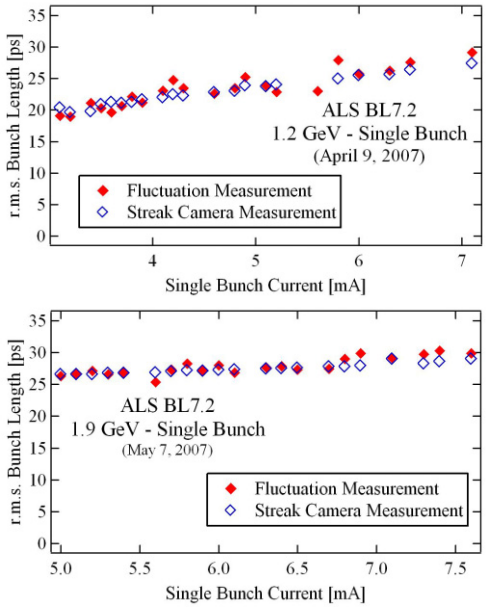

Figure 4: Examples of fluctuation and streak-camera bunch length measurements at the ALS for different beam parameters.

The typical rms difference between the streak camera and the fluctuation data was ~ 4 %. This is larger than the 2% contribution due to (4). The extra error is probably associated with the shot noise term that in our measurements was comparable to δ^2 and to the nonzero experimental error in the streak camera measurements.

Equation (3) and (5) show the dependency of the fluctuations on the transverse beam size. This situation can represent a limitation when the transverse beam size is not known a priori or when it varies shot to shot or turn to turn. In this case, by splitting the light from the source in two paths and using for each of them a bandpass filter with different central wavelength but same bandwidth, it is in principle possible to discriminate between the transverse and longitudinal components. This can be done by exploiting the fact that the longitudinal term depends only on the bandwidth of the filters while the transverse ones depend only on their central wavelength. By combining the results between the two branches it is then possible to remove the dependence of the measurement on the transverse size and measure the bunch length also in cases where the transverse beam size changes or is not known. This modified scheme is presently under test at the ALS.

We are also planning to test the system by coupling the light from the source to the measurement setup by an optical fibber. This will allow having the monitor components separated from the source area for an easy accessibility and tuning of the system.

A technique based on [3, 4] has been also successfully tested for measuring the length of the x-ray pulses in random emission processes [8, 9].

Pseudo-single bunch.

ALS as well as other light sources, dedicates several weeks per year to a mode of operation where two high current bunches are stored into diametrically opposed buckets. This special mode allows users to perform experiments requiring a long relaxation time. The photons from the main bunches excite their samples and the gap between the two bunches (~ 330 ns) permits data taking during the sample relaxation without the contaminating radiation from other bunches. During standard multibunch operation at the ALS ~ 280 contiguous buckets of the 328 available are filled with electrons. A single high current bunch (the "camshaft") is then injected in the remaining ~100 ns gap of empty buckets. Unfortunately, for most of the long relaxation time experiments, the empty bucket gap is too small for them to take data.

Table 3: Fast kicker system characteristics

Parameter	**Value**
Kicker type	Stripline
Electrode length	0.6 m
Characteristic impedance	50 Ohm
Deflection angle	73 μrad/kV
Pulse amplitude	1 kV
Repetition rate	~ 3 MHz (max)
Kicker Pulse width	~ 60 ns FWHM
Shot to shot stability	< 2.5 x 10^{-3}

To overcome this problem and to allow data taking for these experiments during standard multibunch operation, a new scheme of operation has been developed and is under test at the ALS.

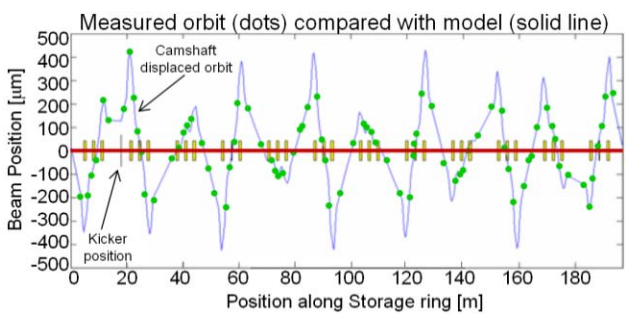

Figure 5: Theoretical and measured camshaft displaced orbit.

A fast kicker system capable of selectively kicking turn by turn the camshaft without perturbing the other bunches in the ring was constructed and installed in the ALS ring. Table 3 shows the main parameters of the system. By using such a kicker to synchronously kick the camshaft, one can force it on a stable vertically displaced orbit. The users in the beamlines where the displacement is large

enough, can collimate out the photons from the other bunches and take the radiation only from the displaced camshaft, and operate in this way in a pseudo-single bunch mode parasitically to the standard multibunch operation.

Figure 5 shows the remarkable agreement between the theoretical displaced camshaft orbit (solid line) and the actual orbit (dots) measured when the kicker was operated at 1.522 MHz (ALS revolution frequency) with a ~750 V excitation (~ 55 μrad kick). The figure also shows how in some of the beamlines (position along the ring) the displacement is large enough to allow them to operate in the pseudo-single bunch mode.

By kicking the bunch every n-th turn instead of every turn, distorted orbits closing in n-turns can be generated. In this way, one can control the "repetition rate" of the pseudo single bunch and also create the required displacement in all beamlines.

The displacement amplitude can be controlled by exploiting the fact that the orbit is proportional to $1/\sin(\pi\nu)$. By means of small changes in the vertical tune ν, one can tune the displacement to the desired amplitude.

Local single bunch-closed bumps can be also obtained if more than one kicker is used.

Initial tests of the system at the ALS have been very encouraging and promising but before the pseudo-single bunch can become an official mode of operation, extensive further tests need to be done. For example, the transparency of the operation for the all the "normal" beamlines not using the pseudo-single bunch must be systematically and carefully investigated. More detailed information on the system can be found elsewhere [10].

FPGA based "bunch cleaning"

In the previous section, we described the special mode of operation of the ALS where two high current bunches are stored in the ring for allowing experiments requiring a long relaxation time. During this time, the gap between the two bunches must be free of electrons to avoid data contamination from photons radiated by undesired electrons stored in these nominally empty buckets. Unfortunately at the ALS and in other rings as well, because of imperfect injection, some of the "empty" buckets can be populated with electrons at a level of the order of 0.1% respect to the number of particles in the main bunches. Additionally as time flows, diffusion effects can progressively populate originally empty buckets. These contamination mechanisms can represent a severe limitation for a number of users that require bunch "purity" of 10^{-4} or better. For those users a bunch cleaning technique capable of removing the undesired particles is then required.

The cleaning system we presently use at the ALS is based on the scheme in operation at the Spring 8 storage ring [11] and tested at the ESRF [12]. The system layout is shown in Fig. 6, two signals are mixed together, amplified and sent to a transverse kicker that applies the excitation to the beam. One of the signals is a sinusoidal excitation at the frequency of one of the transverse tune sidebands, while the other is a pseudo-square wave synchronous with the ring RF and with zero amplitude crossing at the position of each of the bunches that needs to be preserved. After the mixing, the resulting signal is still a resonant excitation at the selected tune frequency but with zero amplitude at the position where "good" buckets are located. Such a signal, properly amplified and applied to the beam through the kicker, allows for the removal of the electrons in the undesired bunches by exciting them on very large transverse oscillations ending on the vacuum chamber walls.

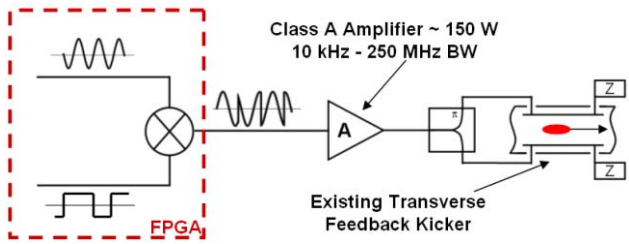

Figure 6: Bunch cleaning system layout.

Differently to the Spring 8 case, in the ALS implementation, the generation of both the signals and their mixing are performed digitally by using a low cost Xilinx demo-board (HW-V4-ML403-USA) with a 4VFX12 Virtex-4 FPGA clocked at the ALS 500 MHz RF. The board also includes a DAC for the generation of the analogical output signal, and an imbedded Power-PC that allows network control of all the settings and functionality of the system.

At the ALS the bunch cleaning is performed in the storage ring right after injection, exciting the beam at one of the vertical tune sidebands. The sinusoidal frequency is actually swept over a bandwidth of 4 kHz to account for tune shift on amplitude effects. The kicker, a stripline with a transverse shunt impedance of ~ 9 kΩ, is one of the transverse feedback kickers. Despite this fact, the cleaning procedure is fully compatible with the transverse feedback operation (the high current bunches are not excited by the cleaning system) and no use of scrapers is required during the cleaning operation.

The system has been extensively tested and has been regularly used in operation during the last few years. It showed a remarkable stability making the cleaning procedure straightforward and reliable. The perturbation on the good bunches during the cleaning is extremely small and even if the cleaning is presently performed with the shutters closed, there is the concrete possibility of doing it during users' data taking in a completely transparent way.

Figure 7 shows a measurement of the time required for the system for performing the cleaning. The top track is the excitation signal amplitude (switched ON for t=0) while the bottom track is the sum signal from a beam position monitor. From this measurement, one can estimate a time constant for the cleaning of ~ 0.4 s. It must

be remarked that during this measurement the system was not fully optimised so significantly shorter time constants should be potentially achievable. The level of purity after a cleaning cycle is better than ~ 10^{-6}, beyond the measurement capability of our bunch purity monitor.

More detailed information on the system can be found elsewhere [13].

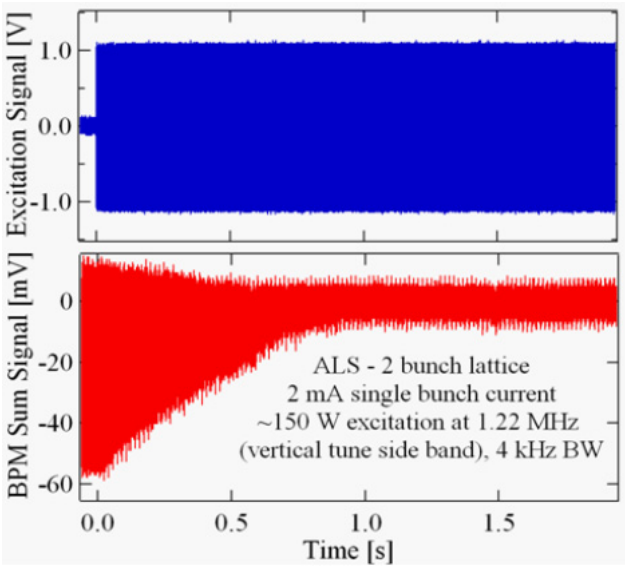

Figure 7. Cleaning time measurement. Top track: cleaning signal amplitude. Bottom track: sum signal from a beam position monitor.

CONCLUSIONS

Despite being the oldest 3rd generation synchrotron light source in the world, ALS is still delivering quality beam with characteristics that compare well with the ones of the more recent storage ring based light sources. This is due to the continuous upgrade of the storage ring, of the beamlines and of the instrumentation and beam diagnostic systems that allow to control and tune the ALS to its maximum performance.

ACKNOWLEDGEMENTS

The authors acknowledge contributions from J. Byrd, S. De Santis, J. Guo, M. Hertlein, J. Kirz, D. Li, K. Robinson, R. Schoenlein, C. Steier, and A. Trensim.

REFERENCES

[1] A. Jackson, *et al*., Proceedings of 1994 European Particle Accelerator Conference, London, England, June 1994, p. 107.
[2] H. Nishimura, *et al.*, Proceedings of 2007 Particle Accelerator Conference, Albuquerque, New Mexico, USA, 1997 p.. 1170.
[3] M. Zolotorev, G. Stupakov, SLAC PUB 7132 (1996).
[4] M. Zolotorev, G. Stupakov, Proceedings of the 1997 Particle Accelerator Conference, Vancouver, B.C., Canada, May 1997, p. 2180.
[5] P. Catravas *et al*., Phys. Rev. Letters **82**, 5261 (1999).
[6] V. Sajaev, *Determination of Longitudinal Bunch Profile using Spectral Fluctuations of Incoherent Radiation*, Proceedings of EPAC 2000, Vienna.
[7] SRW code, http://www.esrf.eu/Accelerators/Groups/InsertionDevices/Software/SRW
[8] E. Saldin, *et al*., Opt. Commun. **148**, 383 (1998).
[9] M. Yabashi, *et al*., Phys. Rev. Letters **97**, 084802 (2006).
[10] G. Portmann, *et al*., this conference.
[11] H. Suzuki, *et al*., Nuclear Instruments and Methods in Physics Research A **444** (2000) 515-533.
[12] E. Plouviez, ESRF Machine Technical Note 01-04/MDT.
[13] M. Chin, *et al*., this conference.

DEVELOPMENT OF BEYOND STATE-OF-THE-ART DIAGNOSTIC TECHNIQUES WITHIN THE EUROPEAN NETWORK DITANET

C.P. Welsch

University of Heidelberg, GSI, Darmstadt and MPI-K, Heidelberg, Germany
on behalf of the DITANET consortium

Abstract

The development of new particle accelerators with unprecedented beam characteristics has always driven the need for an intense R&D program in diagnostic techniques. The successful operation of these machines is finally only possible with an adequate set of beam instrumentation.

DITANET is a large European network between several research centers, Universities, and partners from industry that aims for the development of beyond-state-of-the-art diagnostic techniques for future accelerator facilities. This includes research projects focusing on beam profile, current, and position measurements, as well as on particle detection techniques and related electronics. A particular focus of the consortium is the training of young researchers in this multi-disciplinary field and to thus prepare them for their future careers in academia or industry.

This contribution will introduce the network participants, present the general structure of DITANET, and give an overview of its research and training activities.

INTRODUCTION

Beam diagnostics is a rich field in which a great variety of physical effects are made use of and consequently provides a wide and solid base for the training of young researchers. Moreover, the principles that are used in any beam monitor or detector enter readily into industrial applications or the medical sector, which guarantees that training of young researchers in this field is of relevance far beyond the pure field of particle accelerators. Beam diagnostics systems are essential constituents of any particle accelerator; they reveal the properties of a beam and how it behaves in a machine. Without an appropriate set of diagnostic elements, it would simply be impossible to operate any accelerator complex let alone optimize its performance.

Future accelerator projects will require innovative approaches in particle detection and imaging techniques to provide a full set of information about the beam characteristics. Since a long time, Europe has played a major role in this field and the declared goal of this network is to pave the way for world-class research with particle accelerators. This will only be possible by a joint training effort, where knowledge and technology transfer are encouraged, where close collaboration with industry is an integral part of the network, and where leading research centers and major universities work closely together.

Marie Curie Initial Training Networks (ITN) are aimed at improving the career perspectives of researchers who are in the first five years of their career by offering structured training in well defined scientific and/or technological areas as well as providing complementary skills and exposing the researchers to other sectors including private companies.

DITANET - "**DI**agnostic **T**echniques for particle **A**ccelerators - an initial training **NET**work" - covers the development of advanced beam diagnostic methods for a wide range of existing or future accelerators, both for electrons and ions. The proposed developments in profile, current, and position measurement techniques clearly stretch beyond present technology and will mark the future state of the art.

The network comprises almost all of the European expertise in this field, either in the form of the network members themselves or as associate partners, having well-proven expertise in finding solutions to the technological challenges related to the development of cutting edge diagnostic techniques. This stimulates on one hand the search for the most advanced methods and technologies and ensures at the same time a comprehensive training of young researchers who will get the unique possibility to become experts not only in their main research field, but also in related techniques.

DITANET consists of the following network participants: University of Heidelberg (coordinator, Germany), CEA (France), CERN (Switzerland), DESY (Germany), GSI (Germany), HIT GmbH (Germany), IFIN-HH (Romania), Stockholm University (Sweden), Royal Holloway University of London (UK), and the University of Seville/Centro Nacional de Aceleradores (Spain).

It is complemented by twelve associated partners from all over the world: ESRF (France), idQuantique (Switzerland), INFN-LNF (Italy), Instrumentation Technologies (Slovenia), MPI for Nuclear Physics (MPI-K), PSI (Switzerland), THALES (France), Thermo Fisher

Scientific (USA), TMD Technologies Limited (UK), TU Prague (Czech Republic), ViALUX (Germany), and WZW Optics (Switzerland).

NETWORK STRUCTURE

The DITANET Marie Curie Initial Training Network forms a consortium which comprises the ten participants and a roughly equal number of associated partners. It is the goal of the governance structure to profit from the individual expertise of the parties involved while maintaining an effective decision making and controlling process.

The governance structure is sketched in the following figure 2. Its key bodies are the Supervisory Board, the Coordinator assisted by the Management Office in scientific, management and financial matters, and the DITANET Steering Committee.

Whenever required, a spin-off board will complement this structure.

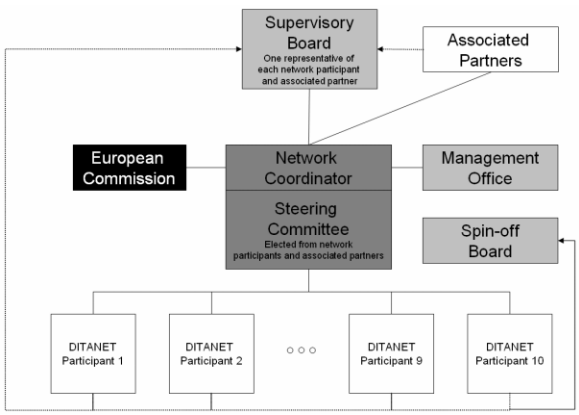

Figure 1: DITANET structure

A Consortium Agreement is presently being concluded between the partners. It regulates the management and organizational structure of the network and the demarcation of responsibilities between its different entities. It also regulates intellectual property issues such as pre-existing know-how, patents and accession rights.

RESEARCH

DITANET covers the development of advanced beam diagnostic methods for a wide range of existing or future accelerators, both for electrons and ions.

The DITANET projects can be split into six thematic packages as depicted in figure 2.

All projects within DITANET involve an extremely wide spectrum of technologies in various fields, including optics, mechanics, cryogenics, electronics, as well as data acquisition and processing, and thus require a multi-disciplinary approach. The aim of this network is thus to set up the frame for a truly inter-European network with the objective of strengthening interdisciplinary communication between the participating laboratories, partners from industry and university groups.

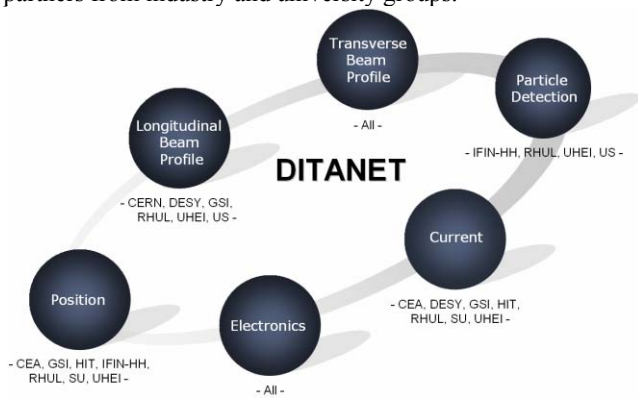

Figure 2: Overview of DITANET work packages

The accelerator projects that will be covered within DITANET range from the next generation of linear colliders (ILC, CLIC) and the most advanced high energy accelerators (LHC, FAIR), to innovative light sources (X-FEL) and novel low-energy storage ring projects (DESIREE, USR).

Some examples of the research projects within DITANET are outlined in the following sections.

The Large Hadron Collider (LHC)

The Large Hadron Collider [1] will boost protons and heavy ions to very high energies and bring them in collision. The particles will be grouped in bunches separated by empty spaces. The distance between two consecutive bunches is 25ns and their total number is 2 x 2808 . The particles that for a reason or another escape from the bunches will eventually be lost potentially quenching a magnet, or even damaging the machine. For this reason it is very important to monitor and study the distribution of the particles in the rings, and in particular to monitor the protons drifting out of the RF buckets or drifting into what is called the abort gap.

The monitor that will be developed by an Early Stage Researcher (ESR) must have a large dynamic range (10^6) and a fast time resolution (50ps). The solution proposed consists of a two-parts system, one with the required dynamic range but smaller time resolution (100ns) used to monitor the protons population in the mentioned abort gap, the other with a lower dynamic range (10^4) and full time resolution for the measurement of the protons population inside the bunches and in the empty spaces between them.

Both systems are based on the detection of single photons of synchrotron radiation emitted by the beam. In the first case the high dynamic range is achieved by using gated photomultipliers that are gated on the abort gap interval. In the second case the fast response is achieved by using state-of-the-art Avalanche Photo Diodes (APD) and time-to-digital converters.

Fast Wire Scanners for the XFEL Project

The performance of future projects based on (superconducting) Linacs like the ILC [2] and XFEL [3] depends critically on the correct matching of the phase space in the different parts of the machine. Even slight changes, e.g. in the injector region, might result in loss of performance by orders of magnitude. Therefore, a precise control of the beam sizes at different locations in the machine is required.

Due to the high load of their beams and the requirement of non destructive measurements screens cannot be used to determine the beam sizes during standard operation. Also the currently used types of wire scanners [see e.g. 4, 5] are not suitable. Due to the low speed of the existing types, the wire would burn within a bunch train. Scanner speeds of 10-20 m/s with a position resolution of 1 micron are necessary to get the required endurance. In the frame of a project for an Early Stage Researcher (ESR) a novel, continuously rotating wire scanner that is synchronized to the beam will be developed. High demands are put on synchronization and vacuum technology together with the requirement of a roughly 1 μm resolution.

Beam Diagnostics for CLIC

One of the major decisions in particle physics over the next 3 years will be to decide on the next major accelerator to access the multi-TeV energy scale. The CLIC two-beam acceleration scheme [6] is one of the candidates for the next accelerator for the high-energy frontier, and the CLIC Test Facility (CTF3) at CERN [7] is the unique facility to test the CLIC acceleration principle and to prove the feasibility of associated RF systems.

In addition to the RF accelerating systems themselves, a host of beam diagnostics will need to be developed to cope with the challenging environment of CLIC. There exists space at the CLEX area of the CTF3 facility to build a new Instrumentation Test Beam (ITB). One of the first tasks of the trainee will be to design the machine optics for the ITB in collaboration with the CERN experts and to work with the CLIC diagnostics team to optimize the layout and functionality for future key diagnostics projects.

In addition to the ITB design, the Early Stage Researcher (ESR) with work with TMD technologies to assess the opportunities for RF system development and to identify a fruitful new line of R&D where the expertise of TMD can be combined with the expertise at RHUL and CERN to develop a new product of use to the CTF3/CLIC project.

The system design work will be complemented by frequent data taking and machine operation at CTF3. This combination of practical experience, beam-line design, and industrial collaboration, will provide a unique training opportunity.

The Ultra-Low Energy Storage Ring (USR)

To enable the efficient investigation of some very essential questions regarding the physics with low-energy antiprotons and possibly exotic highly charged ions, a novel electrostatic cooler synchrotron, the ultra-low energy storage ring (USR) [8,9], and a state-of-the-art in-ring spectrometer [10] will be developed in the QUASAR group at the Kirchhoff Institute for Physics/Max-Planck Institute for Nuclear Physics in close collaboration with the GSI Atomic Physics Division, and other groups from the University of Heidelberg.

The aim of the USR will be to slow down antiprotons as well as possibly highly charged ions (up to bare uranium) to very low energies between 300 and 20 keV/q. This will provide world-wide unique conditions for both in-ring studies with an intensity of up to 10^{12} cooled and stored antiprotons or highly charged ions per second, as well as for experiments requiring extracted slow beams. In the frame of an Early Stage Researcher (ESR) project, the beam diagnostic elements as they are required for a successful operation of such a machine will be developed.

The boundary conditions of the USR project put very high demands on the machine's instrumentation: In order to ensure reasonable life times in the ring, ultimate vacuum pressures have to be realized extending to below 10^{-14} mbar if highly charged ions shall be stored and slowed down. Hence, an approach considered in the present study is to cryogenically cool the vacuum chambers of the USR to a temperature of only a few Kelvin. The extremely low vacuum pressure of the (cooled) USR together with a beam energy of only 20 keV and low currents of singly charged antiprotons between 1 nA and 1 uA require the development of new diagnostic methods as most of the standard techniques will no longer work.

Beam Tracking for FAIR

In order to study the nuclear structure of weakly-bound nuclei, knowledge about reactions induced by them should be improved. The existing Radioactive Ion Beam (RIB) facilities and the new ones (SPIRAL II, FAIR) provide an ideal environment to study such nuclides. From an experimental viewpoint, the detection and reconstruction of the particle trajectories is a key parameter to obtain good experimental resolution. In particular, the low energy branch of the FAIR facility will produce exotic beams, with large emittance and low energy resolution. These beams need to be tracked by detectors that allow obtaining the velocity and direction of each particle of the beam. Secondary emission detectors (SeD) have been proved to be adequate for this purpose [11], for very low beam intensity (10^3 pps). However, new developments are required to use SeD detectors to track the intensities expected at the low energy branch at FAIR [12].

The 3 MV tandem accelerator at the Centro Nacional de Aceleradores (CNA) at the University of Seville, along

with a specifically designed tracking chamber offers an excellent opportunity to test the position and time signals of the tracking detectors, and correlate them with the known properties of the low energy beams.

This project will focus on the operation of different types of beam detectors (Diamond Detectors, Secondary Emission Detectors, Multi-wire Chambers) to track ion beams produced at the CNA, and to design prototypes of detectors to be used in the HISPEC-DESPEC experiment at the FAIR facility.

TRAINING

Young researchers participating in the network program will not only get the possibility to perform state-of-the-art research, they will also get a much wider training in the domain of beam diagnostics by interaction with other network participants and close collaboration with associated partners from the industrial sector. This includes regular exchanges of trainees between the partners that will thus get the possibility to participate in ongoing R&D work at linked institutes and universities.

This way, DITANET will provide a cohesive, flexible framework for the training and professional development of researchers in beam diagnostic techniques for particle accelerators, with a strong focus on possible applications of these principles in industry. The network will thus contribute to overcoming institutional and disciplinary boundaries and add value to the training of the researchers over and above that which could be provided by a single network partner.

The network members have a long record of successfully training young researchers and the necessary capacities to ensure a high-level training and close supervision. Mutual recognition of the training acquired at the different participating institutes is a core element of the DITANET joint training scheme.

While helping young researchers to put together their individual training plan at each of the institutes, DITANET will also promote a multidisciplinary training in the wider field of beam diagnostic techniques. This means that all young researchers within the network will have the opportunity to learn enough about other involved disciplines to be able to design, install and operate most of the key detectors used in accelerator physics. This responds to the need for strong interdisciplinary skills and expert knowledge in a range of different diagnostic techniques.

DITANET will organize one week courses on beam diagnostic techniques in spring 2009 and fall 2010 that will be open to all network participants as well as to external participants. Details on these courses will be published on the DITANET web site [13].

RECRUITMENT

DITANET's focus is the training of early stage researchers, i.e. PhD candidates, in next-generation diagnostic techniques for particle accelerators. Thus the main fraction of the researchers to be recruited (91%) is early-stage researchers.

High priority will be given to a recruitment strategy based on international competition. All positions are presently published in both online resources and relevant international journals, ensuring open access for interested applicants. Appointments will be made on the basis of direct comparison between the applications and qualification for the respective topic. The ultimate goal will be to ensure a multicultural network composition with the possibility for each trainee to experience the benefits of cultural diversity.

Particular attention is paid to promote gender issues by addressing this point in all position openings and explicitly encouraging women to apply. The participating institutions support this attempt by family-friendly policies, including flexible approaches to career breaks and support for return from career breaks. The possibility of part-time work and child minding services close to the working place is already established at many of the network partners and shall be offered wherever possible.

Furthermore, a special mentorship program will be established in the context of this network to accompany and promote female doctoral students and young Post-docs throughout their work in the network. The main objectives are to strengthen understanding, extend networking both laterally and vertically, and to develop effective strategies for the advancement of women, i.e., bottom up and top down.

INVOLVEMENT OF INDUSTRY

The participation of industry is an integral part of DITANET. As shown in the beginning of this article, a number of private companies are included as associated partners to the network. They are members of the supervisory board to ensure that industry-relevant aspects are covered in the different projects carried out within the network and to enhance knowledge transfer. In addition, one third of the DITANET Steering Committee members come from industry.

From the beginning, the DITANET management encouraged the involvement of these partners in the training program at the highest possible level. This led to the participation of HIT GmbH as a full network member with a PhD project that will be hosted by this company. In addition, the associated partner THALES, who is considered as a world-wide leader in the development of klystron technology, will host the trainee from CEA during up to 25% of the PhD project, thus taking over a considerable part of the training.

WZW Optics , Vialux, Thermo Fisher and idQuantique are among the leading companies in the field of optics, scientific cameras and detector systems. Instrumentation Technologies from Slovenia and TMD technologies from the UK have long-standing links to accelerator laboratories and have pushed the development of beam diagnostic techniques on various occasions in the past.

All companies as well as the other associated partners from academia (TU Prague, MPI for Nuclear Physics) and research (PSI, INFN, ESRF) have agreed to host the DITANET trainees during some weeks up to several months. This ensures that every trainee will get the possibility to realize an extended research stay at a leading partner institute from industry and to take part in its R&D efforts.

Thereby it is guaranteed that all trainees will be provided with a true multi-disciplinary and inter-sectorial training, where they will not only work on their main project, but learn about neighboring fields and get a view of possible applications and of the impact of their work in the industrial sector.

These measures will complement the scientific training and actively bridge between the academic and the industrial sectors within DITANET.

CONCLUSION

The largest ever coordinated EU education action for young researchers in the field of beam diagnostic techniques for particle accelerators has been awarded to a consortium of ten groups from all over Europe within the EU-Marie Curie program for initial training networks. The joint effort in setting up DITANET and the corresponding administrative and training-related boundary conditions will guarantee a continuous training of young researchers in this field. Close collaboration between the network participants and the associated partners with a very prominent role of industry, will ensure that the basis for DITANET is laid in a true international approach with a clear long term perspective.

REFERENCES

[1] O.S. Brüning, et al., "LHC Design Report", CERN, Geneva (2004)
[2] International Linear Collider, Reference Design Report, ILC Global Design effort and World Wide Study (2007)
[3] Massimo Altarelli, (ed.) et al., "XFEL: The European X-Ray Free-Electron Laser. Technical design report.", DESY-06-097 (2006)
[4] M. Sachwitz, et al., "Wire Scanners in the Undulator Section of the VUV-FEL DESY", Proc. of 7th European Workshop on Beam Diagnostics and Instrumentation for Particle Accelerators, Lyon, France (2005)
[5] K.Wittenburg, "Conventional Wire Scanners at TESLA", Tesla Report 2000-18
[6] R.W.Assmann, et al., “A 3 TeV e+e- Linear Collider Based on CLIC Technology”, CERN 2000–008
[7] G. Geschonke, A. Ghigo (ed.) et al., “CTF3 Design Report”, CERN/PS 2002-008 (RF)
[8] C.P. Welsch, M. Grieser, J. Ullrich, A. Wolf, ”An ultra-low-energy storage ring at FLAIR”, NIM A 546 (2005) 405–417
[9] C.P. Welsch, M. Grieser, J. Ullrich, A. Wolf, ”Layout of the USR at FLAIR”, Proc. Europ. Part. Acc. Conf., Edinburgh, Scotland (2006)
[10] C.P. Welsch, M. Grieser, A. Dorn, R. Moshammer, J. Ullrich, ”Exploring Sub-Femtosecond Correlated Dynamics with an Ultra-low Energy Electrostatic Storage Ring”, AIP Conf. Proc. 796 (2005) p. 266-271
[11] A. Drouart et al, NIMA 579 (2007) 1090
[12] http://www.gsi.de/fair/index_e.html
[13] http://www.ditanet.uni-hd.de

List of Authors

Italic papercodes indicate primary authors

— Z —

Institutes List

ANL
Argonne
- Borland, M.
- Bui, H.
- Conde, M. E.
- Decker, G.
- Donley, L.
- Dooling, J. C.
- Gai, W.
- Li, Y. L.
- Lien, M. K.
- Lill, R. M.
- Nemeth, K.
- Norum, W. E.
- Pasky, S. J.
- Pietryla, A. F.
- Power, J. G.
- Sereno, N.
- Sun, X.
- Wang, J.
- Yao, C.

BESSY GmbH
Berlin
- Böhlick, D.
- Dirsat, M.
- Kamps, T.
- Lipka, D.
- Quast, T.
- Rudolph, J.
- Schenk, M.

BNL
Upton, Long Island, New York
- Fedurin, M. G.
- Pinayev, I.
- Singh, O.

Bira
Albuquerque, New Mexico
- Babel, S. R.
- Cohen, S.

CASA
newport news
- Liu, C.

CEA
Gif-sur-Yvette
- Abbon, P.
- Delagnes, E.
- Jeanneau, F.
- Marroncle, J.
- Mols, J.-Ph.
- Pancin, J.

CELLS-ALBA Synchrotron
Cerdanyola del Vallès
- Olmos, A.
- Perez, F.

CERN
Geneva
- Boccardi, A.
- Bravin, E.
- Caspers, F.
- Dabrowski, A. E.
- Dehning, B.
- Gasior, M.
- Jones, O. R.
- Kroyer, T.
- Lefevre, T.
- Sapinski, M.
- Serrano, J.
- Steinhagen, R. J.

CNU
Newport News, Virginia
- Hewitt, C.

DESY
Hamburg
- Siemens, M.
- Vilcins, S.
- Wittenburg, K.

Diamond
Oxfordshire
- Rehm, G.
- Thomas, C. A.

Dimtel
San Jose
- Teytelman, D.

ELETTRA
Basovizza
- Danailov, M. B.
- Ferianis, M.
- Veronese, M.

ESRF
Grenoble
- Scheidt, K. B.

FZD
Dresden
- Arnold, A.
- Staufenbiel, F.
- Teichert, J.

Fermilab
Batavia
- Anderson, T. G.
- Briegel, C. I.
- Dysert, R.
- Eddy, N.
- Fellenz, B. J.
- Fliller, R. P.
- Gianfelice|-|Wendt, E.
- Haynes, W.
- Hu, M.
- Jansson, A.
- Kamerdzhiev, V.
- Kazakevich, G. M.
- Lebedev, V. A.
- Lipton, R. J.
- Lumpkin, A. H.
- Nicklaus, D. J.
- Prieto, P. S.
- Rechenmacher, R.
- Ruan, J.
- Semenov, A.
- Slimmer, D.
- Thurman|-|Keup, R.
- Voy, D. C.
- Wendt, M.
- Yang, M.-J.
- Zagel, J. R.

GSI
Darmstadt
- Becker, F.
- Forck, P.
- Guetlich, E.
- Haseitl, R.
- Hoffmann, T.
- Kowina, P.
- Ondreka, D.
- Reiter, A.
- Schwickert, M.
- Welsch, C. P.

HIT
Heidelberg
- Peters, A.

I-Tech
Solkan
- Baricevic, B. B.
- Karcnik, T.
- Kosicek, A.
- Poucki, V.

IHEP Beijing
Beijing
- Cao, J.
- Zhao, Y.

INFN Gruppo di Cosenza
Arcavacata di Rende (Cosenza)
- Schioppa, M.

INFN-Roma
Roma
- Iacoangeli, F.
- Valente, P.

INFN/LNF
Frascati (Roma)
- Bocci, A.
- Boscolo, M.
- Bossi, F.
- Buonomo, B.
- Cestelli Guidi, M.
- Chiadroni, E.
- Clozza, A.
- Drago, A.
- Grilli, A. G.
- Marcelli, A.
- Mazzitelli, G.
- Murtas, F.
- Piccinini, M.
- Quintieri, L.
- Raco, A. R.
- Raimondi, P.
- Sensolini, G.
- Sorchetti, R. S.

INOA
Firenze
- Gambicorti, L.

JLAB
Newport News, Virginia
- Allison, T. L.
- Evtushenko, P.
- Freyberger, A.
- Musson, J.

KEK
Ibaraki
- Flanagan, J. W.
- Fukuma, H.
- Funakoshi, Y.
- Honda, T.
- Ieiri, T.
- Mitsuhashi, T. M.
- Obina, T.
- Ohmi, K.
- Tadano, M.
- Terunuma, N.
- Tobiyama, M.
- Urakawa, J.
- Obina, T.
- Tadano, M.

KIP
Heidelberg
- Welsch, C. P.

LAL
Orsay
- Arnaud, N.
- Breton, D.
- Stocchi, A.
- Variola, A.
- Viaud, B. F.

LANL
Los Alamos, New Mexico
- Gilpatrick, J. D.
- Gonzales, F.
- Martinez, D.
- Power, J. F.
- Sedillo, J. D.

LBNL
Berkeley, California
- Baptiste, K. M.
- Barry, W.
- Bieniosek, F. M.
- Byrd, J. M.
- Chin, M. J.
- De Santis, S.
- Hertlein, M. P.
- Julian, J.
- Kwiatkowski, S.
- Leemans, W.
- Leitner, D.
- Low, R.
- Matlis, N. H.
- Ni, P. N.
- Plate, D. W.
- Plateau, G. R.D.
- Portmann, G. J.
- Robin, D.
- Sannibale, F.
- Sonnad, K. G.
- Strohmeier, M. M.
- Todd, D. S.
- Toth, C.
- Weber, J. M.
- Zisman, M. S.
- van Tilborg, J.

MBI
Berlin
- Klemz, G.
- Will, I.

National Instruments
Austin
- Bonal, D. A.
- Ravindran, M. M.

NewPath Research L. L.C.
Salt Lake City
- Hagmann, M. J.

NewPath
Salt Lake City, Utah
- Hagmann, M. J.

Northern Illinois University
DeKalb, Illinois
- Maxwell, T. J.
- Mihalcea, D.
- Piot, P.

ORNL
Oak Ridge, Tennessee
- Blokland, W.
- Jeon, D.
- Long, C. D.
- Menshov, A. A.
- Nesterenko, I.
- Pogge, J.

PSI
Villigen
- Behrmann, G. J.
- Dehler, M. M.

Royal Holloway, University of London
Surrey
- Blair, G. A.

SLAC
Menlo Park, California
- Akre, R.
- Anderson, D. E.
- Cheng, W. X.
- Corbett, W. J.
- Decker, F.-J.
- Ding, Y. T.
- Dowell, D.
- Emma, P.
- Fisher, A. S.
- Fox, J. D.
- Frisch, J. C.
- Gilevich, A.
- Hays, G. R.
- Hering, P.
- Huang, Z.
- Iverson, R. H.
- Johnson, R. G.
- Krasnykh, A.
- Limborg|-|Deprey, C.
- Loos, H.
- Mastorides, T.
- May, J.

- McCormick, D. J.
- Medvedko, E. A.
- Miahnahri, A.
- Nelson, J.
- Nuhn, H.-D.
- Olsen, J. J.
- Pivi, M. T.F.
- Rivetta, C. H.
- Seryi, A.
- Smith, S. R.
- Smith, T. J.
- Straumann, T.
- Turner, J. L.
- Van Winkle, D.
- Welch, J. J.
- White, G. R.
- Woodley, M.
- Wu, J.
- Xu, J.
- Young, A.

SOLEIL
Gif-sur-Yvette
- Cassinari, L.
- Denard, J.
- Filhol, J.-M.
- Hubert, N.
- Nadji, A.
- Nadolski, L. S.
- Pedeau, D.

Stanford University
Stanford, Califormia
- Ratner, D. F.

TU Darmstadt
Darmstadt
- Hoffmann, D. H.H.

UMD
College Park, Maryland
- Beaudoin, B. L.
- Bernal, S.
- Feldman, D. W.
- Feldman, R.
- Fiorito, R. B.
- Kishek, R. A.
- O'Shea, P. G.
- Papadopoulos, C. F.
- Reiser, M.
- Shkvarunets, A. G.
- Stratakis, D.
- Sutter, D. F.
- Thangaraj, J. C.T.

Università degli Studi di Firenze
Firenze
- De Sio, A.
- Emanuele, E. P.

Università di Roma II Tor Vergata
Roma
- Cianchi, A.

VIGO System S. A.
Ozarow Maz.
- Piotrowski, J. P.

YerPhI
Yerevan
- Arutunian, S. G.
- Mailian, M. R.
- Vasiniuk, I. E.

roma3
Rome
- Branchini, P.

PARTICIPANTS

Allison, Trent
Thomas Jefferson Nat. Acc. Fac.

Anderson, Terry
Fermi National Laboratory

Arutunian, Suren
Yerevan Physics Institute

Baricevic, Borut
Instrumentation Technologies

Becker, Frank
GSI

Bentson, Lynn
Stanford Linear Accelerator Center

Bergoz, Julien
Bergoz Instrumentation

Blair, Grahame
Royal Holloway Univ. of London

Buonomo, Bruno
INFN-LNF

Burgada, Giovanni
CAEN Technologies,Inc.

Byrd, John
Lawrence Berkeley National Laboratory

Cameron, Peter
Brookhaven National Lab. - NSLS II

Cao, Jianshe
IHEP, CAS, China

Cheng, Weixing
Stanford Linear Accelerator Center

Chew, Joseph
Lawrence Berkeley National Laboratory

Chin, Mike
Lawrence Berkeley National Laboratory

Condon, Martha
Lawrence Berkeley National Laboratory

Corbett, Jeff
Stanford Linear Accelerator Center

De Monte, Raffaele
Sincrotrone Trieste SCPA

De Santis, Stefano
Lawrence Berkeley National Laboratory

Decker, Glenn
Argonne National Laboratory

Dehler, Micha
Paul Scherrer Institut

Dehning, Bernd
CERN

Delerue, Nicolas
John Adams Institute - Univ. of Oxford

Dietrich, Juergen
Forschungszentrum Juelich

Duan, Ming
Fujikura Ltd.

Enzone, Dan
Kepco Inc

Evtushenko, Pavel
Thomas Jefferson Nat. Acc. Fac.

Falcone, Roger
Lawrence Berkeley National Laboratory

Fedurin, Mikhail
Brookhaven National Lab. - NSLS

Ferianis, Mario
Sincrotrone Trieste SCPA

Fischer, Tom
Kepco Inc

Fiorito, Ralph
University of Maryland

Fisher, Alan
Stanford Linear Accelerator Center

Foley, Sean
Fujikura Ltd.

Forck, Peter
GSI

Fox, John
Stanford Linear Accelerator Center

Frisch, Josef
Stanford Linear Accelerator Center

Gasior, Marek
CERN

Gilpatrick, J D
Los Alamos National Laboratory

Hagmann, Mark
NewPath Research

Hettel, Robert
Stanford Linear Accel. Center - SSRL

Hoffmann, Tobias
GSI

Hubert, Nicolas
Synchrotron SOLEIL

Ieiri, Takao
KEK

Jacobs, Ken
UW-Madison

Jordan, Kevin
Thomas Jefferson Nat. Acc. Fac. - FEL

Kamerdzhiev, Vsevolod
Fermi National Laboratory

Kamps, Thorsten
BESSY

Kilian, Jack
Echotek Product Group

Kolski, Jeffrey
Indiana University / LANL

Kono, Joy
Lawrence Berkeley National Laboratory

Kosicek, Andrej
Instrumentation Technologies

Kurtz, James
Echotek Product Group

Kuske, Peter
BESSY

LeBlanc, Greg
Australian Synchrotron

Lefevre, Thibaut
CERN

Lipton, Ronald
Fermi National Laboratory

Long, Cary
Oak Ridge National Laboratory - SNS

Lumpkin, Alex
Fermi National Laboratory

Marroncle, Jacques
CEA/SACLAY

Martin, Donald
Stanford Linear Acc. Center - SSRL

Mastorides, Themistoklis
Stanford Linear Accelerator Center

Maxwell, Timothy
Northern Illinois University

Mazzitelli, Giovanni
INFN - LNF

McCrady, Rodney
Los Alamos National Laboratory

Medvedko, Evgeny
Stanford Linear Accelerator Center

Musson, John
Thomas Jefferson Nat. Acc. Fac.

Obina, Takashi
KEK - Photon Factory

Pasquinelli, Ralph
Fermi National Laboratory

Payne, Stephen
Rutherford Appleton laboratory

Perez Rodriguez, Francisco
CELLS

Pinayev, Igor
Brookhaven National Lab. - NSLS II

Pogge, James
Ok Ridge National Laboratory

Portmann, Gregory
Lawrence Berkeley National Laboratory

Power, John
Los Alamos National Laboratory

Power, John
Argonne National Laboratory

Prieto, Peter
Fermi National Laboratory

Ravindran, Murali
National Instruments

Richter, Brian
GMW Associates

Ruelas, Marcos
RadiaBeam Technologies

Russo, Thomas
Brookhaven National Laboratory

Sannibale, Fernando
Lawrence Berkeley National Laboratory

Sapinski, Mariusz
CERN

Sarkar, Surajit
Massachusetts General Hospital

Scarvie, Tom
Lawrence Berkeley National Laboratory

Schmickler, Hermann
CERN

Sedillo, James
Los Alamos National Laboratory

Sereno, Nicholas
Argonne National Laboratory

Serrano, Javier
CERN

Sexton, Daniel
Thomas Jefferson Nat. Acc. Fac. - FEL

Shea, Thomas
Oak Ridge National Laboratory

Shkvarunets, Anatoly
University of Maryland

Singh, Om
Brookhaven National Lab. - NSLS-II

Smith, Stephen
Stanford Linear Accelerator Center

Solar, Borut
Instrumentation Technologies

Sun, Xiang
Argonne National Laboratory

Teytelman, Dmitry
Dimtel, Inc.

Thangaraj, Jayakar
University of Maryland

Thomas, Cyrille
Diamond Light Source

Thurman-Keup, Randy
Fermi National Laboratory

Tobiyama, Makoto
KEK Accelerator Laboratory

Todd, Damon
Lawrence Berkeley National Laboratory

Trovato, Giuseppe
Sincrotrone Trieste SCPA

Van Tilborg, Jeroen
Lawrence Berkeley National Laboratory

Veronese, Marco
Sincrotrone Trieste SCPA

Welsch, Carsten
Kirchhoff Institute for Physics

Wendt, Manfred
Fermi National Laboratory

Wissmann, Mark
Thomas Jefferson Nat. Acc. Fac.

Wittenburg, Kay
DESY

Xu, Jiajing
Stanford Linear Accelerator Center

Yau, Chih Yuan
Argonne National Laboratory

Zagel, James
Fermi National Laboratory

Zhao, Ying
Inst. of High Energy Phys. - Acc. Center

Ziomek , Chris
ZTEC Instruments

Zisman, Michael
Lawrence Berkeley National Laboratory

PARTICIPATING VENDORS

CAEN Technologies, Inc.
1140 Bay Street, Suite 2C
Staten Island, NY 10305, USA
Phone +1.415.624.4837
Fax +1.718.556.9185
www.caentech.com

Dimtel, Inc.
2059 Camden Avenue, Suite 136
San Jose, CA 95124, USA
Phone: +1 650.862.8147
Fax: +1 603.907.0210
www.dimtel.com

Echotek Product Group
555 Sparkman Drive, Suite 400
Huntsville, AL 35816, USA
Phone: +1 256.489.0455
Fax: +1 256.721.9266
www.mc.com

Fujikura Ltd.
170 Ridgeview Circle
Duncan, SC 29334, USA
Phone: +1 864.433.5570
www.afltele.com

GMW Associates
955 Industrial Road
San Carlos, CA 94070, USA
Phone: +1 650.802.8292
Fax: +1 650.802.8298
gmw.com

Instrumentation Technologies
Velika pot 22
SI-5250 Solkan, Slovenia
Phone: +386.5.33.52.600
Fax: +386.5.33.52.601
www.i-tech.si

KEPCO, Inc.
131-38 Sanford Avenue
Flushing, NY. 11355, USA.
Phone: +1 718.461.7000
Fax: +1 718.767.1102
www.kepcopower.com

National Instruments
11500 N Mopac Expwy
Austin, TX 78759-3504, USA
Phone: +1 888.280.7645
Fax: +1 512.683.8411
www.ni.com

ZTEC Instruments
7715 Tiburon St. NE
Albuquerque, NM 87109, USA
Phone: +1 505 924 0596
Fax: +1 505 342 0222
www.ztecinstruments.com


Radiation
– Bipolar
– CMOS
– SOI
Single eve
Practical C
My point of vi
REGISTRATION


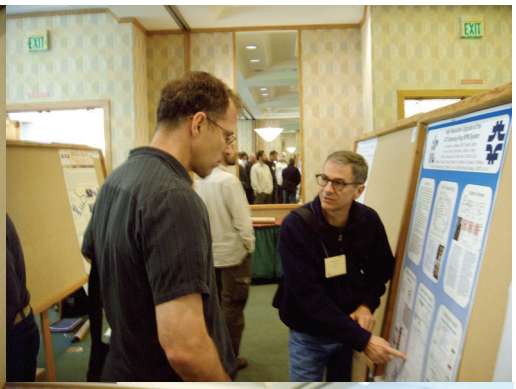
EXIT
EXIT






NO DIVING
FROM PIER

Looking toward BIW10...